The 45th Congress on Science and Technology of Thailand

การประชุมวิชาการวิทยาศาสตร์และเทคโนโลยีแห่งประเทศไทย ครั้งที่ 45 (วทท45)

PROCEEDINGS BOOK

"Seedling Innovation For Sustainable Development"

"ต้นกล้านวัตกรรมสู่การพัฒนาอย่างยั่งยืน"

7 – 9 October 2019
Mae Fah Luang University, Chiang Rai
THAILAND

ทรงพระเจริญ

PROCEEDINGS BOOK

The 45th Congress on Science and Technology of Thailand (STT45)

Seedling Innovation for Sustainable Development

October 7-9, 2019

Mae Fah Luang University,
Chiang Rai, Thailand

Organized by:
The Science Society of Thailand under the
Patronage of His Majesty the King
In Association with
Mae Fah Luang University

The 45th Congress on Science and Technology of Thailand

Editor-in-chef:

Professor Dr.Pranut Potiyaraj	Chulalongkorn University
Associate Professor Dr.Surat Laphookhieo	Mae Fah Luang University
Associate Professor Dr.Onruthai Pinyakong	Chulalongkorn University

Advisory Board:

Associate Professor Dr.Napavarn Noparatnaraporn	The Science Society of Thailand under the Patronage of His Majesty the King
Associate Professor Dr.Saiwarun Chaiwanichsiri	The Science Society of Thailand under the Patronage of His Majesty the King
Professor Emeritus Dr.Piamsook Pongsawasdi	The Science Society of Thailand under the Patronage of His Majesty the King
Professor Dr.Sujitra Wongkasemjit	Mae Fah Luang University
Assistant Professor Dr.Uraiwan Intatha	Mae Fah Luang University

Editorial Secretary:
Ms.Sirada Aromchuen
Mr.Weerasak Chongfuengprinya

Published by	The Science Society of Thailand Under the Patronage of His Majesty the King Mae Fah Luang University, Chiang Rai, Thailand
Published date	October 2019 (available in PDF version only)
ISBN (e-book)	978-616-8155-09-7

Editorial committee:

Section A: AGRICULTURAL SCIENCE / BIOTECHNOLOGY

Associate Professor Dr.Nuttha Thongchul	Chulalongkorn University
Associate Professor Dr.Aphichart Karnchanatat	Chulalongkorn University
Dr.Somrudee Nilthong	Mae Fah Luang University
Dr.Niramon Suntipabvivattana	Mae Fah Luang University

Section B: BIOLOGICAL SCIENCE

Associate Professor Dr.Tuangporn Suthiphongchai	Mahidol University
Professor Dr.Supachitra Chadchawan	Chulalongkorn University
Associate Professor Dr.Chanitra Thuwajit, MD	Mahidol University
Assistant Professor Dr.Noppadon Kitana	Chulalongkorn University
Assistant Professor Dr.Ekachai Chukeatirot	Mae Fah Luang University
Dr.Pattana Kakumyan	Mae Fah Luang University

Section C: CHEMISTRY

Professor Dr.Vatcharin Rukachaisirikul	Prince of Songkla University
Professor Dr.Orawon Chailapakul	Chulalongkorn University
Professor Dr.Thawatchai Tuntulani	Chulalongkorn University
Professor Dr.Pornthep Sompornpisut	Chulalongkorn University
Associate Professor Dr.Weena Siangproh	Srinakharinwirot University
Assistant Professor Dr.Yaowapa Sukpondma	Prince of Songkla University
Assistant Professor Dr.Chittreeya Tansakul	Prince of Songkla University
Dr.Kanchana Watla-iad	Mae Fah Luang University
Dr.Patcharanan Choto	Mae Fah Luang University
Dr.Thitipone Suwanwong	Mae Fah Luang University

Section D: POLYMER & MATERIALS SCIENCE / NANOTECHNOLOGY

Professor Dr.Supon Ananta	Chiang Mai University
Associate Professor Dr.Taweechai Amornsakchai	Mahidol University
Associate Professor Dr.Darunee Vattanasiriweach	Mae Fah Luang University

Section E: ENERGY / ENVIRONMENTAL & EARTH SCIENCES

Associate Professor Dr.Prasert Reubroycharoen	Chulalongkorn University
Associate Professor Dr.Kraichat Tantrakarnapa	Mahidol University
Assistant Professor Dr.Rungrote Nilthong	Mae Fah Luang University
Dr.Panate Manomaivibool	Mae Fah Luang University

Section F: PHYSICS / APPLIED PHYSICS

Associate Professor Dr.Pisith Singjai	Chiang Mai University
Assistant Professor Dr.Suthee Vattanasiriweach	Mae Fah Luang University
Dr.Somwan Chumphongphan	Mae Fah Luang University

Section G: MATHEMATICS/ STATISTICS/ COMPUTER SCIENCE

Associate Professor Dr.Chartchai Leenawong	King Mongkut's Institute of Technology Ladkrabang
Assoc. Prof. Wg.Cdr.Dr.Tossapon Boongoen	Mae Fah Luang University
Dr.Theeradech Mookum	Mae Fah Luang University

Section H: FOOD SCIENCE & TECHNOLOGY

Associate Professor Dr.Kanitha Tananuwong	Chulalongkorn University
Associate Professor Dr.Saroat Rawdkuen	Mae Fah Luang University
Dr.Somruedee Thaiphanit	Siam University
Dr.Nattaya Konsue	Mae Fah Luang University

Section SP1: CRYSTALLOGRAPHY

Professor Dr.Nongnuj Muangsin	Chulalongkorn University
Associate Professor Dr.Kuakarun Krusong	Chulalongkorn University
Assistant Professor Dr.Kittipong Chainok	Thammasat University

Content

SESSION A: AGRICULTURAL SCIENCE & BIOTECHNOLOGY 7

A_001_OF: COMPARISON OF ANTIOXIDANT ACTIVITY AND STILBENE COMPOUNDS PRODUCED BY TAINAN9 AND KALASIN2 PEANUT HAIRY ROOT CULTURE ELICITED WITH A COMBINATION OF METHYL JASMONATE, CYCLODEXTRIN, AND PARAQUAT 8

A_007_OF: PROTEIN HYDROLYSATE PRODUCTION FROM DEFATTED RICE BRAN BY INNER ENZYME OF RICE MALT PLUS BROMELAIN 14

A_009_PF: EVALUATION OF FORMIC ACID IN CONTROLLING *Tropilaelaps* MITES IN LABORATORY 20

A_010_PF: EFFICACY OF NATIVE PLANT EXTRACTS (GINGER AND MARIGOLD) IN CONTROLLING RICE WEEVIL: *Sitophilus oryzae* L. 25

A_013_OF: EVALUATION OF THE CYTOTOXICITY AND GENOTOXICITY OF THE EXTRACTS FROM *Halymenia durvillei* 33

A_017_OF: DATA REDUNDANCY IN PAIRED-END DNA SEQUENCE ALIGNMENTS 40

A_018_OF: SAFETY ASSESSMENT OF THE ETHANOLIC EXTRACT OF *Caulerpa lentillifera* IN VITRO SYSTEM 50

A_019_OF: EFFICIENCY OF *Caulerpa lentillifera* AND *Halymenia durvillei* EXTRACTED SUBSTANCES IN ANTI-OXIDATION 56

A_020_PF: ANTIFUNGAL ACTIVITY OF CRUDE EXTRACTS FROM LICHEN *Parmotrema tinctorum* (Despr. ex Nyl.) Hale AGAINST *Pythium* spp. CAUSAL AGENTS OF DAMPING-OFF DISEASE OF MARIGOLD (*Tagetes erecta* L.) 62

A_022_OF: TOTAL PHENOLIC CONTENT, TOTAL FLAVONOID CONTENT AND ANTIOXIDANT ACTIVITY OF THE CULTURE FILTRATE EXTRACT FROM *Ganoderma lucidum* 67

A_023_PF: DETECTION OF *atzB* GENE IN TROPICAL *Trichoderma harzianum* ISOLATED FROM ATRAZINE CONTAMINATED SOIL IN CENTRAL REGION OF THAILAND 73

A_027_PF: ANTIMICROBIAL ACTIVITY OF A NISIN-CONTAINING BACTERIAL CELLULOSE FILM FROM RICE WASHING DRAINAGE (RWD) 77

A_029_PF: WHICH IS THE SUITABLE TRANSPLANTED FRAME FOR CULTIVATING THE LICHEN *Parmotrema tinctorum* FOR SUSTAINABLE UTILIZATION? 82

A_031_OF: STUDIES ON MICROBIAL BIOMASS CARBON AND NITROGEN TURNOVER DERIVED FROM SUGARCANE RESIDUES INCORPORATED INTO A SANDY LOAM SOIL 87

SESSION B1: BIOCHEMISTRY 94

B1_004_OF: B1_004_OF: ANTIOXIDANT AND CYTOPROTECTIVE EFFECT OF *Arthrospira platensis* PROTEIN HYDROLYSATE 95

B1_007_PF: *Aquilaria crassna* LEAVE CRUDE EXTRACT ENHANCES GLUCOSE CONSUMPTION AND DECREASES GLUCONEOGENESIS IN HEPG2 CELLS 102

SESSION B2: MICROBIOLOGY 108

B2_003_PF: ISOLATION AND PHYSIOLOGICAL CHARACTERIZATION OF BENEFICIAL ANAEROBIC MICROBIOTA IN COMMERCIAL CHICKEN GUTS 109

B2_007_OF: CHARACTERIZATIONS OF TRIMETHOPRIM-SULFAMETHOXAZOLE RESISTANCE IN ENTEROBACTERIACEAE ISOLATED FROM SONGKLANAGARIND HOSPITAL 115

B2_008_OF: CHARACTERISTICS OF BACTERIOPHAGES AGAINST *Vibrio* spp. 120

B2_009_OF: TESTING THE PHENOTYPIC EFFECTS OF *Acinetobacter baumannii* ANTIBIOTIC RESISTANT GENE IN *Escherichia coli* BY USING A HIGH-THROUGHPUT CLONING APPROACH 126

B2_011_PF: ANTIBACTERIAL AND ANTIBIOFILM ACTIVITIES OF RAMBUTAN (*Nephelium lappaceum* L.) PEEL EXTRACT ON *Vibrio parahaemolyticus* and *Escherichia coli* ISOLATED FROM FOODS 135

SESSION B3: MOLECULAR BIOLOGY 142

B3_001_PF: DRAFT INTESTINAL MICROBIOTA OF SEA CUCUMBER (S*tichopus horrens*) FOR AQUACULTURE SYSTEMS 143

B3_003_PF: PHYSIOLOGICAL FUNCTION ANALYSIS OF NOVEL GENE CASSETTE CONFERRING PARAQUAT SUSCEPTIBILITY IN *Pseudomonas aeruginosa* 150

B3_011_PF: EXPRESSION ANALYSIS OF *Drosophila melanogaster* INNATE IMMUNITY GENES DURING *Pseudomonas aeruginosa* INFECTION 157

B3_012_PF: TRANSCRIPTIONAL RESPONSES OF *Pseudomonas aeruginosa* TO REACTIVE CHLORINE STRESS 163

B3_013_PF: FUNCTIONAL CHARACTERIZATION OF A GENE ENCODING A PUTATIVE GLUTATHIONE S-TRANSFERASE ON METAL AND ANTIMICROBIAL RESISTANCE IN *Pseudomonas aeruginosa* 169

SESSION B4: BIOMEDICAL SCIENCE 177

B4_005_PF: OPTIMISATION OF HIGH RESOLUTION MELTING CURVE ANALYSIS (HRMA) TO DETECT MUTANT CALRETICULIN IN *JAK2* NEGATIVE MYELOPROLIFERATIVE NEOPLASM PATIENTS 178

B4_007_OF: PlASMA EXOSOME miR-21 AS THE INTERSTITIAL FIBROSIS AND TUBULAR ATROPHY(IF/TA) BIOMARKER IN KIDNEY TRANSPLANTATION 184

B4_008_PF: THE STUDY OF *UT2B17* POLYMORPHISM IN REPRESENTATIVE THAI MUSLIM POPULATION IN SONGKHLA PROVINCE 189

B4_009_PF: BIOLOGICAL ACTIVITIES OF PAPER MULBERRY EXTRACT (*Broussonetia papyrifera* (L.) Vent.) 194

SESSION B5: BIODIVERSITY 199

B5_002_OF: GENETIC DIVERSITY AND REINTRODUCTION SOURCE OF THE COMMON BUTTERFLY LIZARD, *Leiolepis belliana* (SQUAMATA: AGAMIDAE), ON PHRA ISLAND, CHON BURI PROVINCE 200

B5_004_OF: EFFECTS OF HYPO-OSMOTIC SHOCK ON THE RESPONSE OF HEMOLYMPH OSMOLALITY IN THE MUD CRAB *Scylla olivacea* (Herbst, 1796) 205

B5_006_OF: OVIPOSITIONAL PREFERENCES AND LARVAL DEVELOPMENT OF TAWNY COSTER *Acraea terpsicore* (LINNAEUS, 1758) (LEPIDOPTERA: NYMPHALIDAE) ON FOUR PASSION VINES 212

B5_008_OF: AVIFAUNA IN PUBLIC PARKS IN BANGKOK AND THE EFFECTS OF PARK AREA 221

B5_020_PF: DIVERSITY OF FOLIICOLOUS LICHENS ON *Acrostichum aureum* L. IN MANGROVE FOREST FROM CHUMPHON PROVINCE 229

B5_025_PF: BIODIVERSITY OF DISCOLICHES IN MANGROVE FOREST AT CHUMPHON PROVINCE, THAILAND 235

B5_028_PF: SYSTEMATIC REVIEWS OF RHINOBATIFORMES IN THAI WATERS BASED ON 80 MORPHOMETRIC CHARACTERS 240

B5_030_OF: GENETIC DIVERSITY OF THE ISLAND FLYING-FOX, *Pteropus hypomelanus* (CHIROTERA: PTEROPODIDAE), IN THAILAND 247

SESSION C1 ANALYTICAL CHEMISTRY 253

C1_001_OF: FLUORESCENT DETERMINATION OF SOLUBLE PYROPHOSPHATE LEVEL IN SYNOVIAL FLUID AS A MARKER OF PSEUDOGOUT DISEASE 254

C1_002_PF: A CHEMICAL SENSOR FOR FORMALDEHYDE DETECTION USING NITROGEN-DOPED GRAPHENE QUANTUM DOTS 259

C1_003_PF: IN-HOUSE METHOD VALIDATION FOR TOTAL ACID NUMBER IN BIODIESEL BY POTENTIOMETRIC TITRATION 265

C1_006_OF: SPECIFIC AND SENSITIVE DETECTION METHOD FOR CHROMIUM (VI) IN ORANGE JUICE USING DOUBLE REACTIONS 271

C1_007_PF: ENANTIOMERIC SEPARATION OF 1-PHENYLALKANOLS BY GC USING METHYLATED BETA-CYCLODEXTRIN CHIRAL STATIONARY PHASE 282

C1_010_PF: ALTERNATIVE COLORIMETRIC DETERMINATION OF 2-NAPHTHOL FOR SCREENING OF ALPHA-GLUCOSIDASE ASSAY 289

C1_012_PF: APPLICATION OF SILVER AMALGAM ELECTRODE FOR ANODIC STRIPPING VOLTAMMETRIC DETERMINATION OF CADMIUM IN CONTAMINATED SOIL AND PLANT 295

C1_013_PF: PAPER-BASED LINER FOR HEADSPACE COLORIMETRIC DETERMINATION OF VOLATILE COMPOUNDS 303

SESSION C2: INORGANIC CHEMISTRY 307

C2_001_PF: SYNTHESIS AND CHARACTERIZATION OF A FLUORESCENT CHEMOSENSOR BASED ON ANTHRAQUINONE DERIVATIVE FOR METAL IONS DETECTION 308

C2_005_PF: SYNTHESIS OF TiO_2-SiO_2 COMPOSITE AND ITS APPLICATION AS A PHOTOCATALYST FOR OXIDATIVE DESULFURIZATION 314

C2_006_PF: CYTOTOXICITY OF GOLD(III) PORPHYRIN COMPLEXES AND THEIR DERIVATIVE ON MCF7 CELL LINES 319

C2_008_PF: COUMARIN-BASED SEMICARBAZIDE AS "TURN-OFF" FLUORESCENT SENSOR FOR Cu^{2+} DETECTION 325

SESSION C3: ORGANIC & MEDICINAL CHEMISTRY 331

C3_002_PF: QUANTITATIVE DETERMINATION OF PHENOLIC AND TANNIN CONTENTS AND ANTIOXIDANT ACTIVITY OF PAPER MULBERRY 332

C3_003_PF: SYNTHESIS AND CYTOTOXICITY OF TETRAHYDROCURCUMIN PYRAZOLE INDOLE DERIVATIVES 336

C3_004_PF: FORMALDEHYDE FLUORESCENT SENSORS FROM 1,8-NAPHTHALIMIDE DERIVATIVES 342

C3_005_OF: THE PRELIMINARY STUDIES ON THE SYNTHESIS AND THE CYTOTOXICITY TOWARDS HepG2 AND Huh7 OF A NEW SERIES OF SORAFENIB ANALOGUES: REPLACEMENT OF ARYL UREA WITH A TRIAZOLE RING 348

C3_006_PF: DESIGN AND SYNTHESIS OF OFF/ON FLUORESCENT pH SENSOR BASED ON RHODAMINE 6G 359

C3_007_PF: XANTHONES FROM THE ROOTS OF *Cratoxylum cochinchinense* 364

C3_008_PF: DEVELOPMENT OF AN ASYMMETRIC DIELS-ALDER REACTION OF *O*-NAPHTHOQUINONES 374

C3_010_OF: KINETIC STUDY OF CONJUGATE ADDITION OF AMINES INTO ALKYNOIC ESTER 381

C3_011_PF: STUDY THE EXTRACTION OF *Stephania venosa* (BLUME) SPRENY. TUBERS 388

C3_014_PF: CHEMICAL CONSTITUENTS OF *Garcinia cowa* LEAVES 393

C3_016_PF: CHEMICAL SYNTHESIS OF GLYCOSYL DITHIOCARBAMATE USING LACTOSE ISOLATED FROM WHEY AS PRECURSOR 401

C3_018_PF: POTENT VASORELAXANT CAGED POLYPRENYLATED XANTHONES FROM THE RESIN OF *Garcinia hanburyi* 407

SESSION C4: PHYSICAL & THEORETICAL CHEMISTRY 411

C4_003_OF: ENHANCING SENSITIVITY AND SELECTIVITY OF SURFACE-ENHANCED RAMAN SCATTERING DETECTION BY CHEMOMETRIC METHOD 412

C4_004_PF: MOLECULAR DOCKING STUDIES OF DONEPEZIL-COUMARIN HYBRID AS NOVEL MULTI TARGET hAChE AND hMAO-B INHIBITORS 421

C4_005_PF: LASER-INDUCED BREAKDOWN SPECTROSCOPY STUDY OF RED-COLORED ANCIENT GLASS BEADS FROM KHLONG THOM ARCHAEOLOGICAL SITE 431

SESSION D: POLYMER & MATERIALS SCIENCE_NANOTECHNOLOGY 436

D_001_PF: ZINC OXIDE DOPED WITH COPPER(II) OXIDE SUPPORTED ON CELLULOSE FLAKES FOR DEGRADATION OF METHYLENE BLUE 437

D_002_OF: MODIFICATION OF PECTIN BY 3-(DIMITHYLAMINO) PROPYLAMINE 442

D_007_PF: EFFECTS OF LOW DOSE OF GOLD NANOPARTICLES ON PERICYTES BIOLOGY 449

D_015_PF: SYNTHESIS OF HIGH MOLECULAR WEIGHT POLY(ε-CAPROLACTONE) USING TITANIUM(IV) *n*-BUTOXIDE AS EFFECTIVE INITIATOR 456

D_019_PF: PORTABLE ELECTROCHEMICAL SENSOR FOR FENITROTHION ANALYSIS 461

D_028_OF: NATURAL RUBBER FILM MODIFIED BY METHYLTRICHLOROSILANE FOR CREATING SUPERHYDROPHOBIC SURFACE 467

D_033_PF: NOVEL AND FACILE FABRICATION OF MAGNETICALLY MESOPOROUS CARBON MONOLITHS FOR REMOVAL OF TERACYCLINE 472

D_037_OF: ENHANCING HYDROPHOBICITY OF PVDF HOLLOW FIBER MEMBRANE BY PLASMA INDUCED AND GRAFTED WITH CHLOROALKYLSILANES 479

D_044_PF: PREPARATION AND CHARACTERIZATION OF KAFFIR LIME OIL MACROCAPSULES 485

D_054_OF: SYNTHESIS AND STRUCTURAL PROPERTIES OF METAL DOPED Li NIKEL-RICH NMC POWDER MATERIALS FOR HIGH SPECIFIC CAPACITY 491

SESSION E: ENERGY_ENVIRONMENTAL & EARTH SCIENCE 497

E_002_PF: ARCHITECTURE ELEMENTS AND STRATIGRAPHY OF ANCIENT MUN RIVER, NAKHON RATCHASIMA, NORTHEASTERN THAILAND 498

E_004_PF: ACTIVITY OF $PtIrO_2$/C FOR REGENERATIVE PEM FUEL CELL 507

E_005_PF: $NiCo_2S_4$/N-rGO AS A BIFUCNTIONAL OXYGEN REACTION ELECTROCATALYST FOR RECHARGEABLE ZINC-AIR BATTERIES 513

E_006_OF: THE STUDY OF BASEFLOW SEPARATION AT WATERSHEDS IN CHIANG RAI, THAILAND 518

E_008_PF: PREPARATION OF NiCoS CATALYSTS FOR RECHARGEABLE ZINC-AIR BATTERIES 525

E_010_PF: HYDROGEN PRODUCTION AND COD REMOVAL FROM BIODIESEL WASTEWATER USING COUPLED SEMICONDUCTOR PHOTOCATALYST 529

E_012_OF: ORGANIC GEOCHEMICAL CHARACTERISTICS OF COAL DEPOSITS IN LAMPANG PROVINCE 535

E_013_OF: RECONSTRUCTION OF SEA LEVEL FLUCTUATION AND PALEOENVIRONMENTAL CHANGES IN KHAO SAM ROI YOT NATIONAL PARK, CHANGWAT PRACHUAP KHIRI KHAN DURING THE LATE HOLOCENE 545

E_014_OF: USING INFORMATION AND COMMUNICATION TECHNOLOGY TO SUPPORT THE MANAGEMENT OF HOUSEHOLD HAZARDOUS WASTE: A CASE OF CHIANG RAI PROVINCIAL ADMINISTRATIVE ORGANIZATION 551

E_015_OF: ESTIMATING LONG-TERM GROUND-LEVEL PM10 CONCENTRATIONS OVER NORTHERN THAILAND USING A SATELLITE-BASED 557

E_020_PF: SOME PETROCHEMICAL FEATURES OF GRANITIC ROCKS ALONG HIGHWAY 1D, XIENGKHOUANG TO XAISOMBOUN PROVINCES, LAO PDR 564

E_021_OF: DEVELOPMENT OF LITHIUM METAL OXIDE AS A CATHODE MATERIAL FOR LITHIUM ION BATTERIES 575

E_022_OF: CHARACTERISTICS OF BIOCHAR FROM TEA RESIDUAL FOR SOIL AMENDMENT 582

E_024_OF: PALEOSEISMIC EVIDENCES OF THE DOI WIANG LA FAULT SEGMENT, MAE HONG SON FAULT, NORTHERN OF THAILAND 584

E_027_OF: PHYSICOCHEMICAL CHARACTERIZATION OF SLOW PYROLYSIS BIOCHAR FROM *Robusta* SPENT COFFEE GROUNDS UTILIZED FOR SOIL AMENDMENT 592

E_028_OF: SIMULATION OF SHALLOW LANDSLIDES SUSCEPTIBILITY MAP IN THE TOP OF PHU TUB BERK MOUNTAIN, PHETCHABUN, THAILAND 597

E_029_PF: LOW ASH BIOMASS PELLET FROM CORN STALK: EFFECT OF CALCIUM CARBONATE BASE ADDITIVE ON FUELS AND ASH QUANTITIES 603

SESSION F: PHYSICS & APPLIED PHYSICS 608

F_001_PF: STRUCTURAL AND PHYSICAL PROPERTIES OF $SnS_{1-x}Se_x$ SOLID SOLUTION THIN FILMS PREPARED BYCLOSE SPACED SUBLIMATION METHOD 609

F_002_PF: EFFECTS ON TRIBOLOGICAL BEHEVIORS OF SYNTHETIC HYDROCARBON BASED LUBRICANT FOR MICROELECTRONIC APPLICATIONS 619

F_003_PF: FABRICATION AND CHARACTERIZATION OF $(CdS)_{1-x}(ZnTe)_x$ AND $CuSbS_2$ THIN FILMS FOR PHOTODIODE APPLICATION 624

F_004_OF: FLOW CROSSOVER DURING COLLISIONLESS MAGNETIC RECONNECTION 635

F_005_OF: VERIFICATION OF CURLING PROBE MEASUREMENT IN DC PLASMA 640

F_006_PF: HEAT TREATMENT OF MOGOK ZIRCON, MYANMAR 647

F_008_PF: EFFECT OF SINTERING TEMPERATURES ON DENSITY AND VICKERS MICRO-HARDNESS OF BZT CERAMICS PREPARED BY MOLTEN SALT METHOD 654

SESSION G: MATHEMATICS / STATISTICS / COMPUTER SCIENCE 658

G_001_PF: EDGE-ODD GRACEFUL LABELING IN THE CONTEXT OF DUPLICATION OF GRAPH ELEMENTS 659

G_002_OF: EXPLORING DATA CLASSIFICATION MODELS FOR IDENTIFICATION OF CKD PROGRESSION INTERVAL: A CASE STUDY 663

SESSION H: FOOD SCIENCE & TECHNOLOGY 669

H_009_PF: COMPARISON OF EXTRACTION TECHNIQUES USING DHS-TENAX TA, SBSE AND SPME FOR ANALYSIS OF DRIED CHILI VOLATILES 670

H_010_PF: EFFECTS OF JIAOGULAN ON HEXANAL CONTENT IN *SAI-UA* (NORTHERN STYLE HERBAL-PORK SAUSAGE) 679

H_013_PF: INFLUENCE OF STEVIA CONCENTRATION AND GUAR GUM ON RHEOLOGY AND PHYSICO CHEMICAL PROPERTIES OF GUAVA JUICE 687

SESSION SP1: CRYSTALLOGRAPHY 695

SP1_004_PF: THERMAL ANALYSIS OF PHASE TRANSITION AND CRYSTALLIZATION OF $EuBa_2Cu_3O_{7-\delta}$ POWDER PREPARED BY SOLID-STATE REACTION 696

SP1_005_PF: A NEW ZINC(II) COORDINATION POLYMER BASED ON 5-NITROISOPHTHALATE; SYNTHESIS, CRYSTAL STRUCTURE AND HIGHLY SENSITIVE FLUORESCENCE SENSING PROPERTIES OF SMALL MOLECULES AND METAL IONS 703

Author Index 710

SESSION A:
AGRICULTURAL SCIENCE
& BIOTECHNOLOGY

A_001_OF: COMPARISON OF ANTIOXIDANT ACTIVITY AND STILBENE COMPOUNDS PRODUCED BY TAINAN9 AND KALASIN2 PEANUT HAIRY ROOT CULTURE ELICITED WITH A COMBINATION OF METHYL JASMONATE, CYCLODEXTRIN, AND PARAQUAT

Pakwuan Wongshaya[1], Anupan Kongbangkerd[2], Apinun Limmongkon[1,*]
[1]Department of Biochemistry, Faculty of Medical Science, Naresuan University, Phitsanulok 65000, Thailand
[2]Department of Biology, Faculty of Science, Naresuan University, Phitsanulok 65000, Thailand
[*]e-mail: apinunl007@yahoo.com

Abstract: Peanuts (*Arachis hypogaea*) can produce valuable secondary metabolites, such as stilbenes compounds to defend against oxidative stress. *In vitro* hairy root culture is a convenient method to produce large quantities of plant secondary metabolites. In this study, peanut hairy roots derived from 2 different peanut cultivars; Tainan9 (T9-K599) and Kalasin-2 (K2-K599) were used for elicitation assay and antioxidant stilbene compound determination. They were cultured and elicited with a combination of 3 elicitors, paraquat (PQ), methyl jasmonate (MeJA) and cyclodextrin (CD). The antioxidant activity, total phenolic compounds and stilbene compounds namely *trans*-resveratrol, *trans*-arachidin1 and *trans*-arachidin 3 were compared between peanut hairy root cultivars. The results showed a higher production of stilbene compounds with antioxidant activity in K2-K599 compared to T9-K599 hairy root culture. This indicated that hairy root derived from different peanut cultivar might process distinct levels of an antioxidant defense mechanism to protect it against oxidative stress.

Introduction: Plants use enzymatic and non-enzymatic antioxidants as a defense mechanism against herbivores, pathogens, and other stresses. Non-enzymatic antioxidant molecules are generally secondary metabolite substances with various structures, such as phenolic compounds. Secondary metabolites have been identified in various plants and possess antioxidants, antiviral and antibacterial activity.[1] Sobolev et al.[2] reported that peanuts contain many bioactive compounds such as *trans*-arachidin and resveratrol. These compounds are characterized in the stilbenoid group, which are biologically phytoalexin active substances for the protection of plants against fungal infections and other environmental toxins.[3]

Nowadays, the biotechnological approach can be applied to enhance secondary metabolites by using *Agrobacterium rhizogenes* to induce hairy root in plants. In addition, the strategy to use elicitors to induce plant secondary metabolites was extensively studied in several reports. Yang et al. reported that peanut hairy root can produce resveratrol, piceatannol, arachidin-1, and arachidin-3 after elicited with methyl jasmonate (MeJA) and methyl-β-cyclodextrin (CD).[4] MeJA acts as a signaling molecule to activate the defense mechanism in plants. The CD are cyclic oligosaccharides bonds with glycosidic that can form inclusion complexes with organic molecules were reported to act as a plant elicitor. Somboon et al. studied the schematic diagram of the defense pathways of peanut hairy root, after being treated with different approaches of paraquat (PQ), MeJA and CD. The high induction of stilbene compounds was observed in the pretreatment of PQ, followed by the application of MeJA plus CD. [5]

The aim of this study is to determine the antioxidant activity, total phenolic compounds and the amount of stilbene compounds as a defense mechanism of peanut hairy root after being elicited with a combination of MeJA, CD and PQ elicitors. To our knowledge, this is the first report to investigate the response of peanut hairy root by using a combination of MeJA, CD, and PQ as the elicitors at the same time. The results of bioactive compounds and antioxidant activity will be compared between peanut hairy root cultivar Kalasin2 and Tinan9 to investigate the defense mechanism levels of different cultivars.

Methodology:

Plant material: The two different cultivars of peanut hairy root cultures transformed with *A. rhizogenes* K599 namely Kalasin2 (K2-K599) and Tinan9 (T9-K599) were used in the elicitor experiment. The hairy roots were cultured with B5 agar medium and were sub-cultured every 14 days.

Elicitor treatments: A total of 5g of peanut hairy roots were cut and transferred into 150 ml of half MS liquid medium with 3% sucrose. The combination of 100 µM MeJA, 6.87 µM CD and 500 µM PQ were used as the elicitors at the same period of elicitation, respectively. The peanut hairy roots were then cultured at 25 °C under continuous darkness and shaken at 150 rpm for 24, 48 and 72 hours with three biological replications.

Hairy root culture medium extraction: The culture medium was extracted three times with ethyl acetate (ratio 1:1). The organic phase was evaporated by rotary evaporation under vacuum at 40 °C. The crude extracts were dissolved in ethanol for further analysis.

The antioxidant ABTS assay: Free radical scavenging activity was determined by ABTS (3-ethylbenzothiazoline-6-sulphonic acid) radical cation decolorization assay. The ABTS radicals can be scavenged by antioxidant compounds and become decolorized. The reaction was prepared by 198 µl of $ABTS^{\cdot+}$ solution and 2 µl of peanut hairy root crude extract. The absorbance was measured at 6 min after the initial mixing at 734 nm. Trolox was used as a standard substance and antioxidant activity was calculated as Trolox equivalent antioxidant capacity (TEAC) mM Trolox per gram of the crude extract.

The antioxidant DPPH assay: The total free radical scavenging capacity of the extracts were evaluated using the DPPH (2,2-diphenyl-1-picrylhydrazyl) to obtain an absorption at 515 nm. The solution contained 100 µl of DPPH radicals, 90 µl of ethanol and 10 µl of crude extract. After incubation in the dark at room temperature for 30 min, the solution was determined. The Trolox was used as the standard and the antioxidant activity was exhibited as TEAC value, mM Trolox per gram dry weight of the crude extract.

The antioxidant FRAP assay: The FRAP (Ferric reducing antioxidant power) assay was used to investigate the properties of electron donating antioxidants. The FRAP solution was prepared by mixing 300 mM acetate buffer, 10 ml TPTZ in 40 mM HCl and 20 mM $FeCl_3.6H2O$, then determined by adding 2 µl of crude extract to 198 µl of FRAP reagent and incubated at room temperature for 5 min, and the absorbance was measured at 593 nm. The ascorbic acid was used as the standard and the antioxidant activity represented as ascorbic acid equivalent (AAE), mM ascorbic acid per gram dry weight of the crude extract.

Total phenolic compound: The total phenolic contents were determined spectrophotometrically according to the Folin-reagent method. The yellow solution of the Folin-reagent can turn blue when it reacts with electrons from phenolic compounds which measure its absorbance at 765 nm. The solution was prepared by adding 2 µl of crude extract to 178 µl of water, followed by the addition of 10 µl Folin reagent and 10 µl of sodium carbonate (20% w/v). The absorbance of the solution was measured after incubation for 30 min at 765 nm. The amount of phenolic compounds was expressed as gallic acid equivalents (GAE) in mg per gram dry weight of the crude extract.

High-performance liquid chromatography (HPLC): The stilbenoid compounds were analyzed by the HPLC method according to Somboon et al.[5] protocol. The C18 reverse-phase column was used as the stationary phase and the mobile phase consisted of acetonitrile and 2% formic acid in water with a flow rate at 1 ml/min. The *trans*-resveratrol chromatogram was detected at UV 306 nm and *trans*-arachidin-1, *trans*-arachidin-3 were detected at UV 340 nm. The amount of each stilbene compound was expressed as µg/g DW of hairy roots.

Results and Discussion:

Antioxidant activity and total phenolic compounds: K2-K599 and T9-K599 hairy root, were elicited with a combination of elicitors MeJA, CD, and PQ for 24, 48 and 72 hours. The antioxidant activities were determined using ABTS, DPPH and FRAP assay. The crude extract with antioxidant activity can inhibit the $ABTS^{\cdot+}$ radical cation and expressed the activity as the TEAC value. The ABTS antioxidant activity of K2-K599 and T9-K599 peanut hairy root crude extract is shown in Figure 1. (a) which demonstrated that K2-K599 hairy root elicited with elicitors performed higher antioxidant activity than T9-K599 hairy root and the control group. The K2-K599 peanut hairy root culture elicited with elicitors for 72 hours exhibited the highest TEAC value of 359.84±104.14 mM Trolox per gram of the dry weight of the crude extract, which showed a significant difference compared to T9-K599 peanut hairy root and the control group.

The antioxidant ability to inhibit the DPPH radical was determined by the DPPH assay. As the result shown in Figure 1. (b), the highest antioxidant activity was found in K2-K599 peanut hairy root culture elicited for 72 hours with a value of 162.85±39.70 mM Trolox per gram of the dry weight of the crude extract, showed a significant difference compared to T9-K599 peanut hairy root and the control group at every time point.

The investigation of the antioxidant ability to reduce Fe^{3+} was determined by the FRAP method. As the result shown in Figure 1. (C), the K2-K599 peanut hairy root culture elicited with elicitors for 72 hours represented the highest AAE value of 276.16±26.14 mM ascorbic acid per gram of the dry weight of the crude extract which was significantly different when compared to T9-K599 peanut hairy root and the control group at every time point.

The total phenolic compounds result determined by the Folin–Ciocalteu method is shown in Figure 1. (d). The K2-K599 hairy root elicited at 72 hours expressed the highest levels of phenolic compounds with the GAE value of 189.77±110.30 mg gallic acid per gram of the dry weight of the crude extract. In accordance to the results of the total antioxidant activity determined by 3 different methods, the phenolic contents of K2-K599 hairy root at 72 hours elicitation, displayed a significant difference when compared to T9-K599 peanut hairy root and the control group at every time point. With the results of antioxidant activity and total phenolic compounds, K2-K599 peanut hairy root demonstrated higher antioxidant activity and phenolic contents than T9-K599 peanut hairy root. This is in agreement with the results of Limmongkon et al.[6] which reported the higher antioxidant activity and total phenolic compound of germinated peanut cultivar than Tainan9 cultivar.

The HPLC result of stilbene compounds: A sample of stilbene compound was analyzed by the HPLC method as shown in Figure 2. (a-d) and Figure 3. (a-c), which showed that the K2-K599 peanut hairy root culture represented a higher amount of *trans*-resveratrol, *trans*-arachidin1, and *trans*-arachidin3, than the T9-K599 peanut hairy root culture, which was in accordance with the results of antioxidant activity and total phenolic compounds. Interestingly, the *trans*-resveratrol content of K2-K599 peanut hairy root was the highest after 24 hours elicitation with a value of 964.98±319.90 µg per gram of the dry weight of the crude extract, but decreased upon higher elicitation time (Figure 3. (a)).

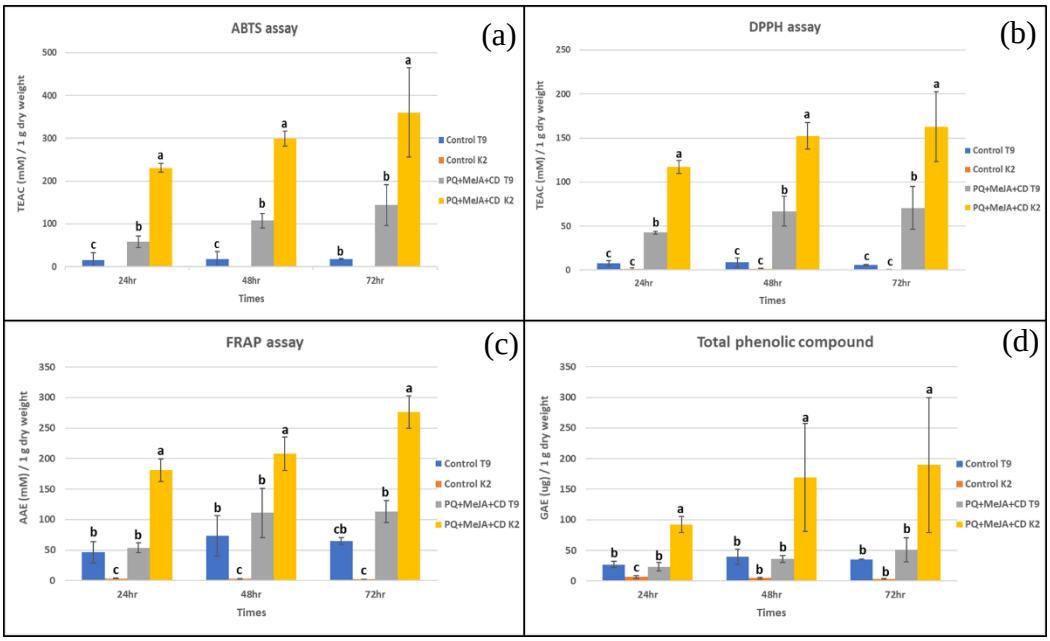

Figure 1. Antioxidant activity of peanut hairy root culture medium crude extracts elicited with PQ+MeJA+CD at 24, 48 and 72 hours measured by the ABTS assay (a), DPPH assay (b), FRAP assay (c) and total phenolic compounds (d). The data represents the mean ± standard deviation of three biological replicates. Different lowercase letters represent significant differences between different peanut hairy root genotype at each time point ($p<0.05$).

In contrast to K2-K599, the *trans*-resveratrol content detected in T9-K599 peanut hairy root showed an increasing amount of it with a higher elicitation time. The *trans*-arachidin1 and *trans*-arachidin3 amounts increased after elicitation period in both K2-K599 and T9-K599 peanut hairy root and exhibited the highest amount after 72 hours of elicitation. The highest amount of *trans*-arachidin1 and *trans*-arachidin3 detected in K2-K599 peanut hairy root at 72 hours was 180,600.54±43,329.01 and 78,465.15±7,427.24 µg per gram of the dry weight of the crude extract, respectively (Figure 3. (b-c)). Our results were in accordance with the study of Yang et al[4] which showed the peanut hairy root culture elicited with MeJA and CD also exhibited high amounts of *trans*-arachidin1 and *trans*-arachidin3 with increasing elicited time points.

Effect of combination elicitor on peanut hairy root culture: The combination of elicitor MeJA, CD and PQ can induce oxidative stress in plant cells. Ekmekci and Terzioglu[7] reported that the increasing concentration of PQ elicited wheat can increase oxidative stress in cells which could decrease the efficiency of photosynthesis (PSII). Plants can protect themselves by using secondary metabolites as antioxidant defense mechanisms. This study demonstrated a high amount of stilbene compounds with high antioxidant activity in peanut hairy root, elicited with the combination of MeJA, CD and PQ, might act as free radical generator, pathogen mimic and signaling transduction molecules. With all the combinations of elicitation molecules at the same time, peanut hairy root might provoke the defense mechanisms to confront all possible stresses by producing stilbene compounds.

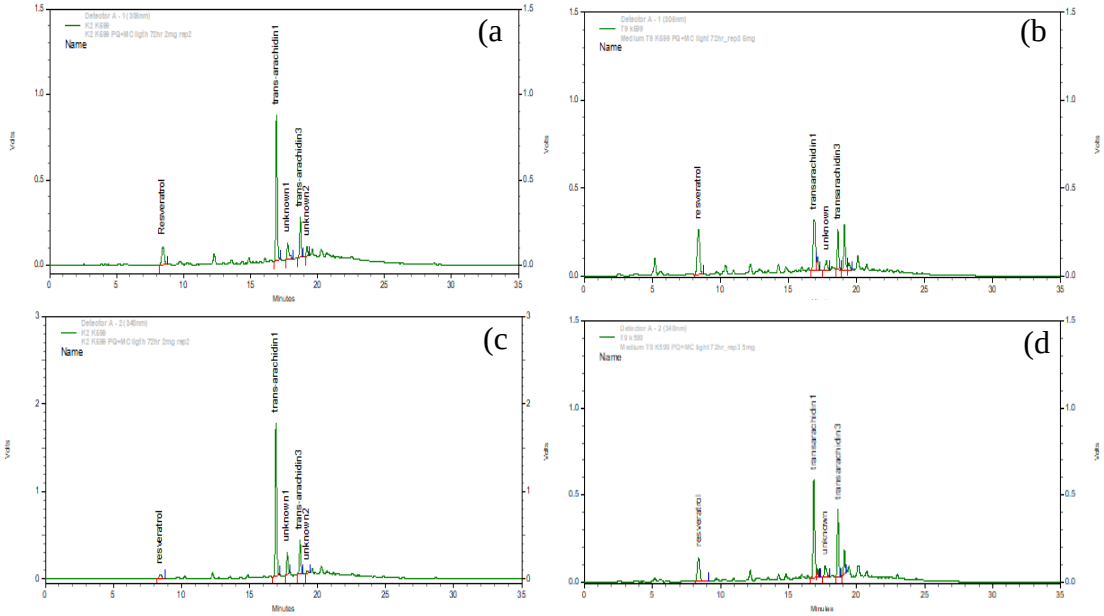

Figure 2. The HPLC chromatograms of peanut hairy root culture medium crude extracts elicited with PQ+MeJA+CD. (a) K2-K599 (306 nm), (b) T9-K599 (306 nm), (c) K2-K599 (340 nm) and (d) T9-K599 (340 nm)

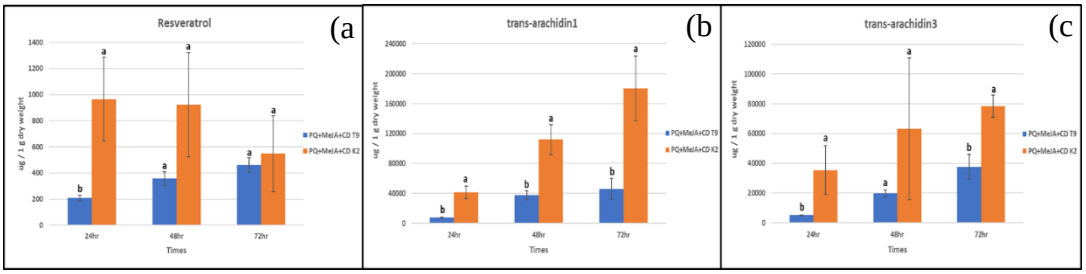

Figure 3. The amount of stilbenoid group of peanut hairy root culture medium crude extracts elicited with PQ+MeJA+CD at 24, 48 and 72 hours analysis by the HPLC method indicated the amount of (a) *trans*-resveratrol, (b) *trans*-arachidin1 and (c) *trans*-arachidin3. The data represents the mean ± standard deviation of three biological replicates, and different lowercase letters represent significant differences between different peanut hairy root genotypes at each time point ($p<0.05$).

In addition to secondary metabolites, other defense mechanisms, such as antioxidant enzymes and pathogenesis-related (PR) proteins had previously been described by Soomboon et at.[5], who also proposed a difference strategy for elicited peanut hairy root, and showed that pre-exposure to MeJA+CD followed by PQ, exhibited high antioxidant activity at 24 and 48 hours. However, pre-exposure of PQ followed by MeJA+CD exhibited the highest amounts of *trans*-resveratrol, *trans*-arachidin1 and *trans*-arachidin3 compared with other strategies. The results indicated that peanut hairy root can use different defense mechanisms while struggling with other elicitation stresses. With our present elicitation strategy of using a combination of MeJA, CD, PQ at the same time, the *trans*-arachidin1 at 48 hours after elicitation was detected in a higher amount (111,9630.01±200,83.81 µg per gram of the dry weight

crude extract) compared to the elicitation with pre-exposure PQ followed by MeJA+CD as described previously by Soomboon et at.[5]

Conclusion: The present study demonstrated the defense mechanisms of different peanut hairy roots, derived from 2 different cultivars, K2-K599 and T9-K599 while elicited with a combination elicitor of MeJA, CD and PQ. Both peanut hairy root genotypes presented non-enzymatic antioxidant activity with different level of antioxidant stilbene compounds. The K2-K599 exhibited a higher production of *trans*-resveratrol, *trans*-arachidin1, *trans*-arachidin3 and antioxidant activity, compared to the T9-K599 type. The alteration of the phytochemical content may be due to the peanut cultivar which can be strongly influenced by its genotypes, and the regulation of secondary metabolites production in both. Therefore, the correct peanut hairy root cultivar should be taken into consideration for the production process of secondary metabolites.

References:

1. Makkar HP, Siddhuraju P, Becker K. Plant secondary metabolites: Springer; 2007.
2. Sobolev VS, Khan SI, Tabanca N, Wedge DE, Manly SP, Cutler SJ, et al. Journal of Agricultural and Food Chemistry. 2011;59(5):1673-82.
3. Akinwumi CB, Bordun MK-A, Anderson DH. International Journal of Molecular Sciences. 2018;19(3).
4. Yang T, Fang L, Nopo-Olazabal C, Condori J, Nopo-Olazabal L, Balmaceda C, et al. J Agric Food Chem. 2015;63(15):3942-50.
5. Somboon T, Chayjarung P, Pilaisangsuree V, Keawracha P, Tonglairoum P, Kongbangkerd A, et al. Phytochemistry. 2019;163:11-22.
6. Limmongkon A, Janhom P, Amthong A, Kawpanuk M, Nopprang P, Poohadsuan J, et al. Asian Pacific Journal of Tropical Biomedicine. 2017;7(4):332-8.
7. Ekmekci Y, Terzioglu S. Pesticide Biochemistry and Physiology. 2005;83(2-3):69-81.

Acknowledgements: This work was supported by the National Research Council of Thailand 2018 [grant number R2561B028].

A_007_OF: PROTEIN HYDROLYSATE PRODUCTION FROM DEFATTED RICE BRAN BY INNER ENZYME OF RICE MALT PLUS BROMELAIN

Yupakanit Puangwerakul*, Suvimol Soithongsuk
Food Technology Faculty, Rangsit University, PathumThani, Thailand
*e-mail: lombiotec@yahoo.com

Abstract: Soluble protein hydrolysate produced from defatted rice bran plus rice malt were hydrolyzed by inner enzyme extraction and by inner enzyme plus bromelain extraction. The hydrolysate from the two methods had different protein content of 6.33 and 9.06%, respectively. Moreover, the extracted protein from the second method had higher degree of solubility, emulsion activity and DPPH scavenging activity. However, protein hydrolysate powder produced by inner enzyme extraction had higher foaming ability and contained vitamin B1, B3 and B6 more than the second method. For the amino acid composition, it was found that protein hydrolysate powder produced from different method had mostly essential amino acids met the standard for child and adult intake recommendation of FAO/WHO/UNU. Protein hydrolysate powder had excellent solubility at 92-98%. The ACE-inhibitory activity from protein hydrolysate powder produced from defatted rice bran by inner enzyme extraction and by inner enzyme plus bromelain extraction were 27.50 and 26.43%, respectively.

Keywords: Rice protein, Rice malt, Defatted rice bran, ACE-inhibitory activity

Introduction: Rice protein has many bioactive properties, it can reduce blood pressure by inhibition of ACE activity, inhibit microorganism growth, reduce blood cholesterol and blood clotting, enhance mineral absorption, act as antioxidant and pain relieving agent (1). The researches about ACE inhibition property by rice protein was studied by using extracted protein from different part of rice such as seed, bran and rice dregs sake lee by-product from sake precipitate. These researches focus on protein extraction process by chemical method using concentrated alkali and commercial enzymes. There is also a research using defatted rice bran as a raw material for rice protein extraction by dissolving in alkaline solution followed by precipitation with acid which resulting in low protein content (2, 3). This extraction method caused the crosslinking and rearrangement of the protein molecules resulted in nutritional value reduction and forming of toxic substance such as lisinoalanine (4). The study of suitable condition for protein extraction from Hom Mali rice bran using bacterial endopeptidase, a commercial enzyme showed the ACE inhibition property of the rice protein (5). However, there are no researches using rice protein from defatted rice bran extracted by inner enzyme from rice malt during mashing process as my previous research (6). Therefore, it is interesting to do the research to increase the %yield of the rice protein and extend its production scale to commercial scale to add more value of the extracted protein including study of its functional properties especially on ACE inhibition. The objectives of this research were to study the soluble protein extraction from defatted rice bran by inner enzyme from rice malt plus commercial enzyme and to evaluate the functional properties of the extracted protein.

Methodology:

Raw material : Defatted rice bran, which is a by-product of rice bran oil production, was kindly given byThai Ruam Jai Vegetable Oil Co., Ltd. The powder of PathumThani1rice malt was purchased from Chalerm Phra Kiat Community Enterprise.

Study on optimal conditions for protein extraction: To study the protein extraction by using inner enzyme from rice malt, the rice malt and defatted rice bran were ground to a fine particles approximately 150-200 micron in size. Then, the defatted rice bran was mixed with the rice malt at a ratio of 1: 2 and water was added to the mixed raw materials at a ratio of 5:1.

The pH was adjusted to 4.5-5.0 and temperature was controlled at 30-35 °C (usually the pH and temperature were in this range without adjusting). The mixture was continuously stirred at 100 rpm for 4 hrs. After that, it was heated at 95 °C for 15 min, then the supernatant was separated as a method of Yupakanit and Suvimol (6).

According to protein extraction using inner enzyme plus commercial enzyme, bromelain activity of 96.54 unit/g was used. The extraction process was the same but the pH of the suspension was adjusted to 6.0 and bromelain was added to the suspension at a concentration of 15% (w/w) and the extraction temperature was controlled at 50 °C. After 4 hrs., the suspension was heated at 95 °C for 15 min, then the supernatant was separated as a method of Yupakanit and Suvimol (6). The supernatant from the two extraction methods were analyzed for soluble protein content by Lowry's method (7).Phytic acid content were determined by method of Haug and Lantzsch (8). ACE inhibitory activities were determined by method of Li *et al.* (2005) (9). Antioxidant activities were determined by DPPH radical scavaging method (10). The yields were expressed as percent by calculation.

Evaluation of physical and functional properties of rice extracted protein: The rice protein was extracted from defatted rice bran by using inner enzyme and inner enzyme plus commercial enzyme as the first experiment but the scale of extraction were done in batch 1,000 liter. The supernatant were separated by filtration through 10 micron filter cloth followed by filter press before concentrated by vacuum evaporator at 70 °C to obtain 20-25 °Brix. Subsequently, the concentrated solutions were spray-dried to become a protein powder by spray dryer using inlet temperature of 190 °C and outlet temperature of 90 °C followed the method of Yupakanit *et al.* (11). The rice protein powder from the two extraction methods were analyzed for physical, chemical and functional properties compared to the protein powder commercial standard such as protein solubility, foaming ability, emulsion activity index capacity by the method of Benjakul and Morrissey (12).

Statistical analysis: Three replications of each experiment were performed. All data were analyzed by SPSS. Significant difference ($p \leq 0.05$) among various treatments was detected by using Duncan's multiple range tests.

Results and Discussion:

Optimal condition for protein extraction: The different protein extraction methods affected on soluble protein and phytic acid content as shown in Table1. Using inner enzyme from rice malt plus bromelain could extracted soluble protein as 95% yield and could reduce phytic acid content more than using inner enzyme alone. Moreover, the extracted protein solution showed higher antioxidant activity than using only inner enzyme method. The result showed in Table1.

Table 1 Quality and % Yield of soluble protein from different extraction methods

Items	Extraction method using inner enzyme	Extraction method using inner enzyme plus bromelain
Phytic acid (mg/100g)	168 ± 6.55^{a}	98 ± 7.55^{b}
Soluble protein (%)	2.54 ± 0.52^{b}	3.12 ± 0.65^{a}
ACE inhibitory activity (%)	8.93 ± 0.22^{a}	9.35 ± 0.21^{a}
Antioxidant activity (%)	25.86 ± 5.10^{b}	42.08 ± 5.55^{a}
% Yield of soluble protein	77.67^{b}	95.41^{a}

Mean value±standard deviation of three replications. The different superscript was significant difference value at $p \leq 0.05$.

The results clearly showed that the amount of phytic acid in the extracred protein supernatant obtained from the extraction method using inner enzyme plus bromelain was

significantly lower than using only inner enzyme from rice malt because the pH of the extraction condition using bromelain was 6.0 which was the optimal pH of phytase. Konietzny and Greiner (13) also indicated that optimal pH of phytase was 4.5-6.0 which was consistent with the optimal pH of 5.0-5.5 reported by Baruah et al. (14). The protein extraction method using inner enzyme plus bromelain could reduced 66% of phytic acid compared to 41% using only inner enzyme from rice malt. The former data of Yupakanit and Suvimol (6) was also showed the similar results that using inner enzyme from rice malt could reduce 30-40% of phytic acid. Liu et al. (15) explained that natural phytic acids are combined with protein molecules as a complex structure, therefore after protein hydrolysis by protease the complex molecules are destroyed and phytic acids are released as a free form. Then, natural phytase in the raw materials can easily hydrolyze phosphodiester bond of the phytic acid molecules to inositol and orthophosphate as final products.

Moreover, extracted protein supernatant from the method using inner enzyme plus bromelain showed a high % antioxidant activity of 42. The result was in accordance with the researchs of Geo et al. (16); Gennis and Jonas (17); Panya and Kilara (18) who supported that hydrolysis of rice protein by protease produced soluble and smaller peptides. These peptides such as arginine, leucine and valine had antioxidant activity (19; 20). The similar results of Ortiz and Wagner (21) indicated that supernatant obtained from hydrolysis of protein from rice and other plants such as soybean, mung bean, defatted rice bran and bromelain had better antioxidant activity. It was because bromelain is the enzyme specifically cleave the peptide chain at lysine, alanine, tyrosine and glycine that are the hydrophobic amino acids. These amino acids can improve the functional properties of protein. According to ACE inhibition activity of the extracted protein supernatant, there was no significant difference between the two methods.

Large scale production of protein powder: Considering the benefit of rice protein, production of rice protein powder by inner enzyme from rice malt and inner enzyme plus bromelain methods were compared. The properties of protein powder from the two methods were shown in Table 2. It was found that protein powder from the second method had significantly higher solubility and emulsifying capacity may be because of the higher short peptide chains. Many functional properties of protein such as solubility, foaming capacity, emulsifying capacity including antioxidant activity are due to amphiphilic nature of protein molecules that compose of hydrophobic and hydrophobic amino acids (17; 18). Hydrolysis of protein produce small peptide chains and amino acids which increase surface area among protein molecules with air, water and fat (16; 18).

Table 2 Physicochemical qualities and functional properties of protein powder from different extraction methods

Items	(unit)	Protein powder		Commercial Protein Specification (Nutrition Limited Partnership)
		Extraction method using inner enzyme	Extraction method using inner enzyme plus bromelain	
Color	(°EBC)	3.25± 0.25 [a]	3.38± 0.20 [a]	-
Water activity		0.267± 0.015 [a]	0.254± 0.030 [a]	<0.5
Moisture content	(%)	4.22± 0.35 [a]	4.10± 0.28 [a]	<5.0
pH		4.34± 0.15 [b]	6.22± 0.38 [a]	5.0-6.0
Solubility	(%)	92.14± 0.55[b]	98.16± 0.65 [a]	Completely soluble in water
Foaming ability	(%)	45.35± 1.12 [a]	26.26± 1.97 [b]	-
Emulsion activity index	(m^2/g)	10.74± 0.88 [b]	16.65± 0.70 [a]	-

Mean value±standard deviation of three replications. The different superscript in the same row was significant difference value at p≤0.05.

According to foaming property, protein powder hydrolyzed by using only inner enzyme from rice malt had significantly higher foaming property due to lower degree of hydrolysis. Cai et al. (22) also found that hydrolysis of pine nut (*Pinus gerardiana*) by alcalase at higher degree of hydrolysis resulted in decreasing of foaming property of protein. They indicated that at 5% degree of hydrolysis, foaming property of protein was higher than at 25% degree of hydrolysis and protein hydrolysate that composed of large peptide size over 10 kDa had good functional properties. Study of soybean hydrolysis using trypsin and chymotrypsin by Calderon de la barca et al. (23) showed that foaming and emulsifying properties of soybean hydrolysate hydrolyzed by trypsin and chymotrypsin decreased when decreasing of protein molecules.

Chemical properties of rice protein powder: The chemical properties of rice protein powder from large scale production using inner enzyme from rice malt and inner enzyme plus bromelain were compared as shown in Table 3. The protein powder obtained from protein hydrolysis using inner enzyme plus bromelain method had protein content of 9.06% significantly higher than 6.33% protein content of the method using only inner enzyme. However, the protein powder from the method using only inner enzyme contained more amount of soluble vitamin B_1, B_3 and B_6 than the method using inner enzyme plus bromelain because of the lower temperature during the extraction process. The different kinds and amount of amino acids in the protein powder obtained from different processes were detected. The results showed that the 3 main amino acids of the protein powder from the method using inner enzyme were glutamic acid followed by phenylalanine and aspartic acid respectively and were phenylalanine followed by glutamic acid and aspartic acid respectively for the protein powder from another method. Both protein powder from the two methods contained all essential amino acids and their amount were met the standard requirement of children (except methionine and lysine) and standard requirement of adults (except methionine) as recommended by FAO/WHO/UNU (24). However, it was found that the amount of bitter amino acids such as threonine, proline, glycine, valine. methionine, leucine and trypyophan in the protein powder obtained from the method using inner enzyme plus bromelain were higher than the method using only inner enzyme.

Table 3 Chemical properties of protein powder from different extraction methods

Items (unit)		Extraction method using inner enzyme	Extraction method using inner enzyme plus bromelain	FAO/WHO/UNU Child	Adult
Protein content	(g/100g)	6.33	9.06		
Vitamin	B1 (mg/100g)	0.72 (Claim High)	0.34 (Claim High)		
	B3 (mg/100g)	28.61 (Claim High)	6.82 (Claim High)		
	B5 (mg/100g)	3.03 (Claim High)	5.74 (Claim High)		
	B6 (mg/100g)	2.64 (Claim High)	0.52 (Claim High)		
Amino acid (mg/100g)	Aspartic acid	826.33 (11.21%)	1,089.47(10.95%)	3.4%	0.9%
	Threonine	280.06(3.80%)	350.29(3.52%)		
	Serine	363.28	404.42		
	Glutamic acid	1,222.74(16.59%)	1,325.96(13.32%)		
	Proline	392.46	580.43		
	Glycine	304.57	339.33		
	Alanine	384.15	479.19		
	Cystine	46.11	50.81		
	Valine	408.68(5.55%)	521.80(5.24%)	3.5%	1.3%
	Methionine	24.50(0.33%)	42.60(0.43%)	2.5%	1.7%
	Isoleucine	288.60(3.92%)	412.93(4.15%)	2.8%	1.3%
	Leucine	547.04(7.42%)	697.72(7.01%)	6.6%	1.9%
	Tyrosine	326.20	362.58(3.64%)		
	Phenylalanine	832.56(11.30%)	1,942.45(19.52%)	6.3%	1.9%
	Histidine	168.18(2.28%)	189.99(1.91%)	1.9%	1.6%
	Lysine	261.69(3.55%)	421.85(4.24%)	5.8%	1.6%
	Arginine	593.54	661.65(6.65%)		
	Tryptophan	52.78(0.72%)	78.54(0.80%)		
*Phenolic compound	(mg/100gGAE)	158.12± 15.65 [a]	153.46± 17.10 [a]	-	
*Antioxidant activity(%)		47.45± 2.55[b]	72.20± 4.55 [a]	-	
*ACE inhibitory activity (%)		27.50± 2.14[b]	26.43± 2.35[b]	-	

* Mean value±standard deviation of three replications. The different superscript in the same row was significant difference value at $p \leq 0.05$.

Conclusion: Extraction of protein from defatted rice bran by hydrolysis with inner enzyme from rice malt plus bromelain had an advantage in terms of higher % yield, soluble protein content, % ACE inhibition activity and antioxidant activity including lower amount of phytic acid. Moreover, functional properties of the protein powder obtained from this method such as solubility and emulsifying property were better than from the extraction method using only inner enzyme. However, the amount of some bitter amino acids in the protein powder processed by using inner enzyme plus bromelain were found more than the process using only inner enzyme.

.

References:
1. Korhonen M.P., Pihlanto A. Int. Dairy J. 2006; 16: 945-960.
2. Jiamyangyuen S.,Srijesdaruk V.,Harper W.J. Sci.Technol.2005; 27(1):55-64.
3. Chen L.,Houston D.F. Recovery of Protein.1970; 47: 72-79.
4. De Groot A.P., Slumps P. J. Nutr.1969; 98:45-56.
5. Thawornchinsombat S., Kokkaew H. Thai petty patent no.4844. 2008.
6. Puangwerakul Y., Suvimol Soithongsuk S. The 44th Congress on Science and Technology of Thailand (STT44). 2018.
7. Lowry O H, Rosebrough N J, Farr A L, Randall R J. J. Bio. Chem. 1951;193: 265-275.
8. Haug W, Lantzsch H J. J. Sci Food Agric.1983; 34(12):1423-1426.
9. Li G.H,Liu H.,Shi Y.H.,LeG.W.J.Pharm Biomed Anal.. 2005; 37:219-224.
10. American Association of Cereal Chemists. 20th Ed., AOAC. 2000.
11. Puangwerakul Y.,Soithongsuk. S.uvimol . Proceeding of RSU International Research Conference April,28. 2017.
12. Benjakul S.,Morrissey M. J Agri. and Food Chem.1997; 45: 3423-3430.
13. Konietzny U, Greiner R. Int. J. Food Sci. Technol.2002; 37(7):791-812.
14. Baruah K, Sahu N P, Pal A K, Debnath D. NAGA. 2004;27 (3): 15-19.
15. Liu B L, Rafig A, Tzeng Y M, Rob A. Enzyme Microbio. Technol. ;1998;22: 415-428.
16. Guo X., Zhang J., Ma Y., Tian S. J Food Process Pres. 2013; 37: 245-253.
17. Gennis R.B.,Jonas A. Annu. Rev. Biophys Bioeng. 1977;6 :195-238.
18. Panyam D., Kilara A. Trends Food Sci.Tech. 1996;71:120-125.
19. Saldivar S., Othon S.R. CRC Press Taylor&Francis Group,Boca Raton.2010:81-107.
20. Xie Z., huang J.,Xu X.,Jin z. Food Chem. 2008; 111: 370-376.
21. Ortiz M.S.E., Wagner J.R. Food Res. Int. 2002; 35:515-518.
22. Cai L., Xiao l., Liu C., Ying T. Food Bioprocess Tech. 2013;6: 2109-2117.
23. Calderon de la Barca A.M.,Ruiz-Salazar R.A., Jara-marini M.E. J. Food Sci. 2009;65:246-253.
24. FAO/WHO/UNU. (1985). Series No.724.1985. WHO Tech. Rep. : 121.

Acknowledgements: This study was financially supported by the Research Institute of Rangsit University Research Institute. The authors would like to thank the Thai Ruam Jai Vegetable Oil Co., Ltd. for the raw materials provided.

A_009_PF: EVALUATION OF FORMIC ACID IN CONTROLLING *Tropilaelaps* MITES IN LABORATORY

Puncharat Promsuvong, Kitiphong Khongphinitbunjong, Khanobporn Tangtrakulwanich*
Bioscience, School of Science, Mae Fah Luang University, Chiang Rai, 57100, Thailand
*e-mail: khanobporn.tan@mfu.ac.th

Abstract: The evaluation of formic acid at different concentrations to control bee mites (*Tropilaelaps mercedesae*) was compared by bioassay experiment using formic acid at concentrations 98%, 90%, 80%, 70%, and 60% and 0% as control treatment respectively. The result showed that there were significant differences ($P < 0.0001$) in increasing mortality rate of the mites among these concentrations. The 98% and 90% of formic acid could cause the mite to die within 1 hr after the mites were exposed to these concentrations. While the 60%, 70% and 80% concentrations of formic acid could cause the mortality to the mites after being exposed at least for 2 hrs. All pupae showed normal characteristics for 7 days after being exposed to every concentration of formic acid treatment. On the 8th day, all pupae in every concentration showed deflated abdomen, brown color of the bodies, none responsive nor movement which indicated mortality except for the control treatment. The pupae in the control treatment died on the 11th day after the experiment was started. Result of study showed benefit of using formic acid as miticide. However, further study is needed to verify the optimal concentration of formic acid to be applied in the field apiary.

Keywords: formic acid, pupae bee, *Tropilaelaps* mites

Introduction: Honey bees are social insects. There are classified into casts according to their roles and functions in their colonies. They are considered economic insects because their products can be used in food industry and some can be the ingredient of cosmetics. They are also good pollinators which make a lot of people want to rear them in order them in order to pollinate their plants. The most popular honey bee species which people rear around the world is European honey bee *Apis mellifera* L.[1] This species originated in Europe and was brought to Thailand since 1940 and kept in the Chulalongkorn University. However, the rearing activity of this European honey bees started in 1977.[2] Nowadays, rearing European honey bee has become popular in Thailand because farmers can get a lot of honey yield from rearing this species.[3] However, the bee keepers have faced with the problems of rearing this species. One of the biggest problem is the mite infestation. Along with to get rid of the mite infestation is very difficult.

There are two species of mites in Thailand infesting the European honey bees. These are *Varroa destructor* and *Tropilaelaps mercedesae* or *Tropilaelaps* mites. The two species of mites causing problem in beekeeping around the world are *Varroa* mites and *Tropilaelaps* mites. However, the *Tropilaelaps* mites are said to infest European honey bees in Asia only. There is still lack of information on this. The life cycle of and specific time to infest the honey bees is needed to be studied more in detail. The predominant problem of beekeeping in Thailand is *Tropilaelaps* mites.[1] *Tropilaelaps* mites causes injury to honeybee brood by direct feeding on bee blood "hemolymph". *Tropilaelaps* mites not seriously damage adult bees, if the infestation is not serve. However, *Tropilaelaps* is a brood disease. If the female mites infest brood cells deterioration will occur including distorted wings and shortened abdomen.

The current methods to control these mites which have been adopted by the beekeepers are manipulating the combs to capture the mites or using chemicals to fumigate in order to get rid of the mites. However, beekeepers tend to use chemical methods because it gives a good and fast result in getting rid of the mites.

Using chemical to control mite infestation during the flowering of plants results in contamination of chemical in honey product and harmful for honeybees. However, the

beekeepers still choose this method because of rapid result and they can be sure the mite infestation will be in control. The chemicals that they use can be Sulphur combine with naphthalene to fumigate the combs or by using Folbex VA paper tape inserting in the combs. And the Folbex VA chemicals will be released inside the comb.[4]

Another approach to control the mites is to use the chemicals which is not harmful to the bees but it can kill the mites. Formic acid could be the candidate for serving as alternative chemical. Actually formic acid is a natural chemical produced by some insects. Formic acid is an irritating chemical present in the sprayed venom of some ant species and in the secretion released from some stinging insects. It is a relatively inexpensive treatment for *Tropilaelaps* mites. And there is a gaining in popularity of using formic acid to resist the mite infestation compare to other treatment.[5] However, formic acid can reduce worker longevity.[6] And when apply formic acid to control mites, the dosage concentration must be in concerns. The high dose of formic acid can also become dangerous to the honey bees. At high concentration, it can become corrosive and produces dangerous fume.[7] Therefore, the appropriate concentration of formic acid is very important. The concentration must be able to kill the mites but cause no adverse effect to the honeybees.

Because incidence of the *Tropilaelaps* mites have increased dramatically, therefore this study was aimed to investigate the appropriate concentration of formic acid to inhibit mite infestation and cause no harm to the European honeybee.

Methodology:

Preparation of Tropilaelaps mercedesae and pupae bees: The mites and honey bee pupae were kindly provided by Dr. Kitiphong Khongphinitbunjong and Miss Krisana Narapong, School of Science, Mae Fah Luang University.

Experiment1 (Investigation of Effect of Formic Acid Concentrations on Tropilaelaps mites): The Whatman filter paper was cut into pieces (1x3cm). The pieces of paper were dropped the formic acids with the concentrations of 98%, 90%, 80%, 70% and 60% with the volume of 20 microliters respectively. Each concentration on the paper was placed in the glass tube with the length of 20 cm at one end of the tube. Twenty microliters of distilled water were dropped at the Whatman filter paper which were size of 1x3 cm and placed in the other end of the glass tube to serve as control treatment. Six pupae of honeybees were released to the tube and the number of individual moving to either end of the tube were observed at the time of 1 hour, 2 hours, 3 hours, 12 hours, 24 hours, and 48 hours, respectively. The experiment was arranged in Completely Randomized Design (CRD). And each treatment was replicatesd three times.

Experiment2 (Investigation of Effect of Formic Acid Concentrations on Honeybee Pupae): The arrangement of the experiment was the same as described in Experiment1. But for the Experiment 2 the 11 mites were released to the glass tube and the number of individuals moving to either end of the tube was observed at the time of 1 hour, 2 hours, 3 hours, and every 12 hours until 12 days, respectively. Observation to change of pupae bee from white eye to pink eye. The concentrations of formic acid tested in this experiment were the same as the concentrations tested in Experiment 1. The control treatment was also distilled water applied in the piece of paper and placed at one end of the glass tube. The experiment was arranged in Complete Randomized Design (CRD). And each treatment was also replicated three times.

Data collected from Experiment1 and Experiment2 were calculated for percentage of repellency using this formula:

$$PR = (Nc - Nt / Nc + Nt) \times 100$$

PR= Percentage of repellency

Nc= Number of individuals in control

Nt= Number of individuals in treatment

The statistical tool to analyze the data was One Way Analysis of Variance. The multiple comparisons were compared by Duncan's multiple range test.

Results:

Investigation of effect of formic acid concentrations on Tropilaelaps mites: There were significant differences in increasing mortality rate of the mites among formic acid at concentration 98%, 90%, 80%, 70%, 60%, compared to control treatment (0%) respectively (P<0.0001, Figure 1). The most effective concentration which could kill the mites were 90% and 98 % of formic acids. The mites died within 1 hour after being exposed to these concentrations. There were no significant differences in efficacy of formic acids at the concentrations of 90% and 98%. The formic acid concentrations of 60%, 70%, and 80% did not show any significant differences in causing death to the mite. And these concentrations of 60%, 70%, and 80% showed the efficacy of causing death to the mites after the mites were exposed to them within 2hrs.

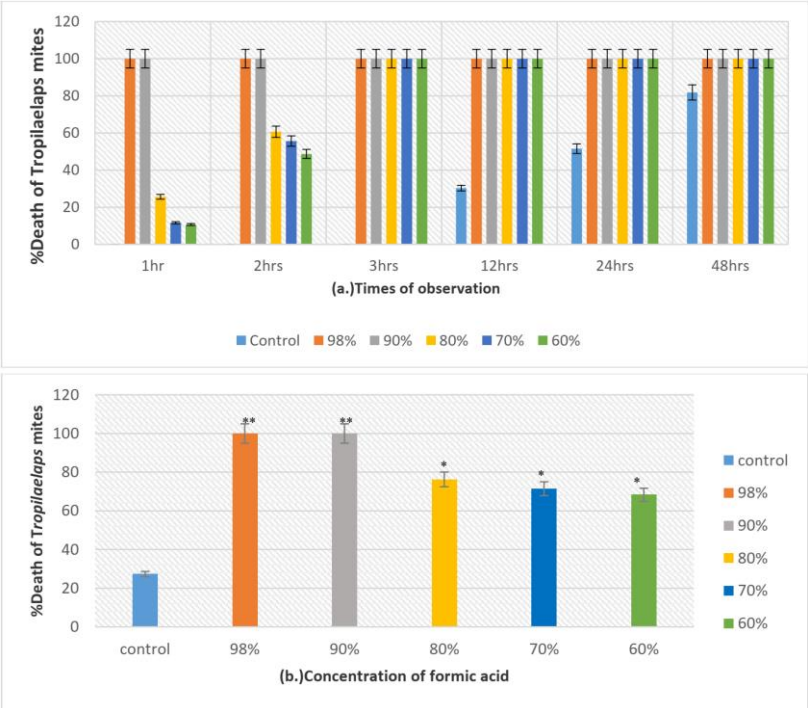

Figure 1. Average of percent death for investigation effect of formic acid concentrations on *Tropilaelaps* mites. (a.) Times of observation and (b.) Observed the concentration of formic acid within 48 hrs. (*, **) indicate significant differences at P<0.05 (ANOVA followed by Duncan's multiple range test, SPSS version 21)

Investigation of effect of formic acid concentrations on pupae bee: There was no effect of these formic concentrations on the *Apis mellifera* pupae within the first 7 days after having been exposed to the acids. All pupae showed normal characteristics. On the 8th day, all pupae in every concentration showed deflated abdomen, brown color of the bodies, none responsive nor movement which indicated mortality except for the control treatment. The pupae in the control treatment died on the 11th day after the experiment was started.

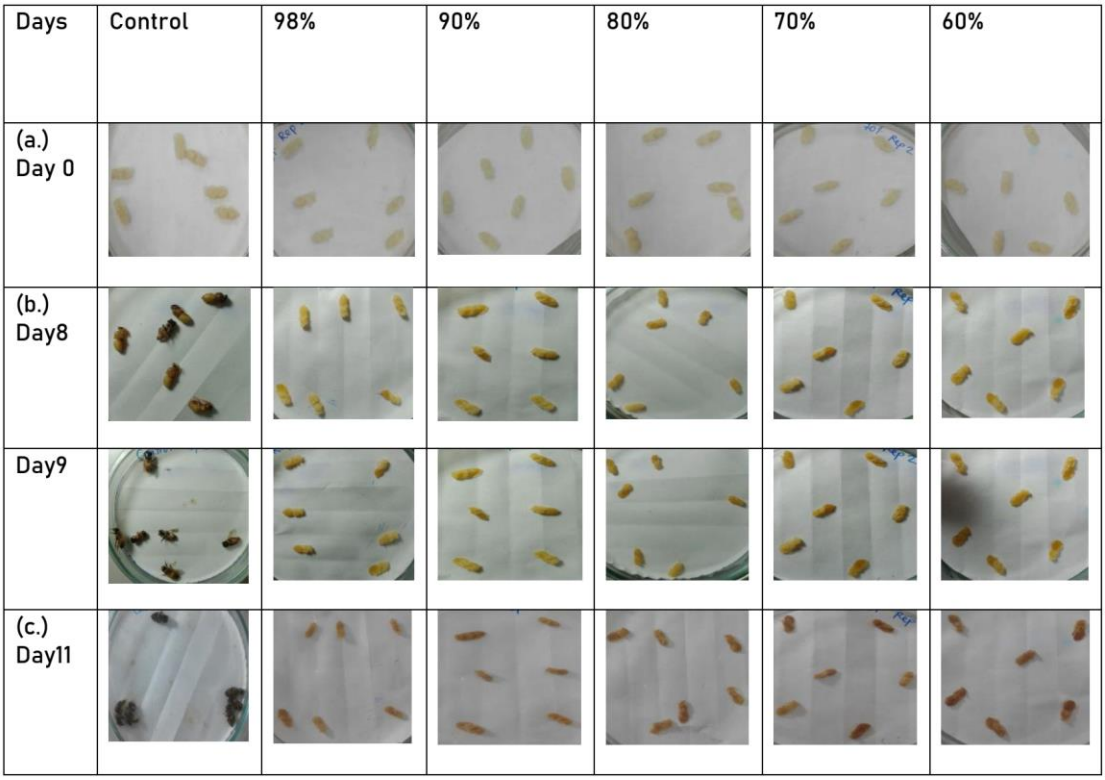

Figure 2. Average of percent death for investigation effect of formic acid concentrations on Pupae bees. (a.) Observed the characteristic of pupae on day 0 (b.) Observed the characteristic of pupae on day 8 (c.) Observed the characteristic of pupae in day 11.

Discussion: The bioassay presented in our study showed that formic acid can be an inexpensive product to be used as acaricide. Our result revealed that the concentrations of 90% and 98% had the same efficacy in killing the *Tropilaelaps* mites after the mites were exposed to these concentrations within 1 hr. When the lower concentrations were exposed to these mites such as 60%, 70% and 80% of formic acid liquid solution, the mites died more slowly than the concentrations of 90% and 98%. Formic acid was tested to control the *Varroa* mites from many studies.[8] Their results showed that the formic acid was effective in controlling the *Varroa* mites which were similar as our results. "Soft" acaricides[9] like formic acid, oxalic acid, lactic acid and thymol are active compounds that present a low risk of residues in hive products. Among them, formic acid is the only one that is effective both against phoretic (on bees) and reproductive phases (in the capped brood) of the mite[9] it has been largely applied by beekeepers and studied since the '80s in European countries.[10] However, the disadvantages of formic acid treatments could be: mortality of the queen, depletion of the colony, swarming of the hive and reduction in productivity.[11] When we tested all concentrations of formic acid with the bee pupae, we did not find the mortality occur in bee pupae at any concentration during the first 7 days of being exposed to the formic acid. However, all pupae died on the 8th day after being exposed to the formic acid at every concentration tested except for the control (0% concentration). The pupae in control treatment could continue living until the 11th day and then died off. There was a report that formic acid suppressed the brood area and colony production.[12] Some studies found that formic acid could improve bee colonies that were more heavily infested with *Varroa* mites [13] and formic acid also

can have a negative effect on colony well-being.[14] However, all these studies were conducted in the field apiary not in the laboratory condition as our study.

Conclusion: Our result showed clear benefit to the use of formic acid to get rid of the *Tropilaelaps* mites infesting the *Apis mellifera*. However, it was very difficult to determine the exact concentration of the formic acid to be effective in killing the mites but had no adverse effect on the pupae. Further study is needed to verify the optimal concentration of formic acid to be applied in the field apiary.

References:

1. Wongsiri S, Chanchao C, Deowanish S, Aemprapa S, Chaiyawong T, Petersen S, Leepitakrat S. Bee World. 2000; 81:20-29.
2. Winston ML, Otis GW, Taylor Jr OR. J Apic Res. 1979; 18: 85-94.
3. Oottamadilok K. Master Thesis, Chulalongkorn University. 1982. 15pp.
4. Marchetti S, Barbattini R, d'Agaru M. APIDOLOGIE. 1984; 15:363-378.
5. Elzen PJ, Eischen FA, Baxter JR, Elzen GW, Wilson WT. APIDOLOGIE. 1999; 30:13-17.
6. Underwood RM, Currie RW. EXP APPL ACAROL. 2003; 29: 303-313.
7. Malviya, R, Chaudhary R. J. Hazard. Mater. 2006; 137: 267-276.
8. Pettis JS, Rose R, Chaimanee V. PLoS One. 2017; 12:doi.org/10.1371/journal.pone.0188063.
9. Rosenkranz P, Aumeier P, Ziegelmann B. Pathol. 2010; 103:96-119
10. Elzen, PJ, Westervelt D. Am. Bee J. 2002; 142: 291-292.
11. Bolli HK, Bogdanov S, Imdorf A, Fluri P. APIDOLOGIE. 1993; 24:51-57.
12. Ostermann D, Curries R. J Econ Entomol. 2004; 97:1500-1508.
13. Hoppe H, Ritter W, Stephen EWC. Am Bee J. 1989; 129: 739-742.
14. Ostermann,DJ. Master thesis, University of Manitoba, Canada. 2002. 20pp.

Acknowledgements: I would like to express my appreciation to our senior project advisor, Dr. Khanobporn Tangtrakulwanich and co-advisor, Dr. Kitiphong Khongphinitbunjong for guidance and encouragement. Without valuable assistance, this work would not have been completed. I am deeply grateful for experimental place at Mae Fah Luang University.

The special acknowledgement goes to Miss. Krisana Narapong and Miss Benyapa Ruangwut for their support and cooperation.

A_010_PF: EFFICACY OF NATIVE PLANT EXTRACTS (GINGER AND MARIGOLD) IN CONTROLLING RICE WEEVIL: *Sitophilus oryzae* L.

Kanchana Kiriyadee, Wimonsiri Kaewsamer, Wisanu Maneerat, Khanobporn Tangtrakulwanich*
Bioscience, School of Science, Mae Fah Luang University, Chiang Rai, 57100, Thailand, School of Science.
*email: khanobporn.tan@mfu.ac.th

Abstract: The bio-assay was conducted under laboratory condition in order to investigate the efficacy of 2 plant extracts, marigold (*Tagetes erecta* L.)and ginger (*Zingiber officinale* Roscoe) in order to investigate the efficacy of each extracts in controlling rice weevil (*Sitophilus oryzae*). The experiments were set as the repellency test, fumigant test, and contact toxicity test. The solvents used in the crude extraction were hexane, ethyl acetate, and dichlolomethane, respectively. Repellency test revealed that there was no significant in efficacy of both crude extracts in repelling rice weevil. The fumigant test showed that ginger crude extract had more efficacy in knocking down the weevils than marigold did when ethyl acetate and dichlolomethane were used as solvents for extraction. For the contact toxicity test, ginger crude extract showed higher potential in increasing mortality than the marigold extracts when hexane was used as solvent in extraction. Overall results, ginger crude extract showed more promising efficacy in controlling rice weevil than the marigold crude extract. The GC/MS analyses revealed that ginger crude extract had the main compounds as Hexamethylcyclotrisiloxan (27.159%) Octamethylcyclotetrasiloxane (12.928 %) and 1,3,3-Trimethyl-2-Oxabicyclo[2.2.2]octan-6-ol (11.005 %) respectively. Further study is needed to verify the bio active compound affecting the rice weevils.

Keywords: Ginger, Marigold and Controlling Rice Weevil

Introduction: Rice is a cereal that is one of the most important to the people of Asia. Most of these people are consuming rice as the main food. Rice is consumed or processed into product which rice is harvested, abraded, and polished. After that the processed rice will be stored in shed. It has been found that in many countries where rice and wheat are grown in warm climate area, the dominant insect which destroys rice is the rice weevil, *Sitophilus oryzae L.*[1,2] This insect can damage both paddy field and harvested rice. The insects damaging rice start at the female using her mouth to penetrate the leaf of the rice to lay eggs. Eggs are laid within individual kernels. The grub-like larvae consumes the grain from within. Pupation occurs in the kernel and then the adult will penetrate the rice causing small round hole leaving behind a hollow kernel and leads to loss of nutrients within the grain.[3] The level of insect infestation is an important quality factor of food grains and represents a serious and continuing problem for the grain and milling industries. Growing rice is the main occupation of farmers in Northern Thailand. For storage of rice in the upper north, most of farmers store harvested rice in sacks.[4] From the annual rice yield, there is a loss of productivity at every stage of harvesting. The total loss of all steps is about 16.83% and most of the loss occurs during storage which is about 5%.[5] The major problem that occurs while storing harvested rice is the destruction of insect pests in the ware house and rice weevil is one of the major insect pests that destroy rice in the ware house. Prevention and getting rid of rice weevil consist of chemicals and non-chemical techniques to get rid of rice weevil. However, these chemical use is expensive.[6] Another way to prevent rice weevil is fumigation which is highly effective way but the rice will be contaminated by the fumigant.[7] Therefore the way to control rice weevil which is not expensive and not harmful is very important.

In Thailand, there are many varieties of plants. It has been recorded that all plant species found in Thailand are around 12,000 species. Among these plants, more than 1000

species produced bioactive substances. Especially used as a traditional medicine for the treatment of diseases.[8] In addition, the intellectual knowledge in controlling insect pests has been adopted from generation to generation. Extracts from herbs can be used to control insect pests in grains. [9,10,11] According to the documented study, the plant essential oils such as monoterpenes, D-limonene, linalool and terpeneole were found to inhibit the rice weevil feeding activity.[12] Marigold (*Tagetes spp.*) has the smell that can repel a lot of insects. [13] Moreover, the root of ginger (*Zingiber officinale* Roscoe) has been shown to deter insect and activities. [14] The chemicals found in marigolds are pyrethrin, carotent, D-limonene. These chemicals have bad foul odors which agitate most insects and cause them to escape from the plant. Zingiberene, zingiberol and bisabolene are found in ginger rhizomes. These chemicals also have the property of repelling many insects.[14] This study is aimed to investigate the efficacy of crude extracts of marigold and ginger rhizome in controlling the rice weevil. If the result shows that extracts from these plants can have negative effect on rice weevil, it can be used to be an alternative approach to control rice weevil which is good for environment. Moreover, it can lead to promote the use of native plants to control pests instead of purchasing expensive chemicals that have serious adverse effect on the rice products and environment.

Methodology:

Extraction crude extract: The plant samples were extracted to get the crude. The solvent used for extraction will be hexane, ethyl acetate, and dicholomethane respectively. The crude extracts will be used to conduct repellency test, fumigant test, and contact toxicity test of the rice weevil. After that, the crude extracts which show promising result in controlling rice weevils will be investigated for bio active compounds by using gas chromatography-mass spectrometry (GCMS).

Rearing Insects: The adult rice weevil *Sitophilus oryzae* L were collected from the rice sacks which have infested with this insects. After that, the rice weevils were kept at the plastic box containing 5 kilograms of rice. The box were left for a few days to have the insects mate and increase in numbers. The plastic box were kept in the laboratory laboratory at 29-32°C relative humidity 70-80%. When the experiment is started, the insects were collected from this box and sorted for the adult insects which have the age of 7 days.

Bioassay Study Test the efficiency extracts of essential oils and insect repellents (Repellency Test): The crude extracts were mixed with solvent and made them to the concentrations of 0.5, 1.0, 1.5, 2.0 and 2.5% respectively. Two hundreds microliter of each concentration were dropped on the 1 x 1 cm Whatman No. 1 filtered paper. Then the dropped filter paper were placed on one end of the glass tube with 20 cms in length. The other end of the tube were the 1x1 cm of filtered paper which has the 200 micro litter of each solvent to serve as control treatment. Twenty individuals of 7 days old rice weevils were released to the glass tube. A para film were used to seal both ends of the tube to prevent insects from escaping the tube. The numbers of individuals going to either end (treatment VS control) were observed at 1, 2, 3, 4, and 5 hours respectively.

After that, data were calculated for the percentage of repellency using the formula:

$$PR = (Nc-Nt/(Nc+Nt) * 100$$

PR = Percentage repellency
Nc = number of insects found on Control
Nt = number of insects found on Treatment

Calculated data were analyzed by One Way Anova. The multiple comparison were analyzed by Duncan's Multiple Range test.

Fumigant Test: The filter paper with the size of 1.5 x 4 cm were dropped with the crude extracts with the concentrations which showed the good results from the repellency test. That

candidate concentration were calculated for the volume of 55, 70, 85, and 100 microliter respectively. The paper which has been dropped with each volume will be set dry for 2 minutes and placed under the cap of 50 ml Duran bottle. The 20 individuals of rice weevils were released to the bottle. Then the bottle were closed tightly with the caps which has the filter paper placed underneath. The mortality date were observed at 6, 12, and 24 hrs. The control treatments were each solvent (hexane, ethyl acetate, di chloromenthane applied in the same manner as described above. Each treatment will be repeated 5 times. The information were analyzed by One Way Anova and the multiple comparison will be done by Duncan's Multiple Range Test.

Contact Toxicity Test: The Whatman filter paper No. 1 were placed in a glass petri dishes which have the diameter of 9 cm. After that, the 1 milliliter of the crude extracts with the concentration of 0.5, 1.0, 1.5, 2.0 and 2.5 % respectively. The prepared paper was let dry at the room temperature for 3-5 minutes. The 20 individuals of rice weevils were released in the petri dishes and the caps of the petri dishes were sealed tightly and wrapped with Para film. The mortality rate were observed at 24, 48, and 72 hours respectively. All treatments were repeated 5 times. The data were analyzed by One Way Anova and the multiple range comparison were done by Duncan's Multiple Range Test.

Results:

Percent Yeild: The percent yield of crude extract from ginger when hexane, Dichoromethane, and Ethyl Acetate were used as solvents for extraction were 0.0378%, 0.6837%, 1.0835% respectively. And the percent yield of crude extracts from marrigold when hexane, Dichoromethane, and Ethyl Acetate were used as solvents for extraction were 1.0125%, 4.5372%, and 13.5101% respectively.

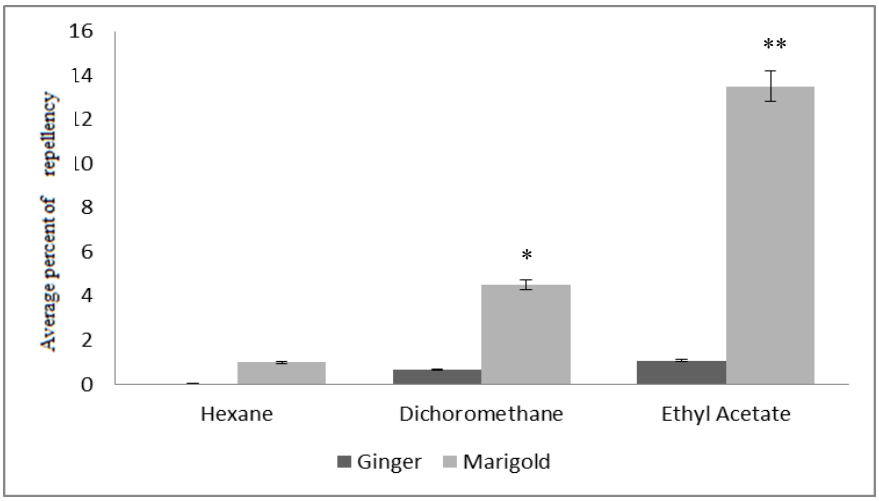

Figure 1. The percent yield of crude extract from ginger when hexane, Dichoromethane, and Ethyl Acetate were used as solvents for extraction process. (*,**) indicate significant differences at $P < 0.05$ (ANOVA Followed by Duncan's Multiple Range test, SPSS version 21).

Repellency Test: The result of repellency test showed that there were no significant differences in efficacy of ginger crude extract and marigold crude extracts when hexane, ethyl acetate, and dicholomethane were used as solvents in extraction process. Both crude extracts from three solvents showed the average percentage of repellency of 60%.

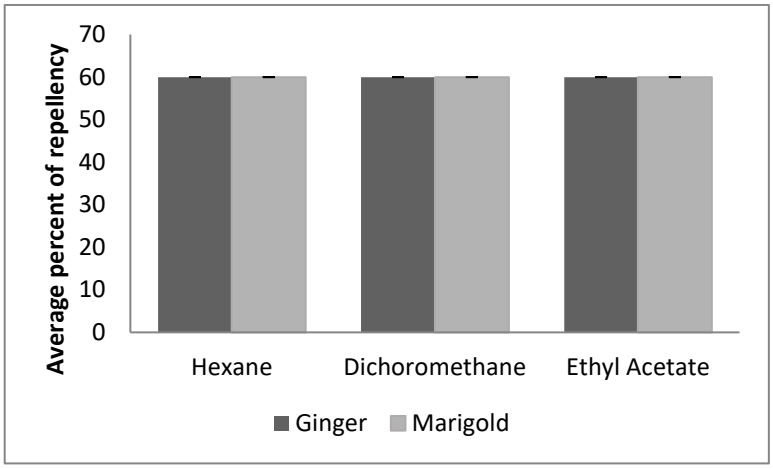

Figure 2. eThe average percent of repellency in efficacy of ginger crude extract and marigold crude extracts when hexane, ethyl acetate, and dicholomethane were used as solvents in extraction process.

Fumigant Test: The result of fumigant test revealed that ginger crude extract had more efficacy in increasing mortality of rice weevil than marigold crude extract when ethyl actate and dicholomethane were used as solvents for extraction (Figure 1, 2). But when hexane was used as solvent for extraction, there was no significant differences between ginger and marigold crude extracts in causing the mortality in rice weevils. Ethyl acetate and dicholomethane fumigant test showed the efficacy of killing the insects within 6 hrs after the insects were exposed to the crude extracts whereas hexane fumigant test showed the efficacy of killing insects after 24 hrs when insects were exposed to the crude extracts (Figure3). There were no differences in concentrations used among crude extracts in causing the mortality of insects.

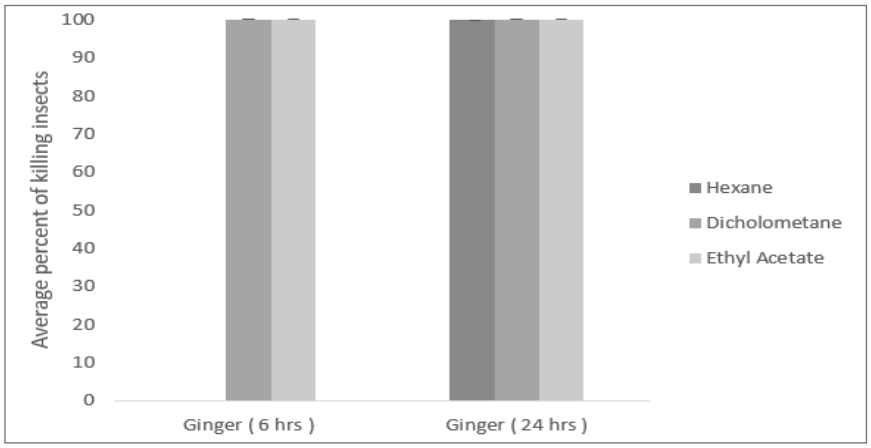

Figure 3. The average percent of fumigant test of ginger when hexane, ethyl acetate, and dicholomethane were used as solvents in extraction process.

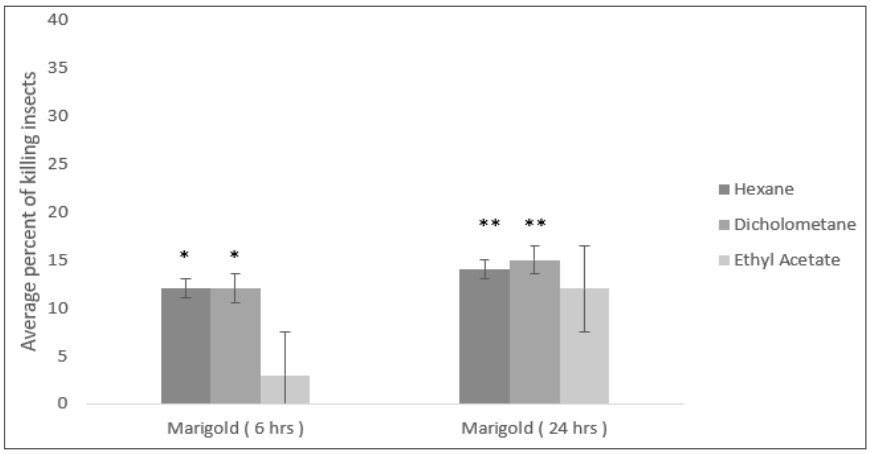

Figure 4. The average percent of fumigant test of marigold when hexane, ethyl acetate, and dicholomethane were used as solvents in extraction process. (*,**) indicate significant differences at P < 0.05 (ANOVA Followed by Duncan's Multiple Range test, SPSS version 21).

Contact Toxicity Test: The result of contact toxicity test showed that ginger crude extract had higher potential in causing mortality in rice weevils than marigold crude extracts when hexane was used as solvent in extraction (Figure 5). And both crude extracts showed higher potential in killing insects after 24 hrs when insects were exposed to the treatments. There was no significant differences in concentrations used among the crude extract in causing the mortality of insects. There was no significant difference in efficacy of ginger and marigold crude extracts in increasing mortality of the insects when ethyl acetate and dicholomethane were used as solvents for extraction.

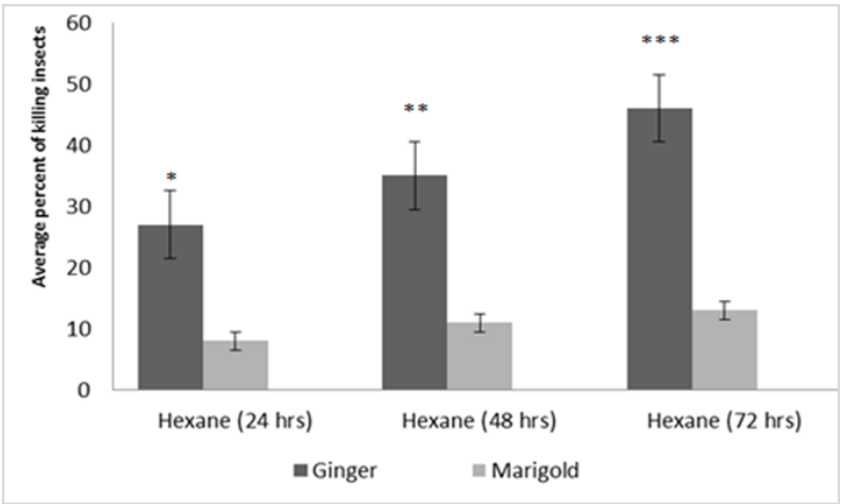

Figure 5. The average of contact toxicity test of ginger crude extract and marigold crude extracts when hexane, ethyl acetate, and dicholomethane were used as solvents in extraction process. (*,**,***) indicate significant differences at P < 0.05 (ANOVA Followed by Duncan's Multiple Range test, SPSS version 21).

Gas chromatography and Mass spectrometry (GC/MS) Analysis: The GC/MS analyses showed that ginger crude extract had the main compounds as Hexamethylcyclotrisiloxan (27.159%) Octamethylcyclotetrasiloxane (12.928%) and 1,3,3-Trimethyl-2-Oxabicyclo[2.2.2]octan-6-ol

(11.005 %) respectively. For the GC/MS analysis of marigold crude extract, the main compounds revealed from this analysis were 2,2,4,6,6-pentamethylheptane (37.023%) *n*-Heptane (28.462%) and 3-methylpentanal (10.149%) respectively (Table 1,2).

Table 1. The list of chemical constituents identified from crude extract of ginger (*Zingiber offinale* Roscoe)

No	RT	Chemical Compounds	% area
1	3.3841	Hexamethylcyclotrisiloxane	27.159
2	4.0659	*N*-Ethyl-1,3-dithioisoindoline	6.579
3	7.0737	6-Methyl-5-hepten-2-one	3.911
4	7.2727	Octamethylcyclotetrasiloxane	12.928
5	14.5638	α-Terpinolene	6.844
6	15.9176	1,3,3-Trimethyl-2-Oxabicyclo[2.2.2]octan-6-ol	11.005
7	16.1525	p-Menth-2-en-7-ol	6.656
8	16.6614	*cis*-1,3,3-Trimethyl-2-oxabicyclo[2.2.2]octan-5-ol	2.711
9	17.2552	δ-3-Carene	4.807
10	17.4378	4-Iodo-2,6-dioxa-adamantane	6.198
11	26.6471	1-(1,5-Dimethyl-4-hexenyl)-4-methylbenzene	5.042
12	27.1593	α-Cedren i	2.581
13	27.6715	β-Bisabolene	1.687
14	28.2587	β-Sesquiphellandrene	1.893

Table 2. The lists of chemical constituents identified from crude extract of marrigold (*Tagetes erecta*)

No	RT	Chemical Compounds	% Relative peak area
1	0.7972	2-Methyl-Butanal	2.591
2	0.9636	Methyl-cyclopentane	1.467
3	1.1267	Cyclohexane	0.902
4	1.952	3-methylpentanal	10.149
5	2.1086	Cyclohexane	4.022
6	2.4609	*n*-Heptane	28.462
7	3.1166	1-Methylcyclopentanol	5.741
8	3.3744	*N*-Ethyl-1,3-dithioisoindoline	5.637
9	7.0803	2,2,4,6,6-Pentamethylheptane	37.343
10	8.2579	2,2,4,4,6,8,8-Heptamethylnonane	3.27
11	11.6539	3,6-Bis-(*N,N*-dimethylamino)-9-methylcarbazole	0.416

Discussion: Repellent and insecticidal activity of two plant extracts were tested on rice weevils (*Sitophilus oryzae*). The solvents used in the extraction procedure were hexane, Ethyl Acetate and Dicholoromethane. From the result Ethyl Acetate being used as solvent in extraction procedure showed the highest amount of percent yield in both ginger (*Zingiber officinale* Roscoe) and marigold (*Tagetes erecta* L.). Dicholoromethane when used as solvent in extraction gave the second highest yield but hexane used as solvent gave

the lowest yield. When repellency test was conducted, the result showed no significant differences between the two plant extracts in the ability to repel insects. Other study conducted by.[15] revealed that the essential oil of ginger could repel the maize grain weevil (Sitophilus zeamail Motchusky). Their result supported our study that ginger could repel the rice weevil. Marigold (*Tagetes erecta* L.) crude extract was reported to repel the mosquito when extracted with ethanol. [16] However, their study showed that the potential of marigold as repellent was not that effective. Our repellency test was not set quite effectively during the experiment. We chose the test tubes and released the insects, let insects choose which arm of the test tubes they would go between the treatment arm (crude extract) and the control arm. We did not perform the experiment in the dark. The light could interfere with the way the insects chose because insects tend to go the arms which brighter than the darker ones. Our fumigant test revealed that ginger crude extract had more efficacy in increasing mortality of rice weevil than marigold crude extract when ethyl actate and dicholomethane were used as solvents for extraction and both plant crude extracts showed the efficacy of killing the rice weevils faster than when hexane was used as solvent in extraction. As we mentioned above, Ethyl Acetate gave the highest yield when used as solvent in extraction and followed by Dicholomethane. The higher amount of yield may have given the higher amount of active compounds that can increase the mortaility rate of insects. Ethyl Acetate and Dicholomethane have higher polarity of solvent than hexane. Ethyl Acetate was reported to be killing agent for insects. [17] The Ethyl Acetate we used in the fumigant test as solvent for extraction could have synergistic effect with plant crude extracts and cause high mortality of the rice weevils. Dicholomethane has been used in many crude extractions nowadays because of its polar and miscible with many organic solvents.[18] However, there has been no report that Dicholomethane itself can kill insects.Hexane is non polar solvent and can be used to extract compounds which can be soluble in it. However, the two plants when extracted by hexane did not give such high yield. This could be that both ginger and marigold could be extracted for more yield if the high polarity of solvents are used. From our contact toxicity test, ginger crude extract from hexane showed higher mortality of insects than marigold crude extract from the same solvent. And the effect of the hexane ginger crude extract on killing the rice weevils occurred within 24 hrs. From our result ginger crude extract seemed to work better to control rice weevils compared to marigold crude. However, the efficacy of the ginger extract depends on the solvent used for extraction and depend on the mode of action that it will be applied as repllent, fumigant or contact toxicity. Ginger was reported to have Zingiberene, Zigiberol and Bisabolene which have ability to repel insects. [19] However, only β-Bisabolene was revealed from our GC/MS analysis. Marigold plants produce a number of potentially bioactive compounds, among which α-therthienyl is recognized as one of the most toxic. This sulfur-containing compound is abundant in marigold tissues, including roots. It has nematicidal, insecticidal, fungicidal, antiviral, and cytotoxic activities, and it is believed to be the main compound responsible for the nematicidal activity of marigold.[20] However, our GC/MS analysis did not show such compound.

Conclusion: Ginger and marrigold have potential to be used as natural insecticide to control rice weevil. However, further study is needed to be conducted to verify the potential of these extracts when use as repellent. The mode of action which gives the highest potential in controlling the rice weevil could be as fumigation. The result of this study can be applied in pest management in stored product.

References:

1. Sinha AK, Sinha KK. J Stored Prod Res.1990; 26: 223-226.
2. Bata YA. Crop Prot. 2004; 23:103-108.
3. Kamara JS, Kanteh SM, Bockari-Gevao SM, Jalloh S. Int J Agri For. 2014; 4:19-23.

4. Oudtakarn N. J Wittayakarn Chadkarn.2006; 3: 84-94.
5. Tienchoompol P, Noimanee P, Pankasemsook T, Chanbang Y, Klaitin R, Ketnak K. Postharvest Newsletter. 2015;14: 1-3.
6. Toonthisong S, Choomchaihan P. 2013. The 14th TSAE National Conference and the 6th TSAE 2013. (in Thai)
7. Zettler JL, Cuperus GW. J Econ Entomol. 1990; 83: 1677-1681.
8. Wanset S, Onchomchant D. J. Thai Traditional & Alternative Medicine. 2018; 16:421-453.
9. Su HCF. J Entomol Sci. 1990; 25: 16-20.
10. Malik MM, Naqvi SHM. J Stored Prod Res. 1984; 20: 41-44.
11. Dunkel FV, Sears LJ. J Stored Prod Res. 1998; 34: 304-321.
12. Tripathi AK, Prajapati V, Gupta R, Kumar S. JMAPS. 1999; 21: 408-430.
13. Kimutai A, Ngeiywa M, Mulaa M, Njagi PGN, Ingonga J, Nyamwamu LB et al. BMC Res Notes. 2017; 10: 1-9.
14. Amuji CF, Echezonal BC, Dialoke SA. IJAT. 2012; 8: 2023-2031.
15. Yang K, Wang CF, You CX, Geng ZF, Sun RQ, Guo SS, Du SS, Liu ZL, Deng W. J Asia-Pac Entomol.2014; 17: 459-466.
16. Amrutha P, Priya BS, Lakshamamasenthil S, Jenifer AA, Pillai LS, Suja G, Vinothkumar T. ICPJ. 2013; 2: 170-176.17.
17. Loru L, Sassu A, Fois X, Pantaleoni RA. Int J Entomol. 2010; 46: 422-424.
18. Rossberg M, Lendle W, Pfleiderer G, Togel A, Dreher EL, Langer E, Mann T. Chlorinated hydrocarbons. Ullmann's Encyclopedia of Industrial Chem. Wiley-VCH Weinheim. 2006. doi:10.1002/14356007.a06_233.pub2
19. Limpaphayom V, Laohakunjit N, Duzzadeelawan P, Vamasiri K. KUMTT Res Develop J. 2014; 37: 297-312.
20. Topp E, Millar S, Bork H, Welsh M. Effects of marigold (Tagetes sp.) roots on soil microorganisms. Biol Fert Soils. 1998; 27:149-154.

Acknowledgement: We wish to express our appreciation to our senior project advisor, Dr. Khanobporn Tangtrakulwanich and Co-advisor Dr. Wisanu Maneerat for advice, guidance and encouragement throughout the course of our study. We are deeply grateful for experimental place at Mae Fah Luang University.

A_013_OF: EVALUATION OF THE CYTOTOXICITY AND GENOTOXICITY OF THE EXTRACTS FROM *Halymenia durvillei*

Athit Chaiwichien[1], Supawadee Osotprasit[1], Tepprit Samrit[1], Pornanan Kuekai[1], Krai Meemon[2], Nakorn Niamnont[3], Montakan Tamtin[4], Prasert Sobhon[2], Narin Changklungmoa[1,*]
[1]Faculty of Allied Health Sciences, Burapha University, Long-Hard Bangsaen Road, Saen Sook Sub-district, Mueang District, Chonburi 20131, Thailand
[2]Department of Anatomy, Faculty of Science, Mahidol University, Rama VI Rd., Bangkok 10400, Thailand
[3]Department of Chemistry, Faculty of Science, King Mongkut's University of Technology Thonburi, Bang Mod, Bangkok 10140, Thailand
[4]Phetchaburi Coastal Aquaculture Research and Development Center, Coastal Aquatic Feed Research Institute, Phetchaburi 76100, Thailand
*e-mail: narin_bio@hotmail.com

Abstract: *Halymenia durvillei* (HD), a species of Madagascar marine coasts red algae, is believed to have potential for pharmacological, nutritional and cosmetic applications. However, such potentials only make sense when devoid of any adverse on health consequences. Thus, the aim of this work was to investigate cytotoxicity and genotoxicity of ethanolic (HD-ET) and aqueous (HD-AQ) extracts. The cytotoxicity was evaluated by MTT assays in L929 and HaCaT cell lines. The genotoxicity was studied by comet assay and micronucleus test in TK6 cell line. The cytotoxicity studies indicated low toxicity to non-toxicity of HD-ET and HD-AQ. In addition, HD-ET and HD-AQ did not show genotoxicity *in vitro* against TK6 cells, at 10–1000 µg/ml. In conclusion, *H. durvillei* at popular concentrations used (or popularly used concentrations), in nutraceuticals or infusion, may be consumed safely because it did not show any cytotoxic or genotoxic effects in in vitro. This is encouraging and justifies further investigation on studies in *in vivo* to confirm the safety of *H. durvillei* extracts.

Introduction: Algal products have been used in many applications such as for the food, nutraceutical, cosmetic and pharmaceutical industries and also pollution control such as water treatment [1]. Macroalgae or seaweeds contain many bioactive substances like polysaccharides, proteins, lipids, polyphenols, flavonoids, carotenoids, etc., their many properties give seaweed as a great potential supplement in functional food and for the extraction of compounds. Commercially carotenoids are used as food colorants and in nutritional supplements, with an estimated global market for US$ 935 million dollars in 2005. Taking only the pair of astaxanthin–canthaxanthin in the international market in 2000, can easily be reached to amount of 150 million US dollars/year [1]. Regarding agar of algae, agar is a valuable and expensive product in the market, about 10,000 tons of agar are produced worldwide from species of the red algal families *Gelidiaceae* and *Gracilariaceae*, reported to be valued at US$200 million [2]. In last 25 years, the market of carrageenan, most of agar from algae has grown by at least 5% per year. In 1996, the Philippines exported $94 million worth of carrageenan from farm raised and natural sources of *Eucheuma cottonii* and *Eucheuma spinosum* [2]. In present, the cosmetic prospective of the large variety of algae species have more received increasing interest. Currently, there are ranges of pharmaceutical and nutraceuticals products derived from algae. Some of them include photoprotective, antivirals & antifungals, neuroprotective products, therapeutic proteins, and drugs etc.

The genotoxic and cytotoxic potential of each drug or new chemical entity (NCE) must be checked and validated by the regulatory authorities to be a part of the safety evaluation process. Any NCE presented as a potential drug especially cosmetic must be tested for a basic toxicological profile. The data that obtained are used for efficacy and safety of the drugs or NCE between risks and benefit associated with the potential drug, and it is assessed by several guidelines such as Organization for Economic Cooperation and Development (OECD)

or International Conference on Harmonization (ICH) guidelines [3]. Toxicity testing helps to identify the chemical influences to somatic or germ cell alteration. Genotoxicity is dangerous in the long term, because they might be present at a very low dose, but continuous exposure can also result in damaged DNA [4]. The OECD prescribed genotoxic tests, four in vitro assays are commonly used for analysis are bacterial reverse mutation test (Ames test; TG 471), the in vitro mammalian chromosome aberration test (TG 473), the mammalian cell micronucleus test (TG 487), and the mammalian cell comet assay (TG 489) [5].

The toxicity test of the extract is absolutely necessary for evaluate the toxicity or safety of that product due to food and drug toxicity is another important cause of the disease. Hence, toxicity is important in for pharmacological potential of the extracts, especially in cell toxicity and genome toxicity that lead to cell mutations. At present study, seaweed-derived products are rapidly developed into dietary supplements for pharmaceutical or nutraceutical benefits and cosmetic products for both domestic consumption and exportation. The basal data of toxicity should be rapidly and fully established to support the product development. The data should establish quantity of active compound in seaweeds that safety for consumers.

Methodology:

Seaweed material: Halymenia durvillei (HD), Rhodophyta, a red seaweed was receipted from Phetchburi Coastal Fisheries Research & Development center, Thailand.

Extraction and fractionation of marine algae: The dried powdered seaweed was immersed with 95% ethanol (dried seaweed 1 kg: ethanol 3 liters) at room temperature for 7 days as an ethanol fraction (HD-ET). The obtain extract of ethanolic extracts was separated by aqueous as an aqueous fraction (HD-AQ) receipted from Asst. Prof. Nakorn Niamnont, Department of Chemistry, Faculty of Sciences. King Mongkut's University of Technology Thonburi. Both fractions were subjected to determine the cytotoxicity activity by MTT assay. And to determine the genotoxic activity by comet assay and micronucleus assay. All extracts were dissolved in 100% Dimethyl Sulfoxide (DMSO) as 1 mg/ml stock solution and stored at -20°C.

Cell lines: Mouse areolar fibroblast cells (L929), Human keratinocyte cells (HaCaT) and Human lymphoblast cells (TK6) were purchased from ATCC.

Cell culture: The mouse fibroblast (L929) and Human keratinocyte (HaCaT) cell lines were maintained as exponentially growing cultures in a basal culture medium containing Dulbecco's Modified Eagle Medium (DMEM) supplemented with 1 g/L D-Glucose, L-Glutamine, 110 mg/L Sodium Pyruvate, Penicillin G (10 U/ml), Streptomycin (10 µg/ml), and 10% heat-inactivated fetal bovine serum (cell culture medium), for Human lymphoblast (TK6) cell lines were culturing in RPMI 1640 cell supplemented with L-Glutamine, Penicillin G (10 U/ml), Streptomycin (10 µg/ml), and 10% heat-inactivated fetal bovine serum (cell culture medium). All cell lines were cultured in incubated at 37° C in a humidified atmosphere of 95% air and 5% of CO_2 incubator. Culture medium was routinely subcultured twice a week to maintain the optimum conditions for the exponential growth.

Determination of cell viability by MTT assay: The concentration of 10, 50, 100, 200, 500 and 1000 µg/ml (v/v), 3 replicates per concentration from all samples, including total ethanolic and aqueous fractions, were tested for Mouse fibroblast (L929) and Human keratinocyte (HaCaT) cell lines. Samples were dissolved in DMSO (Dimethyl Sulfoxide) and further diluted with cell culture medium. The final DMSO concentration used was 1% of total volume of the medium in all treatments, including the control group. Cells with no treatment as negative controls.

For the MTT assay, 8 x10^3 cells/wells of each cells in culture medium were seeded into 96-well plate and incubated for 24 h until cell attachment before addition of extracts. After the incubation period, the cells were treated with seaweed extracts for 24 and 48 h. After 24 and 48 h of incubation, complete culture medium containing various concentrations of samples were discarded and 1 ml of MTT (5mg/ml) in phosphate buffered serum (PBS) was added to culture medium for final concentration 0.5 mg/ml, was added to each well. The plates were

incubated at 37° C for 3 h. At the end of the incubation period, the medium was removed and 100 µl cell DMSO was added to each well to dissolve insoluble formazan crystals. The formazan crystals were quantified by reading the absorbance wavelength at 570 nm on a microplate reader.

Cell viability in MTT assays was calculated as a percentage of untreated cells (control value). The cytotoxicity value was presented as IC50 (the median growth inhibitory concentration) of the reagents. IC50 values were calculated by GraphPad Prism 7 software.

Determination of genotoxicity by comet assay: The concentration of 10, 50, 100, 200, 500 and 1000 µg/ml (v/v), 3 replicates per concentration from all samples, including total ethanolic and aqueous extracts fraction, were tested for Human lymphoblast (TK6) cell line. Samples were dissolved in DMSO and further diluted with cell culture medium. The final DMSO concentration used was 1% of total volume of the medium in all treatments, including the control group. Cells with no treatment as negative controls and 98 mM H_2O_2 treatment were examined as positive controls for comet assay.

For comet assay, 2 x10^5 cells/well of lymphoblast cells in the culture medium were seeded into 24-well plate and incubated for 24 h before addition of extracts. After the incubation period, the cells were treated with seaweed extracts for 24 and 48 h. After 24 and 48 h of incubation, aliquots of 1 × 10^5 cells were centrifuged for 5 min at 3000 rpm, then incubation media was removed and the pellet was washed with PBS pH 7.4. The cells in PBS were resuspended in molten low melting point (LMP) agarose at a ratio of 1:10 (v/v). 100 µl of cells in molten low melting point agarose were laid on a glass microscope slide pre-coated with 1% normal melting point agarose. After gel solidification at room temperature, slides were placed in a Coplin jar and immersed in ice-cold lysis solution (2.5 M NaCl, 0.1 M EDTA, 10 mM Tris base, pH10, supplemented with 1% Triton X-100) for overnight at 4 °C (protected from light), to lyse the cells and separated DNA from histones. The lysis solution was removed and slides were immersed in DNA unwinding solution (0.3M NaOH, 1mM EDTA pH 13) for 20 min in the dark at room temperature for DNA unwinding, followed by gel electrophoresis for 20 minutes at 20 V. Finally, slides were neutralized with neutralization buffer (0.4M Tris, pH 7.5) for 5 min. The slides were stained with a SYBR Green and images were immediately used a fluorescence optical microscope with a 400× magnification and the image analysis software CometScore 2.0.

For evaluation of DNA damaged by comet assay, slides were analyzed 100 cells per concentration per slide. Tail DNA% (tail DNA content as a percentage of comet DNA content), tail length, and tail moment were used to determine genotoxicity.

Determination of genotoxicity by micronucleus test: The concentration and extract fractions of micronucleus test as the same of comet assay were tested for Human lymphoblast (TK6) cell line. Cells with no treatment as negative controls and mitomycin C 1 mg/ml treatment were examined as positive controls.

For micronucleus test, 2 x10^5 cells/wells of lymphoblast cells in the culture medium were seeded into 24-well plate and incubated for 24 h before addition of extracts for 24 and 48 h. After 24 and 48 h of incubation, cells were centrifuged at 3000 rpm for 5 minutes, then the cells were resuspended in fresh culture medium and transferred to a new 24-well plate, cytochalasin B 6 µg/ml was added to the cells for 24 h to collected the cells at a binucleated stage by prevent cytokinesis occurred after nuclear division. After the incubation period, cells were harvested by centrifugation at 3000 rpm for 5 min, the supernatant was removed and the cells were subjected to a hypotonic solution (5 ml KCl, 0.075 M), followed by another centrifugation, then the cells were fixed with methanol/glacial acetic acid (3:1), centrifuged, and the pellet was resuspended in a small volume of fresh fixative and 20 µl per drops were laid on a clean microscope slides. After dried, cells were stained with 2% Giemsa–Romanowski solution for 10 min, micronuclei (MN) formations were

scored in 1000 binucleated (BNC) cells under a light microscope (40x). One thousand cells per dose were examined and the frequency (%) of micronucleated cells were determined.
Statistical analysis: One-way analysis of variance (ANOVA) was used followed by Tukey's test to discriminate significant differences between extracts and controls or vehicle. These analyzes were performed using GraphPad Prism 7 for Windows. Results are presented as mean ± standard deviation (S.D.). The significance level was inferred at $p < 0.05$ or $p < 0.001$ for all statistical tests.

Results and Discussion:
Cytotoxicity activities of algae extracts: L929 and HaCaT cell viability: The ethanolic and aqueous fractions obtained from *H. durvillei*, were tested for their cytotoxicity on two cell lines. The result showed no significant change of cell viability at all concentration of algae extract 10-1000 µg/mL between two extracts fraction of algae extract as shown by Figure 1-2. However, the addition of HD-ET (10 and 50 µg/mL) on L929 cell after 48 h exposure showed increased cell viability by up to 156.88% and 152.66%, respectively. The increasing cell viability of L929 cell may be involve cell proliferation effect of HD-ET which contains a large number of carotenoids and other compounds identified from *H. durvillei* include alkaloids, flavonoids, terpenoids, steroids, glycoside and saponins (unpublished results of our research group from King Mongkut's University of Technology Thonburi). On the other hand, an increasing concentration of HD-ET show slightly decreased cell viability of L929 cell in a dose-dependent manner. This is probably due to their side-effects from excessively exposure of bioactive compounds in a dose-dependent manner of HD-ET on L929 cell that leads to the mild cytotoxic effect or the production of toxic secondary metabolites, for surviving in the environment [14]. Nevertheless, this result didn't show noticeable toxicity to cells whose cell viability was above 80%. Several studies reveal several bioactive compounds from plants or algae are possibly safe but often toxic if consumed excessively and it is not known yet if long-term use or higher doses are safe [15,16,17].

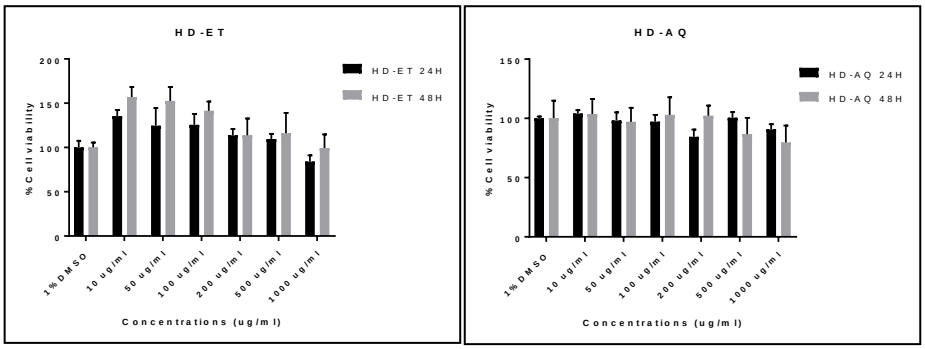

Figure 1. The viability of L929 mouse fibroblasts after a 24 h and 48 h exposure to HD-ET and HD-AQ (10–1000 µg/mL) was assessed using MTT assay.

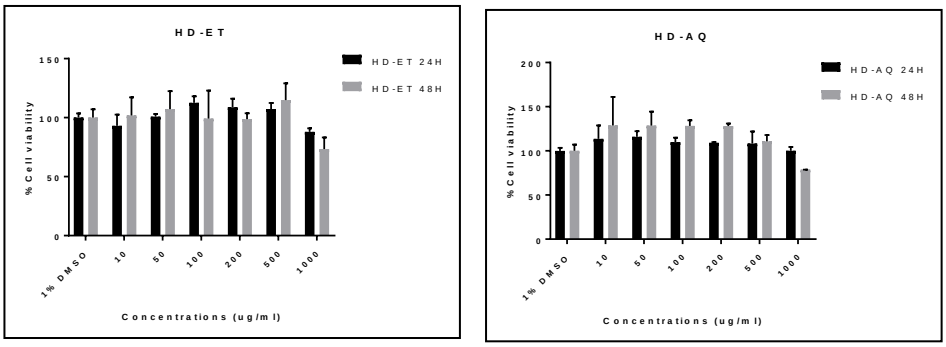

Figure 2. The viability of HaCaT mouse keratinocyte after a 24 h and 48 h exposure to HD-ET and HD-AQ (10–1000 µg/mL) was assessed using MTT assay.

Table 1. The calculated IC50 value of ethanolic and aqueous fractions of HD (µg/mL). Results are shown as mean ± SD.

Fraction	Cell Lines (MTT assay)[a]	
	L929	HaCaT
Ethanolic	>1000	>1000
Aqueous	>1000	>1000

[a] Key to cell lines employed: L929 (Mouse areolar fibroblast cells), and HaCaT (Human keratinocyte cells).

Genotoxicity activities of algae extracts: TK6

DNA damage of TK6 Human lymphoblast cells induced by HD extracts: The comet assay is already recognized as the most sensitive method available for measuring DNA damage. In this assay, there were no significantly changed in tail length, percentage of DNA in tail and tail moment after TK6 Human lymphoblast were treated with HD extracts at the examined concentrations (Table 2).

Table 2. Changes in the levels of DNA damage (tail length, % DNA in tail and tail moment) in TK6 human lymphoblast.

Group	Concentration (µg/ml)	Tailing Cell (n = 100)		
		Tail length ± S.D.	% Tail DNA ± S.D.	Tail moment ± S.D.
Negative (control)	-	1.23 ± 1.38	4.05 ± 2.50	0.07 ± 0.11
Positive (98 mM H_2O_2)	-	38.97 ± 6.78	44.05 ± 9.04	17.68 ± 6.57
Ethanolic fraction	1000	3.71 ± 1.63	4.81 ± 2.20	0.17 ± 1.66
	500	3.44 ± 2.36	4.22 ± 1.21	0.14 ± 1.23
	200	2.89 ± 1.23	4.12 ± 2.32	0.12 ± 0.66
	100	2.95 ± 1.95	3.56 ± 1.22	0.11 ± 1.21
	50	3.01 ± 2.21	3.94 ± 2.13	0.12 ± 0.39
	10	2.23 ± 1.52	2.97 ± 2.68	0.06 ± 0.21
Aqueous fraction	1000	1.40 ± 1.03	6.31 ± 3.10	0.08 ± 0.07
	500	1.62 ± 0.36	5.32 ± 3.54	0.05 ± 1.23
	200	1.48 ± 2.89	5.61 ± 2.64	0.08 ± 1.58
	100	2.33 ± 1.22	4.36 ± 2.11	0.10 ± 2.22
	50	3.54 ± 2.49	6.20 ± 2.32	0.22 ± 2.65
	10	2.02 ± 1.33	2.05 ± 1.20	0.04 ± 1.57

S.D. = standard deviation; H_2O_2 = hydrogen peroxide

Values are given as mean ± S.D. of three experiments in each group. * $p < 0.001$ *vs.* control

Our data indicated that the DNA damage caused by HD-ET and HD-AQ extracts was not occurred with the concentration increasing and there was no significant difference between all of dosage level.

Chromosomal damage of TK6 Human promyeloblast cells induced by HD extracts: The results of the micronucleus test are given in Table 3. It can be seen that only the positive control (1 mg/ml Mitomycin C) induced micronuclei in a statistically significant way. Whereas, HD-ET and HD-AQ extracts were shown no significantly induce micronuclei in the TK6 cells.

Table 3. The frequency of micronuclei in TK6 human lymphoblast cells. The control group was untreated-cells, whereas MMC positive control group was 1 µg/ml of mitomycin C treatment.

Fraction	Concentration (µg/ml)	% Micronucleus
Negative	-	0
Positive (MMC)	1	57.89*
Ethanolic	1000	0
Aqueous	1000	0

SD = standard deviation
* Significantly different from negative control ($p < 0.001$) (ANOVA Tukey test);
In all cases 1000 binucleated cells (BC) were analyzed.

Conclusion: In conclusion, according to our results, the ethanolic (HD-ET) and aqueous (HD-AQ) fractions do not have cytotoxic and genotoxic effects. (or are not cytotoxic and genotoxic effects). To the best of our knowledge, this is the first report on the evaluation of the genotoxic and cytotoxic effects of the tested algae extract or fractions. It shows that they can (so far) be considered safe in terms of their potential *in vitro* cytotoxic and genotoxic properties. This is encouraging with respect to further investigations on their therapeutic value.

References:

1. Cardozo KH, Guaratini T. Comp Biochem Physiol C Toxicol Pharmacol. 2007 ;146(1-2): 60-78.
2. West, J. Agarophytes and carrageenophytes. In: Leet, W.S., Dewees, C.M., Klingbeil, R., Larson, E.J. (Eds.). 2001; pp. 286–287.
3. OECD. 2016.
4. OECD. 2014.
5. Dixit M, Kumar A. In Vitro Toxicology. 2017; pp. 67-89
6. Ames BN, McCann J. Mutat Res 1975;31(6):347–64.
7. Evans HJ. 1976. p. 1–29.
8. Galloway SM, Armstrong MJ. Environ Molec Mutagen 1987; 10:1–175.
9. Gatehouse D, Haworth S. Mutat Res June 1994;312(3):217–33.
10. Kirsch-Volders M. Mutat Res 1997; 392:1–4.
11. Maron DM, Ames BN. Mutat Research 1983;113(3–4):173–215.
12. OECD. 2016.
13. Phillips DH, Arlt VM. Exs Suppl 2009; 99:87–110.
14. Sirikantaramas S, Yamasaki M, Saito K. Phytochemistry Reviews 2008, 7:467
15. Wink M. Front Physiol. 2018 11;9:364.
16. Galati G, O'Brien PJ. Free Radic Biol Med. 2004 1;37(3):287-303.
17. Vidak M, Rozman D, Komel R. Molecules. 2015 23;20(10):19406-32.

Acknowledgements: This research was supported financially by Research and Researchers for industries (RRI) and Agricultural Research Development Agency (ARDA).

A_017_OF: DATA REDUNDANCY IN PAIRED-END DNA SEQUENCE ALIGNMENTS

Eliot Cline, Anant Eungwanichayapant*
School of Science, Mae Fah Luang University, Thailand
*e-mail: anant@mfu.ac.th

Abstract: Illumina sequencers generate paired-end reads by sequencing both ends of a DNA fragment. Sequencing libraries contain variable-length fragments. Fragment length determines the distance between the 3' ends of the reads in a pair. They overlap when this distance is less than twice the read length. The overlapping portion is redundant, as the same part of the fragment was sequenced twice. Variant detection software overestimates read-depth in these areas of overlap. This paper studied how data redundancy affects variant detection.

A simulated tomato genome containing known variants was created, from which paired-end reads were generated at multiple mean fragment lengths and standard deviations (relative to mean fragment length). Reads were aligned to the published tomato reference genome. Software was developed to merge the overlapping pairs into a single read. Variants were called on the merged and unmerged data and the results compared.

Reads generated at small standard deviations showed very few overlapping pairs after alignment. For large standard deviations, up to 26% of read-pairs overlapped and contained 12% redundant data. However, removing the redundant data did not have a major effect on variant detection performance.

Introduction: DNA sequencing machines typically produce short sequences of between hundreds to thousands of base pairs in length. These sequencer "reads" can be used in a variety of bioinformatics pipelines. Paired end reads are synthesized from a single DNA template, but two short reads are created. One covers bases starting at one end of the template, while the other read covers bases at the other end of the template.

Assembled genomes can be used as a reference to which sequencing reads are aligned. Read alignment, or mapping, is usually a first step in variant calling. Variants that can be called using read alignments include single nucleotide polymorphisms (SNP) and small insertions and deletions (INDEL).

This investigative study used the popular Bowtie2[1] software for read mapping. The VarSim[2] genome simulation tools were used to create a reference genome implanted with large numbers of variants of different types. The ART[3] program was used to create simulated sequencer reads. The ART read simulator can simulate reads from a number of Illumina sequencers.

When the length of a DNA template fragment is less than twice the read length, paired-end sequencing reads will overlap. The overlapping region in the reads is redundant, as the same piece of the fragment is sequenced twice. Redundancy in paired-end read data is not well studied. There are software tools that detect overlapping pairs by comparing the ends of read-pairs with each other, but this is done with the raw, unaligned read data. Most studies have focused on merging overlapping pairs into a single read and then combining the merged reads with the non-overlapping pairs and using this data for genome or transcriptome assembly, as in the studies by Magoc[4], Liu[5] and Zhang[6].

Paired-end data sets can have over 20% of read pairs overlap. To what extent does this redundancy contribute to the estimated depth at a given position and influence the decisions made by variant calling software? Nucleotides in the overlapping portions of paired-end reads can get counted twice depending on the calling software used, resulting in erroneous, over-estimates of read depth.

Errors in the ends of overlapping read-pairs can also be interpreted as SNPs by variant callers. Since the overlapping portion comes from the same DNA fragment, that part

of the two reads should be exactly the same for both reads in the pair. Any differences in those regions must be due to sequencing error in one, or both, of the reads.

It is not known if redundancy has any effect, positive or negative, on variant calling. In Illumina data the 5' and 3' ends of reads contain the most sequencing errors[7]. It is in those regions where overlap occurs. The expectation was that the presence of redundant data should not be beneficial to any downstream analysis after read mapping. A software tool was developed to merge the overlapping portions in paired-end alignments. Experiments to quantify the effects on SNP and INDEL calling were carried out.

Methodology: In this experiment the simulated reads were mapped to the Heinz SL2.50 reference genome[8] using Bowtie2. The aligned reads are output in the Sequence Alignment/Map (SAM) format[9]. Variants were called with the FreeBayes variant calling software. A C++ program was written to identify the overlapping portions of read pairs and merge the two reads into a single, longer read. These reads were written out to a new SAM file together with all the non-overlapping read pairs. SNPs and INDELs were then called on both the merged and unmerged SAM files using the FreeBayes software and the results were compared.

The C++ program also outputs statistics about the number of overlapping read pairs, total number of nucleotides covered by the overlapping portions and the percentage of the data set found in the overlapping regions.

Merging the aligned, overlapping reads directly in the SAM file turned out to be a challenging problem. Reads can be aligned to portions of the reference genome containing insertions or deletions. This means that certain parts of the genome may be missing from the reads or that certain parts of the reads may be missing from the genome.

The key to resolving these issues is the CIGAR string and MD tag. The CIGAR string is part of every record in a SAM file and is used to describe how a read aligns to its reference sequence. The MD tag is an optional tag that describes variations from the reference sequence. In the case of INDELS we find that often there is an INDEL in one read and not in its mate. Very frequently there is a base mismatch between the two reads. These inconsistencies need to be resolved before the read pair can be merged.

In the simplest case the two reads of an overlapping pair will not align to any INDELs and their CIGAR strings will be identical. The orientation of reads in a pair, with respect to the reference sequence, determines which ends of the reads will overlap. During sequencing, one read will come from the forward strand of the DNA fragment and the other will come from the reverse strand. If the first read in the pair came from the forward strand and the second read from the reverse strand, the 3' end of the first read will overlap the 5' end of the second read. The opposite case also frequently occurs. This is illustrated in Figure 1.

Other orientations are possible. Both reads can come from either the forward or reverse strands. This usually happens when there is a translocation or inversion in the sequenced sample. Overlap is rare in these cases and is not considered here.

Figure 2 shows a more complicated overlap situation. The first read has a one base deletion near the end of the overlapping region while the second read has a five-base insert. The red lines above and below the read sequences delineate the parts of the reads that correspond to their CIGAR strings. The bases highlighted in green are mismatches between the read sequences.

```
Orientation: F1R2
CIGAR: 100M (both reads)

    5'                                                                                                  3'
R1  CCTAGGGCGGTGATGTCATGCCACG  TTCGACATTGTCAAACCGTGTGTGGTATCCAAGGCCAGTAATATCATCTCACGCCCAACGTTGCAGACTGTGTGT
R2                             TTCGACATTGTCAAACCGTGTGTGGTATCCAAGGCCAGTAATATCATCTCACGCCCAACGTTGCAGGCTGTGTGT  GCTGTCCAAGGGCGGTGAGGTCATG
                               5'                                                                                                     3'

Orientation: F2R1
CIGAR: 100M (both reads)

                               5'                                                                                                     3'
R1                             ACACACAGTCTGCAACGTTGGGCGTGAGATGATATTACTGGCCTTGGATACCACACACGGTTTGACAATGTCGAA  CGTGGCATGACATCACCGCCCTAGG
R2  CATGACCTCACCGCCCTTGGACAGC  ACACACAGCCTGCAACGTTGGGCGTGAGATGATATTACTGGCCTTGGATACCACACACGGTTTGACAATGTCGAA
    5'                                                                                                  3'
```

Figure 1.The two simplest cases of overlapping pairs.

To merge the reads, one of the mismatched bases must be used in the new, merged read. To choose which one, the base-call quality scores for each base are compared. The base with the highest score is used and its quality score is set to the difference between the two, original base-call scores. Inserted bases are removed from the reads while deletions in one read are patched with the bases from the other read. The merged read is shown in the bottom of the figure.

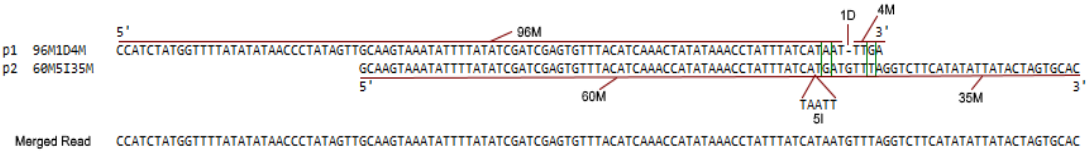

Figure 2.A more complicated overlap.

Figure 3 shows an example of a read-pair with mismatches and a large deletion in the area of overlap. The bottom part of the figure is a zoomed-in view of the overlap region. Note that one read has two inserts and two mismatches in the overlapped area. The second read is missing 17 bases from the reference sequence and the first read's last six bases protrude into the deleted part of the second read.

To resolve INDELs and mismatches, the software first expands the read and quality sequences of the read pairs to incorporate dashes to represent deleted bases. Then for each read in the pair, two new sequences are created.

One is a sequence of the CIGAR operations for each position in the read. The other is the information encoded in the MD tag. A '=' character represents an exact match between the read and the reference. An 'I' says that the base at a given position in the read is an insert relative to the reference, while a '-' means that a particular position in the read is a deletion relative to the reference. The program then scans and compares these sequences, building the merged read one base at a time.

In the case of deletions, if a base is present in the first read, but not in the second read, the first read's base is added to the merged read. If there is an insert in one read but not in the other, the inserted bases are skipped and not added to the merged read. However, if the insert is present in both reads, the inserted base is added to the merged read.

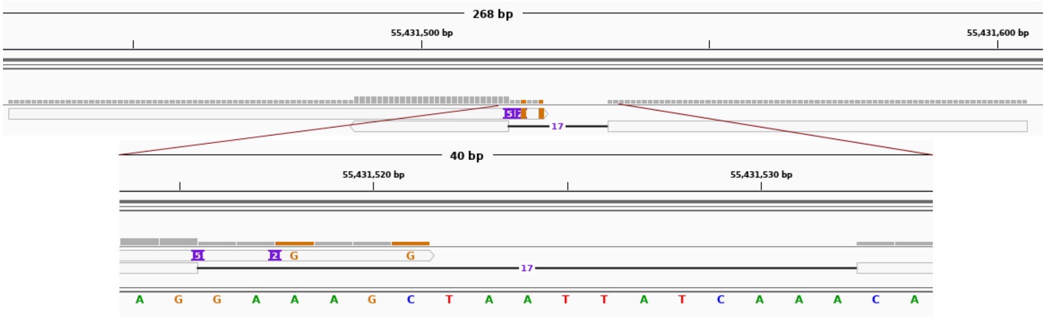

Figure 3. Example of mismatches and INDELs in overlaps.

Mismatches are handled by examining the MD sequence and the quality values for both reads at the mismatched position. If both bases at that position are different from the reference, the base with the highest quality score is used in the merged read, and its quality score is set to the absolute value of the difference between the two scores. This is the same method used in the FLASH read-merging software. If one of the two mismatched bases is the reference base, then the reference base is used in the merged read and its quality score is set to that of the reference base. Figure 4 illustrates how this works.

```
1) Original CIGAR, MD tags and read/quality sequences

R1  87M5I2M2I4M  89A2C0
CCAAGCTGTCTTACTAGCTTAATCTTCTTTTTTCACCTGCAATAGGTATCCATCCGGGCAGAAGCTGATCGTGACCAGTGAAGAAAGCAATCGATTGAGG
C?CFFDFDGDH@GEJJICCHJIII0JJIHEJBGIIBJIGAIGD?HJJ(?8FJHJDHG;BJD94HFHIDBBDJDG;;E3>F=DDDC9BD@DDDDD@@D<DD

R2  27M17D73M    27^GAAAGCTAATTATCAAA73
GAAGCTGATCGTGACCAGTGAAGAAAGCAATCGATTGAGGTTCTGACAAAGTTGCTTCAGACACATCAGGCTTTTCACCTGAGCATGGTAGAGCGATCAT
(2DB>DABDCDFD&DHDFDBDEFCDD?;DI:EIH:JCIIIHHDJCIDG@IHG=D?HJC*J5EH)HE0HCCGJGJIJHGJJJEFIGJIHDHH2FDFF=C?@


2) Expansion of read sequences, quality sequences, CIGAR and MD tag

CCAAGCTGTCTTACTAGCTTAATCTTCTTTTTTCACCTGCAATAGGTATCCATCCGGGCAGAAGCTGATCGTGACCAGTGAAGAAAGCAATCGATTGAGG
C?CFFDFDGDH@GEJJICCHJIII0JJIHEJBGIIBJIGAIGD?HJJ(?8FJHJDHG;BJD94HFHIDBBDJDG;;E3>F=DDDC9BD@DDDDD@@D<DD
MMMMMMMMMMMMMMMMMMMMMMMMMMMMMMMMMMMMMMMMMMMMMMMMMMMMMMMMMMMMMMMMMMMMMMMMMMMMMMMMMMMMMMMIIIIIMMIIMMMM
=======================================================================================IIIII==IIA==C


GAAGCTGATCGTGACCAGTGAAGAAAG-----------------CAATCGATTGAGGTTCTGACAAAGTTGCTTCAGACACATCAGGCTTTTCACCTGAGCATGGTAGAGCGATCAT
(2DB>DABDCDFD&DHDFDBDEFCDD?-----------------;DI:EIH:JCIIIHHDJCIDG@IHG=D?HJC*J5EH)HE0HCCGJGJIJHGJJJEFIGJIHDHH2FDFF=C?@
MMMMMMMMMMMMMMMMMMMMMMMMMMMDDDDDDDDDDDDDDDDDMMMMMMMMMMMMMMMMMMMMMMMMMMMMMMMMMMMMMMMMMMMMMMMMMMMMMMMMMMMMMMMMMMMMMMMMM
===========================-----------------=========================================================================
```

Figure 4. Resolving mismatches and INDELs in overlaps.

The CIGAR string for the merged read is built base-by-base as they are being added to the read. The MD tag is discarded and not included in the merged read's SAM record. The output of the software is a new SAM file containing the non-overlapping read pairs and the merged reads. Figure 4 above shows a detailed example for an actual read-pair.

Simulated reads were generated at two different lengths. For each read length, two mean fragment lengths were used. For each fragment length two levels of standard deviation were tested. This resulted in a total of 16 BAM files. The details are shown in Table 1.

Table 1. Parameters for generating simulated reads.

Read length	Coverage	Fragment Length (bp)	Std Deviation[a]
100bp	5x, 20x	250, 450	5, 50
250bp	5x, 20x	625, 825	5, 50

[a]Standard deviation is expressed as a percentage of read length.

Mean fragment lengths and their standard deviations were chosen by examining actual SAM files of alignments of 100bp reads. Statistics were calculated using several of the SAM files from the 150 Tomato Genomes project[10]. Mean fragment length for these files ranged from as low as around 200bp up to 480bp. Standard deviations ranged from approximately 4.5% to 59% of mean fragment length. All of the reads were generated from the Illumina HiSeq family of sequencing machines.

The HiSeq platform does not produce reads longer than 100bp. The 250bp reads were simulated using the Illumina MiSeq platform profile in ART. Mean fragment lengths for the 100bp reads are 2.5 and 4.5 times the read length. This is a bit different for the 250bp reads as the recommended maximum fragment size for the Illumina MiSeq platform is 900bp. For the 250bp reads, mean fragment lengths are 625bp and 825bp, or 2.5 and 3.3 times read length.

Results and Discussion: Merging reads most often results in modification to the overlap area. That includes removing inserted bases from one or both reads, using bases from one read that were deleted in the other and, in the case of mismatches, choosing a single base from one read over a base in the other read. The number of overlapping pairs and the number of modified bases varies with the mean fragment length and its standard deviation in the population of reads in an alignment file. Table 2 and Table 3 summarize the results of merging the overlapping reads for each of the BAM files. The first two columns show the mean fragment length and fragment length standard deviation for the alignments at each of the two coverage levels. The columns "Olp Pairs" and "Pct Total" show the total number of overlapping pairs in the alignment and percentage of the total number of read pairs that overlap. "Olp Bases" and "Pct Total" show the total number and percentage of base-pairs in the overlapping regions, respectively. "Modified" shows the total number of mismatched bases that were changed or removed.

Table 2. Results of merging 100bp read pairs.

5x Coverage							
Frag Len	*StdDev*	*Ttl Pairs*	*Olp Pairs*	*% Ttl*	*Olp Bases*	*% Ttl*	*Modified*
250	13	36556847	3571	0.01	74783	0.002	3590
450	23	36342891	1054	0.003	47634	0.001	3087
250	125	36530334	9508156	26.028	431135220	11.802	8914609
450	225	36327980	2870817	7.902	131009003	3.606	2737357
20x Coverage							
250	13	146215651	13965	0.01	274932	0.002	13268
450	23	145362718	4319	0.003	199188	0.001	12334
250	125	146117991	38042558	26.034	1725414348	11.808	35678356
450	225	145302525	11489060	7.91	524342717	3.609	10968319

Table 3. Results of merging 250bp read pairs.

5x Coverage							
Frag Len	*StdDev*	*Ttl Pairs*	*Olp Pairs*	*% Ttl*	*Olp Bases*	*% Ttl*	*Modified*
250	13	36556847	3571	0.01	74783	0.002	3590
450	23	36342891	1054	0.003	47634	0.001	3087
250	125	36530334	9508156	26.028	431135220	11.802	8914609
450	225	36327980	2870817	7.902	131009003	3.606	2737357
Read length: 250bp							
250	13	146215651	13965	0.01	274932	0.002	13268
450	23	145362718	4319	0.003	199188	0.001	12334
250	125	146117991	38042558	26.034	1725414348	11.808	35678356
450	225	145302525	11489060	7.91	524342717	3.609	10968319

Read populations with lower mean fragment length and lower standard deviations have fewer reads overlapping. Those with standard deviations of only 5% of fragment length have very few overlapping pairs, and very few bases that have been modified. For these files it is not necessary to call SNPs as it is quite obvious that there will be little or no benefit to merging reads in this case.

Alignment files with standard deviations of 50% of mean fragment length show a very different picture. With up to 26% of read-pairs overlapping and nearly 12% of the total data set being redundant, it is reasonable to expect read merging might be a sensible thing to do. Therefore, variants were called on only the SAM files with standard deviation of 50% of mean fragment length.

Table 4 shows the results of SNP calling performed on the merged and unmerged data sets for the 100bp reads. Total true positive calls with a quality score over 20 show only very small differences between the merged and unmerged data sets. Total false positive calls with a score over 20, too, are largely unchanged after merging overlapping reads. This is the case for both coverage levels and mean fragment lengths. If anything, in most cases there is a slight increase in the number of false positives after filtering and a slight decrease in true positives after filtering.

Table 4. 100bp SNP calling results.

Mean Fragment Length: 250								
	TP (Q > 20)		FP (Q > 20)		Total TP		Total FP	
	unmerged	*merged*	*unmerged*	*merged*	*unmerged*	*merged*	*unmerged*	*merged*
5x	160399	159474	698	704	187601	187638	41511	39873
20x	187994	187826	1280	1282	197307	197476	3174	3113
Mean Fragment Length: 450								
5x	155607	155263	4734	4814	184066	184018	85403	85514
20x	183191	183095	10497	10693	195640	195727	35321	35743

Table 5 shows the SNP calling results results for 250bp reads. The results are very similar to those for the 100bp reads. For all read lengths, mean fragment lengths and standard deviations the total number of true and false positive calls, regardless of the score, changes very little after merging reads.

Table 5. 250bp SNP calling results.

Mean Fragment Length: 625								
	TP (Q > 20)		FP (Q > 20)		Total TP		Total FP	
	unmerged	*merged*	*unmerged*	*merged*	*unmerged*	*merged*	*unmerged*	*merged*
5x	164301	162889	1178	1157	183486	183131	50225	51203
20x	187645	186763	1444	1500	195661	195618	7997	7724
Mean Fragment Length: 825								
5x	163310	162508	1093	1084	183079	182760	50316	50182
20x	186228	185744	1729	1753	195002	194954	8559	7893

Tables 6 and Table 7 shows the results for INDEL calling for 100bp reads and 250bp reads, respectively. The same pattern exists for INDEL calling as it does SNP calling. The spread in totals between the unmerged and merged data is even smaller for INDELs than for SNPs.

Table 6. 100bp INDEL calling results.

Mean Fragment Length: 250								
	TP (Q > 20)		FP (Q > 20)		Total TP		Total FP	
	unmerged	*merged*	*unmerged*	*merged*	*unmerged*	*merged*	*unmerged*	*merged*
5x	62250	61786	647	625	65094	64986	1147	1089
20x	65900	65840	927	920	66543	66530	1218	1205
Mean Fragment Length: 450								
5x	61165	60992	1097	1092	64754	64720	8563	8628
20x	65659	65650	2193	2228	66445	66451	4910	5002

Table 7. 250bp INDEL calling results.

Mean Fragment Length: 625								
	TP (Q > 20)		FP (Q > 20)		Total TP		Total FP	
	unmerged	*merged*	*unmerged*	*merged*	*unmerged*	*merged*	*unmerged*	*merged*
5x	63441	63094	192	189	65816	65713	1992	1520
20x	66447	66384	243	235	67094	67082	790	679
Mean Fragment Length: 825								
5x	62904	62551	106	113	65004	64888	384	230
20x	66374	66314	143	136	66954	66943	271	224

As Table 2 and Table 3 show, for certain combinations of mean fragment length and standard deviation, a significant portion of data sets are redundant. Up to 26% of read-pairs can overlap, with the overlapping portions comprising up to 12% of an entire data set. In that specific case, there were over 35 million nucleotides that differed between the overlaps in the two reads in a pair. This should theoretically not be the case as the overlapping portions of two reads come from the same part of the sequenced fragment. Additionally, these nucleotides are in the most error-prone regions of reads.

Therefore, it does come as somewhat of a surprise that there was no significant reduction in false positive SNP calls (Tables 3 and 4). One explanation for this is that the spatial distribution of sequencing errors is random, so bases representing a possible alternate allele do not necessarily occur at the same genomic position in enough reads covering that position.

The number of true positive SNP calls in the merged-read data sets decreased slightly compared to the unmerged-read data. There are two explanations for this. Firstly, in the case that nucleotides in the same genomic position in the overlapping portion of a read pair differ from each other, it is impossible to know exactly which one is erroneous. One could be a real SNP and the other sequencing error, or both could be sequencing error, or one could be sequencing error and the other the reference allele. If neither of the bases is the reference allele the software chooses the base with the highest base-call quality score, but this does not guarantee that it is the correct base. If one of the bases is the reference allele, it is chosen

over the possible alternate allele. While this is a reasonable thing to do, it is not guaranteed to be the correct choice every time.

The other reason that true positive calls are reduced after merging reads has to do with the behavior of the FreeBayes software. Ideally the calculation of read-depth would only take into account one of the reads in a pair in the area where they overlap. FreeBayes does not do this, so depth is overestimated in those areas. This overestimation seems to have no ill-effects on SNP calling with the unmerged data, but clearly reduces the confidence of SNP calls with the merged data.

Figure 3 illustrates this behavior. In the top part of the figure, the two reads highlighted in brown are an unmerged pair. The small gap in the in the reads represents a two-base deletion relative to the reference sequence. Note that there are four reads covering that position.

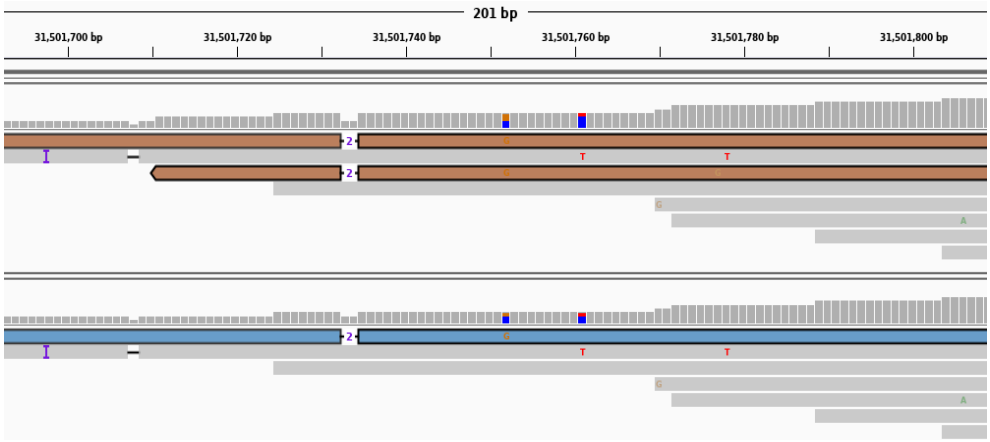

Figure 3. Inserted bases excised from one read in a pair.

Two show the deletion and two do not. This is an actual heterozygous variant implanted into the simulated tomato genome, and it was correctly called using the unmerged data set. The lower part of the figure shows the merged read highlighted in blue. The same deletion is present, but now only in one read. Note that read depth here has now been reduced to three, and FreeBayes did not call the variant.

For INDEL calling, the reduction of the number of true positive calls in the merged-read data does not come as a surprise. The software developed for this study removes inserted bases from the overlapping portions of read-pairs if the insertion does not occur in both reads at the same position.

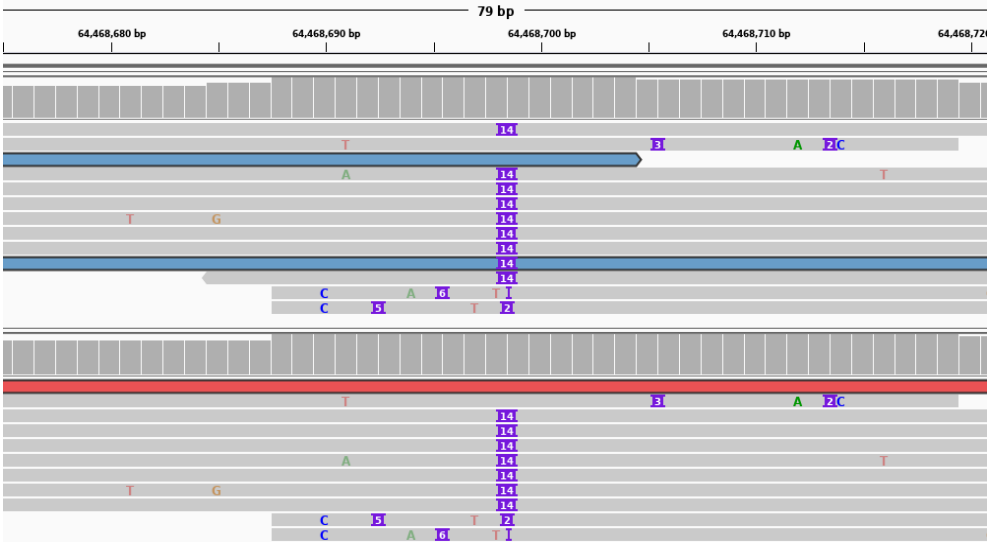

Figure 4. Inserted bases excised from one read in a pair.

Figure 4 shows a 14-base insertion in several reads at the same genomic position, which was correctly called in the unmerged data. The merged read in the bottom figure has had the inserted bases removed. This reduces by two the number of reads supporting this variant and was enough to cause it not to be called in the merged data set, most likely because the mapping quality of reads at this position is quite low.

A similar problem occurs with deletions. Bases that were deleted from one read of a pair may be present in the other. In this case they are incorporated into the merged read. In some cases, this can reduce the confidence of the variant calling software that a deletion actually exists. This is shown in Figure 5.

The reason for removing inserted bases from, or incorporating deleted bases in, a merged read is that it is impossible to know whether or not the INDEL is due to sequencing error when a read-pair is considered in isolation from other reads covering the same position. In the vast majority of cases it is the correct thing to do, but not in every case. Results could be improved by taking the other reads into consideration to help decide whether an INDEL or a SNP is a real feature of a read.

There are some other interesting observations that can be made from the SNP and INDEL calling results. As expected, the number of false positive SNP calls is much higher for the 5x coverage data than for the 20x coverage data. In some cases, the difference is more than an order of magnitude. Yet, FreeBayes assigns most of them a very low-quality score, with only a handful having a quality score over 20.

The number of false positives creeps up as mean fragment size increases. This is more apparent for the shorter read lengths. The reason for this is that read-depth is somewhat lower for the larger mean fragment length data sets. This may be an artifact of the ART read simulator, because there is no particular reason for this to be the case. Read depth is a function of the number of mapped reads, read length and haploid genome size, so mean fragment length should not have an effect on overall read depth.

SNP calling performance was best for the 100bp reads at 250bp mean fragment length and 20x coverage, recovering around 93.5% of the total number of SNPs implanted into the genome. This, again, may well be due to the higher read depth for the smaller mean fragment size data sets. This is almost certainly due to the behavior of the ART read simulator.

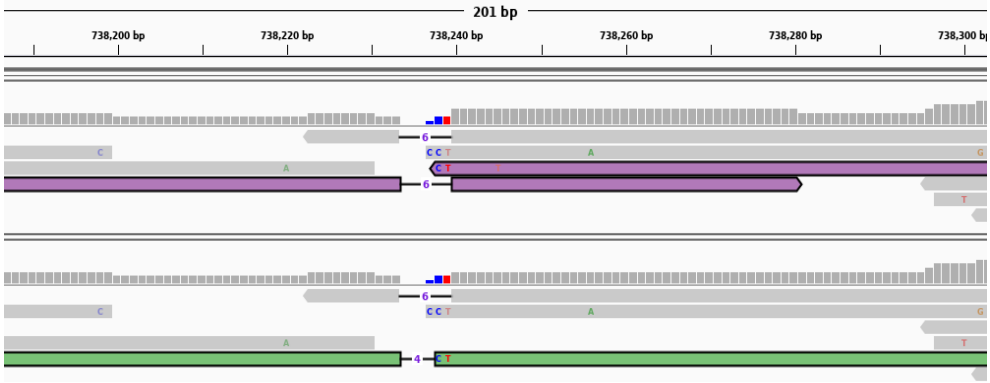

Figure 5. Deleted bases are incorporated into the merged read.

Conclusion: Overall it is apparent that redundancy in paired-end alignments is not a big problem, and that it is probably better to leave the overlapping pairs of reads alone, rather than merging them into a single read. In theory, the redundant portions of read-pairs should offer an opportunity to correct base-call errors. However, even in the most extreme case the number of possible erroneous bases was barely over 1% of the total number of bases in the alignment.

This may have implications for using such tools as FLASH to merge reads prior to mapping, or genome assembly. Using a pure kmer approach for merging reads may introduce more base call errors into the merged reads, thereby causing more problems than it solves.

This study only examined the consequences of merging overlapping read pairs. It is possible base call errors could be corrected by combining information in all reads at positions within read-pair overlaps with the redundant information in overlapping pairs. This could reduce false positive calls and would be an interesting project for future research.

References:

1. Langmead B, Salzberg S. Nature Methods 2009;9:357-9.
2. Mu JC, et al. Bioinformatics. 2015;31:1469-1471.
3. Huang W, Li L, Myers JR, Marth GT. Bioinformatics. 2012;28:593-594.
4. Zhang J, Kobert K, Flouri T, Stamatakis A. Bioinformatics. 2014;30:614-620.
5. Magoc T, Salzberg SL. Bioinformatics. 2011;27:2957-2963.
6. Liu B, et al. Bioinformatics. 2012;28:2870-2874.
7. Schirmer M, D'Amore R, Ijaz UZ, Hall N, Quince C. BMC bioinformatics. 2016;17:125.
8. The Tomato Genome Consortium, et al. Nature. 2012;485:635-641.
9. Heng L, et al. Bioinformatics. 2009;25:2078-2079
10. Aflitos S, et al. The Plant Journal. 2014;80:136-148.

A_018_OF: SAFETY ASSESSMENT OF THE ETHANOLIC EXTRACT OF *Caulerpa lentillifera* IN VITRO SYSTEM

Supawadee Osotprasit[1], Athit Chaiwichien[1], Tepparit Samrit[1], Pornanan Kueakhai[1], Prasert Sobhon[2], Krai Meemon[2], Nakorn Niamnont[3], Montakan Tamtin[4], Narin Changklungmoa[1,*]
[1]Faculty of Allied Health Sciences Burapha University, Chonburi, Thailand
[2]Faculty of Science, Department of Anatomy, Mahidol University, Bangkok, Thailand.
[3]Faculty of Science, Department of Chemistry, King Mongkut's University of Technology Thonburi, Bangkok, Thailand.
[4]Coastal Aquatic Feed Research Institute, Coastal Fisheries Research and Development Bureau, Department of Fisheries, Phetchaburi, Thailand.
*e-mail: narin_bio@hotmail.com

Abstract: *Caulerpa lentillifera* (sea grape) that have been widely used for the pharmaceutical industry, herbal medicines and medical supplies. In this study, we attempted to evaluate the cytotoxicity and genotoxicity of sea grape extract in ethanol fraction. The extract was evaluated cytotoxicity assays by MTT and LDH assay on hepatocyte cell (FL83B). In addition, to test genotoxicity by the comet assay in vitro performed using lymphoblast cell (TK6) for detecting DNA damage. Our results demonstrated the cytotoxicity of sea grape extract, that showed high cell viability and low LDH activity. For genotoxicity to use three different parameters were performed: tail length, %tail DNA and tail moment were not different from the control group. In conclusion, sea grape extract showed no cytotoxic and genotoxic effects on both cell types under the conditions studied in vitro. Therefore, our results indicated that ethanol fraction of *C. lentillifera* safe for consumption and supplementary food.

Introduction: The toxicity test is very popular, especially in the development of medicines and products. In order to obtain information on toxicity to various systems and risk assessment before bring the product used. Force all chemicals both imported and new produced need pass the toxicity test and register toxicological data, this is to tell about the safety of chemicals to use. Therefore, toxicity of the extract is important to evaluate before develop and apply to humans, especially cytotoxicity and genotoxicity that causes mutations, degradation and death or proliferation, and abnormal cells occur as cancer cells. A number of in vitro tests are gaining wide acceptance in order to replace in vivo cytogenetics with in vitro cytogenetics.[1] In recent years, the interagency coordinating committee on the validation of alternative method and European counterparts has validated of in vitro tests.[2] The most common ones generally assess cell viability or toxicity have many tests. Each method has different limitations, should choose to use internationally accepted methods such as using OECD test guideline, product toxicity test data will be accepted (Mutual Acceptance of Data - MAD) in the European Union. At present, many types of extracts have been developed for food, pharmaceutical, herbal and pharmaceutical industries.

C.lentillifera (sea grape) is seaweed that can be found in the Thai sea and has been studied for commercial culture from the department of fisheries since 1993. *C.lentillifera* is a popular edible species high minerals, dietary fibers, vitamin A, vitamin C, and several essential unsaturated fatty acids.[3] Recently report, the activities of *C.lentillifera* showed anti-cancer,[4] anti-oxidative, and lipid-lowering[3]. Also, *C.lentillifera* has been used traditionally in the Philippines for the treatment of diabetes. At present, sea grapes can be cultured in many ways and can be produced in many places. Pharmaceutical industry, herbal medicines and medical supplies in Thailand are industries that are worth several hundred million baht, both production for domestic and export. Thus, this project aim to test the toxicity of the sea grape extract.

Methodology:

Plant material and extraction: C.lentillifera was receipted from Phetchaburi Coastal Fisheries Research & Development center, Thailand. The algae were extensively washed with tap water, and dried at room temperature. The dried *C.lentillifera* was extracted with 95% ethanol as an ethanol fraction (CLET). Ethanol extract of *C.lentillifera* was then filtered, and evaporated under vacuum. The extracts receipted from Asst.Prof.Dr. Nakorn Niamnont of King Mongkut's University of Technology Thonburi, Thailand. The extracts were dissolved in 100% DMSO as 1 mg/ml stock solution and stored at -20°C.

Cell culture: Mouse Hepatocyte cells (FL83B) and human lymphoblast cells (TK6) were purchased from American Type Culture Collection (ATCC). Briefly, FL83B cells were grown in DMEM with 1 g/L D-glucose, L-glutamine, 110 mg/L sodium pyruvate, penicillin G (10 U/ml), streptomycin (10 µg/ml), and 10% fetal bovine serum (cell culture medium). For TK6 cell were grown in RPMI 1640 with L-glutamine, penicillin G (10 U/ml), streptomycin (10 µg/ml), and 10% fetal bovine serum (cell culture medium). All cell lines were cultured at 37°C in a humidified incubator with 5% CO_2 atmosphere. The culture media was changed every 2–3 days. The logarithmic cells were harvested before performing each experiment.

MTT assay: The cell viability was measured by employing an MTT assay as described previously by Mosman (1983).[5] The cytotoxicity tests were performed in triplicate for controls and treatments on Mouse Hepatocyte cells (FL83B). The cells were seeded into 96-well plates at a density of $8x10^3$ cells per well, containing 100 µl of the respective culture medium, for 24 h at 37°C. After this time, the medium was discarded, and cells were treated for 24 and 48 h with various concentrations of the extracts as 10, 50, 100, 200, 500 and 1000 µg/ml in the culture medium, and 1% DMSO diluted in the culture medium as a control. MTT salt was dissolved in PBS (stock solution; 5 mg/mL). After treatments, the reaction media was removed, the MTT was dissolved in culture medium (working solution: 10:100 µl v/v; 0.5 mg/ml) and added to each well for incubation by 3 h at 37°C. Finally, the MTT was removed, and 100 µl/well DMSO was added to solubilization of the formazan crystals. The plates bremained gently shaking for at least 15 min and were then read with a microplate spectrophotometer (VersaMax Microplate Reader) at a wavelength of 690 nm absorbance value (background signal from the instrument) and 570 nm. The percentage of viable cells was calculated after normalization with the negative control (1%DMSO), which was considered as 100% cell viability, and calculated as follow equation;

$$\% \text{ Cell viability} = [\text{Abs}_{(\text{sample})}/\text{Abs}_{(\text{blank control})}] \times 100$$

LDH assay: Cytotoxicity was analyzed by LDH assay (sigma-aldrich, Roche). The experiments were performed in triplicate to each control and concentration. Mouse Hepatocyte cells (FL83B) were seeded into 96-well plates at density of $8X10^3$ cells per well of triplicate wells and allowed to grow for 24 h. After this time, the cell was treated with many concentrations of the extracts 10, 50, 100, 200, 500 and 1000 µg/ml in the culture medium for 24 and 48 h, 5 µl/well lysis buffers (high control) incubate the plate for an additional 15 minutes and 50 µl culture medium plus 50 µl assay medium (low control). The cell culture supernatants were collected to measure the released LDH by transfered 50 µl to a new 96-well plate. Then, the cell culture supernatants add 100 µl reaction mixture (freshly prepared) to each well on the 96-well plate and incubate 5–10 minutes in a dark room. Finally, the cell culture supernatants add 50 µl stop solution to each well into the 96-well plate. And then, the results were analyzed by ELISA reader to measure the absorbance of the samples at 492 nm and the reference wavelength should be more than 690 nm. The percentage of LDH activity were calculated as follow equation:

$$\% \text{ LDH activity} = [(Ab_{(sample)} - Abs_{(high\ control)}) / (Ab_{(high\ control)} - Abs_{(low\ control)})] \times 100$$

Single-Cell Gel Electrophoresis Assay (comet assay): Comet assay was carried out to measure the DNA damage. TK6 cells ($2x10^5$) were seeded in 24-well plate, maintain the plate incubator with 5 % CO_2 and 37°C for 24 h and treat with extract concentrations 10, 50, 100, 200, 500 and 1000 µg/ml in the culture medium for 24 and 48 h, H_2O_2 10 µM (Positive control), and 10% FBS in RPMI medium (negative control). After incubation, the cells were collected 100 µl of TK6 cell was centrifuge 4,500 rpm for 5 minutes and the supernatant was discarded, resuspend with 100 µl PBS pH 7.4. This cell suspension was transferred to agarose-coated slides, which were coverslipped. The coverslips were removed, and the slides were immersed in a freshly prepared lysis solution (2.5M NaCl, 100mM EDTA, 10mM Tris, pH 10) for overnight, at 4°C in dark. Next, the slides were transferred to unwinding solution (300mM NaOH and 1mM EDTA pH > 13) for 30 min at room temperature in a dark room and electrophoresis was conducted under standard conditions (20 V; 300 mA; 1 Vcm^{-1}) for 30 min. The slides were neutralized with 0.4M Tris pH 7.5 for 5 min and stained with SYBR® Green. The samples were analyzed using a fluorescence microscope (Olympus with 40X magnification, immediately) with the aid of the Comet Score 2.0 software. The results were indicated by the single-cell gel electrophoresis assay and conducted by examining at least 50 randomly selected and nonoverlapping cells per culture well, in a blind analysis. These cells were scored visually, according to tail and head (nucleus) size.

Statistics: All data were analyzed by GraphPad Prism®7 software (version 7.0) and shown as means ± standard deviation (SD). Comparisons between the extracts and controls were conducted by using one-way analysis of variance (ANOVA) followed by Duncan's *post hoc* comparisons. Differences were considered statistically significant at $p < 0.001$.

Results and Discussion:

Cytotoxicity: The viability of hepatocyte cells by ethanol fraction from *C.lentillifera* extract was investigated by MTT assay and showed in Figure 1. After treatment both 24 and 48 h, IC50 was calculated as more than 1,000 µg/ml, when compared with the blank control, viability showed no significant in the concentration of 10, 50, 100, 200 and 500 µg/ml at 24 h. but decrease significantly of 1,000 µg/ml. For 48 h, the results showed no significant in the concentration of 10, 50, 100 and 200 µg/ml but decrease significantly of 500 and 1,000 µg/ml (Figure 1). The activation of hepatocyte cells by *C.lentillifera* extract were increased no significant over the entirely tested low concentrations when compared with the blank control. These results suggested that *C.lentillifera* no cytotoxicity when to test by MTT assay for cell viability. Moreover, the low concentrations could stimulate the growth of hepatocyte cells. Figure 2 showed the effects of *C.lentillifera* extract on the cytotoxicity, as measured by the lactate dehydrogenase (LDH) release assay, indicated that cell death or membrane permeability. IC50 of *C.lentillifera* extract was more than 1,000 µg/ml at 24 and 48 h. These results suggested that *C.lentillifera* no cytotoxicity when analyzed by LDH assay for LDH activity.

The MTT assays are based on detecting the decrease in viable cell metabolism.[6] The MTT assay measured the enzymatic conversion of tetrazolium salt in the mitochondria. Whereas, the LDH assay is based on detecting cell membrane damage by measuring the release of LDH is a stable cytoplasmic enzyme that is found in all cells. LDH is rapidly released into the cell culture supernatant when the plasma membrane is damaged, a key feature of cells undergoing apoptosis, necrosis, and other forms of cellular damage.[7] These results related to cytotoxicity absence are in agreement, for example, with a previous study carried out by Consistent, Reiko et al. (2012)[8] evaluated the cytotoxicity of polysaccharides isolated from *C.lentillifera* on macrophage cells by MTT assay after 24 h.

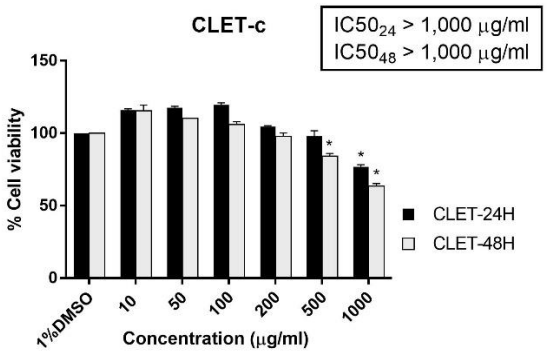

Figure 1.Cell viability of hepatocyte cells treated with *C.lentillifera* extract for 24 and 48 h, assessed by the MTT assay. Data expressed as mean ± standard deviation of the percentage of cell viability in relation to 1%DMSO (100% cell viability), calculated from two technical replicates. * $p < 0.001$ vs. 1%DMSO

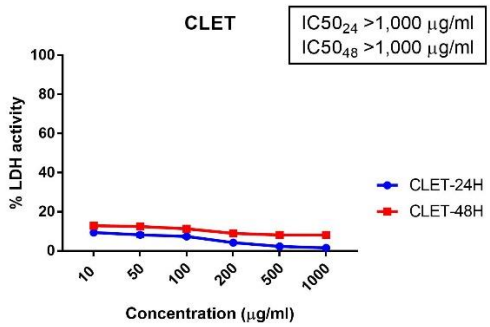

Figure 2.LDH activity of hepatocyte cells treated with *C.lentillifera* extract for 24 and 48 h, assessed by the LDH assay. Data expressed as mean ± standard deviation of the percentage of LDH activity in relation to high control (100% LDH activity), calculated from two technical replicates. NC: negative control. * $p < 0.001$ vs. low control.

Genotoxicity: TK6 cell was a well known recommended cell line for in vitro evaluations of DNA damage through the comet assay due to its high accuracy (90%) to test many genotoxic chemicals.[9] The adequate reliability of the comet assay to predict the genotoxic potential of a test item is well described. Despite the satisfactory performance of this assay, there are some reports of confounding factors that may compromise the confidentiality of the results and increase the uncertainty of the risk assessment. In the present study, following visual examination of the slides, no evidence of overt toxicity was noted on the slides, i.e. there was no substantial increase in background debris and/or increase in the incidence of excessively damaged cells (i.e. non-detectable cell nuclei, hedgehog or ghost comets). To evaluate whether the *C.lentillifera* extracts affect genes, a single cell gel electrophoresis assay (comet assay) was performed with the lymphoblast cell lines (TK6). After treatment, the results were calculated as 3 parameters, and important parameter was %Tail DNA. The administration of the test item had no effect on the %tail DNA intensity in the lymphoblast cell. Consistent, although at concentration 1,000 µg/ml of *C.lentillifera* extracts were not caused cell cytotoxicity in hepatocyte cell (Figure 1), there was slightly detectable genotoxicity in the lymphoblast cell lines (Figure 3). By the proportion of tail DNA increased after *C.lentillifera* treatment but no significant. The positive control showed clear, unequivocal increases in %tail DNA intensity (Table 1). The performance of the negative and positive controls was consistent

with a valid assay. These results suggested that *C.lentillifera* showed no genotoxicity when to test comet assay for DNA damage. There are many examples from study on DNA damage for example showed this type of response with resveratrol (RES) treatment. In cultured human lymphocytes, high concentrations of RES-induced DNA damage while low concentrations showed protective effects on reactive oxygen species-induced DNA damage.[10] Altogether the reports demonstrate good performance of the comet assay, but highlight the need to deepen the understanding of factors that may generate contradictory results and the necessity for careful consideration of study design when using the comet assay as a measure of in vivo genotoxicity.

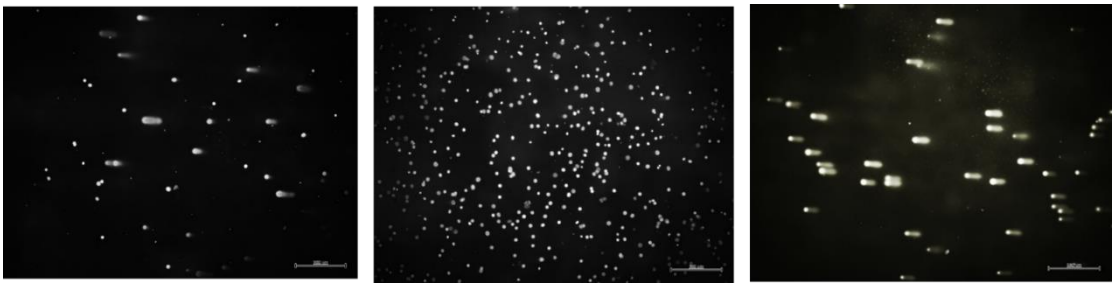

(A) (B) (C)

Figure 3.Genotoxicity measured by comet assay. The expression of DNA damage in comet where strand breakers and alkylating agents analyzed by Comet Score 2.0 software. (A) *C.lentillifera* extract concentration 1,000 µg/ml. (B) Negative control. (C) Positive control.

Table 1. Genotoxicity measured by comet assay. Show calculated three parameters for tail length, %tail DNA and tail moment in TK6 cells treated with *C.lentillifera* extract for 24 h.

Group	Tail Length ± SD	%Tail DNA ± SD	Tail moment ± SD
Negative control	0.7 ± 1.04	10.66 ± 2.15	0.08 ± 0.12
Positive control (98 mM H_2O_2)	59.42 ± 52.39*	80.03 ± 13.83*	44.19 ± 42.56*
CLET 1,000 µg/ml	19.14 ± 21.08	34.84 ± 23.75	10.42 ± 13.18

S.D = Standard Deviation; H_2O_2 = Hydrogen Peroxide

Significant results from the control group are calculated and marked with asterisks (* $p < 0.001$).

Conclusion: In this study, toxicity studies were conducted to determine the possible toxic effects of *C.lentillifera* extract in the cellular level and to provide credible information for the future application. To make the result more convincing, hepatocyte cell lines and lymphoblast cell lines (TK6) were employed in our study for cytotoxicity and genotoxicity, respectively. Our findings revealed that *C.lentillifera* extract could no significant cause cell damage in hepatocyte cells. In the genotoxicity test, significant toxic effects were not observed from lymphoblast cell, followed by the treatment with *C.lentillifera*. Overall, our findings provided important information for the further use of *C.lentillifera* in the food industry and supplement products.

References:

1. Walum E, Clemedson C, Ekwall B. Toxicol In Vitro. 1994;8(4):807–12.
2. Council NR. Washington, DC: National Academies Press. 2006.
3. Matanjun P, Mohamed S, Muhammad K, Mustapha NM. J Med Food. 2010;13(4):792-800.
4. Maeda R, Ida T, Ihara H, Sakamoto T. Biosci Biotechnol Biochem. 2012;76(5):1032-4.

5. Mosmann, T. J. Immunol. 1983;65:55–63.
6. Fotakis G and Timbrell JA. Toxicology Letters. 2006;160(2):171–177.
7. Priti K, Arvindhan N, Pradeep D. Cold Spring Harb Protoc. 2018(7).
8. Reiko M, Tomoaki I, Hideshi I, Tatsuji S. Food & Nutrition Science Regular Papers. 2012(3);76:501-505.
9. Hong Y, Jeon H, Ko K, Kim J, Yi J, Ahn I, Kim T, Lee J. Mutat. Res. 2018;827:59–67.
10. Heger A, Ferk F, Nersesyan A, Szekeres T, Kundi M, Wagner K, Haidinger G, Mišík M, Knasmüller S. Mutat. Res. 2012;749:82–86.

Acknowledgements: This research was supported by the Thailand Research Fund (TRF), research and researcher for industry (RRi) and The Agricultural Research Development Agency (Public Organization).

A_019_OF: EFFICIENCY OF *Caulerpa lentillifera* AND *Halymenia durvillei* EXTRACTED SUBSTANCES IN ANTI-OXIDATION

Tepprit Samrit[1], Athit Chaiwichien[1], Supawadee Osotprasit[1], Narin Changklungmoa[1], Krai Meemon[2], Montakan Tamtin[3], Nakorn Niamnont[4], Prasert Sobhon[2], Pornanan Kueakhai[1,*]
[1]Faculty of Allied Health Sciences, Burapha University, Long-Hard Bangsaen Road, Saen Sook Sub-district, Mueang District, Chonburi 20131, Thailand
[2]Faculty of Science, Department of Anatomy, Mahidol University, Bangkok, Thailand,
[3]Department of Fisheries, Coastal Aquatic Feed Research Institute, Coastal Fisheries Research and Development Bureau, Petchaburi, Thailand,
[4]Faculty of Science, Department of Chemistry, King Mongkut's University of Technology Thonburi, Bangkok, Thailand.
e-mail: earn_patho@hotmail.com, pornanan@buu.ac.th (P. Kueakhai)

Abstract: Free radicals are an atom or molecule that have one or more unpaired electrons and can react quickly with a micromolecule and macromolecule that cause of many diseases. Antioxidants were mostly found in plants such as herb and seaweeds. *Caulerpa lentillifera* (CL) and *Halymenia durvillei* (HD) are seaweeds that classified in Chlorophyta and Rhodophyta phylum. They were cultivated in tropical and subtropical region for food and water waste treatment. The aim of the present study was to evaluate the antioxidant and anti-inflammation effect of CL and HD extracts. In this study, seaweeds were extracted by ethanol (ET), hexane (HE) and ethyl acetate (EA) solutions. The antioxidation effect demonstrated by DPPH scavenging assay and ABTS scavenging assay. The result of DPPH and ABTS scavenging assay found CL and HD extract contained antioxidation compound in EA, HE, and ET fraction. The EA fraction was highest antioxidant effect.

Introduction: Marin algae or seaweeds are important in ecology. They are a group of species from the Protista kingdom comes in various colors such as green (Chlorophyta), red (Rhodophyta) and brown (Phaeophyta), and also various shapes in form of sphere, board leaves, and delicate finger. Seaweeds have been used to commercial because, they are rapid growly and high product volume. In 2016, the value is given above for exports of seaweeds products about USD 1.7 billion[1]. Product of seaweeds increased from in 2005 to more than 15.7 million tons in 2015 At present they have many products and benefited from seaweed such as food, fertilizers, pharmaceuticals, cosmetics, wastewater treatment, and biochemicals[2].

Biochemical from seaweeds are high benefits. In Previous studies, biochemical functionalities of seaweed have many effects to prevent and treatment such as antibacterial, anti-cancer, anti-osteoporosis, anti-viral, anti-obesity, antifungal, antileishmanial, anti-diabetic, antitumor, anti-inflammation and antioxidant[3-4]. In the future biochemicals were discovered from seaweeds will use too many products for health care, as a food supplement, drugs, and cosmetics. The products were high commercial value and increased commercial value of seaweeds[5]. In Thailand, seaweed farming was cultivated and harvested in many countries. Many seaweeds can be cultivated high yields such as sea grape (*C. lentillifera*) and dragon's breath (*H. durvillei*). Support activities in a value chain by technology development can be increased commercial value of seaweeds in Thailand. Previous researchers have reported the effects of green algae and red algae. Sea grape (*C. lentillifera*) and dragon's breath (*H. durvillei*) are native to tropical areas. Seagrape is a green seaweed, popular edible and include high essential mineral, vitamins, and macronutrients. Dragon's breath is a red seaweed. It was found highly sulfated and pyruvylated[6]. However, the effect of sea grape and dragon's breath weren't expected studied.

Free radicals are an atom or molecule that have one or more unpaired electron and can react quickly with a micromolecule and macromolecule. Two types of free radicals were found in organism include oxygen-based and nitrogen base radicals. Oxygen-based radicals

were called reactive oxygen species (ROS) such as superoxide anion, hydrogen peroxide, hydroxyl radical, and peroxyl radicals. Nitrogen-based radicals reactive were called reactive nitrogen species (RNS) such as nitric oxide, and peroxynitrite[7]. These can induce many problems in organism such as DNA damage, mitochondria impairment. The natural antioxidant contained in many seaweeds[8-9]. That can protect damage from free radicals by provide electron or hydrogen atoms.

Here, we were studied about antioxidant effect of *C. lentillifera* and *H. durvillei* extraction. That was increased commercial value to seaweeds product from Thailand.

Methodology:

Biological material: Caulerpa lentillifera (green algae) and *Halymenia durvillei* (red algae) were collected from the seaweed farming in Phetchaburi. Algae were dried, and next seaweeds were extracted by ethanol, hexane, and ethyl acetate solutions. The extracts were evaporated with rotary evaporator that provided by Asst.Prof.Dr. Nakorn Niamnont (the King Mongkut's University of Technology Thonburi). Crude extracts were dissolved with Dimethyl sulfoxide (DMSO, Sigma) and were adjusted 100 mg/ml for algae extraction stock solution, stored in dark and -20 °C.

DPPH scavenging assay: Scavenging of 2,2-Diphenyl-1-picrylhydrazyl (DPPH) radicals' assay was adjusted form Xie and Schaich, 2014[10]. The DPPH solution was purchased from EMD Millipore corporation, Germany ($C_{18}H_{12}N_5O_6$, Mw 394.3 g/mol). The solution was dissolved to 0.002 g of DPPH in absolute methanol to obtain constant volume by filling 1.0 mL (5.0 mM DPPH the stock solution, store in dark and -20 °C). After that dilutes in absolute methanol to generate a 0.1 mM DPPH working solution. In this assay has a four group, I) 0.1 mL of stock algae sample solutions were diluted with methanol (250, 500, 750, 1000, 1500, and 2000 µg/mL), and mixed with 0.1 mL of methanol in 96-well plate ($A_{sample+Met}$). II) 0.2 mL of methanol in 96-well plate (A_{Met}). III) 0.1 methanol in 96-well plate ($A_{DPPH+Met}$). IV) 0.1 mL of stock algae sample solutions were diluted with methanol ($A_{Sample+DPPH}$). After that, 0.1 mL DPPH solution (0.1 mM of DPPH) were added to III and IV groups. Positive control will be used 0.1 mL of vitamin C (L-ascorbic acid, $C_6H_8O_6$, Sigma). The vitamin C was diluted with methanol (2, 4, 6, 8, and 10 µg/mL), then 0.1 mL of DPPH (0.1 mM DPPH) were mixed with positive control group in 96-well plate. The solution was mixed and left at room temperature and dark about 30 min. after that the absorbance of solution at 517 nm was measured.

ABTS scavenging assay: Scavenging of ABTS assay was adjusted from Re, et al., 1998. 2,2′-Azino-bis (3-ethylbenzothiazoline-6-sulfonic acid) diammonium salt solution (ABTS) was purchased from EMD Millipore Corporation, Germany. ABTS radical cation (ABTS+) was produced by reacting 8 mM ABTS stock solution with 5 mM ammonium persulfate in 5 mL of methanol. That was incubated at room temperature in the dark about 18 hours. ABTS and ammonium persulfate reacted at a ratio of 2:1. The ABTS working solution was diluted with 5 mL of methanol (total 10 mL of ABTS working solution). This method has a four-group like DPPH assay. I) 0.1 mL of algae extract solutions were diluted with methanol (250, 500, 750, 1000, 1500, and 2000 µg/mL) and mixed with 0.1 mL of methanol in 96-well plate ($A_{sample+Met}$). II) 0.2 mL of methanol in 96-well plate (A_{Met}). III) 0.1 methanol in 96-well plate ($A_{\mathrm{ABTS+}Met}$). IV) 0.1 mL of stock algae sample solutions were diluted with methanol ($A_{\mathrm{sample+ABTS}}$) and 0.1 mL ABTS solution (ABTS working solution) were added to III and IV groups. The positive control was used 0.1 mL of vitamin C (L-ascorbic acid, $C_6H_8O_6$, Sigma). The vitamin C were diluted with methanol (2, 4, 6, 8, and 10 µg/mL), then ABTS working solution was mixed with a positive control group in 96-well plate. The solution was mixed and incubated at room temperature and dark about 20 min. after that, the absorbance of a solution at 734 nm was measured.

DPPH and ABTS analytical procedure: In the analytical procedure, the result of DPPH and ABTS assay was repeated three times. After that, measurement at six points of sample concentrations, positive and negative control were calculated as following equation

$$\%\ \text{scavenging effect} = \left[\frac{(A_{DPPH/\text{ABTS}+Met} - A_{Met}) - (A_{Sample+DPPH/ABTS} - A_{sample+Met})}{(A_{DPPH/\text{ABTS}+Met} - A_{Met})}\right] \times 100$$

Next, the half maximal effective concentration (EC50) of various samples and positive control were calculated with the regression line equation. In this step, we generated respective regression line by trend line and correlation with percent of DPPH scavenging effect or ABTS scavenging effect (y) and concentration (x) by graph prism 7 software (graph prism, Inc., version 7.04). Correctly respective regression line was a high positive association ($R^2 \leq 0.9$). Concentration of samples were calculated when the percent of scavenging effect (y) in the equation was substituted with 50%. The average value of three repetitive measurements were calculated.

Results and Discussion:

DPPH scavenging assay activity: DPPH free radical solution is unstable form. That reacted with antioxidant and change color because can be quenched by both electrons and hydrogen atom. In this study, DPPH solution was used to determine antioxidation effect of CL and HD in 3 fractions. DPPH radical scavenging effects of all tested fraction increased with increasing concentrations of samples. EC5 is the extracted concentration providing 50% of radical scavenging effect. That values were calculated from line equation of % DPPH Scavenging effect and concentration.

Vitamin C was used as positive control. It was mainly antioxidant in many foods. The EC50 of vitamin C was 6.66 µg/ml.

CL extract was had antioxidation effect (Fig 1A). The highest antioxidation effect was EA fraction (EC50 = 535.90 µg/mL). The HE fraction was higher antioxidation effect than ET fraction (EC50 = 2,947.41 and 3,088.77 µg/mL). HD extract was had antioxidation effect (Fig 1B). The highest antioxidation effect was EA fraction (EC50 = 571.20 µg/mL). The HE fraction was higher antioxidation effect than ET fraction (EC50 = 1,081.35 and 3957.08 µg/mL).

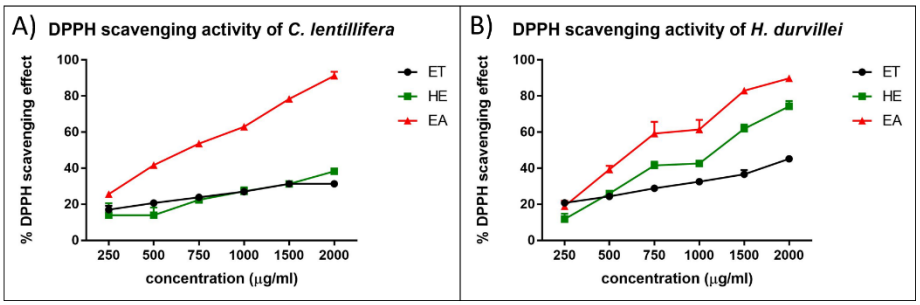

Figure 1. DPPH scavenging of algae extracts A) *C. lentillifera* extract. B). *H. durviillei* extract.

Table 1. DPPH scavenging and EC50 of *C. lentillifera* extract

Fraction	% DPPH scavenging effect						EC50 (µg/ml)
	250 µg/ml	500 µg/ml	750 µg/ml	1,000 µg/ml	1,500 µg/ml	2,000 µg/ml	
CLET	1.21 ±1.99	5.54 ±2.96	11.30 ±1.06	15.34 ±1.23	21.98 ±0.81	31.68 ±1.65	3,088.77
CLHE	13.97 ±6.68	13.98 ±4.23	22.44 ±0.91	27.18 ±2.16	31.26 ±1.49	38.27 ±0.59	2,947.41
CLEA	25.64 ±1.84	41.69 ±0.34	53.64 ±1.64	62.99 ±1.8	78.41 ±0.41	91.25 ±2.29	535.90

Table 2. DPPH scavenging and EC50 of *H. durviillei* extract

Fraction	% DPPH scavenging effect						EC50 (µg/ml)
	250 µg/ml	500 µg/ml	750 µg/ml	1,000 µg/ml	1,500 µg/ml	2,000 µg/ml	
HDET	-3.45 ±0.90	1.02 ±0.26	5.05 ±8.72	8.94 ±1.44	14.35 ±2.00	22.22 ±2.77	3,957.08
HDHE	11.82 ±3.00	25.97 ±1.11	41.56 ±2.08	42.65 ±1.33	61.88 ±2.36	74.26 ±2.94	1,081.35
HDEA	18.95 ±3.01	39.26 ±2.04	59.23 ±6.53	61.43 ±5.32	82.98 ±0.49	89.82 ±0.38	571.20

ABTS scavenging assay activity: The ABTS solution can react with free radical such as ammonium persulfate, potassium persulfate, and hydrogen peroxide. That was transferred to radical form (ABTS+ free radical). The ABTS+ can be derived electrons and hydrogen atom from antioxidation solution. In this study ABTS solution were induced with ammonium persulfate and used to determine antioxidant effect of CL and HD in 3 fractions. ABTS radical scavenging effects of all fractions were increased with increasing concentrations of samples. The EC50 was extracted concentration providing 50% of radical scavenging effect. That values were calculated from line equation of % ABTS Scavenging effect and concentration.

Vitamin C was used to positive control. That was found in many foods. The EC50 of vitamin C was 4.82 µg/ml.

The CL extract was had antioxidation effect (Fig 2A). The highest antioxidation effect was CLEA fraction (EC50 = 712.42 µg/mL). The CLET fraction higher antioxidation effect than CLHE fraction (EC50 = 2,022.75 and 2,546.60 µg/mL). The HD extract was had antioxidation effect (Fig 2B). The highest antioxidation effect was HDEA fraction (EC50 = 668.73 µg/mL). The HDHE fraction was higher antioxidation effect than HDET fraction (EC50 = 1,639.87 and 3,555.92 µg/mL).

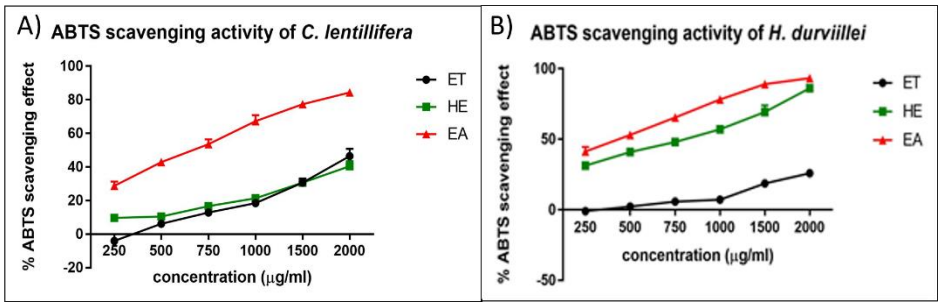

Figure 2. ABTS scavenging of algae extracts A) *C. lentillifera* extract. B). *H. durviillei* extract.

Table 3. DPPH scavenging and EC50 of *C. lentillifera* extract

Fraction	% ABTS scavenging effect						EC50
	250	500	750	1,000	1,500	2,000	(µg/ml)
CLET	-4.08 ±2.74	6.13 ±2.72	12.80 ±1.00	18.43 ±0.91	30.62 ±2.42	46.46 ±2.63	2,022.75
CLHE	9.70 ±1.81	10.43 ±1.36	16.67 ±1.06	21.36 ±1.19	30.69 ±1.29	40.41 ±3.02	2,546.60
CLEA	28.75 ±2.55	42.85 ±1.83	53.51 ±2.96	67.25 ±3.55	77.30 ±0.37	84.37 ±0.97	712.42

Table 4. ABTS scavenging and EC50 of *H. durviillei* extract

Fraction	Concentration (µg/ml)						EC50
	250	500	750	1,000	1,500	2,000	(µg/ml)
HDET	-0.88 ±4.30	2.32 ±2.56	5.83 ±2.12	7.15 ±1.06	18.65 ±0.57	25.90 ±0.40	3,555.92
HDHE	31.28 ±2.93	40.92 ±2.30	48.01 ±0.99	57.11 ±0.60	69.36 ±4.75	86.18 ±1.59	1,639.87
HDEA	41.28 ±3.34	53.06 ±1.48	65.48 ±2.44	78.20 ±1.90	89.05 ±0.76	93.27 ±0.99	668.73

CL and HD have an antioxidant effect similar to many red and green seaweeds such as *Gracilariopsis longissima*, *Hydropuntia cornea*, *Halopithys incurva* [12], *Chaetomorpha linumx*[13], and *Ulva rigida* [14]. The EA fraction has the highest antioxidant effect. Maybe the HDEA fraction consists high concentration of flavonoid, terpenoid, steroids, glycoside and saponins and the CLEA fraction consist high concentration of alkaloids, tannins, terpenoids, and Glycoside. The ET and HE fraction consist of many pigments such as chlorophyll and phycobilin. which interfered absorbance. The CLET fraction maybe consists of alkaloids, flavonoid, phenols, tannins, terpenoid, steroids, glycoside, and saponins. The HDET maybe consists of alkaloids, flavonoid, terpenoid, steroids, glycoside, and saponins. The CLHE may be consist of alkaloids, flavonoid, terpenoid, and glycoside. The Antioxidant properties of each fraction relate the type of phytochemicals and concentration of phytochemicals. Besides, antioxidant effects measured by ABTS assay was strongly positively correlated to that by DPPH assay. ABTS and DPPH solutions are limited as they use non physiological radicals. However, the limitation of ABTS and DPPH assays were more strongly correlated with total phenolics than another phytochemical. In addition, the DPPH assay was greater determined in the highly pigmented extracts[15].

Conclusion: In this study, The CL and HD were extracted by ethanol, hexane, and ethyl acetate solvent. The algae extracts were separated by high to low polarity. Next, we used DPPH and

ABTS assay for measured antioxidation scavenging effect. CL and HD extracts showed antioxidant effects. CLEA and HDEA fractions contained the highest antioxidant effects. Further studies are required to identify and isolate phytochemicals form each fraction.

References:

1. Ananthanawat C, Vilaivan T, Hoven VP. Sens Actuators B. 2009; 137:215–221.Food and Agriculture Organization of the United Nations (FAO). The State of World Fisheries and Aquaculture 2018; 1:17.
2. Brown ES, Allsopp PJ, Magee PJ, Gill CI, Nitecki S, Strain CR, McSorley EM. Nutrition Reviews. 2014; 72: 205-216.
3. Fernando IPS, Nah JW, Jeon YJ. Environ Toxicol Pharmacol. 2016; 48: 22-30.
4. Carson MA, Clarke SA. Mar Drugs. 2018; 16:340.
5. Meksuk Ch. Thammaapipon S. Business Review Journal, 2017;9, 68-80.
6. Fenoradosoa TA, Delattre C, Laroche C, Wadouachi A, Dulong V, Picton L, Andriamadio P, Michaud P. Int J Biol Macromol. 2009; 45:140-145.
7. Kehrer JP, Klotz LO. Crit Rev Toxicol. 2015;45:765-798.
8. Mellouk Z, Benammar I, Krouf D, Goudjil M, Okbi M, Malaisse W. Exp Ther Med. 2017 ;13:3281-3290.
9. Shin T, Ahn M, Hyun JW, Kim SH, Moon C. Acta Histochem. 2014; 116(5) :669-74.
10. Xie J, Schaich KM. J Agric Food Chem. 2014; 62: 4251-4260.
11. Re R, Pellegrini N, Proteggente A, Pannala A, Yang M, Rice-Evans C. Free Radic Biol Med. 1999; 26:1231-1237.
12. Álvarez-Gómez F, Korbee N, Figueroa FL. J Phycol. 2019
13. Stabili L, Acquaviva MI, Angilè F, Cavallo RA, Cecere E, Del Coco L, Fanizzi FP, Gerardi C, Narracci M, Petrocelli A. Mar Drugs. 2019 ;17
14. Cruces E, Rautenberger R, Cubillos VM, Ramírez-Kushel E, Rojas-Lillo Y, Lara C, Montory JA, Gómez I. J Phycol. 2019
15. Floegela A, Kim DO, Chung SJ, Koo SI, Chun KO. Journal of Food Composition and Analysis. 2011; 24: 1043-1048

Acknowledgements: This research was supported by Agricutural Research Development Agency (Public Organization), ARDA

A_020_PF: ANTIFUNGAL ACTIVITY OF CRUDE EXTRACTS FROM LICHEN *Parmotrema tinctorum* (Despr. ex Nyl.) Hale AGAINST *Pythium* spp. CAUSAL AGENTS OF DAMPING-OFF DISEASE OF MARIGOLD (*Tagetes erecta* L.)

Muthita Molsil*, Patchara Mongkolsuk, Vasun Poengsungnoen, Mongkol Phaengphech, Onuma Piasai, Kawinnat Buaruang
Lichen Research Unit. Department of Biology. Faculty of Science. Ramkhamhaeng University. Huamark, Bangkapi, Bangkok 10240, Thailand
*e-mail: mumi-401@hotmail.com

Abstract: Damping-off in marigolds caused by *Pythium* spp. can damage young marigolds leading to collapse of seeding, and cause severe economic losses. The objective of this study was to investigate the antifungal activity of lichen crude extracts, *Parmotrema tinctorum* (Despr. ex Nyl.) Hale, against *Pythium* spp. causal agents of damping-off disease of marigold (*Tagetes erecta* L.). Two hundred grams of the investigated lichen thalli were cut and macerated in 500 mL of acetone for 48 hrs. The extracts were concentrated with rotary evaporator at 40 °C. The lichen crude extract was dissolved in dimethyl sulphoxide (DMSO) and tested against two isolated strains of *Pythium* spp. (Py-R7, Py-RM4) by poisoned food method with five different concentrations; 3,000, 1,000, 500, 100 and 50 µg/mL. Fungicide metalaxyl and DMSO were used as positive and negative controls. .EC_{50} was calculated using Probit analysis. The crude extract at 3,000 µg/mL inhibited 87% and 78% mycelial growth of Py-R7 and Py-RM4, respectively. In contrast, the crude extracts at concentrations of 500, 100 and 50 µg/mL were less active to reduce the growth of both fungal strains (less than 50% mycelial growth inhibition). The EC_{50} values of crude extracts on Py-R7 and Py-RM4 were 436.5 and 630.9 µg/mL, respectively.

Introduction: Lichens are symbiotic organisms of fungi (mycobiont) and algae or cyanobacteria (photobiont or phycobiont). Lichen-forming fungi produce a great number of various secondary metabolites, and most of them are unique. The lichen substances are produced by the mycobiont[1,2], and accumulate in cortex or medullary layers of lichen thalli. Approximately 1,050 secondary compounds have been reported[3] which many of them have various biological activities such as antifungal, antiviral and antiprotizoal[4].

Parmotrema tinctorum (Despr. ex Nyl.) Hale is a cosmopolitan lichen species belonging to the family Parmeliaceae. This lichen is characterized by large foliose thalli with broad lobes and the present of two lichen substances viz. atranorin and lecanoric acid. The crude extracts and lichen acids from this lichen have been reported to have antifungal activities. Kekuda and Vinayaka (2016)[5] studied methanol crude extracts of *P. tinctorum* against fungi isolated from seeds of maizes and groundnuts. Lecanoric acid was tested against the fungus *Cladosporium sphaerospermum*, a dematiaceous saprophytic fungus. The results revealed that the compound had potent fungitoxic activity[6]. Shivanna et al. (2014)[7] evaluated the antifungal activity of the acetone, ethyl acetate and methanol extracts of *P. tinctorum* against *Fusarium oxysporum* f. sp. *capsici*, causing Fusarium wilt of chili pepper. The results showed that both ethyl acetate and methanol extracts had the efficiency to reduce mycelial growth of the plant pathogen, whereas the acetone extract had no activity to control the growth of mycelial.

Marigold (*Tagetes erecta* L.) is one of the important economic flowers and normally it can resist to insect issues however, fungal diseases in marigold plants are the problems. Many diseases causing by fungi were reported such as leaf spots (*Alternaria tenuissima*) and flower blight (*Alternaria zinniae*)[8]. Damping-off is another serious problem, caused by *Pythium* spp. that damage or weaken young marigolds leading to collapse of seeding. The aim of this study was to evaluate antifungal activity of crude extracts of *Parmotrema tinctorum* against *Pythium* spp. isolated from disease marigolds.

Methodology:
Collection and Identification of Lichen: *Parmotrema tinctorum* was collected from Khao Yai National Park -on 26 September 2017. The specimens of lichens were carefully separated from the substrate. The samples were identified based on morphological, anatomical and chemical tests (potassium hydroxide (K), calcium hypochlorite (C) and p-phenylenediamine (P)) and the secondary metabolites were characterized by thin layer chromatography[9].
Preparation of lichen crude extracts: Lichens were cleaned of substrata and shade dried at room temperature for 3 days. The dried samples were cut to small piece (ca. 2×3 mm). Two hundred grams of cut lichen were soaked with 500 ml of acetone and incubated on a shaker for 48 h at room temperature. Then the mixture was filtered through Whatman No. 1 filter paper and maceration of residue was repeated until the extractions were clear. The filtrate was concentrated in vacuo at 50 °C by using rotary evaporator. The crudes extracts were weighed and stored in a desiccator at 25 °C for further assays.
Plant pathogenic fungi isolation: The marigolds with symptoms of damping-off disease were collected from agricultural fields in Nonthaburi and Pathumthani provinces during July 2017 - October 2018. The isolation of *Pythium* spp., causal agents of damping-off disease, was made by tissue transplanting method and identified on the basis of their morphological and anatomical structures[10,11]. The pure fungal strains (Py-R7, Py-RM4) were maintained on potato dextrose agar (PDA) slants at 25 °C.
Antifungal activity assay: Antifungal activity assay was carried out by the poisoned food method. The plant pathogenic fungi were inoculated on PDA plates and incubated at 25°C for 3 days to obtain young and active colonies. The lichen crude extracts were dissolved in dimethyl sulphoxide (DMSO; the final concentration did not exceed 0.2%) and then mixed with worm PDA medium (45-50 °C) to obtain five different concentrations (3,000, 1,000, 500, 100 and 50 µg/mL). After the agar and lichen extracts were mixed together, approximately 15 ml was poured into each of 5 Petri plates and allowed to solidify at room temperature. The colony margin of fungal pathogens was cut with 5 mm diameter of sterile cork borer. Then transferred to the center of the agar plates containing different lichen extract concentrations and then the plates were incubated at 25±1 °C. Colony diameters were measured when the positive control had reached the edge of the plates. The PDA with fungicide metalaxyl and with 0.2% of DMSO were used as positive and negative controls, respectively. For each treatment was repeated five times. Percentage inhibition of mycelial growth is evaluated by comparing and measuring the colony diameter of the poisoned plates (with lichen extract) and non-poisoned plate (without lichen extract). The antifungal activity of the lichen extracts in terms of percentage inhibition of mycelial growth (PIMG) was calculated using the formula:

$$PIMG = C - T / C \times 100$$

Where, C = Average of diameter increase of mycelial growth in control plate and T = Average of diameter increase of mycelial growth in treatment plate. All observed data were analyzed by using statistical software package SPSS. The comparison differences between lichen extracts and metalaxyl against both plant pathogenic fungi were done by t-test ($P < 0.05$) and significant differences of concentrations were determined by using Duncan's multiple range analysis. The means effective inhibitory concentration (EC_{50}) against plant pathogenic fungal was calculated according to probit analysis[12].

Results and Discussion: The effects of different acetone crude extract concentrations from *Parmotrema tinctorum* (3000, 1000, 500, 100 and 50 µg/mL) on mycelial growth of *Pythium* spp., Py-R7 and Py-RM4, were shown in Table 1. The antifungal activity was found in all of the different concentrations and the activity of crude extract was significantly enhanced

by increasing of the concentrations (Table 1 and Figure 1). In addition, each concentration showed significant differences to reduce the radial growth of the tested fungi (Table 1.). At concentration 3,000 µg/mL of the crude extract showed the highest mycelial growth inhibition of both Py-R7 and Py-RM4 by 87.1% and 77.8 %, respectively. Whereas, the metalaxyl completely inhibited the mycelial growth of both fungal strains at the same concentration. Another strong mycelial growth inhibition was found at 1,000 µg/mL which reduced the growth of Py-R7 and Py-RM4 by 74.1% and 62.4%, respectively. Our results are similar to the previously reported by Kekuda et al. (2016)[13] who also found that the extracts from *P. tinctorum* had antifungal activities against several plant pathogenic fungi viz. *Helminthosporium* sp, *Curvularia* sp. *Alternia* sp., *Mucor* sp., *Penicillium* sp. and *Rhizopus* sp. The mycelial growth was suppressed lower than 50% at concentration of 500 and 100 µg/mL. In contrast, the metalaxyl reduced more than 80% of both plan pathogens at the same concentration. The two fungal strains were only slightly affected by crude extracts at 50 µg/mL (Figure 2). The comparison of the effect of different crude extract concentrations in the growth inhibition of both Py-R7 and Py-RM4 showed that Py-R7 was more significantly affected by the extract than Py-RM4 at 3000, 500 and 50 µg/mL.

The EC_{50} values of lichen crude extracts against Py-R7 and Py-RM4 were 436.5 and 630.9 µg/mL which was higher than metalaxyl with 8.32 and 7.94 µg/mL, respectively. Even though, the EC_{50} values in this study appear to be higher than the EC_{50} values of metalaxyl. However, we think the EC_{50} values obtained in this study are reasonable because lichen crude extract are generally a mixture of active and non-active compounds whereas the metalaxyl used in this investigation is one of the best fungicides to control lower fungi such as *Pythium* spp. or *Phytophthora* spp. The results of this study were concordance with Mongkolsuk et al. (2009)[14], who reported that the EC_{50} values of lichen crude extracts from *Parmotrema tinctorum* against *Pythium deliense*, causal agent of damping-off of seedling, was 548 µg/mL.

Table 1. Effect of different concentrations of acetone crude extracts from *Parmotrema tinctorum* and metalexyl on the mycelial growth of *Pythium* spp.

Concentration	Percentage of mycelial inhibition[A]				t-test[B]			
	Py-R7		Py-RM4					
	(1)	(2)	(3)	(4)	(1) vs (2)	(3) vs (4)	(1) vs (3)	(2) vs (4)
50 µg/mL	12.7±7.43[a]	86.7±1.36[a]	10.0±2.48[a]	86.7±1.36[a]	-21.886**	-60.517**	0.760	0.000
100 µg/mL	19.8±1.64[b]	88.9±0.0[a]	14.8±4.11[b]	88.0±1.22[a]	-93.770**	-38.174**	2.523*	1.633
500 µg/mL	44.2±0.92[c]	95.6±6.09[b]	45.4 ±1.13[c]	95.6±6.09[b]	-18.645**	-18.098**	-1.859	0.000
1,000 µg/mL	74.1±1.44[d]	100±0.0[c]	62.4 ±3.08[d]	100±0.0[c]	-39.959**	-27.236**	7.658**	-
3,000 µg/mL	87.1±1.68[e]	100±0.0[c]	77.8 ±0.00[e]	100±0.0[c]	-17.103**	-	12.385**	-
p-value	<0.001	<0.001	<0.001	<0.001				

[A]Values are percentage of mycerial inhibition. Means (n = 5) in each column followed by the same superscript letter(s) are not significantly different in the percentages of mycelial growth inhibition. Data reported are mean values ± standard deviation.

[B]Data was analysed by *t*-test compared between (1) (2) (3) and (4)

(1) and (3) = Crude extract of *Parmotrema tinctorum*

(2) and (4) = Metalaxyl

*p<0.05, ** p<0.01

Plant pathogenic fungi	Efficacy of five concentrations of *Parmotrema tinctorum* acetone crude extracts and metalaxyls against *Pythium* spp. *in vitro*				
	50 µg/mL	100 µg/mL	500 µg/mL	1,000 µg/mL	3,000 µg/mL
Py-R7 (lichen crude extracts)	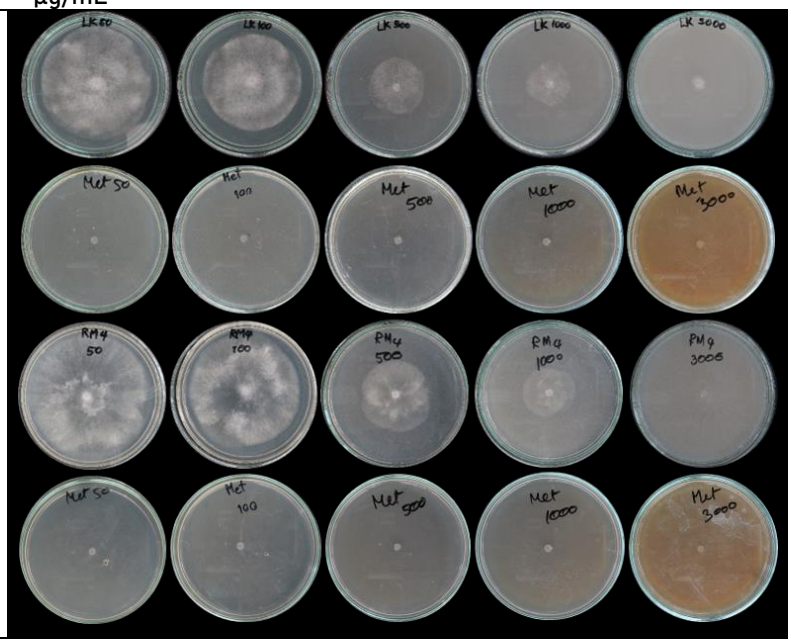				
Py-R7 (metalaxyl)					
Py-RM4 (lichen crude extracts)					
Py-RM4 (metalaxyl)					

Figure 1. Mycelial growth inhibition of *Parmotrema tinctorum* on acetone crude extract and metalaxyl PDA medium against *Pythium* spp., at 25±1 °C for 2 days.

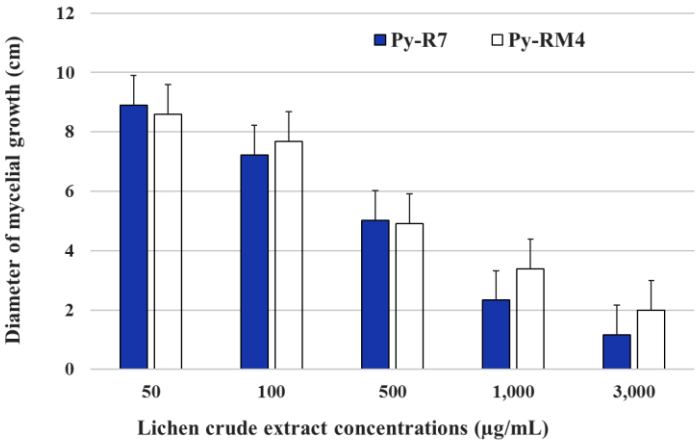

Figure 2. Growth inhibition of *Pythium* spp. (Py-R7 and Py-RM4) by acetone crude extracts of *Parmotrema tinctorum*.

Conclusion: The crude extracts of lichen *Parmotrema tinctorum* showed the antifungal activity against *Pythium* spp. causal agents of damping-off disease of marigolds. The treatments were more effective to Py-R7 than Py-RM4. The antifungal activity of lichen observed in this study could be related to the presence of bioactive secondary metabolites in the extracts. The next study should focus on the application of this inhibitory activity against *Pythium* spp. in the

condition of the potted plants and might include a larger number of fungal isolations and lichen species.

References:

1. Elix J.A. Lichen Biology. 1996; 486: 155-180.
2. Huneck S. Naturwissenschaften. 1999; 86: 559–570.
3. Stocker-Wörgötter E. Nat. Prod. Rep. 2008; 25 (1): 188–200.
4. Halama P. Haluwin C. V. Bio Control. 2004; 49: 95–107.
5. Kekuda P. T.R. Vinayaka K.S. Sci. Technol. Arts Res. J. 2016; 5 (1): 80-83.
6. Gomes A. T. Honda N. K. Roese F. M. Muzzi R. M. Marques M. R. Rev. Bras. Farmacogn. 2002; 12: 74–75.
7. Shivanna R. Garampalli R. H. Adv. Appl. Sci. Res. 2014; 5 (5): 273-277.
8. Chandel S. Teixeira da Silva J. A. Sharma C. Floriculture ornamental biotech. 2010; 4 (1): 79-83.
9. Orange A. James P.W. F.J. White. British Lichen Society; 2001; 101.
10. Van der Plaats-Niterink A. J. Studies in Mycology. 1981; 21: 1–244.
11. Teymoori1 S. M. H. Shahri K., Rahnama Afzali H. Crop Protection. 2012; 13: 239-247.
12. Finney D.J. Probit analysis. 1978; 508.
13. Kekuda P. T. Vinayaka K. S. STAR Journal; 2016: 5 (1); 80.
14. Mongkolsuk P. Manoch L. Buaruang1 K. Poengsungnoen1 V. and Siripong P. The 47th Kasetsart University Annual Conference: Plants; 2009: 571-576.

Acknowledgements: We are grateful to office of Khao Yai National Park for co-operation in field works. The authors also thank the owners of marigold agricultural fields for specimen collection and thank also the Lichen Research, Department of Biology, Faculty of Science, Ramkhamhaeng University for laboratory facility.

A_022_OF: TOTAL PHENOLIC CONTENT, TOTAL FLAVONOID CONTENT AND ANTIOXIDANT ACTIVITY OF THE CULTURE FILTRATE EXTRACT FROM *Ganoderma lucidum*

Puttachard Hensanghong[1], Rungnapa Tangchitcharoenkhul[2], Janpen Tangjitjaroenkun[3,*]
[1]Program in Natural Product Science and Technology, Faculty of Science at Si Racha, Kasetsart University, Si Racha Campus, Thailand
[2]Graduate school, Suan Dusit University, Bangkok, 10300, Thailand
[3]Department of Resources and Environment, Faculty of Science at Si Racha, Kasetsart University, Si Racha Campus, Thailand
*e-mail: xjanpen@gmail.com, sfscijpt@src.ku.ac.th

Abstract: *Ganoderma lucidum* has been recognized as a medicinal mushroom for over 2000 years. The extract from fruiting body of *G. lucidum* has been attributed to numerous bioactivities including anti-microbial, anti-inflammatory and antioxidant. In the present study, the mycelial submerged culture of the *G. lucidum* were performed using potato dextrose broth at 25°C for 21 days under static condition. The culture filtrate was extracted with two equal volume of ethyl acetate. The ethyl acetate extract of *G. lucidum* get yields 0.58 g. The total phenolic content was 55.56 ± 5.06 mg GAE/g DW. The total flavonoid content was 71.63 ± 1.05 mg QE/g DW. The screening of antioxidant activity by thin layer chromatography autographic assay found the bleaching color from purple to yellow between 5 and 10 minutes. The quantitative determination of antioxidants used 3 assays, DPPH radical scavenging activity found IC_{50} values of 870.07 ± 26.07 µg/mL, 2,2'-azino-bis[3-ethylbenzthiazoline-6-sulfonic acid] (ABTS) free radical scavenging activity IC_{50} values of 235.81 ± 9.28 µg/mL and ferric reducing antioxidant power assay (FRAP) found 216.031 ± 3.738 mmol Fe_2SO_4 equivalent/g DW, respectively. The culture filtrate extract of *G. lucidum* exhibited a good free radical scavenging activity and also it contained high contents of total phenolic and total flavonoid compounds. This study demonstrates that this extract could be a potential source of natural antioxidants.

Introduction: *Ganoderma lucidum* is a basidiomycota belonging to the family of Ganodermataceae. It is a saprophyte.[1] In China is called Lingzhi, whereas in Japan is called Reishi or Mannentake. In nature, it grows in the subtropical and temperate climate zones, in the forests of Asia, Europe and America.[2] *G. lucidum* can be found growing on living and dead wood of deciduous species under high humidity and indistinct lighting conditions.[3] The fruiting body of *G. lucidum* has large, dark color with a glossy exterior and look like a woody texture.[4]

Amongst the more than 2000 classes of *G. lucidum*, black Lingzhi and red Lingzhi have been investigated to discover potential health-beneficial properties.[3] It has been recognized as a medicinal mushroom for over 2000 years and its powerful effects have been documented in ancient scripts and has a long history of use for promoting health in China, Japan, and other Asian countries. The Chinese are called Lingzhi as the "mushroom of immortality".[5]

It has been reported that *G. lucidum* contains over 400 bioactive compounds, including triterpenoids, polysaccharides, nucleotides, sterols, steroids, fatty acids and proteins. These compounds have important biological activities, such as anti-tumour, anti-microbial, anti-atherosclerotic, anti-inflammatory, hypolipidemic, anti-diabetic, anti-oxidative, anti-aging, anti-fungal, immunomodulatory activity and anti-viral (specifically against herpes simplex virus and human immunodeficiency virus (HIV)) effects.[3]

In this study was to identify the antioxidant potential of ethyl acetate extract from culture filtrate of *G. lucidum* (GL extract). The extract was evaluated for DPPH free radical scavenging activity, ABTS free radical scavenging activity, ferric reducing antioxidant power and reducing power capacity and for phenol and flavonoid content.

Methodology:

Mushroom strains: Cultures of *G. lucidum* were obtained from Department of Agricultural, Biotechnology research and development office, Thailand.

Mycelium culture: G. lucidum were inoculated into potato dextrose agar (PDA) plates and incubated at room temperature for 3-7 days to allow growth of the mycelium. Afterwards cut mycelium using a cork borer no.3 and inoculated 5 pieces in 250 mL potato dextrose broth (PDB). The culture was incubated at room temperature in static condition for 15 days to allow fungal growth.

Extraction: The mycelial fermentation broth was filtered through filter paper (Whatman no.1) and extracted two times with ethyl acetate in the ratio of 1:1 (v/v). Ethyl acetate layer was collected and concentrated by evaporating to dryness at 40 °C. Afterwards the crude extract was store in amber bottle and weighed.

Screening of antioxidant activity: The GL extract test screening of antioxidant by thin layer chromatography autographic assay. The GL extract was spot on TLC (Thin layer chromatography) silica gel GF_{254}. The TLC plate was developed in solvent system contain ethyl acetate mixed with methanol in the ratio of 1:1. The TLC plate was observed under UV light at 254 and 365 nm. It was sprayed with 2,2-diphenyl-1-picrylhydrazyl ($DPPH^{\bullet}$) to detect the bleaching color of $DPPH^{\bullet}$ from purple color to yellow color.

Total phenolic content: The Folin-Ciocalteu reagent was used for the determination of the total phenolic content of the GL extract following the method by Nazemiyeh *et al.* with some modifications.[6] Gallic acid was used as positive controls. The GL extract at various concentrations 125 µL was mixed with 125 µL of Folin- Ciocalteu reagent and 1250 µL of 7% Na_2CO_3. The mixture was stand at room temperature for 30 minutes. The absorbance of the mixture was measured at 715 nm. The results were expressed as gallic acid equivalents in milligram per gram of dry weight (mg GAE/g DW). The test was repeated for 3 times.

Total flavonoid content : The aluminum chloride colorimetric method was used for the determination of the total flavonoid content of the GL extract following the method by Kamtekar *et al.* with some modifications.[7] Quercetin was used as positive controls. The GL extract at various concentrations 250 µL was mixed with 1250 µL of distilled water and 75 µL of 5% $NaNO_2$. The mixture was shaken in room temperature for 5 minutes. Then the mixture was added 150 µL of 10% $AlCl_3$, 500 µL of 1M NaOH and 270 µL of distilled water. The mixture was shaken in room temperature for 5 minutes. The absorbance of the mixture was measured at 415 nm. The results were expressed as quercetin equivalents in milligram per gram of dry weight (mg QE/g DW). The test determinations were carried out in triplicate.

Determination antioxidant activity

DPPH radical scavenging activity: The free radical scavenging activity of the samples was determined using the stable $DPPH^{\bullet}$ radical which was performed according to the method of Tangjitjaroenkun *et al.* with some modifications.[8] The GL extract at various concentrations was diluted with ethanol. The diluted extract 250 µL was mixed with 250 µL of $DPPH^{\bullet}$ solution (2.4 mg DPPH powder in 100 mL of ethanol) in 96-well microtitter plates. The mixture was shaken vigorously and stand for 30 minutes in the dark. The absorbance of the mixture was measured at 520 nm. The inhibition of DPPH free radicals was calculated as % inhibition by the following equation:

$$\% \text{ inhibition} = [(A_{blank}-A_{extract}) / A_{blank}] \times 100$$

Where A_{blank} is the absorbance of blank, and $A_{extract}$ is the absorbance of sample or standard. The results were expressed as extract concentration providing 50% inhibition (IC_{50}) was calculated using the graph by plotting inhibition percentage against extract concentration.

Butylated hydroxytoluene (BHT) was used as positive controls. The results were expressed as the mean±SD of three replicates

2,2'-azino-bis[3-ethylbenzthiazoline-6-sulfonic acid] (ABTS) free radical scavenging activity: The free radical scavenging activity of the samples was determined using the stable 2,2'-azino-bis[3-ethylbenzthiazoline-6-sulfonic acid] ($ABTS^{\bullet+}$) which was performed according to the method of Tangjitjaroenkun *et al.* with some modifications.[8] The $ABTS^{\bullet+}$ was prepared of 7 mmol of ABTS in distilled water mixed with 2.45 mmol potassium persulfate ($K_2S_2O_8$) and incubated in the dark at room temperature for 16 hours. The $ABTS^{\bullet+}$ solution was diluted with deionized water and measured the absorbance of 0.8 ± 0.02 at 734 nm. An amount of 50 µL of GL extract at various concentrations was mixed with 450 µL of $ABTS^{\bullet+}$ solution. The mixture was stand for 1 minute. The absorbance of the mixture was measured at 734 nm. The inhibition of $ABTS^{\bullet+}$ radicals was calculated as % inhibition by the following equation:

$$\% \text{ inhibition} = [(A_{blank}-A_{extract}) / A_{blank}] \times 100$$

Where A_{blank} is the absorbance of blank, and $A_{extract}$ is the absorbance of sample or standard. The results were expressed as extract concentration providing 50% inhibition (IC_{50}) was calculated using the graph by plotting inhibition percentage against extract concentration. Trolox was used as positive controls. The test determinations were carried out in triplicate.

Ferric reducing antioxidant power (FRAP) assay: The total reducing capacity was determined by using FRAP assay which was performed according to the method of Tangjitjaroenkun *et al.* with some modifications.[8] The FRAP reagent was prepared of 300 mM acetate buffer (pH 3.6), 10 mM 2,4,6-tripyridyl-s-triazine (TPTZ) in 40 mM HCl and 20 mM $FeCl_3 \cdot 6H_2O$ solution in the ratio of 10:1:1 (v/v/v) and incubated in a water bath at 37 °C. An amount of 60 µL GL extract at various concentrations was mixed with 1.8 mL of the FRAP reagent and 180 µL of distilled water. The mixture was incubated for 4 minutes. The absorbance of the mixture was measured at 593 nm. The results were expressed as mmol of $Fe_2SO_4 \cdot 7H_2O$ equivalent per gram of dry weight (mmol Fe_2SO_4 equivalent/g DW). Ferrous sulfate (Fe_2SO_4) was used as the standard. The results were expressed as the mean±SD of three replicates

Results and Discussion:

Mycelium and extraction: G. lucidum was cultivated in PDA. After incubated 3-5 days, the mycelium has white color showed in Figure 1. The mycelium in PDA were cut and inoculated in PDB (10 L) for 15-20 days. The mycelial fermentation broth was extracted with ethyl acetate. The ethyl acetate extract of *G. lucidum* get yields 0.58 g of dark brown color and sticky showed in Figure 2.

Figure 1. The mycelium of *G. lucidum* in PDA after incubated 3-5 days

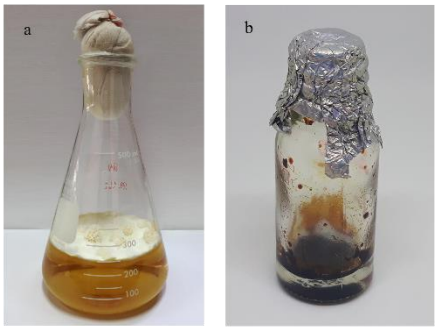

Figure 2. (a) Mycelial fermentation in submerge culture of *G. lucidum* for 15-20 days; (b) The crude extract of *G. lucidum*

Screening of antioxidant activity: The GL extract was spot on TLC. The TLC plate was developed in suitable solvent system (ethyl acetate:ethanol, 1:1). The band on TLC are showed under UV 254 and UV 365. When sprayed DPPH• on TLC found the bleaching color from purple to yellow between 5 and10 minutes are given in Figure 3. The yellowish bands on the purple background were considered as antioxidants from GL extract. The rapidity of bleaching color showed potential of antioxidant of GL extract.

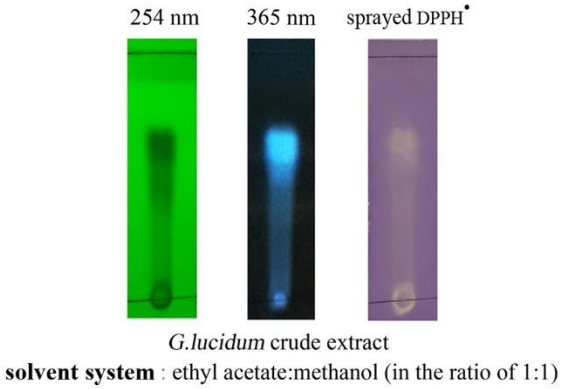

Figure 3. Band of extract under UV 254, UV 365 and bleaching color of DPPH• on TLC

Total phenolic and total flavonoid content: Phenolic acids are a major class of phenolic compounds, widely occurring in the plant

kingdom especially in fruits and vegetables.[9] Phenolic compounds have redox properties, which allow them to antioxidants.[10] The result of total phenolics content of GL extract was measured by Folin-Ciocalteu reagent was found 55.56 ± 5.06 mg GAE/g DW. Flavonoids suppress reactive oxygen formation, chelate trace elements involved in free-radical production, scavenge reactive species and protect antioxidant defenses.[10] The flavonoid content of GL extract was measured by aluminum chloride colorimetric method was found 71.63 ± 1.05 mg QE/g DW.

In another report on the total phenolic content and total flavonoid content from *G. lucidum*, Ćilerdžić *et al.* reported that *G. lucidum* BEOFB 432 have total phenolic content value of 134.89 ± 2.58 µg GAE/mL of culture filtrate and total flavonoid content value of 42.20 ± 1.47 µg QE/mL of culture filtrate.[11] Furthermore, the methanol extracts from mycelia of *G. lucidum* Karst. on PDB and sweet corn media have the total polyphenols value of 13.15 ± 1.89 GAE mg/g and 8.18 ± 0.44 GAE mg/g, respectively.[12] In addition, the culture broth of *G. lucidum*

have total phenol content as 0.557 mg GAE/g extract.[13] From these research indicated that the culture filtrate, mycelial extract and culture filtrate extract of *G. lucidum* contained high phenolic and flavonoid contents. The phenolic compounds have ability to chelate metal ions involved in the production of free radicals and have ability to inhibit some enzymes involved in radical generation.[14] In addition, the flavonoids can prevent injury caused by free radicals in various ways. Flavonoids are oxidized by radicals, resulting in a more stable, less-reactive radical. Flavonoids interfering with inducible nitric-oxide synthase activity. In addition, flavonoids have ability to scavenging of oxygen-derived free radicals.[15] Therefore, phenolic and flavonoids compounds are important antioxidant components.

Determination of antioxidant activity: The antioxidant activity of the GL extract was evaluated by DPPH radical scavenging activity, ABTS free radical scavenging activity and FRAP assay show in Table 1.

In the $DPPH^{\bullet}$ assay, the extract was evaluated in term of hydrogen donating ability.[8] The GL extract showed IC_{50} value of 870.07 ± 26.07 µg/mL, while BHT was found IC_{50} value of 32.34 ± 7.35 µg/mL

ABTS free radical scavenging activity was evaluated in based on the scavenging of the radical cation ($ABTS^{\bullet+}$) by antioxidants in the extract.[8] The GL extract showed IC_{50} value of 235.81 ± 9.28 µg/mL, while trolox was found IC_{50} value of 2.32 ± 0.03 µg/mL

In the FRAP assay, the extract was evaluated in based on the reduction of ferric tripyridyltriazine (Fe^{3+}-TPTZ) complex to the ferrous tripyridyltriazine (Fe^{2+}-TPTZ) formed by the action of electron donating.[16] The GL extract showed FRAP value of 216.03 ± 3.74 mmol Fe_2SO_4 equivalent/g DW

Table 1. Antioxidant activity of *Ganoderma lucidum* extract

	DPPH radical scavenging IC_{50} (µg/mL)	ABTS free radical scavenging IC_{50} (µg/mL)	FRAP (mmol Fe_2SO_4 equivalent/g DW)
GL extract	870.07 ± 26.07	235.81 ± 9.28	216.03 ± 3.74
BHT	32.34 ± 7.35	-	-
Trolox	-	2.32 ± 0.03	-

In another report on the antioxidant activity of *G. lucidum*, Ćilerdžić *et al.* reported that *G. lucidum* BEOFB 432 fermentation broth have the percentage $DPPH^{\bullet}$ scavenging activity of 39.67% ($DPPH^{\bullet}$).[11] In addition, the methanol extracts from mycelia of *G. lucidum* Karst. on PDB and sweet corn media have the percentage DPPH scavenging activity of 22.14 ± 3.25 % and 12.84 ± 2.03 %, respectively.[12] Ai-lati *et al.* reported that the fraction of polysaccharide from *G. lucidum* in submerged fermentation have the highest scavenging rate of 89.02% ($DPPH^{\bullet}$) and 69.53% ($ABTS^{\bullet+}$).[17] The culture filtrate, mycelial extract and culture filtrate extract of *G. lucidum* have the potential of antioxidant activity by different assays including DPPH radical scavenging activity, ABTS free radical scavenging activity and FRAP assay. These results showed that the culture filtrate extract of *G. lucidum* (GL extract) could be used for natural antioxidant supplemented because the antioxidants defensed from damage by free radicals and decreased risk of chronic diseases including heart disease, type 2 diabetes and cancer.[18]

Conclusion: The GL extract was contained high phenolic and flavonoid contents. Phenolic and flavonoid compounds are important antioxidant components. The contents of total phenolic and total flavonoid compounds could affect the antioxidant activity. The free radical scavenging activities of the GL extract was assessed against $DPPH^{\bullet}$, $ABTS^{\bullet+}$ and ferric reducing ability (FRAP). Therefore, the GL extract could be used as natural antioxidant supplement.

References:
1. Babu P D, Subhasree R S. Am-Euras. J. Bot. 2008;1:107–110.
2. Siwulski M, Sobieralski K, Golak-Siwulska I, Sokół S, Sękara A. Herba Pol. 2015;61:105–118.
3. Cör D, Knez Ž, Hrnčič M K. Molecules. 2018;23:694.
4. Soksawatmakhin S, Boonyahotra W. JAASP. 2013;2:262–268.
5. Hennickeab F, Cheikh-Alic Z, Liebischa T, Maciá-Vicentea J G, Bodecd H B, Piepenbringa M. Phytochemistry. 2016;127:29–37.
6. Nazemiyeh H, Khodaie L, Bamdad S, Delazar A. BioImpacts. 2012;2:47–53.
7. Kamtekar S, Keer V, Patil V. JAPS. 2014;4:61–65.
8. Tangjitjaroenkun J. Asian J Pharm Clin Res. 2018;11:271–276.
9. Tinrat S. KKU Res.j. 2016;21:1–11.
10. Baba S A, Malik S A. JTUSCI. 2015;9:449–454.
11. Ćilerdžić J, Kosanić M, Stajić M, Vukojević J, Ranković B. International Journal of Medicinal Mushrooms. 2016;18:397–404.
12. Darsih C, Indrianingsih A W, Apriyana W, Nur Hayati S, Rosyida V T, Nisa K, Ratih D, Indirayati N. EES. 2019;251:012015.
13. Sarnthima R, Khammaung S, Sa-ard P. J Food Sci Technol. 2017;54:3724–3730.
14. Pereira D M, Valentão P, Pereira J A, Andrade P B. molecules. 2009;14:2202–2211.
15. Nijveldt R J, van Nood E, van Hoorn D E C, Boelens P G, van Norren K, and van Leeuwen P A M. Am J Clin Nutr. 2001;74:418–425.
16. Rajurkar N S, Hande S M. Indian J Pharm Sci. 2011;73:146–151.
17. Ai-lati A, Liu S, Ji Z, Zhang H, Mao J. BIOENGINEERED. 2017;8:565–571.
18. Rahman K. Clin Interv Aging. 2007;2:219–236.

Acknowledgements: We would like to thank Department of Resources and Environment, Faculty of Science at Si Racha, Kasetsart University for financial support. We thank Ms. Teeraya Jittarom and Mr. Nuttapong Ponganiwat for the technical assistance.

A_023_PF: DETECTION OF *atzB* GENE IN TROPICAL *Trichoderma harzianum* ISOLATED FROM ATRAZINE CONTAMINATED SOIL IN CENTRAL REGION OF THAILAND

Gun Anantasomboon[1,*], Intira Tampayak[2]
[1]Anatomy Unit,
[2]Microbiology Unit, Department of Medical Science, Rangsit University, Patumthani, Thailand
*e-mail: ananta_rsu@yahoo.com

Abstract: *Trichoderma* spp. is tropical fungus currently used as biological control agent due to their ability to antagonize other plant pathogenic fungi, as well as to degrade some agrochemicals. Among herbicides, atrazine, is intensively used in sugarcane, corn and sorghum fields. Due to the toxicity and persistence of atrazine in the environment, bioremediation using microorganisms have been studied to remove atrazine from contaminated soil and water. This study aimed to investigate the tropical *Trichoderma* spp. that may has unique capability in atrazine degradation or toleration. Fifty isolates of fungal strain from atrazine contaminated corn and sugar cane fields from Kampahaengphet, Nakornpathom and Ratchaburi provinces were cultured in modified medium agar containing 50 mg/L of atrazine for 15 days, then the *atzB* gene investigations of eight survival isolates were determined by using PCR analysis. All of eight survival isolates were finally identified for specific fungal stain by PCR and DNA sequencing analyses, respectively. The results showed that six fungus isolates were positive *atzB*-PCR analysis and classified as *Trichoderma harzianum*. Therefore, the selected strain of tropical *T. harzianum* from central region of Thailand may benefit for the agriculture and the global environment to reduce or to degrade atrazine in contaminated soil.

Introduction: Atrazine (2-chloro-4-(ethylamino)-6-(isopropylamino)-s-triazine) is a selective herbicide widely used in agricultural fields to control the emergence of broadleaf and grassy weeds in corn, sugar cane, sorghum, cotton, residential lawns, golf courses and other crops, which is moderately mobile and highly persistent in soil[1], surface water, groundwater and agricultural products. The persistence of this herbicide in environment is a serious problem for economy loss and health[2], as well as the limitation of biocontrol of plant diseases by some competitive bacteria and fungi. Effects of atrazine for health are risks for cancer formation, malformation of embryo and fetus, respiratory and digestive signs. In 2004, atrazine is a prohibited herbicide for the European Union[3]. In Thailand, atrazine has been imported and used for many decades. Annual cost of atrazine imports in the year 2013 is high as a top-ten of the world countries[4]. The reduction of atrazine is found to be influenced by the metabolic action of habituated microorganisms[5]. The usage of selective microorganisms for atrazine degradation is probably in a practical. Alabouvette[6] reported that some bacteria and fungi in temperate zone such as *Aspergillus*, *Rhizopus*, *Fusarium*, *Pseudomonas*, *Agrobacterium*, *Clavibacter*, *Arthrobacter* and *Escherichia coli*[5] have a capacity in atrazine destruction and reduction. Cai and co-workers[7] reported that the *Arthrobacter* sp. isolated from waste water unit in atrazine producing plant in China has a specific property in atrazine destruction and used atrazine as a nitrogen source for its growth. In the year 2010, mechanism for atrazine degradation in bacteria was firstly reported that it begins from the Hydrolytic dechlorination by using atrazine chlorohydrolase (AtzA), controlled by *atzA* (*trzA*) gene, followed by the Hydrolytic deamination processes by using Hydroxyl-atrazineethylamino-hydrolase (AtzB) and N-isopropyl-ammelide isopropyl–amino-hydrolase (AtzC), controlled by *atzB* (*trzB*) and *atzC* (*trzC*), respectively. After that, atrazine was transformed as cyanuric acid and finally changed to be non-toxic substances, CO_2 and NH_3[8]. *Trichoderma viridae* is known as a competitive fungus for control of plant diseases in temperate zone. It also found to degrade the atrazine rapidly[9]. However, there is lacking data of some tropical fungi, such as *Trichoderma* spp. that may contain an atrazine degradation property. This research aimed to

examine the *atzB* gene of atrazine-tolerant fungi that were isolated from contaminated agricultural fields in central region of Thailand. Selection of tropical *Trichoderma* spp. with atrazine degrade element is beneficial for plant disease control and environmental protection.

Methodology:

Fungal isolation from atrazine contaminated fields: Atrazine contaminated soils were collected from 6 corn and sugarcane fields in Kampahaengphet, Nakornpathom and Ratchaburi provinces. One kilogram of surface soil from each source was kept, filtered and preserved at 4 °C until used. Fifty mg of soil was hydrated with 25 ml sterile water. Then, the fungal culture was performed on Martins'agar plate with Dilution Plate Technique (0.5, $0.5x10^{-1}$, $0.5x10^{-2}$ ml) at 28 °C, for 5 days.

In vitro selection of atrazine tolerant fungus: Selection of each fungal isolates on the center of Czapek-dox agar (D-glucose 1% w/v), with atrazine (50 mg/L) at 28 °C, for 15 days. Identify the surviving fungus under microscope by its morphology and color of hypha[10].

analysis of atzB gene in atrazine tolerant fungus: Pick up hyphae of each isolate of atrazine tolerant fungus from the previous step into 1.5 ml microcentrifuge tube, add liquid nitrogen, lysis buffer and then extract for DNA[11]. DNA samples were preserved at -70 °C. Then, the PCR analysis with a specific primer set[12] (Table 1.) was applied to detect *atzB* gene fragment of atrazine tolerant fungus.

Table 1.Demonstrating the specific primers[12] for *atzB* gene examination of *Trichoderma* spp.

atzB-F primer:	5' TCACCGGGGATGTCGCGGGG 3'
atzB-R primer:	5' CTCTCCCGCATGGCATCGGG 3'

Identification of fungal stain: The atrazine tolerant isolates were sent to investigate for fungal stain at the First BASE laboratories Co. Ltd., Selangor, Malaysia.

Results and Discussion:

Fungal isolation from atrazine contaminated fields: Fungal isolation from 6 corn and sugarcane fields in Kampahaengphet, Nakornpathom and Ratchaburi provinces that were contaminated with atrazine revealed 50 isolates on Martins'agar plate at 28 °C, at 5 days (Figure1).

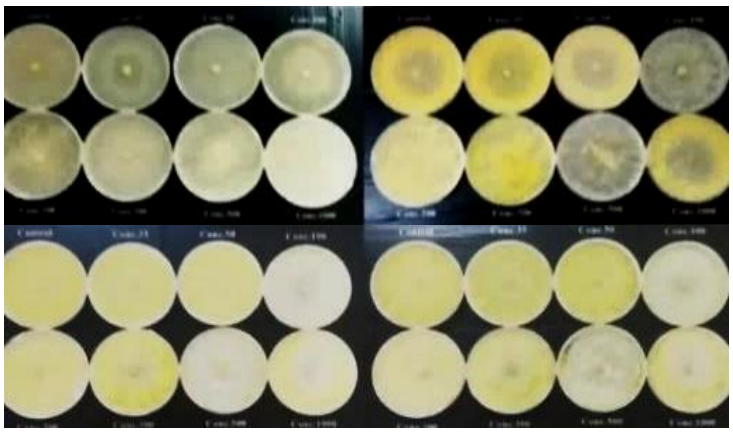

Figure 1. Photograph showing samples of fungal isolated from atrazine contaminated corn and sugarcane fields

In vitro selection of atrazine tolerant fungus: Selection of atrazine tolerant fungus was performed under an Enrichment Culture technique. Fungal isolates from the previous method were separately cultured on Czapek-dox agar with atrazine (50 mg/L), at 28°C. After 15 days of culture period, eight surviving fungal isolates were obtained. The tolerant isolates were fully growth on culture plates. Under microscopic observation, hyphae of all isolates were similar to *Trichoderma* spp.

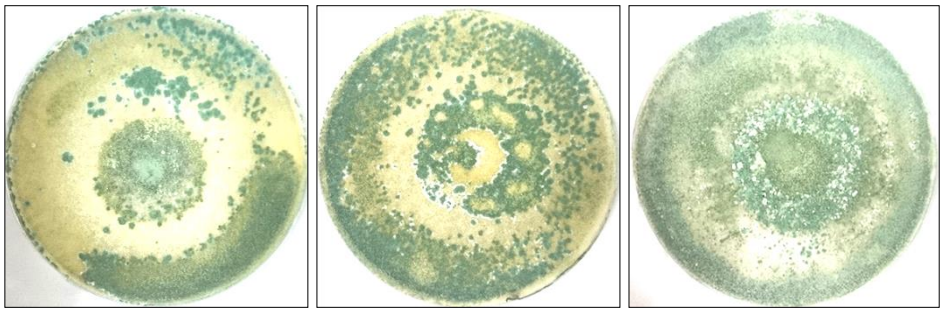

Figure 2. Photograph demonstrating sample of fungal isolates which are survive and tolerant from high concentration of atrazine (50 mg/L) on Czapek-dox agar for 15 days.

PCR analysis of atzB gene in atrazine tolerant fungus: Detection of *atzB* fragment of 8 isolates by using PCR and Agarose Gel Electrophoresis exhibited PCR product at 560 bp with isolates 1-6 and showed negative result with isolates 7-8 (Figure3). Result revealed the detection of *atzB* gene in 6 fungal isolates (lane 1-6).

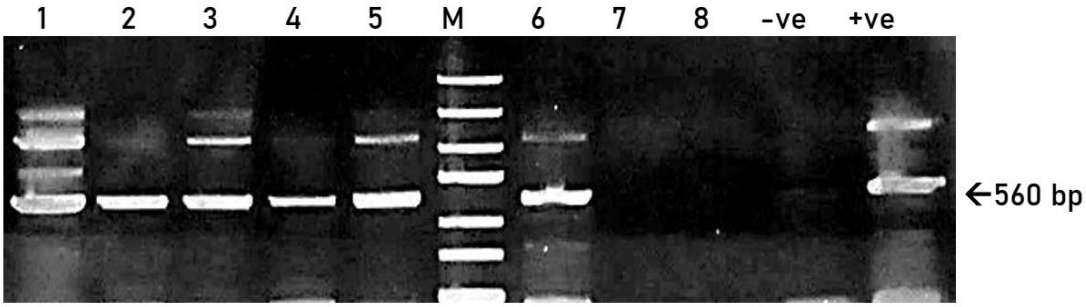

Figure 3. Gel-electrophoresis showing a result of *atzB* gene-PCR analysis of 8 isolates of fungus that are survive and tolerant to a high concentration of atrazine (50 mg/L) on Czapek-dox cultural plate. Positive *atzB*-PCR band (560 bp) was found with 6 isolates (lane 1-6), M = DNA ladder.

4. Identification fungal stain: Result from 18s rRNA fragment analysis revealed that the fungal isolates 1-6 (contains *atzB* gene) were *T. harzianum*, whereas isolates 7-8 were *T. asperellum.*

Conclusion: Since result on the positive PCR detection of *atzB* fragment with 6 isolates of tropical fungus that were survive and tolerant from a high concentration of atrazine (50 mg/L) in Czapek-dox medium with 15 days culture period, all 6 isolates (isolates 1-6) identity to *Trichoderma* spp. by gross morphology and color of hypha. The result correlated to a formation of clear zone during the day 1-5. It was different from the result of 2 isolates that were negative of *atzB*-PCR (isolates 7&8) and did not formation of clear zone. Another result

of fungal stain investigation revealed that all 6 isolates are *T. harzianum*. It is possible that the selected stain of *T. hazianum* from our study has an atrazine degrading property as be found in some bacteria. Normal process for atrazine degradation is involved by many enzymes including the Hydroxyl-atrazineethylamino-hydrolase (AtzB)[8,11]. This study demonstrates a method for selection of tropical *T. harzianum* which is tolerant to high concentration of atrazine *in vitro*. The selected isolates may be further used as a biocontrol of plant disease in atrazine contaminated fields[12,13], as well as for atrazine elimination form soil[14].

References:

1. Cohen SZ, Greege SM, Carsel RF, Enfield CG. Treatment and Disposal of Pesticide Wastes. 1984;p.297-325.[doi:10.1021/bk-1984-0259.ch018]
2. Hayes TB, Collins A, Lee M, Mendoza M, Noriega N, Stuart AA, Vonk A. Proceedings of the National Acad of Sci. 2002;99(8):5476-5480.
3. Sass JB, Colangelo A. Int J Occup Environ Health. 2006;12(3):260-267.
4. Tawatsin A, Thavara U, Siriyasatien P. Med Res Archiv. 2015;3:1-10.
5. Solomon RDJ, Kumar A, Santhi VS. J Zhejiang University SCIENCE B. 2013;14(12):1162-1172.
6. Alabouvette C, Olivain C, Steinberg C. European J of Plant Pathol. 2006;114(3):329-341.
7. Cai B, Han Y, Liu B, Ren Y, Jiang S. Letters in Appl Microbiol. 2003;36(5):272-276.
8. Sene L, Converti A, Secchi GAR, Simão RDCG. Brazilian Archives of Biol and Technol. 2010;53(2):487-496.
9. Muthuselvam M, Arunkumar S. J Pure and Appl Microbiol. 2009;3(2):661-666.
10. Howell CR. Plant Disease. 2003;87(1):4-10.
11. Chomczynski P, Sacchi N. Analy Biochem. 1987;162(1):156-159.
12. De Souza ML, Wackett LP, Sadowsky MJ. Appl Environ Microbiol. 1998;64(6):2323-2326.
13. Arbeli Z, Fuentes C. FEMS Microbiol Ecol. 2010;73(3):611-623.
14. Pelcastre MI, Ibarra JRV, Navarrete AM, Rosas JC, Ramirez CAG, Sandoval OAA. Tropical Subtropical Agroecosystems. 2013;16(2):265-276.

Acknowledgements: This study was supported by a research grant for permanent staffs (No.7/54) from the Research Institute, Rangsit University, Patumthani, Thailand. We would like to appreciate for this funding.

A_027_PF: ANTIMICROBIAL ACTIVITY OF A NISIN-CONTAINING BACTERIAL CELLULOSE FILM FROM RICE WASHING DRAINAGE (RWD)

Pipat Sudying, Phimchanok Jaturapiree*
Department of Biotechnology, Faculty of Engineering and Industrial Technology, Silpakorn University, Muang, Nakhon Pathom 73000 Thailand
*e-mail: phimchanok@hotmail.com

Abstract: Among available packaging materials, cellulose products have attracted increasing interest due to their edibility, biodegradability and potential as a good carrier of a wide range of antimicrobial agents. A bacterially produced cellulose film containing nisin was developed and used in a proof-of-concept study to control *Bacillus cereus*, *Escherichia coli* and *Staphylococcus aureus*. Bacterial cellulose pellicles were produced by *Komagataeibacter nataicola* Li1 from rice washing drainage (RWD) as the renewable carbon source. Using inexpensive waste materials as substrates in fermentation media could significantly reduce the bacterial cellulose production cost. Moreover, it also has an environmentally friendly effect by the removal of this waste from the environment. Bacterial cellulose films from rice washing drainage containing nisin showed effectiveness in controlling *B. cereus* and *S. aureus*, indicating that the use of active bacterial cellulose films would be a promising method to enhance the safety and extend the shelf life. Substantial work is still required, however, to make the production of active bacterial cellulose films economically feasible.

Introduction: Nisin is a natural antimicrobial polypeptide produced by some strains of the lactic acid bacterium *Lactococcus lactis* subsp. Nisin is an effective bactericidal agent against Gram-positive bacteria including strains of *Lactococcus*, *Streptococcus*, *Staphylococcus*, *Micrococcus*, *Pediococcus*, *Lactobacillus*, *Listeria* and *Mycobacterium* [1]. Gram-positive spores like *Bacillus* and *Clostridium* spp. are particularly susceptible to nisin, with spores being more sensitive than vegetative cells [2]. In contrast, many Gram-positive bacteria are resistant to nisin due to their ability to synthesize an enzyme, nisinase, which could inactivate nisin [3]. The bacteriocin nisin is not generally active against Gram-negative bacteria, fungi and virus [4]. This compound has been approved for use as a food preservative by the Joint FAO/WHO Expert Committee on Food Additives and granted Generally Recognized As Safe (GRAS) status for use in cheese products in the United States [5]. The antimicrobial activity of nisin depends on many factors, direct addition of nisin to food surfaces may lead to some loss of its activity, because it migrates towards the center of the food which can result in an associated dilution and depletion of its effect. Besides, nisin may be inactivated by some components of the food they are present in [6].

Active packaging, defined as packaging which performs some role other than that of a barrier to the outside environment. Active packaging generally either acts to increase or indicate the shelf life or safety of products, is of increasing interest to food producers [7]. It has been suggested that antimicrobial agents could also be incorporated into food packaging films to create an active packaging system that will maintain their activity during food storage. Controlled release of such agents from packaging films could inhibit the growth of target microorganisms over time and thus extend the shelf life of packaged products [8].

Bacterial cellulose (BC), an exopolysaccharide produced by various species of bacteria, such as those of the genera *Aerobacter, Agrobacterium*, *Alcaligenes, Azotobacter, Pseudomonas*, *Rhizobium*, *Rhodobacter, Sarcina*, and *Salmonella* [9, 10]. BC has certain better demonstrates unique properties for most uses than cellulose from plants, such as high purity, good shape retention, high water binding capacity, high degree of crystallinity, water retention value, tensile strength and moldability [11]. Because of these properties and susceptibility to biological, chemical, and physical modifications, this natural biomaterial found numerous

applications in fabrication of bioproducts and is considered a "bio-base" for the development of novel materials in various fields [12], such as micro blood vessel [13], three-dimensional scaffold material for tissue engineering of bone and cartilage [14]. That the carbon source may determine the cost of each production process, and in the case of cellulose production it is even up to 65% of the entire cost of biotechnological process [15]. Traditional sources of carbon for microbial fermentation are sugars such as glucose, fructose and sucrose. More recently, some agricultural and industrial wastes can be used as the growth medium for BC production, such as Waste beer yeast [16], wastewater after lipid fermentation [17] and wastewater of candied jujube [18] Using inexpensive waste materials as substrates in fermentation media could significantly reduce the bacterial cellulose production cost. Moreover, also has an environmentally friendly effect by the removal of this waste from the environment. The previous report, we success to screen and isolate for bacterial capable of producing bacterial cellulose using rice washing drainage as the carbon source under static condition. The bacterial *Komagataeibacter nataicola* Li1 was isolated from apple [19]. The aim of this study was to develop bacterial cellulose films from rice washing drainage containing nisin to the antimicrobial activity. The study would benefit in providing a potentially low-cost and environmentally-friendly active packing film.

Methodology: *Bacterial strains*: *Bacillus cereus, Escherichia coli*, *Komagataeibacter nataicola* Li1 and *Staphylococcus aureus*. The bacterial strains were provided from the Department of Biotechnology, Faculty of Engineering and Industrial Technology, Silpakorn University, Thailand. *K. nataicola* Li1 was used as the microorganism for BC production. *B. cereus, E. coli* and *S. aureus* were used for the antimicrobial activity assay and were subcultured overnight at 37 °C in nutrient broth before use.
Culture media: The seed medium contained (g/L): glucose 30, peptone 7.5, yeast extract 10, disodium hydrogen phosphate 7.5, citric acid 0.5, and pH 6.0 [20]. The rice washing drainage was used as the culture medium for BC production. Then rice washing drainage was centrifuged at 12,000 rpm for 10 min to remove particles, and the supernatant was collected as a stock solution the preparation of rice washing drainage (RWD) medium. The RWD medium was adjusted a total sugar concentration to 4 g/L and then yeast extract 5 g/L, Potassium dihydrogen phosphate 3 g/L, magnesium sulphate heptahydrate 2 g/L, ammonium sulfate 5 g/L were added, and the pH was adjusted to 4.5 [19].
Preparation of bacterial cellulose films for absorption: *K. nataicola* Li1 was cultivated in 250 mL flask containing 100 mL of seed medium and incubated at 30°C under static culture conditions for 4 days. To prepare the inoculum, the prepared seed inoculum (5% v/v) was then transferred into the RWD medium and incubated at 25˚C under static culture conditions for 13 days. After cultivation, the cellulose was picked from the surface and treated with 0.1 N NaOH at 90 ˚C for 10 min to dissolve the microorganisms [19]. The cellulose was immersed in distilled water for overnight or until the pH of the water became neutral. The diameter of purified cellulose films was confirmed as 11.5 mm using digital calipers.
Nisin solution preparation: Nisin powder from *Lactococcus lactis*, 2.5% (balance sodium chloride and denatured milk solids) was purchased from Sigma-Aldrich (Gillingham, Dorset, UK). A nisin solution of 50,000 $IUml^{-1}$ was prepared by dissolving 0.5 g of nisin in 10 ml of 0.01 M HCl. The solution was centrifuged at 3000×g for 15 min in a sterile centrifuge tube to remove insoluble whey proteins. The supernatant was filtered and kept into a sterile tube as a stock solution at 4 °C [21]. This solution was diluted with 0.01M HCl to obtain a nisin solution of 1250, 2500 and 10000 $IUml^{-1}$.
Nisin absorption assays: The purified cellulose films were soaked in 10 ml of nisin solution 1250, 2500 and 10000 $IUml^{-1}$ in a sterile 50 ml centrifuge tube at 4 °C for 6 h. under static conditions to allow absorption of nisin. After soaking, the cellulose pieces were removed from the nisin solution and immersed briefly in sterile distilled water to remove non-absorbed

nisin. The films were then immersed briefly in 15% glycerol to make them flexible and dried at 50 °C. Cellulose films soaked in a 0.01M HCl solution without nisin were used as a control [22].
Antibacterial activity of bacterial cellulose films: The modification of the diffusion assay is used to evaluate the antimicrobial activity of the cellulose films after nisin absorption. *B. cereus,*
E. coli and *S. aureus* were grow overnight at 37 °C in nutrient broth, its absorbance was adjusted at 600 nm and diluted to attain viable cell count of 10^{-7} CFU/ml using Spectrophotometer. The sterile cotton swab was dipped into the broth cultures of *B. cereus, E. coli* and *S. aureus* were streaked separately on nutrient agar plates. Subsequently, cellulose films were placed on the agar surface. The agar plates were then incubated at 37 °C for 24 h and the antimicrobial activity of cellulose films was determined by measuring the diameter of inhibition zones around the films.

Results and Discussion:
Antibacterial activity of bacterial cellulose films containing nisin: The antibacterial activity of the bacterial cellulose films from rice washing drainage containing nisin produced in this study against *Bacillus cereus*, *Escherichia coli*, and *Staphylococcus aureus* was recorded in Table 1 and illustrated in Figure 1. The results revealed that the bacterial cellulose itself has no antimicrobial activity as no zone of inhibition is observed for the control samples (Table 1 and Figure 1Ai, Bi and Ci). Bacterial cellulose films containing nisin solution 10,000 $IUml^{-1}$ effective active against *B. cereus* and *S. aureus* inhibition zone were 4.97 ± 0.860 and 2.75 ± 0.068 mm respectively. The diffusion assay showed that there was no inhibition zone around cellulose films containing nisin from solutions of concentration lower than 1,250 IU ml^{-1}, while all concentration of nisin is not active against *E. coli*, due to *E. coli* is a Gram-negative bacterium (Table 1 and Figure 1Bii, Biii and Biv) [4]. Results of antimicrobial activity of bacterial cellulose films from rice washing drainage containing nisin can be suggested that *E. coli* was the most resistant strain to nisin, while *B. cereus* and *S. aureus* were the most susceptible strains to nisin respectively.

Table 1. Antimicrobial screening test of bacterial cellulose films from rice washing drainage containing nisin against some bacterial strains.

Nisin concentration ($IUml^{-1}$)	Inhibition zones (mm)		
	B. cereus	*E. coli*	*S. aureus*
0	0.0 ± 0.0	0.0 ± 0.0	0.0 ± 0.0
1,250	0.0 ± 0.0	0.0 ± 0.0	0.0 ± 0.0
2,500	1.33 ± 0.750	0.0 ± 0.0	0.77 ± 0.077
10,000	4.97 ± 0.860	0.0 ± 0.0	2.75 ± 0.068

Data are means of three replicates (n = 3) ± standard error.

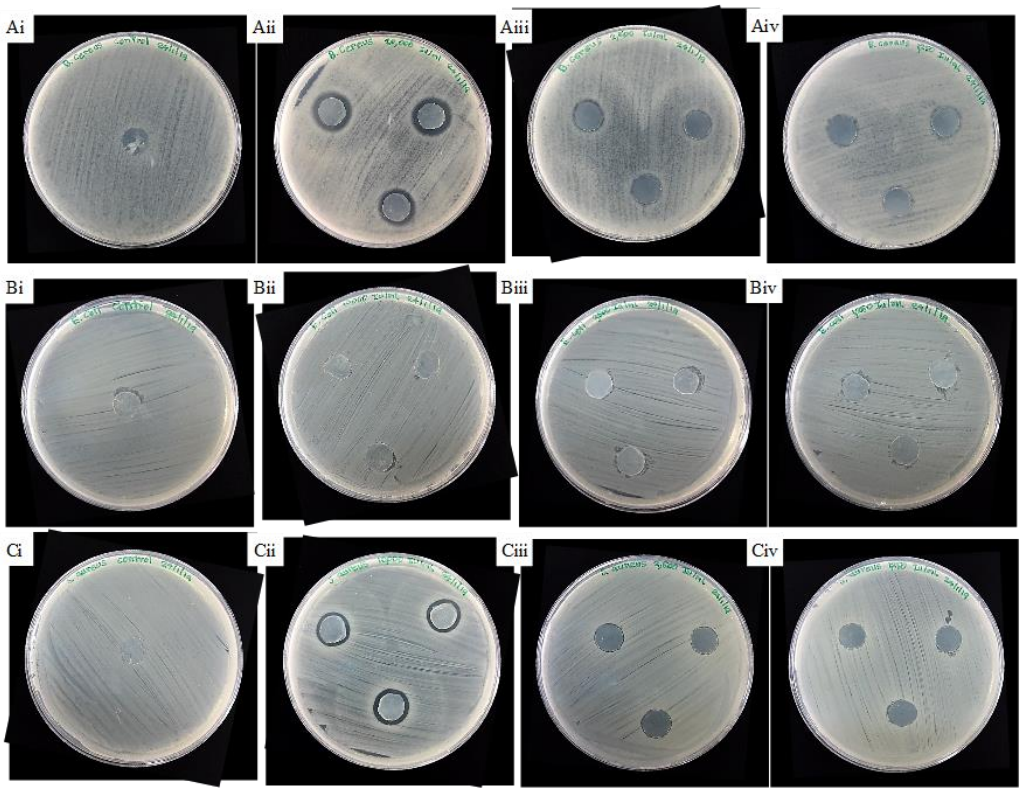

Figure 1. Antimicrobial activity of bacterial cellulose films against *Bacillus cereus* (A), *Escherichia coli* (B), and *Staphylococcus aureus* (C). Bacterial cellulose film exposed to a nisin solution of 0 (i), 1250 (ii), 2500 (iii) and 10000 (iv) $IUml^{-1}$.

Conclusion: The study shows that it is feasible to develop bacterial cellulose films from rice washing drainage into active packaging materials by the incorporation of nisin. Nisin-containing bacterial cellulose films showed effectiveness in controlling *B. cereus* and *S. aureus*, indicating that the use of active bacterial cellulose films would be a promising method to enhance the safety and extend the shelf life.

References:

1. Sahl H-G, Jack R W, Bierbaum G. Eur. J. Biochem.1995; 230:827-853.
2. Delves-B J, Blackburn P, Evans R J, Hugenholtz J. Antonie Van Leeuwenhoek. 1996; 69: 193-202.
3. Abee T, Krockel L, Hill C. Int. J. Food Microbiol. 1995; 28:169-185.
4. Boziaris I S, Adams M R. Int. J. Food Microbiol. 1999; 53:105-113.
5. Hurst A. In: Branen, A.L., Davidson, P.M. (Eds.), Antimicrobials in Foods. Marcel Dekker, New York. 1983; pp. 327–351.
6. Rose N L, Sporns P, Stiles M E, McMullen L M. J. Food Sci. 1999; 64:759–762.
7. de K N, van B M, Rijk R. Sipilaeinen-M T, Paseiro L P, de M B. Food Addit. Contam. 2002; 19:144–162.
8. Quintavalla S, Vicini L. Meat Sci. 2002; 62:373–380.
9. Brown R. M. J. J. Polym. Sci. 2004; 42(3): 487-495.
10. Chawla R P, Bajaj B I, Survase A S, Singhal, S R. Food Sci. Biotechnol. 2009; 47(2): 107–124.
11. Tanskul S, Amornthatree K, Jaturonlak N. Carbohydrate Polymers. 2012; 92(1):421-428.

12. Dourado F, Ryngajllo M, Jedrzejczak-K M, Bielecki S, Gama M. In Bacterial Nanocellulose Amsterdam: Elsevier. 2016; 1-17.
13. Klemm D, Schumann D, Udhardt U, Marsch S. Prog. Polym. 2001; 26(9):1561-1603.
14. Jiang J H, Ling W Y, Ru J S, Huang Y, he F, Zao W Y. Key Engineering Materials. 2007; 923-926.
15. Jedrzejczak-K M, Kubiak K, Ludwicka K, Bielecki S. In Bacterial Nanocellulose. Amsterdam: Elsevier. 2016; 19-46.
16. Lin D, Lopez-S P, Li R, Li Z. Bioresour. Technol. 2014; 151:113-119.
17. Huang C, Guo H J, Xiong L, Wang B, Shi S L, Chen X F, Lin X Q, Wang C, Luo J, Chen X D. Carbohydrate Polymers, 2016; 136:198-202.
18. Li Z, Wang L, Hua J, Jia S, Zhang J, Liu H. Carbohydrate Polymers. 2015; 120:115-119.
19. Sudying P, Laingaumnuay N, Jaturapiree P. Key Engineering Materials. 2019; Accepted Manuscript.
20. Fan X, Gao Y, He W, Hu H, Tian M, Wang K, Pan S. Carbohydrate Polymers. 2016; 151: 1068-1072.
21. Komitopoulou E, Boziaris I S, Davies E A, Delves-B J, Adams M R, Int. J. Food Sci. Technol. 1999; 34:81–85.
22. Nguyen V T, Gidley M J, Dykes G A. Food Microbiology. 2008; 25:471–478.

Acknowledgements: The authors wish to thank the Department of Biotechnology, Faculty of Engineering and Industrial Technology, Silpakorn University the Silpakorn University Research, Innovation and Creativity Administration Office for financial support.

A_029_PF: WHICH IS THE SUITABLE TRANSPLANTED FRAME FOR CULTIVATING THE LICHEN *Parmotrema tinctorum* FOR SUSTAINABLE UTILIZATION?

Mongkol Phaengphech[1]*, Wetchasart Polyiam[1], Chaiwat Boonpeng[1], Kansri Boonpargob[1]
Lichen Research unit, Department of Biology, Faculty of Science, Ramkhamhaeng University, Bangkok, Thailand
*e-mail: mongkolpp@gmail.com

Abstract: Carbon assimilation in lichens depends largely on available atmospheric humidity. Maintaining optimal thallus water content can prolong carbon fixation and increase lichen production. The objective of this study was to develop transplanted frames that prolong optimal thallus water content. Three small and three large frames were made, standing 45° above the ground facing the East. Enclosing beneath each frame with either shading net, shading net lining with plastic sheet, or open (control). Six thalli of the lichen *Parmotrema tinctorum* were fixed over the surface of each frame. Thallus relative water content (RWC), chlorophyll fluorescence (Φ_{PSII}) and microclimate were measured from 5 a.m. to 1 p.m. for 4 days during 25 to 28 January 2019. The result showed that the frame that surrounded by the shading net lining with plastic sheet could maintain higher and longer humidity inside the frame. Consequently, the transplanted lichens on this frame showed evidently higher thallus water content than the others. Temperatures were not different among all frames. This result suggested that walling the lower surface of the frames with the combination of shading net and plastic sheet was suitable for lichen transplantation. This information is essential for cultivation of lichens for sustainable utilization. More importantly, further study under varying environment needs to be carefully assessed.

Introduction: Lichens are obligate symbiotic organisms between fungi and algae and/or cyanobacteria. They produce novel products that are different from other organisms and could be used for pharmaceutical purpose, cosmetic, foods, beverages etc.[1] In addition, lichens are well recognized as effective bioindicators of air quality.[2]

The lichen *Parmotrema tinctorum* (Despr. ex Nyl.) Hale used as an experimental material for this study distributes across all ecosystems in Thailand and was commonly found in Khao Yai National Park. It has been utilized successfully for silk dying and a bioindicator of air quality.[2] It also metabolizes secondary substances that have potential to be used for pharmaceutics. However, the growth rate of the lichen is very slow (9.86-10.71 mm/yr.)[3] because it has a relatively short period of time for carbon assimilation. Photosynthesis of lichens depends largely on atmospheric moisture which terminates in the late morning when air humidity drops and thallus runs out of water.[4,5] As such, natural lichen biomass is not sufficient for utilization. It is essential to develop method that enable to increase lichen production such as prolong optimal thallus water content for longer and higher carbon assimilation. Previous studies revealed that soil watering under transplanted frames could increase lichen growth rate,[6] nevertheless the growing biomass remained under utilization demand, as a result further experiments are needed.

The main objective of this study was to develop transplanted frames that allow longer optimal thallus water content that essential for longer photosynthesis process.

Methodology: This experiment was performed at the secondary forest in Khao Yai National Park (KYPN), Thailand.

Six transplanted frames made up from PVC pipes, lining the square surface area with black polyethylene net and a 50% black shading net. They composed of two sizes, three large (L) frames (200x70 cm or 1.4 m^2) and three small (S) frames (50x70 cm or 0.35 m^2) (Figure 1a and Table 1). Each frame stands 45° inclination on the ground, facing east. All four sides underneath the frames were enclosed by 50% black shading net and/or a plastic sheet. Six

thalli of *P. tinctorum* were fixed on top of each frame for measuring thallus water content and chlorophyll fluorescence. All frames stood under 50% black shading net.

Table 1. Condition of the transplanted frames.

Frame No.	Size	Underneath frame walling	abbreviation
1	Small (50x70 cm)	None (Control)	S_C
2	Small (50x70 cm)	50% black shading net	S_N
3	Small (50x70 cm)	Plastic sheet and 50% black shading net	S_{P+N}
4	Large (200x70 cm)	None (Control)	L_C
5	Large (200x70 cm)	50% black shading net	L_N
6	Large (200x70 cm)	Plastic sheet and 50% black shading net	L_{P+N}

Approximately 10 liters of natural water was sprinkled with flow rate of 1 L/min. beneath each small frame. Whilst the larger frames received a double supplied of 20 liters. The watering was applied during 7 and 9 a.m. every day during experiment. Thallus water content was calculated from the six lichen thalli fixing on each frame using the formula according to Barták,[6] They were expressed as a relative water content (RWC); (FWa-DW)/(FWw-DW) x 100 (% water status of thalli), where FWa is fresh weight of actually hydrated thallus, FWw is fresh weight of fully hydrated thallus of the day, and DW is dry weight of dehydrated thallus. Chlorophyll fluorescence parameter (yield or Φ_{PSII}) that was used to determine the physiological active period of the lichens were conducted by a Pulse Amplitude Modulation Fluorometer, MINI-PAM (Walz Inc. Germany). Relative humidity (RH), air temperature (temp.) inside and outside the transplanted frames were recorded, while photosynthetically active radiation (PAR) was measured over the frame. This experiment was repeated for 4 days during 25 to 28 January 2019, and from 5 a.m. to 1 p.m.

Statistical differences of the data were tested using Student's t-test by IBM SPSS Statistics version 20 (IBM Corporation, USA), and graphs were created by SigmaPlot version 11 (Systat Software, Inc., USA).

Figure 1. Lichen transplanting
(a) Thallus of the lichen *Parmotrema tinctorum*. (b) fragmented thalli of lichen over the large and small transplanted frames, and (c) measuring microclimate.

Results and Discussion: The consequences of frame size on relative humidity (RH) underneath the surface, and relative water content (RWC) of the lichens transplanted over it remain unclear. The RH and RWC were similar when underneath the frames were open (Figure 2). However, with only enclosing net below the frame caused RH and RWC of the large frame was higher than the small one. Contradictory, this effect was reversed in the frames with surrounded by net and plastic underneath.

It was clear that enclosing underneath the frames with a combination of net and plastic sheet (P+N) resulted in higher humidity under the frames and the lichen thalli than those without them (Figure 2 and Table 2). Thallus water content over the small frame that the underneath bound with net and plastic sheet (S_{P+N}) had RWC significantly higher ($p<0.001$) than those over the large frame with similar bounding (L_{P+N}). In addition, Table 2 shows that the S_{P+N} could maintain inside RH above 80% for about 45 minutes longer than the control (S_C). Similarly, at 9 a.m., the transplanted lichens had evidently higher RWC (46%) than the others. This amount of water was enough to maintain its high physiological activity, as showed by the chlorophyll fluorescence parameter (Φ_{PSII}), for almost double at 9 a.m. This was probably because of; (i) the smaller surface area of the transplanted frame delayed water evaporation; (ii) enclosing underneath the frame with plastic sheet and shading net helped to hold high moisture. It indicated that the S_{P+N} frame could prolong optimal thallus water content, and consequently extend period of carbon assimilation of the lichen.[4]

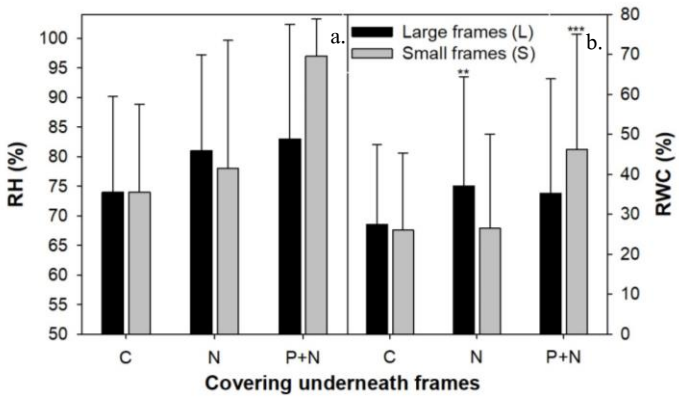

Figure 2. Microclimate and thallus water content of the lichen at the transplanted frames (a) Relative humidity (RH) inside the frames, and (b) relative water content (RWC, % water status of thalli) of the lichen thalli at 9 a.m. Denotes type of wall covering under the frames: C control, open without covering, N enclosed with 50% black shading net, and P+N bound with plastic sheet and 50% black shading net. Asterisks on top of the bars denote statistically significant differences between the pair (** $p<0.01$, *** $p<0.001$) by Student's t-test.

Table 2. Time and period of relative humidity (RH) below 80% under the transplanted frame, thallus water content (RWC) and chlorophyll fluorescence (Φ_{PSII}) of *Parmotrema tinctorum* at 7 and 9 a.m.

Transplanted frame	Time RH below 80% (a.m.)	80% RH longer than Control (min.)	RWC (%)		Φ_{PSII}	
			7 a.m.	9 a.m.	7 a.m.	9 a.m.
L_C (Control)	8.51	-	99	27	0.71	0.28
L_N	9.01	10	97	37	0.73	0.27
L_{P+N}	9.10	18	99	35	0.69	0.26
S_C (Control)	8.52	-	99	26	0.72	0.23
S_N	8.57	5	98	27	0.73	0.32
S_{P+N}	9.37	45	96	46	0.70	0.48

Previous studies observed that frames walled with plastic sheet accumulated heat beneath them. They enhanced the respiration rates. This study modified the former ones by

using 50% black shading net lining with the plastic sheet. Assuming that the shading net may reduce light intensity and temperature. We found that temperature inside the current frames were comparable with the open frames (control), all of which were 1-2 °C above the ambient air (Figure 3b).

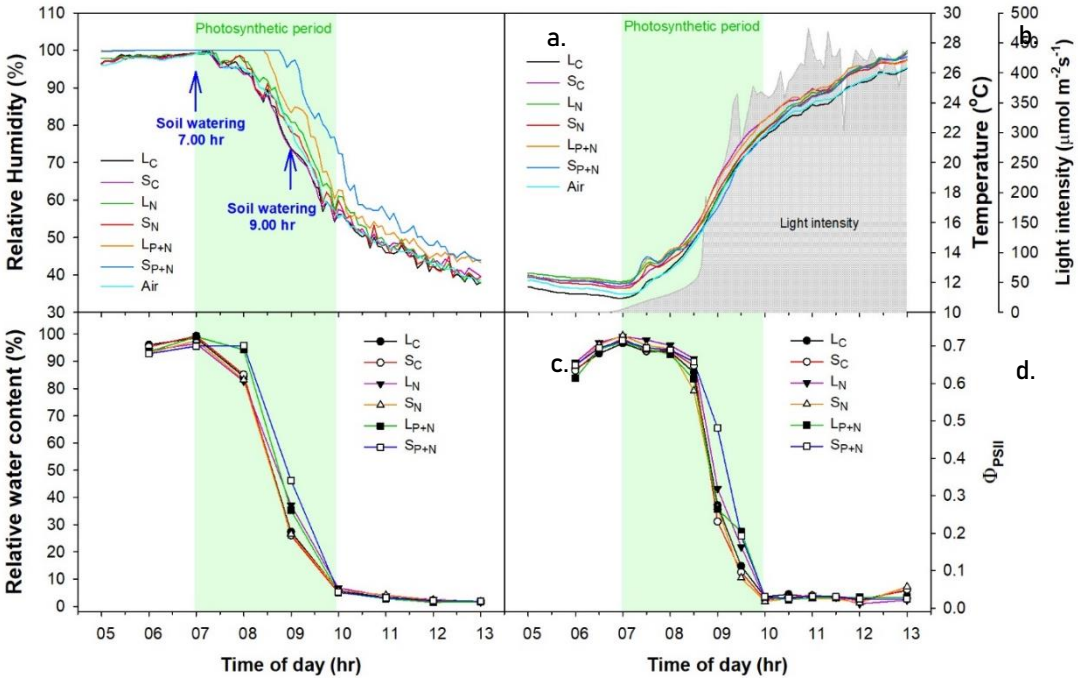

Figure 3. Microclimate and efficiency of photosystem of the lichen at the transplanted frames (a) Relative humidity (RH) (b) temperature and light intensity (c) thallus relative water content (RWC) and (d) efficiency of PSII (Φ_{PSII}) of the lichens. Data was measured and recorded at 5 a.m. to 13 a.m. during 25 to 28 January 2019. Denotes type of wall covering under the large (L) and small (S) frames: C control, open without covering, N enclosed with 50% black shading net, and P+N bound with plastic sheet and 50% black shading net.

Watering the ground under the transplanted frames could increase growth rates of the transplanted lichens.[3] However, maximizing growth rate of the transplanted lichen by an extra supply of water remained controversial. Soil watering at 7 a.m. did not increase RH (Figure 3a) because air humidity still saturated (98-100% of RH). Providing water at 9 a.m. increased ca. 5-6% of air humidity in the L_{P+N} and S_{P+N} for a short period time. However, it could not help to retain thallus water content. This was probably caused by water was used up readily for photosynthesis in the early morning under the sunlight and unable to quickly reabsorb from the frame or the atmosphere, including relatively low volume (10 liters/frame) of soil watering. Therefore, we suggest providing soil water at 7-8 a.m., or intermittently until 9 a.m. because the thallus remains hydrated and physiologically active. Delayed watering, when thallus almost dried out and inactive, make it difficult to reactivate again other than extra respiration cost.

The lichens from all frames dried out at about 10 a.m. Their photosynthesis terminated as showed by the chlorophyll fluorescence parameter (Figure 3d). This was because of low atmospheric humidity resulted from intense sunlight and elevated temperature,[4,5] and more importantly, used up of water by photosynthesis.

Conclusions: This experiment suggested that time and volume of soil watering, 7 a.m. and 10 liters, under the transplanted frames of 50x70 cm. enclosed by plastic and shading net under the surface was the best for cultivating lichens. However, watering pattern and frame size could be further modified under different environment.

References:

1. Rankovic´ B, Studzińska-Sroka E, FaŁtynowicz W. 2015;16:34-43.
2. Boonpeng C, Polyiam W, Sriviboon C, Sangiamdee D, Watthana S, Nimis PL, Boonpragob K. 2017;24:12393–12404.
3. Phaengphech M, Polyiam W, Boonpargob K. 2018;44:226-230.
4. Palmqvist K, Sundberg B. 2000;23:1–14.
5. Phaengphech M, Fuangkaew P, Polyiam W, Watthana S, Boonpargob K. 2016;42: 611-615.
6. Barták M. 2014;39:379-400.

Acknowledgements: We would like to thank Miss Wipawan Laekpet for assistance in fieldwork, the officers at Khao Yai National Park for kind cooperation, and our colleagues at the Lichen Research Unit, Ramkhamhaeng University. This study was funded by the National Research Council of Thailand (NRCT).

A_031_OF: STUDIES ON MICROBIAL BIOMASS CARBON AND NITROGEN TURNOVER DERIVED FROM SUGARCANE RESIDUES INCORPORATED INTO A SANDY LOAM SOIL

Walaiphan Chuwongpanich[1], Natthapol Chittamart[1,*], Saowanuch Tawornpruek[1], Surachet Aramrak[1], Kazumichi Fujii[2]
[1]Department of Soil Science, Faculty of Agriculture, Kasetsart University, Bangkok, 10900, Thailand
[2]Forestry and Forest Products Research Institute, Tsukuba 305-8687, Japan
[*]email: fagrnpc@ku.ac.th

Abstract: Organic amendments have been widely used to increase organic matter in sandy soil, consequently improving its fertility and productivity. However, identifying the most effective organic amendment needs to be studied. Here, three organic amendments including sugarcane leaf residues sugar and K-humate were incubated in Korat soil series and followed by evaluating changes in microbial biomass carbon and nitrogen and the nitrogen mineralization turnover into the soil after applying those organic amendments.

The results revealed that at the end of incubation, the contents of microbial biomass carbon (MBC) were observed in the significantly respective order of leaf residue amended soil (52.52 mg kg^{-1} soil), K-humate amended soil (39.98 mg kg^{-1} soil) and sugar amended soil (29.48 mg kg^{-1} soil). Meanwhile, the contents of microbial biomass nitrogen (MBN) increased in all treatments over the control during incubation. The soil amended with K-humate had the lowest C:N ratio and released the highest mineral N content of 35 mg kg^{-1} soil at the end of incubation periods. Our findings imply that sugarcane leaf and completely decomposed organic materials such as K-humate can provide carbon and nitrogen source turnover into the coarse and medium-textured soils.

Keywords: Microbial biomass Carbon, Microbial biomass Nitrogen, Nitrogen Mineralization, Korat soil series

Introduction: Most of the arable soils in Northeast Thailand are generally sandy, acidic and infertile. Their mineralogy dominated by quartz and kaolinite, respectively, because of their parent materials have been strongly weathered[1] and derived from sandy sedimentary rock. The sandy soils in northeast Thailand have very low organic matter (<10 g kg^{-1}) and total nitrogen (<0.3 g kg^{-1}) demonstrated that these soils have potentially low to very low nutrient status for crop production.[2] Organic matter is a key soil amendment to improve fertility and productivity of sandy soils. Liming, green manure and organic fertilizers (e.g. compost and animal dung) were also successfully improved organic matter content and increasing crop yield but these practices have some limitations in finding, preparing and application of organic fertilizers.[1] On the other hand, these soils are recently used for economic crops e.g. sugarcane cassava, and paddy rice. The residues from these crops have potential to be used as organic amendment to improve soils fertility but necessary to investigate their decomposition and turnover rates for properly used. Sugarcane plantation generates a lot of fresh residues which have potential for incorporating into soil to provide nutrients source for plant growth rather than the residues are burned after harvesting cane yield. Thus, the turnover rate of organic carbon and nitrogen of cane residues is a key factor for evaluating potential use of cane residues as soil fertility amendment. The application of fresh organic residues into the soil can temporary activates diverse microbial populations that do promote short-term change in the turnover of organic matter (SOM) into the soils. Soil microbial biomass (SMB) acts as a reservoir of plant nutrients and is a major determinant for governing the nutrient (like N, P, and S) availability in soils.[3]

On the other hand, incorporation of crop residues into the soils provides the energy and nutrients for microbial growth and activity, acts as a driving force for

the mineralization–immobilization processes in the soil and is a source of nitrogen (N) for plants.[4] The N availability from these residues depends on the amount of N mineralized or immobilized during decomposition. The study reported that one of the tools to achieve synchronization is the use of plant residues with different natures and qualities. Application of residues with a high C/N ratio results in immediate net N immobilization while residues with a low C/N ratio result in net N mineralization, showing that mineralization–immobilization turnover (MIT) can be influenced differently by chemical components of added plant materials.[5]

Sugarcane residues, usually considered a problem, when managed correctly may improve soil organic matter dynamics and nutrient cycling, thereby creating a rather favorable environment for plant growth. The proper management and utilization of sugarcane residues are essential for the improvement of soil quality and crop productivity, especially in infertile sandy soils. In addition, it is important to evaluate mineralization of organic residues to release the nutrients required for crop growth and development[6] that may reduce the need for mineral fertilizer[7] and reduce costs for farmers. Therefore, this study aimed to evaluate the effect of different sugarcane waste and by-products on change of soil microbial biomass carbon and nitrogen in a sandy loam infertile soil from northeast Thailand that can be implied for appropriate crop residues management in this region.

Methodology:

Study area: A representative Korat soil series (Kt) was collected from cassava field in Tha Ang subdistrict, Chok Chai district, Nakhon Ratchasima province, Thailand (14°50'11.5"N 102°11'01.5"E). The soil had sandy loam topsoil with very strongly acid (pH 5) and low fertility status (Table 1).

Table 1. Some physicochemical properties of Korat soil series.

Soil property	Unit	Value
Bulk density	(g cm^{-3})	1.0
Particle size distribution		
Sand	(g kg^{-1})	790
Silt	(g kg^{-1})	130
Clay	(g kg^{-1})	80
Textural class		Sandy Loam
pH (1:1 H_2O)		5.0
Organic matter	(g kg^{-1})	8.0
Total N	(g kg^{-1})	15
Organic C	(g kg^{-1})	4.6

Experiment: The experiment was laid out in complete randomized design (CRD) with three replications. The soil samples were pre-incubation under aerobic conditions for 7 days at 27°C and controlled water content was adjusted to 60% of the water holding capacity (WHC) by adding distilled water to stabilize the metabolic activities. Then, soils sample were incubation at 27°C for 21 days (Control). Under the same condition, the soil samples were treated with the same rate of three different organic materials in a quantity is 10-folds of microbial biomass carbon including leaf sugarcane residue (Leaf residue) which were dried in an oven-dried at 65 °C and ground in a vibrating mills, sugars (Sugar) was extracted from sugarcane juice at 100°C and then was freeze-dried, and K-humate (K-humate) was extracted from filter cake following the procedures presented by Asing et al.[8] The chemical characteristics of sugarcane residue used in this study are shown in Table 2.

Sub-samples from treatments were taken from each incubation beaker at 3,7,14 and 21 days of the incubation period to determine contents of soil microbial biomass carbon (MBC),

soil microbial biomass nitrogen (MBN). During the incubation, distilled water was added by weight method every day to keep the soil moisture stable at 60% of the water holding capacity during period of the incubation.

Calculations: Microbial biomass carbon (MBC) and microbial biomass nitrogen (MBN) were determined using the chloroform fumigation-extraction method[9]. Fumigation was conducted using alcohol-free chloroform (CH_3Cl_3) for lysing the cells. Both fumigated and unfumigated samples were extracted with 0.5 M K_2SO_4 at 1:5 soil weight: extractant volume ratio for 60 minutes by shaking at 200 rev min^{-1} and filtered with filter papers. Microbial biomass carbon (MBC) was calculated by the following equation [10]

$$MBC = \frac{EC}{KEC}$$

where EC = (organic C extracted from fumigated from fumigating soils)-(organic C extracted from non-fumigate soils) and KEC factor equal 0.45.[11]

Microbial biomass nitrogen (MBN) was calculated by the following equation.[10]

$$MBN = \frac{EN}{KEN}$$

where EN = (organic N extracted from fumigated from fumigating soils)-(organic N extracted from non-fumigate soils) and KEN equal 0.54.[12]

In the K_2SO_4 extracts of the non-fumigate samples, the Mineral-N were determined using BL-TEC Auto-analyzer.

Statistics Analysis: Analysis of variance between treatments was done by IBM SPSS Statistics (Version 21) and to compare mean of examined parameters by Duncan's multiple range test significant difference test at 95% confidential level ($p \leq 0.05$).

Results and Discussion:

Initial properties of organic materials: The chemical components of organic materials used in the experiment (Table 2) showed that sugarcane leaf has the highest carbon content, whereas K-humate had lowest carbon content. Total nitrogen content was significantly highest in sugarcane leaf and lowest in sugar. The low carbon content and high N content in K-humate resulted in low C:N ratio. The carbon: N ratio was significantly the lowest in K-humate (K-humate < Leaf residue < Sugar) indicating that this material was more decomposable than fresh sugarcane leaf and sugar.

Table 2. Chemical component properties of the sugarcane residues used in the 21-day incubation experiment

Material	%C (DM)	SE	N % (DM)	SE	C:N ratio	SE
Leaf residue	44.32 a	(0.27)	1.49 a	(0.02)	29.8 b	(0.20)
Sugar	35.98 b	(0.24)	0.25 c	(0.01)	145.3 a	(0.20)
K-humate	22.98 c	(0.02)	1.27 b	(0.01)	18.1 c	(0.20)

Notes: C=carbon, N=nitrogen, DM=dry matter. Different letters in the column indicate significant differences ($p \leq 0.01$). Values shown are means (n=3; standard errors in parentheses).

*Changes in Microbial Biomass Carbon in Korat soil*s *series*: The amount of microbial biomass C (MBC) in all treatment was significantly higher than that in control throughout the incubation period. The OM-amended soils produced biomass C in the range of 29.48-419.76 mg kg^{-1} soil, where it was only 17.46-54.50 mg kg^{-1} soil in control (Figure 1). The OM-amended soils increased MBC rapidly within 3 days and substantially decreased, except in Leaf residue

treatment that slightly increased after 3 days and reached a constant level only after 14 days of incubation. These results are similar to the finding obtained by Paul et al. [13]. A significantly higher amount of biomass C (419.76 mg kg^{-1} soil) was observed in Sugar treated because sugar addition to soil stimulates soil microbial activity and changes the size of the soil microbial biomass followed by K-humate (149.360 mg kg^{-1} soil) after 3 days of incubations (Figure 1) and leaf residue (80.12 mg kg^{-1} soil) after 7 days of incubations, respectively. At the end of incubation, the significantly higher amount of biomass C was also observed in leaf residue amended soil (52.52 mg kg^{-1} soil), followed by K-humate amended soil (39.98 mg kg^{-1} soil) and Sugar amended soil (29.48 mg kg^{-1} soil) demonstrated that sugarcane leaf provided biomass C in long run. The amount of biomass C in OM-amended soils was over the control of 47-670 % and the production of biomass C in Sugar-amended soil was highest of 69-670 % between organic materials (Figure2).

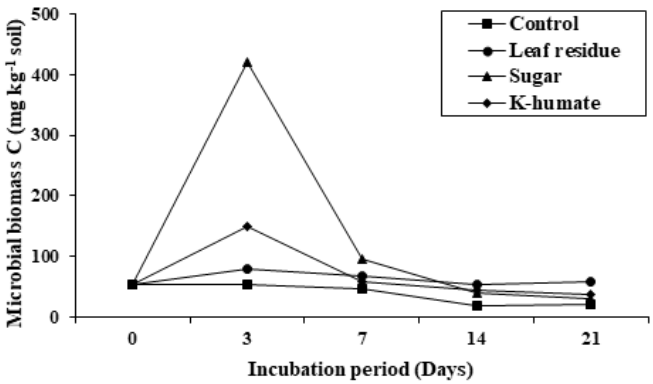

Figure 1. Changes in Microbial Biomass Carbon in Korat soil with organic materials

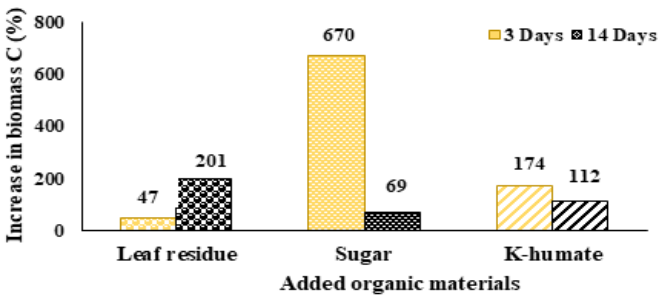

Figure 2. Percentage of increase in biomass C over control in Korat soil amended with OM after 14 days of incubation.

Changes in Microbial Biomass Nitrogen in Korat soil series: Microbial biomass Nitrogen content increased in all treatments over control during incubation. Biomass N formation accounted from 6.9-16.8 mg kg^{-1} soil in OM-amended soil and 3.9-13.5 mg kg^{-1} soil in control (Figure 3). The amount of microbial biomass N in all OM amended soils significantly increased with 3 days and decreased then reached a constant level after 14 days of incubation. Addition of sugarcane residue in soils significantly increased the microbial biomass N in soils over control in all treatment (Fig 3.). After added organic material to soil the amount of microbial biomass N in all treatment soil increased within 3 days. The interaction of type and level showed a strong effect to increase microbial biomass N by K-humate amended soil on day 21. At the end of incubation, the significantly higher amount of biomass N was also observed in

Sugar amended soil (16.8 mg kg^{-1} soil), followed by leaf residue amended soil (15.0 mg kg^{-1} soil) and K-humate amended soil (13.5 mg kg^{-1} soil) Figure 4 shows that the increase in the amount of biomass N in OM-amended soils over the control ranged from 0.4-111 %. After finished incubation, Figure 4 shows the production of biomass N in K-humate amended soil can stimulate microbial biomass N highest (111 %) over control.

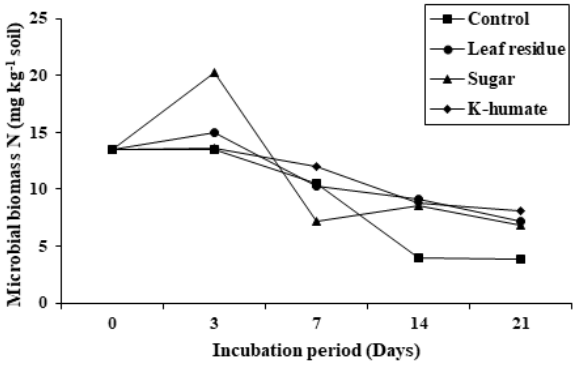

Figure 3. Changes in microbial biomass nitrogen in Korat soil with organic materials.

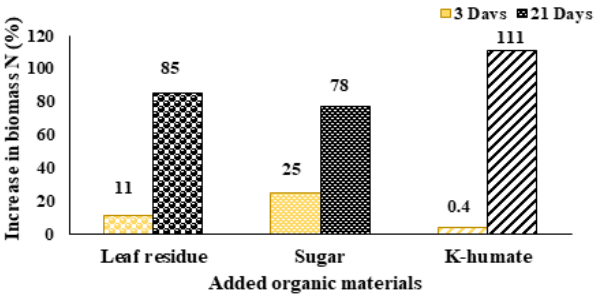

Figure 4. Percentage of increase in biomass C over control in Korat soil amended with OM after 21 days of incubation.

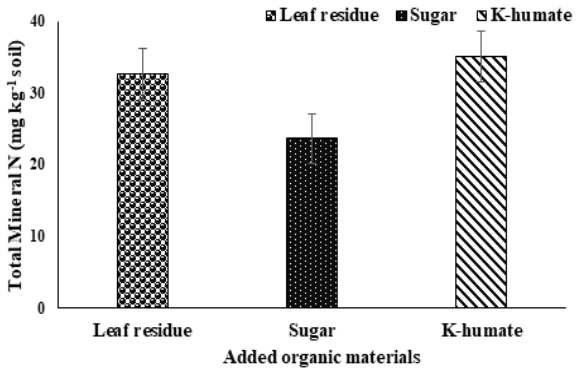

Figure 5. Total Mineral N content in Korat soil amended with different organic material after 21 days of incubation.

Nitrogen mineralization in Korat soils series: As microorganisms break down dead organic matter (from plants, animals, and microbes) during decomposition, the nitrogen are released as dissolved organic matter (DOM) by the action of exo-enzymes and then the DOM is

mineralized to mineral forms that can be used by plant and microorganisms. Nutrients release after soil micro-flora (SMB) death has been pointed out as an important source of plant nutrient N.[14] Figure 5 shows that N released from the soil amended with K-humate having the lowest C:N ratio produced the highest amount of mineral N reached 35 mg kg^{-1} soil throughout the incubation periods of 21 days. These results are similar to the finding obtained by Paul et al. [13]. Mineral N released from the control of 55 mg kg^{-1} soil. Our results were supported by Parton et al. 2007 found the net N release started when the average C/N ratio of leave litter is less than 40. Moreover, the N released from Sugar found the net immobilization. These results are also similar to the finding obtained by Paul et al.[13] and Arunachalam et al.[15] who found that close relationship between N mineralization rate and C/N ratio was negatively correlated. The critical value of substrate C/N ratio between immobilization and mineralization is considered to be 25. The C/N ratio higher than 25, microbes immobilized N from environment because microbial growth is limited by N. On the contrary, when C/N ratio below 25, N mineralization begins as a result of microbial growth is limited by C and N is relatively sufficient.

Conclusion: Incorporation of sugarcane leaf into the soils provides the energy and nutrients for microbial growth and activity, acts as a driving force for the mineralization–immobilization processes in the soil and is a source of nitrogen (N) for plants. At the end of incubation, the significantly higher amount of biomass C has also observed in leaf residue amended soil that sugarcane leaf provided biomass C and suitable for use as soil amendment in long run. High microbial biomass can increase nutrient availability to crop especially C, whereas K-humate amended soil is a good source of nutrients to crops due to K-humate can stimulate high microbial biomass N content (111 %) over control. In addition, N released from the soil amended with K-humate have the lowest C:N ratio that produces the highest amount of mineral N reached 35 mg kg^{-1} soil at the end of incubation periods. Our results imply that sugarcane leaf and completely decomposed organic materials like K-humate can provide carbon and nitrogen source turnover into the coarse and medium-textured soils.

References:

1. Wada H. Management of Tropical Sandy Soils for Sustainable Agriculture. 2005, 27th November-2nd December. Khon Kaen, Thailand.
2. Kheoruenromne I, Suddhiprakarn A, Kanghae. P. Kasetsart J. (Nat. Sci.). 1998; 32:355-373.
3. Singh Y, Singh B, Timsina, J. Advances in Agronomy. 2005; 85:269-303.
4. Stevenson F. J, Jansson S. L, Persson, J. agronmonogr. 1982; 22:229.
5. Abiven S, Recous S, Reyes V, Oliver R. Biology and Fertility of Soils. 2005;42:119-128.
6. Diacono M, Montemurro F. Sustainable Agriculture. 2011;2:761-786.
7. Mohanty M, Reddy K. S, Probert M. E, Dalal R. C, Rao, A. S, Menzies N. W. Soil Biology and Biochemistry. 2008;222:719-726.
8. Asing J, Wong N. C, Lau S. Trop. Agric. and Fd. Sc. 2009;37:211-223.
9. Vance E. D, Brookes P. C, Jenkinson D. S. Soil Biology and Biochemistry. 1987;19:703- 707.
10. Engelking B, Flessa H, Joergensen R. G. Soil Biology and Biochemistry. 2008;40:97-105.
11. Wu J, Joergensen R. G, Pommerening B, Chaussod R, Brookes P. C. 1990;22:1167-1169.
12. Jenkinson D. S, Powlson D. S. Soil Biology and Biochemistry. 1976;8:209-213.
13. Paul G. C, Solaiman A. R. M. Communications in Soil Science and Plant Analysis. 2005;35:2433-2447.
14. Van der Heijdenv G. A, Bardgett R. D, Van Straalen N. M. Ecology Letters. 2008;11: 296–310.
15. Arunachalam A, Maithani K, Pandey H. N, Tripathi R. S. Forest Ecology and Management. 1998; 109:151-161.

Acknowledgments: We are grateful to thank the Center for Advanced Studies for Agriculture and Food, Institute for Advanced Studies, Kasetsart University under the Higher Education Research Promotion and National Research University Project of Thailand, Office of the Higher Education Commission, Ministry of Education, and Thailand (CASAF) for the financial support in student exchange program in Forestry and Forest Products Research Institute, Japan

SESSION B1:
BIOCHEMISTRY

B1_004_OF: B1_004_OF: ANTIOXIDANT AND CYTOPROTECTIVE EFFECT OF *Arthrospira platensis* PROTEIN HYDROLYSATE

Nattaya Wongyai, Damratsamon Surangkul, Sarawut Sattayakawee, Chayaphon Sripannam, Krit Tantanarat, Amnat Phetrungnapha*
Department of Biochemistry, Faculty of Medical Science, Naresuan University, Phitsanulok 65000, Thailand.
*e-mail: amnatp@nu.ac.th

Abstract: Muscle aging is a complex process that is usually associated with a decrease in muscle mass, strength, and velocity of contraction. One of the most striking effects of muscle aging is known as sarcopenia, a condition characterized by loss of skeletal muscle mass and function. Accumulation of the reactive oxygen species (ROS) is one of the important factors leading to decrease of muscle mass. Therefore, reduction and prevention of ROS is crucial for protection of muscle mass loss. This research aims to study the antioxidant effect of protein hydrolysate produced from blue-green algae, *Arthrospira platensis*. Total protein of *A. platensis* was extracted and hydrolyzed with alcalase. The antioxidant activity of *A. platensis* protein hydrolysate (APH) was determined by using ABTS radical scavenging assay. The result showed that APH exhibited 90.10 ± 0.53% scavenging activity at the concentration of 100 µg/ml. Further study in L6 rat skeletal muscle cells indicated that APH could protect and recover the cells from H_2O_2-induced oxidative damage. However, gene expression analysis demonstrated that APH could not stimulate the expression of antioxidant genes such as SOD1, Gpx1, and CAT. The results obtained from this study will be useful for developing APH as a dietary supplement.

Keyword: Sarcopenia, antioxidant, protein hydrolysate, *A. platensis*

Introduction: Oxidation is an essential reaction in all living organisms. During the oxidative metabolic process, free radicals and reactive oxygen species (ROS) are formed [1]. Excess ROS are usually quite harmful and result in oxidative stress that can damage other cellular components such as DNA, proteins, lipids [2], which may lead to diseases such as cancer, cardiovascular disease, diabetes mellitus, neurological disorders, and Alzheimer's disease [1]. Muscle mass loss, known as sarcopenia or the decline of skeletal muscle tissue with age, is also caused by the accumulation of ROS in muscle cell. A previous study has showed drastically increased ROS production during the aging process because of an altered function of the respiratory chain and an insufficient function of the antioxidant cellular defenses [2]. Therefore, reduction and prevention of ROS are crucial for protection of muscle mass loss in the elderly.

Antioxidants are the chemical compounds that can donate electrons or hydrogen atoms to the free radical to create a complex, protecting the human body from free-radical damage and retarding the progress of many diseases [1]. In recent years, protein hydrolysate and bioactive peptides produced from animal and plant proteins can exhibit an antioxidant activity [3,4]. This research aims to study the antioxidant effect of protein hydrolysate produced from the blue-green alage, *Arthrospira platensis. A. platensis* contains 60-70% high-quality proteins by weight, essential amino acids, vitamins, essential fatty acids, β-carotene, and other nutritional components. Previous studies have shown that peptides isolated from *A. platensis* protein hydrolysate could inhibit proliferation of cancer cells [5] and exhibited antioxidant activity [1]. In this study, *A. platensis* protein was hydrolyzed by using alcalase. An antioxidant activity of *A. platensis* protein hydrolysate (APH) was then studied by using the ABTS radical scavenging assay. The protective and recovery effects of APH against oxidative damage were studied using a model of L6 rat skeletal muscle cell. Furthermore, the ability of APH to stimulate the expression of antioxidant gene in L6 cells was also investigated.

Methodology:

Cultivation of A. platensis and Protein extraction: A. platensis strain strain TISTR 8217 were purchased from Thailand Institute of Scientific and Technological Research (TISTR). They were cultured in in Zarrouk's medium for 3 weeks and collected by centrifugation. Protein extraction was performed by using freeze-thaw method. The total protein concentration was measured by Lowry's method.

Preparation of APH: A. platensis protein was dissolved in 20 mM sodium phosphate buffer pH 7.8 and hydrolyzed separately using 2% alcalase (v/w). The hydrolysis reaction was incubated at 50°C for 24 h. Subsequently, the reaction was incubated at 95°C for 5 min to inactive enzyme activity, followed by centrifugation at 5,000 g for 15 min. The supernatant were collected and was separated by ultracentrifugation with 10 kDa cut-off.

ABTS radical scavenging assay: ABTS radical scavenging activity was determined according to modified method of Re and clique [6]. The stock solutions of 7 mM ABTS and 140 mM potassium persulfate solution were prepared. The working solution was then prepared freshly by mixing both stock solutions in an equal volume and allowing them to react for 14 h at room temperature in the dark. The solution was then diluted by distilled water to obtain an absorbance at 743 (A_{734}) of 0.70 ± 0.02. Various concentrations of APH were allowed to react with 150 µl of the ABTS solution for 6 min and A_{734} were then determined. ABTS radical mixed with 20 mM sodium phosphate buffer was used as the control ($A_{control}$), while ABTS radical solution mixed with APH was used as the sample solution (A_{sample}). The ABTS radical scavenging activity was calculated according to the following equation:

$$\text{ABTS radical scavenging activity (\%)} = [A_{control} - A_{sample} / A_{control}] \times 100$$

L6 rat skeletal muscle cell and cell culture: An L6 cell line was obtained from ATCC and cultured in DMEM supplemented with 10% (v/v) FBS and penicillin-streptomycin and maintained at 37°C and 5% CO_2.

L6 rat skeletal muscle cell differentiation: Approximately 3×10^3 of L6 cells/well were plated into a 24-well plate and cultured for 24 h in DMEM supplemented with 10% (v/v) FBS and penicillin-streptomycin at 37°C and 5% CO_2 for 24 h. Then, FBS concentration was decreased from 10% to 2% for cell differentiation. The cells with 70-80% confluence were used in further experiments.

Cytotoxicity of APH: The differentiated L6 cells were treated with various concentrations of APH, including 0, 125, 250, 500, 750, 1,000, 1,250 µg/ml. The cells were incubated for 24 h at 37 °C and 5% CO_2. Then, the cell viability was determined by using MTT assay.

Cytoprotective effect of APH: The differentiated L6 cells were treated with various concentrations of APH (0, 125, 250, 500, 750, 1,000 and 1,250 µg/ml) and incubated for 24 h. Subsequently, H_2O_2 was added to cell at a concentration of 800 µM and the cells were incubated for 3 h. Then, the cell morphology was observed under microscope. The morphology of the APH-treated cells was compared with the control cells without APH.

H_2O_2 detoxification effect of APH: The differentiated L6 cells were treated with 800 µM H_2O_2 and incubated for 3 h. Subsequently, APH was added to cells at various concentrations (0, 125, 250, 500, 750, 1,000, and 1,250 µg/ml) and the cells were incubated for 24 h. Then, the cell morphology was observed under microscope. The morphology of the APH-treated cells was compared with the control cells without APH.

Reverse transcription polymerase chain reaction (RT-PCR) of antioxidant genes: SOD1 (Superoxide dismutase1), Gpx1 (Glutathione peroxidase 1) and CAT (Catalase) mRNA expression levels were determined by RT-PCR. The differentiated L6 cells were treated with various concentrations of APH (0, 125, 250, 500, 750, 1,000 and 1,250 µg/ml) and incubated for

24 h. Then, total RNA was extracted and converted into cDNA by reverse transcription using ReverTra Ace® qPCR RT Master Mix (Toyobo). The PCR mixture included 12.5 µl of Econo Taq® Plus Green 2X master mix (Lucigen), 1 µl of the single- stranded cDNA, 0.5 µl of gene-specific primer set (10 µM), and 10.5 µl sterile H_2O in a final volume of 25 µl. The PCR condition was as follows: Initial denaturation at 95 °C for 2 min, followed by 30 cycles of 94 °C for 30 s, 58 °C for 30 s, and 72 °C for 30 s. The final extension was 72 °C for 7 min. The mRNA expression of each target gene was normalized to ß-actin in each sample. The gene-specific primers were as follows: SOD1, forward, 5'-ATT GTG TCC ATT GAA GAT CGT GTG A-3', reverse 5'-GCT TCC AGC ATT TCC AGT CTT TGT A-3', GPX1, forward, 5'-AGT TCG GAC ATC AGG AGA ATG GCA-3', reverse 5'-TCA CCA TTC ACC TGC CAC TTC TCA-3', CAT, forward, 5'-GCA GGA AGA CTT GCA CAG GA-3', reverse 5'-ATG GGA AGG TTT CTG CCT CC-3'; β-actin, forward, 5'-TGT CCA CCT TCC AGC AGA TGT-3', reverse 5'-AGC TCA GTA ACA GTC GCG CTA GA-3'. After amplification, RT-PCR products were separated by 2% agarose gel electrophoresis and visualized under UV light.

Results and Discussion:

Antioxidant activity of APH: The hydrolysate was assayed for its antioxidative activity using ABTS radical scavenging method with the concentration up to 300 µg/ml. The results in Figure 1 showed that APH exhibited the antioxidant activity. The antioxidant activity of APH significantly increased in a dose-dependent manner. Notably, as the concentration increased from 10 to 100 µg/ml, the scavenging activity increased rapidly from 37.82 ± 1.33 % to 90.10 ± 0.53 %. These results indicate that APH exhibited an antioxidant activity. Similar to our study, Yu et. al showed DPPH scavenging activity of *Spirulina platensis* protein lysate [1].

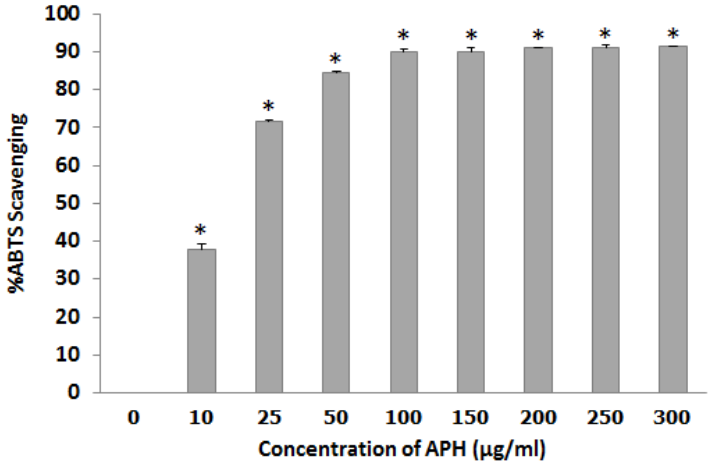

Figure 1. ABTS (2,2'-azino-bis (3-ethylbenzthiazoline-6-sulphonic acid)) radical scavenging activity of APH. APH was diluted in 20 mM sodium phosphate buffer to obtain the concentration of 10-300 µg/ml. All data represent the mean ± standard deviation. The asterisks (*) represent significant difference.

Cytotoxicity of APH: The percent viability of the L6 cells after incubating with various concentration of APH was determined by using MTT assay. The result showed that APH exhibited cytotoxicity to L6 cells in a dose-dependent manner (Figure 2). The percent viability was significantly decreased at the concentration higher than 750 µg/ml. This suggested that APH has low toxicity to the cells.

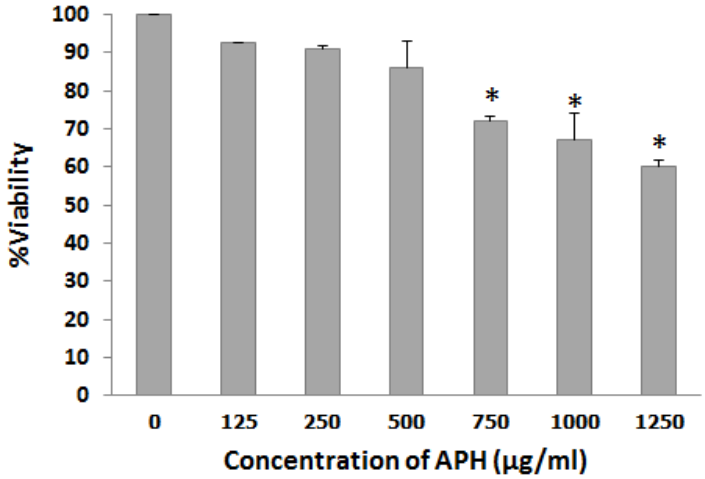

Figure 2. Cytotoxic of APH on L6 rat skeletal muscle cell.
Differentiated L6 cells were treated with various concentrations of APH for 24h.
The cell viability was determined by using MTT assay. The asterisks (*) represent significant difference.

Protective effect of APH: The results in Figure 3 showed the protective effect of APH. The fibroblast-like shape was observed in the control cells. Comparing to the control, the morphology of the cells treated with 800 µM H_2O_2 showed the round shape, indicating the oxidative damage from H_2O_2. Obviously, in the wells containing APH, the fibroblast-like cells were observed similar to the control. The amount of fibroblast-like cells was increased with APH concentration. This suggests that, PH has the ability to protect cells from H_2O_2-induced oxidative damage.

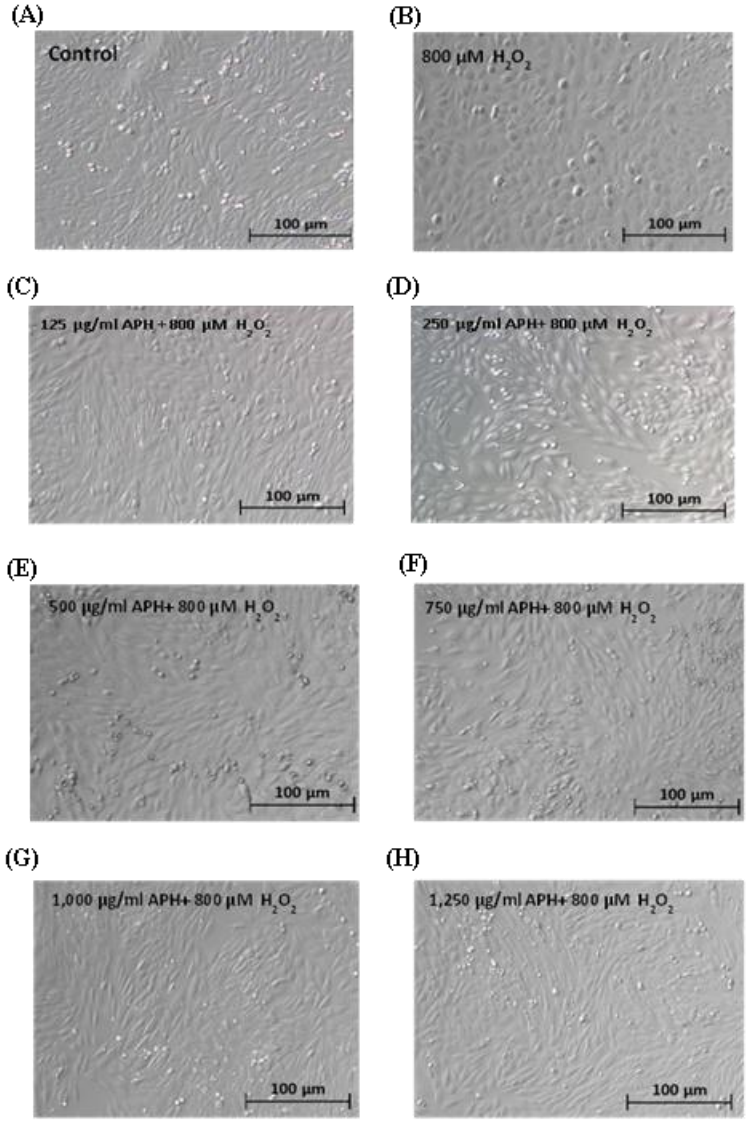

Figure 3. Cytoprotective effect of APH on L6 cell.
(A) The morphology of control cells cultured under normal condition. (B) The morphology of the cells treated with 800 µM H_2O_2 only. (C-H) The morphology of the cells treated with various concentration of APH for 24 h followed by 800 µM H_2O_2 for 3 h.

H_2O_2 Detoxification by APH: The results in Figure 4 showed that APH can detoxify H_2O_2. The fibroblast-like shape was observed in the control cells. Comparing to the control, the morphology of the cells treated with 800 µM H_2O_2 showed the round shape and detached from 24-well plate, indicating the damage from H_2O_2. Obviously, in the wells containing APH, the fibroblast-like cells were observed similar to the control. The amount of fibroblast-like cells was increased with APH concentration. This suggests that, APH has the ability to detoxify and recover the cells from H_2O_2-induced oxidative damage.

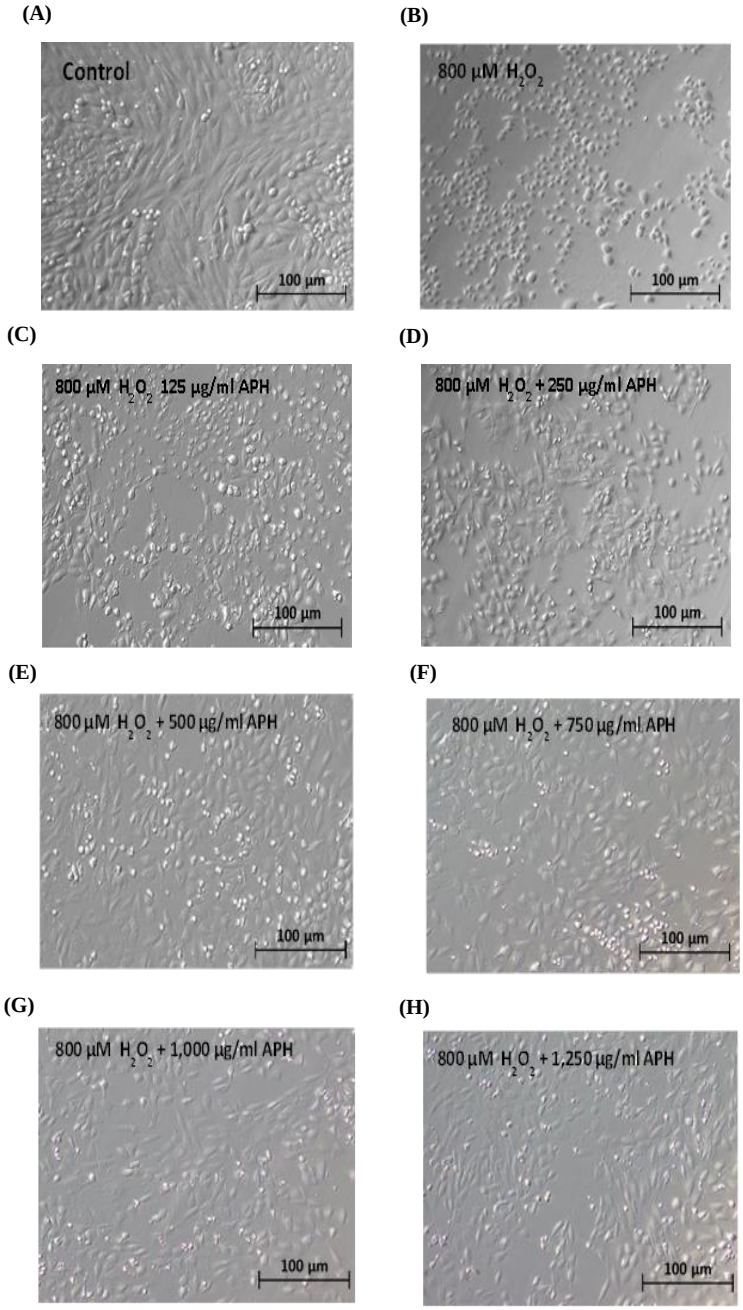

Figure 4. H_2O_2 Detoxification by APH on L6 cell.
(A) The morphology of control cells cultured under normal condition. (B) The morphology of the cells treated with 800 µM H_2O_2 only. (C-H) The morphology of the cells treated with various concentration of 800 µM H_2O_2 for 3 h followed by APH for 24 h.

Effect of treatment by APH on expression of SOD1, GPX1 and CAT genes: The mRNA expression level of SOD1, GPX1 and CAT genes levels were determined by RT-PCR. The housekeeping gene, β-actin was used to normalize RNA form each well. The result showed relative expression of SOD1, GPX1 and CAT genes after treated with various concentration of APH. The

results indicated that APH has no effect on the expression of SOD1, GPX1 and CAT genes when compared with control group. It is possible that APH exhibited an antioxidant activity and had the ability to protect and recover the cells from oxidative conditions because APH contained more aromatic amino acid, including tryptophan and phenylalanine that could readily donate electrons to free radicals [7].

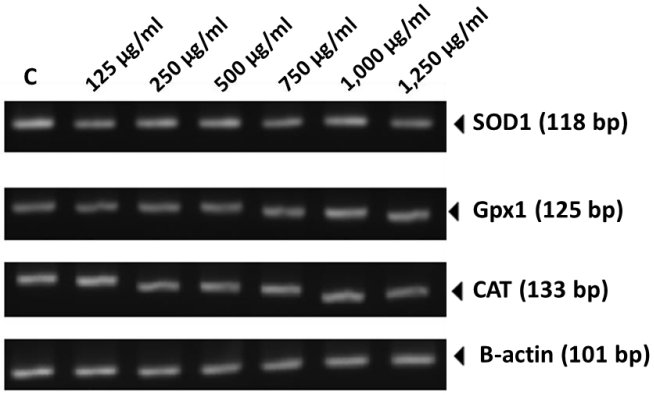

Figure 5. The mRNA expression of antioxidant genes in L6 cells treated with APH. RT-PCR was carried out to detect the expression of SOD1, GPX1, CAT and β-actin after treated with various concentration of APH.

Conclusion: We demonstrated that APH exhibits an antioxidant activity and has low toxicity to the L6 rat skeletal muscle cells. Furthermore, APH can protect and recover the cells from H_2O_2-induced oxidative damage but has no effect on the expression of antioxidant genes including SOD1, GPX1 and CAT.

References:

1. Yu J, Hu Y, Xue M, Dun Y, Li S, Peng N, et al. Purification and Identification of Antioxidant Peptides from Enzymatic Hydrolysate of *Spirulina platensis*. J Microbiol Biotechnol. 2016;26(7):1216-23.
2. Fulle S, Protasi F, Di Tano G, Pietrangelo T, Beltramin A, Boncompagni S, et al. The contribution of reactive oxygen species to sarcopenia and muscle ageing. Exp Gerontol. 2004;39(1):17-24.
3. Chen N, Yang H, Sun Y, Niu J, Liu S. Purification and identification of antioxidant peptides from walnut (*Juglans regia L.)* protein hydrolysates. Peptides. 2012;38(2):344-9.
4. Liu J, Jin Y, Lin S, Jones GS, Chen F. Purification and identification of novel antioxidant peptides from egg white protein and their antioxidant activities. Food Chem. 2015;175:258-66.
5. Zhang B, Zhang X. Separation and nanoencapsulation of antitumor polypeptide from *Spirulina platensis.* Biotechnol Prog. 2013;29(5):1230-8.
6. Re R, Pellegrini N, Proteggente A, Pannala A, Yang M, Rice-Evans C. Antioxidant activity applying an improved ABTS radical cation decolorization assay. Free Radical Biology and Medicine. 1999;26:1231–37.
7. Pyne PK, Bhattacharjee P, Srivastav PP. Microalgae (*Spirulina Platensis*) and Its Bioactive Molecules: Review. Indian J Nutri. 2017;4(2): 2326-95.

Acknowledgements: This study was financially supported by the grants from Biodiversity-based Economy Development Office (BEDO).

B1_007_PF: *Aquilaria crassna* LEAVE CRUDE EXTRACT ENHANCES GLUCOSE CONSUMPTION AND DECREASES GLUCONEOGENESIS IN HEPG2 CELLS

The anti-diabetic effects of *Aquilaria crassna* leaves crude extract on HepG2 Cells

Phanupol Mongkolsiri[1], Sarawut Jitrapakdee[1], Netiya Karaket[2], Pinnara Rojvirat[2,*]

[1]Department of Biochemistry, Faculty of Science, Mahidol University, Thailand

[2]Division of Interdisciplinary, Mahidol University (Kanchanaburi campus), Thailand

*e-mail: pinnara.roj@mahidol.ac.th

Abstract: Type 2 diabetes mellitus (T2DM) is a chronic metabolic disease characterized by elevated plasma glucose which can further cause cardiovascular complications. *Aquilaria crassna* L. is the medicinal plant that has been reported to show several medicinal properties including an anti-diabetic effect in an animal model. The current study aims to determine the mechanism by which *A. crassna* leaves extract (ALE) lowers glucose level. To verify the objective, HepG2 cell line was used as a model to examine the effects of the ALE on glucose metabolism. Our study demonstrates that the ethanolic extract of *A. crassna* leaves at the concentration up to 25 µg/mL did not produce the cytotoxic effect in HepG2 cells. Treatment of HepG2 cells at concentrations of 6.25, 12.5 and 25 µg/mL increased glucose consumption by approximately, 14%, 44%, and 82%, respectively. Furthermore, treatment of HepG2 cells with ALE at a concentration of 25 µg/mL suppressed the expression of a key gluconeogenic gene, glucose-6-phosphatase gene by 56%, indicating its action to reduce endogenous glucose production. The finding suggests that ALE possesses an anti-diabetic activity *in vitro* at least in part by increasing glucose consumption and reducing gluconeogenesis.

Introduction: Type 2 diabetes mellitus (T2DM) is a complex, chronic metabolic disorder which can lead to further complications including cardiovascular disease, renal failure, blindness, and stroke[1]. World Health Organization (WHO) reported that 422 million people worldwide are affected by diabetes. Diabetes Association of Thailand also reports that over 4 million are affected by this disease and estimated the cost of treatment up to $ 1,400 million a year. T2DM is caused by insulin resistance of target tissues, combined with defective insulin secretion from pancreatic islets. As the result of insulin resistance, peripheral tissues cannot uptake glucose from plasma while liver constitutively produces glucose even during postprandial period, causing elevated plasma glucose[2]. *In vivo* study showed that the enhanced hepatic glucose production is caused by increased expression of glucose-6-phosphatase (G6Pase), one of key gluconeogenic enzymes[3,4]. The current treatment of T2DM has been focused on improving insulin sensitivity of target tissues and reduced hepatic glucose production. Although metformin is the most prescribed drug, it can cause a severe lactic acidosis because this drug acts by inhibiting oxidative phosphorylation[5]. Thus new active compounds from medicinal plants with an anti-diabetic effect without the toxicity have been screened to replace the current drug.

The Agarwood (*Aquilaria crassna* L.) is a medicinal plant in traditional Thai medicine which was reported to have several bioactive properties including anti-bacterial[6], protective effect on brain cells , anti-nitric activity in the body and anti-diabetic[7] activity with no toxicity to the cells. Recently, Manok S. *et al.* reported the anti-diabetic effect of *A. crassna* leaves extract in streptozotocin-induced T2DM mice. Although *A. crassna* has previously been reported to have an anti-hyperglycemic effect in mice model[8], the exact mechanism underlying this action is unknown. Therefore this research is aimed at investigating the mechanism of the anti-diabetic property of *A. crassna* leaves extract using HepG2 cell line as a model.

Methodology:

Leaves collection and extraction: Fresh *A. crassna* leaves were collected from Mahidol University, Kanchanaburi campus, Kanchanaburi, Thailand, 2017. The leaves were cleaned and dried in a hot air oven (50°C) for 24 h before grinding into powder. One hundred grams of leave powder was macerated in 1 liter of 95% ethanol for 72 h at room temperature. The extract was filtered through a 0.45 μm filter paper and concentrated using a rotary evaporator to produce the *A.crassna* leaves crude extract (ALE). The ALE was stored at -20 °C until used. Before used, ALE was dissolved in DMSO at the concentration of 200 mg/ml before sterilizing filtration by passing through a 0.22 µm millipore filter paper.

Cell culture: HepG2, Hepatocellular carcinoma cell line: ATCC: HB-8065, were grown in DMEM-high glucose medium (Gibco) supplied with 10% ($^{v}/_{v}$) fetal bovine serum (Gibco) and 1% ($^{v}/_{v}$) antibiotic-antimycotic (100 units/ml penicillin and 100 µg/ml streptomycin) (Gibco) at 37°C with 5% CO_2. The cells were sub-cultured using trypsin following standard cell culture technique.

MTT assay: 1 x 10^4 HepG2 cells were plated into 96-well plate containing DMEM-high glucose supplemented with 10% ($^{v}/_{v}$) FBS and 1% ($^{v}/_{v}$) Pen/Strep for 24 h. The cells were treated with 0, 6.25, 12.5, 25.0 and 50.0 µg/mL of ALE or 5 mM Metformin as the control. However, the final concentration of DMSO was 0.2% ($^{v}/_{v}$) in all conditions. After 24 h treatment, the culture medium was replaced with MTT assay medium containing 2 mg/mL MTT in DMEM-high glucose . After 2h of incubation, the medium was removed, and the purple formazan was dissolved in 200 µL DMSO before measuring the absorbance at 540 nm.

Hepatic glucose consumption assay: 2 x 10^5 HepG2 cells were plated into 24-well plate in DMEM low glucose (5 mM glucose) supplemented with 10% FBS and 1% ($^{v}/_{v}$) Pen/Strep. After 24 h, cells were then maintained in the serum free medium for another 24 h before treating with various concentrations of ALE and 5 mM metformin as positive control in DMEM high glucose medium (25 mM glucose) for 24 h. Then, culture medium was collected to determine the concentration of remaining glucose using glucose (GO) assay kit (Sigma) following instruction manual. The protein content of treated cells was extracted using cell culture lysis buffer (Promega) before collected the supernatant protein solution by centrifugation at 13,000 rpm, 4°C for 10 min. The supernatant was determined using Quick Start™ Bradford Protein Assay (Bio-Rad).

Glucose consumption (mM/µg) was calculated by subtracting the initial glucose concentration (mM) with remaining glucose concentration (mM) and normalized with total protein (µg). Each condition was performed in triplicate, and all results of three independent experiment were analyzed in relative to that of the control.

Quantitative analysis of gluconeogenic gene expression: HepG2 cells were plated into 6-well plate in density as 1 x 10^6 cells per well under DMEM-low glucose supplemented with 10% ($^{v}/_{v}$) FBS and 1% ($^{v}/_{v}$) Pen/Strep for 24 h. Then, the medium was replaced into DMEM-high glucose without serum. After 24 h, the cells were treated with 0, 6.25, 12.5 and 25.0 µg/mL ALE in DMEM-low glucose at 37 °C for 24 h before treatment under gluconeogenic substrate medium for 4 h. The treated cells were harvested and total RNA were extracted using TRIzol Reagent (Gibco) following manufacturer's instructions. Total RNA was converted into cDNA in a 20 µl revers-transcription reaction mixture containing 1x ImPromII reaction buffer, 3 mM $MgCl_2$, 0.5 mM dNTPs, 1 unit of ImProm-II™ Reverse Transcriptase (Thermofisher), 2000 µg of total RNA and 200 ng of random hexamer (Promega). qPCR of glucose-6-phosphatase (G6Pase) and fructose-1,6-bisphosphatase (FBPase) was performed using SYBR Green in a 12 µl-reaction mixture containing 1x KAPA SYBR Green PCR master mix, 0.2 µM forward primer, 0.2 µM reverse primer and 2 µl of cDNA template. The primers used to detect G6Pase mRNAs in HepG2 are 5'-GGGAAAGATAAAGCCGACCTAC-3' (forward primer) and 5'-CAGCAAGGTAGATTCGTGACAG-3' (reverse primer). The primers used to detect FBPase expression in HepG2 were 5'-AGCCTTCTGAGAAGGATGCTC-3' (forward primer) and

5'-GTCCAGCATGAAGCAGTTGAC-3' (reverse primer). SYBR Green qPCR was carried out in a Mx3000P Q-PCR system (Agilent Technologies) under thermal profiles as follows: initial denaturation at 95°C for 5 min, followed by 40 cycles of denaturation at 95°C for 30 s, annealing at 58°C for 90 s, extension at 72°C for 30 s, and final extension at 72°C for 30 s.

qPCR of pyruvate carboxylase (PC) expression was performed using Taq-man probe in a 12 µL reaction mixture containing 1x KAPA probe fast qPCR master mix, 0.2 µM forward primer (5'-GATGACTTCACAGCCCAG-3'), 0.2 µM reverse primer (5'-GATGACTTCACAGCCCAG-3') and 2 µl of cDNA template. Taq-man probe qPCR were performed by Mx3000P Q-PCR system (Agilent Technologies) under thermal profile as follows: 95°C for 5 min, 40 cycles at 95°C for 40 sec and 58°C for 90 sec.

The expression of G6Pase, FBPase, and PC was normalized to that of 18s rRNA and presented as relative gluconeogenic mRNA expression under the expression fold change by comparative CT method (ΔΔCT Method)[9].

Statistical analysis: The results were shown as means of relative activity ± standard deviations of three independent experiments (n=3). Statistical analysis was tested using One-Way ANOVA of variance over 95% confidence interval followed post-hoc Tukey HSD Test and a difference in the mean p value < 0.05 was considered significantly different as a symbol as "*". (*$p < 0.05$, **$p < 0.01$ and ***$p < 0.001$).

Results and discussion:

Effects of A. crassna leaves extract (ALE) on cell viability of HepG2 cells: To examine the cytotoxicity of the ALE and metformin on HepG2 cells, the MTT assay was performed. HepG2 cells were treated with five different concentrations of ALE and 5 mM metformin . As shown in Figure 1, ALE at concentrations of 3.125-25 µg/mL did not show the cytotoxic effect in HepG2 cells. In contrast to 50 µg/mL of ALE caused 35% reduction of cell viability compared to that of the control. In addition, 5 mM of metformin also showed no cytotoxic effect. Therefore, ALE at concentrations of 3.125-25 µg/mL were used in further experiments and 5 mM of metformin could be used as a positive control.

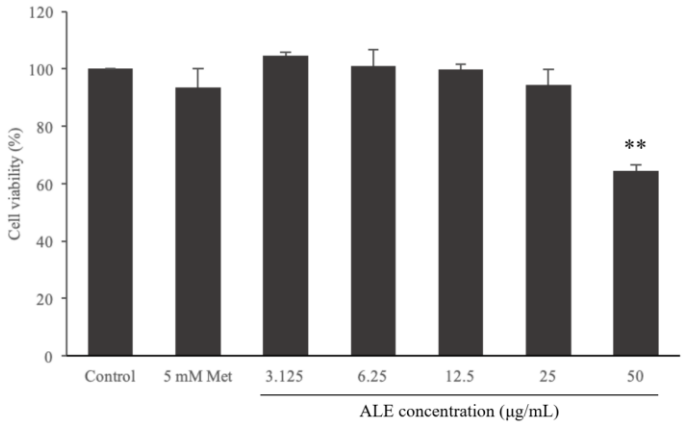

Figure 1: The cytotoxicity effect of ALE and metformin on HepG2 cells. The results of MTT assay was shown as the relative of cell viability compared with that of the control which was arbitrarily set to 100%.

A. crassna leaves extract (ALE) stimulates hepatic glucose utilization in HepG2 cells: Hepatocytes typically consume 50-60% of an oral glucose load[10] therefore in vitro the effect of ALE on glucose utilization was performed using HepG2 cells as model. The ALE at concentrations of 6.25, 12.5, and 25 µg/mL were tested for the glucose consumption in HepG2

cells. As shown in Figure 2, treatment of ALE at every concentration increased hepatic glucose utilization to 1.14-, 1.44- and 1.82-fold, respectively (*p<0.01*). Likewise, 5 mM Metformin as a positive control also stimulated HepG2 glucose utilization up to 1.69-fold. Thus, ALE affected glucose metabolism by stimulating glucose utilization in a dose-dependent manner and the net hepatic glucose utilization of the highest concentration of ALE was similar to metformin, an anti-diabetic drug.

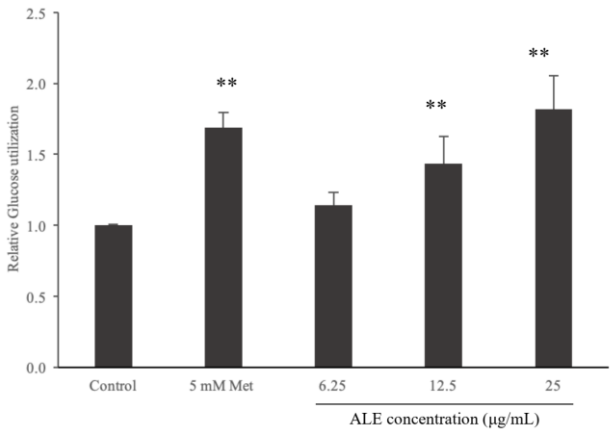

.Figure 2: The effect of ALE on glucose consumption in HepG2 cells. The result was normalized with total protein and shown as fold change of glucose consumption compared with the control group which was arbitrarily set as 1-fold. **

A. crassna leaves extract (ALE) suppressed the expression of key gluconeogenic enzyme in HepG2 cells: Type 2 diabetes is caused by an excessive production of hepatic glucose during fasting[11]. In addition, 90% of hepatic glucose production is contributed by gluconeogenic pathway[12]. Pyruvate carboxylase (PC), fructose-1,6-bisphosphatase (FBPase) and glucose-6-phosphatase (G6Pase) are key enzymes in this pathway. For positive control, metformin was used because of its action on inhibiting hepatic gluconeogenesis[13]. Metformin ameliorates hyperglycemia by suppressing hepatic glucose production.

To examine the effect of ALE on hepatic gluconeogenesis by measuring expression of these three key gluconeogenic enzymes, qRT-PCR analysis was performed. As shown in Figure 3, treatment of cells with 5 mM metformin reduced the expression of PC, FBPase and G6Pase mRNA by 63%, 61% and 44%, respectively. ALE at all concentrations did not affect the expression of both PC and FBPase gene while it reduced expression of G6Pase gene by 29%, 39% and 56% following treatment with 6.25, 12.5, and 25 µg/mL of ALE, respectively (Figure 3C). G6Pase regulated the gluconeogenesis at terminal step by dephosphorylated glucose-6-phosphate[14] into free glucose which can diffuse outside the cell and it was up-regulated in type 2 diabetic patients[15]. From our result, ALE showed the de-regulation of G6Pase expression that might be represent with the decreasing of hepatic glucose release on HepG2 model[16]. This was consistent with the previous *in vivo* study about effect of ALE on reduction of plasma glucose[8] which is a major cause of hyperglycemia in T2DM.

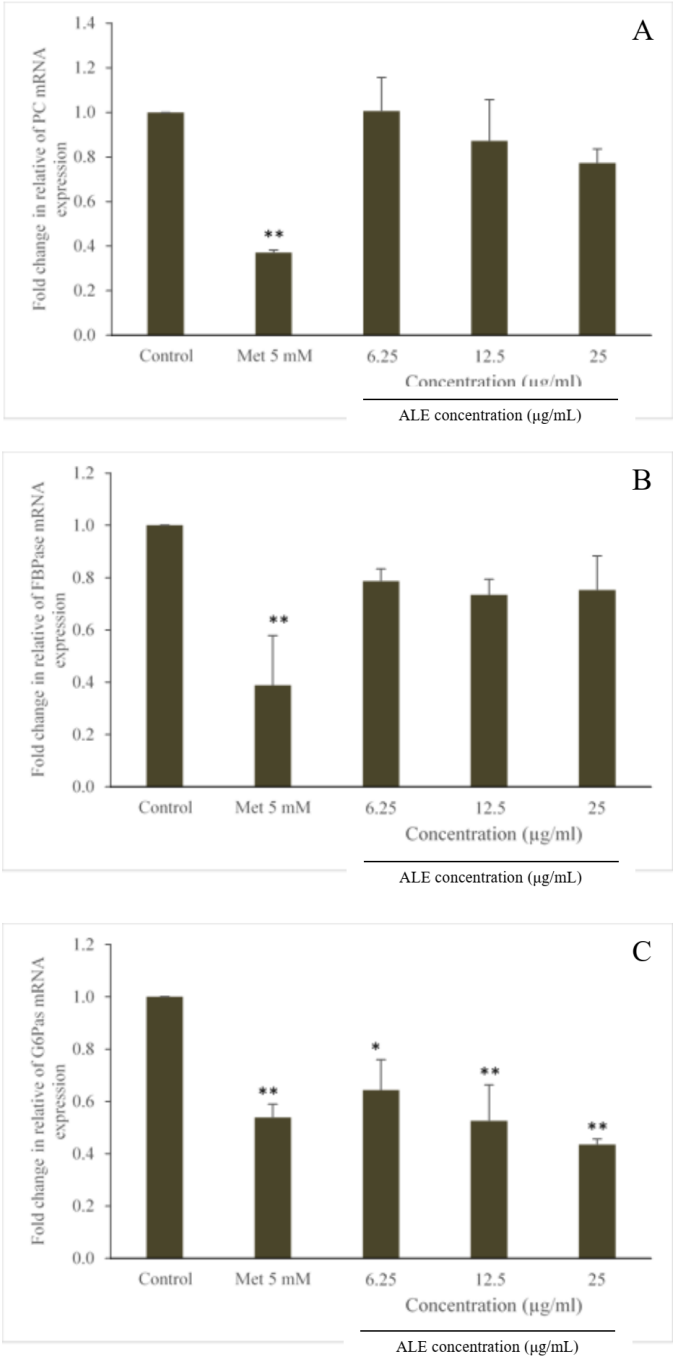

Figure 3: Effect of ALE on gluconeogenic gene expression in HepG2 cells. The result is shown as the relative expression level of target genes, normalized with 18sRNA and the value of control was arbitrarily set to 1-fold.

Conclusions: In summary, the results from this study indicates that *A. crassna* leaves extract exhibited an anti-diabetic effect by increasing hepatic glucose utilization and suppressing mRNA expression of G6Pase, a key gluconeogenic enzyme in HepG2 cells without toxicity.

Acknowledgements: This work was supported by the National Research Council of Thailand (NRCT) and Plant Genetic Conservation Project Under the Royal Initiation of Her Royal Highness Princess Maha Chakri Sirindhorn.

References

1. American Diabetes A. Diabetes Care. 2009;32 Suppl 1:S62-67
2. Roden M. Wien Klin Wochenschr. 2016;128 Suppl 2:S37-40
3. Andrikopoulos S, Proietto J. Diabetologia. 1995;38:1389-1396
4. Postic C, Dentin R, Girard J. Diabetes Metab. 2004;30:398-408
5. Cameron AR, Logie L, Patel K, Erhardt S, Bacon S, Middleton P, Harthill J, Forteath C, Coats J T, Kerr C, Curry H, Stewart D, Sakamoto K, Repiscak P, Paterson M J, Hassinen I, McDougall G, Rena G. Redox Biol. 2018;14:187-197
6. Kamonwannasit S, Nantapong N, Kumkrai P, Luecha P, Kupittayanant S, Chudapongse N. Ann Clin Microbiol Antimicrob. 2013;12:20
7. Sattayasai J, Bantadkit J, Aromdee C, Lattmann E, Airarat W. J Ayurveda Integr Med. 2012;3:175-179
8. Manoka S, Sungthong B, Sato H, Sugiyama E, Sato VH. Nat Prod Commun. 2016;11:757-761
9. Schmittgen TD, Livak KJ. Nature Protocols. 2008;3:1101-1108
10. Ferrannini E, Bjorkman O, Reichard GA, Jr., Pilo A, Olsson M, Wahren J, DeFronzo RA. Diabetes. 1985;34:580-588
11. Sharabi K, Tavares CD, Rines A K, Puigserver P. Mol Aspects Med. 2015;46:21-33
12. Konig M, Bulik S, Holzhutter HG. PLoS Comput Biol. 2012;8:e1002577
13. Wollen N, Bailey CJ. Biochemical Pharmacology. 1988;37:4353-4358
14. van Schaftingen E, Gerin I. Biochem J. 2002;362:513-532
15. Clore JN, Stillman J, Sugerman H. Diabetes. 2000;49:969-974
16. Okamoto T, Kanemoto N, Ban T, Sudo T, Nagano K, Niki I. Arch Biochem Biophys. 2009;491:46-52

SESSION B2:
MICROBIOLOGY

B2_003_PF: ISOLATION AND PHYSIOLOGICAL CHARACTERIZATION OF BENEFICIAL ANAEROBIC MICROBIOTA IN COMMERCIAL CHICKEN GUTS

Benya Nontaleerak[1], Janista Thumrongtharadol[1,2], Khwannarin Khemsom[2], Saifon Nopnipa[2], Watanalai Panbangred[1,3], Adisak Romsang[1,2,*]
[1]Department of Biotechnology, Faculty of Science, Mahidol University, Bangkok 10400, Thailand
[2]Center for Emerging Bacterial Infections, Faculty of Science, Mahidol University, Bangkok 10400, Thailand
[3]Mahidol University and Osaka University: Collaborative Research Center for Bioscience and Biotechnology, Faculty of Science, Mahidol University, Bangkok 10400, Thailand
*e-mail: adisak.rom@mahidol.ac.th

Abstract: Globally, sustainable poultry production drives secure and quality of nutritional protein sources in human. Chicken's gastrointestinal tract contains a complex microbiota that functions in an increase in nutrients' digestion and absorption, enhancement on immune system and prohibition against pathogens. In this study, particular group of microorganisms was isolated from commercial chicken guts using selective media. Twelve morphologically different colonies were successfully grown on de Man, Rogosa & Sharpe Agar (MRS) at 41°C under an anaerobic condition. Supplementation of calcium carbonate exhibited a clear zone surround these strains inferring their acid producer property. The results from well diffusion assay showed that a 72-hour culture secretion from these isolated strains could inhibit the growth of both *Bacillus subtilis* and *Escherichia coli*. Treating the tested culture secretions with sodium hydroxide (NaOH) for adjusting the pH to 6.0 resulted in a decreased inhibitory effect against the tested bacteria. However, the NaOH-treated secretion from the isolated strains EBI-01 and EBI-03 conferred the growth inhibition against *B. subtilis*. Finally, the *16S rRNA* sequencing was done in these two strains and they were belonged in the *Lactobacillus* genus, which could be further analyzed in term of their phylogenic tract and probiotics properties. A better understanding of commercial chicken guts' microbiota will provide us novel chances for sustainably improving poultry health and production.

Introduction: Chicken is a major food source for humans. The chicken productivity has been rising rapidly for meeting the demand of global population. It is important to understand the mechanisms involved in growth and nutrient absorption in chicken. In the chicken's gastrointestinal tract, the complex microbiota plays a crucial role in nutrients' absorption, enhancing nutrient absorption, strengthening the immune system and prohibition against pathogens.[1] Thereby, it affecting both growth and health of chicken. The highly productive chickens have been developed by selection for genetic traits. Nonetheless, the role of productivity and health outcomes could be influenced by selection of elite microbiota. Microbiota is a symbiotic community of probiotic and pathogenic microorganisms. The composition of the microbiota changing over time. The succession of gastrointestinal colonization by various bacteria may be influenced by several factors including diet, age and the use of antibiotics and probiotics.[2] The presence of pathogenic bacteria in the chicken microbiota is important to animal and human health for enhancement on immune system. But some bacteria can cause illness in humans and have been reported in the chicken microbiota i.e. *Salmonella enterica, Escherichia coli* and *Clostridium perfringens*.[3,4] Moreover, these bacteria can act as a reservoir for the dissemination of antibiotic resistance gene to other pathogenic bacteria.[5-7] However, commensal bacteria could transform into pathogens or resistant bacteria when they acquire genetic material encoding virulence factors or antibiotic resistant gene, respectively.[8,9]

Commercial probiotics compose multiple strains of beneficial bacteria. A diversity of microbial species have been purposed as probiotics, including species of *Bacillus*, *Bifidobacterium*, *Enterococcus*, *E. coli*, *Lactobacillus*, *Lactococcus*, *Streptococcus*, a variety of

yeast species, and undefined mixed cultures.[10] Among the potential probiotics, lactic acid bacteria (LAB) are reported to have important effects in animals.[11] Not only LAB can be found in gastrointestinal tract but also found in any environment that rich mainly in carbohydrates, such as plants, fermented foods, the mucosal surfaces of humans, terrestrial and marine animals. LAB are Gram-positive either rod-shaped (bacilli) or spherical (cocci) and usually grow under microaerophilic to strictly anaerobic conditions and non-spore forming.[12] In addition, LAB strain should be able to tolerant to acid and bile in the gut.[13] LAB are characterized by an increased tolerance to acidity (low pH range). This characteristic helps LAB to compete with other bacteria in a natural fermentation, as they can withstand the increased acidity from organic acid production (e.g. lactic acid). Furthermore, the colonization ability that specific to adhere to the intestinal epithelium of the hosts and antibacterial effects toward pathogen are major characteristics in the selection of LAB as probiotic candidates because these can compete against enteric pathogens and reduce their colonization.[14] LAB have been proposed as probiotics for the prevention of various enteric diseases which can inhibit the growth of *E. coli* and *Salmonella* species and the improvement of overall health for many years.[15] Because LAB are common inhabitants in the gastrointestinal system of animals, it is generally not possible to avoid the entry of these microorganisms into the human food chain.[16] Even though the microbes are killed by cooking process, the genetic materials are remained. If the bacteria in the chicken are genetically resistant to the antibiotics, it may cause the bacteria in the human become resistance. Therefore, understanding the roles of the chicken microbiota is essential for reducing the number of infected chickens in the poultry industry. The encouragement of gastrointestinal probiotics could be effective for substitution antibiotics.[17,18] In this study, the bacterial isolation, identification and characterization in chicken's gut were focused. Due to an oxygen level in the chicken's gut is extremely low[19], this study focused on bacteria that grow under microaerophilic to strictly anaerobic conditions. These results could be a preliminary data for further experiments to investigate the beneficial probiotics in commercial chicken guts for better chicken productivity and quality.

Methodology:

Bacterial isolation from chicken guts: Chicken guts' samples were obtained from several commercial sources of famous brands in Thailand. To obtain the microbiota in chicken gut's, the secreted liquid was freshly isolated from the chicken guts using closed-containment pouring and homogenization techniques. Then the sample was 10-fold serial diluted and immediately transferred into the particular selective medium de Man, Rogosa & Sharpe Agar (MRS). The agar plates were incubated at 41°C under an anaerobic condition for 48 hours. Calcium carbonate was supplemented into the MRS medium to determine an acid production of each isolated culture. The results were analyzed by observing a clear zone surround these strains.

pH determination: The acidity of each isolated culture was observed to characterize the acid-producing bacteria by measuring a pH value. The pH determination was done by using pH meter with manually adjusted calibration. The results were analyzed in means and standard deviation (SD) from three biologically independent experiments.

Well diffusion assay: Well diffusion assay was used to determine a growth inhibition effect of the isolated culture on the representative of different Gram bacteria. In this study, *Bacillus subtilis* was used as a representative of Gram-positive bacteria while *Escherichia coli* was selected one from Gram-negative bacteria. The secreted liquid into the medium was collected at 24-hour, 48-hour and 72-hour from each isolated strain with a similar level of cell concentration. 50 µL secretion was dropped into the 7 mm-well mediated in the NA agar plate with an overlay of either *B. subtilis* or *E. coli* culture. The plates were incubated at 37°C for 18 hours. The presence and the size of clear zone around the well was determine as an inhibition level against these bacteria. Treating the tested culture secretions with sodium

hydroxide (NaOH) to the pH magnitude of 6.0 was done and used for further analysis in the well diffusion assay. The results were analyzed in means and SD from three biologically independent experiments.

16S rRNA sequencing: The molecular DNA technique was applied based on the unique sequence profile of the *16S rRNA*-coding gene in each bacterial strain. The oligonucleotides as primers were particularly designed in the highly conserved gene-coding region as 5' CCTACGGGAGGCAGCAG 3' (as a forward primer) and 5' ATTACCGCGGCTGCTGG 3' (as a reverse primer). The proofreading Phusion polymerase chain reaction was used to amplify the selected fragment, which was further analyzed by gel electrophoresis, isolated by DNA-gel extraction kit and send these purified DNA samples to the commercial DNA sequencing company (Macrogen). The bioedit software was required for analyzing the precision of the nucleotide bases and the online bioinformatics tools were used to compare the analyzed DNA sequences to the reference sequences in the scientific databases.

Statistical analysis: Group data are presented as means ± SD. Student's *t*-test analysis was used to determine differences between means using the SPSS (version 17.0; SPSS Inc.) statistical package. Unless otherwise is stated, p values of < 0.05 were considered significant.

Results and Discussion: Particular group of microorganisms was isolated from commercial chicken guts using a selective medium. Chicken guts' samples were obtained from several commercial sources of famous brands in Thailand. Microbiota was freshly isolated from the chicken guts and immediately transferred into the MRS agar as described in the methodology. After incubated at 41°C under an anaerobic condition for 48 hours, several colonies were found on the medium and the amount of CFU was depended on the dilution level. 96 colonies were patched on the fresh MRS medium supplemented with calcium carbonate and incubated at 41°C under an anaerobic condition for 48 hours. Twelve morphologically different clones were exhibited a clear zone surround these strains inferring their acid producer property and the pure culture of these clones was collected in the laboratory stock as an assigned code (EBI-01 to EBI-12) as shown in the Figure 1.

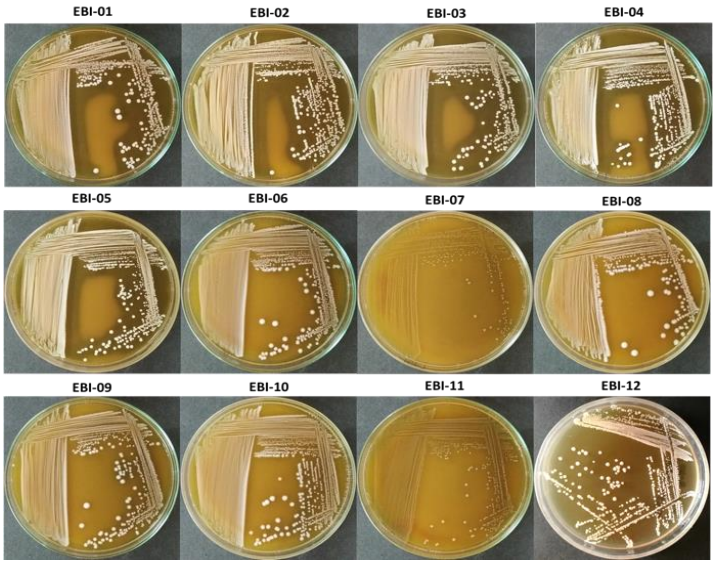

Figure 1. Pure culture of twelve morphologically different clones of the isolated microbiota from commercial chicken guts

To determine the acid production from each isolated strain, the pH of the culture was measured at 24-hour, 48-hour and 72-hour incubation times as previously described in the

methodology. The results showed that all of the 12 cultures mediated an acidic pH of the medium with the average magnitude of 3.9±0.3 and the range of 3.4 to 4.4 at the 24-hour incubation time. The decreased level of pH was observed in the culture further incubated until 48 hours and 72 hours with the average magnitude of 3.5±0.3 and 3.2±0.3; and the range of 3.0 to 4.0 and 2.7 to 3.7, respectively. These results indicated the acid production property of these isolated strain, which confirmed the observation of the clear zone in the MRS agar supplemented with $CaCO_3$. Moreover, an isolated strain EBI-04 expressed the lowest pH at all tested incubation times.

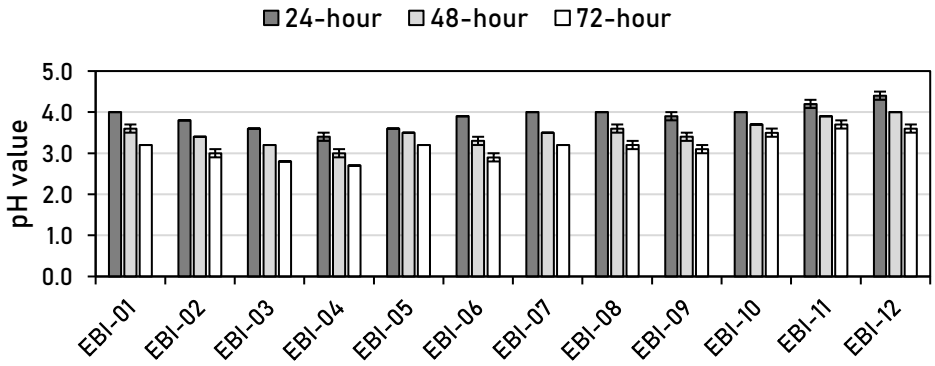

Figure 2. Determination of acid production of the isolated microbiota from commercial chicken guts

To test whether these isolated cultures can inhibit the growth of other bacteria (*Bacillus subtilis* and *E. coli* were used as a representative of different Gram strains), the well diffusion assay was performed as previously mentioned in the methodology. The results showed in the Table 1 that a 72-hour culture secretion from all of these isolated strains could inhibit the growth of both *B. subtilis* and those from 9 isolated strains could inhibit the growth of *Escherichia coli*. Moreover, an isolated strain EBI-04 expressed the widest inhibition zone among all chicken gut-isolated cultures in all tested incubation times suggesting this strain could be potentially as a beneficial microbiota isolated from the commercial chicken guts. However, the lower pH and the higher inhibition effect could be mainly resulted from the acid-mediated culture. It needed to test whether these isolated strains may produce any pH-independent bioactive compound.

Table 1. Growth inhibition zone against different Gram bacteria mediated by the secretion of chicken gut-isolated cultures

chicken gut-isolated cultures	*Bacillus subtilis*			*Escherichia coli*		
	24 hour (mm)[a]	48 hour (mm)[a]	72 hour (mm)[a]	24 hour (mm)[a]	48 hour (mm)[a]	72 hour (mm)[a]
EBI-01	ND	8.0±1.0	9.0±1.0	ND	ND	8.0±0.5
EBI-02	7.0±0.0	8.0±0.5	9.5±2.0	ND	ND	8.0±1.0
EBI-03	8.0±1.0	9.0±1.0	11.0±1.5	ND	8.0±0.5	9.0±1.0
EBI-04	8.5±1.0	10.0±1.0	12.0±2.0	8.0±0.0	9.0±0.5	10.5±2.0
EBI-05	8.0±0.5	8.0±0.5	9.0±1.0	ND	ND	7.0±0.0
EBI-06	ND	9.0±0.0	10.0±1.0	ND	8.0±1.0	9.0±0.5
EBI-07	ND	8.0±1.0	9.0±0.5	ND	ND	8.0±0.0
EBI-08	ND	7.0±0.5	9.0±1.0	ND	ND	7.0±1.0
EBI-09	ND	7.0±0.5	9.5±0.5	ND	ND	8.0±1.0
EBI-10	ND	7.0±0.0	8.0±0.5	ND	ND	ND
EBI-11	ND	ND	7.0±1.0	ND	ND	ND
EBI-12	ND	ND	7.0±1.0	ND	ND	ND

[a]Means±SD; ND denoted as not detected clear zone.

We extended the well diffusion experiments by treating the tested culture secretions with sodium hydroxide (NaOH) for adjusting the pH to 6.0 as described in the methodology. The results showed in the Table 2 that an inhibitory effect against *E. coli* was not found in any NaOH-treated secretion of chicken gut-isolated cultures. Only NaOH-treated secretion from the isolated strains EBI-01 and EBI-03 conferred the growth inhibition against *B. subtilis* with the inhibition zone of 7.5±0.5 mm and 7.5±0.5 mm, respectively.

Table 2. Growth inhibition zone against different Gram bacteria mediated by the NaOH-treated secretion of chicken gut-isolated cultures

NaOH-treated secretion	*Bacillus subtilis*			*Escherichia coli*		
	24 hour (mm)[a]	48 hour (mm)[a]	72 hour (mm)[a]	24 hour (mm)[a]	48 hour (mm)[a]	72 hour (mm)[a]
EBI-01	ND	ND	7.5±0.5	ND	ND	ND
EBI-02	ND	ND	ND	ND	ND	ND
EBI-03	ND	ND	7.0±0.5	ND	ND	ND
EBI-04	ND	ND	ND	ND	ND	ND
EBI-05	ND	ND	ND	ND	ND	ND
EBI-06	ND	ND	ND	ND	ND	ND
EBI-07	ND	ND	ND	ND	ND	ND
EBI-08	ND	ND	ND	ND	ND	ND
EBI-09	ND	ND	ND	ND	ND	ND
EBI-10	ND	ND	ND	ND	ND	ND
EBI-11	ND	ND	ND	ND	ND	ND
EBI-12	ND	ND	ND	ND	ND	ND

[a]Means±SD; ND denoted as not detected clear zone.

Finally, the partial *16S rRNA* sequence in these two strains was PCR-amplified, submitted for DNA sequencing by Macrogen Company and analyzed by a bioinformatics tools

compared with the reference sequences in the NCBI database as previously mentioned in the methodology. The preliminary results suggested that both strains were belonged in the *Lactobacillus* genus and the results paralleled to those in the previous studies[19,20]. They could be further analyzed in term of their phylogenic tract and probiotics properties.

Conclusion: Twelve morphologically different colonies were isolated from commercial chicken gut samples. They were successfully grown and provide a clear zone on MRS agar supplemented with $CaCO_3$ inferring their acid producer property. A 72-hour culture secretion from these isolated strains could inhibit the growth of both *Bacillus subtilis* and *Escherichia coli*. Treating the tested culture secretions with NaOH for adjusting the pH to 6.0 resulted in a decreased inhibitory effect against the tested bacteria. However, the NaOH-treated secretion from the isolated strains EBI-01 and EBI-03 conferred the growth inhibition against *B. subtilis*. Finally, the *16S rRNA* sequencing was done in these two chicken gut-isolated strains and they were belonged in the *Lactobacillus* genus, which could be further analyzed in term of their phylogenic tract and probiotics properties. Herein, we isolated at least two beneficial microbiota from the commercial chicken guts. A better understanding of commercial chicken guts' microbiota will provide us novel chances for sustainably improving poultry health and production.

References:

1. Shang Y, Kumar S, Oakley B, Kim WK. Front Vet Sci. 2018;5:254.
2. Stanley D, Hughes RJ, Moore RJ. Appl Microbiol Biotechnol. 2014;98(10):4301-10.
3. Clavijo V, Florez MJV. Poult Sci. 2018;97(3):1006-21.
4. Oakley BB, Lillehoj HS, Kogut MH, Kim WK, Maurer JJ, Pedroso A, et al. FEMS Microbiol Lett. 2014;360(2):100-12.
5. Fricke WF, McDermott PF, Mammel MK, Zhao S, Johnson TJ, Rasko DA, et al. Appl Environ Microbiol. 2009;75(18):5963-71.
6. Castellanos LR, Donado-Godoy P, Leon M, Clavijo V, Arevalo A, Bernal JF, et al. PLoS One. 2017;12(1):e0170777.
7. Nandi S, Maurer JJ, Hofacre C, Summers AO. Proc Natl Acad Sci U S A. 2004;101(18):7118-22.
8. Farthing MJ. Best Pract Res Clin Gastroenterol. 2004;18(2):233-9.
9. van den Bogaard AE, Stobberingh EE. Int J Antimicrob Agents. 2000;14(4):327-35.
10. Patterson JA, Burkholder KM. Poult Sci. 2003;82(4):627-31.
11. Chou LS, Weimer B. J Dairy Sci. 1999;82(1):23-31.
12. Klein G, Pack A, Bonaparte C, Reuter G. Int J Food Microbiol. 1998;41(2):103-25.
13. Thirabunyanon M, Boonprasom P, Niamsup P. Biotechnol Lett. 2009;31(4):571-6.
14. Taheri HR, Moravej H, Tabandeh F, Zaghari M, Shivazad M. Poult Sci. 2009;88(8):1586-93.
15. Tellez , G. , S. E. Higgins, A. M. Donoghue, and B. M. Hargis. J. Appl. Poult. Res. 2006;15:136–144.
16. Aquilanti L, Garofalo C, Osimani A, Silvestri G, Vignaroli C, Clementi F. J Food Prot. 2007;70(3):557-65.
17. Cheng G, Hao H, Xie S, Wang X, Dai M, Huang L, et al. Front Microbiol. 2014;5:217.
18. Anadon A, Martinez-Larranaga MR, Aranzazu Martinez M. Regul Toxicol Pharmacol. 2006;45(1):91-5.
19. Rinttila, T. and Apajalahti, J. J Appl Poultry Res, 2013;22(3):647-658.
20. Amit-Romach, E., Sklan, D. and Uni, Z. Poult. Sci. J. 2004;83(7):1093-1098.

Acknowledgements: This research was supported by a grant from Mahidol University to the Department of Biotechnology, Faculty of Science, Mahidol University under A.R.'s project.

B2_007_OF: CHARACTERIZATIONS OF TRIMETHOPRIM-SULFAMETHOXAZOLE RESISTANCE IN ENTEROBACTERIACEAE ISOLATED FROM SONGKLANAGARIND HOSPITAL

Kalyarat Kaewnirat[1], Sarunyou Chusri[2], Rattanaruji Pomwised[3,*]
[1]Department of Biomedical Sciences, Faculty of Medicine, Prince of Songkla University, Hat Yai Campus, Songkhla, Thailand
[2]Department of Internal Medicine, Faculty of Medicine, Prince of Songkla University, Hat Yai Campus, Songkhla, Thailand
[3]Department of Microbiology, Faculty of Science, Prince of Songkla University, Hat Yai Campus, Songkhla, Thailand
*e-mail: rattanaruji.p@psu.ac.th

Abstract: The objective was to investigate *sul* genes and their related with class I integron in Enterobacteriaceae isolated from patients. Thirty-five bacterial isolates were recovered from 29 patients who were admitted to the medicine ward, Songklanagarind hospital. The isolates were identified as *Klebsiella pneumoniae* (85.7%), *Escherichia coli* (8.6%), *Enterobacter cloacae* (2.9%), and *Proteus mirabilis* (2.9%) by biochemical testing. The *sul1* gene was mostly found in these isolates (94.3%) and almost associated with *intI1* gene (82.8%). The *sul2* gene was found 20.0% of all isolates and *sul3* was not found in our study. From our study, we can conclude that now the occurrence rate of the *sul1* gene was very high, and it might have increased the opportunity to spread to other bacteria species.

Introduction: The combination of sulfonamides and trimethoprim have been used for the treatment of bacterial infection since 1968. They have a synergistic effect and broad-spectrum antibacterial. Both drugs affect bacterial folic acid synthesis. Sulfonamides inhibit dihydropteroate synthetase (DHPS), which catalyzes the formation of dihydrofolate from para-aminobenzoic acid. Trimethoprim inhibits dihydrofolate reductase (DHFR) which catalyzes the formation of tetrahydrofolate from dihydrofolate. However, using sulfonamides or trimethoprim alone has a side effect. Sulfonamides can induce serious side effects such as hypersensitivity or toxic reactions. Trimethoprim has less side effect than sulfonamides. It can cause rashes and other hypersensitivity (1).

Sulfonamides-trimethoprim has been used to treat urinary tract infection, which is mostly caused by *E. coli* or other Enterobacteriaceae. However, these bacteria very quickly develop resistance against this drug. The sulfonamides resistance mostly occurs from genes, *sul1*, *sul2*, and *sul3,* which encode DHPS enzyme. Among these genes, *sul1* is the most prevalent and also locates on class I integron and conjugative plasmids (2). The *sul2* is generally found on nonconjugative plasmids, transmissible multiresistance plasmids, or insertion element common region (ISCR2) element. While *sul3* is rarely found but it associates with plasmid-borne sulfonamide resistance genes (3). Identification of integron is defined by the presence of an integrase gene (*intI*). The amino acid sequence of the *intI* gene can be divided integron into 'classes' which carry *intI1* defined as class 1, *intI2* as class 2, and *intI3* as class 3. Mostly, *intI1*, *intI2*, and *intI3* were associated with mobile genetic elements, but *intI4* and others were involved with chromosomal integrons (4). Moreover, in the class I integron can carry multiresistant genes in its gene cassette. Forty-seventy percent of clinical isolates of gram-negative pathogenic bacteria carried class I intergron. Generally, class I integron embedded in diverse plasmids and transposons, which facilitate their horizontal transfer into a wide range of pathogenic bacteria (5). Additionally, the people who stay in a tropical or subtropical zone combined with poor hygienic, also have a high risk for the dissemination of resistant gram-negative bacteria in the community (1). So, in this study, we investigated the prevalence of *sul1*, *sul2*, and *sul3* genes and also a class I integron that

involves with the *sul1* gene in Enterobacteriaceae from patients in medicine ward, Songklanagarind hospital.

Methodology:

Bacterial isolation and identification: Thirty-five bacterial isolates were recovered from 29 patients who were admitted to the medicine ward, Songklanagarind hospital from February 28 to April 18, 2017 (ethical reference no: 59-352-14-1). Patients with signed of any bacterial infections were excluded in this study. Briefly, the bacteria were isolated from rectal, throat, and environmental swabs on MacConkey agar (MAC.) by streaking plate technique. The plates were incubated at 37 °C for 24 hours. The isolates were stored in 10% glycerol at -80 °C and identified by biochemical testing (table 1) (6).

Table 1 The interpretation of biochemical testing for *K. pneumoniae*, *E. coli*, *E. cloacae*, and *P. milirabilis*

Species	indole	MR	VP	citrate	H_2S	urea	LDC	motile	D-glucose	sucrose
K. pneumoniae	-	-	+	+	-	+	+	-	+	+
E. coli	+	+	-	-	-	-	+	+	+	+/-
E. cloacae	-	-	+	+	-	+	-	+	+	+
P. milirabilis	-	+/-	+	+	+	-	+	+	-	-

Antimicrobial susceptibility testing: The bacteria were cultured on tryptic soy agar (TSA) (Beckton Dickinson, USA). The single colony of bacteria was picked into Mueller-Hinton broth (MHB) incubated at 37 °C for 3-6 hours, adjusted turbidity to 0.5 McFarlandand and streaked the bacteria on Mueller Hinton agar (MHA) (HiMedia, India). All the isolates were determined with trimethoprim-sulfamethoxazole (1.25/23.75 µg) susceptibility and incubation at 37°C for 16–18 hours. *Escherichia coli* ATCC 25922 and *Pseudomonas aeruginosa* ATCC 27853 were used as quality control.

Identification of sul1 gene, sul2 gene, sul3 gene, and class I integron by PCR method: The DNA was extracted by a boiling method by using 100˚C for 10 minutes to break the cell wall, and the DNA will be released. This DNA was used as the DNA template in this experiment. PCR amplifications were carried out in 25 µl volumes containing 15.9 µL of deionized water, 5 µl of 5X reaction buffer (5 mM dNTPs, 15 mM MgCl2, stabilizers and enhancers) (Bioline, UK), 0.1 µl of 5U My Taq DNA polymerase (Bioline, UK), 1 µl of each 10 µM primer (table 2), and 2 µl of DNA template. Amplifications of *sul1* gene, *sul2* gene, and *sul3* gene were performed at an initial denaturation step at 95˚C for 5 minutes; 35 cycles of denaturation step at 95˚C for 45 seconds, annealing at 55˚C for 1 minute, and extension at 72˚C for 2 minutes; final extension 72˚C for 5 minutes.

The amplification of class I integron was performed with the same amplification program but at an annealing temperature is 57 °C 1 minutes. The PCR products were separated using electrophoresis in 1% agarose gel at 100 V, 30 min and stained with ethidium bromide. The PCR bands were shown on a UV transilluminator. The *Stenotrophomonas maltophilia,* which harbored the gene and already confirmed by sequencing, was used as a positive control, and *E. coli* ATCC 25922 was used as a negative control.

Results and Discussion:

Bacterial identification and antimicrobial susceptibility testing: Thirty-five isolates were identified as 30 *K. pneumoniae* (85.7%), 3 *E. coli* (8.6%), 1 *E. cloacae* (2.9%), and 1 *P. milirabilis* (2.9%) by biochemical testing which collected from rectal swab (74.3%) and throat swabs (25.7%). Among these isolates, 21 (60%) and 9 (25.7%) *K. pneumoniae* was recovered from rectal swabs and throat swabs respectively. All *E. coli* isolates were obtained from the rectal

swab. An *E. cloacae* and a *P. milirabilis* were isolated from the rectal swab and throat swabs respectively. The resistance to trimethoprim-sulfamethoxazole was present in 34 isolates (97.1%). In Thailand, in 2000-2005, the rate of *E. coli* resistant to trimethoprim-sulfamethoxazole was 62.2%, but now it continues to increase almost 100% resistance (8). Blahna et al. 2006 (7) report that trimethoprim-sulfamethoxazole resistant is raising due to ability in the horizontal transfer of the bacteria, which is concordant with our result. Another study, they collected the isolates from fecal samples from healthy volunteers in Phitsanulok province, Northern Thailand. The result from their study show 48.5 % of isolates resistant to trimethoprim-sulfamethoxazole, which most common found in *E. coli* followed by *E. cloacae* and *K. pneumoniae* (9). Moreover, all bacteria used in this study were colonized suggesting that using antibiotics required more consideration because of the dissemination of resistant genes.

Table 2. Primer used for PCR amplification

Primer	Sequence (5'-3')	Gene	Product size	Reference
Sul1-F	ATGGTGACGGTGTTCGGCATTCTGA	*sul1*	840 bp	(10)
Sul1-R	CTAGGCATGATCTAACCCTCGGTCT			
Sul2-F	GAATAAATCGCTCATCATTTTCGG	*sul2*	704 bp	(10)
Sul2-R	CGAATTCTTGCGGTTTCTTTCAGC			
Sul3-F	GAGCAAGATTTTTGGAATCG	*sul3*	799 bp	(11)
Sul3-R	CATCTGCAGCTAACCTAGGGCTTTGGA			
intI1-F	GGTCAAGGATCTGGATTTGG	*intI1*	457 bp	(12)
intI1-R	ACATGCGTGTAAATCATCGTC			

Table 3. Prevalence of *sul* genes and *intI1* in trimethoprim-sulfamethoxazole resistant Enterobacteriaceae

Isolate	*sul1*	*sul2*	*sul3*	*intI1*
K. pneumoniae (30)	28/30	4/30	-	27/30
E. coli (3)	3/3	3/3	-	3/3
E. cloacae (1)	1/1	-	-	1/1
P. milirabilis (1)	1/1	-	-	1/1
Total (35)	33	7	-	32

Identification of sul genes and their relatedness to class 1 integrons: The *sul1* gene was mostly found in these isolates (94.3%) following the *sul2* gene (20.0%), which was mostly found in *K. pneumoniae* (table 3). Manyah et al. 2017 collected the clinical samples from Tanzanian patients and found that 98% carried *sul1* genes (13). Our study did not found *sul3* gene. However, we found 6 isolates harboring *sul1*, *sul2*, and *intI1* gene together. Co-existence of *sul1* and *sul2* gene was common. The *intI1* gene was found in 32 isolates which associated with *sul1* gene 31 isolates (88.6%). Many reports show that the *sul1* gene is located within the integron (13). It is similar to the previous study; they also found a high prevalence of *intI1* in *K. pneumoniae* (73.3%) (14). In Korea in1980s, *E. coli* isolates were found to carry a single gene cassette in class I integrons while in the 1990s, they found multigene cassette gene in class I integrons. The conjugative plasmid that carries class I integrons may act to be responsible for broad dissemination of a particular type of class I by horizontal transfer (15).

However, we also found 2 isolates that carried the *sul1* gene but not *intI1*. Singha et al. 2015 reported that the *sul1* gene might not be located in *intI1*, but it still can cause sulphonamide resistance. The evident was showed by MIC value from their study (2). Furthermore, in 2018, another report revealed that more than two-thirds of carbapenem-

resistant Enterobacteriaceae were resistant to trimethoprim-sulfamethoxazole. Most of them were carbapenem-resistant *K. pneumoniae*. Susceptibility rate of CRKP to trimethoprim-sulfamethoxazole is varying from 31% to 82%, depending on the region of the world (16). So, our findings show the high occurrence of *sul1* gene, which were almost associated to the class 1 integron. Future study, we will investigate other antibiotic resistance genes that involve in this integron. This type of integron carries not only trimethoprim-sulfamethoxazole resistant gene but also other antibiotic resistance genes which might cause of multidrug-resistant bacteria and lead to a limit of treating bacterial infection.

Conclusion: In this study, Enterobacteriaceae isolates mostly were *K. pneumoniae*. Almost isolates were resistant to trimethoprim-sulfamethoxazole. We found a high occurrence of *sul1* gene and mostly associated with the *intI1* gene, which might make their increase ability of horizontal transfer.

References:

1. Huovinen P. Clin Infect Dis Off Publ Infect Dis Soc Am. 2001;32(11):1608–14.
2. Singha P, Maurya AP, Dhar D, Chakravarty A, Bhattacharjee A. Arch Clin Microbiol. 2015;6(3).
3. Shin HW, Lim J, Kim S, Kim J, Kwon GC, Koo SH. J Microbiol Biotechnol. 2015 ;25(1):137–42.
4. Deng Y, Bao X, Ji L, Chen L, Liu J, Miao J, Chen D, Bian H, Li Y, Yu G. Ann Clin Microbiol Antimicrob. 2015;14(1):45.
5. Gillings M, Boucher Y, Labbate M, Holmes A, Krishnan S, Holley M, Stokes HW. J Bacteriol. 2008;190(14):5095–100.
6. Farmer JJ, Davis BR, Hickman-Brenner FW, McWhorter A, Huntley-Carter GP, Asbury MA, Riddle C, Wathen-Grady HG, Elias C, Fanning GR, Steigerwalt AG, O'Hara CM, Morris GK, Smith, PB, Brenner DJ. J Clin Microbiol. 1985;21(1):46–76.
7. Blahna MT, Zalewski CA, Reuer J, Kahlmeter G, Foxman B, Marrs CF. J Antimicrob Chemother. 2006;57(4):666–72.
8. Polwichai P, Dejsirilert S, Panpetch S, Sawanpanyalert P, Aswapokee N, Mootsikapun P. J Med Assoc Thail Chotmaihet Thangphaet. 2009;92 Suppl 4:S59-67.
9. Niumsup PR, Tansawai U, Na-Udom A, Jantapalaboon D, Assawatheptawee K, Kiddee A, Romgaew T, Lamlertthon S, Walsh TR. Eur J Clin Microbiol Infect Dis Off Publ Eur Soc Clin Microbiol. 2018;37(1):69–75.
10. Toleman MA, Bennett PM, Bennett DMC, Jones RN, Walsh TR. Emerg Infect Dis. 2007;13(4):559–65.
11. Adegoke AA, Okoh AI. Jundishapur J Microbiol. 2014;8(1).
12. Ozkaya E, Aydin F, Bayramoglu G, Buruk CK, Sandalli C. Mikrobiyol Bul. 2014 ;48(2):201–12.
13. Manyahi J, Tellevik MG, Ndugulile F, Moyo SJ, Langeland N, Blomberg B. Microb Drug Resist. 2016;23(1):37–43.
14. Li B, Hu Y, Wang Q, Yi Y, Woo PCY, Jing H, Zhu B, Liu CH. PLOS ONE. 2013;8(9):e75805.
15. Kang HY, Jeong YS, Oh JY, Tae SH, Choi CH, Moon DC, Lee WK, Lee YC, Seol SY, Cho DT, Lee JC. J Antimicrob Chemother. 2005;55(5):639–44.
16. Luterbach CL, Boshe A, Henderson HI, Cober E, Richter SS, Salata RA, Kalayjian RC, Watkins RR, Hujer AM, Hujer KM, Rudin SD, Domitrovic TN, Doi Y, Kaye KS, Evans S, Fowler VG, Bonomo RA, Duyn DV. Open Forum Infect Dis. 2019;6(1):351.

Acknowledgements: We would like to thank the Department of Internal Medicine, Faculty of Medicine, Prince of Songkla University for bacterial isolates used in this research and

Department of Microbiology, Faculty of Science, Prince of Songkla University for research facilities

B2_008_OF: CHARACTERISTICS OF BACTERIOPHAGES AGAINST *Vibrio* spp.

Natwara Dangnordang[1], Ampapan Naknaen[2], Jumroensri Thawonsuwan[3], Noodchanath Kongchouy[4], Rattanaruji Pomwised[1]*
[1]Department of Microbiology, Faculty of Science, Prince of Songkla University, HatYai Campus, Songkhla, Thailand
[2]Department of Environment Management, Faculty of Environment management, Prince of Songkla University, HatYai Campus, Songkhla, Thailand
[3]Coastal Aquatic Animal Health Research Institute, Department of Fisheries, Songkhla, Thailand
[4]Department of Mathematics and Statistics, Faculty of Science, Prince of Songkla University, HatYai Campus, Songkhla, Thailand
*e-mail: rattanaruji.p@psu.ac.th

Abstract: *Vibrio* is a gram-negative short rod curved bacterium with polar flagella with sheaths. *Vibrio* is facultative anaerobe, low tolerance to acid, and prefer alkaline. It can cause diseases in both aquatic animals and humans. Therefore, contamination of *Vibrio* in seafood is the public safety concern. The present study was to isolate vibriophages from marine water, seafood samples, and shrimp aquaculture by double-layer agar plaque assay using *V. vulnificus* VVA5, and VVA6 as host. Five vibriophages, V6T04, V6T12 and V5W07, V5W12, V5W13 with prominent zone, plaques sized 0.1 to 0.5 mm, and phage titers ranged from 104 to 107 were selected for determining host range specificity with 49 *Vibrio* isolates. The result showed that they inhibited 3 main *Vibrio* spp. (*V. parahaemolyticus* and *V. vulnificus* and *V. alginolyticus*) isolated from frozen seafood factories, suggesting that they are broad host range phages. From this result, 2 vibriophages, V5W07, and V6T12 were selected to study further: phage survival determination with various temperature, salinity, pH and chlorine. The result indicated that both vibriophages survived and were active at the temperature 0 °C and 5 °C and stable at 20 ° C, the salinity of 0 – 5 % NaCl and pH 5 – 11 but unable to survive at pH 2 and pH 13. Besides, with increasing concentration of chlorine, the number of phages decreased slightly from 5 to 50 ppm, and all of them cannot survive at chlorine 100 ppm. One-step growth curve revealed that V6T12 phage presented a shorter latent period than V5W07 phage. The results suggested that they might be useful in providing an alternative method to reduce the contamination of the *Vibrio* spp. in industry and aquaculture.

Introduction: *Vibrio* is a gram-negative short rod curved, motile and has polar flagella with sheaths. *Vibrio* is facultative anaerobe, low tolerance to acid and prefer alkaline conditions (1), and can be able to cause diseases in fish, shellfish, mammals, as well as in humans (2). It is one of the most significant pathogens associated with seafood consumption and has frequently caused severe production losses on shrimp and prawn farms (4). Thailand supplies 20 percent of the world trade in shrimp and prawn (3). Frozen industries focus on the chemical process to reduce the bacterial contamination of the product to be acceptable by partner countries (9). Chlorine has been the most frequently used for reducing contaminated bacteria and kills significant pathogens even though it is highly toxic and can generate dangerous carcinogens which affect the health of workers, consumers and causes negative environment and socioeconomic (10). Major international markets have enforced strict quality control on Shrimp, particularly the maximum concentration of applied disinfectants and disease control compounds such as antibiotics and chemicals (6).

Therefore, novel biocontrol strategies should be considered and explored to ensure food safety. Bacteriophage (phage) is a promising approach to combat bacteria since phages are high host specificity (8). Phages infect only a single species of bacteria and are obligate parasites of the bacterial host (7). Phages are easy to be selected because they can be found

in every environment where their bacterial hosts are present (12). To assess the utility of two bacteriophages as a biocontrol, vibriophages were isolated by using *V. vulnificus* VVA5, VVA6 as hosts and their abilities to kill *V. vulnificus* were determined.

Methodology:

Phage isolation and purification: Phages were isolated from 14 shellfish samples and 20 seawater samples collected from open markets throughout Hatyai city, Songkhla and Songkhla lake respectively. V. vulnificus VVA5 and VVA6 were used as host. Briefly, 20 mL of marine water was filtered by 0.22 µm. Filtered water was added to 20 mL of 2X TSB (1%Nacl) or twenty grams of seafood were chopped and then added to 20 mL of TSB (1%Nacl). Then 1 mL of the bacterial host overnight culture was added. The mixture was incubated at 37 °C for overnight at 150 rpm, and then all mixture was centrifuged at 10,000 g for 30 min. After that water sample was filtered by 0.22 µm and tissues were filtered by 0.45 µm and stored at 4 °C with 2% chloroform.

The presence/absence of the bacteriophage was confirmed by double-layer agar plaque assay. Two hundred micro milliliter of the host culture and 200 µL of the filtered sample were added to 3 mL of soft agar (TSB, 1% NaCl, 0.75% agar) and overlaid onto a TSA culture medium. After the top agar was solidified, plates were incubated overnight at 37°C. Plaque formation on the plates was observed.

Single plaque isolations: To obtain a pure phage stock, 100 µL of each serially diluted phage suspension were mixed with 200 µL of host culture were then the mixture was added to 3 mL of soft agar and overlaid onto a TSA. Plates were incubated overnight at 37°C. After incubation, single plaque on TSA plate was collected. Single plaque isolation was performed 3 times to ensure purified phage. Then phage was stored in SM buffer ($MgSO_4 \cdot 7H_2O$, 1M Tris-Cl pH 7.5, NaCl, DW water) with 2% chloroform at 4 °C.

Host range determination: 49 *Vibrio* spp. were used including *V. vulnificus* (n=24), *V. cholerae* (n=1) *V. alginolyticus* (n= 4), *V. parahaemolyticus* (n=14), *V. mimicus* (n=2) and *V. rotitirianus* (n=4). The ability of phages killing was determined by using the spot test onto bacterial lawns. Two hundred µL of each *Vibrio* strain were added to 3 mL of soft agar and overlaid onto a TSA. After the top agar was solidified, 10 µL of phage was spotted onto the overlaid plates and incubated overnight at 37°C. The efficiency of phage infection was determined by an observed clear zone. The results were recorded as (-) Plaques not formed, (+) Hazy plaques and (++) Distinct clear plaques (Table 1).

Phage survival determination: The phage in vitro survival was determined in different parameter including different pH (pH 2, 5, 7, 9, 11 and 13), salinity (0%, 1%, 2%, 3%, 4% and 5%), chlorine (5, 10, 20, 50 and 100 ppm) and temperature (0, 5, 10 and 20 °C). For survival test in different pH and salinity, 10^6 CFU/mL of each phage was incubated at various pH and salinity for 12 hours at room temperature. For survival test in different chlorine concentration and various temperature, 10^6 CFU/mL of each phage was incubated for 1 h at different situations. Amount of each phage after facing different parameters was calculated by using double-layer agar plaque assay.

One-step growth assay: Host bacterial cultures were adjusted to the final concentration of 107 CFU/ml and phage stocks were adjusted to 106 PFU/ml. Five microliters of the phage suspension were added to 5 mL of the bacterial culture and incubated at room temperature for 10 min and then the mixture was centrifuged at 10,000 rpm/min for 5 min to remove supernatant. The pellet was resuspended in 6 mL of TSB and was incubated at 37 °C for 2 h at 150 rpm. Two hundred µL were collected at 5 min interval from 0-120 min. The culture was centrifuged at 10,000 rpm/min for 2 min to obtain the supernatant. The number of phages was calculated by using a double-layer agar plaque assay.

Results and Discussion:

Phage isolation and purification: A total of 82 phages was isolated from 9 shellfish samples and 12 seawater samples. Forty-eight phages were isolated from shellfish and 34 of phage were isolated from seawater. This result could be explained for finding bacteriophages is to look where the host is as for *Vibrio* spp., which natural habitat in seawater and brackish water.
Single plaque isolations: Single plaque isolations were performed to obtain a pure phage stock. From all of 82 phages, 5 phages formed clear plaques, with plaque diameter varying from 0.1 to 0.5 mm. The phage titers ranged from 10^4 to 10^7. Phage titers can indicate the time of phage life cycle from infecting bacteria and generating progeny (11). Five phages were successfully isolated and purified after three times single plaque isolations to study further.
Host range determination: Five phages were selected to determine their host ranges by spot testing on 49 *Vibrio* spp.. Phage V6T04, V6T12, and V5W07, V5W12, V5W13 showed similar host range results (Table 2) suggesting that they might use the same receptors on their host (5). These five phages were lytic phages. Even though they used *V. vulnificus* VVA5 and VVA6 as hosts, they were capable to infect other *V. vulnificus* strains isolated from different sources and different geographical locations indicating that they were broad-host-range phages. They also infected *V. parahaemolyticus* and *V. alginolyticus* species but cannot inhibit *V. cholerae*. These phages are valuable to reduce the contamination of the *Vibrio* spp. in frozen industry and aquaculture. Two phages, V6T12 and V5W07, had capabilities of producing clear zones and showed very broad-host-range, so they were selected to determined phage survival in different stress conditions.
Phage survival determination: The result of phage survival (V6T12 and V5W07) in different pH, salinity, chlorine, and temperature indicated that they survived and were active in 0 °C and 5 °C and stable at 20 °C which was the setting condition identical to the factory. For salinity test, the result showed that they could survive at 0 – 5 % of NaCl and pH 5 – 11 but both of them were unable to survive at pH 2 and pH13. In addition, with increasing concentration of chlorine, the number of phages decreased slightly from 5 to 50 ppm, and all of them cannot survive at chlorine 100 ppm. The result from the resistance to stress conditions implied that these phages could be used as an alternative method to reduce the contamination of the *Vibrio* spp. in industry and aquaculture (Figure 1).
One-step growth assay: The results of the phage one-step growth experiments showed in Figure 2. and the latent period of V6T12 phage presented a shorter latent period at 5 min and V5W07 phage presented a longer latent period at 65 min. The phage burst size and latent periods are important factors to consider when phages are selected as a biocontrol. Phages with high burst sizes and shorter latent periods are more effective in inactivating bacteria (13)

Table 1. Show the level of cleat zone to indicate the efficiency of phage infection

Plaques not formed (-)	Hazy plaques (++)	Distinct clear plaques (+++)
		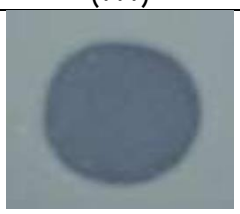

Table 2. Show the level of cleat zone to indicate the efficiency of phage infection

Vibrio spp.	Strains	Source	Phage code.				
			V6T04	V6T12	V5W07	V5W12	V5W13
V. vulnificus	ATCC 27562	Standard	++	++	-	-	-
	DMST 3606	Clinic	-	-	+	+	+
	DMST 4126		-	-	++	-	++
	DMST 4183		+	+	+	-	-
	DMST 31751		++	++	-	-	-
	DMST 31752		++	++	-	-	-
	DMST 31753		+	+	-	-	-
	DMST 32990		++	++	+	+	-
	DMST 32991		-	-	-	-	-
	DMST 32989		-	-	-	-	-
	PSU 039	Biotype 2	-	-	-	-	-
	PSU 025		+	+	-	-	-
	VVA1	Disease in	-	-	-	-	-
	VVA2	fish	+	+	++	++	++
	VVA3		++	++	-	-	-
	VVA4		-	-	-	-	-
	VVA5		-	-	++	++	++
	VVA6		++	++	-	-	-
	VVA7		+	+	-	-	-
	VVA8		++	++	-	-	-
	VVA9		+	+	-	-	-
	FVV11		+	+	++	-	-
	7		-	-	-	-	-
	15	Factory	-	-	++	++	-
V. cholerae	PSU 966 01	Standard	-	-	-	-	-
V. alginolyticus	PSU 6	Standard	-	-	-	-	-
	8		-	+	-	-	-
	13	Factory	-	-	++	++	-
	19		-	-	++	++	-
V. parahaemolyticus	ATCC 17808	Standard	-	-	-	-	-
	SCI		++	++	-	-	-
	1.1		-	++	+	+	+
	1.2		-	-	+	+	+
	1.3		-	-	+	+	+
	2.2		-	-	+	++	+
	B 1.1		-	-	+	+	+
	B 1.2.1		-	-	+	-	-
	B 1.2.2	Factory	-	-	-	-	-
	B 1.3		-	-	+	+	+
	B 2.1		+	+	++	+	++
	B 2.2		-	++	++	++	+
	B 2.3		-	++	++	++	++
	B 3.2		++	++	+	++	+
			++	++	++	++	++

(-) Plaques not formed
(+) Hazy plaques
(++) Distinct clear plaques

Table 2. Show the level of cleat zone to indicate the efficiency of phage infection (Cont.)

Vibrio spp.	Strains	Source	Phage code.				
			V6T04	V6T12	V5W07	V5W12	V5W13
V. mimicus	03	Factory	-	-	-	-	-
	5		-	-	-	-	-
V. rotitirianus	02	Factory	-	-	-	-	-
	14		-	-	-	-	-
	16		-	-	-	-	-
	18		-	-	-	-	-

(-) Plaques not formed
(+) Hazy plaques
(++) Distinct clear plaques

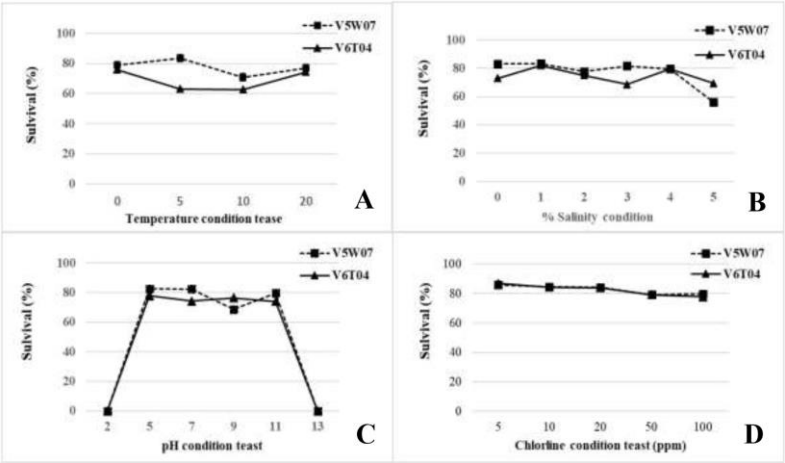

Figure 1. Phage survival of V6T12 and V5W07 by stability test of (A) Temperature, (B) % Salinity, (C) pH, and (D) Chlorine.

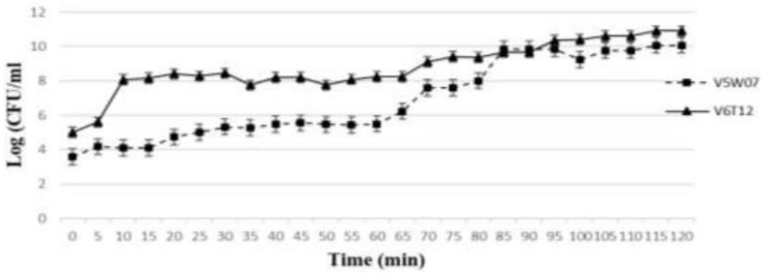

Figure 2. One-step growth curves of V5W07 and V6T12 in the presence of *V. vulnificus* VVA5 and VVA6 as host

Conclusion: In this study, the isolation, characterization, host range, phage survival, and one step growth were investigated. The isolated bacteriophages V6T12 and V5W07 are characterized by broad host range and both of them were capable of surviving within various stress conditions. V6T12 with shorter lytic cycles also increases the efficiency of bacterial inactivation. Phages may be used as an alternative to solutions against bacterial diseases and biocontrol.

References:
1. Bisharat N, Cohen DI, Harding RM, Falush D, Crook DW, Peto T, Maiden MC. Emerging Infectious Diseases.2015;11(1): 30-35.
2. Chang RYK, Wallin M, Lin Y, Leung SY, Wang H, Morales S, Chand HK. Advanced Drug Delivery Reviews.2018;133:76-86.
3. Kalatzis P.G, Bastías R, Kokkari C, Katharios P. Pols One.2016;11(3):1-18.
4. Kawa1 ZD, Skrobek1 GM, Maciejewska B, Delattre AS, Lavigne R. Current Protein and Peptide Science.2012;13:699-722.
5. Mateus LL, Costa YJ, Silva C, Pereira A, Cunha A. Aquaculture.2014;425:167-173.
6. Nakai T, Park SC. Research in Microbiology.2002;153(1):13-8.
7. Osunla CA, Okoh AI. International Journal of Environmental Research and Public Health. 2017;14(10):1188.
8. Patmasiriwat D, Kuik O, Pednekar S. World Shrimp Farming.1998;9:1-34.
9. Phumkhachorn P, Attanachaikunsopon P. African Journal of Microbiology Research. 2010;4:1794-1800.
10. Ramirez1 K, Montoya C, Moreno HS, Campo NC. Pols One. 2018;3(5):1-10.
11. Thompson FL, Iida T, Swings J. American Society for Microbiology.2004;68(3):403- 431.
12. Yang ZQ, Tao XY, Zhang H, Rao SQ, Gao L, Pan ZM, Jiao XA. International Journal of Food Microbiology. 2019;292(2):107-117.
13. Yen M, Cairns1 LS, Camilli1 A. Nature communication. 2017;8:1-7.

B2_009_OF: TESTING THE PHENOTYPIC EFFECTS OF *Acinetobacter baumannii* ANTIBIOTIC RESISTANT GENE IN *Escherichia coli* BY USING A HIGH-THROUGHPUT CLONING APPROACH

Asmita Khaniya*, Iyarit Thaipisuttikul
Department of Microbiology, Faculty of Medicine Siriraj Hospital, Bangkok, Thailand
*e-mail: ashmita.khaniya1@gmail.com

Abstract: *Acinetobacter baumannii* is a major gram-negative nosocomial pathogen found ubiquitously in hospital environments. Currently, *A. baumannii* has been resisted to almost all commercially available antibiotics. The emergence of multidrug resistant (MDR) and extensively drug resistant (XDR) strain in *A. baumannii* is challenging. Unfortunately, colistin is the last line treatment option for XDR *A. baumannii*. Previously, researchers found *A. baumannii* has possessed the mechanism to sense the external environment and induced resistance against colistin. Though, the exact colistin resistance inducer and its regulatory mechanisms were still controversial. The RcnB protein was previously found in *Escherichia coli* as a regulator for nickel and cobalt efflux but the contribution of this protein against colistin in *A. baumannii* is still unknown. However, it was hypothesized as a regulator for nickel and cobalt efflux. Our knowledge up to now on *A. baumannii* resistant mechanism is limited due to the paucity of genetic tools and the narrow host range. This study aimed to test the effect and the suitability of protein (RcnB) from *A. baumannii* to NEB stable *E. coli* host cell by using the previously published high-throughput cloning approach based on homologous recombination in *E. coli.* The *rcnB* gene of *A. baumannii* was amplified with primers incorporated with homologous sequences similar to the vector backbone and was transformed into *E. coli* along with the linearized vector. The transformation was directly performed in *E. coli* by KCM based method within one and half hour. The minimum inhibitory concentration (MIC) of *E. coli* with *rcnB* gene from *A. baumannii* was 2- folds increased compared to *E. coli* with blank before and after induced with Isopropyl β-D-1-thiogalactopyranoside (IPTG). This result suggested that the cloned *rcnB* gene from *A. baumannii* in NEB-stable *E.coli* could function in the same manner as in wild type strain. The cloning technique in this study is less time consuming, easy to perform and economical. Since *A. baumannii* has a narrow host range, it is important to find other alternative hosts to study the function of unknown genes in crucial role of antibiotic resistance. This study could provide the new gateway in the field of molecular genetic analysis of MDR and XDR *A. baumannii* in near future.

Introduction: *Acinetobacter baumannii,* a non-lactose fermenting bacterium, is an opportunistic gram-negative pathogen responsible for causing various nosocomial infections such as bacteremia, pneumonia, meningitis and urinary tract infections in critically ill and hospitalized patients (1). The study carried out in 49 United States (US) hospitals showed that *A. baumannii* is the third most leading cause of death in ICU patients with bacteremia (2). The challenging aspect of *A. baumannii* infection is the emergence of drug resistance i.e. multidrug resistance (MDR) and extensively drug resistance (XDR) strains. The 'MDR *Acinetobacter* species' is defined as the isolates resistant to at least three class of antimicrobial agents including penicillins, cephalosporins, fluoroquinolones and aminoglycosides whereas, 'XDR *Acinetobacter* species' is the isolates resistant to previously mentioned three classes of antibiotic (MDR) and also resistant to carbapenems (3). The study in 2012 by Werarak P *et al,* found *A. baumannii* as a major cause of nosocomial pneumonia (30.4%) in hospitalized adults from 12 tertiary care hospitals in Thailand. The result from antimicrobial susceptibility pattern of these *A. baumannii* disclosed (14.6%) were resistant to 1-2 class of antibiotics, (15.7%) were multidrug-drug-resistant, (69.7%) were extensively-drug-resistant and (81.8%) were found to be resisted to carbapenems (4). However, *A. baumannii* strains were resisting to almost all class of the antibiotics including beta-lactams, fluoroquinolones, tetracyclines,

aminoglycosides and carbapenems. The reported data from National Antimicrobial Resistance Surveillance Thailand 2008-2018 have shown (~60%) of *Acinetobacter* spp were resisted to imipenem (5). Though, carbapenems were considered as a last resort antibiotics in beta-lactams family, but the carbapenems-resistant isolates of *A. baumannii* were reported from all over the world (6).

Nevertheless, colistin is the only last line remaining choice of treatment against XDR *A. baumannii*. Colistin is a cationic antimicrobial peptide in polymyxin family, which interacts with negatively charged lipopolysaccharide of gram negative bacterial cell membrane and caused death via the displacement of divalent cations (7, 8). Unfortunately, the resistant strains of *A. baumannii* against colistin have also been reported (1). To date, there are at least two colistin resistant mechanisms that have been characterized in *A. baumannii*. The first common mechanism is the mutations in two-component system i.e. *pmrAB*, leading to the upregulation of *pmrC* resulting in the addition of positively charged phosphoethanolamine to bacterial lipid A molecules that cause decrease in the affinity of colistin (9). Second, the complete loss of lipopolysaccharide due to the mutations in *lpxACD* (10). Previously, researchers found *A. baumannii* has ability to sense the environmental cues, NaCl, monovalent and divalent cations. Those were identified as an important signals that induced significant tolerance to many antibiotics including colistin (11). Though, the genetic determinants of resistance to colistin in *A. baumannii* was studied, but the mechanism by which it regulates it's tolerance against colistin have not been studied yet. Different colistin resistance mechanisms have been studied in *A. baumannii* however most of them are still unclear (12). Unfortunately, limited molecular tools and the narrow host range makes the study of resistance mechanism of *A. baumannii* even more complicated. Therefore, it is very important to develop the new molecular tools to investigate the suitable and specific colistin resistance mechanism in order to give the way out for the appropriate treatment against the MDR and XDR *A. baumannii*. Though, few studies were carried out to investigate the suitable shuttle vector between *Escherichia coli* and *Acinetobacter* species however, those developed shuttle vectors were somehow unsuitable for the gene expression of MDR and XDR *A. baumannii* because of the extremely limited selectable marker (13, 14).

Although, *A. baumannii* has developed several resistance mechanisms against most of the antibiotics but to find specific resistance mechanism of drug transporter proteins is difficult due to the limited host cell. Till now, several expression vector, methods and the host cell i.e. *E.coli* has been developed to study the function of certain transporter protein of *A. baumannii*. But whether those proteins from *A. baumannii* can function well in *E.coli* is still questionable. Different cloning method has been used for the protein expression but most of them are costly and still time consumable.

The gene that was used in this study is a novel gene (*rcnB*) found in *A. baumannii* which function is still unknown. However, this gene was previously found in *E. coli* and thought to maintain the nickel (Ni) and cobalt (Co) homeostasis in *E. coli* (15). Moreover, it is suggested as an efflux pump regulator gene in *E. coli*, though the function of this gene is still not known in *A. baumannii* against colistin. This study aimed to test the newly adapted *in vivo* cloning technique by using NEB stable *E. coli* competent host cell in order to check the effect of *rcnB* gene (16) and produce a large-scale clone of *A. baumannii rcnB* gene in *E. coli* with the subsequent tested for the change in their MIC levels. The *in vivo* cloning technique does not require any *in vitro* ligation-based reaction but the cloning product occurs directly in *E. coli* cell via recombination machinery. Hence, the primers of inserts (*rcnB*) were designed by adding homologous sequence with respect to the vector backbone.

Material and methods:

Bacterial strains and plasmid: The hypervirulent and colistin resistant *A. baumannii* AB5075-UW strain was kindly gifted by Professor Colin Manoil (Department of Genome Sciences, University of Washington, USA). *E. coli* (NEB stable) and pBS2ndd vector (Addgene plasmid # 97353; http://n2t.net/addgene:97353; RRID: Addgene_97353) were kindly gifted by Asst. Prof. Jamorn Somana (Faculty of Science, Mahidol University). *E. coli* ATCC25922 was used as a quality control strain for micro-broth dilution method according to 2015 CLSI guideline.

The vector pBS2ndd has ampicillin resistant gene marker (amp^R), has *lac* operon inside it and *ndd* gene inserts in *lacZα* region. *ndd* is a lethal gene from bacteriophage T4 that codes for nucleotide disruption protein of host chromosome (16). For this experiment the primers for vector were designed in such a way that it will not amplify *lacZα* region which has *ndd* gene insertion.

PCR Amplification: All primers in this study were designed using Primer 3 software. The primes that were used to amplify vector backbone are given as; forward primer (FP) 5'GTT CTT TAA TAG TGG ACT CTT GTT CCA3' and reverse primer (RP) 5'AGC TGT TTC CTG TGT GAA ATT GTT AT3'. The full circular map of the vector pBS2ndd was given in figure 1.

The complete genome of *A. baumannii* AB5075-UW was available on The National Center for Biotechnology Information (NCBI) database. Genomic DNA of *A. baumannii* AB5075-UW was used as a template to amplify inert (*rcnB*) for the cloning. The primer for insert was designed by adding homologous sequence matching with vector backbone. The primer sequences designed for insert were as follows; forward primer (FP), 5'<u>ATA ACA ATT TCA CAC AGG AAA CAG CT</u>A TGA AAA AGC CTT CTC GTA3', reverse primer (RP), 5'<u>TGG AAC AAG AGT CCA CTA TTA AAG AAC</u> CA GAT GAC GAG TTG GCA TAA3', where the underlined sequences are homologous sequence to the vector backbone and remaining are primer specific to *rcnB* gene. The diagrammatic representation of homologous recombination was given in figure 2. The blue arrow represents the forward and reverse primer for *rcnB* gene whereas the yellow and the purple boxes represent the homologous sequence to the vector.

Colony PCR was performed to verify the insertion of respective insert (*rcnB*) after the successful transformation. The primers were designed to match vector pBS2ndd sequence flanking the insert. The primers were as followed, forward primer (FP), 5'AGT GAG CGC AAC GCA ATT A3'; reverse primer (RP), 5'GAA ATC GGC AAA ATC CCT TA3'. The diagrammatic representation of colony PCR primers designed position was given in figure 3. The figure 3 represents the final recombinant plasmid after transformation, the forward and the reverse colony PCR primers where named as sequencing-FP and sequencing-RP respectively inside the red boxes in figure 3.

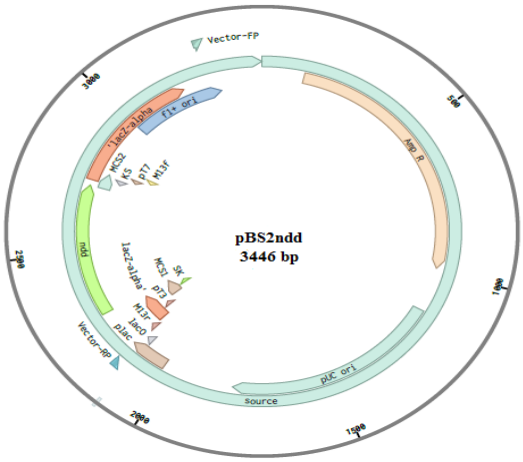

Figure 1: pBS2ndd vector circular map

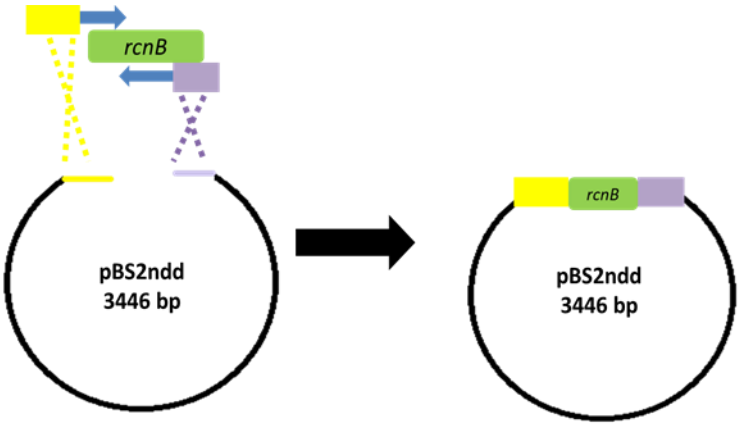

Figure 2: Diagrammatic representation of homologous recombination

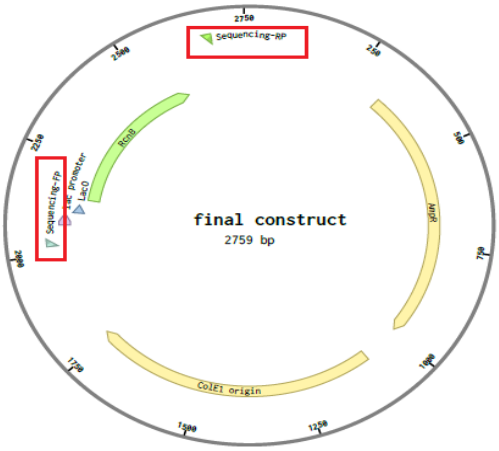

Figure 3: Vector map showing the position of primer designed for colony PCR

In vivo cloning: The linearized vector and PCR product were directly co-transformed into competent cells by KCM (0.5 M KCL, 150 mM $CaCl_2$, 250 mM $MgCl_2$) transformation method. The competent cells were prepared by following TSB protocol (16). The mixture was prepared in a final volume of 50 µl consisting of DNA, vector backbone, 10 µl of 5X KCM solution, and adjusted with sterile water to 50 µl. The *E. coli* competent cells were thawed on ice for approximately 10 minutes and 50 µl of competent cells were then gently mixed with 50 µl of insert and vector mixture. The transformation mixture was immediately incubated on ice for 10 minutes, followed by incubation in room temperature for 10 minutes. After that, 200 µl of Luria-Bertani (LB) broth was added into transformation mixture, which was then incubated at 37°C for 60 minutes at 200 rpm. The transformation mixture was then centrifuged. The supernatant was discarded and 100 µl of LB broth was added into 1.5 ml microcentrifuge tube to resuspend pellet. Finally, transformation culture was spread on the LB agar containing ampicillin and incubated at 37°C for overnight.

Next day, white colonies that were grown in LB agar with ampicillin containing plates were selected to performed colony PCR. Positive result of insert was detected by using specific forward and reverse primer that was designed near insert as mentioned above. The expected size of PCR product was 662 bp. Template DNA was prepared by adding 2 µl of sterile distilled water in sterile PCR tube. After that, single colony was picked up from overnight plate by inoculating micropipette tip then dissolved in a water in a PCR tube. The dissolved colony was then used as template in a 25 µl PCR reaction. As a negative control, the blank vector template without *rcnB* gene insert was used. The expected size for the negative result should be 1349 bp. PCR was carried out with following conditions; Initial denaturation at 95°C for 5 minutes followed by 30 cycles of denaturation at 95°C for 30 seconds, annealing at 50°C for 1 minute, extension at 72°C for 1 minute and then final extension at 72°C for 5 minutes. The colony PCR result was further analyzed by running into 1% gel under the UV transluminator and the band size were further compared by using 100 bp DNA ladder

Antimicrobial susceptibility testing: E.coli strains carrying recombinant plasmids with *rcnB* gene inserts were grown overnight at 37°C in LB agar medium containing 100 µg/ml of ampicillin and 1mM Isopropyl β-D-1-thiogalactopyranoside (IPTG) as a final concentration. The *lac* promoter will be expressed after exposing to the source of lactose i.e. IPTG and that caused the overexpression of *rcnB* gene which is under the control of *lac* promoter. The significantly expressed *rcnB* gene from AB5075-UW in *E. coli* host cell will show the increase in minimum inhibitory concentration (MIC) against colistin when compared to the *E. coli* with blank vector after induction with IPTG. Next day, the antimicrobial susceptibility testing was performed by doing micro-broth dilution method as recommended by CLSI 2015 guideline. The colistin concentration ranges from 0.25 to 256 µg/ml was prepared in 96 well microtiter plate and the result was interpreted by screening the lowest drug concentration that inhibits the visible bacterial growth after overnight incubation at 37°C. The MIC between transformants *E. coli* with AB5075-UW *rcnB* gene insert and the transformants *E. coli* with blank vector (pBS2ndd) induced with and without IPTG were compared.

Results and discussion: The *in vivo* homologous recombination occurred inside the competent cells by utilizing its own DNA repairing mechanism. Based on the result from our study, to yield the optimal recombination, addition of longer homologous bases (26 bp) would be beneficial as it will increase the transformation efficiency (20000 CFU/µg). Our preliminary experiment in which only 18 bp of homologous sequences were added and the transformation efficiency was found to be lower and this showed the concordant result with the previous experiment (17). The transformants colonies were taken for the colony PCR in order to rule out the correct insertion of the gene of interest (*rcnB*), the result showed (100%) positive (15 out of 15) bands on gel electrophoresis shown in figure 4, that represents the band of insert from the 15 colonies those were taken for colony PCR. Furthermore, the recombinant plasmid

from transformants were extracted and analyzed into 1% gel under the UV transluminator. The band size was compared by using 1 Kb plus DNA ladder. The homologous recombination produces circular recombinant plasmid (16) which moves faster in gel than the other forms of plasmid. The result was shown in figure 5 in which this form of plasmid was compared with the linear vector backbone which is 2314 bp in size.

To demonstrate whether NEB stable *E. coli* host cell strain is effective for the expression of *A. baumannii rcnB* gene, MICs of transformants was tested with and without induction with 1mM IPTG. Interestingly, the microbroth dilution result of *E. coli* with *rcnB* gene from AB5075-UW showed the same MIC of 4 µg/ml in both IPTG induced and uninduced condition. However the MIC of *E. coli* alone and with blank vector was 2 µg/ml and 1 µg/ml respectively in IPTG induced and uninduced condition. The result showed 2- folds increased in MIC of *E. coli* with *rcnB* gene insert from AB5075-UW when compared to *E. coli* with and without blank vector. This result suggested that the cloned *rcnB* gene from *A. baumannii* in NEB-stable *E.coli* could function in the same manner as in wild type strain. However, the MIC of uninduced and induced *E. coli* with *rcnB* insert was found to be the same for the colistin which was not expected. But it could be suspected to have a leaky transcription of *lac* promoter because the *lac* operon of the vector lacks *lacI* gene and the *lac* repressor molecule from host cell may not be enough to bind at the *lacO* so that the background expression may occur even in the absence of inducer (18). To rule out this condition, the *E. coli* with blank vector and the *E. coli* with *rcnB* insert were tested on the LB agar containing 2 µg/ml of colistin with and without IPTG induction. While the result showed only one colony of *E.coli* with blank vector on LB agar with 2 µg/ml of colistin whereas no colony was appeared on the LB agar plate with 2 µg/ml of colistin and with IPTG. In contrast with this finding the *E. coli* with *rcnB* gene insert from AB5075-UW can able to grow in 2 µg/ml of colistin with and without IPTG induction. This result was shown in figure 6 and figure 7. Figure 6 represents the growth pattern of *E.coli* with and without *rcnB* insert from AB5075-UW in the presence of 2 µg/ml of colistin while figure 7 represents the growth pattern of *E. coli* with and without *rcnB* gene insert in the plate containing 2 µg/ml colistin and IPTG. This showed the consistent result with the study by Nielsen BL *et al*, in 2007 stated that the expression of *β*-galactosidase in induced and uninduced bacterial cells bearing *lac* promoter based vector by western blot analysis (19). But, our study lacks the result from western bolt analysis in which further study needs to be done to perform sodium dodecyl sulfate-polyacrylamide gel electrophoresis (SDS-PAGE) and western blot in order to check the purified protein product (RcnB) from the transformants that is induced with and without IPTG in order to prove the leaky expression of *lac* promoter.

Conclusion: In summary, we can see the phenotypic differences in NEB stable *E. coli* with *rcnB* gene insertion from AB5075-UW. This evidence suggests that the protein from *A. baumannii* can be functioned well in *E. coli*. Further study on *rcnB* gene resistance mechanism of *A. baumannii* against the colistin is still needed. In addition, *in vivo* cloning is more convenient, easy to perform, inexpensive and less time consuming than *in vitro* methods that require additional enzymatic steps. This approach is suitable for large-scale production of other desired clone and also useful for the proteomic study of *A. baumannii* in near future.

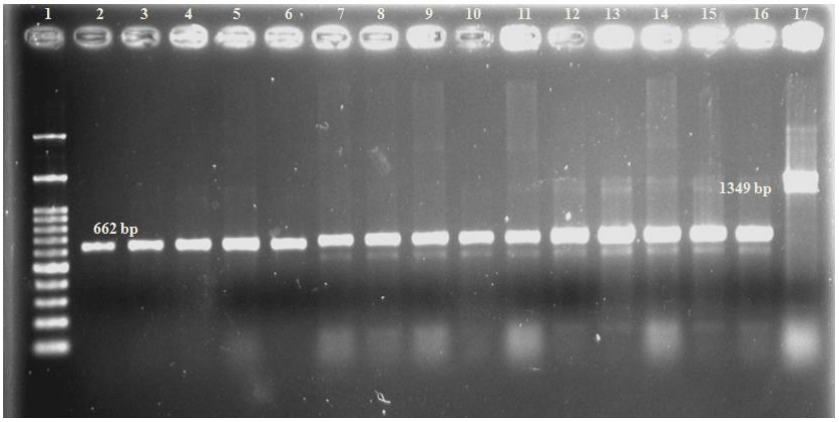

Figure 4: Gel electrophoresis of colony PCR after successful transformation
Lane 1: 100 bp ladder, Lane 2-16: *rcnB* insert (662 bp) and Lane 17: vector product with no insert (1349 bp).

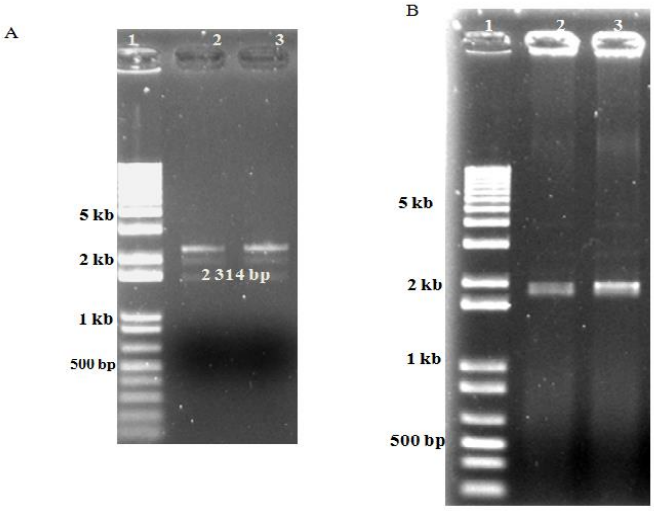

Figure 5: Gel electrophoresis of pBS2ndd vector backbone and gel electrophoresis of recombinant plasmid after extraction
(A) Lane 1: 1 Kb plus DNA ladder, Lane 2-3: PCR amplified linear vector backbone (2314 bp),
(B) Lane 1: 1 Kb plus DNA ladder and lane 2-3: plasmid from transformants

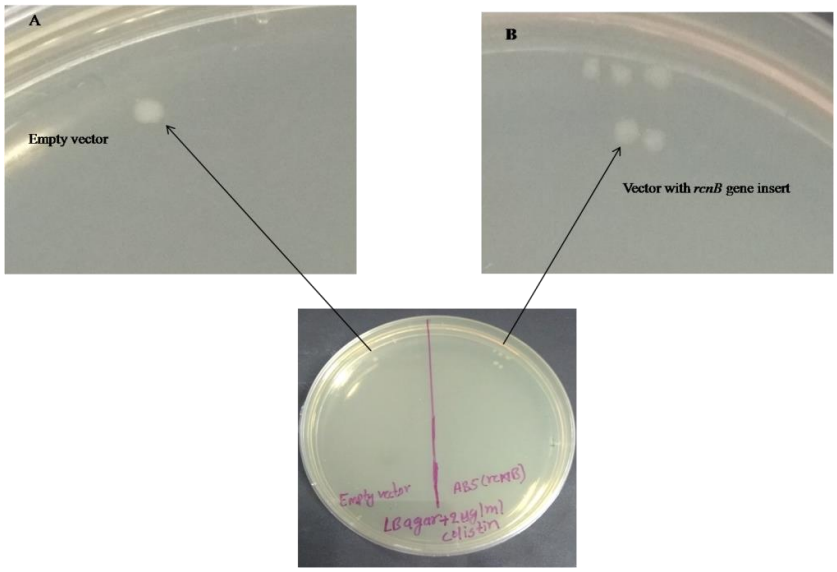

Figure 6: Growth pattern of E.coli with empty/blank vector and with *rcnB* gene insert from AB5075-UW

(A) Colony of *E. coli* with empty/blank vector, (B) Colonies of *E. coli* with *rcnB* gene insertion from AB5075-UW on LB agar containing 2µg/ml of colistin

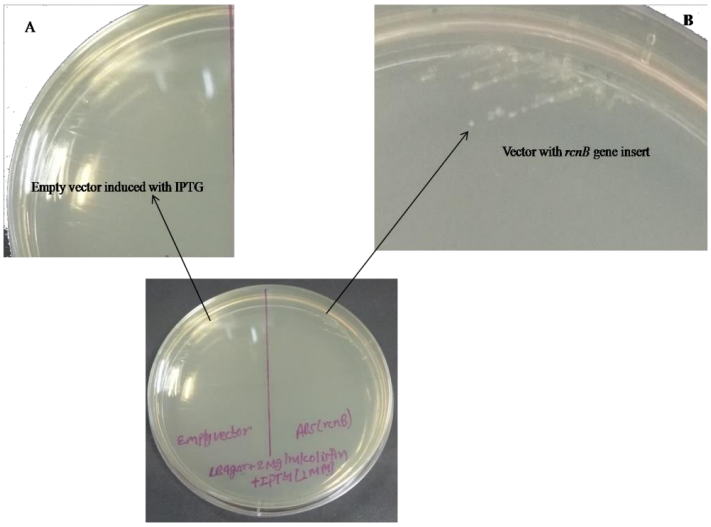

Figure 7: Growth pattern of *E.coli* with empty/blank vector and with *rcnB* gene insert from AB5075-UW

(A) No growth of *E. coli* with empty/blank vector, (B) Colonies of *E. coli* with *rcnB* gene insertion from AB5075-UW on LB agar containing 2µg/ml of colistin and IPTG

References:

1. Shaheer AS, Alp E, Hoopman J, Voss A. J Infect Dis Ther. 2016;4(4):1–5.
2. Wisplinghoff H, Bischoff T, Tallent SM, Seifert H, Wenzel RP, Edmond MB. Clin Infect Dis 2004;39(3):309–17.
3. Manchanda V, Sinha S, Singh N. Multidrug resistant Acinetobacter. J Glob Infect Dis. 2010;2(3):291.

4. Werarak P, Waiwarawut J, Tharavichitkul P, et al. J Med Assoc Thai. 2012;95(2):23-33.
5. The National Antimicrobial Resistant Surviellance Centre, Thailand 2008-20018
6. Nordmann P, Poirel L, Walsh TR, Livermore DM. Trends Microbiol. 2011;19(12):588–95.
7. Biswas S, Brunel JM, Dubus JC, Reynaud-Gaubert M, Rolain JM. Expert Rev Anti Infect Ther. 2012;10(8):917–34.
8. Nation RL, Li J. Curr Opin Infect Dis. 2009;22(6):535–43.
9. Adams MD, Nickel GC, Bajaksouzian S, Lavender H, Murthy AR, Jacobs MR, et al. Antimicrob Agents Chemother. 2009;53(9):3628–34.
10. Moffatt JH, Harper M, Harrison P, Hale JDF, Vinogradov E, Seemann T, et al. Antimicrob Agents Chemother. 2010;54(12):4971–7.
11. Hood MI, Jacobs AC, Sayood K, Dunman PM, Skaar EP. Antimicrob Agents Chemother. 2010;54(3):1029–41.
12. Jamal S, Al Atrouni A, Rafei R, Dabboussi F, Hamze M, Osman M. J Glob Antimicrob Resist. 2018;15:154–63.
13. Hunger M, t Sehmueker R, Kishan V, Hillen W. Gene. 1990;87:45–51.
14. Lucidi M, Runci F, Rampioni G, Frangipani E, Leoni L, Visca P. Antimicrob Agents Chemother. 2018;62(4):1–19.
15. Blériot C, Effantin G, Lagarde F, Mandrand-Berthelot MA, Rodrigue A. J Bacteriol. 2011;193(15):3785–93.
16. Rotchanapreeda T, Ngonsawan W, Klomtun M, Somana J. World J Microbiol Biotechnol. 2018;34(6):1–27.
17. Parrish JR, Limjindaporn T, Hines JA, Liu J, Liu G, Finley RL.J.proteome Res. 2004;582–6.
18. Riggs, P. D. (2018). *Current Protocols Essential Laboratory Techniques*, e23.
19. Nielsen BL Willis VC, Lin CY. Mol Biol Educ. 2007;35(2):133–7.

B2_011_PF: ANTIBACTERIAL AND ANTIBIOFILM ACTIVITIES OF RAMBUTAN (*Nephelium lappaceum* L.) PEEL EXTRACT ON *Vibrio parahaemolyticus* and *Escherichia coli* ISOLATED FROM FOODS

Tittita Aksonkird[1], Sutima Preeprem[2], Nattida Pankaew[3], Pichamon Srisawad[3], Pimonsri Mittraparp-arthorn[1,*]
[1]Department of Microbiology, Faculty of Science, Prince of Songkla University, Hat Yai, Songkhla, Thailand
[2]Microbiology Program, Faculty of Science Technology and Agriculture, Yala Rajabhat University, Yala, Thailand
[3]School of Science, Mae Fah Luang University, Chiang Rai, Thailand
*e-mail: pimonsri.m@psu.co.th

Abstract: *Vibrio parahaemolyticus* and *Escherichia coli* are significant food-borne pathogens associated with acute diarrhea in human. The formation of biofilms by these bacteria plays various roles in nature and also food safety. The aim of this study were to investigate the antibacterial and antibiofilm activities of rambutan peel extract (RPE) on food isolates of *V. parahaemolyticus* and *E. coli*. RPE had the minimum inhibitory concentrations (MICs) values of 0.5 to 1 mg/ml for *V. parahaemolyticus* and ≥4 for *E. coli* isolates. Meanwhile results of minimal bactericidal concentrations (MBCs) values were in the range of 2 to 4 and >4 mg/ml for *V. parahaemolyticus* and *E. coli*, respectively. Moreover, RPE inhibited the biofilm formation and caused the reduction of pre-formed biofilm of both *V. parahaemolyticus* and *E. coli* at the sub-MIC concentrations (0.5 MIC and 0.25 MIC). The results revealed that RPE exhibits antibacterial and antibiofilm activities against *V. parahaemolyticus* and *E. coli*, which can be considered as an alternative substance for inhibit biofilms or removal of these pathogens on food contact surfaces.

Introduction: *Vibrio parahaemolyticus* and *Escherichia coli* are common causative agents of diarrhea diseases worldwide, especially in developing countries. *V. parahaemolyticus* is a halophilic bacteria found in marine environments and can be transmitted to human by consumption of seafood [1]. *E. coli* is normally found as a normal microbiota in worm-blooded animals including humans [2]. Some of this species are pathogens causing food-borne diarrhea such as enterotoxigenic *E. coli* (ETEC), enteroinvasive *E. coli* (EIEC), enteropathogenic *E. coli* (EPEC), enterohemorrhagic *E. coli* (EHEC), and enteroaggregative *E. coli* (EAEC) [3]. Department of Medical Sciences, Ministry of Public Health, Thailand, regulated *V. parahaemolyticus* should not be detected in 25 g of raw seafood and for *E. coli* should not be detected higher than 100 MPN in 1 g of raw meat. For food safety reason, various antibiotics and chemical substances were used during food production and processing to reduce number of these pathogen. There are several reports demonstrated the ability of these bacterial to form biofilms on different types of food contact surfaces which make it difficult to eliminate them and the resistant to sanitizer sodium hypochlorite has been reported [4],[5],[6]. Several natural extracts derived from plants demonstrated antibacterial and antibiofilm properties [7],[8],[9]. In contrast to chemical synthesis substances, they are more acceptable and have been proposed as the alternative way to avoid the problem of some chemical residues which will be harmful to consumers [10]. Rambutan (*Nephelium lappaceum* L.) is commonly grown in every part of South East Asia, including Thailand and rambutan peel is considered as fruit waste. Rambutan peel contains many phytochemical compounds such as saponin and tannin which exhibit various biological activities [11]. Tadtong *et al*. revealed that rambutan peel extract (RPE) contains antibacterial activity against *Staphylococcus aureus*, methicillin-resistant *S. aureus* (MRSA) and *Streptococcus mutans* [12]. Moreover, inhibition of *Enterococcus faecalis*, *S. epidermidis*, *Pseudomonas aeruginosa*, and *Vibrio cholerae* has also

been reported [13]. The aim of this study was therefore to evaluate the antibacterial and antibiofilm activities of RPE against *V. parahaemolyticus* and *E. coli*.

Methodology:

Bacterial strains and culture conditions: V. parahaemolyticus and *E. coli* isolated from food samples were used in this study (Table 1). Species identification of all isolates were confirmed by PCR targeted to *toxR* gene for *V. parahaemolyticus* and *uidA* gene for *E. coli* [14],[15]. Bacteria were grown on Mueller Hinton Broth (MHB; beef extract powder, acid digest of casein, starch) and incubated overnight at 37°C under aerobic conditions. Medium supplemented with 1% of NaCl were used for *V. parahaemolyticus*.

Table 1. Bacterial strains used in this study.

Strain	Source
Vibrio parahaemolyticus	
PSU 166, PSU 476, PSU 5382	Clam
PSU 360	Mussel
PSU 513, PSU 582, PSU 4413, PSU 4415	Bloody clam
PSU 3819	Crab
PSU 3831	Fish
Escherichia coli	
PSU 5026, PSU 5027, PSU 5028, PSU 5029 PSU 5030, PSU 4169, PSU 4170	Thai Beef
PSU 4153, PSU 4159, PSU 4164	Malaysian Beef

Preparation of rambutan peel extract (RPE): Fresh rambutan peels were obtained from a market in Hat Yai, Songkhla, Thailand during June to September 2018. The peels were washed under flowing tap water and dried by sun light. A 100 g of dried rambutan peels were soaked for 5 days in 500 ml of methanol, filtered through double layers of muslin, and evaporated using rotatory vacuum evaporator. The crude extract powder was kept protected from light and stored under 4°C for further experiments [16].

Evaluation of Antibacterial activity of RPE: Antibacterial activity of RPE was preliminary performed using the agar-well diffusion technique. Briefly, bacteria lawn was prepared on Mueller-Hinton agar (MHA) and wells (diameter=6 mm) were made with sterile Pasteur pipette. Then, 50 µl of the desired concentrations of RPE (100, 50, 25 mg/ml) were pipetted into the wells. After incubated for 18 hours at 37°C, the diameters of the growth inhibition zone surrounding the well was measured [17].

Minimum inhibitory concentrations (MICs) and minimum bactericidal concentrations (MBCs): The minimum inhibitory concentrations (MICs) and the minimum bactericidal concentrations (MBCs) of RPE were determined in *V. parahaemolyticus* and *E. coli* isolates using broth microdilution method. Briefly, RPE was dissolved in 100% dimethyl sulfoxide (DMSO) and diluted with MHB to obtain concentrations of 1-4 mg/ml. The bacterial culture was adjusted to 0.5 McFarland and was diluted to 10^5 cfu/ml. A hundred µl of bacterial culture was added into each prepared RPE dilution well and incubated for 18 hours. Bacterial growth was determined by 0.1% resazurin solution and the results were recorded after 4 hours [18].

The minimum bactericidal concentrations (MBCs) of RPE were determined at MIC and higher MIC concentration by subculturing on agar plate which do not contain the extract and incubated for 24 hours. The MBCs were recorded by determining the lowest concentration of RPE that reduces the viability of the initial bacterial inoculum by ≥99.9% [19].

Biofilm formation assay of bacterial isolates: Quantitative biofilm measurement was performed in 96-well microtiter plate assay. A 100 µl of each overnight bacterial culture (10^8 cfu/ml) was incubated for 16 hours. To measure biofilm formation, bacterial cultures were poured out, wash three times with distilled water, stained with 0.1% crystal violet solution, and determined the OD_{570} [20].

Evaluation of antibiofilm effect of RPE: The inhibition of biofilm formation and the degradation of pre-formed biofilm were evaluated at subinhibitory concentrations of RPE (0.5 MIC and 0.25 MIC) by a cover slip-based technique.

Inhibition of biofilm was performed using RPE coated glass cover-slip in 6-well microtiter plate. To coat the cover-slips, each well was inoculated with a desired concentration of RPE and left at room temperature for 2 hours. The RPE-coated cover-slips were introduced into new plates containing bacterial culture and were then incubated for 6 hours. A cover-slip from each well was removed, unattached bacterial cells were rinsed off with phosphate buffered saline (PBS), and biofilms were stained with 0.1% crystal violet.

The effect of RPE on the degradation established biofilms was tested as described previously [21] with some modifications. Briefly, a sterile cover-slip in each well was inoculated with 3 ml of overnight culture of a representative isolate of *V. parahaemolyticus* or *E. coli* and incubated for 16 hours in 6 well plate. The cover-slips with biofilm were washed in PBS to remove the unattached cells, placed in new wells, and stained with 0.1% crystal violet.

The stained biofilms in each experiment were observed by light microscope.

Results and Discussion:

Antibacterial activity of RPE: The agar-well diffusion technique is mainly used for screening antimicrobial activity of plant extracts [22]. In this study, RPE was preliminary tested for its antibacterial activity against *V. parahaemolyticus* (n=10) and *E. coli* (n=10) by this method. The results showed that RPE was active against all isolates and the activity against *V. parahaemolyticus* strains were higher than *E. coli* isolate (Table 2). MIC results of RPE were comparable to those obtained in the agar-well diffusion technique. RPE had the MIC value ranging from 0.5 to 1 mg/ml for *V. parahaemolyticus* and ≥4 for *E. coli* isolates. MBC results showed that *V. parahaemolyticus* was more sensitive to RPE than *E. coli* (Table 2). Previous study has been reported about the antibacterial activity of agricultural by-products [23],[24]. The result showed that rambutan peels extracted with water or 95% ethanol were failed to inhibit *V. parahaemolyticus*. However, the MIC of pomegranate peels extracted with ethanol against *V. parahaemolyticus* was 2.5 mg/ml [25]. Another study also showed that the rambutan peels extracted with ether, methanol, and aqueous at the concentration of 2.5 mg/disc had no antibacterial activity against *E. coli* [11]. These might be due to the reasons that the antibacterial activity of extracts was a result of active phytochemical substances contained in the extract. Moreover, extracted solvent, extraction method, or different rambutan varieties can affect the presence of these compounds in the extracts [12],[26].

Table 2. Antibacterial activity of the RPE against *V. parahaemolyticus* and *E. coli* isolates.

Strain	Diameter of inhibition zone (mm)			MIC (mg/ml)	MBC (mg/ml)
	RPE 100 mg/ml	RPE 50 mg/ml	RPE 25 mg/ml		
Vibrio parahaemolyticus					
PSU 166	14.1	12.4	10.5	1	2
PSU 360	17.8	13.6	13.5	0.5	2
PSU 476	15.3	15.2	15.1	1	2
PSU 513	15.0	14.7	14.5	1	2
PSU 582	18.1	17.2	14.4	1	2
PSU 3819	13.9	11.9	11.2	1	2
PSU 3831	15.6	13.6	12.7	1	2
PSU 4413	15.8	15.3	14.1	1	2
PSU 4415	14.9	14.4	12.8	1	4
PSU 5382	15.0	14.2	12.8	1	2
Escherichia coli					
PSU 5026	8.9	NI	NI	4	>4
PSU 5027	9.5	NI	NI	4	>4
PSU 5028	9.6	NI	NI	4	>4
PSU 5029	8.8	NI	NI	4	>4
PSU 5030	9.4	NI	NI	>4	>4
PSU 4153	9.3	NI	NI	4	>4
PSU 4159	9.1	NI	NI	4	>4
PSU 4164	9.8	NI	NI	4	>4
PSU 4169	9.0	NI	NI	4	>4
PSU 4170	9.1	NI	NI	4	>4

NI: no inhibition.

Biofilm production and effect of RPE on bacterial biofilms: All bacterial isolates were capable to form biofilms on 96-well microtiter plate (data not shown). Several studies have reported *V. parahaemolyticus* and *E. coli* isolated from foods had ability to form biofilms [5]. This study evaluated the different concentrations of RPE (0.5 MIC and 0.25 MIC) to affect the adhesion ability and disrupt pre-formed biofilms and found a biomass reduction on the cover-slip of both conditions compared to that of the control. However, RPE was more active against *V. parahaemlyticus* biofilms than that of *E. coli* (Figure 1 and 2). Increasing the exposure time or the concentration of RPE is therefore required to obtain more effective results. Previous studies evaluated the effect of plant-based extracts on biofilm of clinical isolates [25],[27]. Analyses of phytochemical contents revealed the presence of flavonoids, tannins, and coumarines which are capable of reducing biofilm formation [28]. Rambutan peel contains saponins, flavonoids, and tannins [29]. Tannins have been reported to contain anticarcinogenic activity and antimicrobial activity against *E. coli*, *Enterobacter cloacae*, *Clostridium perfringens*, *Salmonella* Typhimurium, and *Bacteroides fragilis* [30]. Flavonoids contain broad spectrum of chemicals and biological activities including antioxidant and free radical scavenging properties. Furthermore, flavonoids have proven to be antibacterial agents which include ability against multi-drug resistant bacterial isolates including *S. aureus*,

B. cereus, *S. enterica*, Enterohemorrhagic *E. coli* O157:H7 and MRSA [31]. Saponin is a surfactant agent which act as a biofilm dispersant by disintegrate bacterial bond in biofilm, degrading biofilm matrix by disturbing biofilm metabolism then release the bond between the bacteria on the biofilm. When the biofilm dispersed, the other active compound such as xanthone, flavonoid, and tannin will come in and damage the bacteria inside biofilm [32].

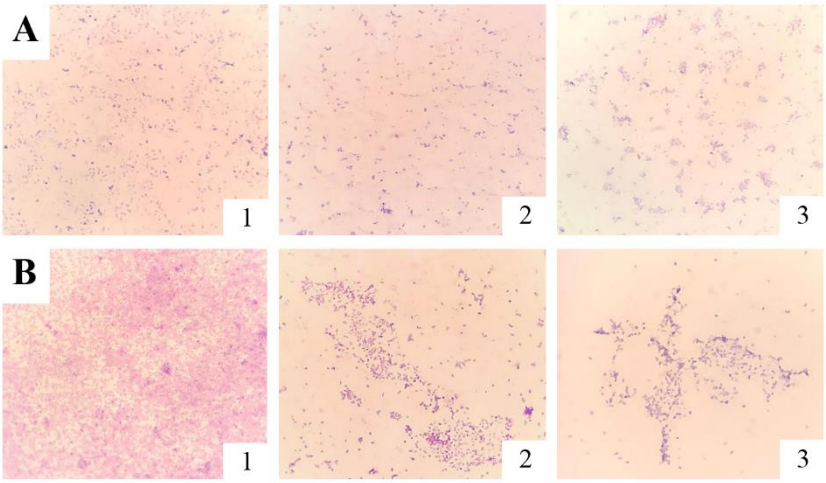

Figure 1. Microscopic analysis of *V. parahaemolyticus* biofilm on glass coverslips in the absence (1) or the presence of RPE at 0.5MIC (2) and 0.25MIC (3). The inhibition of biofilm formation (A) and the degradation of pre-formed biofilm (B) were evaluated.

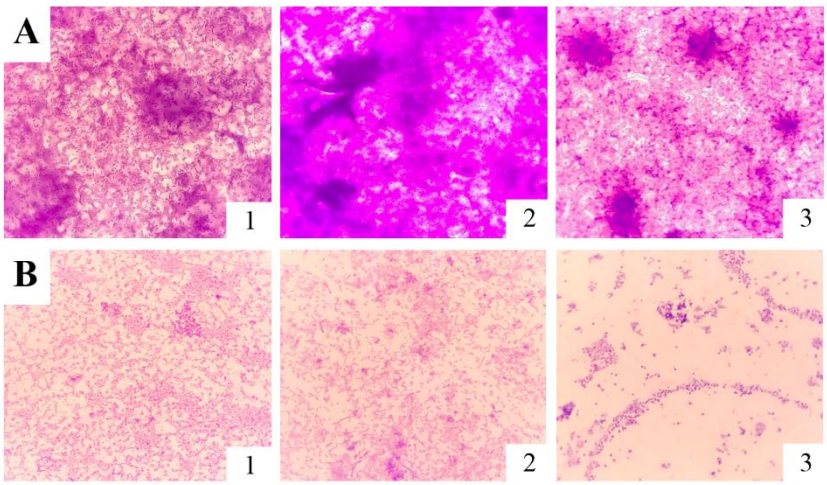

Figure 2. Microscopic analysis of *E. coli* biofilm on glass coverslips in the absence (1) or the presence of RPE at 0.5MIC (2) and 0.25MIC (3). The inhibition of biofilm formation (A) and the degradation of pre-formed biofilm (B) were evaluated.

Conclusion: RPE exhibited antibacterial and antibiofilm activities against *V. parahaemolyticus* and *E. coli.* Therefore, this plant-based compound may be an alternative to chemical for inhibit biofilms or removal of bacteria in food processing environments. Further analyses of the active compounds presence in extract and its mechanisms is needed.

References:

1. Broberg A C, Calder J T, Orth K. Microbes and infection. 2011;13:992-1001.
2. Mohammad K. Iranian journal of microbiology. 2010;2:59–72.
3. Nataro P J, Kaper B J. Clinical microbiology reviews. 1998;11:142-201.
4. Han N, Mizan M, Jahid K I, Ha S. Food Control. 2016;70:161-166.
5. Nesse L L, Sekse C, Berg K, Johannesen C S K, Solheim H, Vestby K L, Urdahl M A. Applied and Environmental Microbiology. 2014;80:2042–2049.
6. Rosa J, Conceição N, Conceição R, Timm C. Ciência Rural. 2018;48:1678-4596.
7. Sanchez E, Rivas-Morales C, Castillo S, Leos Rivas C, Garcia-Becerra L, Ortiz Martinez D. Evidence-Based Complementary and Alternative Medicine. 2016;2016:1-8.
8. Hastuty A. Journal of Microbial Systematics and Biotechnology. 2019;1:19-29.
9. Nikolic M, Vasic S, Durdevic J, Stefanovic O, Comic L. Kragujevac Journal of Science. 2014;36:129-136.
10. Galig S, Garcia-Gutierrez C, Miguelez M E, Villar J C, Lombó F. 2018;9:898-898.
11. Mahmood K, Fazilah A, Yang T A, Sulaiman S, Kamilah H. International Food Research Journal. 2018;25:890-902.
12. Tadtong S, Athikomkulchai S, Worachanon P, Chalongpol P, Chaichanachaichan P, Sareedenchai V. Journal of Health Research. 2011;25:35-37.
13. Thitilertdecha N, Teerawutgulrag, Rakariyatham N. Food Science and Technology. 2008;41:2029-2035.
14. Kim B Y, Okuda J, Matsumoto C, Takahashi N, Hashimoto S, Nishibuchi M. Journal of Clinical Microbiology. 1999;37:1173–1177.
15. Farnleitner H A, Kreuzinger N, Kavka G G, Grillenberger S, Rath J, Mach L R. Applied and Environmental Microbiology. 2000;66:1340–1346.
16. Mistriyani, Riyanto S, Rohman A. Food Research. 2018;2:119-123.
17. Ginovyan M, Petrosyan M, Trchounian A. Biomed central. 2017;17:50-50.
18. The H C, Nazni A W, Nurulhusna H A, Norazah A, Lee L H. Biomed central. 2017;17:36-36.
19. French L G. Journal of Antimicrobial Chemotherapy. 2016;58:1107–1117.
20. Nesper J, Lauriano C, M, Klose K, E, Kapfhammer D, Kraiß A, Reidl J. Infection and Immunity. 2001;69:435-445.
21. Sayem A S, Manzo E, Ciavatta L, Tramice A, Cordone A, Zanfardino A, Felice D M, VarcamontiEmail M. Microbial Cell Factories. 2011;10:71.
22. Balouiri M, Sadiki M, Ibnsouda K S. Journal of Pharmaceutical Analysis. 2016;6:71-79.
23. Guil-Guerrero J L, Ramos L, Moreno C, Zúñiga-Paredes J C, Carlosama-Yepez M, Ruales P. 2016;189:32-49.
24. Widsten P, Cruz D C, Fletcher C G, Pajak A M, McGhie K T. Journal of Agricultural and Food Chemistry. 2014;62:11146-11156.
25. Charoenrak S, Boonprasop S, Sutthirak P, Wongmongkol N. Thai Journal of Agricultural Science. 2011;44:200-203.
26. Sekar M, Jaffar F, Zahari H N, Mokhtar N, Zulkifli A N, Kamaruzaman A R, Abdullah S. Annual Research & Review in Biology. 2014;4:3869-3874.
27. Rehman S, Mujtaba G S, Sabri A N. Jundishapur journal of microbiology. 2016;9:29483-29483.
28. Sanchez E, Morales R C, Castillo S, Leos-Rivas C, Garcia-Becerra L, 1 and Martinez D. Evidence-Based Complementary and Alternative Medicine. 2016:1572697-1572697.
29. Mahmood K. Kamilah H, Alias A K, Ariffin F. Journal of Food Measurement and Characterization. 2018;12:1556-1571.
30. Chung K T, Lu Z, Chou M W. Food and Chemical Toxicology. 1998;36:1053-1060.
31. Alghazeer R, Elmansori A, Sidati M, Gammoudi F, Azwai S, Naas H, Garbaj A, Eldaghayes I. Journal of Biosciences and Medicines. 2017;5:26-48.
32. Sutojo A, Wahjuningrum A.D. The Earth, Planets and Space. 2014;8:2094-3903.

Acknowledgements: This study was supported by grant no. SCI610391a from Prince of Songkla University.

SESSION B3:
MOLECULAR BIOLOGY

B3_001_PF: DRAFT INTESTINAL MICROBIOTA OF SEA CUCUMBER (S*tichopus horrens*) FOR AQUACULTURE SYSTEMS

Wachira Jaengkhao[1], Warapond Wanna[2,*]
[1]Department of Molecular Biotechnology and Bioinformatics, Faculty of Science, Prince of Songkla University, Hat-Yai, Songkhla 90112
[2]Center for Genomics and Bioinformatics Research, Faculty of Science, Prince of Songkla University, Hat-Yai, Songkhla 90112
*e-mail: wwanna_1@hotmail.com

Abstract: 16S rRNA gene sequencing has been used to identify microbiota of many animal species, but that of marine invertebrate organisms is still poor. *Stichopus horrens* (Gamat sea cucumber) is one of highly valued sea cucumber that contains rich nutritional value and pharmacological properties and is widely used in traditional medicine to treat various illnesses. In this study aims to study the microbiota in intestine of *Stichopus horrens* by high throughput sequencing based on 16S rRNA gene sequences, which provide culture-independent information of bacteria and archaea diversity. The results showed that the anterior intestine is dominated by Proteobacteria (65.28%) and Bacteroidetes (12.46%), the posterior intestine is higher in Proteobacteria (92.89%) but lower Bacteroidetes (2.52%), the third dominant were different with Firmicutes 2.36% in anterior intestine while the posterior intestine are high relative abundance of Actinobacteria with 2.45% relative abundance. In conclusion, this study is the first high-throughput study characterizing the microbiota of the intestine of *Stichopus horrens*, which present the core microbiota of intestinal organism, and provides important changes the microbiota in each part of the intestine.

Introduction:

Stichopus horrens or Gamat in Thailand, it is an invertebrate animal in phylum Echinodermata which typically found in deep seas across the coasts in tropical coral reefs around the world including southern part of Thailand.

Gamat is rich in nutritional value and pharmacological properties including rheumatism and wound healing, along with several natural chemicals which useful for antifungal and anticancer properties [1-3] so they are widely used in traditional medicine to treat various illnesses [4, 5].

For this reason, Gamat is very highly valued in foreign countries [6] cause the overfishing Gamat sea cucumber in the natural to consume and export to foreign countries. Which has resulted in a continuous decrease in the amount of natural Gamat sea cucumber [7]. In this study, we aim to characterize the microbiota of the intestinal microbiota in Gamat. We hypothesized that intestinal bacterial community is effect to the immune and growth of sea cucumber so the data from microbiome might help in an aquaculture system of Gamat sea cucumber in Thailand hereafter. In this study, we characterized the microbiota from the anterior intestine or small intestine (AI) and posterior intestine or large intestine (PI) of Gamat sea cucumber to study the differential of intestinal microbiota by using high throughput sequencing based on 16S rRNA gene.

Methodology:

Sample preparation: In July 2018 sea cucumber were collected from Satun coastal fisheries research and development center, Satun province (98 ±0.1g, 14.50 ±0.01cm) the sea cucumber was knocked in the ice bucket for 10 minutes, the surface body was wiped with 70% ethanol before dissection, then the intestine of sea cucumber was collected and separated into two segments anterior intestine (AI) and posterior intestine (PI) with a sterile scalpel. The collecting intestinal samples were stored in the DNA preservation solution DNA/RNA Shield™

(Zymo Research) in a 50 ml sterile tube to completely inactivates infectious (viruses, bacteria, fungi, & parasites) and store in -80 ° C for further DNA extraction.

DNA extraction and library preparation: The intestinal samples of sea cucumbers were extracted genomic DNA followed by a manufacturer's protocol (QIAamp® DNA Stool Mini Kit). The DNA samples have been measuring the quantity of DNA with NanoDrop ™ 2000. The DNA concentration and purity was monitored by run gel electrophoresis with 1% agarose gels before performing polymerase chain reaction (PCR).

Amplicon Generation: According to the concentration, DNA were diluted to 1 ng/µl using sterile water and perform PCR by using a specific primer with the barcode 341F primer (5'CCTAYGGGRBGCASCAG3 ') and 806R (5'GGACTACNNGGGTATCTAAT3 '), which is the location of the V3 and V4 regions of the 16S rRNA gene. All PCR reactions were carried out with Phusion® High-Fidelity PCR Master Mix (New England Biolabs). The PCR products quantification and qualification by using electrophoresis on 2% agarose gel for detection. Samples size between 400-450bp were chosen for further experiments. PCR products were mixed in equal density ratios. The PCR products were purified with Qiagen Gel Extraction Kit (Qiagen, Germany) and the libraries preparation were generated with NEBNext® Ultra TM DNA Library Prep Kit for Illumina then libraries were quantified via Qubit and Q-PCR were analyzed before sequencing by Illumina Hiseq platform.

Bioinformatics analysis

Sequencing data processing: Paired-end reads were assigned to samples based on unique barcode and truncated by cutting off the barcode and primer sequence. Paired-end reads were merged using FLASH (V1.2.7) [8], which merge paired-end reads when at least some of the reads overlap the read generated from the opposite end of the same DNA fragment, then the splicing sequences were called raw tags. Quality filtering on the raw tags was performed with specific filtering conditions to obtain the high-quality clean tags according to the QIIME (V1.7.0) quality-controlled process [9]. The tags were compared with the reference database (Gold database) using UCHIME algorithm [10] to detect chimera and the sequences were removed. Then the effective tags finally obtained.

OTU cluster and species annotation: Sequences analysis were performed to Operational Taxonomic Unit (OTU) by Uparse software (Uparse v7.0.1001) [11], Sequences with ≥97% similarity were assigned to the same OTU. The representative sequence of each OTU were used for further annotation. Species annotation each representative sequence, the GreenGene Database was used based on RDP classifier (Version 2.2) algorithm to annotate taxonomic information then the heat-map were generated to observe the dominant OTU in each sample. OTU abundance information were normalized using a standard of sequence number corresponding to the sample with the least sequences. Subsequent the alpha diversity and Venn diagram were performed base on normalized data from each sample.

Alpha Diversity: Alpha diversity is applied in analyzing the complexity of species diversity by rarefraction curve and 4 indices of alpha diversity were used for present alpha diversity in each sample including Observed species, Chao1, Shannon, Simpson. All these indices in our samples were calculated with QIIME (Version 1.7.0).

Results and Discussion:

Sequencing data processing: The amplicons were sequencing on Illumina HiSeq paired-end platform to generate 250bp paired-end raw reads (Raw PE), and then assembled and pretreated to obtain clean tags, finally the chimeric sequences in clean tags were detected and removed to obtain effective tags. The data output quality control stats show total PE reads equal to 200,778 raw tags (AI 92,588) (PI 108,190), raw tags were assessed assembled the PE end read the total combined reads 128,994 (AI 52,766) (PI 76,228), after trimming barcodes and primers and filtering low quality 71,784 qualified tags were gained (PI 31,962) (AI 39,822) (data not shown).

These tags contained an average length ranged 423 bp that approximated to the length of 16S rRNA V3-V4 region. The effective tags with AI=28.69% and PI=43.81% were clustered into operational taxonomy units (OTU). The statistical dataset of tag number and number of OUTs were showed as followed in figure 1 and 2.

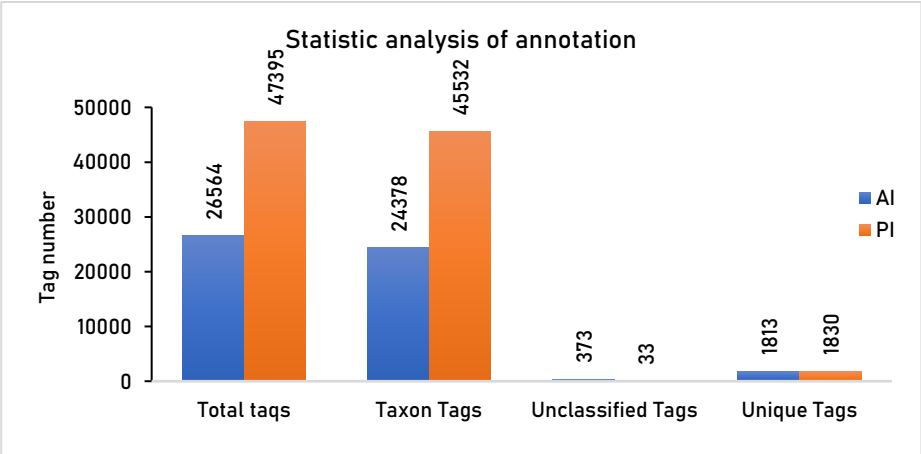

Figure 1. Statistical analysis of annotation
"Tags Number" means the number of tags; "Total tags" means the number of effective tags; "Taxon Tags" means the number of annotated tags; "Unclassified Tags" means the number of unannotated tags; "Unique Tags" means the number of tags with a frequency of 1 and only occurs in one sample

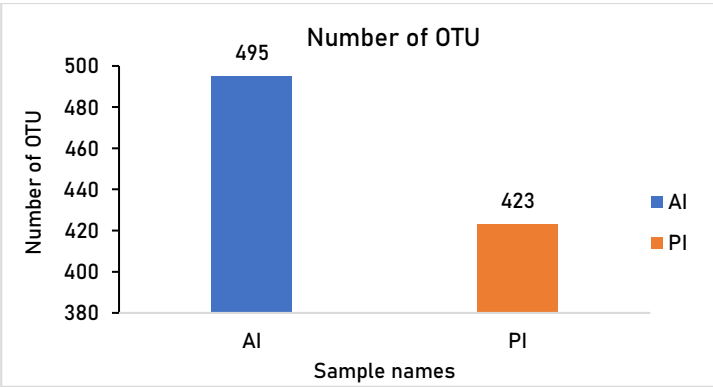

Figure 2. OTUs number of each samples
"Number of OTU" means the number of OTUs which displayed as OTUs in different samples.

Average of 459 OTUs (AI=495, PI=423) were filter by 1000 counted per OTU group to generate heat-map that show the highest taxonomy assignment for each OTU in AI segment and PI segment. The result show 12 OTUs that show the highest relative abundant of OTU including OTU 1,2,3,4,5,6,7,8,10,13,21,206. In AI group are a high relative abundance of Arcrobacters (OTU3), *Alteromonas* sp. (OTU6), *Psychroflexus halocasel* (OTU8), Salinivibrio sp. (OTU13) while PI group high relative abundance of *Vibrio* sp. (OTU1,2,4,5,10,21,206) and *Pseudoalteromonas* sp. (OTU7),

However, the result in some OTU can't be achieved to species level by using Qiime (v.1.7.0). The sequence in each OTUs were BLAST with NCBI database [12], the result showed corresponding to OTU1 *Vibrio tapetis* (identity: 98.83%, E-value: 0), OTU2 *Vibrio pelagius*

(identity: 100%, E-value: 0), OTU3 *Arcobacter pacificus* (identity: 97.52%, E-value: 0), OTU4 *Vibrio alginolyticus* (identity: 100%, E-value: 0), OTU5 *Vibrio tubiashii* (identity: 96.74%%, E-value: 0), OTU6 *Alteromonas mediterranea* (identity: 100%, E-value: 0), OTU7 *Pseudoalteromonas spongiae* (identity: 100%, E-value: 0), OTU8 *Psychroflexus halocasei* (identity: 99.29%, E-value: 0), OTU10 *Vibrio europaeus* (identity: 98.37%%, E-value: 0), OTU13 *Salinivibrio kushneri* (identity: 100%, E-value: 0), OTU_{21} *Vibrio xuii* (identity: 98.83%, E-value: 0), OTU206 *Vibrio hangzhouensis* (identity: 99.07%, E-value: 0).

Table 1. OTU table heat-map filter by 1000 counted per OUT
The counts are colored based on the contribution percentage of each OTU to the total OTU count in one sample (blue: contributes a low percentage of OTUs to sample; red: contributes a high percentage of OTUs).

#OTU ID	OTU 1	OTU 2	OTU 3	OTU 4	OTU 5	OTU 6	OTU 7	OTU 8	OTU 10	OTU 13	OTU 21	OTU 206
AI	122	138	2524	101	440	2313	46	1788	101	1704	151	33
PI	2654	3635	26	1929	1712	21	1286	3	2494	14	2498	1178

These results suggested that the bacterial populations in AI are higher variation of bacteria while PI had highly relative abundant of Vibrio genus the dominant species is *Vibrio pelagius* that are report seemed to improve larval survival turbot (*Scophthalmus maximus*) larvae [13] forms the previous study some of Vibrio species such as *Vibrio tasmaniensis* that are act as a probiotic in the sea cucumber [14] and Vibrio is the most abundant genus that found in sea cucumber *H. glaberrima* and it is consistent with other echinoderms such as the sea urchins *Strongylocentrotus droebachiensis*, *Tripneustes ventricosus* [15] and the ophiuroid *Ophionema* sp., suggested the echinoderms have a high population of Vibrio in the gut, that may serve as reservoirs for the bacteria, however almost of Vibrio genus are pathogen for several marine animals (*V.parahaemolyticus, V.harveyi, V.alginolyticus*) that can inhibit of intestinal micro flora of marine animal that cause low relative abundant of other bacterial species at this point chose to be considered before performing the experiment with the probiotic improvement of Gamat sea cucumber. In addition, in segment AI tended to differ from the PI segment that may be related to the digestion process.

Species relative abundance layout: The top 10 species in the different taxonomic ranks were selected to construct the distribution histogram of relative abundance. The distribution in phylum was shown as follow in figure 5.

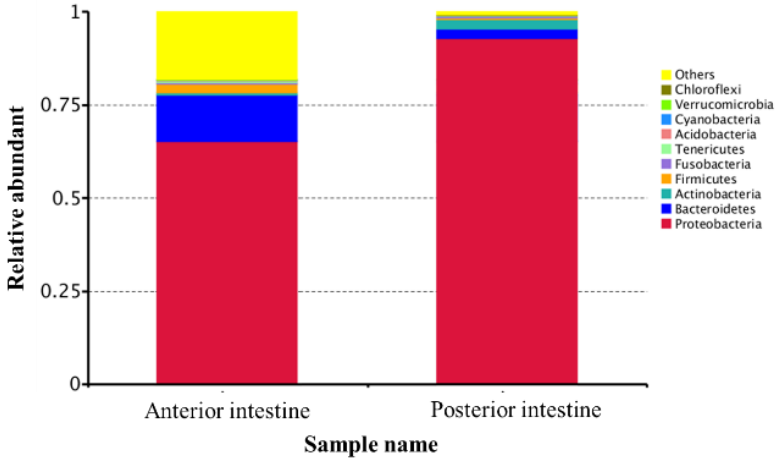

Figure 5. Species relative abundance in phylum
Plotted by the "Relative Abundance" on the Y-axis and "Samples name" on the X-axis.
"Others" represents a total relative abundance of the rest phylum besides the top 10 phyla.

Taxonomy composition intestine of sea cucumber was detected into phylum level, the most dominant OTUs were Proteobacteria with 65% and 92% relative abundant in AI and PI groups, respectively follow by Bacteroidetes 12 and 2 % relative abundant the third dominant in AI are high abundance of Firmicutes 2% while in PI are high relative abundance of Actinobacteria with 2% relative abundance the result showed Bacteroidetes in AI show higher relative abundant then PI group on the other hand PI group are higher relative abundant of Proteobacteria so Bacteroidetes might be an important role in determining the digestion process on anterior intestine in contrast Actinobacteria might be play important role in nutrient absorption on posterior intestine.

Alpha diversity analysis: Alpha diversity was widely used to assess microbial diversity within the community Alpha diversity indices Generally, OTUs were generated by 97% sequence identity was considered to the same OTU. Statistical indices of alpha diversity when the clustering threshold is 97% are summarized as below: Table 2 (Number of reads chosen for normalization cutoff=24751).

Table 2. Alpha Diversity Indices statistics

Sample name	Observed species[a]	Shannon[b]	Simpson[c]	Chao1[d]
AI	486	6.061	0.961	510.022
PI	363	4.595	0.927	470.35

[a] observed species it is the species richness
[b] Shannon it is a value much higher than 0 would be considered more diverse
[c] Simpson if the valued closer to 1 would be considered more diversity.
[d] Chao1 it is how many species are represented by only one individual in the sample

Species diversity curves: Rarefaction curves were used for indicating the biodiversity of the samples. If the curve is steep remain to not cover the bacterial species in the sample in contrast if the curve becomes flatter it means the believable number of samples have been taken. The result show ed the observed species number were covered to boat sample group by 24748 sequencing deep, in addition the result showed that the variation of bacterial diversity in AI group are higher than PI group.

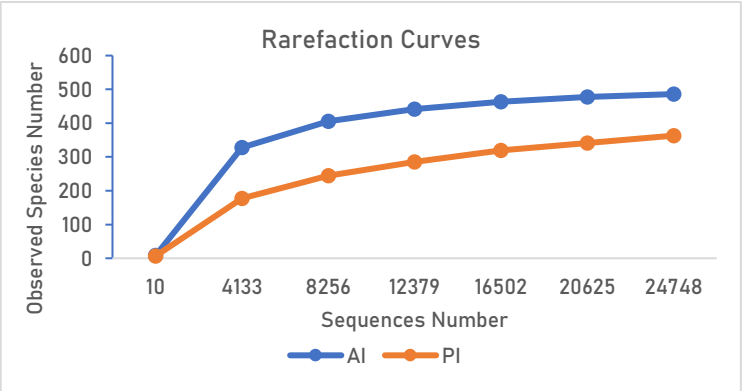

Figure 6. Rarefaction curves. For the rarefaction curves, each curve represents a sample, and can be colored and shaped by each sample name supplied in the mapping file. The sequences number is on the X-axis and the observed species number is on the Y-axis.

Venn diagram: According to the Venn diagram showed the overall were 621 OTUs. The common 228 OTUs were found in both anterior and posterior intestine and the unique number of OTUs in AI segment was 258 and 135 OTUs in PI segment, the results suggest that anterior intestine are higher bacteria diversity than posterior intestine like the rarefaction curve result.

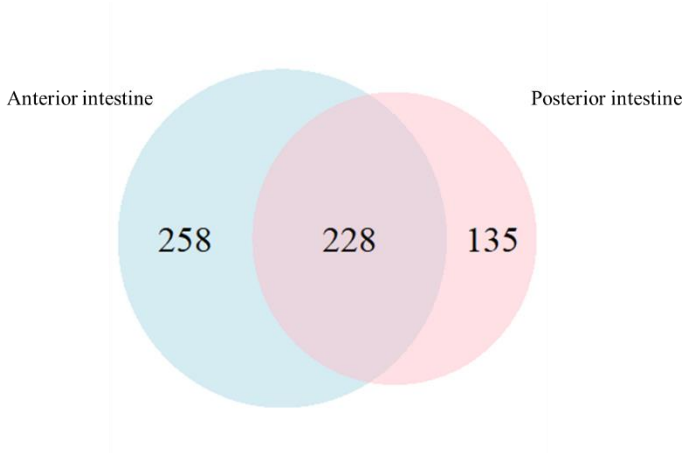

Figure 7. Venn diagram based on OTUs.
Each circle represents the number of OTU in the anterior intestine and posterior intestine of sea cucumber. Values in overlapping parts represent common OTUs. Others are specific OTUs in each sample.

The result from alpha diversity showed that the anterior intestine (AI) was more diversity than posterior intestine (PI), however bacterial composition in this study base on habitat and season of sample collection so it is possible to different varies of microbiome from the wild sea cucumber. The results represent the OTU of microbiota intestine quite different among the two segments of taxonomy and relative abundance (53.09% of unique OTU in AI and 37.02% in PI). The dominent of bacterial composition in anterior intestine and posterior intestine showed a large proportion of Proteobacteria and Bacteroidetes, the results of bacteria composition are similar to other sea cucumber species such as *Holothuria glaberrima* [16] and *Apostichopus japonicus* [17-18], which high relative abundant with

Proteobacteria nonetheless the secondary dominant are varied in each species. On the other hand. We found that the anterior intestine samples high relative abundant with Firmicutes, which all known endospore-forming bacteria [19], which can survive extreme conditions this character may be an important character to survive in anterior intestine part. On the other hand, posterior intestine found Actinobacteria that higher relative abundant, which they play an essential role in recycling refractory biomaterials by decomposing complex mixtures of polymers [20] which may play an important role in posterior intestine of sea cucumber.

However, the bacteria composition in this study present by only one sample of sea cucumber for preliminary data, the result of bacteria composition should be confirmed by repeat and increases samples.

Conclusion: The result of this study indicates that the microbiota in intestinal segments is different between the anterior and posterior of intestine. Which provide the basic information of intestinal microbiota to perform the cultured sea cucumber in the future. In addition, this is not only the first microbiota study by using high-throughput next-generation sequencing in the intestinal of Gamat sea cucumber (*Stichopus horrens*) but also this is the first present the overview of bacterial composition in different intestinal part of Gamat, which presents the core microbiota of intestinal organism, and basic knowledge for the microbial ecology of Gamat in Thailand that might help sea cucumber aquaculture systems in the future.

References:

1. Hawa I., et al., Malaysian Journal of Nutrition, 1999;5:55–59.
2. Ridzwan B.H., Leong T.C. , and Idid S.Z. , Pakistan Journal of Biological Sciences 2003;6:2068–2072.
3. Althunibat O. Y., et al., Acta Biol Hung, 2013;64:10-20.
4. Taiyeb-Ali, et al., Journal of Oral Science, 2003;45:153-159.
5. Subramaniam B. S., et al., International Journal of Pharmaceutical Sciences Review and Research, 2013;20:142-145.
6. Bordbar, S., F. Anwar, and N. Saari, Mar Drugs, 2011;9:1761-805.
7. Choo, P., FAO. 2004.
8. Zhang, J., et al., Bioinformatics, 2013;30:614-620.
9. Bokulich, N.A., et al., Nature methods, 2013;10:57.
10. Edgar, R.C., et al., Bioinformatics, 2011;27:2194-2200.
11. Edgar, R.C., Nature methods, 2013;10:996.
12. Hakim J. A., et al., FEMS Microbiol Ecol, 2016;92.
13. Ringø, E. and O. Vadstein, Journal of Applied Microbiology, 1998;84:227-233.
14. Chi C., et al., Fish Shellfish Immunol, 2014;38:367-73.
15. Guerinot, M. and D. Patriquin, Canadian journal of microbiology, 1981;27:311-317.
16. Pagán-Jiménez, M., et al., PloS one, 2019;14: e0208011.
17. Sha, Y., et al., Microbiology, 2016;85:109-115.
18. Bogatyrenko, E. and L. S. Buzoleva, Microbiology, 2016;85:116-123.
19. Muller, A.L., et al., ISME J, 2014;8:1153-65.
20. Olano C, Méndez C, Salas, J, Marine drugs,2009;7, 210-248.

Acknowledgements: The support from Satun coastal fisheries research and development center is gratefully to support sea cucumbers for this study. Thank you, Department of Molecular Biotechnology and Bioinformatics, Faculty of Science, Prince of Songkla University to support place and equipment. This work scholarship was supported by the Center for Genomics and Bioinformatics Research, Faculty of Science, Prince of Songkla University.

B3_003_PF: PHYSIOLOGICAL FUNCTION ANALYSIS OF NOVEL GENE CASSETTE CONFERRING PARAQUAT SUSCEPTIBILITY IN *Pseudomonas aeruginosa*

Chanapimon Keerathiwattanarat[1], Jintana Duangnkern[2], Khwannarin Khemsom[1,3], Skorn Mongkolsuk,[2] Adisak Romsang[1,3,*]
[1]Department of Biotechnology, Faculty of Science, Mahidol University, Bangkok 10400, Thailand
[2]Laboratory of Biotechnology, Chulabhorn Research Institute, Bangkok 10210, Thailand
[3]Center for Emerging Bacterial Infections, Faculty of Science, Mahidol University, Bangkok 10400, Thailand
*e-mail: adisak.rom@mahidol.ac.th

Abstract: *Pseudomonas aeruginosa* is in the WHO-listed critical concerned opportunistic pathogen in healthcare units and hospitals. It is a Gram-negative bacterium and commonly found in any environments. In response to biological degradation under several circumstances including during host infection or chemically biocide exposure, *P. aeruginosa* has cellular defenses to reactive oxygen species (ROS). Superoxide anion, one of common ROS form, can be generated by agriculture-used biocide named paraquat, one of the most widely used herbicides in the world. *P. aeruginosa* adapted itself to tolerate the paraquat toxicity via its genetic materials and transcriptional control. In this study, we identified the novel gene cassette that contributed to the paraquat resistance. We constructed a specific gene knockout mutant in the *P. aeruginosa* PAO1 strain and compared its growth ability under superoxide generators including paraquat, plumbagin, and menadione exposure. Mutation at the *pqiS* (paraquat inducible susceptibility) in the *P. aeruginosa* PAO1 caused a significantly increased susceptibility (more than 50 folds) against paraquat compared to the PAO1 wild-type strain. Moreover, the paraquat-sensitive phenotype in the *pqiS* mutant was completely restored by an ectopic expression of *pqiS* in the pBBR vector, suggesting a critical role of this gene in response to the paraquat toxicity in *P. aeruginosa*. In-depth analysis of this gene product in further progression may be beneficial to develop an alternative strategy to fight against hospital-acquired infection by this bacterium *P. aeruginosa*.

Introduction: *Pseudomonas aeruginosa* is in the opportunistic pathogen in healthcare units and hospitals. It is a Gram-negative bacterium that can survive in a wide range of environmental conditions.[1] In response to stresses from host immune system during bacterial infection or chemically biocide exposure, *P. aeruginosa* has cellular defenses to reactive oxygen species (ROS). Superoxide anion which is one of ROS can be generated by agriculture-used biocide named paraquat (PQ), one of the most widely used herbicides in the world.[2] PQ interferes intracellular electron transfer system and then inhibits reduction of NADP to NADPH, generating ROS including superoxide, singlet oxygen, hydroxyl and peroxide radical.[3] This is able to damage lipid cell membranes by polymerization of unsaturated lipid compounds.[4] *P. aeruginosa* adapted itself to tolerate the paraquat toxicity via antioxidant enzymes such as superoxide dismutase (SOD). SOD is an enzyme that convert superoxide radicals (O_2^-) to oxygen (O_2) and hydrogen peroxide (H_2O_2), providing cellular defense against reactive oxygen species.[5] Moreover, *P. aeruginosa* displays resistance to many groups of antibiotics such as aminoglycoside.[6] In order to counter the toxicity and antibiotic attack, there are a few principle mechanisms of antimicrobial resistance including enzymatic degradation of antibacterial drugs, alteration of bacterial proteins that are antimicrobial targets, and changes in membrane permeability to antibiotics.[7] Transmembrane protein which is a type of membrane protein plays an important role in molecule transport, so it is one of strategy to transport the compound and drugs outside the cells.[8] Transmembrane protein crosses the phospholipid bilayer of the membrane and this indicates that the transmembrane region must be composed of strongly hydrophobic amino acids.

In this proceeding, a gene encoding a putative *pqiS* found in the *P. aeruginosa* PAO1 genome was analyzed its localization and properties by using *in silico* tools. Different mutants were constructed in order to study the physiological function of *pqiS* mutants towards oxidative stress. In addition, the *pqiS* antibiotic resistance profiles were investigated using commercial discs. These results could be a preliminary data for further experiments to investigate the molecular mechanism of PqiS to complete the oxidative stress-defending network in this pathogenic bacterium.

Methodology:

Bioinformatics analysis: Amino acid sequence and genetic information in FASTA form were obtained from Kyoto Encyclopedia of Genes and Genomes) KEGG website (https://www.genome.jp/kegg/). The sequence was analyzed by using Protscale and LipoP 1.0 for hydrophobic and lipoprotein prediction, respectively.[9, 10]

Bacterial Strains and Growth Conditions: All pathogenic bacterial strains in this study were cultured, maintained and experiments were conducted following procedures approved by the Committee of Biosafety, Faculty of Science, Mahidol University (MUSC2018-015).

In this study, all bacterial strains and plasmids used are listed in Table 1. *E. coli* and *P. aeruginosa* PAO1 were cultivated in Luria-Bertani (LB) broth at 37℃ with shaking at 180 rpm. Exponential phase cells with OD_{600} in between 0.4 to 0.8 were used in all experiments.

Table 1. Bacterial strains and plasmids used in this study

Bacterial strains	Genotypes or characteristics	Sources
E. coli (DH5α)	λ- ϕ80d*lacZ*ΔM15 *recA1 endA1 gyrA96 thi-1 hsdR17* (r_K- m_K^+) *supE44 relA1 deoR* Δ(*lacZYA-argF*) *U169*	Laboratory stock
E. coli (BW20767)	*leu-63*::IS*10 recA1 creC510 hsdR17 endA1 zbf-5 uidA*(ΔMluI)::*pir*$^+$*thi* RP4-2-*tet*::Mu-1*kan*::Tn7	Laboratory stock
PAO1	*P. aeruginosa* wild type	Laboratory stock
pqiS$^-$	*pqiS* mutant, derivative of PAO1 in which *pqiS* was disrupted by pKNOCK*pqiS*, Gm^r	This study
$pKNOCK_{Gm}$	Suicide vector, Gm^r	Laboratory stock
pKNOCK*pqiS*	$pKNOCK_{Gm}$ containing a 207-bp fragment of the *pqiS* coding region, Gm^r	This study
pBBR	Medium-copy-number expression vector, Ap^r	Laboratory stock
pBBR*pqiS*	Full length *pqiS* cloned into pBBR	This study

Molecular Techniques: DNA and RNA preparation, DNA cloning, PCR amplification, and *E. coli* transformation were performed using standard protocols. Transformation of plasmids into *P. aeruginosa* strains was performed using electroporation.

Construction of P. aeruginosa pqiS mutant: The $pKNOCK_{Gm}$ suicide plasmid was used in an insertional inactivation of *pqiS*.[11] DNA fragment in the *pqiS*-coding region was amplified with RTFW (5'-AGTTGTGCCTGCTCACCG-3') and RTRV (5'-GTTGGCTGAGGGCGTAGC-3'), using genomic DNA isolated from wild-type PAO1 as the template. The $pKNOCK_{Gm}$ cut with *Sma*I was ligated with a 207-bp PCR product, generating pKNOCK*pqiS*. This recombinant plasmid was introduced into PAO1 by conjugation. The transconjugants were selected by the gentamicin resistance (Gm^r) phenotype. A single homologous recombination event between the *pqiS* fragment on pKNOCK*pqiS* and its counterpart on the chromosome results in the insertion of the plasmid and inactivation of *pqiS*. The *pqiS* mutant was confirmed by PCR and DNA sequence analyses.

Cloning of full-length pqiS genes: Functional *pqiS*-coding region was PCR amplified from PAO1 genomic DNA using the primers, FLFW (5'-GAGAATCGCAATGCGTTG-3') and FLRV (5'-TGCTCTGAGGGTCACTCG-3'). The PCR products were cloned into the medium-copy-number expression vector pBBR at the *Sma*I site.[12] The resulting plasmids were named pBBR*pqiS* and checked by PCR and DNA sequence analyses.
Plate Sensitivity Assay: To determine the oxidant resistance level, a plate sensitivity assay was performed as previously described.[13] Briefly, exponential-phase cells were adjusted to OD_{600} of 0.1 before making 10-fold serially diluted in fresh LB medium. 10 µl of each dilution was then spotted onto LA plates containing 225 µM PQ, 1.5 mM plumbagin (PB), and 20 mM menadione (MD). The plates were incubated at 37℃ for overnight before the bacterial growths were observed. The experiments were repeated three times and one of the similar representative results was shown.
Disc diffusion assay: Antibiotic susceptibility of *P. aeruginosa* PAO1 and mutant strains were determined by using the Kirby-Bauer disc diffusion method. The bacteria were grown in Mueller-Hinton (MH) broth (Difco, USA) at 37℃ with continuous shaking at 180 rpm under aerobic condition until reach mid-exponential phase. The exponential phase cell with OD_{600} 0.5 was mixed into 20 ml of prewarmed top MH agar (MH broth containing 0.75% Bacto agar) and covered on the 14 cm-dimeter Petri dishes containing 40 ml MH agar. The plates were placed at room temperature to solidify in sterile environment. The antibiotic discs were dropped on the bacteria lawns. The diameter of inhibition zones was measured at the time after aerobically incubating at 37℃ for 18 h. The inhibition zones were recorded. Experiment were repeated independently three times and analyzed in term of means and standard deviations.

Results and Discussion:
Gene organization of the pqiS: P. aeruginosa PAO1 genome contains a 1185-bp open reading frame (ORF) annotated as a hypothetical protein, which named as *pqiP* in this study.[14] Multiple alignment were analyzed by the ClustalW program and found that the amino acid sequence of *P. aeruginosa* PqiS shares 41.73% and 41.99% similarity with PqiS from *Stenotrophomonas maltophilia* and *Salmonella* Thyphimuriym, respectively. Gene organization of the *pqiS* was shown in Figure 1. *In silico* analysis from Pseudomonas genome database predicted the genes encoded for PqiS.

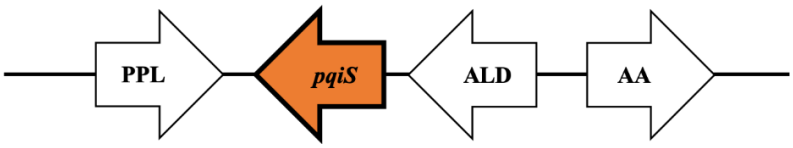

Figure 1. Gene organization of the *pqiS* in *P. aeruginosa*. The arrow indicates the orientation of the transcription. PPL, Phospholipase; *pqiS*, paraquat inducible susceptibility protein; ALD, Aldehyde dehydrogenase; and AA, Amino acid synthase.

Bioinformatics determine the localization of PqiS: To predict the hydrophobicity and localization of PqiS, amino acid sequence downloaded from KEGG website was used to analyze via Protscale. In Figure 2A, the purple line indicates the signal from prediction. The score on y-axis informs the hydrophobicity trends (score > 0, amino acid sequence was a hydrophobic molecule) and the output shows that the score was likely more than 0 which indicated that most of amino acids in PqiS were hydrophobic molecule which had similarity signal pattern to a membrane molecule.

To differentiate the lipoproteins of PqiS, this protein was predicted whether it is lipoprotein signal peptides, other signal peptides, or N-terminal membrane helices in Gram-negative bacteria by using LipoP 1.0. The results in Figure 2B predicted that PqiS was

an N-terminal transmembrane helix (TMH) as LipoP:Best indicated the result hits the highest score of classification.

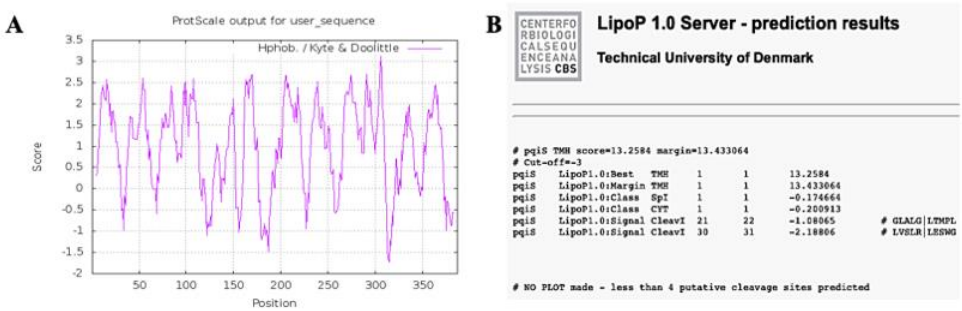

Figure 2. *In silico* analysis to study properties of PqiS. (A) Protscale calculated the hydrophobic score of each amino acid, which was shown as scoring position matrix. (B) LipoP 1.0 predicted that PqiS is a transmembrane helix TMH.

Construction of the pqiS knockout mutant: Amplification of a 207-bp *pqiS* gene fragment was done by PCR with two gene-specific primers RTFW and RTRV from the extracted genomic DNA of the PAO1 culture. The PCR product was ligated into the pKNOCK$_{Gm}$ vector cut with *Sma*I as mentioned in the methods. After analyzing by DNA sequencing, the recombinant plasmid pKNOCK*pqiS* were introduced into host *E. coli* BW20767 by heat shock transformation and selected by gentamicin resistance. Conjugation between PAO1 and BW20767 containing pKNOCK*pqiS* was performed as shown in Figure 3A. The transconjugants were selected from the Gm^r phenotype and checked by molecular analysis before naming as a *pqiS* mutant.

The *pqiS*-knockout mutants were confirmed by PCR amplification using primers BT543 (represented in the pKNOCK$_{Gm}$ vector) and RTRV (represented in the coding region of *pqiS*). The results were shown in Figure 3B as an expected band at 282-bp in size of the PCR products presented in the *pqiS* mutant strains (lanes 2 and 3) as similar as the positive control (lane 1) but not presented in the PAO1 wild-type strains (lanes 4 and 5). Moreover, the correct DNA sequence of the genomic DNA around *pqiS*-coding region was confirmed.

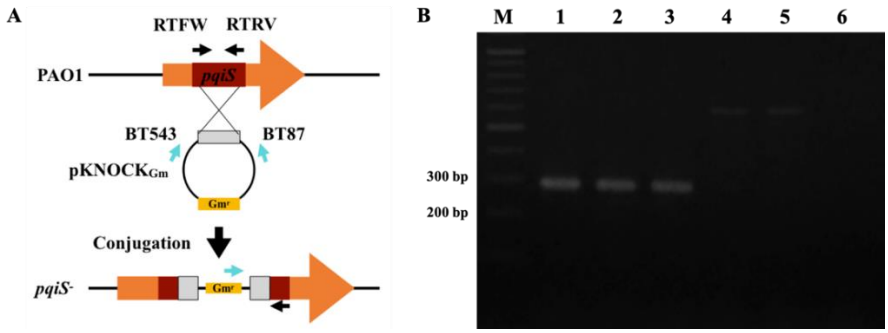

Figure 3. Schematic diagram of *P. aeruginosa pqiS* mutation (A) and confirmation of mutation by PCR amplification (B). Gel electrophoresis showed a size of PCR product amplified from indicated *pqiS*-knockout mutants using primers BT543 and RTRV, giving the expected 282-bp of PCR products. Lane 1, positive control (pKNOCK*pqiS*); lane 2, *pqiS*$^-$/pBBR; lane 3, *pqiS*$^-$/pBBR*pqiS*; lane 4, PAO1/pBBR; lane 5, PAO1/pBBR*pqiS*; lane 6, reagent control; lane M, molecular weight marker (GeneRuler 100-bp DNA ladder; Fermentas).

Construction of the pqiS overexpression and complementation strains: To construct the *pqiS* overexpression and complementation strains, a 1185-bp PCR product containing a *pqiS*-coding region was amplified by using an extracted PAO1 chromosome as template and with primers, FLFW and FLRV. The PCR product was ligated with an expression vector pBBR at *Sma*I site. After checking by DNA sequencing, the recombinant plasmid (pBBR*pqiS*) was transformed into *E. coli* DH5α and selected for ampicillin resistant phenotype. Transformants were screened by PCR (Figure 4B) to confirm plasmid insertion and direction using primers M13R (5'-AAACAGCTATGACCATG-3') and RTRV, and then sequenced to verify the correction of the constructed plasmid.

The overexpression and complemented strains were constructed by transforming with pBBR*pqiS* into the PAO1 wild type and *pqiS* mutant (Figure 4A). After *P. aeruginosa* transformation, the DNA sequence around an ectopic *pqiS* expression cassette was analyzed by DNA sequencing technique. The presence of plasmids was checked by phenol lysis and PCR amplification (Figure 4B).

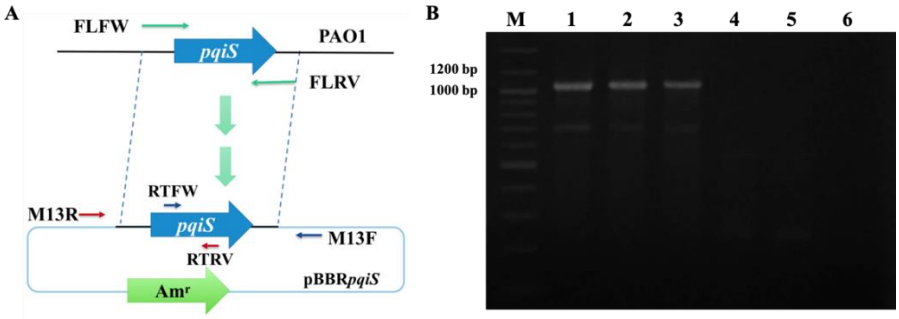

Figure 4. Schematic diagram of the full-length *pqiS* expression vector construction (A) and confirmation by PCR amplification (B). Gel electrophoresis showed a size of PCR product amplified from indicated *pqiS* transformants using primers M13F and RTFW, giving the expected 1055-bp of PCR products. Lane 1, positive control (pBBR*pqiS*); lane 2, PAO1/pBBR*pqiS*; lane 3, *pqiS*$^-$/pBBR*pqiS*; lane 4, PAO1/pBBR; lane 5, *pqiS*$^-$/pBBR; lane 6, reagent control; lane M, molecular weight marker (GeneRuler 100-bp plus DNA ladder; Fermentas).

Physiological function studies against paraquat stress response: To evaluate the physiological role of *P. aeruginosa* PqiS in an oxidative stress response, the plate sensitivity assay was performed to compare the bacterial growth on plate referred to the resistance level of PAO1 wild-type and *pqiS* mutant strains against 225 µM PQ. The results showed in Figure 5 that the *pqiS*-knockout mutant (*pqiS*$^-$/pBBR) exhibited a significantly increased susceptibility level (approximately 50-fold) against methyl viologen (represented by PQ) compared to that in the wild type (PAO1/pBBR), whereas, the overexpressed *pqiS* mutants (PAO1/pBBR*pqiS* and *pqiS*$^-$/pBBR*pqiS*) showed an opposite phenotype, which was observed as a dramatically increased resistant level (more than 10^4-fold) against PQ (225 µM). Since paraquat was proposed to have a redox cycling property, we extended the experiments in to test the resistance level of the *pqiS* mutant against other redox cycling drugs including plumbagin (1.5 mM PB) and menadione (20 mM MD). The result showed in Figure 5 that no difference in the sensitivity level against PB and MD was observed among all tested strains.

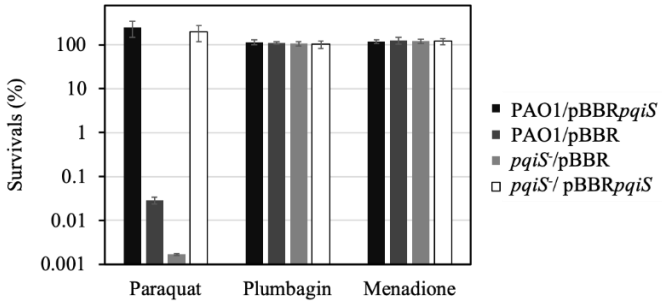

Figure 5. Sensitivities of wild-type *P. aeruginosa* and *pqiS* mutants to oxidants. Exponential-phase cells grown in LB medium were serially diluted (10-fold dilutions), and 10 µl of each dilution was spotted onto LA containing 225 µM paraquat (PQ), 1.5 mM plumbagin (PB), and 20 mM menadione (MD). After incubation at 37°C for approximately 18 h, growth of the bacteria was observed. Data were representatives of three independently replicate experiments.

The results suggest that *P. aeruginosa pqiS* was required for a protection against PQ toxicity and it may be not involved in the redox recycling mechanism. However, the susceptibility assay against PB and MD could not be in the growth inhibition range in the PAO1 wild type. It requires further experiments at the growth inhibition level to confirm the possible explanation. Moreover, PQ has been shown to generate an intracellular superoxide anion in the presence of oxygen (O_2).[15] Next experiment would be to compare a PQ susceptibility level between aerobic and anaerobic conditions, and the superoxide dismutase (SOD) activity assay will be further investigated.

Physiological function of pqiS against antibiotics susceptibility: To analyze the antibiotic susceptibility profile in *P. aeruginosa* wild-type PAO1 and *pqiS* mutant strains, the bacteria were treated with a representative from different groups of antibiotics by using disc diffusion assay as described in the methods. The results showed in Table 2 that the overexpressed *pqiS* mutants (PAO1/pBBR*pqiS*) was more sensitive to 10 µg tobramycin, which is in the aminoglycoside group, compared to the wild type's level.

Table 2. Comparison of antibiotic susceptibility of PAO1 and *pqiS* mutants

Antibiotics (µg)	Inhibition Zone (means ± SD, mm)			
	PAO1/pBBR	*pqiS*-/pBBR	*pqiS*-/pBBR*pqiS*	PAO1/pBBR*pqiS*
β-lactam				
Meropenem (10)	25.9 ± 0.6	25.9 ± 0.9	25.7 ± 0.1	24.9 ± 0.9
Aminoglycoside				
Tobramycin (10)	20.5 ± 0.5	21.0 ± 1.1	19.9 ± 2.1	24.0 ± 1.1*
Quinolone				
Levofloxacin (5)	25.5 ± 0.5	26.0 ± 0.7	25.2 ± 0.3	25.6 ± 0.7
Tetracycline (30)	12.0 ± 1.6	12.3 ± 1.3	12.4 ± 0.6	12.9 ± 0.8
Others				
Fosfomycin (50)	7.3 ± 0.4	7.9 ± 0.8	10.8 ± 0.9	10.0 ± 0.9
Polymyxin B (300)	16.8 ± 0.1	16.1 ± 0.8	15.4 ± 0.7	16.4 ± 0.1

An asterisk (*) indicates a significantly difference ($p < 0.01$) compared to that in the PAO1/pBBR

From the previous study, an iron-sulfur cluster biogenesis machinery including ISC and SUF has a role in aminoglycoside resistance by interfering proton motive force (PMF), which is crucial for aminoglycoside uptake.[16] Moreover, one of the PQ mechanism has been

shown to primarily target the iron-sulfur cluster for cellular damage.[17] Therefore, an overproduction of PqiS, resulting more PMF activity, would provide bacterial uptake of aminoglycoside antibiotics and mediate the tobramycin susceptibility in *P. aeruginosa*. We will further test to elucidate this hypothesis by extending experiments in other aminoglycoside drugs and PMF activity assays.

Conclusion: A novel transmembrane protein (PqiS)-mediated protection methyl viologen toxicity in *P. aeruginosa* was investigated. The bioinformatics analysis predicted that this hypothetical protein had a high hydrophobicity, which referred its location in the cellular membrane. The *pqiS*-knockout mutant showed a significantly increase in the susceptibility against paraquat, but no differences in other redox cycling drugs. This protein could play an important role in PQ detoxification in *P. aeruginosa*. Moreover, the overexpression of *pqiS* mediated an increased susceptibility against aminoglycoside, which may be via the PMF activity. Data indicate that PqiS is a novel paraquat resistance mechanism in *P. aeruginosa* and a design of drug-targeting PqiS, as similar as paraquat mechanism, could be a novel strategy for fighting against infectious diseases from this bacterium.

References:

1. Silby MW, Winstanley C, Godfrey SA, Levy SB, Jackson RW. FEMS Microbiol Rev. 2011;35(4):652-80.
2. Hassan HM, Fridovich I. J Biol Chem. 1978;253(22):8143-8.
3. Dinis-Oliveira RJ, Duarte JA, Sánchez-Navarro A, Remião F, Bastos ML, Carvalho F. Crit Rev Toxicol. 2008;38(1):13-71.
4. Sandy MS, Moldeus P, Ross D, Smith MT. Biochem Pharmacol. 1986;35(18):3095-101.
5. Hassett DJ, Woodruff WA, Wozniak DJ, Vasil ML, Cohen MS, Ohman DE. J Bacteriol. 1993;175(23):7658-65.
6. Pachori P, Gothalwal R, Gandhi P. Genes Dis. 2019;6(2):109-19.
7. Dever LA, Dermody TS. Arch Intern Med. 1991;151(5):886-95.
8. Ghai I, Ghai S. Infect Drug Resist. 2018;11:523-30.
9. Gasteiger E, Hoogland C, Gattiker A, Duvaud S, Wilkins MR, Appel RD, Bairoch A. The Proteomics Protocols Handbook. 2005:571-607.
10. Rahman O, Cummings SP, Harrington DJ, Sutcliffe IC. World J Microbiol Biotechnol. 2008;24(11):2377-2382.
11. Alexeyev MF. Biotech. 1999;26(5):824-826, 828.
12. Kovach ME, Elzer PH, Hill DS, Robertson GT, Farris MA, Roop RM, Peterson KM. Gene. 1995;166(1):175-176.
13. Romsang A, Atichartpongkul S, Trinachartvanit W, Vattanaviboon P, Mongkolsuk S. J Bacteriol. 2013;195(15):3299-3308.
14. Stover CK, Pham XQ, Erwin AL, Mizoguchi SD, Warrener P, Hickey MJ, Olson MV. Nature, 2000;406(6799):959-964.
15. Pavelescu LA. J Med Life. 2015;8:38-42.
16. Vergnes A, Banzhaf M, Duverger Y, Huguenot A, Brochado AR, Su SY, Espinosa L, Loiseau L, Py B, Typas A, Barras F. Science. 2013;340(6140):1583-7.
17. Romsang A, Duang-Nkern J, Leesukon P, Saninjuk K, Vattanaviboon P, Mongkolsuk S. PLoS One. 2014;9(1):e86763.

Acknowledgements: This research was supported by a grant from Mahidol University to the Center for Emerging Bacterial Infections (EBI), Faculty of Science, Mahidol University under A.R.'s project. C.K. was a student under Science Achievement Scholarship of Thailand (SAST) and was supported by a funding from Faculty of Graduate Studies, Mahidol University.

B3_011_PF: EXPRESSION ANALYSIS OF *Drosophila melanogaster* INNATE IMMUNITY GENES DURING *Pseudomonas aeruginosa* INFECTION

Chutimon Tangaiad[1], Saifon Nopnipa[2], Jintana Duangnkern[3], Scorn Mongkolsuk[1,2,3], Adisak Romsang[1,2,*]
[1]Department of Biotechnology, Faculty of Science, Mahidol University, Bangkok 10400, Thailand
[2]Center for Emerging Bacterial Infections, Faculty of Science, Mahidol University, Bangkok 10400, Thailand
[3]Laboratory of Biotechnology, Chulabhorn Research Institute, Bangkok 10210, Thailand
*e-mail: adisak.rom@mahidol.ac.th

Abstract: *Pseudomonas aeruginosa* is a bacterium adapted to infect a wide range of hosts including fruit fly and human. *Drosophila melanogaster* was used as a host model for *P. aeruginosa* infection due to its similar innate immune response (IIR) components as in human. An interaction between *P. aeruginosa* infection and IIR components in *Drosophila melanogaster* host model was less studied. In this study, the *D. melanogaster* gene expression analysis focused on IIR components in IMD, Toll, and other alterative signalling pathways under *P. aeruginosa* infection. End-pointed RT-PCR results showed that all tested genes in IMD pathway were highly expressed in the *P. aeruginosa*-infected fly samples. Whereas slightly induction of the genes in the Toll pathway and no significantly different expression level of genes in the other alternative pathways were observed. The results suggested that the IMD pathway could be a major innate immune system in *D. melanogaster* in response against *P. aeruginosa* infection. The IMD pathway in *D. melanogaster* could generate bactericidal antimicrobial peptides (AMPs), which may be effective against *P. aeruginosa* infection. We further tested to infect the flies with the *fprB* mutant, which is represented as the stress-hypersensitive strain. The gene expression analysis results showed that an induction of the IMD pathway genes was decreased under an infection with the *fprB* mutant suggesting that the IMD pathway in *D. melanogaster* could related to the generation of the stressful condition to the infected bacteria. Data presented are preliminary shown a correlation between *D. melanogaster* innate immunity against stress responsive mechanism in *P. aeruginosa*.

Introduction: *Pseudomonas aeruginosa* has a wide range host including human, mice, insects, nematodes and plants. *Drosophila melanogaster* was used as a host model due to its innate immune response (IIR) system was highly similar in human. Immune Deficiency (IMD) and Toll pathways are mainly responsible for microbial infections in both *D. melanogaster* and human IIR systems. They control antimicrobial peptides (AMPs) production that required to kill invasive microbes. In mammalian, the IMD pathway is shared similarities with the tumor necrosis factor receptor 1 signaling pathway. While the *Drosophila* IMD pathway controls the gene expression responsible for most of the AMP production through an activation of nuclear factor-κB (NF-κB) transcriptional regulator. The induced AMP is primarily responded to Gram-negative bacterial infections.[1] In parallel, the Toll pathway is homologous to the mammalian Toll/IL-1 receptor-signaling pathway, which does not directly recognize bacterial components, but it is responsible for AMP production against fungal and Gram-positive bacterial infections.[2] The Jun N-terminal kinase (JNK) pathway is homologous to the mammalian pathway. In *Drosophila*, JNK signaling involved in the biological processes including apoptosis, stress response and immunity. The JNK pathway mechanisms are activated by TAK1, a kinase that is a part of the IMD pathway, resulting in turn activate Basket. Activation of JNK can also turn on the expression of transcription factors like activator protein-1 (AP1) and other target genes. Moreover, the JNK signaling pathway regulated AMP gene expression of the IMD pathway and

also regulated immune response genes induced after septic injury.[3] In addition to defense pathways against bacterial infection, RNA interference (RNAi) is a major antiviral defense in *Drosophila*.[4] The exogenous dsRNA, that can trigger a second RNAi mechanism, is sensed by the three core proteins of the RNAi including AGO2, Dicer-2, and R2D2, which are associated with cofactors to sense RNAs. Afterward, the RNA-induced silencing complex (RISC) is formed, leading to RNA target cleaved by the AGO2 slicer activity. The AGO-2 and Dicer-2 upregulated when virus infection.[5]

Pseudomonas aeruginosa is a versatile Gram-negative bacterium. It is able to grow even in stress conditions such as oxidative stress and antibiotic exposure that lead to survive in hospital environments. It requires iron for virulence. Iron reacts with oxygen via Fenton reaction, generating the reactive oxygen species (ROS) production.[6-7] Bacteria maintains the intracellular iron by the iron storage proteins such as ferritins and a general ferric iron buffering system such as heme and iron-sulfur clusters. Iron-sulfur clusters are key cofactors of proteins and act as catalysts or redox sensors. Iron-sulfur clusters are found to participate in diverse biological processes such as gene expression, DNA repair, central metabolism and respiration.[8] Ferredoxin $NADP^+$ reductases or FprB catalyze reversible electron transfer between NADPH and electron carrier iron-sulfur cluster proteins such as ferredoxin and flavodoxin. Inactivation of iron-sulfur cluster-containing enzymes releases free iron which leads to Fenton reaction. The inactivation of *fprB* gene lead to increased sensitivity to oxidative stresses.[9] Nowadays, an interaction between *P. aeruginosa* infection and IIR components in *Drosophila melanogaster* host model was less studied. In this study, the *D. melanogaster* gene expression analysis focused on IIR components in IMD, Toll, and other alterative signalling pathways under *P. aeruginosa* infection.

Methodology:

Bacterial strain and conditions: Wild-type PAO1 (PAO1::Tn7T) and Δ*fprB* mutant (Δ*fprB*::Tn7T) strains were cultivated Luria-Bertani (LB) broth (Lennox, USA) at 37°C with shaking at 180 rpm under aerobic condition. The medium was supplemented with 30 µg/ml gentamicin (GM) as required. Exponential-phase cells were used in all experiments.

Drosophila growth conditions and maintenance: Flies were maintained on the preservative-free corn flour Drosophila medium (350 ml water, 32 g corn flour, 9 g yeast, 20 g sugar, and 8 g agar) at the bottom of glass fly-culture vial and kept at 25°C with a 12 h light-dark cycle. All experiments were carried out in 12-day-old adult flies.

RNA extraction: Total RNA extraction was done by the Trizol RNA isolated method as mentioned by Chomczynski and Sacchi[10] and followed by DNase treatment using DNase I (Thermo Scientific, USA) according to the manufacturer's recommendations. The 5-10 flies of each samples was homogenized in 1 ml TRIZOL reagent. Adding 0.2 ml chloroform per 1 ml of TRIZOL reagent for phase separation and collect the colorless upper aqueous phase. The RNA was precipitated by mixing with 0.5 ml isopropyl alcohol per 1 ml of TRIZOL reagent and washed by with 1 ml 75% ethanol per 1 ml of TRIZOL reagent. Finally, the RNA pellet was dry by 1 hour air-dry and dissolved in RNase-free water.

First strand cDNA synthesis was performed by using RevertAid™ Reverse Transcriptase (Thermo Scientific, USA) according to the manufacturer's instructions. The first reaction mixture (5 µg of DNase I-treated total RNA, 0.2 µg of random hexamers and DEPC-treated water in a total volume of 12.5 µl) was heated at 65°C for 5 minutes and placed on ice. The second reaction mixture was mixed with 4 µl of 5x reaction buffer (250 mM Tris-HCl pH 8.3, 250 mM KCl, 20 mM $MgCl_2$, and 50 mM DTT), 0.5 µl (20 units) of RiboLock™ RNase inhibitor and 1 µl (200 units) of RevertAid™ Reverse Transcriptase and incubated at 25°C for 10 minutes

followed by 42°C for 60 minutes and finally terminated by heating at 70°C for 10 minutes. The cDNA was stored at -20°C until used.
RT-PCR: The cDNA was used as a template for PCR by using gene-specific primers. Amplification of *18S rRNA* was required to equilibrate an equal amount of total RNA. Gel electrophoresis was done in order to analyze the band intensity of the particular PCR products. Data was determined by the band intensity compared between infected and uninfected fly samples using ImageJ program and the experiments were done in triplicate independent experiments.
Ethics statement: All *P. aeruginosa* and *D. melanogaster* were raised, maintained and all experiments were conducted following procedures, MUSC2018-015 and MUSC60-052-402, approved by the Committee of Biosafety, Faculty of Science, Mahidol University (MUSC) and the MUSC-Institutional Animal Care and Use Committee (IACUC), respectively.

Results and Discussion: The IMD pathway in *D. melanogaster* against the *P. aerugiosa* infection at 15-hour incubation were determined by end-pointed RT-PCR. In this experiment, the genes Relish (*rel*) and Diptericin (*dptA*) were selected as representative genes. The results showed in Figure 1. Both *rel* and *dptA* genes expressions were increased the *P. aeruginosa*-infected fly samples compared to the uninfected fly samples. Whereas *18S rRNA* expression was similar level in all samples. In the infected condition, innate immune defenses against pathogens are initiated by pattern recognition receptors that bind peptidoglycan (PGN) of both Gram-positive and Gram -negative bacterial cell wall. Drosophila peptidoglycan recognition protein (PGRP) are receptors that recognize diaminopimelic acid (DAP)-type peptidoglycan in Gram-negative bacteria.[11] In the IMD pathway, the receptor sent signaling to activate *rel* expression. The *dptA* gene was produce to kill bacteria.[12] Thus, *rel* and *dptA* genes expressions in the infected fly samples were higher than the uninfected fly samples. These results correlated with among Gram-negatives' infection in *D. melanogaster* that the AMP can exhibit bactericidal activity and NF-kB transcription factor expression coincides with immune responsive genes activation.[13] These results suggest that IMD pathway could be required in *D. melanogaster* response against *P. aeruginosa* infection.

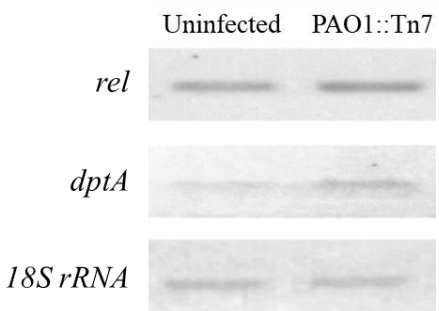

Figure 1. Analysis of IMD pathway expression in *D. melanogaster* during *P. aeruginosa* infection.

Similar to the IMD pathway, the Toll pathway in *D. melanogaster* against the *P. aerugiosa* infection at 15-hour were determined by end-pointed RT-PCR. The genes Dorsal-related immunity factor (*dif*) and Drosomycin (*drs*) were selected as representative genes. The results showed in Figure 2. Both *dif* and *drs* genes expressions were slightly increased in the *P. aeruginosa*-infected fly samples compare to the uninfected fly samples. Whereas *18S rRNA* expression was similar level in all samples. The genes *dif* and *drs* encoding an NFκB transcriptional regulator and an antimicrobial peptide, respectively, against an

infection of Gram-positive bacteria. During an infectious condition, the *Drosomycin* encoding antimicrobial peptide was induced by DIF and Relish (NFκB-liked transcription factors from the IMD pathway).[14] Thus the *Drosomycin* can activate by the Toll pathway was used to kill the bacteria. These results were correlated with the previous study in *P. aeruginosa* PA14 that the *D. melanogaster* genes involved the Toll pathway were activated under *P. aeruginosa* PA14 infection.[2] These results suggest that Toll pathways could be required in response against *P. aeruginosa* infections as same as in the IMD pathway.

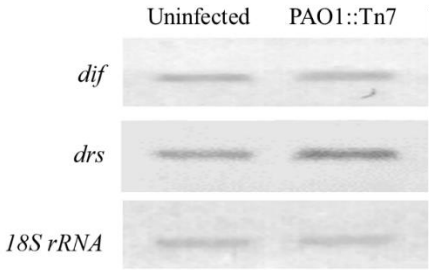

Figure 2. Analysis of Toll pathway expression in *D. melanogaster* during *P. aeruginosa* infection.

The alterative pathways in *D. melanogaster* against the *P. aerugiosa* infection including JNK and RNAi pathways were determined by end-pointed RT-PCR. In this experiment, the genes Basket (*bsk*) and Archipeago (*ago-2*) were selected as representative genes. The results showed in Figure 3. Both *bsk* and *ago-2* genes expressions were not significantly different in the *P. aeruginosa*-infected fly samples compare to the uninfected fly samples. Whereas *18S rRNA* expression was similar level in all samples. The gene *bsk* encodes a serine/threonine-protein kinase, a key component of JNK pathway that phosphorylates Jra transcription factor. While the gene *ago-2* encoding a substrate adaptor component of the SCF-Ago ubiquitin ligase in RNA interference. These results suggested that alterative pathways could not be required in response against *P. aeruginosa* infections.

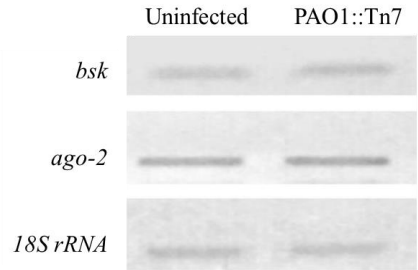

Figure 3. Analysis of Toll pathway expression in *D. melanogaster* during *P. aeruginosa* infection.

The IMD, Toll and alterative pathways in *D. melanogaster* against the Δ*fprB* mutant infection at 15-hour incubation were determined by end-pointed RT-PCR. In the IMD pathway, both *rel* and *dptA* genes expressions were slightly decreased in response to Δ*fprB* mutant-infected fly samples compared to the wild-type PAO1-infected fly samples as shown in figure 4A. Toll and alterative pathways genes expressions were not significantly different in response to Δ*fprB* mutant-infected fly samples compared to the wild-type PAO1-infected fly samples as shown in figure 4B and 4C. Whereas *18S rRNA* expression was similar level in all samples. During an infection, the iron-sulfur clusters was destabilized by antimicrobial

oxidants mediated from host. FprB involved in the redox cycling drugs detoxification and protected bacteria from the host-generated redox-disturbing agents. The Δ*fprB* mutant cannot catalyze reversible electron transfer between NADPH and electron carrier iron-sulfur cluster proteins.[9] The IMD gene expression in Δ*fprB* mutant infection was slightly lower than wild-type PAO1 infection. This suggested that IMD pathway in *D. melanogaster* could related to the generation of the stressful condition to the infected bacteria. Whereas Toll and alterative pathways genes expressions were not different. Thus, *P. aeruginosa fprB* may not require for regulating the Toll and alterative pathways genes in *D. melanogaster*. However, the difference in these expression levels was not clearly quantified. Therefore the Real-time PCR is being investigated in the further experiment.

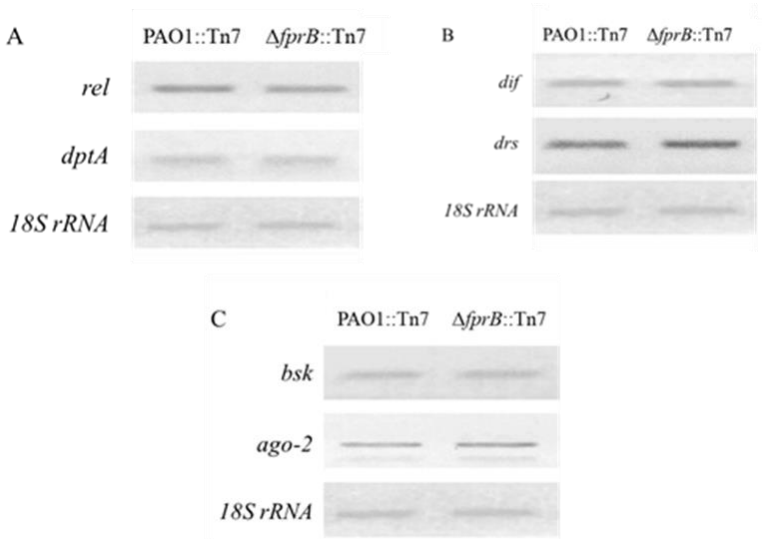

Figure 4. Analysis of genes expressions in *D. melanogaster* during Δ*fprB* mutant infection. A. IMD pathway B. Toll pathway C. Alterative pathways

Conclusion: In this study, the *D. melanogaster* gene expression analysis focused on IIR components in IMD, Toll, and other alterative signalling pathways under *P. aeruginosa* infection. We proposed that the IMD pathway could be a major innate immune system in *D. melanogaster* in response against *P. aeruginosa* infection. The IMD pathway in *D. melanogaster* could related to the generation of the stressful condition to the infected bacteria. Data presented are preliminary shown a correlation between *D. melanogaster* innate immunity against stress responsive mechanism in *P. aeruginosa*.

References:

1. Myllymaki H, Valanne S, Ramet M. J Immunol. 2014;192(8): 3455-3462.
2. Lau GW, Goumnerov BC, Walendziewicz CL, Hewitson J, Xiao W, Mahajan-Miklos S, et al. Infect Immun. 2003;71(7):4059-66.
3. Delaney JR, Stoven S, Uvell H, Anderson KV, Engstrom Y, Mlodzik M. EMBO J. 2006;25(13):3068-77.
4. Xu J, Cherry S. Dev Comp Immunol. 2014;42(1):67-84.
5. Kemp C, Mueller S, Goto A, Barbier V, Paro S, Bonnay F, et al. J Immunol. 2013;190(2):650-658.

6. Reinhart AA, Nguyen AT, Brewer LK, Bevere J, Jones JW, Kane MA, et al. Infect Immun. 2017;85(5): e00764-16.
7. Azam MW, Khan AU. Drug Discov Today. 2019;24(1):350-359.
8. Roche B, Aussel L, Ezraty B, Mandin P, Py B, Barras F. Biochim Biophys Acta. 2013;1827(3):455-69.
9. Romsang A, Duang-Nkern J, Wirathorn W, Vattanaviboon P, Mongkolsuk S. PLoS One. 2015;10(7):e0134374.
10. Chomczynski P, Sacchi N. Anal Biochem. 1987;162(1):156-9.
11. Lim JH, Kim MS, Kim HE, Yano T, Oshima Y, Aggarwal K, et al. J Biol Chem. 2006;281(12):8286-95.
12. Ganesan S, Aggarwal K, Paquette N, Silverman N. Curr Top Microbiol Immunol. 2011;349:25-60.
13. Verma P, Tapadia MG. PLoS One. 2012;7(7):e40714.
14. Tanji T, Hu X, Weber AN, Ip YT. Mol Cell Biol. 2007;27(12):4578–4588.

Acknowledgements: This research was supported by a grant from Mahidol University to the Center for Emerging Bacterial Infections (EBI), Faculty of Science, Mahidol University under A.R.'s project. C.T. was a student under Science Achievement Scholarship of Thailand (SAST) and was supported by a funding from Faculty of Graduate Studies, Mahidol University.

B3_012_PF: TRANSCRIPTIONAL RESPONSES OF *Pseudomonas aeruginosa* TO REACTIVE CHLORINE STRESS

Nannipa Phuphuripan[1], Jintana Duang-nkern[2], Kritsakorn Saninjuk[1], Skorn Mongkolsuk[1,2,3], Adisak Romsang[1,3,*]
[1]Department of Biotechnology, Faculty of Science, Mahidol University, Bangkok 10400, Thailand
[2]Laboratory of Biotechnology, Chulabhorn Research Institute, Bangkok 10210, Thailand
[3]Center for Emerging Bacterial Infections, Faculty of Science, Mahidol University, Bangkok 10400, Thailand
*e-mail: adisak.rom@mahidol.ac.th

Abstract: Reactive chlorine species (RCS) are including strong oxidizing property, which facilitates a powerful antimicrobial activity. RCS play an important role in microbial killing in host defenses mechanism. However, overuse of RCS-containing disinfectants can promote the spread of resistant bacteria. Two P. aeruginosa paralogue genes, *brpR1* and *brpR2,* encoding for a putative transcriptional regulator related to the RCS response were characterized. Purified BrpR1 and BrpR2 were produced in *Escherichia coli* M15 resulting in more than 95% purity based on the intensity under SDS-PAGE. The results in non-reducing SDS-PAGE showed the oligomer structure of both purified proteins and their stability was strongly shown under the RCS treatment with the concentration of less than 1 ppm. *In vitro* electrophoretic mobility shift assay (EMSA) results suggested that RCS promote the binding affinity of BrpR1 to *brpA1* targets but no effect on the binding of BrpR2 protein. In addition, the β-galactosidase activity controlled by *brpA* promoter was showed that their activity strongly increased under RCS treatment particularly in the extended promoter region covering the regulator gene. Data presented suggest that two paralogous BrpR transcriptional regulators control the expression of *brpA* genes under RCS exposure leading to an activation of RCS stress responsive mechanism, which could be a part of RCS tolerance in this versatile bacterium.

Introduction: *Pseudomonas aeruginosa* is an important opportunistic pathogen that cause severe acute and chronic infection in people who are hospitalized or immunocompromised, due to it has developed adaptive mechanisms to live in the environments containing reactive chlorine species (RCS) including sodium hypochlorite (NaOCl), widely used in hospitals.[1,2] Detection of bleach contaminated in the environment was less studied and only developed by chemical synthesis. In addition, during the bacterial infection, human immune system including neutrophil and macrophage cells can produce hypochlorous acid (HOCl), the extremely HOCl generated by the enzyme myeloperoxidase (MPO), to fight against bacteria at sites of inflammation.[3] The HOCl has high reactivity with a wide range of biomolecules including nucleotides, ATP, lipids, amino acid side residues, ascorbate, glutathione and protein thiols, which are essential for cell survivals. Recently, genes in response to RCS-mediated stress including *msrAB*, *fprAB*, and *ttcA* were identified.[4-6] However, all of these genes showed indirect RCS-responsive mechanisms, in which a direct mechanism still be less known. In a previous study, polyphosphate degradation and protein unfolding were found to be major contributors to the bactericidal activity of HOCl.[7]

The aims of this study were to investigate the *P. aeruginosa* BrpR1 and BrpR2 molecular mechanisms against RCS stress by characterization an effect of RCS on purified BrpR to their DNA binding motif, and analysis the promoter activity of RCS-responsive gene targets, *brpA1* and *brpA2*, under RCS exposure.

Methodology:

Bacterial growth conditions: Both *Pseudomonas aeruginosa* (PAO1) and *Escherichia coli* strains were grown aerobically in Luria-Bertani (LB) broth at 37°C with continuous shaking at 180 rpm. Exponential-phase (OD_{600} of about 0.6) cells were used in all experiments unless otherwise stated. *P. aeruginosa* and *E. coli* were raised, maintained and all experiments were conducted following procedure, MUSC2018-015, approved by the Committee of Biosafety, Faculty of Science, Mahidol University.

Construction of recombinant E. coli and P. aeruginosa strains: Cloning procedures were performed using Phusion High-Fidelity DNA Polymerase and restriction enzymes from Thermo-Fisher Scientific Company (USA). All constructs were confirmed by gel electrophoresis, PCR, and DNA sequence analyses supplied by Macrogen, Inc. All plasmids used in this study were listed in Table 1.

Table 1. Plasmids used in this study

Plasmids	Genotypes	Sources
pQE-30Xa-*brpR1*	pQE-30Xa harboring *brpR1* coding cassette	This study
pQE-30Xa-*brpR2*	pQE-30Xa harboring *brpR2* coding cassette	This study
pUC18-mini-tn7t-Gm-*lacZ*	Promoterless driving *lacZ* expression vector	This study
pUC18-mini-tn7t-Gm-1,145-bp-*lacZ*	Promoterless driving *lacZ* expression vector inserted with 1,145-bp of *brpA1* promoter	This study
pUC18-mini-tn7t-Gm-311-bp-*lacZ*	Promoterless driving *lacZ* expression vector inserted with 311-bp of *brpA1* promoter	This study
pUC18-mini-tn7t-Gm-1,121-bp-*lacZ*	Promoterless driving *lacZ* expression vector inserted with 1,121-bp of *brpA*2 promoter	This study
pUC18-mini-tn7t-Gm-312-bp-*lacZ*	Promoterless driving *lacZ* expression vector inserted with 312-bp of *brpA*2 promoter	This study

In vitro assays and promoter analysis were done as previously mentioned.[6] The promoter of BrpR-targeted gene, *brpA1* and *brpA2*, was designed for identifying an important regulatory region involved in transcriptional control of RCS-responsive genes (Figure 1). The series of *brpA1* and *brpA2* promoter fragments in various sizes were amplified and inserted into *Sma*I sites of pUC18-mini-Tn7T-Gm-*lacZ*. The recombinant plasmids were cloned into *E. coli* DH5α for propagation and extraction. The correct orientation of promoter relative to *lacZ* promoter was checked by PCR and was verified the insertion by DNA sequencing. These plasmids were used as a DNA template for amplifying DNA probe in the *in vitro* studies. The extracted plasmids were introduced into *P. aeruginosa* PAO1 chromosome by electroporation.[8] Gentamicin-resistant and carbenicillin-sensitive colonies were selected for Tn7 insertion at the chromosome. To verify an insertion, PCR and DNA sequence analyses was required.

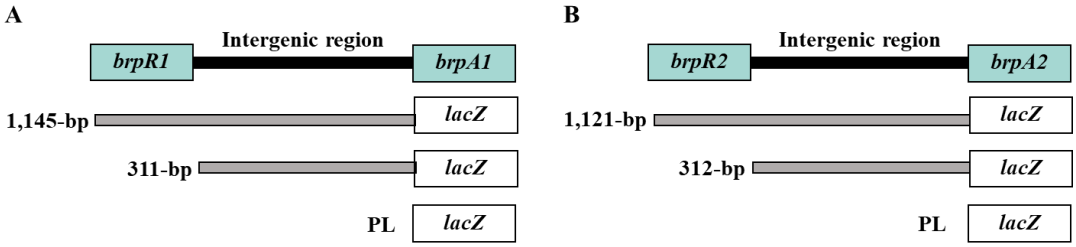

Figure 1. The *brpA* promoter fused *lacZ* are indicated with respect between *brpA* and *brpR* intergenic region (black bars). (A) 1,145-bp and 311-bp indicating the size of *brpA1* promoter fragments were inserted to pUC18-mini-Tn7T-Gm-*lacZ*, respectively. (B) 1,121-bp and 312-bp indicating the size of *brpA2* promoter fragments were inserted to pUC18-mini-Tn7T-Gm-*lacZ*, respectively. PL is a promoterless using as a control.

SDS-PAGE and Non-reducing SDS-PAGE analysis of purified BrpR: Purified BrpR was performed as previously described (Romsang *et al.*, 2018). In brief, functional cassette of *P. aeruginosa brpR1* and *brpR2* encoding for BrpR transcriptional regulators were amplified from *P. aeruginosa* PAO1 genomic DNA and separately cloned into pQE-30Xa expression vector, resulting in N-terminally 6xHistidine-tagged *brpR1* and *brpR2*. The recombinant plasmids were cloned into *E. coli* M15 to produce 6xHis-tagged BrpR by induced with 25 µM isopropyl-β-d-thiogalacto pyranoside (IPTG) and allowed to grow for an hour. Cells were harvested, resuspended in cold-lysis buffer solution, and lysed by sonication. The clear supernatant containing 6xHis-tagged BrpR were applied to Ni-NTA column equilibrated with the binding buffer. The BrpR was eluted and collected to ultra-centrifuge column for concentrating the eluted BrpR.

The concentrated BrpR was analyze by SDS-PAGE and Non-reducing SDS-PAGE with 12.5% polyacrylamide of separating gel and 4% stacking gel. The samples were boiled in water for 5 minutes and immediately loaded into an SDS-PAGE gel. For Non-reducing SDS-PAGE, samples were treated with indicated NaOCl for 30 minute and immediately loaded into gel without boling. To visualize the protein bands, gel was stained with Coomassie blue staining solution for 30 minutes at room temperature with shaking. The gel was then destained by a destaining solution with gentle agitation until observed the clear background and the stained protein bands were visible in blue color.

Electrophoresis Mobility Shift Assay (EMSA): The EMSA experiment was performed as previously described.[9] The forward primers of promoter fragment were labeled with radioactive [γ-^{32}P] ATP by using T4 DNA kinase and purified through the chromatography of Sephadex G-25. DNA probe containing the *brpA* promoters were then amplified by Phusion PCR using pUC18-mini-Tn7T-Gm-*lacZ* inserted promoter as a template, with [γ-^{32}P]-labeled forward primer and the reverse primer. The DNA probes were separated by agarose gel and purified *brpA*-labeled fragments using QIAquick Gel extraction kit. The various concentrations of either BrpR1 or BrpR2 were added to the binding reaction mixture including a DNA probe and binding buffer. After incubating at room temperature for 30 minutes, the reaction mixture was loaded on 5% polyacrylamide gel and electrophoresed at 4°C for 3 hours at 100 V. The gel was dried out and 24-hour exposed to X-ray film (Hyperfilm, Amersham, UK) at -80°C. X-ray film was visualized in developer and fixer solutions (Kodak) according to manufacturer's guidance.

β-galactosidase assay: The β-galactosidase assay was performed as previously described.[10] *P. aeruginosa* strains were exposed with and without sublethal concentrations of NaOCl for 20 minutes. The cells were harvested and then washed with 50 mM phosphate buffer (pH 8.0). The cells were lysed by ultrasonication on ice. The lysate was then added to reaction buffer

containing 1 mg/ml *o*-nitrophenay1-β-D-galactoside (ONPG). The yellow product, an *o*-nitrophenol (ONP), was detected at OD_{420}. Total protein concentration was determined using Bio-Rad protein assay. An enzyme activity was kinetically recorded as ΔA_{420} and the specific activity is expressed as ΔA_{420} per minutes per mg protein.

Results and Discussion:

Formation of purified BrpR and their stability: To study the molecular mechanism of *P. aeruginosa* BrpR1 and BrpR2, RCS-responsive regulators, 6xHis-fused *brpR1* and *brpR2* were constructed in an expression vector system, pQE-30Xa. The purification of these proteins was done by using Ni-NTA resin as described in the methods. Fractions containing purified BrpR1 and BrpR2 were concentrated using Amicon® Ultra spin column (10 kDa molecular weight cut off) for removing contaminated proteins, salts and an imidazole. The concentrated BrpR1 and BrpR2 were analyzed by SDS-PAGE (Figure 2A and 2B, left) to determine the protein purity resulting in more than 95% purity as judged by a major band represent to the 34 and the 33 kDa proteins, respectively. The proteins concentration was determined by Bradford's method and adjusted final concentration to 10 µM for investigation an effect of RCS on BrpR proteins. The formation of purified BrpR1 and BrpR2 were observed on non-reducing gel that shown an oligomer formation of both BrpR1 and BrpR2 with molecular weights corresponding to dimeric, trimeric, tetrameric and multimeric (Figure 2A and 2B, right) The result in Figure 2A and 2B (right), showed that protein aggregation occurred after treated with 10 ppm of NaOCl, suggested that the stability of BrpR1 and BrpR2 under the RCS is less than 1 ppm. To confirm the oligomeric structure, Western blot analysis will be further performed.

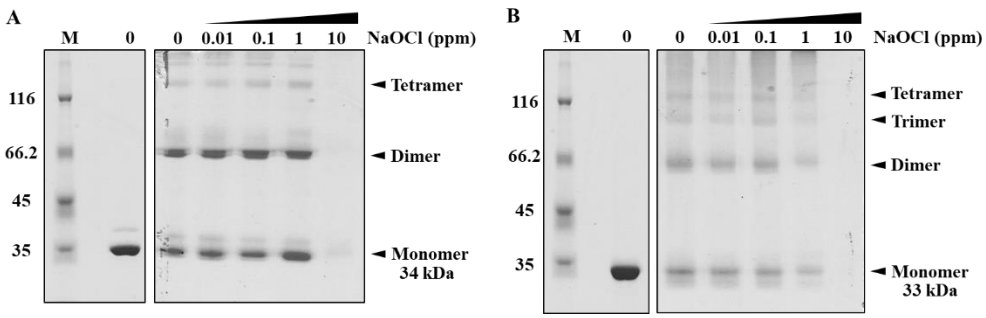

Figure 2. Purified 6xHis-tagged BrpR proteins. SDS-PAGE analysis (left) showed purified BrpR1 (A) and BrpR2 (B) after 10 kDa cut-off membrane purification. Non-reducing SDS-PAGE analysis (right) showed formation and stability of purified BrpR1 (A) and BrpR2 (B) after treated with 0.01, 0.1, 1 and 10 ppm of NaOCl. Unstained protein marker (M) indicates a size of an expected protein band. Arrowheads indicate BrpR1 and BrpR2 bands at 34 and 33 kDa, respectively, and their migration positions of monomers, dimers, trimers and tetramers.

RCS promote the binding affinity of BrpR-brpA in vitro: To investigate an interaction between BrpR1 and BrpR2 and their target promoter, *brpA1* and *brpA2*, respectively, EMSA was conducted using purified *P. aeruginosa* BrpR1 or BrpR2 protein and [γ-^{32}P]-labeled *brpA1* and *brpA2* fragment as mentioned in the methods. The presence of slow-moving bands in non-denaturing gel were indicated that both BrpR1 and BrpR2 proteins bound to the [γ-^{32}P]-*brpA1*amd –*brpA2* promoter fragments, respectively, and the percent shift was calculated using ImageJ program analysis of the shifted band intensity. The results in Figure 3 showed the percent shift of the BrpR-*brpA* promoter complex was increased along the increasing of BrpR protein added into the reaction. Interestingly, the binding affinity, indicated

by %Shifted, of BrpR1-*brpA1* (Figure 3A) was significantly increased after added 0.01 ppm NaOCl into binding reaction mixture according with the characteristic of known RCS-responsive transcriptional regulators such as RclR in *E. coli*.[11] However, NaOCl had no effect on BrpR2-*brpA2* (Figure 3B) interaction *in vitro*. This suggest that BrpR2 may not directly targeted by RCS and control the expression of RCS responsive gene.

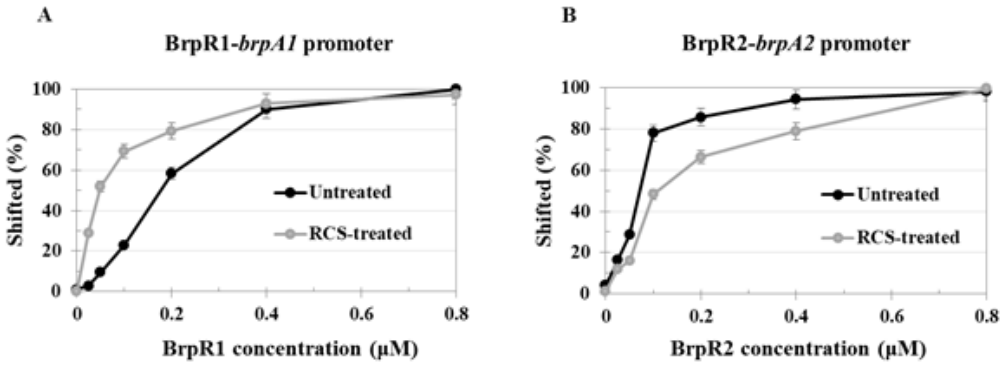

Figure 3. Role of RCS on BrpR-*brpA* interaction *in vitro*. EMSA binding assay of [γ-^{32}P]-P$_{brpA1}$ (A) and [γ-^{32}P]-P$_{brpA2}$ (B) with various concentrations of purified BrpR1 and BrpR2 under untreated (black line) and treated with 0.01 ppm of NaOCl (gray line). Data presented are means and SE of percent shifted band intensities from three independent experiments.

BrpR regulates brpA expression under RCS exposure: To determine whether BrpR controls *brpA* expression under RCS exposure, a promoter-*lacZ* fusion analysis was performed. The *brpA* promoters region designed in Figure 1 was amplified from genomic PAO1 chromosome and transcriptionally fused with a promoterless β-galactosidase (*lacZ*) gene in pUC18-mini-Tn7T-Gm-*lacZ* vector. The constructed plasmids were verified by DNA sequencing before transposed into the PAO1 on *att*Tn7-specific site. The β-galactosidase activity was collected from PAO1 harboring *brpA*-*lacZ*, where *lacZ* was driven by the *brpA* promoter, treating with NaOCl ranging from 0 to 200 ppm. The result in Figure 4 shown that the level of β-galactosidase activity significantly increased under RCS exposures in dose-dependent manner, particularly in 1,145-bp and 1,121-bp. The 1,145-bp and 1,121-bp driven *lacZ*, which are extended promoter region covering the regulator gene, shown an activation of β-galactosidase activity up to 5-fold, while 311-bp and 312-bp driven *lacZ* shown low level of activation suggested that it caused by an incomplete regulatory region in their promoter. In addition, activation of *brpA2* expression provided the highly basal level of activation implied that *brpA2* expression might require more than one regulatory proteins that co-regulate in different stress conditions.

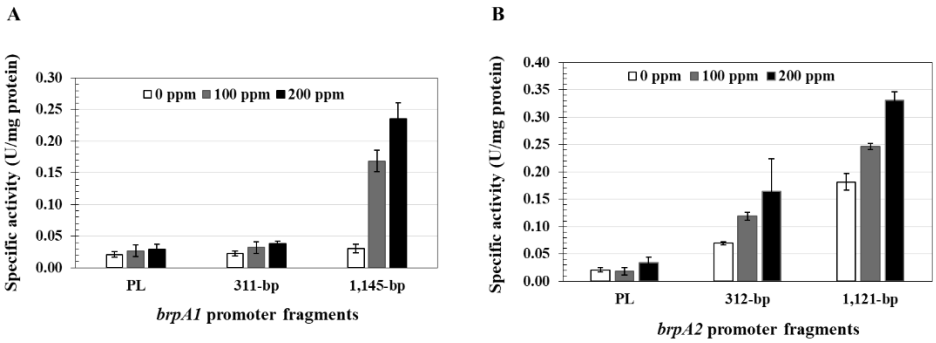

Figure 4. Role of BrpR regulating *brpA*. β-galactosidase activity level in *P. aeruginosa* PAO1 harboring 1,145-bp, 311-bp (A) and 1,121-bp, 312-bp (B) -fused *lacZ* expression under NaOCl treatment ranging from 0 to 200 ppm. Data presented are means and SD from three independent experiments. PL indicates promoterless vector or without DNA promoter inserted.

Conclusion: Overall results showed the oligomeric structure of both purified BrpR1 and BrpR2 that was stabilized under the RCS treatment with the concentration of less than 1 ppm. Both transcriptional regulators were specifically bound their own DNA promoter with an extending regulatory region and this region was required to response against RCS treatment. RCS promote the binding affinity of BrpR1 to *brpA1* targets but no effect on the binding of BrpR2 protein. Indeed, two paralogous BrpR control the expression of *brpA* genes under RCS exposure leading to an activation of RCS stress responsive mechanism, which could be a part of RCS tolerance in this versatile bacterium.

References:

1. Sadikot RT, Blackwell TS, Christman JW, Prince AS. Journal of Respiratory Biology and Criticle Care Medicine. 2005;171(11): 1209-1223.
2. Gray MJ, Wholey WY, Jakob U. Annual Review of Microbiology. 2013;67:141-160.
3. Klebanoff SJ. Journal of Leukocyte Biology. 2005;77(5):598-625.
4. Romsang A, Atichartpongkul S, Trinachartvanit W, Vattanaviboon P, Mongkolsuk S. Journal of Bacteriology. 2013;195(15):3299-3308.
5. Romsang A, Duang-Nkern J, Wirathorn W, Vattanaviboon P, Mongkolsuk S. PLoS ONE. 2015;10(7):e0134374.
6. Romsang A, Duang-Nkern J, Khemsom K, Wongsaroj L, Saninjuk K, Fuangthong, et al. Scientific Reports. 2018;8(1):11882.
7. Groitl B, Dahl JU, Schroeder JW, Jakob U. Molecular Microbiology. 2017;106(3):335-350.
8. Choi KH, Schweizer HP. Nature Protocols. 2006;1(1):153-161.
9. Romsang A, Duang-Nkern J, Leesukon P, Saninjuk K, Vattanaviboon P, Mongkolsuk S. PLoS ONE. 2014;9(1):e86763.
10. Atichartpongkul S, Fuangthong M, Vattanaviboon P, Mongkolsuk S. Journal of Bacteriology. 2010;192(8):2093-2101.
11. Parker BW, Schwessinger EA, Jakob U, Gray MJ. The Journal of Biological Chemistry. 2013;288(45):32574-32584.

Acknowledgements: This research was supported by a grant from Faculty of Science, Mahidol University under A.R.'s project. N.P. is a recipient of scholarship under Institutional Strengthening Program, Faculty of Science, Mahidol University. This work is a part of N.P. thesis master's degree.

B3_013_PF: FUNCTIONAL CHARACTERIZATION OF A GENE ENCODING A PUTATIVE GLUTATHIONE S-TRANSFERASE ON METAL AND ANTIMICROBIAL RESISTANCE IN *Pseudomonas aeruginosa*

Thanaphat Auwattanamongkol[1], Jintana Duang-nkern[2], Skorn Mongkolsuk[2,3], Adisak Romsang[1,3,*]
[1]Department of Biotechnology, Faculty of Science, Mahidol University, Bangkok 10400, Thailand
[2]Laboratory of Biotechnology, Chulabhorn Research Institute, Bangkok 10210, Thailand
[3]Center for Emerging Bacterial Infections, Faculty of Science, Mahidol University, Bangkok 10400, Thailand
*e-mail: adisak.rom@mahidol.ac.th

Abstract: The objective of this study was to identify a novel resistance mechanism in *Pseudomonas aeruginosa* against antimicrobial agents. A Genomic library of *P. aeruginosa* PAO1 strain was constructed by using conventional techniques in recombinant DNA technology. In this study, some modifications from the standard method had been made. The modified library was resulted in higher resistance efficiency with lower false-positive resistance clones compared with that from the conventional library. Testing the library with antimicrobial agents, the modified library gave 4-fold greater number of resistance cassettes compared to that from the conventional library. From DNA analysis of the resistance clones, known genes which are mainly membrane components, transporters of small molecules and metal transporters were found. 30% of unknown genes annotated as a hypothetical protein were obtained. Amongst candidate resistance cassettes, one of them covered a gene encoding a probable glutathione S-transferase (GST). The *gst*-knockout mutant was constructed by an insertional inactivation using pKNOCK system. The *gst*-overexpression mutant was constructed by using pBBR system. The *gst*-knockout mutant exhibited an increased susceptibility against antimicrobial agent such as a bleaching agent compared to the wild type. We extended the experiments against other stresses and found that the *gst*-knockout mutant developed resistance against ferrous salt. Overall data indicated a useful of modified genomic library in *P. aeruginosa* to identify the novel antimicrobial targeting molecules such as *gst* and resistance-related mechanisms including glutathione (GSH) for mapping the genomic resistance network in this pathogen. The correlation between GST and antimicrobial resistance will be elucidated in order to expand the genetic resistance network in this bacterium against antimicrobial agents.

Introduction: The emergence of antimicrobial resistance (AMR) is a serious concern that poses a serious global threat to plants, animals, and human.[1] A change in genetic materials in the bacterial genome causes most of the drug resistances. A development of resistance through genomic mutations and horizontal gene transfer from other sources including other species promotes an increasing resistance to antibiotics threat in pathogens.[2] The main important factor leading to antibiotic resistance in bacteria is a heavy usage of antibiotics around the world, especially in hospitals. This heavy usage of antibiotics in hospitals also promotes the spread of these highly resistant bacteria, which overcome other bacteria that are susceptible to antibiotics.

Multidrug-resistant (MDR) and extensively drug-resistant (XDR), which are highly resistant bacteria, are now increasing the prevalence of chronic and hospital-acquired infections. Infections by multidrug-resistant *Pseudomonas aeruginosa* causes nearly 13% of severe healthcare-associated. Even last line antibiotic or several classes of antibiotics are no longer cure the infection.

Pseudomonas aeruginosa is a Gram-negative, rod-shaped bacterium that can cause disease in animals, plants, and humans. *P. aeruginosa* processes multifactorial mechanisms.

They develop resistance mechanism against antibiotics, which contains more than 50 resistance genes.

Bacteria can be intrinsically resistant to certain antibiotics via mutations in chromosomal genes, but they also can acquire resistance to antibiotics by horizontal gene transfer. *P. aeruginosa* is a bacterium that can develop resistance mechanism against antibiotic because it carries multi-resistance plasmids. This resistance present in some strains makes *P. aeruginosa* very difficult to treat once a host, such as a human or others animal, is infected. The strain inherent resistance to many drug classes; its ability to acquire resistance, via mutations, to all relevant treatments; its high and increasing rates of resistance locally; and its frequent role in serious infections. Intrinsic resistance involves the collaboration of restricted uptake through the outer membrane and secondary resistance mechanisms such as energy-dependent efflux, and β-lactamases. Thus, the importance of low outer membrane permeability is clear because agents that break down the outer membrane permeability barrier.

During bacterial infection, *P. aeruginosa* will be eliminated by the host innate immune system such as reactive oxygen species (ROS).[3] Exposure to ROS, such as superoxide anion or hydrogen peroxide can cause oxidative stress. If bacteria are continuously exposed to various types of oxidative stress from various types of ROS, it will lead to cell death. Therefore, bacteria try to develop defense mechanisms for protection against reactive metabolites. *P. aeruginosa* can produce several antioxidants such as glutathione (GHS), which plays a role in ROS protection and removal, to degrade ROS toxicity.[4]

In this study, we found GST protein that shows around 28% identity to glutathione S-transferase *yibF* of *Escherichia coli*. We constructed the *gst*-knockout mutant by using an insertional inactivation technique using pKNOCK system and *gst*-overexpression mutant using pBBR system. We used plate sensitivity assay to study the physiology and function of the *gst* mutants under oxidative stress and biocide exposure conditions. These results could be a preliminary data for further experiments to identify a novel resistance mechanism in *P. aeruginosa*.

Methodology:

Bacterial strain and conditions: Bacterial strains and primers are provided in Table 1 and 2, respectively.

Table 1. Bacterial strains used in this study

Bacterial strains	Key genotypes	Sources
Escherichia coli DH5α	λ- ϕ80d*lacZ*ΔM15 *recA1 endA1 gyrA96 thi-1 hsdR17*(r_K- m_K^+) *supE44 relA1 deoR* Δ(*lacZYA-argF*) *U169*	Laboratory stock
Escherichia coli BW20767	*leu-63*::IS*10 recA1 creC510 hsdR17 endA1 zbf-5 uidA*(ΔMluI)::*pir*$^+$*thi* RP4-2-*tet*::Mu-1*kan*::Tn7	Laboratory stock
Pseudomonas aeruginosa PAO1	*P. aeruginosa* wild-type strain	Laboratory stock

Table 2. Primers used in this study

Primers	Sequence (5'→3')	Purposes
BT87	CACT TAA CGG CTG ACA TGG	Reverse primer in $pKNOCK_{Gm}$
BT543	TGA CGC GTC CTC GGT AC	Forward primer in $pKNOCK_{Gm}$
FLFW	CCC ATA ACA AGA ACA GGA G	Full length forward primer of *gst*
FLRV	TGG CGC TTC ATC AGG ACG	Full length reverse primer of *gst*
KOFW	CGC TGG CTG GAG GAG TAC	Forward primer for knockout fragment
KORV	GAT GGA CAG CTC GCC GCA	Reverse primer for knockout fragment
M13F	GTA AAA CGA CGG CCA GT	Universal forward primer in pBBR1MCS-4
M13R	AAA CAG CTA TGA CCA TG	Universal reverse primer in pBBR1MCS-4

P. aeruginosa and *E. coli* strains in this study were grown in lysogeny broth (LB) (Lennox, USA) at 37°C under aerobic conditions with continuous shaking at 180 rpm. For mutant selection, the medium was supplemented with an appropriate concentration of antibiotics. Routine cultivation of all pathogenic bacteria was raised, maintained and all experiments were conducted following procedures, MUSC2018-015, approved by the Committee of Biosafety, Faculty of Science, Mahidol University.

Generation of the modified P. aeruginosa genome library: From construction of conventional genomic library followed by METHODS IN MOLECULAR BIOLOGY as previously described.[5] The obtained resistance clones did not provide many resistance clones as expected. In order to get a better representative of a genomic library in *P. aeruginosa*, we modified the experiment from the previous study.[5] Briefly, both chromosomes of *P. aeruginosa* and pBBR1MCS-4 plasmid were independently digested with 6 different restriction enzymes to cover all functional genes. Every resulting ligation mixture was transformed into competent cells (*E. coli* DH5α) using Heat shock technique at 42°C. After that, spread transformants on LA with Ampicillin 100 µg/ml, IPTG, and X-Gal for blue-white screening. Picked only white colonies at the different plates into each LB medium tubes with Ampicillin 100 µg/ml until reaching 800 colonies or 800 tubes (120 clones/day). The new prepared library and PAO1 control were tested with sodium hypochlorite.

Treating antibiotic into the modified genomic library: The modified library was treated with antimicrobial agents in order to find resistance clone compared with the control library (PAO1/pBBR background). The tested concentrations of an antimicrobial agent sodium hypochlorite were ranged from 500 - 800 ppm.

Sequencing: The plasmid extraction was performed according to the manufacturer's instruction protocol. (Thermo Fisher Scientific Inc., Massachusetts, USA). Sequencing was done by Macrogen Company. Bioinformatics was used to identify the region of genes that were inserted. With computer program (Bioedit), sequence results can be analyzed to find inserted fragment compared in pBBR1MCS-4. This result was sequenced with only M13 forward. Size of fragments was predicted as 2000 - 4000 bp. These inserted fragments were BLAST compared in Pseudomonas Genome Database using the strain PAO1 as the reference genome.[8]

Construction of P. aeruginosa gst-knockout mutant: The parental strain *P. aeruginosa* PAO1 wild type and the *gst*-knockout mutant was constructed followed the instruction as previously described.[6] Briefly, 210-bp in the middle of the *gst* coding region was amplified from genomic DNA by using primers KOFW and KORV. Transformants were screened by PCR to confirm plasmid insertion and direction using primers BT534 and KOFW. PCR products were sequenced to verify the correction of an inserted DNA sequence.

Construction of P. aeruginosa gst-overexpression mutant: The full-length *gst* was amplified from PAO1 genomic DNA using the primers FLFW and FLRV. The PCR product was cloned into an expression vector pBBR1MCS-4 at the *Sma*I site. Transformants were screened by PCR to

confirm plasmid insertion and direction. PCR products were sequenced to verify the correction of an inserted DNA sequence.

Plate sensitivity assay: The plate sensitivity assay was performed to compare the bacterial growth on plate referred to the resistance level of PAO1 wild type and several mutant strains against various antimicrobial agents. Plate sensitivity assay was done as previously described.[6] Briefly, cells were cultured to exponential-phase and then were 10-fold serially diluted in LB medium. Spotted 8 µl of each dilution on LA plates 550 µM hydrogen peroxide (H_2O_2), 1000 ppm sodium hypochlorite (NaOCl), 4.3 mM $FeCl_3$ and 4 mM $FeSO_4$. The plates were incubated at 37°C for 18 h, and bacterial growth was compared.

Results and Discussion:

Generation of the modified P. aeruginosa genome library: Resistance clones obtained from conventional genomic library followed by previously described[5] did not cover the entire resistance cassettes. The modification of how-to construct a genomic library had been made in order to get many fragments as possible. To create a better representative of a genomic library, conventional library was constructed by digesting *P. aeruginosa* with only one restriction enzyme. Only one enzyme to digest the entire bacterial genome might not represent all functional genes in the genome and always exhibit similar missing genes during repetition or experiments. From an *in siligo* analysis, the expected experimental of when the genomic DNA of *P. aeruginosa* was independently digested with 6 different restriction enzymes into multiple and different fragments (Figure 1).

Spot test was performed to compare the modified library with a control library. Cell concentration of the modified library was 3.75×10^9 CFU/ml in a similar level as the control library and could be used for calculation of the resistance efficiency.

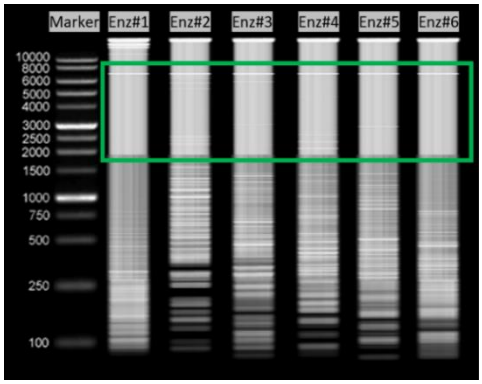

Figure 1. Digested genomic DNA of *P. aeruginosa* by multiple enzymes. Result from digestion of genomic DNA. Chosen fragment sizes (2,000 - 8,000 bp) were compared by using Lane marker (M) in the first column; Lane 2 - 7 were genomic DNA digested with 6 different restriction enzymes

Treating antibiotic into the modified genomic library: To test the modified genomic library and to find resistance clone, treated sodium hypochlorite into the lab constructed library to find resistance clone compared with PAO1 wild type (control). Cell concentration of the first PAO1 library and PAO1 control was 1.3×10^9 CFU/ml. Cell concentration of the modified library and control library was 3.8×10^9 CFU/ml. Table 3 shows comparison between resistance efficiency of the first library and the modified library when treating with sodium hypochlorite (NaOCl). Retransformation and resistance confirm test showed that only 9 resistance isolates were

obtained from the conventional *P. aeruginosa* genomic library, whereas more than 72 resistance isolates were from the modified genomic library in this study.

Table 3. Resistance analysis in *P. aeruginosa* of conventional and modified constructed libraries after treated with sodium hypochlorite

NaOCl	Control (pBBR)			Library (inserted pBBR)		
	Conventional	Modified	Fold	Conventional	Modified	Fold
No. of resistance colonies	No colony	No colony	-	6	>300	>50
Resistance efficiency	(0)	(0)	0	(4.6×10^{-8})	($>7.9 \times 10^{-8}$)	>1.72

After analysis of gene-harboring vectors, 44 antibacterial agents-resistance genes including 63.6% function-annotated genes and 36.4% uncharacterized genes in the modified *P. aeruginosa* genomic library was discovered while only 9 resistance genes consisted of 77.8% function-annotated genes and 22.2% uncharacterized genes was found in the conventional library. From DNA analysis, most of known genes are encoded lipoprotein membrane components, efflux proteins (to transport small molecules) and metal transporters. Interestingly, there is a candidate resistance cassette covered the gene called *gst* which is glutathione S-transferase encoding at cytoplasmic. Glutathione S-transferase is part of a superfamily of enzymes that responsible in phase II detoxification reactions. Not only for the detoxification but also the protection against chemical, oxidative stresses and antimicrobial resistance.[7] In the resistance cassette, it contains 4 genes as following:

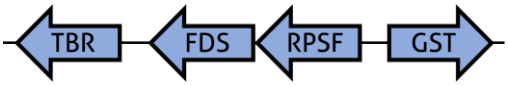

Figure 2. Gene organization of selected resistance cassette from the modified *P. aeruginosa* genomic library. An online Bioinformatics analysis was applied and physical mapping with the *P. aeruginosa* PAO1 online database was retrieved from Pseudomonas Genome Database [8]

Construction of P. aeruginosa gst-knockout mutant: The 210-bp PCR product was cloned into $pKNOCK_{Gm}$ cut with *Sma*I, generating pKNOCK-*gst*. The ligation was confirmed by seeing shifted band up from the control due to inserted fragment from phenol extraction indicated by the red arrow in Figure 3A. Transformants were screened by PCR as previously described in material and method (Figure 3B). This recombinant plasmid was conjugated into PAO1. The *gst*-knockout mutant was confirmed by PCR.

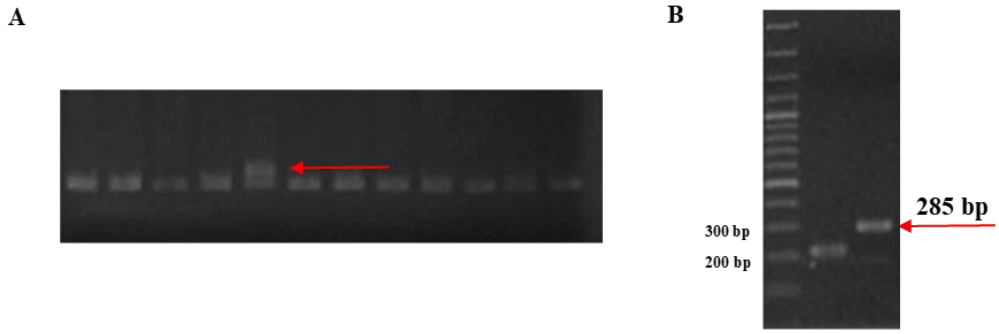

Figure 3. Construction of *P. aeruginosa gst*-knockout mutant was confirmed by checking pKNOCK-*gst* with phenol extraction (A). Shifted up band indicates an insertion in the plasmids. The confirmed plasmid insertion and direction of homologous recombination of *gst* fragment on pKNOCK-*gst* and its complemented on PAO1 chromosome was confirmed by PCR amplification. (B) Only the template of an insertional inactivation of *gst* would be amplified and shown in gel

Construction of P. aeruginosa gst-overexpression mutant: The 822-bp PCR product was cloned into pBBR1MCS-4 cut with *Sma*I, generating pBBR-*gst*. The ligation was confirmed by seeing shifted band up from the control due to inserted fragment from phenol extraction indicated by the red arrow (Figure 4A). Transformants were screened by PCR as previously described in material and method (Figure 4B).

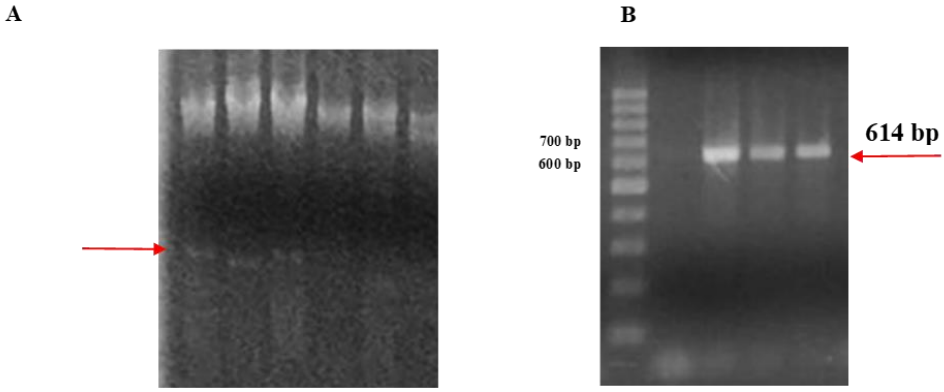

Figure 4. Construction of *P. aeruginosa gst*-overexpression mutant was confirmed by checking pBBR-*gst* with phenol extraction (A). Shifted up band indicates an insertion in the plasmids. (B) Confirmation of the inserted full-length gene in plasmid by PCR amplification

Plate sensitivity assay: The plate sensitivity assay was performed to determine the resistance level against various stress conditions including oxidative stress, stress-mediated biocides, and high iron concentration among *P. aeruginosa* wild type and mutant strains as described in the methods. The results in Figure 5 show that pKNOCK-*gst* mutant (*gst*/pBBR) was increased in the resistance level to hydrogen peroxide (3-fold), $FeCl_3$ (7-fold) and $FeSO_4$ (2-fold) than the PAO1 parental strain (PAO1/pBBR). But, pKNOCK-*gst* mutant shows decreased resistance level against NaOCl. Whereas, overexpressed *gst* mutants (PAO1/pBBR*gst*) was decreased in the resistance level to hydrogen peroxide (2-fold),

$FeCl_3$ (2-fold) and $FeSO_4$ (3-fold) than the PAO1 parental strain but shows increased resistance against NaOCl.

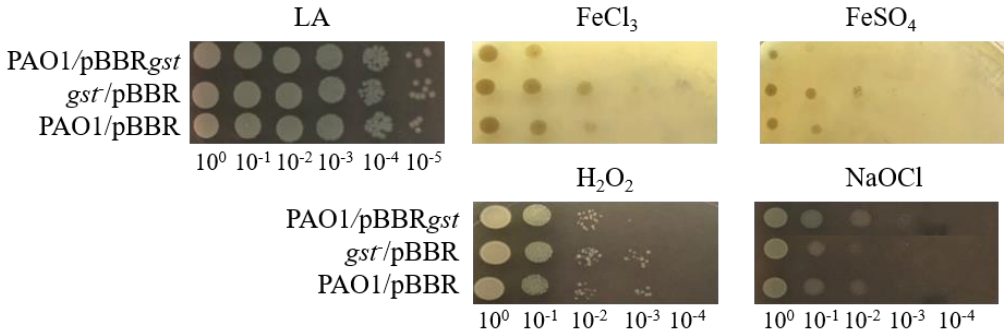

Figure 4. Determination of *P. aeruginosa* susceptibility level under various chemical treatments. The wild type (PAO1) and the *gst* mutants were grown in LB medium at 37°C overnight. Cultures were 10-fold serially diluted in LB, and 8 µl were directly spotted onto LA plates containing indicated oxidants. Each spot represents a 10-fold serial dilution. Data presented was a representative of three similar results

The results suggest that *gst* was required for a balancing of GSH:GSSG ratio. GSH is considered as the antioxidant of the cell. Glutathione can prevent damage to important cellular components caused by reactive oxygen species such as free radicals, hydrogen peroxide, and heavy metals.[9] Malfunction of *gst* responsible for glutathione S-transferase leads to accumulation of intracellular GSH. When bacteria encounter with oxidative stress-mediated agents such as hydrogen peroxide, GSH that accumulated inside would protect the oxidative damages. Moreover, hydrogen peroxide could react with accumulated intracellular free iron undergoing the Fenton's reaction caused oxidative stress. These stresses could be eliminated by the accumulated GSH. These are reasons that pKNOCK-*gst* mutant was increased in the resistance level to hydrogen peroxide and iron excess conditions.

NaOCl can target lipids, fatty acids and essential proteins in several compartments in bacteria, that essential to GSH production and GST activity, leading to lethality. Without GTS activity, glutathione disulfide (GSSG) is accumulated and causes highly toxic due to its ability to reacts with free sulfhydryl groups.[10] Additionally, the increases in GSH and/or a reduction of the GSH/GSSG pool is associated with growth stimulation by nutrients and growth factors.[11] Moreover, the GSH/GSSG redox can activate several signaling pathways.[12]

Conclusion: Multiple restriction enzyme digestions with independent cultivation of each clones proves to be a better way to represent the whole *P. aeruginosa* genome due to greater number of different fragments, higher resistance efficiency, low plasmid instability, and less false positive resistance clones. The resistance clones obtained from the modified library contains functional *gst* gene. We found that the *gst*-knockout mutant exhibited a reduced susceptibility to iron- and hydrogen peroxide conditions but had an increased sensitivity against NaOCl exposure. Whereas, overexpressed gst mutants exhibited a reduced susceptibility to NaOCl but had an increased sensitivity to iron- and hydrogen peroxide conditions. The modified genomic library and study of physiological studies could be a preliminary data for further experiments to identify a novel resistance mechanism in *P. aeruginosa* in order to extend the antibacterial agents-resistance network in *P. aeruginosa* and the using of antiseptic or the disinfectant in households and in hospitals may allow the bacteria to resist an antibiotic.

References:
1. Pachori P, Gothalwal R, Gandhi P. Genes Dis. 2019;6(2):109-19.
2. Oliver A, Mulet X, Lopez-Causape C, Juan C. Drug Resist Updat. 2015;21-22:41-59.
3. Cifani N, Pompili B, Anile M, Patella M, Diso D, Venuta F, et al. PLoS One. 2013;8(8):e71717.
4. Wongsaroj L, Saninjuk K, Romsang A, Duang-Nkern J, Trinachartvanit W, Vattanaviboon P, et al. PLoS One. 2018;13(10):e0205815.
5. Bordi C. Methods Mol Biol. 2014;1149:555-63.
6. Romsang A, Atichartpongkul S, Trinachartvanit W, Vattanaviboon P, Mongkolsuk S. J Bacteriol. 2013;195(15):3299-308.
7. Allocati N, Federici L, Masulli M, Di Ilio C. FEBS J. 2009;276(1):58-75.
8. Winsor GL, Griffiths EJ, Lo R, Dhillon BK, Shay JA, Brinkman FS. Nucleic Acids Res. 2016;44(D1):D646-53.
9. Pompella A, Visvikis A, Paolicchi A, De Tata V, Casini AF. Biochem Pharmacol. 2003;66(8):1499-503.
10. Smirnova GV, Oktyabrsky ON. (Mosc). 2005;70(11):1199-211.
11. Jones DP. Methods Enzymol. 2002;348:93-112.
12. Sen CK. Curr Top Cell Regul. 2000;36:1-30.

Acknowledgements: We thank Khwannarin Khemsom for her technical assistance. This research was supported by a grant from Faculty of Science, Mahidol University under A.R.'s project. T.A. is a recipient of scholarship under Institutional Strengthening Program, Faculty of Science, Mahidol University. This work is a part of T.A. thesis master's degree.

SESSION B4:
BIOMEDICAL SCIENCE

B4_005_PF: OPTIMISATION OF HIGH RESOLUTION MELTING CURVE ANALYSIS (HRMA) TO DETECT MUTANT CALRETICULIN IN *JAK2* NEGATIVE MYELOPROLIFERATIVE NEOPLASM PATIENTS

Htoo Pyei Hlaing[1], Jarichad Toosaranont[1], Rattaphan Lamoon[2], Dusit Jit-ueakul[3], Boonrat Tassaneetrithep[4], Archrob Khuhapinant[2], Chalermchai Mitrpant[1,5,*]

[1]Department of Biochemistry, Faculty of Medicine, Siriraj Hospital, Mahidol University, Bangkok, Thailand

[2]Division of Haematology Department of Medicine, Faculty of Medicine Siriraj Hospital, Mahidol University, Bangkok, Thailand

[3]Department of Internal Medicine, Faculty of Medicine Vajira Hospital, Navamindradhiraj University, Bangkok, Thailand

[4]Office for Research and Development, Faculty of Medicine Siriraj Hospital, Mahidol University, Bangkok, Thailand

[5]Perron Institute for Neurological and Translational Science, Perth, Western Australia, Australia

*e-mail: chalermchai.mit@mahidol.edu

Abstract: Myeloproliferative neoplasms are chronic haematologic malignancies characterized by abnormally increased production of blood cells in bone marrow. Chronic myeloid leukemia (CML), polycythemia vera (PV), essential thrombocythemia (ET), and primary myelofibrosis (PMF) are included in this group and three major clonal markers associated with these diseases are somatic mutation on Janus kinase 2 (*JAK2)*, thrombopoietin receptor (*MPL*) or calreticulin (*CALR*). In our previous work, we used heteroduplex mobility assay (HMA) to detect somatic mutation of CALR in patients with essential thrombocythemia or primary myelofibrosis. Our HMA assay using 6% polyacrylamide gel electrophoresis (PAGE) can detect 52 base pair deletion (type I mutation), 5 base pair insertion (Type II mutation) and other types of mutations. However, the limit of detection was at 25% for type I mutation. We optimized the high-resolution melting analysis (HRMA) to detect type I CALR mutation. Wild type and mutant alleles were isolated and re-amplified to perform the Sanger sequencing to confirm its identity. Amplified wild type allele was used for assay optimization using different pairs of primer encompassing exon9 of *CALR*. Mixture of wild type and mutant amplicons were prepared as 50%, 25%, 12.5%, 6.25%, 3.125%, 1.5% and 0.75% respectively, and were utilized to determine limit of detection. Limit of detection of our assay was at 6.25%. The work provides information on the assay that could be used for diagnosis in this group of patients.

Introduction: Myeloproliferative neoplasms (MPNs) are a group of chronic haematological diseases where bone marrow abnormally produces increased number of blood cells [1]. First, the term was described as myeloproliferative disorders by Dameshek in 1950 [2]. According to World Health Organization classification in 2008, MPNs is divided into four major types namely chronic myelogenous leukemia, polycythemia vera, essential thrombocythemia and primary myelofibrosis [3]. Of these, chronic myelogenous leukemia is the Philadelphia-chromosome positive neoplasm and the other three are Philadelphia negative diseases [4].

According to the data collected from two large health plans in the United States of America during 2008 to 2010, out of 1000,000 patients with MPN, it has been observed that 44-57 cases have polycythemia vera, 38-57 cases have essential thrombocythemia and only 4-6 cases are of primary myelofibrosis [5]. Statistical analysis of incidence of MPN in another study showed that the disease occurs in 1.95 persons in 100,000 [6].

Somatic mutation of genes regulating proliferation of blood cell occurs in subpopulation in bone marrow which in turn leads to bone marrow overproduction of blood

cells, and makes the hypercellularity of bone marrow. The affected hematopoietic progenitor lies in the myeloid linage [7]. The predominant features of individual are increased platelet count in ET whereas bone marrow fibrosis, osteosclerosis, and extramedullary haematopoiesis can be seen in PMF [1, 3].

Genetic studies reported driver mutations in MPNs. The first mutation to be discovered is the gain-of-function mutation in *Janus kinase 2* gene [8, 9]. Other molecular markers identified in MPN are thrombopoietin receptor (*MPL*) gene mutation [9, 10] and calreticulin gene mutation [11].

In hematopoietic cells, *JAK2* involves in signaling pathways of cytokines and growth factors and phosphorylates the tyrosine residues on the cytokine receptors when the receptors are activated by its ligands. The somatic mutation of *JAK2* gene leads to the change in protein structure by the substitution of valine to phenylalanine at 617 amino acid [3]. The mutation results in that the hematopoietic stem cells in myeloid and erythroid lineages become cytokine independent increased phosphorylation of the substrates [11, 12]. This type of mutation is the most associated with polycythemia vera and the studies showed that 92% of PV patients carry *JAK2*V617F mutation [13]. Approximately 50 to 60% of the patients with ET or PMF carry this mutation [8].

In ET and PMF patients, *MPL* mutation in *MPL* is seen in 5-10% of the cases [11]. *MPL*, myeloproliferative leukemia virus oncogene, encodes thrombopoietin receptor and base substitution mutation, W515L mutation in exon10, was found associated with ET and PMF. This results in constitutive activation of thrombopoietin receptor and increase in growth and proliferation of megakaryocytes [10].

Calreticulin gene mutation was reported to be associated to ET and PMF patients and mutation on *CALR* almost mutually exclusive to mutation on *JAK2* exclusive. Recent study has shown that in ET and PMF patients who are *JAK2* and *MPL* non-mutated, *CALR* mutations were found in 67% and 88% in *JAK2* negative ET and PMF patients respectively. Thirty six types of deletion or insertion of *CALR* have been described and of these, the two major types are Type 1 (52 base pairs deletion) and Type 2 (5 base pair insertion). Both major types happen at the exon 9 of the gene and results in the frameshift of the sequence. The alternative reading frame caused by both mutations is the same [11].

We previously designed primer pairs spanning on *CALR* exon 9 and the heteroduplex mobilization was used to identify mutations. In this study, we further developed High resolution melting curve analysis (HRMA) to identify different mutations on *CALR* gene. The work provides information on the assay that could be used for diagnosis in this group of patient.

Materials And Methods

DNA Samples: DNA from patients with myeloproliferative neoplasm (ET or PMF) who was confirmed for type I calreticulin mutation (52 base pair deletion) was used in for this experiment. The study was approved by Human Subjects Protection Committee of Faculty of Medicine Siriraj Hospital (ethical clearance number Si665/2015).

Generating template of wild type and mutant alleles and optimization of HRMA

Polymerase Chain Reaction: Exon 9 of calreticulin gene was amplified by polymerase chain reaction using the enzyme *Taq* DNA polymerase (New England BioLabs, England) with approximately 100ng of DNA template. PCR cycling condition was performed for 40 cycles of 94 °C for 30 seconds, 55 °C for 1 minute and followed by an extension step at 72 °C for 1 minute. The forward primer designed is (5' ctgtccaaagcaagggctat 3') named as forward-primer 4 and the reverse primer is (5' acagagacattatttggcgcg 3') named as reverse-primer 7. Detection of mutation was observed by fragment size analysis.

PCR products mixed with loading dye were loaded onto 6% polyacrylamide gel electrophoresis followed by an electrophoresis at 100V for 1 hour. The gel was subsequently stained with ethidium bromide and visualized by gel documentation using ImageQuant LAS 4010 (General Electric Healthcare Life Sciences, Bukinghamshire, UK). The 100 base pairs DNA ladder (New England Biolabs Inc, Massachusetts, USA) was used as a reference to identify the size of the PCR products.

Isolation of the mutated bands and optimization: The type of mutation expected to see by PCR is the deletion type so that the mutated bands were seen at the lower position compared to site of wild type DNA on gel electrophoresis. Mutant alleles were isolated by band stabbing method or pieces of cut-off mutant band and re-amplified by PCR by 30 cycles of 94 °C for 30 seconds, the annealing temperature 55 °C for 1 minute followed by final extension of 72 °C for 1 minute. The primers used were forward-primer 4 and reverse-primer 7.

Purification of the isolated PCR products and Sanger sequencing: The isolated PCR products were cleaned up by the use of GenepHlow™ Gel/ PCR kit (Geneaid Biotech Ltd, Taiwan) according to the manufacturer's protocol. The purified isolated products were sent for sequencing. The nucleotide sequences were detected and the results were observed as the chromatograms. Sequences were analyzed by using BioEdit Sequence Alignment Editor Version 7.2.5 (Ibis Biosciences, Carlsbad, CA, USA) to align to NCBI reference sequence (NC_000019.10).

Limit of detection: The PCR product of one mutated sample which has been confirmed by Sanger sequencing was selected to determine the limit of detection. Serially half-dilution of mutant band in wild type product was performed for seven folds given a percentage of mutant ranging from 50%, 25%, 12.5%, 6.25%, 3.13%, 1.56% and 0.78% respectively. Afterwards, all the diluted products were undergone amplification by PCR. The resultant bands were visualized by electrophoresis and loading on 6% polyacrylamide, and the same template was used for high resolution melt curve analysis (HRMA).

*High resolution melt curve analysis (HRMA):*50 ng of template DNA was added into HRMA reaction which contained 5 µl of 2× Precision Melt Supermix (Bio-Rad), 0.5 µl each of forward and reverse primers. Seven primer pairs targeting *CALR* exon9 were tested. Forward and Reverse primer sequences are all listed in Table 1. The optimized PCR conditions were as follows: initial denaturation at 95 °C for 2 min, followed by 40 cycles of 95 °C for 10 sec, 61 °C for 30 sec and 72 °C for 30 sec. During the HRM stage, the PCR product was then denatured at 95 °C for 30 sec, cooled to 60 °C for 1 min, and melted from 65 °C to 95 °C at the speed of 0.2 °C/ step and held for 10s at each step with continuous data acquisition. CFX Manager software version 3.1 (Bio-Rad) was used to set up the sample arrangement, define PCR conditions, to analysed amplification plots and melting graphs. Post-qPCR HRM analyses of the melt curves were performed using Precision Melt Analysis™Software version 1.2 (Bio-Rad).

Results: Isolated wild type was initially chosen as a template to identify primer pair with unique single peak of melting temperature (Tm) from tested seven different combinations of primer pair. Figure 1 showed a Figure of primer pair on calreticulin gene that was used to generate template fragment, Heteroduplex mobility assay and High resolution melting curve analysis (Figure 1). The amplicon generating from combinations of primer pair with Forward primers 4, Reverse primer 2 or reverse primer 5 yielded double peak (Figure 1). Both Fwd5/Rev1 and Fwd5/Rev6 pairs yielded a single peak; however Fwd 5/Rev1 pair was chosen as the base of the melting peak was narrower and the amplicon size is smaller. The chosen pair was further tested using template of wild type, mutant or a mixture of 50% mutant preparation. Our HRMA assay can clearly separate mutant from wild type peak, while 50% mutant preparation gave rise Tm peak locating between two peaks of wild type and mutant

alleles (Figure 2). From our result, T_m Difference between wild type and mutant (52 base pair deletion) were 2-3 degree and this difference was comparable to the T_m difference which were predicted by uMelt, an online melting curve prediction software hosted by The University of Utah (Data not shown). [14]

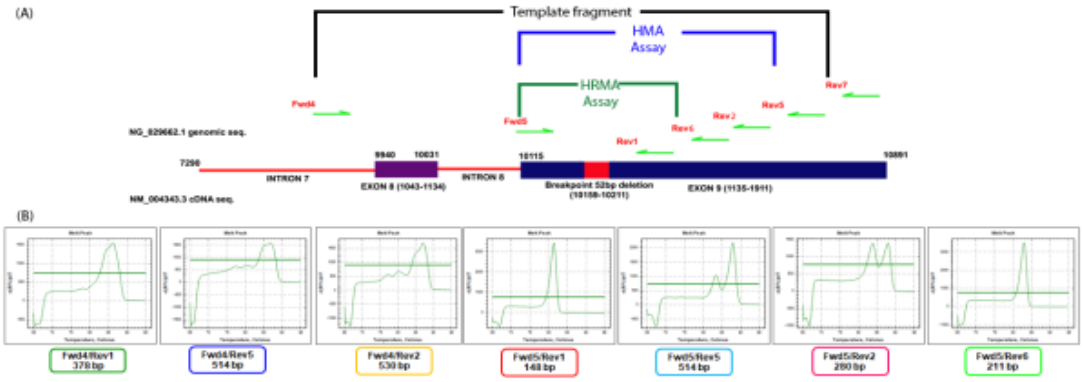

Figure 1: (A) Schematic diagram demonstrated location of primer used for generating template fragment, heteroduplex mobility assay and High-resolution melting curve analysis (HRMA) with peaks of melting temperature (B), which were generated from HRMA on wild type allele.

We further tested this primer pair on mixture of different percentage of mutant allele; i.e. 50%, 25%, 12.5%, 6.25%, 3.13%, 1.56% and 0.78%. Our HRMA assay can differentiate heteroduplex peak ranging from 50%-6.25% mutant (Figure 2B), while the heteroduplex mobility assay (HMA) was able to differentiate mutant allele at the limit of detection comparable to HRMA assay (Figure 2). Although our HRMA results on different template dilution was able to differentiate 0.78% from Wild type, our HRMA was not able to clearly differentiate 6.25% from 3.12% samples or 1.56% from 0.78% sample. We confidently claimed that limit of detection of our assay was at 6.25%.

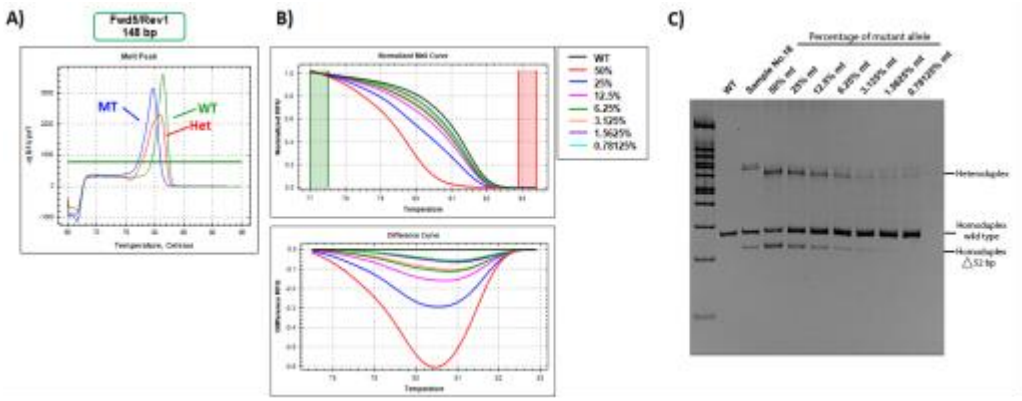

Figure 2: Graphs demonstrated peaks (A) and normalized melting curves (B) of HRMA analysis on a serial dilution of mutant allele for seven folds, i.e. 50%, 25%, 12.5%, 6.25%, 3.13%, 1.56% and 0.78%, while HMA (C) were also tested on these serial dilutions of mutant allele.

Table 1: List of primers to amplify *Calreticulin*

Name of primer	Sequence
Forward 4	5' CTGTCCAAAGCAAGGGCTAT 3'
Forward 5	5' CCTGCAGGCAGCAGAGAAAC 3'
Reverse 1	5' CCTCATCCTCCTCATCCTCA 3'
Reverse 2	5' AAAGTTCTCGAGTCTCACAGA 3'
Reverse 5	5' ACAGAGACATTATTTGGCGCG 3'
Reverse 6	5' CTCTCTACAGCTCGTCCTTG 3'
Reverse 7	5' GTGAGGGCTGAAGGAGAATC 3'

Discussion: In this current study, we developed an assay that is possibly used to detect type I CALR mutation in patients with MPN. Assay can clearly differentiate mutant allele or heteroduplex from wild type *CALR*. Based on our finding, the limit of detection was at 6.25%. This aforementioned limit of detection (LOD) was the HRMA/HMA result on artificial mixture of isolated full-length Calreticulin and the 52 bp deletion allele at the ratio of 1 to 1 based upon gel densitometry, and it is not then directly translated for percentage of mutation we can detect in clinical setting. The next step to develop this assay is to design primer and probe to simultaneously detect two common mutant *CALR* alleles, i.e. 52 base pair deletion and 5 base pair insertion.

References

1. Campbell, P.J. and A.R. Green, *The Myeloproliferative Disorders.* New England Journal of Medicine, 2006. 355(23): p. 2452-2466.
2. Tefferi, A., *The history of myeloproliferative disorders: before and after Dameshek.* Leukemia, 2008. 22(1): p. 3-13.
3. Tefferi, A., *Myeloproliferative neoplasms: A decade of discoveries and treatment advances.* American Journal of Hematology, 2016. 91(1): p. 50-58.
4. Tefferi, A. and J.W. Vardiman, *Classification and diagnosis of myeloproliferative neoplasms: The 2008 World Health Organization criteria and point-of-care diagnostic algorithms.* Leukemia, 2007. 22(1): p. 14-22.
5. Mehta, J., et al., *Epidemiology of myeloproliferative neoplasms in the United States.* Leukemia & Lymphoma, 2014. 55(3): p. 595-600.
6. Park, E.H., et al., *Nationwide statistical analysis of myeloid malignancies in Korea: incidence and survival rate from 1999 to 2012.* Blood Res, 2015. 50(4): p. 204-17.
7. de Freitas, R.M. and C.M. da Costa Maranduba, *Myeloproliferative neoplasms and the JAK/STAT signaling pathway: an overview.* Revista Brasileira de Hematologia e Hemoterapia, 2015. 37(5): p. 348-353.
8. James, C., et al., *A unique clonal JAK2 mutation leading to constitutive signalling causes polycythaemia vera.* Nature, 2005. 434(7037): p. 1144-1148.
9. Tefferi, A., *Novel mutations and their functional and clinical relevance in myeloproliferative neoplasms: JAK2, MPL, TET2, ASXL1, CBL, IDH and IKZF1.* Leukemia, 2010. 24(6): p. 1128-1138.
10. Pikman, Y., et al., *MPLW515L Is a Novel Somatic Activating Mutation in Myelofibrosis with Myeloid Metaplasia.* PLoS Medicine, 2006. 3(7): p. e270.
11. Klampfl, T., et al., *Somatic Mutations of Calreticulin in Myeloproliferative Neoplasms.* New England Journal of Medicine, 2013. 369(25): p. 2379-2390.
12. Jatiani, S.S., et al., *JAK/STAT Pathways in Cytokine Signaling and Myeloproliferative Disorders: Approaches for Targeted Therapies.* Genes & Cancer, 2010. 1(10): p. 979-993.
13. Tefferi, A., et al., *The clinical phenotype of wild-type, heterozygous, and homozygous JAK2V617F in polycythemia vera.* Cancer, 2006. 106(3): p. 631-635.

14. Dwight, Z., R. Palais, and C.T. Wittwer, *uMELT: prediction of high-resolution melting curves and dynamic melting profiles of PCR products in a rich web application.* Bioinformatics, 2011. 27(7): p. 1019-20.

B4_007_OF: PlASMA EXOSOME miR-21 AS THE INTERSTITIAL FIBROSIS AND TUBULAR ATROPHY(IF/TA) BIOMARKER IN KIDNEY TRANSPLANTATION

Sunaree Saejong[1], Natavudh Townamchai[2], Poorichaya Somparn[3], Pattarin Tangtanatakul[4], Asada Leelahavanichkul[5,*], Nattiya Hirankarn[5]
[1]Medical Microbiology Interdisciplinary Program, Graduate School, Chulalongkorn University, Bangkok 10330, Thailand
[2]Center of Excellence in Solid Organ Transplantation, Division of Nephrology, Department of Medicine, Chulalongkorn University, Bangkok 10330, Thailand
[3]Center of Excellence in Systems Biology, Faculty of Medicine; Chulalongkorn University, Bangkok 10330, Thailand
[4]Department of Transfusion Medicine and Clinical Microbiology, Faculty of Allied Health Sciences; Chulalongkorn University, Bangkok 10330, Thailand
[5]Center of Excellence in Immunology and Immune-Mediated Diseases, Department of Microbiology, Faculty of Medicine; Chulalongkorn University, Bangkok 10330, Thailand
*e-mail: a_leelahavanit@yahoo.com

Abstract: Interstitial fibrosis and tubular atrophy (IF/TA) are major cause of chronic allograft rejection in post kidney transplantation (post-KT). A non-invasive biomarker to diagnose and predict IF/TA is still absent. Plasma exosomes has possibly become a potential biomarker in various conditions including fibrosis since plasma exosomes is found to carry microRNAs(miRs) which modulate the interaction between cell. In this study, we aim to investigate whether the expression of miR-21 in plasma exosomes are associated with the severity of IF/TA in post-KT patients. The plasma samples of post-KT-patients were categorized into 4 groups based on histopathology including IF/TA grade I (5-25%) (n=5), grade II (26-50%) (n=5), grade III (≥50%) (n=5) and stable graft function(n=5). Isolated plasma exosomes and miR-21 expression were characterized by nanoparticle tracking analysis and qPCR (quantitative Polymerase Chain Reaction), respectively. The correlation between miR-21 expression and kidney functions was evaluated. The result showed that plasma exosomes miR-21 expression was significantly increased in patients with IF/TA grade II when compared to patients with stable graft function ($p < 0.01$), while IF/TA grade I and III were not significantly different ($p = 0.9634$, $p=0.8657$ respectively). Plasma exosomes miR-21 expression was not significantly correlated with serum creatinine and proteinuria. This data suggested that plasma exosomes miR-21 might represent the pathological changes during a progression of fibrosis specifically in patients with IF/TA grade II but not in the patients with IF/TA grade I and III. Increasing sample size is necessary to validate the association between plasma exosomes miR-21 and IF/TA.

Introduction: Interstitial fibrosis and tubular atrophy (IF/TA) are major causes of chronic allograft rejection in post kidney transplantation (post-KT). The incident of IF/TA in kidney allografts is significantly increasing around 40% after 3-6 months of transplantation and increasing to 65% within 2 years after transplantation.(1) Nowadays, kidney biopsy is the gold standard to identify the pathological cause of post-KT rejection including IF/TA.(2) Notwithstanding, it is an invasive method and difficult routine procedures. Thus, the development of non-invasive biomarker to monitor allograft rejection is necessary. Innovative biomarkers which are accurate, sensitive, specific and able to identify IF/TA in noninvasive method to monitor renal graft status in early and long-term graft functions are needed.

Exosomes which are the extracellular vesicles size around 40-200 nm, comprise of many cellular compartments including mRNA, microRNA (miR), pre-microRNA, DNA, proteins, lipids, other cell surface markers and major histocompatibility complex (MHC) molecules. Exosome secreted from many cell types into the biological fluid such as plasma, serum, breast milk, sweat, saliva, tears, amniotic fluid and urine.(3-9) It has been studied that exosomes can

deliver their cellular compartments (miRNA, mRNA) from original cell to the target cell leading to regulate gene expression and modulate the function of the cell . [10, 11]

MicroRNAs (miRNAs, miR) are small non-coding RNA molecules containing 22-25 nucleotides. They regulated gene expression by complementary binding to 3'UTR target mRNA. The binding causes the degradation or inhibition of translation and resulted in silencing of gene expression. In addition, miRNAs are easily detected more than mRNA and very stable in liquid body substance such as plasma, serum, urine and saliva. Moreover, miRNAs are high abundant in the exosome.[12-16]

Therefore, miRNAs in the exosomes may potential be a good non-invasive biomarker. In this study, plasma miR-21 in the exosome will be explored as non-invasive biomarker for interstitial fibrosis and tubular atrophy. Vahed SZ and colleagues have found that urinary miR-21 could discriminate IF/TA recipients and normal allograft function with an area under the Receiver Operating Characteristic (ROC) curve of 0.89 ($P < 0.001$) with 85% sensitivity and 80% specificity.[17] Nirmalya and colleagues found that TGF beta up-regulated miR-21 resulted in decreased PTEN expression and activated Akt to phosphorylate tuberin/PRAS40 which enhanced mTORC1 activation. This events led to mesangial cells hypertrophy and mesangial cells matrix expansion.[18] Another study also found that circulating miR-21 levels were increased in severely patients with IF/TA grade 3. Receiver operating characteristic curve analysis showed the diagnostic tool to predict severe kidney fibrosis (IF/TA grade III) of circulating miR-21 levels with area under the curve (AUC): 0.891 and 89% of sensitivity and 70% of specificity.[19] Based on these previous evidence, we hypothesized that miR-21 in plasma exosome might be a good predictive marker for IF/TA progression.

Methodology:

Patients and samples: The study is conducted in 20 post-KT patients at Chulalongkorn university. All patients signed informed consent. The peripheral bloods of the patients were collected when the patients had kidney biopsy. The IF/TA score was identified by kidney biopsy in concordance with the standard of 2015 update Banff classification. Samples from post-KT patients were categorized into 4 groups; patients with IF/TA grade I (5-25%), grade II (26-50%), grade III (≥50%) and stable graft function, based on histopathology. Patients with serology positive for BK virus, cytomegalovirus (CMV) and re-transplanted patients were excluded as exclusion criteria. Patients information, serum creatinine and proteinuria level were collected from medical record.

Exosome isolation: Plasma were incubated with thrombin to remove fibrin clot and centrifuged at 10,000 rpm, room temperature for 5 minutes to collect supernatant. The collected supernatants were precipitated with 24% polyethylene glycol (PEG) and incubated at 4°C approximately 12-20 hours. After that, the precipitate samples were centrifuged at 1,500g for 30 minutes. The supernatants were discarded, resuspended and retrieved the exosome pellets with 1xPBS. The suspended pellets were processed for Nano sight tracking and the RNA preparation.

Nanoparticle tracking analysis: The suspended exosome pellets were homogeneously diluted in 1:200 particle-free PBS (0.02 µm filtered) and measured the size and concentration of exosome by using NanoSight NS300 (Malvern Panalytical Instruments Company, United Kingdom).

RNA isolation and complementary DNA (cDNA) Synthesis: Total RNA was isolated from plasma exosome pellets using the miRNeasy (QIAGEN) then quantified by NanoDrop 1000 (Thermo Fisher Scientific). Total RNA (10 ng/µl) was reverse-transcribed into cDNA using specific stem loop primer for miR-21 (assay ID: 000397)
and Taqman MicroRNA Reverse Transcription Kit (Applied biosystems). The spike-in control cel-39 (cel-miR-39-3p, QIAGEN Thailand) was used as endogenous control for data normalization.

Real-time qPCR: The miR-21 expression was evaluated using Taqman® MicroRNA Assays from the Thermo Fisher Scientific with particular primers and probes for miR-21 (assay ID: 000397) in samples of patients with IF/TA grade I, II, III and stable graft function. Cel-miR-39 (assay ID : 000200) was also used to normalize the plasma samples. Real-time qPCR was performed on the 7500 Real-Time PCR System (Applied Biosystems).
Data Analysis: The data were analyzed by SPSS software (version 22, IBM Corporation, New York, USA) and GraphPad Prism version 7.0 software (LaJolla, CA, USA). One-way ANOVA was performed to analyze the expression of miR-21. A p-value less than 0.05 was accepted as statistically significant.

Results and discussion:
Clinical characteristic of the post-kidney transplant patients: Twenty post-transplant patients between 2017 and 2019 were recruited in this study. Five post-transplant patients with IF/TA of each group were investigated. The clinical characteristic of the post-kidney transplant patients is showed in Table 1.

Table 1. Clinical characteristic of the post-kidney transplant patients

	Stable (n=5)	IF/TA I (n=5)	IF/TA II (n=5)	IF/TA III (n=5)
Gender				
Female	4	3	4	2
Male	1	2	1	3
Ages (years)				
Range	20-67	20-67	39-65	36-64
Mean ± SEM	43.2±9.238	42±9.915	47.2±4.630	52.6±5.845

Plasma exosomes extraction and purity: To validate exosome pellets which were isolated from the plasma, the particle size distribution of exosomes was acquired by nanoparticle tracking analysis. The characteristic of exosomes was small vesicle which had 30-200 nm diameter in range.(20, 21) The result showed that the particle in suspension of plasma exosomes had the peak of diameter in the range of 115 nm and 154 nm (Figure1). Thus, this confirm that the precipitated pellets from plasma are composed of exosomes.

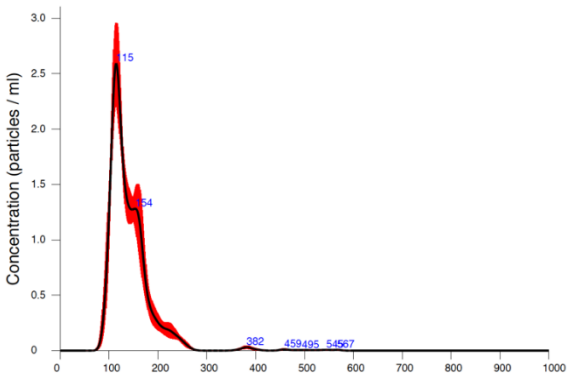

Figure 1. Plasma exosomes analysis by nanoparticle tracking analysis. X-axis determine size of particle and y-axis showed the number of particles.

Plasma exosome miR-21 associated with IF/TA: We identified the miR-21 expression in patients with IF/TA grade I, II and III compared with stable graft function, we found that plasma exosomes miR-21 expression was significantly increased in patients with IF/TA grade II compared to patients with stable graft function ($p < 0.01$), while IF/TA grade I and III were not

significantly different (p = 0.9634, p=0.8657 respectively) (Figure 2). This result suggested that miR-21 in plasma exosome associated with IF/TA during active fibrosis and might be used as fibrosis biomarker. Our result was consistent with previous studies that circulation miR-21 in the plasma or serum was up-regulated in patients with IF/TA.[17, 19] Moreover, the function of miR-21 has been studied to involve with renal fibrosis.(18) It was found that donor tubular cell can secrete miR-21 which packed into micro-vesicle and transport to recipient tubules. The delivered miR-21 is targeting to decrease PTEN leading to phosphorylation of AKT signaling which decrease the expression E-cadherin and increase the expression of α-SMA and fibronectin in renal tubules which could be implicated with renal fibrosis.(22)

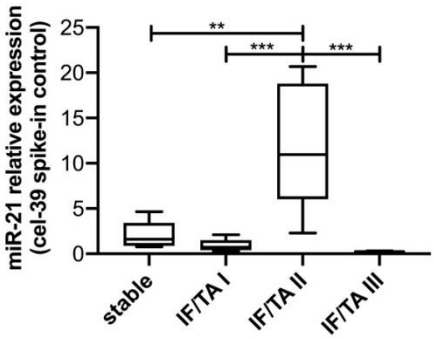

Figure 2. The expression levels of plasma exosome miR-21 in patients with IF/TA grade I, II III and stable graft function was analyzed by qPCR. (** *p < 0.01*, *** *p < 0.001*, n = 20).

The correlation of plasma exosome miR-21 with serum creatinine and proteinuria: We examined the correlation of miR-21 expression in plasma exosome with serum creatinine and proteinuria. We found that there were no correlation in plasma exosome miR-21 with serum creatinine and proteinuria in patients with IF/TA grade I, IF/TA grade II and IF/TA grade III (Figure 3).

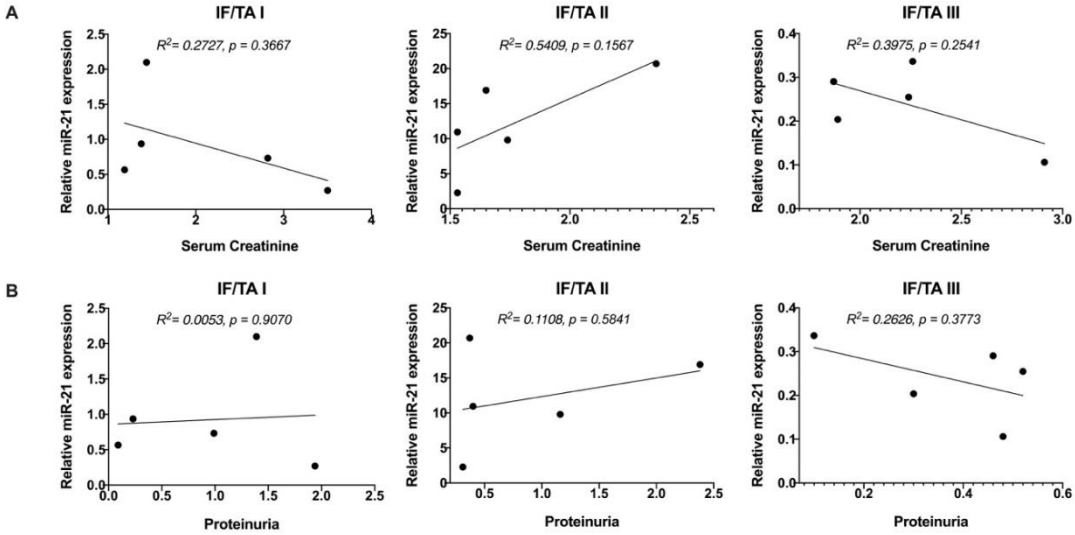

Figure 3. The Pearson's correlation of plasma exosome miR-21 in patients with IF/TA grade I, II and III and serum creatinine (A) and proteinuria (B). A p-value less than 0.05 is accepted as statistically significant.

Conclusion: The present study found the up-regulated plasma exosome miR-21 in patients with IF/TA grade II. Although the expression was not correlated with the severity of IF/TA or kidney function. It is interesting to further explore why plasma exosomes miR-21 was specifically elevated in the IF/TA grade II. This might suggest that the pathological etiology of IF/TA class II was different from IF/TA class I and III. However, the study was conducted in a relatively small number of samples, larger cohort of post-KT patients are needed to confirm the results and might help us to identify the specific biomarker for IF/TA.

References:

1. Boor P, Floege J. Am J Transplant. 2015;15(4):863-86.
2. Korbet SM. Clin J Am Soc Nephro. 2012;7(10):1545-7.
3. Admyre C, Johansson SM, Qazi KR, Filen JJ, Lahesmaa R, Norman M, et al. J Immunol. 2007;179(3):1969-78.
4. Gallo A, Tandon M, Alevizos I, Illei GG. Plos One. 2012;7(3).
5. Keller S, Rupp C, Stoeck A, Runz S, Fogel M, Lugert S, et al. Kidney Int. 2007;72(9):1095-102.
6. Lawson C, Vicencio JM, Yellon DM, Davidson SM. J Endocrinol. 2016;228(2):R57-R71.
7. Li QL, Bu N, Yu YC, Hua W, Xin XY. Clin Med Oncol. 2008;2:461-7.
8. Qiu SQ, Duan XB, Geng XR, Xie JX, Gao H. Asian Pac J Allergy. 2012;30(2):107-13.
9. Street JM, Barran PE, Mackay CL, Weidt S, Balmforth C, Walsh TS, et al. J Transl Med. 2012;10.
10. Alexander M, Hu RZ, Runtsch MC, Kagele DA, Mosbruger TL, Tolmachova T, et al. Nat Commun. 2015;6.
11. Valadi H, Ekstrom K, Bossios A, Sjostrand M, Lee JJ, Lotvall JO. Nat Cell Biol. 2007;9(6): 654-U72.
12. Eulalio A, Huntzinger E, Izaurralde E. Cell. 2008;132(1):9-14.
13. Fabian MR, Sonenberg N, Filipowicz W. Annu Rev Biochem. 2010;79:351-79.
14. Filipowicz W, Bhattacharyya SN, Sonenberg N. Nat Rev Genet. 2008;9(2):102-14.
15. Kasinath BS, Feliers D, Sataranatarajan K, Ghosh Choudhury G, Lee MJ, Mariappan MM. Am J Physiol Renal Physiol. 2009;297(5):F1153-65.
16. Vasudevan S, Tong YC, Steitz JA. Science. 2007;318(5858):1931-4.
17. Zununi Vahed S, Omidi Y, Ardalan M, Samadi N. Clin Biochem. 2017;50(1-2):32-9.
18. Dey N, Ghosh-Choudhury N, Kasinath BS, Choudhury GG. Plos One. 2012;7(8):e42316.
19. Glowacki F, Savary G, Gnemmi V, Buob D, Van der Hauwaert C, Lo-Guidice JM, et al. Plos One. 2013;8(2).
20. de la Torre Gomez C, Goreham RV, Bech Serra JJ, Nann T, Kussmann M. Front Genet. 2018;9:92.
21. Yu LL, Zhu J, Liu JX, Jiang F, Ni WK, Qu LS, et al. Biomed Res Int. 2018.
22. Zhou Y, Xiong MX, Fang L, Jiang L, Wen P, Dai CS, et al. Am J Pathol. 2013;183(4):1183-96.

B4_008_PF: THE STUDY OF *UT2B17* POLYMORPHISM IN REPRESENTATIVE THAI MUSLIM POPULATION IN SONGKHLA PROVINCE

Sirikanya Anantasena, Wandee Udomuksorn*
Department of Pharmacology, Faculty of Science, Prince of Songkla University, Hat Yai, Songkhla 90110, Thailand
*e-mail: wandee.u@psu.ac.th

Abstract: The human UDP glucuronosyltransferase 2B17 (UGT2B17) is an enzyme in phase 2 metabolism which has a major role in xenobiotic and endobiotic glucuronidation, especially testosterone. UGT2B17 is encoded by *UGT2B17* gene. The *UGT2B17* polymorphism may affect to an abnormal transcription and lack of enzyme activity. A deletion polymorphism in *UGT2B17* gene has a high prevalence in Asian. However, there is no report in Thai population. The purpose of this study was to investigate *UGT2B17* polymorphism in representative Thai-Muslim population in Songkhla province. Fifty genomic DNAs were extracted from Thai-Muslim neonates cord blood samples and then were amplified the exon1 region of *UGT2B17* gene by PCR. The mutations were detected by direct sequencing. The result showed that 35 of the 50 neonates (70%) were homozygous deletion (del/del), 10 (20%) were heterozygous deletion (del/ins), and 5 (10%) were wild type homozygous insertion (ins/ins) of *UGT2B17* gene. There was 60 bps insertion at position -111 in the promoter region of *UGT2B17* gene and the sequence became to be *UGT2B15* gene, which indicated that this sample lack of *UGT2B17* gene. Conclusions, *UGT2B17* deletion polymorphism is the highest prevalence in representative Thai-Muslim population which is similar to Japanese and Korean.

Introduction: UDP-glucuronosyltransferases (UGTs) are major enzymes in phase II drug- metabolizing enzymes and catalyze the glucuronide conjugation reaction, which the glucuronyl group of uridine 5'-diphosphoglucuronic acid (UDPGA) conjugates with polar groups of various substrates, including xenobiotic as well as endobiotic, such as bilirubin, bile acids, and hormones. A glucuronide product is hydrophilic, more polar and facilitating excreted from the body into bile or urine. The human UGTs are encoded by the *UGTs* gene, which they can be classified into four subfamilies including *UGT1*, *UGT2*, *UGT3*, and *UGT8* [1]. For *UGT2B17* gene encodes UGT2B17 enzyme is containing six exons and spans over 30 kbs, which is located on chromosome 4q13.2 [2]. The nucleotide sequence of *UGT2B17* shares over 95% identities with *UGT2B15* cDNA and may have resulted from gene duplication event. *UGT2B17* was expressed in testis, prostate, liver, uterus, and mammary gland [3, 4]. UGT2B17 catalyzed the glucuronidation of steroid hormones (testosterone and its metabolites), exemestane, and vorinostat [5, 6, 7].

Polymorphic gene deletion of the *UGT2B17* has been detected in high prevalence of 67% in Asian but low prevalence of 9% in Caucasians population, which led to no protein expression, lack of enzyme activity, and abolishing the glucuronidation of its substrates [8]. For example, The *UGT2B17* deletion polymorphism has been detected to be associated with low urinary testosterone levels and increased prostate cancer risk [9]. Besides, *UGT2B17* polymorphism was found to be correlated with individual variability of 17β-DHE levels in the plasma of women taking exemestane and was proposed to be the cause of severe exemestane adverse effects [6]. A previous study, *UGT2B17* polymorphisms ((ins/ins), (del/ins), and (del/del)) in healthy boys were discovered to be related to the timing of male pubarche, which the boys with del/del has delayed pubic hair development [5]. There were some reports about *UGT2B17* polymorphisms in Japanese and Korean population [10, 11]. Nevertheless, there is no report about *UGT2B17* polymorphisms in Thai population. So the aim of this study was to investigate the *UGT2B17* polymorphisms in representative Thai-Muslim population in Songkhla province, Thailand.

Methodology:

Study populations and genomic DNA extraction: Fifty Thai-Muslim neonatal cord blood samples were collected at Songkhla hospital. Their parents were Muslim and living in southern Thailand. Pregnant women who came to give birth at Songkhla Hospital would be received information about the project study and protocols, including benefits to be received and signed a consent form to join the project. All protocols were approved under human ethic permission code SUB.EC 52-231-19-2-3 from Human Research Ethics Committee (HREC), Faculty of Medicine, Prince of Songkla University. The entire genomic DNAs were extracted by using Illustra™ blood genomicPrep Mini Spin Kit (GE Healthcare, UK). Fifty genomic DNAs were stored at -80°C until analysis.

Polymerase chain reaction (PCR) conditions and sequencing analysis of UGT2B17gene: Neonatal genomic DNAs were amplified to determine the exon 1 of the *UGT2B17* gene by PCR with specific primer, including forward primer (5'- CCTCTCACCTGCCACTGTTC -3') and reverse primer (5'- TGGACACACGACTTACCTAGA -3'). Each reaction consisted of 2 µl of PCR buffer ($MgCl_2$ free), 1.5 mM $MgCl_2$, 0.5 µM of each primer, 0.2 mM dNTPs, and 0.5 µl *Taq* DNA polymerase in a total volume of 20 µl. PCR conditions consisted of an initial denaturation at 94°C for 4 min, followed by 40 cycles of denaturation at 95°C for 30 sec, an annealing 56.9°C for 30 sec, an extension 72°C for 1 min. Then the PCR products were identified the actual size 1,000 bps by 1.5% gel electrophoresis and were sent to the First Base Laboratories (Selangor, Malaysia) for gene sequencing.

Statistical analysis: Allele frequency and genotype frequency were calculated and Hardy-Weinberg equilibrium test using SNPAlyze software version 8 (Trail) (Dynacom Co. Ltd., Japan).

Results and Discussion: The genomic DNAs were extracted from fifty Thai-Muslim neonates cord-blood. Twenty four males and twenty six females genomic DNAs were amplified and sequenced the exon 1 region of *UGT2B17* gene, which was an unique exon and has been reported 3 known SNPs such as 253G>T (Asp85Tyr), 489A>G (Glu163Glu), and 541G>A (Val181Ile). Genbank accession number NG_017033.1 was used for the reference sequence of the *UGT2B17* gene. Distributions of the Thai-Muslim neonates *UGT2B17* gene according to the investigation of genotypes were as follows: 5 (10%) wild-type (wt) homozygous, 10 (20%) heterozygous deletion, and 35 (70%) homozygous deletion. The allele frequency of *UGT2B17* gene insertion in Thai-Muslim neonates was 0.2 (Table 1). Interestingly, the highest prevalence (67-75%) of a polymorphic gene deletion of the *UGT2B17* has been reported in Asian population [10, 11].

Table 1. Characteristics of *UGT2B17* polymorphism, including ins/ins, del/ins and del/del

Genotype	Male	Female	Total
	n (%)	n (%)	n (%)
Ins/ins	1 (2)	4 (8)	5 (10)
Del/ins	4 (8)	6 (12)	10 (20)
Del/del	19 (38)	16 (32)	35 (70)
Del[a]	23	22	
Allele frequency ins	0.2		

Abbreviations: n, number; del, deletion; ins, insertion.
[a]All subjects with deletion, including (del/ins) and (del/del).

The primers in this study were designed to cover the area of -215 at least and all nucleotide sequence of exon 1. The electropherograms of the polymorphic *UGT2B17* gene were

shown in Figure 1 and 2. The figure 1 showed the different between wt homozygous of *UGT2B17* with heterozygous variant of del/ins at nucleotide position -111. The figure 2(A) showed wt homozygous of *UGT2B17* and figure 2(B) showed homozygous of del/del of *UGT2B17* and then, the sequence of that sample became to *UGT2B15* gene, which was indicated an absent of *UGT2B17* gene.

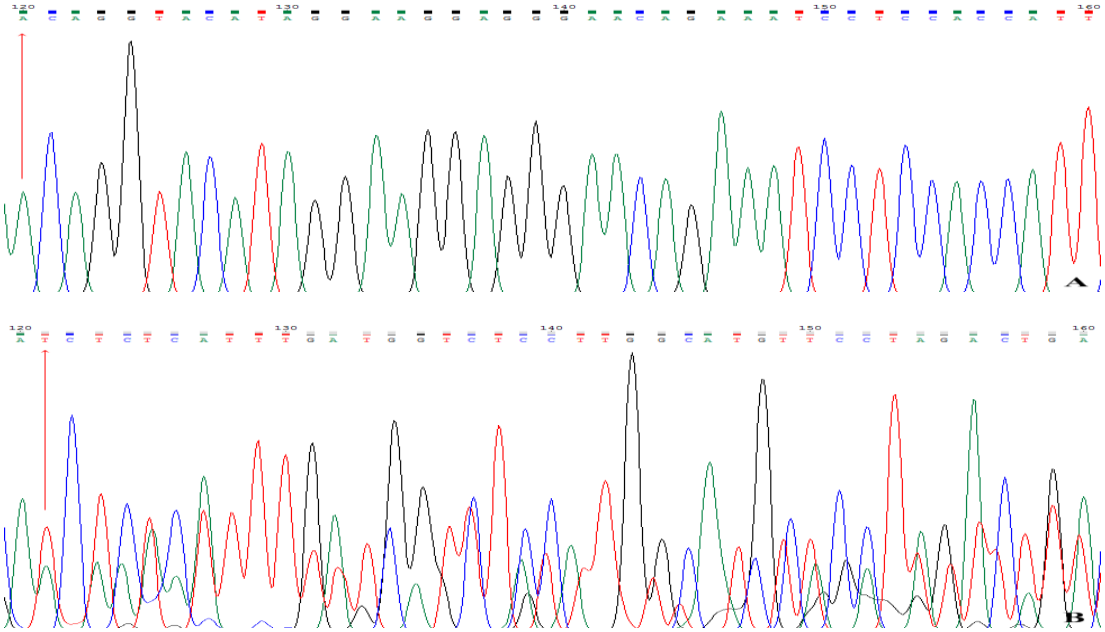

Figure 1. Electropherograms for the *UGT2B17* gene; A=wild-type, B=heterozygous deletion. The red arrow showed the position of nucleotide changes.

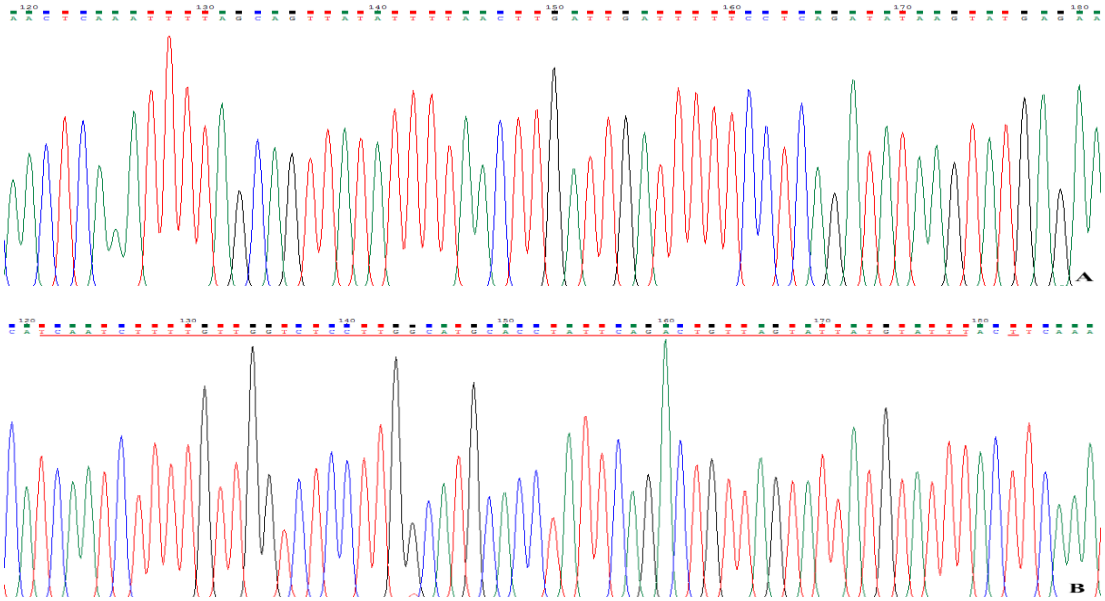

Figure 2. Electropherograms for the *UGT2B17* gene; A=wild-type, B= homozygous deletion. The red line showed the position of nucleotide changes.

From this study, the prevalence of *UGT2B17* null polymorphism was 70% of the study population, which was according to the previous study in Japanese population, which showed that *UGT2B17* deletion polymorphism was found 75% and might be associated with a risk for the development of upper aero digestive tract (UADT) cancer (head and neck squamous carcinoma, and esophageal cancer). Major risk factors for UADT-cancer were alcohol and tobacco because mucosal membranes of head, neck, and esophagus could be directly exposed to carcinogens via alcohol drink and tobacco smoke. UGT2B17 could be responsible for the glucuronidation of ethanol in alcoholic drinks and carcinogens in tobacco smoke. Thus, *UGT2B17* deletion polymorphism could be decreased elimination of ethanol and carcinogens so it might be a risk for UADT-cancer [10]. In contrast, the prevalence of *UGT2B17* null polymorphism in Caucasians, African Americans, Danish, and Swedish were 11%, 17%, 9%, and 3%, respectively [12, 4, 5, 9] (Table 2). In the previous study, the polymorphic of the *UGT2B17* gene was strongly correlated with the testosterone excretion, which homozygous deletion of the *UGT2B17* gene had no or negligible amounts of urinary testosterone. This genotype is absent of the UGT2B17 enzyme, this enzyme seems to be one of the most important enzymes for testosterone glucuronidation *in vivo* [11]. The *UGT2B17* deletion polymorphism was found to be related to prostate cancer risk in Caucasians but it was not found to be related in African Americans [4]. Moreover, Caucasian prostate cancer patients in Sweden were found to be associated with lack of UGT2B17 enzyme [9]. Since the null expression of *UGT2B17* gene is the majority in representative Thai-Muslim population, the further study should be performed to determine the association of an enzyme activity with protein expression in prostate tissue and the study of the correlation with prostate cancer or UADT-cancer in Thai population.

Table 2. The prevalence of *UGT2B17* polymorphism in each ethnic population

UGT2B17 genotypes	n (%)	Allele frequency	reference
Thai			
UGT2B17 [+][a]	15 (30)	0.2	This study
UGT2B17 null[b]	35 (70)	0.8	This study
Japanese			
UGT2B17 [+]	760 (25)	nd	[10]
UGT2B17 null	2,332 (75)	nd	[10]
Koreans			
UGT2B17 [+]	22 (33)	0.33	[11]
UGT2B17 null	44 (67)	0.67	[11]
Caucasians			
UGT2B17 [+]	73 (89)	0.86	[12]
UGT2B17 null	9 (11)	0.14	[12]
African Americans			
UGT2B17 [+]	94 (83)	0.83	[4]
UGT2B17 null	19 (17)	0.17	[4]
Danish			
UGT2B17 [+]	609 (91)	nd	[5]
UGT2B17 null	59 (9)	nd	[5]
Swedish			
UGT2B17 [+]	156 (97)	0.81	[9]
UGT2B17 null	5 (3)	0.19	[9]

Abbreviations: n, number; nd, no data

[a] *UGT2B17* [+] = wild type homozygous and heterozygous

[b] *UGT2B17* null = mutant homozygous deletion

Conclusion: This study suggests that the highest prevalence of *UGT2B17* deletion polymorphism can be found in representative Thai-Muslim population in Songkhla province which is similar to the prevalence in Japanese and Korean.

References:

1. Yang N, Sun R, Liao X, Wang G. Pharmacological Research. 2017;121:169–183.
2. Beaulieu M, Levesque E, Tchernof A, Beatty B G, Belanger A, Hum D W. DNA and Cell Biology. 1997;16:1143-1154.
3. Beaulieu M, Levesque E, Hum D W, Belanger A. The Journal of Biological Chemistry. 1996;271:22855-22862.
4. Park J, Chen L, Ratnashinge L, Sellers T A, Tanner J, Lee J, Dossett N, Lang N, Kadlubar F F, Ambrosone C B, Zachariah B, Heysek R V, Patterson S, Pow-Sang J. Cancer Epidemiology, Biomarkers & Prevention;15:1473-1478.
5. Mouritsen A, Busch A S, Aksglaede L, Rajpert-De Meyts E, Juul A. Endocrine Connections. 2018;7:460-465.
6. Luo S, Chen G, Truica C, Baird C C, Leitzel K, Lazarus P. The Pharmacogenomics Journal;18:295-300.
7. Bock K W. Biochemical Pharmacology;96:77-82.
8. Martín-Escudero P, Muñoz-Guerra J A, García-Tenorio S V, Garde E S, Soldevilla-Navarro A B, Galindo-Canales M, Prado N, Fuentes-Ferrer M E, Fernández Pérez C. Steroids;141:104-113.
9. Karypidis A H, Olsson M, Andersson S O, Rane A, Ekström L. The Pharmacogenomics Journal;8:147-151.
10. Urashima M, Nakashima A, Hama T, Suzuki Y, Ohdaira H, Akiba T, Suzuki M, Noya M, Tsumi Y, Mafune A, Toda K, Yokoyama K, Wada K, Kojima H, Okamoto A. Epidemiology;5:1-6.
11. Jakobsson J, Ekström L, Inotsume N, Garle M, Lorentzon M, Ohlsson C, Roh H, Carlström K, Rane A. The Journal of Clinical Endocrinology & Metabolism;9:687-693.
12. Martín-Escudero P, Muñoz-Guerra J, Del Prado N, Canales M G, Ferrer M F, Vargas S, Soldevilla A B, Serrano-Garde E, Miguel-Tobal F, Maestro de las Casas M, Fernandez-Pérez C. Physiological Reports;3:1-7.

Acknowledgments: This study was financially supported by Graduate School, Prince of Songkla University. We thank the Department of Pharmacology, Faculty of Science for providing the laboratory and equipment for the experiment.

B4_009_PF: BIOLOGICAL ACTIVITIES OF PAPER MULBERRY EXTRACT (*Broussonetia papyrifera* (L.) Vent.)

Orawan Wanachewin[1], Rujirek Chaiwongsa[2], Kanyamas Choocheep[2], Prachya Kongtawelert[3], Wipawan pukumpuang[1,*]
[1]Program in Biological Sciences, Chiang Rai Rajabhat University, Chiang Rai, Thailand
[2]Faculty of Associated Medical Sciences, Chiang Mai University, Chiang Mai, Thailand
[3]Thailand Excellence Center for Tissue Engineering and Stem Cells, Department of Biochemistry, Faculty of Medicine, Chiang Mai University, Chiang Mai, Thailand
*e-mail: wipawan.pu@gmail.com

Abstract: This study aimed to evaluate the effects of *B. papyrifera* the antibacterial activities against various bacteria, cytotoxicity against RAW 264.7, and nitric oxide production. Various parts of the plant were extracted using hot water to obtain young leave (YL), old leave (OL), stem (S) and bark (B) extracts. The crude extracts (500 mg/ml) were determined for their antibacterial activity against *Staphylococcus aureus* TISTR 746, methicillin-resistant *Staphylococcus aureus* (MRSA), *Bacillus cereus* TISTR 2372, *Escherichia coli* TISTR 527, *Pseudomonas aeruginosa* TISTR 2370 and *Salmonella enterica* TISTR 2519 using agar disc diffusion method. The result showed that all aqueous extracts exhibited the growth of the tested bacteria with inhibition zone ranged from 7.17 – 10.00 mm. The B extract gave the highest antibacterial against all Gram positive bacteria with inhibition zone ranged from 8.33 – 9.83 mm. In addition, the cytotoxicity on RAW 264.7 cell was evaluated using MTT assay. The anti-inflammatory effect was investigated using *in vitro* a lipopolysaccharide (LPS) induced nitric oxide (NO) production on RAW 264.7 macrophage model. All parts of the extracts (0.1-1000 µg/ml) had low cytotoxicity except S, and B extracts with 1000 µg/ml that caused cell death up to 40%. The S extract at 100 µg/ml possessed the highest inhibitory effect on NO production with 93% inhibition of NO level relative to lipopolysaccharide (LPS)-induced control. In conclusion, *B. papyrifera* is an interesting plant further used for applying as natural health products.

Introduction: *Broussonetia papyrifera* (L.) Vent. also known as paper mulberry, is generally used as material for the making of handmade Sa-paper. In terms of medicinal usage, various parts of the plant are used. For instance, decocted bark is used for the treatment of ascites, and leaves are used to stop bleeding, reduce blood in sputum, and cure dysentery. Together, several purified compounds derived from *B. papyrifera* have been reported regarding their biological activities. For example, radix and fruit extractions exhibited anti-nociception and anti-inflammation in rodents[1]; ethanol extract of fruit parts showed the protective effects in H_2O_2 induced nerve cell, PC12[2], impairment; and seed oil and leave extraction had antibacterial activities [3, 4.] Though there are many publications about the plant's activities in Taiwan, China, and Japan, there are few reports of biological activities of paper mulberry grown in Thailand. Therefore, the study aim to screening anti-bacterial, cytotoxicity, and anti-inflammatory effects of *B. papyrifera* grown in Thailand in expect to use the information in applying to the usage of the plant for other purposes in locals.

Methodology:

Sample collection and extraction method: Paper mulberry was collected from Pang Ha village, Koh Chang, Mae Sai, Chiang Rai, Thailand. The plant sample was divided into 4 parts those were young leaves (YL) (1-3 leaves at the top of a branch), old leaves (OL), stem (S) and bark (B). Each sample was extracted using hot water (1:10 w/v) at room temperature for 72 hours. After that, the extraction was filtrated, evaporated under vacuum using rotary evaporator and then lyophilized to obtain the crude powder.

Antibacterial activity: The antibacterial activity was performed using agar disc diffusion method[5]. The tested bacterial strains including *S. aureus* TISTR 746, MRSA, *B. cereus* TISTR 2372, *E. coli* TISTR 527, *P. aeruginosa* TISTR 2370, and *S. enterica* TISTR 2519 were obtained from Thailand Institute of Scientific and Technological Research (TISTR). The tested bacteria were cultured in Mueller-Hinton Broth (MHB) at 37°C for 18 hours. After that, the turbidity of the bacterial cultures was adjusted to McFarland standard No. 0.5 yielding approximately 1 x 10^8 CFU/ml. Then each culture was swabbed on Mueller-Hinton Agar (MHA) and allowed to air dry. Twenty microliters of plant extracts (500 mg/ml) were dropped in a 6 mm sterile paper disc (Macherey-Nagel), and the discs were placed on the agar compared with 100% Dimethyl sulfoxide (DMSO) as a solvent control. Gentamycin (10 µg/disc) was used as a positive control. The antibacterial activity of each crude extract was evaluated by measuring a diameter of clear inhibition zone after incubating at 37°C for 24 hours.
Cell culture: Murine macrophage cell line RAW264.7 (ATCC® TIB-71™) was obtained from the ATCC (American Type Culture Collection). The cells were cultured in Dulbecco's Modified Eagle Medium (DMEM) supplemented with 10% heat inactivated fetal bovine serum, 100 U/mL penicillin and 100 µg/mL streptomycin. The cells were maintained in monolayer cultures at the temperature 37 °C in 5% CO_2 incubator.
Cytotoxicity on RAW264.7: One hundred microliters of RAW264.7 (1 x 10^4 cells/mL) was cultured in 96-well plate for 24 hours. After that, the cell has been treated with *B. papyrifera* extract in a range of 0.1-1000 µg/ml for additional 24 hours. At the end of treatment, the old media were discarded and refilled with 100 µl of 0.5 mg/ml MTT 3-(4,5-dimethylthiazol-2-yl)-2,5-diphenyltetrazolium bromide solution. The cells were incubated at 37 °C for 4 hours. Then, the solution was removed and precipitated formazan crystal in each well was dissolved by 100 µl DMSO. Optical density (OD) of solution was measured at 540 nm using Thermo Multiskan EX plate reader. Cell viability is presented as a percentage relative to control, which was treated with DMSO.
Nitric oxide production of RAW264.7: RAW264.6 was seeded at density 3 x 10^4 cell/ml in 48-well-plated. Then, cells were deprived and treated with the paper mulberry extract (1 and 10 µg/ml) for 2 hours. Next, the cells were treated with LPS (1 µg/ml) for another 48 hours. 10 and 50 µM Indomethacin was used as a positive control. Cultured media were collected, and nitric oxide level has been examined as the following methods. 50 µl of culture media was mixed with 50 µl Griess reagent. Then, optical density was detected at 540 nm using Thermo Multiskan EX plate reader. NO production is shown as relative levels to control.
Statistical analysis: Three replicates of each sample were used in statistical analysis, and the data were reported as mean ±SD. Analysis of variance (ANOVA) was calculated using the independent T-test, and the Duncan's honestly significant difference (HSD) test at $P < 0.05$.

Results and Discussion:
Antibacterial activity : For preliminary screening, the plant extracts at low concentration could not inhibit any tested bacteria. Therefore, the crude extracts at a concentration of 500 mg/ml were used in this study. The antibacterial activities of various parts of paper mulberry aqueous extracts, including YL, OL, S and B extracts, on six pathogens; *S. aureus* TISTR 746, MRSA, *B. cereus* TISTR 2372, *E. coli* TISTR 527, *P. aeruginosa* TISTR 2370 and *Sal. enterica* TISTR 2519 were shown in Table 1. The result showed that all aqueous extracts could inhibit the growth of *B. cereus* TISTR 2372 with inhibition zone ranged from 7.83 – 10.00 mm. Moreover, B and OL extracts could inhibit all Gram positive bacteria with inhibition zone ranged from 8.33 – 9.83 and 7.17 – 8.50 mm, respectively. Furthermore, S extract could inhibit Gram positive bacteria; MRSA and *B. cereus* TISTR 2372 and Gram negative bacteria; *P. aeruginosa* TISTR 2370 with the inhibition zone of 7.33, 7.83 and 7.50 mm, respectively. The results indicated that the Gram negative bacteria are more resistant to *B. papyrifera* extracts than Gram positive bacteria. Different sensitivities between Gram negative and Gram positive

bacteria might be due to the distinct cell wall structures. The Gram negative bacteria has the outer membrane carrying LPS and porin which made the cell wall impermeable to plant extracts[6]. The previous report found that the methanol extract of *B. papyrifera* leave collected from Margalla Hills, Pakistan could inhibit *Enterobacter faecalis*, *Vibrio cholera*, *B. subtilis*, *P. aeruginosa* and *Klebsiella pneumonia*[7]. According to another report, the prenylated flavonoids isolated from *B. papyrifera* root bark exhibited potent antimicrobial activity *Candida albicans, Saccaromyces cerevisiae, E. coli, S. typhimurium*, *S. epidermis,* and *S. aureus* [8]. However, there are few reports regarding the anti-bacterial activities of paper mulberry in Thailand.

Table 1. Inhibition zones of paper mulberry extracts (YL, OL, S, B) on pathogenic bacteria

Plant extracts (500 mg/ml)	Inhibition zone ± SD (mm)					
	S. aureus TISTR746*	MRSA*	*B. cereus* TISTR2372*	*E. coli* TISTR527	*P. aeruginosa* TISTR2370**	*Sal. enterica* TISTR2519
YL	0	0	10.00 ± 0.50b	0	0	0
OL	8.00 ± 0.50b	7.17 ± 0.29b	8.50 ± 0.00c	0	0	0
S	0	7.33 ± 0.29b	7.83 ± 0.29c	0	7.50 ± 0.00b	0
B	8.33 ± 1.04b	9.83± 0.29a	9.83 ± 0.29b	0	0	0
gentamycin (10 μg/disc)	15.00 ± 0.00a	0	14.67 ± 0.58a	14.33 ± 0.58	9.67 ± 0.29a	16.00 ± 1.73

Data are presented as mean ± standard deviation (SD) of triplicate experiments.
Statistical comparison between groups are Post hoc Duncan test (*) and T-test (**)
Mean values in the same column with different letters are significantly different ($P < 0.05$).

Cytotoxicity on RAW264.7: Water extracts of paper mulberry have relatively low toxicity to mouse macrophage cell line, RAW264.7 (Figure. 1). Every concentration of *B. papyrifera* extracts, excluding the 1000 µg/ml of S and B extracts, exhibited low toxicities (<20% lower number of cells). However, there is a previous report showed that methanol extracts of *B. papyrifera* leaf and bark have strong cytotoxicities on cancer cell lines, such as Hela, HepG2, and MCF-7[9]. This might imply the different biological effects of *B. papyrifera* extracts on different cell lines.

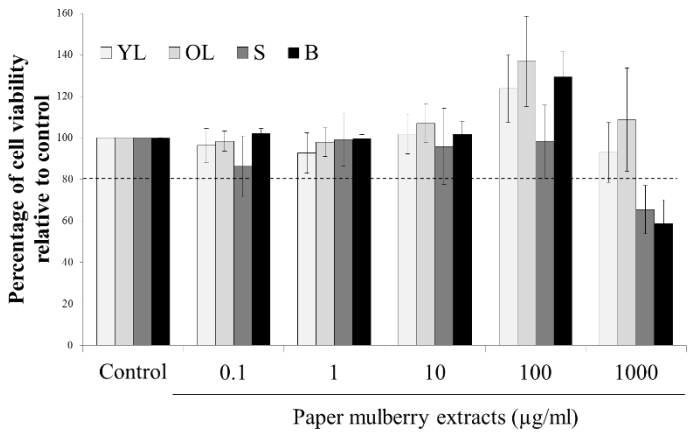

Figure 1. Effects of paper mulberry extracts on RAW264.7 viabilities. Viabilities of control were set as 100% and were used for normalization.

Nitric oxide production of RAW264.7: Nitric oxide (NO) is a signal molecule that plays a key role in the inflammatory process. Several studies show that NO produced by macrophage is involved in the inflammatory process and several inflammation-related pathologies. We tested the protective effects of *B. papyrifera* water extracts on LPS-induced mouse macrophage cell lines. Indomethacin at 10 and 50 µM were used as a positive control. Interestingly, extraction from all parts of *B. papyrifera* exhibited protective effects on LPS-induced inflammation in RAW264.7 cells. S extract of *B. papyrifera* at 100 µg/ml exhibited stronger potency than 50 µM indomethacin, and this part showed the most potent inhibition effect on NO production (Figure 2). Our result is consistent with the previous report by Young and colleagues that leave extract of *B. papyrifera* from Jeju, Korea possess strong NO inhibition[10]. Hence, S extract are further examined for its effects on the expression of inflammatory genes including inducible nitric oxide synthase (iNOS), Interleukin-1beta (IL-1β) and interleukin-6 (IL-6). Together, levels of inflammatory mediator, prostaglandin E2, will be measured.

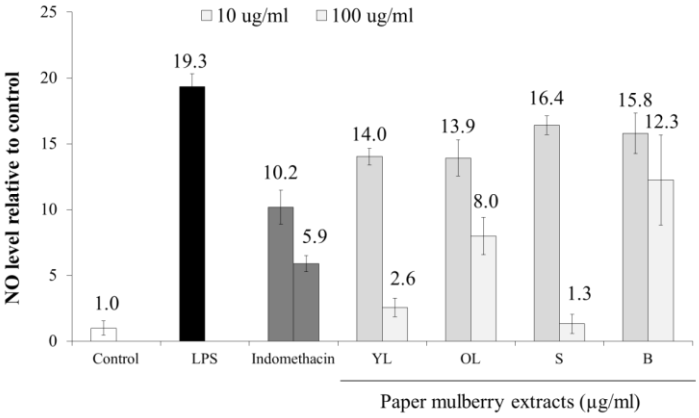

9

Figure 2. Effects of *B.papyrifera* extracts on LPS-induced NO production in RAW264.7 cells. Indomethacin is a NO inhibitor. 10 and 50 µM indomethacin treatment were presented in the first and second bars.

Conclusion: The results from the current study suggested that extracts from *B.papryrifera* has modest anti-bacterial activities and has potent anti-inflammatory effects. Further studies regarding the related molecules and underlying inhibition mechanism are required in order to demonstrate the potential usage of paper mulberry as a food supplement.

References:

1. Lin LW, Chen HY, Wu CR, Liao PM, Lin YT, Hsieh MT, et al. Biosci Biotechnol Biochem. 2008;72(9):2377-84.
2. Mei RQ, Wang YH, Du GH, Liu GM, Zhang L, Cheng YX. J Nat Prod. 2009;72(4):621-5.
3. Kumar NN, Ramakrishnaiah H, Krishna V, Deepalakshmi A. International Journal of Pharmaceutical Sciences and Research. 2015;6(9):3954.
4. Sharma R, Lall N. South African Journal of Science. 2014;110(11-12):01-8.
5. CLSI. Performance standards for antimicrobial disk susceptibility tests; Approved Standard–Twelfth Edition. CLSI document M02-A12. Clinical and Laboratory Standards Institute Wayne, PA; 2015.
6. Martinez de Tejada G, Sánchez-Gómez S, Rázquin-Olazaran I, Kowalski I, Kaconis Y, Heinbockel L, et al. Current drug targets. 2012;13(9):1121-30.

7. Khan AM, Qureshi RA, Gilani SA, Ullah F. Journal of Medicinal Plants Research. 2011;5(18):4665-70.
8. Sohn H-Y, Son K, Kwon C-S, Kwon G-S, Kang S. Phytomedicine. 2004;11(7-8):666-72.
9. Kumar NN, Ramakrishnaiah H, Krishna V, Radhika M. Int J Pharma and Pharmaceu Sci. 2014;6(5):339-42.
10. Yang E-J, Yim E-Y, Song G, Kim G-O, Hyun C-G. Interdisciplinary toxicology. 2009;2(4):245-9.

Acknowledgements: This work was funded and supported by National Research Council of Thailand (NRCT). We also thank Faculty of Science and Technology, Chiang Rai Rajabhat University and Thailand Excellence Center for Tissue Engineering and Stem Cells, Department of Biochemistry, Faculty of Medicine, Chiang Mai University, Chiang Mai, Thailand for providing laboratory facility.

SESSION B5:
BIODIVERSITY

B5_002_OF: GENETIC DIVERSITY AND REINTRODUCTION SOURCE OF THE COMMON BUTTERFLY LIZARD, *Leiolepis belliana* (SQUAMATA: AGAMIDAE), ON PHRA ISLAND, CHON BURI PROVINCE

Nutthanun Khantasup, Thongchai Ngamprasertwong, Nontivich Tandavanitj*
Department of Biology, Faculty of Science, Chulalongkorn University, Bangkok, Thailand 10330
*e-mail: Nontivich.T@chula.ac.th

Abstract: Species translocation has currently been a common practice for conservation of threatened or endangered species. The common butterfly lizard, *Leiolepis belliana* (Hardwicke & Gray, 1827), is among such species, which have experienced population decline and have been reintroduced in the wild. However, information related to population genetic structure and genetic diversity of *L. belliana* is inadequate. The objectives of this study are to assess the genetic diversity and investigate the origin of the putative reintroduced *L. belliana* on Phra Island, Chon Buri Province, which is a conservation site for the butterfly lizards, using mitochondrial cytochrome *b* sequences. Tail tissue samples (n = 9) were collected from Phra Island and some mainland localities. Mitochondrial cytochrome *b* sequences (1,040 bps) revealed no genetic variation (h = 0, π = 0) with one unique haplotype (N = 1). Moreover, comparison of sequences from Phra Island and other mainland localities revealed the potential source of reintroduction, which was possibly southern Thailand. The results obtained from this study highlighted the need for serious conservation plan in the near future to maintain genetic uniqueness and strengthen genetic diversity of *L. belliana* population on the island.

Introduction: Species translocation is one of the most commonly used procedures for wildlife conservation. It accomplished by translocating an endanger species to a new, relative more suitable habitat, which is usually outside the species' original range to overcome detrimental factors resulting in population decline in the original habitat. For this reason, islands potentially serve as suitable habitats for species translocation due to the low level of disturbance and predators.[1] One of the common goals of species translocation is to strengthen the genetic diversity of a small translocated population.[2] Therefore, knowledge regarding the population genetic structure and genetic diversity are necessary for the success of species translocation and conservation.

The common butterfly lizard, *Leiolepis belliana* (Hardwicke & Gray, 1827), is one of the four species of butterfly lizards that is widely distributed in Thailand.[3] It plays important roles in the ecosystem, especially in the control of insect populations, including disease vectors and agricultural pests. However, wild populations have recently experienced noticeable declines as the results of hunting and habitat destruction.[4] Therefore, conservation efforts have been implemented in many parts of Thailand to increase the numbers of the butterfly lizard in the wild. These conservation measures include captive breeding and species translocation programs.

Phra Island, Sattahip District, Chon Buri Province, is located in the Gulf of Thailand and is one of the butterfly lizard conservation sites under the protection of the Royal Thai Navy. According to interviews with naval officers, this particular island has been reputed as a reintroduction site for approximately 20 years. However, within a relatively small habitat (~ 0.5 km^2), butterfly lizard population may potentially experience inbreeding and suffer from loss of genetic diversity, which will hinder the conservation efforts.[5] Therefore, genetic diversity assessment should be conducted, through which the source of the reintroduction individuals should be investigated, in order to assure the effectiveness of future conservation plan. This study examined the genetic diversity of *L. belliana* population on Phra Island using the mitochondrial cytochrome *b* sequences.

Methodology:
Specimens and sampling localities: Tissue samples of *Leiolepis belliana* (n = 9) were collected from Phra Island. To obtain the tissue samples, butterfly lizards were captured by a noose and handled with care. Tail tips were excised and preserved in 95% ethanol. In addition, tissue samples from mainland localities, namely Chon Buri, Prachin Buri, Suphan Buri, Phuket, and Narathiwat Provinces were also included (Figure 1).

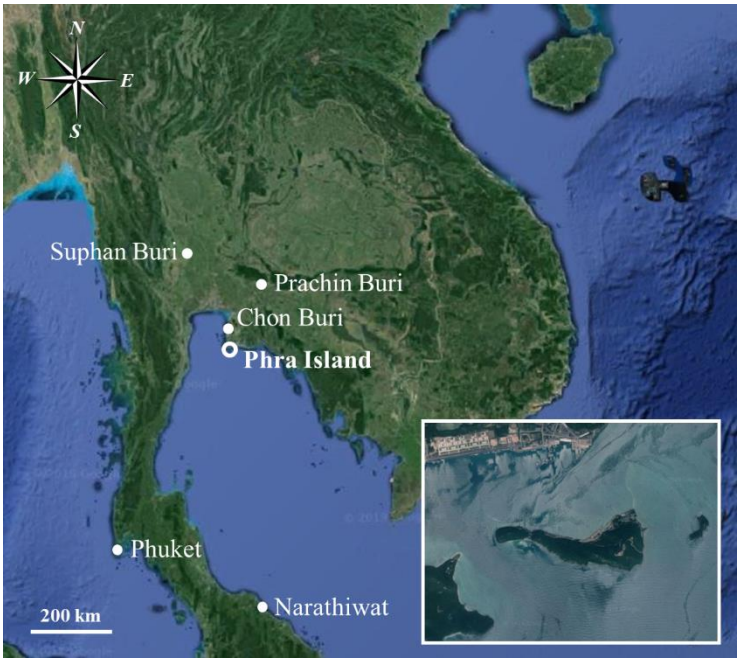

Figure 1.Map of Thailand showing location of Phra Island (small) and localities of other *L. belliana* specimens used in this study (Google Maps, 2019). Retrieved from https://maps.google.com.

DNA extraction, amplification, and sequencing: Total DNA was extracted from tail tissues using PureDireX™ Genomic DNA Isolation Kit (Bio-Helix Co., Ltd., Taiwan). Mitochondrial cytochrome *b* gene was amplified by polymerase chain reactions (PCR), using the forward primer L14910 (5'-GACCTGTGATMTGAAAAACCAYCGTTGT-3')[6] and the reverse primer H16064 (5'-CTTTGGTTTACAAGAACAATGCTTTA-3').[7] The reaction was performed with an initial denaturation step at 94 °C for 7 min followed by 40 cycles of denaturation at 94 °C for 40 sec, annealing at 50 °C for 30 sec, extension at 72 °C for 1 min and end with final extension step at 72 °C for 7 min.[8] Sequencing was performed by a commercial firm (Bioneer Inc., South Korea).
Data analyses: All sequences were manually checked, edited, and aligned using MUSCLE algorithms in MEGA version 7.0.[9] Subsequently, the genetic diversity within Phra Island was evaluated through the calculations of number of haplotypes (*N*), haplotype diversity (*h*) and nucleotide diversity (π) using Arlequin version 3.5.[10] Phylogenetic tree, based on maximum likelihood (ML), was constructed using MEGA version 7.0.[9] Two other *Leiolepis* sequences (*Leiolepis guttata* and *Leiolepis boehmei*) were downloaded from GenBank and assigned as outgroups in the phylogenetic tree. The GTR+I nucleotide substitution model was selected by jModelTest version 2.1.3[11] as the most appropriate nucleotide substitution model. The confident level of tree topology was examined by bootstrap analysis with 1000 bootstrap pseudoreplicates.

Results and Discussion: Mitochondrial cytochrome *b* sequences (n = 9, length = 1,040 bps) obtained from Phra Island revealed only one unique haplotype (N = 1), inferring no genetic variation within the population (h = 0, π = 0). Although parthenogenesis has been reported in *Leiolepis* and it can potentially reduce genetic diversity within a population, *Leiolepis belliana* is evidently a sexually reproduced species.[3] Founder effect may also contributes to the observed low genetic diversity and the uniqueness of the single haplotype because the entire population on the island was possibly established by a few reintroduced individuals[12]. Ultimately, low genetic diversity can lead to reduced fitness, inability to adapt to environmental changes, and, eventually, population extinction.[13] Fundamentally, the results are alarming and are presumably detrimental to the survival and conservation of Phra Island population. Moreover, this study investigated mitochondrial cytochrome *b* gene, which is maternally inherited. Considering the possibility that Phra Island's population is under the influence of founder effect, the current population may have inherited the particular gene from only few female individuals. Even though population size has increased in subsequent generations, with restricted gene flow and no further reintroduction, the low mitochondrial genetic diversity was consequently maintained within the population. With the current data on matrilineal diversity of *L. belliana*, it is of interest to further conduct a molecular analysis on nuclear DNA to see the overall genetic diversity in this population in the future.

According to the maximum likelihood phylogenetic tree, all *L. belliana* specimens were assigned as a strongly supported monophyletic group and were distinct from the outgroups (*L. boehmei* and *L. guttata*). However, *L. belliana* monophyletic clade was further divided into two minor clades, namely clade A and clade B. Clade A was comprised of specimens from eastern (Chon Buri and Prachin Buri) and central Thailand (Suphan Buri). Clade B was comprised of specimens from southern Thailand (Narathiwat and Phuket) in addition to Phra Island (Figure 2). The observed phylogenetic relationship was also reported by Grismer in 2014,[3] where the *L. belliana* were separated into several phylogenetic clades based on their geographical localities and regions. Interestingly, the maximum likelihood phylogenetic analysis grouped specimens from Phra Island together with southern Thailand specimens rather than the expected grouping with specimens from eastern Thailand. It is plausible that *L. belliana* population on Phra Island was comprised of reintroduced individuals from southern Thailand. Evidently, specimens from Phra Island were strongly supported as the sister lineage to specimens from Narathiwat with only two nucleotide differences. This speculation was later confirmed through an interview with the officers from the Royal Thai Navy. Remarkably, our results demonstrated reliable evidence of human interference on the observed phylogenetic relationship. A precise understanding of the population genetic structure, including the source of reintroduced individuals, is an important key to the success of future conservation plan. For instance, if it is necessary to translocate this particular population to a new habitat in the future, the implication of genetic assessment will be helpful in order to determine the suitable relocation site and devise plan to meet conservation goals while maintaining genetic uniqueness of the population. On the other hand, if the population severely suffer from loss of genetic diversity, reintroduction of more butterfly lizard individuals could be conducted to increase the genetic diversity within the island. Nonetheless, the source should be carefully selected to prevent genetic admixture and maintain the genetic uniqueness of the island.

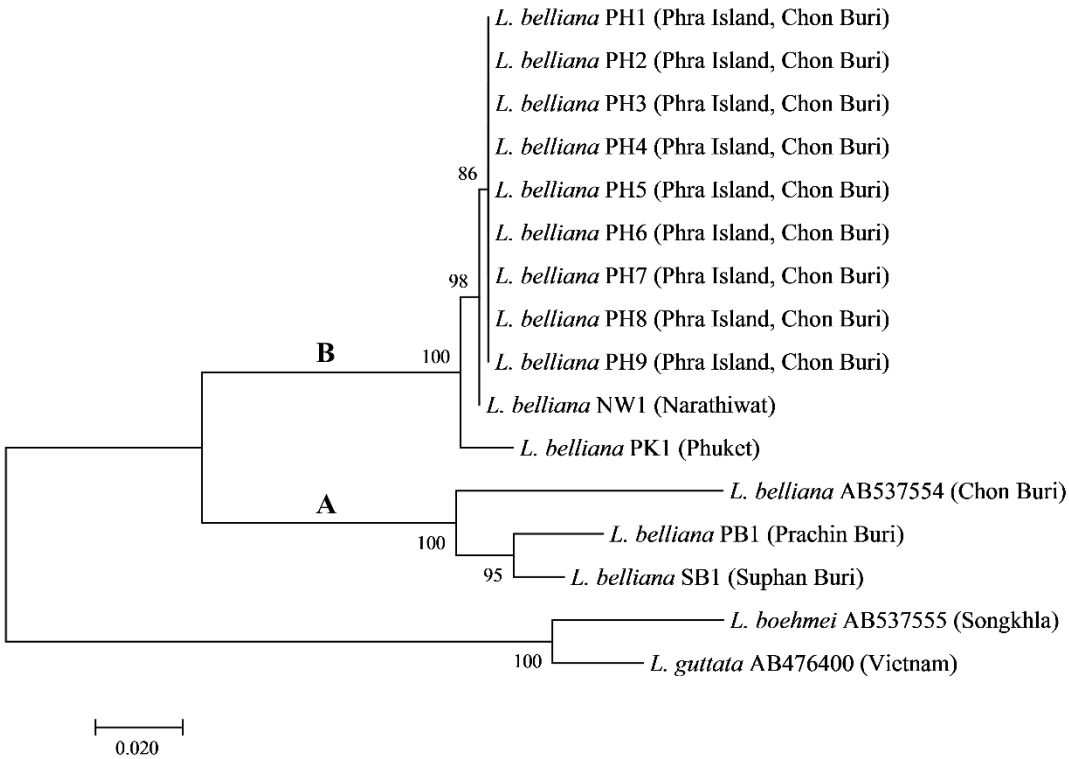

Figure 2. Phylogenetic tree based on maximum likelihood method for *L. belliana* specimens from Phra islands and other localities as inferred from mitochondrial cytochrome *b* sequences. Statistical support of each node was represented by maximum likelihood bootstrap values.

The available GenBank accession numbers of some specimens were given after the species name.

Conclusion: In summary, mitochondrial cytochrome *b* sequences revealed no genetic variation and one unique haplotype was observed among *Leiolepis belliana* population on Phra Island. Furthermore, the maximum likelihood phylogenetic analysis indicated that the possible source of reintroduced individuals was southern Thailand. Hence, future conservation plans should carefully consider the maintenance of the genetic uniqueness of the island. To further our research, we intend to investigate the population genetic structure of *L. belliana* on other islands in the eastern Gulf of Thailand to demonstrate the complete genetic relationship among *L. belliana* populations, leading to the effectiveness of future conservation plan.

References:

1. Conant S. Bioscience. 1988;38:254–257.
2. Griffith B, Scott M, Carpenter JW, Reed C. Science. 1989;245:477–480.
3. Grismer JL, Bauer AM, Grismer LL, Thirakhupt K, Aowphol A, Oaks JR, et al. Biol J Linnean Soc. 2014;113:1080–1093.
4. Aranyavalai V. Agric Technol (Thail). 2008;26:111–115. (in Thai)
5. Frankham R. Heredity. 1997;78:311–327.
6. de Queiroz A, Lawson R, Lemos-Espinal JA. Mol Phylogenet Evol. 2002;22:315–329.
7. Burbrink FT, Lawson R, Slowinski JB. Evolution. 2000;54:2107–2118.
8. Lin LH, Ji X, Diong CH, Du Y, Lin CX. Mol Phylogenet Evol. 2010;56:601–607.

9. Kumar S, Stecher G, Tamura K. Mol Biol Evol. 2016;33:1870–1874.
10. Excoffier L, Lischer EL. Mol Ecol Resour. 2010;10:564–567.
11. Darriba D, Taboada GL, Doallo R, Posada D. Nat Methods. 2012;9:772.
12. Provine WB. Genetics. 2004;167:1041–1046.
13. Amos W, Balmford A. Heredity. 2001;87:257–265.

Acknowledgements: Funding for this research was provided by the Plant Genetic Conservation Project Under the Royal Initiative of Her Royal Highness Princess Maha Chakri Sirindhorn (RSPG) and the Science Achievement Scholarship of Thailand (SAST). We would like to express our sincere gratitude to the Royal Thai Navy (RTN) for their supports during the field surveys on Phra Island, and to Miss Arpapan Prakobkarn for providing tissue samples of *Leiolepis belliana* from Phuket and Narathiwat Provinces. We would like to thank the members of Thai Turtle Laboratory for their precious advice and laboratory assistance. Lastly, we would also like to thank the Department of Biology, Faculty of Science, Chulalongkorn University for the supports.

B5_004_OF: EFFECTS OF HYPO-OSMOTIC SHOCK ON THE RESPONSE OF HEMOLYMPH OSMOLALITY IN THE MUD CRAB *Scylla olivacea* (Herbst, 1796)

Phurich Boonsanit, Supanut Pairohakul*
Department of Marine Science, Faculty of Science, Chulalongkorn University, Bangkok, Thailand
*e-mail: Supanut.P@chula.ac.th

Abstract: The mud crab *Scylla olivacea* are an ecologically and commercially important crab species in Thailand. These crabs inhabit mainly in mangroves where they could face salinity fluctuations. Salinity changes especially acute low salinity could lead to physiological stresses for these mud crabs in term of osmoregulation. Thus, this study aims to examine the effects of hypo-osmotic shock on hemolymph osmolality of the mud crab *Scylla olivacea*. Adult males *S. olivacea* were acclimated at salinity of 25 psu (the control group) for a week prior to the experiment. After the acclimation period, the crabs were transferred from 25 psu to 15 and from 25 psu to 5 psu immediately. Hemolymph osmolality of the crabs in each salinity treatment was measured within 3, 6, 12, 24 and 72 hours as well as 7 days after the exposure to salinity changes. The results showed that the crabs were hyperosmoregulators at salinities of 5, 15 and 25 psu. After acute salinity changes, hemolymph osmolality reached and was constant within 12 and 72 hours after exposure to the salinity of 15 psu and 5 psu respectively. The results demonstrated that *S. olivacea* had well adapted to salinity changes in term of hypo-osmotic shock. Furthermore, different salinity levels of hypo-osmotic shock can also affect osmoregulatory performance of the crabs. The crabs that faced with the lower amplitude of salinity changes showed well responses compared with the higher amplitude.

Introduction: Coastal regions, mangroves and estuaries can be considered as extreme environments due to environmental fluctuations especially salinity. Estuarine animals generally experience with short-term and long-term fluctuations of salinity that can be caused by tides and freshwater runoff[2]. Several studies have been reported that salinity changes can affect various physiological responses of some aquatic animals especially osmoregulation[29]. Thus, osmoregulatory adaptations and acclimations are necessary for living in salinity fluctuating areas as mangroves and estuaries.

Aquatic crustaceans inhabit in various salinity environments such as freshwater, brackish water and fully seawater. They have diverse osmoregulatory adaptations and responses to environmental salinity[28]. According to the studies on crustacean osmoregulation, the exposure to reduced salinities lead to changes in ionic concentrations in their hemolymph especially Na^+ and Cl^- ions. That changes directly influence to their osmotic concentrations or osmolality of hemolymph[3]. Moreover, salinity changes could also alter their cell and body volume. Due to salinity problems, active ion uptake via gill epithelia are one of the crucial mechanisms for maintaining their osmotic and volume regulations for crustaceans[12]. Crustacean gills play important roles in osmoregulation in terms of active ion transport. Gill epithelium consists of ionocytes or osmoregulatory cells which play roles in transbranchial ion transport[9]. Na^+ and Cl^- ions are pumped into hemolymph vessel via activities of Na^+/K^+ ATPase that are located at the basolateral membrane of ionocytes[13]. This can demonstrate that Na^+/K^+ ATPase directly play important roles in osmotic and ionic regulations of crustaceans. Moreover, osmoregulation is an energetic process for the activities of Na^+/K^+ ATPase[19].

The mud crab *Scylla* is a commercially and ecologically important crab that distributes throughout Indo-Pacific Ocean and South China sea. These crabs have high commercial values and high marketing demand in tropical Asia and subtropical Asia[18]. Moreover, they also play important roles as predators and scavenger in mangrove ecosystems[32]. The mud crabs *Scylla olivacea* (Herbst, 1796) are one of mud crabs in genus *Scylla* which are one of the

dominant mud crabs in Thailand. *S. olivacea* inhabits in intertidal mangroves and estuaries where they may face salinity challenges regarding to tides and freshwater runoff[17]. According to their habitats, physiological adaptations and acclimations to salinity changes might be necessary for these crabs for coping with salinity fluctuations. Several studies had been reported that salinity had influences on *S. olivacea* in various aspects. The high mortality of megalopa stage and young crab *S. olivacea* were found when subjected to low salinities[10,15]. Moreover, salinity levels also affected to ovarian development of the female *S. olivacea*[1]. However, the study of physiological responses to reduced salinities in adult *S. olivacea* still has little information especially their osmoregulation.

Generally, salinity regimes in estuaries are controlled by tides and freshwater runoff. However, salinity changes in term of reduced salinities might be resulted from anthropogenic effects. Releasing freshwater from agricultural areas and industries as well as river-mouth dams could cause acute salinity changes in term of hypo-osmotic shock. Hypo-osmotic conditions that were caused by acute changes had been defined as the severe threat to ecological structures and functions in estuarine and coastal regions[22]. Moreover, drastically reduced salinity is one of critical problems in mud crab farms that crab ponds are connected to riverine mangroves or estuarine areas during rainy season. Hypo-osmotic shock can cause to physiological stresses and mortality in estuarine animals. Therefore, this study aims to examine effects of hypo-osmotic shock on physiological responses of *S. olivacea* in term of their osmoregulation. This study may provide a better understanding about physiology of mud crabs that may provide implications for ecological studies and aquaculture of mud crabs in the future.

Methodology:

Experimental animals and preparation: The males *S. olivacea* as adult stage were provided from a private standard farm in Samut Sakhon province, Thailand. Body weight of the crabs was in a range of 150-250 g. The crab species was confirmed species using morphological characters. After that, the crabs were carried to the laboratory at Department of Marine Science, Faculty of Science, Chulalongkorn University, Bangkok. The experimental crabs were individually acclimated in plastic containers with aerated seawater as salinity of 25 psu for one week prior to the experiment. Artificial seawater was utilized throughout the acclimation and experimental periods. The crabs were fed with fish meat throughout the acclimation periods. Seawater in each plastic container was changed 100% every day for preventing elevated ammonium ions. Seawater temperature was in a range of 26-28 ˚C.

The experimental design and protocols: After the acclimation period, only healthy male crabs were used in the experiment. The crabs were transferred immediately into hypo-osmotic conditions including 5 and 15 psu. As mentioned earlier, artificial seawater was applied throughout the experimental period. The crabs that were individually held at salinity of 25 psu were considered as the control group. The animals were fed with fish meat throughout the experiment. Parameters such as salinity, ammonium ion and temperature in each plastic container was randomly checked and controlled every day. Hemolymph samples of the crabs were collected within 3, 6, 12, 24, 72 hours and day 7 after exposure to the hypo-osmotic shock (3 replications per time). Repeated animals were not used in each collecting time to avoid stresses affecting physiological responses.

For hemolymph collecting, the crabs were anesthetized on ice for 15-20 minutes for minimizing painful and stresses. Then, hemolymph samples were withdrawn by inserting a 23.5 g needle with a syringe through arthropodial membrane at the base of swimming legs. Hemolymph samples were collected in a microcentrifuge tube and stored at -20 ˚C for further analyses. A volume of 20 µL of hemolymph samples was measured osmolality by using freezing point osmometer (Fiske® Micro-Osmometer model 210). Hemolymph osmolality was expressed in term of mOsm/kg H_2O. The experimental protocols in this study were approved

by the Animal Care and Use Committee of Faculty of Science, Chulalongkorn University (Protocol review No. 1823014).

Statistical analysesf: The differences in hemolymph osmolality among the salinity treatments were analyzed by one-way ANOVA, followed by the multiple comparison test. Tukey's HSD test was performed for data which had the homogeneity of variances. In contrast, the Games-Howell's test was used for data without the homogeneity of variances. Statistical differences were accepted at $p<0.05$.

Results and Discussion: After the crabs *S. olivacea* had exposed to hypo-osmotic shock including salinities of 5 and 15 psu, the crabs showed different responses of hemolymph osmolality. When the crabs were immediately transferred from 25 psu to 15 psu. Hemolymph osmolality of the animals dramatically decreased within 3 and 6 hours after exposure to the salinity change (Figure. 1). Hemolymph osmolality of the crabs at 3 and 6 hours after the salinity changes was significantly lower than the control group. (ANOVA; $F=11.66$, $p<0.05$, Games-Howell test, $p<0.05$). After that, their hemolymph osmolality increased and was approximately equal to the control group within 12 hours. After 12 hours, hemolymph osmolality of the crabs at 15 psu was not significantly different compared with the control group (25 psu) (ANOVA; $F=11.66$, $p<0.05$, Games-Howell test, $p>0.05$). Moreover, the crabs which were held at salinities of 15 psu and 25 psu showed higher in their hemolymph osmolality than seawater osmolality. (seawater osmolality at 15 psu = 507 mOsmo/kg H_2O; seawater osmolality at 25 psu = 744 mOsmo/kg H_2O)

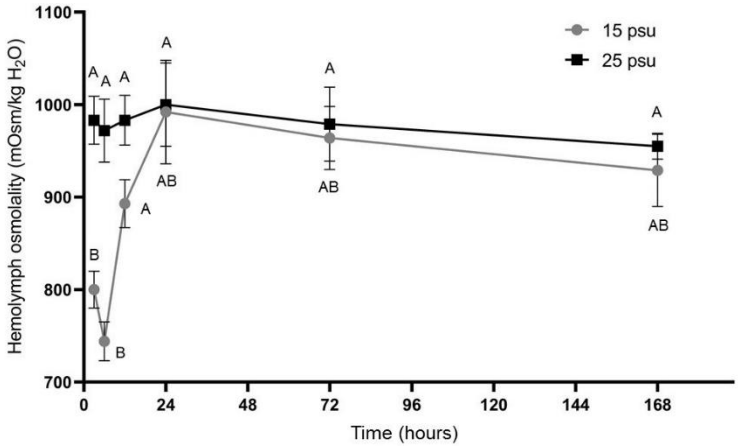

Figure. 1 Hemolymph osmolality of males *S. olivacea* were subjected to 15 psu (grey line) and 25 psu (black line). Data are mean ± S.D. Different letters above data indicate statistically significant differences by Games-Howell test ($p<0.05$).

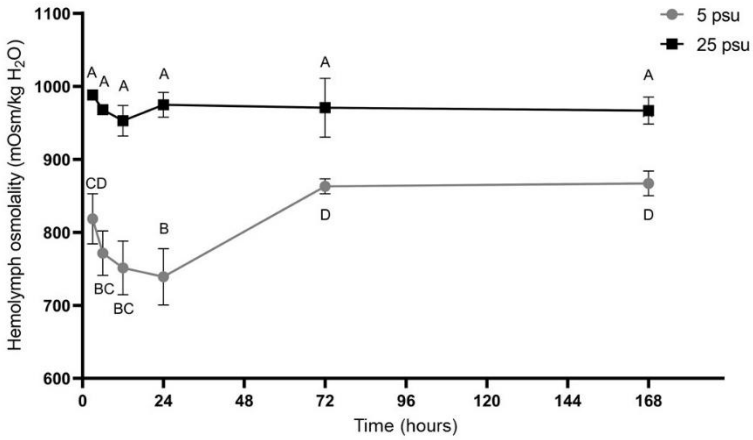

Figure. 2 Hemolymph osmolality of males *S. olivacea* were subjected to 5 psu (grey line) and 25 psu (black line). Data are mean ± S.D. Different letters above data indicate statistically significant differences by Tukey's HSD test (p<0.05).

Hemolymph osmolality of the animals which were transferred from 25 psu to 5 psu rapidly decreased within 24 hours (Figure. 2). After that, their hemolymph osmolality increased and was constant within 72 hours after exposure to hypo-osmotic shock (ANOVA; F=40.72, p>0.05, Tukey's HSD test, p>0.05). After 72 hours, the crabs which were experienced with hypo-osmotic shock also showed significantly lower in hemolymph osmolality compared with the control group (25 psu). However, hemolymph osmolality of the crabs at both 5 and 25 psu had higher than seawater osmolality. (seawater osmolality at 5 psu = 170 mOsmo/kg H_2O; seawater osmolality at 25 psu = 744 mOsmo/kg H_2O)

Acute salinity changes are one of environmental fluctuations that estuarine animal can be encountered. Thus, physiological responses and adaptations are very important for estuarine and intertidal crustaceans[21]. The results showed that *S. olivacea* exhibited the rapid decrease of their hemolymph osmolality when exposed to the hypo-osmotic shock (Figure. 1 and 2). The decrease of hemolymph osmolality may be caused by ionic leakage from their hemolymph to ambient environments. Loss of inorganic ions is directly a result of a dramatically decrease of hemolymph osmolality in crustaceans[4,6]. Hemolymph osmolality of the crabs increased and was constant within 12 and 72 hours after they had transferred to 15 psu and 5 psu respectively (Figure. 1 and 2). The increase of hemolymph osmolality can be resulted from their osmoregulatory responses. Crustaceans respond to maintain their osmotic and ionic concentrations by pumping ions from ambient environments into their hemolymph. Particularly, the crabs that were subjected to 15 psu rapidly stabilized their hemolymph osmolality and showed high osmolality in the initial times (within 24-72 hours). This might reflect short-term acclimation of the crabs to counteract a large reduction of osmotic and ionic concentrations during exposure to reduced salinities. The previous studies indicated that elevated hemolymph osmolality of crustaceans after exposure to reduce salinities were results of gill Na^+/K^+ ATPase activities. Na^+, Cl^- and K^+ ions were pumped into hemolymph space by activities of Na^+/K^+ ATPase that located on gill epithelia[13,25]. Increased activities of Na^+/K^+ ATPase were mostly detected when animals exposed to low salinities. That could indicate important roles of gills and energetic costs of *S. olivacea* in their osmoregulation at low salinities according to high activities of Na^+/K^+ ATPase [14,19,24].

Regarding to osmoregulatory responses of *S. olivacea*, the results indicated that the crabs *S. olivacea* were hyperosmoregulators. They showed higher in hemolymph osmolality than seawater osmolality in salinities of 5, 15 and 25 psu. This osmoregulatory pattern was closely with other crabs in *Scylla* that were reported in *S. serrata*[26] and *S. paramamosain*[7].

Moreover, hyperosmoregulation at the salinity below 30 psu was also found in many crustaceans that lived in estuaries and intertidal habitats e.g. *Hemigrapsus nudus*[8] and *Penaeus chinensis*[6].

S. olivacea showed constant hemolymph osmolality within 12-72 hours after exposure with hypo-osmotic shock could indicate well responses to acute salinity changes. The results are similar with several previous studies that *S. serrata* was able to maintain their hemolymph osmolality within a range of 24- 72 hours after salinity changes[5,30]. In *S. paramamosain*, the previous study found that these mud crabs had better responses to salinity changes compared with *S. serrata* in the previous studies and with *S. olivacea* in the present study. Hemolymph osmolality of mud crabs *S. paramamosain* was constant within 6 hours after exposure with salinity change[19]. Moreover, the current study also found that different levels of hypo-osmotic shock had influence on the osmoregulatory responses of *S. olivacea*. The crabs that were immediately exposed to 5 psu showed delayed responses for maintaining hemolymph osmolality compared with exposure to 15 psu. The results may indicate that the high amplitude of reduced salinities may lead to more physiological stress compared with the lower amplitude of salinity changes for *S. olivacea*.

The differences in osmoregulatory responses of each species may reflect their microhabitats in estuarine areas. Generally, four species of mud crabs *Scylla* have overlapping habitats in estuarine environments. However, some study also suggested that they may show diffrential microhabitats preference. *S. olivacea* preferred to live in intertidal mangroves while *S. serrata* mostly found in coastal water where have higher salinity[11,16]. In contrast, *S. paramamosain* mostly preferred estuarine conditions, they can be found throughout mangrove and estuarine areas[18]. Thus, well responses to salinity changes of *S. paramamosain* may explain their microhabitats and the widely distribution within estuarine conditions.

Intrinsic factors of the experimental animals e.g. sex and body size may influence on physiology of animals. In the present study, adult males *S. olivacea* survived without the mortality throughout the experiment at both salinities of 5 and 15 psu. The results were different from a previous study that LC50 of adult females *S. olivacea* was approximately identified at salinity of 5 psu within 72 hours[1]. The different results may reflect that adults *S. olivacea* have sexual polymorphism in term of salinity adaptations. Males *S. olivacea* seem to have higher salinity tolerance rather than female crabs. The sexual polymorphism in osmoregulation have also been reported in some crustaceans which lived in estuarine environments. Virtually, males showed higher osmoregulatory responses than females e.g. *Chasmagnathus granulatus*[23]. Therefore, further study on the osmoregulation in the mub crab species will be required to complete our understanding on sexual polymorphism on osmoregulatory homeostasis.

According to the results, males *S. olivacea* exhibited abilities for maintaining their osmotic regulations within several days after exposure to acute salinity changes. However, low salinities could cause physiological stresses due to high metabolic demand for their osmoregulation[31]. Moreover, salinity fluctuations especially reduced salinities were also considered as problems in crustacean aquaculture. Reduces salinities and high frequency of salinity changes could affect survival rates and growth as well as physiological energetics of aquatic crustaceans[28]. Regarding to previous studies, aquatic crustaceans that were subjected to low salinities and frequently salinity changes mostly showed low growth rate and feed conversion ratio (FCR). Poor growth rate at low salinities may be resulted from less energy budgets for their somatic production. The most proportion of energy is allocated for supporting osmoregulation which is a high energetic cost [27,33]. Overall, the results demonstrated that *S. olivacea* was an osmoregulator. The crabs might get physiological stress and had high energy expenditure for coping with extreme low salinities. Therefore, salinity levels should be concerned and checked frequently in mud crab aquaculture especially in

natural ponds to prevent adverse effects to the animals and may improve the quality and quantity of the animals.

Conclusion: The present study showed that males *S. olivacea* were osmoregulating crabs which had well osmoregulatory responses to hypo-osmotic shock. The crabs were able to maintain their hemolymph osmolality within 12 and 72 hours after exposure to hypo-osmotic shock at 15 and 5 psu respectively. Moreover, the crabs that subjected to the higher amplitude of reduced salinity showed better response compared with the lower amplitude. The response of hemolymph osmolality to acute salinity changes of *S. olivacea* could reflect their adaptations in term of osmoregulation that allowed them to survive in salinity fluctuating areas as mangroves.

References:

1. Amin-Safwan A, Muhd-Farouk H, Nadirah M, Ikhwanuddin M. Pak J Biol Sci. 2016;19(5): 219-226.
2. Bussell JA, Gidman EA, Causton DR, Gwynn-Jones D, Malham SK, Jones MLM, Reynolds B, Seed R. J. Exp. Mar. Biol. Ecol. 2008;358:78-85.
3. Castille FLJr, Lawrence AL. Comp. Biochem. Physiol. Part A: Mol. Integr. Physiol. 1981;68:75–80.
4. Chen JC, Chen CT. Comp. Biochem. Physiol. 1996;114C:35–38.
5. Chen JC, Chia PG. Comp. Biochem. Physiol. 1997;117A:239–244.
6. Chen JC, Lin JL. Mar. Biol. 1994;120:115-121.
7. Chung KF, Lin HC. Comp Biochem Physiol A Mol Integr Physiol. 2006;144(1):48-57.
8. Corroto FS, Holliday CW. Comp. Biochem. Physiol. 1996;113A:361-368.
9. Freire CA, Onken H, McNamara JC. Physiol. A Mol. Integr. Physiol.2008;151(3):272-304.
10. Gunarto G, Parenrengi A. J. Aquac. Res. Development. 2014;5(5):1-4.
11. Hamasaki K, Matsui N, Nogami M. Fish Sci. 2011;77:49–57.
12. Henry RP. Annu. Rev. Physiol. 1996;58:523-538.
13. Henry RP, Lucu C, Onken H, Weihrauch D. 2012. Front. Physiol. 2012;3:431.
14. Holliday CW. J. Exp. Zool. 1985;233:199-208.
15. Jantrarotai P, Taweechuer K, Pripanapong S. Kasetsart J. (Nat. Sci.). 2002;36:278-284.
16. Keenan CP, Davie PJF, Mann DV. Raffles B. Zool. 1998;46(1):217-245.
17. Lebata MJHL, Le Vay L, Walton ME, Biñas JB, Quinitio ET, Rodriguez EM, Primavera JH. Mar. Freshwater Res. 2009;60(1):
18. Le Vay L. Asian Fish. Sci. 2001;14:101-111.
19. Lucu C, Towle DW. Comp. Biochem. Physiol. A Mol. Integr. Physiol. 2003;135(2):195-214.
20. Lu JY, Shu MA, Xu BP, Liu GX, Ma YZ, Guo XL, Liu Y. Fish. Sci. 2014;81(1):175-186.
21. McNamara JC, Faria SC. J. Comp. Physiol. 2012;182B:997-1014.
22. Montague A, Ley A. Estuaries. 1993;16:703-717.
23. Novo MS, Miranda RB, Bianchini A. J. Exp. Mar. Biol. Ecol. 2005;323:118–137.
24. Palacios E, Bonilla A, Luna D, Racotta IS. Aquaculture. 2004;234:497–511.
25. Péqueux A. J. Crustac. Biol. 1995;15:1–60.
26. Romano N, Wu X, Zeng C, Genodepa J, Elliman J. Mar. Biol. Res. 2014;10(5):460-471.
27. Romano N, Zeng C. Aquaculture. 2006;260:151–162.
28. Romano N, Zeng C. Aquaculture. 2012;334-337:12-23.
29. Rowe CL. Comp. Biochem. Physiol. A. 2002;132:341-351.
30. Tangkrock-Olan N, Ketpadung R. Asian J. Biol. Educ. 2010;4:8-14.
31. Vilas M, Balasaheb K. Int. Res. J. Environment Sci. 2014;3(10):38-42.
32. Viswanathan C, Raffi SM. India. Saudi. J. Biol. Sci. 2015;22:698–705.
33. Ye L, Jiang S, Zhu X, Yang Q, Wen W, Wu K. Aquaculture. 2009;290:140–144.

Acknowledgements: We would like to thank Science Achievement Scholarship of Thailand (SAST) for supporting this research. We are particularly grateful to Samut Songkhram Fishery Research station of Kasetsart University, Samut Songkhram province for finding and supporting experimental animals in this research.

B5_006_OF: OVIPOSITIONAL PREFERENCES AND LARVAL DEVELOPMENT OF TAWNY COSTER *Acraea terpsicore* (LINNAEUS, 1758) (LEPIDOPTERA: NYMPHALIDAE) ON FOUR PASSION VINES

Chitsanuphong Phanthian[1,2], Chatchawan Chaisuekul[2,*]
[1]Zoology Program, Department of Biology, Faculty of Science, Chulalongkorn University, Bangkok 10330, Thailand
[2]Center of Excellence in Entomology: Bee Biology, Biodiversity of Insects and Mites, Department of Biology, Faculty of Science, Chulalongkorn University, Bangkok 10330, Thailand
*e-mail: chatchawan.c@chula.ac.th

Abstract: Acraea terpsicore (Linnaeus, 1758), a common butterfly in SE Asia that utilized wild passion vine plants (genus *Passiflora*) as host plants, is being exposed to several exotic fruits and ornamental *Passiflora* plants due to the expansion of urbanization and globalization. The increasing choices of passion vine plants may affect the preferences of this butterflies. Therefore, this study aimed to compare the ovipositional preferences of adults *A. terpsicore* on 4 passion vine plants between one wild host plant, *Passiflora foetida*, and three exotic cultivated plants, *P. edulis*, *P. x alata-caerulea* and *P. x coccinea-caerulea*, as well as to compare the survivorship and developmental times of *A. terpsicore* caterpillars on these passion vine plants. Wild *A. terpsicore* females were caught from eastern central plain of Thailand for the oviposition preferences experiment in laboratory. From a total of 27 wild mated females, only 8 females oviposited in this study. Most eggs from the total of 457 eggs were found on *P. edulis* (60.54%) and *P. foetida* (33.88%), while limited number of eggs were found on *P. x alata-caerulea* (2.89%) and *P. x coccinea-caerulea* (2.69%). All of caterpillars hatched from eggs on *P. edulis* (100.00%), but they died within 24 hours. In contrast, the caterpillars on *P. foetida* had the lowest hatching rate (11.59%), but most of hatched caterpillars can complete the development to adult. Only caterpillars on *P. foetida* and *P. x coccinea-caerulea* can completed the development to adult. The developmental times of caterpillars on these two plants were not significantly different (Wilcoxon rank sum test with continuity correction, $W = 141$, *P-value* = 0.1012), but pupal stage on *P. foetida* was significantly longer than *P. x coccinea-caerulea* ($W = 169.5$, *P-value* = 0.0016**). Caterpillars of *A. terpsicore* can utilize some exotic plant, *P. x coccinea-caerulea*, probably due to similar morphologies and chemical profile to wild host plant, *P. foetida*.

Introduction: Due to urbanization and globalization, the proliferation of exotic plants has been accelerating and subsequently impacting native flora and fauna. Many exotic plants have been introduced into the new landscapes and replace of native plants for many reasons.[1,2] Some exotic plants have been hybridized and cultivate for increase the yield of productivity or modify the phenotypes of plants.[2] Currently, plants in family Passifloraceae, especially passion vine plants (genus *Passiflora*), had been introduced into Indo-Malayan realm, including Thailand, from Neotropical biogeographic realm for long time and hybridization by plant breeders as the horticultural exotic fruits and cultivated exotic ornamental flowers.[3] Plants in family Passifloraceae have highly evolutionary arm races with butterflies in subfamily Heliconiinae, especially in *Heliconius* spp. which is native to Neotropical realm.[4] On the other hand, butterflies in this subfamily are worldwide distributed and some also have host plants preferences on passion vine plants. Naturally, butterflies have the different level of host plants specialization and preferences according to evolutionary arms race between butterflies and host plants that affected from nutrient content and chemical content in plants leaves.[4,5,6] Moreover, host plants also exhibit the cues which can be used for mate searching in these butterflies.[7] The host plants utilization and preferences of adult butterflies can affect the survivorship of caterpillars and fecundity of those butterflies in next generation.[8] From these reasons, host plant is the most important aspect in microhabitat that will directly affect

to the whole life of butterflies. The presence of exotic plants affect the host plants utilization and preferences of butterflies, especially those exotic plants with close-relationship with wild host plants of these butterflies.[9] Many researches have reported to the shifting of host plants utilization and preferences of butterflies to exotic plants that related with native host plants instead of their own wild host plants, for examples; *Iphiclides podalirius* and *Danaus plexippus* can utilize exotic host plants with the similar performance to native host plants.[10,11,12] In the conservation practice, exotic plants are beneficial to the threatened butterflies in case of habitat loss and extinction of native host plants.[13]

Butterflies in genus *Acraea* have distributions in old world, especially in Afrotropic realm.[14] Most of these butterflies have been classified as polyphagous butterflies that can consumed diverse host plants, including plants in family Passifloraceae, but some species had been recorded to utilized only plants in this family as host plants, including exotic plants in genus *Passiflora.*[14] Butterflies in genus *Heliconius*, a new world group of butterflies, have been studied about performance and preference of adult and caterpillar stages with plants in family Passifloraceae, but few butterflies in genus *Acraea* have been studied, especially the relationship with exotic plants.[3] In Indo-Malayan and Australasia biogeographic realm including Thailand, *Acraea terpsicore* is a very common butterfly, and it originated in India and Sri Lanka, then spread to Southeast Asia and arrived Australasia realm in the past few decades.[15,16] Because of wide distribution of this butterfly species, it has many recorded host plants, including passion vine plants, and it was considered as polyphagous butterfly.[16] Currently, *Passiflora foetida* is recorded as a wild and main host plant of *A. terpsicore*. The ability of host plants shifting and preferences of *A. terpsicore* with passion vine plants can affect the increasing number of passion vine plants in many aspects. This study aimed to compare the ovipositional preferences of adults *A. terpsicore* with passion vine plants and compare the larval performance of caterpillars on passion vine plants in aspects of survivorship and developmental times. We hypothesized that *A. terpsicore* preferred and utilized passion vine plants that have the similar phenotypes to its wild host plants, *P. foetida.*

Methodology: Four passion vine plants*, Passiflora foetida* (a wild *Passiflora* host plants), *P. edulis* (a cultivated *Passiflora* crop plants) *P. x alata-caerulea* (a cultivated *Passiflora* ornamental plant) and *P. x coccinea-caerulea* or *P.* 'Lady Margaret' (a cultivated *Passiflora* ornamental plant), were tested for multiple ovipositional preference choices experiment and larval development of *A. terpsicore*.

Multiple ovipositional preference choices experiment: Ovipositional preferences experiments in laboratory were conducted using wild-caught females of *Acraea terpsicore* from Saraburi (Chulalongkorn University: Center of Learning Network for the Region (CU: CLNR), 14°31'N 101°01'E) and Prachinburi (14°08'N 101°42'E). Sphragis (mating plug) on genital opening of each female was verified to ensure female was already mated. Wild-caught females were kept in cool box for transportation (about 10 Celsius) and used for the experiment in the same day (no later than 8 hours) at Chulalongkorn University, Bangkok, Thailand. This experiment was conducted in 30x30x30 cm^3 transparent acrylic boxes and each female was housed singly. Similar sized plant branches from each of the four tested plants, about 20 cm in length, were placed in 180 ml plastic cups that filled with floral foam (Oasis®) and water, separated by species (1 branch per cup and the leaves on branch were removed until 5 leaves remained). Plastic cups were placed at corner of experimental box in equal distances about 20 cm. The order of plant's branches was randomly assigned in each experimental replication. 9 cm-diameter plastic petri dish, which had 9 cm diameter filter paper filled with 10 ml 0.9% normal saline was placed in the middle of experimental box, and in the middle of the petri dish had 30 ml plastic cup, which filled with cotton wool and 30 ml 20% glucose-water solution as foods for females *A. terpsicore*. The boxes in this experiment was illuminated with 18W fluorescent lamp (Toshiba® 18W daylight fluorescent lamp, 1090 lumen), 15 cm above the boxes

for 24 hours daily during experiment with temperature at 26.36 ± 0.17 °C and humidity at 64.31 ± 0.35 %. Normally, light is the crucial factor for stimulating butterflies to oviposit eggs.[22,23] Therefore, we assumed that the illumination at 24 hours per day will be most effective for stimulating butterflies to oviposit eggs in limited times. Female butterflies were kept in the experiment for 72 hours. After the experiments was terminated in each round, record the amount of eggs in each branch of plants.

Larval development of Acraea terpsicore: Newly oviposit eggs were kept in 9 inch diameter plastic petri dish until they hatched to be caterpillars. Caterpillars were then separated and housed in cluster of 10 to 15 individuals in 30x30x30 cm^3 transparent acrylic boxes and they were provided the corresponded plant materials that they were oviposited during the eggs stage. Then, hatching rate of eggs and survival rate of caterpillars in the first 24 hours after hatched from eggs were recorded. We left the unhatched eggs in plastic petri dish until 10 days for confirmed the activation of embryos in unhatched eggs. If the 10th day of eggs stage, caterpillars had been not hatched from unhatched eggs. These unhatched eggs were classified to inactivated eggs. Excess amount of host plant materials was put in the box and changed daily. Survivorship of caterpillars was checked daily during the change host plants to minimize any disturbance to caterpillars and reduce the stress of caterpillars until they develop into chrysalises. Developmental time (days) of each stage of each individual was recorded. The boxes were under the same condition as the multiple ovipositional preference choices experiment.

Statistical analysis: The proportion of oviposit females to non-oviposit females on each host plants had been compared. The number of oviposit eggs on each plant species had been tested for normality by Shapiro-Wilk normality test. Oviposit eggs and developmental times of each stage were calculated to mean, standard deviation and standard error. Due to the non-parametric data of the oviposit eggs, larval developmental time and pupal development time (Shapiro-Wilk normality test, W = 0.7863, 0.7189 and 0.8174, respectively, *P-value* = 0.0204*, 0.0000*** and 0.0001***, respectively), the number of oviposit eggs on each plant species of multiple oviposition preference choices experiment and developmental times of *A. terpsicore* in each stage were analyzed and compared by using Kruskal-Wallis rank sum test and Wilcoxon rank sum test with continuity correction. Statistical analyses were performed using the *base, stats, ggpubr* and *ggplot2* packages in R version 3.6.0.

Results and Discussion: From the 27 wild females *A. terpsicore*, only 8 females oviposited on plant branches provided in the experiment (33.33% oviposit wild females) and each female oviposited on only 1 plant species in this study. The most frequent of oviposition was found on *P. foetida* followed by *P. edulis* and female oviposited on *P. x alata-caerulea* and *P. x coccinea-caerulea* on 1 individual on each plant species (Figure 1.) The total of 484 eggs were found on all of 4 passion vine plants in this experiments (Figure 1.). The majority of eggs were found on *P. edulis* (146 ± 48.5 eggs per female or 60.54%) and followed by *P. foetida* (41 ± 31.82 eggs per female or 33.88%). While, few eggs were found on *P. x alata-caerulea* (14 eggs or 2.89%) and *P. x coccinea-caerulea* (13 eggs or 2.69%) (Figure 2.). Even though number of eggs on *P. edulis* were the highest, but the frequency of oviposition was lower than *P. foetida* and the number of eggs and frequency of oviposition on *P. foetida* is also higher than the other 2 plant species.

Although *A. terpsicore* was classified as a polyphagous butterfly, the utilization of *A, terpsicore* on other plants besides *P. foetida* had been not found at sampling sites. Furthermore, other three cultivated plants had been not found within 10 kilometers around the sampling sites. Normally, female butterflies would prefer to oviposit on the host plants that they were imprinted during juvenile stage[7], which we hypothesized in this case is *P. foetida*, a wild host plant. Meanwhile, visual and chemical cues the important to stimulate female butterflies to oviposit eggs.[17,18] First, butterflies can recognize their host plants species and

locations that they complete their development, and come back to mate and oviposit by observing shapes and texture of leaves and height of plants.[4,7,17] Then, females will the confirm the quality and quantity of suitable chemical profiles of plants by chemoreceptors at tarsi, antennae and mouthparts before decide to oviposition to ensure the success development of their offspring.[18,19]

The plant species in this study can be divided into 2 groups based on leaf morphologies, which are a hard-glabrous leaf group with *P. edulis* and *P. x alata-caerulea* and a soft-trichomous leaf group with *P. foetida* and *P. x coccinea-caerulea*. The leaves of soft-trichomous leaf group are covered with hairy trichomes. While, leaves of hard-glabrous leaf group are not covered with trichomes, but covered with thick cuticle layer that affects the toughness of leaves and makes leaves glabrous. The shape of all plants in this study are three-lobed shape leaf, but *P. x coccinea-caerulea* has characteristic of polyphylly that might affect the recognition of females to avoid oviposit on this plant species. While, *P. edulis* and *P. x alata-caerulea* have distinctively different leaf morphologies from *P. foetida*. Nevertheless, the key chemicals group for host plants searching-cues of *A. terpsicore* is cyanogenic glycoside[15], and all of plant species in this study contain cyanogenic glycoside in different forms[22], and possibly could attract females to oviposit. Otherwise, the oviposition of *A. terpsicore* in this study could not be concluded due to the low number of oviposit females and there was not significantly different between plant species (Kruskal-Wallis rank sum test, chi-squared (x^2) = 2.875, df = 3, *P-value* = 0.4113). For the further study, more oviposited females will be required for better results analysis and conclusion.

Total 338 caterpillars were hatched from oviposit eggs of multiple ovipositional preference choices experiment. Most caterpillars were hatched from eggs on *P. edulis* and all of oviposited eggs on *P. edulis* hatched to be caterpillars (293 caterpillars (86.69%), hatching rate = 100.00%). While, some oviposit eggs on *P. x alata-caerulea* and *P. x coccinea-caerulea* were also high hatching rate (13 caterpillars (3.84%), hatching rate = 92.86% and 13 caterpillars (3.84%), hatching rate = 100.00% respectively). In contrast, some caterpillars hatched from oviposit eggs on *P. foetida* (19 caterpillars (5.63%), hatching rate = 11.59%) (Figure 3A). The majority of inactive eggs was found on *P. foetida*, although sphragis was confirmed. The activation of eggs had affected by maternal health and environmental conditions, such as temperature and humidity.[24,25] The in active eggs in this study probably occurred by accidentally erroneous conditions in experimental box or female individuals.

Conversely, all of newly hatched caterpillars on three passion vine plants, *P. foetida*, *P. x alata-caerulea* and *P. x coccinea-caerulea*, can survived through the first 24 hours after hatched from eggs (24 hrs survival rate = 100.00%), except all of caterpillars on *P. edulis* (24 hrs survival rate = 0.00%) (Figure 3B). The hatching rate of eggs on *P. foetida* seem to be the lowest of all plant species in this experiment, but the all of newly hatched caterpillars on *P. foetida* can survived through the first 24 hours after hatching. In contrast, although the hatching rate of caterpillars on *P. edulis* was 100.00%, but all newly hatched caterpillars on *P. edulis* died within the first 24 hours after hatching. Moreover, the hatching rate of eggs on *P. x alata-caerulea* was also high and all newly hatched caterpillars could survive through the first 24 hours, but caterpillars on *P. x alata-caerulea* were gradually died later and there were no caterpillars that fed on this plant had developed to chrysalises.

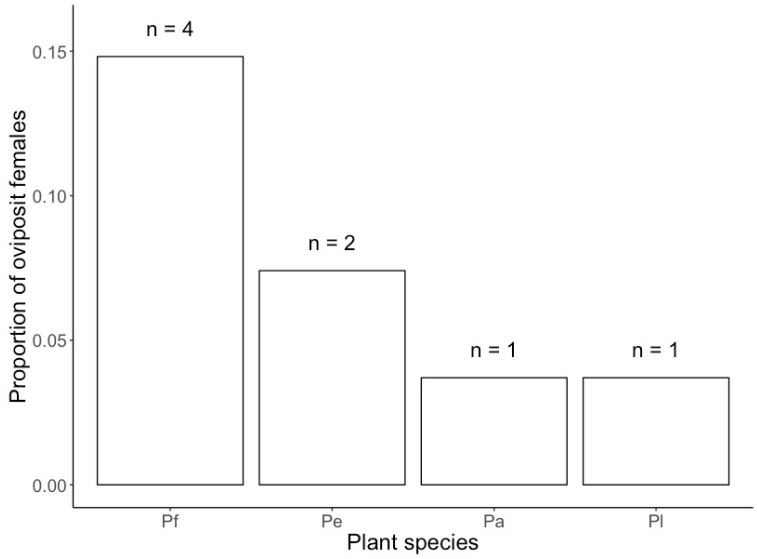

Figure 1. Proportion of 8 oviposit female from 27 wild caught females in multiple ovipositional preference choices experiment. (Pf = *P. foetida*, Pe = *P. edulis*, Pa = *P. x alata-caerulea* and Pl = *P. x coccinea-caerulea*)

Figure 2. Mean number of *A. terpsicore*'s oviposit eggs per female on each plant species in multiple ovipositional preference choices experiment. (Pf = *P. foetida*, Pe = *P. edulis*, Pa = *P. x alata-caerulea* and Pl = *P. x coccinea-caerulea*)

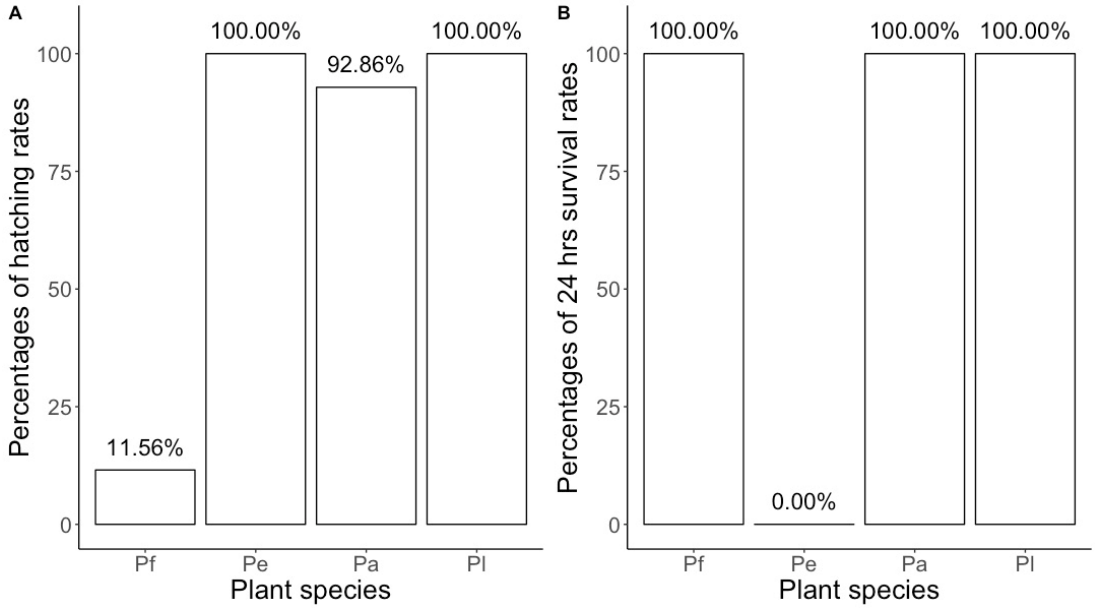

Figure 3. The percentages of (A) hatching rate and (B) survival rate in the first 24 hours of *A. terpsicore*'s newly hatched caterpillars in laboratory (Pf = *P. foetida*, Pe = *P. edulis*, Pa = *P. x alata-caerulea* and Pl = *P. x coccinea-caerulea*)

The developmental times of *A. terpsicore*'s embryos in active eggs on the all plant species were equal at 4 days and not more or less (Figure 4.). Only 16 caterpillars on *P. foetida* and 13 caterpillars on *P. x coccinea-caerulea* can complete the development to be adult butterflies. The total developmental times of *A. terpsicore* on *P. foetida* (31.06 ± 0.53 days) was not significantly different to *P. x coccinea-caerulea* (30.15 ± 0.34 days) (Wilcoxon rank sum test with continuity correction, *W* = 141, *P-value* = 0.1012). The larval stage of *A. terpsicore* on *P. foetida* (20.19 ± 0.43 days) were similar to larval stage on *P. x coccinea-caerulea* (20.08 ± 0.29 days) (Wilcoxon rank sum test with continuity correction, *W* = 103, *P-value* = 0.9810). In contrast, the pupal stage of *A. terpsicore* on *P. foetida*, a wild host plant, (6.88 ± 0.20 days) was significantly longer than pupal stage on *P. x coccinea-caerulea*, an exotic *Passiflora* plant, (6.08 ± 0.08 days) (Wilcoxon rank sum test with continuity correction, *W* = 169.5, *P-value* = 0.0016**) (Figure 4.).

The toughness of leaves in hard-glabrous leaf group can affect the ability of consumption because of mandibles of newly hatched caterpillars of *A. terpsicore* cannot chewed these hard leaves[5], and it caused newly hatched caterpillars on *P. edulis* cannot feed on the leaves of this plant species and died within the first 24 hours after hatched. Although the caterpillars on *P. x alata-caerulea* did not die in the first 24 hours after hatched, they consumed only underneath layers of leaves (Figure 5.) and had low growth rate when compared with caterpillars on *P. foetida* and *P. x coccinea-caerulea*. Finally, the caterpillars on *P. x alata-caerulea* died before becoming chrysalises as the results in this study. When caterpillars feed on soft-trichomous leaves group, they can consume the whole leaves (Figure 5.) and can complete the development. Normally, trichomes have function to protect plants from the settle down of newly hatched caterpillars, but some species of caterpillars can adapt to utilize these trichomes.[3] The newly hatched caterpillars can consume the soft trichomes and gradually invade the layers of leaves matter.[20,21] The presence of trichomes possibly help to increase the survivorship of caterpillars.[3,20,21] From this results, caterpillars

of *A. terpsicore* has ability to utilize the passion vine plants with trichomes that affected from evolutionary arms race between plant in genus *Passiflora* and *A. terpsicore*.
On the other hand, chemicals and nutrients content of leaves is the important aspect of survivorship of caterpillars.[3,5,19] The data of nutrients content of passion vine plants, for examples; carbohydrate, protein and lipid, still are limited. However, the defensive chemical contents of passion vine plants has been presented by many researches, and those researches concluded that defensive chemicals is the key factors to evolutionary arms race and adaptation between caterpillars and host plants.[3,4] The key defensive chemicals in *Passiflora* that affected to evolutionary arms race between plants in this genus and caterpillars in subfamily Heliconiinae is a group of toxins, particularly cyanogenic glycosides.[3] Nonetheless, the same group of plants probably contain the different defensive chemicals profiles that affect specification and survivorship of butterfly.[4,23]

Dhawan et al. (2004) examined the chemical contents in some passion vine plants.[22] The key cyanogenic glycosides of most *Passiflora* in this study have cyclopentenyl structures, for examples; deidaclin in *P. foetida* (simple monoglycoside cyclopentenyl structure), tetraphyllin B sulphate in *P. foetida* and *P. x alata-caerulea*); but the key cyanogenic glycoside of *P. edulis* has aromatic structure.[22] In the case of hybrid plants of *P. x alata-caerulea* and *P. x coccinea-caerulea*, *P. x alata-caerulea* is the hybrid between *P. alata* and *P. caerulea* and *P. x coccinea-caerulea* is the hybrid *P. coccinea* and *P. caerulea*.[2] The defensive chemicals of *P. caerulea* is comprised of high density of tetraphyllin B sulphate and epitetraphyllin B sulphate that are cyclopentenyl structures.[22] Similar to *P. caerulea*, the defensive chemicals of *P. coccinea* has the high density of passicoccin that are also cyclopentenyl structure.[22] In contrast, the defensive chemicals of *P. alata* is comprised of high density of flavonoids.[22] Therefore, *P. x coccinea-caerulea*, a hybrid of *P. coccinea* and *P. caerulea*, possibly contain the high density of cyclopentenyl glycosides and comprising with the morphologies of leaves that allow caterpillars can consumed and survived on *P. x coccinea-caerulea*. In contrast, *P. x alata-caerulea* contain high flavonoid toxins from *P. alata*, and caterpillars cannot detoxify and died later[21] in addition to combination with leaves toughness, caterpillars cannot survive on this plants. Although, *P. edulis* contains different structure of cyanogenic glycoside, caterpillars cannot consume leaves of this plant, probably due to leaf toughness, and died within 24 hours. Leaf toughness affect the survivorship of newly hatched caterpillars because caterpillars cannot settle down on plant's leaves, while the defensive chemicals affect survivorship of caterpillars because caterpillars cannot detoxify unadapt toxins and died from the toxins. However, the effects of chemicals to caterpillars of *Acraea* butterflies still require further studies.

Naturally, short lifespan phytophagous insects (type III survivorship curve), including butterflies, have ability to search suitable host plants to oviposit eggs for the best performance in survivorship of their offspring on host plants according to principle of "mother knows best" or preference-performance hypothesis.[18,26] In this study, females oviposit on other unadapt plant in addition to wild host plants, but caterpillars could not complete their development on *P. edulis* and *P. x alata-caerulea* that probably represented mother does not ever knows best.[27] These females were search for different cues, such as leaf shape and climber plants, instead of external morphologies and chemical profiles. We suggest that females that already oviposit in wild before caught might chose *P. foetida* for oviposit in laboratory, but further researches are remained to be validated. Moreover, female's chemoreceptors might identify cyanide groups with glycoside chemicals in cases of cyanogenic glycoside, but females might not distinguish the structure of cyanogenic glycoside that affect survivorship of their offspring, which further study in the physiology of chemoreceptors of *A. terpsicore* on cyanogenic glycoside could elucidate.

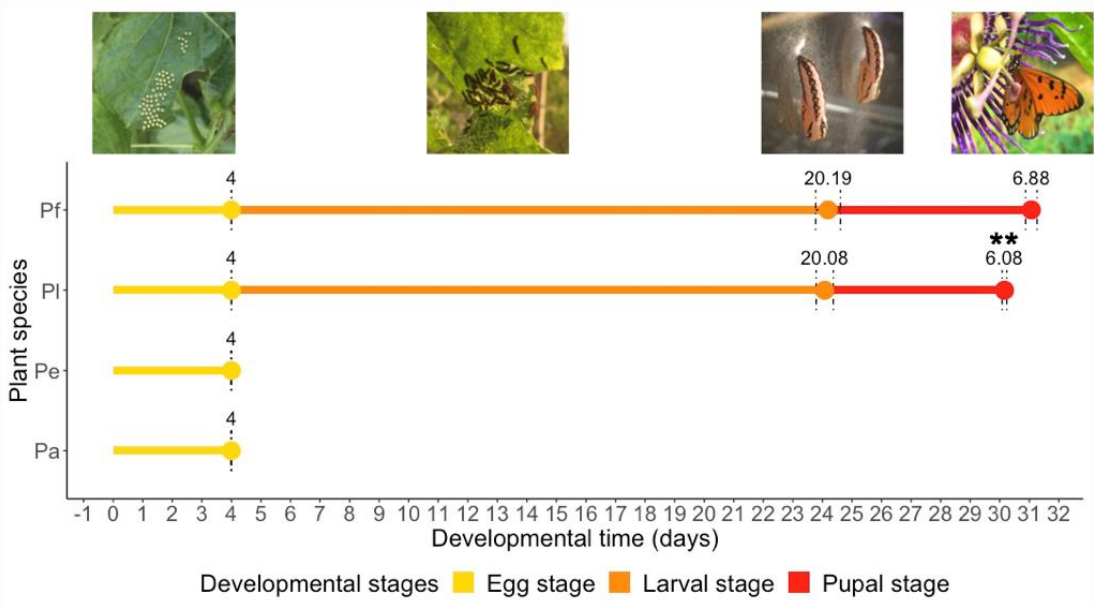

Figure 4. Mean developmental times of each developmental stages of *A. terpsicore* in laboratory on each plant species (Pf = *P. foetida*, Pe = *P. edulis*, Pa = *P. x alata-caerulea* and Pl = *P. x coccinea-caerulea*), ** represented to significantly different between developmental time in pupal stage of *A, terpsicore* on *P. foetida* and *P. x coccinea-caerulea* (Wilcoxon rank sum test with continuity correction, *W* = 169.5, *P-value* = 0.0016**)

Figure 5. Eating patterns of caterpillars on *P. x alata-caerulea* (Left) and caterpillars on *P. foetida* (Right) during the 2nd instar of larval stage.

Conclusion: From the results, caterpillars can utilize some exotic plants with similar morphologies and chemical structures to wild host plants as host plants, and these exotic host plants have equivalent the performance and potential to the wild host plant. The close proximity of different plant species may confuse the female butterflies for correct host plant selection, for example; *P. edulis*, but caterpillars cannot utilize all of passion vine species.

Caterpillars of *A. terpsicore* can utilize only some exotic passion vine plants, *P. x coccinea-caerulea*, which probably have similar morphologies and chemical profile to the wild host plant, *P. foetida*, and they can complete the development within 32 days. In contrast, *A. terpsicore* may be an important pest of some passion vine plants with trichomes and thin leaves. This study is the initial work to explore relationship between plants and heliconiid butterfly in SE Asia, especially exotic and hybrid plants.

References:

1. D'Antonio C, Meyerson LA. Restor Ecol. 2002;10: 703-713.
2. Abreu PP, Souza MM, Santos EA, Pires MV, Pires MM, and Almeida AAF. 2008. Euphytica. 2008;166: 307-315.
3. Hamilton AW, Holttum RE. J Malay Branch Royal Asiatic Soc. 1930;8: 318-329.
4. Castro ECP, Zagrobelny M, Cardoso MZ, Bak S. Biol Rev. 2018;93: 555-573.
5. Thomas CD. Nature. 1990;347: 237-237.
6. Shobana K, Murugan K, Kumar NA. J Insect Physiol. 2010;56: 1065-1070.
7. Estrada C, Gilbert LE. Anim Behav. 2010;80: 231-239.
8. Schultz CB, Dlugosch KM. Oecologia. 1999;119: 231-238.
9. Forister ML, Scholl CF. Am Nat. 2012;179: 805-810.
10. Graves SD, Shapiro AM. Biol Conserv. 2003;110: 413-433.
11. DiTommaso A, and Losey JE. Entomol Exp Appl. 2003;108: 205-209.
12. Stefanescu C, Jubany J, and Dantart J. Anim Biodiv Conserv. 2006;29: 83-90.
13. Severns PM, Warren AD. Anim Conserv. 2008;11: 476-483.
14. Silva-Brandao KL, Wahlberg N, Francini RB, Azeredo-Espin AML, Brown KS, Paluch M, Lees DC, Freitas AVL. Mol Phylogenet Evol. 2008;46: 515-531.
15. Braby MF, Thistleton BM, Neal MJ. Austral Entomol. 2014;53: 288-297.
16. Braby MF, Bertelsmeier C, Sanderson C, Thistleton BM, Schonrogge K, Christie F. Insect Conserv Diver. 2014;7: 132-143.
17. Arikawa K, Takagi N. Zool Sci. 2001;18: 175-179.
18. Renwick JAA, Chew FS. Annu Rev of Entomol. 1994;39: 377-400.
19. Barros HCH, Zucoloto FS. J Insect Physiol. 1999;45: 7-14.
20. Gilbert LE. Science 1971;172: 585.
21. Cardoso MZ. Neotrop Entomol. 2008;37: 247-252.
22. Dhawan K, Dhawan S, and Sharma A. J Ethnopharmacol. 2004;94: 1-23.
23. Engler HS, Gilbert LE. J Chem Ecol. 2007;33: 25-42.
24. Geister LT, Lorenz WM, Hoffmann HK, Fischer K. Front Zool. 2008;5: 10.
25. Geister LT, Lorenz WM, Hoffmann HK, Fischer K. J Comp Physiol B. 2009;179: 87-98.
26. Jaenike J. Theor Popul biol. 1978:14: 350-356
27. Adar S, Dor R. Behav Prosess. 2018;147: 1-4.

Acknowledgements: We would like to thank the Plant genetic conservation project under the Royal initiative of Her Royal Highness Princess Maha Chakri Siridhorn and Chulalongkorn center of learning network for the region, Saraburi campus for providing the grants, facility and accommodation during the study. The research was supported by the 90th Anniversary of Chulalongkorn University Fund (Ratchadaphiseksomphot Endowment Fund).

B5_008_OF: AVIFAUNA IN PUBLIC PARKS IN BANGKOK AND THE EFFECTS OF PARK AREA

Sutanan Pinmaneenopparat, Pongchai Dumrongrojwatthana*
Department of Biology, Faculty of Science, Chulalongkorn University, Bangkok 10330, Thailand
*e-mail: pongchai.d@chula.ac.th

Abstract: In an urbanizing world, public parks in urban landscape could play an important role in diversity conservation especially for birds. Park area was identified as a key factor that influence the bird diversity in the park. But scientific research to prove this is still scarce in Thailand. Thus, this study was conducted to survey bird diversity in 24 public parks in Bangkok metropolis and test relationships between diversity indicators and park area. A total of 71 species of birds were found and 51 species were resident species. *Copsychus saularis*, *Pycnonotus blanfordi*, *Passer montanus* and *Psilopogon haemacephalus* were observed in every park. More than half of the observed species were found less than 33% of study sites. Two species which have conservation status were found in the area. Within 24 parks, resident species richness ranged between 14 to 37 with an average of 22±5. The number of species of resident birds were increase with the park area. In conclusion, the public park in the city can provide habitats for birds including migratory species and even species with conservation status and the large parks tend to harbor more resident bird species.

Introduction: Urban area has been expanding and it causes species diversity loss on a global scale including birds.[1, 2] To conserves diversity in natural habitat, conservationists previously focused on large continuous natural reserve area.[3, 4] However, conservation outside protected area is still required to maintain diversity, especially in urbanizing situation.[5] Public park, main green space in the cities established for providing ecosystem services to citizen, is reported that it could support various of bird species and plays important role for the conservation.[1, 6, 7] When a park is viewed as a green space island in build-up matrix, a larger park typically supports higher bird diversity than a smaller one.[8-12] Yet, there were few studies on birds in urban setting in tropical area, especially in Southeast Asia.[2] Thus, we aim to study about effect of park area on bird diversity in public park in such area.

Bangkok, a capital and the most populated city of Thailand, continues to grow more population and expands its urban area. There are approximately 8,150 parks including street parks, junction parks and monument parks scattered in Bangkok, accounting for 2.4% of the total area. Thirty-seven of them are main public parks managed by the Office of Public Park, Environment Department, Bangkok Metropolitan Administration which all the parks are man-made and the size ranges from 0.5 to 103 ha. Two previous studies in the area found that park area was not an important factor explaining the richness,[13, 14] but there was another study could detect their relationship.[15] However, only few parks were explored and used in the analysis. Therefore, the objective of this paper is to test the correlation between park area and species richness and abundance by using data from 24 main public parks in Bangkok.

Methodology:

Bird census: Twenty-four main public parks varied in size were selected as study sites from throughout Bangkok (Figure 1., Table 1.). Park area was estimated using QGIS 2.18, after manually digitized the park boundary following the official park plan and satellite images taken in 2018. Intensive searching method was used to survey bird composition twice in each park during April to October 2018. To ensure that most of park area would be surveyed, census routes were assigned systematically using grid sampling.[16] The 100 m sampling grids were used for the parks that were smaller than 25 ha (n=19), and 200 m sampling grids were used for the larger parks (n=5). Every grid cell which contained more than 50% of accessible area was surveyed for 5 to 10 minutes. Any bird seen or heard within the park boundary were recorded, except bird flying over the area. Each survey lasted from 6:30 to 10:30 in the morning

and 15:00 to 18:00 in the evening. The censuses were done only on sunny days to avoid biases from weather variation.

Residential status of each species was interpreted by compiling breeding behavior described in reference books[17, 18] and using all year round records from eBird online database.[19] In this study, bird with resident status was a species that presumably breeds in Bangkok area and lives throughout year. Winter visitors, passage migrants and nomadic species were considered as migratory species. The international conservation status of bird species was retrieved from the IUCN Red List of Threatened Species,[20] while the national conservation status of birds was taken from the species list of Bird Conservation Society of Thailand or BCST.[21] Taxonomic data and specific name of the observed species followed Lynx and Birdlife international field guide.[18]

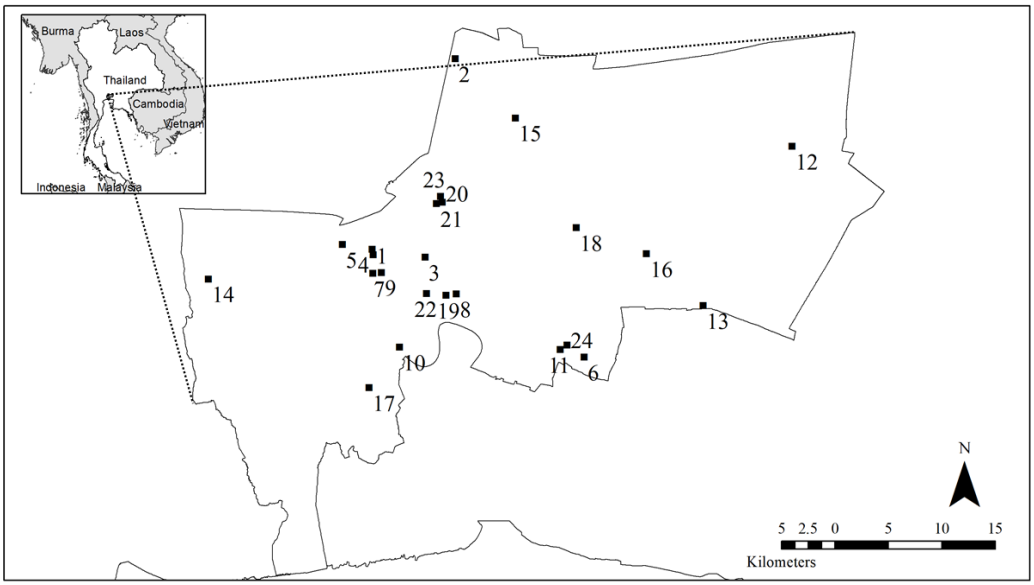

Figure 1. Location of 24 study sites where birds were surveyed in Bangkok, Thailand. (The park description was listed by number in Table 1.).

Data analysis: After we pooled data from the two surveys, resident species richness and resident species abundance were calculated. Only resident bird data was used because their occurrences were directly related to the habitat quality as they use the study sites throughout their lives. We then test for correlation among species richness, abundance and park area with Spearman correlation and explored the effect of park area on resident species richness by using linear regression since it distributed normally.

Table 1. Park area and bird diversity indicators of 24 public parks

	Public park	Area (ha)	Total Richness	Resident Richness	Resident Abundance	Shannon's index
1	Santichaiprakan Public Park	1.4	16	15	50	2.088
2	Rommani Thungsikan Park	2.7	20	19	84	2.348
3	Santiphap Park	3	20	20	37	2.707
4	Suan Luang Rama VIII Park	3.1	18	18	73	2.381
5	Park in Commemoration of H.M. the King's 80 birthday (Bangkok Noi)	3.3	27	26	81	2.777
6	Maha Chakri Sirindhorn's 50th Birthday Park	3.3	16	14	60	2.135
7	Saranrom Park	4	23	19	86	2.455
8	Benchasiri Park	4.2	19	17	204	1.020
9	Rommaninat Park	4.5	19	18	116	2.241
10	Public Park in Commemoration of H.M. the King's 6th Cycle Birthday	4.9	22	21	204	2.079
11	Wanadharm Park	4.9	28	24	130	2.161
12	Nong Chok Park	5.7	27	24	157	2.423
13	Phra Nakhon Park	8	29	24	140	2.511
14	Thawiwanarom Park	8.2	23	21	84	2.666
15	Ram Indra Sport Park	8.6	28	25	107	2.697
16	Her Majesty the Queen's 60th Birthday Park	8.8	24	22	107	2.589
17	Thonburirom Park	11	28	24	131	2.719
18	Seri Thai Park	11	22	18	118	2.350
19	Benchakitti Park	23	25	22	112	2.760
20	Chatuchak Park	26	17	17	148	2.020
21	Queen Sirikit Park	28	31	26	165	2.702
22	Lumphini Park	57	26	24	416	2.152
23	Wachirabenchatat Park	59	34	31	338	2.534
24	Suan Luang Rama IX Park	75	44	37	402	2.717
	Total	368.6	71	51	3543	2.832
	Mean±SD	15±20	24±6	22±5	148±102	2.385±0.382

Results and Discussion:

Species diversity: In total, 71 species were observed across 24 public parks (Table 2.). Fifty-one species were residents, 18 species were migrants to Bangkok area and 2 species unusually occurred in the area which they were possibly released from captivity. *Pycnonotus blanfordi*, *Copsychus saularis*, *Passer montanus* and *Psilopogon haemacephalus* were found in every park. When we classified birds into 3 groups by relative frequency range, more than a half of resident species were found in less than 33% of the sites (28 species), 17 species were observed in more than 66% of the sites and there were only 6 species that had relative frequency between 0.33 and 0.66. From the total of 71 species, there were 2 species with conservation status. *Pycnonotus jocosus* was listed as a vulnerable species (VU) at the national level and *Ploceus hypoxanthus* was rated as a near threatened species (NT) on a world scale.

Looking at the park level (Table 1.), we found that the resident species richness ranged from 14 to 37 species across 24 parks with an average of 22±5 species. Mean resident bird abundance was 147±101 birds per park which was strongly affected by amount of a few urbanophilic species, including *Columba livia*, *Passer montanus* and *Geopelia striata*. These species were also the three most abundant species in total. Santiphap Park had lowest

resident abundance (73 observations) and Lumphini Park had highest abundance (416 observations). Regarding the frequency of the observed species, there were more species with lower frequency compare with the more common species which this finding was consistent with the previous studies[22]. For the common species, they were generally widespread species which can adapt to forage and nest in urban condition, so their population were larger and easier to be detected.

Table 2. Bird species, residential status, relative frequency and abundance from the 24 public parks

Family	Scientific name	Status[a]	Relative frequency (%)	Abundance
Family Columbidae	*Columba livia*	R	96	1626
	Geopelia striata	R	96	536
	Spilopelia chinensis	R	88	183
	Streptopelia tranquebarica	R	42	176
	Treron curvirostra	R	4	6
	Treron vernans	R	33	46
Family Cuculidae	*Cacomantis merulinus*	R	75	40
	Centropus sinensis	R	13	4
	Eudynamys scolopaceus	R	88	88
	Phaenicophaeus tristis	R	4	1
Family Rallidae	*Amaurornis phoenicurus*	R	21	11
Family Ciconiidae	*Anastomus oscitans*	R	13	6
Family Ardeidae	*Ardea intermedia*	M	4	2
	Ardeola bacchus	M	17	4
	Ardeola speciosa	R	21	17
	Bubulcus ibis	R	4	10
	Butorides striata	R	21	21
	Egretta garzetta	R	29	28
	Ixobrychus sinensis	R	8	4
	Nycticorax nycticorax	R	8	4
Family Phalacrocoracidae	*Microcarbo niger*	R	4	1
Family Charadriidae	*Vanellus indicus*	R	4	3
Family Strigidae	*Glaucidium cuculoides*	R	4	6
Family Meropidae	*Merops philippinus*	M	17	11
Family Coraciidae	*Coracias affinis*	R	25	33
Family Alcedinidae	*Halcyon pileata*	M	4	1
	Halcyon smyrnensis	R	4	1
Family Megalaimidae	*Psilopogon haemacephalus*	R	100	164
Family Oriolidae	*Oriolus chinensis*	M	33	20
Family Campephagidae	*Pericrocotus cinnamomeus*	R	21	23
Family Aegithinidae	*Aegithina tiphia*	R	75	90
Family Rhipiduridae	*Rhipidura javanica*	R	96	188
Family Dicruridae	*Dicrurus annectens*	M	4	1
	Dicrurus leucophaeus	M	13	3
	Dicrurus macrocercus	M	13	7
	Dicrurus paradiseus	R	4	1
Family Monarchidae	*Terpsiphone incei*	M	4	1
Family Laniidae	*Lanius cristatus*	M	42	11
Family Corvidae	*Corvus macrorhynchos*	R	58	383

Family	Scientific name	Status[a]	Relative frequency (%)	Abundance
Family Cisticolidae	*Orthotomus atrogularis*	R	4	2
	Orthotomus sutorius	R	71	51
	Prinia inornata	R	33	30
Family Pycnonotidae	*Pycnonotus aurigaster*	R	4	4
	Pycnonotus blanfordi	R	100	361
	Pycnonotus goiavier	R	50	63
	Pycnonotus jocosus[VU]	R	8	2
Family Phylloscopidae	*Phylloscopus coronatus*	M	8	2
	Phylloscopus inornatus	M	4	1
Family Leiothrichidae	*Garrulax chinensis*	C	4	1
	Garrulax leucolophus	C	4	4
Family Sturnidae	*Acridotheres grandis*	R	96	366
	Acridotheres tristis	R	96	498
	Gracupica contra	R	58	76
	Gracupica nigricollis	R	58	103
	Sturnia malabarica	M	4	3
Family Muscicapidae	*Copsychus saularis*	R	100	368
	Cyornis glaucicomans	M	4	1
	Ficedula albicilla	M	8	2
	Ficedula zanthopygia	M	4	2
	Muscicapa dauurica	M	54	20
Family Dicaeidae	*Dicaeum cruentatum*	R	96	154
Family Nectariniidae	*Anthreptes malacensis*	R	63	51
	Cinnyris jugularis	R	79	94
Family Ploceidae	*Ploceus hypoxanthus*[NT]	R	4	1
	Ploceus philippinus	R	4	16
Family Estrildidae	*Lonchura punctulata*	R	29	27
	Lonchura striata	R	17	37
Family Passeridae	*Passer domesticus*	R	50	103
	Passer flaveolus	R	13	6
	Passer montanus	R	100	973
Family Motacillidae	*Motacilla tschutschensis*	M	4	1

[a]Residential status; R = Resident, M = Migrant, C = Possibly released from captivity
[NT]species with Near Threaten status in global level [21]
[VU]species with Vulnerable status in national level [20]

Park area and species diversity: The park area, the number of species and abundance of resident birds were positively correlated ($p<0.05$). A larger park tends to have more resident species and contains more birds than a smaller park (Figure 2.). Moreover, richness has linear relationship with park area ($p<0.001$). This finding was also supported by previous studies in urban area[8-10]. The park with highest number of resident species was the largest one, Suan Luang Rama IX park (75 ha), and the park with fewest bird species was one of the five smallest parks, Maha Chakri Sirindhorn's 50th Birthday Park (3.3 ha). The reasons behind the park area is that large park usually contains various types of habitat which can support bird with different requirements.[23] For instance, the larger parks with dense vegetation area, yard and pond could support some forest species, grassland species and aquatic species, respectively. However, size of each habitat type limits an occurrence of a species by an availability of resource[24]. For example, *Phaenicophaeus tristis* and *Orthotomus atrogularis* are considered as forest edge species. They require relatively large continuous dense tree area compared

with common urban species. A park that has continuous dense tree area smaller than the species requirement should not be able to support these species.

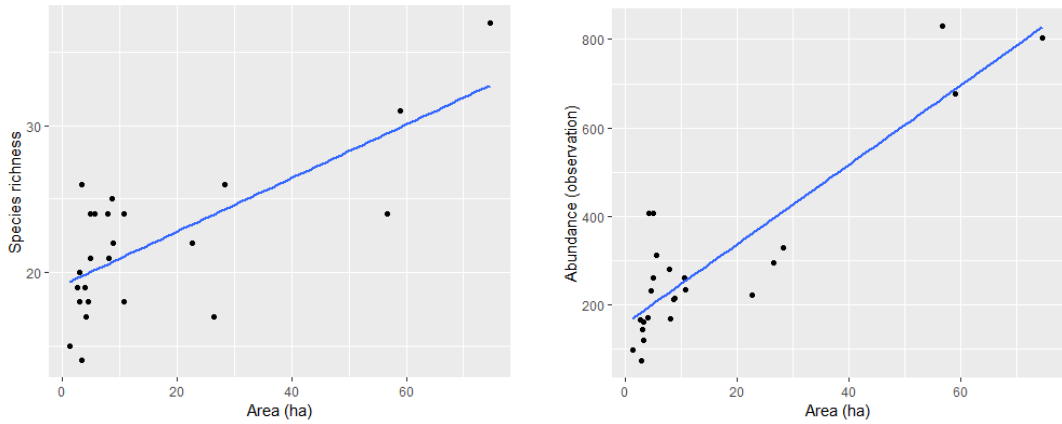

Figure 2. Correlation between park area and species richness (left) and abundance (right).

Role of Bangkok public parks and species diversity conservation: Results from our study showed that public parks in Bangkok could support at least 6.7% of bird species found in Thailand, including both resident and migratory bird species. Most of species found in the site were native to the area. This also supports that the urban bird community in tropical is likely to be dominated by native urban exploiters rather than few exotic species.[25] Among 18 migrants, most of them were non-breeding visitors to Thailand. Some species using public parks in Bangkok as stopover sites of their migration which were *Phylloscopus coronatus*, *Ficedula zanthopygia*, *Dicrurus annectens*, *Cyornis glaucicomans* and *Terpsiphone incei*. Apart from the migrants, *Garrulax chinensis* and *Garrulax leucolophus* which typically found as resident in broadleaf evergreen forest and mixed deciduous forest[18] were observed in Queen Sirikit Park. We believed that they might be unintentionally released from the nearby weekend market where wildlife trading has been reported.[26] Moreover, the public parks in Bangkok also harbors some birds with conservation status. *Pycnonotus jocosus*, a nationally vulnerable species, was observed in 2 parks, Phra Nakhon Park and Her Majesty the Queen's 60th Birthday Park. This species has been trapped for the pet trade and has declined in population which was a cause that it had been listed in the national conservation species account. However, the status on a global scale is least concern due to their occurrence elsewhere. Another IUCN NT species, *Ploceus hypoxanthus* was observed in Suan Luang Rama IX park which is the biggest park in this study. Nevertheless, it was rated it as least concern in Thailand due to its capability to expand the population observed recently.[21]

Implication for conservation and further study: Our results suggest that public parks with larger area could support more bird species because they likely provide more resource in both qualitative and quantitative ways. Therefore, to establish new public park, its size should be as large as possible. Moreover, enlarge the existed parks might be another solution but it is difficult to implement nowadays. However, human disturbance,[8, 27] vegetation composition, structure and pattern[10, 28, 29] and park management[28] were reported from publications across the world as predictors of the avian diversity in urban area. Thus, in the further study, we planned to test relationship between occurrence of each bird species in parks and several park characteristics, including park area, human disturbance and amount of vegetation both inside and outside the park in order to identify major factors and design park for bird and other wildlife conservation in this region.

Conclusion: In this study, the avian diversity in 24 parks in Bangkok area was explored. A total of 71 species were recorded in the area, 51 species were residents. Interestingly, there were one near threatened species according to the IUCN Red List of Threatened Species, and 1 vulnerable species in the national account existing in the urban area. This showed the important role of public park on bird conservation. From our results, park area was an important factor that influence resident species richness in public park. However, there were more factors which has not been tested in the area. Thus, further studies should aim to identify other factors related to bird diversity in public parks.

References:

1. Savard J-PL, Clergeau P, Mennechez G. Landscape Urban Plann. 2000;48:131-142.
2. Marzluff JM, Bowman R, Donnelly R. Avian ecology and conservation in an urbanizing world. New York: Springer Science & Business Media; 2001.
3. Santos T, Telleria JL, Carbonell R. Biol Conserv. 2002;105:113-125.
4. Margules CR, Pressey RL. Nature. 2000;405:243.
5. Fischer J, Lindenmayer DB, Manning AD. Front Ecol Environ. 2006;4:80-86.
6. Blair R. Ecol Soc. 2004;9:2.
7. Urbanová T. J Plan Lit. 2010;24:123-136.
8. Fernández-Juricic E. Ecol Res. 2000;15:373-383.
9. Crooks KR, Suarez AV, Bolger DT. Biol Conserv. 2004;115:451-462.
10. Murgui E. Global Ecol Biogeogr. 2007;16:319-329.
11. Huang Y, Zhao Y, Li S, von Gadow K. Urban For Urban Green. 2015;14:1027-1039.
12. Shih W-Y. Urban Ecosyst. 2018;21:379-393.
13. Soonthornsarathool V. Relationship among birds, plants and park management in Bangkok (in Thai) [Master Thesis]. Bangkok: Chulalongkorn University; 1999.
14. Wongtirawatana S, editor Adaptation of Birds to Bangkok Public Park Habitats (in Thai). The 40th Kasetsart University Annual Conference; 2011; Bangkok: Kasetsart University.
15. Chaiyarat R, Wutthithai O, Punwong P, Taksintam W. Urban Ecosyst. 2019;22:201-212.
16. Sutherland WJ, Newton I, Green R. Bird ecology and conservation: a handbook of techniques. New York: Oxford University Press; 2004.
17. Round P. The Birds of the Bangkok Area. Bangkok: White Lotus; 2008.
18. Treesucon U, Limparungpatthanakij W. Birds of Thailand. Barcelona: Lynx Edicions; 2018.
19. Sullivan BL, Wood CL, Iliff MJ, Bonney RE, Fink D, Kelling S. Biol Conserv. 2009;142:2282-2292.
20. The IUCN Red List of Threatened Species [Internet]. 2019 [cited 19/6/2019]. Available from: http://www.iucnredlist.org/
21. Revised Checklist of Thai birds October 2018 [Internet]. 2018. Available from: https://www.bcst.or.th/wp-content/uploads/2018/11/Checklist_ThaiBirds_2018_for_download.xlsx.
22. Lennon JJ, Koleff P, Greenwood JJD, Gaston KJ. Ecol Lett. 2004;7:81-87.
23. Zanette L, Doyle P, Trémont SM. Ecology. 2000;81:1654-1666.
24. Storch D, Izling AL, Gaston KJ. J Anim Ecol. 2003;72:509-519.
25. Wolff PJ, DeGregorio BA, Rodriguez-Cruz V, Mulero-Oliveras E, Sperry JH. Trop Conserv Sci. 2018;11:1-10.
26. Round P. Nat Hist Bull Siam. 1990;38:1-43.
27. Chang H-Y, Lee Y-F. Urban Ecosyst. 2016;19:257-274.
28. Shwartz A, Muratet A, Simon L, Julliard R. Biol Conserv. 2013;157:285-292.
29. Kang W, Minor ES, Park C-R, Lee D. Urban Ecosyst. 2015;18:857-870.

Acknowledgements: This project was supported by Development and Promotion of Science and Technology Talents Project and Department of Biology, Faculty of Science, Chulalongkorn

University. The authors would like to thank Public Park Office, Environment Department, Bangkok Metropolitan Administration, Bird Conservation Society of Thailand for their support and assistance with this project.

B5_020_PF: DIVERSITY OF FOLIICOLOUS LICHENS ON *Acrostichum aureum* L. IN MANGROVE FOREST FROM CHUMPHON PROVINCE

Udomrak Meethong*, Pachara Mongkolsuk, Kawinnat Buaruang
Lichen Research Unit, Department of Biology, Faculty of Science, Ramkhamhaeng University, Bangkok, 10240
*e-mail: gateudomrak@gmail.com

Abstract: Foliicolous lichens grow entirely on the living leaves of vascular plants. Thailand has high foliicolous lichens with about 180 species which most of them were reported from the high altitudes in northern and northeast parts. Whereas, a few of foliicolous lichens in mangrove forest have been studied. The aim of this study was to investigate the diversity of foliicolous lichens on *Acrostichum aureum* L. in mangrove forests of Chumphon province. A total of 152 specimens were collected from living leaves of *Acrostichum aureum* L. during 14-16 February 2018. The external morphology was determined under a dissecting binocular microscope. The anatomical characters of the thallus and ascomata were studied by free hand section and observed under a compound microscope. Lichen substances were characterized by spot tests. In the present study 5 families, 6 genera and 7 species were recorded including *Arthonia lividula* Vain., *Byssoloma subdiscordans* (Nyl.) P. James, *Calopadia fusca* (Müll. Arg.) Vězda, *Calopadia puiggarii* (Müll. Arg.) Vězda, *Dirinaria confluens* (Fr.) D.D. Awasthi, *Porina nitidula* Müll. Arg. and *Tricharia demoulinii* Sérus. Among them, *Porina nitidula* was commonly found with 70 observing specimens. The key to all species of foliicolous lichens that colonizing on live leaves of *Acrostichum aureum* L. was provided together with their pictures.

Introduction: Chumphon province is located at the top of the southern region (10° 29'N/99° 11'E) on the east coast of Thailand approximately 6,010 km^2. The general geography is long and narrow comprising of high mountains and lowlands. In addition, there are plains along the coast of the Gulf of Thailand, which is plentiful of mangrove forests and several of mangrove plants such as *Acrostichum aureum* L.

Acrostichum aureum L. is a species of fern that grows in mangrove swamps. This plant is one of the interesting mangrove phorophyte for species diversity study of foliicolous lichens because of its glossy, thick, broad and large leaves that are suitable for growth of lichens on leaves, called foliicolous lichens.

Foliicolous lichen grows and reproduces on surfaces living leaves consisting of the upper surface (epiphyllous) and occasionally at lower surface (hypophyllous). Most of them are found in tropical areas where high humidity and low light intensity prevail[1] and with more than 800 species have been reported worldwide.[2]

The foliicolous lichens in Thailand were first reported by Boonpragob *et al.*[3], who examined specimens from a few sites in Khao Yai National Park and listed 34 lichen species. Papong *et al.*[1] published a new species and 71 new records of foliicolous species collected from five different forest types in Khao Yai National Park. The rich number of foliicolous lichen species were reported by Aptroot *et al.*[4], who studied lichen mainly microlichens from Chiang Mai province. Buaruang *et al.*[5] published a checklist of lichens in Thailand with 1,292 taxa of which about 180 are foliicolus lichens. It is clearly seen that most collections of foliicolous lichens have been reported in Thailand mainly from the high altitude of northern and northeastern parts. Therefore, the objective of this study was to study the diversity of foliicolous lichens that live on *Acrostichum aureum* L., in the mangrove forest from Chumphon province.

Methodology: A total of 152 samples of the foliicolous lichens growing on the leave of *Acrostichum aureum* L. in mangrove forests of Chumphon province were collected from two

collection sites; (1) Bang Son Subdistrict, Pathio District (10° 41.494'N 99° 19.870'E) and (2) Bang Nam Chuet Subdistrict, Lang Suan District (10° 3.470'N 99° 8.271'E) (Figure 1), during 14-16 February 2018. All the specimens were air dried with wood panel in room temperature for a week before identification. The external morphological characters of thallus and ascomata were examined with an Olympus SZ30 stereomicroscope and images were made by microscope Eye-Piece Camera (Dino-Eye). The anatomical features were investigated by hand-cut section of thalli and ascoma by razor blade. The iodine reaction of the hymenium and ascospores were studied in Lugol's iodine solution. All sections were mounted in water and observed under light microscope (Olympus CH). Lichen chemistry of thalli and ascomata were characterized by spot tests as follow Lucking 2008, Swinscow and Krog 1988, Ferraro and Lucking 1997, Singh,and Pinokiyo 2018. The specimens were identified by comparing by own description and specimens in the herbarium of lichen research unit of Ramkhamhaeng University.

Results and Discussion: The foliicolous lichens that colonize on live leaves of *Acrostichum aureum* L. in the mangrove forest of Chumphon Province were identified to seven species belonging to six genera in five families. The lists of lichen species and number of specimens together with their photobionts were shown in Table 1. Two genera of photobionts were observed namely *Phycopeltis* and *Trebooxia* (Table 1 and Figure 2) of which five species of lichenized fungi were found associated with photobiont genus *Trebooxia* and other two lichen species were symbiosis with the algal genus *Phycopeltis*. Family Pilocarpaceae dominated with 3 species namely *Byssoloma subdiscordans* (Nyl.) P. James, *Calopadia fusca* (Müll. Arg.) Vězda and *Calopadia puiggarii* (Müll. Arg.) Vězda and the rest families with one species each were recorded (Table 1). Study area site, Lang Suan district (2) had more species diversity of lichens than site Pathio district (1). All seven species were found in the study site (2) whereas only two species namely *Calopadia puiggarii* and *Porina nitidula* were observed in the site (1). *Porina nitidula* was commonly found in this study with 70 specimens, following by *Calopadia fusca*, *Byssoloma subdiscordans* and *Arthonia lividula* with 18, 18 and 16 specimens, respectively. The foliicolous lichens on *Acrostichum aureum* L. were dominated by crustose growth form with 6 species and foliose growth form with one species (Table 1.). *Byssoloma subdiscordans* (Nyl.) P. James and *Dirinaria confluens* (Fr.) D.D. Awasthi, that grows as foliicolus are also found as corticolous.[9] Whereas, *Arthonia lividula* Vain., *Calopadia puiggarii* (Müll.Arg.) Vězda and *Tricharia demoulinii* Sérus have been reported in Thailand as only foliicolous lichens.[1,4,5] In addition, all seven species found in this study have never been reported in mangrove forest of Thailand so far. Thus, we constructed the key for lichens that colonized on leaves of *Acrostichum aureum* L. for the first time on the basis of their morphological, anatomical and chemical characters.

Figure 1. A. Map of two collection sites in Chumphon province; (1) Pathio district, (2) Lang Suan district. B. *Acrostichum aureum* L. hosted of foliicolous lichens. C. Mangrove forest at Chumphon province.

Table 1. List of foliicolous lichen on *Acrostichum aureum* L. in the mangrove forest of Chumphon province.

Family	Lichen species	Growth form	Photobionts	Number of specimens		
				Site 1	Site 2	Total
Arthoniaceae	*Arthonia lividula*	Crustose	*Phycopeltis*	-	16	16
Caliciaceae	*Dirinaria confluens*	Foliose	*Treboxia*	-	8	8
Gomphillaceae	*Tricharia demoulinii*	Crustose	*Treboxia*	-	14	14
Pilocarpaceae	*Byssoloma subdiscordans*	Crustose	*Treboxia*	-	18	18
	Calopadia fusca	Crustose	*Treboxia*	-	5	5
	Calopadia puiggarii	Crustose	*Treboxia*	3	18	21
Porinaceae	*Porina nitidula*	Crustose	*Phycopeltis*	27	43	70
Total specimens				30	122	152

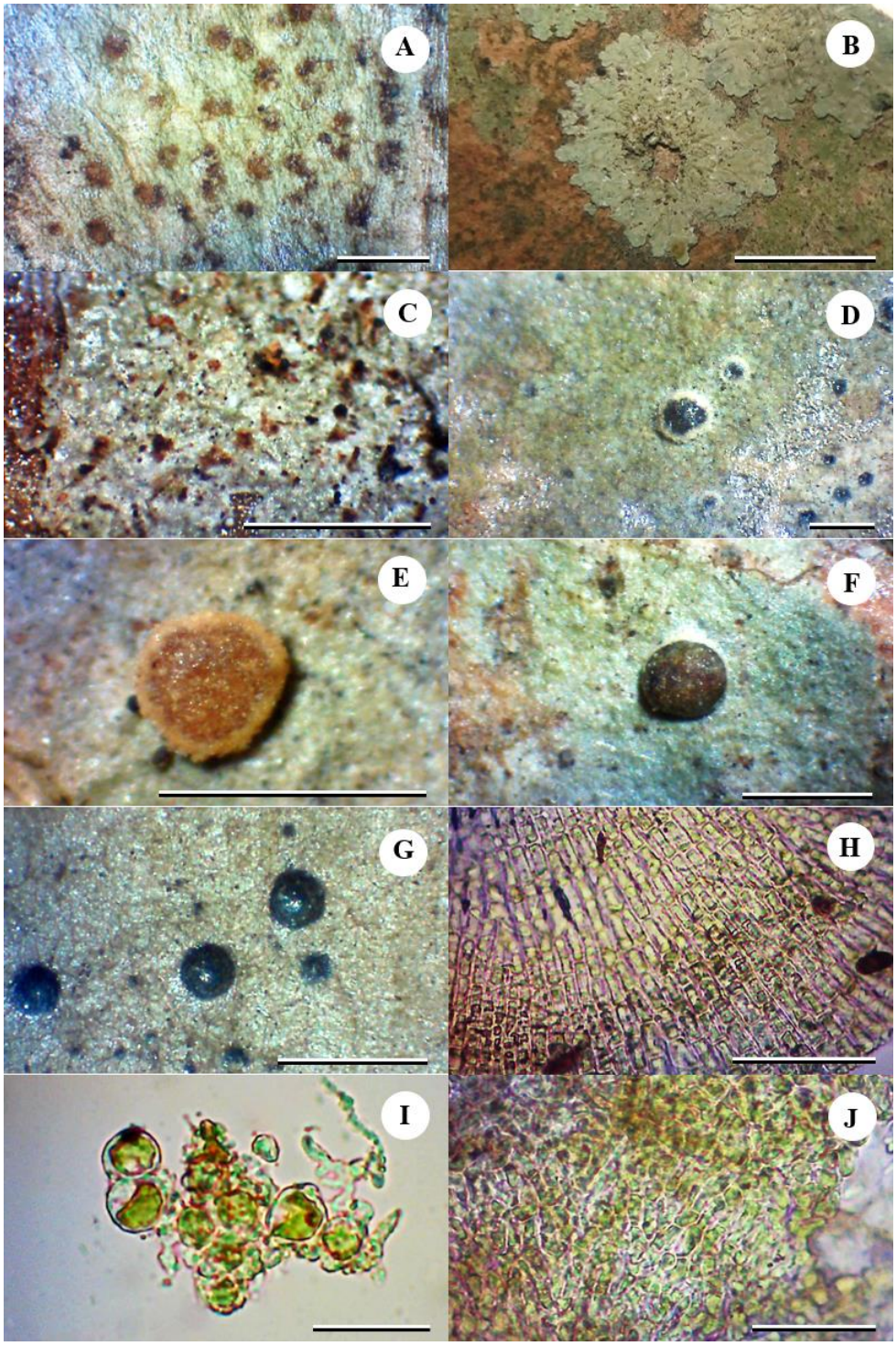

Figure 2. Foliicolous lichens and their photobionts that colonize on *Acrostichum aureum* L. A. *Arthonia lividula*, B. *Dirinaria confluens*, C. *Tricharia demoulinii*, D. *Byssoloma subdiscordans*, E. *Calopadia fusca*,), F. *Calopadia puiggarii*, G. *Porina nitidula*,

H. Photobiont *Phycopeltis* (*Arthonia lividula*) I. Photobiont *Treboxia* (*Dirinaria confluens*), J. Photobiont *Phycopeltis* (*Porina nitidula*). Scale for A–G = 0.5 mm.; for H-J = 50 µm.

Key to foliicolous lichens on *Acrostichum aureum* L. in Chumphon province

1a. Thallus foliose.....	*Dirinaria confluens*
1b. Thallus crustose.....	2
2a. Ascomata perithecia; photobiont trentepohlioid (*Phycopeltis*).....	*Porina nitidula*
2b. Ascomata apothecia; photobiont chlorococcoid (*Trebouxia*) or trentepohlioid (*Phycopeltis*).....	3
3a. Apothecia irregular lirellate brownish, pale margin and lacking algae; ascospore transversely septate, small (6–25 × 2–8 µm); photobiont trentepohlioid (*Phycopeltis*).....	*Arthonia lividula*
3b. Apothecia disc-like; photobiont chlorococcoid (*Trebouxia*).....	4
4a. Apothecia yellowish to dark brown to black; sterile setae present, black.....	*Tricharia demoulinii*
4b. Apothecia greyish brown to dark brown; setae absent.....	5
5a. Apothecia black, margin well-developed and densely byssoid, pure white; ascospore oblong-ellipsoid, transversely septate.....	*Byssoloma subdiscordans*
5b. Apothecial disc dark brown; ascospore muriform.....	6
6a. Apothecia light brown to reddish brown; hypothecium light brown.....	*Calopadia fusca*
6b. Apothecia greyish brown to dark brown; hypothecium dark brown.....	*Calopadia puiggarii*

Conclusion: One hundred and fifty-two specimens of foliicolous lichens on *Acrostichum aureum* L. in the mangrove forest from Chumphon province were classified into 5 families 6 genera and 7 species. The highest lichen species diversity found on *Acrostichum aureum* L. was in family Porinaceae with three species. *Porina nitidula* was species that commonly found in two study sites. All of seven species have never been found in magrove forests of Thailand before. Therefore, the findings of this study lead to a better understanding of the diversity and distribution of foliicolous lichens in the southern part of Thailand.

References:

1. Papong K, Boonpragob K, Lücking R. Lichenologist, 2007;39:47-56.
2. Lucking R. Flora Neotropica Minograph. 2008;103:1-866.
3. Boonpragob K, Homchantara N, Coppins BJ, McCarthy PM, Wolseley PA. Botanical Journal of Scotland. 1998;50:209-219.
4. Aptroot A, Saipunkaew W, Sipman HJM, Sparrius LB, Wolseley PA. Fungal Diversity. 2007;24:75-134.
5. Buaruang K, Boonpragob K, Mongkolsuk P, Sangvichien E, Vongshewarat K, Polyiam W, Rangsiruji A, Saipunkaew W, Naksuwankul K, Kalb J, Parnmen S, Kraichak E, Phraphuchamnong P, Meesim S, Luangsuphabool T, Nirongbut P, Poengsungnoen V,

Duangphui N, Sodamuk M, Phokaeo S, Molsil M, Aptroot A, Kalb K, Lücking R, Lumbsch HT. Myco Keys. 2017;23:1-91.
6. Singh KP, Pinokiyo A. Indian journal of forestry additional. 2018;4:1-335.
7. Swinscow TDV, Krog H. Macrolichens of East Africa. 1988:78-82.
8. Ferraro L.I., Lucking, R. Phyton. 1997;37(1):61-70.
9. Rashmil S., and Rajkumar HG. Int.J.Curr.Microbiol.App.Sci. 2015;4(6):250-256.

Acknowledgements: We are grateful to the office of the Mangrove Conservation, Department of Marine and Coastal Resources for their kind cooperation, and also thanks the Lichen Research Unit at the Department of Biology, Faculty of Science, Ramkhamhaeng University for laboratory facilities. This study was financially supported by the National Research Council of Thailand for the project "Biodiversity of Lichen in Mangrove Forest at Western Sea Coast on the Gulf of Thailand, DNA Barcoding and Managing and Developing Database and Lichen Herbarium, Ramkhamhaeng University".

B5_025_PF: BIODIVERSITY OF DISCOLICHES IN MANGROVE FOREST AT CHUMPHON PROVINCE, THAILAND

Phimpisa Phraphuchamnong*, Kawinnat Buaruang, Patchara Mongkolsuk
Lichen Research Unit. Department of Biology. Faculty of Science. Ramkhamheang University. Huamark, Bangkapi, Bangkok 10240, Thailand
e-mail: phimna191@gmail.com

Abstract: The Discolichens are a lichenized discomycetes is a group of lichens with disc-shaped fruiting bodies (apothecia), which fruiting bodies of this type will produce ascospore in ascus. During February 2018, six hundred and forty-four discolichens samples collected from seventeen phorophytes in mangrove forests at Chumphon province were compiled and taxonomically catalogued into nine families twelve genera and twenty-three species (plus two species to be expected). Whereas the highest species diversity was *Cresponia proximata,* followed by *Malmidea aurigera*, *Bacidia submedialis*, and *Lecanora helva* frequently found respectively.

Introduction: Chumphon is one of the southern provinces on the Gulf of Thailand. The area 6,010.5 square kilometers. Chumphon province is divided into three types; the central plains area, the area in the west is high mountains, and coastal plains. The province which consists of six coastal districts into Lamae, Lang Suan, Muang Chumphon, Pathio, Sawi, and Thung Tako. A total 164.0 square kilometers of mangrove forest in Chumphon province. Four mangrove forest study sites consist of Lang Suan (4.1 km^2), Muang Chumphon (22.9 km^2), Pathio (7.5 km^2) and Sawi (10.6 km^2) [22], [23]. Always we found the crustose lichen are abundant on phorophytes tree. Discolichens in this study is a group of lichen-forming fungi (Ascomycota). This group is characterized to as crustose lichens with disc-like apothecia (fruiting bodies). The apothecia disc may be exposed, flat, convex or concave and normally upraised on the thallus. Two types of apothecia were found, the margin of an apothecia can be concolorous that have been called lecanorine, which the margin entirely fungi with algae, but apothecia with only a proper margin are referred to as lecideine or biatorine, which the margin entirely fungal without algae. Ascospores are produced within the ascus with the distinguished variety of colorless ascospores type as simple, polarilocular, septate, muriform or sub-muriform ascospores [6]. Objectives of research for in order update lichen database in Thailand and collected discolichens samples in mangrove forest are indispensable for the known taxonomy, diversity and distribution as well as an information for the conservation and sustainable utilization of biodiversity resource.

Methodology: Discolichens were collected from mangrove forest of Chumphon province Latitude: 10° 29' 20.39" N, Longitude: 99° 10' 27.00" E. All specimens were examined for their morphological, anatomical and chemical characteristics. Chemicals were clarified by using spot test and Thin Layer Chromatography (TLC). Preliminarily color tests for lichen substances are usually carried out with the following reagents according to Elix's method [8]. Thin layer chromatography was performed according to the standard method of White and James [20]. Taxa were determined to morphology and anatomy structures according to Awasthi (2) Brodo et. al (3), Kantvilas et. al (4), Lumbsch (12) and Rambold (16).

Results and Discussion: The taxa of six hundred and forty-four discolichens samples in mangrove forest at Luang Suan, Muang Chumphon, Pathio and Sawi district of Chumphon province were collected and catalogued into nine families twelve genera and twenty-three species (plus two species to be expected). Discolichens was founded on phorophytes, a total of eight families, eleven genera and seventeen species. Mostly found in the family Rhizophoraceae. The List of lichen-taxa on seventeen phorophyte trees in mangrove forest is

shown in table 1. Proportion of number of species among families of discolichens is shown in Figure 2. The highest discolichens species diversity is in family Lecanoraceae and Ramalinaceae (5 taxa). The second highest is in Malmideaceae and Pilocarpaceae (4 taxa). Observation on the occurrence of lichens on the various phorophytes revealed that twenty-three species are growing on the various mangrove trees. However, the highest species diversity of lichen was recovered twenty-four taxa on *Excoecaria agallocha* and *Rhizophora mucronata* with sixteen species, followed by *Rhizophora apiculata* with fifteen species. However*, Kandelia candel* and *Thespesia populnea* were discovered for one species of discolichen. Besides, *Cresponia proximata* (Nyl.) Egea & Torrente, *Malmidea aurigera* (Fée) Kalb, Rivas Plata & Lumbsch. *Bacidia submedialis* (Nyl.) Zahlbr, and *Lecanora helva* Stizenb.were frequently found.

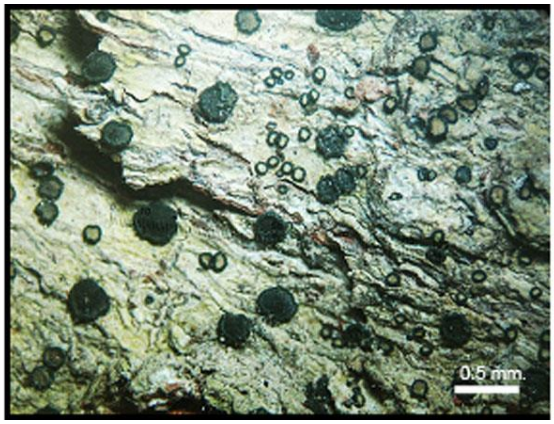

Cresponia proximata figure (left)

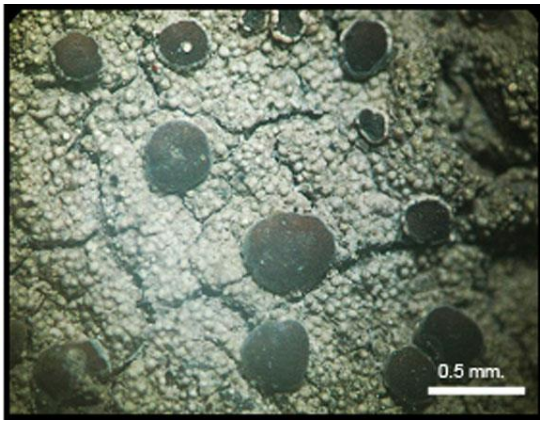

Malmidea aurigera figure(right)

Bacidia submedialis figure (left)

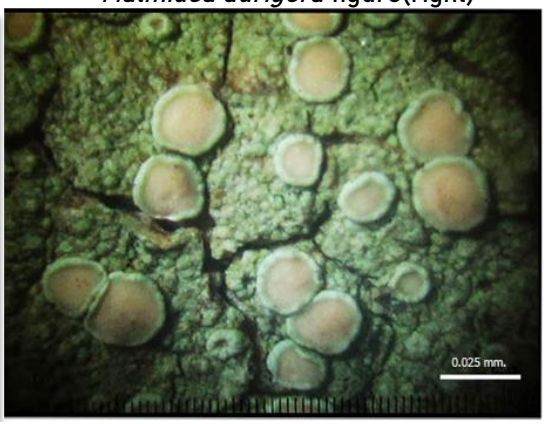

Lecanora helva figure(right)

Figure 1. Four common species

Table1. List of Lichen-taxa on phorophyte trees of mangrove forest in Chumphon province.

Lichen taxa	Phorophyte																	Total specimens
	1	2	3	4	5	6	7	8	9	10	11	12	13	14	15	16	17	
COENOGONIACEAE																		
Dimerella lutea (LS, SW)						1						1						2
Dimerella pineti (LS, MC, PT, SW)						3		3				1		1			1	9
LECANORACEAE																		
Lecanora astrothelin (LS)													1					1
Lecanora conizaeoides (MC)													3					3
Lecanora helva (LS, PT, SW)	4	5		12		5	1	2			1	7	17	6			1	61
Lecanora leproplaca (SW)	6													1				7
Lecanora tropica (LS, MC, PT)								1	1				1					3
LETROUITIACEAE																		
Letrouitia domengensis (LS)								1										1
Letrouitia leprolytoides (LS, PT, SW)				4		12		1				1					1	19
MALMIDEACEAE																		
Malmidea aurigera (LS, MC, PT, SW)			2	15	15	10	1	4		1		34	12			1		95
Malmidea inflata (LS)						2						1	2					5
Malmidea perplexa (LS, MC, SW)				2		3		7				4	25		1		1	43
Malmidea piae (LS, SW)					1	2												3
OPEGRAPHACEAE																		
Cresponea proximata (LS, MC, PT, SW)			2	42	7	21		8				29	61	1		1	4	176
PILOCARPACEAE																		
Byssoloma subdiscoedans (PT)													2	1				3
Calopadia fusca (LS)						1						1	4					6
Calopadia subcoerulescens (LS, MC, SW)						1		1		1			3					6
Fellhanera bouteillei (LS,PT)						3							8	1				12
RAMALINACEAE																		
Bacidia igniarii (MC)								3										3
Bacidia phacodes (LS, MC, SW)			3	1		3		2				6	18					33
Bacidia rubella (LS, PT)												3	1	2				6
Bacidia submedialis (LS, MC, PT, SW)		2	4	3	5	7		6			1	18	37	2				85
Lecania Chum1. (LS,MC,PT)						1		1				22	20					44
ROCCELLACEAE																		
Bactrospora cf. *medians* (LS, MC, PT, SW)		3		2		3		1			1	4		2			1	17
TELOCHISTACEAE																		
Caloplaca Chum1. (SW)	1																	1
Total of lichen species	11	10	11	81	28	78	2	41	1	2	3	132	215	17	1	2	9	644

Note: 1= *Avicennia alba* Blume.; 2= *Avicennia offcinalis* L.; 3= *Bruguiera gymnorrhiza* (L.) Savigny.; 4= *Bruguiera parviflora* Roxb.; 5= *Ceriops decandra* (Griff.) Ding Hou.; 6= *Excoecaria agallocha* L.; 7= *Ficus benghalensis* L.; 8= *Hibiscus tiliaceus* L.; 9= *Kandelia candel* (Linn.) Druce.; 10= *Lumnitzera litorea* (Jack) Voigt; 11= *Lumnitzera racemosa* Wild.; 12= *Rhizophora apiculata* Blume; 13= *Rhizophora mucronata* Poir.; 14= *Sonneratia alba* J.SM.; 15= *Thespesia populnea* (L.) Sol. ex Correa.; 16= *Xylocarpus granatum* Koenig; 17= *Xylocarpus moluccensis*

(Lam.) M. Roem.; (LS)= Lang Suan, (MC)= Muang Chumphon, (PT)= Pathio, and (SW)= Sawi district.

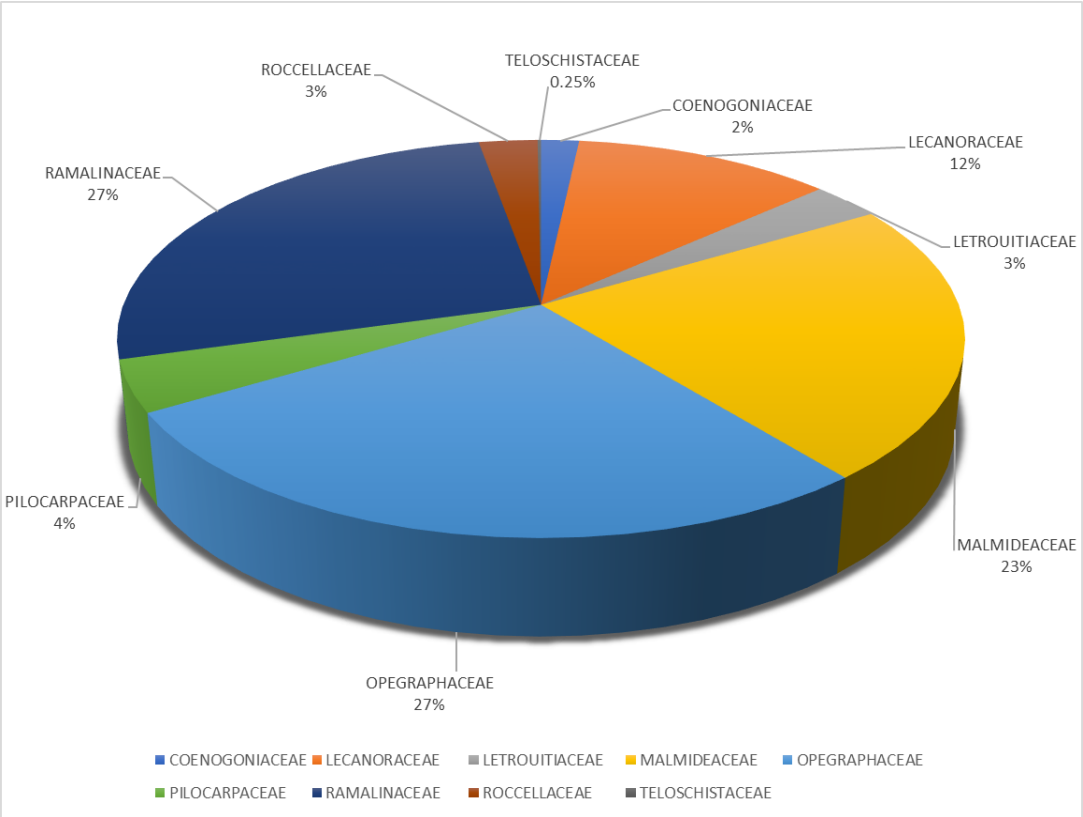

Figure 2. Proportion of number of species among nine families of Discolichens.

Conclusion: Six hundred and forty-four discolichens samples in mangrove forest in Chumphon province. Twenty-two species were found in Lung Suan, fourteen species in Sawi, Twelve species in Pathio and only eleven species in Muang Chumphon district. Discolichens from seventeen substrates were scrutinized and taxonomically classified in nine families twelve genera and twenty-three species (plus two species). *Rhizophora mucronata* Poir is the highest discolichens species rich (seventeen species) because it is the dominant tree in mangrove forest, while *Kandelia candel* (Linn.) Druce and *Thespesia populnea* (L.) Sol. ex Correa. are only one species. However, the dominant species are *Cresponea proximata* (Nyl.) Egea & Torrente. was found in four study sites at Phatio, Luang Suan, Mueng Chumphon and Sawi district respectively. The lichen communities that occur in mangroves forest are indicate their smooth of the tree barks, tolerance to hot, humid and saline breeze environmental conditions prevailing in mangrove, it would be an interesting aspect to study in detail the environmental factors and the physiology of these lichens enabling them for the successful colonization in mangrove forest.

References:

1. Aptroot, A., Saipunkaew, W., Sipman, H. J. M., Sparrius, L. B., & Wolseley, P. A. (2007). New lichens from Thailand, mainly microlichens from Chaing Mai. Fungal Diversity, 24: 75-134.
2. Awasthi DD. (1991). Bilo. Lichen. 40: 66-75.
3. Brodo JM, Culberson WL, Culberson CF. (2008). Bryologist. 111 (3): 363-423.

4. Elix, J. A. (2009). Letrouitiaceae. Flora of Australia 57: 483-493.
5. Gintaras Kantvilas, (2016). A synopsis and key for the lichen genus Caloplaca (Teloschistaceae) on Kangaroo Island, with the description of two new species, Journal of the Adelaide Botanic Gardens 29: 53–69
6. Kalb, K., Rivas Plata, E., & Lumbsch, H. T. (2011). The phylogenetic position of Malmidea, a new genus for the Lecidea piperis- and Lecanora granifera-groups (Lecanorales, Malmideaceae) inferred from nuclear and mitochondrial ribosomal DNA sequences with special reference to Thai species. Bibliotheca Lichenologica.
7. Kantvilas G, (2016). Journal of the Adelaide Botanic Gardens. 29: 53-69.
8. Kantvilas G, Elix JA, (2007). Lichenologist. 38 (2): 135-141.
9. Kantvilas G, Papong K, Lumbsch HT. (2010). Lichenologist. 42 (5): 557-561.
10. Kenan Yazici1 & Ali Aslan, (2009). Lichen species new to Turkey and Asia, Mycotaxon, 108: 463–466
11. Lugo AE, Snedarker SC. (1974). Annual Review of Ecology and Systematics. 5: 39-64.
12. Lumbsch HT. (2004). Flora of Australia. 56A: 11-62.
13. Mongkolsul P, Buaruang B, Polyiam P, Vongshewarat K, Phokaeo S, Seeiam D, Nirongbut P, Sangwisut T, Sodamuk M. (2011). The 37th Congress on Science and Technology of Thailand.
14. McCarthy PM., Elix J. A. (2018). New species and record of lichens from the Cook Islands, South Pacific Ocean. Australasian Lichenology. 82: 1-79
15. Nash, T.H., Ryan, B.D., Gries, C., Bungartz, F., (eds.), (2004). Lichen Flora of the Greater Sonoran Desert Region. Vol 2.
16. Rambold, G. (1989). Biblo. Lichen. 34: 10-69.
17. Papong K, Lumbsch HT. (2011). Lichenologist. 43: 299-320.
18. Phraphuchamnong P, Buaruang B, Mongkolsul P. (2018). The 44th Congress on Science and Technology of Thailand.
19. Sriprang V, Monkolsuk P. (2010). Thai Journal of Botany 2: 47-53.
20. White FJ, Jame PW. (1985). British Lichen Society Bulletin. 57: 1-41.
21. Wolseley PA, Aguirre-Hudson B, McCarthy PM. (2002). Catalogue of the lichens of Thailand. Bull Nat Hist Mus Bot. 32: 13–59.
22. Mangrove Forest Resources Research and Development Group, Mangrove Forest Resources Conservation Bureau Department of Marine and Coastal, Mangrove Forest Research Project Report. 2006.
23. Mangrove Forest Resources Conservation Bureau Department of Marine and Coastal,Marine and coastal resource information of Chumphon. 2018.

B5_028_PF: SYSTEMATIC REVIEWS OF RHINOBATIFORMES IN THAI WATERS BASED ON 80 MORPHOMETRIC CHARACTERS

Apinya Huskul[1], Tassapon Krajangdara[2], Jes Kettratad[3,*]
[1]Department of Marine Science, Faculty of Science, Chulalongkorn University, Bangkok, Thailand
[2]Upper Andaman Sea Fisheries Research and Development Center (Phuket), Phuket, Thailand
[3]Department of Marine Science, Faculty of Science, Chulalongkorn University, Bangkok, Thailand
*e-mail: jes.kettratad@gmail.com

Abstract: Intensive systematic reviews of the fishes in the order of Rhinobatiformes has been attempted in the past. Most studies utilized single diagnostic character approach which could not give overall differences among species. We opted to use principal component analysis and discriminant function analysis of 80 morphometric characters from 50 specimens. Our specimens were collected from two sources: the fish market and museum collection. Principal component score plot reviewed 9 distinct clusters: *Rhina ancylostoma, Rhynchobatus australiae*, *R. laevis*, *Glaucostegus thouin*, *G. granulatus, G. obtusus*, *Rhinobatos annandalei*, *R. ranongensis*, and the last cluster was *G.* cf *granulatus*. Discriminant function analysis suggested only one specimen of *R. australiae* could be misidentified with *R. laevis*. Characters that are useful for species identification of fish in order Rhinobatiformes included first dorsal-fin anterior margin, first dorsal-fin length, interspiracular space, first dorsal-fin base, pectoral-pelvic space, pre-first dorsal length, pre-second dorsal length, pelvic-fin length, pelvic-fin base, pectoral-fin base, eyeball length, corneal length, anterior nasal flap length, spiracle length, interdorsal space, preorbital length, prenarial length and pelvic-fin posterior margin.

Introduction: Fishes in the order of Rhinobatiformes has an intermediate body form between sharks and rays. They are considered as threatened species in Thailand. Unfortunate only few works have been done on this group of fish in Thai waters. Most studies are catch survey. [6] Currently, there were 13 species of fishes in this order in Thai waters.[1] The most distinct morphology among them is the shark rays which had a round snout and clear distinct lunate tail. The other members had similar morphological features includes: dorso-ventrally flatten head, pointy snout and not so well developed caudal fin. Previously, most studies of fish in this order used the univariate analysis [3] which could not represent the overall similarity of the taxa used in the study. In the morphological study, it is important to consider about sexual dimorphism. There is no sexual dimorphism in order Rhinobatiformes but size had been one of the issues that would affect the interpretation of the difference in shape. It is important that the size effect should be eliminated before making inference on the shape differences. None of the earlier studies address this issue.[3] Recent works mainly focused on molecular data[2]. Therefore, in this study, we used full suites multivariate analysis of 80 morphometric characters which we minimize the size effect on the interpretation for the fish in this group.

Methodology:
Sample collecting: This research focuses on batoids in order Rhinobatiformes in Thai waters which included 14 species in 4 families. Family Rhinidae includes one species which is *Rhina ancylostoma* Bloch & Schneider, 1801, family Rhynchobatidae includes four species which are *Rhynchobatus australiae* Whitley, 1939, *R. laevis* (Bloch & Schneider, 1801), *R. palpebratus* Compagno & Last, 2008 and *R. springeri* Compagno & Last, 2010, family Rhinobatidae includes eight species which are *Glaucostegus granulatus* (Cuvier, 1829), *G.* cf *granulatus* (Cuvier, 1829), *G. obtusus* Müller & Henle, 1841 , *G. thouin* (Anonymous [Lacepede],

1798), *G. typus* (Bennett, 1830), *Rhinobatos annandalei* Norman, 1926, *R. ranongensis* Last, Séret & Naylor, 2019, *R. lionotus* Norman, 1926 and family Platyrhinidea includes one species which is *Platyrhina psomadakisi* White & Last, 2016. (Tassapon Krajangdara and Somchai Vibunpant, 2018) However, only eight species (fifty specimens) were found during the research which are *Rhina ancylostoma* (one specimen from fish market) , *Rhynchobatus australiae* (fourteen specimens from fish market and two specimens from department of fisheries collection), *R. laevis* (two specimens from department of fisheries collection), *Glaucostegus granulatus* (one from department of fisheries collection), *G.* cf. *granulatus* (eight specimens from fish market), *G. obtusus* (one specimen from fish market), *G. thouin* (five specimens from department of fisheries collection) , *Rhinobatos annandalei* (nine specimens from fish market) *and R. ranongensis* (seven specimens from fish market and one specimen from Department of Fisheries collection; Figure 1). Fresh specimens were collected from the fish market in Samut Sakhon and Ranong province. They were preserved in 10% neutral formaldehyde solution for at least 1month before the measurements which is the same preservation method as the specimen from Department of Fisheries collection. Preserved specimens which kept in the Department of Fisheries collection was measured under permission. The measurements were taken with an analog vernier caliper.

Morphometric measurements: Seventy-eight characters measurement follows Compagno, 2008. The measurement includes total length (TOT), fork length (FOR), precaudal length (PCL), pre-second dorsal length (PD2), pre-first dorsal length (PD1), prepelvic length (PP2), snout-vent length (SVL), prespiracular length (PSP), prebranchial length (PG1), head length (HDL), preorbital length (POB), preoral length (POR), prenarial length (PRN), interdorsal space (IDS), dorsal-caudal space (DCS), pectoral-pelvic space (PPS), pelvic- caudal space (PCS), disc width (DW), disc length (DL), disc thickness (DT), snout-greatest width (Snout), snout width at base (SWB), corneal length (COL), corneal height (COH), eyeball length (EYL), eyeball height (EYH), interorbital space (INO), spiracle length (SPL), spiracle height (SPH), eye-spiracle space (ESL), interspiracular space (INS), nostril width (NOW), internarial space (INW), anterior nasal flap length (ANF), first gill slit height (GS1), second gill slit height (GS2), third gill slit height (GS3), fourth gill slit height (GS4), fifth gill slit height (GS5), inter 1st gill (ING1), inter 5th gill (ING5), head height (HDH), trunk height (TRH), trunk width (TRW), abdomen height (ABH), abdomen width (ABW), caudal peduncle height (CPH), caudal peduncle width (CPW), vent length (VNL), pectoral-fin length (P1L), pectoral-fin anterior margin (P1A), pectoral-fin base (P1B), pectoral-fin height (P1H), pectoral-fin posterior margin (P1P), pectoral-fin inner margin (P1I), pelvic-fin length (P2L), pelvic-fin anterior margin (P2A) ,pelvic-fin base (P2B), pelvic-fin height (P2H), pelvic-fin posterior margin (P2P), pelvic-fin inner margin length (P2I), pelvic-fin span (P2S), first dorsal-fin length (D1L), first dorsal-fin anterior margin (D1A), first dorsal-fin base (D1B), first dorsal-fin height (D1H),

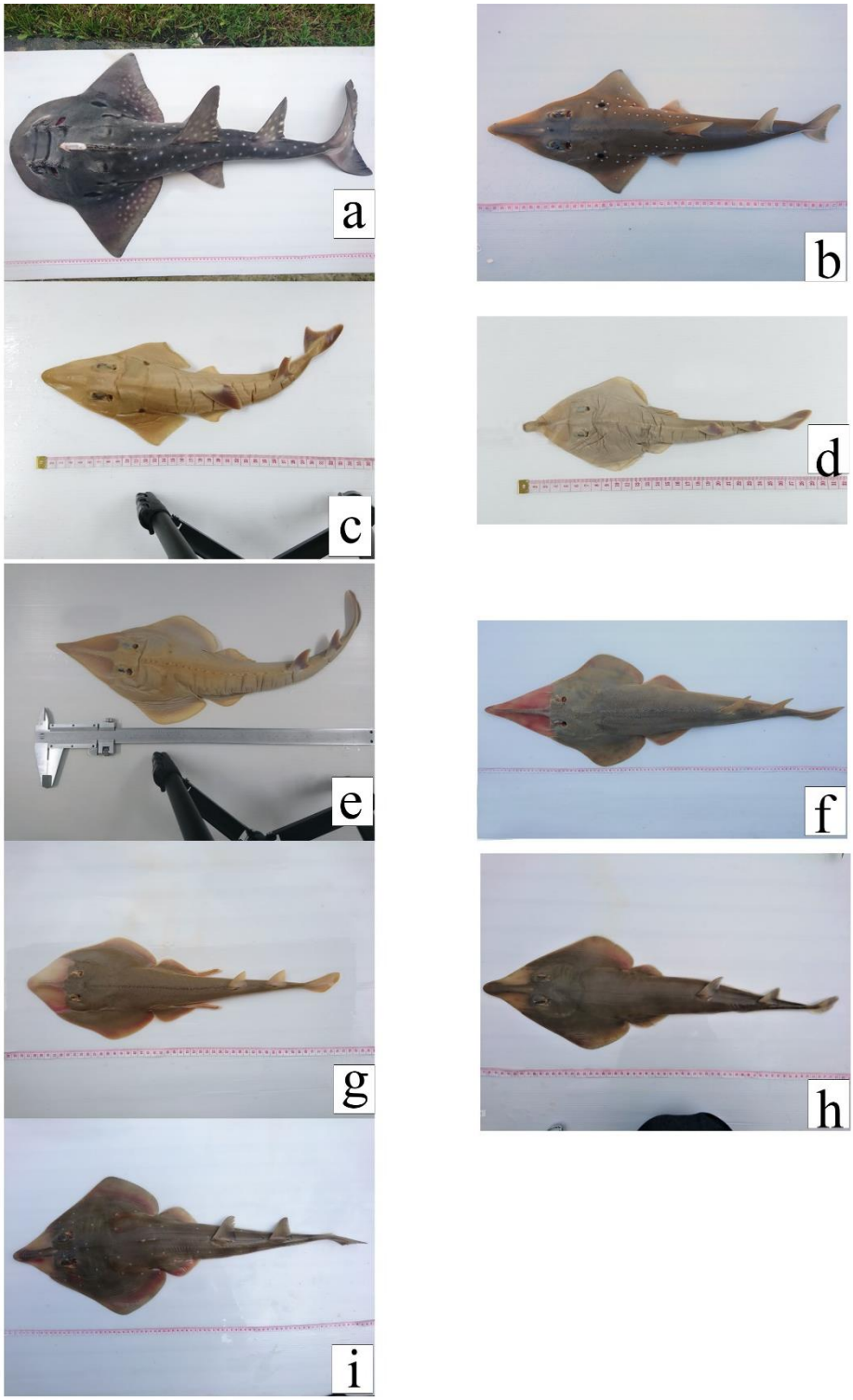

Figure 1. (a) *Rhina ancylostoma*, (b) *Rhynchobatus australiae*, (c) *R. laevis*, (d) *Glaucostegus thouin*, (e) *G. granulatus*, (f) *G.* cf *granulatus*, (g) *G. obtusus*, (h) *Rhinobatos ranongensis*, (i) *R. annandalei*

first dorsal-fin posterior margin (D1P), first dorsal-fin inner margin (D1I), second dorsal-fin length (D2L), second dorsal-fin anterior margin (D2A), second dorsal-fin base (D2B), second dorsal-fin height (D2H), second dorsal-fin posterior margin (D2P), second dorsal-fin inner margin (D2I), dorsal caudal margin (CDM), preventral caudal margin (CPV), lower postventral caudal margin (CPL), upper postventral caudal margin (CPU).

Statistical analysis: STATGRAPHICS Centurion XV, version 15.2. 06 was used for the analysis. Each character was plotted against the total length and used to find outliers. The values outside of the 95 % interval from the predicted line are considered as outliers. The characters with no outliers were saved as residuals. All the residuals were used for principal component analysis (PCA). Scatter plot of the principal component loading 1,2, and 3 (PC1, PC2, and PC3) explained significantly difference between species. The characters which have high eigenvalues were used in Discriminant Factorial Analysis (DFA) to test the effectiveness of the characters in predicting different species

Results and Discussion:

Principle component analysis: Principle component 1 and 2 explained 58.01% of the variance in the data. Principal component score plot reviewed nine groupings: *Glaucostegus thouin*, *G. granulatus*, *G. obtusus, Rhina ancylostoma, Rhinobatos annandalei, R. ranongensis, Rhynchobatus australiae, R. laevis,* and *G.*cf *granulatus. Rhina ancylostoma* (shark ray) is the most distant from the other group (Figure 2). Based on the Principal component score plot and the loading, *R. ancylostoma* tended to have broader head than the rest by estimated from the space between spiracular and pectoral fin size (INS, P1B, P1P, P1L). The space between pectoral fin and pelvic fin (PPS) in *R. ancylostoma* tends to be wider and also both of its dorsal fins (D2L, D1H, D1B) tend to be larger than the rest. Including the *R. ancylostoma* in the PCA analysis would cause less resolution among the relationship to the other members.

To reviews the variance among the rest of the member, we, therefore removed *R. ancylostoma* from the second PCA. With the *R. ancylostoma* removed from the second PCA analysis, principal component score plot reviews much more distinct grouping among the rest of Rhinobatid member while PC1 and PC3 explained (49.57%) of the variance found among the data (Figure 3). To further refine the distinguish power and pinpoint the characters that responsible for the majority of the variances of the data, ten characters which had loading (more than 0.10 and less than -0.16) from each PC1 and PC3 of the second PCA that excluded the *R. ancylostoma* were used on the subsequent third PCA. The characters that had high loading on PC1 were PD1, PD2, P2L, P2B, P1B,D1A, D1L, INS, D1B, and PPS while ten characters had high loading on PC3 were POB, PRN2, PRN1, PSP2, PSP1, EYL, COL, ANF, SPL and IDS (Table 1). Based on the loading and the principal component score plot, family Rhynchobatidea which include *Rhynchobatus australiae* and *R. laevis* tend to have both of dorsal fins larger (D2L, D1B, D1A) and wider space between pectoral fin and pelvic fin (PPS) than Rhinobatids (Figure 4). These characters were the fix differences between the family Rhynchobatidea and family Rhinobatidae.[4] Family Rhinobatidae which include : *Glaucostegus thouin*, *G. granulatus*, *G. obtusus, Rhinobatos annandalei, R. ranongensis* and *G.* cf *granulatus*, tent to have both of the dorsal fins origin on more posterior on the body (PD1, PD2) and larger pectoral fin and larger pelvic fin than the member of family Rhynchobatidae as suggested in previous studied.[4] Furthermore, *G.* cf *granulatus* is a potential new species due to the overall distinct morphological form from the rest of the family*. Glaucostegus* cf *granulatus* tend to have the longer body (PD1, PD2) than the rest of the member of the order. This characters could be affected by the longer head (PRN1, PRN2, POB) (Figure 4) which were significantly different (all P-value<0.05) with other family members.

Discriminant function analysis: The Wilk's Lambda (0.0000234074) for both discriminant functions suggest that both axes explained significant variance (P value= 0.0000). Most of the prediction (98.00%) have similar results from initial identification based on the SEAFDEC

identification guide.[1] Only one specimen identified as *R. australiae* from the initial identification was predicted as *R. laevis* which was considered as only 2.00% misidentified from all of the specimens. Discriminant function score plot clearly showed the grouping according to the PCA(Figure 5).

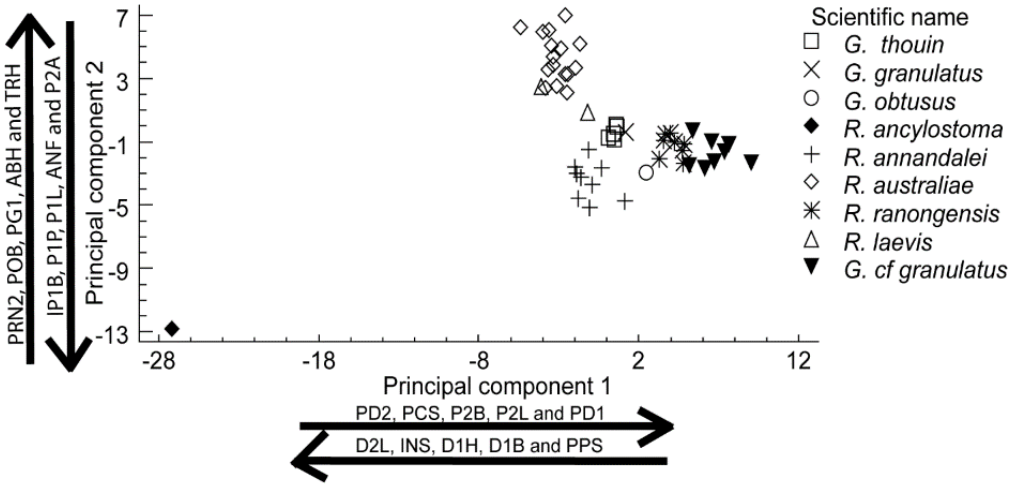

Figure 2. Scatter plot of Principal component 1 vs 2. Principal component 1 explains 39.64% of the total variance and Principal component 2 explains 18.37% of the total variance. This plot explains 58.01% of the total variance. The arrow point to the increased values of the characters.

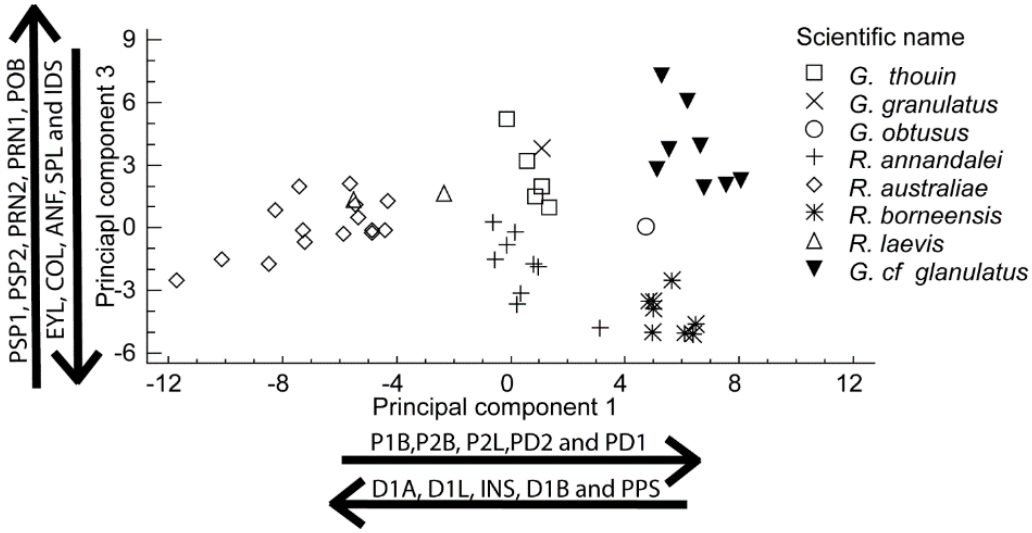

Figure 3. Comparison between scatter plot without *R. ancylostoma* of PC1 vs PC3. Principal component 1 explains 38.03% of the total variance. Principal component 3 explains 11.54% of the total variance. This plot explains 49.57% of the total variance. The arrow point to the increased values of the characters.

Table 1. The ten characters with high eigenvalues of the principal component 1 and 3 from the principal component analysis of 20 morphometric characters:PD1, PD2, P2L, P2B, P1B,D1A, D1L, INS, D1B, PPS, POB, PRN2, PRN1, PSP2, PSP1, EYL, COL, ANF, SPL and IDS

Characters	PC1	Characters	PC3
PD1	0.165546	POB	0.283916
PD2	0.150676	PRN1	0.259529
P2L	0.132629	PRN2	0.252811
P2B	0.127231	PSP2	0.214242
P1B	0.108005	PSP1	0.20505
D1A	-0.17819	EYL	-0.260445
D1L	-0.17803	COL	-0.216417
INS	-0.177	ANF	-0.177022
D1B	-0.17637	SPL	-0.165233
PPS	-0.17266	IDS	-0.16159

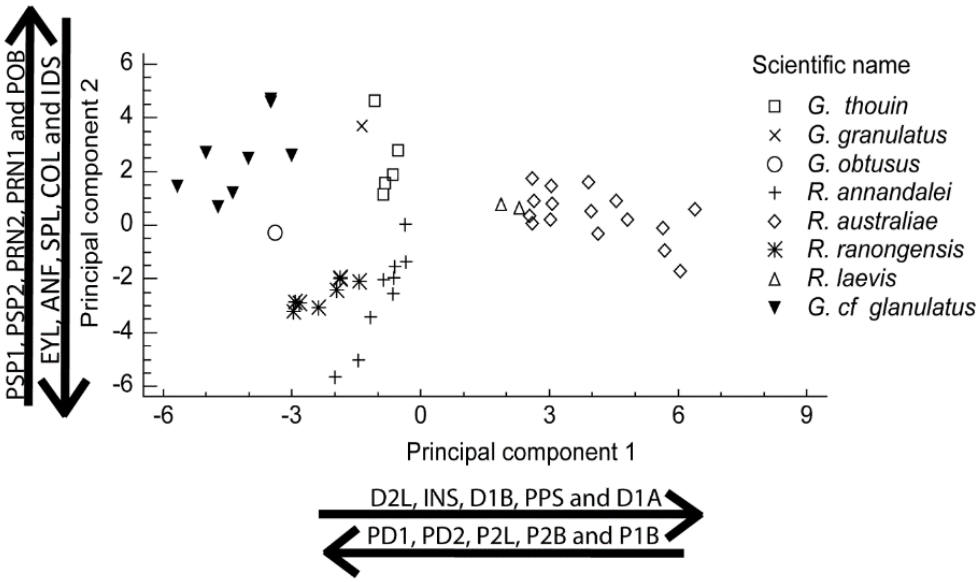

Figure 4. Scatter plot of Principal component 1 and 2 without *R. ancylostoma* from the PCA of the most 20 significant characters: PD1, PD2, P2L, P2B, P1B,D1A, D1L, INS, D1B, PPS, POB, PRN2, PRN1, PSP2, PSP1, EYL, COL, ANF, SPL and IDS. The arrow on each axis points to the increased eigenvalues of the characters. Principal component 1 explains 52.60% of the total variance. Principal component 2 explains 28.10% of the total variance.

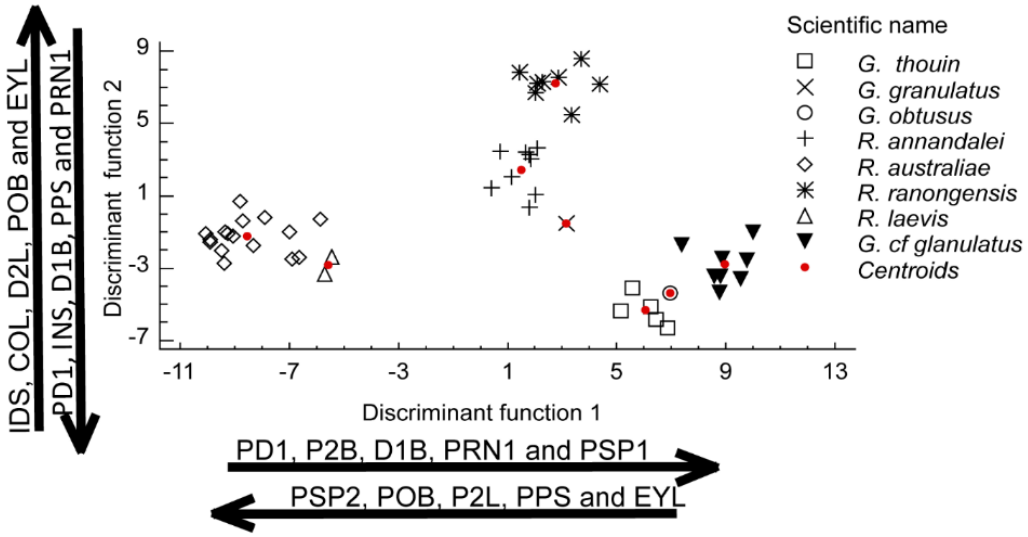

Figure 5. Scatter plot of Discriminant function 1 and 2. Discriminant function 1 explained 67.00% of the total variance. Discriminant function 2 explained 22.57% of the total variance. This plot explains 89.57% of the total variance. The arrow point to the increased values of the character loading (on each arrow) on each discriminant function

Conclusion: This study clearly showed the nine distinct morphological species which could be distinguished based on twenty characters: PD1, PD2, P2L, P2B, P1B, D1A, D1L, INS, D1B, PPS, POB, PRN2, PRN1, PSP2, PSP1, EYL, COL, ANF, SPL, and IDS. The most distinct form was *Rhina ancylostoma,* the only member of Rhinidae which could be separated from the rest by having the broader head, larger dorsal fins, larger pectoral fin, and more developed lunar caudal fin. *Rhynchobatus australiae* and *R. laevis* the member of Rhynchobatidae were easily identified from rest based on the space between the pectoral fin and pelvic fin and predorsal length. The other five members of Rhinobatidae were distinguished apart by these characters the space between the pectoral fin and pelvic fin, predorsal length, Pectoral fin base, pelvic fin base, and pelvic fin length. One potential new species was found *G.* cf *granulatus* which were differentiated from the rest of rhinobatids based on the head length and body length.

References:

1. Ali A, Pek Khiok Lim A. SEAFDEC. 2017
2. Cerutti-Pereyra F, Meekan M. PLoS One. 2012;7
3. Compagno L, Last P. CSIRO. 2008: 227-240.
4. Compagno L, Last P. FAO. 1999:1418-1433.
5. Krajangdara T, Vibunpant S. DOF, 2018
6. Last P, Bernard S. Zootaxa, 2016;4117.4: 451-475.

Acknowledgements: We thank the Department of Fisheries of Thailand for permission to measure specimens in their collection and accommodation during field trips.

B5_030_OF: GENETIC DIVERSITY OF THE ISLAND FLYING-FOX, *Pteropus hypomelanus* (CHIROTERA: PTEROPODIDAE), IN THAILAND

Patcharapon Jumsri, Nontivich Tandavanitj, Thongchai Ngamprasertwong*
Department of Biology, Faculty of Science, Chulalongkorn University, Bangkok 10330, Thailand
*e-mail: thongchai.n@chula.ac.th

Abstract: Study on genetic diversity can provide vital information for conservation of threatened species, including island flying fox *Pteropus hypomelanus,* a species with high extinction risk due to limited dispersal ability, small home range, and high hunting pressure. In Thailand, *P. hypomelanus* can be found on islands along the coasts of the Gulf of Thailand and the Andaman Sea. This study aims to investigate the genetic diversity of *P. hypomelanus* in Thailand. DNA was extracted from fecal samples (n = 40) obtained from 6 localities in both Eastern and Southern Thailand. Mitochondrial control region (D-Loop) was amplified and sequenced. A total of 26 haplotypes (585 bps) were obtained and 24 haplotypes were specifically assigned to certain sampling localities, indicating population isolation and limited gene flow between islands. Overall nucleotide diversity ($\pi \pm$ SD) was 0.034 ± 0.004, whereas overall haplotype diversity ($h \pm$ SD) was 0.970 ± 0.013. Genetic diversity of Thai *P. hypomelanus* was lower and colony size was smaller on non-protected islands compared to those designated on protected islands. The results suggested that there is a potential risk of local extinction on non-protected islands, and hence proper management to conserve this species at local scale should be implemented. These genetic diversity data could be useful as baseline data for subsequent population genetic studies and conservation in the future.

Introduction: Island populations are at a higher risk of extinction compared to mainland populations due to low genetic variation and inbreeding depression, leading to reduced adaptability to environmental changes. Population genetic diversity assessment can provide information for estimating extinction risk[1,2,3] and initiating conservation plan[4].

The genus *Pteropus* (Chiroptera: Pteropodidae), commonly known as flying foxes, is comprised of 65 recognized species. Most flying foxes are island-dwelling species that occur in remote area with small population size, which make them extremely sensitive to human disturbance or habitat conversion. Flying foxes are becoming either threatened or endangered due to deforestation and hunting[5]. The extinction risk in this genus is possibly higher in small-sized species with small home range, such as *P. hypomelanus*.

Pteropus hypomelanus (Temminck, 1853), also known as the island flying fox or variable flying fox, is distributed in the Indo-Australian region[6]. It roosts in colonies of 10 – 1000 individuals[7]. Roosting sites are usually restricted to small off-shore islands, but bats may visit mainland's coastal area to feed. Thus, they play important ecological roles as important seed dispersers and pollinators of economically important fruits, such as durian (*Durio ziberthinus*)[8]. Although, *P. hypomalnus* is listed as Least Concern by the IUCN[9] and as Near Threatened in Thailand Red Data, information regarding roosting sites, population size and genetic diversity are inadequate. This study investigated the genetic diversity of *P. hypomelanus* population in Thailand using the mitochondrial D-loop. A clear understanding of genetic diversity of this species is important for conservation management in Thailand.

Methodology:

Field survey and sample collection: Field surveys were conducted between March 2018 and May 2019 in both the Gulf of Thailand and the Andaman Sea (Figure 1). Fecal samples were collected from four islands in the Gulf of Thailand, namely Khram Yai Island (~21 km^2, n = 10), Chan Island (~0.5 km^2, n = 7), Mun Nai Island (~0.5 km^2, n = 5) and Talu Island (~1.5 km^2, n = 8), and two islands in the Andaman Sea, namely Miang Island (~1 km^2, n = 4) and Hin Dum Island (~0.1 km^2, n = 6). The minimum number of individuals in each colony was estimated based on

visual encounter surveys. To determine whether there was an increase or decrease in population size, we relied on data from field observations and personal interviews, where field data were not available. Only fresh and isolated fecal samples were collected under the roosting trees. In order to avoid collecting samples from the same individual, the minimum distance between each fecal sample was kept at 5 meters. In the field, all samples were kept in lysis buffer, and later transported to the laboratory and stored at -20 °C.

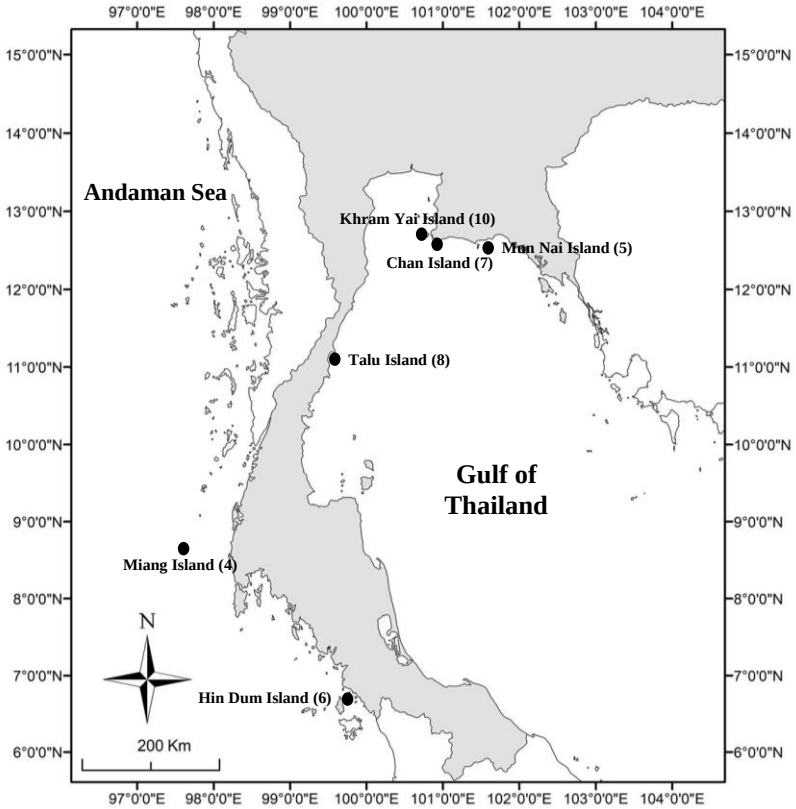

Figure 1. Sampling locations of *P. hypomelanus* on islands along the coast of the Gulf of Thailand and the Andaman Sea. Sample size is shown in parenthesis.

DNA extraction, amplification, and sequencing: Total genomic DNA was extracted from fecal samples using AccuPrep® Stool Genomic DNA Extraction Kit (Bioneer Inc., South Korea). DNA fragment was amplified from the mitochondrial control region (D-loop) by polymerase chain reaction (PCR), using the forward primer Pv_dlpL (5'-AACACCCAAAGCTGATATTCTACT-3') and the reverse primer Pv_dlpR (5'-CGTATGCGTATGCGTATGTC-3')[10]. Amplification was performed in a programmable thermocycler according to the following protocol: the initial denaturing step at 94 °C for 3 min, followed by 35 cycles of denaturing step at 94 °C for 1 min, annealing step at 54 °C for 1 min and then extension step at 74 °C for 1 min. A final extension at 74 °C for 5 min was included after the last amplification cycle. Amplicons were purified using AccuPrep® PCR Purification Kit (Bioneer Inc., South Korea) and sequenced using an ABI 3730XL DNA sequencer (Bioneer Inc., South Korea). Primer Pv_dlpL was used as a sequencing primer.
Data analyses: Sequences were aligned using ClustalW in MEGA 7.0 software[11]. To examine the genetic diversity, number of haplotypes (H), haplotype diversity (h), and nucleotide diversity (π) were calculated using DnaSP v.6 software[12].

Results and Discussion: D-loop sequences (n = 40) revealed a total of 26 haplotypes, 24 of which were specific to certain island. Two haplotypes (H11, H14) were shared among the sampling localities. H11 was detected at four sampling localities both in the Gulf of Thailand and the Andaman Sea, whereas H14 was shared between two islands in the Gulf of Thailand (Table 1). Low number of shared haplotypes and relatively high number of island-specific haplotypes suggested that gene flow between islands was limited and populations were isolated. This particular species is thought to have a limited long-distance dispersal ability[10,13]. Based on a previous study of the same species in Malaysia, no significant correlation between genetic and geographic distances was observed, but significant pairwise F_{ST} values inferred clear genetic differentiation among island populations[10]. Behavioral traits, such as site fidelity, or philopatry, may have contributed to the observed genetic differentiation and limited gene flow. However, the results were based on mitochondrial DNA sequences and the speculation regarding limited dispersal ability may be female-biased. Further assessment of nuclear genes will present a clearer representation of *P. hypomelanus* dispersal ability.

The overall haplotype diversity ($h \pm$ SD) was 0.970 ± 0.013, whereas nucleotide diversity ($\pi \pm$ SD) was 0.034 ± 0.004. Based on the results, the overall genetic diversity of *P. hypomelanus* was relatively high and comparable to the value reported from Malaysia and a closely related species, *P. melanotus natalis,* on the Christmas Island[14] (Table 2). Regardless of the high overall genetic diversity, localized genetic assessment at small-scale is necessary for population conservation, especially when haplotype distribution and frequency suggested that *P. hypomelanus* are isolated island population.

At all sampling localities, high haplotype diversity (0.786 – 1.000) and nucleotide diversity (0.010 – 0.055) were observed (Table 2). Highest haplotype diversity (h = 1.000) was found in colonies roosted on Miang Island and Mun Nai Island, and highest nucleotide diversity (π = 0.055) was found in colony roosted on Chan Island. Lowest haplotype diversity (h = 0.786) and nucleotide diversity (π = 0.010) were found in colonies roosted on Talu Island and Hin Dum Island, respectively. Interestingly, when comparing among all sampling localities, *P. hypomelanus* colonies roosted on protected islands (Khram Yai Island, Chan Island, Mun Nai Island and Miang Island) were characterized by relatively higher genetic diversity and larger colony size (> 300 individuals). In contrast, relatively low genetic diversity was observed in colonies roosted in non-protected islands, namely Talu Island (h = 0.786 ± 0.151) and Hin-Dum Island (h = 0.800 ± 0.172). As such, it is possible that the presence of threats such as tourism, habitat alteration and destruction on non-protected islands was detrimental and consequently led to population decline[15], which was confirmed through field data. It is crucial that proper conservation measures are implemented on these islands to avoid further population decline and allow the population to recover.

Nonetheless, it should be mentioned that the high haplotype diversity observed in some sampling localities may be overestimated due to small sample size. Addition samples from those particular islands will provide more conclusive evidence.

Table 1. Haplotype frequency observed at each sampling locality in the Gulf of Thailand and the Andaman Sea based on mitochondrial D-loop sequences (585 bps).

Haplotype	Gulf of Thailand				Andaman Sea	
	Khram Yai (n = 10)	Chan (n = 7)	Mun Nai (n = 5)	Talu (n = 8)	Similan (n = 4)	Hin Dum (n = 6)
H1	0.300	-	-	-	-	-
H2	0.100	-	-	-	-	-
H3	0.100	-	-	-	-	-
H4	0.100	-	-	-	-	-
H5	-	0.143	-	-	-	-
H6	-	0.143	-	-	-	-
H7	-	0.143	-	-	-	-
H8	-	0.285	-	-	-	-
H9	-	0.143	-	-	-	-
H10	-	-	0.200	-	-	-
H11	0.100	0.143	0.200	-	0.250	-
H12	-	-	0.200	-	-	-
H13	-	-	0.200	-	-	-
H14	0.300	-	0.200	-	-	-
H15	-	-	-	0.500	-	-
H16	-	-	-	0.125	-	-
H17	-	-	-	0.125	-	-
H18	-	-	-	0.125	-	-
H19	-	-	-	0.125	-	-
H20	-	-	-	-	0.250	-
H21	-	-	-	-	0.250	-
H22	-	-	-	-	0.250	-
H23	-	-	-	-	-	0.170
H24	-	-	-	-	-	0.490
H25	-	-	-	-	-	0.170
H26	-	-	-	-	-	0.170

Table 2.Overall genetic diversity of *P. hypomelanus* in Thailand compared to previously studies in Malaysia and Christmas Island based on the mitochondrial D-loop sequences.

Species	Population	Number of base pair	Number of haplotype (H)	Haplotype diversity ($h \pm$ SD)	Nucleotide diversity ($\pi \pm$ SD)
P. hypomelanus (n = 40)	Thailand	585	26	0.970 ± 0.013	0.034 ± 0.004
P. hypomelanus[10] (n = 80)	Malaysia	747	35	0.943 ± 0.015	0.040 ± 0.004
P. melanotus natalis[14] (n = 28)	Christmas Island	390	18	0.942 ± 0.029	0.074

Table 3. Genetic diversity and estimated colony size of *P. hypomelanus* at 6 sampling localities.

Locality	Protection	Minimum colony size	Population trend	Haplotype diversity (h ± SD)	Nucleotide diversity (π ± SD)
Gulf of Thailand					
Khram Yai Island	Protected area	500	No data	0.867 ± 0.085	0.016 ± 0.002
Chan Island	Protected area	300	Stable	0.952 ± 0.096	0.055 ± 0.007
Mun Nai Island	Protected area	300	Stable	1.000 ± 0.126	0.012 ± 0.005
Talu Island	Non-protected area	100	Decline	0.786 ± 0.151	0.031 ± 0.005
Andaman Sea					
Miang Island	Protected area	600	Stable	1.000 ± 0.177	0.040 ± 0.016
Hin Dum Island	Non-protected area	200	Stable	0.800 ± 0.172	0.010 ± 0.005

Conclusion: Mitochondrial D-loop sequences (585 bps) of *P. hypomelanus* (n = 40) revealed a total of 26 haplotypes, 24 of which were island-specific haplotypes, suggesting that gene flow between islands was limited and populations were isolated. The overall genetic diversity, in terms of haplotype diversity (h ± SD) and nucleotide diversity (π ± SD), were 0.970 ± 0.013 and 0.034 ± 0.004, respectively. Compared to protected areas, relatively lower genetic diversity and colony size were observed on islands located in non-protected areas. Therefore, in conjunction with limited gene flow, populations on non-protected islands are more vulnerable and should be considered as top priority for population monitoring and conservation programs. This study provided one of the first data on genetic diversity of *P. hypomelanus* in Thailand, which serve as baseline data for biodiversity assessment, conservation, and future studies.

References:

1. Berry RJ. Biol J Linn Soc. 1986;28:205–230.
2. Frankham R. Conserv Biol. 1998;12:665–675.
3. Plante Y, Vega-Pla JL, Lucas Z, Colling D, de March B, Buchanan F. Heredity. 2007;98: 594–602.
4. Ralls K, Ballou JD, Dudash MR, Eldridge MDB, Fenster CB, Lacy RC, Sunnuck P, Frankham R. Conserv Lett. 2017;11:1–6.
5. Mickleburgh SP, Huston AM, Racey PA. Oryx. 2002;36:18–34.
6. Jones DP, Kunz TH. Mamm Species. 2000;639:1–6.
7. Lekagul B, McNeely JA, Mammals of Thailand. 1977.
8. Aziz SA, Clements GR, McConkey KR, Srithongchuay T, Pathil S, Hafizi Abu Yazid MN, Campos-Arceiz A, Forget PM, Bumrungsri S. Ecol Evol. 2017;7:8670–8684.
9. Francis C, Rosell-Ambal G, Bonaccorso F, Heaney L, Molur S, Srinivasulu C. The IUCN Red List of Threatened Species. 2008.
10. Olival KJ, Population Genetic Structure and Phylogeography of Southeast Asian Flying Foxes: implications for conservation and disease ecology. 2008.
11. Kumar S, Stecher G, Tamura K. Mol Biol Evol. 2016;33:1870–1874.
12. Rozas J, Ferrer-Meta A, Sanchez-DelBarrio JC, Guirao-Rico S, Libardo P, Ramos-Onsins SE. Mol Biol Evol. 2017;34:3299–3302.
13. Mickleburgh SP, Hutson AM, Racey PA. Old World Fruit Bats: an action plan for their conservation. 1992.
14. Phalen DN, Hall J, Ganesh G, Hartigan A, Smith C, De Jong C, Field H, Rose K. J Mammal. 2017;98:428–437.
15. Brown VA, Brooke AN, Fordyce JA, McCracken GF. Conserv Gent. 2011;12:933–941.

Acknowledgements: Funding for this research was provided by the Plant Genetic Conservation Project under the Royal Initiative of Her Royal Highness Princess Maha Chakri Sirindhorn (RSPG). We thank the Royal Thai Navy, the Department of Eastern Marine and Coastal Resources Research Center (EMCOR), and the members of Thai Turtle Laboratory for the advice. Lastly, we would also like to thank the Department of Biology, Faculty of Science, Chulalongkorn University for the supports.

SESSION C1
ANALYTICAL CHEMISTRY

C1_001_OF: FLUORESCENT DETERMINATION OF SOLUBLE PYROPHOSPHATE LEVEL IN SYNOVIAL FLUID AS A MARKER OF PSEUDOGOUT DISEASE

Nattha Yongwattana[1], Wannee Thepsing[1], Supasara Ounsuk[1], Tulyapruek Tawonsawatruk[2], Itaru Hamachi[3], Akio Ojida[4], Jirarut Wongkongkatep[1,*]
[1]Department of Biotechnology, Faculty of Science, Mahidol University, Bangkok 10400, Thailand
[2]Department of Orthopedics, Faculty of Medicine Ramathibodi Hospital, Mahidol University, Bangkok 10400, Thailand
[3]Department of Synthetic Chemistry and Biological Chemistry, Graduate School of Engineering, Kyoto University, Kyoto 615-8510, Japan
[4]Graduate School of Pharmaceutical Sciences, Kyushu University, Fukuoka 812-8582, Japan
*e-mail: jirarut.chu@mahidol.ac.th

Abstract: Pseudogout is one of the joint inflammations caused by the deposition of calcium pyrophosphate (CaPPi) crystal in the affected joint. The formation of crystal starts from inorganic pyrophosphate (PPi), which is generated from the decomposition reaction of an extracellular adenosine triphosphate (ATP), then forms complex with calcium to create CaPPi crystal and deposit in articular cartilage leading to pseudogout disease. Nowadays, there are few diagnostic methods such as radiography and polarized light microscopy for the crystal observation, but the discrepancy of the methods seems to be problematic. Therefore, the purpose of this study is to apply the PPi specific sensor for fluorescent detection of soluble PPi in synovial fluid of the arthritis patients. The sensor comprised of xanthene as a fluorophore and the Dpa/Zn(II) as two specific binding sites for PPi. Each patient synovial fluid was titrated with the sensor in aqueous solution for the evaluation of PPi level. The sensor displays a rapid detection of the soluble PPi with a large fluorescence enhancement, showing that the patient with high level of PPi in synovial fluid have high possibility to be pseudogout. Furthermore, the ENLITEN® ATP Assay System showed that the ATP levels of the patient synovial fluids were 3-order lower than the detection limit of the sensor, demonstrating that this sensor is promising for the diagnosis of pseudogout disease.

Introduction: Nowadays, the aging population is increasing rapidly along with many chronic diseases. Calcium pyrophosphate deposition disease or pseudogout is one of the arthritis diseases occurred in the joint of many elderly patients. The deposition of calcium pyrophosphate crystals in affected joint is the main culprit of pseudogout, inorganic pyrophosphate (PPi) is generated from the extracellular adenosine triphosphate (ATP), then forms crystals with calcium in the pericellular matrix of articular cartilage. Thus, the concentration of soluble PPi in patient synovial fluid can be used as a biomarker to evaluate the possibility to be pseudogout disease. In addition, the patient with excess CaPPi crystal deposition manifest as swelling, redness, and pain in the affected joint[3]. Furthermore, the culprit and clinical symptom of pseudogout look almost exactly the same as gout disease, but gout causes by the deposition of monosodium urate crystals[4]. At present, there are few diagnostic methods available for differentiation between gout and pseudogout, such as radiography for detection of crystals, unfortunately the results can easily lead to misdiagnosis due to the clinical picture of both diseases look quite similar and also depend on the technician. Therefore, this research aimed to apply xantheneDpa-Zn (II) complex as a PPi specific sensor for the detection of soluble PPi in synovial fluid of the arthritis patients using the fluorescence technique. The highly sensitive xantheneDpa-Zn (II) complex will provide the reliable and rapid method for the detection of pseudogout disease from gout and other joint inflammation symptoms.

Methodology:

Chemicals and reagents: XantheneDpa-Zn(II) complex ($C_{39}H_{34}N_6O_4Zn_2{\cdot}2ClO_4{\cdot}3H_2O$), referred hereafter as Dpa sensor was originally synthesized at Professor Akio Ojida's laboratory, Kyushu University, JAPAN. Enliten® kit (ATP, ATP-free water, luciferase/luciferin reagent) was purchased from Promega, Madison, USA. HEPES, minimum 99.5% titration ($C_8H_{18}N_2O_4S$) was purchased from Sigma, St. Louis, USA. Magnesium chloride ($MgCl_2$) was purchased from Merck, Darmstadt, Germany. Sodium chloride (NaCl) was purchased from LobaChemie, Mumbai, India.

Synovial fluid (SF) samples of patients with joint inflammation symptom: Patient SF was kindly provided by Dr. Tulyapruek Tawonsawatruk, Department of Orthopaedics, Faculty of Medicine, Ramathibodi Hospital, Mahidol University, 270 Rama 6 Road, Bangkok 10400 THAILAND. Patient SF was the waste from the therapeutic treatment of those patients with joint inflammation symptom. The obtained Patient SF samples were used in accordance with the ethical approval of the Ramathibodi Hospital, Mahidol University, Bangkok, Thailand (Documentary Proof of Ethical Clearance Committee on Human Rights Related to Research Involving Human Subjects, based on the declaration of Helsinki, Faculty of Medicine Ramathibodi Hospital, Mahidol University Reference No. MURA2017/317). The Patient SF were kept at -20°C prior analysis.

Preparation of SF sample: The Patient SF was pipetted into eppendorf tube and centrifuged at 12,000 rpm for 10 minutes to separate the supernatant and precipitate. The clear supernatant of SF in the upper phase was used for analysis of soluble PPi level.

Analysis of ATP concentration in Patient SF: The standard curve of ATP was constructed using ENLITEN® kit. ATP standard (10^{-7} M) provided in the ENLITEN® kit was diluted to 10^{-17} in ATP-free water. Luciferase/Luciferin solution (50 µL) and the diluted ATP standard (10^{-7}-10^{-17} M) (5 µL) were pipetted into 384-well plate and analysed for the luminescence intensity using microplate reader (TECAN Spark 10M, Tecan Group Ltd., Mannedorf, Switzerland). The amount of ATP in Patient SF was measured at 0, 1, 2, 3, 4, 5, 6, 24 h during thawing period at room temperature by using ENLITEN® kit. Luciferase/Luciferin solution (50 µL) and the Patient SF (5 µL) were pipetted into 384-well plate and analysed for the luminescence intensity using microplate reader (TECAN Spark 10M, Tecan Group Ltd., Mannedorf, Switzerland).

Analysis of soluble PPi concentration in Patient SF: To a solution of 1 µM Dpa sensor in 50 mM HEPES buffer (3 ml), pH 7.4 in a quartz cell at 25°C, the clear supernatant of Patient SF was serially added using the volume between 1-10 µL/each titration. The fluorescence emission spectrum was observed on spectrofluorometer (JASCO FP6500, Japan). The standard curve of Dpa sensor toward PPi was constructed using 0.01-5 µM of PPi solution for titration using similar procedure. The lowest detection limit of Dpa sensor toward ATP was confirmed using ATP stock solution diluted in ATP free water obtained from ENLITEN® kit using similar procedure.

Results and Discussion:

Analysis of ATP concentration in Patient SF: The time-course ATP concentrations of Patient SF samples during thawing at 27°C were determined through the ENLITEN ® ATP Assay kit in order to check the level of ATP and the PPi related enzyme activity available in the Patient SF. The ENLITEN® ATP Assay System showed that the initial concentration of ATP was picomolar level, and the highest ATP concentration observed was approximately 0.1-2 nanomolar at 3 hours when the Patient SF was thawed to room temperature (Figure 1), indicating that some ATP specific enzymes were still active even after the storage of the SF sample under -20°C. However, such ATP concentration was approximately 3-order below the lower detection limit

of Dpa sensor, suggesting the suitability of using this sensor for fluorescent detection of the soluble PPi in Patient SF.

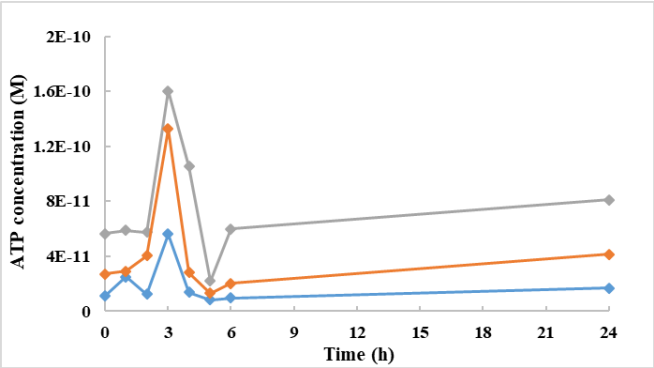

Figure 1. Variation of ATP concentrations in 3 samples of Patient SF during thawing period.

Performance of Dpa sensor for detection of soluble PPi: The performance of Dpa sensor toward PPi was firstly tested in a 50 mM HEPES buffer (pH 7.4). An increase in fluorescence emission centred at 520 nm was observed when the solution of Dpa sensor was titrated with soluble PPi as shown in Figure 2a and a large fluorescent enhancement (F/F_0 > 100) was observed (Figure 2b). The fluorescent intensity was then displayed the saturation curve with the upper limit of quantification (ULOQ) of 2.2 µM. The sensor also exhibited the lower limit of quantification (LLOQ) of 0.39 µM and the middle point of quantification (MPOQ) of 0.9 µM as shown in Figure 2b.

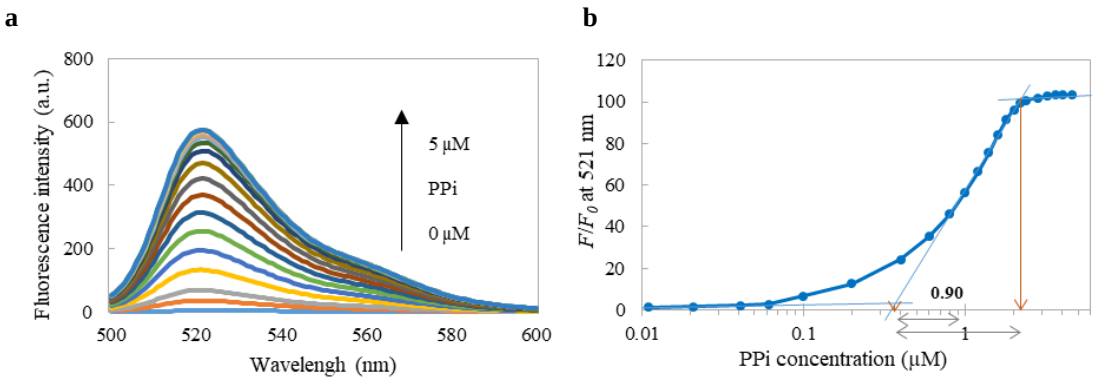

Figure 2. (a) Fluorescence spectral changes of Dpa sensor upon addition of PPi (0-5 µM). (b) Change in fluorescence intensity (F/F_0) at 521 nm of Dpa sensor upon addition of PPi. Conditions: 1 µM Dpa sensor in 50 mM HEPES (pH 7.4), λ_{ex}=488 nm, 25°C.

Analysis of soluble PPi concentration in Patient SF: Patient SF was diluted serially and then the titration was performed to the solution of Dpa sensor in 50 mM HEPES buffer (pH 7.4). The fluorescence emission of the Dpa sensor was largely increased upon the addition of the clear supernatant of Patient SF, indicating the presence of soluble PPi in the Patient SF (Figure 3). However, in order to calculate the concentration of the soluble PPi in the synovial fluid, it could be problematic to use the vertical axis of F/F_0 for the calculation because the F/F_0 of the Dpa sensor varies largely due to the different microenvironment of the fluorescent sensor. It is well-known that the fluorescent properties of the substance is highly sensitive, which allow the extremely low detection limit in comparison with UV technique. On the other hand,

fluorescent technique can provide a high fluctuation when analyzed in a non-uniform environment such as different ionic strength and composition of buffer.

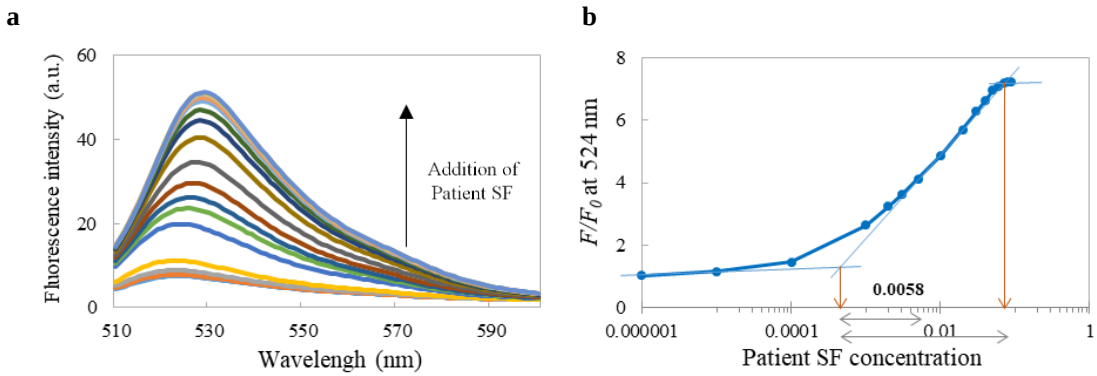

Figure 3 (a) Fluorescence spectral changes of Dpa sensor upon addition of the clear supernatant of Patient SF sample 1. (b) Change in fluorescence intensity (F/F_0) at 524 nm of Dpa sensor upon addition of the clear supernatant of Patient SF sample 1. Conditions: 1 µM Dpa sensor in 50 mM HEPES (pH 7.4), λ_{ex}=488 nm, 25°C.

Synovial fluid is a complex biological fluid, comprising of various component such as sodium ions (136 mM), potassium ions (4 mM), calcium ion (1.5-2.4 mM), protein, albumin, mucoprotein, hyaluronic acid, sialic acid, glucose and a number of cells[1] and the characteristic of the SF is different between the normal and the inflammatory cases. It is impossible to control the assay environment of the Dpa sensor after addition of SF sample to be under similar condition for all tests. Table 1 revealed that the F/F_0 of the Dpa sensor after addition of Patient SF samples varied largely from 4.8 to 21.3, which was significantly lower than F/F_0 of 100 observed in the sole HEPES buffer (50 mM, pH 7.4) (Figure 2). To achieve the highest accuracy in fluorescence sensing, the use of the vertical axis of F/F_0 for calculation of the PPi concentration was avoided then the comparison between the MPOQ of the standard and each SF samples was used instead. Table 1 summarized the amount of soluble PPi content in the Patient SF which ranged from 0.03 to 0.18 nmole PPi/µL of SF. The Dpa sensor demonstrated a high possibility to be a specific soluble PPi sensing for investigation of the amount soluble PPi in Patient SF, which related with pseudogout disease.

Table 1 The amount of soluble PPi in 8 Patient SF samples

Patient SF sample	Maximum value of F/F_0 observed	MPOQ	The amount of PPi calculated (nmol/µl)
1	7.2431	0.0058	0.1552
2	9.9730	0.0090	0.1000
3	21.3401	0.0092	0.0978
4	19.6606	0.0230	0.0391
5	4.8613	0.0050	0.1800
6	8.0283	0.0090	0.1000
7	18.8429	0.0180	0.0500
8	12.6311	0.0088	0.1023

Conclusion: The ENLITEN® ATP Assay System showed that the level of ATP in SF sample was varied during thawing at 27°C, however, Dpa sensor was not disturbed by such ATP presented in the Patient SF because the highest ATP level was approximately 3-order below the lower

detection limit of Dpa sensor. Furthermore, the level of the soluble PPi in Patient SF detected fluorescently by Dpa sensor, can be adopted as a marker of pseudogout disease with suitable control. We strongly believe that the fluorescent detection of soluble PPi using Dpa sensor could be a rapid and sensitive method for an improvement of the preciseness and accuracy of diagnostic method of pseudogout disease.

References:

1. Hearn PR, Russell RG. Formation of calcium pyrophosphate crystals in vitro: implications for calcium pyrophosphate crystal deposition disease (pseudogout). Ann Rhem Dis. 1980;39(3):222-7.
2. Ojida A, Takashima I, Kohira T, Nonaka H, Hamachi I. Turn-on fluorescence sensing of nucleoside polyphosphates using a xanthene-based Zn(II) complex chemosensor. Am Chem Soc. 2008;130:12095-12101.
3. Rosenthal AK, Ryan LM. Calcium pyrophosphate deposition disease. N Engl J Med. 2016;374(26):2575-2584.
4. Stanway J, Marianayagam T, Ellis S. Crystal arthropathies. Medicine. 2018;46(3):181-6.

Acknowledgements: This research was supported by Center of Excellence on Medical Biotechnology (CEMB), S&T Postgraduate Education and Research Development Office (PERDO), Office of Higher Education Commission (OHEC), Thailand.

C1_002_PF: A CHEMICAL SENSOR FOR FORMALDEHYDE DETECTION USING NITROGEN-DOPED GRAPHENE QUANTUM DOTS

Teerapong Jantarat[1,3], Chotika Neamchey[1,3], Proespichaya Kanatharana[1,3], Panote Thavarungkul[2,3], Dhassida Sooksawat[1,3], Chongdee Thammakhet-Buranachai[1,3,*]
[1]Department of Chemistry and Center of Excellence for Innovation in Chemistry (PERCH-CIC), Faculty of Science, Prince of Songkla University, Hat Yai, Songkhla 90112, Thailand
[2]Department of Physics, Faculty of Science, Prince of Songkla University, Hat Yai, Songkhla 90112, Thailand
[3]Center of Excellence for Trace Analysis and Biosensor, Prince of Songkla University, Hat Yai, Songkhla 90112, Thailand
*e-mail: chongdee.t@psu.ac.th

Abstract: Formaldehyde (FA) is a one of the most concerned contaminants in food especially seafood since it has illegally been used as seafood preservative to keep them fresh and to prevent a spoilage from transportation. There is a need, therefore, of the analytical method for FA detection which can be applied to detect this compound in seafood samples. Herein, we propose a nitrogen doped graphene quantum dots (N-GQDs) based chemical sensor. N-GQDs was easily synthesized in the microwave oven under mild condition, the obtained N-GQDs provided bright blue fluorescent emission under the UV-radiation. Several techniques were used to characterize N-GQDs including, UV-Vis spectrophotometry, fluorescence, and FT-IR. The fluorescence intensity N-GQDs decrease linearly with the concentration of FA in the range of 2.5 – 100 mg L^{-1}. In addition, the selectivity of the developed sensor was investigated using the analogous carbonyl compound and the existential interferences in seafood samples such as different types of salts. The results showed that N-GQDs provided the response to only acetaldehyde whereas no response from other compounds was observed. We believe that after optimization, the sensor can be applied to detect FA in real sample.

Introduction: Currently, the contamination in food from pesticides, insecticides, antibiotics, food additives, and food preservatives is a serious problem and gaining a great concern since most of these compounds are harmful to human health and the environment in either short term or long-term aspect[1-3].

Concerning of contamination of formaldehyde (FA) in food especially seafood is crucial because it has illegally been used as seafood preservative to avoid a spoilage from transportation and to remain fresh after fishery. FA can cause serious problems on human body for example, eyes, throat and nose irritation, nasal congestion, central nervous system damage, immune system disorders, blindness and respiratory disease[4]. Furthermore, FA has been classified as a 1A carcinogen group (probably carcinogenic to humans) by the International Agency for Research on Cancer[5] and the US Environmental Protection Agency has been limiting the amount of FA in taking per day (acceptable daily intake; ADI) at 0.2 mg.kg^{-1} by weight of consumer[6]. Due to toxicity of FA, an easy, sensitive, selective, rapid method for detection of FA contamination in seafood is very important to develop.

Several conventional techniques for FA detection were reported such as high-performance liquid chromatography (HPLC)[7], and gas chromatography (GC)[8]. Even though these techniques provide high sensitivity to FA, but they need a high skill operator, require expensive instrument, and long analysis time[9, 10]. Nowadays, the development of FA sensing has been fabricated for several techniques, such as electrochemical[11], optical[12, 13], and piezoelectric sensors[14]. Among these techniques, optical sensors especially fluorescent sensors are alternative tools to be used for detection of various types of target molecules including FA due to easy operation, rapid, and low cost[15]. There are however reports using the specific dyes for FA sensing, for example, aza-Cope rearrangement reaction[16, 17], but there is

a need of using the toxic organic solvent for the reaction. Consequently, the biocompatibility and environmentally friendly sensor is needed.

Carbon-based nanomaterials are interested to be used in sensing fabrication due to their good properties such as excellent physicochemical properties, environmentally friendly[18, 19]. Nitrogen-doped graphene quantum dots (N-GQDs) is one type of carbon-based nanomaterials which strongly exhibited fluorescent emission because of the electron delocalization in sp^2 hybridization of N-GQDs skeleton. They also showed good properties such as quantum size effects, photostability, good biocompatibility, large specific surface areas, and water solubility[20-23]. Due to highly abundant nitrogen doped of N-GQDs, they have a potential to be reacted with FA and change the oxidation state affecting the decreasing fluorescent signal of N-GQDs. Therefore, N-QGDs will potentially be applied to detect FA since redox reaction can cause the electron transferring of nitrogen atoms of N-GQDs to FA leading to a significant fluorescence quenching[22]. Therefore, we herein proposed the chemical sensor utilizing N-GQDs to react with FA resulting in the decrease of fluorescent emission of N-GQDs.

Methodology:

Materials: All chemicals are commercially available and are of analytical grade. Formaldehyde was purchased from Sigma-Aldrich (St. Louis, MO, USA), Citric acid and urea were purchased from Loba Chemie (Mumbai, India). Acetaldehyde was purchased from Merck (Hohenbrunn, Germany). Ammonium chloride, sodium bicarbonate, and potassium phosphate were purchased from Merck (Darmstadt, Germany).

Synthesis of nitrogen-doped graphene quantum dots: The synthesis of N-GQDs was slightly adopted from Ma's work[24]. N-GQDs is easily synthesized using a microwave oven. Urea and citric acid were used as precursors for the synthesis. In the procedure, 0.30 g urea and 0.30 g citric acid were dissolved in 10 mL DI water to obtain the clear and transparent solution. Then the solution was transferred to the microwave oven and heated at 600 W approximately 4-5 min until obtained the dark-brown solid of N-GQDs. The dark-brown solid was then re-dispersed with 10 mL DI water and kept at 4°C for the further use.

Characterization of graphene quantum dots: The synthesized N-GQDs was characterized using several techniques. The fluorescent spectra were recorded on a LS 55 PerkinElmer Fluorescence Spectrometer. Absorption spectrum was investigated using an AvaSpec-ULS2048 StarLine Versatile Fiber-optic Spectrometer. Fourier Transform Infrared spectrum (FT-IR) was studied from a Spectrum BX FTIR spectrometry and recorded the transmitting wavenumber range of 400–4000 cm^{-1}. The pellets sample were prepared with dried KBr.

FA detection procedure: N-GQDs was dispersed in DI water and FA solutions were prepared in the 0.10 mM phosphate buffer pH 7.0. Then 100 µL FA solution and 100 µL N-GQDs were mixed and incubated for 15 min. After the incubation, the mixture solution was transferred to a quartz cuvette and the fluorescent emissions were recorded from 380 – 640 nm using the excitation wavelength at 340 nm. For the selectivity testing, as the same conditions with the sensing protocol, but FA solution was substituted by other interferences.

Results and Discussion:

Characterization of graphene quantum dots: As shown in Figure 1., the absorption spectrum of N-GQDs was performed and shown the maximum absorption wavelength at 340 nm (Figure. 1A) and the emission spectra of N-GQDs are shown the strongest fluorescent emission at 460 nm when the excitation was stimulated at 340 nm (Figure. 1B) indicating the N-GQDs was successfully synthesized. In order to observe the fluorescent emission of N-GQDs and possibly detect of FA using N-GQDs, Figure. 1D showed the comparison of photographs of the fluorescent emission under the white-light (a) and UV-light (b) with different conditions, (1) the blank solution, (2) N-GQDs, and (3) N-GQDs with FA. The results could be observed that there was no fluorescence from the blank solution whereas the

bright-blue fluorescent emission could be seen by the naked-eye under UV-light. Furthermore, after the FA solution was added into the N-GQDs, the bright-blue fluorescence was turned off showing the possibility to be used the N-GQDs to detect FA.

FT-IR was further used to characterize N-GQDs as the result was shown in Figure 1C. The FT-IR peaks showed that O-H stretching at around 3,450 cm^{-1}, C-H stretching at 2,780 cm^{-1}, C=O vibrations at around 1718 cm^{-1}, C=C vibration at around 1658 cm^{-1}, carboxyl C-OH vibrations at 1,400 cm^{-1}, hydroxyl C-OH vibrations at 1,082 cm^{-1}. According to the FT-IR, the results were consistent with the N-GQDs were encapsulated with the hydrophilic functional group, mainly carboxylic group (COOH). Furthermore, the synthesized N-GQDs were easily dispersed in water which confirmed the results. Additionally, Dan Qu and coworkers explained the synthesized mechanism which the formation of pyrrolic structure via the dehydration between carboxylic group of citric acid used as a precursor transferring into graphene sheets, and the nitrogen atom in urea entered in the structure to increase the fluorescent quantum yield[23].

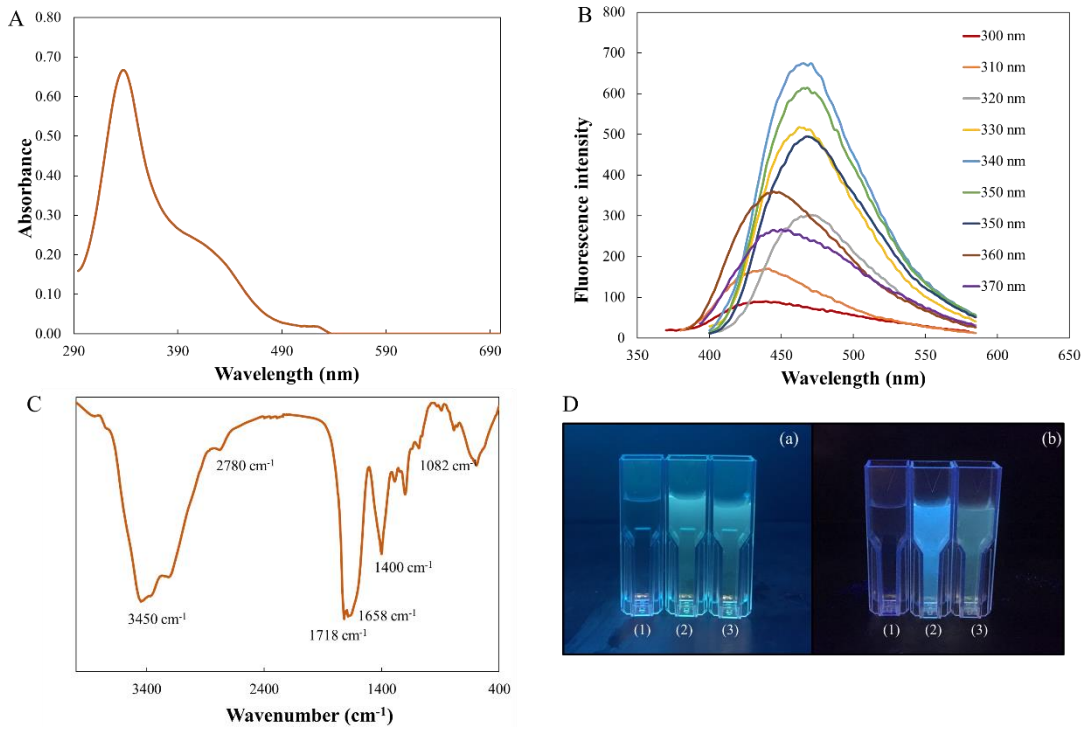

Figure 1. (A) Absorption spectrum of N-GQDs, (B) emission spectra of N-GQDs with different exciting wavelengths, (C) FT-IR spectrum of N-GQDs, (D) Photograph of the N-GQDs under the white-light (a), and UV-radiation (b) which are the blank solution (1), N-GQDs (2), and N-GQDs with FA.

The preliminary study of FA detection and sensor performances: As the results from Figure 2., The photograph of the fluorescent emission under UV-light obviously decreased after adding the high concentration of FA (Figure. 2A). The sensing mechanism might be explained by the reaction between N-GQDs and FA. N-GQDs was an electron-rich species which electron can be transferred to FA molecules; therefore, the decrease of fluorescent emission could be observed. Then, in order to construct the FA sensor, the fluorescent signals were recorded showing the response in Figure. 2B. The response of N-GQDs emission to the different concentration of FA dropped with the increase of FA concentration. Then,

the fluorescent signals were plotted to the linear correlation between the ratio of blank signal and sensor's response (F_0/F), and FA concentration (Figure. 2C). The linear range of the sensor is between 2.5-100 mg. L^{-1} which the linear regression equation was related to $F0/F = 0.0032C_{FA} + 0.9831$ (Figure. 2D). At the moment, the lowest FA concentration at 2.5 mg L^{-1} was detectable using the developed sensor, however, if the optimization of the sensor was carried out, it was expected that under the optimal condition, the detected concentration can be pushed down to the level of μg L^{-1}.

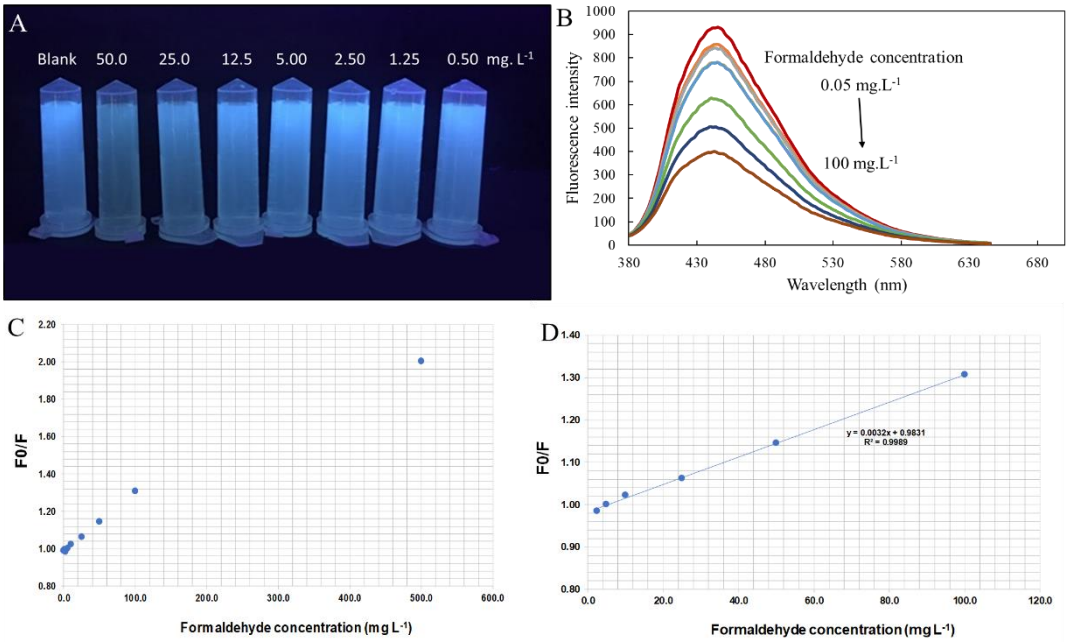

Figure 2. (A) The photograph under UV radiation of N-GQDs mixed with FA in different concentration, (B) The reduction of fluorescent signal of N-GQDs responding to the different concentration of FA, (C) The plot of fluorescent ratio (F0/F) and FA concentration, (D) The linear dynamic range of the developed sensor

The selectivity of the sensor was tested with the analogue carbonyl compound (acetaldehyde) and existentially interferences (potassium ion, ammonium ion, and sodium bicarbonate) in the real seafood samples with the concentration of each interferences at 400 mg. L^{-1}. As a result from Figure 3., the developed sensor showed no responses to other interferences except to acetaldehyde which the fluorescent signal obviously reduced from the blank indicating that the sensor provided the responses with the compounds consists of carbonyl group. However, in seafood, no acetaldehyde was previously reported as a contaminant, so, the developed sensor still have a good promising to be used as a FA sensor and we expected that after optimization the affecting parameter, the sensor will provide better analytical performances for FA detection.

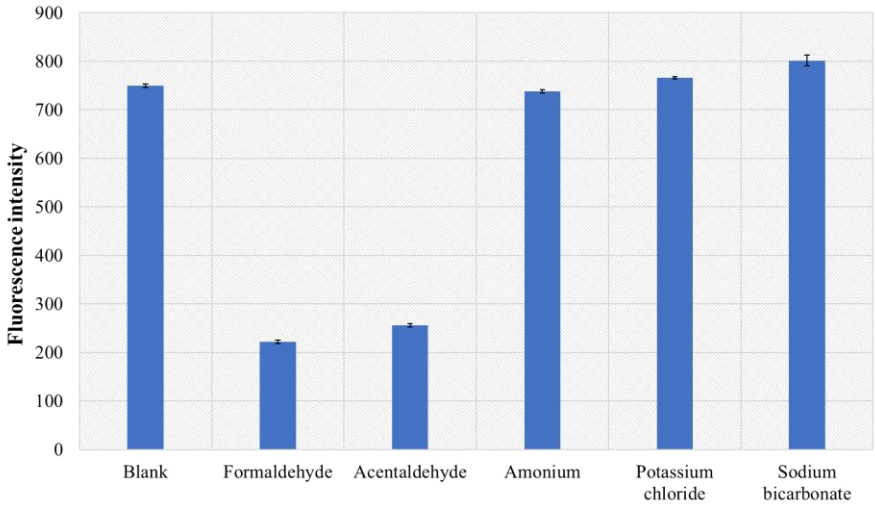

Figure 3. The selectivity of the developed sensor

Conclusion: We developed a chemical sensor for FA detection utilizing the fluorescence turned off. Citric acid and urea were used as precursors. The synthesis of N-GQDs carried out a hydrothermal process using microwave oven for only 5 min. The synthesized N-GQDs exhibited the bright-blue fluorescent emission and provided the strongest emission wavelength at 460 nm. Furthermore, we tried to use the synthesized N-GQDs to fabricate a chemical sensor for FA detection. The results showed that N-GQDs could react to FA affecting the decreased of their fluorescent quantum yield that provided the opportunity to be used N-GQDs for the fabrication of FA sensor. The selectivity of a developed sensor was investigated using acetaldehyde and other existentially content in seafood, the result indicated that N-GQDs responded to acetaldehyde only. We however believe that the developed sensor has a potential to be applied to detect FA in seafood even acetaldehyde affected the sensor because there is no report about the amount of acetaldehyde in seafood.

References:

1. Laszlo N, Lanyi K, Laczay P. Food Chem. 2018;267:178-186.
2. Narenderan S. T, Meyyanathan S. N, Karri V. Food Chem. 2019;289:384-395.
3. Huang Y, Shi T, Luo X, Xiong H, Min F, Chen Y, Nie S, Xie M. Food Chem. 2019;275:255-264.
4. ATSDR, Toxicological Profile for Formaldehyde, Agency for Toxic Substances and Disease Registry, 1999.
5. IARC, IARC Monographs Volume 100F Formaldehyde, International Agency for Research on Cancer, 2007.
6. EPA, Toxicity and Exposure Assessment for Children's Health, U.S. Environmental Protection Agency, 1999.
7. Wang H, Ding J, Du X, Sun X, Chen L, Zeng Q, Xu Y, Zhang Z, Zhao Q, Ding L. Food Chem. 2012;131:380-385.
8. Bianchi F, Careri M, Musci M, Mangia A. Food Chem. 2007;100:1049-1053.
9. Nael G. Y, Hasan S, Maha M. A. Arab. J. Chem. 2015;8:487-494.
10. Weng X, Chon C. H, Jiang H, Li D. Food Chem. 2009;114:1079-1082.
11. Trafela S, Zavašnik J, Šturm S, Rožman K. Z. Electrochim. Acta. 2019;309:346-353.
12. Shahvar A, Saraji M, Shamsaei D. Sens. Actuators B Chem. 2018;273:1474-1478.
13. Li P, Zhang D, Zhang Y, Lu W, Wang W, Chen T. ACS Sens. 2018;3:2394-2401.
14. Wang L, Gao J, Xu J. Sens. Actuators B Chem. 2019;293:71-82.

15. Chaiendoo K, Boonchiangma S, Promarak V, Ngeontae W. Colloid Polym. Sci. 2018;296:1995-2004.
16. Yang H, Fang G, Guo M, Ning P, Feng Y, Yu H, Meng X. Sens. Actuators B Chem. 2018;270:318-326.
17. Zhao X, Ji C, Ma L, Wu Z, Cheng W, Yin M. ACS Sens. 2018;3:2112-2117.
18. Zhu X, Zhang Z, Xue z, Huang C, Shan Y, Liu C, Qin X, Yang W, Chen X, Wang T. Anal. Chem. 2017;89:12054-12058.
19. Wang W, Wang Z, Liu J, Peng Y, Yu X, Wang W, Zhang Z, Sun L. Ind. Eng. Chem. Res. 2018;57:9144-9150.
20. Liu Q, Guo B, Rao Z, Zhann B, Gong J. R. Nano Lett. 2013;13:2436-2441.
21. Bhunia S. K, Dolai S, Sun H, Jelinek R. Sens. Actuators B Chem. 2018;270:223-230.
22. Li H-J, Sun X, Xue F, Ou N, Sun B-O, Qian D-J, Chen M, Wang D, Yang J, Wang X. ACS Sustain Chem Eng. 2018;6:1708-1716.
23. Qu D, Zheng M, Zhang L, Zhao H, Xie Z, Jing X, Haddad R. E, Fan H, Sun Z. Sci Rep. 2014;4:5294-5302.
24. Ma J. L, Yin B. C, Wu X, Ye B. C. Anal. Chem. 2017;89:1323-1328.

Acknowledgements: The authors wish to sincerely thank for financial support from the Center of Excellence for Innovation in Chemistry (PERCH-CIC); PSU Research Fund (Grant no. SCI610483M); the Center of Excellence for Trace Analysis and Biosensors; Department of Chemistry and Department of Physics, Faculty of Science, Prince of Songkla University Ministry of Higher Education, Science, Research and Innovation is gratefully acknowledged. The authors also thank the Development and Promotion of Science and Technology Talents Project (DPST), the Institute for the Promotion of Teaching Science and Technology (IPST) for the financial support.

C1_003_PF: IN-HOUSE METHOD VALIDATION FOR TOTAL ACID NUMBER IN BIODIESEL BY POTENTIOMETRIC TITRATION

Songsuda Promthong, Watchara Kaewsuwan*
Scientific Equipment Center, Prince of Songkla University, Hat Yai Campus, Songkhla, 90110, Thailand
*e-mail: watchara.kae@psu.ac.th

Abstract: The use of certified reference materials (CRMs) in the total acid number (TAN) measurement for the method of validation is well recommended. However, the cost of the CRMs is very expensive. To reduce the service cost and provide the biodiesel producers in the method for the accurate study, this research article aimed to develop an in-house method validation for assessing the accuracy (% Recovery) of the total acid number (TAN) determination in the biodiesel sample refers to ASTM D664. Pure formic acid (98-100 %) has been chosen to be a representative acid in the biodiesel sample. The total acid number in the studied biodiesel sample was found at (0.4384±0.0083) mg KOH/g (n=3). The suitable volume of standard formic acid spiking in the biodiesel sample was found at 2 µL and 4 µL. The accuracy at 2 µL and 4 µL of standard spiking showed acceptable values of (84.17±2.33) % and (94.20±3.35) %, respectively. Therefore, the development of in-house method validation for the total acid number in the biodiesel sample was successfully developed and can be applied to verify the testing at the scientific equipment center. The method is not only cost-effective but also reliable and good recovery.

Keywords: Potentiometric autotitrator, Biodiesel sample, Standard formic acid, % Recovery

Introduction: The total acid number (TAN) is an indicator of acidic compounds in petroleum products. It is a crucial parameter for assuring the quality of petroleum products. Since petroleum products present a high TAN value it can generate solid deposit in parts of the engine and also can cause engine corrosion in storage tanks.[2] TAN is defined by the American Society for Testing and Materials (ASTM), according to ASTM D664, the TAN in petroleum products, lubricants, and biodiesel is the quantity of base, expressed as milligrams of potassium hydroxide per gram of sample (mg KOH/g) required to titrate a sample with the specified endpoint by potentiometric titration.[1,6] It is the measurement of the electric potential change as each volume of the titrant is added to the biodiesel sample under continuous stirring, thus the measured electric potential is the result of the reaction between the biodiesel sample and the titrant. Various samples were measured the TAN value include biodiesel, commercial biodiesel, and bio-oils etc.[2,4,6] Consequently, the certified reference materials (CRMs) are the most extensively used for the method's accuracy investigation, however, the CRMs are very expensive. Therefore, to reduce the cost of purchasing CRMs, various acids is an alternative for method validation such as hydrochloric acid (HCl) and benzoic acid solutions.[6] In this work, to provide a simple method for accuracy testing for crude palm oil producers and a simple reagent as standard formic acid has been examined.

Methodology:
Chemicals and Reagents: Toluene, propanol-2-ol and potassium hydroxide (KOH) were purchased from RCI Labscan (Bangkok, Thailand). Potassium hydrogen phthalate (KHP) and pure formic acid were purchased from Merck (Darmstadt, Germany).
Instruments: Potentiometric autotitrator, 794 Basic Titrino, Metrohm, Switzerland. Analytical balance 4 digits, Mettler Toledo ME204, Switzerland. Oven, Memmert ULE 600, Schwa Bach, Germany. Deionized (DI) water system was purchased from Human Corporation ZENEER NAVI UP 900 (Seoul, Korea).

Preparation of 0.1 M of alcoholic KOH solution in propanol-2-ol:[4] Prepared by dissolving 5.6 g of potassium hydroxide in propanol-2-ol and stir well. After that, transferred the solution to a 1 liter of a volumetric flask, filled to the mark and kept the solution in an amber reagent bottle.

Preparation of titration solvent:[4] Prepared by a mixing 1 liter of titration solvent consist of 500 mL of toluene, 5 mL of deionized (DI) water and 495 mL of propanol-2-ol and mix well.

Standardization of alcoholic KOH solution:[4] Dried the potassium hydrogen phthalate (KHP) at (105±2) °C and kept in a desiccator, then weighed the KHP about 0.1 g and dissolved with 90 mL of titration solvent and took the beaker to test by placing it on the test stand of potentiometric autotitrator for determined the exact concentration as shown in Figure 1.

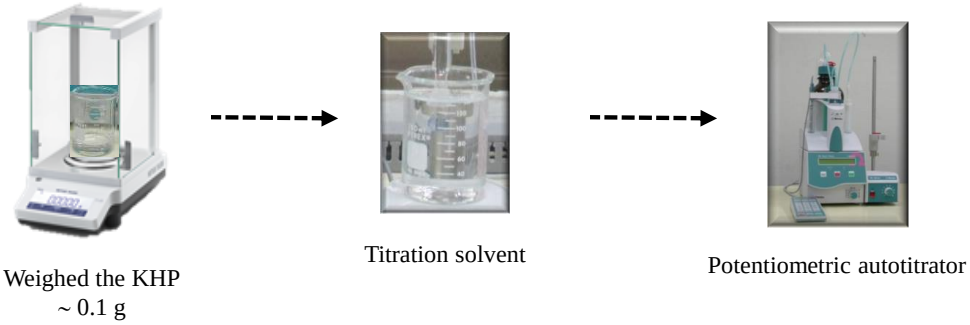

Figure 1. The standardization procedure of alcoholic KOH solution.

Blank titration procedure: Added 90 mL of the titration solvent and took the beaker to test by placing it on the test stand of potentiometric autotitrator for determined the volume of blank titration as shown in Figure 2.

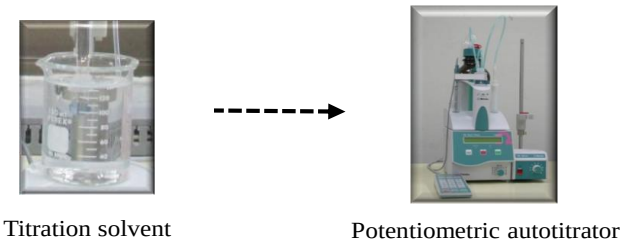

Figure 2. The blank titration testing procedure.

The total acid number procedure: In general, the total acid number (TAN) in the biodiesel sample is less than 0.5 mg KOH/g.[3,4] Therefore; the ASTM D664 gives the following indications in Table 1.

Table 1. Recommended size of the tested portion[1]

Acid number (mg KOH/g)	Mass of test portion (g)	Accuracy of weighing (g)
0.05 to < 1.0	20.0 ± 2.0	0.10
1.0 to < 5.0	5.0 ± 0.5	0.02
5.0 to < 20	1.0 ± 0.1	0.005
20 to < 100	0.25 ± 0.02	0.001
100 to < 260	0.1 ± 0.01	0.0005

The total acid number of biodiesel sample procedure: Weighed the biodiesel sample about 20 g and recorded the exact weight, then added 90 mL of the titration solvent and took the beaker to test by placing it on the test stand of potentiometric autotitrator for determined the TAN value as shown in Figure 3.

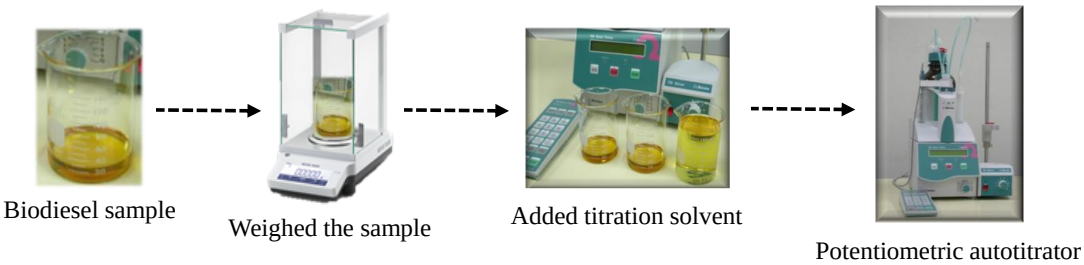

Figure 3. The total acid number testing procedure of the biodiesel sample.

The total acid number of spiked standard formic acid in the biodiesel sample procedure: Weighed the biodiesel sample about 20 g, added 2 µL and 4 µL of standard formic acid and recorded the exact weight, then added 90 mL of the titration solvent and took the beaker to test by placing it on the test stand of potentiometric autotitrator for determined the TAN value as shown in Figure 4.

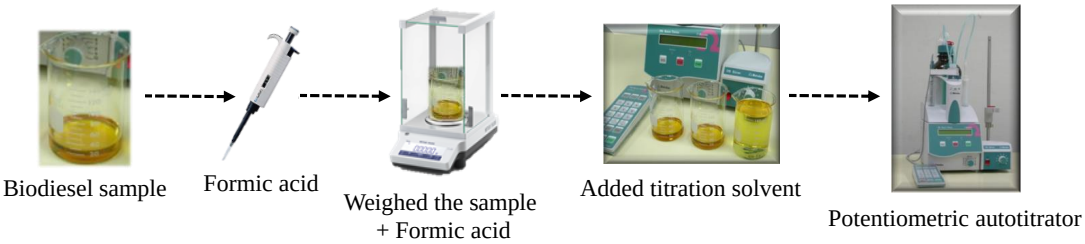

Figure 4. The total acid number testing procedure for spiked 2 µL and 4 µL of standard formic acid in the biodiesel sample.

The total acid number of standard formic acid procedure: Weighed the titration solvent about 20 g, added 2 µL and 4 µL of standard formic acid and recorded the exact weight, then added 90 mL of the titration solvent and took the beaker to test by placing it on the test stand of potentiometric autotitrator for determined the TAN value as shown in Figure 5.

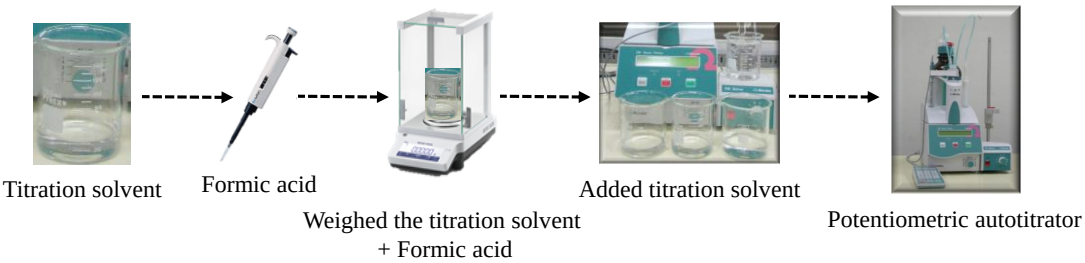

Figure 5. The total acid number testing procedure for spiked 2 µL and 4 µL of standard formic acid.

Results and Discussion:

The results of the total acid number (TAN) in the biodiesel sample by potentiometric titration can be determined by the volume of alcoholic KOH solution was obtained from the potentiometric titration curve as shown in Figure 6. (Replicate 1), and can be calculated as the following equation (1).[2,4,6]

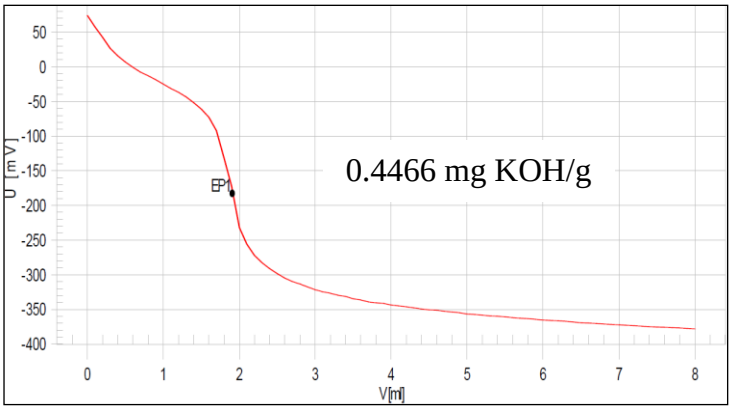

Figure 6. Potentiometric titration curve of the total acid number in the biodiesel sample (Replicate 1).

$$\text{Total Acid Number (mg KOH/g)} = (A-B) \times M \times 56.1/W \qquad (1)$$

Where; A is the volume of alcoholic KOH solution used to titrate sample to endpoint (mL), B is volume corresponding to A for blank titration (mL), M is the concentration of alcoholic KOH solution (mol/L), W is sample mass (g).

*The total acid number of biodiesel sample*s: From the testing procedures in Figure 3, 4 and 5 of biodiesel sample, spiked standard formic acid in the biodiesel sample and standard formic acid titration reaches to the specified endpoint, the total acid number all of them will be displayed on the screen of potentiometric autotitrator, the all results as shown in Table 2., for within-sample (n=3) and Table 3., for difference samples (n=1).

Table 2. The total acid number of biodiesel sample (Within-sample, n=3).

Replicates	Total Acid Number, TAN (mg KOH/g)					%	%
	Biodiesel sample	Spiked (2 µL)[a]	Standard (2 µL)[b]	Spiked (4 µL)[c]	Standard (4 µL)[d]	Recovery @ 2 µL	Recovery @ 4 µL
Replicate 1	0.4466	0.5762	0.1495	0.7266	0.2909	86.6890	96.2530
Replicate 2	0.4384	0.5685	0.1585	0.7133	0.2863	82.0820	96.0182
Replicate 3	0.4301	0.5531	0.1469	0.6609	0.2555	83.7304	90.3327
Average	0.4384	0.5659	0.1516	0.7003	0.2776	84.1671	94.2013
SD	0.0083	0.0118	0.0061	0.0347	0.0192	2.3343	3.3524
% RSD	1.8820	2.0783	4.0144	4.9603	6.9346	2.7734	3.5587

[a]TAN for spiked 2 µL of standard formic acid in the biodiesel sample
[b]TAN for 2 µL of standard formic acid
[c]TAN for spiked 4 µL of standard formic acid in the biodiesel sample
[d]TAN for 4 µL of standard formic acid

Table 3. The total acid number of various biodiesel samples (Difference samples, n=1).

Samples	Total Acid Number, TAN (mg KOH/g)					% Recovery @ 2 µL	% Recovery @ 4 µL
	Biodiesel sample	Spiked (2 µL)[a]	Standard (2 µL)[b]	Spiked (4 µL)[c]	Standard (4 µL)[d]		
Sample 1	0.2112	0.3499	0.1566	0.4968	0.2982	88.5696	95.7746
Sample 2	0.2244	0.3573	0.1566	0.4856	0.2982	84.8659	87.5922
Sample 3	0.3873	0.5515	0.1846	0.7274	0.3537	88.9491	96.1549
Sample 4	0.0941	0.2506	0.1573	0.3874	0.3115	99.4914	94.1573

[a]TAN for spiked 2 µL of standard formic acid in the biodiesel sample
[b]TAN for 2 µL of standard formic acid
[c]TAN for spiked 4 µL of standard formic acid in the biodiesel sample
[d]TAN for 4 µL of standard formic acid

% Recovery calculations: The accuracy (% Recovery) of the test method can be calculated as the following equation (2).

$$\% \text{ Recovery} = \frac{(TAN_{\text{Spiked sample}} - TAN_{\text{Sample}}) \times 100}{TAN_{\text{Formic acid}}} \quad (2)$$

Where; $TAN_{\text{Spiked sample}}$ is the total acid number of spiked standard formic acid in the biodiesel sample (mg KOH/g), TAN_{Sample} is the total acid number of biodiesel sample (mg KOH/g), $TAN_{\text{Formic acid}}$ is the total acid number of standard formic acid (mg KOH/g).

In the case of spiked 2 µL of standard formic acid, we would like to show the accuracy (% Recovery) of the test method (Average ± SD).

$$\% \text{ Recovery} = \frac{(TAN_{\text{Spiked sample}} - TAN_{\text{Sample}}) \times 100}{TAN_{\text{Formic acid}}}$$

$$\% \text{ Recovery} = \frac{(0.5659 - 0.4384) \times 100}{0.1516}$$

$$\% \text{ Recovery} = 84.17 \pm 2.33 \ \%$$

In the case of spiked 4 µL of standard formic acid, we would like to show the accuracy (% Recovery) of the test method (Average ± SD).

$$\% \text{ Recovery} = \frac{(TAN_{\text{Spiked sample}} - TAN_{\text{Sample}}) \times 100}{TAN_{\text{Formic acid}}}$$

$$\% \text{ Recovery} = \frac{(0.7003 - 0.4384) \times 100}{0.2776}$$

$$\% \text{ Recovery} = 94.20 \pm 3.35 \ \%$$

From the results, the accuracy (Average % Recovery) of the test method for spiked 2 µL and 4 µL of standard formic acid in the biodiesel sample is (84.17±2.33) % and (94.20±3.35) % respectively, which can be accepted according to AOAC requirements (80-110%, AOAC).[5]

Comparison of the developed method and other methods: A comparison of the developed method with other reported methods for the total acid number (TAN) in various sample as shown in Table 4. It can be observed that, cannot compare due to each method using different chemicals for accuracy testing. However, the average % recovery with RSD value of the developed method was acceptable value according to AOAC.[5]

Table 4. Comparison of the developed method and other methods.

Sample types	TAN ± SD (mg KOH/g)	Chemical studied	% Recovery	References
Biodiesel	0.4348 ± 0.0083	Formic acid	84.2 – 94.2	In this work.
Bio-oils	1544.21 ± 4.66	Hydrochloric acid	100.4	[6.]
	461.39 ± 3.52	Benzoic acid	100.4	
Biodiesel	0.2901 ± 0.0028	Commercial biodiesel	-	[4.]
	0.3844 ± 0.0029			

Conclusion: The developed in-house method validation for accuracy (% Recovery) assessment of the total acid number (TAN) in the biodiesel samples was successfully established and can be applied the test method for biodiesel producers. Moreover, it has several advantages including cost-effective, easy to use, reliable, and good recovery.

References:

1. ASTM D664-17: Standard Test Method for Acid Number of Petroleum Products by Potentiometric Titration.
2. Tubino M, Aricetti AJ. J. Braz. Chem. Soc. 2011;22:1703-1081.
3. Department of Energy Business, Ministry of Energy.
4. Santos E, Souza E, Ramos T, Silva M, Fiorucci A. Orbital: Electron. J. Chem. 2018;10:47-53.
5. AOAC, 2013. Guidelines for Single-Laboratory Validation of Chemical Methods for Dietary Supplements and Botanicals. 1-32.
6. Shao J, Agblevor AF. American Journal of Biomass and Bioenergy. 2015;4:1-9.

Acknowledgements: This work was supported by the budget of Scientific Equipment Center, Prince of Songkla University. We would like to thanks Asst. Prof. Chulaluk Phathanasakpinyo, Director of Scientific Equipment Center, Asst. Prof. Dr. Wilairat Cheewasedtham, Deputy Director of Scientific Equipment Center and Mrs. Roosanee Kulvijitra, Head of Scientific Research Equipment Services for a consultant and support the personnel of Scientific Equipment Center to develop the knowledge from routine work to research work.

C1_006_OF: SPECIFIC AND SENSITIVE DETECTION METHOD FOR CHROMIUM (VI) IN ORANGE JUICE USING DOUBLE REACTIONS

Indiah Ratna Dewi[1,*], Chatchai Putson[2], Thitima Rujiralai[1, 3], Wilairat Cheewasedtham[1]
[1]Analytical Chemistry and Environment Research Unit, Division of Chemistry, Department of Science, Faculty of Science and Technology, Prince of Songkla University, Pattani 94000 Thailand
[2]Center of Excellence in Nanotechnology for Energy (CENE), Prince of Songkla University, Hatyai, Songkhla 90112, Thailand
[3]Department of Chemistry and Center of Excellence for Innovation in Chemistry, Faculty of Science, Prince of Songkla University, Hat Yai, Songkhla 90112, Thailand
*e-mail: indiah.dardanela@gmail.com

Abstract: The specific and sensitive method for hexavalent chromium determination in aqueous solution has been developed based on two chemical reactions, complex formation with dithizone (DTZ) and redox oxidation. The analysis were carried out based on absorbance measurement by mean of spectrophotometry, which the ratio of absorbance at A_{370}/A_{550} was investigated. The optimum reducing agent and chromium (VI) ratio and DTZ concentration in the system were 25:1 and 0.03 mM, respectively. The color of the reactions changed from dark green to red and further changed into magenta after reacted with the chromium hexavalent. In comparison with the conventional method which employed only complex formation reaction which diphenylcarbazide (DPC) is used as chromium (VI) complexing agent, this developed method shows higher sensitivity than that of DPC for up to 1.4 times. The linearity range of the developed method was found in the concentration range of 0 to 10 µg mL^{-1} of chromium (VI) with very satisfied mean recovery of 94.29%. Moreover, the specificity of DTZ complexation and redox reaction was profen by no intering effect by other major metal element in water, such as iron (II) and manganese (II). In addition, some commercial orange juice samples from supermarket have been investigated using this deleveloped method.

Introduction: The determination of hexavalent chromium (Cr(VI)) in samples, such as waste water, surface water, ground water, or even in food and beverages are very important due to its high toxicity, causing health problems such as liver damage, pulmonary congestions, vomiting, and severe diarrhea[1]. The United States Environmental Protection Agency has demonstrated Cr(VI) as one of the 17 chemicals posing the greatest threat to humans and set the standard for Cr(VI) in drinking water should not exceed 50 µg L^{-1} [2]. The available techniques for Cr(VI) determination, such as ion chromatograpyh (IC), atomic absorption spectrometry (AAS), inductively coupled plasma (ICP) are expensive and require technical skills, and simpler method for this determination is reported using spectrophotometric technique, by adding the metal complaxing agent prior to the determination[3]. The common complexing agent used is 1,5-diphenylcarbazide (DPC) which can form a red-violet chromium-DPC complex. However, certain substances such as molybdenum, vanadium, and mercury, may interfere if the chromium concentration is relatively low (<0.5 mg L^{-1}), so it necessary to improve the specificity and sensitivity of Cr(VI) determination.

Diphenylthiocarbazone, also known as dithizone, is a type of chromogenic reagent that contains several N-donor atoms, -NH as well as –SH groups which are excellent for analytical and and spectroscopic applications. This compound is specific for chelating heavy metal ions such as Pb(II), Cd(II), Cu(II), Hg(II), and Co(II)[4] that can perform various colored complexes with metal ions but not with Cr(VI) since it gives a similar color with Zn(II). In the other hand, it's a well known that dichromate ($Cr_2O_7^{2-}$) is a strong oxidising agent together with peroxide (H_2O_2) and permanganate (MnO_4^-). Recently, very few works has used dithizone for Cr(VI) determination.

Fruit juice is widely consumed as a good source of vitamin C, carotenoids, minerals, and various kinds of antioxidants and dietary fibre to meet the micronutrients need, which can protect against degenerative and chronic disease[5]. Consuming fruit juices is a convenient way for adults and children to get part of the recommended 4.5 or more cups of fruits and vegetables each day[6]. However, they can be contaminated by toxic elements, such as arsenic, cadmium, chromium, lead, mercury, manganese or nickel. Those trace elements may be expected to be influenced by the nature of the fruit, the mineral composition of the soil, the composition of irigation water, the weather conditions, and also the agricultural practices such as types and amounts of fertilizers and pesticides used[7,8]. Due to this pollution, our food and bevereges are also getting contaminated[9]. In some fruit juices samples, such as apple, pomegranate, tomato, guava, mixed fruit, mango, litchi, cranberry and orange, pesticides were found below the tolerance limit, i.e. 0.01 to 1.0 mg kg^{-1}, by Food Safety and Standard Authority of India (FSSAI). Some pesticides like chlorpyrifos in orange juice and Deltamethrin in ginger garlic were detected above the permissible limit at 1.08 and 1.28 mg kg^{-1}, respectively[10]. Hence, it is very important to evaluate industrial fruit juices to guarantee food safety and consumer safety.

The aim of this study was to develop the specific and sensitive method for Cr(VI) determination by using the dithizone-LN complexing agent and to investigate the Cr(VI) content in commercial orange juice samples.

Methodology:

Chemicals and instrumentation. Dithizone (1,5-diphenylthiocarbazone) and nitric acid (HNO_3) were purchased from Merck (Germany), diphenylcarbazide ($C_{13}H_{14}N_4O$) and potassium dichromate ($K_2Cr_2O_7$) were from LOBA Chemie (India), cobalt nitrate ($Co(NH_3)_2.6H_2O$) from ANaPURE (Hong Kong), iron sulphate ($FeSO_4.7H_2O$) from Ajax Finechem (Australia), manganese oxide (MnO) from Fluka Chemica (Switzerland). Phosphoric acid was purchased from JT Baker (USA), acetone from Fisher (USA), and ethanol from RCI Labscan (Thailand).
All chemicals used were of analytical grade. Deionized (DI) water was chosen as the water source. The UV-Visible absorbance spectra were analyzed using spectrophotometer Biochrom Libra S22 (Country). All glasswares and tubes used were soaked in 10% of nitric acid and rinsed until no acidity left with DI water.

Dithizone-LN complex system. In order to optimize the LN concentration, into a 1.5-mL clear eppendorf tube, 300 µL of 2.5 ppb DTZ were added, then 300 µL of various concentration LN as follows 2.5, 5, 10, 20, and 30 ppm were added in different tubes respectively, followed by vortex mixing for 30 second and kept for 1 minute to let the complex reaction completed. The fixed amount of 400 µL of 1 ppm Cr(VI) was then added with vortex mixing for 30 seconds and kept for 5 minutes prior to measurement of the absorption spectra within 250 – 800 nm wavelength.

To optimize the dithizone concentration, 300 µL of DTZ in following concentration of 0.06, 0.125, 0.25, 0.5, 0.75, and 1.5 ppb were added into 1.5-mL clear eppendorf tubes, followed by 300 µL of 100 ppm LN, vortex mixed and stand for 1 minute. The fix amount, 400 µL of 1 ppm Cr(VI) was then added with vortex mixing for 30 seconds and stand for 5 minutes prior to measurement of the absorption spectra within 250 – 800 nm wavelength.

The characterization of the dithizone-LN complex was studied by observing the absorption spectra of DTZ, mixture of LN and Cr(VI) (LN+Cr), complex between DTZ and LN (DTZ-LN), complex between DTZ and Cr(VI) (DTZ-Cr), and mixed complex of DTZ + LN and Cr(VI) (DTZ-LN-Cr). All systems were vortexed for 30 seconds and kept for 5 minutes prior to measurement of the absorption spectra within 250 – 800 nm wavelength. The color changes of each system were recorded by using mobile camera.Error! Reference source not found.

Validation method. In the chromium determination according to EPA Method number 7196A, a 1000 ppm of Cr(VI) standard stock solution was prepared from dried potassium

dichromate. Series of Cr(VI) concentration solutions of 0, 0.01, 0.05, 0.1, 0.25, 0.5, 1, 2.5, 5, and 10 ppm were prepared freshly prior to use by diluting with DI water. For the linearity study, 300 µL of 2.5 ppb DTZ, 300 µL of 100 ppm LN were added into eppendorf tubes, mixed well and subsequently added with 400 µL of different concentrations of Cr(VI) as previously prepared. The absorption spectra were collected within wavelength of 250 – 800 nm. The absorbance ratio of A370 and A550 were plotted and the linearity range was determined. Blank signals of A370/A550 were measured for the sensitivity test and according to Miller and Miller [11] LOD and LOQ were calculated by the following formulas:

$$LOD = \frac{S_m - Average\ blank\ signal}{m} \qquad \text{Equation (1)}$$

$$LOQ = \frac{10xSD}{m} \qquad \text{Equation (2)}$$

The precision was reported as Relative Standard Deviation (RSD) percentage, checked using 10 ppm of Cr(VI) after the complexation reaction step as above details. The specificity of redox reaction between LN and Cr(VI) was investigated by replacing LN with other major metal elements in water, which were 100 ppm of iron (II) and manganese (II). The characteristics peak at 270, 370 and 550 nm were observed.

Matrix interference. A series of Cr(VI) standard solution of 0, 0.01, 0.05, 0.1, 0.25, 0.5, 1 ppm at the same amount, were added into DTZ-LN system which already contained 400 µL of orange juice digested sample, according to the complexation reaction step. The absorptions were recorded at wavelength of 270, 370 and 550 nm. The absorbances ratio of A370/A550 were calculated and plotted. The statistical significant of difference of the two slopes was examined.

Cr(VI) determination in orange juice samples. Twelve orange juice samples with different brands were acquired from supermarkets. An aliquot of 1 mL of the samples was transferred into test tube, and after the addition of 1 mL of 65% HNO_3 and 1 mL of DI water, the tube was heated (±90°C) in waterbath for 10 minutes in open tube, and continued heating up to 60 minutes in closed tube for complete digestion. After that, the resulting solution was made up to 5 mL with DI water for further analysis. The digested orange juice samples were kept at 4°C, modified from that of Tormen[12]. For each test, 300 µL of 2.5 ppb DTZ, 300 µL of 100 ppm LN were added in the tubes, mixed, the subsequently added with 400 µL of digested sample. The absorbance ratio at A370/A550 were calculated and plotted to the standard curve. For accuracy study, the recovery percentage was carried out by adding 200 µL of 1 ppm Cr(VI) in all samples tubes prior to absorption measurements. As a comparation, the EPA method number 7196A[13] which is used diphenylcarbazide as the complexing agent was employed. The result for both methods was then compared.

Results and Discussion:

Dithizone-LN complex system. The complex reaction between DTZ and LN was characterized at the wavelength of 430 and 530 nm. Here, the concentrations of LN were varied, to find the optimum concentration of LN which could be complexed by DTZ (Figure 8). As seen in Figure 8., the absorbances at 430 nm were decreased and at 530 nm were increased when higher concentration of LN added in the system (Figure 8.). By calculating the absorbance ratio of A_{530}/A_{430}, the optimum concentration of LN was found to be 20 ppm (Figure 8.).

a. b.

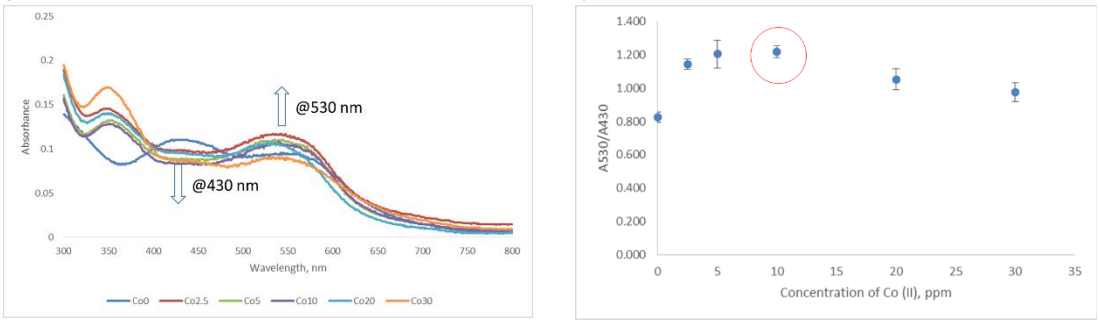

Figure 8. Optimization of LN concentrations, (a) color of system, (b) UV-Vis absorbance spectra of system, and (c) the intensity of A_{530}/A_{430} of various LN concentrations

The characteristic peaks of dithizone optimization in the system were at 370 and 550 nm. It showed that increasing of DTZ concentration caused decreasing the absorbance (Figure 9.). The intensity was also calculated by the ratio of A_{370}/A_{550}. The optimal amount of dithizone concetration was 0.5 ppb as seen at Figure 9.

a. b.

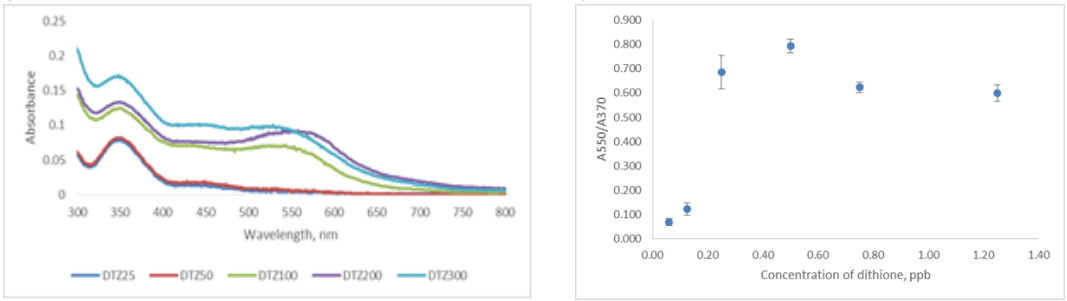

Figure 9. Optimization of dithizone concentrations, (a) UV-Vis absorbance spectra of system and (b) the intensity of 550/470 of various DTZ concentrations

The spectra characters of the DTZ-LN systems were carried out by observation of the color and UV-Visible spectrum of each system as given in Error! Reference source not found.. Ten ppm of LN and 10 ppm of Cr(VI) showed colorless, dithizone at the studied concentration gave green color, complex of DTZ-LN was red, complex DTZ-Cr(VI) was pink but complex DTZ-LN-Cr was reddish purple or magenta. In this system, characteristic peaks of DTZ were found at 430 and 600 nm wavelength. When LN added, those two peaks were dissaperad, and there was new peak at 500 nm as the characteristics peak for DTZ-LN complex. The green DTZ color is changed by LN, probably due to its suitable coordination with nitrogen and sulfur atoms which present in DTZ. Those atoms serve as donors and form a penta-heterocycles chelating complex between LN and DTZ molecules as $[LN(DTZ)_2]^{2+}$, with the formation of the 2:1 (DTZ:LN) binding ratio[14]. Further, this 500 nm peak was shifted to 550 nm after Cr(VI) addition and new peak was obtained at 370 nm. The peak at 550 nm is expected as LN dithizonate, as previous finding from Eschwege[15] which has maximum wavelength at 547 nm. Here, Cr(VI) can oxidize the $[LN(DTZ)_2]^{2+}$ to be $LN(DTZ)_3$. The proposed reaction is illustrated in Figure 10.

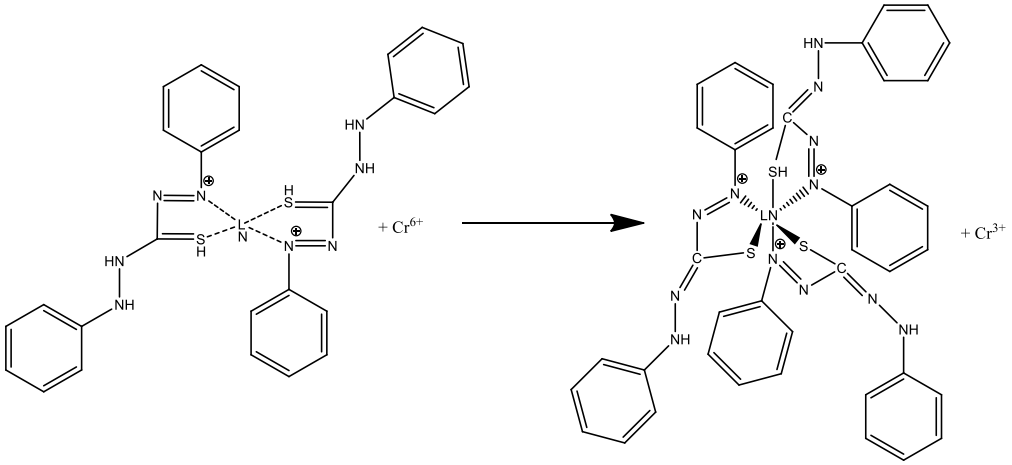

Figure 10. Proposed reaction of Cr(VI) determination by double reaction of DTZ-LN complex

The characteristic colors in Figure 11 was clearly showed the shifting of all peaks, and the absorbance peaks at wavelength of 270, 370, and 550 nm, were determined as the maximum wavelength of the complex system, which would be used for the absorbance measurements for the next experiments.

a.

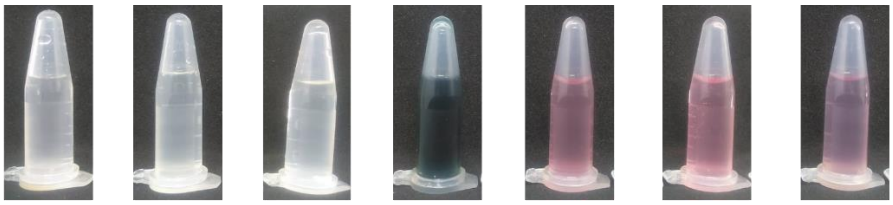

COLORLESS 10 ppm of LN | COLORLESS 1 ppm of Cr^{6+} | COLORLESS LN-Cr^{6+} | GREEN 0.1 mM of Dithizone (DTZ) | RED DTZ-LN complex | PINK DTZ-Cr^{6+} complex | MAGENTA (REDDISH PURPLE) DTZ-LN-Cr^{6+} complex

b.

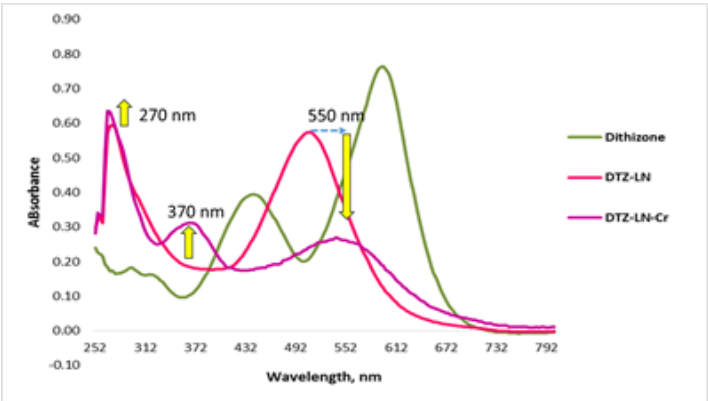

Figure 11. The characteristic colors and peaks of dithizone-LN-chromium complex system

The intensity of the Cr(VI) standard solution color was decreased for the lower concentration of Cr(VI). It was confirmed by the sprectra in Figure 12, which the intensity of

absorbances peak at 550 nm were decreased for higher concentrations of Cr(VI). In other hand, the absorbances peaks at 370 nm were increased as the result of higher Cr(VI), and the absorbances peak at 270 nm were also increased as the result of higher turbidity of the system.

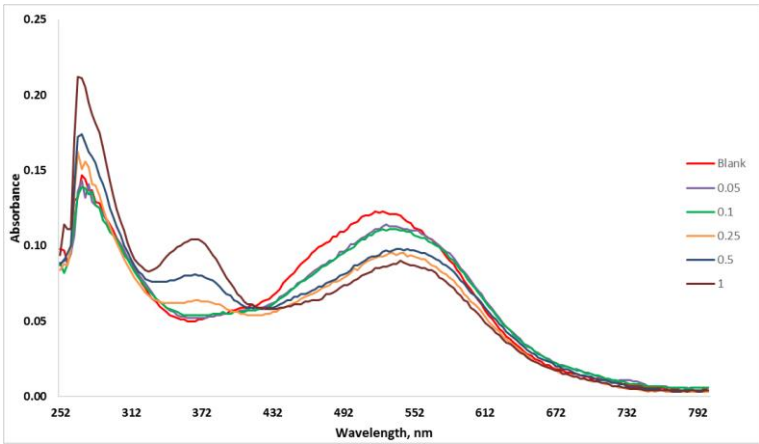

Figure 12. UV Visible absorbance spectra of Cr(VI) standard solution

From the absorbances data of Cr(VI) standard curve at 270, 370, and 550 nm, four possibilities were obtained, which were single wavelength curve at 270 nm, 370 nm, and 550 nm, respectively, the absorbance intensity ratio between 270 and 370, the intensity ratio between 270 and 550, and the intensity ratio between 370 and 550. Among those possibilities, the highest intensity and linearity was found to be 0.9951 at A_{370}/A_{550} as shown in Figure 13.

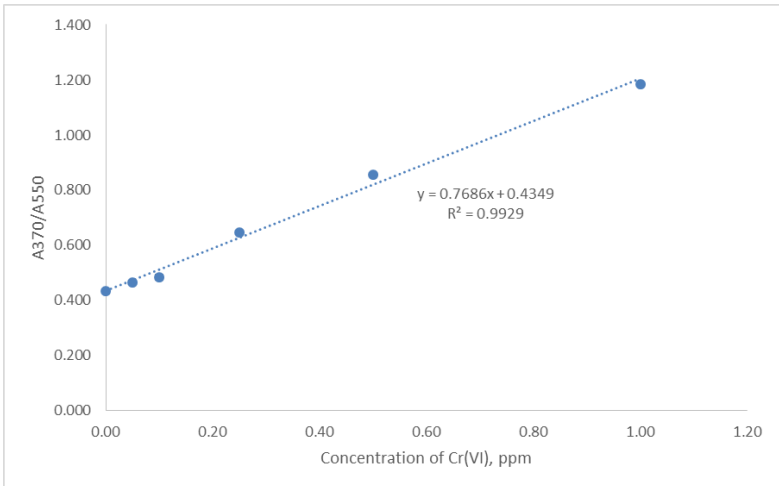

Figure 13. The Cr(VI) standard curve possibilities in DTZ-LN system

Method Validation. The Cr(VI) determination using DTZ-LN compexing agent method employing spectrophotometry performed good linearity, sensitivity, recovery, and precision. All values were in the acceptable and reliable range of validation. Compare with the established method with diphenylcarbazide, the developed method has range of linearity at 0.0 – 10.0 ppm of Cr(VI), higher molar absorptivity, lower LOD and LOQ, and lower %RSD. The results of validation were summerized in Table 1.

Table 1. Validation method values of the developed method *vs* the standard method

Validation method	Dithizone-LN	Diphenylcarbazide[13]
Linearity range	Ranging from 0.0 – 10.0 ppm, r^2 = 0.9849	Ranging from 0.0 – 10.0 ppm, r^2 = 0.9968
Sensitivity		
- Slope	0.218	0.169
- LOD	0.050 ppm	0.070 ppm
- LOQ	0.168 ppm	0.232 ppm
Recovery	81 to 118%	82 to 116%
Precision (%RSD)	2.56%	6.12%

[13] EPA Method 7196A

In the developed system, Cr(VI) can oxidized LN divalent to be LN trivalent while Cr hexavalent is reduced to be Cr trivalent. To assess the specificity of LN-Cr redox reaction, LN was replaced by 100 ppm of Fe(II) and Mn(II) and the UV Vis absorbance spectra was investigated. From Figure 14. UV-Visible spectrum of DLNCr, DFeCr, and DMnCr . DTZFeCr and DTZMnCr had shown no peak at 370 nm, where it was showing Cr(VI) characteristic peak in th system (Figure 14).

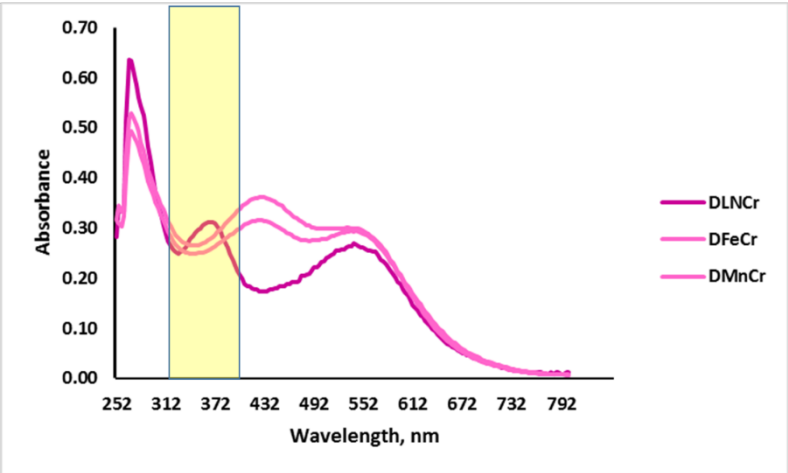

Figure 14. UV-Visible spectrum of DLNCr, DFeCr, and DMnCr complex

Matrix interferences. In order to verify the matrix interferences, the standard addition method was conducted according to Froes[16] and Garcia[17]. When same amount of various concentrations of Cr(VI) standar was added in to DTZ-LN system which contained digested sample, both curves gave positive correlation with high coefficients about 0.976 at the concentration range tested (0 to 1 ppm). The comparison of the slopes of the curves revealed no significant difference at 95% confidence level (p=0.11). It means that the matrix of digested orange juices sample no matrix interference (Figure 15).

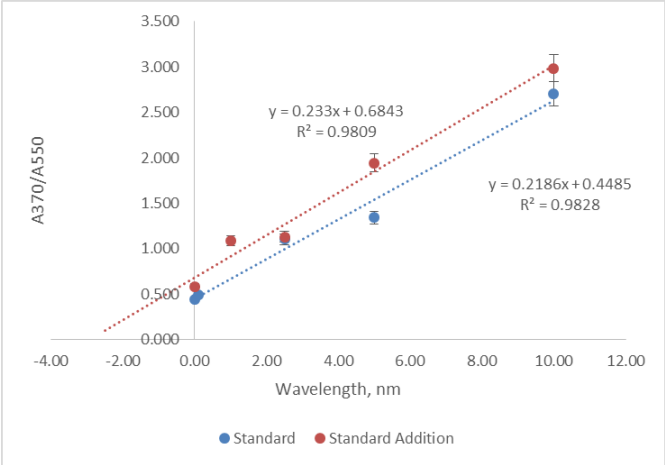

Figure 15. Standard addition curve for matrix interference study

Cr (VI) determination in orange juices with dithizone-LN system. Orange juice samples were prepared by wet digestion for 60 minutes. The appearence of the sample and the digested samples were shown in Figure 16. Nitric acid could destroy the organic matrix of the orange juice samples and left into clear solutions.

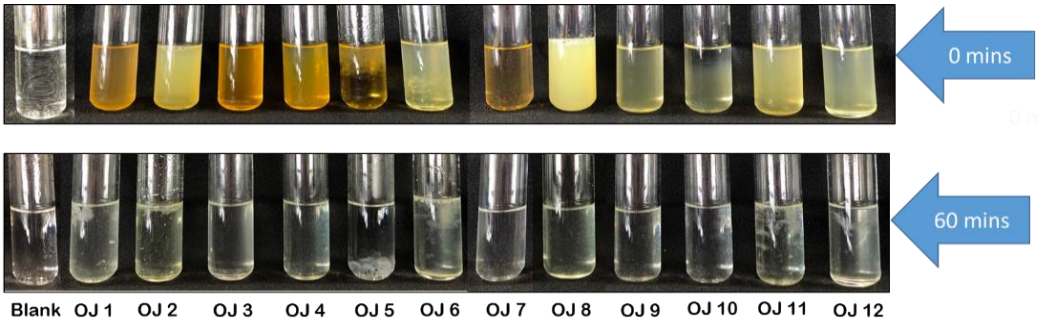

Figure 16. The appearence of orange juice samples and digested orange juice samples

Those digested sample were then added into dithizone-LN system, and the color were shown in Error! Reference source not found.Sample with code OT5, OT7, OT8, and OT9 showed the magenta color, but Cr(VI) could not be detected in any of the samples. As comparison, some previous study reported that the average value of chromium content in orange juice or orange drink in Spain was 5.75 ppb[17], in Nigeria was 0.002 ppb (canned package)[18], and in Poland was 0.009 ppm[19].

Figure 17. Color of digested orange juice sample in dithizone-LN complex system

Cr (VI) determination in orange juices with dihenylcarbazide. The common complexing agent that is used for Cr(VI) determination is diphenylcarbazide (DPC) using spectrofotometry. DPC-Cr(VI) complex had high linearity range from 0 to 10 ppm with 0.9968% linearity. The color shaded from colorless into violet as shown in Figure 18.

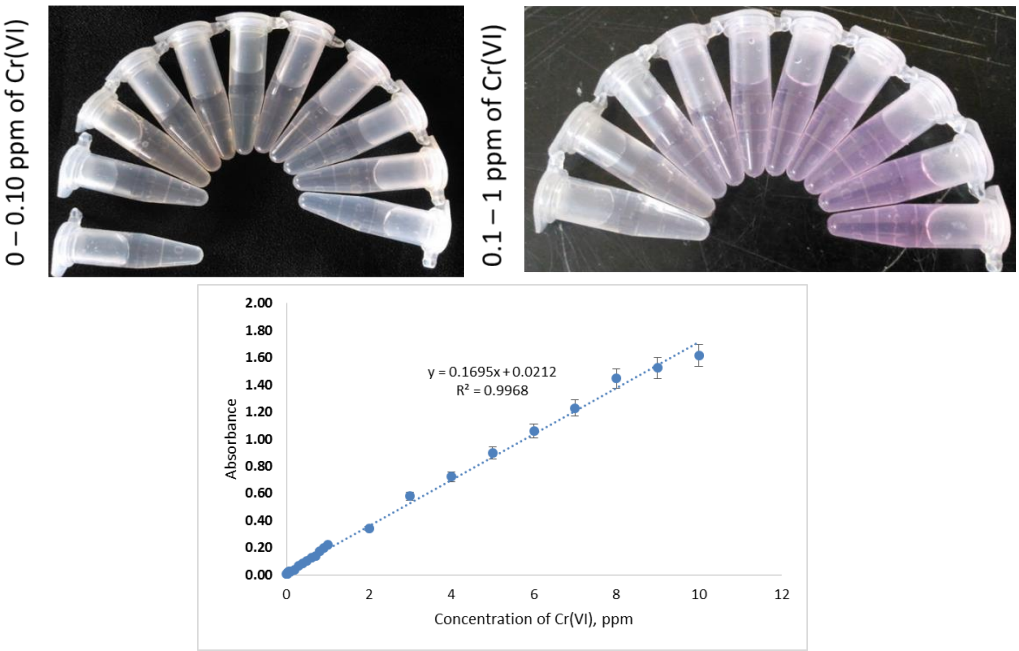

Figure 18. Diphenylcarbazide-chromium(VI) complex and its linearity

According to Figure 19, the Cr(VI) content could not be determined by color changes. Confirming the result from the proposed method, Cr(VI) could not be detected in all samples with this standard method.

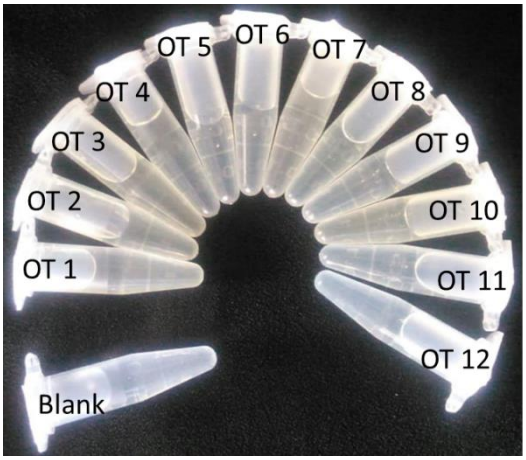

Figure 19. Color of Cr(VI) complexed with diphenylcarbazide in orange juice samples

Conclusion: In summary, the study of the based on double reaction led us to develop and optimize a specific and sensitive spectrophotometric analytical method for the determination of Cr(VI) in aqueous media. The main point of interest of this developed method is it can be easily applied in the real samples with organic matrix samples after sample pre-treatment applied. This method performed linearity (r^2: 0.9849) in the range of 0.0 – 10 ppm of Cr(VI), recovery (81 – 118%), precision (%RSD: 2.56), and more specific than the standard EPA Method 7196A which only use single reaction with diphenylcarbazide. The sensitivity (LOD: 0.050 ppm, LOQ: 0.168 ppm) is similar to the maximum permissive level in drinking water, which is 0.05 ppm according to the World Health Organization (WHO). The studied orange juice samples are free of Cr(VI), so those are suitable to be consumed to improve on the overall nutritional needs of consumer.

References:

1. Han A, Zhang H, Sun J, Chuah G, Jaenicke S. J. Water Process Eng. 2017:17:63–69.
2. Jin W, Du H, Zheng S, Zhang Y. Electrochim. Acta. 2016:1–55.
3. Danwittayakul S, Thanaboonsombut A. NU Sci. J. 2009:6:64–72.
4. Mudasir M, Karelius K, Aprilita NH, Wahyuni ET. Biochem. Pharmacol. .2016:4:1839–1849.
5. Harmankaya M, Gezgin S. Environ. Monit. Assess. 2012:184:5415–5420.
6. Farid SM, Enani MA. Med. J. Islam. World Acad. Sci. 2010:18:31–38.
7. Anastácio M, dos Santos APM, Aschner M, Mateus L. Toxicol. Reports. 2018:5: 434–439.
8. Ciavatta C, Manoli C, Cavani L, Franceschi C, Sequi P. J. Environ. Prot. 2012:2012: 1532–1541.
9. Pramod HP, Davendra HJ. Res. Chem. Environ. 2014:4:163–168.
10. Dwivedi BC, Tiwari H, Gaur VK. Int. J. Chem. Stud. 2018:5:259–285.
11. Miller JN, Miller JC. Statistics and Chemometrics for Analytical Chemistry. 2010.
12. Tormen L. Torres DP, Dittert IM, Araújo RGO, Frescura FLA, Curtius AJ. J. Food Compos. Anal. 2011:24:95–102.
13. EPA.Method 7196A.1992:1–6.
14. Tavallali H, Deilamy-Rad G, Parhami A, Mousavi SZ. J. Photochem. Photobiol. B Biol. 2013:125:121–130.
15. Von Eschwege KG, Van As L, Joubert CC, Swarts JC, Aquino MAS, Cameron TS. Electrochim. Acta. 2013:112:747–755.
16. Froes RES, Neto WB, e. Silva NOC, Naveira RLP, Nascentes CC, da Silva JBB. Spectrochim. Acta - Part B At. Spectrosc. 2009:64:619–622.

17. García EM, Cabrera C, Sánchez J, Lorenzo MJ, López MC. Sci. Total Environ. 1999:241: 143–150.
18. Iwegbue CMA, Nwozo SO, Ossai EK, Nwajei GE. Am. J. Food Technol. 2008:3:220–223.
19. Szymczycha-Madeja A, Welna M. Food Chem. 2013:141:3466–3472.

Acknowledgements: The authors wish to acknowledge the financial support granted by Graduate School, Prince of Songkla University (The Thailand's Education Hub for Southern Region of ASEAN Countries Project Office of the Higher Education Commission), other facilities from Faculty of Science and Technology and some equipments supported by Lin Shing Enterprise (Thailand) Co. Ltd.

C1_007_PF: ENANTIOMERIC SEPARATION OF 1-PHENYLALKANOLS BY GC USING METHYLATED BETA-CYCLODEXTRIN CHIRAL STATIONARY PHASE

Suchada Muangsri, Aroonsiri Shitangkoon*
Department of Chemistry, Faculty of Science, Chulalongkorn University, Bangkok 10330, Thailand
*e-mail: aroonsiri.s@chula.ac.th

Abstract: Chiral alcohols are useful chemicals for many industries. Enantiomers of a chiral compound have identical physical and chemical properties. However, they may show different biological activities and, in some cases, one enantiomer may show unwanted property. Gas chromatography (GC) is a useful technique for analyses of enantiomeric purity of volatile alcohols. In this study, enantiomeric separation of eleven chiral 1-phenylalkanols were examined by GC using a capillary column of 15 m long, 0.25 mm i.d. and a 0.25 µm thick film of stationary phase. Heptakis(2,3-di-*O*-methyl-6-*O*-*tert*-butyldimethylsilyl)-β-CD mixed with polysiloxane was used as a chiral stationary phase. The effects of type and position of substituent on alcohol structure as well as column temperature on retention and enantioselectivity were studied. Ten chiral alcohols could be separated into their enantiomers using this stationary phase. Results showed that a small methyl substituent at the stereogenic center provided better enantioselectivity than a larger phenyl substituent. Methyl group substituted at the *para*-position of the aromatic ring provided better enantioselectivity than other types of substituent. Optimum condition for complete enantiomeric separation of each chiral alcohol was also obtained. In this study, enantiomers of 1-(4-methylphenyl) ethanol could be separated with shortest analysis time in less than 2 minutes.

Introduction: Chiral compounds display identical physical and chemical properties except for the direction of rotating polarized light[1]. However, each enantiomer of a chiral compound may show different properties, such as bioactivity, toxicity or clinical activity. Chiral alcohols are among useful intermediates for pharmaceutical and agrochemical industries[2]. In pharmacy, optically active drugs are needed because single enantiomers showed improvement in solubility, dissolution and stability. In many cases, the use of a racemic mixture of a chiral drug may be wasteful and may lead to side effect or adverse reactions[3]. Therefore, pure optically active drugs are required and determination of their enantiomeric purity is necessary.

Chromatography and capillary electrophoresis are well-known and popular techniques for the analysis of chiral compounds of different classes. For small organic compounds such as alcohols, capillary gas chromatography (GC) is a suitable technique[4]. In most cases, direct analysis of chiral compounds using chiral GC stationary phases are preferred.

Cyclodextrin (CD) derivatives are among the most popular compounds to be used as chiral GC stationary phases. CDs are cyclic oligosaccharides of 6, 7 or 8 glucose units linked by α-1,4-glycosidic bonds, called α-, β- and γ-cyclodextrins, respectively. CD molecules have a cavity in their structures. This characteristic enables CD to form an inclusion complex with various types of analytes. An analyte, as a guest, can enter into the cavity of CD (host) by physical forces. GC stationary phases based on CD derivatives showed good selectivities towards many classes of chiral compounds as well as isomers[5].

Generally, factors affecting enantioselectivity of each derivatized CD are size of CD as well as type and position of substitution. Previous reports showed that derivatized β-CDs were the most frequently used CD derivatives in GC stationary phases[6]. The *tert*-butyldimethylsilyl group substituted at 6-position of CD with different types of substitution at 2- and 3-positions of CD showed good enantioselectivities for many classes of compounds[7]. Furthermore, the analyte structure is another important factor for successful enantiomeric separation. The

objective of this work was to study the enantiomeric separation of eleven alcohols by capillary gas chromatography using heptakis(2,3-di-*O*-methyl-6-*O*-*tert*-butyldimethylsilyl)-β-CD (Figure 1) as a chiral stationary phase. The structure of eleven alcohols used in this study was based on 1-phenylalkanols with different type and position of substituents (Figure 2). The effects of type and position of substituent on alcohol structure on retention factor (k′) and enantioselectivity (α) were studied as a function of temperature. In addition, the optimum condition for complete enantiomeric separation of each chiral alcohol was also determined.

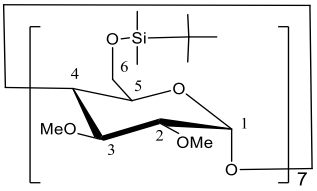

Figure 1. Structure of heptakis(2,3-di-*O*-methyl-6-*O*-*tert*-butyldimethylsilyl)-β-CD.

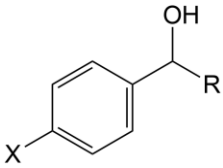

	alcohol #	
X	R = Me	R = Ph
H	1	-
F	2	7
Cl	3	8
Br	4	9
Me	5	10
OMe	6	11

Figure 2. Structures of eleven chiral alcohols.

Methodology:
Chiral alcohols: All racemic alcohols were prepared from their corresponding ketones. The ketone (2 mmol) and sodium borohydride (4 mmol) were mixed in ethanol (10 mL) and refluxed for 3 hours. After the reaction was complete, the solvent was removed under vacuum. The white solid was dissolved in 2 M hydrochloric acid. The aqueous solution was extracted twice with dichloromethane. The combined organic solution was evaporated to dryness. The obtained alcohols were characterized by ^{1}H and ^{13}C NMR (Bruker AV-400 spectrometer) using $CDCl_3$ as a solvent. Chiral alcohols were directly analyzed by GC without derivatization.
GC analyses: All GC measurements were performed on an Agilent 7890B gas chromatograph equipped with a split injector and a flame ionization detector. Both injector and detector were set at 250 °C. Hydrogen was used as a carrier gas with an average linear velocity of 50 cm/sec. A chiral column of 15 m long, 0.25 mm i.d. with a 0.25 µm thick film of stationary phase was used. The stationary phase contained a mixture of heptakis (2,3-di-*O*-methyl-6-*O*-*tert*-butyldimethylsilyl)-β-CD in polysiloxane. Each chiral alcohol was diluted in dichloromethane. Each alcohol solution was analyzed isothermally at least in duplicate at 5-7 different temperatures of 10 °C intervals. The retention factor (k′), enantioselectivity (α), and resolution (Rs) were calculated from chromatograms[8]. The optimum temperature for each chiral alcohol was also determined by adjusting the column temperature until a resolution of at least 1.5 was obtained.

Results and Discussion: Direct GC analyses of eleven chiral alcohols using heptakis (2,3-di-*O*-methyl-6-*O*-*tert*-butyldimethylsilyl)-β-CD as a chiral stationary phase were

performed. The effects of type and position of substituent on alcohol structure on retention factor (k′) and enantioselectivity (α) were studied. From chromatograms, all underivatized alcohols showed symmetric peak shapes. The retention factor (k') of each enantiomer related to column temperature (T) according to

$$\ln k' = -\frac{\Delta H}{RT} + \frac{\Delta S}{R} - \ln \beta.$$

where ΔH = enthalpy change
ΔS = entropy change
T = absolute temperature (Kelvin)
R = universal gas constant
β = volume ratio of mobile phase to stationary phase

Linear relationships between ln k' versus 1/T for each enantiomer for all analytes were obtained with correlation coefficient (R^2) greater than 0.9990. Plots of ln k' versus 1/T of the more retained enantiomers of alcohols 1-11 were shown in Figure 3.

For all analytes, as the column temperature decreased, retention factors of analytes increased. It can be seen that, at the same temperature, alcohol 1 (1-phenylethanol) was the least retained analyte (lowest k' value). Alcohol 9, with bromo-substitution at *para*-position of the aromatic ring and phenyl-substitution at the stereogenic center, was the most retained analyte under the same condition. The type of substitution clearly affected retention. Retention factors of alcohols 7-11, with phenyl-substitution at the stereogenic center, were higher than alcohols 1-6, with methyl-substitution at the stereogenic center. For halogen-substituted alcohols, retention factors increased with the order of F < Cl < Br, as shown by the increased retention factors of alcohols 2 < 3 < 4 and 7 < 8 < 9.

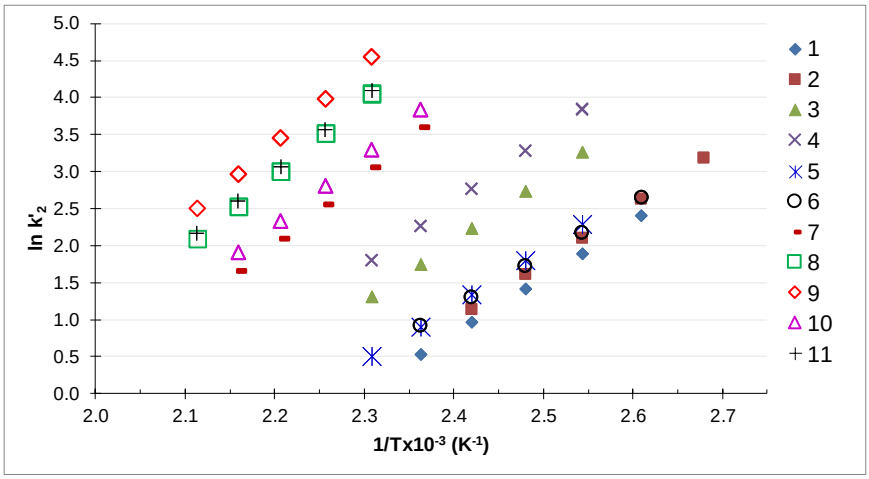

Figure 3. Plots of ln k' versus 1/T of the more retained enantiomers of all alcohols.

When a chiral compound can be separated into their enantiomers, two peaks will be observed. Relationships between ln α versus 1/T for all alcohols were shown in Figure 4. From eleven chiral alcohols used in this work, ten could be separated into their enantiomers with different enantioselectivities. Only enantiomers of alcohol 7 could not be separated by this stationary phase.

(a)

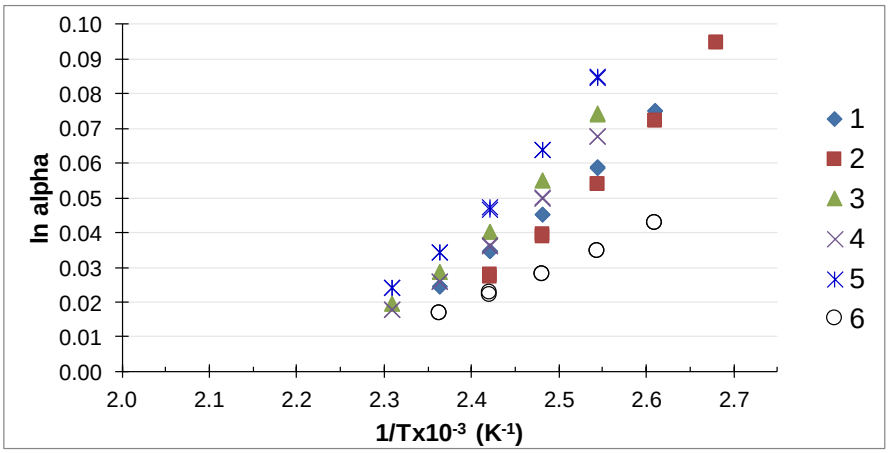

(b)

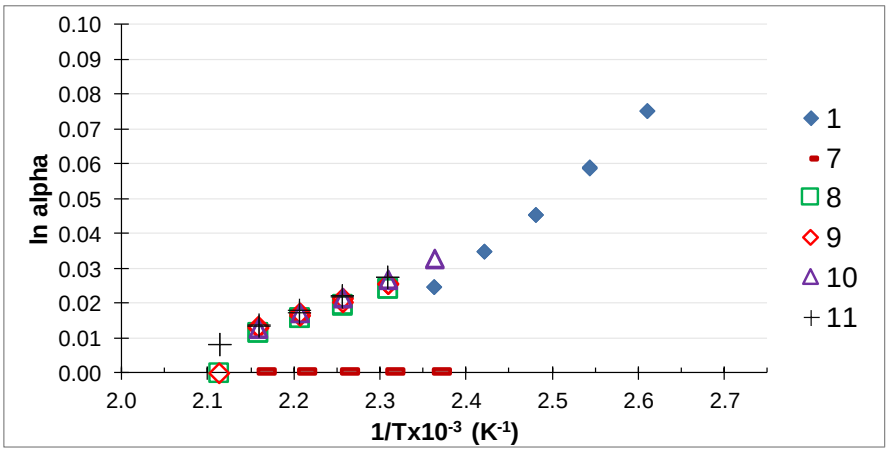

Figure 4. Plots of ln α versus 1/T of alcohols (a) 1-6 and (b) 1 and 7-11.

Enantioselectivities of 1-phenylethanol (1) and *para*-substituted 1-phenylethanols (2-6) at different isothermal temperatures were compared in Figure 4(a). It can be seen that, at the same temperature, alcohol 5 (with methyl substitution at *para*-position on the aromatic ring) showed the highest enantioselectivity (highest α value). While alcohol 6 (with methoxy substitution) has the lowest enantioselectivity. For alcohol 1 and three halogen-substituted 1-phenylethanols (2-4), their enantioselectivities varied between alcohols 5 and 6.

To improve the GC separation of enantiomers, the column temperature is generally decreased. From plots of ln α versus 1/T of alcohols in Figure 4(a), alcohols 2 and 5 showed steeper slopes compared to other alcohols, suggesting that their enantioselectivities could be easily increased by lowering the column temperature. If the column temperature was decreased, the increases in enantioselectivities of alcohols 2 and 5 were larger than the increase in enantioselectivity of alcohol 6 (with a shallow slope). Chromatograms for the separation of alcohols 5 and 6 were compared in Figure 5. The decrease in column temperature by 10 °C from 130 to 120 °C resulted in an increase of enantioselectivity for alcohol 5 from 1.066 to 1.088. Lower values and a smaller increase of enantioselectivity for alcohol 6, from 1.029 to 1.035, were observed. The increases in retention for both alcohols were not much different, as shown by similar k' values in Figure 3.

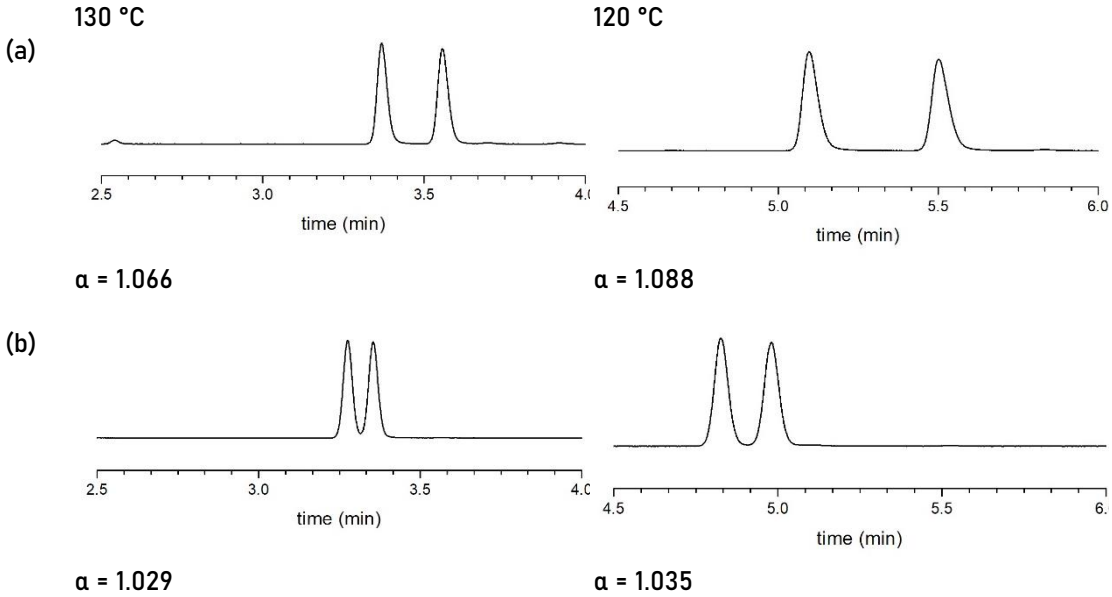

Figure 5. Chromatograms of alcohols (a) 5 and (b) 6 at 130 and 120 °C.

The effect of type of substitution at the stereogenic center on enantioselectivity was also studied. Enantioselectivities of 1-phenylethanol (1) and *para*-substituted 1-diphenylmethanols (7-11) at different isothermal temperatures were compared in Figure 4(b). All *para*-substituted 1-diphenylmethanols (7-11), with two large phenyl groups at the stereogenic center, showed poorer enantioselectivities compared to alcohol 1. Alcohol 7, with fluoro substitution, showed no separation at all temperatures studied. In addition, alcohols 8-11 showed shallow slope of ln α versus 1/T plots, suggesting that the decrease in column temperature for these alcohols would result in increased retention factors (longer analysis times) with small improvement in enantioselectivities.

Finally, the optimum temperatures for complete enantiomeric separation of each alcohol were determined. The column temperature for each alcohol was adjusted until a resolution (Rs) of 1.5 was obtained. The isothermal temperatures, retention factors of the more retained enantiomers (k'_2) and other parameters at the optimum condition for each alcohol were shown in Table 1.

Table 1. Optimum column temperatures and other chromatographic parameters for complete enantiomeric separations of eleven alcohols (Rs ≥ 1.5).

alcohol #	temperature (°C)	$t_{R,2}$ (min)	k'_2	α	Rs
1	135	2.162	3.290	1.040	1.55
2	133	2.697	4.341	1.036	1.55
3	145	4.170	7.323	1.032	1.53
4	146	6.421	11.715	1.030	1.55
5	147	1.921	2.812	1.038	1.55
6	125	4.062	7.012	1.032	1.51
7	no separation	-	-	-	-
8	164	23.672	46.155	1.023	1.58
9	169	29.271	57.193	1.021	1.55
10	162	12.832	24.562	1.026	1.51
11	169	19.163	37.173	1.023	1.54

Clearly, enantiomers of *para*-substituted 1-diphenylmethanols (8-11) could be completely separated with long retention (k'_2 > 20). For all *para*-substituted 1-phenylethanols (2-6), with smaller methyl group at the stereogenic center, their enantiomers could be completely separated with shorter retention (k'_2 < 12). The influence of type of substitution at the *para*-position on the aromatic ring was observed. Methyl-substituted alcohols, 5 and 10, showed the shortest retentions for 1-phenylethanols and 1-diphenylmethanols, respectively. The retention at optimum condition of 1-phenylalkanols increased with the type of substituent in the order of methyl < methoxy < chloro < bromo. Fluoro substitution was an exception, as it provided good enantioseparation with short retention for alcohol 2 but it deterred the separation of alcohol 7. Among eleven alcohols in this work, enantiomers of alcohol 5 could be separated with the shortest analysis time. Enantiomers of three alcohols (1, 2 and 5) could be separated in less than 3 minutes (Figure 6).

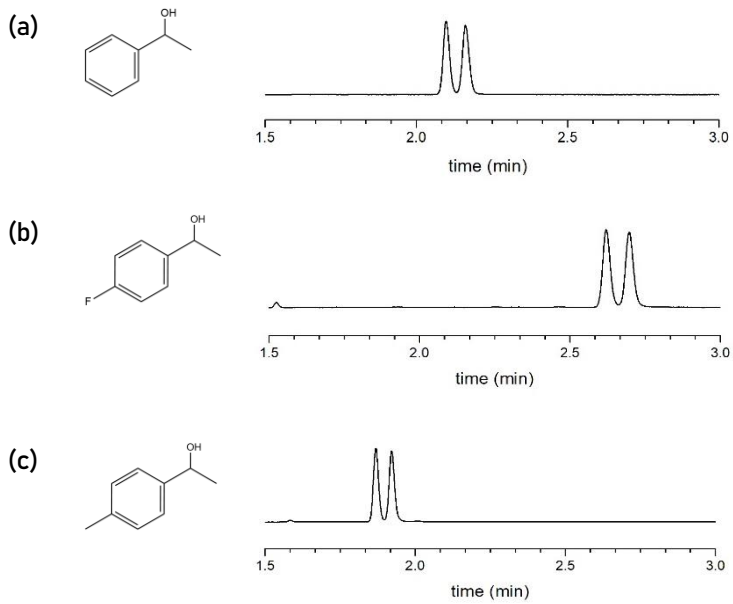

Figure 6. Chromatograms of alcohols (a) 1, (b) 2 and (c) 5 at their optimum temperatures.

Conclusion: Eleven chiral alcohols were synthesized and directly analyzed by GC using heptakis(2,3-di-*O*-methyl-6-*O*-*tert*-butyldimethylsilyl)-β-CD as a stationary phase. All alcohols were based on 1-phenylalkanols with different type of substitution at the *para*-position on the aromatic ring and at the stereogenic center. The effect of column temperature and analyte structure on retention and enantioselectivity were studied. Larger phenyl group at the stereogenic center led to low enantioselectivities. Methyl group substituted at the *para*-position on the aromatic ring led to higher enantioselectivities and shorter analysis times for complete separation.

References:

1. Roos G, Roos C. Organic Chemistry Concepts. 2015;43-54.
2. Kataoka M, Kita K, Wada M, Yasohara Y, Hasegawa J, Shimizu S. Appl Microbiol Biotechnol 2003;62:437-445.
3. Somagoni JM, Faga CM, Madhsudan RY. Int J Pharm Sci Nanotech. 2009;1:309-316.
4. Volker S. Trend Anal Chem. 2002;21:647-661.
5. Astray G, Gonzalez-Barreiro C, Mejuto JC, Rial-Otero R, Simal-Gadara J. Food Hydrocolloids. 2009;23: 1631-1640
6. Zoltan J. Trend. Anal Chem. 2002;21:379-388.
7. Timothy JW. Anal Chem. 2002;74:2863-2872.
8. Robards K, Haddad PR, Jackson PE. Principles and Practice of Modern Chromatographic Method. 1994;74-159.

C1_010_PF: ALTERNATIVE COLORIMETRIC DETERMINATION OF 2-NAPHTHOL FOR SCREENING OF ALPHA-GLUCOSIDASE ASSAY

Lalida Chanchaem[1], Plaipol Dedvisitsakul[1], Kanchana Watla-iad[1,2,*]

[1]School of Science, Mae Fah Luang University, Muang, Chiang Rai 57100, Thailand

[2]Center of Chemical Innovation for Sustainability, School of Science, Mae Fah Luang University, Muang, Chiang Rai 57100, Thailand

*e-mail: kanchana.wat@mfu.ac.th

Abstract: The aim of this study is to study an alternative colorimetric method for determination of 2-naphthol that will be used for α-glucosidase inhibitory activity. Since a well-known method for the assay, this enzyme is to use *p*-nitrophenyl α-D-glucopyranoside (*p*NPG) as the substrate. When α-glucosidase hydrolyzed the glycosidic bond, it will release *p*-nitrophenol, which can absorb light at maximum wavelength of 405 nm. However, the color of plant extract has become problematic in the assay since the compounds in the extracts usually exhibited overlapping absorption spectrum with *p*-nitrophenol. So, we focused on developing an alternative colorimetric detection system based on creating derivatives of 2-naphthol with several reactants such as $FeCl_3$, $K_3[Fe(CN)_6]$, NaOCl and diazonium salt. Results showed that 2-naphthol reacting with diazonium salt could present the red shift spectrum of the product solution to the maximum absorption wavelength of around 540 nm. This shift in absorption property could solve the interference of the plant extracts. In addition, analytical characteristics such as LOD and LOQ, obtained from using the diazonium salt reacted with 2-naphthol were 0.006 mM and 0.015 mM, respectively. Therefore, the diazoniun salt would be further developed for the colorimetric detection of the released 2-naphthol produced from enzymatic reaction when use *β*-naphthyl α-D-glucopyranoside as the substrate in α-glucosidase assay.

Introduction: In recent years, type-2 diabetes mellitus (DM) has increased all over the world and about 366 million patients are expected[1]. Deficient production of insulin resulted in the imbalance of insulin and hydrolysis of glucose. Consequently, level of glucoses in blood is raised up after meal. Nowadays, acarbose, a pseudotetrasaccharide which is an inhibitor of α-glucosidase and pancreatic α-amylase, was used in DM treatments to maintain glucose balance. However, acarbose has exposed side effects such as flatulence, nausea and vomiting[2]. So, plant extracts obtained from natural sources have been investigated for α-glucosidase inhibition. In the enzymatic assay, *p*-nitrophenyl α-D-glucopyranoside (*p*NPG) was usually used as the substrate for assay of α-glucosidase activity. The enzyme catalyzes the breaking of *p*NPG to release *p*-nitrophenol and α-D-glucopyranoside as the products. In this assay, the color of the released *p*-nitrophenol is yellow with maximum wavelength of 405 nm. In this regard, the α-glucosidase assays of plant extracts have become problematic with interference of compounds in plants that presents absorbance at around the detection range of *p*NPG assay[3]. Therefore, development of alternative colorimetric methods for the assay of α-glucosidase in the presence of plant extracts would be useful.

2-Naphthol or *β*-naphthol is a phenolic compound constituting naphthalene structure with hydroxyl group located at the *β*-position. Generally, 2-naphthol is colorless, but it can be ionized in water to be anionic fluorescent forms by delocalization of electron in the two aromatic rings[4]. Moreover, 2-naphthol is the precursor for manufacturing of dyes, pigments and pharmaceuticals[5] such as Sudan I (red dye), Sudan II (red dye) and Sudan III (reddish-brown dye). Interestingly, 2-naphthol can be changed from being colorless to visible color by increasing number of the aromatic rings or conjugated system. These properties have potential suggested that 2-napthol can be colorimetric detecting compound developed as the conjugated molecule of α-D-glucopyranoside substrate of α-glucosidase.

Generally, oxidizing agents, metallic transition and diazonium salt are used as chemical reagents for reaction of phenolic compounds. Alkaline oxidizing agent such ferric chloride ($FeCl_3$) and potassium ferricyanide ($K_3[Fe(CN)_6]$) and strong oxidizing agent such hydrogen peroxide (H_2O_2), potassium permanganate ($KMnO_4$), potassium manganate (K_2MnO_4) and sodium hypochlorite (NaOCl) were also reported for coupling reaction of phenolic and naphthol compounds too. In addition, horseradish peroxidase (HRP) was used as a catalyst for naphthol oxidation[6] and 5,10,15,20-tetraarylporphyrinatoiron (III) chlorides was also used[7]. Moreover, transition metals such as Cr, Cu and Ru have been also utilized as catalysts for this reaction[8,9,10]. However, the coupling reactions of naphthol compound using metallic transitions as catalysts have complicated process, customized times, and spineless costs. In addition, azo-group of aromatic amine could use to link with nucleophilic group of phenol was studied[11]. Diazonium salt have been also studied for α-glucosidase assay[12,13].

This research, compound of 2-naphthol released from enzymatic reaction was preformed color developing by using various chemical reagents (Figure 1.). The reactions of 2-naphtol with oxidizing agents ($FeCl_3$, $K_3[Fe(CN)_6]$ and NaOCl) and diazonium salts were studied for the screening absorption spectrum and color shade of chemical reactions. Moreover, effect of solvents and pH on the absorption and color shade of the 2-naphthol reaction were investigated. Finally, analytical characteristics of selected reactions were studied for future applying to evaluate the α-glucosidase inhibitory (AGHi) activity.

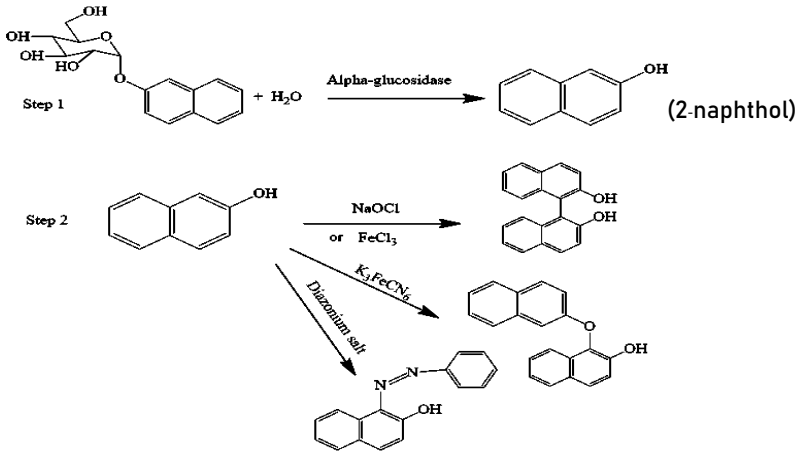

Figure 1. Chemical reaction of 2-naphthol released from enzymatic process (step 1) using various oxidizing agents and diazonium salt [14,15,16].

Methodology:

Chemicals and Materials: Compound of 2-naphthol (99 %w/w grade) was obtained from Loba Chemine, India. Phosphate buffer (PBS, 20.00 mM) at pH 6.8 and pH 8.0 were prepared from di-sodium hydrogen phosphate dihydrate, $Na_2HPO_4.2H_2O$ (RCI Labscan, Thailand) and sodium dihydrogen orthophosphate dihydrate, $NaH_2PO_4.2H_2O$ (Ajax Finechem, New Zealand. Dimethyl sulfoxide (DMSO) (RCI Labsacn, Thailand) used for dissolving 2-naphthol was diluted to 20 %v/v by phosphate buffer (PBS, pH 6.8). Oxidizing agents such as Iron (III) chloride ($FeCl_3$), potassium ferricyanide ($K_3[Fe(CN)_6]$) and sodium hypochlorite (NaOCl) were bought from Sigma-Aldrich Corporation. All oxidizing agents were prepared in different buffer solutions. Sodium borate buffer (1.0 M) has pH 9.0 and pH 10.0 were prepared from boric acid (H_3BO_3, Sigma Aldrich, USA) and sodium hydroxide (NaOH, RCI Labscan, Thailand). The pHs of buffer solution were adjusted by using NaOH and hydrochloric acid solution (HCl, Merck,

Germany). Other, sodium carbonate (Na_2CO_3) was obtained from Loba Chemine, India. Aniline solution (5 %w/v) was prepared by dissolving aniline (PRS Panreac, Spain) in 1.00 M of sulfuric acid (H2SO4, Merck, Germany) and then heated until all of aniline was completely dissolved. Aluminum chloride hexahydrate ($AlCl_3.6H_2O$, Merck, Germany) and sodium nitrite solutions ($NaNO_2$, RCI Labscan, Thailand) were prepared by dissolving them with DI water. Ethanol (10 %v/v) was prepared from dilution of 99.99 %w/w ethanol (Merck, Germany) with distilled water (DI). A spectrophotometer (Ocean optics, USA) including light source HL-2000 and ocean optics USB 4000 was used for the detection of the absorption spectrum of reactions.

The reactions of 2-naphthol with oxidizing agents: The coupling reactions of 2-naphthol were done by using three differences oxidizing agents which were $FeCl_3$, NaOCl, and $K_3[Fe(CN)_6]$. For the oxidation of 2-naphthol with $FeCl_3$, 3.20 mM of 2-napthol (220 µL) was mixed with 150 µL of 0.125 M $FeCl_3$ dissolved in various solvents (10 %v/v ethanol, 1 %v/v HCl, PBS buffer (pH 6.8) and DI). The same procedures were done by changing the oxidizing agent to 0.125 M of $K_3[Fe(CN)_6]$, and 12%w/v of NaOCl dissolved in alkaline solution (pH 8.0 to pH 10.0), respectively. All reactions were diluted with DI water to 1160 µL before the analysis with an Ocean Optics spectrometer in the range of 200 nm to 900 nm.

The reaction of 2-naphthol with diazonium salt: A diazonium salt was generated from the reaction of aniline and nitrite compounds. Then, 2-naphthol standard solution (2.30 mM, 20 µL) was sequentially mixed with 1.00 M $NaNO_2$ (50 µL), 5 %w/v aniline (50 µL), and 1.00 M $AlCl_3$ (50 µL). The reaction was diluted to 500 µL with distilled water before investigating the absorption spectrum by an Ocean Optics spectrophotometer.

Analytical characteristics: For the oxidation reactions of 2-naphthol, calibration of 2-naphthol standard was investigated in the range of 0.10 mM to 0.60 mM for the selected oxidizing agents ($K_3[Fe(CN)_6]$) dissolved in a particular solvent (10 %v/v ethanol, PBS (pH 6.8) and distilled water). In case of the coupling reaction of 2-naphthol with diazonium salt, the concentration of 2-naphthol standard was prepared in the range of 0.01 mM to 0.05 mM for calibration plotting. The analytical characteristics such as determination coefficient (R^2), limit of detection (LOD) and limit of quantitation (LOQ) were investigated.

Results and Discussion: The development of colorimetric methods for the screening of α-glucosidase inhibitory (AGHi) activity using derivatives of 2-naphthol as chromophores were studied (Figure 1). Spectra of the oxidative coupling compounds of 2-naphthol obtained from using various oxidizing agents and diazonium salt were shown in Figure 2. Redshift spectra (higher maximum wavelength) were observed from the products produced from the oxidative coupling reactions of 2-naphthol with NaOCl, and $K_3[Fe(CN)_6]$. However, the spectral shift was not observed from the reaction of 2-naphthol with $FeCl_3$ in different solvent systems. Observation of product color and maximum wavelength obtained from using various experimental conditions were summarized on Table 1.

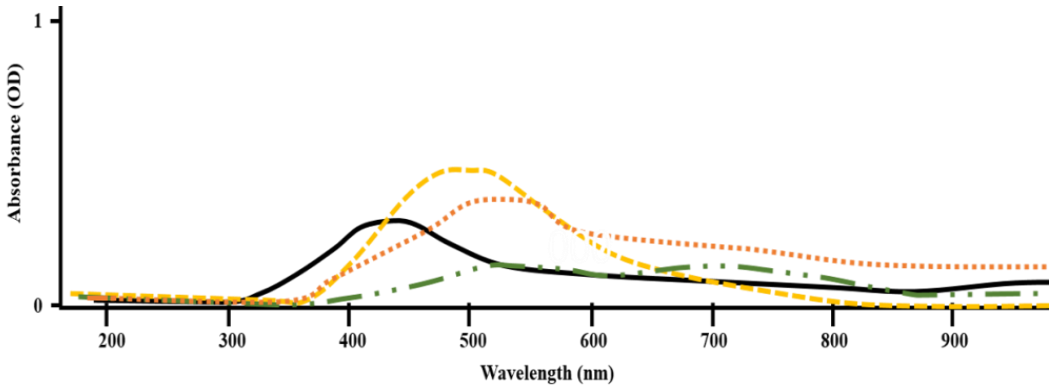

Figure 2. Absorption spectra of the derivatives of 2-naphthol obtained from using $FeCl_3$ in HCl (––), $K_3[Fe(CN)_6]$ in phosphate buffer pH 6 (– –), NaOCl in phosphate buffer pH 8 (– ··) and azonium coupling 2-naphthol (··) as reagents for the reaction.

Table 1. Maximum wavelength and color shade of the derivatives of 2-naphthol obtained from the coupling reaction of 2-naphthol with various oxidizing agents dissolved in different solvents and diazonium salt.

Oxidizing agents	Solvents	Observation	Solution color	Maximum wavelength (nm)
$FeCl_3$	1 %v/v HCl	white colloid		-
	10 %v/v ethanol	faded orange with yellow of iron solution		450
	phosphate buffer pH 6.8	faded orange with yellow of iron solution		450
	DI-water	faded orange with yellow of iron solution		450
$K_3[Fe(CN)_6]$	1 %v/v HCl	faded yellow of iron solution		450
	10 %v/v ethanol	faded orange		500
	phosphate buffer pH 6.8	faded orange		500
	DI-water	faded orange		500
NaOCl	DI-water	clear solution		-
	phosphate buffer pH 8.0	yellow with fade green		750
	borate buffer pH 9.0	dark green		540,750
	borate buffer pH 10.0	dark green		540,750
	0.1 M NaOH	greenish dark		540,750
Diazonium salt	DI-water	faded orange		540

It was found that dissolving $K_3[Fe(CN)_6]$ in different solutions could likely shift the color of the reaction to faded orange color. This could be explained that the Fe^{3+} ion in $K_3[Fe(CN)_6]$ can oxidize 2-naphthol more than that of $FeCl_3$ because the positive charge of potassium ion is important for reducing electrostatic repulsive forces of the complex, which resulted in the facilitated electron transfer[18]. In addition, the faded orange color of solution observed from the experiment was consistent with the results reported by Scott[15]. In contrast, the color of product solution obtained by using NaOCl dissolved in different solvent systems slightly increased to dark greenish color due to high pH affected the ionization of OCl^{-}[19]. We speculated that the dark greenish color might be 1,1'-Bi-2-naphthol as reported by Ni et al.[14]. However, this dark greenish color was still overlapping with the color of plant extract usually observed. Besides, reaction between 2-naphthol and diazonium salt could extend the original conjugated system of 2-naphthol resulted in higher maximum absorption wavelength, which was in the range of absorption of orange color. The orange compound presented from the reaction of diazonium salt and 2-naphthol was speculated to be 1-phenylazo-2-naphthol as reported by Mkpenie[16].

From the results described above, $K_3[Fe(CN)_6]$ and diazonium salt were selected as the alternative colorimetric reactants for the determination of 2-naphthol. These protocols could be developed for α-glucosidase assay using *β*-naphthyl α-D-glucopyranoside as the substrate. The analytical characteristics obtained from both methods were compared in Table 2. A good linear calibration curve was observed when using $K_3[Fe(CN)_6]$ as reagents with R-square of 0.997, 1.000, and 0.998 for dissolving $K_3[Fe(CN)_6]$ in 10 %v/v ethanol, phosphate buffer, and DI-water, respectively. However, the protocol that using diazonium salt as reagent is more sensitive than other method with the LOD and LOQ at 0.006 mM and 0.015 mM, respectively. The diazonium salt could rapidly react with 2-naphthol because it is weak electrophile[20]. Therefore, diazonium salt was sensibility more than $K_3[Fe(CN)_6]$. So, reaction of diazonium salt with 2-naphthol compound would be used for further development of colorimetric method for screening AGHi.

Table 2. Analytical characteristics obtained from using the $K_3[Fe(CN)_6]$ and diazonium salt as reactants to react with 2-naphthol

Analytical characteristics	10%v/v ethanol	$K_3[Fe(CN)_6]$ in Phosphate buffer pH 6.8	DI-water	Diazonium salt in DI-water
R^2	0.997	1.000	0.998	0.981
Slope	0.747	0.786	0.807	5.919
LOD (mM)	0.029	0.012	0.026	0.006
LOQ (mM)	0.063	0.029	0.051	0.015

Conclusion: Colorimetric method for the detection of 2-napthol using various oxidizing agents and diazonium salts were studied for further screening of α-glucosidase inhibitory (AGHi) activity.

The coupling reaction of 2-naphthol with $K_3[Fe(CN)_6]$ and diazonium salt could extend the conjugated system resulted in presenting higher maximum wavelength of the absorption spectrum. However, the reaction of diazonium salt showed the lowest LOD and LOQ than other reagents. The product obtained from the reaction of diazonium salt and 2-naphthol was exposed to orange-red color with maximum wavelength at 540 nm, which could reduce the interference from the color of plant extract. So, the reaction of the diazonium salts and 2-naphthol would be alternative colorimetric method for further screening of AGHi.

References:
1. Wild S, Roglic G, Green A, Sicree R, King H. Diabetes care. 2004;27(5):1047-1053.
2. Toeller M. EJCI. 1994;24:31-35.
3. Aoki K, Muraoka T, Ito Y, Terauchi Y. Intern Med. 2010;49:1085-1087
4. Tokutake S, Yamaji N, Kato M. Pharm Bull. 1990; 8:13-18.
5. Wu D, Hurtubise R. Talanta. 1993;40:901-907.
6. Tao Y, Bentley WE, Wood TK. Appl Microbiol Biotechnol. 2005;68:614-621.
7. Brignac J, Patel V. ANAL LETT.1974;7:195-203.
8. Chauhan S, Kalra B, Mohapatra P. J Mol Catal A Chem. 1999;137:85-92.
9. Lee E, Cao T, Torruellas C, Kozlowski C. JACS. 2014;136:6782-6785.
10. Kim Y, Takizawa S, Oh K. ORG BIOMOL CHEM. 2016;14:7191-7196.
11. Matsushita M, Kamata K, Yamaguchi K, Mizuno N. JACS. 2005;127:6632-6640.
12. Guerin F, Ali B, Rollet J, Souchier C, Czyba C. J. Androl. 1986;64:1102-1107.
13. SimõesPires A, Hmicha B, Marston A, Hostettmann K. Phytochem Anal. 2009;6:511-515.
14. Ni X, Li X, Li Z, Cheng P. Org Chem Front. 2016;3:1154-1158.
15. Scott I. Chem Soc. 1965;19:1-35.
16. Mkpenie N, Essien E. Am Chem Sci J. 2015;8
17. Kazeem I, Adamson O, Ogunwande A. BioMed research international. 2013.
18. McDonald D, Hamilton A. JACS. 1973;95:7752-7758.
19. Oakes J, Gratton P. JCS PERKIN II. 1998;10:2201-2206.
20. Ouellette J, Rawn D. Org Chem. 2014;1: 843-872.

Acknowledgements: This work is supported by the Scientific and Technological Instrument Center and the Center of Chemical Innovation for Sustainability, School of Science, Mae Fah Luang University. The Ministry of Science and Technology (Thailand) is acknowledged for financial support (256109A3070015).

C1_012_PF: APPLICATION OF SILVER AMALGAM ELECTRODE FOR ANODIC STRIPPING VOLTAMMETRIC DETERMINATION OF CADMIUM IN CONTAMINATED SOIL AND PLANT

Mangheny Godfrey [1], Kawinthida Moolsarn[2], Chidkamon Thunkhamrak[2], Jaroon Jakmunee[1,2,3,*]
[1]Master Degree Program in Environmental Science, Environmental Science Research Center, Faculty of Science, Chiang Mai University, Chiang Mai, 50200, Thailand
[2]Department of Chemistry and Research Laboratory for Analytical Instrument and Electrochemistry Innovation, Faculty of Science, Chiang Mai University, Chiang Mai 50200, Thailand
[3]Center of Excellence for Innovation in Chemistry, Faculty of Science, Chiang Mai University, Chiang Mai 50200, Thailand
*e-mail: jaroon.jakmunee@cmu.ac.th, jakmunee@gmail.com

Abstract: Heavy metals such as cadmium and lead are persistent contaminants in the environment. The analysis and remediation of heavy metals need an analytical method that is reliable, convenient to use, and low-cost. In this research, the silver amalgam electrode was developed for anodic stripping voltammetric (ASV) determination of cadmium and lead. This electrode is more environment-friendly than the commonly used hanging mercury drop electrode. Its property is similar to mercury electrode but lower in toxicity and easy preparation. The optimization of the ASV method with using of silver amalgam electrode was carried out. Under the optimum conditions, the linear analytical ranges of cadmium were 20-80 µg L^{-1} and 90-800 µg L^{-1} and lead were 10-80 µg L^{-1} and 150-1000 µg L^{-1}. Moreover, detection limits were 2.0 and 0.01 µg L^{-1} for cadmium and lead, respectively. The method had percentage recoveries for the determination of those metals in ranges of 81.9-114.1 for cadmium and 86.4-109.5 for lead. The proposed method was applied for the determination of cadmium in soil and plant from a cadmium contaminated site in Tak province. The method is potentially used in the phytoremediation study of cadmium.

Introduction: Heavy metal environmental pollution is a worldwide challenge especially cadmium which is readily available and mobile to plants and animals. Thailand for some time has had a problem of environmental pollution especially heavy metal pollution due to growing (and after inception of) industrialization. The heavy metal pollution has come with its associated health and social challenges which have prompted a need for sustainable approaches in this regard, some studies have been conducted to determine cadmium levels in soils and identify the origin of Cd in the vicinity of the zinc mine at Mae sot, *Tak* province [1]. The total soil cadmium in Thailand ranges from 0.01 to 1.3 mg Cd kg^{-1} (or 37 mg kg^{-1}) with a mean value of 0.03 mg Cd kg^{-1}, whereas EU/EEC permissible Cd level (3.0 mg Cd/kg soil), however the Thai standard stands at 0.15 mg Cd/kg soil; but Mae sot Area, Tak province where a zinc mine and related human activities stands at 0.5-284 mg Cd/kg [2,3].. However, in one such a case study, soil samples from agricultural areas around the *Pha Te* village, the Mae Sot District, have total soil Cd and Zn concentrations range from 0.63 to 30.4 mg Cd kg^{-1} and 14.4 to 594 mg Zn kg^{-1} respectively, yet by the world health organization standards these values are high especially for agricultural lands[1,4,5], therefore the need for soil/environment remediation.

The analysis and remediation of heavy metals need an analytical method that is reliable, convenient to use, and low-cost. The standard methods for determination trace amounts of cadmium are atomic absorption spectroscopy (AAS) [6,7] and inductively couple plasma-mass spectrometry (ICP-MS) [8]. The limitation of these methods are sample preparation, high cost, long analysis time, high cost of instrument, non-simultaneous analysis, and used high reagent consumption. Anodic stripping voltammetry (ASV) is an inexpensive alternative technique that can determine cadmium at trace level [9-12]. ASV provides more advantages such as simultaneous analysis, used low reagent consumption and short time

analysis. This electroanalytical technique is based on the applying of electrical potential to working electrode (WE), the analyte (heavy metal ions) is electrochemically reduced at electrode surface of WE in the deposition step, and then scanning the potential to positive direction in the stripping step, which causes the accumulated metal to oxidize and return back to the solution. The monitoring of electrical current which is relating directly to concentration of the analyte is carried out in this step.

At early time, a hanging mercury drop electrode (HMDE) [13] was commonly used as WE because of its wide negative potential window (-2.0 to +0.4 V) due to many metal analysis but it has many disadvantages such as toxic for life and environment, uncontrolled size of drop or surface of electrode, and unstable. Therefore, silver amalgam electrode was developed. Silver amalgam electrode resembles to HMDE which was combined between silver (Ag^0) and mercury (Hg^0). In 2002, Baś and Kowalski developed a silver surface for mercury film electrode (Hg(Ag)FE) [14]. They used a silver wire (0.05 cm of diameter) is dipped in mercury and applied to determine heavy metals. Some metallic impurities were deposited, stripped and measured. Piech et al. [15] demonstrated a renewable mercury film silver based electrode that followed Baś method for manganese(II) traces determination. Silver solid amalgam electrode (AgSAE) was developed in the latter [16-21]. Although, AgSAE has low toxicity than HMDE, it remains to use liquid mercury. Therefore, silver amalgam microwire electrode was developed [22,23]. It was prepared by plating mercury on the silver microwire. This method showed lower mercury consumption, lower toxicity, and renewable electrode.
In this work, we developed the silver amalgam electrode by coating mercury on silver wire for cadmium(Cd) and lead(Pb) determination via anodic stripping voltammetry. The developed electrode was applied for ASV determination of cadmium in soil and plant that collected for a cadmium contaminated site in Tak province. The developed method shows good performance and potentially useful for environmental study of the cadmium and lead. The results indicated that cadmium is accumulated in the *A. spinosus* plant, so it is potentially useful for phytoremediation of cadmium by using this plant.

Methodology:
Chemicals and materials: Acetic acid (CH_3COOH) was purchased from Lab scan (Thailand), Cd chloride dihydrate ($CdCl_2.2H_2O$) was purchased from Fluka (Switzerland), hydrochloric acid (HCl), Pb(II) nitrate ($Pb(NO_3)_2$), mercury(II) nitrate ($Hg(NO_3)_2$) and nitric acid 65 %w/v (HNO_3) were purchased from Merck (Germany). Sodium acetate trihydrate ($CH_3COONa.3H_2O$) was obtained from Carlo Erba (Italy). Acetate buffer solution (0.04 M) was prepared by dissolving 1.3608 g $CH_3COONa.3H_2O$ with deionized (DI) water, adjusted pH to 4.5 with 0.04 M acetic acid and brought up to 250 mL with DI water. Hg(II) solution was prepared by dissolving 0.1713 g $Hg(NO_3)_2$ with 10 mM nitric acid and brought up to 25 mL with DI water. 200 mg L^{-1} standard solution of Pb and Cd was prepared by dissolving 0.02 g of Pb and Cd with 0.1 M hydrochloric acid and 0.1 M nitric acid, respectively and brought up to 100 mL with DI water.
Silver amalgam electrode preparation: The 0.16 mm diameter of silver wire was polished with glass paper and covered the un-react site with an insulator. After that, the silver wire was put into a polypropylene pipette tip and setting it in an electrochemical cell. The voltammetric cell consisted of silver/silver chloride (Ag/AgCl) electrode as a reference electrode (RE), a stainless steel rod as an auxiliary electrode (AE), and a silver wire electrode as a working electrode (WE). An aliquot of 10 mM HNO_3 20 mL that contained 2 mM Hg(II) was pipetted into the voltammetric cell. Silver amalgam film was prepared by applying the constant potential at -0.4 V for 900 s to the WE.
Cadmium and lead determination: ASV was performed by using a Metrohm 757 VA Computrace voltammograph (Metrohm, Switzerland). In the first step, Pb and Cd standard solutions were added into the voltammetric cell that contained acetate buffer pH 7.4. Then, potential of -0.9 V vs Ag/AgCl was applied to the WE for 180 s of deposition time and rested the system

about 5 s. The stripping step was performed by scanning the potential from -0.9 V to 0.0 V with 0.05 V s^{-1} of scan rate. A voltammogram was obtained and the peak currents were directly proportional to the concentrations of the analytes.

Sample collection and preparation: Soil and mature plant samples were collected from the Padaeng, zinc mine area in Mae Sot district, Tak province (16°40.187'N 98°36.62'E). The respective sampling sites were chosen on the basis of being farmlands and proximity to the water bodies which run around and within the mine area. Soil samples were extracted by EPA method 3050B [24] (wet acid digestion, HNO_3/H_2O_2 regime). The plants parts were separated into leaves, roots, stem and floral (reproductive parts) after the drying processes. The samples were carefully crush-milled to powder forms using mortar-pestle and blender as necessary, packed in aluminum foil and kept in a secure dry storage till further process of acid-digestion. The respective plants parts were then processed according to EPA method 3050B.

Results and Discussion:

Preparation of the silver amalgam electrode: The silver amalgam electrode was electrochemically prepared by depositing mercury onto the silver wire. The deposition time of mercury on the silver wire was studied. The potential of -0.4 V vs Ag/AgCl was applied in HNO_3 solution contained 2 mM Hg(II) for different deposition time and monitoring the current of Cd and Pb of 100 and 400 ppb, respectively. The results as shown in Figure 1 indicated that deposition time of 300 s provided lowest current and gradually increase to the highest current at 900 s. When time increased to 1200 s, the current decreased and saturated because of the limiting of electrode surface. Therefore, 900 s was selected for forming mercury on silver wire.

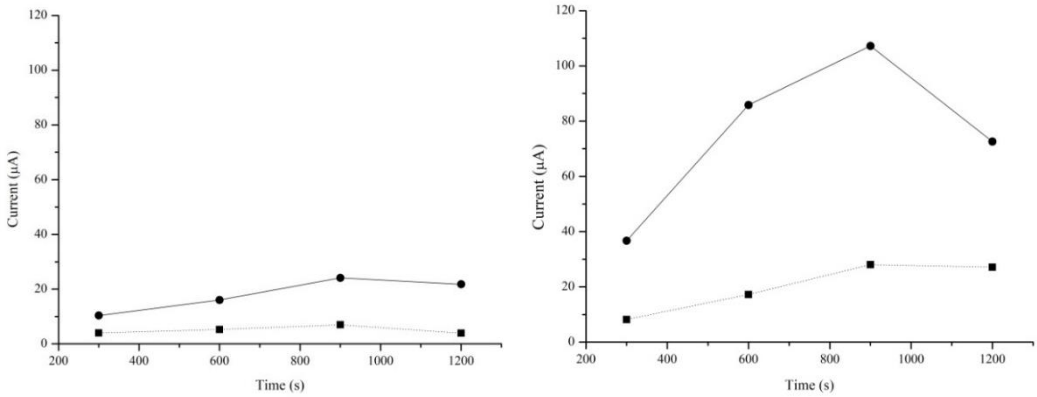

Figure 1. Optimization of deposition time of mercury on silver wire electrode: 100 μg L^{-1} (a) and 400 μg L^{-1} (b) of Cd (dot line) and Pb (solid line) concentration.

Effect of deposition time of Cd and Pb: In deposition step, Cd and Pb were deposited on electrode surface, so the deposition time is necessary to study. It was studied in the range of 30 - 600 s in 50, 100 and 500 μg L^{-1} of Cd and Pb. The results were plotted between deposition time and current as shown in Figure 2a-2c. Each deposition time illustrated difference current due to each metal ion. Increasing time in 30-180 s provided rapidly increased current until 300 s the highest current was established. However, deposition time of more than 300 s gave decreasing current because metals on electrode surface are saturated. In addition, the

current related directly with concentration (C) and deposition time (t_d) as shown in equations:

$$i_p \propto C \cdot t_d$$
$$i_p = k \cdot C \cdot t_d$$

Thus, 300 s of deposition time was selected as an optimum condition.

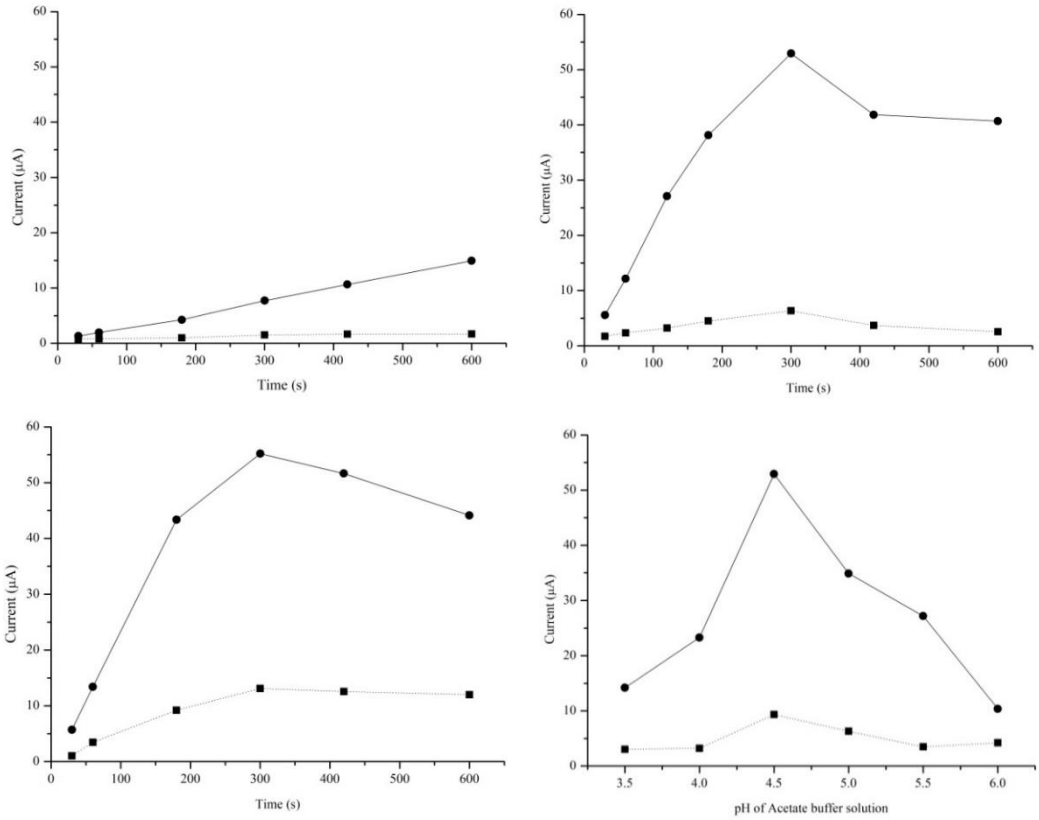

Figure 2. Optimization of deposition time of Cd and Pb: 50 μg L^{-1} (a), 100 μg L^{-1} (b) and 500 μg L^{-1} (c) of Cd (dot line) and Pb (solid line), and optimization of pH of the acetate buffer (d).

Effect of pH of acetate buffer solution: pH of acetate buffer solution affect to mobility of ion in the electrolyte. The 0.04 M acetate buffer was used with the range of pH of 3.5 - 6.0 and containing 50 μg L^{-1} Cd and Pb. Figure 2d showed the effect of pH. Both of Cd and Pb showed the same trend, at the low pH indicated low current and the current greatly increased to the highest at pH 4.5. Furthermore, at pH higher than 4.5, the decrease of current occurred again. Therefore, acetate buffer solution at pH 4.5 was selected.

Calibration graph: The silver amalgam electrode was used for determination of Cd and Pb, following the condition selected from the above studies, i.e., 900 s of forming mercury on silver wire, 300 s of deposition time of the analyte, and pH 4.5 of acetate buffer. The proposed electrode provided voltammograms as shown in Figure 3. A direct relationship of current and concentration of Cd and Pb is shown in Figure 4a-4d. However, the response current offered 2 linear calibration ranges. Linear calibration graph of Cd was in the range of 20-80 μg L^{-1} and 90-800 μg L^{-1} with detection limit (3SD) of 2.00 μg L^{-1} and Pb was in the range of 10-80 μg L^{-1} and 150-1000 μg L^{-1} with detection limit (3SD) of 0.01 μg L^{-1}, respectively.

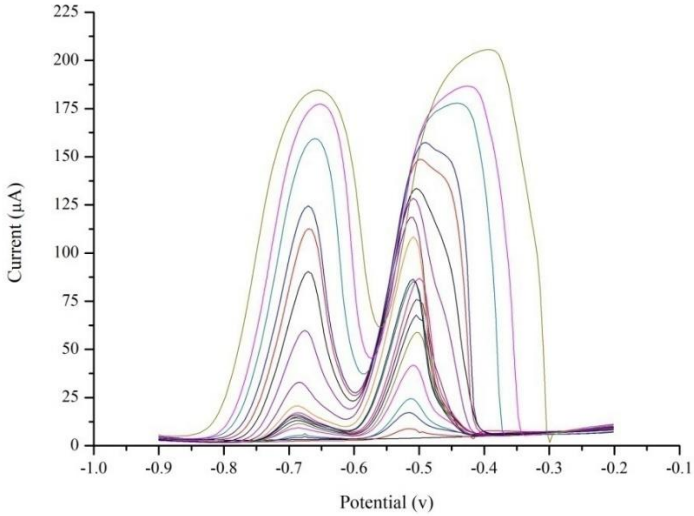

Figure 3. Anodic stripping voltammogram of silver amalgam electrode in pH 4.5 of acetate buffer for determination of Cd and Pb in 10-5000 μg L^{-1}.

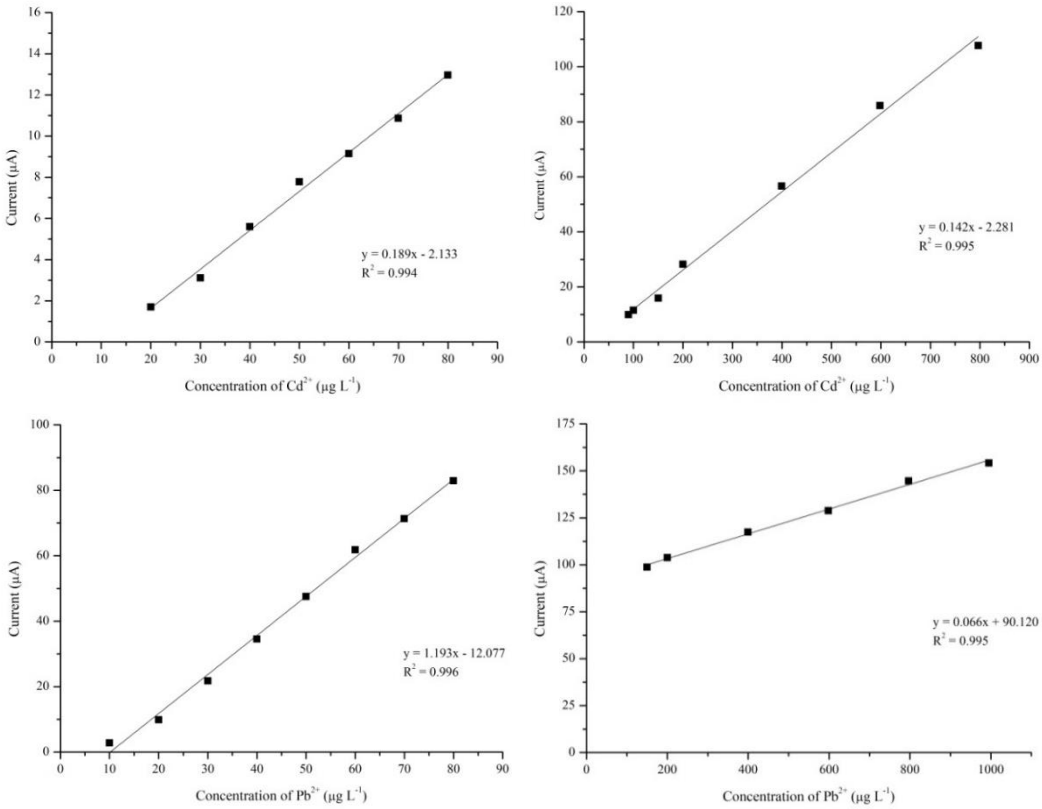

Figure 4. Calibration graph of Cd in the range of 20-80 μg L^{-1} (a), 90-800 μg L^{-1} (b) and Pb in the range of 10-80 μg L^{-1} (c), 150-1000 μg L^{-1} (d).

Repeatability and Reproducibility: Under the optimum conditions, the repeatability and reproducibility were studied from the current response to 100 µg L^{-1} Cd and Pb, using the same electrode and different electrodes, respectively. The results of the relative standard deviation (RSD) of repeatability indicated 2.48% and 1.65% (N=9) of Cd and Pb, respectively. Moreover, RSD of reproducibility indicated 1.14% and 1.06% (N=9) of Cd and Pb, respectively.
Determination of cadmium in soil and plant digested samples: The developed method was applied for determination of Cd in soil and plant collecting from a cadmium contaminated sites. The quantification was performed by standard addition method. Sample was pipetted in to an electrochemical cell and standard solution of Cd and Pb were added. The results are shown in Table 1.

Table 1 Cadmium concentrations (mg kg^{-1}) in the soil and *A.spinosus* collected from-near zinc mine area, Mae Sot district, Tak province

Site No.	Site description	Cd content, mg kg^{-1}			
		Soil	Root	Leave	Stem
1	Mae Tao Mai 1	54.22	53.94	147.72	101.75
2	Mae Tao Mai 2	5.54	ND	ND	ND
3	Mae Tao Mai 3	5.65	ND	10.28	5.65
4	Pa de village 1	1.03	5.65	6.45	2.21
5	Pa de village 2	1.31	3.29	4.68	3.10
6	Pa de village 3	2.84	2.89	6.64	3.68

The preliminary result indicated that the native *A. spinosus* plant accumulated Cd in its various organs with highest concentration being in the leaves, and had the potential to be adapted as a phytoextractor. As shown in Figure 5, the concentrations of Cd in the plant are directly related to the Cd content in the soil. As comparison to Thailand standard soil Cd levels: 0.01-1.3 mg or 37 Cd kg^{-1} soil; EU/EEC permissible Cd level (3.0 mg Cd kg^{-1} soil), high Cd levels were found in Mae Sot area (0.5 - 284 mg Cd kg^{-1}). These results basically correlate with those of other studies [1,2,25] regards the cadmium accumulation, and the current situation at the Mae Sot mine area. These plants were sampled at an approximate distance of 500 m from each other.

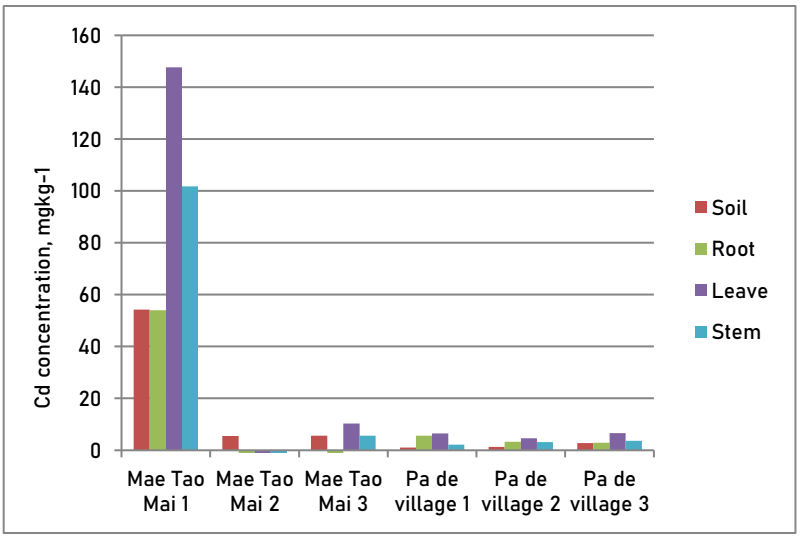

Figure 5. Distribution of cadmium in the Mae sot samples with that of Mae Tao Mai 1 area showing highest concentration of Cd in *A.spinosus*

Conclusion: In this work, we demonstrated that silver amalgam electrode can be simply prepared and used in ASV for determination of Cd and Pb. Silver wire electrode was electrochemically coated with Hg to form amalgamated electrode. Under the optimum condition, it can determine Cd and Pb with low detection limits. The proposed electrode was applied to determination of Cd in soil and plant digests. Further, *A.spinosus* plant species collected from Mae Sot mine area, Tak province showed phyto-extraction characteristics with higher concentration in the leaves correlating with area soil concentrations with those of the plant under this investigation. This study sought to assess this plant's heavy metal extraction capabilities/capacity on cadmium contaminated soil under green-house conditions.

References:

1. Akkajit P. Applied Environmental Research. 2015;37:71.
2. UNEP. Final review of scientific Information on cadmium. New York: UNEP Chemicals Branch, DTIE. 2010.
3. Simmons R, Pongsakul P, Saiyasitpanich D, Klinphoklap S. Environmental Geochemistry and Health. 2005;27:501.
4. Morais S, Osta FG, Pereira MD. Heavy Metals and Human Health. Intechopen. 2012;-: 227-246.
5. Lugwisha HE, Othman OC. International Journal of Environmental Monitoring and Analysis. 2014;2:313.
6. Duarte AT, Dessuy MB, Silva MM, Vale MGR, Welz B. Microchemical Journal. 2010;96:102.
7. Bagheri H, Afkhami A, Saber-Tehrani M, Khoshsafar H. Talanta. 2012;97:87.
8. Minnich MG, Miller DC, Parsons PJ. Spectrochimica Acta Part B: Atomic Spectroscopy. 2008;63:389.
9. Bonfil Y, Kirowa-Eisner E. Analytica chimica acta. 2002;457:285.
10. Mamani MCV, Aleixo LM, de Abreu MF, Rath S. Journal of pharmaceutical and biomedical analysis. 2005;37:709.
11. Abbasi S, Khodarahmiyan K, Abbasi F. Food chemistry. 2011;128:254.
12. Yi WJ, Li Y, Ran G, Luo HQ, Li NB. Sensors and Actuators B: Chemical. 2012;166:544.
13. Li Y, Xue H. Analytica chimica acta. 2011;448:121.
14. Baś B, Kowalski Z. Electroanalysis. 2002;14:1067.
15. Piech R, Baś B, Kubiak WW. Journal of Electroanalytical Chemistry. 2008;621:43.
16. Jiranek I, Peckova K, Kralova Z, Moreira JC, Barek J. Electrochimica Acta. 2009;54:1939.
17. Niaz A, Fischer J, Barek J, Yosypchuk B, Bhanger MI. Electroanalysis. 2009;21:1719.
18. Strasunske K, Mikkelsen Ø, Billon G. Electroanalysis. 2010;22:501.
19. Danhel A, Yosypchuk B, Vyskocil V, Zima J, Barek J. Journal of Electroanalytical Chemistry. 2011;656:218.
20. Danhel A, Mansfeldova V, Janda P, Vyskocil V, Barek J. Analyst. 2011; 136:3656.
21. Deýlová D, Vyskočil V, Barek J. Electrochimica Acta. 2012;62:335.
22. Bi Z, Salaün P, van den Berg CMG. Analytica Chimica Acta. 2013;769:56.
23. Espada-Bellido E, Bi Z, van den Berg CMG. Talanta. 2013;105:287.
24. US EPA, http://www.epa.gov/osw/hazard/testmethods/sw846/pdfs/chap3.pdf; SW-846 Update V. US EPA METHOD 3050B, (1996, December 2). pp. 1-12.
25. Kitana J, Achayapunwanich O, Thammachoti P, Othman MS, Khonsue W, Kitana N. Environment Asia. 2015;8:16.

Acknowledgements: MG thanks the Thailand International Cooperation Agency (TICA) for providing him a financial support for International Program in Environmental Science fellowship at Chiang Mai University. The authors would like to thank Chiang Mai University,

Thailand Research Fund, and Center of Excellence for Innovation in Chemistry for partial financial support.

C1_013_PF: PAPER-BASED LINER FOR HEADSPACE COLORIMETRIC DETERMINATION OF VOLATILE COMPOUNDS

Kamonwan Meesuwan, Waleed Alahmad, Pakorn Varanusupakul*
Chemical Approaches for Food Applications Research Group, Faculty of Science, Chulalongkorn University, Bangkok, Thailand
Department of Chemistry, Faculty of Science, Chulalongkorn University, Bangkok, Thailand
*e-mail: pakorn.v@chula.ac.th

Abstract: This work presented a simple alternative method for simultaneous extraction and determination of volatile compounds in complex matrix samples by combining headspace technique with paper based colorimetric method. The method used a paper loaded colorimetric reagent attached to the liner of the cap (paper-based liner) for direct detection of the volatilized compounds in headspace extraction mode. The paper was attached to the liner of the cap. A sample was placed in a vial sealed with the paper-based lined cap. The method was tested for determination of alcohol using ethanol as a model and aldehyde using hexanal as a model in complex matrix samples. Ethanol volatilized and reacted with potassium dichromate in sulfuric acid on the paper forming a green color spot. Hexanal volatilized and reacted with 2,4 dinitrophenylhydrazine reagent on the paper resulting in an intense yellow color spot. The color image was taken by a digital camera and proceeded by Image J program in RGB mode and the blue intensity was taken for quantification. For determination of alcohol, the sample was heated at 40 °C for 5 min. The method was applied for determination of alcohol content in stomahic mixtures. The linear calibration ranged from 0-7 % (v/v) of ethanol with $r^2 > 0.96$ was obtained. The recovery of 94-120% and the relative standard deviation of less than 3% were achieved. For determination of hexanal, the sample was heated at 70 °C for 10 min. The linear calibration ranged from 0-100 ppm of hexanal with $r^2 > 0.98$ was obtained. The method was applied for determination of hexanal in grille chicken breast. The recovery of 108% and the relative standard deviation of less than 2% were achieved. The method was rapid and low cost. The paper-based liner would not directly contact the samples minimizing the interference due to color or suspended particles in the matrix.

Introduction: Paper-based analytical devices (µPADs) have received a lot of attentions these days because it is simple to use, portable, environmental friendly and easy to fabricate in low cost. Generally, µPADs are fabricated from filter paper designating reaction flow path and detection zone confined by hydrophobic barrier [1]. Colorimetric method has been widely used in µPADs for detection of target analytes because it is selective, easily observed by naked eyes and simply proceeded by economical image processing software. µPADs have been employed mainly as sensor probes for screening as well as for quantitative analysis [2]. Like other analytical devices, µPADs have encountered some limitations when applied to samples with complex matrices such as dirty samples, color samples and samples containing suspended particles that may interfere color reading. For these reasons, sample preparation steps are required.

Headspace sampling/extraction has been the method of choice for determination of volatile compounds, because it is simple and relatively clean from the matrix interference. Generally, the sample is placed in the sealed vial and let it equilibrate. The analyte is taken from the headspace by either direct sampling or solid phase microextraction for further analysis by gas chromatograph. The method requires relatively expensive equipment and instrument. In this work, a low cost µPAD with colorimetric method combined with headspace sampling/extraction for simultaneous extraction and determination of volatile compounds in complex matrix samples is presented.

Methodology: Paper-based liner was made of filter paper (Whatman filter paper No. 1). A piece of filter paper was circled by a permanent marker (12 mm i.d.) making a hydrophobic barrier to contain a drop of colorimetric reagents; i.e., potassium dichromate in sulfuric acid for determination of alcohol [3] and 2,4 dinitrophenylhydrazine reagent for determination of aldehyde [4]. The paper was attached to the liner of the vial cap making a paper-based lined cap. The sample was placed in a vial sealed with the paper-based lined cap. The sample was heated. The analyte vaporized and reacted with the colorimetric reagents on the paper-based liner to form the color or change the color. The paper-based liner was taken off. The image of the paper-based liner was taken by the digital camera (the same parameter setup) under the photo booth where the light conditions had been controlled. The color image was processed in RGB mode using ImageJ program. The blue intensity was chosen for quantitative analysis of both alcohol and aldehyde. The process was schematically summarized in Figure 1. All working standard solutions were freshly prepared by diluting appropriate amounts in deionized water. Parameters affecting the sensitivity were studied and optimized. The analytical merits such as linear range, %Recovery and %RSD were reported. The methods were applied to real samples purchased from local supermarket.

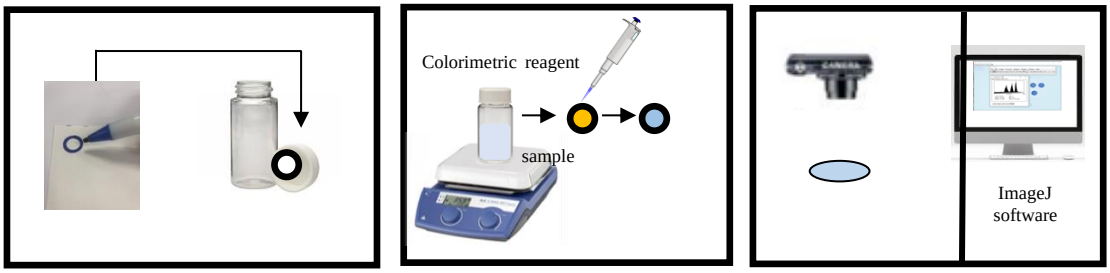

a) Paper-based cap liner b) Headspace colorimetric detection c) Color image processing

Figure 1. Schematic process of paper-based liner for headspace colorimetric determination of volatile compounds; a) fabrication of paper-based liner; b) headspace extraction and colorimetric detection; c) color image processing by ImageJ software.

Results and Discussion: The volatile compounds could be extracted from the samples to the headspace by heating and stirring. The green color was developed on the paper-based liner for alcohol detection and the intense yellow color was observed on the paper-based liner for aldehyde detection. According to the RGB values in the image processing software, the blue values were substantially changed for varied parameters so that the blue intensity was chosen for detection of both analytes. The extraction time profiles of both ethanol and hexanal were investigated at various heating temperatures. The results were shown in Figure 2. For ethanol, the blue intensity increased with increased temperature while, for hexanal, the blue intensity decreased with increased temperature. At high temperature, despite the more volatile compound being extracted, the colors on paper-based liners were affected by the moisture from the samples that may cause alteration in color reading. The effect was significant for determination of ethanol probably because ethanol was more soluble than hexanal. In addition, the extraction time profiles show that the equilibriums were observed at 5 min for ethanol and for 10 min for hexanal. For these reasons, the extraction temperature of 40 °C and 70 °C were chosen for ethanol and hexanal, respectively for further study.

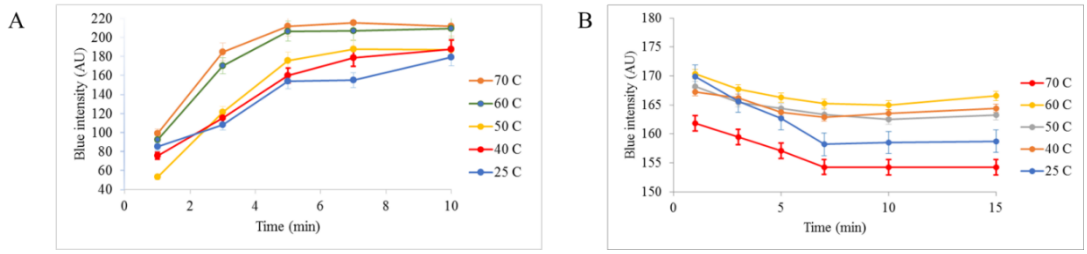

Figure 2. Extraction time profiles of a) 3% ethanol; b) 5 ppm hexanal using paper-based liner headspace colorimetric determination

For application to the real samples, calibration curves were established. The blue intensities subtracted by the blue intensity of the controlled blank (Δ blue intensity) were plotted against various concentrations of analyte. The linear calibration curves for determination of ethanol and hexanal were displayed in Figure 3. For ethanol, the linear range of 0-5% (v/v) of ethanol was achieved with coefficient of determination (r^2) greater than 0.96 (Figure 3a). For hexanal, the linear range of 0-100% (v/v) of hexanal was achieved with coefficient of determination (r^2) greater than 0.98 (Figure 3b).

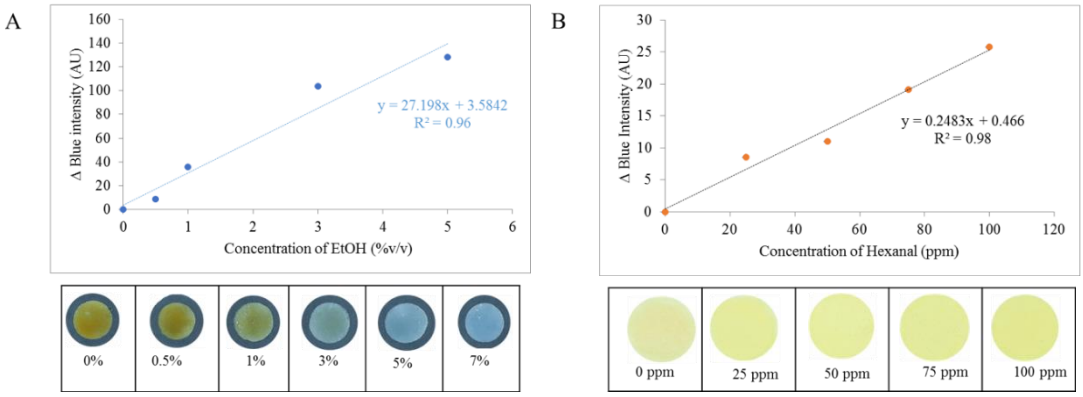

Figure 3. Linear calibration curves between Δ blue intensity at various concentrations of a) ethanol (40 C, 5 min) and b) hexanal (70 C, 10 min)

The methods were tested and evaluated for their accuracy and precision by applying to the real samples and spiked samples. For determination of ethanol, the method was applied for determination of alcohol content in stomachic mixture and salol et menthol mixture. The stomachic mixture was red-brown colored liquid while the salol et menthol mixture was white suspension. The method was directly applied to the samples without any pretreatment. The results were summarized in Table 1. The alcohol content in stomachic mixture was labeled as 6.65%. The sample was diluted with MilliQ water (1:1) prior to use. The alcohol content in stomachic mixture obtained by our method was 3.4% with relative error of 6%. The recovery of spiked sample with 0.5% ethanol was 94% with %RSD less than 2%. The alcohol content in salol et menthol mixture obtained by our method was 1.2% compared to its label of 1% giving the relative error of 20%. The recovery of spiked sample with 0.5% ethanol was 120% with %RSD less than 3%.

For determination of hexanal, because hexanal is an aroma compound, which has been known as a main characteristic meat flavor for chicken and pork[5], the method was applied for determination of hexanal in grilled chicken breast. The results were reported in

Table 2. The hexanal was found around 21 ppm in the grilled chicken breast sample. The recovery of spiked sample with 5 ppm hexanal was 108% with %RSD less than 3%.

Table 1. Method performance in determination of ethanol

Sample	Blue intensity (N=3)	SD	RSD	%EtOH	%Recovery
Stomachic mixture	147.40	2.6	1.8	3.4	
Stomachic mixture + spiked 0.5% EtOH	160.11	0.9	0.5	3.8	94%
Salol et Menthol Mixture	87.63	2.9	3.3	1.2	
Salol et Menthol Mixture + spiked 0.5% EtOH	104.41	0.6	0.6	1.8	120%

Table 2 Method performance in determination of hexanal

Sample	Blue intensity (N=3)	SD	RSD	Hexanal (ppm)	% Recovery
Grilled chicken breast	5.69	2.6	2.8	21	
Grilled chicken breast + spiked 5ppm	7.45	0.8	1.7	28	108

Conclusion: A simple method using paper-based lined cap combined with headspace technique was presented for determination of volatile compounds. The design demonstrated the advantage for direct determination of ethanol and hexanal from such complex matrix samples such as suspended drugs, colored samples and food samples without any pretreatment.

References:

1. Ratnarathorn N, Chailapakul O, Henry CS et al. Talanta. 2012;99:552-7.
2. Kaneta T, Alahmad W, Varanusupakul P. Applied Spectroscopy Reviews. 2009;137:215–221.
3. Phansi P, Sumantakul S, Wongpakdee T et al. Anal Chem. 2016;88:8749-8756.
4. van Leeuwen SM, Hendriksen L, Karst U. J Chromatogr A. 2004;1058:107-112.
5. Goodridge CF, Beaudry RM, Pestka JJ et al. J Agric Food Chem. 2003;51:7533-7539.

SESSION C2:
INORGANIC CHEMISTRY

C2_001_PF: SYNTHESIS AND CHARACTERIZATION OF A FLUORESCENT CHEMOSENSOR BASED ON ANTHRAQUINONE DERIVATIVE FOR METAL IONS DETECTION

Chawanakorn Kongsak[1,2], Praput Thavornyutikarn[1,*]
[1]Department of Chemistry, Faculty of Science, Chiang Mai University, Chiang Mai 50200, Thailand
[2]Graduate School, Chiang Mai University, 239 Huay Kaew Road, Muang, Chiang Mai 50200, Thailand
*e-mail: praput.th@cmu.ac.th

Abstract: To improve the sensing performance toward metal ions in trace amount, a fluorescent sensor (compound 1) based-on anthraquinone derivative was developed and synthesized combining unique tridentate dipicolylamine (DPA) units as receptor moieties with the overall yields of 47%. The designed sensor 1 showed the absorption maxima in range of 260-430 nm with relatively high molar absorptivities. The emission peak of sensor 1 was observed at *ca.* 511 nm and its Stokes shift was calculated as 79 nm. Moreover, The preliminary optical studies of chemosensor 1 revealed the significant enhancement of fluorescence intensity in the presence of Zn(II) and Cd(II) ions compared to pure chemosensor.

Introduction: Metal ions play important roles regarding several biological functions in living organisms.[1] They can be classified into two groups: (i) alkali and alkaline earth metal ions such as Na(I), K(I), Ca(II), Mg(II), and (ii) transition metal ions, for example, Fe(II), Zn(II), Cu(II), Mn(II), Cd(II). Among these transition metal ions, Cu(II) is important for human bodies by acting as parts of many enzymes and many organ systems.[2] Zn(II) actively involves in many enzymes and is an essential part of both DNA and RNA metabolisms.[3] Nevertheless, other transition metal ions also have received significant attention due to their severe effects to environments and related health issues to human and biotic lives.[4-5] For example, lead, cadmium and mercury ions are highly toxic and possess no useful role in the living organisms. Unfortunately, many transition metal ions are typically presented in the environment in very low quantities called "trace amount", so the efficient detection techniques for these chemical species are in urgent needs. Typical conventional methods employ for the detection of heavy metal ions including cold vapor atomic absorption spectrometry, atomic absorption spectroscopy (AAS), electrochemistry (cyclic voltammetry (CV) and square wave voltammetry (SWV)), and photoelectrochemical techniques.[6-9] However, these methods are relatively expensive, tedious, unwieldy, and complicated in terms of instrumentation and sample preparation.[10] To overcome these obstacles, fluorescent chemosensors have become the better choices due to their high sensitivity and selectivity with possibly low detection limits toward metal ions.[11] Interestingly, anthraquinone derivatives could provide promising optical properties depending on the type and position of substituent groups. Combining with unique tridentate ligand, 1-(2-pyridinyl)-*N*-(2-pyridinylmethyl)methanamine or dipicolylamine (DPA) and amide linkers could further improve the metal sensing abilities of such chemosensors. In this study, an anthraquinone-derivatized chemosensor with DPA moieties at 1,8-positions was synthesized and characterized as showed in Figure 1. The optical properties and the preliminary complexation studies of a novel chemosensor was also performed and discussed.

Methodology:
Material: All chemicals were of analytical grade, purchased from Aldrich, Acros, Carlo Erba, TCI, and RCI Labscan and used as acquired. Methanol was dried over Na, distilled, and stored over molecular sieve 3 Å before use. Dimethylformamide (DMF) was also dried over CaH_2 and distilled prior to use under reduced pressure. All reactions were carried out under inert nitrogen atmosphere to avoid moisture and oxygen. Analytical thin-layer chromatography (TLC) separations were performed on Merck silica gel 60 on F_{254} aluminum plates and the

visualization was performed under a 254 nm ultraviolet lamp. ^{1}H and ^{13}C-NMR spectra were recorded on a Bruker Avance 400 MHz spectrometer and the chemical shifts were reported as δ values in the unit of part per million (ppm). All NMR spectra were measured in DMSO-d_6 and the chemical shifts were related to the solvent residue peaks as internal references (^{1}H: δ 2.50, ^{13}C: δ 39.5 for DMSO-d_6). The coupling constant (J values) were given in Hertz (Hz) and NMR spin multiplicities were represented as s (singlet), d (doublet), t (triplet), m (multiplet), dd (doublet of doublet), td (triplet of doublet), br. (broad). MALDI-TOF mass spectra were obtained from a Bruker Daltonics Microflex™ spectrometer using dithranol and/or α-cyano-4-hydroxycinnamic acid as matrices. UV-Vis spectra were recorded on a UV-1800 Shimadzu UV-Vis spectrophotometer (250-700 nm). Fluorescence spectra were recorded on a RF-5301PC Shimadzu spectrofluorophotometer (400-800 nm). Both optical techniques were performed using standard 10 nm size fluorimeter quartz cuvettes. Solutions of sensor 1 and particular metal perchlorates was prepared using UV-IR grade solvents.

Synthetic Methods:

1,8-Diaminoanthraquinone (3). This compound was synthesized *via* a literature procedure with slight modification.[12] 1,8-Dinitroanthraquinone (2, 4.4865 g, 15.04 mmol) was dissolved in anhydrous EtOH then mixed with the solution of $Na_2S{\cdot}9H_2O$ (14.4633 g, 60.22 mmol) in 250 mL of DI water at room temperature. The resulting solution was then refluxed for 6 hour. After that, the reaction solution was cooled and then poured into an ice/water (150 mL). The precipitate was collected by vacuum filtration and then recrystallized from EtOH to obtain a red-purple solid (3, 3.4178 g, 95%). ^{1}H-NMR (400 MHz, DMSO-d_6) δ 7.85 (br. s, 4H, -NH_2), 7.45 (dd, J = 8.29, 7.35 Hz, 2H), 7.35 (dd, J = 7.35, 1.16 Hz, 2H), 7.15 (dd, J = 8.29, 1.16 Hz, 2H). ^{13}C-NMR (100 MHz, DMSO-d_6) δ 187.8, 183.4, 151.5, 133.7, 133.5, 123.5, 114.9, 113.1. MALDI-TOF calculated for $C_{14}H_{12}N_2$ = 238.07, found = 238.15.

N,N'-(9,10-dioxo-9,10-dihydroanthracene-1,8-diyl)bis(2-chloroacetamide) (5). This compound was prepared by dissolving 1,8-dianinoanthraquinone (3, 4.0000 g, 16.85 mmol) in dry dimethylformamide (DMF) (170 mL) then subsequently cooled in an ice bath. 2-Chloroacetyl chloride (4, 5.7091 g, 4.026 mL, 50.55 mmol) in dry DMF (20 mL) was added into the reactant solution and continuously stirred for 24 hour. After that, a solution of diisopropylethylamine (DIPEA, 2.1777 g, 3.0 mL, 16.85 mmol) in dry DMF (20 mL) was added into the reaction mixture and the solution was further stirred for an hour at room temperature. The resulting solution was poured into an ice/water mixture (200 mL). The precipitate was collected by filtration and recrystallization from EtOH to afford yellow power (5, 6.0912 g, 92%). ^{1}H-NMR (400 MHz, DMSO-d_6) δ 12.62 (s, 2H, -NH amide), 9.01-8.99 (m, 2H), 8.08-7.93 (m, 4H), 4.58 (s, 4H). There were no satisfied details regarding its ^{13}C-NMR due to the low solubility of 5 in DMSO-d_6.

1-(2-Pyridinyl)-N-(2-pyridinylmethyl)methanamine (DPA, 9). This compound was prepared *via* two-step synthesis, modified from literature work.[13] First step: a mixture of 2-pyridinecarboxaldehyde (6) (22.5200 g, 20.00 mL, 210.25 mmol) and 2-(aminomethyl)-pyridine (7) (22.0290 g, 21.00 mL, 203.71 mmol) were dissolved in 150 mL of dry methanol at 0 °C and stirred for 3 hour to give imine product (8) without any further separation. Second step: sodium borohydride ($NaBH_4$) (8.0107 g, 0.2118 mol) was added in small portions to the solution mixture previously mentioned and stirred at room temperature for 24 hour. Then conc. HCl was added dropwise into the resulting solution to adjust the pH of solution to about 4. During this process, NaCl was precipitated from the solution. The mixture was filtered and washed thoroughly with DI water and methanol. The combined filtrate was evaporated to dryness under reduced pressure and re-dissolved in DI water. Furthermore, NaOH was slowly added into the solution until the pH of solution became basic, then extracted with dichloromethane, and the combined organic layers was dried with anhydrous $MgSO_4$. After all volatile organic solvents were removed *in vacuo*, yellow oil of 9 was obtained (30.1015 g, 75%). ^{1}H-NMR (400 MHz, DMSO-d_6) δ 8.50 (d, J = 5.02 Hz, 2H), 7.72 (td, J = 7.71, 1.78 Hz, 2H), 7.45 (d, J = 7.71 Hz, 2H),

7.21 (dd, *J* = 5.02, 1.78 Hz, 2H), 3.85 (s, 4H). ^{13}C-NMR (100 MHz, DMSO-d_6) δ 160.0, 148.7, 136.3, 121.8, 121.7, 54.0.

N,N'-(9,10-dioxo-9,10-dihydroanthracene-1,8-diyl)(2-(bis(pyridin-2-ylmethyl) amino)acetamide) (1). A mixture of 5 (2.1272 g, 5.454 mmol) and potassium iodide (KI, 0.8759 g, 5.276, 5.28 mmol) were dissolved in 70 mL of dry DMF. Then, solution of DPA (9, 2.7675 g, 2.50 mL, 13.89 mmol) in 30 mL of dry DMF was added into the reaction flask and heated to 70 °C with constant stirring for 48 hour. After that, DIPEA (1.7808 g, 2.40 mL, 13.77 mmol) was added in the reaction mixture and the reaction vessel was subsequently cooled to room temperature. The mixture was poured into an ice/water (150 mL) to formed yellow precipitate. The crude product was then filtered and recrystallized from acetone to afford compound 1 as an orange-yellow solid (2.8069 g, 72%). ^{1}H-NMR (400 MHz, DMSO-d_6) δ12.32 (s, 2H, -NH amide), 8.94 (dd, *J* = 8.25, 1.29 Hz, 2H), 8.40 (d, *J* = 4.87 Hz, 4H), 7.94 (dd, *J* = 7.78, 1.29 Hz, 2H), 7.87 (t, *J* = 8.25, 7.78 Hz, 2H), 7.64 (td, *J* = 7.69, 1.77 Hz, 4H), 7.50 (d, *J* = 7.69 Hz, 4H), 7.15 (dd, *J* = 7.35, 4.87 Hz, 4H), 3.88 (s, 8H), 3.43 (s, 4H). ^{13}C-NMR (100 MHz, DMSO-d_6) δ 189.2, 182.2, 170.5, 157.8, 148.8, 140.4, 136.4, 135.3, 133.1, 126.0, 123.1, 122.3, 121.6, 119.4, 59.9, 58.4.

Preliminary studies of metal ions selectivity by spectrophotometric techniques: Solution of compound 1 was prepared in chloroform at 5.00×10^{-5} M while the metal solutions were prepared by dissolving in acetonitrile. Various divalent metal salts such as $Zn(ClO_4)_2{\cdot}6H_2O$, $Cu(ClO_4)_2{\cdot}6H_2O$, $Ni(ClO_4)_2{\cdot}6H_2O$, $Co(ClO_4)_2{\cdot}6H_2O$, $Fe(ClO_4)_2{\cdot}6H_2O$, $Mn(ClO_4)_2{\cdot}6H_2O$, and $Cd(ClO_4)_2{\cdot}xH_2O$ were chosen to use in the preliminary studies. All metal ion solutions were prepared as 5 mole equivalents comparing to the solution of 1.

Results and Discussion:

Synthetic part: The complete synthetic pathways of compounds 1 is summarized in Figure 1. To synthesize compound 1, 1,8-diaminoanthraquinone (2) was reduced *via* Zinin reaction using sodium sulfide ($Na_2S{\cdot}9H_2O$) to give 1,8-diaminoanthraquinone (3) in high yield of 95%. After that, compound 5 was successfully obtained in 92% yield by acylation of compound 3 with 2-chloroacetyl chloride (4) in the presence of DIPEA as a base. Subsequently, compound 5 was reacted with 1-(2-pyridinyl)-*N*-(2-pyridinylmethyl)methanamine or DPA (9) *via* S_N2 reaction to finally give sensor 1 in 72% yield. In addition, DPA which is a part of receptor moieties, was synthesized by the condensation reaction between 2-pyridinecarboxaldehyde (6) and 2-(aminomethyl)pyridine (7) which initially formed an imine intermediate (8), then the addition of sodium borohydride ($NaBH_4$) fully afforded compound 9 in 75% yield.

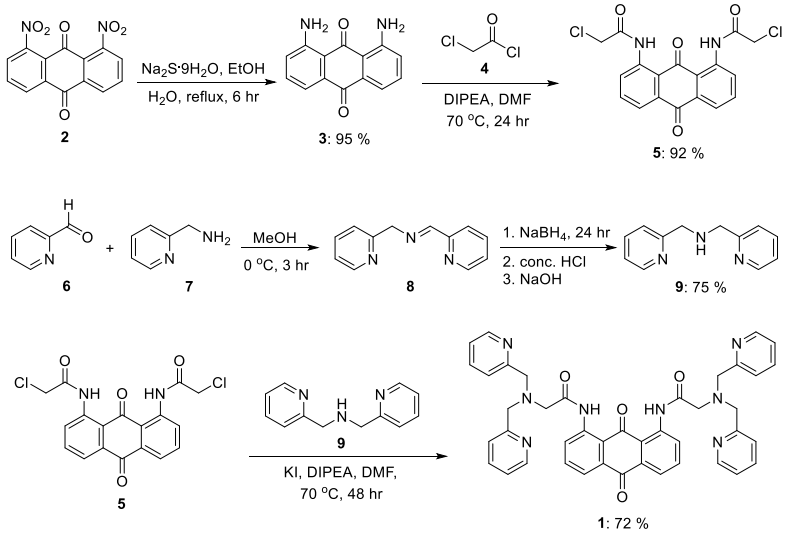

Figure 1. Synthetic route of compound 1.

Photophysical properties: The photophysical properties of compound 1 in chloroform (5.00×10^{-5} M) was recorded and investigated using both UV-Visible and fluorescence spectrophotometric techniques. The optical data are showed and summarized in Table 1 and Figure 1. From absorption spectra, compound 1 exhibited only two absorption bands at 268 nm which had very high molar absorptivity and 426 nm. Furthermore, compound 1 was excited at 400 nm and exhibited approximate fluorescence emission band at 511 nm. These results can be used for calculation of Stokes shifts which is about 79 nm for compound 1.

Table 1. Photophysical properties of chemosensor 1 in chloroform.

Sensor	Absorption		Emission	
	λ_{max} (nm)	ε ($M^{-1}cm^{-1}$)[a]	λ_{max} (nm)	Stokes shift
1	268	77106	-	-
	426	20000	511	79

[a]Molar absorptivity (ε) were calculated from Beer-Lambert Law (A = εlc; A: absorbance at maxima absorption band, l: the length of cuvette which was 1 cm, c: concentration of sensor 1 solution which was both 5.00×10^{-5} M)

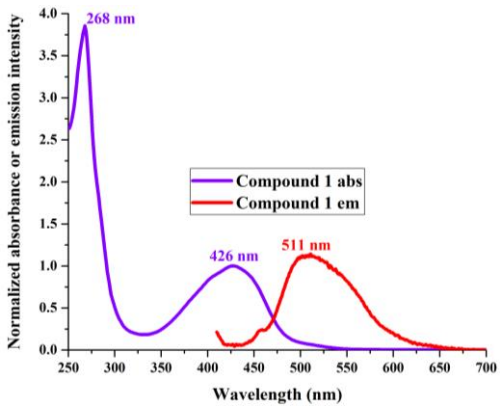

Figure 1. Normalized absorption and emission spectra of sensor 1 in chloroform (5.00×10^{-5} M for UV-visible and fluorescence spectrophotometric studies).

Preliminary studies of metal ions selectivity by spectrophotometric techniques: For UV-visible spectroscopic studies in Figure 2 (left), 5 mole equivalents of various transition metal ions at 10 µL were individually added to solution of 1 (2.5 mL) in quartz cuvettes. Addition of all divalent metal ions results in little blue shift of the absorption band at 432 nm and slightly decreased the absorbance of this peak as showed in partial UV-Vis spectrum in Figure 2 (right). These results were possibly stemmed from the increasing energy gap between non-bonding and π* orbitals of an anthraquinone core upon the complexation with metal ions. Nevertheless, there is no significant spectral change from the UV-Vis results so this spectroscopic technique could not be used for further metal selectivity studies between compound 1 and transition metal ions.

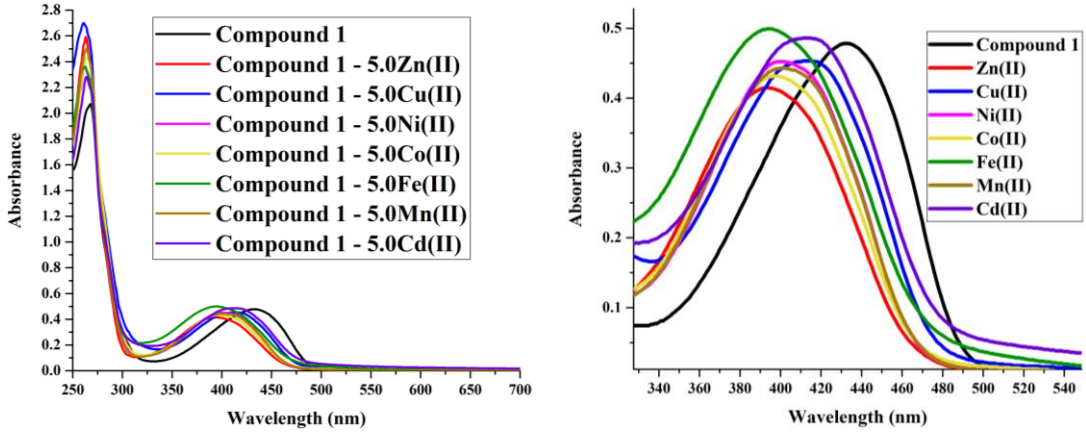

Figure 2. UV-Vis spectra of compound 1 with various divalent metal ions at 5 mole equivalents (left) and partial UV-Vis spectra in range of 330-550 nm (right).

For fluorescence investigation, the free compound 1 displayed relatively weak fluorescence emission intensity at 511 nm with excitation at 400 nm. This compound could possibly undergo photoinduced electron transfer (PET) phenomenon between an anthraquinone core linked with DPA moieties. Upon the addition of divalent metal ions into the solution of 1, the results could be classified as two groups. First, the fluorescence quenching metal ions, for instance, Cu(II), Ni(II), Co(II) and Fe(II) ions, reduced the intensity of 1 and only Cu(II) caused hypsochromic shift. Another group was the emission enhancing metal ions such as Zn(II), Mn(II), and Cd(II) ions which enhance the fluorescence intensity of compound 1 as showed in Figure 3 (left). The emission wavelength of sensor 1 was slightly moved to longer wavelength (520 nm) in the presence of Zn(II) whereas the addition of Cd(II) caused slight hypochromic shift (509 nm). To significantly illustrate the results of metal ions, the fluorescence intensity were all compared and calculated to normalized fluorescence intensity bar graph which calculated from $F-F_0/F_0$ formula (F: intensity of addition metal ions at 520 nm and F_0: intensity of pure sensor 1 at 520 nm) in Figure 3 (right). Only Zn(II) and Cd(II) ions significantly enhanced the fluorescence intensity of 1 for 16 and 22 times, respectively. This results suggested that the compound 1 has relatively high sensitivity toward Zn(II) and Cd(II) ions which possibly affected by the presence of full-filled electron configuration of both ions.

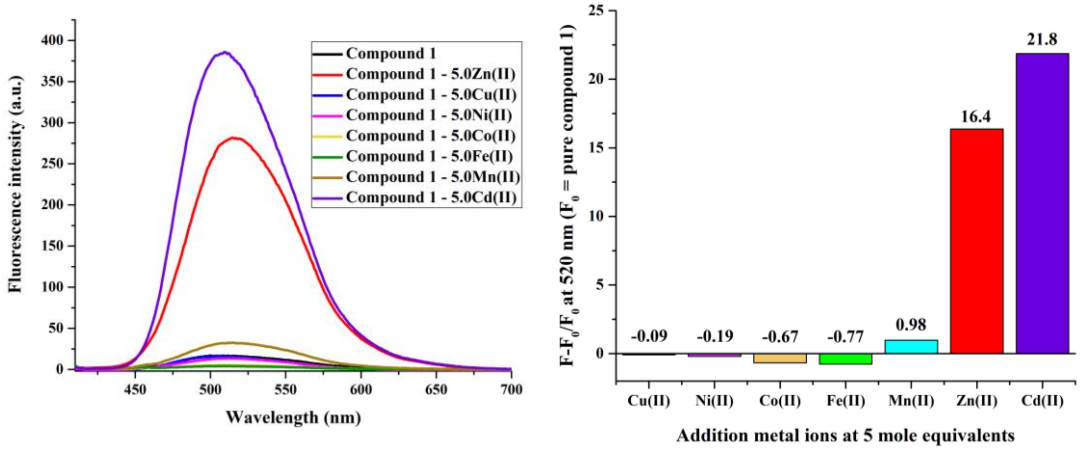

Figure 3. Fluorescence spectra of compound 1 with various divalent metal ions at 5 mole equivalents (left) and normalized bar graph (right).

Conclusion: An anthraquinone-based fluorescent chemosensor 1 containing DPA-amide linkage was successfully synthesized in overall moderate yields (47 %). The photophysical results revealed the potential application of chemosensor 1 for the detection of Zn(II) and Cd(II) due to the large enhancements of its fluorescence intensity at 520 nm. Other transition metal ions have no significant influence in terms of their fluorescence emission intensity compared to that of the free form of sensor 1.

References:

1. McRae R, Bagchi P, Sumalekshmy S, Fahrni J. Chem. Rev. 2009;109:4780-4827.
2. Kim BE, Nevitt T, Thiele DJ. Nat. Chem. Biol. 2008;4:176-185.
3. Que EL, Domaille DW, Chang CJ. Chem. Rev. 2008;108:1517-1549.
4. Campbell L, Dixon DG, Hecky RE. J. Toxicol. Environ. Health, Part B. 2003;6:325-356.
5. Kim HN, Ren WX, Kim JS, Yoon J. Chem. Soc. Rev. 2012;41:3210-3244.
6. Konieczka P, Misztal-Szkudlińska M, Namieśnik J, Szefer P. Pol. J. Environ. Stud. 2010;19:931-936.
7. Álvarez MS, Gutiérrez E, Rodríguez A, Sanromán MÁ, Deive FJ. Ind. Eng. Chem. Res. 2014;53:8615-8620.
8. Li X, Yu P, Yang L, Wang F, Mao L. Anal. Chem. 2012;84:9416-9421.
9. Dutta M, Das D. Trends Anal. Chem. 2012;32:113-132.
10. Huy GD, Zhang M, Zuo P, Ye BC. Analyst. 2011;136:3289-3294.
11. Quang DT, Kim JS. Chem. Rev. 2010;110:6280-6301.
12. Porter HK. The Zinin Reduction of Nitroarenes. In Organic Reactions, (Ed.). John Wiley and Sons, Inc. 2011.
13. Wong YL, Mak CY, Kwan HS, Lee HK. Inorganica Chim. Acta. 2010;363: 1246-1253.

Acknowledgements: This study is financially supported by the Thailand Research Fund (TRF) grant (Grant No. MRG5980191) and the Nation Research Council of Thailand (NRCT) *via* Chiang Mai University (Grant No. 347978) The authors would like to thank the Department of Chemistry, Faculty of Science, Chiang Mai University and Center of Excellence for Innovation in Chemistry (PERCH-CIC) for the access of laboratory instruments and facilities. CK is a recipient of the Science Achievement Scholarship of Thailand (SAST) and would like to thank for the SAST for his financial supports and Graduate School, Chiang Mai University.

C2_005_PF: SYNTHESIS OF TiO_2-SiO_2 COMPOSITE AND ITS APPLICATION AS A PHOTOCATALYST FOR OXIDATIVE DESULFURIZATION

Tu Thi Phuong Nguyen[1], Pawnprapa Pitakjakpipop[2], Wipark Anutrasakda[1,*]
[1]Department of Chemistry, Faculty of Science, Chulalongkorn University, Bangkok 10330, Thailand
[2]National Metal and Materials Technology Center (MTEC), 114 Thailand Science Park, Pathumthani, Thailand
*e-mail: wipark.a@chula.ac.th

Abstract: TiO_2-SiO_2 was synthesized by a facile sol-gel method. XRD, N_2 adsorption-desorption, SEM and UV-Vis DRS were used to characterize the photocatalyst. The photocatalytic properties of TiO_2-SiO_2 composite was studied by oxidative desulfurization process using dibenzothiophene (DBT) in dodecane as a model oil. The XRD analysis identified that TiO_2-SiO_2 has anatase phase with low crystallinity. Since TiO_2-SiO_2 has higher surface area, its photocatalytic activity was better than commercial TiO_2 (P25). Under UV irradiation, the DBT conversion over TiO_2-SiO_2 photocatalyst could reach 63% within 3 hours.

Introduction: The demand for transportation fuel has been increasing in most countries for the past three decades, especially for diesel fuel. Hence, the sulfur content in diesel fuel is an environmental concern because of the release of SO_x during combustion, which is associated with various ecological damages and health problems[1, 2]. Many strict rules and regulations have been implemented worldwide to limit the sulfur content of fuel to very low level[3]. Therefore, deep desulfurization technologies have been a promissing solution to meet the demand of very stringent environmental regulations. Along with conventional hydrodesulfurization, many alternative desulfurization technologies for removing sulfur in diesel have been investigated such as adsorptive desulfurization (ADS)[4, 5], oxidative desulfurization (ODS)[6, 7] and extractive desulfurization (EDS)[8, 9]. Among them, photocatalytic oxidative desulfurization is one of the most convenient methods in deep sulfurization of fuels due to its low cost and mild conditions[10, 11].

The use of TiO_2 in catalytic applications has been extensively examined because this material possesses many advantages including low cost, high photo-stability, non-toxicity and feasibility for large scale production [12, 13]. Several studies claimed that the deposition of TiO_2 on the surface of mesoporous silica (SiO_2) is a promising method for creating active catalyst with anatase nanocrystallites dispersed on the high surface area of SiO_2. In addition, the presence of SiO_2 has been shown to hinder the phase transition of TiO_2 from anatase to rutile, which is preferable for photocatalytic properties[14-16]. However, most studies of TiO_2-SiO_2 photocatalyst focused on the degradation of organic pollutants. There are only few studies in relation to desulfurization[17].

In this study, TiO_2-SiO_2 was synthesized via sol-gel method. The obtained material was used as a photocatalyst in a green ODS process where dibenzothiophene (DBT) was used as a model refractory sulfur-containing compound in diesel.

Methodology:

Material preparation: Briefly, 4 g titanium (IV) butoxide was dissolved in a mixture of 40 mL of absolute ethanol and 5 mL of isopropanol and magnetically stirred for 30 min to obtain a homogeneous and transparent solution. Then, the solution was slowly dropped into a mixture of SiO_2 in deionized water to form a white precipitate with the TiO_2/SiO_2 weight ratio of 1/1. The excess water was evaporated at 90°C until the mixture became slurry. The obtained gel was then dried at 110°C overnight and calcined at 450°C for 2 h.

Characterization: The crystalline phase of the materials was examined by X-Ray diffraction (XRD) using Rigaku with Cu Kα radiation source worked at 40 kV and 30 mA. The surface

properties of photocatalysts were identified by N_2 adsorption-desorption using BEL Japan BELSORP-mini 28SP instrument. The morphologies of samples were observed by a scanning electron microscope (SEM-Jeol-JSM-IT100). Absorption edge and the band gap of the photocatalysts were determined by Ultraviolet-visible diffuse reflectance spectroscopy (UV-Vis DRS) using UV-3600 Plus.

Photocatalytic oxidative desulfurization: A 50 ppm of dibenzothiophene (DBT) in dodecane was used as the model oil. Briefly, 100 mg of the photocatalyst was added into a bottle containing 5 mL model oil with the light source (UV light) located beside the bottle. After that, the suspension was kept in the dark for 30 min to attain adsorption-desorption equilibration of pollutant on the catalyst. Then, the light was switched on. The treated fuel was taken out after 3h and filtered through a 0.22 µm membrane filter. The initial and final concentrations of DBT were measured using GC-FID. The photocatalytic activity was evaluated based on sulfur removal (%), which was calculated using the following equation:

$$\text{Sulfur removal (\%)} = [(C_i - C_f)/C_i] \times 100\%$$

Where C_i, C_f are initial and final concentrations (ppm) of sulfur in fuel before and after irradiation, respectively.

Results and discussion:

Characterization of the photocatalysts:

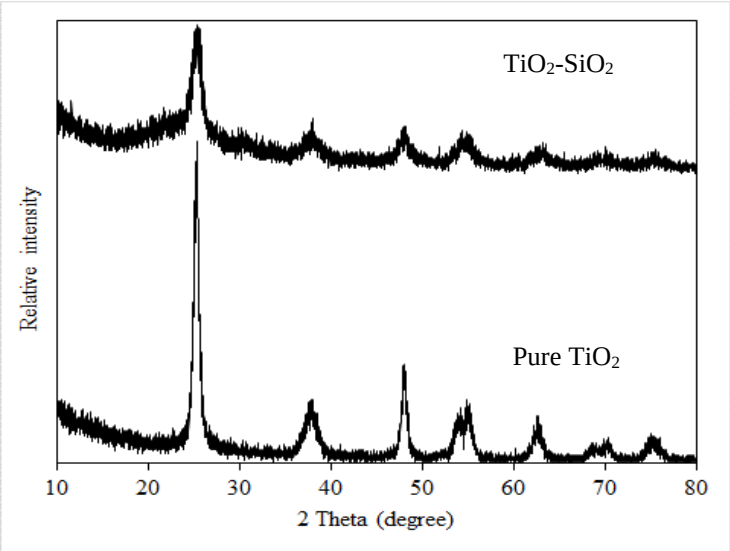

Figure 1. XRD patterns of pure TiO_2 and TiO_2-SiO_2

XRD patterns of pure TiO_2 and TiO_2-SiO_2 composite are shown in Figure 1. The results demonstrates that pure TiO_2 has strong diffraction peak at 2θ = 25.3°, 37.9°, 48.0°, 54.0°, 55.1°, 62.7°, 68.9 and 75.2°, corresponding to (101), (004), (200), (105), (211), (204), (116) and (215) planes of anatase TiO_2, respectively (JCPDS-NO. 01-075-2547). For the TiO_2-SiO_2 composite, all diffraction peaks were assigned to anatase phase. However, the intensities of these peaks were significantly decreased due to the addition of a large amount of SiO_2 into TiO_2 matrix, consequently inhibiting the growth of crystallite anatase.

Table1. Textural properties of TiO_2, SiO_2 and TiO_2-SiO_2

Sample	S_{BET} (m^2/g)	V_{tot} (cm^3/g)	D (nm)
Commercial TiO_2	46.3	0.13	11.54
SiO_2	417.2	0.60	5.71
TiO_2-SiO_2	243.7	0.40	6.64

(S_{BET} = specific surface area, V_{tot} = pore volume, D = pore diameter)

The specific surface area of TiO_2 can be enhanced significantly by using SiO_2 as a support. As shown in Table 1, the surface area of TiO_2-SiO_2 (243.7 m^2/g) was significantly higher than that of pure TiO_2 (P25) (46.3 m^2/g) since the inhibition of the individual crystallization during preparation, which was consistent with the result of XRD analysis. In addition, the high porosity of TiO_2-SiO_2 (0.4 cm^3/g) facilitate the mass transfer of reactants and reaction intermediates, hence the photocatalytic activity is expected to be improved[18].

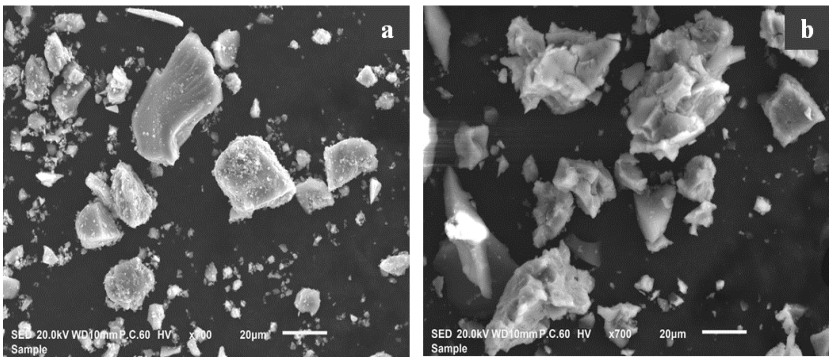

Figure 2. SEM images of TiO_2 (a) and TiO_2-SiO_2 (b)

Figure. 2 shows the SEM images of TiO_2 and TiO_2-SiO_2. It can be seen that the TiO_2 contained different sizes of particles. Smaller TiO_2 particles had strong tendency to agglomerate on the surface of the bigger ones. In case of TiO_2-SiO_2, it had rougher surface, leading to a larger surface area than TiO_2. From Figure 3, the EDX results show that TiO_2-SiO_2 was composed of Ti, Si and O with Ti dispersed on Si and O, indicating that TiO_2-SiO_2 was successfully synthesized. The EDX analysis also confirms that the weight ratio of SiO_2 to TiO_2 is about 0.9:1, which agrees with the theoretical value.

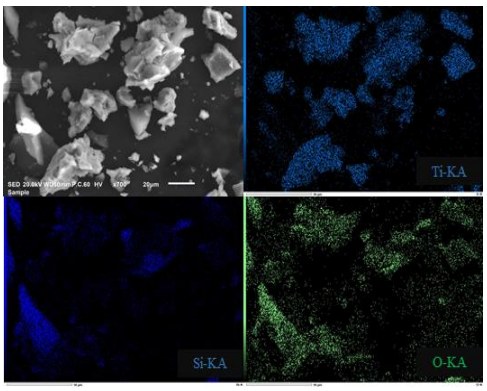

Figure 3. EDX mapping analysis of TiO_2-SiO_2

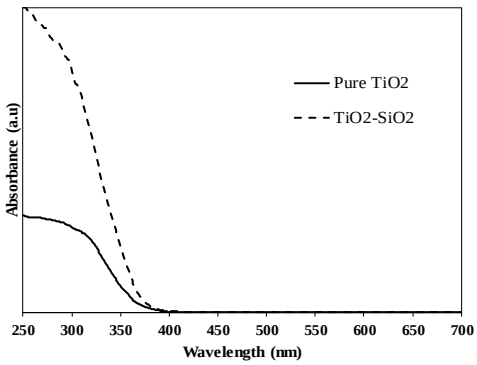

Figure 4. UV-Vis diffuse reflectance spectra of pure TiO_2 and TiO_2-SiO_2

UV-Vis spectroscopy was used to investigate the optical properties of the prepared catalyst (Figure 4). The results show that the absorption spectra of pure TiO_2 and TiO_2-SiO_2 had strong absorption peaks in the UV region. According to the Tauc plot equation, the band gaps of pure TiO_2 and TiO_2-SiO_2 were 3.14 and 3.17 eV, respectively.

Photocatalytic property: The desulfurization performance of the pure TiO_2 and pure SiO_2 were compared with that of the TiO_2-SiO_2 composite (Figure 5). Under UV light irradiation, TiO_2 produced electrons in conduction band and holes in valence band. These photogenerated species could form $^{\bullet}OH$ or $^{\bullet}O_2^-$ radical, which have strong oxidizing properties, leading to the oxidization of DBT to $DBTO_2$. The experimental results show that TiO_2-SiO_2 exhibited higher performance than SiO_2 and TiO_2 for sulfur removal. Interestingly, the photocatalytic activity of TiO_2-SiO_2 was 2.7 times greater than that of TiO_2, even though there was only 50 wt.% of TiO_2 active sites in the TiO_2-SiO_2 composite.

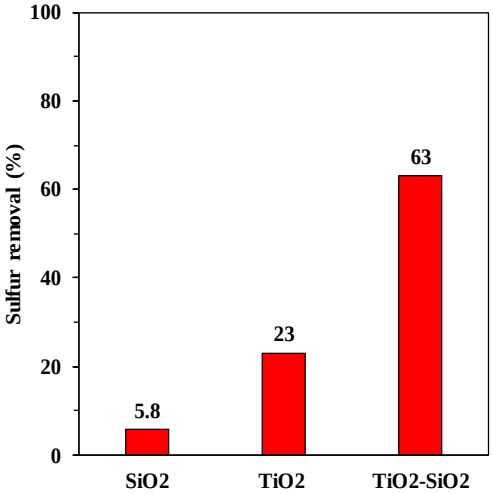

Figure 5. Desulfurization of SiO_2, TiO_2 and TiO_2-SiO_2 under catalytic conditions: 100 mg of photocatalyst, 50 ppm of DBT in 5 mL dodecane, UV ligand (□ = 365 nm) after 3 hours of UV light irradiation in ODS system

Conclusion: The TiO_2-SiO_2 composite was successfully synthesized by simple sol-gel method. The prepared composite had low crystallinity and a high surface area of 243.7 m^2/g. It also exhibited greater performance for removing sulfur compound in model oil under UV irradiation than commercial TiO_2. The addition of SiO_2 into TiO_2 could enhance the surface area of TiO_2 and hence improve the photocatalytic activity in ODS system.

References

1. Song, C.; Ma, X. Appl. Catal. B: Environ. 2003; 41 (1), 207-238.
2. Roy, P.; Sardar, A. J. Eng. Process. Tech. 2015; 6 (2), 1-7.
3. Guo, W.; Wang, C.; Lin, P.; Lu, X. Appl. Energy. 2011; 88 (1), 175-179.
4. Dehghan, R.; Anbia, M. Fuel Process. Technol. 2017; 167, 99-116
5. Xiong, J.; Luo, J.; Yang, L.; Pang, J.; Zhu, W.; Li, H. J. Ind. Eng. Chem. 2018; 64, 383-389.
6. Lorençon, E.; Alves, D. C. B.; Krambrock, K.; Ávila, E. S.; Resende, R. R.; Ferlauto, A. S.; Lago, R. M. Fuel. 2014; 132, 53-61.
7. Abdul-Kadhim, W.; Deraman, M. A.; Abdullah, S. B.; Tajuddin, S. N.; Yusoff, M. M.; Taufiq-Yap, Y. H.; Rahim, M. H. A. J. Environ. Chem. Eng. 2017; 5 (2), 1645-1656.

8. Li, F.-t.; Kou, C.-g.; Sun, Z.-m.; Hao, Y.-j.; Liu, R.-h.; Zhao, D.-s. J. Hazard. Mater. 2012; 205-206, 164-170.
9. Jha, D.; Haider, M. B.; Kumar, R.; Balathanigaimani, M. S. Chem. Eng. Res. Des. 2016; 111, 218-222.
10. Zhou, X.; Li, J.; Wang, X.; Jin, K.; Ma, W. Fuel Process. Technol. 2009; 90 (2), 317-323.
11. Zarrabi, M.; Entezari, M. H.; Goharshadi, E. K.. RSC Adv. 2015; 5 (44), 34652-34662.
12. Hoffmann, M. R.; Martin, S. T.; Choi, W.; Bahnemann, D. W. Chem. Rev. 1995; 95 (1), 69-96.
13. Lu, S.-y.; Wu, D.; Wang, Q.-l.; Yan, J.; Buekens, A. G.; Cen, K.-f. Chemosphere. 2011; 82 (9), 1215-1224.
14. Reidy, D. J.; Holmes, J. D.; Morris, M. A. Ceram. Int. 2006; 32 (3), 235-239.
15. Perathoner, S.; Lanzafame, P.; Passalacqua, R.; Centi, G.; Schlögl, R.; Su, D. S. Microporous Mesoporous Mater. 2006; 90 (1), 347-361.
16. Besançon, M.; Michelin, L.; Josien, L.; Vidal, L.; Assaker, K.; Bonne, M.; Lebeau, B.; Blin, J.-L., New J. Chem. 2016; 40 (5), 4386-4397.
17. Xu, M.; Yang, L.; Li, J. China Petroleum Process. Petrochemical Tech. 2017, 19, 59-67.
18. Mahyar, A.; Behnajady, M.; Modirshahla, N. Indian J. Chem. 2010, 49, 1593-1600.

Acknowledgements: The "Scholarship Program for Asean Countries", Chulalongkorn University is gratefully acknowledged.

C2_006_PF: CYTOTOXICITY OF GOLD(III) PORPHYRIN COMPLEXES AND THEIR DERIVATIVE ON MCF7 CELL LINES

Tossapon Phromsatit[1], Premjit Arpornmaeklong[2], Yuki Shirosaki[3], Thapong Teerawatananond[4], Supakorn Boonyuen[1,*]

[1]Department of Chemistry, Faculty of Science and Technology, Thammasat University, Pathumthani 12120, Thailand

[2]Faculty of Dentistry, Thammasat University, Pathumthani 12120, Thailand

[3]Department of Materials Science, Faculty of Engineering, Kyushu Institute of Technology, Kitakyushu, Japan

[4]Department of Chemistry, Faculty of Science and Technology, Valaya Alongkorn Rajabhat University, Pathumthani 12120, Thailand

*e-mail: chemistrytu@gmail.com

Abstract: A new series of gold porphyrin complexes containing different meso-substituent groups (phenyl, methoxyphenyl, butyloxyphenyl, octyloxyphenyl, and dectyloxyphenyl) were synthesized. All synthesized compounds have been fully characterized by mass spectrometry, UV-visible and fluorescence spectroscopy. The electronic absorption band showed a small red-shift as the number of carbon atoms in the alkyl long chain was increased due to the electronic effect of the alkyl groups. Gold(III) porphyrin complexes continue to be explored for their potential utility as anticancer agent. The *In vitro* anticancer activity of gold(III) porphyrin complexes have been investigated. As judged from MTT assay, all gold(III) porphyrin complexes exhibited the cytotoxicity on MCF7 cell lines. Especially, the AuTPP and AuTOMPP show the cytotoxicity with IC50 value 0.50 µM and 40.47 µM, respectively.

Introduction: Cancer is a major public health problem worldwide and is the second leading cause of death globally and accounted for 8.8 million death in 2018.[1] Cancer can affect almost any part of the body and has many an atomic and molecular subtype that each requiring specific management strategies.[2] The chemotherapy, as a viable alternative, was first considered in the 1940s when nitrogen mustards were used against lymphornas.[3] Chemotherapy or chemo usually refers to the used of medicines or drug to treat cancer. The chemotherapy drug target cell at different phase of the process of forming new cells (cell cycle). The cancer cells tend to form new cell more quickly than normal cell and this make a better target for chemotherapy drug.[4] The most well-known chemotherapy drug is cisplatin or *cis*-diamminedichloroplatinum (II).[5] This compound was first described by Michele Peyrone in 1845.[6] Since the serendipitous discovery that cisplatin can arrest cell division of *E. coli*, platinum coordination complexes have been widely investigated as anticancer agent.[7] The success of cisplatin as an anticancer metal-pharmaceutical drug has simulated the use of metal including gold in anticancer medicine.[8] Due to the gold(III) complex are isoelectronic ($5d^8$) and isostructure (square-planar) with platinum(II) and so have attracted interest as potential anticancer agent. The medical properties of gold have been explored throughout the history of civilization.[9] Perviously, it was reported that the promising gold(III) candidates are the prophyrinato derivatives developed by Che and Sun, which included the complex $[Au(TPP)]^+$. This compound shows good activity in nasopharyngeal and hepatocellular carcinoma, colon cancer neuroblastoma, melanoma, and promyelocytic leukemia.[10] In this work, a series of gold porphyrin complexes contain different meso-substituent groups (phenyl, methoxyphenyl, butyloxtphenyl, octyloxyphenyl, and dectyloxyphenyl) were synthesized and characterized. The cytotoxicity of gold(III) porphyrin complexes were observed on MCF7 cell line by using MTT assay.

Methodology:

Synthesis of gold(III) porphyrin complexes: All free base porphyrins were prepared according to the literature method.[11] The gold(III) porphyrin complexes were synthesized with the corresponding free base by following the published procedure[12]. The gold(III) tetraphenylporphyrin (AuTPP) complex was prepared by refluxing tetraphenylporphyrin (TPP) in glacial acetic acid with sodium acetate and excess $KAuCl_4$ for 3 h. After completion the reaction was checked by TLC. The crude product was obtained by removed acetic acid and wash withCH_2Cl_2 and water. The product was purified by silica gel column chromatography (CH_2Cl_2/MeOH 5/1 v/v) to afford AuTPP as a purple crystalline solid in 16% yield. Mass m/z (ESI) calcd for $AuC_{44}H_{28}N_4$: 809.6. Found 808.9 $[M+H^+$. Other gold(III) porphyrin complexes were synthesis similarly with AuTPP.

The gold(III) tetrakis(4-methoxyphenyl)phenyl-porphyrin (AuTOMPP) was obtained as purple crystals in 10% yield. Mass m/z (ESI) calcd for $AuC_{48}H_{36}N_4O_4$: 929.8. Found 929.4 $[M+H]^+$.

The gold(III) tetrakis(4-butyloxyphenyl)phenyl-porphyrin (AuTOBPP) was obtained as purple crystals in 21% yield. Mass m/z (ESI) calcd for $AuC_{60}H_{60}N_4O_4$: 1098.1. Found 1097.4 $[M+H]^+$.

The gold(III) tetrakis(4-octyloxyphenyl)phenylporphyrin (AuTOOPP) was obtained as purple crystal in 18% yield. Mass m/z (ESI) calcd for $AuC_{76}H_{92}N_4O_4$: 1322.5. Found 1322.2 $[M+H]^+$.

The gold(III) tetrakis(4-dectyloxyphenyl)phenylporphyrin (AuTODPP) was obtained as purple crystal in 22% yield. Mass m/z (ESI) calcd for $AuC_{84}H_{108}N_4O_4$: 1434.7. Found 1434.9 $[M+H]^+$.

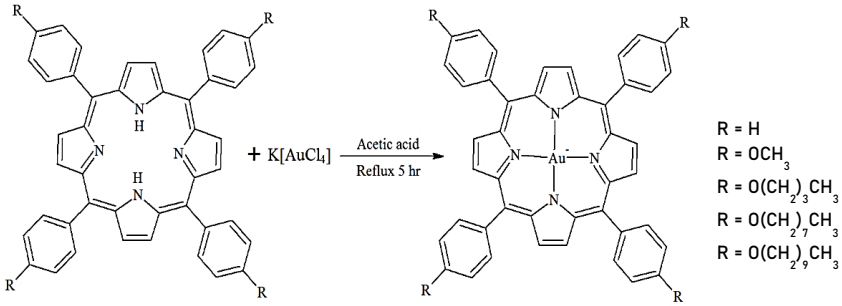

Figure 1. Synthetic route of gold(III) porphyrin complexes

Cell lines and cell culture: The human breast cancer cell line MCF7 was maintained in E-MEM(+) medium. The E-MEM(+) medium was supplemented with 10% Fetal bovine serum (928676), 1% MEM-Non essential amino acid (Gibco, Lot. 1237722), 1% of 200 mM L-Glutamine (Gibco, Lot. 1240196), 1% of PEST (Gibco, Lot. 1221644), and 1% Fungizone (Gibco, Lot 1465402). The MCF7 cell lines were maintained at 37°C in a humidified incubator with an atmosphere of 5% carbon dioxide.

Samples preparation: The gold(III) porphyrin solutions were prepared by dissolving each gold(III) porphyrins in DMSO at concentrations of 1.5, 1.0, 0.5 and 0.25 mM, respectively. Then the stock solutions were diluted with E-MEM(+) medium to obtain working concentrations of DMSO at 1s% (V/V) and working concentration of each compound are 150, 100, 50, and 25 µM respectively.

MTT assay: MCF7 cells were seeded in 96-well plates with a seeding density of 1.0×10^4 cells/well for 24 h. Then, culture medium was changed to control and tested culture media. A control sample was 1% (V/V) DMSO in E-MEM(+) medium. After that, MTT assay was performed at 24 h and 48 h incubation in control and tested culture media. In brief, MTT assay was performed as followed. Experiments were initiated by replacing the culture medium in each well with 100 µL of sample solutions and incubated at 37 °C in the 5% CO_2 incubator. After 24 and 48 h of incubation, the tested cultured media were replaced by culture medium with 10% MTT reagent, 10 µl of MTT reagent (Lot. MKCC5045) in 100 µl culture medium. After that, the plates were incubated at 37 °C in the 5% CO_2 incubator for 4 h. At the end of the incubation

period, the medium was removed and the intracellular formazan was solubilized with 100 µL DMSO and quantified by reading the absorbance at 560 nm on a microplate reader with UV scan instrument. Percentage of cell viability was calculated based on the absorbance measured relative to the absorbance of cells exposed to the negative control. The percentage of cell viability was calculated as follow:

$$\%\ cell\ viability = \frac{OD\ of\ treated\ cells}{OD\ of\ untreated\ cells} \times 100$$

Results and Discussion:

UV-visible spectroscopy: The absorption spectra of all gold(III) porphyrin complexes were recorded in dichloromethane at room temperature. The absorption spectra data of all compounds are summarized in Table 1. The absorption spectra of the gold(III) porphyrin complexes exhibited strong absorption (Soret band) between 409 - 425 nm and weak adsorptions (Q band) around 500-700 nm, both of which can be assigned to π⟶π* electronic transitions. The very intense Soret band assigned to the S0⟶S2 transition is found at shorter wavelengths. In contrast, the Q bands assigned to the S0⟶S1 transitions appear at longer wavelengths.[12] The absorption spectrum of free base porphyrins displayed one Soret band with four Q-bands, whereas the gold(III) porphyrin complexes exhibited one soret band and one Q-band due to the symmetry change of metalloporphyrin complexes. These spectral features were previously explained by Au^{III}-N bonding interactions, consequently leading to stabilization of the HOMO levels, and an increase in the HOMO–LUMO gap with respect to that of the metal-free porphyrin. As the experimental results, the electron effects of the functional groups have no affect to the changes in the UV-Vis absorption of complexes due to the para-substituted of porphyrin as the similar electronegativity (electron-donating) moved slightly toward short wavelength.

Table1 Absorption data of gold(III) porphyrin complexes in CH_2Cl_2

Porphyrin	Absorption	
	S band (nm)	Q band (nm)
AuTPP	406	519
AuTOMPP	418	521
AuTOBPP	419	525
AuTOOPP	419	526
AuTODPP	419	526

[a] All solution was prepared in the concentration of 10 µM, in CH_2Cl_2 (n =3, %RSD ≤ 1.6) and measured in the wavelength range of 200-800 nm.

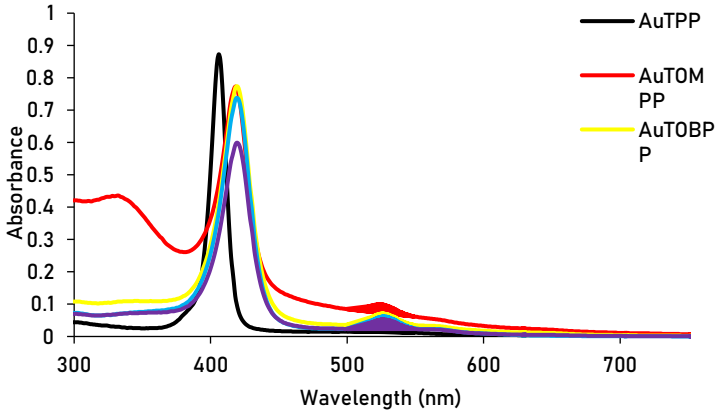

Figure 2. Absorption spectra of all gold(III) porphyrin complexes

Fluorescence spectroscopy: The emission spectra of gold(III) porphyrin complexes were recorded in dichloromethane using fluorescence spectroscopy. The gold(III) porphyrin complexes were excited at each λ_{max}, while the emission spectra appeared in range 500 – 900 nm. The emission data of all compounds were summarized in Table 2. The energy difference between HOMO and LUMO was calculated in terms of the energy gap (E_{gap}). The estimated energy gap was determined from intersection of UV-vis absorption (Q band) referred to the energy for exciteing electron from ground state to excited state and fluorescence emission referred to energy that electron release from excited state back to ground state by using the equation $E_{gap} = hc/\lambda$. The previous work by *Ventura B. et. al.* calculated the energy gab of TPP at 1.92 eV.[14] However, the gold(III) complexes showed only one Q band as shown in Figure 2. The estimated energy gaps of all gold(III) porphyrins complexes were tried by using the different between absorption and emission wavelength and calculate with $E_{gap} = hc/\lambda$. The estimated energy gaps of all synthesized porphyrins were summarized in Table 2. The gold(III) porphyrin complexes exhibited a lower energy gap around 2.1 eV that related to the donating electron of the long chain substituent group at *para*- position.

Table 3 emission data and the estimated energy gap of gold(III) porphyrins complexes in CH_2Cl_2

porphyrin	Dichloromethane		
	Absorption wavelength (nm)	Emission wavelength (nm)	E_{gap} (ev)
AuTPP	406	611, 650, 824	2.20[a]
AuTOMPP	418	503, 718, 848	2.00[a]
AuTOBPP	419	658, 858	2.10[a]
AuTOOPP	419	659, 854	2.10[a]
AuTODPP	419	657, 854	2.10[a]

[a] Calculate by using average of wavelength between Q-band and emission band

Cytotoxicity: The cytotoxicity effect of different dose of gold(III) porphyrin complexes on human breast cancer cell (MCF7) was investigated by MTT assay. The results showed that all compounds exhibited the cytotoxicity effect on MCF7 cell lines. The AuTPP showed the lowest % cell viability than other complexes in all test concentration. At the same concentration, AuTPP and AuTOMPP showed the most prominent anticancer activity with % cell viability lower than other three gold(III) porphyrin compounds (AuTOBPP, AuTOOPP, and

AuTODPP) due to the solubility and disorderly of meso-substituent group. Figure 2 shows % cell viability of MCF7 cell lines after treated with gold(III) porphyrin complexes for 24 h and 48 h. Figure 3 show images of staining of MCF7 cell line after treated with 25 µM gold(III) porphyrin complexes for 24 h. The staining demonstrated levels of cell cytotoxicity of gold (III) porphyrin complexes, from the highest to the lowest, as followed AuTPP > AuTOMPP ≥ AuTOBPP ≥ AuTOOPP ≥ AuTODPP, respectively.

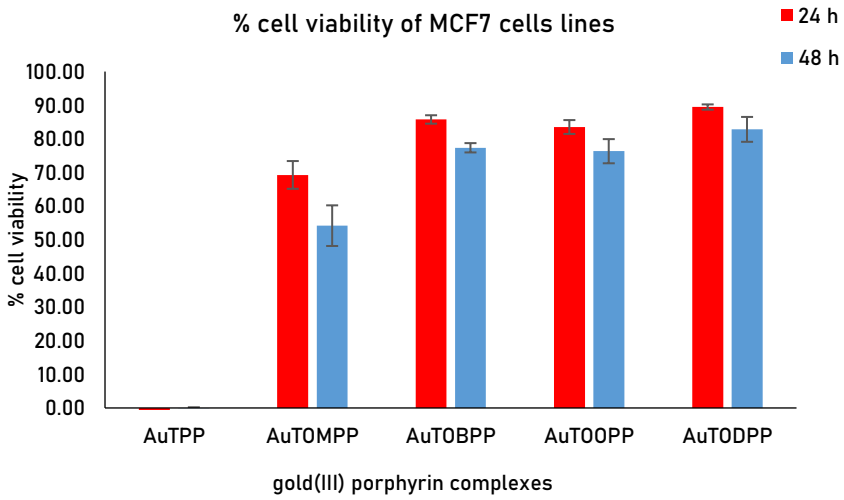

Figure 2. Demonstrating percent cell viability of MCF7 cell line after treated with gold(III) porphyrin complexes for 24 h and 48 h

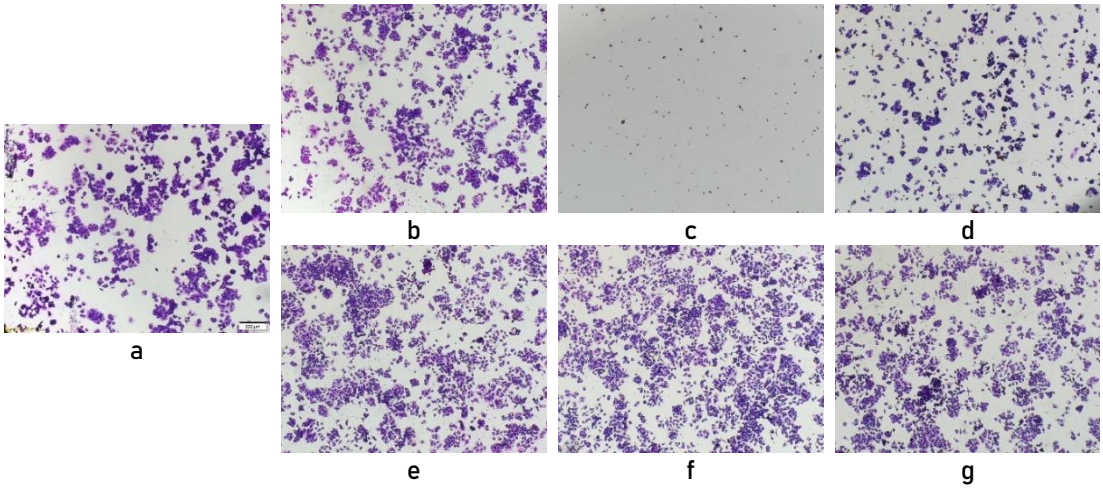

Figure 3 Staining images of MCF7 cell line a) control, b) 1%DMSO, and c) 25 µM of AuTPP, d) AuTOMPP, e) AuTOBPP, f) AuTOOPP, and g) AuTODPP.

The inhibitory concentrations required to inhibit cell growth by 50% compared with control (IC_{50} values) were evaluated from the dose dependence of cells 24 h after exposing to the compounds. The AuTOMPP exhibited IC50 value as 40.47 µM. Regarding AuTPP, the complex exhibited % cell viability lower than 2% at all test concentrations. Therefore, working concentrations of AuTPP complex for cytotoxicity test on MCF7 cell lines were lower than concentrations of other compounds (10, 5, 1, and 0.5 µM) and the IC50 value at 0.5 µM was

calculated. In contrast, IC50 of AuTOBPP, AuTOOPP, and AuTODPP cannot be calculated due to all three compounds showed %cell viability higher than 80% at all doses.

Conclusion: Gold(III) porphyrin complexes were successfully synthesized with approximately 20% reaction yields. The expected synthesized structures were confirmed by mass spectroscopy (MS). The UV-visible absorption spectra of the compounds showed one Soret band and one Q band in the dichloromethane solution. The absorption spectra exhibited a small red shift when the number of carbon atom at *meso*-substituent were increased. The gold(III) porphyrin complexes exhibited two emission peaks at around 650 nm and 850 nm, respectively, when excited at the maximum absorption. Cell cytotoxicity test of MCF7 cell lines demonstrated markedly high cytotoxicity effects of AuTPP and AuTOMPP complexes on MCF7 cell line with IC50 value at 0.50 µM and 40.47 µM, respectively. Whereas, AuTOBPP, AuTOOPP, and AuTODPP complexes exhibited low cytotoxicity effects or low anticancer activity on MCF7 cell line with % cell viability higher than 80%.

References:

1. http://www.nci.go.th Retrieved June 20, 2019.
2. Romero-Canelon I, Sadler P.J. *Inorg. Chem.* 2013;52(21):12276-12291.
3. https://www.cancer.org/treatment/treatments-and-side-effects/treatmenttypes/chemotherapy.html Retrieved June 20, 2019.
4. Dasari S, Tchounwou P.B. *Eur. J. Pharmacol.* 2014;740:364-378.
5. Kauffman G. B, Pentimalli R, Doldi S, Hall M. D. *Met. Rev.* 2010;54:250–256.
6. Cisplatin; Lippert, B., Ed.; Wiley VCH: Zurich, Switzerland, 1999
7. To Y.F, Sun R.W, Chen Y, Chan V.S, Yu W.Y, Tam P.K, Che C.M, Lin C.L. *Int. J. Cancer.* 2009;124(8):1971-1979.
8. Milacic V, Dou Q.P*. Coord. Chem. Rev.* 2009;253(11-12):1649-1660.
9. Sun R.W.-Y, Che C.M. *Coord. Chem. Rev.* 2009;253(11-12):1682-1691.
10. Tu S, Wai-Yin Sun R, Lin M.C, Tao Cui J, Zou B, Gu Q, Kung H.F, Che C.M, Wong B.C. Cancer 2009;115(19): 4459-4469.
11. Alan A. J. Org. Chem. 1967;32:476 – 476.
12. Liang S, Huasheng C, Zonglei Z, Qian Y, Haibo T, Aihua X, Cunde W. J. Inorg. Biochem. 2012;108:47-52.

Acknowledgements: We are grateful to the Department of Chemistry, Faculty of Science and Technology, Thammasat University and Science Achievement Scholarship of Thailand (SAST), for financial support and supports for all experiments, and Department of Materials Science, Faculty of Engineering, Kyushu Institute of Technology, Kitakyushu, Japan for a study on cell cytotoxicity. Last but not least, we most appreciated in support from "Japan Student Services Organization (JASSO)" for a scholarship.

C2_008_PF: COUMARIN-BASED SEMICARBAZIDE AS "TURN-OFF" FLUORESCENT SENSOR FOR Cu^{2+} DETECTION

Pichayanan Srisuwan[1,2], Anirut Suppasombut[1,2], Morakot Kaewpet[1,2], Dhassida Sooksawat[1,2,]*
[1]Department of Chemistry and Center of Excellence for Innovation in Chemistry (PERCH-CIC), Faculty of Science, Prince of Songkla University, Hat Yai, Songkhla, 90110, Thailand
[2]Center of Excellence for Trace Analysis and Biosensor, Prince of Songkla University, Hat Yai, Songkhla, 90110, Thailand
*e-mail: dhassida.s@psu.ac.th.

Abstract: The development of probes for specific Cu^{2+} detection has been widely interested due to the adverse effects to environmental system of Cu^{2+}. Fluorescent chemosensors have become the effective technique to monitor the amount of Cu^{2+} because of their advantages such as high sensitivity and selectivity, low cost and fast response. In this work, a highly sensitive and selective coumarin-based semicarbazide as fluorescent chemosensor for Cu^{2+} detection, CS1, has been synthesized and characterized. CS1's fluorescence was quenched in the presence of Cu^{2+} and behaved as a "turn-off" fluorescent chemosensor. Trace amount of Cu^{2+} was detected by spectrofluorometric method in CH_3CN: H_2O (9:1 v/v). The ligand exhibited excitation and emission maxima at 370 nm and 482 nm, respectively. After addition of Cu^{2+} concentration to CS1 solution, blue shift of absorption band was observed. Based on fluorescence titration with Cu^{2+} concentration was calculated, a good linear range was obtained (R^2= 0.9996). CS1 also exhibits good selectivity for Cu^{2+} over a range of other metal ions. Further study would be applying the sensor to analyse Cu^{2+} in environmental sample.

Introduction: Recently, detection of metal ions used in biological and environmental has gained a lot of attention from researchers due to their harm on ecosystems and human health. Transition metal ions including copper are also essential trace elements in biological systems. Copper is used extensively in agriculture and industry, particularly in electrical wiring. The production of copper has elevated due to high demand from various sources. Copper is also a metal pollutant because of its widespread applications. The normal average concentration of Cu^{2+} in blood is in the range of 15.7–23.6 µM. The limit of concentration for Cu^{2+} in drinking water has been set by The U.S. Environmental Protection Agency (EPA), is 20 µM[1]. In addition, too much copper in human body can cause eminent health problems. Excessive amounts of Cu^{2+} can cause serious diseases like amyotrophic lateral sclerosis[2], Alzheimer's disease[3], Parkinson's disease[4], Wilson's disease[5] and Menkes syndrome[6]. Moreover, copper deficiency in humans can also result in anemia, neutropenia and bone abnormalities[7]. Hence, the detection of Cu^{2+} concentration needs an efficient, selective and highly sensitive method[8, 9].

A number of methods for Cu^{2+} detection have been developed including atomic absorption spectrometry[10], inductively coupled plasma atomic emission spectroscopy[11], and electrochemical techniques[12, 13]. However, there are some drawbacks for these methods, such as expensive instrumentation and complicated sample preparation. These adverse effects lead to the development of other simple and sensitive methods for detection of Cu^{2+}. Because of their strengths such as high selectivity and sensitivity, real time analysis and very fast response towards complexation, many fluorescent chemosensors for Cu^{2+} ion detection have been reported. A fluorescent chemosensor is a compound incorporating binding site(s) for selectively hold an analyte and a fluorophore as a signaling unit upon chemical change[14]. Among fluorescent dyes or fluorophores, coumarin exhibits interesting fluorescence properties. It can be used in media with a wide range of polarity, pH, viscosity. Therefore, many studies involving spectroscopic property of coumarin have been published[15, 16]. Previously, coumarin derivatives have been reported to act as on-off fluorescence chemosensors and applied to determine Cu^{2+} content in real water sample which exhibited good selectivity and sensitivity[17].

Herein, we reported the synthesis of a coumarin-based semicarbazide as a fluorescent chemosensor CS1 for Cu^{2+} detection which induced a fluorescence quenching upon addition of Cu^{2+} concentration. The process of binding was confirmed by UV-vis absorption and fluorescent measurement. Further studies to apply CS1 chemosensor for detection of Cu^{2+} in the real water sample is yet to be determined.

Methodology:

Synthesis and Characterization: Compound CS1 was synthesized through the route shown in Scheme 1. The synthesis of ethyl nitroacetate (2) was carried out according to the reported procedure[18], which was obtained 33% as an oil. After that, nitro-coumarin (4) was produced by condensation reaction of 4-(diethylamino)salicylaldehyde (3) and ethyl nitroacetate (2) with 37% as a yellow powder. Amino-coumarin (5) was obtained through reduction of (4) with HCl and $SnCl_2$ as catalyst without further purification with 75% as an orange powder[19]. In the final reaction CS1 was synthesized from a reaction of compound 5 with 4-nitrophenyl chloroformate and hydrazine hydrate with 73%. The structure of CS1 was determined by ^{1}H-NMR, ^{13}C-NMR spectroscopy.

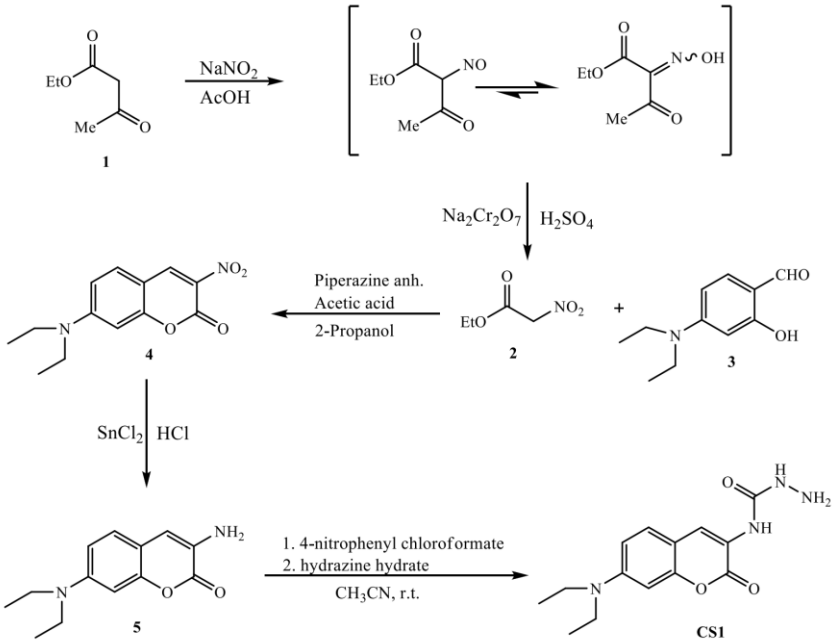

Scheme 1. Synthetic route of CS1.

Synthesis of ethyl nitroacetate (2): An aqueous solution of $NaNO_2$ (1.8 g, 25.71 mmol) in water 2.5 ml was added to a mixture of ethylacetoacetate (23.51 mmol) in acetic acid (4 mL). Then the solution mixture was stirred at 15 °C for 1 h and poured into 60 mL and ice-cold water. After 16 h, the suspension was extracted with chloroform and the organic layer was dried over anhydrous Na_2SO_4 and evaporated under reduced pressure to afford isonitrosoacetoacetate as an oily residue (2.5 g). In the second step, a solution of potassium dichromate (15.6 mmol) in water (10 mL) and conc. H_2SO_4 (3.75 mL) was added to a suspension of isonitrosoacetoacetate (2.5 g) in water (6 mL). The resulting mixture was stirred for 6 h at 20°C and then poured into 10 mL of ice-cold water and heated to room temperature. The mixture was then extracted with chloroform and the organic layer was neutralized by saturated solution of sodium bicarbonate, washed with brine, dried over anhydrous Na_2SO_4

and evaporated to obtain ethyl nitroacetate 2 as oil in 33% yield. ^{1}H NMR (300 MHz, $CDCl_3$) δ 5.16 (s, 2H), 4.32 (t, *J* = 6.9 Hz, 2H), 1.31 (q, *J* = 7.1, 4.8 Hz, 3H).

Synthesis of nitro-coumarin (4): Ethyl nitroacetate (2.83 mmol) was added to a solution of 4-(diethylamino)salicylaldehyde (2.58 mmol) in 1-butanol (15 mL). A catalytic amount of anhydrous piperazine and acetic acid were added to the reaction mixture. After reflux for 24h, the reaction mixture was cooled down to room temperature. A solid compound (4) was precipitated and isolated in pure form (yield 37%). ^{1}H NMR (300 MHz, $CDCl_3$) δ 8.71 (s, 1H), 7.43 (d, *J* = 9.1 Hz, 1H), 6.70 (dd, *J* = 9.1, 2.4 Hz, 1H), 6.47 (d, *J* = 2.3 Hz, 1H), 3.50 (q, *J* = 7.2 Hz, 4H), 1.27 (t, *J* = 7.2 Hz, 6H). ^{13}C NMR (75 MHz, $CDCl_3$) δ 158.7, 154.5, 153.4, 143.3, 132.5, 126.7, 111.1, 106.1, 96.7, 77.4, 77.2, 76.9, 76.5, 45.4, 30.8, 12.3.

Synthesis of amino-coumarin (5): A solution of compound 4 (0.763 mmol) in 5 ml conc. HCl, and tin chloride ($SnCl_2$) (5.0 mmol) was added slowly over 15 minutes. After stirred for 6 h at room temperature, the reaction mixture was neutralized by an aqueous solution of NaOH (4 N). Then the crude product was extracted with ethylacetate. Anhydrous $MgSO_4$ was added to the organic phase and it was concentrated under reduced pressure. Finally, amino-coumarin (5) was obtained in high yield (75%). ^{1}H NMR (300 MHz, $CDCl_3$) δ 7.09 (d, *J* = 8.7 Hz, 1H), 6.69 (s, 1H), 6.55 (dd, *J* = 8.7, 2.4 Hz, 1H), 6.50 (d, *J* = 2.3 Hz, 1H), 3.35 (q, *J* = 7.1 Hz, 4H), 1.16 (t, *J* = 7.1 Hz, 7H).

Synthesis of CS1: Amino-coumarin (5) 1.0 mmol was dissolved in acetonitrile. After stirred at ambient temperature for 20 min, 4-nitrophenyl chloroformate 1.5 mmol was added to the coumarin solution. After 12 h, hydrazine monohydrate 3.3 mmol was added slowly to the reaction mixture, and the solution turned yellow. After 2 h, the solvent was removed under reduced pressure. Probe CS1 was obtained as a yellow powder after purification by crystallization from methanol (73%). ^{1}H NMR (300 MHz, $CDCl_3$) δ 8.71 (s, 1H), 8.35 (s, 1H), 7.28 (d, *J* = 9.0 Hz, 1H), 6.61 (dd, *J* = 8.8, 2.5 Hz, 1H), 6.51 (d, *J* = 2.4 Hz, 1H), 6.13 (s, 1H), 3.88 (s, 2H), 3.39 (q, *J* = 7.1 Hz, 4H), 1.19 (t, *J* = 7.1 Hz, 6H). ^{13}C NMR (75 MHz, $CDCl_3$) δ 159.8, 157.1, 152.2, 148.8, 128.2, 123.1, 119.7, 109.5, 108.7, 97.5, 77.4, 77.2, 77.2, 76.9, 76.5, 44.7, 12.4.

Results and Discussion:

The preliminary study of CS1 chemosensor performances: the absorption spectrum of CS1 was investigated and the maximum absorption wavelength was shown at 370 nm (Figure 1).

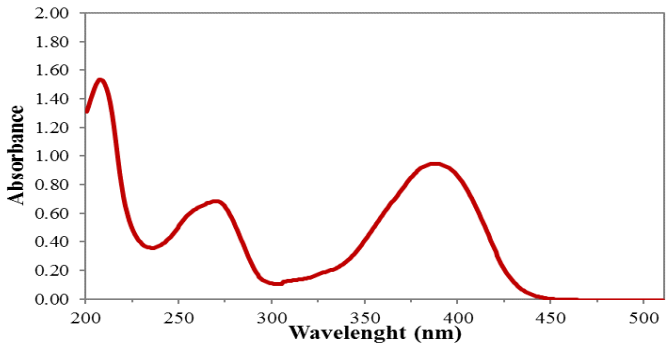

Figure 1. UV absorption spectrum of CS1 in CH_3CN: H_2O (9:1 v/v).

The emission spectral measurements of CS1 with and without increasing concentrations of Cu^{2+} ions were determined in CH_3CN: H_2O (9:1 v/v) shown in Figure 2. According to Figure 2a, in the absence of Cu^{2+} ions, CS1 exhibits an emission maximum at 482 nm with the excitation wavelength at 370 nm. Upon the addition of Cu^{2+} ions to CS1 solution, emission intensity at 482 nm gradually decreased and blue shifted from 482 nm to 440 nm. The plot of the linear correlation was investigated between $I_0/(I_0-I)$ as a function of

1/[Cu^{2+}], whereas I_0 is the fluorescence intensity of the free ligand CS1, I is the fluorescence intensity of CS1-Cu^{2+} complex. A good linear relationship was obtained which the linear regression equation was related to $I_0/(I_0-I)$ = 0.2346(1/[Cu^{2+}]) + 0.5766 (R^2 = 0.0996).

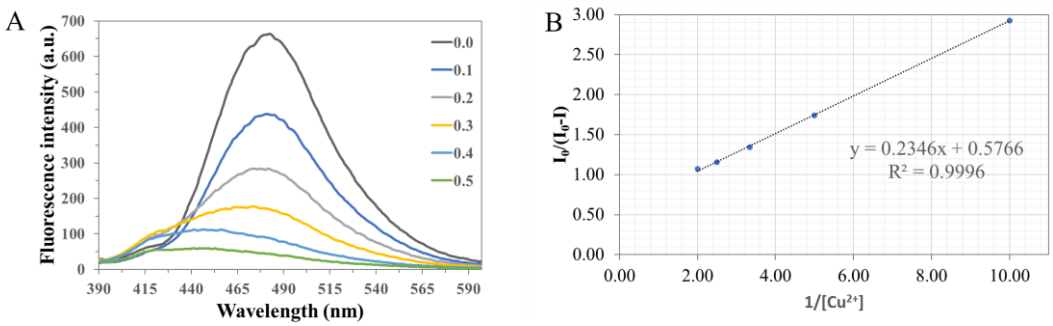

Figure 2. (A) Changes in the fluorescence spectra of CS1 (1 µM) in CH_3CN/H_2O (9:1 v/v) as a function of added [Cu^{2+}] = 0-0.5 µM (each addition 0.1 µM).; (B) Calibration plot for relative emission intensity of CS1 versus Cu^{2+} ions

One of the most important characteristics for cation-selective chemosensor is the selectivity. Thus, the interference on the fluorescence intensity of the proposed Cu^{2+} chemosensor was investigated. In this study, Cu^{2+}, K^+, Ca^{2+}, Co^{2+}, Mg^{2+}, Ni^{2+} and Zn^{2+} (10 equiv) were added to the compound CS1 (1 µM) solution, and the fluorescence spectra was observed. The fluorescence emission intensity at 482 nm significantly decreased as a result of binding with Cu^{2+}. The other metal ions showed no significant fluorescent change. Compared to the other cations, compound CS1 exhibited good selectivity for Cu^{2+}, indicating that CS1 has a good anti-interference ability in detecting Cu^{2+} (Figure 3A and 3B). In addition, naked eye colorimetric changes of probe CS1 in the presence of various metal ions were also observed. The CS1 only stimulated with Cu^{2+} ions which showed color changing from colorless to yellow, while other metal ions had no color change under white light and UV-lamp (Figure 3C and 3D).

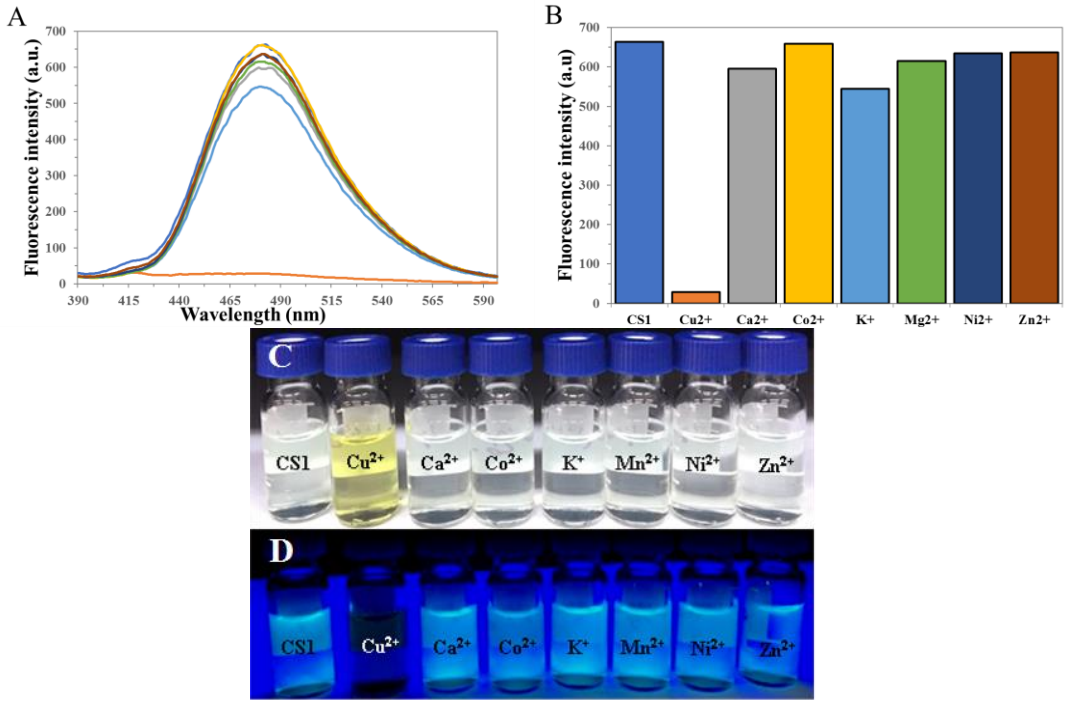

Figure 3. (A) and (B) Fluorescence changes of CS1 (1 μM) (a) with different cations (10 equiv). (C) and (D) Chromogenic and Fluorogenic changes of a 1.0 mM solution of CS1 in CH_3CN: H_2O (9:1) in the presence of 10 equiv of each cation.

Conclusion: In summary, a new coumarin-based semicarbazide as "turn-off" fluorescent chemosensor, CS1 was successfully synthesized and characterized. A linear curve was obtained in the plotting of relative emission intensity against 1/[Cu^{2+}] (R^2=0.9996). CS1 exhibits a significantly quenched fluorescence in the presence of Cu^{2+} over a range of metal cations. The detection was highly sensitive and selective which almost unaffected by the common coexisting metal ions. In addition, only Cu^{2+} ion added to CS1 chemosensor exhibits naked eye colorimetric changes from colorless to yellow and fluorescence color changes under day light and UV lamp.

References:

1. Jung H S, Kwon P S, Lee J W, Kim J I, Hong C S, Kim J W, Yan S, Lee J Y, Lee J H, Joo T, Kim J S. Journal of the American Chemical Society. 2009;131:2008-2012.
2. Valentine J S, Hart P J. Proceedings of the National Academy of Sciences. 2003;100:3617.
3. Hung Y H, Bush A I, Cherny R A. Journal of biological inorganic chemistry : JBIC : a publication of the Society of Biological Inorganic Chemistry. 2010;15:61-76.
4. Lee J C, Gray H B, Winkler J R. Journal of the American Chemical Society. 2008;130: 6898-6899.
5. Madsen E, Gitlin J D. Annual review of neuroscience. 2007;30:317-337.
6. Vulpe C, Levinson B, Whitney S, Packman S, Gitschier J. Nature genetics. 1993;3:7-13.
7. Henkin R I, Schulman J D, Schulman C B, Bronzert D A. The Journal of pediatrics. 1973;82:831-837.
8. Khan B, Shah M R, Ahmed D, Rabnawaz M, Anis I, Afridi S, Makhmoor T, Tahir M N. Journal of Hazardous Materials. 2016;309:97-106.

9. Moussa H, Merlin C, Dezanet C, Balan L, Medjahdi G, Ben-Attia M, Schneider R. Journal of Hazardous Materials. 2016;304:532-542.
10. Faghihian H, Hajishabani A, Dadfarnia S, Zamani H. International Journal of Environmental Analytical Chemistry. 2009;89:223-231.
11. Tomalová I, Foltynová P, Kanický V, Preisler J. Analytical Chemistry. 2014;86:647-654.
12. Zhu Z, Su Y, Li J, Li D, Zhang J, Song S, Zhao Y, Li G, Fan C. Analytical Chemistry. 2009;81:7660-7666.
13. Niamnont N, Khumsri A, Promchat A, Tumcharern G, Sukwattanasinitt M. Journal of Hazardous Materials. 2014;280:458-463.
14. Czarnik A W. Accounts of Chemical Research. 1994;27:302-308.
15. Razi S S, Srivastava P, Ali R, Gupta R C, Dwivedi S K, Misra A. Sensors and Actuators B: Chemical. 2015;209:162-171.
16. Mani K S, Rajamanikandan R, Murugesapandian B, Shankar R, Sivaraman G, Ilanchelian M, Rajendran S P. Spectrochimica Acta Part A: Molecular and Biomolecular Spectroscopy. 2019;214:170-176.
17. Chao J-B, Zhang Y, Wang H-F, Zhang Y-B, Huo F-J, Yin C-X, Qin L-P, Wang Y. Journal of Coordination Chemistry. 2013;66:3857-3867.
18. Sharma R, Priyanka, Katiyar D, l-Proline catalyzed condensation of salicylaldehydes with ethyl nitroacetate: an efficient access to 3-nitrocoumarins, 2016.
19. Kumar A, Mondal S, Kayshap K S, Hira S K, Manna P P, Dehaen W, Dey S. New Journal of Chemistry. 2018;42:10983-10988.

Acknowledgements: This work was supported by the Faculty of Science Research Fund, Prince of Songkla University, Contract no. 1-2560-02-005. Centre of Excellence for Innovation in Chemistry (PERCH-CIC), Center of Excellence for Trace Analysis and Biosensor (TAB-CoE) and Department of Chemistry, Faculty of Science, Prince of Songkla University.

SESSION C3:
ORGANIC &
MEDICINAL CHEMISTRY

C3_002_PF: QUANTITATIVE DETERMINATION OF PHENOLIC AND TANNIN CONTENTS AND ANTIOXIDANT ACTIVITY OF PAPER MULBERRY

Banthot Chomsawan[1,*], Jinda Sirita[1], Piyada Yodsoontorn[1], Kanlaya Jumpatong[2]
[1]Faculty of Science and Technology, Chiang Rai Rajabhat University, Chiang Rai 57100, Thailand
[2]School of Science, University of Phayao, Chiang Rai 56000, Thailand
*e-mail: banthod49@gmail.com

Abstract: This research aimed to determine the quantity of phenolic and tannin contents and antioxidant activity of paper mulberry ethanol extract and to evaluate physical and chemical properties and product satisfaction of the appropriate formulation of soap containing paper mulberry extract. It was found that the dry old leaf extract of paper mulberry gave the highest percent yield (5.09 ± 0.19) and phenolic content (262.25 ± 9.17 mg GAE /100g) while the dry young leaf extract contained the highest tannin content (213.16 ± 24.26 mg/100g). The highest antioxidant activity with IC_{50} value of 0.29 ± 0.02 mg/mL was found in the dry bark extract. When comparing the quantity of phenolic, tannin and antioxidant contents in paper mulberry extract, it showed to be statistically different ($p<0.05$). The dry bark extract was selected for soap production. Moreover, the results indicated that the appropriate ratio for glycerin, paper mulberry bark extract and essential oil was 98.5:0.5:1 which gave clear, brown-green lumps of soap with high foaming volume. The percentage of weight lost after soaking in the water, the corrosion and crevice rate were similar to those of soap products in the market with pH 9.94, chloride content of 0.020 ± 0.0006% w/w and no free hydroxide which corresponded with Thai Industrial Standard 29-2002 and the standard of community product 665/2010. The overall consumer satisfaction was 3.78 ± 0.42, which was high satisfaction.

Introduction: Paper mulberry (*Broussonetia papyrifera*) is a plant in the same family of mulberry trees. Most of its fiber is from bark and can be used as a good quality material to produce umbrellas, artificial flowers, lamps, fans, kites, various greeting cards, drawing paper, chemical wrapping paper and several useful substances used in hospitals. It is also a medicinal plant used in the treatment of various diseases. Leaves are used for promoting diuresis, treatment of toxic from insect bites and stings and dermatophytosis treatment. Ripen fruits are used to promote kidney functions and relieve fatigue. The barks of the trunk are used for treatment of hemorrhage, coughing, vomiting. The latex from stems can be used to treat edema, bites and stings from insects.[1] Substances found in paper mulberry are kazinol F, broussochalcone A and papyriflavonol A, etc. In addition, various parts of plant contain different kinds of essential substances. For example, kazinol F can be extracted from the root, providing ability to inhibit tyrosinase activity during melanin production. Thus, it is used in cosmetics and skin treatment.[2] It is reported that the extract of paper mulberry is able to reduce pigments as it inhibits tyrosinase, resulting in lower enzyme concentration than when treated with kojic acid, vitamin C and hydroquinone.[2] Both ethanol and petroleum ether extracts contain antioxidants in a high-performance group such as hydroxytoluene (BHT). However, clinical trials regarding skin lightening effects are lacking. A patch test using 1% paper mulberry extract revealed no significant skin irritation at 24 h and 28 h.[3]

From the literature review, different parts of plant and extraction methods of paper mulberry affect the quantity and quality of essential substances and antioxidants. Therefore, we are interested in determining and comparing the content of polyphenols, tannins, and antioxidant substances of paper mulberry extracts which are obtained from various parts of paper mulberry collected from Chiang Rai Province and to develop glycerin soap product containing paper mulberry extract. Physical properties including colors, smell, foaming and chemical properties such as pH values will be determined. We hope that the knowledge from this research could be used as a guideline for production of paper mulberry extract soap.

Methodology:

Materials and chemicals: Young leaves, old leaves, barks and stems of paper mulberry (*Broussonetia Papyrifera*) were collected from Ban Pang Ha, Koh Chang district, Mae Sai, Chiang Rai. Chemicals included absolute ethanol (MERCK), acetone (CARLO ERBA), DPPH (SIGMA), Folin–Ciocalteu reagent (SIGMA), gallic acid (MERCK), tannic acid (SIGMA), trolox (Aldrich). All chemicals were analytical grade or equivalent.
Preparation of paper mulberry extracts: Various parts of paper mulberry were thoroughly rinsed with clean water, dried in the shade, then smashed and cut into small pieces. The dry paper mulberry was prepared by oven-drying at 50 °C. Samples were soaked in 95% ethanol (1:10 weight per volume) for 72 h, and then filtered. The solvent was evaporated by rotary vacuum evaporator. Then, samples were freeze-dried and used for further analysis.
Determination of total phenolic content (adapted from Savitree Mongkolsilp)[4]: The 1.0 mL extract in methanol at the concentration of 1 mg/mL was added to a test tube containing 2.5 mL of 10% v/v Folin-Ciocalteu reagent and 2.0 mL distilled water. Solution was mixed and set aside for 6 min before adding 1.25 mL of 7.5% w/v sodium carbonate and left in the dark at room temperature for 2 h. The absorbance measurement was achieved at 765 nm wavelength using ethanol as a blank to analyze the amount of all polyphenols in the gallic acid form and compare with a standard curve to determine gallic acid equivalents (mg GAE/100g).
Determination of tannin content: The extract at concentration of 2.0 mg/mL in methanol was added into a test tube containing 0.2 mL Folin-Ciocalteu reagent and 2.0 mL of 7% w/v sodium carbonate. Then, the mixture was shaken and left in the dark for 60 min before measuring absorbance with UV-Vis spectrophotometer at a wavelength of 760 nm to calculate the amount of total tannins by comparing with a standard curve of tannic acid.
Antioxidation activity test (adapted from Joo-Shin Kim)[5]: Various concentrations of mulberry extract in methanol (1.0 mL) was added into a test tube. Then, a solution of 2.0 mL of 0.2 mM DPPH was added. The mixture was kept in the dark at room temperature for 30 min before measurement of the absorbance at 517 nm wavelength in triplicate. When Ac is the absorbance of DPPH mixed with methanol and As is the absorbance of DPPH mixed with sample solution, the formula used for calculation is as follows:

$$\% \text{ inhibition} = \frac{Ac - As}{Ac} \times 100$$

Average yield percentage, total phenolic content, tannins and antioxidant activity (IC_{50}) of extracts from various parts of paper mulberry were analyzed statistically using t-test.
Preparation of mulberry extract soap: The paper mulberry extracts were used as an ingredient in transparent glycerin soap. Four different ratios of glycerin, the extract, and essential oils (100:0:0, 99:0:1, 98.5:0.5:1 and 98:1:1) were studied.
Study of physical and chemical properties of paper mulberry extract soap: Physical properties included general characteristics, color, foaming, the percentage of soap weight lost after washing with water, soap corrosion and crevice occurrence.
Chemical properties included pH measurement, chloride test and free sodium hydroxide test. The criteria used of glycerin soap was based on Thai Industrial Standard 29-2002, community product standard 665/2010 and survey of consumer satisfaction.

Results and Discussion: The results of percentage yield, total phenolic content, tannins and antioxidant activity (IC_{50}) of the extracts from different parts of paper mulberry are shown in Table 1.

Table 1. The percentage yield, quantities of total phenols, tannins and IC_{50} values.

Plant parts	% yield	total phenolics mg GAE/100g	tannins mg/100g	IC_{50} (mg/mL)
Fresh young leaves	2.84 ± 0.28	143.21 ± 9.66	167.07 ± 6.11	0.78 ± 0.05
Fresh old leaves	3.06 ± 0.15	155.93 ± 15.27	46.95 ± 2.12	0.58 ± 0.04
Fresh barks	2.11 ± 0.03	146.91 ± 16.83	45.48 ± 4.49	0.40 ± 0.04
Fresh stems	1.90 ± 0.26	49.17 ± 9.46	13.56 ± 1.83	1.40 ± 0.06
Dry young leaves	3.68 ± 0.46	179.07 ± 12.17	213.16 ± 24.26	0.53 ± 0.00
Dry old leaves	5.09 ± 0.19	262.25 ± 9.17	80.66 ± 4.98	0.56 ± 0.02
Dry barks	2.10 ± 0.14	181.18 ± 9.56	52.30 ± 4.56	0.29 ± 0.02
Dry stems	1.07 ± 0.18	47.08± 10.59	12.69 ± 2.62	0.77 ± 0.04

From Table 1, it was found that the highest percent yield was obtained from dry old leaves while the second highest was from dry young leaves. The extract with the highest quantity of phenolic compounds was from dry old leaves, followed by dry young and fresh old leaves. The highest antioxidant activity was found in dry barks, followed by fresh barks and dry young leaves. When compared the quantities of total phenolics, tannins and antioxidant activities of the extracts from different parts of paper mulberry using t-test, they were significantly different ($p < 0.05$). In addition, the extracts from dry young leaves, old leaves and barks showed higher phenolic and tannin contents than the extracts from fresh plant. The extract of the dry bark showed the highest antioxidant activity even though the amounts of total phenolics and tannins were not the highest.

The dry bark extract of paper mulberry was used as a natural ingredient in soaps. The tests showed that the appropriate ratio of glycerin, paper mulberry extract and essential oil was 98.5:0.5:1, resulting in clear, brown-green and high foaming lumps. The weight lost percentage after washing, corrosion and crevice rates was comparable to those of products available in the market (benchmark product) with pH value of 9.94, chloride content of 0.020 ± 0.0006% w/w and no free hydroxide. The soap properties were equivalent to an industrial product standard TIS 29-2002 and community product standard 665/2010. The overall consumer satisfaction was 3.78 ± 0.42, which was high satisfaction.

Conclusion: The extract of dry old paper mulberry leaves had the highest percent yield and phenolic content (5.09 ± 0.19 and 262.25 ± 9.17 mg GAE/100g, respectively) while the highest tannin content was detected in dry young leaves (213.16 ± 24.26 mg/100g). The highest antioxidant activity with IC_{50} value of 0.29 ± 0.02 with mg/mL was from dry barks. Different parts of plant gave different amounts of phenols, tannins and antioxidants significantly ($p < 0.05$). Furthermore, the dry bark extract was selected for soap production, as a natural ingredient. The results of some property tests showed that it was in accordance with Thai Industrial Standard 29-2002 and community product standard 665/2010. It could be used as a guideline for production of paper mulberry extract soap in industry. Further study will involve in the isolation and structure elucidation of active ingredients in the plant.

References:

1. Han Q, Wu Z, Huang B. Int J Biol Macromol. 2016;92:116–24.
2. Zong-Ping Z, Ka-Wing C, Jianfei C, Jiajun W, Mingfu W. Food Chem. 2008;106:529-535.
3. Rashmi S, Pooja A, K Vijay G. J Cutan Aesthet Surg. 2013;6(1):4–11.
4. Savitree M, Isara P, Nittaya S, Worapan S. SWU J Pharm Sci. 2004;9(1):32–35.
5. Joo-Shin K. J Food Sci. 2005;70:C208–C213.

Acknowledgements: We would like to thank the National Research Council of Thailand for the sponsorship and the support experimental devices and analysis tool provided by Chiang Rai Rajabhat University and we would like to thank Ban Pang Ha community, Koh Chang district, Mae Sai, Chiang Rai for the generous providing of plant samples.

C3_003_PF: SYNTHESIS AND CYTOTOXICITY OF TETRAHYDROCURCUMIN PYRAZOLE INDOLE DERIVATIVES

Manatchanok Pattanasing, Chopaka Thongbumrer, Boon-ek Yingyongnarongkul, Mayura Thongchuang, Vachiraporn Ajavakom*
Department of Chemistry and Center of Excellence for Innovation in Chemistry, Faculty of Science, Ramkhamhaeng University, Bangkok 10240, Thailand
*e-mail: satcharoen@yahoo.com

Abstract: Tetrahydrocurcumin Pyrazole Indole (TPI) derivatives were designed and synthesized by combining three important heterocyclic units into one molecule in order to create a novel type of biologically active compounds. Construction of pyrazole ring on tetrahydrocurcumin (THC) were carried out successfully by utilizing glacial acetic acid as a catalyst and subsequent coupling with corresponding indole acids (n = 1-3). The present work also aimed to improve the cytotoxic activity of the THC against cancer cells. The cytotoxicity studies of the synthesized and related compounds were described herein. THC bearing an indole scaffold linked with three methylene units (n = 3) exhibited better cytotoxic activities than the parent THC against human cervical adenocarcinoma (HeLa), prostate cancer (PC3), human colon adenocarcinoma (HT29) and human breast adenocarcinoma (MCF-7) cell lines with IC_{50} values of 7.00±0.839 µM, 12.93±1.631, 11.53±0.505 and 21.31±0.794 µM, respectively.

Introduction: Tetrahydrocurcumin (THC), which is a curcumin derivative naturally found in metabolic system,[1] could be simply prepared herein by the hydrogenation reaction of curcumin. Many synthetic chemists have used the 1,3-dicarbonyl unit in THC molecule as a substrate in structural modification process to explore the novel possibility on biological usefulness. Recently, the construction of tetrahydrocurcumin pyrazole (TP) derivative was reported and this compound also showed the cytotoxic activity against some cancer cell lines,[2] as THC and pyrazole were well known with their bioactivities.[3-6] Therefore, we conceptually design to attach the indolic moiety into the TP core structure based on the hybrid strategy. As natural compounds containing indole unit were found in many plants and marine natural products, there have been the numerous investigations involving the drug discovery and development process with hope to find lead compounds.[7-12] Particularly, the indolic compounds have received attention as they exhibited antioxidant,[13-15] anti-HIV,[16-18] anti-microbial,[19-23] anti-rheumatoidal,[24] anti-convulsant,[25] anti-inflamatory[26-28] and anticancer[29-31] properties. Accordingly, the combination of these two anti-carcinogenic units might provide very interesting synergistic effect and significantly improved activities. Our research group has investigated the synthesis of hybrid compounds as anticancer agents. The incorporation of indole moiety with TP derivative by using the amide coupling is presented. It would be interesting to investigate the cytotoxic activity of synthesized hybrid molecules against different types of cancer cell lines.

Methodology:
General procedure: All chemicals were used as received from standard chemical suppliers unless otherwise stated. All reactions were monitored by thin layer chromatography (TLC) on aluminum sheets coated with silica gel containing a fluorescent indicator (Merck) and were visualized under UV light with wavelength 254 nm, iodine or potassium permanganate solution. Flash column chromatography was carried out on Silica 60 (Fisher Matrix). Evaporation refers to rotary evaporation of solvent. IR spectra were recorded on a Perkin-Elmer Spectrum GX 60237 and Perkin-Elmer FT-IR spectrum 400 spectrometers. Spectra of solid samples were recorded as ATR. The ^{1}H and ^{13}C NMR spectra were measured on a Bruker AVANCE 400 spectrometer and a Burker ASCEND 400 spectrometer operating at 400 MHz. The chemical shifts (δ_H and δ_C) were recorded in ppm with reference to residual

solvent signal, $CDCl_3$ (δ_H 7.24, δ_C 77.23). High resolution mass spectra (HRMS) were recorded on a Bruker Daltomics microOTOF-QII mass spectrometer with an electrospray ionization (ESI) source.

Procedure for the synthesis of tetrahydrocurcumin pyrazole (TP): To a stirred solution of THC (190 mg, 0.51 mmol) in glacial acetic acid (10 mL) was added hydrazine monohydrate (86 µL, 1.78 mmol). The reaction mixture was stirred at 65 °C for 5 h. The reaction was concentrated under reduced pressure to give a crude residue. Water (10 mL) and ethyl acetate (10 mL) were added. The organic phase was separated and the aqueous phase was extracted with EtOAc (3 × 10 mL). The combined organic phases were washed with brine (10 mL), dried over anhydrous Na_2SO_4, filtered and concentrated under reduced pressure to give a crude product. Purification was performed by column chromatography on silica gel eluting with 4% $MeOH/CH_2Cl_2$ to afford TP (115 mg, 61%).

TP: yellow solid; R_f = 0.63; mp 79–81 °C. ^{1}H NMR (400 MHz, $CDCl_3$) δ 6.81 (2H, d, J = 7.9 Hz, ArH), 6.66 (2H, d, J = 8.0 Hz, ArH), 6.64 (2H, s, ArH), 5.83 (1H, s, CH), 4.46 (2H, s (br), OH), 3.82 (6H, s, 2×OCH_3), 2.90-2.82 (8H, m, 4×CH_2); ^{13}C NMR (100 MHz, $CDCl_3$) δ 148.3 (2×$C_{Pyrazole}$), 146.5 (2×$C_{Ar}OCH_3$), 144.0 (2×$C_{Ar}OH$), 133.2 (2×C_{Ar}), 120.9 (2×CH_{Ar}), 114.3 (2×CH_{Ar}), 111.1 (2×CH_{Ar}), 102.7 (COCHCO), 55.9 (2×OCH_3), 50.7 (CH_2), 35.3 (2×CH_2), 29.2 (CH_2); IR ν_{max} neat (cm^{-1}): 2935 (w), 2879 (w), 1334 (m), 1155 (s), 1101 (m), 814 (m); HRMS (ESI): Calcd. for $C_{23}H_{23}N_2O_4$: 391.1652 found 391.1658.

Typical procedure for the synthesis of tetrahydrocurcumin pyrazole indole (TPI) derivatives

To a stirred solution of the corresponding indole acid (0.10 mmol) in DMF (0.5 mL) was added EDCI (0.10 mmol), HOBt (0.10 mmol) and a solution of TP (0.08 mmol) in DMF (2 mL). The reaction mixture was stirred at room temperature for 15 h before it was quenched with water (10 mL). The organic phase was separated and the aqueous phase was extracted with EtOAc (3 × 15 mL). The combined organic phases were washed with brine (10 mL), dried over anhydrous $MgSO_4$, filtered and concentrated under reduced pressure to give the crude product as a brown oil. Purification was accomplished by column chromatography on silica gel eluting with 8% $EtOAc/CH_2Cl_2$ to afford the corresponding TPI derivatives (TPI1- TPI3).

TPI1: pale yellow viscous oil; R_f = 0.74. ^{1}H NMR (400 MHz, $CDCl_3$) δ 8.11 (1H, s, NH), 7.70 (1H, d, J = 7.8 Hz, ArH_{Indole}), 7.35 (1H, d, J = 8.1 Hz, ArH_{Indole}), 7.17 (1H, t, J = 7.6 Hz, ArH_{Indole}), 7.12 (1H, t, J = 7.8 Hz, ArH_{Indole}), 7.08 (1H, s, CH_{Indole}), 6.82 (1H, d, J = 8.0 Hz, ArH_{THC}), 6.77 (1H, d, J = 8.4 Hz, ArH_{THC}), 6.68 (2H, s, ArH_{THC}), 6.63-6.10 (2H, m, ArH_{THC}), 5.92 (1H, s, =CH_{THC}), 5.51 (1H, s (br), OH), 5.45 (1H, s (br), OH), 3.80 (3H, s, OCH_3), 3.78 (3H, s, OCH_3), 3.20 (2H, t, J = 7.6 Hz, CH_{2THC}), 2.91 (4H, s, CH_{2THC}), 2.80 (2H, t, J = 7.6 Hz, CH_{2THC}); ^{13}C NMR (100 MHz, $CDCl_3$) δ 171.9 (C=O), 171.2 (C=N_{THC}), 155.2 ($C_{Ar}OCH_3$), 148.1 ($C_{Ar}OCH_3$), 146.4 ($C_{Ar}OH$), 143.8 ($C_{Ar}OH$), 143.7 (=CNCO), 136.0 ($C_{ArIndole}$NH), 133.3 (C_{ArTHC}), 132.9 (C_{ArTHC}), 127.5 ($C_{ArIndole}$), 123.8 (=$CH_{ArIndole}$NH), 122.1 (2×CH_{ArTHC}), 121.0 ($CH_{ArIndole}$), 119.6 ($CH_{ArIndole}$), 119.1 ($CH_{ArIndole}$), 114.3 (CH_{ArTHC}), 114.1 ($CHAr_{THC}$), 111.1 (CH_{ArTHC}), 111.0 (CH_{ArTHC}), 110.9 ($CH_{ArIndole}$), 109.6 ($CH_{ArIndole}$), 108.4 (CH_{THC}), 60.3 (OCH_3), 55.8 (OCH_3), 36.3 ($CH_{2Indole}$), 34.6 (CH_{2THC}), 30.6 (CH_{2THC}), 21.0 (CH_{2THC}), 20.2 ($CH_{2Indole}$), 14.2 (CH_{2THC}); IR ν_{max} neat (cm^{-1}): 3391 (w), 2926 (w), 2858 (w), 1716 (s), 1513 (s), 1454 (m), 1428 (m). HRMS (ESI): Calcd. for $C_{31}H_{31}N_3O_5Na$: 548.2164 found 548.2155.

TPI2: white solid; Rf = 0.55; mp 126–127 °C. ^{1}H NMR (400MHz, $CDCl_3$) δ 7.97 (1H, s, NH), 7.67 (1H, d, J = 7.8 Hz, ArH_{Indole}), 7.34 (1H, d, J = 8.0 Hz, ArH_{Indole}), 7.18 (1H, dd, J = 7.3, 7.6 Hz, ArH_{Indole}), 7.11 (1H, dd, J = 7.7, 7.1 Hz, ArH_{Indole}), 7.04 (1H, s, =CH), 6.81 (1H, d, J = 8.6 Hz, ArH_{THC}), 6.80 (1H, d, J = 7.8 Hz, ArH_{THC}), 6.68 (2H, s, ArH_{THC}), 6.67 (1H, d, J = 7.8 Hz, ArH_{THC}), 6.67 (1H, d, J = 7.6 Hz , ArH_{THC}), 5.92 (1H, s, =CH_{THC}), 5.48 (1H, s, OH), 5.47 (1H, s, OH), 3.84 (3H, s, OCH_3), 3.81 (3H, s, OCH_3), 3.52 (1H, t, J = 7.4 Hz, CH_{2THC}), 3.52 (1H, t, J = 7.8 Hz, CH_{2THC}), 3.25-3.20 (4H, m, CH_{2THC}), 2.85-2.80 (6H, m, $CH_{2Indole}$, 2×CH_{2THC}); ^{13}C NMR (100 MHz, $CDCl_3$) δ 173.4 (C=O), 171.2 (C=$N_{Pyrazole}$), 155.3 ($C_{Ar}OCH_3$), 147.7 ($C_{Ar}OCH_3$), 146.4 ($C_{Ar}OH$), 143.9 ($C_{Ar}OH$), 143.8 (=CNH), 136.3 ($C_{ArIndole}$NH), 133.2 (C_{ArTHC}), 133.0 (C_{ArTHC}), 127.3 ($C_{ArIndole}$), 122.0 (CH_{ArTHC}), 121.6 (CH_{Ar}THC), 121.1

($CH_{ArIndole}$), 119.3 ($CH_{ArIndole}$), 118.9 ($CH_{ArIndole}$), 115.1 ($C_{ArIndole}$), 114.2 (2×$CH_{ArIndole}$), 114.1 (2×CH_{ArTHC}), 111.1 ($CH_{ArIndole}$), 110.9 (CH_{ArTHC}), 109.4 (CH_{ArTHC}), 60.4 (OCH_3), 55.5 (OCH_3), 36.3 (CH_{2THC}), 34.5 (CH_{2THC}), 30.5 (CH_{2THC}), 21.3 (CH_{2THC}), 20.2 ($CH_{2Indole}$), 14.2 (CH_{2THC}); IR ν_{max} neat (cm^{-1}): 3404 (w), 2934 (w), 2845 (m), 1720 (s), 1509 (s), 1449 (m), 1433 (m); HRMS (ESI): Calcd. for $C_{32}H_{33}N_3O_5Na$: 562.2312 found 562.2305.

TPI3: white solid; Rf = 0.63; mp 138–139 °C. ^{1}H NMR (400MHz, $CDCl_3$) δ 7.94 (1H, s (br), NH), 7.62 (1H, d, J = 7.8 Hz, ArH_{Indole}), 7.34 (1H, d, J = 8.0 Hz, ArH_{Indole}), 7.17 (1H, d, J = 7.4 Hz, ArH_{Indole}), 7.09 (1H, d, J = 7.6 Hz, ArH_{Indole}), 7.09 (2H, d, J = 7.6 Hz, ArH_{THC}), 6.82 (2H, d, J = 8.5 Hz, ArH_{THC}), 6.69 (2H, s, ArH_{THC}), 6.68 (2H, d, J = 8.5 Hz, ArH_{THC}), 5.91 (1H, s CH), 5.47 (3H, s, OH), 5.46 (3H, s, OH), 3.85 (3H, s, OCH_3), 3.84 (3H, s, OCH_3), 3.23-3.18 (4H, m, $CH_{2Indole}$, CH_{2THC}), 2.90-2.81 (6H, m, $CH_{2Indole}$, 2×CH_{2THC}), 2.17 (2H, quintet, J = 7.4 $CH_{2Indole}$); ^{13}C NMR (100 MHz, $CDCl_3$) δ 174.1 (C=O), 171.2 (C=$N_{Pyrazole}$), 155.1 ($C_{Ar}OCH_3$), 147.1 (2×$C_{Ar}OCH_3$), 147.7 (2×$C_{Ar}OCH_3$), 146.4 ($C_{Ar}OH$), 143.9 ($C_{Ar}OH$), 143.8 (=CNH), 136.4 ($C_{ArIndole}NH$), 133.3 ($C_{Ar\ THC}$), 133.0 ($C_{Ar\ THC}$), 127.9 ($C_{ArIndole}$), 121.9 (CH_{ArTHC}), 121.4 ($CH_{Ar\ THC}$), 121.0 ($CH_{ArIndole}$), 119.2 ($CH_{ArIndole}$), 118.9 ($CH_{ArIndole}$), 115.9 ($C_{ArIndole}$), 114.2 ($CH_{ArIndole}$), 111.0 ($CH_{Ar\ THC}$), 110.9 (4×CH_{ArTHC}), 109.3 ($CH_{Pyrazole}$), 60.4 (OCH_3), 55.9 (OCH_3), 35.2 (CH_{2THC}), 34.6 (CH_{2THC}), 34.4 (CH_{2THC}), 30.5 (CH_{2THC}), 24.8 (CH_2CO), 21.0 ($CH_{2Indole}$), 14.2 ($CH_{2Indole}$); IR ν_{max} neat (cm^{-1}): 3403 (w), 2938 (w), 2841 (w), 1720 (m), 1509 (s), 1454 (m), 1433 (m), 1371 (m); HRMS (ESI): Calcd. for $C_{33}H_{35}N_3O_5Na$: 576.2468 found 576.2462.

Results and Discussion: The initial target was the synthesis of THC pyrazole indole (TPI) derivatives by the direct condensation of hydrazide indoles with THC (Figure 1). The synthesis commenced by building the methyl ester of the commercially available indole acid with a different number of methylene linkers (n = 1-3). Subsequent nucleophilic addition reaction of indole methyl esters by treatment with hydrazine monohydrate provided the corresponding indole hydrazides (n = 1-3) in excellent yields. The synthetic hydrazides were then exposed to the direct condensation by using *p*-toluenesulfonic acid (*p*-TSA) as a catalyst in ethanol and heated at 45 °C for 5 h. The reaction of indole hydrazides and THC did not provide the desired products. When the indole hydrazide with one methylene group between carbonyl and indole core structure (n =1) was reacted with THC, it was found that only starting material THC and TP were obtained in 40% and 49% yields, respectively. The similar result was observed in the case of using the indole hydrazide (n = 2) which provided the higher yield of TP in 60% yield and 20% yield of recovered starting material. By extending the linking chain, the use of the indole hydrazide (n = 3) for the direct condensation was attempted. Unfortunately, the reaction did not proceed successfully, but only 40% of the starting material and 35% of TP were obtained (Figure 1). It is believed that the formation of TPs involved hydrolysis of amide functionality in TPIs.

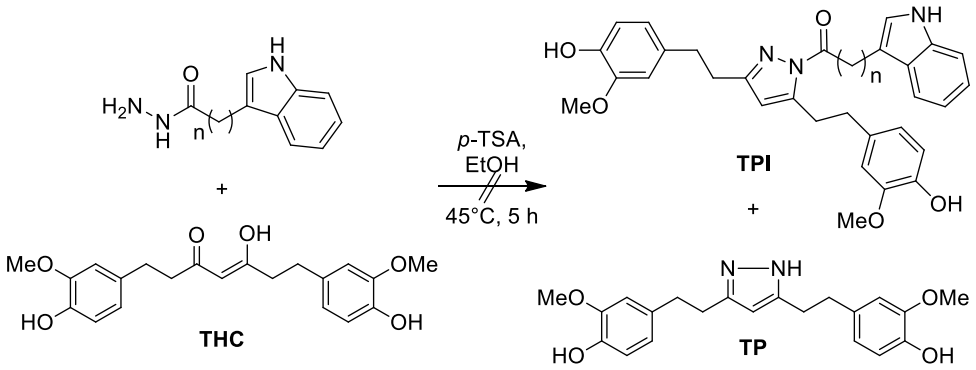

TPI1, n=1, 0%, **TP**, 49%, **THC**, 40%
TPI2, n=2, 0%, **TP**, 60%, **THC**, 20%
TPI3, n=3, 0%, **TP**, 35%, **THC**, 40%

Figure 1. Attempted synthesis of THC pyrazole indoles (TPI) by direct condensation

In order to obtain the target TPI derivatives, an alternative method by using the simple coupling method was explored. The synthesis of TP by the condensation of 1,3-dicarbonyl group in THC molecule with hydrazine monohydrate in the presence of acetic acid as a catalytic solvent was achieved, followed by heating at 65 °C for 5 h, resulting in formation of the expected product in good yield.[3,32] The TP product was then further coupled with the corresponding indole acids (n = 1-3) in the presence of the coupling agents EDCI and HOBt for amide bond formation to produce the desired TPI products in moderate to good yields (Figure 2).

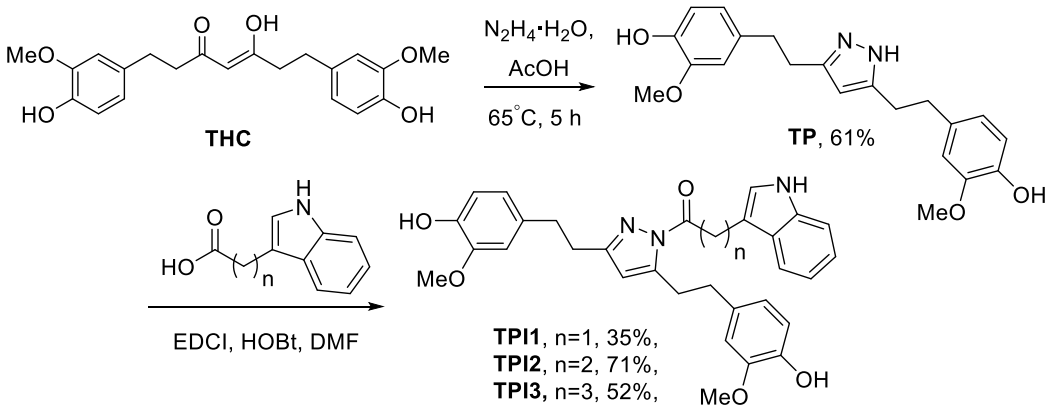

Figure 2. The synthesis of TPI derivatives

THC, TP and three TPI derivatives were evaluated for *in vitro* cytotoxic activity against four cancer cell lines including HeLa, PC-3, HT-29 and MCF-7 cell lines (Table 1).

Table 1. Cytotoxic activity of the synthesized compounds

Compound	Cell lines (IC_{50} (µg/mL))			
	HeLa	PC-3	HT-29	MCF-7
THC	51.69 ± 1.393	50.01 ± 2.53	52.53 ± 0.970	27.71 ± 4.405
TP	31.22 ± 3.997	48.67 ± 2.50	53.64 ± 1.757	57.80 ± 4.463
TPI1	29.08 ± 0.533	28.65 ± 4.55	27.12 ± 0.916	35.42 ± 1.66
TPI2	25.55 ± 0.808	17.41 ± 1.26	23.92 ± 0.435	29.20 ± 1.882
TPI3	7.00 ± 0.839	12.93 ± 1.63	11.53 ± 0.505	21.31 ± 0.793
Doxorubicin	0.68 ± 0.044	0.67 ± 0.068	1.65 ± 0.221	0.317 ± 0.045

The preliminary studies of the cytotoxic activity of the synthesized compounds revealed that the hydrogenated curcumin (THC) exhibited relatively higher cytotoxic activity against MCF-7 cell lines than other three cancer cell lines. TP differing from THC in the replacement of the 1,3-dicarbonyl moiety with a pyrazole unit displayed comparable inhibitory activity against PC-3 and HT-29 cell lines, better activity against HeLa and much lower activity against MCF-7 as shown in Table 1. Interestingly, TPI1, which was derived from the coupling of indole acid (n =1) to TP, demonstrated better cytotoxicity against all cancer cell lines compared to those of TP. Moreover, when TPI2 with longer linking chain (n = 2) showed higher activity against all tested cell lines with the IC_{50} values of 25.55 ± 0.808, 17.41 ± 1.26, 23.92 ± 0.435 and 29.20 ± 1.882 µg/mL for HeLa, PC-3, HT-29 and MCF-7 cell lines, respectively.

As expected, TPI3, containing methylene carbon (n = 3) in the linking chain, exhibited the most potent cytotoxicity with IC_{50} values against HeLa, PC-3, HT-29 and MCF-7 cell lines of 7.00 ± 0.839, 12.93 ± 1.63, 11.53 ± 0.505 and 21.31 ± 0.793 µg/mL, respectively. Especially, TPI3 was approximately 3.7-fold more potent than that of TPI2 against HeLa cell lines. However, all of TPIs were much less active than the reference drug, doxorubicin. As the relationship between "n" and cytotoxicity against cancer cells has never been reported, the further work for the development of these types of compounds with longer methylene linking chain will be investigated in order to obtain TPI analogues with better cytotoxic activity against these cell lines.

Conclusion: THC, TP and TPI derivatives were successfully synthesized and evaluated for their anticancer properties. Among them, TPI3 displayed the most potent activity against HeLa, PC-3, HT-29 and MCF-7 cell lines. In addition, this investigation revealed the synergistic effect between three important components; THC, pyrazole, and indole moieties.

References:

1. Prasad S, Tyaki AK, Aggarwal BB. Cancer Res Treat. 2014;46(1):2–18.
2. Mahal A, Wu P, Jiang Z-H, Wei X. Nat Prod Bioprospect. 2017;7:461–469.
3. Xu X-Y, Meng X, Li S, Gan R-Y, Li Y, Li H-B. Nutrients. 2018;10:1–33.
4. Wright LE, Frye JB, Gorti B, Timmermann BN, Funk JL. Curr Pharm Des. 2013;19(34): 6218–6225.
5. Rajeswari A, Sabesan M. Inflammopharmacology. 2008;16:96–99.
6. Yoysungnoen B, Bhattarakosol P, Patumraj S, Changtum C. BioMed Research International. 2015:1–11.
7. Gul W, Hamann MT. Life Sci. 2005;78:442–453.
8. Brandi G, Paiardini M, Cervasi B, Fiorucci C, Filippone P, Marco CD, Zaffaroni N, Magnani M. Cancer Res. 2003;63:4028–4036.
9. Nguyen HH, Lavrenov SN, Sundar SN, Nguyen DHH, Tseng M, Marconett CN, Kung J, Staub RE, Preobrazhenskaya MN, Bjeldanes LF, Firestone GL. Chem-Biol Interact. 2010; 186: 255–266.
10. Singh P, Mittal A, Bhardwaj A, Kaur S, Kumar S. Bioorg Med Chem Lett. 2008;18:85–89.
11. Chadha N, Silakari O. Eur J Med Chem. 2017;134:159–184.
12. Sravanthi TV, Manju SL. Eur J Pharm Sci. 2016;91:1–10.
13. Kim WG, Lee IK, Kim JP, Ryoo IJ, Koshino H, Yoo ID. J Nat Prod 1997;60:721–723.
14. Maharaj DS, Glass BD, Daya S. Biosci Rep. 2007;27:299–320.
15. Shanthi G, Perumal P, Rao U, Sehgal PV. Indian J Chem. 2009;48B:1319–1323.
16. Ravichandran V, Shalini S, Venkateskumar K, Dhanaraj SA. Famacia. 2016;64:745–756.
17. Sanna G, Madeddu S, Gilliberti G, Piras S, Struga M, Wrzosek M, Kobiak-Tomaszewska G, Koziol AE, Savchenko O, Lis T, Stefanska J, Tomaszewski P, Skrzycki M, Szulczyk D. Molecules. 2018;23:1–17.
18. Silvestri R, Artico M, Bruno B, Massa S, Novellino E, Greco G, Marongiu ME, Pani A, De Montis A, La Colla P. Antiviral Chem Chemother. 1998;9:139–148.
19. Pereira ER, Sancelme M, Towa J-J, Prudhomme M, Martre A-M, Mousset G, Rapp M. J Antibiot. 1996;46:380–385.
20. Pathak VN, Gupta R, Gupta N. Indian J Chem. 2008;47B:1303–1307.
21. Ambrus JI, Kelso MJ, Bremner JB, Ball AR, Casadei G, Lewis K. Bioorg Med Chem. 2008;18:4294–4297.
22. Gurkok G, Altanlar N, Suzen S. Chemotherapy. 2009;55:15–19.
23. Panchal RG, Ulrich RL, Lane D, Butler MM, Houseweart C, Opperman T, Williams JD, Peet NP, Moir DT, Nguyen T, Gussio R, Bowlin T, Bavari S. Antimicrob Agents Chemother. 2009;53;4283–4291.

24. Hasan H, Ismail H, El-Orfali Y, Khawaja G. BMC Complement Altern Med. 2018;18:1–12.
25. Gitto R, De Luca L, Ferro S. Bioorg Med Chem. 2009;17:1640–1647.
26. Rani P, Srivastava VK, Kumar A. Eur J Med Chem. 2004;39:449–452.
27. Vo QV, Trenerry C, Rochfort S, Waddeson J, Leyton C, Hughes AB. Bioorg Med Chem. 2014;22:856–864.
28. MacDonough MT, Strecker TE, Hamel E, Hall JJ, Chaplin DJ, Trawick ML, Pinney KG. Bioorg Med Chem. 2013;21:6831–6843.
29. Zhang F, Zhao Y, Sun L, Ding L, Gu Y, Gong P. Eur J Med Chem. 2011;46:3149–3157.
30. Zhou Y, Duan K, Zhu L, Liu Z, Zhang C, Yang L, Li M, Zhang H, Yang X. Bioorg Med Chem Lett. 2016;26:460–465.
31. Fortes MP, da Silva PBN, da Silva TG, Kaufman TS, Militão GCG, Silverira CC. Eur J Med Chem. 2016;118:21–26.
32. Jordan BC, Kumar B, Thilagavathi R, Yadhav A, Kumar P, Selvam C. Chem Biol Drug Des. 2018;91(1):332–337.

Acknowledgements: This work was supported by the Center of Excellence for Innovation in Chemistry (PERCH-CIC), Research and development Institute and the Department of Chemistry, Faculty of Science, Ramkhamhaeng University. We would like to thank Assistant Professor Dr. Anawat Ajavakom from Department of Chemistry, Chulalongkorn University for his valuable advice.

C3_004_PF: FORMALDEHYDE FLUORESCENT SENSORS FROM 1,8-NAPHTHALIMIDE DERIVATIVES

Apicha Maharat[1,3], Paitoon Rashatasakhon[2,3,*]
[1]Program of Petrochemistry and Polymer Science, Faculty of Science, Chulalongkorn University, Phayathai Road, Pathumwan, Bangkok 10330, Thailand
[2]Department of Chemistry, Faculty of Science, Chulalongkorn University, Bangkok 10330, Thailand
[3]Nanotec-CU Center of Excellence on Food and Agriculture, Department of Chemistry, Faculty of Science, Chulalongkorn University, Bangkok 10330, Thailand
[*]E-mail: paitoon.r@chula.ac.th; Fax: +66 (2) 2187598; Tel: +66 (2) 2187633

Abstract: Three derivatives of 1,8-naphthalimide were systematically designed and synthesized in order to investigate the effect of substitution pattern on their photophysical properties and sensing behaviors towards formaldehyde in aqueous media. The key substituents, the hydrazino ($-NHNH_2$) and the 2-methoxyethylamino groups ($-NHCH_2CH_2OCH_3$), were installed at the 4-position of 1,8-naphthalimide by a nucleophilic replacement, and at the imide position by a condensation reaction with 1,8-naphthalic anhydride precursor. All target compounds were obtained in good overall yields of 60-80%. Due to the photo-induced electron transfer, these compounds were relatively less emissive compared to typical 1,8-naphthalimide derivatives. A preliminary screening revealed that their fluorescence signals increase upon addition of formaldehyde. The compound with two hydrazine groups exhibited the 5-fold fluorescence enhancement by formaldehyde in 5% aqueous acetic acid solution with a detection limit of 3.0 ppm.

Introduction: Formaldehyde has been involved in many applications such as building materials, household products, cosmetics, drug, and food. However, it has been classified as a toxic and carcinogenic substance.[1, 2] Even at a low concentration, formaldehyde can cause severe health conditions including allergies, brain infarction, and headache.[3, 4] In order to raise awareness of this highly toxic chemical, the International Agency for Research on Cancer (IARC) categorized formaldehyde in Group I as carcinogenic to humans, while the World Health Organization (WHO) suggested a daily limit of formaldehyde exposure to 0.15 mg/kg of the body weight.[5] Therefore, newly developed and more effective detection methods for formaldehyde is of great importance.

A number of analytical techniques such as high-performance liquid chromatography (HPLC), gas chromatography (GC), mass spectrophotometry (MS), quartz crystal microbalance (QCM) have been used for qualitative and quantitative analysis of formaldehyde.[6, 7, 8, 9] Although they often provide excellent sensitivity and precision, the issues on high instrument costs, complicated operation, and tedious sample preparation could sometime prevent the use of these techniques. To this end, fluorescence spectroscopy has become a favorable analytical method since it could avoid the above-mentioned drawbacks, yet could still provide high sensitivity and selectivity.

In this work, we report a design and synthesis of three fluorescent probes for formaldehyde which contain a highly fluorescent 1,8-naphthalimide core and a reactive hydrazino group ($-NHNH_2$) that could serve as a reacting site with formaldehyde. The structures of these target compounds are shown in Figure 1. The different substitution position of the hydrazine and the hydrophilic 2-methoxyethyl group in R1 and R2 could lead to different sensitivity towards formaldehyde detection, thus allowing us to understand the substituent effect on fluorescent sensing mechanism for this class of compounds.

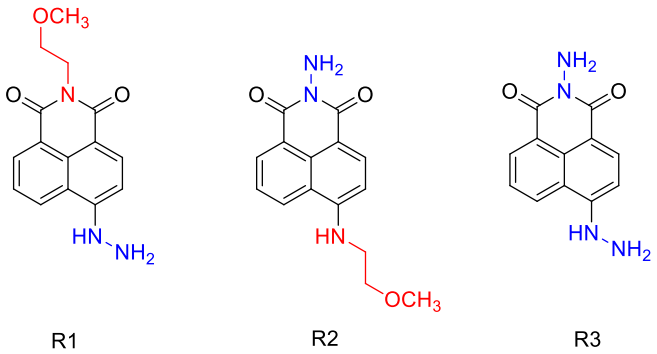

Figure 1. Structures of naphthalimide derivatives R1-R3

Methodology: All reagents and solvents used in the reactions were reagent grade purchased from Sigma–Aldrich (USA), Fluka®(Switzerland), or Merck®(Germany). Solvents for reaction workup and chromatography were bulk commercial grade and distilled prior to use. Analytical thin layer chromatography (TLC) was carried out on Merck Kieselgel 60 F254 aluminum-backed silica plates (Merck KgaA, Darmstadt, Germany). Flash column chromatography was performed using Merck Kieselgel 60G silica gel and eluting with the solvent system stated. ^{1}H NMR spectra was determined on a Varian Mercury NMR spectrometer, which operated at 400 MHz. Absorption spectra were measured by using Shimadzu UV-2550 UV–vis spectrophotometer. Fluorescence spectra were recorded on a Varian Cary Eclipse spectrofluorometer.

Synthesis of R1: This compound was prepared per a literature procedure with a slight modification.[10] A mixture of 4-bromo-1,8-naphthalic anhydride (5.00 g, 18.04 mmol), 2-methoxyethylamine (3.14 mL, 36.08 mmol) and glacial acetic acid (50 mL) were heated under reflux for 4 h. After the reaction was completed, the reaction mixture was allowed to cool to room temperature. The resulting solid was filtered, washed with water, and dried under vacuum. This initial product was then mixed with 80% hydrazine hydrate (2.32 mL, 47.84 mmol) and ethanol (40 mL) and the mixture was refluxed for 2 h. After cooling to room temperature, the reaction mixture was evaporated to yield the crude product, which was further purified by column chromatography on silica gel using hexane/ethyl acetate (2:1, v/v) as the eluent to afford R1 as an orange solid in 87% yield. ^{1}H NMR (400 MHz, DMSO-d_6) δ 9.10 (s, 1H, -*NH*), 8.56 (d, *J* =7.7 Hz, 1H, -C^{7}_{aro}*H*), 8.36 (d, *J* = 7.7 Hz, 1H, -C^{5}_{aro}*H*), 8.24 (d, *J* = 8.5 Hz, 1H, -C^{2}_{aro}*H*), 7.59 (t, *J* = 7.7 Hz, 1H, -C^{6}_{aro}*H*), 7.21 (d, *J* = 8.5 Hz, 1H, -C^{3}_{aro}*H*), 4.67 (s, 2H, -NH_2), 4.19 (t, *J* = 6.2 Hz, 2H, -OCH_2), 3.55 (t, *J* = 6.2 Hz, 2H, -NCH_2), 3.25 (s, 3H, -*OCH3*); ^{13}C NMR (100 MHz, DMSO-d_6) δ 163.69, 162.82, 153.08, 134.10, 130.47, 129.20, 128.15, 123.92, 121.50, 118.33, 107.26, 103.89, 68.83, 57.86, 38.07.

Synthesis of R2: A mixture of 4-bromo-1,8-naphthalic anhydride (1.00 g, 3.61 mmol), hydrazine hydrate (0.70 mL, 14.4 mmol) and ethanol (10 mL) was stirred under reflux for 2 h. After cooling to room temperature, the resulting solid was filtered, washed with water, and dried under vacuum. The crude product was mixed with 2-methoxyethylamine (0.90 mL, 10.3 mmol) and glacial acetic acid 10 mL. The reaction was heated under reflux for 4 h. After the reaction was completed and allowed to cool to room temperature, a portion of CH_2Cl_2 (50 mL) was added, and the organic phase was washed with DI water. The organic phase was then dried over anhydrous Na_2SO_4 and concentrated under reduced pressure. The residue was purified by column chromatography using a mixture of hexane/ethyl acetate (1:1, v/v) as the eluent to give R2 as a light brown solid in 60% yield. ^{1}H NMR (400 MHz, DMSO-d_6) δ 8.69 (d, *J* = 7.9 Hz, -C^{7}_{aro}*H*), 8.43 (d, *J* = 7.9 Hz, 1H, -C^{5}_{aro}*H*), 8.24 (d, *J* = 8.6 Hz, 1H, -C^{2}_{aro}*H*), 7.85 (t, *J* = 5.1 Hz, 1H, -*NH*), 7.68 (t, *J* = 7.9 Hz, 1H, -C^{6}_{aro}*H*), 6.81 (d, *J* = 8.6 Hz, -C^{3}_{aro}*H*), 5.73 (s, 2H, -NH_2), 3.63 (t, *J* = 5.1 Hz, 2H, -OCH_2), 3.58 (t, *J* = 5.0 Hz, 2H, -NCH_2). 3.30 (s, 3H, -*OCH3*); ^{13}C NMR (100 MHz, DMSO-d_6)

160.10, 159.94, 150.80, 134.08, 130.38, 128.38, 127.75, 124.09, 121.22, 120.02, 107.09, 103.82, 69.68, 58.08, 42.56.

Synthesis of R3: A mixture of 4-bromo-1,8-naphthalic anhydride (1.00 g, 3.61 mmol), hydrazine hydrate (0.88 mL, 18.04 mmol) and ethanol (10 mL) was heated under reflux for 3 h. After cooling to room temperature, the precipitates were filtered, washed with water, dried under vacuum. The crude product was recrystallized twice using ethanol to afford R3 as an orange solid in 90% yield. The ^{1}H-NMR spectrum of this compound was in good agreement with the literature report.[11] ^{1}H NMR (400 MHz, DMSO-d_6) δ 9.20 (s, 1H, -*NH*), 8.62 (d, *J* = 7.5 Hz, 1H, -C^{7}_{aro}*H*), 8.42 (d, *J* = 7.5 Hz, 1H, -C^{5}_{aro}*H*), 8.28 (d, *J* = 8.7 Hz, 1H, -C^{2}_{aro}*H*), 7.64 (t, *J* = 7.5 Hz, 1H, -C^{6}_{aro}*H*), 7.24 (d, *J* = 8.7 Hz, 1H, -C^{3}_{aro}*H*), 5.72 (s, 2H, -NNH_2), 4.69 (s, 2H, -$NHNH_2$); ^{13}C NMR (100 MHz, DMSO-d_6) 160.17, 160.00, 153.48, 134.42, 134.32, 130.71, 130.46, 128.22, 127.21, 124.08, 118.49, 104.10.

Results and Discussion: The synthesis of R1-R3 is shown in Scheme 1. Starting from the commercially available 4-bromo-1,8-naphthalic anhydride, a condensation with 2-methoxyethylamine in glacial acetic acid followed by a nucleophilic aromatic replacement of the bromine group using hydrazine afforded R1 in an excellent yield of 87%. By switching the reaction order, compound R2 was achieved in a moderate yield of 60%. This lower yield of R2 was caused by the unexpected formation of a by-product (R3) in the reaction of 4-bromo-1, 8-naphthalic anhydride with hydrazine. Attempts to improve the yield of R2 by lowering the amount of hydrazine were unsuccessful since the competing reaction could still occur while the unreacted starting material remained. In the synthesis of R3, both condensation and nucleophilic substitution occurred in one pot and the target compound was obtained in an excellent yield of 90% after double recrystallization.

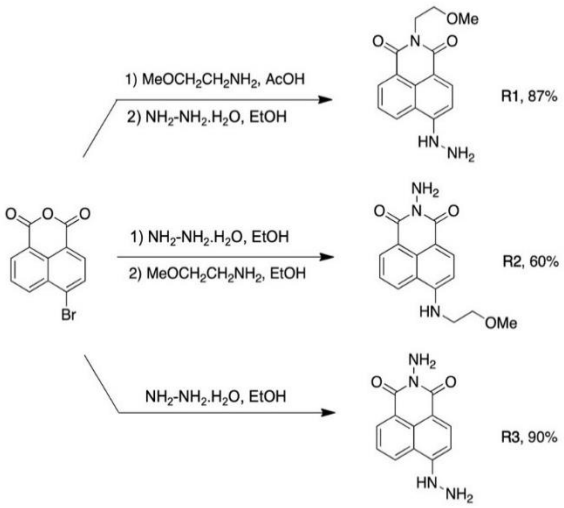

Scheme 1. Synthesis of R1-R3

The photophysical properties studies of R1-R3 were investigated in DMSO solution. The results are compiled in Table 1, while the UV-Vis and fluorescence spectra are shown in Figure 2. The maximum absorption wavelengths appeared at 416, 447, and 400 nm for compounds R1, R2 and R3, respectively. The molar extinction coefficients of these compounds were ranging between 3.5 x 10^3 and 8.4 x 10^3 M^{-1} cm^{-1}. The molar extinction coefficient for R2 was significantly higher than the others because the substitution of 2-methoxyethylamino at the 4-position of naphthalimide may result in a more extensive conjugated system. Each

fluorophore showed a single maximum emission wavelength at 515, 528 and 520 nm, respectively. This resulted in the green emission of R1-R3 under the blacklight. The longest emission maxima in R2 may result from the internal charge transfer from the electron-donating NH group to the electron-withdrawing naphthalimide C=O. The lowest quantum yield of R3 may result from the photo-induced electron transfer process from hydrazino group to the naphthalimide core.

Table 1. Photophysical properties of R1-R3 in DMSO.

Compound	Absorption		Emision	
	λ_{max} (nm)	ε (M^{-1} cm^{-1})	λ_{max} (nm)	Φ[a]
R1	416	4843	515	0.10
R2	447	8437	528	0.14
R3	400	3595	520	0.05

[a]Quinine sulfate in 0.1 M H_2SO_4 was used as the reference.

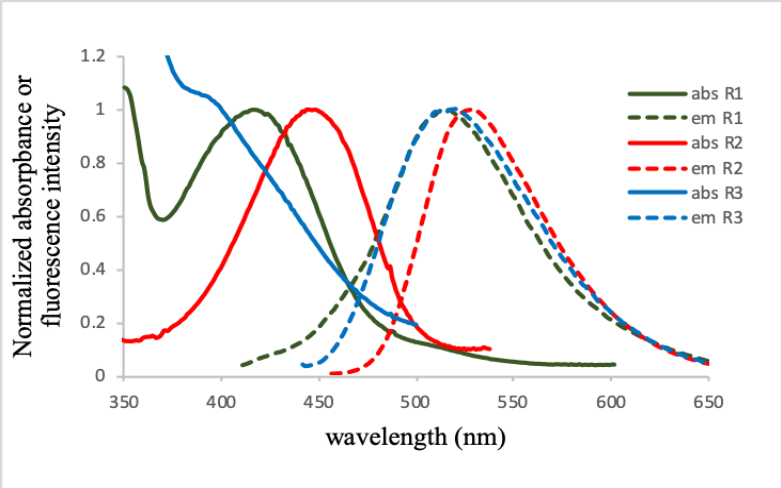

Figure 2. Normalized absorption and emission spectra of R1-R3 in DMSO.

With these three compounds in hands, their stock solutions were prepared in DMSO at 1 mM. Several samples of aldehyde such as formaldehyde, terephathaldehyde, naphthaldehyde, 3-methoxybenzaldehyde, 2-nitrobenzaldehyde, propionaldehyde, acetaldehyde, valeradehyde, and nonanal were also prepared in DMSO at 10 mM. The stock solutions of sensors (R1-R3) and analytes (aldehyde samples) were diluted with 5% acetic acid solution in water to achieve the final concentration of R1-R3 at 10 µM. The results in Figure 3 indicate that only R3 displayed an excellent selectivity towards formaldehyde with a 4.5-folds fluorescence enhancement. The impressive sensitivity of R3 towards formaldehyde may attribute to its lowest starting quantum yield, which can be enhanced upon a reaction between the hydrazino unit and formaldehyde. The formation of formaldehyde hydrazine could inhibit the photo-induced electron transfer, thus enhancing the emission signal. Meanwhile, the exceptional selectivity towards formaldehyde may result from its high reactivity in hydrazine formation with the sensor. The detection limit at three-time noise for the detection of formaldehyde using R3 was estimated to 0.1×10^{-3} mM or 3.0 ppm (Figure 4). A detailed investigation of the sensing mechanism is currently in progress and will be reported in due course.

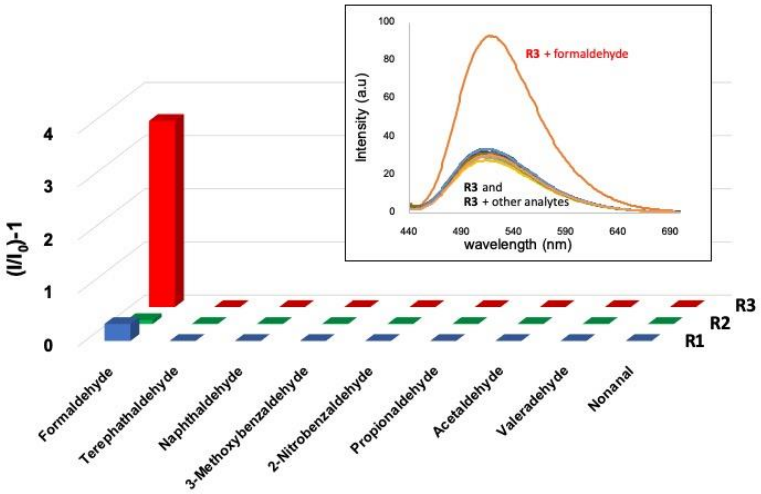

Figure 3. Fluorogenic responses of R1-R3 (10 µM) towards various aldehydes (1 mM). Inset shows the emission spectra of R3 in the presence of various aldehydes.

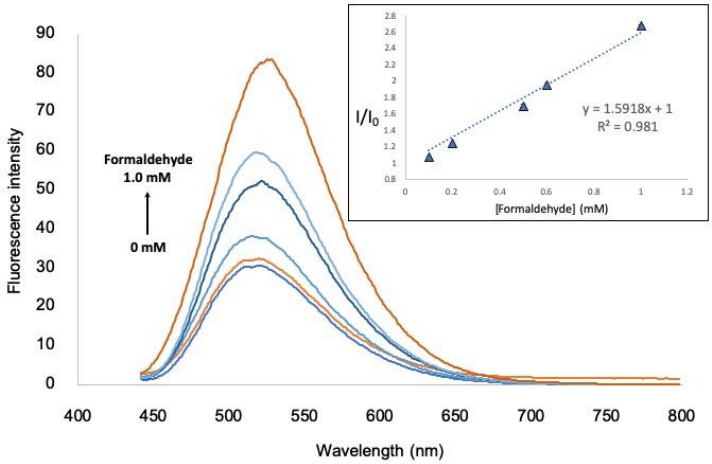

Figure 4. Fluorescence responses of R3 (10 µM) towards formaldehyde (0.1-1.0 mM)

Conclusion: Three derivatives of nathalimide were successfully synthesized from 4-bromo-1,8-naphthalic anhydride. Compound R3 exhibited an outstanding selective fluorescent enhancement towards formaldehyde with detection limit of 1.5 mM. The proposed sensing mechanism involving the inhibition of PET process between the hydrazine and naphthalimide moieties upon the formation of formaldehyde hydrazine is currently in progress.

References:

1. Powers PO. Ind Eng Chem Res. 1953;45:1063-1066.
2. Salthammer T. Angew Chem. 2013;52:3320-3327.
3. Saiki R, Park H, Ishii I, Yoshida M, Nishimura K, Toida T, Tatsukawa H, Kojima S, Ikeguchi Y, Pegg AE, Kashiwagi K, Igarashi K. Biochem Biophys Res Commun.2011;404:1044-1049.
4. Unzeta M, Sole M, Boada M, Hernandez M. J Neural Transm (Vienna). 2007;114:857-862.

5. Cogliano VJ, Grosse Y, Baan RA, Straif K, Secretan MB, El Ghissassi F. Environ Health Perspect. 2005;113:1205-1208.
6. Wahed P, Razzaq MA, Dharmapuri S, Corrales M. Food Chem. 2016;202:476-483.
7. Kato S, Burke PJ, Koch TH, Bierbaum VM. Anal Chem. 2001;73: 2992-2997.
8. Serrano M, Gallego M, Silva M. J Chromatogr A. 2016;1437:241-246.
9. Vellingiri K, Deep A, Kim KH, Boukhvalov DW, Kumar P, Yao Q. Sens Actuators B. 2017;241:938-948.
10. Vongnam K, Muangnoi C, Rojsitthisak P, Sukwattanasinitt M, Rashatasakhon P. Biosens Bioelectron. 2016;86:472-476.
11. Jiang SQ, Zhou ZY, Zhuo SP, Shan GG, Xing, LB, Wang HN, Su ZM. Dalton Trans. 2015;44:20830-20833.

Acknowledgements: This work is supported by the Nanotechnology Center (NA- NOTEC), NSTDA, Ministry of Science and Technology, Thailand.

C3_005_OF: THE PRELIMINARY STUDIES ON THE SYNTHESIS AND THE CYTOTOXICITY TOWARDS HepG2 AND Huh7 OF A NEW SERIES OF SORAFENIB ANALOGUES: REPLACEMENT OF ARYL UREA WITH A TRIAZOLE RING

Sarinya Palakhachane[1], Yuwaporn Ketkaew[2], Natthaya Chuaypen[2], Pisit Tangkijvanich[2], Apichart Suksamrarn[3], Panupun Limpachayaporn[1,*]

[1]Department of Chemistry, Faculty of Science, Silpakorn University, Nakhon Pathom 73000, Thailand

[2]Center of Excellence in Hepatitis and Liver Cancer, Faculty of Medicine, Chulalongkorn University, Bangkok 10330, Thailand

[3]Department of Chemistry and Center of Excellence for Innovation in Chemistry, Faculty of Science, Ramkhamhaeng University, Bangkok 10240, Thailand

*e-mail. panupun.lim@gmail.com, limpachayaporn_p@silpakorn.edu; tel. +66 34 255797; fax. +66 34 271356

Abstract: As a preliminary result, seven triazole-containing sorafenib analogues were synthesized successfully *via* Huisgen 1,3-dipolar cycloaddition (click reaction) followed by nucleophilic aromatic substitution. The structure of sorafenib (1), a multikinase inhibitor approved by the Food and Drug Administration of the United States (US FDA) for treatment of hepatocellular carcinoma (HCC), was modified by replacement of aryl urea with a 1,2,3-triazole linked to various substituted phenoxy ring. The *in vitro* cytotoxicity data revealed that the unsubstituted analogue 2a (R = H) was almost inactive. Compound 2e (R = *o*-NO_2) exhibited promising inhibitory activities with IC_{50} values of 72.0 and 52.5 μM towards HepG2 and Huh7, respectively, whereas 2d (R = *p*-F) and 2g (R = *p*-NO_2) inhibited Huh7 selectively with IC_{50} values of 64.4 and 21.1 μM, respectively. The most active synthetic inhibitors, 2e and 2g, were still ca. 19-fold and 7-fold, respectively, less active towards HepG2 and Huh7 compared to sorafenib (1). However, the preliminary results suggested that the triazole-containing sorafenib structure had the potential to be further developed for the improvement of anti-HepG2 and Huh7 activities. The substitution at the *o*- or *p*-position on the phenoxy part with a suitable functional group was the key factor for the successful activity improvement.

Introduction: Cancer is one of the most lethal disease with the second major of death worldwide at present.[1] Especially, hepatocellular carcinoma (HCC) is the sixth new cause of cancer in 2018.[2] It is one of the most serious health problems with a high mortality rate in Thailand.[3] The factors promoting liver cancer are alcoholism,[4] unbeneficial eating,[5] over body mass index (BMI)[6] as well as hepatitis B and C virus infection.[7] In the nineteen century, the operational methods for treatment of cancer are surgery, transplantation and chemotherapy depending on the stage, organ and type of cancer. However, chemotherapy can cause the molecular damages to both of cancer and normal cells.[8] The patients with HCC are usually diagnosed in malignant and metastasis phases.[9-10] The symptom cannot be recognized until the advanced stage leading to inefficient therapy in most cases. Nowadays, liver cancer at the advanced stage can be treated with the targeted drug sorafenib.[11]

Sorafenib (1) is a multikinase inhibitor which was approved by the Food and Drug Administration of the United States (US FDA) for the treatment of advanced HCC and renal cell carcinoma (RCC) in 2005.[11] Sorafenib inhibits a wide range of kinases including vascular endothelial growth factor (VEGFR),[12] RAS mutation,[13] and irregularity of MAP kinase pathways,[8] which are overexpressed in HCC and associated with cell growth, angiogenesis and cell proliferation.[14] However, sorafenib can prolong the survival of the HCC patients by less than 1 year.[8] Furthermore, FDA reports adverse effects such as hypertension, dermatitis, rash and hand-foot skin reaction, diarrhea and fatigue.[15] Additionally, sorafenib has low bioavailability leading to the use of high dosage of the drug.[16]

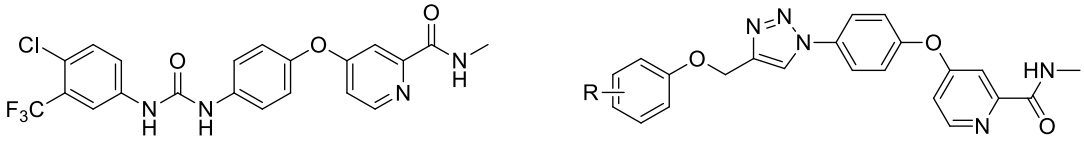

Figure 1. The chemical structure of sorafenib (1) and the general structure of 1,2,3-triazole-containing sorafenib analogues 2a-2g.

Due to the aforementioned disadvantageous profiles of sorafenib, many organic and medicinal chemists are, therefore, interested in the development of new anti-cancer agents for the treatment of HCC and other cancers relying on modification of the originally approved drug sorafenib. In the literature, the structure of sorafenib (1) was derivatized by replacement of picolinamide moiety,[17-18] benzene core[19-20] and diaryl urea.[21-23] Substituting picolinamide with trifluoromethyl imidazole[17] and indazole[18] resulted in inhibitory activities in variety of cancer cell lines including HepG2 and improved toxicity. Instead of a plain benzene core, incorporation of halogen into the benzene core, such as 2-chloro (Lenvatinib and Tivozanib),[20] 2-fluoro (Regorafenib)[20] and 3-fluoro,[19] improved anti-cancer activities significantly. The modification of aryl urea of sorafenib has limited examples. Disappointedly, attachment of 4,5-dihydro-1*H*-pyrazole with urea part of sorafenib led to decreased inhibitory activities towards HepG2 and other target cancer cell lines compared to sorafenib.[23] In addition, various amide groups,[22] thiazole[21] and 1,3,4-thiadiazole[21] were placed at the aryl urea of sorafenib. The urea-modified versions enhanced anti-cancer activities in PCL/PRF5, HeLa, A549, H460 and HT29. Replacing a 1,2,3-trizole at the urea part inhibited HT-29 and MCF-7, and was able to induce apoptosis in HT-29.[24] Unfortunately, their activities against human cancer cell lines were not reported. However, it was proven that modification at aryl urea of sorafenib by replacing with a heterocycle such as a triazole ring inhibited several cancer cell lines.

Herein, we aimed to synthesize a new series of 1,2,3-triazole-containing sorafenib analogues which the aryl urea was replaced by 1,2,3-triazole linked to a substituted phenoxy ring in order to improve the cytotoxicity towards human cancer cell lines (HepG2 and Huh7). These preliminary results will be our important guideline for design, synthetic methodology and improvement of anti-cancer activities of the inhibitors in the next generation.

Methodology:

Design: Most researchers are interested in sorafenib analogues, which aryl urea moiety must exist in the structure. However, urea fragment is usually aggregated itself[25] and its hydrogen bond donor, and acceptor characters introduced binding with varied plasma proteins.[26] For this reason, the new series of sorafenib analogues was challenged our group to replace aryl urea part by 1,2,3-triazole. According to X-ray co-crystal structure of sorafenib, *N*-methyl picolinamide, benzene core, and aryl urea interacted well in the ATP adenine pocket, hydrophobic pocket and hydrophobic pocket of B-raf and VEGFR2.[27] Thus, replacing aryl urea with 1,2,3-triaozle ring linked to lipophilic substituted phenoxy group might be possible to maintain or improve binding efficiency leading to similar or increased anti-HepG2 and Huh7 activities. Moreover, the triazole structure exists in many biologically active agents[28] including anti-cancer agents[24, 29] and is resistant to metabolism,[30] as well as, it can provide hydrogen bond acceptors and π-π interaction with the targets. Therefore, we designed a new series of 1,2,3-triazole-containing sorafenib analogues 2a-2g as depicted in Figure 1.

Materials: Chemicals and reagents used were purchased from Acros Organics, Sigma-Aldrich and Tokyo Chemical Industry (TCI). All reagents received were analytical grade

and used without purification, unless stated otherwise. Deionized water was used in this experiment. Preparative chromatographic separations were performed on silica gel 63-200 µm purchased from Merck. All reactions were followed by TLC analysis using precoated silica gel 60 TLC sheets (Merck) with fluorescent indicator (254 nm) and visualized with a UV lamp (254 and 365 nm).

Instruments: ^{1}H, ^{13}C and ^{19}F NMR spectra were recorded on a Bruker AVANCE III HD in Fourier transform mode at the field strength specified on a 300 MHz spectrometer. Spectra were obtained in $CDCl_3$ and DMSO-d_6 solutions using 5 mm diameter tubes, and chemical shifts in ppm (part per million) are quoted relative to either the internal standards, TMS (δ_H 0.00) or CF_3COOH (δ_F -76.55) or the residual signals of either $CDCl_3$ (δ_H 7.26, or δ_C 77.22) or DMSO-d_6 (δ_H 2.50, or δ_C 39.51). Data are reported as follows: chemical shifts, multiplicity, coupling constant. Multiplicities in the ^{1}H and ^{19}F NMR spectra are described as: s = singlet, d = doublet, t = triplet, q = quartet, m = multiplet, br = broad; coupling constants (*J*) are reported in Hz. High-resolution mass spectra (HRMS) are recorded using a Bruker Daltonics MicroTOF mass spectrometer with ESI+ mode and reported with ion mass/charge (*m/z*) ratios as values in atomic mass units.

Synthesis: 4-Azidophenol (7)[1] and 4-chloro-*N*-methyl picolinamide (9)[2] were prepared using the procedures reported previously. The syntheses of the required precursors, triazole rings and target sorafenib analogues were accomplished using the following procedures.

General procedure for propargyl derivatives: To a stirred suspension of phenol derivatives and Cs_2CO_3 in CH_3CN was added neat propargyl bromide or 80% propargyl bromide in THF dropwise. The resulting suspension was stirred at room temperature or heated to reflux. The reaction mixture was diluted with water and extracted with EtOAc to provide propargyl derivatives (5a-5g), which was purified by column chromatography to give the desired product.

Synthesis of (pro-2-yn-1-yloxy)benzene (5a): Phenol (3a) (0.20 mL, 2.27 mmol), propargyl bromide (4) (80% w/w in toluene, 0.40 mL, 2.34 mmol), Cs_2CO_3 (0.94 g, 2.90 mmol) and CH_3CN (6.0 mL) were heated at reflux for 5 h. The crude product was purified by silica gel column chromatography (hexane) to give 5a (130.3 mg, 0.99 mmol, 44%) as a peach liquid. ^{1}H NMR (300 MHz, $CDCl_3$) δ 2.52 (t, *J* = 2.4 Hz, 1H), 4.69 (d, *J* = 2.4 Hz, 2H), 6.99 (m, 3H), 7.31 (m, 2H); ^{13}C NMR (75 MHz, $CDCl_3$) δ 30.9, 55.7, 76.7, 113.8 (2C), 121.9, 129.5 (2C), 157.6.

Synthesis of 1-fluoro-2-(pro-2-yn-1-yloxy)benzene (5b): 2-Fluorophenol (3b) (1.40 g, 12.5 mmol), propargyl bromide (4) (80% w/w in toluene, 2.5 mL, 20.8 mmol), Cs_2CO_3 (3.94 g, 12.1 mmol) and CH_3CN (70 mL) were heated at reflux for 4 h. The crude product was purified by silica gel column chromatography (hexane) to give 5b (1.72 g, 11.5 mmol, 92%) as a colorless oil. ^{1}H NMR (300 MHz, DMSO-d_6) δ 3.61 (t, *J* = 2.3 Hz, 1H), 4.88 (d, *J* = 2.4 Hz, 2H), 6.94-7.02 (m, 3H), 7.11-7.26 (m, 1H); ^{13}C NMR (75 MHz, DMSO-d_6) δ 56.4, 78.7, 78.8, 115.7, 116.2 (d, $^{2}J_{FC}$ = 17.3 Hz), 121.9 (d, $^{3}J_{FC}$ = 6.8 Hz), 124.7 (d, $^{3}J_{FC}$ = 3.8 Hz), 145.0 (d, $^{2}J_{FC}$ = 9.8 Hz), 151.9 (d, $^{1}J_{FC}$ = 242.3 Hz); ^{19}F NMR (282 MHz, DMSO-d_6) δ -136.4 (s, 1F).

Synthesis of 1-fluoro-3-(pro-2-yn-1-yloxy)benzene (5c): 3-Fluorophenol (3c) (0.7 mL, 7.19 mmol), propargyl bromide (4) (0.6 mL, 7.91 mmol), Cs_2CO_3 (4.32 g, 13.3 mmol) and CH_3CN (50 mL) were stirred at room temperature for 24 h. The crude product was purified by silica gel column chromatography (hexane) to give 5c (1.05 g, 7.00 mmol, 97%) as a colorless liquid. ^{1}H NMR (300 MHz, $CDCl_3$) δ 2.53 (t, *J* = 2.3 Hz, 1H), 4.67 (d, *J* = 2.3 Hz, 2H), 6.67 (m, 3H), 7.24 (m, 1H); ^{13}C NMR (75 MHz, $CDCl_3$) δ 56.0, 75.9, 78.1, 102.8 (d, $^{2}J_{FC}$ = 24.8 Hz), 108.4 (d, $^{2}J_{FC}$ = 21.8 Hz), 110.6 (d, $^{4}J_{FC}$ = 3.4 Hz), 130.3 (d, $^{3}J_{FC}$ = 9.8 Hz), 158.8 (d, $^{3}J_{FC}$ = 3.8 Hz), 163.5 (d, $^{1}J_{FC}$ = 243.8 Hz); ^{19}F NMR (282 MHz, $CDCl_3$) δ -112.2 (s, 1F).

Synthesis of 1-fluoro-4-(pro-2-yn-1-yloxy)benzene (5d): 4-Fluorophenol (3d) (1.20 g, 10.7 mmol), propargyl bromide (4) (80% w/w in toluene, 2.02 mL, 11.2 mmol), Cs_2CO_3 (4.33 g, 13.2 mmol) and CH_3CN (30 mL) were heated at reflux for 4 h. The crude product was purified

by silica gel column chromatography (hexane) to give 5d (1.22 g, 8.14 mmol, 76%) as a colorless liquid. ^{1}H NMR (300 MHz, $CDCl_3$) δ 2.51 (t, *J* = 2.4 Hz, 1H), 4.64 (d, *J* = 2.4 Hz, 2H), 6.95 (m, 4H); ^{13}C NMR (75 MHz, $CDCl_3$) δ 56.5, 75.7, 78.5, 115.9 (d, $^{2}J_{FC}$ = 23.2 Hz, 2C), 116.2 (d, $^{3}J_{FC}$ = 8.0 Hz, 2C), 153.7 (d, $^{4}J_{FC}$ = 2.2 Hz), 157.8 (d, $^{1}J_{FC}$ = 237.7 Hz); ^{19}F NMR (282 MHz, DMSO-d_6) δ -124.8 (s, 1F).

Synthesis of 1-nitro-2-(prop-2-yn-1-yloxy)benzene (5e): 2-Nitrophenol (3e) (1.27 g, 9.10 mmol), propargyl bromide (4) (0.7 mL, 9.23 mmol), Cs_2CO_3 (5.08 mg, 15.6 mmol) and CH_3CN (50 mL) were stirred at room temperature for 24 h. The crude product was purified by silica gel column chromatography (15% EtOAc:hexane) to give 5e (1.61 g, 9.06 mmol, quantitative yield) as a yellow solid. ^{1}H NMR (300 MHz, $CDCl_3$) δ 2.59 (t, *J* = 3.0 Hz, 1H), 4.86 (d, *J* = 3.0 Hz, 2H), 7.10 (td, *J* = 7.5, 1.1 Hz, 1H), 7.27 (dd, *J* = 8.5, 1.1 Hz, 1H), 7.56 (ddd, *J* = 8.1, 7.4, 1.7 Hz, 1H), 7.86 (dd, *J* = 8.1, 1.7 Hz, 1H); ^{13}C NMR (75 MHz, $CDCl_3$) δ 57.2, 77.1, 77.2, 115.5, 121.4, 125.7, 134.0, 140.4, 150.8.

Synthesis of 1-nitro-3-(prop-2-yn-1-yloxy)benzene (5f): 3-Nitrophenol (3f) (1.50 g, 10.8 mmol), propargyl bromide (4) (1.0 mL, 13.2 mmol), Cs_2CO_3 (7.12 g, 21.9 mmol) and CH_3CN (70 mL) were stirred at room temperature for 24 h. The crude product was purified by silica gel column chromatography (15% EtOAc:hexane) to give 5f (1.81 g, 10.5 mmol, 97%) as a yellow solid. ^{1}H NMR (300 MHz, $CDCl_3$) 2.59 (t, *J* = 2.4 Hz, 1H), 4.79 (d, *J* = 2.4 Hz, 2H), 7.31 (ddd, *J* = 8.3, 2.5, 0.9 Hz, 1H), 7.47 (t, *J* = 8.2 Hz, 1H), 7.83 (t, *J* = 2.3 Hz, 1H), 7.88 (ddd, *J* = 8.2, 2.2, 0.9 Hz, 1H); ^{13}C NMR (75 MHz, $CDCl_3$) δ 56.3, 76.7, 77.3, 109.6, 116.6, 121.9, 130.1, 149.1, 157.9.

Synthesis of 1-nitro-4-(prop-2-yn-1-yloxy)benzene (5g): 4-Nitrophenol (3g) (515 mg, 3.70 mmol), propargyl bromide (4) (80% w/w in toluene, 0.7 mL, 4.09 mmol), Cs_2CO_3 (1.51 g, 4.63 mmol) and CH_3CN (20 mL) were heated at reflux for 4 h. The crude product was purified by silica gel column chromatography (15% EtOAc:hexane) to give 5g (651 mg, 3.67 mmol, quantitative yield) as a yellow solid. ^{1}H NMR (300 MHz, $CDCl_3$) δ 2.59 (t, *J* = 3.0 Hz, 1H), 4.81 (d, *J* = 3.0 Hz, 2H), 7.07 (d, *J* = 9.0 Hz, 2H), 8.24 (d, *J* = 9.0 Hz, 2H);^{13}C NMR (75 MHz, DMSO-d_6) δ 56.3, 78.2, 79.1, 115.0 (2C), 125.8 (2C), 141.4, 162.3.

General procedure for click reaction: To a stirred mixture of propargyloxy derivatives (5a-5g) and 4-azidophenol (7) in 50% *n*-BuOH in water was added sodium ascorbate and 1M aq. $CuSO_4$ sequentially. The reaction mixture was stirred at 60 °C for a given reaction time. The resulting solution was diluted with iced water, followed by 10% aq. NH_3 and stirred for another 5 min. The precipitate was collected with a Buchner filter and air-dried overnight. Purification of the crude products by silica gel column chromatography provided the desired products (8a-8g).

Synthesis of 4-(4-(phenoxymethyl)-1H-1,2,3-triazol-1-yl)phenol (8a): (Pro-2-yn-1-yloxy) benzene (5a) (200 mg, 1.51 mmol), 4-azidophenol (7) (229 mg, 1.69 mmol), sodium ascorbate (15.0 mg, 0.08 mmol), 1M aq. $CuSO_4$ (75 µL) and 50% *n*-BuOH in water (4.5 mL) were stirred at 60 °C for 2 h. Purification of the crude product by silica gel column chromatography (50% EtOAc:hexane) gave 8a (247.4 mg, 0.93 mmol, 62% yield) as a white solid. ^{1}H NMR (300 MHz, DMSO-d_6) δ 5.21 (s, 2H), 6.93 (m, 3H), 7.07 (m, 2H), 7.30 (m, 2H), 7.67 (d, *J* = 8.9 Hz, 2H), 8.75 (s, 1H), 9.97 (br s, 1H); ^{13}C NMR (75 MHz, DMSO-d_6) δ 61.0, 114.7 (2C), 116.1 (2C), 120.9, 122.0 (2C), 122.7, 129.2, 129.9 (2C), 143.5, 157.8, 158.0.

Synthesis of 4-(4-((2-fluorophenoxy)methyl)-1H-1,2,3-triazol-1-yl)phenol (8b): 1-Fluoro-2-(pro-2-yn-1-yloxy)benzene (5b) (900 mg, 6.00 mmol), 4-azidophenol (7) (817 mg, 6.05 mmol), sodium ascorbate (98.7 mg, 0.498 mmol), 1M aq. $CuSO_4$ (300 µL) and 50% *n*-BuOH in water (20 mL) were stirred at 60 °C for 2 h. Purification of the crude product by silica gel column chromatography (50% EtOAc:hexane) gave 8b (979 mg, 3.43 mmol, 57%) as a brown solid. ^{1}H NMR (300 MHz, DMSO-d_6) δ 5.29 (s, 2H), 6.95 (d, *J* = 8.9 Hz, 2H), 6.98 (td, *J* = 4.7, 1.6, 1H), 7.16 (m, 1H), 7.23 (ddd, *J* = 11.8, 8.1, 1.6 Hz, 1H), 7.40 (td, *J* = 8.5, 1.5 Hz, 1H), 7.69 (d, *J* = 8.9 Hz, 2H), 8.79 (s, 1H), 9.98 (br s, 1H); ^{13}C NMR (75 MHz, DMSO-d_6) δ 62.0, 115.6, 116.1 (d, $^{2}J_{FC}$ = 18.0 Hz), 116.1 (2C), 121.5 (d, $^{3}J_{FC}$ = 7.5 Hz), 122.1 (2C), 123.0, 124.8 (d, $^{3}J_{FC}$ = 3.8 Hz), 128.7, 143.0, 145.9

(d, $^{2}J_{FC}$ = 10.4 Hz), 151.8 (d, $^{1}J_{FC}$ = 242.0 Hz), 157.9; ^{19}F NMR (282 MHz, DMSO-d_6) δ -136.4 (s, 1F); HRMS (ESI+) *m/z*: calcd. for $C_{15}H_{13}FN_3O_2$ $[M+H]^+$ 286.0992, found 286.0987.

Synthesis of 4-(4-((3-fluorophenoxy)methyl)-1H-1,2,3-triazol-1-yl)phenol (8c): 1-Fluoro-3-(pro-2-yn-1-yloxy)benzene (5c) (844 mg, 5.62 mmol), 4-azidophenol (7) (991 mg, 7.33 mmol), sodium ascorbate (104 mg, 0.53 mmol), 1M aq. $CuSO_4$ (272 μL) and 50% *n*-BuOH in water (20 mL) were stirred at 60 °C for 4 h. Purification of the crude product by silica gel column chromatography (50% EtOAc:hexane) gave 8c (1.30 g, 4.57 mmol, 81%) as a brown solid. ^{1}H NMR (300 MHz, DMSO-d_6) δ 5.23 (s, 2H), 6.78 (td, *J* = 8.7, 2.4 Hz, 1H), 6.95 (m, 4H), 7.33 (m, 1H), 7.67 (d, *J* = 8.9 Hz, 2H), 8.75 (s, 1H), 9.97 (br s, 1H); ^{13}C NMR (75 MHz, DMSO-d_6) δ 61.5, 102.4, (d, $^{2}J_{FC}$ = 24.8 Hz), 107.7 (d, $^{2}J_{FC}$ = 21.0 Hz), 111.2 (d, $^{4}J_{FC}$ = 3.0 Hz), 116.2 (2C), 122.2 (2C), 123.0, 128.8, 130.8 (d, $^{3}J_{FC}$ = 10.5 Hz), 143.2, 158.0, 159.6 (d, $^{3}J_{FC}$ = 11.3 Hz), 163.1 (d, $^{1}J_{FC}$ = 241.5 Hz); ^{19}F NMR (282 MHz, DMSO-d_6) δ -113.0 (s, 1F); HRMS (ESI+) *m/z*: calcd. for $C_{15}H_{13}FN_3O_2$ $[M+H]^+$ 308.0809, found 308.0811.

Synthesis of 4-(4-((4-fluorophenoxy)methyl)-1H-1,2,3-triazol-1-yl)phenol (8d): 1-Fluoro-4-(prop-2-yn-1-yloxy)benzene (5d) (928 mg, 6.18 mmol), 4-azidophenol (7) (878 mg, 6.50 mmol), sodium ascorbate (98.2 mg, 0.50 mmol), 1M aq. $CuSO_4$ (300 μL) and 50% *n*-BuOH in water (18 mL) were stirred at 60 °C for 2 h. Purification of the crude product by silica gel column chromatography (50% EtOAc:hexane) gave 8d (383 mg, 21.7 mmol, 62%) as a white solid. ^{1}H NMR (300 MHz, DMSO-d_6) δ 5.18 (s, 2H), 6.94 (d, *J* = 8.9 Hz, 2H), 7.12 (m, 4H), 7.66 (d, *J* = 8.9 Hz, 2H), 8.75 (s, 1H), 9.96 (br s, 1H); ^{13}C NMR (75 MHz, DMSO-d_6) δ 61.6, 115.9 (d, $^{2}J_{FC}$ = 25.1 Hz, 2C), 116.1 (d, $^{3}J_{FC}$ = 10.1 Hz, 2C), 116.1 (2C), 122.0 (2C), 122.8, 128.7, 143.4, 154.3 (d, $^{4}J_{FC}$ = 1.8 Hz), 156.7 (d, $^{1}J_{FC}$ = 234.6 Hz), 157.8; ^{19}F NMR (282 MHz, DMSO-d_6) δ -125.2 (s, 1F); HRMS (ESI+) *m/z*: calcd. for $C_{15}H_{13}FN_3O_2$ $[M+H]^+$ 286.0992, found 286.0981.

Synthesis of 4-(4-((2-nitrophenoxy)methyl)-1H-1,2,3-triazol-1-yl)phenol (8e): 1-Nitro-2-(prop-2-yn-1-yloxy)benzene (5e) (859 mg, 4.85 mmol), 4-azidophenol (7) (853 mg, 6.31 mmol), sodium ascorbate (84.2 mg, 0.43 mmol), 1M aq. $CuSO_4$ (240 μL) and 50% *n*-BuOH in water (20 mL) were stirred at 60 °C for 3 h. Purification of the crude product by silica gel column chromatography (50% EtOAc: hexane) gave 8e product (1.21 g, 3.88 mmol, 80%) as a brown solid. ^{1}H NMR (300 MHz, DMSO-d_6) δ 5.43 (s, 2H), 6.94 (d, *J* = 9.0 Hz, 2H), 7.15 (ddd, *J* = 8.0, 7.2, 1.4 Hz, 1H), 7.67 (d, *J* = 9.0 Hz, 2H), 7.67 (m, 2H), 7.88 (dd, *J* = 8.1, 1.6 Hz, 1H), 8.77 (s, 1H), 9.98 (br s, 1H); ^{13}C NMR (75 MHz, DMSO-d_6) δ 62.5, 115.7, 116.1 (2C), 121.1, 122.1 (2C), 123.1, 125.0, 128.6, 134.4, 139.9, 142.2, 150.6, 157.9; HRMS (ESI+) *m/z*: calcd. for $C_{16}H_{13}F_3N_3O_2$ $[M+H]^+$ 313.0937, found 313.0937.

Synthesis of 4-(4-((3-nitrophenoxy)methyl)-1H-1,2,3-triazol-1-yl)phenol (8f): 1-Nitro-3-(prop-2-yn-1-yloxy)benzene (5f) (902 mg, 5.09 mmol), 4-azidophenol (7) (998 mg, 7.38 mmol), sodium ascorbate (115 mg, 0.58 mmol), 1M aq. $CuSO_4$ (240 μL) and 50% *n*-BuOH in water (20 mL) were stirred at 60 °C for 4 h. Purification of the crude product by silica gel column chromatography (50% EtOAc:hexane) gave 8f (1.53 g, 4.89 mmol, 96%) as a brown solid. ^{1}H NMR (300 MHz, DMSO-d_6) δ 5.38 (s, 2H), 6.95 (d, *J* = 8.9 Hz, 2H), 7.55 (ddd, *J* = 8.3, 2.3, 1.2 Hz, 1H), 7.62 (t, *J* = 8.2 Hz, 1H), 7.67 (d, *J* = 8.9 Hz, 2H), 7.85 (ddd, *J* = 8.2, 2.1, 1.2 Hz, 1H), 7.91 (t, *J* = 2.1 Hz, 1H), 8.80 (s, 1H), 9.98 (br s, 1H); ^{13}C NMR (75 MHz, DMSO-d_6) δ 61.8, 109.2, 115.9, 116.1 (2C), 122.1 (2C), 122.2, 123.0, 128.7, 130.8, 142.8, 142.8, 157.9, 158.5; HRMS (ESI+) *m/z*: calcd. for $C_{15}H_{13}N_4O_4$ $[M+H]^+$ 313.0937, found 313.0927.

Synthesis of 4-(4-((4-nitrophenoxy)methyl)-1H-1,2,3-triazol-1-yl)phenol (8g): 1-Nitro-4-(prop-2-yn-1-yloxy)benzene (5g) (200.7 mg, 1.13 mmol), 4-azidophenol (7) (200.1 mg, 1.48 mmol), sodium ascorbate (18.3 mg, 0.09 mmol), 1M aq. $CuSO_4$ (57 μL) and 50% *n*-BuOH in water (10 mL) were stirred at 60 °C for 2 h. Purification of the crude product by silica gel column chromatography (50% EtOAc:hexane) gave 8g (222.1 mg, 0.71 mmol, 63% yield) as a brown solid. ^{1}H NMR (300 MHz, DMSO-d_6) δ 5.40 (s, 2H), 6.95 (d, *J* = 9.0 Hz, 2H), 7.31 (d, *J* = 9.0 Hz, 2H), 7.68 (d, *J* = 9.0 Hz, 2 H), 8.24 (d, *J* = 9.0 Hz, 2H), 8.81 (s, 1H), 9.99 (br s, 1H); ^{13}C NMR (75 MHz,

DMSO-d_6) δ 61.9, 115.4 (2C), 116.1 (2C), 122.1 (2C), 123.1, 125.9 (2C), 128.6. 141.1, 142.5. 157.9, 163.2; HRMS (ESI+) *m/z*: calcd. for $C_{15}H_{13}N_4O_4$ $[M+H]^+$ 313.0937, found 313.0936.

General procedure for the synthesis of the inhibitors: A stirred suspension of triazole phenol derivatives (8a-8g), 4-chloro-*N*-methylpicolinamide (9), *t*-BuOK and K_2CO_3 in dried DMF (5 mL) was heated to 80-85 °C for a given reaction time. The resulting suspension was cooled to room temperature, diluted with water, and extracted with EtOAc. The organic phase was dried over anh.Na_2SO_4, filtered and concentrated under reduced pressure to provide the crude product, which was purified by silica gel column chromatography to give the desired products (2a-2g).

Synthesis of N-methyl-4-(4-(4-(phenoxymethyl)-1H-1,2,3-triazol-1-yl)phenoxy) picolinamide (2a): A mixture of 8a (102.1 mg, 0.38 mmol), 9 (148 mg, 0.87 mmol), *t*-BuOK (41.8 mg, 0.37 mmol) and K_2CO_3 (55.5 mg, 0.40 mmol) in dried DMF (5 mL) was stirred at 80-85 °C for 10 h. The crude product was purified by silica gel column chromatography (50% EtOAc:hexane) to afford 2a (118 mg, 0.29 mmol, 76%) as a white solid. ^{1}H NMR (300 MHz, $CDCl_3$) δ 3.20 (d, *J* = 6.0 Hz, 3H), 5.33 (s, 2H), 7.02 (m, 4H), 7.31 (m, 5H), 7.76 (d, *J* = 2.5 Hz, 1H), 7.78 (d, *J* = 9.0 Hz, 2H), 8.06 (br s, 1H), 8.44 (d, *J* = 5.6 Hz, 1H); ^{13}C NMR (75 MHz, $CDCl_3$) δ 26.2, 61.9, 110.4, 114.5, 114.8 (2C), 121.1 (2C), 121.4, 122.0, 122.7 (2C), 129.6 (2C), 134.3, 145.6, 150.0, 152.5, 154.1, 158.1, 164.3, 165.5; HRMS (ESI+) *m/z*: calcd. for $C_{22}H_{19}N_5O_3Na$ $[M+Na]^+$ 424.1386, found 424.1374.

Synthesis of 4-(4-(4-((2-fluorophenoxy)methyl)-1H-1,2,3-triazol-1-yl)phenoxy)-N-methylpicolinamide (2b): A mixture of 8b (304 mg, 1.06 mmol), 9 (208 mg, 1.22 mmol), *t*-BuOK (246 mg, 2.19 mmol) and K_2CO_3 (176 mg, 1.27 mmol) in dried DMF (10 mL) was stirred at 80-85 °C for 24 h. The crude product was purified by silica gel column chromatography (50% EtOAc:hexane) to afford 2b (118 mg, 0.28 mmol, 27%) as an orange brown solid. ^{1}H NMR (300 MHz, DMSO-d_6) δ 2.78 (d, *J* = 4.9 Hz, 3H), 5.31 (s, 2H), 6.97 (m, 1H), 7.19 (m, 3H), 7.38 (td, *J* = 8.5, 1.1 Hz, 1H), 7.46 (m, 3H), 8.02 (d, *J* = 9.6 Hz, 2H), 8.55 (d, *J* = 5.6 Hz, 1H), 8.82 (q, *J* = 4.9 Hz, 1H), 8.94 (s, 1H); ^{13}C NMR (75 MHz, DMSO-d_6) δ 26.3, 62.1, 109.7, 114.9, 115.9, 116.4 (d, $^2J_{FC}$ = 17.3 Hz), 122.0 (d, $^3J_{FC}$ = 6.8 Hz), 122.5 (2C), 122.9 (2C), 123.6, 125.2 (d, $^3J_{FC}$ = 3.8 Hz), 134.2, 143.8, 146.0 (d, $^2J_{FC}$ = 10.5 Hz), 152.1 (d, $^1J_{FC}$ = 241.5 Hz), 151.0, 152.7, 153.7, 164.1, 165.4; ^{19}F NMR (282 MHz, DMSO-d_6) δ -136.7 (s, 1F); HRMS (ESI+) *m/z*: calcd. for $C_{22}H_{19}FN_5O_3$ $[M+H]^+$ 420.1472, found 420.1456.

Synthesis of 4-(4-(4-((3-fluorophenoxy)methyl)-1H-1,2,3-triazol-1-yl)phenoxy)-N-methylpicolinamide (2c): A mixture of 8c (274 mg, 0.96 mmol), 9 (237 mg, 1.60 mmol), *t*-BuOK (219 mg, 1.95 mmol) and K_2CO_3 (270 mg, 1.95 mmol) in dried DMF (10 mL) was stirred at 80-85 °C for 20 h. The crude product was purified by silica gel column chromatography (50% EtOAc:hexane) to afford 2c (213 mg, 0.51 mmol, 53%) as a white solid. ^{1}H NMR (300 MHz, DMSO-d_6) δ 2.79 (d, *J* = 4.9 Hz, 3H), 5.26 (s, 2H), 6.79 (td, *J* = 8.3, 1.9 Hz, 1H), 6.92 (dd, *J* = 8.2, 2.0 Hz, 1H), 6.98 (dt, *J* = 11.3, 2.3 Hz, 1H), 7.24 (dd, *J* = 5.6, 2.6 Hz, 1H), 7.35 (m, 1H), 7.47 (m, 3H), 8.03 (d, *J* = 8.9 Hz, 2H), 8.56 (d, *J* = 5.6 Hz, 1H), 8.81 (q, *J* = 8.4 Hz, 1H), 8.97 (s, 1H); ^{13}C NMR (75 MHz, DMSO-d_6) δ 26.2, 61.5, 102.5 (d, $^2J_{FC}$ = 24.8 Hz) 107.8 (d, $^3J_{FC}$ = 21.0 Hz), 109.6, 111.3 (d, $^4J_{FC}$ = 3.0 Hz), 114.7, 122.4 (2C), 122.7 (2C), 123.3, 130.9, 131.0, 134.1, 143.7, 150.7, 153.0 (d, $^2J_{FC}$ = 68.3 Hz), 159.5 (d, $^3J_{FC}$ = 10.5 Hz), 163.1 (d, $^1J_{FC}$ = 241.5 Hz), 163.8, 165.3; ^{19}F NMR (282 MHz, DMSO-d_6) δ -113.2 (s, 1F); HRMS (ESI+) *m/z*: calcd. for $C_{22}H_{19}FN_5O_3Na$ $[M+H]^+$ 420.1472, found 420.1473.

Synthesis of 4-(4-(4-((4-fluorophenoxy)methyl)-1H-1,2,3-triazol-1-yl)phenoxy)-N-methylpicolinamide (2d): A mixture of 8d (112 mg, 0.39 mmol), 9 (102 mg, 0.60 mmol), *t*-BuOK (126 mg, 1.12 mmol) and K_2CO_3 (78.8 mg, 0.57 mmol) in dried DMF (5 mL) was stirred at 80-85 °C for 16 h. The crude product was purified by silica gel column chromatography (50% EtOAc:hexane) to afford 2d (57.1 mg, 0.136 mmol, 35%) as a white solid. ^{1}H NMR (300 MHz, DMSO-d_6) δ 2.80 (d, *J* = 4.9 Hz, 3H), 5.24 (s, 2H), 7.14 (m, 4H), 7.26 (dd, *J* = 5.6, 2.6 Hz, 1H), 7.50

(m, 3H), 8.05 (d, *J* = 9.0 Hz, 2H), 8.57 (d, *J* = 5.6 Hz, 1H), 8.82 (q, *J* = 4.8 Hz, 1H), 9.00 (s, 1H); ^{13}C NMR (75 MHz, DMSO-d_6) δ 26.0, 61.6, 109.4, 114.6, 115.9 (d, $^{2}J_{FC}$ = 23.0 Hz, 2C), 116.1 (d, $^{3}J_{FC}$ = 8.0 Hz, 2C), 121.9 (2C), 122.5 (2C), 123.1, 134.0, 143.7, 150.6, 152.6, 153.3, 154.3 (d, $^{4}J_{FC}$ = 2.3 Hz), 156.7 (d, $^{1}J_{FC}$ = 234.8 Hz), 163.7, 165.1; ^{19}F NMR (282 MHz, DMSO-d_6) δ -125.8 (s, 1F); HRMS (ESI+) *m/z*: calcd. for $C_{22}H_{18}FN_5O_3Na$ $[M+Na]^+$ 442.1291, found 442.1290.

Synthesis of N-methyl-4-(4-(4-((2-nitrophenoxy)methyl)-1H-1,2,3-triazol-1-yl)phenoxy)picolinamide (2e): A mixture of 8e (306 mg, 0.98 mmol), 9 (186 mg, 1.10 mmol), *t*-BuOK (226 mg, 2.02 mmol) and K_2CO_3 (257 mg, 1.86 mmol) in dried DMF (10 mL) was stirred at 80-85 °C for 17 h. The crude product was purified by silica gel column chromatography (50% EtOAc:hexane) to afford 2e (161 mg, 0.36 mmol, 37%) as a white solid. ^{1}H NMR (300 MHz, DMSO-d_6) δ 2.80 (d, *J* = 4.8 Hz, 3H), 5.46 (s, 2H), 7.16 (t, *J* = 7.5 Hz, 1H), 7.25 (dd, *J* = 5.6, 2.6 Hz, 1H), 7.47 (d, *J* = 8.7 Hz, 3H), 7.63 (d, *J* = 7.8 Hz, 1H), 7.70 (td, *J* = 8.6, 1.4 Hz, 1H), 7.87 (dd, *J* = 8.1, 1.4 Hz, 1H), 8.04 (d, *J* = 8.9 Hz, 2H), 8.56 (d, *J* = 5.6 Hz, 1H), 8.83 (q, *J* = 4.7 Hz, 1H), 8.96 (s, 1H); ^{13}C NMR (75 MHz, DMSO-d_6) δ 26.3, 62.6, 109.8, 114.9, 115.9, 121.5, 122.5 (2C), 122.9 (2C), 123.7, 125.2, 134.1, 134.7, 140.8, 143.2, 150.7, 150.9, 152.6, 153.7, 164.0, 165.4; HRMS (ESI+) *m/z*: calcd. for $C_{22}H_{18}N_6O_5$ $[M+H]^+$ 447.1417, found 477.1413.

Synthesis of N-methyl-4-(4-(4-((3-nitrophenoxy)methyl)-1H-1,2,3-triazol-1-yl)phenoxy)picolinamide (2f): A mixture of 8f (300 mg, 0.96 mmol), 9 (188 mg, 1.10 mmol), *t*-BuOK (226 mg, 2.02 mmol) and K_2CO_3 (257 mg, 1.86 mmol) in dried DMF (10 mL) was stirred at 80-85 °C for 17 h. The crude product was purified by silica gel column chromatography (50% EtOAc:hexane) to afford 2f (161 mg, 0.36 mmol, 38%) as a white solid. ^{1}H NMR (300 MHz, DMSO-d_6) δ 2.79 (d, *J* = 4.8 Hz, 3H), 5.41 (s, 2H), 7.25 (dd, *J* = 5.6, 2.6 Hz, 1H), 7.48 (dd, *J* = 5.4, 2.6 Hz, 3H), 7.59 (m, 2H), 7.86 (d, *J* = 7.8 Hz, 1H), 7.91 (t, *J* = 2.2 Hz, 1H), 8.04 (d, *J* = 8.9 Hz, 2H), 8.56 (d, *J* = 5.6 Hz, 1H), 8.82 (q, *J* = 4.7 Hz, 1H), 8.99 (s, 1H); ^{13}C NMR (75 MHz, DMSO-d_6) δ 26.0, 61.8, 109.3, 109.4, 114.6, 116.0, 122.2, 122.3 (2C), 122.6 (2C), 123.3, 130.8, 134.0, 143.3, 148.8, 150.6, 152.6, 153.4, 158.5, 163.7, 165.1; HRMS (ESI+) *m/z*: calcd. for $C_{22}H_{18}N_6O_5$ $[M+H]^+$ 447.1417, found 477.1418.

Synthesis of N-methyl-4-(4-(4-((4-nitrophenoxy)methyl)-1H-1,2,3-triazol-1-yl)phenoxy)picolinamide (2g): A mixture of 8g (303 mg, 0.9 mmol), 9 (192 mg, 1.13 mmol), *t*-BuOK (256 mg, 2.28 mmol) and K_2CO_3 (257 mg, 1.86 mmol) in dried DMF (10 mL) was stirred at 80-85 °C for 29 h. The crude product was purified by silica gel column chromatography (50% EtOAc:hexane) to afford 2g (77.9 mg, 0.17 mmol, 18%) as a white solid. ^{1}H NMR (300 MHz, DMSO-d_6) δ 2.80 (d, *J* = 4.9 Hz, 3H), 5.45 (s, 2H), 7.26 (dd, *J* = 5.6, 2.6 Hz, 1H), 7.33 (d, *J* = 9.2 Hz, 2H), 7.50 (m, 3H), 8.06 (d, *J* = 8.9 Hz, 2H), 8.26 (d, *J* = 9.2 Hz, 2H), 8.57 (d, *J* = 5.6 Hz, 1H), 8.81 (q, *J* = 4.7 Hz, 1H), 9.05 (s, 1H); ^{13}C NMR (75 MHz, DMSO-d_6) δ 26.0, 61.9, 109.4, 114.6, 115.4 (2C), 122.3 (2C), 122.6 (2C), 123.5, 125.9 (2C), 134.0, 141.2, 143.0, 150.6, 152.6, 153.4, 163.2, 163.2, 165.1; HRMS (ESI+) *m/z*: calcd. for $C_{22}H_{18}N_6O_5Na$ $[M+Na]^+$ 469.1236, found 469.1229.

Cytotoxicity towards HepG2 and Huh7 using MTT assay: HepG2 or Huh7 cell lines were seeded in 96-well plates at the concentration of 4.5 x 10^4 cells/200 µL DMEM medium culture/well followed by incubation at 37 °C under 5% CO_2 atmosphere for 24 h. The medium was removed from the plates. The synthetic analogues and sorafenib were dissolved in DMSO. Stock drug and sample solutions were diluted with complete medium. The cells were treated with various concentrations of compounds and sorafenib including the control (0.1% DMSO). Then, the treated cells were incubated for 48 h. Subsequently, the medium was removed and the cells were washed with PBS. MTT solution (100 µL, 0.5 mg/mL) was added to the cells. The treated cells were incubated at 37 °C for 3 h. The MTT solution was removed and DMSO (100 µL) was added. Then, the absorbance was measured at 570 nm.

Results and Discussion: The designed triazole-containing sorafenib analogues 2a-2g were synthesized successfully starting from different substituted phenols 3a-3g as illustrated in

Scheme 1. Phenols 3a-3g with and without a substituent (e.g. F and NO_2) at different positions on the phenoxy ring were treated with propargyl bromide (4) under basic conditions to yield alkynes 5a-5g in good to excellent yields. Subsequently, the 1,2,3-triazole ring was constructed smoothly in the presence of $CuSO_4$ and sodium ascorbate *via* Huisgen 1,3-dipolar cycloaddition (click reaction) between the obtained alkynes 5a-5g and *p*-azidophenol (7), which was prepared *via* diazotization followed by substitution of *p*-aminophenol (6),[31] to furnish various triazole-containing phenols 8a-8g with good to excellent yields. After coupling of 8a-8g with *N*-methyl 4-chloropicolinamide (9),[32] the target 1,2,3-triazole-containing sorafenib analogues 2a-2g were delivered with the yields of 18-76%. The structures of all target compounds were elucidated using ^{1}H and ^{13}C nuclear magnetic resonance (NMR) and high-resolution mass spectrometry (HRMS). In the case of fluorinated analogues, the ^{19}F NMR spectra were additionally collected.

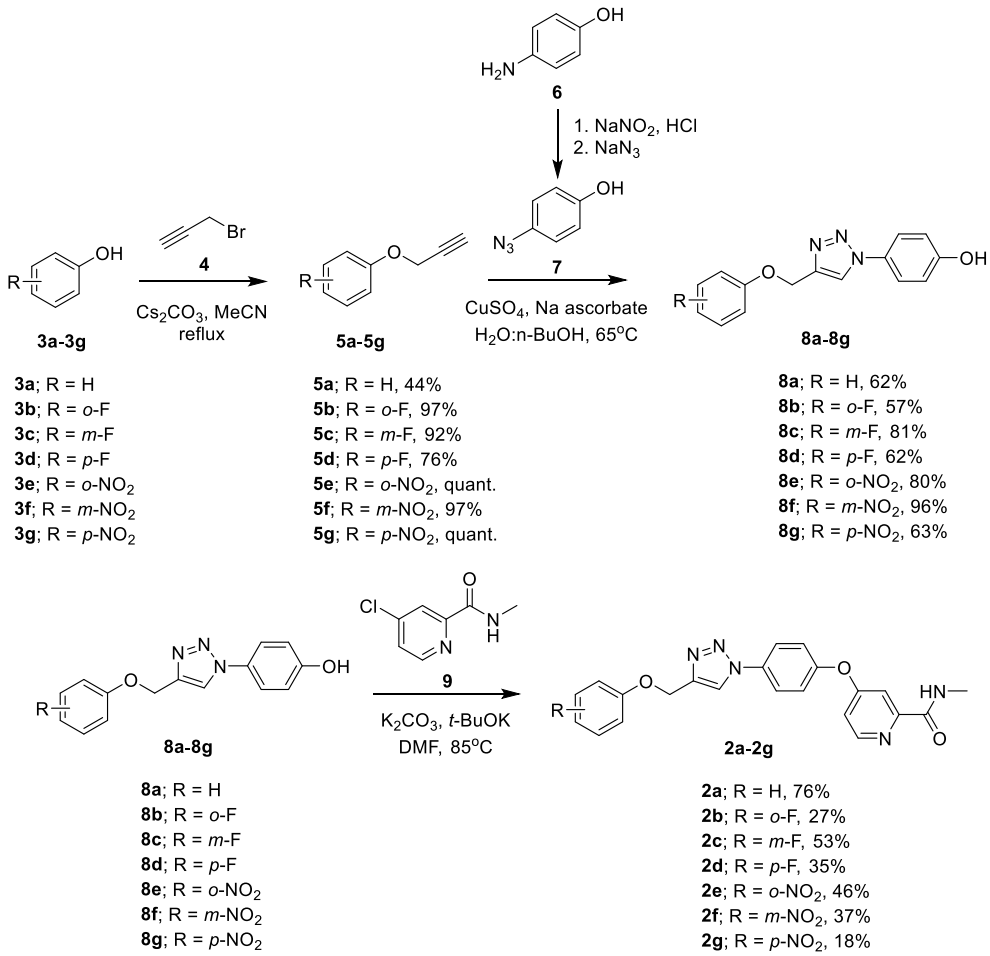

Scheme 1. Synthetic routes to the target triazole-containing sorafenib analogues 2a-2g starting from various substituted phenols 3a-3g.

The biological activities of the synthetic analogues 2a-2g were investigated *in vitro* in human cancer cell lines; HepG2 and Huh7, using MTT assay. The inhibitory properties of the sorafenib derivatives towards HepG2 and Huh7 were indicated in IC_{50} values (half-maximal inhibitory concentration) as reported in Table 1.

Table 1. *In vitro* Inhibitory potencies towards HepG2 and Huh7 of the triazole-containing sorafenib analogues 2a-2g compared to those of the original sorafenib. The activities were expressed as IC_{50} values in the micromolar range (μM).

Compound	R	IC_{50} (μM)	
		HepG2	Huh7
2a	H	234 ± 86	351 ± 181
2b	*o*-F	>300	>300
2c	*m*-F	>300	>300
2d	*p*-F	>500	64.4 ± 5.5
2e	*o*-NO_2	72.0 ± 5.5	52.5 ± 0.8
2f	*m*-NO_2	>100	>300
2g	*p*-NO_2	>500	21.1 ± 5.9
Sorafenib		3.87 ± 1.74	2.93 ± 0.65

The results showed that the unsubstituted phenoxy analogue 2a (R = H) exhibited poor inhibitory activities towards HepG2 and Huh7 with IC_{50} = 234 μM and >300 μM, which were ca. 60-fold and 120-fold lower potencies than sorafenib, respectively. To attempt to improve the inhibitory efficiency, substitution at the various position of the phenoxy ring might be needed. Preliminarily, F and NO_2 were attached to the *o*-, *m*- and *p*-position of the phenoxy ring. As a result, the synthetic analogues 2d (R = *p*-F), 2e (R = *o*-NO_2) and 2g (R = *p*-NO_2) expressed improved IC_{50} values against either HepG2 or Huh7 with IC_{50} values less than 100 μM. The analogue 2e (R = *o*-NO_2) exhibited promising inhibitory properties towards both HepG2 and Huh7 with IC_{50} values 72.0 and 52.5 μM (ca. 19-fold and 18-fold less active than sorafenib), respectively, while 2d (R = *p*-F) and 2g (R = *p*-NO_2) inhibited Huh7 selectively with IC_{50} values 64.4 and 21.1 μM (ca. 22-fold and 7-fold less active than sorafenib), respectively. The analogues tended to inhibit preferably Huh7 to HepG2. Obviously, the presence of a substituent, such as F and NO_2, at *p*-position could help to enhance the anti-Huh7 activity, whereas the analogue 2e with *o*-NO_2 had potential to inhibit HepG2 with IC_{50} value less than 100 μM. According to the results, all the synthetic analogues were not as active as the lead compound, sorafenib. However, the preliminary results informed us that the triazole-containing structure has the potential to be further developed for the improved inhibitory properties towards the human cancer cell lines. Furthermore, the sorafenib analogues might be biologically active towards other cancer cell lines as reported in the literature.[33-34]

Conclusion: Seven 1,2,3-triazole-containing analogues of sorafenib were synthesized successfully *via* Huisgen 1,3-dipolar cycloaddition and nucleophilic aromatic substitution. Their cytotoxicity towards HepG2 and Huh7 were still less active than the mother compound, sorafenib. In most promising cases, the analogues exhibited up to ca. 19-fold and 7-fold less active than sorafenib towards HepG2 and Huh7, respectively. However, the preliminary results implied that the triazole-containing analogues of sorafenib had the potential for further development to be anti-HepG2 and Huh7 agents. Furthermore, it was evident that introduction of a suitable substituent at *o*- or *p*-position on the phenoxy ring of the analogues could improve inhibitory properties towards human cancer cell lines.

References:

1. Parkin D, Bray F, Ferlay J, Pisani P. CA Cancer J Clin. 2005; 55: 74-108.
2. Bray F, Ferlay J, Soerjomataram I, Siegel R, Torre L, Jemal A. CA Cancer J Clin. 2018; 68: 394-424.
3. Vatanasapt V, Sriamporn S, Vatanasapt P. Jpn J Clin Oncol 2002; 32: S82-91.

4. Adami H, Hsing A, McLaughlin J, Trichopoulos D, Hacker D, Ekbom A, Persson I. Int J Cancer. 1992; 51: 898-902.
5. Steinmetz K, Potter J. Cancer Causes Control. 1991; 2: 325-57.
6. Rapp K, Schroeder J, Klenk J, Stoehr S, Ulmer H, Concin H, Diem G, Oberaigner W, Weiland S. Br J Cancer. 2005; 93: 1062-1067.
7. Chuang S, La Vecchia C, Boffetta P. Cancer Lett. 2009; 286: 9-14.
8. Daher S, Massarwa M, Benson A, Khoury T. J Clin Transl Hepatol. 2018; 6: 69-78.
9. Michl P, Pauls S, Gress T. Best Pract Res Clin Gastroenterol. 2006; 20: 227-251.
10. Zhang Z, Niu B, Chen J, He X, Bao X, Zhu J, Yu H, Li Y. Biomaterials. 2014; 35: 4565-4572.
11. Llovet J, Ricci S, Mazzaferro V, Hilgard P, Gane E, Blanc J, de Oliveira A, Santoro A, Raoul J, Forner A, Schwartz M, Porta C, Zeuzem S, Bolondi L, Greten T, Galle P, Seitz J, Borbath I, Haussinger D, Giannaris T, Shan M, Moscovici M, Voliotis D, Bruix J. N Engl J Med. 2008; 359: 378-390.
12. Moon W, Rhyu K, Kang M, Lee D, Yu H, Yeum J, Koh G, Tarnawski A. Mod Pathol. 2003; 16: 552-557.
13. Calvisi D, Ladu S, Gorden A, Farina M, Conner E, Lee J, Factor V, Thorgeirsson S. Gastroenterology. 2006; 130: 1117-1128.
14. Hira E, Ono T, Dhar D, El-Assal O, Hishikawa Y, Yamanoi A, Nagasue N. J Cancer. 2005; 103: 588-598.
15. Wood L. Clin J Oncol Nurs. 2009; 13: 13-8.
16. Wang X, Fan J, Liu Y, Zhao B, Jia Z, Zhang Q. Int J Pharm. 2011; 419: 339-346.
17. Zhan W, Li Y, Huang W, Zhao Y, Yao Z, Yu S, Yuan S, Jiang F, Yao S, Li S. Bioorg Med Chem. 2012; 20: 4323-4329.
18. Zhao C, Wang R, Li G, Xue X, Sun C, Qu X, Li W. Bioorg Med Chem Lett. 2013; 23: 1989-1992.
19. Mannion M, Raeppel S, Claridge S, Zhou N, Saavedra O, Isakovic L, Zhan L, Gaudette F, Raeppel F, Deziel R, Beaulieu N, Nguyen H, Chute I, Beaulieu C, Dupont I, Robert M, Lefebvre S, Dubay M, Rahil J, Wang J, Ste-Croix H, Robert M, Besterman, J, Vaisburg A. Bioorg Med Chem Lett. 2009; 19: 6552-6556.
20. Musumeci F, Radi M, Brullo C, Schenone S. J Med Chem. 2012; 55: 10797-10822.
21. Li W, Zhai X, Ding L, Sun L, Chen X, Gong P, Sun T. Molecules. 2011; 16: 5130-5141.
22. Moku B, Ravindar L, Rakesh K, Qin H. Bioorg Chem 2019; 86: 513-537.
23. Wang M, Xu S, Lei H, Wang C, Xiao Z, Jia S, Zhi J, Zheng P, Zhu W. Bioorg Med Chem. 2017; 25: 5754-5763.
24. Ye W, Yao Q, Yu S, Gong P, Qin M. Molecules. 2017; 22: 1759.
25. Stumpe M. Grubmuller H. J Phys Chem B. 2007; 111: 6220-6228.
26. Alam P, Chaturvedi S, Anwar T, Siddiqi M, Ajmal M, Badr G, Mahmoud M, Khan R. J Lumin. 2015; 164: 123-130.
27. Wan P, Garnett M, Roe S, Lee S, Niculescu-Duvaz D, Good V, Jones C, Marshall C, Springer C, Barford D, Marais R. Cancer Genome P. Cell. 2004; 116: 855-67.
28. Haider S, Alam M, Hamid H. J Inflamm Cell Signal. 2014; 1: e95.
29. Yan S, Liu Y, Chen Y, Liu L, Lin J. Bioorg Med Chem Lett. 2010; 20: 5225-5228.
30. Agalave S, Maujan S, Pore V. Chem Asian J. 2011; 6: 2696-2718.
31. Ryu B, Emrick T. Macromolecules. 2011; 44: 5693-5700.
32. Wang Y, Liu J, Yu X, Yang D, Zhang L, Zhao G. Chem Res Chinese U. 2013; 29: 454-459.
33. Xiang Q, Zhan M, Li Y, Liang H, Hu C, Huang Y, Xiao J, He X, Xin Y, Chen M, Lu L. Artif Cells Nanomed Biotechnol. 2019; 47: 83-89.
34. Yoon S, Lee E, Choi J, Chung T, Kim D, Im J, Bae M, Kwon J, Kim H, Park Y, Wang H, Woo H. Oncogene. 2018; 37: 4443-4454.

Acknowledgements: This research was financially supported by the Development and Promotion of Science and Technology Talent Project (DPST), the DPST research grant 19/2558

from the Institute for the Promotion of Teaching Science and Technology (IPST), The Thailand Research Fund (RTA5980008), Department of Chemistry, Faculty of Science, Silpakorn University and Center of Excellence in Hepatitis and Liver Cancer, Chulalongkorn University.

C3_006_PF: DESIGN AND SYNTHESIS OF OFF/ON FLUORESCENT pH SENSOR BASED ON RHODAMINE 6G

Siriphong Somprasong, Torsak Luanphaisarnnont*
Department of Chemistry and Center of Excellence for Innovation in Chemistry (PERCH-CIC), Faculty of Science, Mahidol University, Bangkok 10400, Thailand
*e-mail: torsak.lua@mahidol.ac.th

Abstract: Development of pH sensors is important for many applications. Fluorescent probes have been among the most useful tools to monitor the pH. This research investigated the off/on fluorescent pH sensor based on structural modification of rhodamine 6G. Probe 1 was designed and synthesized. Its photophysical properties and its ability as a pH sensor were also investigated.

Introduction: The pH plays an important role in many applications from industry production to cellular processes. Intracellular pH plays significant roles in many biological systems, including regulation of cell growth, cell adhesion, endocytosis, enzymatic catalysis and ion transport.[1] Nowadays, many methods have been developed to construct pH sensors such as acid-base indicator titration and potentiometric titration.[2-4] Measurement of pH by fluorescent-based techniques has been among the most important tools for detecting and imaging applications because of its simplicity, low cost, high selectivity, high sensitivity, and application in real-time monitoring.[5] Fluorescent probes for detection of pH based on naphthalene[6], naphthalimide[7], phenyldiazo[8], indole[9], flavones[10], quinolone[11], and bodipy[12] have been developed. One class of commercially available compounds containing a xanthene core is rhodamine (Figure 1), which has been used extensively in sensor development and its applications due to its high quantum yield, excellent photostability and ability to detect by naked-eye. Development of new sensors with capability of turning on and off in response to pH is important. Herein, this research develops an off/on fluorescence probe for detection of pH level based on rhodamine 6G.

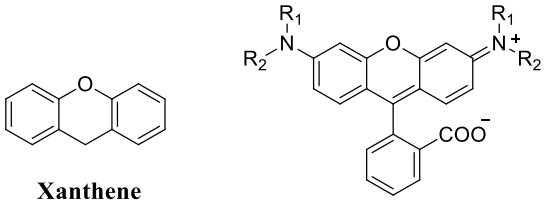

Figure 1. The structures of xanthene and rhodamine

Methodology:
General methods and reagents: Starting reagents and organic solvents were purchased from commercial sources and were used without further purification unless otherwise noted. Deionized water was used in all experiments. ^{1}H NMR (400 MHz) and ^{13}C NMR (100 MHz) spectra were recorded in deuterated chloroform ($CDCl_3$) and deuterated dimethylsulfoxide (DMSO-d_6) by using a Bruker Avance 400 MHz NMR spectrometer. Data are reported as following: (br = broad, s = singlet, d = doublet, t = triplet, q = quartet, p = pentet, and m = multiplet; coupling constant(s) in Hz, integration). Mass spectrometric data were obtained with high resolution mass spectra (HRMS) on a Bruker microTOF spectrometer in the ESI mode. Thin layer chromatography (TLC) was performed on aluminium sheets pre-coated with a Merck silica gel 60 F254 plate and compounds were visualized under UV light. A Merck silica gel 60 (0.063 – 0.200 mm) was used as stationary phase on column chromatography.

Synthesis of rhodamine 19 ethylenediamine: To a solution of rhodamine 6G (1g, 2.09 mmol) in ethanol (25 mL) was added ethylenediamine (1 mL, 14.96 mmol) dropwise. The solution was refluxed for 12 hours. The reaction mixture was cooled at room temperature and poured into water. The solid precipitate was filtered, washed with water and dried to give rhodamine 19 ethylenediamine as a pale pink solid (0.932 g, 98 %), which was used in the next step without further purification. ^{1}H NMR (400 MHz, $CDCl_3$), δ 7.87 (m, 1H, ArH), 7.43 (m, 2H, 2 × ArH), 7.02 (m, 1H, ArH), 6.31 (s, 2H, 2 × xanthene ArH), 6.19 (s, 2H, 2 × xanthene ArH), 3.51 (t, *J* = 4.7 Hz, 2H, 2 × Ar<u>NH</u>), 3.38 (br, 2H, NH_2), 3.18 (m, 6H, 2 × $\underline{CH_2}CH_3$ and $\underline{CH_2}NCO$), 2.51 (t, *J* = 5.9 Hz, 2H, $\underline{CH_2}NH_2$), 1.87 (s, 6H, 2 × xanthene Ar$\underline{CH_3}$), 1.28 (t, *J* = 7.1 Hz, 6H, 2 × $CH_2\underline{CH_3}$). ^{13}C NMR (100 MHz, $CDCl_3$), δ 169.4 (C=O), 153.8 (aromatic), 151.9 (2 × xanthene), 147.8 (2 × xanthene), 133.0 (aromatic), 130.9 (aromatic), 128.4 (aromatic), 128.3 (2 × xanthene), 124.1 (aromatic), 123.1 (aromatic), 118.4 (2 × xanthene), 105.6 (2 × xanthene), 96.7 (2 × xanthene), 65.8 (spiro-carbon), 42.5 ($\underline{CH_2}NCO$), 41.0 ($\underline{CH_2}NH_2$), 38.5 (2 × $\underline{CH_2}CH_3$), 16.9 (2 × xanthene Ar$\underline{CH_3}$), 14.9 (2 × $CH_2\underline{CH_3}$). LC-HRMS (ESI+): *m/z* $[M+H]^+$ calcd for $C_{30}H_{36}O_4N_2$: 457.2598; found 457.2605.

Synthesis of probe 1: To a suspension of 2-chloro-1-methylpyridinium iodide (134.4 mg, 0.526 mmol) in dichloromethane (5 mL) was added benzoic acid (65 mg, 0.526 mmol) and rhodamine 19 ethylenediamine (200 mg, 0.438 mmol) and then slowly added trimethylamine (147 µL). The reaction mixture was stirred at room temperature for 12 hours. After the completion of the reaction, the solvent was removed in vacuo and purified by column chromatography (silica gel: EtOAc/Hexane, 1/2, v/v) to give probe 1 as a white solid (205.4 mg, 84 %). ^{1}H NMR (400 MHz, DMSO-d_6), δ 8.28 (t, *J* = 5.4 Hz, 1H, <u>NH</u>CO), 7.80 (m, 1H, ArH), 7.69 (d, *J* = 7.3 Hz, 2H, 2 × ArH), 7.48 (m, 3H, xanthene ArH and 2 × ArH), 7.39 (t, *J* = 7.3 Hz, 2H, 2 × ArH), 6.94 (m, 1H, ArH), 6.26 (s, 2H, 2 × xanthene ArH), 6.13 (s, 2H, 2 × xanthene ArH), 5.03 (t, *J* = 5.3 Hz, 2H, Ar<u>NH</u>), 3.19 (m, 2H, $\underline{CH_2}NCO$), 3.11 (m, 4H, 2 × $NH\underline{CH_2}CH_3$), 3.02 (m, 2H, $\underline{CH_2}NHCO$), 1.83 (s, 6H, 2 × xanthene Ar$\underline{CH_3}$), 1.20 (t, *J* = 7.1 Hz, 6H, 2 × $CH_2\underline{CH_3}$). ^{13}C NMR (100 MHz, DMSO- d_6), δ 167.7 (C=O), 166.0 (C=O), 154.0 (aromatic), 151.0 (2 × xanthene), 147.7 (2 × xanthene), 134.2 (aromatic), 132.8 (aromatic), 131.1 (aromatic), 130.0 (aromatic), 128.3 (aromatic), 128.2 (2 × aromatic), 127.5 (2 × xanthene), 127.1 (2 × aromatic), 123.6 (aromatic), 122.4 (aromatic), 118.3 (2 × xanthene), 104.5 (2 × xanthene), 95.8 (2 × xanthene), 64.5 (spiro-carbon), 39.3 ($\underline{CH_2}NCO$), 38.0 ($\underline{CH_2}NH_2$), 37.5 (2 × $\underline{CH_2}CH_3$), 17.0 (2 × xanthene Ar$\underline{CH_3}$), 14.2 (2 × $CH_2\underline{CH_3}$). LC-HRMS (ESI+): *m/z* $[M+H]^+$ calcd for $C_{30}H_{36}O_4N_2$: 561.2860; found, 561.2859.

UV-Vis absorption and fluorescence emission studies: UV-Vis and fluorescence spectra were measured in 0.1 M sodium phosphate buffer solution using an Agilent Cary-60 UV–Visible spectrophotometer and a Horiba FluoroMax4+ spectrofluorometer, respectively. All pH values were measured using a Mettler Toledo pH meter. Probe 1 (5 µM) in 3 mL of 0.1 M buffer solution with various H^+ concentrations was stirred for 20 minutes and then transferred to a quartz cuvette for analysis. The absorption spectra were collected from 400 to 700 nm. The emission spectra were measured with excitation wavelength at 510 nm and collected from 400 to 700 nm.

In the selectivity experiments, the metal ion solutions were prepared from chloride and acetate salts. The metal solution (5 µM) was added to a 3 mL buffer solution of probe 1. The absorption and emission spectra were then measured.

Results and Discussion:

Design of probe 1: Probe 1 was designed based on the ring-opening ability of rhodamine under different pH conditions. Changing the ester functional group to an amide functional group would allow further structural modification by installing the substituent at the nitrogen atom of the amide. Ethylenediamine was used as a linker and the other nitrogen atom was modified as an amide functional group. The mechanism of probe 1 as a fluorescent pH sensor was

proposed based on its ring-opening ability (Scheme 1). Under acidic condition, protonation of the carbonyl group of the lactam led to ring opening. The enhanced delocalization in the open-form rendered the molecule fluorescent. This ring-opening mechanism would allow probe 1 to act as a pH sensor.

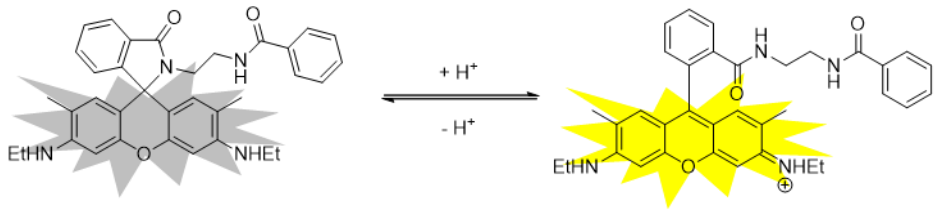

Scheme 1. The proposed mechanism of probe 1

Synthesis of probe 1: Probe 1 was synthesized by a two-step procedure (Scheme 2) and confirmed by ^{1}H NMR, and ^{13}C NMR spectra. A rhodamine 19 ethylenediamine was synthesized by amide formation between commercially available rhodamine 6G and ethylenediamine in ethanol under reflux to afford a pink pale solid in 98 %. The product was subjected to Mukaiyama amide formation with benzoic acid under basic condition to yield the desired probe 1 in 84 %.

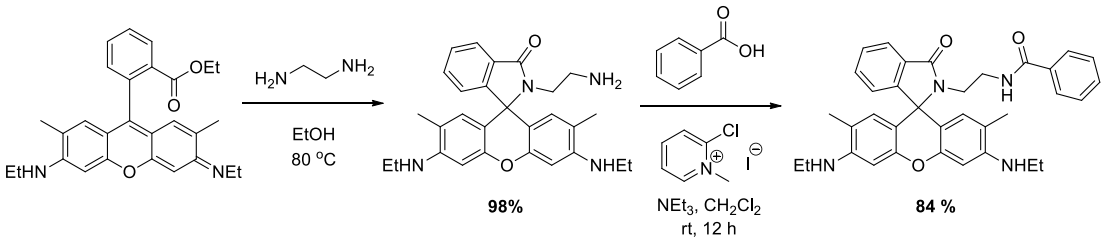

Scheme 2. Synthesis of probe 1

Optical properties: The photophysical properties of probe 1 were investigated. Absorption spectra of probe 1 depended on the pH (Figure 2). At higher pH (pH > 5), no absorption within 450 – 600 nm region was observed; however, when the pH decreases (pH < 5), a new absorption band was observed at 530 nm. The absorption reached maximum when the pH was 2.05. The colorless solution turned pink, which can be observed by naked-eye. This color change confirmed that probe 1 can act as a pH sensor.

Fluorescence properties of probe 1 were also studied at different pH conditions (Figure 3A). When the pH decreases, the fluorescence intensity increases. When pH is lower than 5.05, probe 1 exhibited fluorescence properties with a maximum fluorescence at 555 nm with a Stoke's shift of 25 nm. At pH 2.28, probe 1 showed the highest fluorescence intensity, which is 700-fold higher than the fluorescence when pH is greater than 6.05. This result suggested that probe 1 can act as a fluorescent pH sensor.

The acidity constant (K_a) of probe 1 was determined by fluorometric titration. The data form the titration (Figure 3B) were used to calculate the pK_a from a sigmoidal curve fitting of the Henderson-Hasselbach-type mass action according to Equation 1, where I is the observed fluorescence intensity at a fixed wavelength, I_{max} and I_{min} are the corresponding maximum and minimum intensity, respectively. The pK_a of probe 1 was calculated to be 3.83.

$$pK_a = pH - \log \frac{I_{max} - I}{I - I_{min}} \quad (1)$$

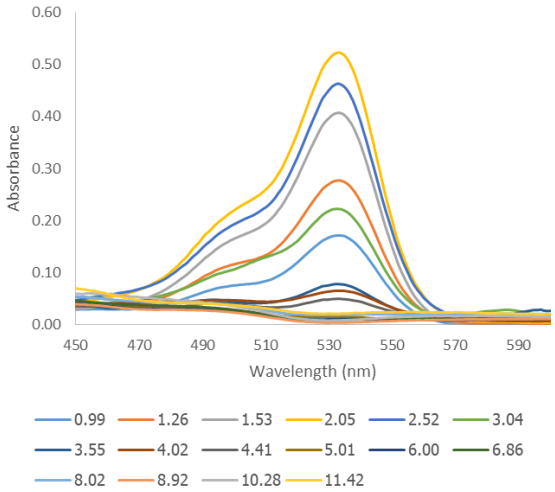

Figure 2. Absorption spectra of probe 1 (5 µM) in 0.1 M sodium phosphate buffer with different pH

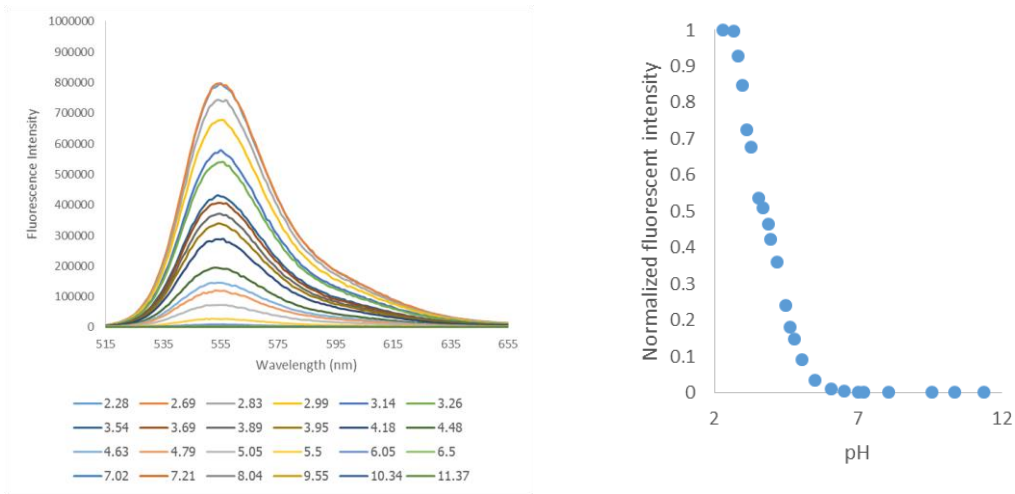

(A) (B)

Figure 3. (A) Fluorescence spectra of probe 1 (5 µM) in 0.1 M sodium phosphate buffer solution with different pH conditions and (B) Fluorescence intensity (555 nm) of probe 1 (5 µM) in buffer solution; λ_{ex} = 510 nm

Selectivity studies: The selectivity of probe 1 as a fluorescent sensor was investigated. Fluorescent intensity of probe 1 in the presence of various metal ions was determined because some metal ions can bind with the nitrogen or oxygen atom of the probe, which cause the spirolactime ring opening to render fluorescence intensity. In the presence of metal ions including K^+, Na^+, Mg^{2+}, Ca^{2+}, Cu^{2+}, Ag^+, Fe^{2+}, Fe^{3+}, Co^{2+}, Hg^{2+}, Ba^{2+}, Al^{3+}, Pb^{2+}, Cd^{2+}, Zn^{2+}, Mn^{2+} and Ni^{2+} at pH 7.24, probe 1 showed minimal fluorescent intensity enhancement at 555 nm (Figure 4). This result suggested that probe 1 is highly selective for H^+.

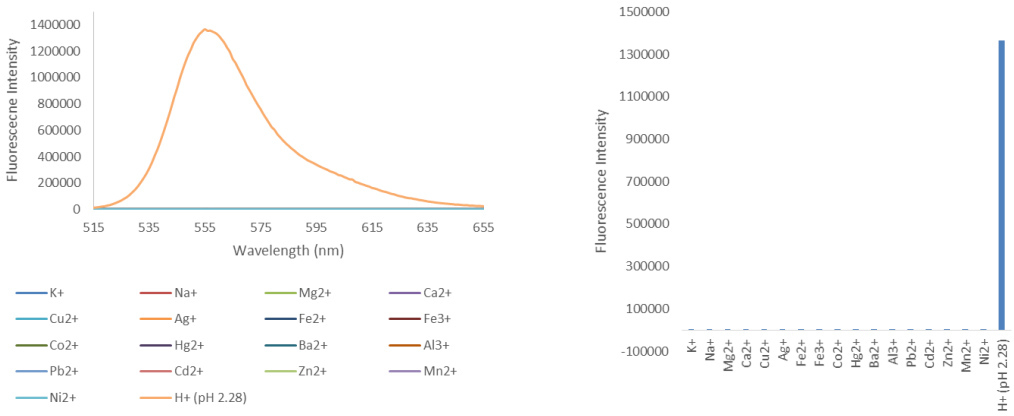

(A) (B)

Figure 4. (A) Fluorescence spectra of probe 1 (5 µM) in 0.1 M sodium phosphate buffer solution with different metal ions and protons and (B) Fluorescence responses of probe 1 upon addition of various metal ions (100 µM) and pH at 2.28; λ_{ex} = 510 nm and λ_{em} = 555 nm

Conclusion: The off/on fluorescence probe based on a rhodamine was developed as a pH sensor. Photophisical properties of probe 1 suggested that it can be used as a pH sensor by naked-eye or fluorescence spectroscopy. Probe 1 showed enhancement of visible absorption and fluorescence intensity when pH is lower than 5. The probe is highly selective for pH. Further development of probe 1 is ongoing and will be reported in due course.

References:

1. Webb BA, Chimenti M, Jacobson MP, Barber DL. Nat Rev cancer. 2011;11:671–677.
2. Gameiro P, Reis S, Lima JLFC, de Castro B. Anal chim acta. 2000;405:167–172.
3. Maskula S, Nyman J, Ivaska A. Talanta. 2000;52:91–99.
4. Paixao TRLC, Kosminsky L, Bertotti M. Sens Actuators B. 2002;87:41–46.
5. Draxler S, Lippitsch ME. Sensors Actuators B. 1995;29:199–203.
6. Mao Z, Hu L, Zhong C, Zhang H, Liu B-F, Liu Z. Sensors Actuators B. 2015;219:179–184.
7. Chen L, Li J, Liu Z, Ma Z, Zhang W, Du L, Xu W, Fang H, Li M. RSC Adv. 2013;3:13412–13416.
8. Cao X-J, Chen L-N, Zhang X, Liu J-T, Chen M-Y, Wu Q-R, Miao J-Y, Zhao B-X. Anal Chim Acta. 2016;920:86–93.
9. Niu W, Nan M, Fan L, Wong MS, Shuang S, Dong C. Dyes Pigments. 2016;126:224–231.
10. Voicu M, Ionescu S, Gatea F. Spectrochim Acta Part A. 2014;123:303–308.
11. Li G, Zhu D, Xue L, Jiang H. Org Lett. 2013;15:5020–5023.
12. Ying L-Q, Branchaud BP. Bioorg Med Chem Lett 2014;21:3546–3549.

Acknowledgements: This research was supported by Thailand Reach Fund (MRG6180248), Center of Excellence for Innovation in Chemistry (PERCH-CIC), and Department of Chemistry, Faculty of Science, Mahidol University.

C3_007_PF: XANTHONES FROM THE ROOTS OF *Cratoxylum cochinchinense*

Peeravat Natrsanga, Santi Tip-pyang*
Center of Excellence in Natural Products Chemistry, Department of Chemistry, Faculty of Science, Chulalongkorn University, Bangkok 10330, Thailand
*e-mail: Santi.Ti@chula.ac.th

Abstract: Six known xanthones namely cratoxylumxanthone A (1), 9-hydroxycalabaxanthone (2), macluraxanthone (3), 10-*O*-methylmacluraxanthone (4), 6-deoxyjacareubin (5), and β-mangostin (6) were isolated from the roots of *Cratoxylum cochinchinense* (Lour.) Blume. Their structures were characterized by spectroscopic methods as well as comparison with those reported in the literature. Their cytotoxicity was evaluated against (KB, Hela S-3, HT-29, MCF-7 and Hep G2 cell lines). Compounds 2 and 3 showed significant cytotoxicity towards both KB and Hela S-3 cells with the respective IC_{50} values of 7.39 and 6.07 µM (for 2) and 1.60, 1.85 µM (for 3). Moreover, 2 exhibited good cytotoxicity against HT-29 cells with IC_{50} value of 8.11 µM, whereas 3 showed a potent cytotoxicity against MCF-7 cells with IC_{50} value of 1.18 µM.

Introduction:

Cratoxylum cochinchinense (Lour.) Blume (Figure1) is a shrubby tree belonging to the family *Hypericaceae*, which is widely distributed in Southeast Asia. It has been extensively used in traditional medicine to treat a number of diseases including cough, diarrhea, fever, and ulcer. Its young fruit has also used as a food spice.[1] From previous phytochemical investigations of the stems, bark and roots of *C. cochinchinense*, diverse chemical constituents such as xanthones, flavonoids, tocotrienols, and triterpenoids have been described.[2-9] Many of these compounds demonstrated a number of interesting biological activity such as antioxidants, antimalarial, antibacterial, anti-HIV and cytotoxicity. This plant was also first collected from the Northern part of Thailand. Herein, we reported the isolation and structure elucidation of six known xanthones, cratoxylumxanthone A (1), 9-hydroxycalabaxanthone (2), macluraxanthone (3), 10-*O*-methylmacluraxanthone (4), 6-deoxyjacareubin (5), and β-mangostin (6), from the dichloromethane extract of the roots of *C. cochinchinense*. The cytotoxic evaluation of the compounds against five human cancer cell lines was also reported.

Methodology:

General experimental procedures: NMR spectra were recorded on a Bruker 400 AVANCE spectrometer and chemical shifts were reported in ppm referenced to solvent residues (δ_H 7.25 and δ_C 77.0 ppm for $CDCl_3$; δ_H 2.05 and δ_C 29.0 and 206.0 ppm for acetone-d_6). Silica gel 60 Merck cat. Nos. 7734 and 7749 were used as absorbent for open column chromatography (CC) and Chromatotron®, respectively. Thin layer chromatography (TLC) was performed on precoated Merck silica gel 60 F_{254} plates (0.25 mm thick layer) and visualized with 10% H_2SO_4–MeOH solution. Melting points were determined on a Fisher–John apparatus and are uncorrected.

Plant Material: The roots of *C. cochinchinense* were collected in Lumpang Province, Northern Thailand, in April 2018 and identified by Dr.Suttira Sedlak, a botanist at the Walai Rukhavej Botanical Research Institute, Mahasarakham University.

Figure 1. The morphological illustration of *Cratoxylum cochinchinense* (Lour.) Blume

Extraction and Isolation: The roots of *C. cochinchinense* (7.6 kg) were extracted with CH_2Cl_2 (3 x 5 L) at room temperature for 1 week. The combined extract was evaporated to give a yellowish brown gum (174.95 g), was subjected to silica gel CC by using hexane (2 L), 1:1 hexane–CH_2Cl_2 (3 L, CH_2Cl_2 (3 L) and 9:1 CH_2Cl_2–MeOH (3 L), yielding fourteen fractions (A1–A14). Fraction A7 (13 g) was subjected to silica gel CC by using a system of hexane–CH_2Cl_2 (1:1 and 1:9, 800 mL each) and CH_2Cl_2–MeOH (1:0, 95:5 and 90:10, 800 mL each) to give five subfractions (B1-B5). The combined subfractions B3 and B4 (4.0 g) were further purified on Chromatotron® with a system of hexane–EtOAc (3:1, 2:1 and 1:1, 500 mL each) to yield 2 (1.7 mg) and 6 (3.0 mg). Fraction A8 (10.0 g) was subjected to silica gel CC by using isocratic elution of hexane–CH_2Cl_2 (30:70, 1 L) and using a system of CH_2Cl_2–MeOH (1:0, 95:5 and 90:10, 1 L each) to afford nine subfractions (C1-C9). Fraction C3 (2.0 g) was also applied to a Sephadex LH-20 CC using CH_2Cl_2–MeOH (1:1, 900 mL) followed by Chromatotron® using isocratic elution of hexane–EtOAc (90:10, 500 mL) to give 1 (1.1 mg) and 5 (7.8 mg), respectively. The combined subfractions H5 and H6 (5.0 g) were subjected to Sephadex LH-20 CC using CH_2Cl_2–MeOH (1:1, 500 mL) then purified by Chromatotron® with a system of hexane–EtOAc (3:1, 2:1 and 1:1, 800 mL each) to furnish 3 (2.0 mg) and 4 (8.0 mg) respectively. All isolated compounds were identified on the basis of their spectroscopic data as well as comparison with those reported in the literature.

Cratoxylumxanthone A (1)[5] was obtained as a yellow powder; m.p. 231–232°C; UV (MeOH) λ_{max} (log ε) 254 (4.47), 266 (4.52), 331 (4.06), 380 (3.03) nm; IR (KBr) ν_{max} 3420, 2920, 1645, 1610,1580, 1465, 1286, 1192, 1102 cm^{-1}; HRESIMS *m/z* $[M + H]^+$409.1647 (Calcd for $C_{24}H_{25}O_6$, 409.1651); ^1H NMR (400 MHz, $CDCl_3$) and ^{13}C NMR (100 MHz, $CDCl_3$) in Table 1.

9-Hydroxycalabaxanthone (2)[14] was obtained as a yellow solid; m.p. 156-157°C; UV (MeOH) λ_{max} (log ε) 243 (4.40), 319(4.08), 358 (4.00) nm; IR (KBr) ν_{max} 3420, 2920, 1645, 1610,1580, 1465, 1286, 1192, 1102 cm^{-1}; HRESIMS *m/z* $[M + H]^+$409.1644 (Calcd for $C_{24}H_{25}O_6$, 409.1651); ^1H NMR (400 MHz, $CDCl_3$) and ^{13}C NMR (100 MHz, $CDCl_3$) in Table 2.

Macluraxanthone (3)[15] was obtained as yellow needles; m.p. 170-172°C; UV (MeOH) λ_{max} (log ε) 227 (4.12), 241 (4.15), 282 (4.53), 310 (4.00), 336 (4.16), 380 (3.88) nm; IR (KBr) ν_{max} 3340,3260, 2955,1655, 1575 cm^{-1}; HRESIMS *m/z* $[M + H]^+$ 395.1423 (Calcd for $C_{23}H_{23}O_6$, 395.1416); ^1H NMR (400 MHz, acetone d_6) and ^{13}C NMR (100 MHz, $CDCl_3$) in Table 2.

10-*O*-Methylmacluraxanthone (4)[16] was obtained as a yellow-green powder; m.p. 236-238°C; UV (MeOH) λ_{max} (log ε) 205(3.85), 282 (3.95), 336 (3.57) nm; IR (KBr) ν_{max} 3336, 2964, 2929,1649, 1623, 1571, 1520, 1465, 1444, 1418, 1324, 1286, 1258, 1200,1184, 1144 cm^{-1}; HRESIMS *m/z* $[M + H]^+$ 409.1632 (Calcd for $C_{24}H_{25}O_6$, 409.1651);^1H NMR spectrum (400 MHz, $CDCl_3$) and ^{13}C NMR (100 MHz, $CDCl_3$) in Table 3.

6-Deoxyjacareubin (5)[17] was obtained as a yellow powder; m.p. 210-212°C; UV (MeOH) λ_{max} (log ε) 236 (4.34), 249sh. 280sh. 292 (5.65), 310sh, 340sh, 375 (3.60) nm; IR (KBr) ν_{max} 3460, 3420,2960,2920, 1645, 1625 cm^{-1}; HRESIMS *m/z* $[M + H]^+$ 311.0832 (Calcd for $C_{18}H_{15}O_5$, 311.0851); ^1H NMR spectrum (400 MHz, $CDCl_3$) and ^{13}C NMR (100 MHz, $CDCl_3$) in Table 3.

β-Mangostin (6)[18] was obtained as yellow gum; UV (MeOH) λ_{max} (log ε) 245 (4.44), 262 (4.43), 312 (4.23), 349(3.74) nm; IR (KBr) ν_{max} 3420,2923,2910, 1645, 1595,1456 cm^{-1}; HRESIMS *m/z* $[M + H]^+$ 425.1986 (Calcd for $C_{25}H_{29}O_6$, 425.1919); ^1H NMR spectrum (400 MHz, $CDCl_3$) and ^{13}C NMR spectrum (100 MHz, $CDCl_3$) in Table 4

Cytotoxicity Assay: The isolated compounds were evaluated for their cytotoxicity against cervix adenocarcinoma (Hela S3), epidermoid carcinoma (KB), adenocarcinoma (HT-29), breast adenocarcinoma (MCF-7) and hepatocellular carcinoma (Hep G2) using an MTT colorimetric method.[13] Doxorubicin was used as the reference substance. 3-(4,5-Dimethylthiazol-2-yl)-2,5-diphenyl-tetrazolium bromide (Sigma Chemical Co., USA) was dissolved in saline to make a 5 mg/mL stock solution. Cancer cells (3×10^3 cells) suspended in 100µg/wells of MEM medium containing 10% fetal calf serum (FCS, Gibco BRL, Life Technologies, NY, USA) were seeded onto a 96-well culture plate (Costar, Corning Incorporated, NY 14831, USA). After 24 h of pre-incubation at 37 °C in ahumidified atmosphere of 5% CO_2/95% air to allow cellular attachment, various concentrations of test solution (10µL/well) were added and these were then incubated for 48 h under the above conditions. At the end of the incubation, 10µL of tetrazolium reagent was added into each well followed by further incubation at 37 °C for 4 h. The supernatant was decanted, and DMSO (100µL/well) was added to allow Formosan solubilization. The optical density (OD) of each well was detected using a Microplate reader at 550 nm and for correction at 595 nm. Each determination represented the average means of six replicates. The 50% inhibition concentration (IC_{50}value) was determined by curve fitting.

Results and Discussion: The CH_2Cl_2 extract from the roots of *C. cochinchinense* was fractionated through various chromatographic methods to afford six known xanthones (1-6) as shown in Figure 2. All of isolated compounds were characterized by using spectroscopic data as well as by comparison with the previously reported data of the known compounds. They were identified as cratoxylumxanthone A (1), 9-hydroxycalabaxanthone (2), macluraxanthone (3), 10-*O*-methylmacluraxanthone (4), 6-deoxyjacareubin (5), and β-mangostin (6).

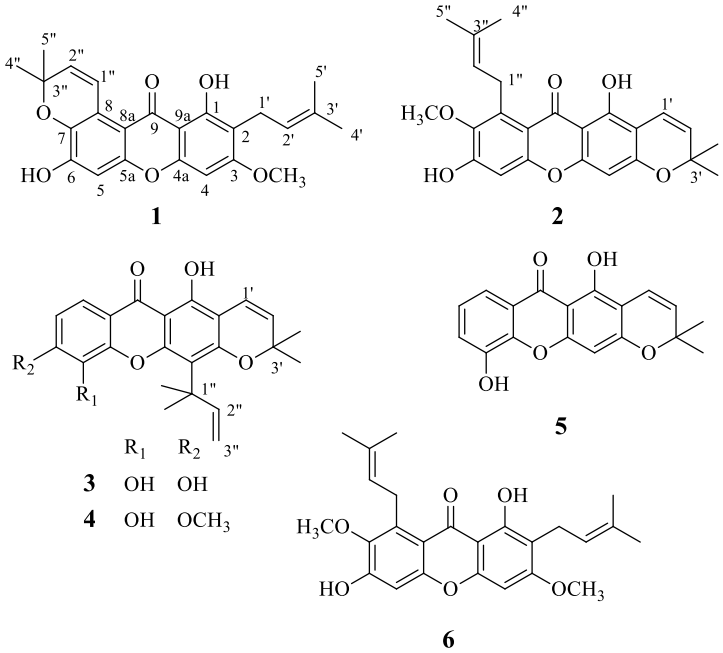

Figure 2. Structures of 1–6 isolated from the roots of *C. Cochinchinense*.

Compound 1 was obtained as a yellow powder (m.p. 231–232 °C). A molecular formular of $C_{24}H_{24}O_6$ was suggested by HRESIMS data *(m/z* = 409.1647 $[M + H]^+$, calcd for $C_{24}H_{25}O_6$, 409.1651). The UV spectrum showed absorption bands at 254, 266, 331, 380 nm, which were characteristics of a hydroxylated xanthone[5]. The ^{1}H NMR spectrum (Table 1) displayed signals for a chelated hydroxy proton at δ_H13.34 (1H, *s*, 1-OH), aromatic proton singlets at δ_H 6.36 (1H, *s*, H-4) and 6.82 (1H, *s*, H-5), and a methoxy group at δ_H 3.90 (3H, *s*, 3-OCH_3). The methoxy group was accommodated at C-3 of ring A based on HMBC cross peak. The presence of a prenyl group was indicated by signals for an olefinic proton at δ_H 5.23 (1H, *m*, H-2′), methylene protons at δ_H 3.35 (2H, *d*, *J* = 7.2 Hz, H-1′), and two methyl groups at δ_H 1.69 (3H, *s*, H-4′) and 1.80 (3H, *s*, H-5′). The correlation of H-1′ to C-1, C-2 and C-3 in the HMBC spectrum (Table 1) established that the prenyl unit was at C-2 of ring A. Furthermore, a dimethylchromene ring was determined from the resonances of two *cis*-olefinic protons at δ_H 8.03 (1H, *d*, *J* = 10.2 Hz, H-1″) and 5.83(1H, *d*, *J* = 10.2 Hz, H-2″), and a singlet for two methyl groups at δ_H 1.50 (6H, *s*, H-4″ and H-5″). The HMBC correlation of H-1″ to C-7 and H-2″ to C-8 indicated the connectivity of dimethylchromene moiety with ether linkage at C-7. The ^{13}C NMR spectrum displayed 24 signals including a carbonyl carbon (δ_C 183.0), twelve quaternary carbons, five methines, one methylene and five methyls (Table 2). The ^{1}H and ^{13}C NMR spectrum of 1 was also compared with those of cratoxylumxanthone A reported in the literature.[5]

Table 1. ^{1}H, ^{13}C and HMBC NMR data of cratoxylumxanthone A (1) in $CDCl_3$ (400 MHz for ^{1}H, 100 MHz for ^{13}C)

Position	cratoxylumxanthone A (1)		
	δ_H (J in Hz)	δ_C	HMBC correlations
1	-	159.6	-
2	-	111.4	-
3	-	163.6	-
4	6.36, (*s*)	88.9	C-2, C-3, C-4a,C-9a
4a	-	155.4	-
5	6.82, (*s*)	102.2	C-5a, C-6, C-7, C-8a
5a	-	153.0	-
6	-	150.7	-
7	-	136.7	-
8	-	119.7	-
8a	-	108.7	-
9	-	183.0	-
9a	-	104.0	-
1′	3.35, (*d*, 7.2)	21.3	C-1, C-2, C-3, C-2′, C-3′
2′	5.23, (*m*)	121.3	-
3′	-	130.0	-
4′	1.69, (*s*)	25.8	C-3′, C-2′, C-5′,
5′	1.80, (*s*)	17.7	C-3′, C-4′, C-2′,
1″	8.03, (*d*, 10.2)	122.3	C-7, C-3″
2″	5.83, (*d*, 10.2)	131.7	C-8, C-3″
3″	-	77.2	-
4″	1.50, (*s*)	27.3	C-2″, C-3″
5″	1.50, (*s*)	27.3	C-2″, C-3″
1-OH	13.34, (*s*)	-	C-1, C-2, C-9a
3-OCH_3	3.90, (*s*)	55.8	C-3
6-OH	6.15, (*s*)	-	C-5, C-6, C-7

Compound 2 was obtained as a yellow solid (m.p. 156-157 °C). Its molecular formula was deduced as $C_{24}H_{24}O_6$ by HRESIMS data (*m/z* = 409.1644 $[M + H]^+$, calcd for $C_{24}H_{25}O_6$, 409.1651). The UV and IR spectrum displayed characteristic of a 1,3,6,7-tetraoxygenated xanthone.[14] The ^{1}H NMR spectrum (Table 2) displayed signals for a chelated hydroxy proton at δ 13.68 (1H, *s*, 1-OH), two aromatic proton singlets at δ_H 6.15 (1H, *s*, H-4) and 6.73 (1H, *s*, H-5) and one methoxy group at δ_H 3.76 (3H, *s*, 7-OCH_3). The presence of a prenyl group was assigned based on signals for an olefinic proton at δ_H 5.24 (1H, *m*, H-2″), methylene protons at δ_H 4.01 (2H, *d*, J = 7.2 H, H-1″) and two methyl groups at δ_H 1.68 (3H, *s*, H-5″) and 1.77 (3H, *s*, H-4″). The presence of dimethylchromene ring was indicated by the coupling pattern of *cis*-olefinic protons at δ_H 5.47 (1H, *d*, J = 10.2 Hz, H-2′) and 6.65 (1H, *d*, J = 10.2 Hz, H-1′), and two singlet for methyl groups at δ_H 1.67 (each 3H, *s*, H-4′ and H-5′). The ^{13}C NMR spectrum displayed 24 carbons including a carbonyl carbon (δ_C 181.5), twelve quaternary carbons, five methines, one methylene and five methyls (Table 2). The ^{1}H NMR and ^{13}C NMR data of compound 2 was identical to the data previously reported for 9-hydroxycalabaxanthone.[14]

Table 2. ^{1}H and ^{13}C NMR data of compounds 2 and 3 (400 MHz for ^{1}H, 100 MHz for ^{13}C)

Position	2 (in $CDCl_3$)		3 (in acetone d_6)	
	δ_H (J in Hz)	δ_C	δ_H (J in Hz)	δ_C
1	-	157.7	-	159.4
2	-	103.6	-	105.9
3	-	159.8	-	160.1
4	6.15, (*s*)	93.8	-	114.2
4a	-	156.0	-	154.8
5	6.73, (*s*)	101.5	-	133.4
5a	-	155.5	-	146.8
6	-	154.5	-	150.8
7	-	142.7	7.00, (*d*, 8.7)	113.4
8	-	136.9	7.60, (*d*, 8.7)	118.9
8a	-	112.1	-	115.3
9	-	181.5	-	181.7
9a	-	104.5	-	103.6
1′	6.65, (*d*, 10.2)	115.6	6.79, (*d*, 11.0)	116.4
2′	5.47, (*d*, 10.2)	123.2	5.78, (*d*, 11.0)	128.2
3′	-	77.8	-	79.0
4′	1.67, (*s*)	28.3	1.52, (*s*)	28.0
5′	1.67, (*s*)	28.3	1.52, (*s*)	28.0
1″	4.01, (*d*, 7.2)	26.5	-	41.8
2″	5.24, (*m*)	126.9	6.52, (*dd*, 17.2, 11.0)	152.9
3″a	-	131.8	5.05, (*d*, 17.2)	107.2
3″b			4.89, (*d*, 11.0)	
4″	1.77, (*s*)	18.1	1.74, (*s*)	29.9
5″	1.68, (*s*)	25.6	1.74, (*s*)	29.9
1-OH	13.68, (*s*)	-	13.90, (*s*)	-
6-OH	6.28, (*s*)	-	-	-
7-OCH_3	3.76, (*s*)	61.6	-	-

Compound 3 was obtained as yellow needles (m.p. 170-172 °C). Its molecular formula was determined as $C_{23}H_{22}O_6$ by HRESIMS measurement at *m/z* 395.1423 $[M + H]^+$ (calcd for $C_{23}H_{23}O_6$, 395.1416) The UV and IR data of 3 showed characteristics of a xanthone skeleton.[15] The ^{1}H NMR spectrum (Table 2) showed the presence of signals for a chelated hydroxy proton at δ_H 13.90 (1H, *s*, 1-OH) and two *ortho*-coupled aromatic protons at δ_H 7.00 (1H, *d*, J = 8.7 Hz, H-7), and 7.60 (1H, *d*, J = 8.7 Hz, H-8). The occurrence of dimethylchromene ring was inferred from signals at δ_H 5.78 (1H, *d*, J = 11.0 Hz, H-2′), 6.79 (1H, *d*, J = 11.0 Hz, H-1′) and two methyl group at δ 1.52 (each 3H, *s*, H-4′ and H-5′). In addition, the splitting pattern and coupling constants of three olefinic protons at δ_H 6.52 (1H, *dd*, J = 17.2, 11.0 Hz, H-2″), 5.05 (1H *d*, J = 17.2 Hz, H-3″a) and 4.89 (1H, *d*, J = 11.0 Hz, H-3″b) indicated the presence of a terminal alkene as a part of a 1,1-dimethylallyl group which also displayed two singlets for methyl groups at δ_H 1.74 (each 3H, *s*, H-4″ and H-5″). The ^{13}C NMR data displayed 23 carbons including a carbonyl carbon (δ_C 181.7), twelve quaternary carbons, five methines, one methylene and four methyls in Table 2. The ^{1}H NMR and ^{13}C NMR spectrum of 3 suggested that compound 3 was macluraxanthone.[15]

Compound 4 was isolated as a yellow-green powder (m.p. 236-238 °C) with a molecular formula $C_{24}H_{24}O_6$ determined by HRESIMS (*m/z* = 409.1632 $[M + H]^+$, calcd for $C_{24}H_{25}O_6$, 409.1651). The UV and IR data of 4 showed characteristics of a xanthone skeleton.[16]

The ^{1}H NMR spectrum (Table 3) indicated the presence of the dimethylchromene ring, 1,1-dimethylallyl group, and two *ortho*-coupled aromatic protons of 4 which were closely related to those of 3. The difference was the presence of the ^{1}H NMR signal for a methoxy group at δ_H 3.90 (3H, *s*, 6-OCH_3). The ^{13}C NMR data displayed 24 carbons including a carbonyl carbon (δ_C 182.3), twelve quaternary carbons, six methines and five methyls in Table 3. Comparison of the ^{1}H and ^{13}C NMR spectrum of 4 with previous reported as 10-*O*-methylmacluraxanthone.[16]

Table 3. ^{1}H and ^{13}C NMR data of compounds 4 and 5 (400 MHz for ^{1}H, 100 MHz for ^{13}C)

Position	4 (in $CDCl_3$)		5 (in $CDCl_3$)	
	δ_H (*J* in Hz)	δ_C	δ_H (*J* in Hz)	δ_C
1	-	157.4	-	160.1
2	-	105.9	-	105.9
3	-	160.1	-	157.2
4	-	114.2	6.38, (*s*)	95.4
4a	-	154.8	-	156.7
5	-	133.4	-	147.5
5a	-	145.6	-	146.0
6	-	151.4	7.45, (*dd*, 7.8, 1.8)	120.5
7	6.89, (*d*, 8.7)	109.4	7.32, (*t*, 7.8)	124.9
8	7.73, (*d*, 8.7)	118.9	7.72, (*dd*, 7.8, 1.8)	115.8
8a	-	115.3	-	121.7
9	-	181.7	-	182.3
9a	-	103.6	-	104.6
1′	6.74, (*d*, 11.0)	116.4	6.68, (*d*, 11.0)	116.3
2′	5.68, (*d*, 11.0)	128.2	5.78, (*d*, 11.0)	128.6
3′	-	79.0	-	79.3
4′	1.45, (*s*)	28.2	1.48, (*s*)	29.0
5′	1.45, (*s*)	28.2	1.48, (*s*)	29.0
1″	-	41.8	-	-
2″	6.59, (*dd*, 17.2, 11.0)	151.9	-	-
3″a	5.05, (*d*, 17.2)	107.4	-	-
3″b	4.92, (*d*, 11.0)		-	-
4″	1.64, (*s*)	29.8	-	-
5″	1.64, (*s*)	29.8	-	-
1-OH	13.50, (*s*)	-	13.32, (*s*)	-
5-OH	6.21, (*s*)	-	9.15, (*br s*)	-
6-OCH_3	3.90, (*s*)	57.1	-	-

Compound 5 was obtained as a yellow powder (m.p. 210-212°C). Its molecular formula was determined as $C_{18}H_{14}O_5$ by HRESIMS measurement at *m/z* 311.0832 $[M + H]^+$ (calcd for $C_{18}H_{15}O_5$, 311.0851). The UV and IR data of 5 showed characteristics of a xanthone skeleton.[16] The ^{1}H NMR spectrum displayed signals for a chelated hydroxy proton at δ_H 13.32 (1H, *s*, 1-OH), broad singlet of hydroxy group at δ_H 9.15 (1H, *br s*, 5-OH) and aromatic proton singlets at δ_H 6.38 (1H, *s*, H-4). Moreover, the splitting pattern and coupling constants of a 1,2,3-trisubsituted benzene moiety in ring B were observed at δ_H 7.32 (1H , *t*, *J* = 7.8 Hz, H-7), 7.45 (1H, *dd*, *J* = 7.8, 1.8 Hz, H-6), 7.72 (1H , *dd*, *J* = 7.8, 1.8 Hz, H-8). The proton signals of a dimethylchromene ring were inferred from signals for two *cis*-olefinic protons at δ_H 5.78

(1H, *d*, *J* = 11.0 Hz, H-2′), 6.68 (1H, *d*, *J* = 11.0 Hz, H-1′) and two methyl groups at δ 1.48 (each 3H, *s*, H-4′ and H-5′). The ^{13}C NMR data displayed 18 carbons including a carbonyl carbon (δ_C 181.5), nine quaternary carbons, six methines and two methyls (Table 3). From the above evidence with the literature data, the structure of 5 was determined as 6-deoxyjacareubin.[17]

Compound 6 was obtained as a yellow gum. Its molecular formula was deduced as $C_{25}H_{28}O_6$ based on HRESIMS data (*m/z* = 425.1986 $[M + H]^+$, calcd for $C_{25}H_{29}O_6$, 425.1919). UV and IR data of 6 revealed the xanthone character of the compound. The ^{1}H NMR spectrum (Table 4) displayed signals for a chelated hydroxy proton at δ_H 13.34 (1H, *s,* 1-OH), two aromatic protons at δ_H 6.24 (1H, *s*, H-4), 6.76 (1H, *s*, H-5), and two methoxy groups at δ_H 3.78 (3H, *s*, 3-OCH_3) and 3.85 (3H, *s*, 7-OCH_3). On the basis of HMBC cross peaks, these two methoxy groups were placed at C-3 of ring A, and C-7 of B ring, respectively. The characteristic signals of two prenyl groups were indicated by signals for two olefinic protons at δ_H 5.22 (2H, *m*, H-2′) and 5.23 (2H, *m*, and H-2″), two sets of methylene protons at δ_H 3.35 (2H, *d*, *J* = 7.2 Hz, H-1′), 4.05 (2H, *d*, *J* = 7.2 Hz, H-1″), and four methyl groups at δ_H 1.68 (3H, *s*, H-4′), 1.69 (3H, *s*, H-4″), 1.80 (3H, *s*, H-5′), 1.84 (3H, *s*, H-5″). The correlations of H-1′ to C-1, C-2 and C-3 (Table 4) revealed that the prenyl group was located at C-2 of ring A, while H-1″ to C-7, C-8 and C-8a indicated that the prenyl group was placed at C-8 of ring B. The ^{13}C NMR data displayed 25 carbons including a carbonyl carbon (δ_C 181.8), twelve quaternary carbons, four methines, two methylenes and six methyls (Table 4). The ^{1}H and C^{13} NMR spectra of 6 were identical to those of β-mangostin.[18]

Table 4. ^{1}H, ^{13}C and HMBC NMR data of β-mangostin (6) in $CDCl_3$ (400 MHz for ^{1}H, 100 MHz for ^{13}C)

Position	β-mangostin (6)		
	δ_H (*J* in Hz)	δ_C	HMBC correlations
1	-	159.7	-
2	-	111.3	-
3	-	163.5	-
4	6.24, (*s*)	88.7	C-2, C-3, C-4a,C-9a
4a	-	155.7	-
5	6.76, (*s*)	101.1	C-5a, C-6, C-7, C-8a
5a	-	155.2	-
6	-	154.4	-
7	-	142.5	-
8	-	137.2	-
8a	-	112.4	-
9	-	181.8	-
9a	-	103.2	-
1′	3.35, (*d*, 7.2)	21.2	C-1, C-2, C-3, C-2′, C-3′
2′	5.22, (*m*)	122.3	-
3′	-	131.5	-
4′	1.80, (*s*)	17.8	C-3′, C-2′, C-5′,
5′	1.68, (*s*)	25.8	C-3′, C-4′, C-2′,
1″	4.05, (*d*, 7.2)	26.4	C-7, C-8, C-8a, C-2″, C-3″
2″	5.23, (*m*)	123.2	-
3″	-	132.1	-
4″	1.84, (*s*)	18.0	C-3″, C-2″, C-5″
5″	1.69, (*s*)	25.8	C-3″, C-4″, C-2″
1-OH	13.34, (*s*)	-	C-1, C-2, C-9a
3-OCH_3	3.78, (*s*)	55.8	C-3
6-OH	-	-	-
7-OCH_3	3.85, (*s*)	62.1	C-7

Cytotoxicity: In previous research many xanthones showed a remarkable cytotoxicity.[9,11,12] Therefore, all isolated compounds (1-6) were evaluated cytotoxicity against five human cancer cell lines (KB, Hela S-3, HT-29, MCF-7 and Hep G2 cell lines) using modified MTT method.[13] However, this is the first report of the evaluation of 2 for their cytotoxicity against the Hep-G2 cells. The results of cytotoxicity were shown in Table 5. Most of the tested compounds showed moderate to weak cytotoxicity, except 2 and 3 which showed significant activity towards both KB and Hela S-3 cells with IC_{50} values of 7.39, 6.07 and 1.60, 1.85 µM, respectively. The active compounds (2 and 3) with IC_{50} values lower than 10 µM toward these two cancer cell lines were further evaluated against the other three cell lines, comprising HT-29, MCF-7, and Hep G2 cells. Compound 2 showed good cytotoxicity against HT-29 cells with IC_{50} value of 8.11 µM while 3 showed a potent cytotoxicity against MCF-7 cells with IC_{50} value of 1.18 µM (Table 5).

Table 5. Cytotoxicity of isolated compounds (1-6) from the roots of *C. Cochinchinense*.

Compounds	IC_{50} (µM) ± SD				
	KB	Hela S-3	HT-29	MCF-7	Hep G2
1	26.44 ± 2.61	10.50 ± 0.86	N.T.	N.T.	N.T.
2	7.39 ± 0.15	6.07 ± 0.59	8.11 ± 0.43	13.67 ± 0.31	27.72 ± 0.61
3	1.60 ± 0.02	1.85 ± 0.19	14.58 ± 0.14	1.18 ± 0.04	10.57 ± 0.74
4	53.01 ± 4.88	35.12 ± 2.63	N.T.	N.T.	N.T.
5	28.01 ± 0.84	13.42 ± 0.91	N.T.	N.T.	N.T.
6	24.99 ± 3.16	14.383 ± 2.67	N.T.	N.T.	N.T.
Doxorubicin	0.02 ± 0.01	0.13 ± 0.01	0.59 ± 0.03	1.29 ± 0.02	0.99 ± 0.17

Note: $IC_{50} \leq 10$ µM = good activity, 10 µM < $IC_{50} \leq 30$ µM = moderate activity, 30 µM < $IC_{50} \leq 100$ µM = weak activity, $IC_{50} > 100$ µM = inactive.
N.T.; the compounds were not tested.

Conclusion: Six xanthones, which were isolated from the roots of *C. cochinchinense*, were identified as cratoxylumxanthone A (1), 9-hydroxycalabaxanthone (2), macluraxanthone (3), 10-*O*-methylmacluraxanthone (4), 6-deoxyjacareubin (5), and β-mangostin (6). Compounds 2 and 3 showed the most potent cytotoxicity towards both KB and Hela S-3 cells with IC_{50} values of 7.39, 6.07 and 1.60, 1.85 µM, respectively. Furthermore, 2 exhibited good cytotoxicity against HT-29 cells with IC_{50} value of 8.11 µM, while 3 revealed significant cytotoxicity against MCF-7 cells with IC_{50} value of 1.18 µM.

References:

1. Laphookhieo S, Maneerat W, Buatip T, Syers J.K, *Can J Chem.* 2008;86:757–760.
2. Duan Y.H, Dai Y, Wang G.H, Chen L.Y, Chen H.F, Zeng D.Q, Li Y.L Yao X.S, *J Asian Nat Prod Res*. 2015;17:519–531.
3. Udomchotphruet S, Phuwapraisirisan P, Sichaem J, Tip-pyang S, *Phytochemistry*. 2012;17:148–151.
4. Boonnak N, Karalai C, Chantrapromma S, Ponglimanont C, Fun H.K, Kanjana-Opas A, Chantrapromma K, Kato S, *Tetrahedron.* 2009;65:3003–3013.
5. Phuwapraisirisan P, Udomchotphruet S, Surapinit S, Tip-Pyang S, *Nat Prod Res* 2006;20:1332–1337.
6. Bennett G.J, Harrison L.J, Sia G.L, Sim K.Y, *Phytochemistry*. 1993;23:1245–1251.
7. Nguyen L.H.D, Harrison L.J, *Phytochemistry*. 1998;50:471–476.
8. Mahabusarakam W, Nuangnaowarat W, Taylor W.C, *Phytochemistry.* 2006;67:470–474.
9. Ren Y, Matthew S, Lantvit D.D, Ninh T.N, Chai H, Fuchs J.R, Soejarto D.D, De Blanco E.J.C, Swanson S.M, Kinghorn A.D, *J Nat Prod.* 2011;74:1117–1125.

10. Rukachaisirikul V, Phainuphong P, Sukpondma Y, Phongpaichit S, Taylor W.C, *Planta Med*. 2005;71:165–170.
11. Laphookhieo S, Syers J.K, Kiattansakul R, Chantrapromma K,Chem Pharm Bull. 2006;54:745–747.
12. Reutrakul V, Anantachoke N, Pohmakotr M, Jaipetch T, Sophasan S, Yoosook C, Kasisit J, Napaswat C, Santisuk T, Tuchinda P, *Planta Med*. 2007;73:33–40.
13. Kongkathip N, Kongkathip B, Siripong P, Sangma C, Luangkamin S, Niyomdecha M, Pattanapa S, Piyaviriyagul S, Kongsaeree P, *Bioorg Med Chem*. 2003;11:3179–319.
14. Sen A.K, Sarkar K.K, Mazumder P.C, Banerji N, Uusvuori R, Hase T.A, *Phytochemistry*. 1980;19:2223–2225.
15. Iinuma M, Tosa H, Tanaka T, Yonemori S, *Phytochemistry.* 1993;35:527-532.
16. Gunasekera S.P, Selliah S, Sultanbawa M.U.S, *J Chem Soc, Perkin Trans* 1. 1975;1: 1539–1544.
17. Chilpa R.R, Estrada M.J, Muniz E.E, *J Chem Ecol*. 1997;23:1901-1911.
18. Sim W.C, Lain G.C, Aspollah S.M, *Res J Chem Environ.* 2011;15(2):62-66.

Acknowledgements: The authors are grateful to 90th Anniversary of Chulalongkorn University Fund (Ratchadaphiseksomphot Endowment Fund).

C3_008_PF: DEVELOPMENT OF AN ASYMMETRIC DIELS–ALDER REACTION OF *O*-NAPHTHOQUINONES

Watcharapon Prasitwatcharakorn, Torsak Luanphisarnnont*
Department of Chemistry and Center of Excellence for Innovation in Chemistry (PERCH-CIC), Faculty of Science, Mahidol University, 272 Rama VI Road, Ratchathewi, Bangkok, 10400, Thailand
*e-mail: torsak.lua@mahidol.ac.th

Abstract: Complex chiral carbocycles are important structural motifs in organic chemistry because they can be found in many biologically active and useful natural products and synthetic compounds. One powerful method to synthesize such carbocycles is an asymmetric Diels–Alder reaction which can rapidly assemble the complex carbocycles in high yield and regioselectivity. This work focuses on the development of a catalytic asymmetric Diels–Alder reaction of *o*-quinones using substituted prolinols as chiral catalysts. These chiral catalysts can catalyze the reaction with moderate efficiency, giving the desired complex chiral carbocycle products in moderate yield, excellent regioselectivity, and moderate enantioselectivity.

Introduction: *o*-Quinones are important because a large number of natural products have an *o*-quinone core structure. Many of them exhibit a biological activity or play a significant role in redox processes in biological systems (Figure 1).[1–6] In addition, *o*-quinones are also key intermediates in syntheses of many natural products and pharmaceutical compounds such as (–)-morphine[7] (Scheme 1) and pygmaeocin C.[8]

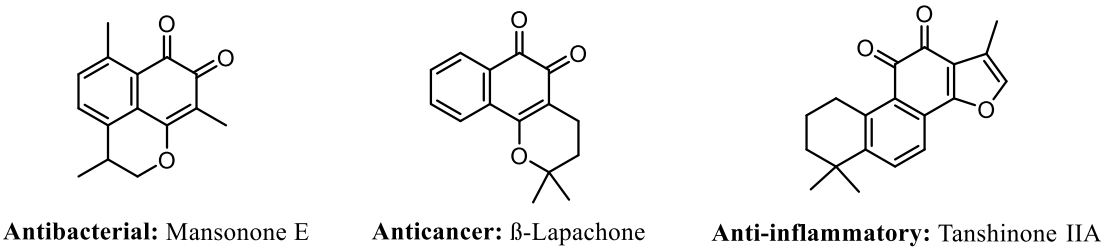

Figure 1. Example of bioactive *o*-quinones

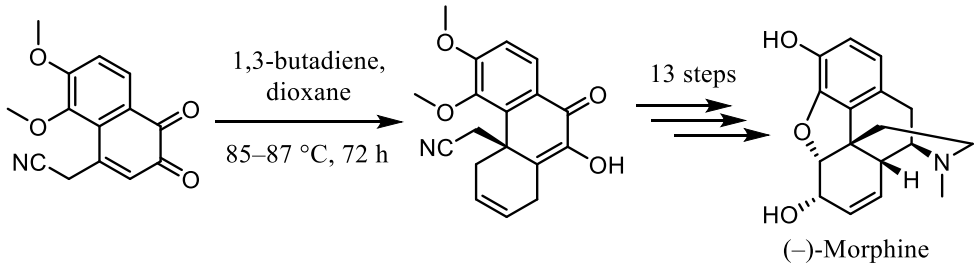

Scheme 1. *o*-Quinones as a key intermediate in (–)-morphine synthesis

o-Quinones can undergo concerted cycloaddition reactions. From the structural feature of *o*-quinones, they can participate in the cycloaddition reactions in four different modes which are carbodiene, heterodiene, carbodienophile, and heterodienophile. Catalytic asymmetric Diels–Alder reactions of *o*-quinones have been investigated. In 2006, Lectka and co-workers disclosed a catalytic enantioselective [4+2] cycloadditions of ketene enolates and *o*-quinones (Scheme 2a).[9] *o*-Chloranil was used as hetero-diene to react with

in-situ generated ketene enolate from acetyl chloride in the presence of benzoylquinidine and Hünig's base to give the products in high yield and excellent enantioselectivity. In 2007, an inverse-electron-demand hetero Diels–Alder reaction of *o*-quinone and *in-situ* generated enamines from aldehydes was studied by Dixon and co-workers (Scheme 2b).[10] A tetrahalo-*o*-benzoquinones was used to react with enamines and provided the products in moderate to high yield and good enantioselectivity.

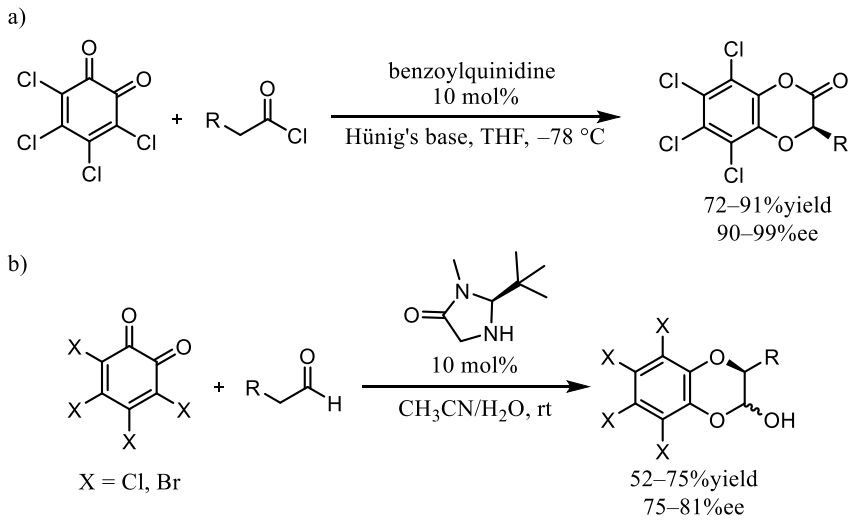

Scheme 2. Catalytic asymmetric Diels–Alder reactions of *o*-quinones a) A catalytic enantioselective [4+2] cycloadditions of *o*-quinones and ketene enolates b) An inverse-electron-demand hetero Diels–Alder reaction of *o*-quinone and enamines

Although some catalytic asymmetric reactions of *o*-quinones have been reported, a catalytic asymmetric reaction in which *o*-quinones act as carbodienophile has not been studied. Herein, this research presented the development of an asymmetric Diels–Alder reaction of *o*-naphthoquinone using chiral prolinols as chiral catalysts (Scheme 3).

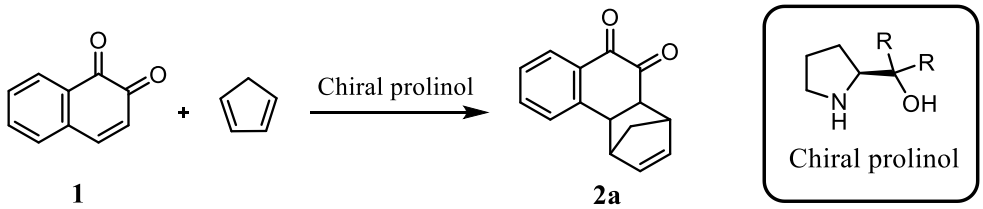

Scheme 3. Asymmetric Diels–Alder reaction of *o*-naphthoquinone

Methodology:

General Procedures.: ^{1}H-NMR and ^{13}C-NMR spectra were obtained from a 400 MHz NMR spectrometer. Chemical shifts are reported in ppm from tetramethylsilane or the residual solvent resonance as an internal standard ($CDCl_3$ at δ_H 7.26 and δ_C 77.0). Data are reported as follows: (br = broad, app = apparent, s = singlet, d = doublet, t = triplet, q = quartet, m = multiplet; coupling constant(s) in Hz, integration). Enantioselectivity was determined by a chiral AS-H HPLC column.

Materials.: Commercial reagents were purchased from Sigma Aldrich, TCI, Merck, and Alfa Aesar and used without purification unless otherwise noted.

General procedure for the synthesis of Prolinol 7a–7d.: To a 250 mL two-necked round-bottomed flask equipped with a Teflon coated magnetic stir bar, a condenser and an addition funnel under nitrogen atmosphere was added magnesium turning (0.13 g, 5.45 mmol) and dry tetrahydrofuran (10 mL). A solution of aryl bromide in dry tetrahydrofuran (20 mL) was slowly added *via* the addition funnel. The reaction was heated to 50 °C until the Grignard's reagent was formed. Next, a solution of *N*-Boc-*S*-proline methyl ester (5) (0.50 g, 2.18 mmol) in dry tetrahydrofuran (20 mL) was slowly added and the reaction was heated to reflux for 3 h. The reaction was then cooled to room temperature, and saturated aqueous ammonium chloride (20 mL) was added. Then, the reaction mixture was extracted with EtOAc (3×100 mL), and the combined organic layer was washed with water (2×100 mL) and brine (2×100 mL), respectively. The organic layer was dried with anhydrous sodium sulfate, filtered and evaporated to dryness in vacuum. Next, to a 100 mL round–bottomed flask equipped with a Teflon coated magnetic stir bar was added substituted *N*-Boc-*S*-prolinol (6a–6d) (1.41 mmol), sodium hydroxide (NaOH, 0.57 g, 14.2 mmol) and ethanol (50 mL). The reaction was heated to reflux for 2 h. The reaction was cooled to room temperature. Then, the reaction mixture was extracted with EtOAc (3×100 mL), and the combined organic layer was washed with water (2×100 mL) and brine (2×100 mL), dried with anhydrous sodium sulfate, filtered, and evaporated to dryness in vacuum. The crude reaction was purified by column chromatography over silica gel (20% EtOAc/hexanes).

S-Diphenyl(pyrrolidin-2-ly)methanol (7a).: The compound was synthesized according to the general procedure. Bromobenzene (0.86 g, 5.45 mmol) was used as the aryl bromide. The product was obtained as a white solid (0.16 g, 55%). ^{1}H NMR (400 MHz, $CDCl_3$): δ_H 7.57 (d, *J* = 8.4, 2H), 7.50 (d, *J* = 8.4, 2H), 7.31–7.26 (m, 4H), 7.18–7.14 (m, 2H), 4.26 (t, *J* = 7.7 Hz, 1H), 3.04–2.98 (m, 1H), 2.97–2.89 (m, 1H), 1.78–1.54 (m, 4H). The ^{1}H NMR was found to be identical to the published data.[11]

S-Bis(3,5-dimethylphenyl)(pyrrolidin-2-yl)methanol (7b).: The compound was synthesized according to the general procedure. 1-Bromo-3,5-dimethylbenzene (1.0 g, 5.45 mmol) was used as the aryl bromide. The product was obtained as a white solid (0.39 g, 58%). ^{1}H NMR (400 MHz, $CDCl_3$): δ_H 7.21 (s, 2H), 7.12 (s, 2H), 6.82 (s, 2H), 4.29 (t, *J* = 4.1 Hz, 1H), 3.01–2.91 (m, 2H), 2.32 (s, 6H), 2.30 (s, 6H), 1.79–1.57 (m, 4H). The ^{1}H NMR was found to be identical to the published data.[12]

S-Bis(3-methoxyphenyl)(pyrrolidin-2-yl)methanol (7c).: The compound was synthesized according to the general procedure. 1-Bromo-3-methoxybenzene (1.02 g, 5.45 mmol) was used as the aryl bromide. The product was obtained as a white solid (0.38 g, 56%). ^{1}H NMR (400 MHz, DMSO-d_6): δ_H 7.25–7.12 (m, 4H), 7.05–7.01 (m, 1H), 7.01–6.96 (m, 1H), 6.78–6.68 (m, 2H), 4.74 (m, 1H), 3.75 (s, 3H), 3.71 (s, 3H), 3.19–3.10 (m, 2H), 1.98–1.75 (m, 4H); ^{13}C NMR (100 MHz, $CDCl_3$): δ_C 159.7, 146.4, 146.3, 129.8, 129.5, 118.4, 118.0, 112.7, 112.2, 112.1, 112.0, 65.6, 55.4, 55.3, 47.2, 26.4, 24.5.

S-Bis(4-methoxyphenyl)(pyrrolidin-2-yl)methanol (7d).: The compound was synthesized according to the general procedure. 1-Bromo-4-methoxybenezene (1.02 g, 5.45 mmol) was used as the aryl bromide. The product was obtained as a white solid (0.41 g, 60%). ^{1}H NMR (400 MHz, DMSO-d_6): δ_H 7.43 (d, *J* = 8.8 Hz, 2H), 7.31 (d, *J* = 8.8 Hz, 2H), 6.80 (q, *J* = 5.5 Hz, 4H), 4.17 (t, *J* = 7.6 Hz, 1H), 3.69 (s, 3H), 3.68 (s, 3H), 2.88–2.78 (m, 2H), 1.62–1.53 (m, 2H), 1.49–1.34 (m, 2H). The ^{1}H NMR was found to be identical to the published data.[12]

*S-Pyrrolidin-2-lymethanol (7e).:*To a 250 mL two-necked round-bottomed flask equipped with a Teflon coated magnetic stir bar and a condenser under nitrogen atmosphere was added L-proline (3) (1.0 g, 8.69 mmol), sodium borohydride (1.30 g, 34.76 mmol) and iodine (4.41 g, 17.38 mmol). The reaction was stirred at room temperature for 5 hours, and then heated to reflux for 20 hours. The reaction was cooled to room temperature and dried with anhydrous sodium sulfate, filtered, and concentrated in vacuum. The product was obtained as a yellow

oil (0.47 g, 53%). ^{1}H NMR (400 MHz, $CDCl_3$): δ_H 3.56–3.45 (m, 2H), 3.34–3.25 (m, 1H), 3.24–3.13 (m, 1H), 2.90–2.78 (m, 2H), 1.83–1.57 (m, 3H), 1.41–1.27 (m, 1H). The ^{1}H NMR was found to be identical to the published data.[13]

1,4-Dihydro-1,4-methanophenanthrene-9,10-dione (2b).: To a 5 mL vial equipped with a teflon coated magnetic stir bar was added 1,2-naphthoquinone (1) (7.91 mg, 0.05 mmol), *S*-Bis(3-methoxyphenyl)(pyrrolidin-2-yl)methanol (7c) (3.13 mg, 0.01 mmol), cyclopentadiene (8.26 mg, 0.125 mmol) and chloroform (1 mL). The reaction mixture was stirred at 50 °C for 24 hours. The reaction was cooled to room temperature and concentrated under vacuum. The ^{1}H NMR of the crude product was obtained using dimethyl sulfone as a standard. The NMR yield and endo/exo selectivity were determined using the reported ^{1}H NMR spectrum of *endo*-5,6-benzotricyclo[6.2.1.0^{2,7}]undec-9-ene-3,4-dione (2a).[14]: The crude reaction was purified by column chromatography over silica gel (20% EtOAc/hexanes) to give the product as a red solid (4.11 mg, 37%). ^{1}H NMR (400 MHz, $CDCl_3$): δ_H 8.03 (d, J = 7.5 Hz, 1H), 7.48–7.43 (td, j = 7.6, 1.3 Hz, 1H), 7.48–7.43 (m, 2H), 6.93–6.91 (m, 1H), 6.77–6.75 (m, 1H), 4.20 (s, 2H), 1.63 (s, 1H), ^{13}C NMR (100 MHz, $CDCl_3$): δ_C 182.4, 175.2, 149.0, 144.3, 139.5, 135.4, 132.8, 130.9, 130.6, 130.3, 125.2, 70.1, 50.4, 47.9; HPLC chiral AS-H column (10% IPA/hexane, flow rate = 1 mL/min) t_{major} = 24.3 min t_{minor} = 21.4 min. Enantiomeric excess = 17%.

Results and Discussion: To study a Diels–Alder reaction of *o*-quinone, 1,2-naphthoquinone (1) and cyclopentadiene were chosen as the model substrates. From the ^{1}H NMR spectrum of the thermal Diels–Alder reaction, *endo*-5,6-benzotricyclo[6.2.1.0^{2,7}]undec-9-ene-3,4-dione (2a) was obtained as a sole product. Then, the endo/exo-selectivity was determined using NOESY technique. The presence of cross peaks between protons at δ_H 3.96, 3.48, and 3.36 with two protons at δ_H 1.69–1.62 suggested that only the endo adduct was obtained. After purification by column chromatography, the product 2a was unexpectedly transformed to 1,4-dihydro-1, 4-methanophenanthrene-9,10-dione (2b). It is expected that the transformation occurred by SiO_2-promoted oxidation.

Chiral prolinols were chosen as a chiral catalyst in this work because they can be easily synthesized from L-proline (3) and their structures can be easily modified. The chiral prolinol derivatives were synthesized in three-step (Table 1). Firstly, the base-catalyzed esterification of the *N*-Boc-L-proline (4) was performed and the desired methyl ester (5) was obtained in 60%. Secondly, a Grignard's reaction of *N*-Boc-L-proline methyl ester (5) with various aryl magnesium bromides was performed to give the products (6a–d). The last step was the deprotection of the Boc group with sodium hydroxide to afford the chiral prolinol derivatives (7a–d). The combined yields for the second and the third steps were reported in Table 1.

Table 1. Syntheses of L-prolinol derivatives with different substituents

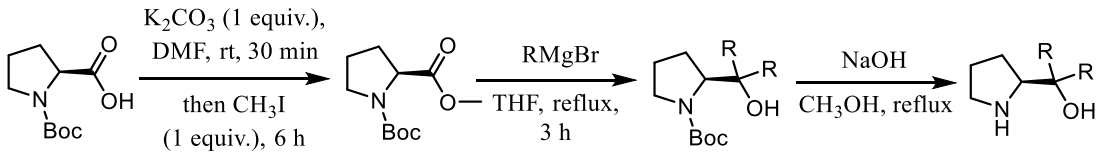

Entry	R-	Yield (%)
1	Ph- (7a)	55
2	3,5-MeOPh- (7b)	56
3	*m*-MeOPh- (7c)	55
4	*p*-MeOPh- (7d)	60

The synthesis of pyrrolidin-2-ylmethanol (7e) was achieved by the reduction of L-proline (3) using $NaBH_4$ and I_2 under reflux condition to give the desired product in 60% yield.

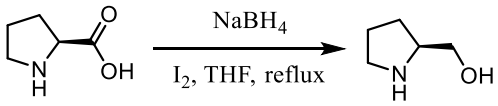

3 **7e**

The optimization of the reaction was investigated (Table 2). For the temperature screening, the reaction was performed using 1,2-naphthoqunone (1) and cyclopentadiene at 5 °C, room temperature, and 50 °C. The result showed that the yield of the product increased when the temperature was increased (entry 1–3). The effect of solvent was also studied. Four types of solvent including non-polar solvents (hexanes and toluene), chlorinated solvent (chloroform), polar aprotic solvents (diethyl ether, ethyl acetate, and acetonitrile), and polar protic solvent (methanol), were employed (entry 4–10). In case of non-polar solvents, when hexane was used, trace amount of the product 2a was observed. In contrast, the reaction in toluene gave the product 2a in 30%. The difference in the yields may come from the solubility of 1,2-naphthoqunone (1), which is insoluble in hexane but soluble in toluene. Because chloroform gave the highest yield, it was chosen as the optimal solvent for further optimization.

Table 2. Optimization of the reaction condition

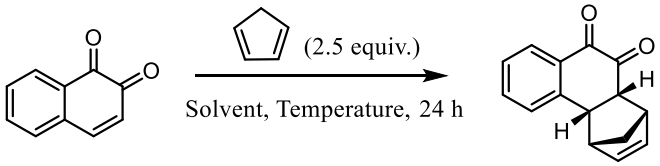

1 **2a**

Entry	Temperature (°C)	Solvent	Yield (%)[a]
1	0	$CHCl_3$	4
2	rt	$CHCl_3$	33
3	50	$CHCl_3$	46
4	50	Hexane	1
5	50	Toluene	31
6	50	$CHCl_3$	46
7	50	Et_2O	16
8	50	EtOAc	10
9	50	CH_3CN	38
10	50	CH_3OH	40

[a]NMR Yield

The reaction was monitored at different times. The yields at 2, 4, 6, 12, 24 and 48 h were determined. As time passed, the yields of the product gradually increased until 24 h, after which the yield appeared to plateau. The optimal time for the reaction was chosen to be 24 h.

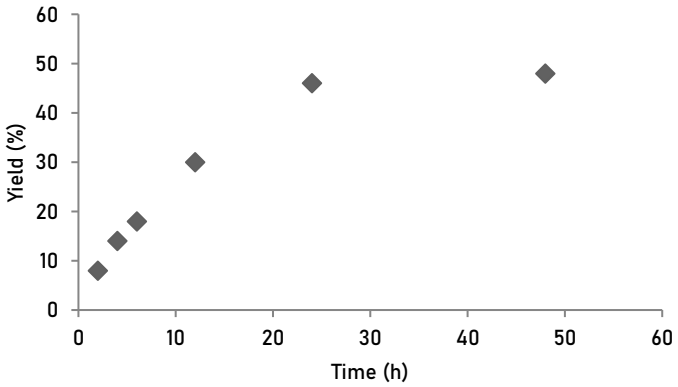

Figure 3. The plot between yield and time

Screening of chiral catalysts was performed to find the best catalyst that gave the highest enantioselectivity. The reaction was performed using standard condition with 20 mol% of a chiral catalyst. Surprisingly, the ^{1}H NMR spectrum of the crude reaction not only showed the product 2a but also the product 2b. It is expected that the chiral catalyst promoted the air oxidation of 2a. From the results (Table 3), the reactions gave the product in moderate yield and *S*-bis(3-methoxyphenyl)(pyrrolidin-2-ly)methanol (7c) is the best catalyst for enantioselectivity with 17% ee.

Table 3. Catalyst screening

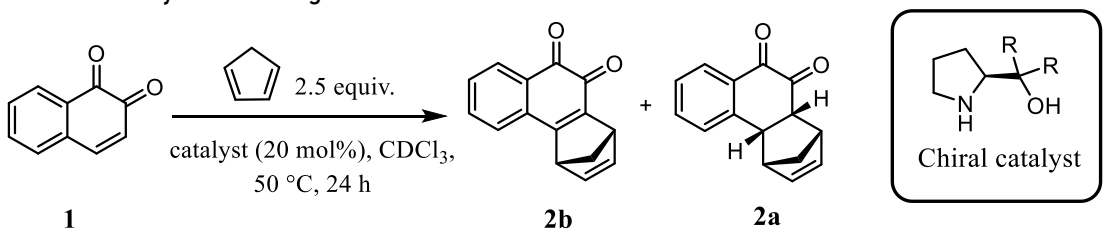

Entry	Catalyst	R	Ratio (2b:2a)	Yield (%)[a]	ee (%)[b]
1		H- (7e)	1.6:1	13	10
2		Ph- (7a)	>99:1	31	6
3	Prolinol	3,5-diMePh- (7b)	>99:1	41	11
4		*m*-MeOPh- (7c)	>99:1	37	17
5		*p*-MeOPh- (7d)	>99:1	35	13

[a]NMR Yield
[b]determined from 2b

Conclusion: Asymmetric Diels–Alder reactions of *o*-naphthoquinones can be achieved using chiral prolinols. The reaction yielded the desired product in low to moderate yield, high endo/exo selectivity, and low enantioselectivity. Further development of the reaction using other chiral catalysts will be investigated.

References:

1. Pardee A, Li Y, Li C. Curr Cancer Drug Tar. 2002;2:227–242.
2. Iwatsuki M, Otoguro K, Ishiyama A, Namatame M, Nishihara-Tukashima A, Hashida J, Ōmura S. J Antibiot. 2010;63:619–622.

3. Bian J, Xu L, Deng B, Qian X, Fan J, Yang X, Zhang X. Bioorg Med Chem Lett. 2015;25: 1244–1248.
4. Hairani R, Mongkol R, Chavasiri W. Bioorg Med Chem Lett. 2016;26:5300–5303.
5. Ma S, Zhang D, Lou H, Sun L, Ji J. J Ethnopharmacol. 2016;188:193–199.
6. Hillard E, de Abreu F, Ferreira D, Jaouen G, Goulart M, Amatore C. Chem Commun. 2008;2612–2628.
7. Gates M, Newhall W. J Am Chem Soc. 1948;70:2261–2263.
8. El Had M, Guardia J, Ramos J, Taourirte M, Chahboun R, Alvarez-Manzaneda E. Org Lett. 2018;20:5666–5670.
9. Bekele T, Shah M, Wolfer J, Abraham C, Weatherwax A, Lectka T. J Am Chem Soc. 2006;128:1810–1811.
10. Hernandez-Juan F, Cockfield D, Dixon D. Tetrahedron Lett. 2007;48:1605–1608.
11. Jiang X, Zhang B, Zhang Y, Lin L, Yan W, Wang R. Chirality. 2010;22:625–634.
12. Mathre DJ, Jones TK, Xavier LC, Blacklock TJ, Reamer RA, Mohan JJ, Jones ETT, Hoogsteen K, Baum MW, Grabowski EJJ. J Org Chem. 1991;56:751–762.
13. Boyle GA, Govender T, Kruger HG, Maguire GEM. Tetrahedron Asymmetry. 2004;15: 2661–2666.
14. Valiulin RA, Arisco TM, Kutateladze AG, J Org Chem. 2011;76:1319–1332.

Acknowledgements: This research was supported by Thailand Reach Fund (MRG6180248), Development and Promotion of Science and Technology Talents Project (DPST), and the Department of Chemistry, Faculty of Science, Mahidol University. We also thank the Central Instrumental Facility (CIF) at the Faculty of Science, Mahidol University for research facilities.

C3_010_OF: KINETIC STUDY OF CONJUGATE ADDITION OF AMINES INTO ALKYNOIC ESTER

Peerawat Saejong[1], Panchika Prangkio[2], Torsak Luanphaisannont[1,3,*]
[1]Department of Chemistry, Faculty of Science, Mahidol University
[2]Department of Chemistry, Faculty of Science, Chiang Mai University
[3]Center of Excellence for Innovation in Chemistry (PERCH-CIC), Faculty of Science, Mahidol University
*e-mail: torsak.lua@mahidol.ac.th

Abstract: Unsaturated hydrocarbon functional groups are important in organic chemistry. One important reaction of these functional groups is the conjugate addition. The reaction is among the most important reactions in organic and biological chemistry as it is a basis of many synthesis applications and biological processes. Although the kinetic reactivity of alkenes and allenes in a conjugate addition has been investigated, the study of alkynes is still limited. This research investigated the kinetic behavior of alkynoic ester in a conjugate addition in comparison with alkenes and allenes. The rate of the conjugate addition of amine into alkynoic ester is faster than that of allenic and alkenic ester.

Introduction: The conjugate addition reactions are among the carbon-carbon bond formation reactions. They are important tools in biological[1,2] and chemical[3] applications. The conjugate acceptor is commonly unsaturated compounds that are attached to an electron-withdrawing group. Development of conjugate addition reactions of alkynoic esters with various nucleophiles has been reported. Examples of such nucleophiles are alkene,[4] allene,[5] and alkyne.[6] Due to the advantages of conjugate addition of alkyne, the reactions are frequently investigated. These substrates in conjugate addition reaction also react with various nucleophiles, which are organometallic nucleophiles[7], stabilized carbanion[8], and heteroatoms[9].

Although the conjugate addition reaction of alkyne is widely used, the reaction behavior has not been well investigated. Thermodynamic behavior of the alkyne has been studied in comparison with other unsaturated functional groups such as alkenes and allenes. The comparison of hydrogenation energy of propene, allene, and propyne was investigated. The enthalpies of hydrogenation of one π bond of alkene, allene, and alkyne are −30, −41, and −39 kcal/mol, respectively.[10,11] Therefore, the order of thermodynamic reactivity from highest to lowest is allene, alkyne, and alkene, respectively.

Although the comparative thermodynamic reactivity of these functional groups has been reported, their kinetic reactivity was not well studied. Previously, the comparison of kinetic reactivity between alkenes and alkynes has been investigated in bromination reaction. Alkenes underwent bromination reaction faster than alkynes.[12] In addition, the pulse radiolysis reaction of alkenes and alkynes was used to determine their relative rate in radical reaction. The rate of both groups were comparable.[13] Therefore, the kinetic reactivity depends on types of reaction. Herein, this research investigated the kinetic reactivity of alkenes, allenes and alkynes in a conjugate addition reaction by competition experiments and comparison of absolute kinetic rates.

Methodology:

General Procedures. ^{1}H-NMR and ^{13}C-NMR spectra were obtained from Bruker Avance 400 MHz NMR spectrometer. Chemical shifts were reported in ppm from tetramethylsilane with the residual solvent resonance as an internal standard ($CDCl_3$ at δ 7.26). Data were reported as follows: br = broad, s = singlet, d = doublet, t = triplet, q = quartet, m = multiplet; coupling constant(s) in Hz, integration. Thin layer chromatography was performed on aluminium sheet laminated by a Merch silica gel 60 F254 plate and compounds were visualized under UV light.

Merck silica gel 60 (0.063 – 0.200 nm) was used as a stationary phase on column chromatrography.

Materials. Commercial reagents were purchased from Sigma Aldrich, TCI, Merck, and Alfa Aesar and used as received unless otherwise noted.

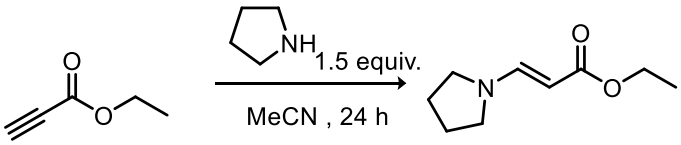

Ethyl(E)-3-(pyrrolidine-1-yl)acrylate. Ethyl propiolate (1 equiv.) was dissolved in acetonitrile while stirring with Teflon-coated magnetic bar. Pyrrolidine (1.5 equiv.) was added to the solution. The reaction was stirred for 24 hours. The solvent was evaporated. The reaction mixture was purified by column chromatography to yield the target molecule in 61 % yield) as a yellow liquid. The ^{1}H NMR spectrum was found to be identical to the published data.[14] ^{1}H NMR (400 MHz, $CDCl_3$): δ 7.65 (d, J = 12.8 Hz, 1H), 4.47 (d, J = 12.8 Hz, 1H), 4.12 (q, J = 7.1 Hz, 2H), 3.25 (br, 4H), 1.92 (br, 4H), 1.25 (t, J = 7.1 Hz, 3H).

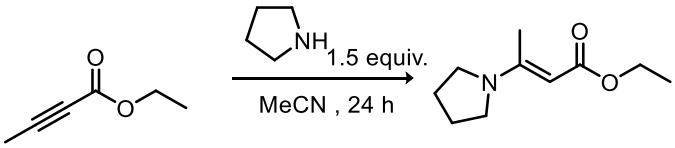

Ethyl(E)-3-(pyrrolidine-1-yl)bu-2-enoate. Ethyl butynoate(1 equiv.) was dissolved in acetonitrile while stirring with Teflon-coated magnetic bar. Pyrrolidine (1.5 equiv.) was added to the solution. The reaction was stirred for 24 hours. The solvent was evaporated to give the product in 79% yield as a yellow liquid. The ^{1}H NMR spectrum was found to be identical to the published data.[15] ^{1}H NMR (400 MHz, $CDCl_3$): δ 4.45 (s, 1H), 4.08 (q, J = 7.2 Hz, 2H), 3.27 (br, 4H), 2.45 (s, 3H), 1.92 (br, 4H), 1.24 (t, J = 7.2 Hz, 3H).

General NMR competition experiment. The stock solutions of ethyl propiolate (180 mM), ethyl butynoate (180 mM), ethyl allenoate (180 mM), ethyl acrylate (180 mM), pyrrolidine (180 mM), and 1,3,5-trimethoxybenzene (60mM) were freshly prepared in chloroform-d. In NMR tube, the ethyl propiolate solution (0.018 mmol, 100 µL) was added followed by 1,3,5-trimethoxybenzene solution (0.006 mmol, 100 µL) as an internal standard. Then, chloroform-d (200 µL) and the ethyl allenoate solution (0.018 mmol, 100 µL) were added. The pyrrolidine solution (0.018 mmol, 100 µL) was added. After 1 hour, the NMR spectrum (Figure 1) of the reaction mixture was obtained to determine the remaining starting material and product.

NMR competition experiment between ethyl allenoate and ethyl acrylate. The experiment was performed following the general NMR competition experiment. Ethyl acrylate was used instead of ethyl propiolate.

NMR competition experiment between ethyl butynoate and ethyl acrylate. The experiment was performed following the general NMR competition experiment. Ethyl butynoate and ethyl acrylate were used instead of ethyl propiolate and ethyl allenoate, respectively.

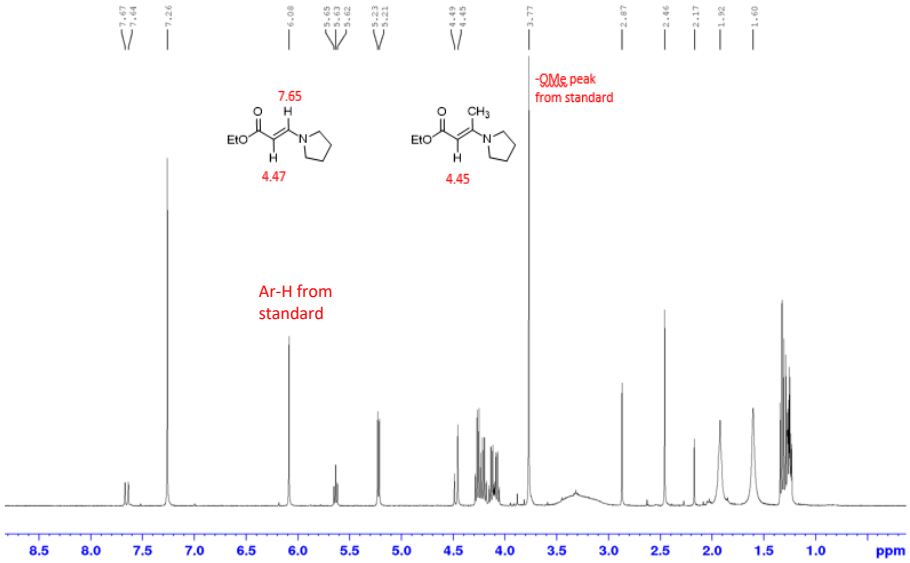

Figure 1. ^{1}H NMR spectrum of competition experiment between ethyl allenoate and ethyl propiolate

UV kinetic experiments. The stock solutions of ethyl propiolate (150 µM) and pyrrolidine (150 µM) in chloroform were prepared. To analyze the reaction, a cuvette with a 1 cm path length was filled with chloroform (1 mL) followed by the ethyl propiolate solution (1 mL). Then, the pyrrolidine solution (1 mL) was added to the cuvette. UV spectra of the reaction were recorded using an Agilent Cary-60 UV–Visible spectrophotometer. The absorbance at 290 nm was used to determine the concentration at different times (Figure 2).

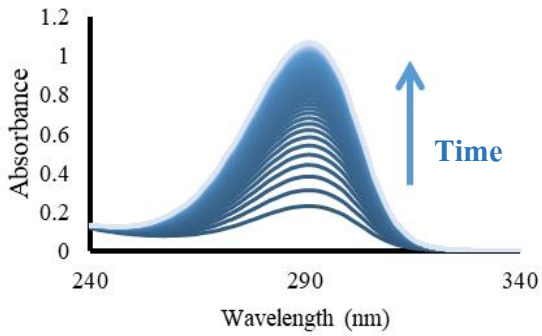

Figure 2. UV spectra of the conjugate addition reaction between ethyl propiolate and pyrrolidine

Results and Discussion: The competition experiments of α,β-unsaturated esters in the conjugate addition reaction with amine were performed (Table 1). Ethyl acrylate, ethyl allenoate, ethyl butynoate, and ethyl propiolate were used as model substrates. Pyrrolidine was chosen as a nucleophile because of its high reactivity and selectivity. The conjugated product was obtained as a single isomer (*E*-isomer), which simplifies the reaction monitoring.

Table 1. Competition experiments of pyrrolidine and various α,β-unsaturated esters

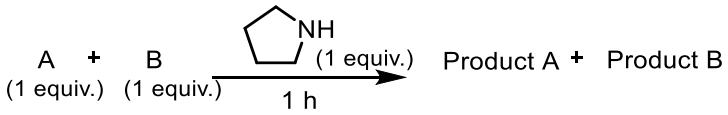

Entry	Compound A	Compound B	Ratio of Product A : Product B
1	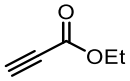	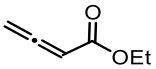	1.14 : 1
2	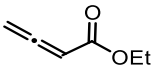	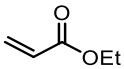	>20 : 1
3	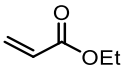	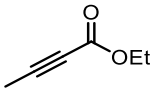	15.2 : 1

The result from the competition experiments showed that the conjugate addition of ethyl propiolate was slightly faster than that of ethyl allenoate. Allenoate reacted much more rapidly than acrylate. When acrylate and butynoate were compared, acrylate underwent conjugate addition faster than butynoate. From these results, ethyl propiolate underwent conjugate addition faster that allenoate, acrylate, and butynoate, respectively.

A pseudo-first order method was used to determine the absolute rate of the bimolecular reaction. The method could simplify a complex second-order kinetic to a simple first-order kinetic by using a large excess amount (>10 times) of one substrate. This large excess allows consideration of that substrate as a constant. The rate of the conjugate addition reaction of pyrrolidine into ethyl propiolate was performed using the pseudo-first order approach. In this case, pyrrolidine was used at a large excess. The graph in Figure 3 was plotted between the natural log of the concentration of ethyl propiolate and time. The slope of this plot showed pseudo first order rate constant at this concentration of pyrrolidine. The conjugate addition reactions of ethyl propiolate with various concentrations of pyrrolidine (10, 20, 30, 40, and 50 times) were performed. The plot between the concentration of pyrrolidine and pseudo first order rate constant (Figures 4 and 5) was used to determine the absolute rate constant. The slope of the plot was the absolute rate constant.

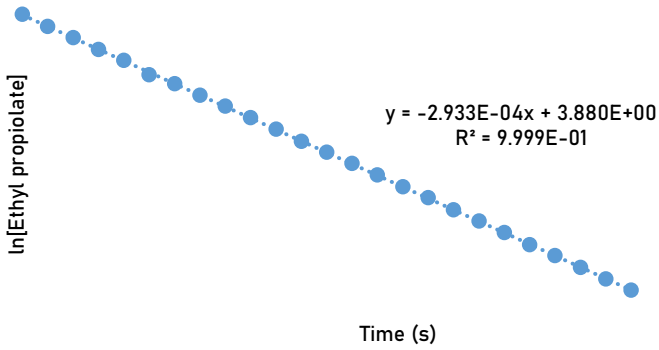

Figure 3. Example of a pseudo-first order plot between ln[Ethyl propiolate] and time (a conjugate addition reaction between ethyl propiolate 50 µM and pyrrolidine 1000 µM)

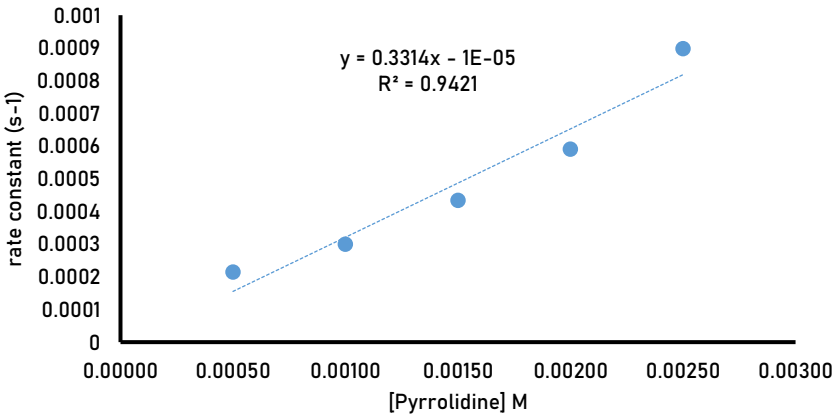

Figure 4. A plot to determine the absolute rate constant of ethyl propiolate in a conjugate addition reaction with pyrrolidine

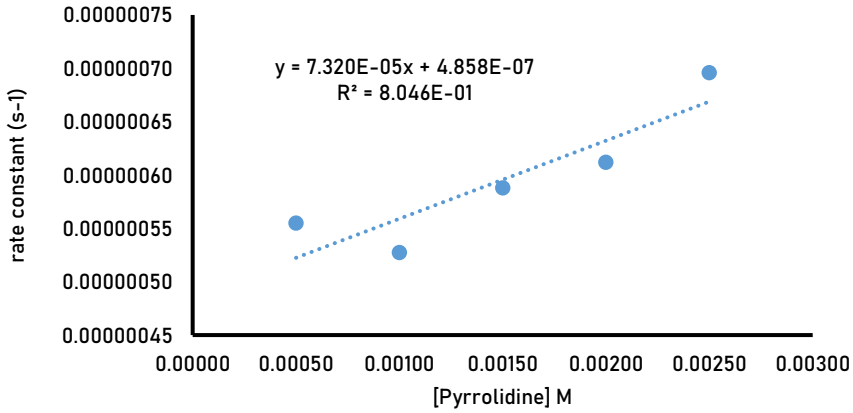

Figure 5. A plot to determine the absolute rate constant of ethyl butynoate in a conjugate addition reaction with pyrrolidine

The results (Table 2) showed that the order of the rate of conjugate addition reaction from fastest to slowest was propiolate, allenoate, acrylate, and butynoate, respectively. Ethyl allenoate and ethyl propiolate underwent the conjugate addition reaction faster than ethyl acrylate by approximately 100 folds. Ethyl acrylate was faster than ethyl butynoate by 100 folds. The order of the rate by the pseudo-first order approach agreed well with that from the competition experiment.

Table 2. The absolute rate constants of ethyl propiolate, ethyl allenoate, ethyl acrylate, and ethyl butynoate in conjugate addition reaction with pyrrolidine

Entry	Substrate	Rate constant ($M^{-1}s^{-1}$)
1	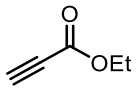	0.331
2	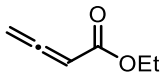	0.299*
3	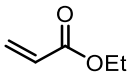	2.33×10^{-3}*
4	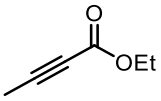	7.32×10^{-5}

*The data were from reference[16]

Conclusion: The absolute rate constant of conjugate addition reaction of alkene, allene and alkyne was investigated using two methods, competition experiment and pseudo-first order approach. Both methods agree with each other. The order of the rate of the conjugate addition was propiolate, allenoate, acrylate, and butynoate, respectively.

References:

1. Zhang Y, Zhou X, Xie Y, Greenberg MM, Xi Z, Zhou C. J Am Chem Soc. 2017;139: 6146–6151.
2. Fontaine SD, Reid R, Robinson L, Ashley GW, Santi DV. Bioconjugate Chem. 2015;26:145–152.
3. Ballini R, Barboni L, Bosica G, Fiorini D, Palmieri A. Pure Appl Chem. 2006;78: 1857–1866.
4. Ondrusa A.E, Movassaghi M. Chem Commun. 2009:4151–4165.
5. Yasumitsu T, Teruhisa T, Shin-ichiro M, Yasuyuki K. J Org Chem. 1985;50:1542–1544.
6. Crisp G.T, Millan M.J. Tetrahedron. 1998;54:637–648.
7. Corey E. J, Alfonso T. J Am Chem Soc. 1984;106:462–463.
8. Lan Q, Wang X, Maruoka K. Tetrahedron Lett. 2007;48:4675-4678.
9. Crisp G.T, Millan M. J. Tetrahedron Lett. 1998;54:637–648.
10. Kistiakowsky G.B, Ruhoff J.R, Smith H.A, Vaughan, W.E. J Am Chem Soc. 1936;58:146–153.
11. Kistiakowsky G.B, Ruhoff J.R, Smith H.A, Vaughan, W.E. J Am Chem Soc. 1935;57:876–882.
12. Chiappe C, Pieraccini D. J Org Chem. 2004;69:6059–6064.
13. Yamamoto S, Yamamoto Y, Hayashi K. Bull Chem Soc Jpn. 1991;64: 346–351.

14. Onkar SN, Maheshwar ST, Manoranjan K, Shaifali, Rahul U, Sushil KM. Asian J Org Chem.2018;7:776-780
15. Elena F, Stefania F, Lucio P, Paolo A.T. Tetrahedron Lett.1999;40:4413-4416
16. Kiattisewee C, Kaidad A, Jiarpinitnun C, Luanphaisarnnont T. Monatsh Chem. 2018;149 : 1059-1068.

Acknowledgement: This research was supported by Thailand Reach Fund (MRG6180248), Development and Promotion of Science and Technology Talents Project (DPST), and the Department of Chemistry, Faculty of Science, Mahidol University. We also thank the Central Instrumental Facility (CIF) at the Faculty of Science, Mahidol University for research facilities.

C3_011_PF: STUDY THE EXTRACTION OF *Stephania venosa* (BLUME) SPRENY. TUBERS

Warabhorn Boonyarat*, Chiraphat Phromthong
Department of Chemistry, Faculty of Science and Technology, Muban Chombueng Rajabhat University, Ratchaburi, Thailand
*e-mail: wara.boon.ell@gmail.com

Abstract: *Stephania venosa* (Blume) Spreng. is an important herb to treat to various diseases. This importance of treating is therefore study of the significant substances in the plant has be extracted by ethanol and methanol solvents. The Mayer's reagent was tested the alkaloids. The separation and purification of the substance were used Thin layer chromatography (TLC) and column chromatography. We found that the extraction solutions were yellow color of precipitate when tested with the reagent. The retention factor (R_f) range of alkaloids was between 0.22-0.25 cm. The purification of the extraction solutions which, it was shown only one line on TLC plate and the R_f was about 0.24 cm. Therefore, the substances were extracted from *Stephania venosa* (Blume) Spreng. that was the alkaloid group. The advantage of extraction methods is that found the substance in plant and used to treat the diseases.

Introduction: Thailand is the place that a lot of herbs and medicines. Applying various herbs for medicinal was used because in the past, there was no medical field, as in the present, therefore, herbs must be used to treat various diseases. From the properties of herbs, consequently, the origin of modern medicine. The popularity of herbs today makes certain herbs are still in demand and expensive because some species are rare herbs. The using of herbs for the villagers are directly used and blending many herbs that are used to treat diseases. The examples of herbs in Ratchaburi that is the province in Thailand, such as karen pepper, Kaffir lime, black Phlai, *Stephania venosa* (Blume) Spreng., Bellyache bush, Black Galingale, Curcuma aeruginosa Roxb, Turmeric, and others. We interested in studying important substances in herbs to treat the diseases by means of extracting important substances to study each property.

Stephania venosa (Blume) Spreng named in Thai as "Sa-Bu-Leud", belongs to the Menispermaceae family.[1] The plant has been traditionally used as tonic drug and treatment of various diseases in South East Asian countries.[2] The various benefits of plant are shown in the table 1. A Thai herbal plant has anti some cancer without making standardize of the material. Thus, comparison thin layer chromatography (TLC). Three mobile phases were tested, including 1) Toluene Ethyl acetate-Diethylamine (7:2:1) 2) Chlorofrom-Acetone- Diethylamine (5:4:1) and 3) Chloroform- Methanol (9:1).[3]

Table 1. Properties of *Stephania venosa* (Blume) Spreng.in various parts for treatment.

Part	Properties
Tuber	Treatment of cancerous or non-cancerous chronic ulcers, leukorrhea, diarrha[4], hyperputun, and dysentery[5,6]
Whole plant	Appplied treatment of spine tuberculosis, inflammation lof Pattakaat line[7], abscess[8,9], treatment of venereal diseases and worm[5], treatment of fever infected wound and pruritic rach
leaves	Used as antidiarrheal and antidysenteric[5,10]
roots	Treatment of infected wound and abcess[5], applied treatment of granular stomatitis, aphthous ulcer, cancerous or non-cancerous chronic ulcers[8], rheumarthritis, hepatitis and cold[5]

The results of three mobile phases could effectively distinguish chemical constituents from the extracts from each part of *Stephania venosa*. The crude ethanolic extract was

performed various fractionations and further isolated to obtain pure constituent that could lead to the further study on the detail mechanisms of action of this active substance for future application as new drug for ovarian cancer.[11] This importance of treating is therefore study of the significant substances in the plant has be extracted by ethanol and methanol solvents.

Methodology: Provided large tubers of *Stephania venosa* (Blume) Spreng. were purchased from Ratchaburi Province, Thailand. The tubers were cleaned, peeled, sliced into pieces, dried in a hot air oven at 40-50°C, and then powdered. The sample was extracted in 95% methanol and 95% ethanol for 7 days. The extract solution was filtered to remove residue with filter paper Whatman No. 1. Then the solution was added to the concentration with the evaporator. The Mayer's reagent was tested the alkaloids. The extracts that have been placed on the TLC and preparing the mobile phase 3 system was 1) Toluene Ethyl acetate-Diethylamine (7:2:1) 2) Chlorofrom- Acetone- Diethylamine (5:4:1) and 3) Chloroform- Methanol (9:1) [3]. Rf calculation was used to examine the important substances that occur on TLC sheets under UV light at wavelengths of 254 and 365 nm. The separation and purification of the substance were used by the column chromatography.

Results and Discussion: The phytochemical examination is a rough test that used to predict the plants. They were tested substances containing which, alkaloids as a component. The alkaloid substances of the extract from the *Stephania venosa* (Blume) Spreng. will rely on white or cream-induced reactions.[12] Figure 1. can be seen that when the alkaloids react with the reagent Meyer solution. It was found that the extraction with ethanol and methanol resulted in white or cream color. The results in the experiment was the positive test according to the theory. Therefore, the solutions from the extraction was the alkaloid.

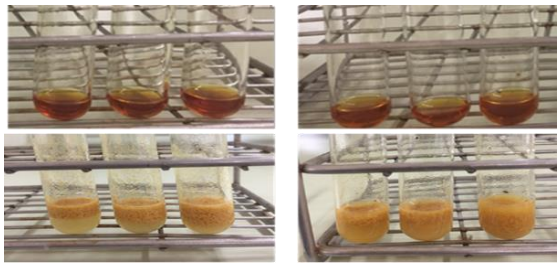

(a) (b)

Figure 1. Meyer Reagent Test Of extracts obtained from solvents
(a) ethanol and (b) methanol.

The determination of the important substances extracted with 95% ethanol and 95% ethanol solvent of the *Stephania venosa* (Blume) Spreng. using TLC technique. The TLC form of the extract was examined under UV light at the 254 nm wavelength, it was found that the characteristics of the TLC could distinguish important substances and there was no drag on the tail. In the 2nd and 3rd systems, there was a clear separation of the strip (Figure.2). The considering both solvents, they can be used together to separate important substances. The results were from TLC that showed in the R_f value of the substance in table 2. It can be indicated that there were more than 10 substances from the extract. R_f values were in the range of 0.05-0.91 cm. The R_f of alkaloid was in the range of 0.22-0.25 cm.[13] In addition, the separation from TLC was not purify that to purify of the substance we used the column chromatography.

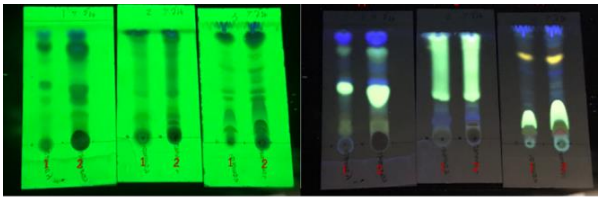

(a) (b)

Figure 2. TLC chromatograms of (1) 95% ethanol and (2) 95% methanol extraction of *Stephania venosa* (Blume) Spreng in 3 mobile phase Toluene–Ethyl acetate–Diethylamine (7:2:1), Chloroform–Acetone-Diethylamine (5:4:1) and Chloroform–Methanol (9:1) under UV lamp (a) 254 and (b) 365 nm.

Table 2. R_f value of *Stephania venosa* (Blume) Spreng from mobile phase1, 2 and 3 in 95% ethanol and 95% methanol.

R_f	Distant (cm)					
	Mobile phase 1		Mobile phase 2		Mobile phase 3	
	Ethanol	Methanol	Ethanol	Methanol	Ethanol	Methanol
1	0.9	0.88	0.88	0.88	0.91	0.91
2	-	-	0.84	0.81	-	0.82
3	0.78	0.74	0.79	0.75	0.73	-
4	0.66	0.65	0.69	0.67	-	0.63
5	0.56	0.55	0.6	0.58	-	-
6	0.41	0.43	0.41	0.41	0.45	0.43
7	0.35	-	0.32	-	0.28	0.3
8	0.17	0.21	0.22	0.24	-	0.19
9	-	0.13	0.11	0.13	0.17	0.13
10	-	-	0.05	0.07	-	-
Total	7	7	10	9	5	7

The substance obtained from the column chromatography separation in each color group was tested, TLC found that the color bands in the group (a) the time period that the t_1-t_3 did not show the color bands at the wavelength of 365 nm. Suggestion that in the first substance, there was no extracted substance mixed with the mobile phase solution. In the group of color bands (b) time period t_4-t_6, which can be seen that there was only one substance and it was in the same line of the three times. The band color group (c) period t_7-t_9, which can be seen that there was a single substance and in the same direction of the three times. Therefore, the group color bands (b) and (c) were the same substance, which can be confirmed by the average R_f value. It was about of 0.23 cm (Table 3) but the substances released in the group color band (c) will be lighter than the group color bands (b). The method of separation by column chromatography can separate the substances to be pure however the result from column chromatography cannot confirm the type of substance.

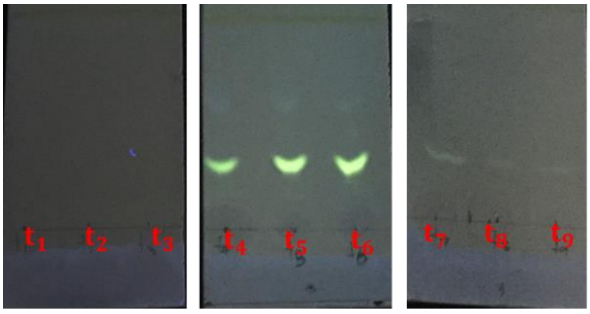

(a) (b) (c)

Figure 3. t_1-t_9 chromatography in all 3 phases under UV light at 365 nm.

Table 3. R_f value of t_1-t_9 at 365 nm.

R_f	Distance (cm)
t_1	-
t_2	-
t_3	-
t_4	0.24
t_5	0.22
t_6	0.22
t_7	0.25
t_8	0.25
t_9	0.23

Conclusion: The studying important substances in the *Stephania venosa* (Blume) Spreng. by using ethanol and methanol extraction solvents for 7 days. The extracted solution was tested to determine the alkaloids using the reagent Mayer. It was found that the white and cream color sediment showed in the extracted substances. Therefore, the extractions were alkaloids. The extract obtained by TLC was exposed to UV radiation at 254 and 365 nm that there were more than 10 substance and R_f values were between 0.05 – 0.91 cm. the R_f value of alkaloids were in the range of 0.22-0.25.[13] The extraction was purified by column chromatography method, which found that the substance was purified when tested on TLC and shining at wavelength 365 nm. Only one substance was released and the R_f value was about 0.23 cm. that was confirm by Flieger's research.

References:

1. Forman L. L. Menispermaceae. Flora Thailand. 1991, 5:300–65.
2. Kongkiatpaiboon S, Duangdee N, Prateeptongkum S, Tayana N, Inthakusol W. Simultaneous HPLC analysis of crebanine, dicentrine, stephanine and tetrahydropalmatine in *Stephania venosa*. Revista Brasileira de Farmacognosia. 2017, 27:691-7.
3. Pranakorn Y, Wichiankham C, Chaiyaveij D, Pranakhon R. The Study of Thin Layer Chromatogram of Leaves, Bulbs, and Latex Crude Extract from *Stephania venosa* (Blume) Spreng in Three Mobile Phases. Songklanakarin Journal of Plant Science. 2016, 3:31-7.
4. Boonyaphapas N, Folk A. medicinal plants 4thEdn, Faculty of Pharmacy, Mahidol University; National Center for Genetic Engineering and Biotechnology. 2000.
5. Pongboonrod S. Plants from abroad and Thailand, properties of the drug from abroad and Thai drug. 1stEdn. Bangkok. 1950.

6. Rujjanawate C, Kanjanapothi D, Amornlerdpison D, Somwong R, Hargreave O. 20th Annitersary HRH Princess MahaChakriSirindhorn Herbs Garden. PTT Public, Bangkok. 2005.
7. S.r.o.a. S, Tipmala P. Tell the symptoms and cure, and illustration. Augsoncharountusana Printing, Bangkok. 1940.
8. Veesapen V, Wutisan S, Wanaudon S, Nunchuntee A, Rawarin N, Chanawech A. Ancient pharmacopoeia from WatSrisompon, aumporChaingyoun, Mahasarakam province. Technical Paper No. 2. Northeast Bailan inscribed conservation project, Mahasarakam University, Siritam Offset Printing, UbonRatchathani. 2005.
9. Traditional medical school faculty, Pharmacopoeia stone inscriptions in WatPhachetuponwimolmungkararam (Wat Po) Bangkok. His Majesty King Rama. 1832.
10. Saralamp P, Chuaku W, Temsiririrkkul R, Clayton T. Plants from abroad and Thailand, properties of the drug from abroad and Thai drug. 1stEdn. Bangkok. 1996.
11. Montririttigri K, Moongkarndi P, Joongsomboonkusol S, Chitkul B, Pattanapanyasat K. Apoptotic Activity of Aporphine from Stephania venosa on Human Ovarian Cancer Cells. 2008.
12. Ayoola G, Coker H, Adesegun S, Adepoju-Bello A, Obaweya K, Ezennia E. Phytochemical Screening and Antioxidant Activities of Some Selected Medicinal Plants Used for Malaria. Therapy in Southwestern Nigeria. 2008.
13. Flieger J. Thin-Layer (Planar) Chromatography. III / ALKALOIDS/ Thin Layer (Planar) Chromatography. 2000.

Acknowledgements: The supporting of Chemicals and locations were from the Science and Applied Science Center, Faculty of Science and Technology, Muban Chombueng Rajabhat University, Ratchaburi Thailand.

C3_014_PF: CHEMICAL CONSTITUENTS OF *Garcinia cowa* LEAVES

Piyaporn Phukhatmuen[1,3], Surat Laphookhieo[1,3], Rawiwan Charoensup[2,4], Wisanu Maneerat[1,3,4,*]
[1]School of Science, Mae Fah Luang University, Chiang Rai 57100, Thailand
[2]School of Integrative Medicine, Mae Fah Luang University, Chiang Rai 57100, Thailand
[3]Center of Chemical Innovation for Sustainability (CIS), Mae Fah Luang University, Chiang Rai 57100, Thailand
[4]Medicinal Plant Innovation Center, Mae Fah Luang University, Chiang Rai 57100, Thailand
*e-mail: wisanu.man@mfu.ac.th

Abstract: *Garcinia cowa* Roxb. *ex* DC. (Cha-Muang) has been used in folklore as an edible plant for culinary and therapeutic to treat fever, reduce phlegm, laxatives and improve blood circulation. The chemical investigation of the ethyl acetate leaf extract from *G. cowa* led to the isolation of six known compounds including friedelin (1), *β*-friedelinol (2), oleanane-12-ol (3), guttiferone I (4), 1,7-dihydroxyxanthone (5) and 1-hydroxy-7-methoxyxanthone (6). The structures of all isolated compounds were established by ^{1}H and ^{13}C NMR spectroscopic data. The structures of all isolated compounds were established by comparisons of their ^{1}H and ^{13}C NMR spectroscopic data with those reported in the literature.

Introduction: *Garcinia cowa* Roxb. ex DC. (Clusiaceae), known as 'Cha Muang' in Thailand is an evergreen tree or shrub that has an outstanding feature of yellow latex in several parts and sour taste.[1] It is widely distributed in Asia and tropical areas.[2] Its leaves are edible and commonly used as a food ingredient and used in therapeutic of traditional medicine for treat fever, reduce phlegm, laxatives and improve blood circulation.[3] The chemical constituents of this plant are xanthones,[4] benzophenones,[5] triterpenes[6] and flavonoids.[7] Some of isolated compounds from *G. cowa* display the pharmacological properties such as cytotoxic,[8] antioxidant,[9] anticancer,[10] antibacterial[11] and antidiabetic[12] activities. However, its leaves are rarely investigated. This study aimed to isolate the chemical constituents from *G. cowa* leaves by chromatographic techniques and to identify their structures by spectroscopic data. Herein, six known compounds including three triterpenes (1–3), one benzophenone (4) and two xanthones (5 and 6) were isolated and structural elucidation of isolated compounds was reported.

Methodology:

General experimental procedure: The NMR spectra were recorded using AVANCE NEO 500 MHz Bruker spectrometer in acetone-d_6 and chloroform-*d* with tetramethylsilane as an internal standard. Silica gel C60 (0–20 mm, SiliCycle® Inc.) and silica gel G60 (60–200 mm, SiliCycle® Inc.) were used to perform quick column chromatography (QCC) and column chromatography (CC), respectively. Analytical thin-layer chromatography (TLC) was performed with the precoated plates of silica gel 60 F_{254}.

Plant material: The leaves of *G. cowa* were collected from Thasud, Chiang Rai province, Thailand in 2018 and was identified by Assoc. Prof. Dr. Nijsiri Ruangrungsi, botanical specialist. A voucher specimen (MFU-NPR0186) was deposited at the Natural Products Research Laboratory, School of Science, Mae Fah Luang University.

Extraction: The air-dried and crushed *G. cowa* leaves (1.7 kg) were extracted at room temperature for three days using distilled EtOAc (5 L) and concentrated under reduced pressure to provide the EtOAc extract (465.74 g, % yielded = 27.36 % w/w).

Isolation: The EtOAc extract (100.5 g) was separated by quick column chromatography (QCC) over silica gel with mixtures of hexanes–EtOAc from 0 to 100% EtOAc to afford four fractions (GC1E–GCE4). Fraction GCE1 (12.46 g) was subjected to column chromatography (CC) with 10:90 hexanes:EtOAc to obtain compounds 1 (8.1 mg), 2 (11.4 mg) and 3 (1.3 mg). Fraction GCE2

(3.70 g) was subjected to reversed-phase CC (C-18, 80:20 MeOH: H_2O) to obtained two fractions (GCE2A and GCE2B). Fraction GCE2A (1.47 g) was subsequently purified by CC with 80:20 hexanes:EtOAc to give compound 4 (6.2 mg). Fraction GCE3 (6.32 g) was isolated by reversed-phase CC (C-18, 80:100 MeOH: H_2O) to obtain three fractions (GCE3A-GCE3C). Compound 5 (13.8 mg) was isolated from fraction GCE3A by Sephadex LH-20 CC using 100% MeOH. Compound 6 (2.7 mg) was isolated from fraction GCE4 (11.5 mg) with by CC with 15:85 hexanes: EtOAc.

Structure elucidation: The structures of the isolated compounds were elucidated by comparison of their physical property and ^{1}H and ^{13}C NMR spectroscopic data as shown in Tables 1-3 with those previously reported.

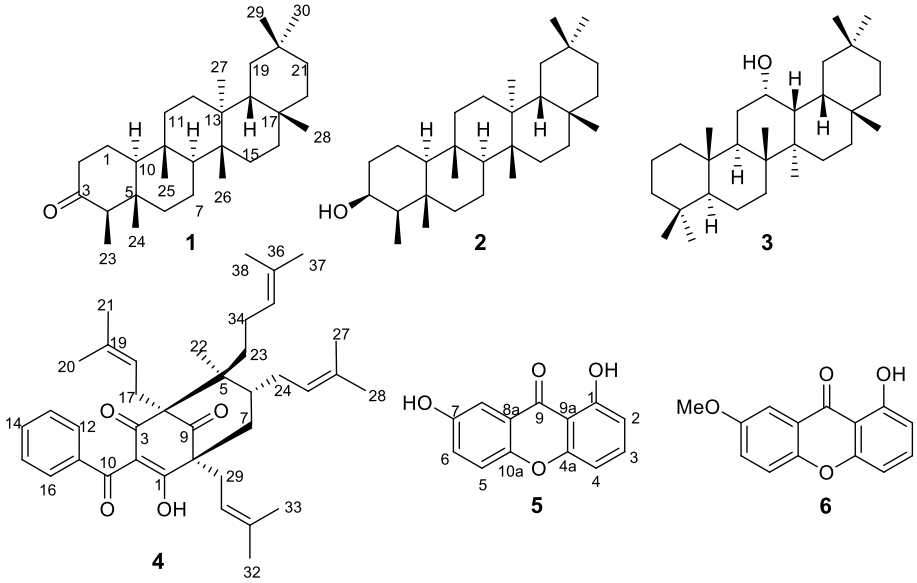

Figure 1. Isolated compounds from *G. cowa* leaves

Results and Discussion:

The phytochemical investigation of the leaf extract of *G. cowa* resulted in six known compounds (Figure 1) including three triterpenes, a benzophenone and two xanthones. They were identified as friedelin (1),[13] *β*-friedelinol (2),[14] oleanane-12-ol (3),[15] guttiferone I (4),[16] 1,7-dihydroxyxanthone (5)[17] and 1-hydroxy-7-methoxyxanthone (6)[18] by analysis and comparison of their spectroscopic data with those reported.

Three known triterpene (1–3) were classified as pentacyclic triterpenes which composed of five isoprene units (C30). Their structures are derived from the acyclic precursor squalene which exists in their free form to give the difference on stereochemistry, substituent groups and ring structure.[19] Compound 1 was obtained as a white solid. The ^{13}C NMR data contained 30 carbon signal for eight methyl carbons, eleven methylene carbons and three methine carbons related with the ^{1}H NMR spectrum that showed signals for methylene protons at δ_H 1.27 (2H, m, H-16), 1.29 (2H, m, H-15), 1.31 (2H, m, H-22), 1.39 (2H, m, H-19), 1.45 (2H, m, H-12), 1.48 (2H, m, H-11), 1.52 (2H, m, H-7), 1.55 (2H, m, H-6), 1.58 (2H, *m*, H-2) and 2.24-2.33 (2H, *m*, H-1), signals for methine protons at δ_H 2.37-2.41 (1H, *m*, H-3), 1.95-1.99 (1H, *m*, H-2) and 1.74-1.76 (1H, *m*, H-6) together with eight methyl groups at δ_H 1.18 (3H, *s*, H-23), 1.05 (3H, *s*, H-24), 1.01 (3H, *s*, H-25), 1.00 (3H, *s*, H-26), 0.95 (3H, *s*, H-27), 0.89 (3H, *s*, H-28), 0.87 (3H, *s*, H-29) and 0.73 (3H, *s*, H-30). According to comparison of the ^{1}H and ^{13}C NMR data with the literature data, compound 1 was identified as friedelin.[13]

Compound 2 was obtained as a white solid. The ^{1}H and ^{13}C spectroscopic data were similar to those of 1 except that compound 2 displayed an oxymethine proton at δ_H 3.73 (1H, *s*, H-3) and an oxymethine carbon at δ_C 72.7 (C-3) instead of the carbon carbonyl signal at δ_C 212.1 at C-3 in 1. Therefore, compound 2 was assigned as β-friedelinol or 3β-hydroxyfriedelane.[14]
Compound 3 was obtained as a white solid. The ^{1}H and ^{13}C NMR data of 3 were closely related to those of compound 2 except that the oxymethine signal of 3 (δ_H 4.17) appeared at higher field than that in 2 (δ_H 3.73), suggesting that the oxymethine proton in 3 was present in the different position. Comparison of the ^{13}C NMR data of 3 with those reported data for oleanan-12-ol[15] (Table 1) indicated that compound 3 was oleanan-12-ol with a hydroxy group at C-12 and the rearrangement of the methyl groups at C-5, C-9 and C-13 in 2 to C-4, C-10 and C-8 in 3, respectively.

Table 1. ^{1}H (500 MHz) and ^{13}C (125 MHz) NMR spectroscopic data of compounds 1-3 in $CDCl_3$ compared with their references.

Position	1		friedelin[13]		2		β-friedelinol[14]		3		oleanane-12-ol[15]	
	δ_H (mult., J in Hz)	δ_C	δ_H (mult., J in Hz)	δ_C	δ_H (mult., J in Hz)	δ_C	δ_H (mult., J in Hz)	δ_C	δ_H (mult., J in Hz)	δ_C	δ_H (mult., J in Hz)	δ_C
1	2.24-2.33 (2H, *m*)	22.2	-	22.3	1.49 (2H, *m*)	15.9	-	15.8	2.28-2.25 (2H, *m*)	38.4	-	38.5
2	1.58 (2H, *m*)	41.2	-	41.5	1.47 (2H, *m*)	36.4	-	36.1	2.16-2.14 25 (2H, *m*)	28.1	-	28.2
3	-	212.1	-	213.2	3.73 (1H, *s*)	72.7	3.74 (1H, *s*)	72.8	1.38-1.36 (2H, *m*)	34.6	-	34.7
4	-	57.8	-	58.2	-	48.8	-	49.1	-	38.9	-	39.4
5	-	42.0	-	42.2	-	37.9	-	37.8	1.86-1.84 (1H, *m*)	53.3	-	53.3
6	1.55 (2H, *m*)	41.1	-	41.3	1.44 (2H, *m*)	41.8	-	41.7	1.33 (2H, *m*)	18.4	-	18.4
7	1.52 (2H, *m*)	18.2	-	18.6	1.42 (2H, *m*)	17.5	-	17.5	1.65-1.62 (2H, *m*)	33.7	-	33.7
8	2.41-2.37 (1H, *m*)	52.9	2.38-2.37 (2H, *m*)	53.1	-	52.9	-	53.2	-	40.2	-	40.2
9	-	37.3	-	37.5	-	37.3	-	37.1	1.29 (1H, *m*)	47.4	-	47.3
10	1.99-1.95 (1H, *m*)	58.9	1.97-1.94 (1H, *m*)	59.5	1.91-1.89 (1H, *m*)	61.5	-	61.3	-	50.1	-	50.1
11	1.48 (2H, *m*)	35.1	-	35.6	1.39 (2H, *m*)	35.6	-	35.3	1.27 (2H, *m*)	22.8	-	22.9
12	1.45 (2H, *m*)	30.0	-	30.5	1.36 (2H, *m*)	30.7	-	30.6	4.16 (1H, *s*)	79.1	4.12 (1H, S)	79.1
13	-	38.1	-	38.3	-	38.7	-	38.4	-	44.6	-	44.7
14	-	38.5	-	39.7	-	39.8	-	39.7	-	42.4	-	42.1
15	1.29 (2H, *m*)	32.1	-	32.4	1.34 (2H, *m*)	32.3	-	32.3	1.15-1.13 (1H, *m*)	28.8	-	28.4
16	1.27 (2H, *m*)	35.6	-	36.0	1.31 (2H, *m*)	35.4	-	35.5	1.22-1.20 (1H, *m*)	24.6	-	24.3
17	-	29.9	-	30.0	-	30.2	-	30.0	-	31.2	-	31.1
18	1.76-1.74 (1H, *m*)	42.5	1.77 (1H, *m*)	42.8	1.75-1.73 (1H, *m*)	42.9	-	42.8	-	43.8	-	43.5
19	1.39 (2H, *m*)	34.9	-	35.4	1.30 (2H, *m*)	35.3	-	35.2	1.19 (1H, *m*)	36.3	-	36.1
20	-	28.0	-	28.2	-	28.6	-	28.2	-	28.8	-	28.5
21	1.34 (2H, *m*)	32.4	1.34 (2H, *m*)	32.8	1.27 (2H, *m*)	32.5	-	32.8	1.18 (2H, *m*)	32.5	-	32.6
22	1.31 (2H, *m*)	38.8	-	39.2	1.24 (2H, *m*)	39.4	-	39.3	1.16 (2H, *m*)	39.7	-	39.9
23	1.18 (3H, *s*)	7.9	1.18 (3H, *s*)	6.8	1.17 (3H, *s*)	11.6	1.15 (3H, *s*)	11.6	1.07 (3H, *s*)	28.9	1.07 (3H, *s*)	28.3
24	1.05 (3H, *s*)	14.9	1.05 (3H, *s*)	14.7	1.00 (3H, *s*)	16.7	0.98 (3H, *s*)	16.4	0.93 (3H, *s*)	16.8	0.94 (3H, *s*)	16.6
25	1.01 (3H, *s*)	17.8	1.01 (3H, *s*)	18.0	0.99 (3H, *s*)	18.5	0.97 (3H, *s*)	18.2	0.89 (3H, *s*)	13.2	0.91 (3H, *s*)	13.5
26	1.00 (3H, *s*)	19.1	0.99 (3H,*s*)	20.3	0.98 (3H,*s*)	20.3	0.96 (3H,*s*)	20.1	0.88 (3H, *s*)	26.9	0.87 (3H,*s*)	26.6
27	0.95 (3H, *s*)	20.2	0.95 (3H, *s*)	18.7	0.96 (3H, *s*)	18.8	0.94 (3H, *s*)	18.6	0.83(3H, *s*)	19.8	0.85 (3H, *s*)	19.5
28	0.89 (3H, *s*)	31.9	0.89 (3H, *s*)	32.1	0.94 (3H, *s*)	32.0	0.92 (3H, *s*)	32.1	0.76 (3H, *s*)	30.5	0.78 (3H, *s*)	30.7
29	0.87 (3H, *s*)	34.7	0.87 (3H, *s*)	35.0	0.93 (3H, *s*)	35.2	0.91 (3H, *s*)	35.0	0.75 (3H, *s*)	33.5	0.76 (3H, *s*)	33.4
30	0.73 (3H, *s*)	34.6	0.73 (3H, *s*)	31.8	0.86 (3H, *s*)	31.9	0.84 (3H, *s*)	31.8	0.60 (3H, *s*)	30.4	0.62 (3H, *s*)	30.2

Table 2 ^{1}H (500 MHz) and ^{13}C (125 MHz) NMR spectroscopic data of compound 4 in $CDCl_3$ compared with guttiferone I in C_5D_5N

	4		guttiferone I[16]	
Position	δ_H (mult., J in Hz)	δ_C	δ_H (mult., J in Hz)	δ_C
1	-	192.6	-	195.3
2	-	122.7	-	119.1
3	-	187.5	-	192.7
4	-	77.5	-	69.6
5	-	49.6	-	51.8
6	2.01 (1H, *m*)	41.9	1.67 (1H, *m*)	42.0
7	1.99 (2H,*m*)	39.6	1.45 (2H,*m*)	43.3
8	-	60.4	-	64.1
9	-	207.9	-	208.6
10	-	193.7	-	198.2
11	-	137.4	-	139.0
12	7.62 (1H, *dd*, 8.1)	128.0	7.38 (1H *dd*, 8.0)	129.9
13	7.30 (1H, *dd*,8.1)	127.4	7.50 (1H *dd*, 8.0)	129.0
14	7.46 (1H, t, 7.3)	131.7	7.54 (1H *t*, 7.5)	133.8
15	7.30 (1H, *dd*, 7.3)	127.4	7.50 (1H *dd*, 7.5)	129.0
16	7.62 (1H, *dd*, 8.1)	128.0	7.38 (1H *d*, 8.0)	129.9
17	2.03 (1H, *m*)	39.6	2.65 (1H, *m*)	26.3
18	5.07 (1H, *m*)	122.1	4.87 (1H, *m*)	120.9
19	-	133.1	-	135.3
20	1.74 (3H,*s*)	26.1	1.63 (3H,*s*)	18.3
21	1.67 (3H,*s*)	24.4	1.66 (3H,*s*)	26.6
22	1.15 (3H, *s*)	13.7	0.82 (3H,*s*)	16.3
23	1.92 (2H,*m*)	36.7	1.66 (2H,*m*)	37.2
24	2.17 (2H, *m*)	40.3	2.00 (1H,*m*)	30.1
25	5.08 (1H, *m*)	123.7	5.04 (1H,*m*)	123.4
26	-	130.8	-	134.7
27	1.69 (3H,*s*)	16.7	1.58 (3H,*s*)	18.2
28	1.68 (3H,*s*)	16.4	1.66 (3H,*s*)	25.9
29	2.54 (2H, *m*)	28.5	2.49 (2H,*m*)	31.5
30	5.06 (1H, *m*)	119.2	5.11 (1H,*m*)	120.9
31	-	137.5	-	135.6
32	1.63 (3H,*s*)	24.3	1.69 (3H,*s*)	18.4
33	1.62 (3H,*s*)	15.2	1.63 (3H,*s*)	26.3
34	1.94 (2H,*m*)	27.3	1.95 (2H,*m*)	24.3
35	5.05 (1H, *m*)	123.7	4.96 (1H,*s*)	125.3
36	-	130.7	-	132.6
37	1.64 (3H,*s*)	18.1	1.56 (3H,*s*)	17.9
38	1.70 (3H, *s*)	15.2	1.71 (3H,*s*)	26.0

The ^{1}H and ^{13}C NMR data (Table 2) revealed that compound 4 was categories of polyprenylated benzophenones core structure.[20] The ^{13}C NMR data of 4 showed signals of a 2,4,6-trisubstituted-3-hydroxycyclohex-2-ene-1,5-dione skeleton including a cyclohexanone carbonyl [δ_C 207.9 (C-9)], β-hydroxy-1,3-enone [δ_C 192.6 (C-1), 122.7 (C-2) and 187.5 (C3)] and two quaternary carbon [δ_C 77.5 (C-4) and 60.4 (C-8)]. The ^{1}H NMR spectra showed signals of a benzoyl group at δ_H 7.30 (2H, *t*, J = 8.1 Hz, H-13, H-15), 7.46 (1H, *t*, J = 8.1 Hz, H-1 4) and 7.62 (2H, *t*, J = 8.1 Hz, H-12, H-16). The ^{1}H and ^{13}C NMR spectra of 4 showed four isoprene units [δ_H/δ_C 2.03

(1H, *m*, H-17)/39.6, 5.07, (1H, *m*, H-18)/122.1, 1.74 (3H, *s*, H-20)/26.1, 1.67 (3H, *s*, H-21)/24.2, 1.92 (2H, *m*, H-23)/36.7, 2.17 (2H, *m*, H-24)/40.3, 5.08 (1H, *m*, H-25)/123.7, 1.69 (3H, *s*, H-27)/16.7, 1.68 (3H, *s*, H-28)/16.4, 2.54 (2H, *m*, H-29)/28.5, 5.06 (1H, *m*, H-30)/119.2, 1.63 (3H, *s*, H-32)/24.3, 1.62 (3H, *s*, H-33)/15.2, 1.94 (2H, *m*, H-34)/27.3, 5.05 (1H, *m*, H-35)/123.7, 1.64 (3H, *s*, H-37)/18.1 and 1.70 (3H, *s*, H-38)/15.2; δ_C 133.1 (C-19), 130.8 (C-26), 137.5 (C-31) and 130.7 (C-36)]. The isoprene groups were located at C-4, C-5, C-6 and C-8 due to the HMBC correlations of H-18 (δ_H 5.07) to C-4 (δ_C 77.5), H-35 (δ_H 5.05) to C-5 (δ_C 49.6), H-25 (δ_H 5.08) to C-6 (δ_C 41.9) and H-30 (δ_H 5.06) to C-8 (δ_C 60.4). In addition, the benzoyl unit and a methyl group (δ_C 1.15, 3H, s, H-22) were joined at C-1 and C-4, respectively. Finally, the NMR data were similar to those of guttiferone I.[16] Accordingly, compound 4 was assigned as guttiferone I.[16]

Compound 5 was isolated as a yellow solid. The ^{1}H NMR spectrum (Table 3) of 5 contained resonances of xanthone skeleton including a singlet chelated proton (1-OH) at δ_H 12.62, an aromatic trisubstituted ABX system [δ_H 7.51 (1H, d, 9.0, H-5), 7.45 (1H, dd, 9.0 and 3.1, H-6) and 7.64 (1H, d, 3.1, H-8)], an ABC aromatic spin system [δ_H 6.77 (1H, d, 8.2, H-2), 7.71 (1H, t, 8.4, H-3) and 6.99 (1H, dd, 8.4, H-4)]. The ^{1}H NMR resonance for a hydroxyl group was found at δ_H 9.02 (1H, s), which was placed at C-7 due to the correlations of H-5 (δ_H 7.51) and 7-OH (δ_H 9.02) to C-7 (δ_H 154.1). Thus, the structure of compound 5 was established as 1,7-dihydroxyxanthone.[17]

Compound 6 was obtained as a yellow solid. The ^{1}H and ^{13}C NMR spectra of 5 and 6 were similar, but compound 6 exhibited significant differences in the presence of a group of methoxy at δ_H 3.87 (3H, s)/ δ_C 56.8 instead a hydroxyl signal at δ_H 9.02 at C-7 of compound 5. Thus, compound 6 was assigned as 1-hydroxy-7-methoxyxanthone.[18]

Conclusion: In conclusion, the phytochemical investigation of leaves extract of *G. cowa* led to isolation and identification of six known compounds including three triterpenes (1–3), one benzophenone (4) and two xanthones (5 and 6). All isolated compounds were determined by analysis of ^{1}H and ^{13}C NMR spectroscopic data and comparison of these signals with those previously reported data. The results provided a scientific basis on phytochemicals of the leaves of *G. cowa* which may be used as supporting data for further works.

Table 3. ^{1}H (500 MHz) and ^{13}C (125 MHz) NMR spectroscopic data of compounds 5, 6, 1,7-dihydroxyxanthone and 1-hydroxy-7-metoxyxanthone (in acetone-d_6)

	5		1,7 dihydroxyxanthone[17]		6		1-hydroxy-7- metoxyxanthone[18]	
Position	δ_H (mult., J in Hz)	δ_C	δ_H (mult., J in Hz)	δ_C	δ_H (mult., J in Hz)	δ_C	δ_H (mult., J in Hz)	δ_C
1	-	162.6	-	163.0	-	161.6	-	162.1
2	6.77 (1H, *d*, 8.2)	109.6	6.75 (1H, *d*, 8.1)	110.4	6.93 (1H, *d*, 8.3)	109.6	6.93 (1H, *d*, 8.1)	110.4
3	7.71 (1H, *t*, 8.4)	138.4	7.68 (1H, *t*, 8.1)	138.0	7.69 (1H, *t*, 8.3)	138.4	7.69 (1H, *t*, 8.1)	136.8
4	6.99 (1H, *dd*, 8.4)	107.1	6.95 (1H, *dd*, 8.4)	107.0	6.73 (1H, *d*, 8.2)	107.1	6.75 (1H, *d*, 8.0)	107.3
4a	-	157.3	-	157.0	-	157.3	-	156.4
5	7.51 (1H, *d*, 9.0)	119.5	7.50 (1H, *d*,8.8)	119.5	7.52 (1H, *d*,8.9)	119.5	7.53 (1H, *d*,8.7)	119.5
6	7.45 (1H,*dd*, 9.0,3.1)	125.4	7.40 (1H,*dd* ,8.8, 2.7)	126.1	7.40 (1H,*dd*,8.9,3.0)	125.4	7.32 (1H,*dd*,8.7, 2.9)	125.9
7	-	154.1	-	156.5	-	156.1	-	156.6
8	7.64 (1H, *d*, 3.1)	104.5	7.57 (1H, *d*, 2.7)	105.1	7.61 (1H, *d*, 3.0)	103.7	7.58 (1H, *d*, 2.9)	104.9
8a	-	120.7	-	121.0	-	120.7	-	121.1
9	-	184.3	-	181.5	-	184.3	-	182.3
9a	-	108.2	-	108.8	-	108.2	-	108.9
10a	-	151.1	-	149.8	-	151.1	-	151.3
1-OH	12.62 (1H, *s*)	-	12.57 (1H, *s*)	-	12.72 (1H, *s*)	-	12.69 (1H, *s*)	-
7-OH	9.02 (1H,*s*)	-	9.20 (1H, *s*)	-	-	-	-	-
7-OMe	-	-	-	-	3.87 (3H,*s*)	56.8	3.89 (3H,*s*)	56.2

References:
1. Te-chato S. Songklanakarin J Sci Technol. 2007; 29(2): 245–252.
2. Panthong K, Pongcharoen W, Phongpaichit S, Taylor WC. Phytochemistry. 2006; 67 999–1004.
3. Khoo HE, Azlan A, Kong KW, Ismail A. Evid Based Complement Alternat Med. 2016: 1–21.
4. Ansari WH, Rahman W, Barraclough D, Maynard R, and Scheinmann FJ. Chem Soc. 1976; 13:1458–1463.
5. Xu G, Kan WLT, Zhou Y, Song JZ, Han QB, Qiao CF, Cho CH, Rudd JA, Lin G, Xu HX. J Nat Prod. 2010; 73:104–108.
6. Sriyatep T, Siridechakorn I, Maneerat W, Pansanit A, Ritthiwigrom T, Andersen RJ Laphookhieo S. J Nat Prod. 2015; 78(2):265–271.
7. Na Z, Song Q, Hu H. Rec Nat Prod. 2013; 7(3): 220–224.
8. Wahyuni FS, Shaari K, Stanslas J, Lajis N, Hamidi D. Appl Pharm Sci. 2015;5(2):6–11.
9. Sharma A, Joseph GS, Singh RP. J Food Sci Technol. 2014; 51(8): 1626-1631.
10. Wahyuni FS, Hui LS, Stanslas J, Lajis NH, Dachriyanus. J Young Pharmacists.2017; 9(2):296–298.
11. Sridechakorn I, Phakhodee W, Ritthiwigrom T, Promgool T, Deachathai S, Cheenpracha S, Prawat U, Laphookhieo S. Fitoterapia. 2012; 83(8):1430–1434.
12. Bharti SK, Krishnan S, Kumar A, Kumar A. Ther Adv Endocrinol Metab. 2018; 9(3): 81-100.
13. Ho LK, Chang CR, Chang YSJ. Chin Soc-Taip. 1995; 42:93–95.
14. Sousa GF, Duarte LP, Alcantara AFC, Silva GDF, Vieira-Filho SA, Silva RR, Oliveira DM, Takahashi JA. Molecules. 2012; 17:13439–13456.
15. Boar RB, Joukhadar L, Luque MD, Mcghie JF. JCS Perkin. 1977:2104–2109.
16. Merza J, Mallet S, Litaudon M, Dumontet V, Seraphin D, Richomme P. Planta Med. 2006; 72:87–89.
17. Mak NK, Kui W, Zhang M, Wong NSR, Tai LS, Yung KKL, Leung HW. Life Science. 2000; 66(4):347–354.
18. Dharmaratne HRW, Napagoda MT, Tennakoon SB. Nat Prod Res. 2009; 23(6):539–545.
19. Xia Q, Zhang H, Sun X, Zhao H, Wu L, Zhu D, Yang G, Shao Y, Zhang X, Mao X, Zhang L, She G. Molecules. 2014; 19:17478–17535.
20. Olivares EM, Gonzalez JG, Monache FD. Phytochemistry. 1994; 36(2):473–475.
21. Wu S, Long C, Kennelly FJ. Nat Prod Rep. 2014; 31(9):1158–1174.
22. Yong KO, Kuete V, Efferth TJ. Med Plants Res. 2013:351–391.
23. Gutierrez-Orozco F, Failla ML. Nutrients. 2013; 5:3163–3183.

Acknowledgements: This study was supported from the grant provided by The Agricultural Research Development Agency (Public Organization), Thailand and Thesis/Dissertation Support Grant, Mae Fah Luang University. Furthermore, the authors appreciated to thank Center of Chemical Innovation for Sustainability (CIS) and natural product laboratory, Mae Fah Luang University, Chiang Rai, Thailand for laboratory facilities.

C3_016_PF: CHEMICAL SYNTHESIS OF GLYCOSYL DITHIOCARBAMATE USING LACTOSE ISOLATED FROM WHEY AS PRECURSOR

Pranpariya Ponpakdee[1], Panuwat Padungros[2,*]
[1]Program in Petrochemistry and Polymer Science, Faculty of Science, Chulalongkorn University, Bangkok 10330, Thailand
[2]Organic Synthesis Research Unit, Department of Chemistry, Faculty of Science, Chulalongkorn University, Bangkok 10330, Thailand
*e-mail: panuwat.p@chula.ac.th

Abstract: Glycosyl dithiocarbamates (glycosyl DTCs) are efficient monomers in oligosaccharide synthesis. Several syntheses of glycosyl DTCs have been previously reported. The conventional methods; however, required multistep syntheses which involved strictly controlled anhydrous conditions. In this work, 2-chloro-1,3-dimethylimidazolinium chloride (DMC) was investigated as a dehydrative agent for condensation between lactol (1-hydroxy glycoside) and sodium *N,N*-diethyldithiocarbamate (NaDTC; $Na^{+-}SC(S)NEt_2$). The lactol 1 derived from protected galactose was first examined as a model substrate. After several optimizations, galactosyl DTC 2 was afforded in good yields *via* direct anomeric activation with DMC. The galactosyl DTC 2 was further utilized as a glycosyl donor for chemical glycosylation. Coupling between galactosyl DTC 2 and glycosyl acceptor 3 using $Cu(OTf)_2$ as an Lewis acid activator provided the corresponding disaccharide 4 in 61% yield with moderate selectivity. Next, lactose (5) was isolated from liquid whey which kindly donated by cheese factory of the Royal Chitralada project, Bangkok. Isolation of lactose was developed and obtained solid lactose in 39 grams from liquid whey 1 liter, the recovery was 3.9% (w/v). The DMC-mediated activation was then carried out to yield lactosyl DTC 6 intermediate in good yield. Ongoing work focuses on the application of lactosyl DTC 6 as glycosyl donor for the synthesis of prebiotic galacto-oligosaccharide (GOS).

Introduction: Over the past decade, there has been increasing interest in the field of synthesis and evaluation of thioglycosides and their derivatives. Thioglycosides have been introduced as versatile glycosyl donors for chemical glycosylation in oligosaccharide synthesis. Besides, they are further employed as biological inhibitors[1-4] and inducers[5] in various biological and medicinal chemistry. Due to their stability and ability, they can be easily activated under various types of glycosylation conditions, also widely used in a variety of electrophilic and thiophilic promoters[6-8] and readily converted into other types of glycosyl donors.[9,10] Among these potentials, aglycon transfer has been observed as side reaction when using thioglycosides as precursors.[11-13] In addition, intermolecular aglycon transfer is not only a major drawback but also including cross-reactivity side reaction between thiophilic promoter and acceptor.[12] For these reasons, novel glycosyl donors have been extensively developed for employing in glycosylation reaction instead of using the traditional thioglycoside donors.

Glycosyl dithiocarbamates (DTCs), one of the thioglycoside derivatives, are widely used in various chemical syntheses; for instance, as ligands in coordination chemistry[14] and functionalization of metal surfaces.[15] They also play important roles in pharmaceutical research studies to act as antibacterial and antitubercular compounds.[16-18] Especially, they are valuable building blocks for the synthesis of complex oligosaccharides that have been focused to use as alternative donors over thioglycoside sugars. There have been many reports developed for the synthesis of glycosyl DTCs that provide some disadvantages. For example, the nucleophilic substitution of glycosyl halides with DTC salts were employed under basic conditions[19] or the dehydrative substitution of lactols under phase-transfer conditions[20] for preparing the designed glycosyl DTCs. In 2014, Wei and co-workers[21] demonstrated further approach for the glycosyl DTCs synthesis by in situ conversion from perbenzylated epoxyglycals, *via* DMDO epoxidation reaction, treated with Et_2NH and CS_2 that carried out

glycosyl DTCs in high yields (Figure 1a). However, these conventional methods required multistep syntheses which involved strictly controlled anhydrous conditions. To overcome these limitations, a more efficient synthetic method has been required for preparation of glycosyl DTC.

Herein, we reported the investigation of 2-chloro-1,3-dimethylimidazolinium chloride (DMC) as a dehydrative condensing agent for condensation of lactol (1-hydroxyl glycoside) with sodium *N,N*-diethyldithiocarbamate (NaDTC; $Na^{+-}SC(S)NEt_2$) (Figure 1b). Next, the coupling between glycosyl DTC and glycosyl acceptor using Lewis acid activator *via* glycosylation reaction was then illustrated. Lactose that can be isolated from liquid whey was then subsequently examined in the DMC-mediated anomeric activation as well. Furthermore, the investigation of the utility of lactosyl DTC as glycosyl donor was still in progress for focusing on prebiotic galacto-oligosaccharide (GOS) synthesis.

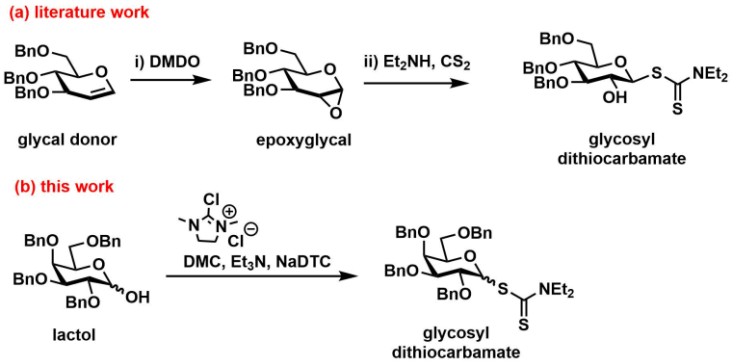

Figure 1. Synthesis of glycosyl DTC *via* (a) DMDO epoxidation reaction (previous work) (b) the direct anomeric activation with DMC (this work).

Methodology:

Materials: All chemical reagents and solvents were purchased from commercial sources and used without further purification. Liquid whey was kindly provided by cheese factory of the Royal Chitralada project, Bangkok Thailand. Thin-layer chromatography (TLC) analysis was monitored with pre-coated aluminium sheets silica gel 60 F_{254} and detected by UV absorption at 254 nm or by staining with *p*-anisaldehyde. The products were purified by flash column chromatography with silica gel 60 (70-230 mesh) and preparative TLC with 0.75 mm silica-coated plates. ^{1}H and ^{13}C NMR spectra were recorded on Bruker Ultrashield 400 Plus NMR spectrometer or Varian Mercury NMR spectrometer operating at 400 MHz (^{1}H) and 100 MHz (^{13}C) in $CDCl_3$ or D_2O.

Methods:

Synthesis of Galactosyl DTC via Direct Anomeric Activation with DMC. 2-chloro-1, 3-dimethylimidazolinium chloride (DMC; 94 mg, 0.56 mmol) was added to a mixture of lactol 1 (100 mg, 0.18 mmol), sodium *N,N*-diethyldithiocarbamate (NaDTC; 250 mg, 1.11 mmol) and triethylamine (232 μL, 1.66 mmol) in acetonitrile (1.85 mL) at 0 °C. The reaction mixture was allowed to stir overnight at room temperature, then quenched with a saturated $NaHCO_3$ solution and extracted with EtOAc (3 x 10 mL). The combined organic layers were washed with brine, dried over Na_2SO_4 and reduced *in vacuo*. The crude product was purified by flash column chromatography on silica gel using 5-50% EtOAc in hexanes gradient to afford an anomeric mixture of galactosyl DTC 2 (77 mg, 82% BRSM; α/β 1:1.3) as a yellow syrup. ^{1}H NMR (400 MHz, $CDCl_3$): δ 7.29 – 7.18 (m, 40H), 6.96 (d, 1H, *J* = 5.6 Hz), 5.69 (d, 1H, *J* = 10.4 Hz), 4.92 – 4.82 (m, 2H), 4.81 – 4.73 (m, 2H), 4.71 – 4.58 (m, 5H), 4.57 – 4.45 (m, 3H), 4.45 – 4.27 (m, 5H), 4.06 – 3.80 (m, 8H), 3.76 – 3.62 (m, 5H), 3.61 – 3.44 (m, 6H), 1.28 – 1.00 (m, 12H).

General Procedure for $Cu(OTf)_2$-Mediated Glycosylation. Glycosyl DTC 2 (40 mg, 0.06 mmol), glycosyl acceptor 3 (41.9 mg, 0.09 mmol) and tri-*tert*-butylpyrimidine (TTBP; 18.3 mg, 0.07 mmol) were dried by azeotropic distillation with toluene-acetonitrile. Activated molecular sieves (3Å) were added to the mixture, dissolved with dried CH_2Cl_2 (1.2 mL) and then stirred for 1 h at room temperature under argon atmosphere to remove trace amount of moisture. The reaction mixture was cooled to -50 °C, treated with anhydrous $Cu(OTf)_2$ (45 mg, 0.12 mmol). After stirred for 5 min, the resulting suspension turned into dark green solution. The mixture was then allowed to stir for overnight at room temperature. After glycosyl DTC 2 was completely consumed as monitored by TLC, the reaction mixture was quenched with a saturated $NaHCO_3$ solution and extracted with CH_2Cl_2 (3 x 10 mL). The combined organic layers were washed with brine, dried over Na_2SO_4 and concentrated under reduced pressure. The dark green syrup was purified by preparative TLC using 2% EtOAc in toluene and then 20% EtOAc in hexanes to give a mixture of the corresponding disaccharide 4 (36 mg, 61%; α/β 1:3) as a pale yellow syrup. *Alpha*: ^{1}H NMR (400 MHz, $CDCl_3$): δ 7.32 – 7.18 (m, 35H), 5.02 – 4.89 (m, 3H), 4.88 – 4.75 (m, 3H), 4.75 – 4.65 (m, 4H), 4.61 – 4.49 (m, 4H, *J* = 18.1, 6.1 Hz), 4.42 (d, 1H, *J* = 12.0 Hz,), 4.35 (d, 1H, *J* = 11.9 Hz), 4.06 – 3.85 (m, 5H), 3.82 – 3.68 (m, 3H), 3.58 (t, 1H, *J* = 9.3 Hz), 3.53 – 3.44 (m, 2H), 3.40 (dd, 1H, *J* = 10.0, 3.7 Hz), 3.28 (s, 3H). *Beta*: ^{1}H NMR (400 MHz, $CDCl_3$): δ 7.33 – 7.14 (m, 35H), 4.87 (t, 3H, *J* = 11.8 Hz), 4.76 – 4.29 (m, 12H), 4.23 (d, 1H, *J* = 7.7 Hz), 4.06 (d, 1H, *J* = 10.5 Hz), 3.90 (t, 1H, *J* = 9.3 Hz), 3.84 – 3.69 (m, 3H), 3.59 – 3.32 (m, 7H), 3.22 (s, 3H).

General Procedure for Isolation of Lactose from Liquid Whey. To a solution of liquid whey (1 L) was heated to boiling in a beaker at 102 °C for 1 h until protein was coagulated. Protein was removed by filtration through cheesecloth. After filtration, liquid whey showed only slight turbidity and was then concentrated by boiling to a volume of 150 mL. The turbid yellow filtrate was allowed to stand open for crystallization in a beaker for several days. Afterward, lactose crystals were gradually formed at the bottom of a beaker. The liquid was decanted into another beaker and then repeated crystallization procedure twice to obtain lactose (5) (39 g, 0.039 g/mL recovery) as a white crystal. ^{1}H NMR (400 MHz, D_2O): δ5.14 (d, 1H, *J* = 3.6 Hz), 4.59 (d, 1H, *J* = 7.9 Hz), 4.37 (d, 1H, *J* = 7.8 Hz), 3.91 – 3.81 (m, 6H), 3.81 – 3.63 (m, 4H), 3.62 – 3.54 (m, 1H), 3.54 – 3.42 (m, 3H), 3.21 (t, 1H, *J* = 8.3 Hz).

Results and Discussion:

Synthesis of Galactosyl DTC via Direct Anomeric Activation with DMC: To improve the drawbacks of the traditional protocol of glycosyl DTCs synthesis, the first attempt to investigate the use of 2-chloro-1,3-dimethylimidazolinium chloride (DMC) as a condensing agent was demonstrated. The one-step synthesis of galactosyl DTC was performed using lactol 1, derived from galactose to use as a model substrate, treated with a commercially available sodium *N,N*-diethyldithiocarbamate (NaDTC), triethylamine and DMC in acetonitrile at 0 °C (Figure 2). To our satisfaction, the corresponding galactosyl DTC 2 was carried out in good yields. This increasing yield of product could be explained by the more stability of perbenzylated galactosyl DTC 2 when comparing with the previous report[22] that showed the hydrolysis product of galactosyl DTC was occurred due to their low stability of unprotected galactosyl DTC species. As a result, the direct anomeric activation mechanism with DMC is proposed as follows (Figure 3). The reaction mechanism initially involves a nucleophilic attack of galactosyl DTC to the 2 position of DMC and subsequently promoting by triethylamine as a general base to the first generate galactosyl intermediate. The resulting β-galactosyl intermediate is then attacked by S_N2 type reaction of DTC salt at anomeric center from α-side leading to the formation of the desired α-galactosyl DTC; on the other hand, the corresponding β-galactosyl DTC is carried out by β-side nucleophilic attack of DTC salt to anomeric center of the α-galactosyl intermediate.

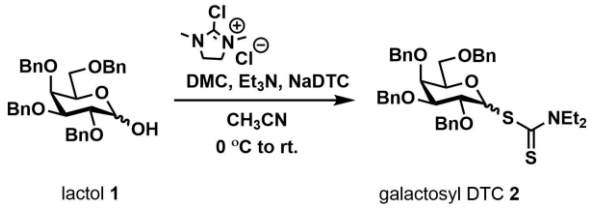

Figure 2. Synthesis of galactosyl DTC 2 *via* Direct Anomeric Activation with DMC.

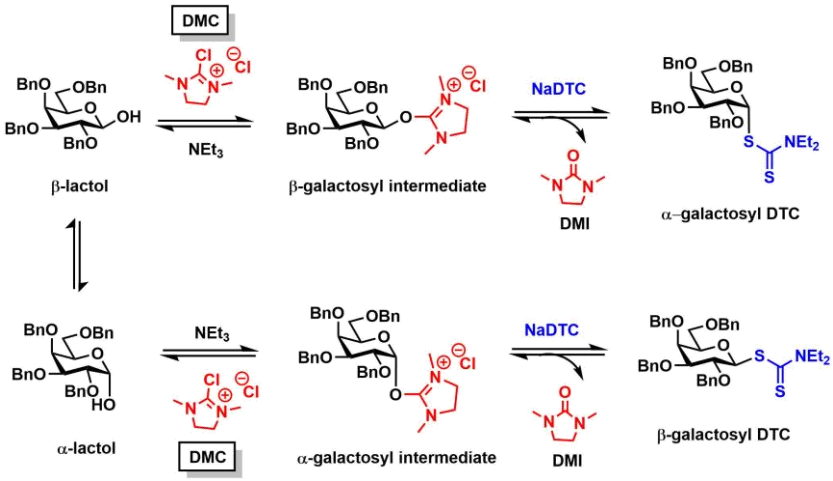

Figure 3. Plausible reaction mechanism of direct anomeric activation with DMC.

Cu(OTf)$_2$-Mediated Glycosylation: We next turned our attention to the glycosylation between galactosyl DTC 2 and glycosyl acceptor 3 to utilize the benefit of the resulting galactosyl DTC 2 as a glycosyl donor. Using the previously reported condition by Wei and co-workers[21], the coupling reaction was performed in the controlled anhydrous conditions by treating galactosyl DTC 2 with glycosyl acceptor 3, TTBP and using Cu(OTf)$_2$ that have high reactivity with the DTC group as an Lewis acid activator at -50 °C to resulted in the desired disaccharide 4 with moderate stereoselectivity in moderate yield (Figure 4). To our success in the synthesis of disaccharides 4, we aimed that the anomeric activation with DMC can be utilized to lactose which was isolated from liquid whey.

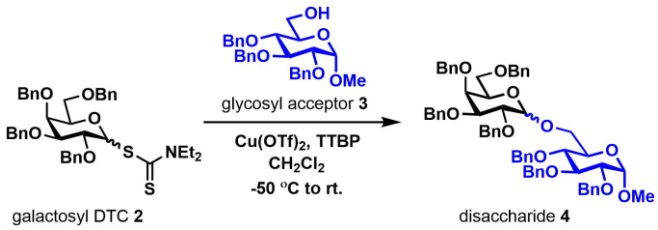

Figure 4. Chemical glycosylation reaction of galactosyl DTC 2 and glycosyl acceptor 3.

Isolation of Lactose from Liquid Whey: To get the most out of liquid whey which is a by-product from the cheese processing, lactose was isolated. Liquid whey was initially boiling at 102 °C for 1 h to remove protein. At the high temperature, the heat destroys protein structure and then protein coagulates that can be removed by filtration. After that, the filtrate was

concentrated by heat and crystallized for several days to obtain white crystal lactose which was 0.039 g/mL recovery.

Synthesis of lactosyl DTC via Direct Anomeric Activation with DMC and its application in the synthesis of prebiotic galacto-oligosaccharide (GOS): To assess the potential utility of this selective activation, the present DMC-mediate reaction is further applicable to unprotected lactose. In order to investigate the utility, the direct anomeric activation of lactose was examined by treating lactose which was isolated from liquid whey with NaDTC, triethylamine and DMC in 1:1 acetonitrile/H_2O at -10 °C. After the reaction was completed, the lactosyl DTC 6 intermediate was provided and was then subsequently acetylated by adding 0.5 mL acetic anhydride in dried pyridine at room temperature for overnight to furnish the acetylated lactosyl DTC 7 product in 45% yield over 2 steps (Figure 5). These results show the feasibility that can be built on to the synthesis of prebiotic-oligosaccharide (GOS).

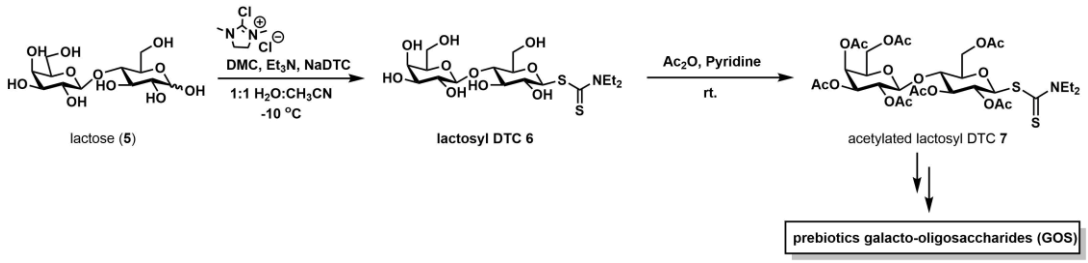

Figure 5. Synthesis of lactosyl DTC 6 and application in the prebiotic-oligosaccharide (GOS) synthesis.

Conclusion: Galactosyl dithiocarbamate (DTC) 2 was successfully prepared from a one-step synthesis *via* direct anomeric activation by using DMC as a dehydrative agent. This beneficial of galactosyl DTC 2 as a glycosyl donor was efficiently utilized in the $Cu(OTf)_2$-mediated glycosylation and obtained disaccharide 4 with moderate stereoselectivity. This one-step synthetic method can further apply to lactose precursor which was isolated from liquid whey to afford the lactosyl DTC 6 intermediate and subsequently built on to the synthesis of prebiotic-oligosaccharide (GOS) in future work.

References:

1. Marino C, Mariño K, Miletti L, Manso Alves MJ, Colli W, de Lederkremer RM. Glycobiology. 1998;8:901–904.
2. Elgemeie GH, Mahdy EM, Elgawish MA, Ahmed MM, Shousha WG, Eldin ME. Z. Naturforsch. C. 2010;65:577–587.
3. Agrawal S, Wozniak M, Luc M, Walaszek K, Pielka E, Szeja W, Pastuch-Gawolek G, Gamian A, Ziolkowski P. Oncotarget. 2017;8:114173–114182.
4. Krol E, Pastuch-Gawolek G, Chaubey B, Brzuska G, Erfurt K, Szewczyk B. Molecules. 2018;23:1435.
5. Birk R, Ikan A, Bravdo B, Braun S, Shoseyov O. Appl. Biochem. Biotechnol. 1997;66:25–30.
6. Xiong DC, Zhang LH, Ye XS. Adv. Synth. Catal. 2008;350:1696–1700.
7. Vibhute AM, Dhaka A, Athiyarath V, Sureshan KM. Chem. Sci. 2016;7:4259–4263.
8. Xu FF, Pereira CL, Seeberger PH. Beilstein J. Org. Chem. 2017;13:1994–1998.
9. Kartha KPR, Field RA. Tetrahedron Lett. 1997;38:8233–8236.
10. Govindarajan M, Kartha KPR. Tetrahedron Lett. 2012;53:5631–5634.
11. Christensen HM, Oscarson S, Jensen HH. Carbohydr. Res. 2005;408:51–95.
12. Li Z, Gildersleeve JC. J. Am. Chem. Soc. 2006;128:11612–11619.

13. Yu F, Nguyen HM. J. Org. Chem. 2012; 77:7330–7343.
14. Hogarth G. Mini-Rev. Med. Chem. 2012;12:1202–1215.
15. Gao D, Scholz F, Nothofer HG, Ford WE, Scherf U, Wessels JM, Yasuda A, von Wrochem F. J. Am. Chem. Soc. 2011;133:5921–5930.
16. Horita Y, Takii T, Chiba T, Kuroishi R, Maeda Y, Kurono Y, Inagaki E, Nishimura K, Yamamoto Y, Abe C, Mori M, Onozaki K. Bioorg. Med. Chem. Lett. 2009;19:6313–6316.
17. Wang MM, Chu WC, Yang Y, Yang QQ, Qin SS, Zhang E. Bioorg. Med. Chem. Lett. 2018;28:3436–3440.
18. Horita Y, Takii T, Kuroishi R, Chiba T, Ogawa K, Kremer L, Sato Y, Lee Y, Hasegawa T, Onozaki K. Bioorg. Med. Chem. Lett. 2011;21:899–903.
19. Gabhe BS, Deshmukh SP. Int. J. Chem. Sci. 2010;8:2083–2088.
20. Szeja W, Bogusiak J. Synthesis 1988;3:224–225.
21. Padungros P, Alberch L, Wei A. J. Org. Chem. 2014;79:2611–2624.
22. Li G, Noguchi M, Kashiwagura H, Tanaka Y, Serizawa K, Shoda SI. Tetrahedron Lett. 2016;57:3529–3531.

Acknowledgements: The authors thank the Royal Chitralada project, Bangkok.

C3_018_PF: POTENT VASORELAXANT CAGED POLYPRENYLATED XANTHONES FROM THE RESIN OF *Garcinia hanburyi*

Rungnapa Noina[1], Ratchanaporn Chokchaisiri[2], Chainarong Tocharus[3], Luckika Panthiya[3], Waraluck Chaichompoo[1], Apichart Suksamrarn[1,*]
[1]Department of Chemistry and Center of Excellence for Innovation in Chemistry, Faculty of Science, Ramkhamhaeng University, Bangkok 10240, Thailand
[2]Department of Chemistry, School of Science, University of Phayao, Phayao 56000, Thailand
[3]Department of Anatomy, Faculty of Medicine, Chiang Mai University, Chiang Mai 50200, Thailand
*e-mail : s_apichart@ru.ac.th

Abstract: *Garcinia hanburyi* (Clusiaceae) known in Thai as "Rong thong", is locally used as traditional medicine for the treatment of internal drastic purgative and externally infected wounds, chronic dermatitis, hemorrhoids, and bedsore. The chemical investigation of the hexane extract of the resin from this plant species resulted in the isolation of three known caged polyprenylated xanthones: gambogin (1), desoxymorellin (2) and desoxygambogenin (3). The structures of these compounds were elucidated using chemical and spectroscopic techniques. All of them showed vasorelaxant activity in rat isolated thoracic aorta. Compound 2 exhibited the most highly potent activity, with EC_{50} of 1.983×10^{-7} M.

Introduction: Hypertension is one of the most common cardiovascular diseases that can cause coronary disease, myocardial infarction and stroke[1] which occur in most countries in the world including Thailand. Hypertension is highly prevalent and one of the leading risk factors for cardiovascular diseases and death in Thailand.[2] Conventional antihypertensives are usually associated with many side effects. The renewed interest in the search for new drugs from natural sources, especially from medicinal plant, has gained global attention. Thus, natural plants and herbs can be the source of drugs, with fewer side effects for treatment of hypertension in future.[3]

The genus *Garcinia* (Clusiaceae) comprises approximately 418 species distributed throughout Asian and southern Africa.[4] In Thailand, there are 30 species of this genus including *Garcinia hanburyi*[5] commonly known as Rong thong. The air-dried resin has been used as a dye and traditional medicine for the treatment of internal drastic purgative and externally infected wounds, chronic dermatitis, hemorrhoids, and bedsore.[6] Previous chemical investigations have reported the isolation of a number of xanthones[7-9] and triterpenoids.[10-12] Their biological activities, such as antibacterial[13], anti-HIV[14], cytotoxic[15], α-glucosidase inhibitory[16] activities were also studied. For the preliminary screening of the crude extracts of plants for anti-hypertensive constituents, we discovered that the *n*-hexane extract of the resin of *G. hanburyi* exhibited vasorelaxant activity in rat isolated thoracic aorta. The present work reports the isolation of three known caged polyprenylated xanthones, gambogin (1), desoxymorellin (2) and desoxygambogenin (3), from the resin of this plant species and their vasorelaxant activity.

Methodology:

General: Optical rotations were measured on a JASCO-1020 polarimeter. IR spectra were recorded on a Perkin-Elmer FT-IR 400 spectrophotometer. ^{1}H and ^{13}C NMR spectra were recorded on a Bruker ASCEND 400 spectrometer. Mass spectra were obtained on a Finnigan LC-Q mass spectrometer. Unless indicated otherwise, column chromatography was carried out using Merck siliga gel 60 (<0.063 mm) and SiliCycle SilicaFlash F 60 (40–63 µm). For TLC, Merck pre-coated silica gel 60 F254 plates were used. Spots on TLC were detected under UV light and by spraying with anisaldehyde-H_2SO_4 reagent followed by heating.

Plant Material: The resin of *G. hanburyi* was purchased from Tai-an-jan herbal store, Bangkok in 2014. A voucher specimen is deposited at the Faculty of Science, Ramkhamhaeng University (Apichart Suksamrarn, No. 090).

Extraction and Isolation : The air-dried resin of *G. hanburyi* (1.0 kg) was extracted successively with *n*-hexane, EtOAc and MeOH at room temperature. The filtered solution of each extraction was evaporated to dryness under reduced pressure at 40–45 °C to give the hexane (47.8 g), EtOAc (272.2 g) and MeOH (43.2 g) extracts.

The hexane extract (47.5 g) was fractionated by column chromatography (Merck silica gel 60, 0.063–0.200 mm, 1500 g), using gradient solvent system of *n*-hexane, *n*-hexane–EtOAc, EtOAc, EtOAc–MeOH and MeOH with increasing amount of the more polar solvent. The eluates were examined by TLC and six combined fractions (H1–H6) were obtained. Fraction H2 (566.8 mg) was chromatographed over silica gel using a gradient solvent system of *n*-hexane, *n*-hexane–EtOAc and EtOAc with increasing amounts of the more polar solvent to give 6 subfractions (H2.1–H2.6). Subfraction H2.4 was chromatographed using *n*-hexane–CH_2Cl_2–EtOAc (4:2:0.1) as eluting solvent system to afford 8 subfractions (H2.4.1–H2.4.8). Subfraction H2.4.7 was purified using column chromatography eluting under isocratic condition of *n*-hexane–EtOAc (5:0.5) to yield gambogin (1) (16.1 mg) and desoxymorellin (2) (28.1 mg). Fraction H3 (8.44 g) was chromatographed over silica gel eluting under isocratic condition of *n*-hexane–EtOAc (4:1) to give 7 subfractions (H3.1–H3.7). Subfraction H3.2 was chromatographed using *n*-hexane–CH_2Cl_2–EtOAc (8:2:0.1) to afford 5 subfractions (H3.2.1–3.2.5). Subfraction H3.2.3 was purified using column chromatography eluting under isocratic condition of *n*-hexane–EtOAc (5:0.5) to yield desoxygambogenin (3) (10.8 mg).

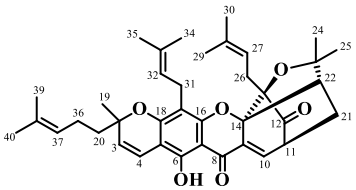

(1)

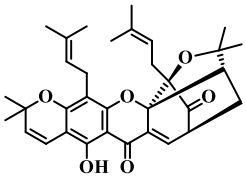

(2)

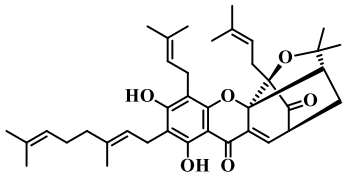

(3)

Gambogin (1). Yellow gum; $[\alpha]_D^{30.7}$ -209.8° (*c* 0.3, $CHCl_3$); ESI-MS (+*ve*): *m/z* 599.3 $[M+H]^+$; ^1H NMR ($CDCl_3$, 400 MHz): δ 1.01 (s, 3H, H-29), 1.25 (s, 3H, H-25), 1.31 (dd, *J* = 13.3, 9.3 Hz, 1H, H_b-21), 1.35 (s, 3H, H-30), 1.38 (s, 3H, H-19), 1.54 (s, 3H, H-39), 1.59 (m, 1H, H-20), 1.63 (s, 6H, H-35, 40), 1.68 (s, 3H, H-24), 1.73 (s, 3H, H-34), 1.75 (m, 1H, H-20) 2.04 (m, 2H, H-36), 2.30 (dd, *J* = 13.3, 4.8 Hz, 1H, H_a-21), 2.44 (d, *J* = 9.3 Hz, 1H, H-22), 2.54 (d, *J* = 7.4 Hz, 2H, H-26), 3.28 (m, 2H, H-31), 3.46 (dd, *J* = 6.9, 4.8 Hz, 1H, H-11), 4.41 (m, 1H, H-27), 5.05 (m, 1H, H-37), 5.19 (m, 1H, H-32), 5.43 (d, *J* = 10.0 Hz, 1H, H-3), 6.66 (d, *J* = 10.0 Hz, 1H, H-4), 7.41 (d, *J* = 6.9 Hz, 1H, H-10), 12.86 (s, 1H, 6-OH); ^{13}C NMR ($CDCl_3$, 100 MHz): δ 16.7 (C-29), 17.6 (C-39), 18.2 (C-34), 21.6 (C-31), 22.7 (C-36), 25.4 (C-21, C-30), 25.6 (C-35,40), 27.3 (C-19), 28.8 (C-26), 29.1 (C-25), 30.1 (C-24), 41.8 (C-20), 46.9 (C-11), 49.1 (C-22), 81.0 (C-2), 83.2 (C-23), 84.6 (C-13), 90.4 (C-14), 100.5 (C-7), 102.6 (C-5), 107.9 (C-17), 116.0 (C-4), 117.8 (C-27), 122.1 (C-32), 123.8 (C-37), 124.7 (C-3), 131.7 (C-33), 131.9 (C-38), 133.7 (C-9, C-10), 134.9 (C-28), 157.4 (C-6), 157.8 (C-16), 160.8 (C-18), 179.8 (C-8), 203.6 (C-12).

Desoxymorellin (2). Yellow gum; $[\alpha]_D^{30.7}$ -253.4° (*c* 0.4, $CHCl_3$); ESI-MS (+*ve*): *m/z* 531.8 $[M+H]^+$; ^1H NMR ($CDCl_3$, 400 MHz): δ 0.99 (s, 3H, H-29), 1.25 (s, 3H, H-25), 1.31 (dd, *J* = 13.3, 9.3 Hz, 1H, H_b-21), 1.33 (s, 3H, H-30), 1.41 (s, 6H, H-19, 20), 1.64 (s, 3H, H-35), 1.68 (s, 3H, H-24), 1.74 (s, 3H, H-34), 2.30 (dd, *J* = 13.3, 4.6 Hz, 1H, H_a-21), 2.46 (d, *J* = 9.3 Hz, 1H, H-22), 2.54 (d, *J* = 7.2 Hz, 2H, H-26), 3.28 (m, 2H, H-31), 3.46 (dd, *J* = 6.9, 4.6 Hz, 1H, H-11), 4.39 (m, 1H, H-27), 5.19 (m, 1H, H-32), 5.49 (d, *J* = 9.9 Hz, 1H, H-3), 6.61 (d, *J* = 9.9 Hz, 1H, H-4), 7.41 (d, *J* = 6.9 Hz, 1H, H-10), 12.86

(s, 1H, 6-OH); ^{13}C NMR ($CDCl_3$, 100 MHz): 16.6 (C-29), 18.2 (C-34), 21.6 (C-31), 25.4 (C-21), 25.6 (C-30), 25.8 (C-35), 28.2 (C-19, C-20), 28.7(C-26), 29.0 (C-25), 30.1 (C-24), 46.9 (C-11), 49.1 (C-22), 78.4 (C-2), 83.2 (C-23), 84.6 (C-13), 90.4 (C-14), 100.5 (C-7), 102.9 (C-5), 108.2 (C-17), 115.5 (C-4), 117.8 (C-27), 122.0 (C-32), 126.1 (C-3), 131.6 (C-33), 133.6 (C-9), 133.7 (C-10), 134.9 (C-28), 157.4 (C-6), 157.7 (C-16), 160.5 (C-18), 179.5 (C-8), 203.6 (C-12).

Desoxygambogenin (3). Yellow gum; $[\alpha]_D^{30.7}$ -135.1° (*c* 1.0, $CHCl_3$); ESI-MS (-*ve*): *m/z* 599.8 [M-H]$^-$; ^{1}H NMR ($CDCl_3$, 400 MHz): δ 0.98 (s, 3H, H-29), 1.26 (s, 3H, H-24), 1.30 (dd, *J* = 13.4, 9.4 Hz, 1H, H_b-21), 1.34 (s, 3H, H-30), 1.57 (s, 3H, H-39), 1.66 (s, 6H, H-25, 40), 1.70 (s, 3H, H-35), 1.75 (s, 3H, H-34), 1.79 (s, 3H, H-19), 2.05 (m, 4H, H-4, 36), 2.30 (dd, *J* = 13.4, 4.6 Hz, 1H, H_a-21), 2.44 (d, *J* = 9.4 Hz, 1H, H-22), 2.53 (d, *J* = 7.6 Hz, 2H, H-26), 3.35 (d, *J* = 7.0, 4H, H-20, 31), 3.46 (dd, *J* = 6.9, 4.6 Hz, 1H, H-11), 4.39 (m, 1H, H-27), 5.03 (m, 1H, H-37), 5.19 (m, 2H, H-3, 32), 6.45 (s, 1H, 18-OH), 7.42 (d, *J* = 6.9 Hz, 1H, H-10), 12.93 (s, 1H, 6-OH); ^{13}C NMR ($CDCl_3$, 100 MHz): 16.2 (C-19), 16.7 (C-29), 17.7 (C-39), 18.0 (C-34), 21.2 (C-4), 22.1 (C-31), 25.5 (C-21, 30), 25.7 (C-35, 40), 26.4 (C-36), 28.8 (C-26), 29.1 (C-25), 30.1 (C-24), 39.7 (C-20), 47.0 (C-11), 49.1 (C-22), 83.1 (C-23), 84.6 (C-13), 90.3 (C-14), 100.8 (C-7), 106.4 (C-17), 107.2 (C-5), 117.8 (C-27), 121.4 (C-3), 121.9 (C-32), 123.8 (C-37), 131.9 (C-38), 133.8 (C-10), 133.9 (C-9, 33), 134.9 (C-28), 139.1 (C-2), 156.3 (C-16), 160.2 (C-6), 163.0 (C-18), 179.7 (C-8), 203.5 (C-12).

Biological Evaluations: Preliminary investigation revealed that the *n*-hexane and EtOAc extracts showed high and moderate vasorelaxant activity in rat isolated thoracic aorta (data not shown). All isolated compounds were subjected to in vitro rat aorta relaxant activity evaluation. The vasorelaxant activity of compounds 1–3 are shown in Table 1.

Results and Discussion: Investigation of the *n*-hexane extract of the resin of *G. hanburyi* has led to the isolation of three known caged polyprenylated xanthones 1–3. The isolated known caged polyprenylated xanthones were identified as gambogin (1)[15], desoxymorellin (2)[17] and desoxygambogenin (3)[15] by comparison of their physical properties and spectral data with those reported in the literature. All the isolated compounds were subjected to in vitro rat aorta relaxant activity evaluation (Table 1). The vasorelaxant reference compound, acetylcholine, was used as the positive control. Compound 2 exhibited the most highly potent activity, with EC_{50} of 1.983×10^{-7} M.

Table 1. Vasorelaxant activity of compounds 1–3.

Compound	EC_{50} (M)
1	1.924×10^{-6}
2	1.983×10^{-7}
3	1.408×10^{-6}
Acetylcholine	3.72×10^{-8}

Conclusion: Three knowns caged polyprenylated xanthone 1–3, were isolated from the resin of *G. hanburyi*. All isolated compounds were subjected to in vitro rat aorta relaxant activity evaluation. Compound 2 exhibited the most active vasorelaxant effect, with the EC_{50} value of 1.983×10^{-7} M.

References:

1. Wonganan O, Tocharus C, Puedsing C, Homvisasevongsa S, Sukcharoen O, Suksamrarn A. Eur J Med Chem. 2013;62:771–776.
2. Tocharoenvanich P, Yipintsoi T, Choomalee K, Boonwanno P, Rodklai A. J Med Assoc Thai. 2008;91:471–478.
3. Tabassum N, Ahmad F. Phcog Rev. 2011;5:30–40.

4. Hemshekhar M, Sunitha K, Sebastin SM, Devaraja S, Kemparaju K, Vishwanath BS, Niranjana SR, Girish KS. Phytochem Rev. 2011;10:325–351.
5. Smitinand, T. Thai Plant Names, Rev. Edit. Bangkok: Office of the Forest Herbarium, Department of Natural Park, Wildlife and Plant Conservation, 2014.
6. Han QB, Wang YL, Yang L, Tso TF, Qiao CF, Song JZ, Xu LJ, Chen SL, Yang DJ, Xu HX. Chem Pharm Bull. 2006;54(2):265–267.
7. Wang LL, Li ZL, Xu YP, Liu XQ, Pei YH, Jing YK, Hua HM. Chin Chem Lett. 2008;19:1221–1223.
8. Deng YX, Guo T, Shao ZY, Xie H, Pan SL. Planta Med. 2013;79: 792–796.
9. Dong B, Zheng YF, Wen HM, Wang XZ, Xiong HW, Wu H, Li W. Nat Prod Res. 2017;31:817–821.
10. Reutrakul V, Anantachoke N, Pohmakotr M, Jaipetch T, Yoosook C, Kasisit J, Napaswat C, Panthong A, Santisuk T, Prabpai S, Kongsaeree P, Tuchinda P. Planta Med. 2010;76:368–371.
11. Wanga HM, Liua QF, Zhaob YW, Liua SZ, Chena ZH, Zhanga RJ, Wangb ZZ, Xiaob W, Zhaoa WM. Nat Prod Res. 2014;16: 20–28.
12. Wang LL, Li ZL, Song DD, Sun L, Pei YH, Jing HK, Hua HM. Planta Med. 2008;74:1735–1740.
13. Sukpondma Y, Rukachaisirikul V, Phongpaichit S. Chem Pharm Bull. 2005;53(7):850–852.
14. Reutrakul V, Anantachoke N, Pohmakotr M, Sophasan S, Yoosook C, Kasisit J, Napaswat C, Santisuk T, Tuchinda P. Planta Med. 2007;73:33–40.
15. Asano J, Chiba K, Tada M, Yoshii T. Phytochemistry. 1996;41:815–820.
16. Chen Y, He S, Tang C, Li J, Yang GZ. Fitoterapia. 2016;109:106–112.
17. Tisdale EJ, Slobodov I, Theodorakis EA. Org Biomol Chem. 2003;1:4418–4422.

Acknowledgements: This work was supported by The Thailand Research Fund (DBG5980003 and DBG6180030). Supports from the Center of Excellence for Innovation in Chemistry (PERCH-CIC), Office of the Higher Education Commission and Ramkhamhaeng University are gratefully acknowledged.

SESSION C4:
PHYSICAL &
THEORETICAL CHEMISTRY

C4_003_OF: ENHANCING SENSITIVITY AND SELECTIVITY OF SURFACE-ENHANCED RAMAN SCATTERING DETECTION BY CHEMOMETRIC METHOD

Nontawat Sricharoen[1,2], Prompong Pienpinijtham[2], Sanong Ekgasit[2], Kanet Wongravee[1,2,*]
[1]Center of Excellence on Petrochemical and Materials Technology, Chulalongkorn University, Bangkok 10330, Thailand.
[2]Sensor Research Unit, Department of Chemistry, Faculty of Science, Chulalongkorn University, Bangkok 10330, Thailand.
*e-mail: kanet.w@chula.ac.th

Abstract: Surface-Enhanced Raman Scattering (SERS) spectroscopy is a rapid and ultrasensitive technique for detecting the vibrational patterns of functional groups of molecules using nanoparticles as substrate. To acquire the analyte signal, the analyte should be immobilized and interacted on the surface of nanoparticles. To differentiate the signal of the analyte, signal patterns of capping agent and analyte must be different, otherwise, SERS signals of both capping agent and analyte will be overlapped and difficult for any further analysis. In the study, the chemometric methods were used to deconvolute the signals in SERS spectra. Multivariate curve resolution-alternative least square (MCR-ALS) was performed to extract the pure spectrum of the capping agent and the analyte from the overlapped signals. In the case, the efficiency of our developed algorithm was tested with the simulated spectra generated by two Gaussian peaks, representing the analyte and capping agent signal, respectively. These two peaks were generated using different condition involving the ratio of concentration between the analyte and the capping agent, noise levels, and resolutions in order to indicate the limitation of the developed method. The results show that, the pure analyte signals were successfully obtained with the R^2 values are higher than 0.99 and the prediction error is <1% and < 5% for calibration samples and validation samples, respectively. The developed program has the potential features to monitor and quantify an analyte in the practical SERS detection.

Introduction: Surface-Enhanced Raman Scattering (SERS) spectroscopy is a rapid and ultrasensitive technique for detecting the vibrational signature of molecule. This technique is widely used in numerous areas for both qualitative and quantitative analyses[1,2]. To enhance the SERS signal, the analyte must be immobilized and interacted with the surface of SERS substrate which might involve some precise metals, such as Ag, Au, or Pt. Therefore, the surface treatment is required in order to induce the analyte migrating to the metal surface. In this case, the combination of Raman signals between capping agents and the target analyte were occurred. Therefore, the functional groups of capping agents and the analyte must be carefully considered and chosen. The capping agent should have functional groups which easily interact with the target analyte. Due to the interaction, the signal patterns between the capping agents and the target analyte can be either partially or completely overlapped. Particularly, amount of the capping agent is excessively added in order to cover an extensive surface of substrate and the analyte is in trace amount. To differentiate the signal of the target analyte might be complicated when the functional groups on capping agent and analyte are similar.

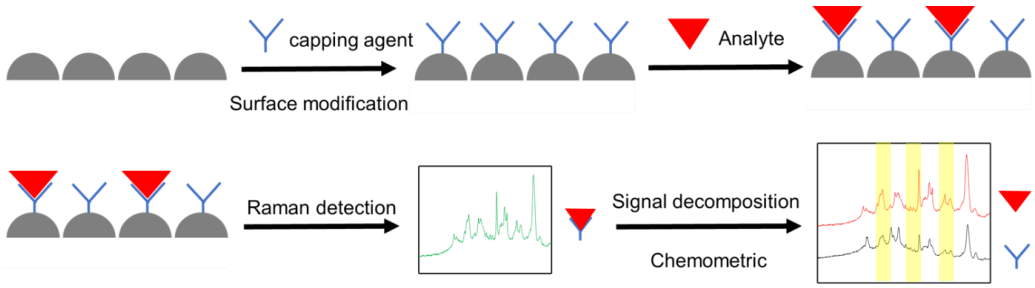

Figure 1 Scheme of our overall study. In SERS detection, surface treatment was particularly performed to modify the surface of SERS substrate in order to induce the immobility of the analyte to be immobilized on the surface. The combination of the SERS signals was acquired. The chemometric techniques were applied here to deconvolute the signals to obtain pure spectrum of the analyte and the capping agent. The yellow highlight shows the different regions between the spectra of the analyte and the capping agent

From the literatures, chemometric methods such as, principal component analysis (PCA), independent component analysis (ICA), and partial least square (PLS) were used to eliminate an irrelevant Raman signals to retain only the target signals.[3-5] However, the significant components were selected using variance underlying in the system. In some cases, most of signals with high variance is related to the undesired signals. To prevent the problems, Multivariate Curve Resolution-Alternative Least Square (MCR-ALS) could be used to extract the spectrum (X) into two significant information involving the concentration profiles (C) and the pure profiles of components (S^T) of the main components in the system. It has been used in various applications such as reaction monitoring, biological system, fingerprint analysis, etc. Simpson *et al.*[6] performed the MCR-ALS in the ultraviolet resonance Raman (UVRR) spectroscopy to monitors the structure of proteins. The signal of the amide I, II, III and S regions of the proteins related α-helical and non-helical derivative structures were successfully deconvoluted by the methods. Forchetti *et al.*[7] applied MCR-ALS technique to the near-infrared spectroscopy (NIR) data of the milk powder to detect and quantify the level of adulterations (whey powder, starch, urea, and melamine). The NIR signals of the adulterants were extracted and determined by MCR-ALS technique with absolute error less than 5%. However, the technique has never been used in the complicated signals from SERS detection.

In the study, the modified MCR-ALS was developed in order to extract the pure spectrum of the main components in the SERS detection system. The system was generated including two main components including a capping agent and a target analyte. The spectra were simulated using the Gaussian function to represent the peak of the capping agent and the peak of the target analyte. The characteristic of the generated spectrum was controlled by various parameters involving the resolution of the peaks, random noise level and the concentration ratio between signal from capping agent and analyte. To evaluate the efficiency of the developed algorithm, the coefficients of determination (R^2) and Root Mean Square Error ($RMSE$) value of the predicted concentrations of the target signals were recorded and monitored. Figure 1 shows the overall schematic of our study.

Methodology

Simulated system: The two Gaussian peaks were generated, using MATLAB (Math work, Inc. Version 2018a) Fuzzy Logic toolbox. The mean value was set equal to 100 and standard deviation value equal to 15 for the analyte signals [X_{ana}] and the standard deviation value equal to 10 for the capping agent signals [X_{cap}]. The width of analyte and capping agent peaks and are constrained to 24 and 57 wavenumbers, respectively. The concentrations of analyte were varied in the ratio of 0.01-1 compared to concentration of capping agent that was fixed at 500

a.u. Then, the random noise was added to the simulated spectra [X_{sim}]. The total spectra of X_{sim} are 200 spectra. The simulated spectra can be written in the form as follow.

$$X_{sim} = [X_{ana} + X_{cap} + X_{noise}] \quad (1)$$

Optimization: In this work, the number of added capping agent spectra, the ratio of concentration of the analyte compared to the capping agent (α), the ratio of noise (μ), and the resolution (*RS*) value of the analyte and capping agent peaks were varied in order to determine the feasibility of the developed method.

- The ratio between the number of simulated and the capping agent spectra was varied by adding capping agent spectra in the amount of 400, 1000, 2000, 5000, 10000, and 20000 spectra. It can be written in the form

$$X_{pre} = [X_{sim}\ ,\ X_{cap}] + X_{noise} \quad (2)$$

- The ratio of noise (μ) was varied at 1%, 5% and 9%.
- The resolution (*RS*) of the two simulated peaks was 1.5 (non-overlap), 0.8, 0.5, and 0 (completely overlap).
- The α (concentration of analyte divided by concentration of capping agent) was set to 0.01-0.2, 0.21-0.40, 0.41-0.60,0. 61-0.80 and 0.81-1.00 compared with the concentrations of the capping agent, in each ratio contains 200 spectra.

Validation set: After obtaining the optimized calculation conditions, the developed procedure was performed on the validation set to examine the reliability of the model. In this set, 50 spectra were generated by using the number of added capping agent spectra, the range of α, the μ, and the *RS* at 50 times, 0.81-1.00., 9%. and 0, respectively.

Multivariate curve resolution-alternative least square: MCR-ALS technique was performed in the simulated spectra (X). The MCR-ALS analysis was achieved using for MCR-ALS program with a graphical user interface (GUI) facility developed by Tauler *et al.*[8] Due to the principal of spectroscopic detection, the spectra (X) are the linear combination of the pure spectra profile (S^T) and concentration profile (C) of the main components in the system with random noise (E).

$$X = C\ .\ S^T + E \quad (3)$$

The pure spectrum of capping agent (S^T_{cap}) was used as initial estimation. The non-negative least square (*nnls*)[9] was used in row and column mode to constraint the output. The spectra (X_{cap}) that contain information of capping agent can be written as follow

$$X_{cap} = C_{cap}\ .\ S^T_{cap} \quad (4)$$

The relative concentration profiles of the capping agent were calculated from eq. (5).

$$C'_{cap} = X_{cap}\ .\ (S^T_{cap})^+ \quad (5)$$

When $(S^T_{cap})^+$ is pseudoinverse of S^T_{cap}, C'_{cap} is the new concentration profile of C_{cap}. To obtain the new spectral profile of capping agent, the C'_{cap} values from (5) were replaced in (4)

$$X_{cap} = C'_{cap}\ .\ S^T_{cap} \quad (6)$$

$$S'^T_{cap} = (C'_{cap})^+\ .\ X_{cap} \quad (7)$$

When $(C'_{cap})^+$ is pseudoinverse of C'_{cap} from the equation (5) and (7), the value of pure spectrum profiles and concentration profile were calculated and it can be substituted into equation (3).

The new spectra that contain the information of pure capping agent signals could be written in the form

$$X'_{cap} = C'_{cap} \cdot S'^{T}_{cap} \quad (8)$$

X'_{cap} is predicted spectra of the capping agent extracted from the simulated spectra (X). The analyte spectra could be calculated by subtraction of the simulated spectra with the predicted spectra of the capping agent which can be written by

$$X_{obs} = |X_{sim} - X'_{cap}| \quad (9)$$

The quality and reliability of the developed techniques might be assessed using the explained data correlation (R^2) and root mean square error (*RMSE*) which can be expressed by

$$RMSE = \sqrt{\frac{1}{n}\sum_{1}^{n}(\boldsymbol{conc}_{\mathrm{act}} - \boldsymbol{conc}_{\mathrm{pred}})^2}$$

Where $conc_{act}$ is actual concentration, and $conc_{pred}$ is predicted concentration. The predictive error could be calculated by compare the *RMSE* values with the minimum range of the actual concentrations which can be expressed by

$$Predictive\ error = \frac{RMSE}{conc_{act}} x\ 100$$

The overall steps of calculation were shown in Figure 2.

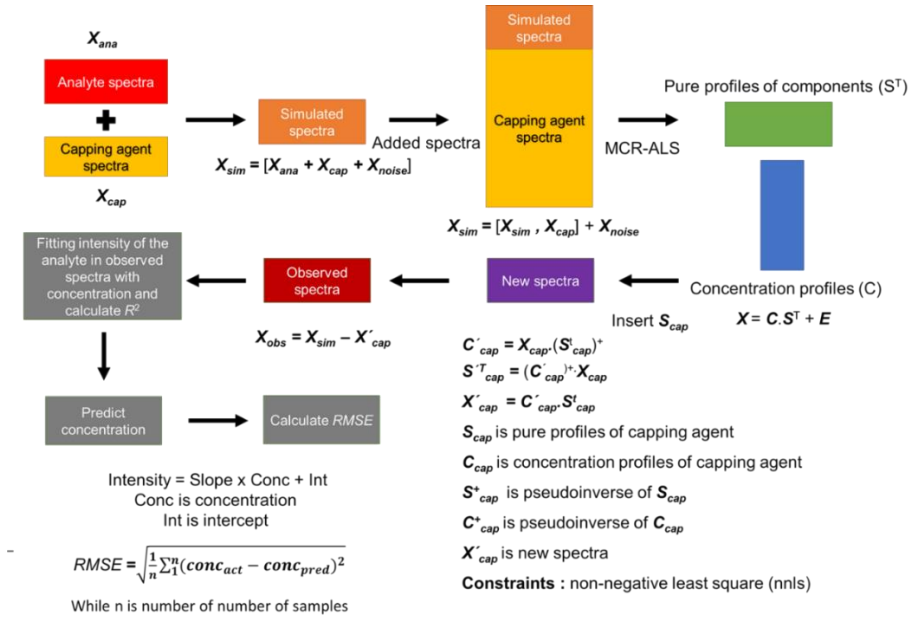

Figure 2 The diagram represent the steps of simulation, calculation and prediction. The simulated spectra (X_{sim}) were generated by the linear combination of the spectra of analyte, capping agent and noise, respectively. The MCR-ALS was applied to the simulated spectra in order to extract the pure spectrum of the capping agent and the analyte. The observed spectra (X_{obs}) were acquired by eliminate the signals of the capping agent to retain only the signals of target analyte. The R^2, predicted concentrations and *RMSE* values were calculated and collected to evaluate the efficiency of the model.

Results and discussion

Simulated spectra: 200 simulated spectra are generated in Figure 3. In all spectra (Figure 3A1-3A4), the smaller and the larger peaks represent the Gaussian peaks of an analyte and a capping agent, respectively. The red and blue lines are the concentration ratio at 0.2 and 0.01, respectively with the brown lines which relate to the moderate concentrations (0.01-0.2). In Figure A1-A4, the *RS* value was adjusted by moving the position of the analyte peak close to the peaks of capping agent. In this system, the *RS* was varied from 1.5 to 0 which express as the clear separated peaks and completely overlapped peak, respectively. In the simulated spectra, the variation of the concentration would affect only on the peak of the target analyte because the concentration of the capping agent was already fixed. The variation on the peak of capping agent appears only from the additional random noise (μ).

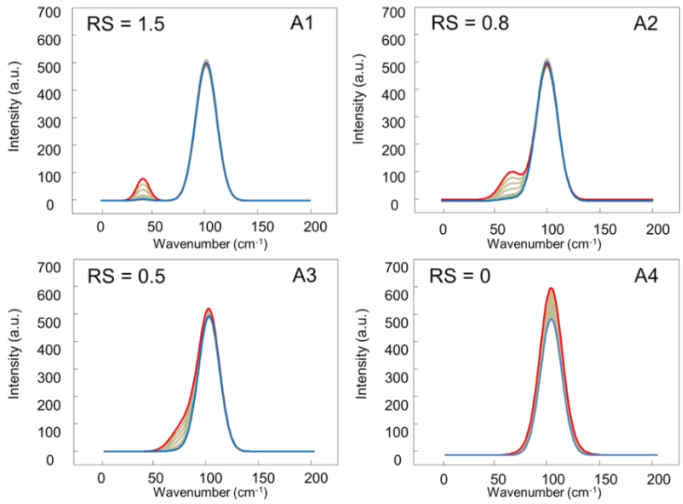

Figure 3 Simulated spectra with *RS* of A1) 1.5, A2) 0.8, A3) 0.5, and A4) 0, respectively. Red line, blue line and grey line show the highest (100 a.u.), the lowest (5 a.u.) and the moderate (10-90 a.u.), respectively. concentration of the analyte. The total number of spectrum in simulated system are 200

There are two major variations presented in the simulated spectra which involves the variation from capping agent and target analyte. The variation from capping agent is originated by the random noise, while the variation of the target analyte comes from the different concentrations. The variance from the target analytes is much higher compared to the capping agent but they are in smaller intensity. To eliminate the signals of capping agent might not be possible. In this section, we try to increase the variance of the capping agent by adding number of spectra (capping agent) in the simulated spectra. The capping agent spectra were added with number of 400, 1000, 2000, 5000, 10000, and, 20000 spectra to investigate an appropriate number of added spectra. The simulated spectra are generated with α = 0.81-1.00, μ = 9%, and *RS* = 0 (completely overlapped peaks). The MCR-ALS was applied to the simulated spectra to extract the major signals and eliminate the signal of the capping agent. The retained spectra which might relate to only the analyte was used further prediction.

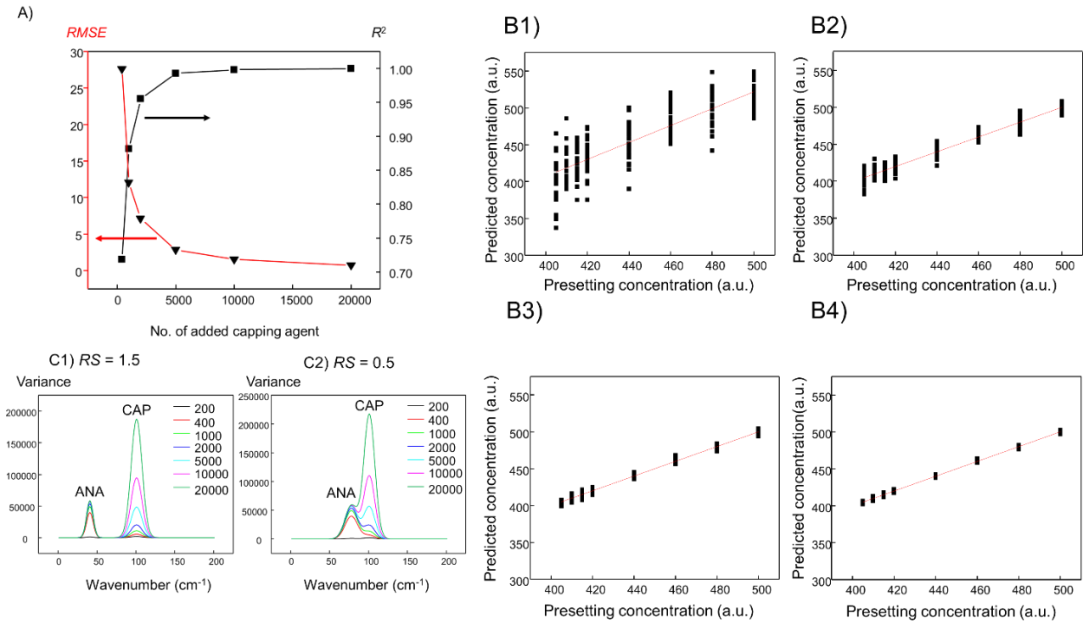

Figure 4 A) The R^2 (black square) and *RMSE* value (triangles) plotted against the number of added capping agent spectra at 400, 1000, 2000, 5000, 10000, and 20000 spectra which equal to 2, 5, 10, 25, 50, and 100 times of the number of simulated spectra, respectively. B) The correlation between actual and predicted concentration of the analyte using the model generated from different added number of capping agent spectra at (B1) 400, (B2) 2000, (B3) 5000 and (B4) 10000. C) Variance of the simulated spectra after the capping agent were added for 200-20000 spectra. The ANA and CAP peaks represent the variance of the analyte and the capping agent signal at RS = 1.5 (C1) and RS = 0 (C2), respectively.

Figure 4A demonstrates the relationship between R^2 and *RMSE* against the number of added spectra. It was found that the R^2 value increases with the decreases of *RMSE* when the number of added spectra increases. This suggests that the number of added spectra has strongly affected on the pure signal extracted from the simulated spectra. However, there is no change in R^2 and *RMSE* values when the spectra were added up to 10000. The variance of each peaks was shown in Figure 4C1-C2, the variance of the capping agent dramatically increases when the capping agent spectra were added, and the variance of capping agent was higher than analyte when the capping agent were added more than 10000 spectra. Consequently, the capping agent spectra were completely extracted out of the analyte peak. The R^2 and *RMSE* values were not changed after 10000 spectra of capping agent were added. This might relate to the ratio of variance between both peaks (the capping agent and the analyte) which is unchanged after this point of insertion. To gain the insight information, the scatter plots of the predicted and presetting concentration values of analyte at different number of added spectra were plotted in Figure 4B1-B4. It can be seen that the higher number of added capping agent spectra, the higher accuracy on prediction is occurred. Figure 4B1 show a bad correlation (R^2~0.7) and prediction (*RMSE* ~30). It suggests that the pure spectra of the capping agent could not be extracted when the lower number of added capping agent spectra was used. In Figure 4B3-B4, the R^2 values are higher than 0.99 due to the increase of the variance from capping agent spectra. Consequently, the capping agent spectra were completely extracted and were separated out from the analyte peak by our developed algorithm. In the case, the pure analyte signals were obtained. In the further analysis, 10000 spectra of capping agent were added to create the model of the pure analyte peak.

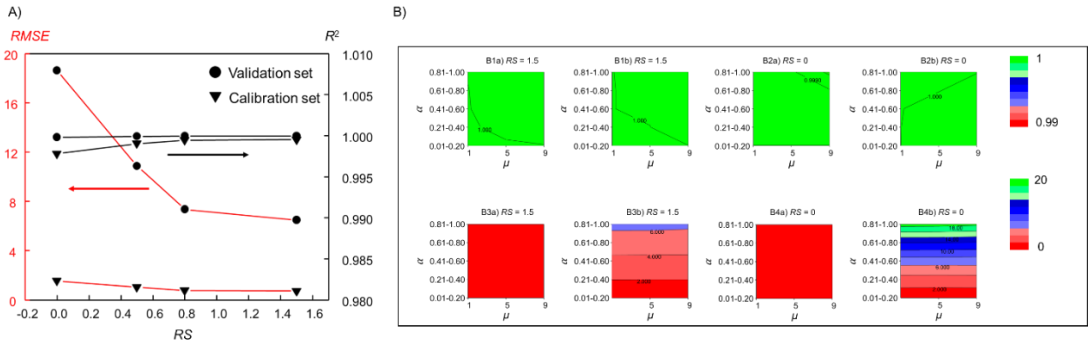

Figure 5 R^2 and *RMSE* at the different *RS*, and various α and μ, A) is the R^2 (black line) and *RMSE* (red line) values at each *RS*. The black squares and circles represent to the calibration and validation set data, respectively. Figure B1-B2 show the contour mapping of R^2 values and Figure B3-B4 demonstrate the *RMSE* values on the a) prediction of calibration samples and b) prediction of validation samples at various ratios of concentration and percentage of noise.

After the number of added spectra was optimized. MCR-ALS was applied to extract the pure spectra of the analyte from different conditions including *RS*, and various concentration ratio and ratios of noise. In figure 5A, the R^2 and *RMSE* values are plotted against the *RS*. It can be seen that the good prediction with R^2 (<0.99) and *RMSE* values (<3) in calibration set were obtained even for the condition which the peaks were completely overlapped (the *RS* equal to 0). To investigate the influences of the parameters (α and μ), the 2D contour plots of R^2 value and *RMSE* value for the calibration set were expressed in Figure 5B1a-B4a. It was found that the prediction performance decreases when the α and μ increases due to the high similarity of variances from capping agent and analyte signals. However, in the calibration sets, the predictions in all conditions are acceptable (R^2 >0.99 and *RMSE* < 1.6). The RMSE of the validation sets were shown in Figure 5B1b-5B4b. It was found that the RMSE values for the validation sets show higher values than the RMSE of calibration sets when the α values higher than 0.4. The overfitting problem was observed at the α values > 0.5 because the RMSE values are small for the calibration set while they raise up for the validation sets. From the results, it shows that our developed algorithm works well when the α not over 0.5. The appropriate prediction was performed on the pure spectra of the analyte in all calibration set. Furthermore, the validation set was used to demonstrate whether the generated model can be used to quantify analyte for the unknown samples. Figure 5A shows that the R^2 value of the validation set is relatively high and in an acceptable value (>0.98) while the *RMSE* value is raised up to 7 (separated peaks) and 20 (overlapped peaks). It suggests that the pure spectrum of the capping agent in the validation set is not be perfectly matched with the pure spectrum of capping agent in the validation set.

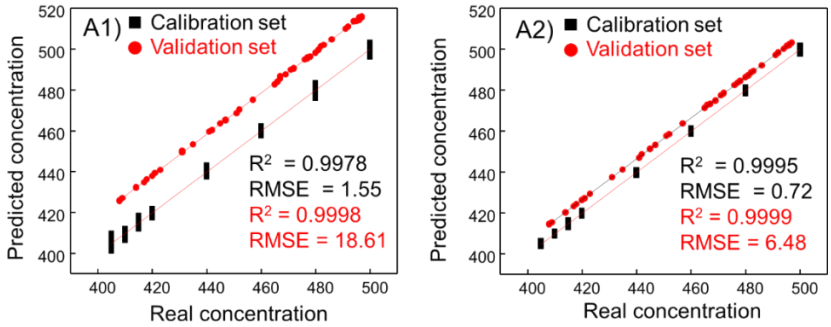

Figure 6 Correlation plot of the presetting concentration (X-axis) and predicted concentration (Y-axis) at (A1) RS = 0 and (A2) 1.5, respectively. Black squares are data from calibration set and red circles are data from validation set

To validate the program, the external simulated validation set has been used. The validation set containing 50 spectra was randomly generated with the α in the range of 0.81-1.00, the RS at 0, 1.5 and the μ at 9%. The matrix of the capping agent spectra which is identical to the one used in the calibration prediction were added to the validation set. The pure profile of capping agent spectra (S_{cap}) calculated from the calibration set were used as an initial estimation. The developed program was performed to extract the capping agent and the analyte signals in the validation set. The R^2 and *RMSE* values of validation set was calculated and was shown in Figure 6. It was found that the good correlation of the predicted concentrations with $R^2 > 0.99$ is obtained for both cases. This suggests that the concentrations were precisely predicted. However, the *RMSE* values of the validation set are increased significantly when the peaks trends to overlap. This might relate the uncomplete extraction of the signals of the capping agent out of the unknown spectra. The residual intensity of the capping agent strongly affects to the accuracy of the prediction but not for the prediction precision. Meanwhile, the developed program would further use in the practical SERS detection.

Conclusion: The simulated spectra were generated by adjusting the factors including the number of added capping agent spectra, the resolution (*RS*), the ratio of concentration (α) and the noise level (μ). The higher number of added capping agent spectra, the higher underlying variance of the capping agent signals in the system were observed. The pure spectra of analyte were completely extracted after number of capping agents were added >10000 spectra. After eliminating the signal from capping agent, the concentration of the analyte was quantified with good R^2 (>0.99) and low *RMSE* values (<1% error) were obtained for the calibration sample in the validation set the R^2 values are more than 0.99 and the *RMSE* values (<5% error). The developed algorithm can extract the analyte signal in the high precision. Furthermore, this developed program will appropriately use in the practical SERS detection.

References

1. Michaels A.M, Nirmal M, Brus L.E. J. Am. Chem. Soc., 1999;121(43):9932-9939.
2. Blackie E.J, Eric C, Le Ru, Etchegoin P.G. J. Am. Chem. Soc., 2009; 131(40):14466-14472.
3. Vrabie V, Gobinet C, Piot O, Tfayli A, Bernard P, Huez R, Manfait M. Biomed Signal Process Control, 2007;2(1):40-50.
4. Hasegawa T, Nishijo J, Umemura J. Chem. Phys. Lett., 2000;317(6):642-646.
5. Meksiarun P, Ishigaki M, Huck-Pezzei V.A.C, Huck C.W, Wongravee K, Sato H, Ozaki Y. Sci. Rep. 2017;7:44890.

6. Simpson J.V, Balakrishnan G, JiJi R.D. Analyst, 2009;134(1):138-147.
7. Forchetti D.A.P, Poppi R.J. LWT., 2017;76:337-343.
8. Jaumot J. de Juan A, Tauler R. Chemom. Intell. Lab. Syst., 2015;140:1-12.
9. Chen J, Richard C, Bermudez J.C.M, Honeine P. IEEE Trans. Signal Process., 2011;59(11):5225-5235.

C4_004_PF: MOLECULAR DOCKING STUDIES OF DONEPEZIL-COUMARIN HYBRID AS NOVEL MULTI TARGET hAChE AND hMAO-B INHIBITORS

Charinee Thonthong, Siritron Samosorn, Pornthip Boonsri*
Department of Chemistry, Faculty of Science, Srinakharinwirot University, Bangkok 10110, Thailand
*e-mail: pornthipb@g.swu.ac.th

Abstract: Designing multitarget-directed-ligands (MTDLs) with simultaneous inhibition of human acetylcholinesterase (hAChE) and human monoamine oxidase type B (hMAO-B) has been targeted as the new potential therapeutic for treatment of Alzheimer's disease (AD). In the present work, a new series of donepezil-coumarin hybrid was designed based on molecular docking to serve as multitarget hAChE and hMAO-B Inhibitors. The hybrids showed no significant difference in binding energies to the hAChE and hMAO-B. Furthermore, the substituent effect on benzene ring for compound A and phenylbenzeneamine ring for compound B, whose design was based on pharmacophores of donepezil, was explored to improve the binding affinity. The results showed that most of compounds obtained similar mode of binding to hAChE and hMAO-B when compared to the reference ligand. Among them, the meta-nitrile substituted group (B8) was identified as the most potent inhibitor to hAChE and hMAO-B with the binding energy values at -12.29 and -12.22 kcal/mol, respectively. More importantly, B8 formed the hydrophobic interactions and strong hydrogen bonding to key residues in the peripheral anionic site (PAS) and catalytic active site (CAS) of the hAChE and have important formed hydrophobic entrance cavity toward the FAD of the hMAO-B. Therefore, we were expected that these novel donepezil-coumarin hybrids could be proposed as the potential multitarget inhibitors for AD therapy.

Introduction: Nowadays, there are only four human acetylcholinesterase (hAChE) inhibitors have been approved by FDA for clinical treatment of AD. Although these drugs can temporarily improve the cognitive and daily function[1], they can not mitigate or halt the progression of AD. Due to the complex etiology disease networks, an efficient therapy is more inclined to discover multifunctional drugs that can simultaneously modulate the complex etiology networks. Therefore, the great efforts on develop multifunctional molecules by incorporating several different active structural fragments into one molecule would reduce the side effects and may add more value on treatment of AD.

The crystallographic structure of hAChE reveals that it has a nearly 20 Å deep narrow gorge which consists of two binding sites: a catalytic active site (CAS) at the bottom of the gorge and a peripheral anionic site (PAS) near the entry of the gorge. The inhibitor can facilitate amyloid fibril formation through the interaction with the PAS of hAChE, giving stable hAChE-Aβ complexes, which are more toxic than single Aβ peptides. Interestingly, the capacity of intact hAChE to promote Aβ assembly can be mimicked by a hydrophobic peptide that contains residues belonging to the PAS of hAChE. Thus, dual site inhibitors that bind simultaneously to the PAS and CAS of hAChE can not only stimulate the cholinergic system, but also inhibit the Aβ aggregation promoted by hAChE.[2]

Human monoamine oxidase B (hMAO-B) is a flavin adenine dinucleotide (FAD)-containing enzyme that is responsible for the oxidative deamination of biogenic and xenobiotic amines and has important functions in the metabolism of neuroactive and vasoactive amines in the central nervous system and peripheral tissues.[3] Furthermore, the activated hMAO-B can also cause disorder of the cholinergic system, destroy cholinergic neurons, and promote the formation of amyloid plaques.[4] Thus, inhibition of hMAO-B provides another potential approach for treating AD. Recently, a multitarget molecules with hAChE and hMAO-B inhibitory activities have been widely reported.[5,6,7] Interestingly, a series of donepezil-coumarin hybrids have been confirmed that the donepezil moiety could inhibit

hAChE and able to bind to the CAS cavity while the coumarin moiety was chosen as anti-Aβ aggregation and able to bind to the PAS via aromatic π-π stacking interactions. Furthermore, the aromatic substitution at donepezil moiety was served as the key binding to the CAS of hAChE which might exert as dual binding mode for the treatment of AD.[8] In view of the importance of hAChE and hMAO-B, designing multitarget-directed-ligands (MTDLs) with simultaneous inhibition of both target enzymes receive much attention in recent years.

Recently, we have been designed the donepezil-coumarin hybrids as the dual binding inhibitors based on molecular docking simulations. Although the nature of each core structures is the main factor affecting to the affinity, it has been proved that the properties of the linker connecting between donepezil and coumarin can substantially modify the binding affinity of hAChE.[9] Therefore, the suitable linker chain lengths ($(-CH_2-)_n$; n = 1-10) were investigated by using molecular docking. The results indicated that the linker chain length (n=3) explores the appropriate binding of the pharmacophores in the active site of hAChE. In addition, the coumarin moiety was observed to bind to the PAS while the phenyl moiety occupied the CAS, whereas the linker oriented in the middle of the gorge between both binding sites as showed in Figure 1. In the present work, we are interested in designing of the novel donepezil-coumarin derivatives based on molecular docking simulations. Then, the binding poses of novel compounds to hAChE and hMAO-B will be further investigated. Finally, the obtained novel compounds will be synthesized (the results are not showed) to be the lead compound for future development as the potent inhibitors to hAChE and hMAO-B.

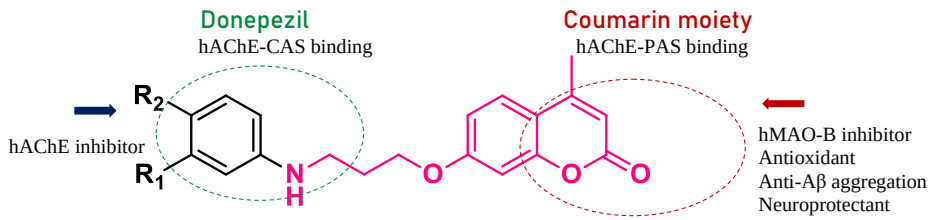

Figure 1. Design strategy for new donepezil-coumarin hybrid.

Molecular Docking Studies: Molecular docking predicts a substrate or drug candidate binds to the target or receptor structure and determine the conformational binding site and direct interacting residues using AutoDock 4.2 program.[10] A computational ligand target docking approach was used to analyze structural complexes of the target protein with ligand in order to understand the structural basis of this protein target specificity. Then, all 27 designed compounds were predicted their drug likeliness properties (Lipinski's rule of five)[11] using Chem3D Ultra 8.0.[12] The molecular docking software included MGL tools 1.5.6 based AutoDock 4.2 (www.scripps.edu) which uses Python 2.5 (www.python.com).

Protein preparation: The X-ray crystal structure of the recombinant human AChE (hAChE) in complex with donepezil (PDB code 4EY7, resolution = 2.35 Å)[13] and human MAO-B (hMAO-B) in complex with 7-(3-chlorobenzyloxy)-4-(methylamino)methyl-coumarin or C18 (PDB code 2V61, resolution = 1.7 Å)[14] were obtained from the Protein Data Bank (PDB) (http://www.rcsb.org/pdb). The protein structures were firstly checked for missing atoms, residues, bonds and contacts. Then, the original crystal ligand, water molecules, heteroatoms, co-crystallized, and solvent were removed using Discovery Studio Visualizer. In case of the hMAO-B isozyme, the FAD co-factor was considered in the docking experiments because of its well-known role into the hMAO inhibition. Autodock Tools (ADT) was used with the default

setting to add missing hydrogen atoms and non-polar hydrogen was merged. Partial charges for proteins were added using Gasteiger–Marsili charges and Kollman charges.
Ligand preparation: The donepezil-coumarin hybrids have been designed computationally (Figure 1). To obtain the stable conformation, the geometry optimization of each compound in 27 hybrid compounds composing of A1-A13 and B1-B14 was performed at B3LYP/6-31G(d,p) method of calculations using the Gaussian 09 program.[15] Then, ADT Tools was used to add Gasteiger charges and flexible torsions were assigned to the ligand.
Molecular docking: The docking studies of each hybrid compound to the hAChE and hMAO-B proteins were carried out using AutoDock 4.2 with the docking parameters set at default values. The active site is the coordinates of the ligand in the original target protein grids. For both proteins, the grid box center was set to the original ligand, and the grid size was set to 60 Å in each dimension. The Lamarckian genetic algorithm, inculcated in the docking program, was employed to satisfy the purpose to search for the best conformers. During the docking process, a maximum of 150 conformers was considered for each compound. The best ranked docking poses of the hybrid compounds to the active site of the hAChE and hMAO-B proteins were obtained according to the binding energy value. Finally, Discovery Studio 4.0 Client's pose viewer utility [www.accelrys.com] was employed for visualizing the docked molecules.

Results and Discussion: To obtain the novel multi-target inhibitors, AutoDock approach was applied to study the binding affinities of the hybrid compounds on hAChE and hMAO-B protein structures. The docking simulations provide insights into the possible binding modes and orientations between ligand and protein. Firstly, the parameters of docking experiment and prepared gird structure were validated by re-docking the original ligand into the target protein. Then, the superposition tool was applied to calculate RMSD value, which was found to be within the acceptable limit of 2 Å on both enzymes. Next, the obtained parameters will be applied for docking of our 27 compounds into the target proteins.
Binding affinity of the hybrids to human AChE: Recently, many researchers confirmed that the donepezil-coumarin hybrid exhibited as the multitarget drugs which donepezil moiety could bind to the CAS cavity while the coumarin moiety was chosen as anti-Aβ aggregation and able to bind to the PAS. Additionally, the substituents at 4-position of coumarin ring could increase the binding affinity of the inhibitor to the PAS of hAChE.[16] Furthermore, the aromatic substitution at donepezil moiety was served as the key binding to the CAS of hAChE which could be used as dual binding mode for the treatment of AD.[8] These obtained results brought us to the designed strategy of the novel donepezil-coumarin hybrid in this work. The different substituents were introduced on 4-position of benzene moiety to investigate the possible effects on dual binding interactions that bind simultaneously to the PAS and the CAS of hAChE. All 27 compounds were docked into the active site of the hAChE, the obtained binding energies (BE) are shown in Table 1.

The binding modes of designed compounds were considered as the important role in selecting the best poses of the docked compounds in comparison to the standard drug donepezil. All 27 compounds showed strong binding energies to hAChE ranging from -9.56 to -12.64 kcal/mol. Interestingly, all B compounds show tight binding interactions toward the hAChE ranging from -11.29 to -12.64 kcal/mol which greater than the reference drug donepezil (-10.25 kcal/mol). The results indicated that our designed strategy based on the donepezil-coumarin hybrid could increase the binding affinity to hAChE. The present results agreed well with the previous work that increasing of aromatic substitution on the benzene moiety (compound B) influence to the mode of binding between the ligand and hAChE.[8]

Table 1. Binding energy (BE) of A1-A13 and B1-B14 to hAChE were obtained from molecular docking studies in comparison to the standard drug.

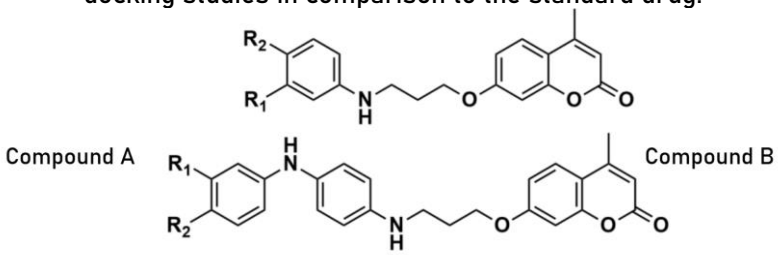

Compound	R_1	R_2	BE (kcal/mol)	Compound	R_1	R_2	BE (kcal/mol)
A1	H	H	-9.56	B1	H	H	-11.88
A2	CH_3	H	-9.83	B2	CH_3	H	-11.59
A3	H	CH_3	-10.51	B3	H	CH_3	-11.33
A4	NH_2	H	-9.92	B4	$COCH_3$	H	-11.91
A5	H	NH_2	-10.36	B5	H	$COCH_3$	-12.00
A6	H	OCH_3	-10.46	B6	NH_2	H	-11.81
A7	H	$COCH_3$	-10.45	B7	H	NH_2	-12.14
A8	H	COOH	-9.68	B8	CN	H	-12.29
A9	H	OH	-10.42	B9	H	CN	-12.64
A10	H	CN	-10.67	B10	OCH_3	H	-11.29
A11	H	F	-9.59	B11	C_2H_5	H	-11.92
A12	H	Cl	-10.19	B12	CH_3	CN	-12.22
A13	H	NO_2	-10.55	B13	CH_3	OCH_3	-12.01
Donepezil	-	-	-10.25	B14	OCH_3	OCH_3	-11.41

Then, the superimpose of all compounds were clearly explained their similar binding mode to the hAChE active site as shown in Figure 2. The binding interactions were observed via π–π stacking and hydrogen bonding interactions between the benzene moiety (Figure 2a) or phenylbenzeneamine part (Figure 2b) pointed to the CAS cavity while the coumarin part can bind to the PAS of hAChE.

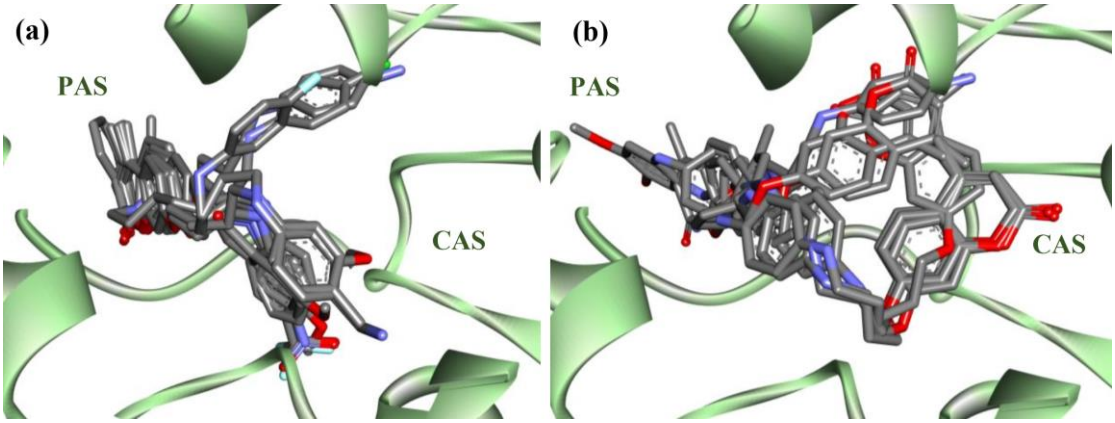

Figure 2. Superimpose of the docking poses for compound A (a) and compound B (b) to hAChE active site.

The effect of either ortho- or meta-substitution on the benzene moiety (A2-A5) and the phenylbenzeneamine moiety (B2-B9) were investigated, the results indicated that para-substitution showed better binding energies than the other one. Furthermore, the different substituents on para-substitution for A (A6-A13) were introduced to improve the binding affinity, the obtained results are not significantly difference. Furthermore, the di-substitution at the phenylbenzeneamine moiety (B12-B14) were also investigated, the binding energy was not greater than the mono-substitution.

We then selected the best binding energies for further investigate the mode of binding. Thus, B9 was the highest binding energy (-12.64 kcal/mol), due to the para-benzonitrile on the phenylbenzenamine could form the strong hydrogen bonding to the ARG296 which increase the binding affinity. The binding conformation of B9 exhibited that the coumarin moiety occupied the PAS of hAChE and it was stabilized by the hydrogen bonding to ALA127, TYR133 and through lone pair-π interactions of GLY120. Similarly to donepezil, the phenylbenzeneamine moiety was located at the CAS of hAChE and interacted with TYR337, TYR341, and TRP86 through van der Waals and hydrophobic interactions. In the middle of the gorge, the linker formed hydrogen bonding to PHE337, TYR133, HIS447, and GLU202.

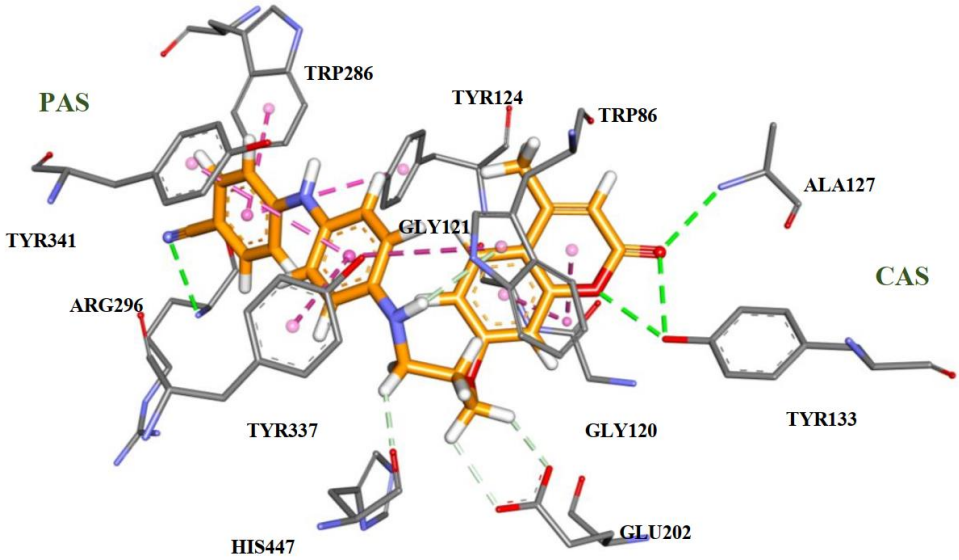

Figure 3. 3D binding interaction of B9 with hAChE active site. Atom colors: orange stick - carbon atoms of B9, gray - carbon atoms of residues of hAChE, dark blue – nitrogen atoms, red - oxygen atoms. The dashed lines represent the interactions between the protein and the ligand.

Binding affinity of the hybrids to human MAO-B: In the present work, the binding mode of the hybrids with respect to hMAO-B was investigated based on the X-ray crystal structure of the hMAO-B in complex with C18 (PDB code 2V61). Molecular docking of 27 compounds toward the hMAO-B were further studied in order to confirm that all compounds can be considered as the multi target inhibitor. Similarity to the hAChE, the substituent effects on donepezil moiety for A and B compounds were calculated in comparison to the reference ligand as shown in Table 2.

Table 2. Binding energy (BE) of A1-A13 and B1-B14 to hMAO-B were obtained from molecular docking studies in comparison to the standard drugs.

Compound	R_1	R_2	BE (kcal/mol)	Compound	R_1	R_2	BE (kcal/mol)
A1	H	H	-10.38	B1	H	H	-12.42
A2	CH_3	H	-11.05	B2	CH_3	H	-11.65
A3	H	CH_3	-11.11	B3	H	CH_3	-11.73
A4	NH_2	H	-10.56	B4	$COCH_3$	H	-12.32
A5	H	NH_2	-10.76	B5	H	$COCH_3$	-11.94
A6	H	OCH_3	-10.63	B6	NH_2	H	-11.84
A7	H	$COCH_3$	-11.50	B7	H	NH_2	-12.22
A8	H	COOH	-10.43	B8	CN	H	-12.22
A9	H	OH	-10.55	B9	H	CN	-11.74
A10	H	CN	-11.07	B10	OCH_3	H	-12.26
A11	H	F	-10.37	B11	C_2H_5	H	-12.55
A12	H	Cl	-11.04	B12	CH_3	CN	-11.13
A13	H	NO_2	-10.58	B13	CH_3	OCH_3	-11.43
C18	-	-	-11.14	B14	OCH_3	OCH_3	-10.62
Safinamide	-	-	-9.79				

The binding energies of 27 compounds to hMAO-B active sites were obtained ranging from -10.37 to -12.55 kcal/mol as showed in Table 2, which greater than the reference drug safinamide (-9.79 kcal/mol). The results indicated that all compounds displayed tight binding interactions to hMAO-B. Then, the different substituent and position effects on the donepezil moiety were investigated for improve the binding affinity of the hybrids. The results display that their binding energies are not significantly different. In addition, the binding mode of compound A were shown in Figure 4a. The docking results indicated that most of novel compounds positioned the coumarin part toward the FAD cofactor and the donepezil moiety toward the hydrophobic entrance cavity which agreed well with the previous results.[17] In the case of compound B, the substitution of the para-phenylbenzeneamine at benzene ring plays the important role to the binding mode of the hybrids as shown in Figure 4b. It was found that most of compound B oriented their conformations similar to compound A except B2, B3, B12, B13, and B14 which pointed the coumarin part toward the entrance cavity resulting in the decrease of the binding energies. The obtained results suggested that either the methyl substituent (B2, B3) or the di-substituent (B12, B13, B14) effect to change the binding mode of the hybrids.

In addition, the binding poses clearly explained that most compounds showed similar mode of binding to the reference drugs. Among them, B11 is the para-C_2H_5 substituent at the phenylbenzeneamine moiety, exhibited the highest binding affinity at -12.55 kcal/mol. The binding pose of B11 to the hMAO-B was shown in Figure 5, phenylbenzeneamine moiety established van der Waals and hydrophobic interactions to ILE199, ILE316, LEU88, PRO102 and through hydrogen bonding with PRO102. Furthermore, the hydrophobic interactions was observed between the coumarin moiety with TYR398, TYR435, LEU171, CYS172, and FAD in the hMAO-B active sites. Finally, the linker which oriented in the middle of the gorge was formed hydrogen bondings to the key residues as PHE168, ILE198 which stabilize the complex.

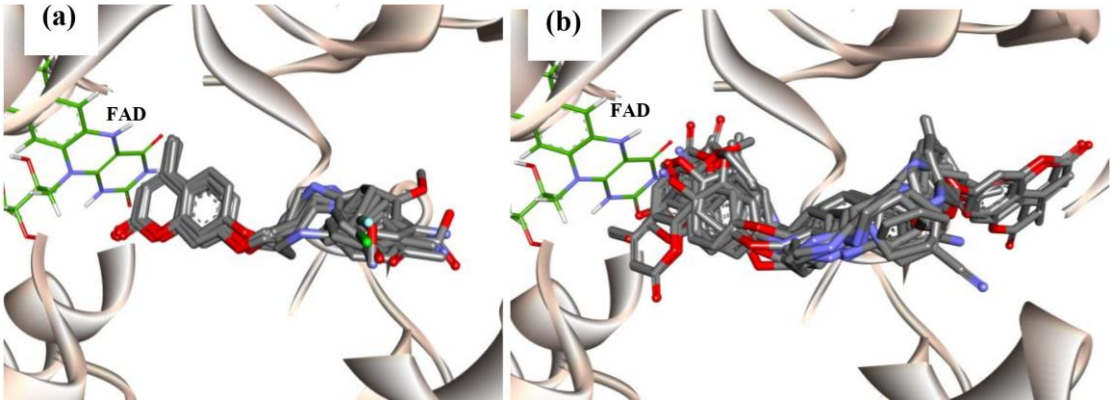

Figure 4. Superimpose of the docking poses for compound A (a) and compound B (b) to hMAO-B active site.

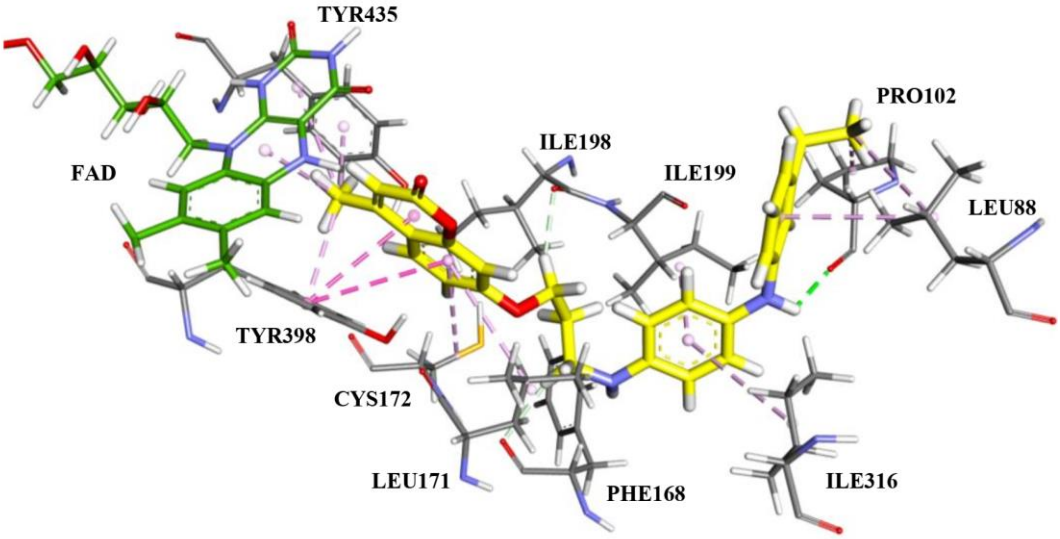

Figure 5. 3D binding interactions of B11 with hMAO-B active sites which yellow stick of carbon atoms represent of B11, while hMAO-B was colored by atom type. The dashed lines represent the interactions between the protein and the ligand.

Multi-target drug of novel donepezil-coumarin hybrids: Recently, the design of multifunctional drugs for the treatment of AD get much attention. Therefore, finding a promising lead compound becomes the key point to develop potential multifunctional agents. In the present work, we are focusing on the novel compound that exhibit the promising binding pose to both hAChE and hMAO-B for further develop as the multi target inhibitor. Overall, the above docking studies of all compounds to both target enzymes provided an explanation for the rationality molecular design. Based on our designed strategy, B8 was chosen as the good candidate for considering to be the lead molecule because it showed the potent binding affinity to both enzymes (-12.22 kcal/mol for hMAO-B and -12.29 kcal/mol for hAChE).

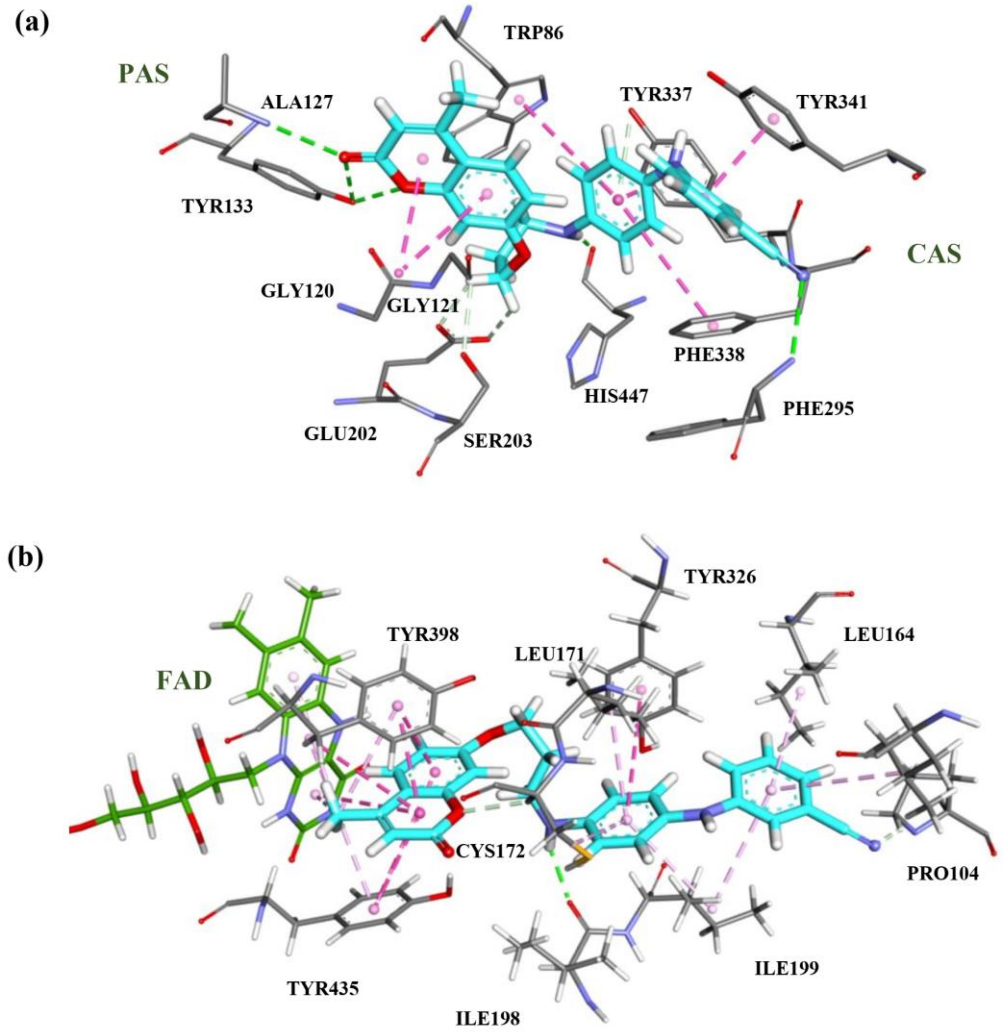

Figure 6. 3D binding interaction of compound B8 to (a) hAChE and (b) hMAO-B. Atom colors: cyan stick - carbon atoms of B8, gray - carbon atoms of residues of hMAO-B, dark blue – nitrogen atoms, red - oxygen atoms. The dashed lines represent the interactions between the protein and the ligand.

B8 is the meta-CN substituent at the phenylbenzeneamine moiety, exhibiting the potent binding affinity. For hAChE binding, B8 can occupy the substrate cavity of the PAS and the CAS which are shown in Figure 6a. The coumarin moiety bound to the PAS of hAChE, establishing strong hydrogen bondings with TYR133, ALA127 and C-H···O interactions through GLU202, SER203. In addition, coumarin moiety generated the amide-π stacking interactions with GLY120, GLY121. Similarly, the benzene moiety located at the CAS of hAChE showed strong hydrogen bonding with PHE295 and HIS447. Furthermore, the benzene moiety which oriented in the CAS of the hAChE also formed the hydrophobic π-π interaction to TRP86, TYR337, PHE338, TYR341 residue.

For hMAO-B, B8 showed similar mode of binding to B11 which are shown in Figure 6b. The phenylbenzeneamine moiety established van der Waals and hydrophobic interactions to LEU171, CYS172, ILE199, TYR326, LEU164, PRO104 and through hydrogen bondings with PRO104 and ILE198. In addition, the coumarin moiety generated the hydrophobic interactions to

TYR398, TYR435, and FAD in the hMAO-B active sites, and through hydrogen bonding with CYS172. The obtained binding interactions indicated that the coumarin part of the novel compound plays an important role for the mode of binding to hMAO-B. Finally, the linker which oriented in the middle of the gorge formed strong hydrogen bonding to the ILE198 residue.
Drug likeliness properties of novel compounds: The drug likeness properties of all designed compounds was investigated according to which an orally active drug should agree to a minimum of four establish criteria for drug likeness including molecular weight (Mw), partition coefficient (cLogP), hydrogen bond donor (HBD), and hydrogen bond acceptor (HBA).[11] The drug properties of 27 compounds was analyzed by Lipinski filter, which highly useful in predicting drug likeness. All compounds show Mw ranging from 309.36 - 460.53 g/mol, cLogP ranging from 0.32 to 3.94, HBD ranging from 1 to 3, and HBA ranging from 4 to 7. The obtained drug likeliness properties indicated that all compounds pass qualified to be used as drugs which are agreement with Lipinski's rule of five.

Conclusion: A series of novel donepezil-coumarin hybrids as multifunctional inhibitors have been designed and evaluated the binding affinities for hAChE and hMAO-B. The obtained results showed that most of designed compounds exhibited strong binding to both enzymes. In addition, the increasing of aromaticity at donepezil moiety (compound B) influence to the better binding affinity of the hybrids. Furthermore, the substituent effect on the donepezil moiety was explored to improve the binding affinities which are not significantly different. For the binding poses to hAChE, all compounds occupied the key interactions toward the CAS and PAS cavities, revealing the dual mode inhibitors. For hMAO-B binding, most of hybrids pointed the coumarin part toward the FAD cofactor and the donepezil moiety into the hydrophobic entrance cavity. Interestingly, B8 is the meta-CN substituent at the phenylbenzeneamine moiety, exhibited the binding affinity to hMAO-B (-12.22 kcal/mol) and hAChE (-12.29 kcal/mol). Finally, *in silico* study confirmed that all compounds fulfilled drug likeliness properties. Further experimental approaches can be applied to prove that the novel donepezil-coumarin hybrid can be further developed as a potential multi target hAChE/hMAO-B inhibitors for Alzheimer's disease.

References:

1. Herrmann N, Chau SA, Kircanski I, Lanctot KL. Drugs. 2011;71:2031-2065.
2. Leon R, Garcia AG, Marco-Contelles J. Med. Res. Rev. 2013;33:139-189.
3. Edmondson DE, Mattevi A, Binda C, Li M, Hubálek F. Curr. Med. Chem. 2004;11:1983-1993.
4. Schedinweiss S, Inoue M, Hromadkova L, Teranishi Y, Yamamoto NG. Alzheimers Res. Ther. 2017;9:57.
5. Bautista-Aguilera OM, Samadi A, Chioua M, Nikolic K, Filipic SJ. Med. Chem. 2014;57: 10455-10463.
6. Farina R, Pisani L, Catto M, Nicolotti O, Gadaleta D, Denora N, Soto-Otero R, Mendez-Alvarez E, Passos CS, Muncipinto G, Altomare CD, Nurisso A, Carrupt PA, Carotti A. J. Med. Chem. 2015;58:5561-5578.
7. Joubert J, Foka GB, Repsold BP, Oliver DW, Kapp E. Eur. J. Med. Chem. 2017;125:853-864.
8. Jiang N, Huang Q, Liu J, Liang N, Li Q, Xie SS. Eur. J. Med. Chem. 2018;146:287-298.
9. Leurs R, Bakker RA, Timmerman H, de Esch IJ. Nat. Rev. Drug Discov. 2005;4:107-120.
10. Morris JS, Friston KJ, Büchel C, Frith CD, Young AW, Calder AJ, Dolan RJ. Brain. 1998; 121:47-57.
11. Lipinski CA. Drug Discov. Today Technol. 2004;1:337-341.
12. Mendelsohn LD. J. Chem. Inf. Model. 2004;44:2225-2226.
13. Cheung J, Rudolph MJ, Burshteyn F, Cassidy MS, Gary EN. J. Med. Chem. 1012;55: 10282-10286.
14. Binda C, Wang J, Pisani L, Caccia C, Carotti A. J. Med. Chem. 2007;50:5848.

15. Frisch MJ, Trucks GW, Schlegel HB, Scuseria GE, Robb MA, Cheeseman JR, Scalmani G, Barone V, Petersson GA, Nakatsuji H, Li X, Caricato M, Marenich AV, Bloino J, Janesko BG, Gomperts R, Mennucci B, Hratchian HP, Ortiz JV, Izmaylov AF, Sonnenberg JL, Williams-Young D, Ding F, Lipparini F, Egidi F, Goings J, Peng B, Petrone A, Henderson T, Ranasinghe D, Zakrzewski VG, Gao J, Rega N, Zheng G, Liang W, Hada M, Ehara M, Toyota K, Fukuda R, Hasegawa J, Ishida M, Nakajima T, Honda Y, Kitao O, Nakai H, Vreven T, Throssell K, Montgomery JA, Peralta JE, Ogliaro F, Bearpark MJ, Heyd JJ, Brothers EN, Kudin KN, Staroverov VN, Keith TA, Kobayashi R, Normand J, Raghavachari K, Rendell AP, Burant JC, Iyengar SS, Tomasi J, Cossi M, Millam JM, Klene M, Adamo C, Cammi R, Ochterski JW, Martin RL, Morokuma K, Farkas O, Foresman JB, Fox DJ, Gaussian, Inc., Wallingford CT. 2016.
16. Xie SS, Lan JS, Wang X, Wang ZM. Bioorg. Med. Chem. 2016;24:1528-1539.
17. Costas-Lago MC, Besada P, Rodríguez-Enríquez F, Vina D, Vilar S, Uriarte E, Borges F, Teran C. Eur. J. Med. Chem. 2017;139:1-11.

Acknowledgements: This work has been fully supported by the grant from Faculty of Science, Srinakharinwirot University. Department of Chemistry, Faculty of Science, Srinakharinwirot University are gratefully acknowledged for providing research facilities. Finally, National e-Science Infrastructure Consortium are thankfully acknowledged for providing computing resources that have partly contributed to the research results reported within this paper.

C4_005_PF: LASER-INDUCED BREAKDOWN SPECTROSCOPY STUDY OF RED-COLORED ANCIENT GLASS BEADS FROM KHLONG THOM ARCHAEOLOGICAL SITE

Krit Won-in[1,*], Jirapant Dutchaneephet[2], Pisutti Dararutana[3]
[1]Department of Earth Science, Faculty of Science, Kasetsart University, Bangkok 10900, Thailand
[2]Institute of Physical Education Phetchabun, Muang District, Phetchabun 67000, Thailand
[3]Retired Army Officer, Royal Thai Army, Bangkok 10900, Thailand
*e-mail: kritwonin@gmail.com

Abstract: This work is the first time in Thailand that a bench-top laser-induced breakdown spectroscopy (LIBS) has been used for examining ancient glass bead samples found at the Khlong Thom archaeological site, Krabi Province in southern Thailand. These samples dated to about the 4th Century AD. The results showed theirs elemental composition which were corresponded with those from X-ray fluorescence spectroscopy such as scanning electron microscope coupled with energy dispersive X-ray spectroscopy (SEM-EDS) and particle-induced X-ray emission spectroscopy (PIXE). It was found that the samples were classified as high magnesia glass and low-magnesia high potash glass which contained same glass chemicals as those from the Roman period. It can be concluded that it was the long distance or exchange connections in the maritime. It is demonstrated that the LIBS is one of potential technique for quick characterization of historical objects.

Introduction: Due to the complex nature of materials and objects of cultural heritage, analytical instruments employed should be very sensitive, spatially resolved, multi-elemental, and versatile. Moreover, they should be as noninvasive as possible and capable of giving complementary details at different scales ranging from the macroscopic to the nanometer level. Quantitative analyses of major, minor, and trace elements of archaeological materials are crucial to answer questions associated with manufacturing technology, raw materials, the origin of these objects and their restoration and protective conservation. Various analytical techniques have been used to analyze the ancient glass composition, which include X-ray fluorescence spectroscopy (XRF), X-ray diffraction (XRD), particle induced X-ray emission (PIXE), X-ray photoelectron spectroscopy (XPS) and X-ray absorption spectroscopy (XAS), inductively coupled plasma coupled to optical emission or mass spectrometry (ICP-OES, ICP-MS) and Raman microscopy [1-4].

Laser-induced breakdown spectroscopy (LIBS) is a practically non-destructive rapid elemental analysis technique and potential alternative techniques used to archaeology related applications such as pigments, icons, pottery, ceramics and metals [5].

It is well known that glasses has been used as ornaments and decorations in Thailand for several hundred years, especially glass bead collected from various regions throughout the country. Although the beads are small objects, they are affected for human beings and also important for archaeologists who studied these, because of their long history. Glass beads are found on the South and the South-East Asia during the end of the 2nd to the beginning of the 1st Century BC came from India [6-7]. Most of them are small annular or globular monochromatic that commonly called the Indo-Pacific bead. Many ancient glass beads are found on historic sites in Thailand; southern, central and eastern provinces [7].

Khlong Thom site or well-known in Khun Lukpud is an archaeological site on the western coast of the Thai–Malay Peninsula, in Khlong Thom district, Krabi Province, southern Thailand. The archaeological resources suggested that it was the earliest site for glass production which dated to about the 4th century AD [8-9].

Methodology: In this work, the LIBS was used to analysis the elemental composition of three red-colored ancient glass beads labelled as KR1, KR2 and KR4, found in the form of red opaque fragments and at the Khlong Thom historical site compared with SEM-EDS and PIXE.

The emission spectra of glass bead samples were recorded using LIBS at the Gem and Jewelry Institute of Thailand (Public Organization), Bangkok (Thailand). The tool consisted of a pulsed G-switched 1064 nm Nd-YAG laser and the detection system.

The structure and chemical compositions of the glass bead samples were analyzed using a scanning electron microscope Hitachi SU1500 SEM coupled with an energy dispersive X-Ray fluorescence spectrometer Horiba Emax EDXRF at Coax Group Corporation Ltd., Bangkok (Thailand).

The chemical compositions of the glass samples were also analyzed using PIXE based on a 2-MeV proton beam produced by a 1.7 MV tandem Tandetron accelerator at the Plasma and Beam Physics Research Facility of Chiang Mai University, Chiang Mai (Thailand). The proton beam was collimated with a diameter of 1 mm, and the beam current on the sample was 10 nA. The detector used to be of Si(Li) type. A 74 µm mylar foil with 0.38% relative hole area was placed in front of the detector as an absorber to reduce the count rate caused by impurities of low atomic numbers. Base pressure in the vacuum chamber was about $6x10^{-6}$ mbar. Quantitative analysis of the PIXE spectra was performed using the GUPIXWIN code.

Results and Discussion: Microstructure of the red-colored ancient glass beads using SEM was shown in Figure 1. The SEM micrographs exhibited the glass corrosion on the surface which indicated the surface detail of the weathering layer [10].

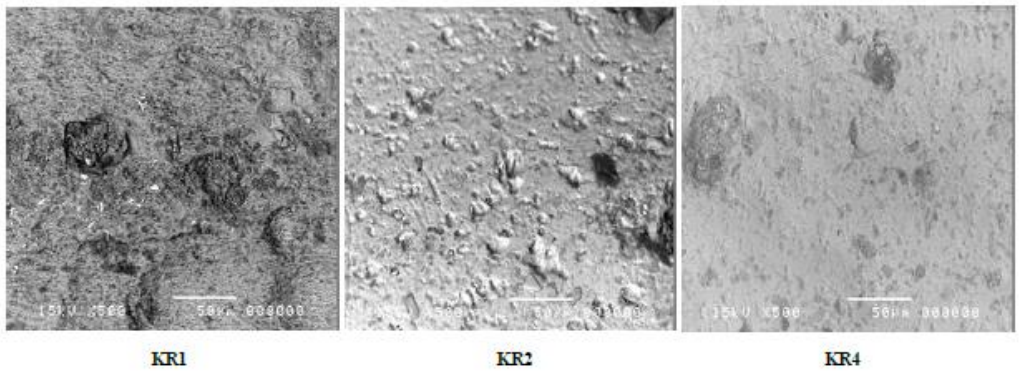

Figure 1. Microstructure of red-colored ancient glass bead samples using SEM

Red-colored ancient glass bead samples were carried out in order to identify composition. The elemental analysis using LIBS was illustrated in Table 1. It was found that the major and minor elements such as Mg, Al, Si, K and Ca were analyzed. Transition metals such as Fe and Cu were detected with a relatively high content. Ti and Sn were also present. However, Pb was non-detectable.

EDS and PIXE analysis showed the same elements in the form of chemical composition, as illustrated in Table 2. Silica (SiO_2), potash (K_2O) and alumina (Al_2O_3) concentrations were between 65.61-73.28 wt%, 12.57-13.46 wt% and 6.00-8.80 wt%, respectively, while the concentrations of magnesia (MgO) and lime (CaO) ranged from 0.24-2.94 wt% and 0.58-1.79 wt%, respectively. Iron content ranged from 1.94 to 2.70 wt% of Fe_2O_3. Titanium content ranged from 0.27 to 0.97 wt% of TiO_2. Iron and titanium normally originated as natural impurities in siliceous sands [11]. However, the enrichment of iron concentration seemed to be high, showed that it may be added as colorant. Manganese content

maximum of 0.10 wt% of MnO. The low ratio of $MnO:Fe_2O_3$ showed that manganese was not intentionally added as a decolorant [11]. Sodium, sulfur, zinc and lead were present and contained up to 0.82 wt% of NaO, 0.42 wt%, 0.29 wt% of ZnO and 0.47 wt% of PbO, respectively. They may be as contaminants in raw materials. Tin was detected with concentration between 1.43-2.06 wt% of SnO_2. However, it may be contaminated from raw materials or added as opacifier. All samples contained important amounts of copper (0.96-3.96 wt% CuO), which played as traditional red colorant. The copper oxide concentration of these samples were same as several red and opaque glasses from Messina (Italy) between the thirteenth to the fourteenth centuries AD that contained 1.20-3.34 wt% CuO [12-13].

It was shown that KR1 and KR2 contained with high content of potash (K_2O; more than 2 wt%) and magnesia (MgO; more than 1 wt%), it was classified that this type of glass was a high magnesia glass (HMG), while the concentration of magnesia in KR3 was less than 1 wt%, it was classified as a low-magnesia high-potash glass (LMHK). Furthermore, these results were corresponded with the previous works which they discussed that the red-colored ancient glass bead sample from the Khlong Thom was a LMHK glass [14], while the one from the Khao Sam Kaeo (Chumphon) was a HMG glass [15]. They were also revealed that the red coloration of the red-colored ancient glass beads found in the south area of Thailand was due to Cu [14-15].

Table 1. The elemental composition of red-colored ancient glass bead samples using LIBS

Element	Weight %			Atomic %		
	KR1	KR2	KR4	KR1	KR2	KR4
C K	17.29	23.37	8.48	26.20	31.99	13.26
O k	46.72	54.54	53.84	53.15	56.05	63.19
Na K	4.31	ND	0.31	3.41	ND	0.25
Mg K	1.02	0.63	0.09	0.77	0.43	0.07
Al K	3.05	1.62	2.26	2.06	0.99	1.57
Si K	15.56	14.78	27.62	10.08	8.56	18.47
P K	0.37	0.24	ND	0.22	0.13	ND
S K	ND	ND	0.16	ND	ND	0.09
Cl K	0.33	ND	0.13	0.17	ND	0.07
K K	1.98	2.94	5.00	0.92	1.23	2.40
Ca K	2.08	0.39	0.21	0.94	0.16	0.10
Ti K	0.44	0.19	0.10	0.17	0.07	0.04
Cr K	ND	ND	0.05	ND	ND	0.02
Mn K	Nd	0.02	ND	ND	0.01	ND
Fe K	2.11	0.45	0.73	0.69	0.13	0.24
Co K	ND	ND	0.02	ND	ND	0.01
Cu L	3.55	0.38	0.36	1.02	0.10	0.11
Zn L	ND	ND	0.11	ND	ND	0.03
Mo L	0.63	ND	ND	0.12	ND	ND
Sn L	0.57	0.45	0.54	0.09	0.06	0.08
Pb M	ND	ND	ND	ND	ND	ND

[a] ND equals with non-detectable elements

Table 2. The chemical composition of red-colored ancient glass bead samples using PIXE and EDS

Composition	Sample (wt%)			PIXE
	KR1	KR2	KR4	LOD (ppm)
NaO	ND[a]	ND	0.82	-
MgO	2.94	2.88	0.24	-
Al_2O_3	8.80	7.41	6.0	0.22
SiO_2	65.61	67.64	73.28	0.24
S	ND	ND	0.42	0.004
K_2O	12.57	13.46	13.27	0.002
CaO	1.16	1.79	0.58	0.007
TiO_2	0.97	0.87	0.27	0.003
MnO	ND	0.09	0.10	0.003
Fe_2O_3	2.70	2.06	1.94	0.005
CuO	3.96	1.74	0.96	0.01
ZnO	ND	ND	0.29	0.01
SnO_2	1.64	2.06	1.43	0.03
PbO	ND	ND	0.47	0.07

[a] For PIXE; ND equals with non-detectable elements
For EDS; ND ≤0.10 wt%

From this work, based on the glass chemistry of the major compositions and the traces of transition metals/oxides, results indicated that the percentage of copper oxide in the red-colored ancient glass bead samples was typical of red opaque glass beads of the Roman period [14]. It was possible that they were produced with slightly compositional differences between glass samples or the use of similar raw materials with different batches [15].

Conclusion: The composition of the red-colored ancient glass bead samples excavated from the Khlong Thom was successfully investigated using LIBS, SEM-EDS and PIXE. These results were good agreement which those from other published. It can be concluded that these glass samples were probably produced at the Khlong Thom, where was the glass work production site in the ancient maritime trade.

The showed results in this work demonstrated the advantages of LIBS analysis to obtain elemental composition about the materials used for making the red-colored ancient glass beads. The results were agreed to compare with an X-ray fluorescence method such as EDS and PIXE. Analysis of LIBS spectra allowed the identification. In conclusion, LIBS is a powerful tool for analysis samples of historical interest leading to characterize of archaeological finding that is highly recommended for archaeological science.

This study possibly led to the historical link of the long distance trade and exchange networks in the maritime along the South-East, the South, the Asia Minor and the East Asia.

References:

1. Nakai I, Matsunaga M, Adachi M, Hidaka K I. J. Phys. IV. 1997: 7: 1033-1034.
2. Quartieri S, Triscari M, Sabatino G, Boscherini F, Sani A. Eur.J.Mineral. 2002: 14: 749-756.
3. Padovani S, Borgia I, Brunetti B, Sgamellotti A, Giulivi A, D'Acapito F. Applied Physics A. 2004: 79: 229-233.
4. Arletti R, Dalconi MC, Quartieri S, Triscari M, Vezzalini G. Applied Physics A. 2006: 83: 239-245.
5. Melessanaki K. Applied Surface Science. 2002: 197-198: 156-163.

6. Lankton JW, Dussubieux L, Gratuze B, Bulletin de L'Ecole Francaise d'Extreme Orient. 2006: 93: 317-351.
7. Thongkam Y. Master Degree of Arts Thesis, Silpakorn University. 2009.
8. Veeraprsert M. Khlong Thom: An ancient bead-manufacturing location and an ancient entrepot, in: Early Metallurgy, Trade and Urban Centres in Thailand and Southeast Asia. White Lotus, Bangkok. 1992.
9. Bronson B. Glass and Beads ant Khuna Lukpad, Southern Thailand. Proceedings of the First Conference of the Association of Southeast Asian Archaeologists in Western Europe, Institute of Archaeology, University College, London, UK, 8-10 September 1986.
10. Won-in K, Thongkam Y, Intarasiri S, Kamwanna T, Dararutana P. IOP Conf. Series: Materials Science and Enineering. 2012: 27: 012015.
11. Sanderson D C, Hunter J R , Warren S E. J Archaeol Sci. 1984: 11: 53-69
12. Arletti R, Dalconi M C, Quartieri S, Triscari M, Vezzalini G. Appl Phys. 2006: 83: 239-245
13. Arletti R, Quartieri S, Vezzalini G, Sabatino G, Triscari M, Mastelloni M A. J Non-Cryst Solids. 2008:354:4962-4969
14. Klysuban W, Thongkam Y, Pongkrapan S, T-Thienpreasert J, Won-in K, Dararutana P. Analytical and Bioanalytical Chemistry. 2011: 339: 3033-3040.
15. Won-in K, Thongkam Y, Kamwanna T, Dararutana P. Journal of Radioanalytical and Nuclear Chemistry. 2012: 294: 247-250.

Acknowledgements: The Gem and Jewelry Institute of Thailand (Public Organization) (Bangkok), the Plasma and Beam Physics Research Facility of Faculty of Science at Chiang Mai University (Chiang Mai) and Coax Group Corporation Ltd. (Bangkok) are thanked for providing the LIBS, PIXE and SEM-EDS apparatus for analysis, respectively. The glass bead samples are supported by the Khlong Thom glass bead working village, at Krabi Province (Thailand). The Department of Earth Sciences at Faculty of Science of Kasetsart University (Bangkok) provided team expertise.

SESSION D:
POLYMER & MATERIALS SCIENCE_NANOTECHNOLOGY

D_001_PF: ZINC OXIDE DOPED WITH COPPER(II) OXIDE SUPPORTED ON CELLULOSE FLAKES FOR DEGRADATION OF METHYLENE BLUE

Saowapa Chotisuwan*, A-aesoh Luebaesa, Jareerat Roumcharoen
Department of Science, Faculty of Science and Technology, Prince of Songkla University, Pattani 94000, Thailand
*e-mail: saowapa.c@psu.ac.th

Abstract: Zinc oxide (1-5 wt %) photocatalysts doped with 1 wt % CuO supported on cellulose flakes (CFs) were prepared for degradation of methylene blue dye. Isolated cellulose fibers from oil palm trunk were dissolved in strong alkaline solution with 0.5 wt % ZnO as additive agent at -10 °C. Then CFs were formed by dropping cellulose solution into coagulation bath of 2 M HCl solution. The photocatalysts supported on CFs were prepared by precipitation to contain 1, 3 and 5 wt % ZnO and 1 wt % CuO. The photocatalysts were characterized by Fourier transform infrared spectroscopy (FT-IR), X-ray diffraction (XRD), and stereoscopic microscopy. It was observed that the particle sizes of CFs were 0.5-3.5 mm. The catalytic performance of the photocatalysts was performed by degradation of methylene blue dye solution. The 5 mg catalysts were dispersed in 50 mL of 1 x 10^{-5} M methylene blue solution at room temperature and irradiated with 20 W daylight lamp for 1 hour. It was found that the degradation efficiency of methylene blue catalyzed by 1 wt% ZnO-1 wt% CuO/CFs gave the optimum value at 68.4±1.5 %.

Introduction: Natural polymers containing large number of hydroxyl groups such as cellulose have been attracted as good adsorbers and applied for wastewater treatment, e.g. removal of methylene blue (MB).[1] Cellulose fibers can be extracted from agricultural biomass including oil palm trunk (OPT). More than 0.72 million hectares has been used for oil palm agriculture in the southern part of Thailand in 2017.[2] Large number of old oil palm trees; more than 20-30 years old, have to be dumped at the replantation due to non-economical harvest. These oil palm tree wastes are usually disposed by burning leads to environmental pollution. Therefore, much effort has been made to use them rather than burning. The OPT biomass composition mainly consists of cellulose, hemicellulose, and lignin. High α-cellulose content up to 41% was reported in fibers of OPT.[3] This characteristic of OPT fibers suggests possibility of cellulose isolation and use for many applications. They can be used as supporting materials for heterogeneous catalysts due to their excellent hydrophilic, thermal, mechanical properties, permeability, nontoxicity, and biodegradable. Methylene blue is cationic thiazine with high toxicity and nonbiodegradable. It is being used in textile, paper, plastic and paint industries. Those wastewater containing MB cause serious environmental pollution, thus there are many methods to remove MB before discard. Phtotocatalysis has been used for degradation of MB in contaminated wastewater into harmless chemicals. Zinc oxide (ZnO) photocatalyst with wide band gap energy of 3.37 eV can be doped with photo-assisted metals such as In, Ag and Ni, to reduce recombination of photogenerated species of ZnO.[4] Therefore, in this work, cellulose flakes were prepared by using isolated cellulose fibers from OPT biomass and used as supporter for ZnO photocatalyst incorporating with CuO to degradation of MB solution.

Methodology:

Isolation of cellulose fibers: Cellulose fibers were isolated from oil palm trunk (*Elaeis guineensis Jacq.*) biomass collected at Krabi province by pretreatment with 2 wt % NaOH solution in an autoclave, then bleached with 3 wt % $Ca(ClO)_2$ solution and finally with 5 wt % oxalic acid solution.[5] The alpha cellulose content of isolated cellulose fibers was determined by TAPPI T203 om-88 method.[6]

Preparation of cellulose flakes and photocatalysts: The 5 wt % isolated cellulose fibers were dissolved in aqueous mixtures of 7 wt % NaOH, 12 wt % urea 0.5 wt % ZnO at -10 °C.[7, 8] Then cellulose flakes (CFs) were formed by dropping the cellulose solution into coagulating bath of 2 M HCl solution and left these CFs in the acid solution for 16 hours. The CFs product was washed with distilled water until pH 7 and dried. The 1, 3 and 5 wt% ZnO containing 1 wt % CuO photocatalysts supported on CFs were prepared by precipitation at room temperature using $Zn(NO_3)_2.6H_2O$ and $Cu(NO_3)_2.6H_2O$ as precursors and characterized by ATR-FTIR (Model Tensor 27, Bruker, USA), XRD (Model X'Pert MPD, Philips, the Netherlands), and stereoscopic microscopy (Carl Zeiss Stemi 2000-C).
Photocatalytic degradation of methylene blue (MB) solution: The degradation of MB dye solution catalyzed by the photocatalyst was performed by dispersion 5 mg catalysts in 50 mL of 1 x 10^{-5} M methylene blue (MB) solution at room temperature. The mixture was kept in the dark for 1 h then irradiated with 20 W daylight lamp for 1 h. The MB degradation efficiency was observed by measurement the absorbance of solution at wavelength 664 nm with Vis spectrophotometer (Biochrom Libra S11, England).

Results and Discussion:
Characterization of isolated cellulose fibers, cellulose flakes and photocatalysts: Cellulose fibers isolated from OPT biomass by alkaline pretreatment were shown in Figure 1 (left). Alkaline pretreatment in an autoclave, bleached with $Ca(ClO)_2$ solution and oxalic acid solution can remove most of lignin and hemicellulose leads to yellow-white cellulose fibers with the length up to 0.1-0.2 mm with rough surface. The percentage yield of cellulose extraction was 70.8±5.1%. Alpha cellulose content of raw OPT fibers determined by TAPPI 203 om-88 method was 77.5±2.1% and it increased up to 82.2±8.0% after extraction. Then, cellulose flakes (CFs) were prepared by dissolution of isolated cellulose fibers in NaOH/urea/water (7/12/81 wt %), and 0.5 wt % ZnO at -10°C and injected to coagulation bath of 2 M HCl solution, then left them there for 16 hours. After drying, the CFs were formed as shown in Figure 1 (right) with broad particle size distribution, mostly 0.5-3.5 mm in diameter with porous and rough surface. These porous and hard agglomerated or regenerated cellulose flakes can be used further as supporting material for metal or metal oxides photocatalysts by interaction via hydroxyl groups of cellulose.

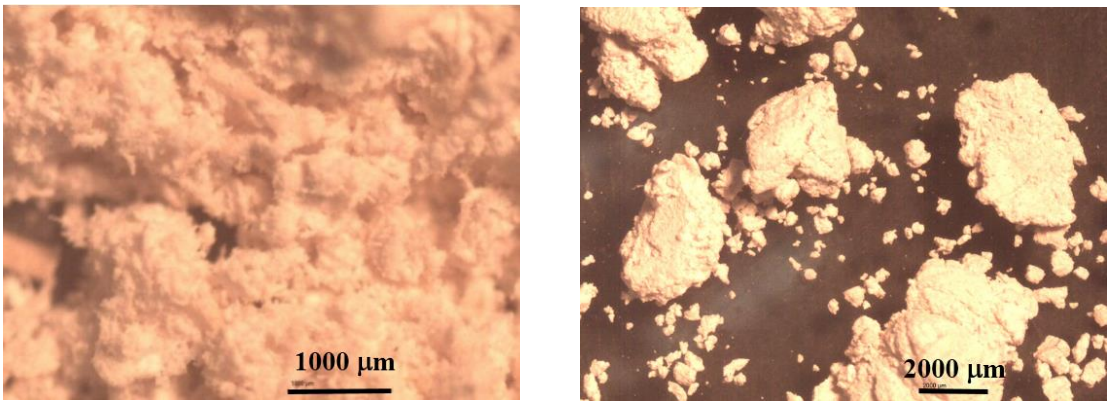

Figure 1. Morphology of isolated cellulose fibers (left) and cellulose flakes (10X) observed by stereo microscope (20X).

The crystallinity of isolated cellulose fibers and CFs were analyzed by XRD (Figure 2). The 2θ diffraction angles at 14.9°, 15.3°, 20.0° and 34.4° of isolated cellulose fibers represented native cellulose I.[1, 9] These XRD peaks were still observed after forming CFs indicating the

crystallinity did not significantly change after crosslinking. However, strong 2θ peaks at 29.7° and 39.8° were also observed indicating calcite interacted on cellulose fibers during bleaching process.[10] This interaction might reduce the dissolution of cellulose fibers and crosslinking of cellulose during cellulose flakes forming.

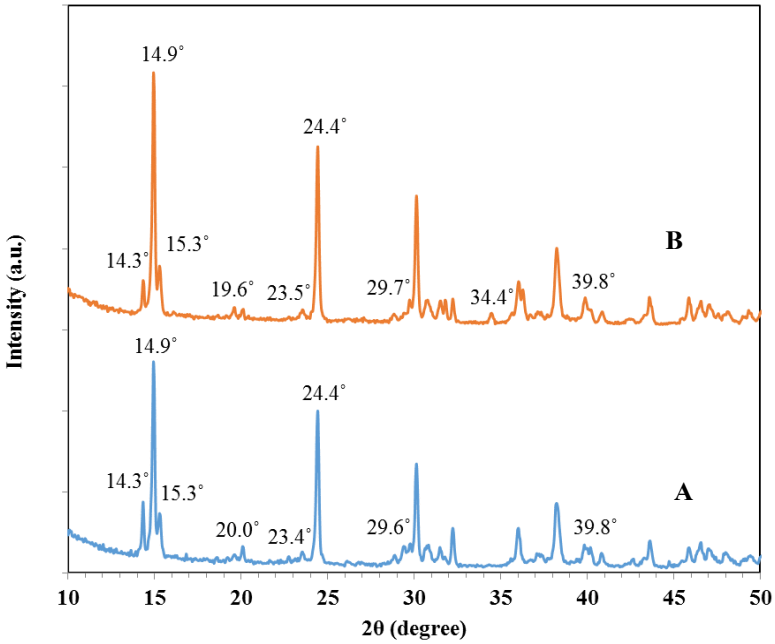

Figure 2. XRD patterns of isolated cellulose fibers (A) and cellulose flakes (B)

The surface functional groups of cellulose fibers, CFs and photocatalysts were determined by FTIR. From Figure 3, the raw OPT fibers, isolated cellulose fibers and CFs showed broad FTIR spectra at 3500-3200 cm^{-1} corresponding to O-H stretching vibration of hydrogen bonded OH groups in cellulose.[11] The aliphatic saturated C-H stretching associated with methylene groups in cellulose was observed at 2900-2928 cm-^{1}.[5] The absorption peak at 1238 cm^{-1} assigning to C-O-C stretching vibration of aryl-alkyl ether linkage in lignin[11] decreased after extraction of cellulose from raw OPT. The functional group C–O, C–C stretching or C–OH bending at 1036 cm^{-1} of hemicelluloses[13] disappeared for isolated cellulose fibers and CFs. The peak at 904-896 cm^{-1} indicated C-H rocking of β-(1 4)-glycosidic linkages of glucose rings of cellulose.[14] FTIR spectra of isolated cellulose fibers (Figure 3B) and CFs (Figure 3C) representing O-H stretching region slightly different after cellulose crosslinking indicating change of hydrogen bonding in cellulose and also crystallinity of cellulose. The total crystallinity index (TCI) of CBs, calculated using the absorption band ratio at around 1371 cm^{-1} and 2900 cm^{-1} was found to be 1.0 – 1.1.[15]

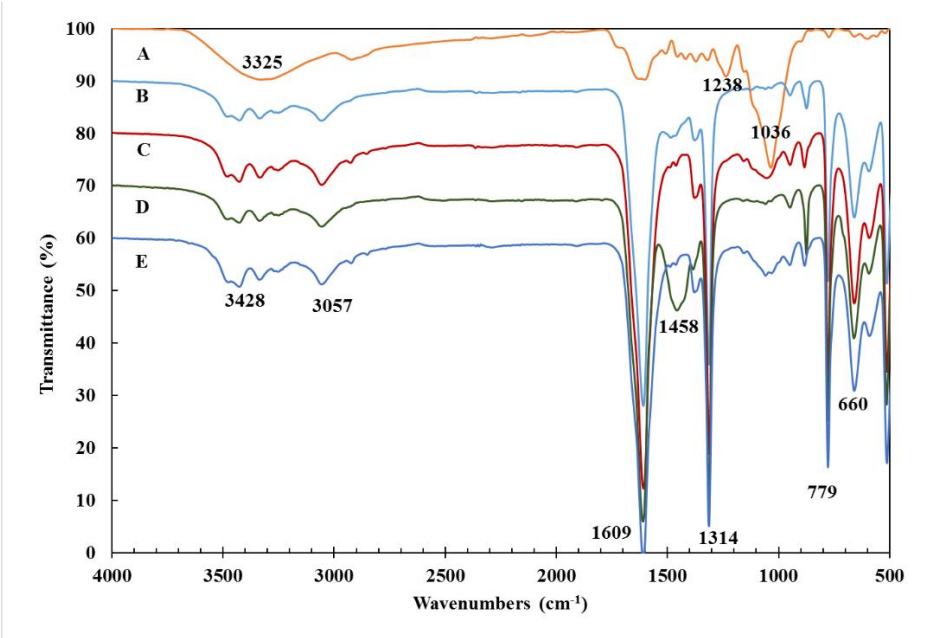

Figure 3. FTIR spectra of raw oil palm trunk fibers (A), isolated cellulose fibers (B), cellulose flakes (C), 1 wt % ZnO/CFs (D), and 1 wt % ZnO-1 wt % CuO/CFs (E).

Photocatalytic degradation of MB solution: The catalytic performance for degradation of MB dye solution by ZnO catalytst supported on CFs was performed at room temperature. The initial concentration of MB solution was fixed at 1 x 10^{-5} M, 50 mL, mixed with 5 mg photocatalyst and stirred in the dark for 1 hour for MB adsorption. The concentration of MB decreased after 1 hour in the dark indicating excellent MB absorption on catalyst and CFs. The MB adsorption on 1 wt % ZnO/CFs was 65.5±19.0%, higher than 3 and 5 wt % ZnO/CFs. After irradiation the mixture with daylight lamp 20 W for 60 minutes, the concentration of MB slightly decreased due to degradation during irradiation time. From Figure 4, the MB degradation by 1 wt % ZnO/CFs incorporating with 1 wt % CuO increased to 68.4±1.5%, higher than 3 and 5 wt % ZnO-1 wt % CuO/CFs and ZnO catalysts without CuO. The increasing of ZnO amount from 3-5 wt % increase degradation efficiency but still lower than 1 wt % ZnO-1 wt % CuO/CFs, possibly due to lower dispersion of CuO and ZnO on CBs than 1 wt% ZnO/CBs. The addition of photo-assisted CuO can reduce recombination of electron-hole of ZnO lead to higher photocatalytic performance. However, low content of ZnO activated by visible light did not complete MB degradation compared to degradation with high content of nano In/ZnO photocatalysts with lower band gap energy.[4] However, the MB adsorption on cellulose might also take the important role to decrease amount of MB in solution rather than degradation by photocatalysts according to slightly increase percentage of degradation after visible light irradiation. Thus, only small amount of MB adsorbed on ZnO can be degraded and hardly to oxidize strong MB adsorption on cellulose.

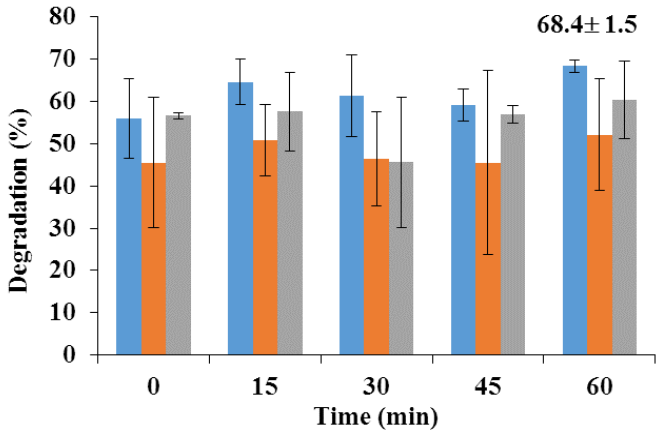

Figure 4. Photocatalytic degradation of MB solution catalyzed by 1 wt % ZnO- 1 wt % CuO/CFs ■, 2 wt % ZnO- 1 wt % CuO/CFs ■, and 5 wt % ZnO- 1 wt % CuO/CFs ■.

Conclusion: Cellulose flakes with particle size 0.5-3.5 mm were prepared by dropping the dissolution of oil palm trunk cellulose fibers in the coagulation bath of 2 M HCl solution. The zinc oxide photocatalysts doped with 1 wt % CuO supported on cellulose flakes can be prepared by precipitation method. The 1 wt % ZnO-1 wt % CuO/CFs gave the optimum MB degradation efficiency at 68.4±1.5 % for 1-hour degradation irradiated by daylight lamp 20 W at room temperature.

References:

1. Dai H. and Hung H. Carbohyd Polym. 2016;148:1-10.
2. Office of Agricultural Economics. http://www.oae.go.th/assets/portals/1/files/ebook/agri_situation2561.pdf. [18th July 2019].
3. Sun R. and Tomkinson J. Sep Purif Technol. 2001;24:529-539.
4. Baeissa E.S. Front Nanosci Nanotech. 2016;2:1-5.
5. Lamaming J., Hashima R., Sulaimana O., Leha C.P., Sugimoto T. and Nordina N.A. Carbohyd Polym. 2015;127:202-208.
6. TAPPI T203 om-88. 1992. Alpha, beta, and gamma cellulose in pulp.
7. Luo X. and Zhang L. J Chromatogr A. 2010;1217:5922-5929.
8. Mohamed S.M.K., Ganesan K., Milow B. and Ratke L. RSC Adv. 2015;5: 90193-90201.
9. Vestena M., Gross, I.P., Muller C.M.O. and Pires A.T.N. Polímeros. 2016;26:327-335.
10. Ciobanu M., Bobu E. and Ciolacu F. Cell Chem Technol. 2010;44: 379-387.
11. Mandal A. and Chakrabarty D. Carbohyd Polym, 2011:86:1291-1299.
12. Jonoobi M., Khazaeian A., Tahir P.M., Azry S.S. and Oksman K. Cellulose. 2011;18: 1085-1095.
13. Baskaran M., Hashim R., Sudesh K., Sulaiman O., Hiziroglu S., Arai T. and Kosugi A. Ind Crop Prod. 2013;51:334-341.
14. Kaushik A. and Singh M. Carbohyd Res. 2011;46:76-85.
15. Yue Y., Han J., Han G., Zhang Q., French A.D. and Wu Q. Carbohyd Polym. 2015, 133: 438-447.

Acknowledgements: This work is a part of the project granted by Research Fund of Prince of Songkla University (SAT610041S).

D_002_OF: MODIFICATION OF PECTIN BY 3-(DIMITHYLAMINO) PROPYLAMINE

Nootcharee Kunkit[1], Thanapon Deekaikam[1], Kiattikhun Manokruang[1,2,*]
[1]Department of Chemistry, Faculty of Science, Chiang Mai University, Chiang Mai 50200, Thailand
[2]Materials Science Research Center, Faculty of Science, Chiang Mai University, Chiang Mai 50200, Thailand
*e-mail: kiattikhun.m@cmu.ac.th

Abstract: Pectin is an anionic and biocompatible polysaccharide that can respond to pH changes. Pectin, thus, is a member of a pH-responsive polymer family. It has been well known that gelation of pectin occurs at acidic pH values and this acidic pH of gelation limits the use of such biomaterials. So, this research aimed to raise the gelation pH of pectin by modifying its chemical structure using 3-(dimethylamino) propylamine. The chemical structure of pectin was modified by the reaction between carboxylic acids of pectin and the primary amine groups of 3-(dimethylamino) propylamine (DMAPA). The carboxylic acid groups on pectin moieties were activated by the use of EDC/NHS coupling so that the amine groups from DMAPA can then react at the active sites, at which the amide formation was a result. The modified pectin copolymers with different DMAPA compositions (pec-*g*-DMAPA0.5, pec-*g*-DMAPA1.0 and pec-*g*-DMAPA1.5) were characterized and successfully confirmed by proton nuclear magnetic resonance spectroscopy (^{1}H-NMR). The grafting percentage values of pec-*g*-DMAPA0.5, pec-*g*-DMAPA1.0 and pec-*g*-DMAPA1.5, as calculated from the ^{1}H- NMR integral bands, were 38%, 42% and 52%, respectively. The grafting percentage obviously depended on DMAPA feeding composition which suggested that the values were increased by increasing DMAPA feeding composition. Also, the pH of the copolymer solutions was increased by increasing DMAPA composition in the pectin backbone.

Introduction: Pectin is one of the complex polysaccharides, mainly found in the primary cell wall of plants. It is consisted mainly of D-galacturonic acid (GalA) units joined in chains by α (1-4) glycosidic linkage. This natural polymer has been a well-known anionic and biocompatible polymer that can respond to pH stimulus (pH-responsive).[1, 2] Pectin is finding increasing applications in the pharmaceutical and biotechnology industry. It has been used successfully for many years in the food and beverage industry as a thickening agent, a gelling agent and a colloidal stabilizer.[3] Pectin also has several unique properties that have enabled it to be used as a matrix for the entrapment and/or delivery of a variety of drugs. The chemical structure of pectin main chain is shown in Error! Reference source not found. (a). The gelation of pectin occurs naturally at pH 3.0 and the commercial pectin demonstrates pH around 2.8-3.6.[4] This gelation in a strong acidic solution is a serious drawback for using pectin as biomedical materials. Therefore, this research aimed to raise the gelation pH of pectin by modifying its chemical structure using 3-(dimethylamino) propylamine (DMAPA) on the pectin backbone.

The chemical structure of DMAPA was shown in Error! Reference source not found.(b). It is a bulk chemical used, such for the synthesis of betaines in shampoos, for curing epoxy resin and as an additive to fuels.[5] DMAPA is positively charged at physiological pH so it can interact with negatively charged on pectin molecules so that the columbic interactions originated between anions from pectin and cations from DMAPA will increase the pH of pectin compared to native pectin at pH 3.0.

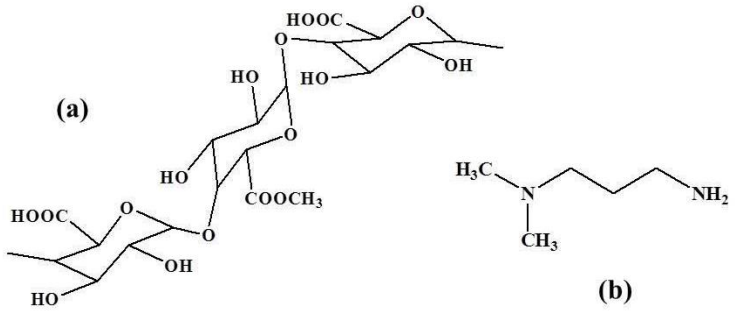

Figure 20. The chemical structures of
(a) pectin main chain and (b) 3-(dimethylamino)propylamine (DMAPA)

Chemical modification of pectin was done in several ways. For example, amidation is considered a simple method for modification of pectin. The common method of this kind of pectin preparation is aminolysis of methyl ester groups of pectin with ammonia in anhydrous methanol (Figure 21). This method is a type of alkaline demethoxylation by the action of ammonia on the ester groups, which then some of methyl ester groups are replaced by amino groups.[6]

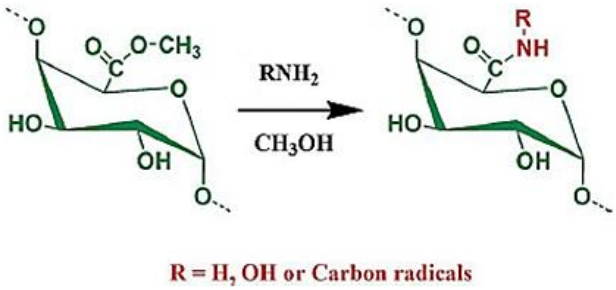

Figure 21. Amidation of pectin.[6]

Grafting on pectin is also possible through the activation of its carboxylic groups. In this approach, 1-ethyl-3-3-dimethylaminopropyl carbodiimide hydrochloride (EDC) and N-hydroxysuccinimide (NHS) were used to activate the carboxylic acids on monosaccharide derivatives to the active groups so that the amine groups can directly react at the active sites.[7] Example of such approach was done by H-L Jiang, *et al.* on the synthesizing chitosans-*graft*-lactobionic acid (LA) copolymer by imine reaction between chitosan and carboxylic group of lactobionic acid (Figure 22).[8]

In this work, pectin was modified with 3-(dimethylamino) propylamine (DMAPA) by use of 1-ethyl-3-3-dimethylaminopropyl carbodiimide hydrochloride (EDC) and N-hydroxysuccinimide (NHS) to activate the acid groups on pectin to the relatively more active sites where the conjugation occurred through the amide bonds.

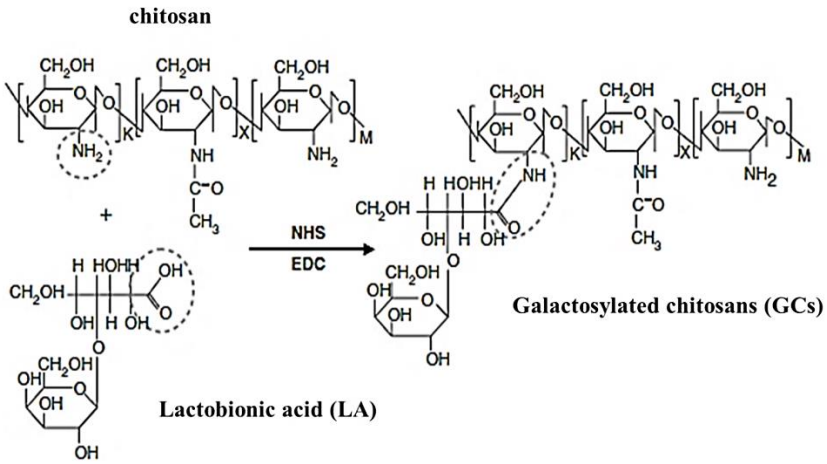

Figure 22. Activation of carboxylic acids for further reaction with amino group as described by H-L Jiang *et al.*[8]

Methodology:

Materials: High methoxy pectin (degree of esterification 70-75%), 3-(dimethylamino) propylamine (DMAPA), N-hydroxysuccinimide (NHS) and Deuterium oxide (D_2O) were purchased from Sigma-Aldrich Company. (1-ethyl-3-(3-dimethylaminopropyl)carbodiimide hydrochloride) (EDC) was purchased from Acros Organics.

Synthesis of Pectin-graft- 3-(dimethylamino)propylamine copolymers: Pectin powder (1.00 g, 5 mmol) was dissolved in 50 ml of deionized water. EDC (5 mmol) and NHS (5 mmol) were added and the reaction was continued for 1 h. DMAPA was added and then the reaction was stirred for 12 h at 4 °C followed by additional 12 h at room temperature.[9] The resulting product was precipitated and washed with methanol. After that, the product pectin-graft-3-(dimethylamino) propylamine (pec-*g*-DMAPA) was dried under vacuum oven for 48 h at 45°C. The feeding compositions of synthesized pec-*g*-DMAPA copolymers were showed in Table 1.

^{1}H-nuclear magnetic resonance (^{1}H-NMR) spectroscopy: The ^{1}H-NMR spectra of native pectin, DMAPA and pec-g-DMAPA copolymers were recorded in deuterium oxide (D_2O) at room temperature by a Varian spectrometer (Model Bruker AVANCE 400 instrument) at a frequency of 400 MHz. The chemical shifts were given in δ (ppm).

Results and Discussion:

Synthesis of Pectin-graft- 3-(dimethylamino)propylamine copolymers: Pectin-graft-3-(dimethylamino) propylamine (pec-*g*-DMAPA) copolymers were synthesized by the use of 1-ethyl-3-3-dimethylaminopropyl carbodiimide hydrochloride (EDC) and N-hydroxysuccinimide (NHS) to activate the acid groups on pectin to the relatively more active sites. Thus, the amine groups from DMAPA can react at the active sites where the conjugation occurred through the amide bonds (Figure 4).

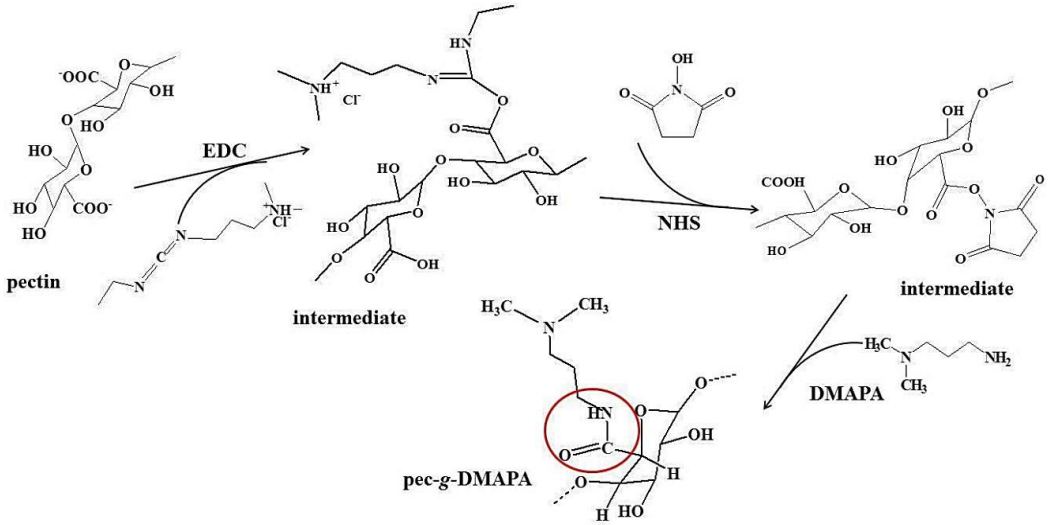

Figure 23. Mechanism of pec-*g*-DMAPA copolymers.

Proton nuclear magnetic resonance spectroscopy (^{1}H-NMR): The ^{1}H-NMR spectra of pectin, DMAPA and pec-*g*-DMAPA copolymers were shown in Figure 24. ^{1}H-NMR spectra of pectin Figure 24 (A) showed methoxy protons (–OCH_3) at 3.8 ppm. The signals of galacturonate and methyl galacturonate residues were seen at 4.9 and 5.1 ppm, respectively. The former corresponded to H-5 protons adjacent to the free carboxyl groups and the latter were a resonance signal of H-5 protons next to the methoxyl groups.[10, 11] The resonance peaks from DMAPA were shown in Figure 24 (b). Three different methylene protons appeared at 2.1, 2.75 and 3.0 ppm and one set of methyl protons appeared at 2.60 ppm. The signal at 2.1 ppm (b) was a signal from the protons between the methylene groups while the signals at 2.6 ppm (d), 3.0 ppm (a) designated the protons next to tertiary amine and the signals at 2.75 ppm (c) designated the protons next to primary amine. The ^{1}H-NMR spectrum of pec-*g*-DMAPA (Figure 24 (c)) showed both resonance peaks originated from pectin and DMAPA. The results confirmed that the grafting reaction was successful.

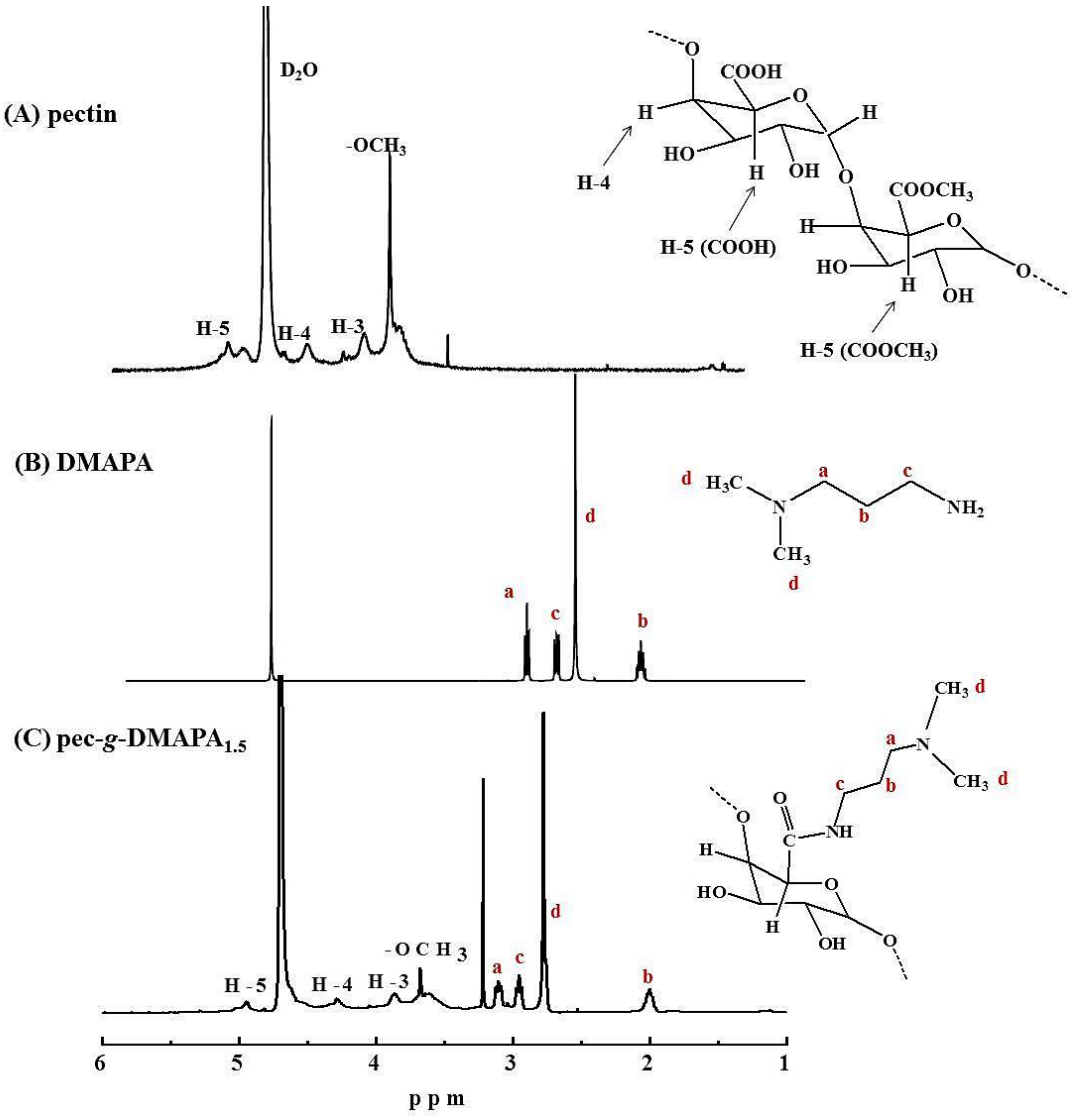

Figure 24. ¹H-NMR spectra of (a) pectin (b) 3-(dimethylamino)propylamine; DMAPA and (c) pec-*g*-DMAPA in D_2O solutions.

Determination of the grafting percentage of pec-g-DMAPA copolymers by proton nuclear magnetic resonance (¹H-NMR) spectroscopy: ¹H-NMR spectrum of the modified pectin confirmed that DMAPA was successfully grafted on the pectin chain and grafting percentage was also calculated from the integral intensities. The percentage of the DMAPA grafted on pectin can be determined by the integration ratio of methoxy proton (H-4) of pectin and the methylene and methyl protons of DMAPA unit using the following equation;

$$grafting\ percentage = \frac{\frac{1}{4}\left(\frac{I_a}{2}+\frac{I_c}{2}+\frac{I_d}{6}+\frac{I_b}{2}\right)}{I_{pec}} \times 100$$

I_a, I_b, I_c, I_d and I_{pec} were integration bands of the methylene and methyl protons of DMAPA and the methoxy proton of pectin (H-4) respectively. The grafting values of DMAPA on

pec-*g*-DMAPA$_{0.5}$, pec-*g*-DMAPA$_{1.0}$ and pec-*g*-DMAPA$_{1.5}$ were found to be 38%, 42% and 52%, respectively, and were shown in Figure 25. The calculated grafting percentage values were also listed in Table 1. The grafting percentage obviously depended on DMAPA feeding composition so that the grafting percentage was increased when increasing DMAPA feeding composition. Also shown in Table 1, the pH of the copolymer solutions was increased by increasing DMAPA composition in the pectin backbone. It was noted that the pH values of copolymer solutions (pH 5.4-5.6) were dramatically higher than that of the native pectin solution (pH 3.0).

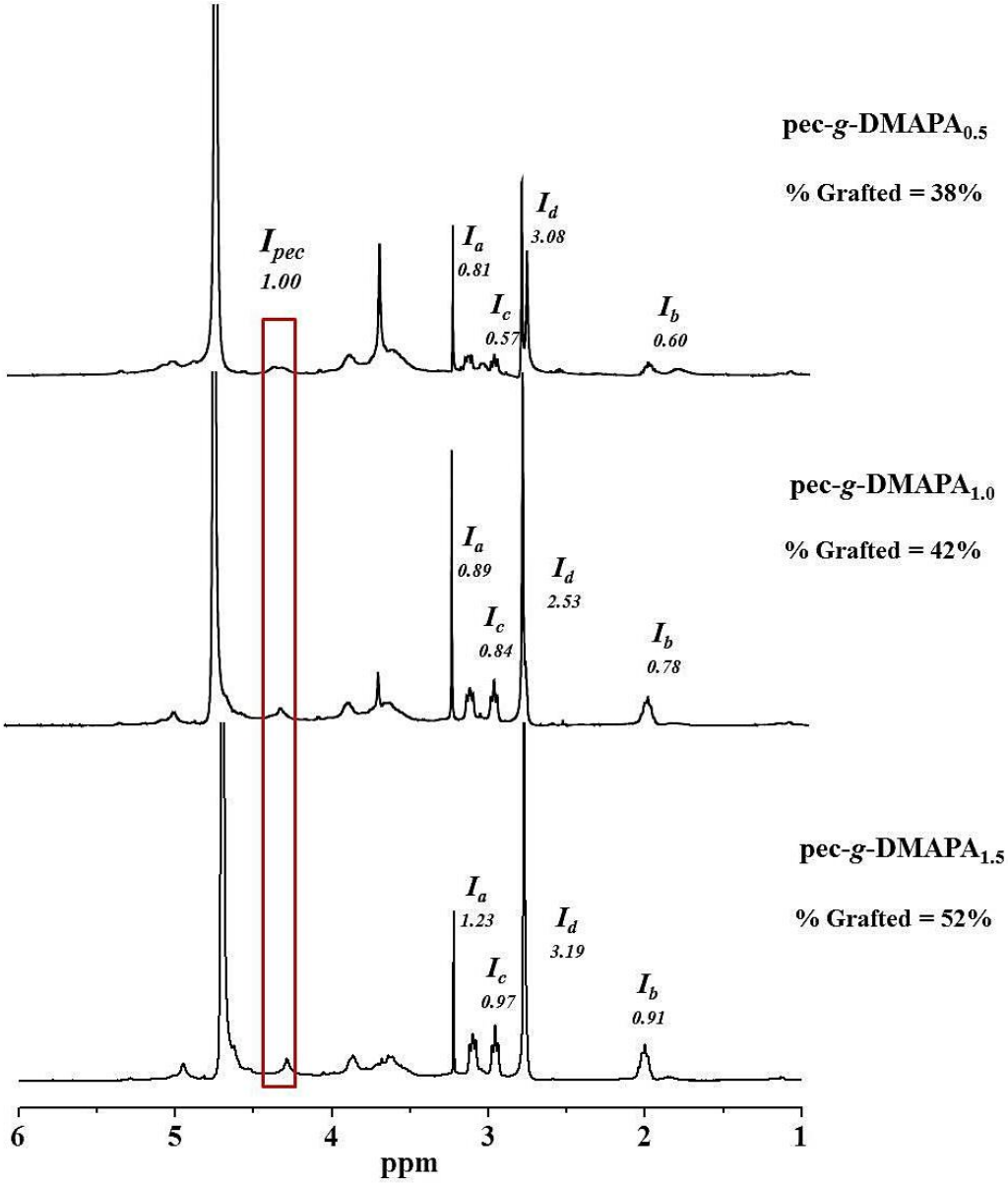

Figure 25. Grafting values for pec-*g*-DMAPA$_{0.50}$, pec-*g*-DMAPA$_{1.0}$ and pec-*g*-DMAPA$_{1.5}$

Table 2. Feeding compositions for the syntheses of pec-*g*-DMAPA copolymers and the pH of the corresponding solutions

product name	pectin (mmol)	DMAPA (mmol)	molar ratio (pectin:DMAPA)	grafting percentage	pH of solution
pec-*g*-DMAPA$_{0.5}$	5.0	2.5	1 : 0.5	38	5.49
pec-*g*-DMAPA$_{1.0}$	5.0	5.0	1 : 1.0	42	5.54
pec-*g*-DMAPA$_{1.5}$	5.0	7.5	1 : 1.5	52	5.64

Conclusion: Pectin was successfully modified by DMAPA in the reaction of EDC/NHS coupling. The modified pectin copolymers (pec-*g*-DMAPA) were successfully confirmed and characterized by ^{1}H-NMR spectroscopy technique, which showed that the grafting percentage values of pec-*g*-DMAPA$_{0.5}$, pec-*g*-DMAPA$_{1.0}$ and pec-*g*-DMAPA$_{1.5}$ were 38%, 42% and 52%, respectively. The grafting percentage obviously depended on DMAPA feeding composition which indicated that the values were increased by increasing DMAPA feeding composition. Also, the pH of the copolymer solutions was increased by increasing DMAPA composition in the pectin backbone.

References:

1. A. Allwyn Sundar Raj*, S.R., R. Jayabalan and T. V. Ranganathan. Scientific Reports 2012; 1(12).
2. Thakur, B.R., R.K. Singh, and A.K. Handa. Crit Rev Food Sci Nutr. 1997; 37(1): p. 47-73.
3. Assaf, S.M., Y.M. Abul-Haija, and M.M. Fares. Journal of Macromolecular Science, Part A. 2011; 48(6): p. 493-502.
4. Owens, H.S., H.A. Swenson, and T.H. Schultz. AMERICAN CHEMICAL SOCIETY. 1954; p. 10-15.
5. Andersen, S.M., M. Heuckendorff, and H.H. Jensen. Organic Letters. 2015; 17(4): p. 944-947.
6. Chen, J, et al.Crit Rev Food Sci Nutr. 2015; 55(12): p. 1684-98.
7. H-L Jiang1, J.-T.K., Y-K Kim1, E-M Kim3, R Arote1, H-J Jeong3, J-W Nah4, Y-J Choi1, T Akaike5, and M.-H.C.a.C.-S. Cho1. Nature Publishing Group.2007.
8. Jiang, H.L., et al. J Control Release. 2008; 131(2): p. 150-7.
9. Huynh, C.T., M.K. Nguyen, and D.S. Lee. Macromolecules. 2011; 44(17): p. 6629-6636.
10. Rosenbohm, C., et al. Carbohydrate Research. 2003; 338(7): p. 637-649.
11. Fajardo, A.R., et al.Carbohydrate Polymers. 2012; 87(3): p. 1950-1955.

Acknowledgements: Authors gratefully acknowledged The Graduate School, Chiang Mai University and Materials Science Research Center, Faculty of Science, Chiang Mai University for the financial supports. Also, the funding was partially supported by Department of Chemistry, Chiang Mai University.

D_007_PF: EFFECTS OF LOW DOSE OF GOLD NANOPARTICLES ON PERICYTES BIOLOGY

Sasikarn Looprasertkul[1], Amornpun Sereemaspun[1,3], Depicha Jindatip[1,2,*]
[1]Department of Anatomy, Faculty of Medicine, Chulalongkorn University and King Chulalongkorn Memorial Hospital, Bangkok, Thailand
[2]Department of Anatomy, Division of Histology and Cell Biology, Jichi Medical University School of Medicine, Tochigi, Japan
[3]Nanobiomedicine Laboratory, Department of Anatomy, Faculty of Medicine, Chulalongkorn University, Bangkok, Thailand
*e-mail: depicha.j@chula.ac.th

Abstract: Pericytes are located on the capillary wall and play an important role in maintaining the vascular system in physiological and pathological conditions. Several studies showed that gold nanoparticles (AuNPs) could inhibit endothelial cells proliferation, migration, invasion and tube formation. However, it should be noted that there was no report on the effect of AuNPs on pericytes. Therefore, the aim of this study was to investigate the alteration of pericyte properties after AuNPs treatment. Human pericytes from the placenta (hPC-PL) were treated with 10 ppm concentration of 20 nm-AuNPs and then observed morphology by light microscopy. Cell migration is evaluated by transwell migration assay. In addition, mRNA expression of the *Ki67* and *PDGFR-β* on pericytes were investigated by reverse transcription quantitative PCR (RT-qPCR). The results showed that 20 nm-AuNPs at 10 ppm significantly reduced cell migration, suppressed cell proliferation, and downregulated *PDGFR-β* mRNA expression of treated pericytes compared with control. Further experiments are required to study the effects of various sizes and doses of AuNPs on the pericytes including endothelial-pericyte tube formation.

Introduction: Pericytes are a perivascular cell, wrap around the capillaries including post-capillary venules and share basement membrane with endothelial cells.[1] They regulate vascular maturation, stabilized blood vessels, and control capillary diameter, hydrostatic balance, and blood flow. Moreover, pericytes can promote endothelial cell survival and migration through paracrine signaling such as PDGF-BB–PDGFR-β signaling.[2-4] Alpha-smooth muscle actin (α-SMC), desmin, neuron-glial antigen 2 (NG2), platelet-derived growth factor receptor-β (PDGFR-β) were markers of pericytes.[1]
Gold nanoparticles (AuNPs) have been generally used in nanomedicine for cell imaging, targeted drug delivery, thermal therapy, anti-angiogenesis and anti-cancer[5-8] because of their low cytotoxicity, good biocompatibility, a low production cost and ease of modifying these AuNPs.[9-11] Nowadays, AuNPs are investigated to inhibit the activity of endothelial cells including cells proliferation, migration, invasion and tube formation by targeting the heparin-binding domain of VEGF-165 with high affinity and specificity.[7, 10]

However, the effects of AuNPs on pericyte functions remained unknown. Therefore, in the present study, the effects of low-dose of AuNPs on pericyte proliferation, migration, and PDGFR-β mRNA expression were investigated.

Methodology:
Gold nanoparticles characterization: Gold nanoparticles (AuNPs), 20 nm diameter, stabilized suspension in citrate buffer were purchased from Sigma-Aldrich (741965, USA). Shape and size distribution of 20-nm AuNPs was confirmed by a transmission electron microscope (TEM; JEM-1400 plus, JEOL, USA). In addition, the absorption spectrum of the AuNPs was measured using a Multiskan GO spectrophotometer (Thermo Scientific, USA).
Cell culture: Human pericytes from the placenta (hPC-PL; Promocell, Germany) were cultured in pericytes growth medium (Promocell) supplemented with 10% SupplementMix (Promocell)

and 1% antibiotic-antimycotic (Gibco, USA) in a humidified incubator at 37°C in a 5% CO_2 incubator.

Reverse transcription-quantitative polymerase chain reaction (RT-qPCR): Pericytes (1×10^5 cells/well) were seeded into 24-well plate and incubated with 10 ppm of 20 nm-AuNPs for 24 h. Total RNA was extracted from pericytes using Trizol reagent (Invitrogen, USA) and RNA was reverse transcribed into cDNA using RevertAid first-strand cDNA synthesis kit (Invitrogen). Next, quantitative real-time RT-PCR amplification was performed on a CFX 96 thermocycler (Bio-rad Laboratories, USA). Reactions were performed in reaction mixture containing AccuPower® 2X Greenstar qPCR Master Mix (BIONEER, Korea), cDNA, each primer and PCR-grade water. The PCR protocol consisted of a pre-denaturation step of 95°C for 15 min, followed by 40 amplification cycles with 15 sec at denaturation 95°C, 20 sec at annealing 60°C and extension 20 sec at 72°C. The melting curve analysis showed only one peak for each PCR product. The qPCR primers, to detect cell proliferation marker (*Ki-67*) and *PDGFR-β* mRNA expression, used in this study are listed in Table 1. GAPDH was taken as an internal control.

Table 1. Oligonucleotide primers used in this study

Primers	Primer sequences (5 ' to 3 ')	Product size (bp)
KI-67-forward	GATCGTCCCAGTGGAGTT	195
KI-67-reverse	CCCCTTCCAAACAAGCAGGT	
PDGFR-β-forward	ACTGCCCAGACCTAGCAGTG	179
PDGFR-β-reverse	CAGGGAAGTAAGGTGCCAAC	
GAPDH-forward	GTGAAGGTCGGAGTCAACGG	107
GAPDH- reverse	TCAATGAAGGGGTCATTGATGG	

Transwell migration assay: Pericytes (1×10^5 cells/well) were seeded into 24-well plate and incubated with 10 ppm for 24 h. Cell migration assay was performed with 8-µm pore size transwell inserts (Corning Inc., USA), 200 µL of 2.5×10^4 cells-treated/well were seeded in the upper chamber and cultured in the serum-free culture medium. Culture medium with platelet-derived growth factor-BB (PDGF-BB; R&D systems, Minnesota) and 10% FBS were used as a chemoattractant in the lower chamber. After 48 h incubation, cells which moved to the lower surface of the membrane were fixed by 4% paraformaldehyde (PFA) for 10 min and stained with 1% crystal violet in 2% ethanol for 20 min. Migrating cells in all area of lower surface of the membrane were counted with inverted-phrase contrast microscope (CKX53, Olympus, Japan).

Statistical analysis: All data were shown as the mean±SEM from three independent experiments. Statistical analyses were carried out using SPSS 23.0 (SPSS Inc., USA) and GraphPad Prism 5.01 (GraphPad Software Inc., USA). Student's t-test was conducted to compare between two groups. A ρ-value was considered statistically significant *$\rho<0.05$, **$\rho<0.01$ and ***$\rho<0.001$.

Results and Discussion: The present study was designed to study the effects of low-dose of AuNPs on pericyte function. To confirm the shape, size of AuNPs, TEM micrographs were taken and. Figure 1A showed that AuNPs were identically spherical shape and the mean±SEM diameter was 20.35±0.20 nm. Figure 1B displayed that the maximum absorption wavelength of 20 nm-AuNPs was 522 nm. According to the previous study in our laboratory, the concentration of AuNPs at 10 ppm was chosen for the next experiments.

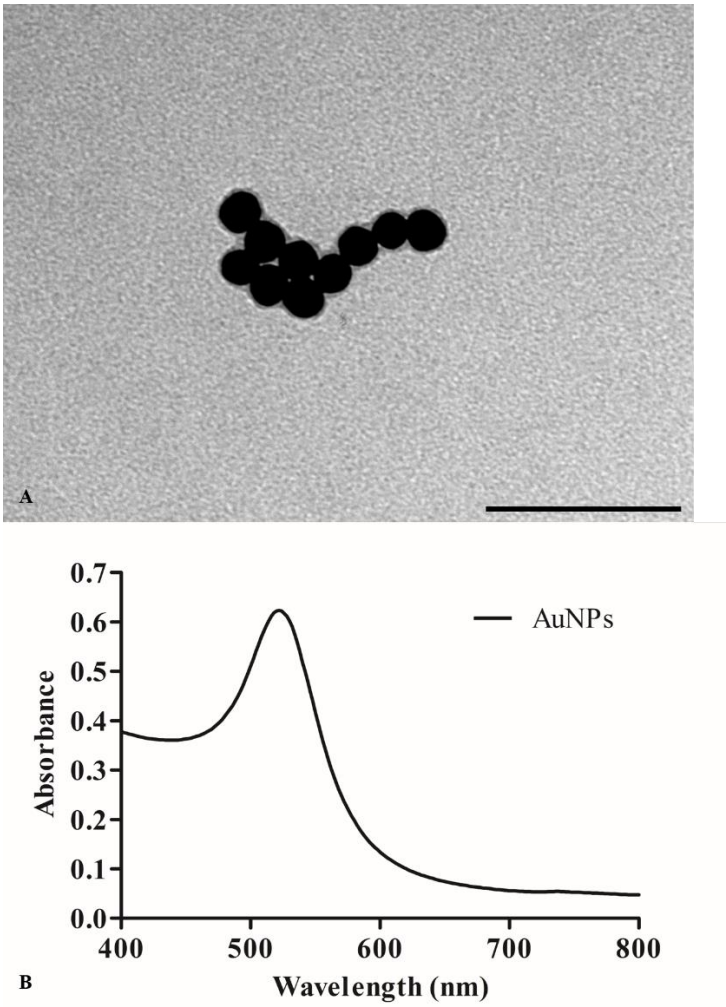

Figure 1. Characterization of AuNPs by TEM (A) and UV-Vis spectroscopy (B). Bar 100 nm

To determine the effect of AuNPS on pericytes proliferation, quantitative real-time RT-PCR was used to investigate the *KI-67* mRNA expression on pericytes. The *KI-67* mRNA expression of AuNPs 10 ppm-treated pericytes was moderately decreased compared with control pericytes (Figure 2, ***$\rho<0.001$). This result resembled the previous study which reported that AuNPs at this concentration could also reduce HUVEC, melanoma cells, and ovarian cancer cells proliferation.[12-14]

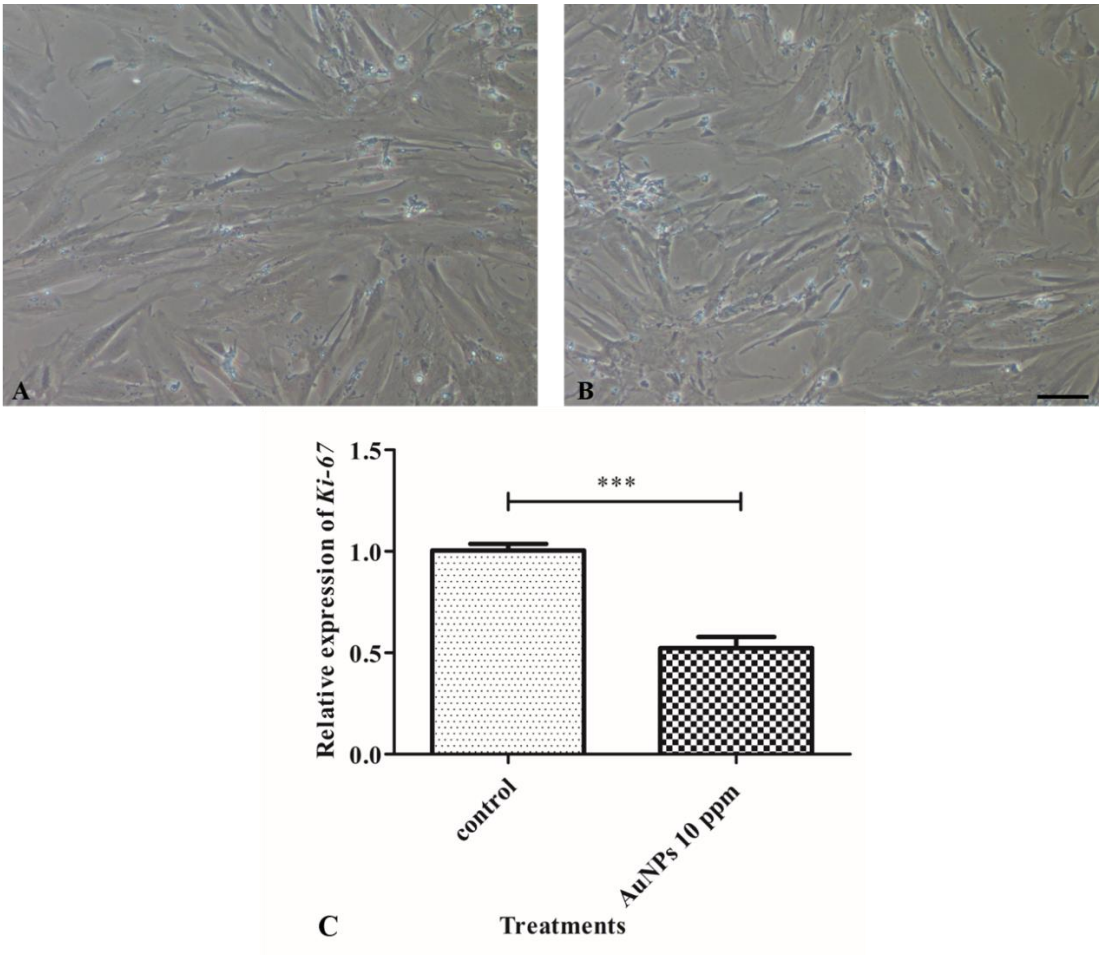

Figure 2. Effects of AuNPs on pericyte proliferation. Note: Control cells in culture medium (A), cells with 10 ppm AuNPs treatment (B), quantitative data of *KI-67* expression (C); ***$p<0.001$. Bar 100 µm

Effect of AuNPs on pericyte migration was examined via transwell migration assay. The AuNPs 10 ppm-treated migrating cells on the lower surface of the membrane were significantly decreased compared with control pericytes (Figure 3, **$p<0.01$). It is well-known that angiogenesis involves the migration of both endothelial cells and pericytes. Taken together with the report of Shen et al. (2018), it indicates that AuNPs could target all vascular cell types which, in turn, antiangiogenesis.[14]

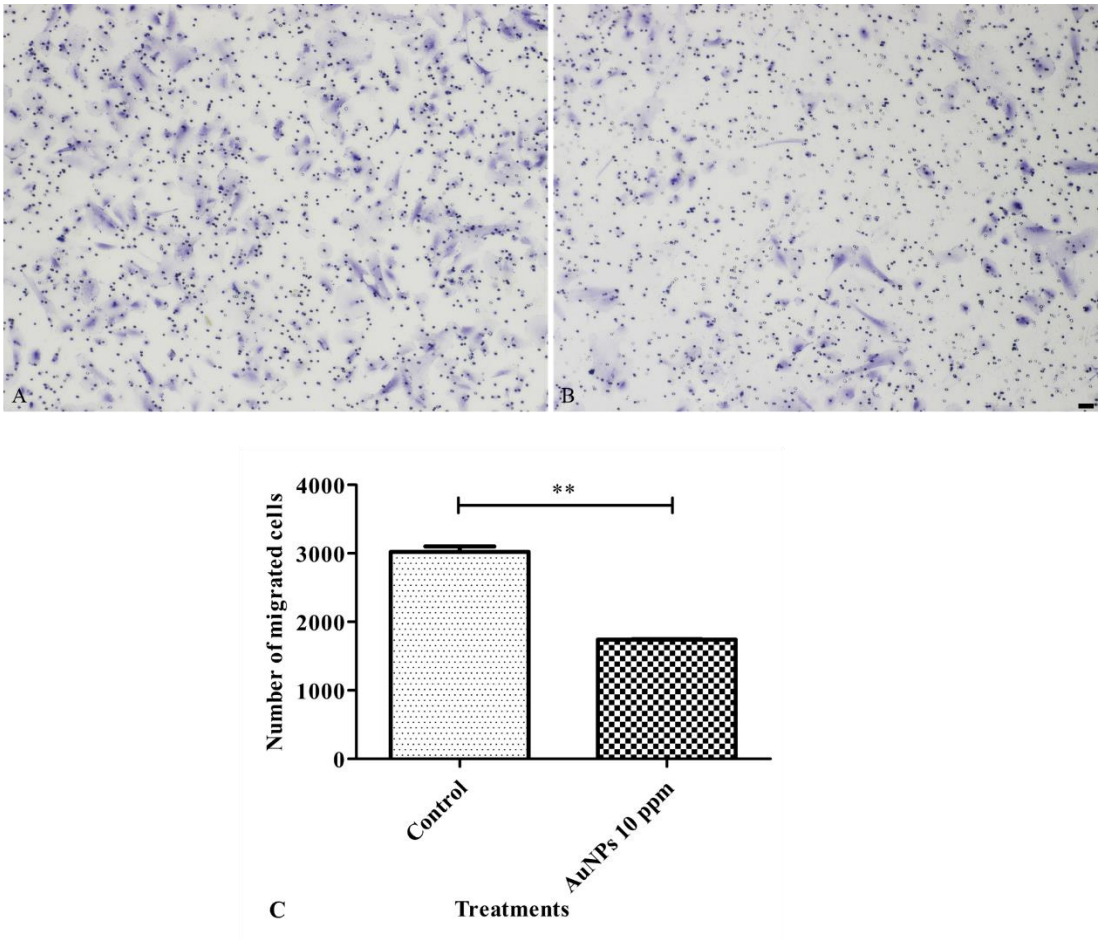

Figure 3. Effects of AuNPs on cell migration of pericytes. Note: Control cells in culture medium (A), cells with 10 ppm AuNPs treatment (B), Number of migrating cells (C); $^{**}\rho<0.01$. Bar 100 µm

The *PDGFR-β* mRNA expression of AuNPs 10 ppm-treated pericytes was decreased compared with control pericytes (Figure 4, $^{***}\rho<0.001$). This result suggested that low-dose AuNPs could affect pericytes biology. It is accepted that PDGF-BB–PDGFR-β signaling in pericyte plays an important role in cells survival, migration, proliferation, differentiation, and recruitment to vessel wall.[1] Therefore, we assume that the alteration of molecular characteristics in pericytes might result in deficit vessel formation.

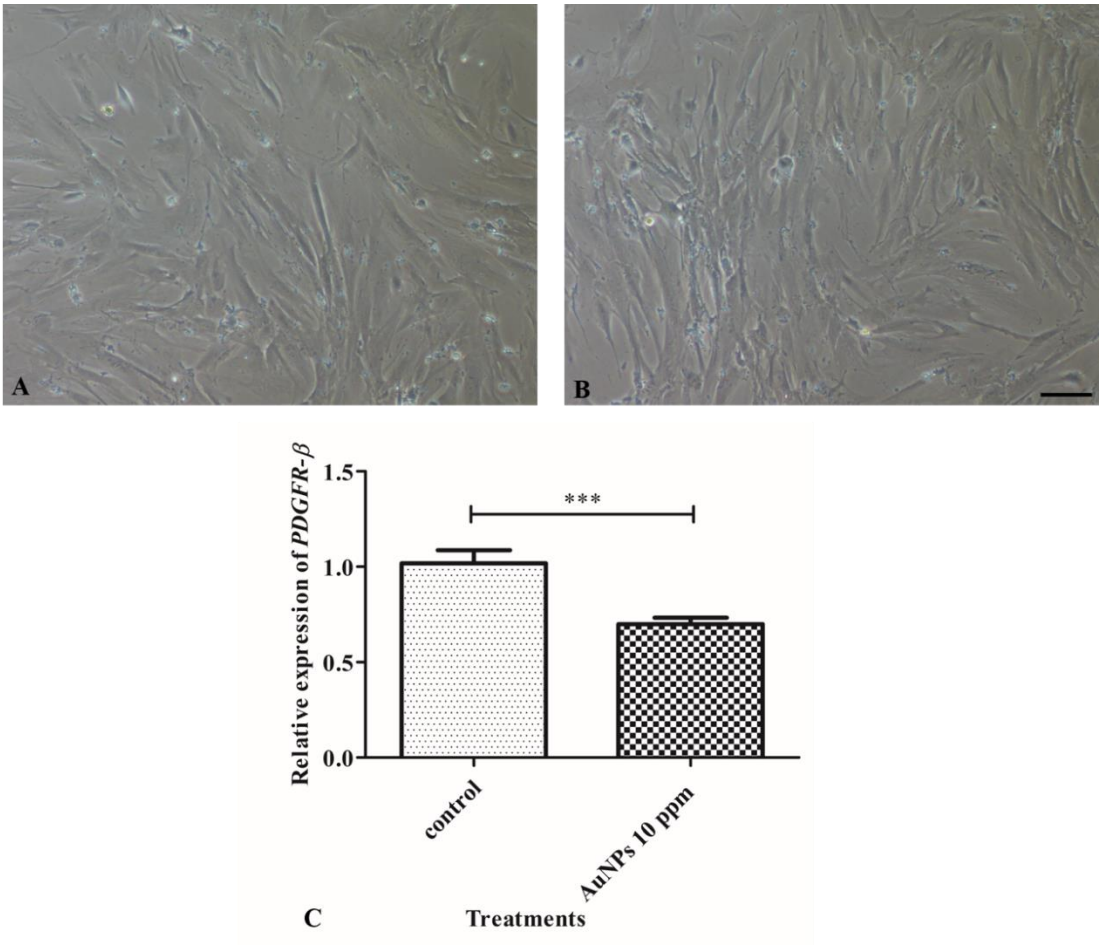

Figure 4. Effects of AuNPs on *PDGFR-β* expression of pericyte. Note: Control cells in culture medium (A), cells with 10 ppm AuNPs treatment (B), quantitative data of *PDGFR-β* expression (C); ***ρ<0.001. Bar 100 µm

Conclusion: The present study suggested that AuNPs are able to change pericyte biology including pericyte proliferation, migration, and *PDGFR-β* mRNA expression. Further study is to assess the effects of various sizes and doses of AuNPs on the pericytes.

References:

1. Sweeney MD, Ayyadurai S, Zlokovic BV. Nat Neurosci. 2016;19:771–783.
2. Winkler EA, Bell RD, Zlokovic BV. Nat Neurosci. 2011;14:1398–1405.
3. Hayden MR, Yang Y, Habibi J, Bagree SV, Sowers JR. Oxid Med Cell Longev. 2010;3:290–303.
4. Kim J, Chung M, Kim S, Jo DH, Kim JH, Jeon NL. PLoS One. 2015;10:e0133880.
5. Chithrani BD, Ghazani AA, Chan WC. Nano Lett. 2006;6:662–668.
6. Jain S, Hirst DG, O'Sullivan JM. Br J Radiol. 2012;85:101–113.
7. Liu FZ, Ma DW, Chen W, Chen XY, Qian YC, Zhao YB, et al. J Nanomater. 2019:1–12.
8. Mukherjee P, Bhattacharya R, Wang P, Wang L, Basu S, Nagy JA, et al. Clin Cancer Res. 2005;11:3530–3534.
9. Roh YJ, Rho CR, Cho WK, Kang S. Invest Ophthalmol Vis Sci. 2016;57:6561–6567.
10. Bhattacharya R, Mukherjee P, Xiong Z, Atala A, Soker S, Mukhopadhyay D. Nano Letters. 2004;4:2479–2481.

11. Wang P, Wang X, Wang L, Hou X, Liu W, Chen C. Sci Technol Adv Mater. 2015;16:034610.
12. Arvizo RR, Saha S, Wang E, Robertson JD, Bhattacharya R, Mukherjee P. Proc Natl Acad Sci U S A. 2013;110:6700–6705.
13. Lu P-H, Li H-J, Chang H-H, Wu N-L, Hung C-FJJoNR. 2017;19:342.
14. Shen N, Zhang R, Zhang HR, Luo HY, Shen W, Gao X, et al. Int J Ophthalmol. 2018;11:1269–1276.

Acknowledgements: We are grateful to the Research Affairs, Faculty of Medicine, Chulalongkorn University for assistance regarding the transmission electron microscope. This work was supported by the Ratchadaphiseksompotch Fund, Faculty of Medicine, Chulalongkorn University, grant number RA61/100.

D_015_PF: SYNTHESIS OF HIGH MOLECULAR WEIGHT POLY(*ε*-CAPROLACTONE) USING TITANIUM(IV) *n*-BUTOXIDE AS EFFECTIVE INITIATOR

Wanich Limwanich[1,*], Winita Punyodom[2,3], Puttinan Meepowpan[2,3]
[1]Faculty of Sciences and Agricultural Technology, Rajamangala University of Technology Lanna, Chiang Mai 50300, Thailand
[2]Polymer Research Laboratory, Department of Chemistry, Faculty of Science, Chiang Mai University, Chiang Mai 50200, Thailand
[3]Center of Excellence in Materials Science and Technology, Chiang Mai University, Chiang Mai 50200, Thailand
*e-mail: wanich.lim@gmail.com

Abstract: In this work, high molecular weight poly(*ε*-caprolactone) (PCL) was synthesized from the ring-opening polymerization (ROP) of *ε*-caprolactone (*ε*-CL) initiated by titanium(IV) *n*-butoxide ($Ti(O\mathit{n}Bu)_4$). The polymerizations of *ε*-CL with different concentrations of $Ti(O\mathit{n}Bu)_4$ initiator (0.025 – 0.200 mol%) were carried out under bulk condition (solvent free process) at 150 °C for 24 h. The molecular weights of the synthesized PCL were determined from the conventional gel permeation chromatography (GPC) technique. From bulk polymerization, $Ti(O\mathit{n}Bu)_4$ could control the polymerization of *ε*-CL and molecular weight of PCL. The physical appearances of the purified PCL were varied from white powder to white fiber. The number average molecular weights (M_n) of the synthesized PCL were in the range of 2.01×10^4 - 4.62×10^4 g/mol with molecular weight distribution (MWD) of 1.80 - 1.93. Furthermore, the values of %yield for the synthesized PCLs were in the range of 90 - 93%. The polymerization mechanism of *ε*-CL with $Ti(O\mathit{n}Bu)_4$ was proposed through the coordination-insertion mechanism. The condition used in this work could effectively improve the molecular weight of PCL obtained from the ROP of *ε*-CL with $Ti(O\mathit{n}Bu)_4$ reported in literature.

Introduction: Biodegradable aliphatic polyesters have considered as important material that can be used to replace the petroleum based polymer in the future. Polylactides and polylactones are the well known biodegradable polyester which can be utilized in many applications [1]. Traditionally, they are synthesized from the ring-opening polymerization (ROP) of cyclic esters through the coordination-insertion mechanism [2]. In this mechanism, many organometallic compounds especially covalent metal alkoxides (MOR) and metal carboxylates (MCOOR) have been used as initiating system. Among these, tin(II) octoate ($Sn(Oct)_2$) is the most frequently and widely used in the ROP of cyclic esters [3]. However, $Sn(Oct)_2$ is not a true initiator because it reacts with hydroxyl containing compounds to form tin(II) alkoxide before initiates polymerization [4]. The direct synthesis of tin(II) alkoxide seems to be an effective route for control of polymerization of cyclic esters and molecular weight of polymers [5]. Other metal alkoxides with different metal centers such as Al(III) [6] Sn(IV) [7] and Ti(IV) [8] were also studied and developed for control synthesis of biodegradable polyesters. Titanium(IV) alkoxide ($Ti(OR)_4$) catches our attention due to its high solubility in monomer, commercially available and high reaction rate.

Li *et al.* [8] reported the kinetics of the ROP of *ε*-caprolactone (*ε*-CL) with the novel double bond containing titanium(IV) alkoxide initiator ($Ti[O(CH_2)_4OCH{=}CH_2]_4$). Differential scanning calorimetry (DSC) was employed to investigate the dependency of polymerization rate with initiator concentration. The number average molecular weight (M_n) and molecular weight distribution (MWD) of PCLs were in the range of 9.40×10^3 - 2.37×10^4 g/mol and 1.76 – 2.36, respectively. Meelua *et al.* [9] also studied the steric interference of $Ti(OR)_4$ structure on the ROP of *ε*-CL by using non-isothermal DSC technique. Titanium(IV) *n*-propoxide, titanium(IV) *n*-butoxide, titanium(IV) *tert*-butoxide and titanium(IV) 2-ethylhexoxide were utilized as initiator in the ROP of *ε*-CL. They found that the activation energy (E_a) for the ROP of *ε*-CL initiated by titanium(IV) *n*-propoxide < titanium(IV)

n-butoxide ≈ titanium(IV) 2-ethylhexoxide < titanium(IV) *tert*-butoxide. Furthermore, they also synthesized PCL by using these $Ti(OR)_4$ initiators via bulk polymerization at 120 °C for 72 h. It was founds that the M_n of the synthesized PCLs were lower 1.88×10^4 g/mol. Moreover, their synthesis process also gave board MWD values (> 3.0) of PCLs.

Therefore, it is interesting that $Ti(OR)_4$ seems to be reactive initiator in the ROP of *ε*-CL but it produces low molecular weight of PCL. This indicates that the synthesis process reported in literatures is not suitable for $Ti(OR)_4$. This impacts our attention to develop the synthesis process that can produce higher molecular weight of PCL by using $Ti(OR)_4$ as initiator. The objective of this work is to synthesize high molecular weight PCL via bulk polymerization by using titanium(IV) *n*-butoxide as initiator. The molecular weight average and MWD of all synthesized PCLs are determined from gel permeation chromatography (GPC) technique. Furthermore, the polymerization mechanism of *ε*-CL with titanium(IV) *n*-butoxide is also described.

Methodology:

Materials preparation: *ε*-Caprolactone (Sigma-Aldrich, 99.0%) was purified by vacuum distillation and kept in round bottom flask under vacuum before used. Titanium(IV) *n*-butoxide (Sigma, 97.0%) was used as received. Methanol (Qrec, 99.0%) and chloroform (LabScan, 99.5%) were used without purification.

Synthesis of poly(ε-caprolactone) via bulk polymerization: *ε*-CL (4 g) with different concentrations of titanium(IV) *n*-butoxide ($Ti(O\mathit{n}Bu)_4$) were weighed in 10 mL dried round bottom flasks which were further closed by glass stopper under nitrogen atmosphere. The prepared reaction flasks were immersed into preheated silicone oil bath at 150 °C for 24 h. After complete 24 h, the flasks were cooled down at room temperature followed by ice bath. The obtained crude PCLs were dissolved in $CHCl_3$ and precipitated in cold methanol. The purified PCLs were dried in vacuum oven until constant weight was reached.

Polymer characterization: The molecular weight averages and molecular weight distribution (MWD) of purified PCLs were determined by gel permeation chromatography (GPC) technique (Waters e2695 GPC) at 35 °C using tetrahydrofuran (THF) as eluent.

Results and Discussion: The ring-opening polymerization (ROP) of cyclic esters with metal containing initiator can be investigated by many techniques such as gravimetry [10], spectroscopy [11] and calorimetry [6, 7, 9]. As reported by Meelua *et al.* [9], the ROP of *ε*-CL with different titanium(IV) alkoxides initiator ($Ti(OR)_4$) can be effectively investigated by differential scanning calorimetry (DSC) technique. In their work, the reactivity of four different $Ti(OR)_4$ initiators such as titanium(IV) *n*-propoxide, titanium(IV) *n*-butoxide, titanium(IV) *tert*-butoxide and titanium(IV) 2-ethylhexoxide has been compared and discussed. They found that the reactivity of $Ti(OR)_4$ in the ROP of *ε*-CL depended on the steric hindrance around Ti-O active center. The reactivity of $Ti(OR)_4$ in the ROP of *ε*-CL was determined in the following order: titanium(IV) *n*-propoxide > titanium(IV) *n*-butoxide ≈ titanium(IV) 2-ethylhexoxide > titanium(IV) *tert*-butoxide. From DSC analysis, the reactivity of titanium(IV) *n*-propoxide and titanium(IV) *n*-butoxide in the ROP of *ε*-CL is high because they initiate the polymerization of *ε*-CL at low temperature (150 °C). They seem to be more reactive than those of tributyltin(IV) alkoxides (Bu_3SnOR; R = Me, Eth, *n*Pr and *n*Bu) initiators that initiate polymerization of *ε*-CL at 180 °C [7]. Furthermore, the obtained DSC polymerization exotherms for the ROP of *ε*-CL initiated by $Ti(OR)_4$ are sharper and more symmetry than Bu_3SnOR initiators. The efficiency of all $Ti(OR)_4$ initiators in the synthesis of PCL is also investigated via bulk polymerization. Their results show that the molecular weight of PCL increases with decreasing of $Ti(OR)_4$ initiators. When compared the molecular weight of the PCL synthesized from the ROP of *ε*-CL with $Ti(OR)_4$ initiators at a similar concentration of 0.010 mol%, it is found

that titanium(IV) *n*-butoxide produces the highest molecular weight of PCL as shown in Table 1.

Table 1. GPC analysis for PCL obtained from bulk polymerization of ε-CL initiated by different $Ti(OR)_4$ initiators at 120 °C for 72 h reported in literature [9].

Initiators	$[Ti(OR)_4]$ (mol%)[a]	M_n (g/mol)[a]	MWD [a]	%Yield (%) [b]
Titanium(IV) *n*-propoxide	0.010	1.29×10^4	2.42	94
Titanium(IV) *n*-butoxide		1.85×10^4	3.13	93
Titanium(IV) *tert*-butoxide		1.57×10^4	3.21	92
Titanium(IV) 2-ethylhexoxide		1.51×10^4	3.64	93

[a] Determined from GPC technique by using THF as eluent.
[b] Calculated from the weight of PCL obtained after filtration.

It is interesting that the number average molecular weight of PCLs synthesized by the ROP of ε-CL using $Ti(OR)_4$ as initiator are low (M_n < 1.88×10^4 g/mol) and MWD values are high (> 3.0). Broad MWD values (> 3.0) indicate that the transesterification reaction occurred that decreases the molecular weight of PCL. Moreover, the molecular weight of PCL does not correspond to the reactivity of $Ti(OR)_4$ initiators. In fact, high molecular weight PCL should be obtained from highly reactive initiators. The results clearly demonstrated that the synthesis condition used in their work seem to be unsuitable for the reactive $Ti(OR)_4$ initiators.

Therefore, we try to improve the effectiveness of $Ti(OR)_4$ in synthesizing high molecular PCL via bulk polymerization. Titanium(IV) *n*-butoxide is selected because it produces high reaction rate and molecular weight of polymer. Firstly, we increase the polymerization temperature from 120 to 150 °C. From our previous work, the increasing of temperature can increase the molecular weight of PCL [6]. Moreover, we also decrease the polymerization time from 72 to 24 h to reduce the transesterification. From the results, it is found that titanium(IV) *n*-butoxide is rapidly and completely dissolved in ε-CL monomer resulting in an accurate initiator concentration. This synthesis condition is suitable for the reactive titanium(IV) *n*-butoxide initiator. The physical appearances of the synthesized PCL are depicted in Figure 1. From Figure 1, the synthesized PCLs are white powder to white fiber. The purified PCLs shown Figure 1 are further analyzed by GPC technique. The GPC analysis of those PCL samples is summarized in Table 2.

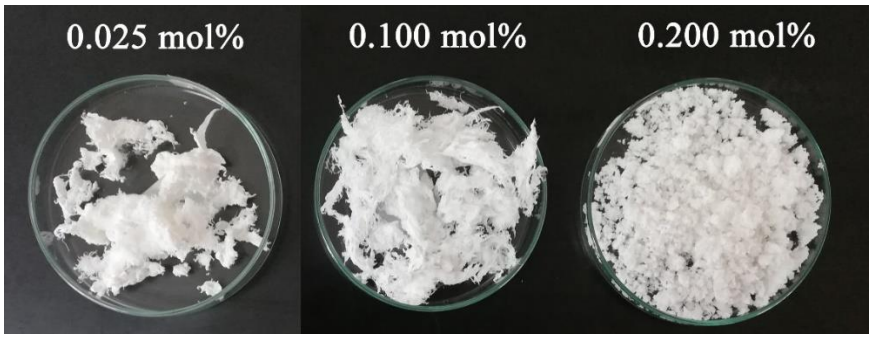

Figure 1. The physical appearances of purified PCL obtained from bulk polymerization of ε-CL initiated by different concentrations of titanium(IV) *n*-butoxide at 150 °C for 24 h.

Table 2. GPC analysis for PCL obtained from bulk polymerization of ε-CL initiated by different concentrations of titanium(IV) *n*-butoxide at 150 °C for 24 h.

[Ti(O*n*Bu)$_4$] (mol%)	M_n (g/mol)[a]	M_w (g/mol)[a]	MWD [a]	%Yield (%) [b]
0.025	4.62×10^4	8.32×10^4	1.80	91
0.100	3.14×10^4	5.84×10^4	1.86	93
0.200	2.01×10^4	4.00×10^4	1.93	90

[a] Determined from GPC technique by using THF as eluent.
[b] Calculated from the weight of PCL obtained after filtration.

From Table 2, it is found that the molecular weights of PCL are controlled by adjusting titanium(IV) *n*-butoxide concentration. The molecular weight of PCL increases with decreasing of titanium(IV) *n*-butoxide concentration similar to literatures [6, 9]. Furthermore, the molecular weights of PCL shown in Table 2 are higher than PCLs synthesized by the condition reported by Meelua *et al.* [9]. The MWD values of the synthesized PCL are also lower than 1.93 suggesting the lower amount of transesterification reaction. The highest M_n for the synthesized PCL obtained from our synthesis condition is 4.62×10^4 g/mol with titanium(IV) *n*-butoxide concentration of 0.025 mol%. In addition, titanium(IV) *n*-butoxide also produces PCL with %yield > 90%. This synthesis condition clearly confirms that titanium(IV) *n*-butoxide acts as an effective initiator that can be used in very low concentration range. For mechanistic consideration, the ROP of ε-CL with titanium(IV) *n*-butoxide is proposed through the coordination-insertion mechanism as shown in Figure 2 [6, 7, 9].

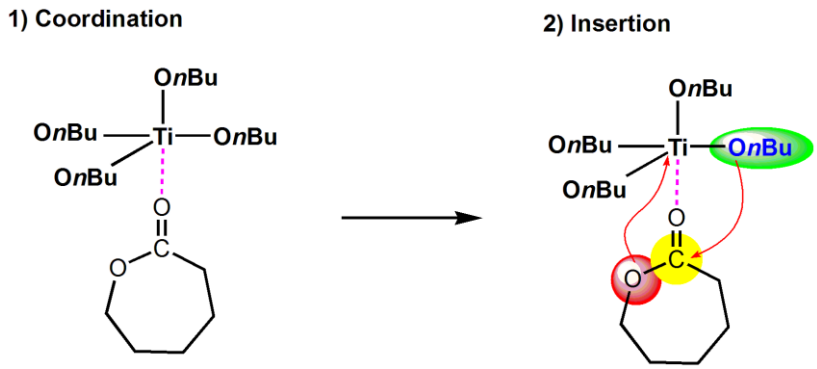

Figure 2. The coordination-insertion ROP of ε-CL with titanium(IV) *n*-butoxide initiator.

This mechanism starts by the coordination of ε-CL with reactive Ti-O bond of titanium(IV) *n*-butoxide. Then, *n*-butoxide group of titanium(IV) *n*-butoxide attacks the carbonyl carbon of ε-CL ring resulting in the cleavage of monomer ring. The opened ε-CL will insert into initiator molecule and convert to propagating specie. Another ε-CL molecule will insert into this propagating specie by the same mechanism to the first molecule yielding PCL. From the obtained results, titanium(IV) *n*-butoxide is considered as one of the powerful candidate initiator for synthesizing high molecular weight biodegradable polyesters.

Conclusion: The ring-opening polymerization of ε-CL initiated by titanium(IV) *n*-butoxide was successfully conducted via bulk polymerization at 150 °C for 24 h. Titanium(IV) *n*-butoxide was completely dissolved in monomer at all concentrations used in this work (0.025 – 0.200 mol%). From bulk polymerization, the molecular weight of PCL was controlled by titanium(IV) *n*-butoxide concentration. The highest molecular weights of PCLs (M_n = 4.62×10^4 g/mol) with 91% of yield was obtained at 0.025 mol% of titanium(IV) *n*-butoxide. The MWD values for all

synthesized PCLs were lower than 1.93 indicating the lower amount of transesterification. The results obtained from this work can be used as template for synthesizing other biodegradable polyesters. Furthermore, the scale up of the synthesis of biodegradable polymers using titanium(IV) *n*-butoxide as initiator is in our attention and still working in laboratory.

References:

1. Cabaret OD., Vaca BM., Bourissou D. Chem Rev. 2004; 101:6147-6176.
2. Stridsberg KM., Ryner M., Albertsson AC. Adv Polym Sci. 2002; 157:41-65.
3. Karidi K., Mantourlias T., Seretis A., Pladis P., Kiparissides C. Eur Polym J. 2015; 72: 114-128.
4. Storey RF., Mullen BD., Desai GS., Sherman JW., Tang CN. J Polym Sci: Part A: Polym Chem. 2002; 40:3434-3442.
5. Kowalski A., Libiszowski J., Duda A., Penczek S. Macromolecules. 2000;33:1964-1971.
6. Limwanich W., Punyodom W., Kungwan N., Meepowpan P. Int J Kinet. 2015; 47:734-743.
7. Limwanich W., Khunmanee S., Kungwan N., Punyodom W., Meepowpan P. Thermochim Acta. 2015; 599:1-7.
8. Li P., Zerroukhi A., Chen J., Chalamet Y., Jeanmaire T., Xia Z. J App Polym Sci. 2008; 110: 3990-3998.
9. Meelua W., Molloy R., Meepowpan P., Punyodom W. J Polym Res. 2012; 19:9799.
10. Purnama P., Jung Y., Hong CH., Han DS., Kim SH. Macromol Res. 2012; 5:515-519.
11. Limwanich W., Meepowpan P., Kungwan N., Punyodom W. Reac Kinet Mech Cat. 2016; 119:381-392.

Acknowledgements: The authors wish to thanks the financial supports from Chiang Mai University (WP, PM). The Department of Chemistry and Materials Science Research Center, Faculty of Science, Chiang Mai University and Faculty of Sciences and Agricultural Technology, Rajamangala University of Technology Lanna are also acknowledged.

D_019_PF: PORTABLE ELECTROCHEMICAL SENSOR FOR FENITROTHION ANALYSIS

Kanyanat Dee-ying, Chaiya Prasittichai*
Department of Chemistry, Faculty of Science, Kasetsart University, Bangkok 10900, Thailand
*e-mail: fscicyp@ku.ac.th or chaiya.pr@ku.th

Abstract: Fenitrothion (FEN) is extensively employed for crop protection from insects. The small amount of FEN has shown to inhibit the activity of acetyl cholinesterase activity causing neurotoxic effect. We report here a novel approach for electrochemical detection of FEN by surface modified halloysite nanotubes (HNTs) electrode. HNTs were surface modified with 3-trihydroxysilyl-1-propanesulfonic acid, mixed with carbon paste and form the electrode. Under the optimal conditions, a linear range from 5-30 ug/L of FEN and detection limit of 0.5 ppm (S/N =3) were obtained from the modified electrode. The modified material was also screen-printed on the flexible materials to form portable electrochemical FEN detector. The results presented here offer an alternative approach for FEN analysis that could be beneficial for several food and agricultural industries.

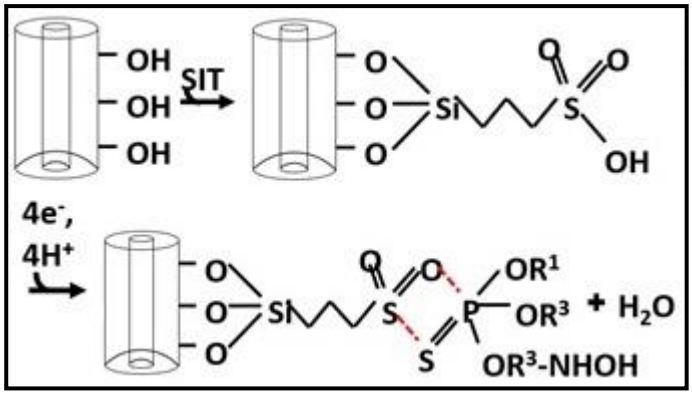

Scheme 1. Schematic diagram of SIT modified HNTs for FEN detection

Introduction: Halloysite (HNTs: $Al_2Si_2O_5(OH)_5$) is a nanotubular structure material, naturally found as a clay. The internal surface of this material is mostly alumina-oxygen octahedrons (Al-O-Al) while external surface is silica-oxygen tetrahedrons (Si-O-Si). HNTs's length, diameter and internal diameter are 800 ±300 nm, 50±10 nm and 15±5 nm, respectively.[3] Due to its long shape and difference surface chemical property, HNTs can be used for a variety of applications such as microbiological culture, load chemicals or biochemical and medical.[5] In addition, HNTs is not a toxin, environment-friendly and inexpensive. As a result, a potential use for this material is vast, especially in biomedical research.

3-trihydroxysilyl-1-propanesulfonic acid (SIT) is a organosilane superacid, comprises of long tail of $Si(OH)_3$ and superacid group at the head of the molecule.[1] Based on its chemical structure, SIT has a characteristic of both inorganic and organic property. Hence, it can be used for a phase transform of the surface from inorganic to organic once this molecule strongly attaches with the surface

Pesticides are synthetic chemicals used for extermination, deportation or inhibit growth of pest such as insect, weed and phytopathy. The agricultural sector in Thailand uses nearly 200,000 tons (nearly 30,000 million THB) a year. This cause strong concerns among consumers that some of this chemical could be left in food and could be accumulated in their body. Fenitrothion (FEN) is one of the prevalent pesticides used for insect control. FEN is an organophosphorus compound that can control insects in farm by covalently binding with enzyme AChE, a vital enzyme used for neurotransmitter production. It is also a dangerous

compound for livestock and human if there is left untreated on the agricultural products. Hence, method of detection organophosphate is essential in terms of food safety perspective.

Methodology:
Materials and chemicals: Halloysite nanoclay and mineral oil were purchased from Sigma-Aldrich (USA). 3-(trihydroxysilyl)-1-propanesulfonic acid (SIT), 30-35% in water, was obtained from Gelest Inc. (USA). Fenitrothion was procured from pestanal. Graphite powder (< 20 µm synthetic) was purchased from Sigma-Aldrich (Switzerland). Conductive epoxy was supplied from Chemtronics (USA). Nickel foam and nickel fiber was obtained from Changsha Lyrun Material Co., Ltd (China). Sodium hydroxide anhydrous pellets, sulfuric acid, ethanol absolute anhydrous, sodium acetate and glacial acetic acid were purchased from Carlo (France). All chemicals used in this paper is A.R. grade or higher. Tuberculin syringe was procured from Nipro (Thailand). All solutions were prepared using deionized water.
Preparation of the modified halloysite: Halloysite nanoclay was added into deionized water and mixed with the SIT solution. The mixture solution was stirred and adjusted pH to 6 with 1 M sodium hydroxide. Then, the mixture was continuously stirred and heated at 70 °C for 24 h. The product was collected by centrifugation and washed with deionized water and 3M H_2SO_4 for three times, respectively. The modified HNTs was dried in oven at 60 °C for 24 h. The final product appeared as white powder. This modified electrode was characterized by scanning electron microscope (SEM), Energy-Dispersive X-ray Spectrometer (EDS) and Fourier-transform infrared spectroscopy (FTIR)
Preparation of the halloysite and modified halloysite treated carbon paste electrode: The halloysite electrode was prepared by mixing the composition of graphite powder: mineral oil: halloysite (65: 30:5) using mortar and pestle. Then, halloysite paste was filled in a dropper until the desired volume. The copper wire was dissected through the halloysite paste to form an electrical connection. The modified halloysite electrode was prepared by similar fashion with the ratio of graphite powder: mineral oil: modified HNTs (65: 30: 5). A standard electrolyte to test the performance of electrodes is 5mM of potassium hexacyanoferrate(II) trihydrate ($K_4Fe(CN)_6$) in 0.1M potassium chloride (KCl).
Electrochemical measurement: Electrochemical measurement was performed in a 3-electrode setup. HHTs or modified HNTs were used as the working electrode, Pt wire as the counter electrode and Ag/AgCl as the reference electrode. The modified electrode was concentration of 20 ppm Fenitrothion in pH 4.9 acetate buffer by differential pulse voltammetry (DPV). Differential pulse voltammetry (DPV) technique was used to determine the amount of analyte. Both electrodes were held at -0.4 V for 150 s before scanned in a negative direction from -0.8 V to -0.8 V.

Results and Discussion: After the modification with SIT, the morphology of modified HNTs was verified by Scanning Electron Microscope (SEM), as shown in Figure 1. As can be seen, the appearance of SIT modified HNTs (Figure 1B) resemble the bare HNTs. This suggest that the surface modification would not interfere the nanotubular structure of HNTs, unlike other treatments. Energy-Dispersive X-ray Spectrometer (EDS), as shown in Figure 1C and Figure 1D, reveal the element compositions of bare HNTs and modified HNTs. As expected, the bare HNTs composes of mainly Al, Si and O elements; the appeared C peak is likely from the adventitious C from the *ex situ* analysis. After the modification, additional S peak noticeably appear in EDS spectrum; this is likely stem from the atomic S in SIT molecule. If using the footprint of SIT molecules at around 5 Å decorated on the HNTs tubular that has the diameter of 50 nm and 800 nm length, the full SIT coverage will have atomic% of S close to 15%. However, the atomic% of S we obtained from EDS was around 6.5 %. This suggests that we only cover half of the HNTs surface by this modification.

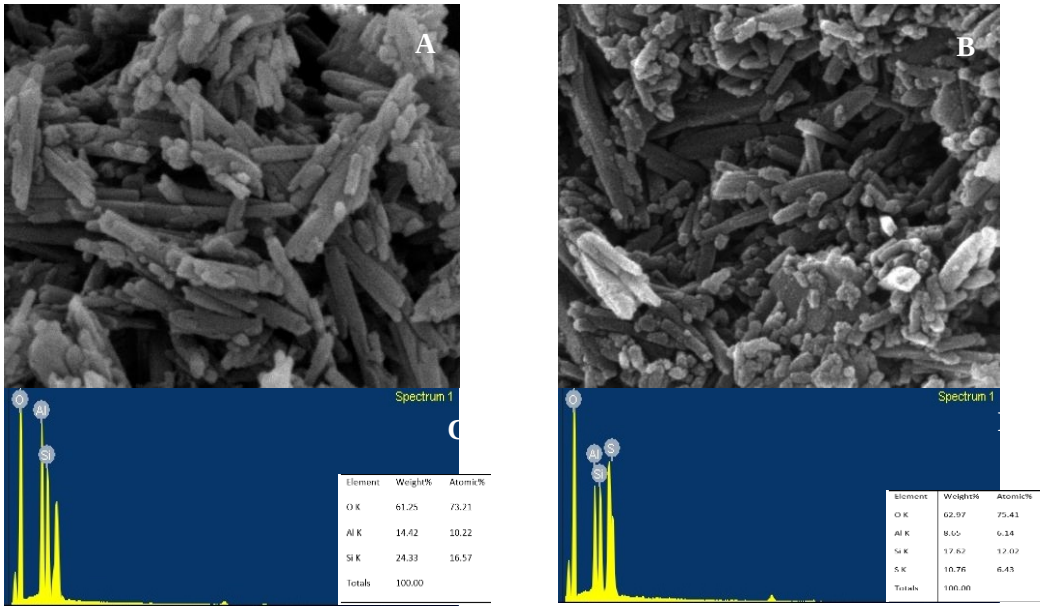

Figure 1. SEM images of (A) bare HNTs and (B) modified HNTs
EDS spectra of (C) bare HNTs and (D) modified HNTs.

Fourier-transform infrared spectroscopy (FTIR) measurement was also performed to confirm the grafting of SIT on HNTs surface. As evident in Figure 2, the additional peak of –OH and –CH FTIR spectrum appear on modified HNTs. This is likely due to the surface treatment of SIT molecules on HNTs. A separate experiment (not shown in this paper) was done to calculate the amount of SIT attachment on the surface and was able to correlate the height of –CH spectrum with the percentage coverage of SIT. Such results will be presented elsewhere. Nonetheless, the result from FTIR experiments here confirmed the grafting (partially) of SIT on the surface of HNTs that could be used for our application.

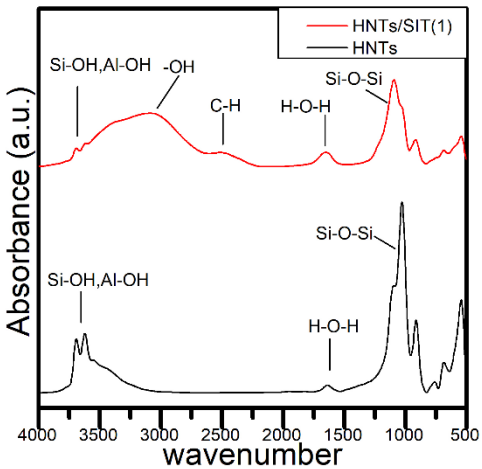

Figure 2. FTIR images of bare HNTs (red) and modified HNTs (black)

After confirming that SIT was able to attach on the surface of HNTs, we were then used this modified material to fabricate the electrode. Figure 3 show the escalation of differential pulse voltammetry (DPV) peaks as the concentration of FEN increases on the modified SIT-HNTs electrode. The linear correlation between peak height and the concentration was observed over the range from 5-30 ppm with a detection limit of 0.5 ppm. We note here that the linear range and detection limit of the measurement could be further extended if the amount of SIT was able to fully cover on the surface of HNTs. Such experiment is currently conducted in our laboratory and will be presented elsewhere.

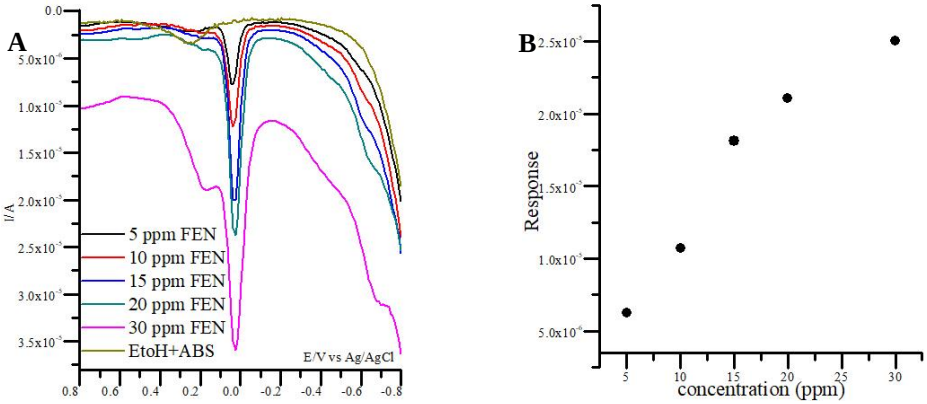

Figure 3. Differential pulse voltammetry (DPV) of FEN on modified HNT electrode in pH 4.9 acetate buffer.

To verify that the modified electrode was able to amplify FEN electrochemical detection, we compared the performance of bare carbon electrode, HNTs electrode and modified HNTs electrode for FEN electrochemical detection. The results, as shown in Figure4, revealed that modified HNTs electrode show a noticeably better performance than those two electrodes. The limit of detection of modified HNTs electrode is about 3 times lower than the HNTs electrode and about 10 times lower than carbon electrode. We reason that the enhanced performance from the modified HNTs electrode is from the combination of two reasons. First is from the increased internal surface area from HNTs that would, in turn, boost the electrochemical FEN detection. Second would be likely from the decorated SIT on HNTs surface that has strong chemical affinity toward phosphoric moiety in FEN molecules. These two factors make the SIT modified HNTs electrode a good candidate for electrochemical detection of FEN or other organophosphate molecules.

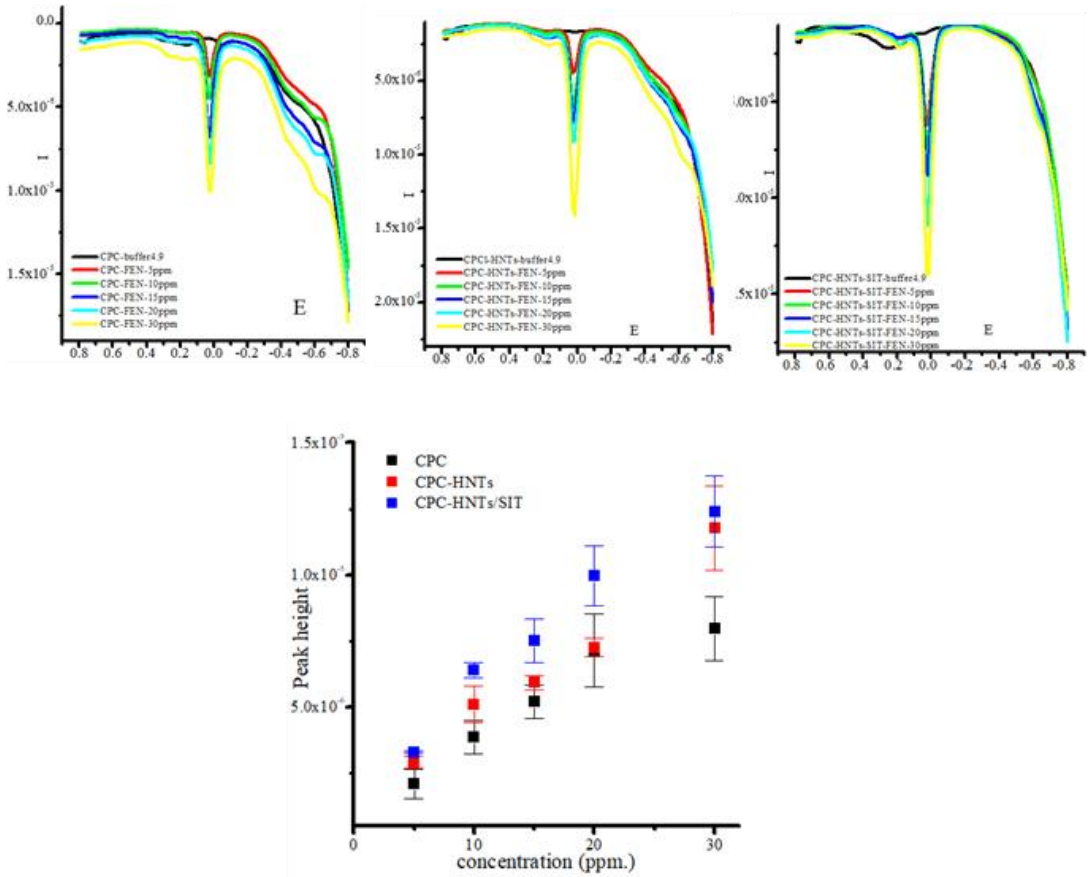

Figure 4 A comparison of differential pulse voltammetry (DPV) of FEN on carbon electrode, HNTs electrode and modified HNTs electrode in pH 4.9 acetate buffer.

Surface modified HNTs was later mixed with carbon paste and screen-printed on flexible substrate to fabricate portable FEN electrochemical sensor. The preliminary results have shown that this portable sensor is capable of sensing FEN. However, there is still a large experimental uncertainty, possibly due to a method in screen print fabrication. However, we believe that this portable sensor could potentially be used for FEN detection that could be useful for Thailand food industry.

Figure 5. A proposed portable modified HNTs screen printed electrode for FEN electrochemical detection

Conclusion: HNTs have been modified with super acid organo compound and were characterized by scanning electron microscope (SEM), Energy-Dispersive X-ray Spectrometer (EDS) and Fourier-transform infrared spectroscopy (FTIR). The surface measurement suggested a partial surface coverage on HNTs surface. The modified materials were then mixed with carbon paste to form electrode. The electrochemical response of modified HNTs electrode was linearly proportional to the concentration of FEN from 5-30 ppm with the detection limit of 0.5 ppm. The results show that this modified HNT electrode maybe an ideal device for FEN electrochemical determination.

References:

1. Jianwen H, Yonghui W, Jing R, Bin W, Tongwen X. Journal of Membrane Science. 2013;433:10-16.
2. Jin W, Masatoshi Y, Takaaki S, Hiroaki S. Sensors and Actuators B: Chemical. 2015;220: 859-863.
3. Raghuvara Y, Daniel P. O, Melgardt M. D. V, VladimirV, Yuri M. L. Int J Pharm. 2017;521: 267-273.
4. Mohammad H. D, Zahra S. N, Mohammad R. M, Mansoreh S, Mohammad A. A, Behzad H, Gordon M, Kaan Y. Chemical Engineering Journal. 2017;310:22-32.
5. Veronika P, Zdenka F, David P, Viera K, Lucy V. Mater Sci Eng C Mater Biol Appl. 2018;91: 94-102.

Acknowledgements: K.D. would like to thank Jutaporn Paothong and Orrapa Cheycharoen for useful discussions. We thank the Department of Chemistry, Faculty of Science, Kasetsart University and the Center of Excellence for Innovation in Chemistry (PERCHCIC) for research supports. We also would like to acknowledge Kasetsart University Research and Development Institute (KURDI) for financial support.

D_028_OF: NATURAL RUBBER FILM MODIFIED BY METHYLTRICHLOROSILANE FOR CREATING SUPERHYDROPHOBIC SURFACE

Patchararujee Ngamdee[1,2], Napida Hinchiranan[1,2,*]
[1]Department of Chemical Technology, Faculty of Science, Chulalongkorn University, Bangkok 10330, Thailand
[2]Center of Excellence of Petrochemical and Materials Technology, Chulalongkorn University, Bangkok 10330, Thailand
*e-mail: patchararujee.n@ku.th, napida.h@chula.ac.th

Abstract: The natural rubber (NR) film with superhydrophobic surface was successfully prepared via hydroxylation of NR to induce the -OH groups, which were the active sites for reacting with methyltrichlorosilane (MTCS), a non-fluorinated water repellent agent. The chemical structure of vulcanized NR (VNR), hydroxylated VNR (OH-VNR) and modified VNR (MTCS-VNR) was determined by using attenuated total reflectance Fourier transform infrared spectroscopy (ATR-FTIR). The results indicated that the OH-VNR prepared by immersing the VNR film in 75% sulfuric acid for 1 h showed the greatest amount of -OH groups in the NR structure. The water contact angles of modified OH-VNR with MTCS was gradually increased to 155° (2 wt% MTCS), which exhibited strong repellence to water as a superhydrophobic NR, while the VNR and modified VNR with similar MTCS content had water contact angles of 99.0° and 116° respectively. The results demonstrated that the -OH functional groups were the effective active sites for MTCS modification leading the superhydrophobic properties.

Introduction: Natural rubber (NR) is an agricultural product that has been produced in many tropical countries, mostly in Thailand. NR have been applied in various applications owing to its high-performance properties, such as good elasticity, high tensile strength, and excellent mechanical strength.[1] However, the NR price in Thailand has been falling for several years due to the sluggish global. In contrast, the amount of imported synthetic rubber products has annually increased especially for medical devices and health-care products. Thus, the modification of NR to have some unique properties those are desired for the market of medical devices and health care can extend the NR demand and its price with simultaneously decrease the amount of imported rubber products. Generally, the medical devices produced from NR have been widely used in forms of medical gloves, extension tubes, syringe plungers and wound dressing.[2] However, these medical devices require essential characteristics such as non-fouling surface for prevent the clogging of any solution in extension tubes and waterproof surface for protecting a wound from contact with water and moisture.[3] Thus, the preparation of highly hydrophobic or superhydrophobic NR surface is necessary.

Hydrophobicity is a physical property of a surface to repel water. When the water contact angle (WCA) is larger than 90°, the surface is considered as a hydrophobic surface. The superhydrophobic surface exhibiting WCA greater than 150° is attractive for industrial applications such as water-proofing, anti-fogging and self-cleaning. The preparation of hydrophobic NR surface can be divided into two ways. One is to modify the NR surface via graft copolymerization with a fluorinated compounds since they can reduce the surface tension to 6.7 mN/m when the surface is enriched with $-CF_3$ groups.[4] However, some fluorinated compounds such as long-chain perfluoroalkyltriethoxysilane (PFAS), perfluorooctyltrichlorosilane (PFOS) and octadecyltrichlorosilane (ODTS) are too expensive for using in the industrial scale. Moreover, they have high toxicity with high persistence to contaminate in the environment.[5] Another way is to modify NR surface using inorganic compounds such as silica or organosilicon monomers to form the three-dimensional silica resulting in the high roughness property. The silane compounds or modify the silica surface can be applied onto the NR surface by spray coating or dipped coating technique.[6] Unfortunately, a superhydrophobic silica coating is easily damaged by scratching off due to no

strong bonding to the NR surface resulting in very weak mechanical resistance.[7] Some previous research directly blended silica with NR to solve the problem of coating methods, but the direct blending could not significantly increase the hydrophobicity of NR surface.[8]
Therefore, the aim of this research was to increase the hydrophobicity of vulcanized NR (VNR) surface by using methyltrichlorosilane (MTCS), a non-fluorinated organosilicon monomer, to form the three-dimensional polysiloxanes through hydrolysis and polycondensation.[9] According to the polarity difference between VNR and MTCS, the VNR structure should be prior modified via hydroxylation to obtain the hydroxyl functional groups (-OH)[10] used as the active sites for reacting with MTCS. The effect of acid types, acid concentration and immersion time of VNR in acid solutions on the amount of -OH functional group in the hydroxylated VNR (OH-VNR) was observed by using attenuated total reflectance Fourier transform infrared spectroscopy (ATR-FTIR). Afterward, the chemical structure of OH-VNR after modifying with MTCS (MTCS-VNR) was analyzed by using ATR-FTIR. The hydrophobicity of the obtained products was also measured via water contact angle measurement.

Methodology:
Materials: The concentrated NR latex (60% dry rubber content (DRC)) preserved in the presence of high ammonia was purchased from Num Rubber & Latex Co., Ltd. (Trang, Thailand). All vulcanizing ingredients were received from the Rubber Research Institute (Thailand). MTCS was obtained from Sigma-Aldrich (USA). Hexane was received from RCI Labscan Ltd. (Thailand). The sulfuric acid (98%) and acetic acid (99.8%) were purchased from QREC (New Zealand). All chemicals used in this research were used as received.
Preparation of VNR film: VNR films were prepared by adding vulcanizing ingredients in the dispersion form (0.3 phr 10% potassium hydroxide, 0.2 phr 20% potassium laurate, 1.0 phr 50% sulfur, 0.2 phr 50% zinc diethyldithiocarbamate, 1.0 phr 50% zinc 2-mercaptobenzothiazole, 0.2 phr 50% zinc oxide and 1.0 phr 50% Wingstay L) into the NR latex and stirred at room temperature for 1 h. After incubation for 3 days, the mixture was casted on a glass mold (5 x 5 x 0.4 in) and left at room temperature for 3 days to obtain VNR-film with a thickness of 0.6 mm.
Preparation of hydroxylated VNR film (OH-VNR): The dry VNR film was immersed in sulfuric acid (50-98 wt%) or acetic acid (99.8 wt%) at room temperature for 1-4 h. After being washed in distilled water and dried at 60 °C in an oven until constant weight, the OH-VNR was collected.
Preparation of MTCS-VNR: The OH-VNR film was immersed into mixture consisting of 1-5 wt% MTCS in hexane. Then, the ultrapure water with equal volume to MTCS was added drop-wise and the mixture was stirred continuously for 1 h at room temperature. The OH-VNR modified by MTCS was subsequently heated at 110 °C for 1 h in an oven and then dried at 60 °C in a vacuum oven for 24 h to obtain the MTCS-VNR film.

Results and Discussion:
Appearance of VNR and OH-VNR films: The appearance of VNR and OH-VNR films obtained from hydroxylation of VNR is shown in Figure 1. It was observed that the color of VNR film (Figure 1a) was darker after immersing in the acetic acid solution (99.8 wt%) or dilute sulfuric acid solution at 50 and 75 wt% (Figure 1b). However, the flexibility of these films was not significantly different from the VNR film. When the VNR was immersed in the 98 wt% sulfuric acid, the obtained OH-VNR film was totally deformed with very poor flexibility possibly due to the over crosslinking generated from high sulfuric concentration (Figure 1c).

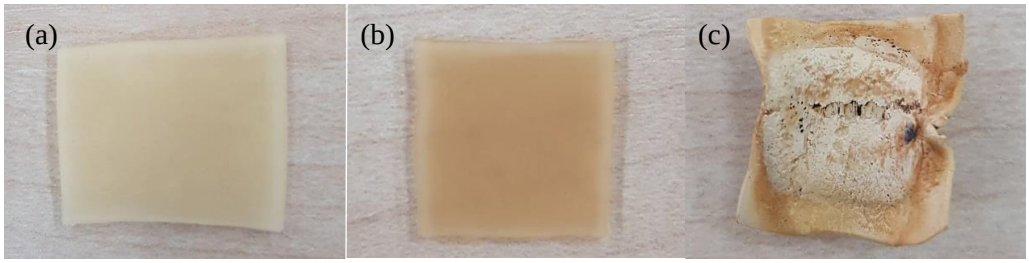

Figure 1. Images of (a) VNR film, (b) OH-VNR film (75 wt% sulfuric acid) and (c) OH-VNR film (98 wt% sulfuric acid)

Effect of reaction parameters on the amount of -OH group in OH-VNR: The effects of acid types, acid concentrations and immersion time for hydroxylation of NR on the amount of -OH group in the OH-VNR were investigated using an ATR-FTIR recorded from 500 to 4,000 cm^{-1}.The spectra of VNR and OH-VNR prepared by immersing the VNR film in 99.8 wt% acetic acid and various concentrations of sulfuric acid for 1 h and MTCS-VNR are shown in Figure 2. For the VNR film, Figure 2a shows the characteristic peaks of NR structure at 2, 849-2,967 cm^{-1} for the stretching vibration of C-H and at 833 cm^{-1} for C-C bending. Since the NR was vulcanized by sulfur, the $-CH_3$ symmetrical and asymmetric stretching vibration at 1,375 cm^{-1} and 1,452 cm^{-1}, respectively including the stretching vibration of C-S band at 752 cm^{-1} of VNR were observed. After hydroxylation in the acid solution, the OH-VNR obtained from the sulfuric acid solution at 75 wt% (Figure 2d) showed the strongest absorption peak at 3,450 cm^{-1} and 1,030 cm^{-1} attributed to the stretching vibration of O-H and C-O, respectively. The amount of -OH group in OH-VNR was calculated from the area of the hydroxyl groups (-OH) band at 3,100-3,600 cm^{-1} using the peak area of $-CH_3$ stretching at 1,452 cm^{-1} as a peak reference. The amount of -OH group in the OH-VNR structure obtained from the immersion in 99.8 wt% acetic acid and sulfuric acid solution with concentrations of 50 wt%, 75 wt% and 98 wt% for 1 h were 0.35, 1.13, 6.05 and 2.79, respectively. Hence, the OH-VNR prepared by immersion in 75 wt% sulfuric acid for 1 h was chosen for further modifying with MTCS.

Modification of OH-VNR using MTCS: The MTCS-VNR films obtained from the reaction between -OH active sites and various amounts of MTCS. Figure 2f shows that the chemical structure of MTCS-VNR film appeared at 754 cm^{-1}, 1,007 cm^{-1} and 1,268 cm^{-1} corresponded to the vibration of Si-O-Si and an asymmetric stretching peak of Si-O-C at 1,080 cm^{-1} indicated the existing of the polysiloxanes. Furthermore, the disappearance of $-CH_3$ peak in the VNR structure showed that the VNR surface was covered by polysiloxanes produced by hydrolysis and polycondensation of MTCS.

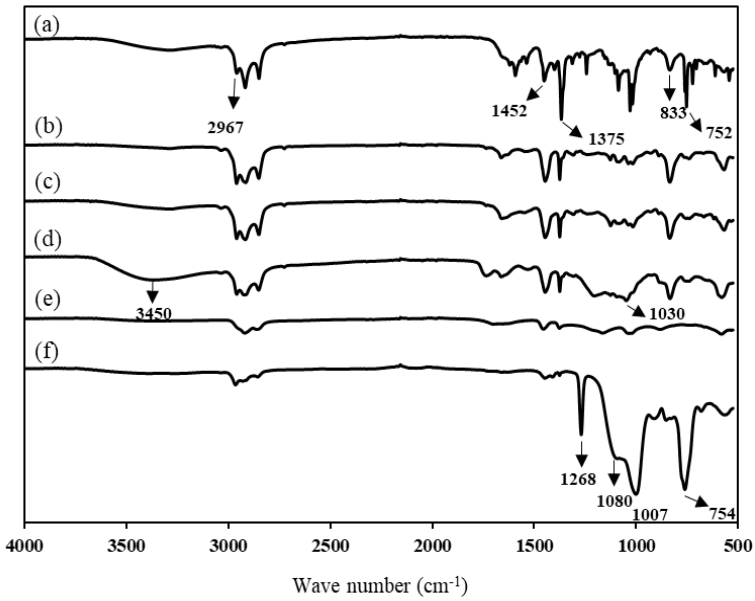

Figure 2. ATR-FTIR of (a) VNR, OH-VNR prepared in (b) 99.8 wt% acetic acid or various concentrations of sulfuric acid: (c) 50 wt%, (d) 75 wt%, (e) 98 wt% for 1 h and (f) modified OH-VNR (75 wt% sulfuric acid for 1 h with 3.70 wt% MTCS

Water contact angle: The hydrophobicity of the MTCS-VNR was demonstrated through the water contact angle measured by using a JC2000D3M device (Powereach, China) at room temperature. Table 1 shows the hydrophobicity of VNR film before and after reacting with MTCS at various concentrations. It results indicated that VNR and OH-VNR films had water contact angles of 99.0° and 64.5°, respectively. When the MTCS-VNR film prepared by using 2 wt% MTCS, the water contact angle of MTCS-VNR film increased to 155° reflecting the superhydrophobic property. Whereas, the VNR film modified with the similar MTCS content showed the water contact angle only 116°. This implied that the -OH functional groups were the effective active sites for MTCS modification leading the superhydrophobic properties.

Table 1. Water contact angle of MTCS-VNR

MTCS concentration (wt%)	Water contact angles (°)	
	VNR	OH-VNR
0	99.0 ± 4.24	64.5 ± 2.09
1.0	118 ± 5.04	151 ± 3.92
2.0	116 ± 4.23	155 ± 5.28
3.0	113 ± 2.96	142 ± 4.22
3.7	125 ± 5.65	149 ± 5.15
5.0	120 ± 6.21	151 ± 7.59

Conclusion: The superhydrophobic vulcanized NR film was successfully prepared via two step modification involving with the hydroxylation of NR and the reaction between -OH functional groups and MTCS used as a water repellent agent. The results indicated the hydroxylated vulcanized NR modified with MTCS provided the superhydrophobicity with a high water contact angle of 155°.

References:
1. Chooprayoon P, Boochathum P, J. Appl. Polym. Sci. 2019;47271:1-10.
2. Phaechamud T, Issarayungyuen P, Int. J. Biol. Macromol. 2016;85:634-644.
3. Wang P, Tan K, Eur. Polym. J. 2000;36:1323-1331.
4. Li Q, Yan Y, Appl Surf Sci. 2016;637:101-108.
5. Shen K, Yu M, Appl Surf Sci. 2017;426:694-703.
6. Wimalasiri V, Weerathunga H, J Nanomater. 2017;1:1-14.
7. Ozbay S, Erbil H, Colloids Surf., A. 2015;481:537-546.
8. Yi Y, Chen Z, J. Phys. Chem. C. 2015;119:20957-20966.
9. Liu H, Kang Y, Appl Surf Sci. 2018;451:223-231.
10. Rasid H, Azhar N, J Polym Res. 2017;24:1-11.
11. Hinchiranan N, Wannako P, Mater. Chem. Phys. 2013;139:689-698.

Acknowledgements: The authors gratefully acknowledge the Department of Chemical Technology, Faculty of Science, Chulalongkorn University for facilities and instrumental support and Center of Excellence on Petrochemical and Materials Technology for the financial support.

D_033_PF: NOVEL AND FACILE FABRICATION OF MAGNETICALLY MESOPOROUS CARBON MONOLITHS FOR REMOVAL OF TERACYCLINE

Parichart Onsri[1], Decha Dechtrirat[2,3], Laemthong Chuenchom[1,*]
[1]Department of Chemistry, Faculty of Science, Prince of Songkla University, Songkhla 90112, Thailand
[2]Department of Materials Science, Faculty of Science, Kasetsart University, Bangkok 10900, Thailand
[3]Specialized Center of Rubber and Polymer Materials for Agriculture and Industry (RPM), Faculty of Science, Kasetsart University, Bangkok, 10900, Thailand
*e-mail: laemthong.c@psu.ac.th

Abstract: Tetracycline (TC), a pharmaceutical antibiotic macromolecule, has been used in suppressing the growth of bacteria in both of humans and animals. The increase use of TC in many fields has spread its contamination to water effluents and then leads to environmental problems. Therefore, the high-efficiency removal of TC from aqueous solution has already become a crucial concern. This work exhibited the novel and facile synthesis of magnetically mesoporous carbon monoliths as an adsorbent for the removal of TC. The materials have been prepared based on carbonization of sodium alginate monolithic sponges in combination with iron ions. The obtained materials were characterized using a Scanning Electron Microscope (SEM) and the porosity was analyzed by N_2 sorption isotherm. A BET specific surface area of a selected sample has been found to be as high as 191.60 m^2/g with large mesopore volume as 76.44%. Interestingly, its porosity is found to be suitable to adsorb large TC molecules. The adsorption capacity of the monolith towards TC was 28.45 mg/g at 24 h. The result of kinetic studies favorably fitted with pseudo-second-order model which reached the equilibrium within 5 h. Furthermore, the materials also exhibited the magnetic properties, enabling the its facile removal from the solution with an external magnet.

Keywords: magnetic, porous carbon, monoliths, adsorption, tetracycline

Introduction: Tetracycline (TC), a pharmaceutical antibiotic macromolecule, is classified as a broad-spectrum drug compound that can practically prevent microbial infections (the chemical structure of TC is shown in Figure 1) [1]. However, the contaminations of TC into surroundings has posed as a possible risk to organism such as humans and animals' health and may therefore motivate allergic reactions, liver detriment, gastro-intestinal infestation and the evolution of bacterial resistance [2]. Adsorption using various types of adsorbents is one of the facile techniques for the treatment of TC [3-5]. Magnetic porous carbon materials have been widely reported as adsorbent for TC removal because of their easy removal from the system after complete adsorption [6-10]. Nevertheless, those magnetic porous carbons are in a powder form in order to increase the contact surface area and adsorption kinetics [11-15]. However, a problem of non-uniform distribution of the magnetic particles makes no guarantee of possessing the magnetic properties for every carbon particles. This could lead to secondary contamination from the non-magnetic carbon particles which are suspended in the aqueous system and cannot be removed using an external magnet. To address this concern, the magnetic porous carbons in a monolithic form is considered to be an alternative to such a powdery system. Nevertheless, no publications have reported adsorption of TC using magnetic porous carbon composite in a monolithic shape. In this study, the novel and facile synthesis of magnetically mesoporous carbon monoliths by using sodium alginate as a carbon source is explained. The sodium alginate sponges were generated *via* a simple freeze-drying process [16]. Magnetic properties were integrated into sodium alginate sponge through the simple *in-situ* addition of Fe^{3+} ions, making the whole synthesis protocol simpler when compared with other reports [17-19]. Interestingly, the magnetically porous carbon monoliths

fabricated here demonstrate a good magnetic stability and high adsorption performance towards TC. Besides, our method developed in this report can be expanded to large-scale productions.

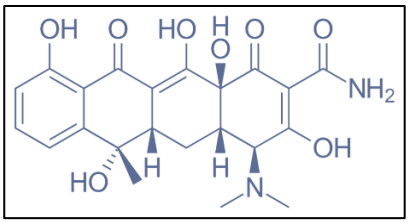

Figure 1. Chemical structure of tetracycline (TC)

Methodology:

Chemicals and reagents: All of chemicals used were analytical grade. Ferric chloride hexahydrate ($FeCl_3 \cdot 6H_2O$, 99.0%) was purchased from Loba Chemie. Hydrochloric (HCl, 37%) was purchased from J.T. Baker. Iron (III) nitrate nonahydrate ($Fe(NO_3)_3 \cdot 9H_2O$) in nitric acid 0.5 mol/L and sodium acetate anhydrous was purchased from ANaPURE. Acetic acid glacial (CH_3COOH) was purchased from RCI Labscan. 1,10- phenanthroline monohydrate was purchased from Merck KGaA. Hydroxylamine hydrochloride was purchased from CARLO ERBA REAGENTI. Deionized water (DI) was used for all experiments.

Synthesis of magnetically porous carbon monoliths: 2.0 g of sodium alginate was first dissolved in 25 ml of DI water. The homogenously viscous transparent yellow solution was then transfer into 24-well plate mold. The white porous sponges were obtained after freeze-drying method and labeled as NaAlg. Then, each of NaAlg was soaked in 10 ml of 5% $FeCl_3 \cdot 6H_2O$ for 24 h in order to make iron species (Fe^{3+}) completely diffuse into NaAlg sponge. The soaked sponges were labeled as NaAlg-Fe. After that, NaAlg-Fe was completely dried in the oven at 70 °C for 2 h. The magnetically porous carbon monolith was obtained after carbonization of NaAlg-Fe under nitrogen atmosphere at 800 °C for 2 h with the heating rate of 1°C/min. The obtained monolith was denoted as NaAlg-Fe-800. The synthesis pathway of magnetically porous materials was showed in Scheme 1.

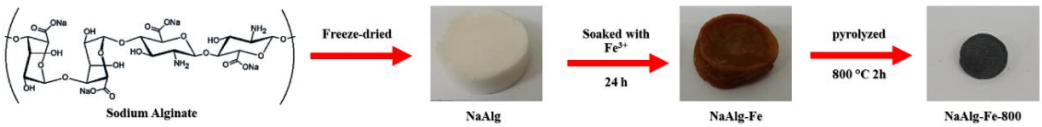

Scheme 1. The synthesis pathway of magnetically porous monoliths

Characterizations of materials: The surface morphology of magnetic carbon materials was observed using a Scanning Electron Microscope (SEM, FEI, Quanta 400). Porosity analysis of magnetic carbon materials was carried out by nitrogen sorption measurements using Surface Area and Porosity Analyzer (Micromeritics, ASAP2460) using N_2 gas at 77 K.

Determination of iron concentration: Iron concentration was analyzed by using UV-Vis spectroscopy. Since iron (II) ions can reacted with *o*-phenanthroline to form the colored complex ions, the intensity of the colored species was measured with calibration method.

Batch adsorption studies: All of adsorption experiments of NaAlg-Fe-800 towards tetracycline were carried out in batch mode with 0.02 g of adsorbent in 50 mL conical flask containers. The batch experiments were carried out in 25 ml of TC with 50 mg/L concentration in a shaker incubator (Model TOL09-FTSH-01, SCIFINETECH), with rotation speed of 250 rpm

at 30±2 °C to reach equilibrium. After complete adsorption experiments, magnetically porous carbon monoliths are conveniently separated from the solution by applying an external magnet. The concentrations of TC before and after adsorption experiments were determined using calibration method, with UV-vis spectrophotometer (UV 2600, Shimadzu) at λ = 357 nm.

For kinetic studies, magnetic adsorbent had been added into 25 mL of 50 mg/L of TC solution set in a shaker incubator, with 250 rpm at RT. Then, 0.5 mL of adsorbate was withdrawn from the solution at a predominant time interval and diluted into appropriate concentration. The adsorption capacity at pre-determined time intervals, q_t (mg/g) of NaAlg-Fe-800 toward tetracycline was calculated using equation (1):

$$q_t = \frac{V\,(C_0 - C_t)}{m} \qquad (1)$$

where C_0 and C_t are the initial concentration and concentration at pre-determined time intervals (t) of tetracycline (mg/L), respectively. V is the volume of tetracycline solution (L), and m is weight of NaAlg-Fe-800 (g).

Results and Discussion: The sponge monoliths can facilely be generated by freeze-drying method. Figure 2B demonstrated that the freeze-dried sponge was in a cylindrical shape with the height of 0.5 cm and diameter of 1.5 cm, similar to the size of the mold used. Since the density of sponge material was rather high (0.88 g/cm^3) (Table 1), the complete diffusion of iron ions into the whole sponge was found to be completely within 24 h (Figure 2A and Figure 2C). This can be confirmed by observing the uniform yellow color of cross-section of NaAlg-Fe (Figure 2D). The proportion of Fe^{3+} uptake into NaAlg sponge was determined by using UV-Vis spectrophotometer at λ= 510 nm, and was found to be 29.286±0.002. After pyrolysis, the magnetic porous carbon monoliths were obtained with the height of ~0.1 cm and diameter of ~0.6 cm (Figure 2E). These materials can float on the water surface since the density of those was only 0.03 g/cm^3 significantly lower than density of water (1 g/cm^3). The floating behavior is even more attractive considering the facile removal from the aqueous system.

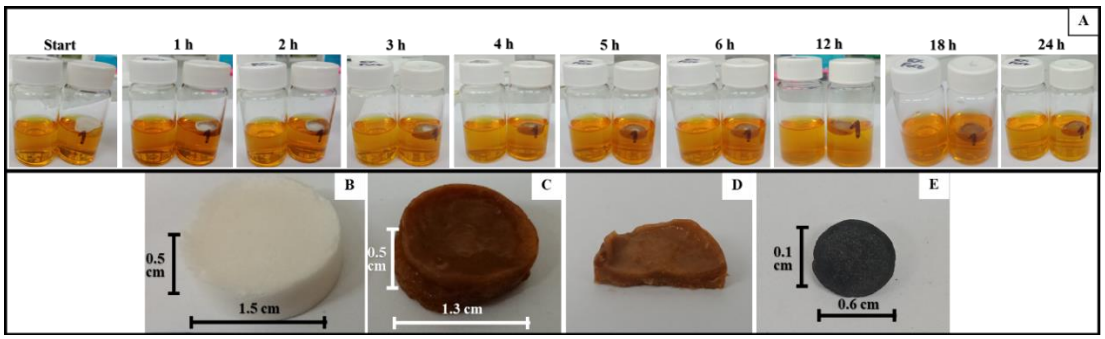

Figure 2. The photograph of time-dependent on diffusion of iron species into NaAlg sponge (A); NaAlg (B); NaAlg-Fe (C); cross-section of NaAlg-Fe (D) and NaAlg-Fe-800 (E)

The densities of the as-prepared NaAlg and the materials incorporated with iron ions are shown in Table 1.

Table1 Data of the prepared monoliths

Samples	Weight (g)	Density (g/cm^3)	% Fe^{3+} uptake	% yield
NaAlg	0.077±0.004	0.88		
NaAlg-Fe	0.086±0.005	0.13	29.286±0.002	
NaAlg-Fe-800	0.0227±0.002	0.03		29.48%

The surface morphology of NaAlg-Fe-800 was observed using SEM technique. In one hand, surface of NaAlg-Fe-800 was permeated with iron particles covered all area of materials (Figure 3A), but many cracks are obviously seen, confirming the open entrance from the sample surface. This smooth morphology may be generated from the direct contact of the surface to the heat during carbonization, leading to the fuse of the outer surface layers.

On the other hand, SEM images of cross-section in Figure 3B demonstrated the existence of macroporous structures indicating to possible rapid accessibility for guest molecules into adsorption sites. The generation of such macropores of such sodium alginate system is typical for the materials undergo freeze-drying process due to the sublimation of ice crystals.

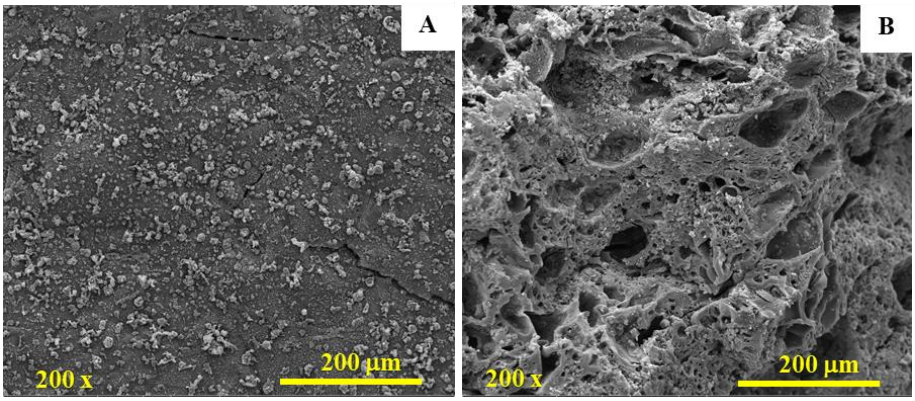

Figure 3. SEM images on surface (A) and cross-section of NaAlg-Fe-800

Porosity analysis of NaAlg-Fe-800 was investigated by using nitrogen sorption isotherm. Figure 4A displayed type IV isotherm indicating to the present of mesoporous structures. The pore size distribution was further studied in detail by fitting with Density Functional Theory (DFT) presented in Figure 4B. Pore size distribution of NaAlg-Fe-800 was obviously observed to possess most of the pores in the range of 2-15 nm. The mesopore sizes found in NaAlg-Fe-800 can be explained by the activation using the iron ions, leading to the formation of mesopores around iron particles. It is interesting to note that our developed synthesis protocol needs no extra toxic activating agents, making our process even facile and environmentally friendly.

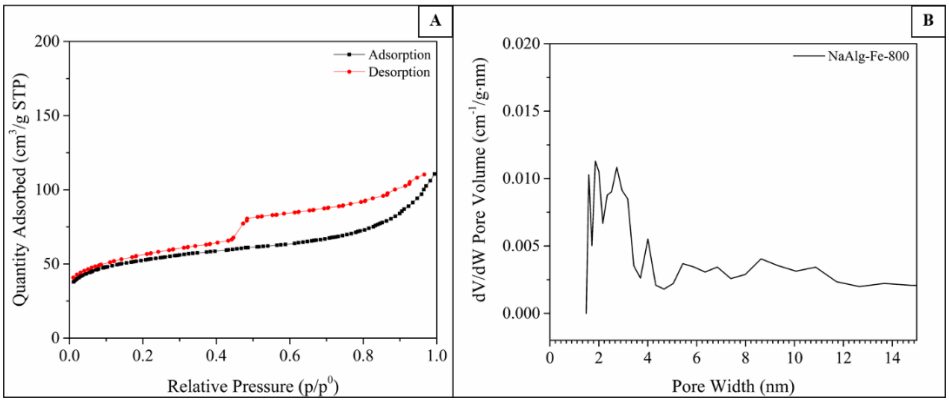

Figure 4. Type IV N_2 adsorption-desorption isotherm (A) and pore size distribution of NaAlg-Fe-800 (B)

Table 2. Calculated data from N_2 sorption measurement of NaAlg-Fe-800

Sample	Specific surface area (m^2/g)[1]	Total pore volume (cm^3/g)	Micropore volume (cm^3/g)[2]	Mesopore volume (cm^3/g)	%Mesopore volume
NaAlg-Fe-800	191.60	0.164	0.038	0.125	76.4

[1]Specific surface area was analyzed by using Brunauer–Emmett–Teller (BET) theory.
[2]Micropore volume was calculated by fitting with *t*-plot.

In addition, NaAlg-Fe-700 illustrated the specific surface area of 191.60 m^2/g and %mesopore volume reached 76.4% (Table 2) which was suitable for adsorption of large molecules, like TC in this case. Interestingly, the high value of specific surface area and %mesopore volume in this study were provided *via* the simple step and without any activation.

Batch adsorption studies : Adsorption efficiency toward TC on the synthesized magnetic porous carbon monoliths, NaAlg-Fe-800, was studied using batch experiments. The result of adsorption kinetic in Figure 5A presented that the adsorption capacity reached to equilibrium within 5 h, with the max adsorption capacity of 28.45 mg/g at 24 h. Furthermore, the adsorption kinetics of TC on NaAlg-Fe-800 was appropriately fitted with pseudo-second-order model (Figure 5B). The insert picture showed that the magnetic properties of NaAlg-Fe-800 can be retained even after adsorption experiments.

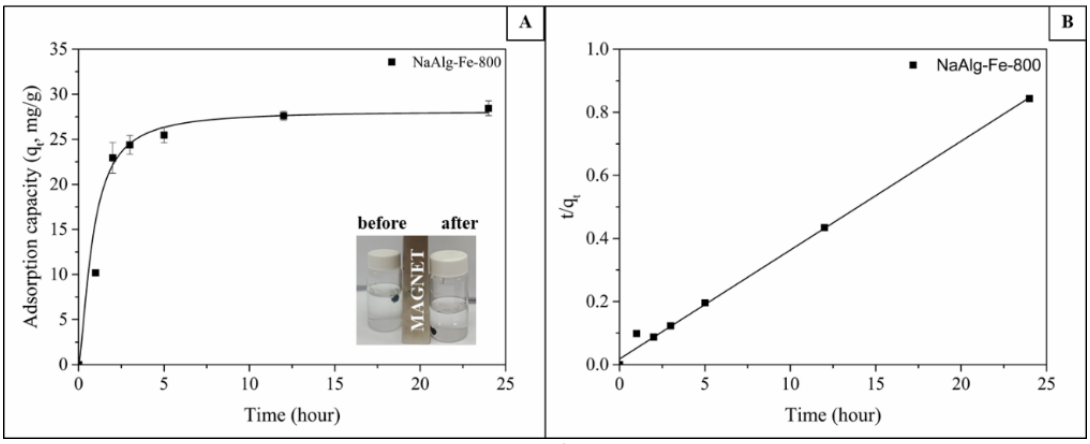

Figure 5. The plot of adsorption capacity (q_t, mg/g) of NaAlg-Fe-800 toward TC vs time (hour) (A); the insert picture of magnetic property of NaAlg-Fe-800 before and after adsorption experiments and pseudo-second-order plot with correlation coefficient (R^2) = 0.9957 (B)

Conclusion: Magnetically mesoporous carbon monoliths were successfully prepared using sodium alginate as a template and carbon source and Fe^{3+} as magnetic precursor through the novel and facile process. The highly %mesopore volume reached to 76.44% was suitable attractive for TC removal. The adsorption capacity of NaAlg-Fe-800 toward TC was high as 28.45 mg/g at 24 h. Our mentioned preparation method in this study was attractive for expansion to large-scale production.

References:

1. Zhang L, Chen L. ACS Appl. Mater. Interfaces. 2016;8:16248-16256.
2. Patyra E, Przenioslo-Siwczynska M, Grelik A, Kwiatek K. MED WETER. 2019;75:280-286.
3. Wan DJ, Wu LR, Liu YD, Chen J, Zhao HL, Xiao SH. J. Am. Chem. Soc. Langmuir. 2019;35:3925-3936.
4. Fan SS, Wang Y, Li Y, Wang Z, Xie ZX, Tang J. ENVIRON SCI POLLUT R. 2018;25: 29529-29540.
5. Chang ZS, Dai JD, Xie AT, He JS, Zhang RL, Tian SJ, Yan YS, Li CX, Xu W, Shao R. IND ENG CHEM RES. 2017;56:9367-9375.
6. Hu AB, Yang XF, You QL, Liu YY, Wang QY, Liao GY, Wang DS. J. Mater. Sci. 2019; 54: 2712-2728
7. Rattanachueskul N, Saning A, Kaowphong S, Chumha N, Chuenchom L. Bioresour Technol. 2017;226:164-172.
8. Alatalo SM, Daneshvar E, Kinnunen N, Mesceriakovas A, Thangaraj SK, Janis J, Tsang DCW, Bhatnagar A, Lahde A. CHEM ENG J. 2019;373:821-830.
9. Aydin S, Aydin ME, Beduk F, Ulvi A. SCI TOTAL ENVIRON. 2019;670:539-546.
10. Zhu XD, Liu YC, Qian F, Zhou C, Zhang SC, Chen JM. Bioresour Technol. 2014;154:209-214.
11. Xie AT, Cui JY, Chen YY, Lang JH, Li CX, Yan YS, Dai JD. J. Alloys Compd. 2019; 784:76-87.
12. Zhu XD, Liu YC, Zhou C, Luo G, Zhang SC, Chen JM. Carbon. 2014;77:627-636.
13. Chen SQ, Chen YL, Jiang H. Ind. Eng. Chem. Res. 2017;56:3059-3066.
14. Tang L, Yu JF, Pang Y, Zeng GM, Deng YC, Wang JJ, Ren XY, Ye SJ, Peng B, Feng HP. CHEM ENG J. 2018;336:160-169.
15. Oladipo AA, Ifebajo AO, Nisar N, Ajayi OA. Wat Sci Tech. 2017;76:373-385.
16. Pettignano A, Tanchoux N, Cacciaguerra T, Vincent T, Bernardi L, Guibal E, Quignard F. Carbohydr. Polym. 2017;178:78-85.
17. Lou JQ, Xu X, Gao YF, Zheng DZ, Wang JY, Li ZG. RSC Adv.2016;6: 112166-112174.

18. Li MF, Liu YG, Liu SB, Zeng GM, Hu XJ, Tan XF, Jiang LH, Liu N, Wen J, Liu XH. J. Colloid Interface Sci. 2018;52:150-159.
19. Ma JQ, Yang QF, Xu DM, Zeng XM, Wen YZ, Liu WP. ENVIRON SCI POLLUT R. 2017; 24: 3820-3828.

Acknowledgements: Parichart Onsri was grateful Department of Chemistry, Faculty of Science, Prince of Songkla University, Thailand for the research facility and Thailand and Science Achievement Scholarship of Thailand for the financial support.

D_037_OF: ENHANCING HYDROPHOBICITY OF PVDF HOLLOW FIBER MEMBRANE BY PLASMA INDUCED AND GRAFTED WITH CHLOROALKYLSILANES

Hanh Le Thi My[1,2,3], Rattachat Mongkolnavin[4], Roongkan Nuisin[5], Sermpong Sairiam[2,3,5,*]
[1]International Postgraduate Program in Hazardous Substance and Environmental Management, Chulalongkorn University, Bangkok 10330, Thailand
[2]Center of Excellence for Environmental and Hazardous Waste Management, Chulalongkorn University, Bangkok 10330, Thailand
[3]Research Program of Industrial Waste Management-Policies and Practices, Center of Excellence for Environmental and Hazardous Waste Management, Chulalongkorn University, Bangkok 10330, Thailand
[4]Department of Physics, Faculty of Science, Chulalongkorn University, Bangkok 10330, Thailand
[5]Department of Environmental Science, Faculty of Science, Chulalongkorn University, Bangkok 10330, Thailand
*e-mail: sermpong.s@chula.ac.th

Abstract: PVDF hollow fiber membranes were modified by plasma activation with different plasma gases (i.e., Ar and O_2) followed by direct grafting with two different chloroalkylsilanes (methyltrichlorosilane (MTCS) and trimethylchlorosilane (TMCS)) at varies of grafting times to enhance the hydrophobicity. The results showed that membrane activated by oxygen plasma gas gave better results compared to which activated by argon plasma gas. In particular, after activated by plasma gases at applied voltage of 8 kV then followed by grafted with 0.02M MTCS for 2h, the water contact angle (WCA) of the modified membrane were increased from 70.5° (original) to 108.1° and 119.4° by Ar and O_2 plasma activation, respectively. Besides, MTCS poses more effect on membrane hydrophobicity enhancement than TMCS. In which, hydrophobic particles were found on membrane surface by SEM using MTCS modification, while the membranes surface grafted by TMCS did not change. The silicon (Si) and oxygen (O) contents on the surface of modified membrane increased compared to the original and activated membranes. The presence of Si on the membrane surface of membranes by EDS proved that PVDF membranes were successfully modified by MTCS. The surface modification under O_2 plasma activation at applied voltage of 8 kV followed by grafting with 0.02M MTCS for 4h showed higher water contact angle.

Introduction: Poly (vinylidene fluoride) (PVDF) membranes is a polymer material that has been widely used in various aspects of the environmental field, such as oil/water separation, salt rejection, water distillation, and wastewater treatment. This material is increasingly popular because of its easy fabrication, its mechanical properties, its excellent chemical resistance ability against corrosive chemicals (such as acid, alkaline), its thermal stability and its high hydrophobic properties.[1,2] Although PVDF membranes are highly hydrophobic, the wetting problem can occur after long-time operation, which can reduce the mass transfer efficiency. To improve the wetting preventable of PVDF membrane, many studies have been focused on improving the hydrophobicity of membrane.

Recently, organosilane has been successfully grafted on the surface of the ceramic membrane to improve the hydrophobicity. Organosilane refers to a molecule which has one Si atom connected with four functional groups, SiX_4. During the grafting process, these functional groups react with -OH groups of ceramic membrane then form hydrophobic membrane. Among them, chloroalkylsilanes have been a great interest for membrane surface modification because of their low cost and their fast-covalent coupling reaction rates.[3] Chloroalkylsilanes have been successfully used for ceramic hollow fiber membrane surface grafting,[4] PVDF membrane surface grafting by chemical vapor deposition,[2] and

cellulose-based paper surface coating.[3] To the best of our knowledge, chloroalkylsilanes have never been used for PVDF hollow fiber surface modification by direct grafting.

To introduce -OH groups onto PVDF membrane surface, chemical activation methods and plasma activation have been used. Chemical modification is a simple method that membranes are immersed onto alkali solution for a short period of time to introduced -OH group onto membrane surface. However, this method effect on physical properties of membrane, even at low solution concentration.[5,6] In contrast, plasma activation method has less effect on membrane properties. In addition, plasma methods also provide more surface binding energy, which enhances the grafting ability of membrane.[7]

Zheng *et al.* (2009) modified PVDF membrane surface by using O_2 plasma activation and grafted by methyltrichlorosilane (MTCS) vapor with the solution concentration of 33 % (w/w). The result showed that the WCA of membranes was increased from 88° to 134° after grafted by chemical vapor.[2] However, the chemical vapor method is very expensive due to a large number of chemicals required for the vapor grafting process. In this work, PVDF hollow fiber membranes were modified by plasma activation and simple direct grafting process by methyltrichlorosilane (MTCS) and trimethylchlorosilane (TMCS) at low concentration to form the hydrophobic membrane surface.

Methodology: To enhance the hydrophobicity, the PVDF hollow fiber membranes were modified using the plasma activation and direct grafting method as follow.

Membrane activation: Plasma activation step was conducted using pulsed inductively coupled plasma (PICP) machine. Three different types of plasma gases, i.e., argon, and oxygen, were used to activate the membrane surface under pressure of 0.25 mbar and plasma activation time of 1 shot. The applied voltage varied from 8 kV to 10 kV.

Membrane grafting: MTCS and TMCS were dissolved to 0.02M by toluene. After being treated with plasma, the activated membranes were immersed in MTCS and TMCS immediately at various grafting times (0.5-4h). Then, the grafted membranes will be rinsed with pure toluene three times to remove any unreacted chemicals from the membranes and were dried at 60°C in an oven for two hours. Finally, the membranes were kept at room temperature (25°C) before characterization.

Characterizations: After being treated by each modifying step, membrane samples were taken to analyze water contact angle by tensiometer (DCAT 11, Dataphysics, Germany), and membrane surface by scanning electron microscopy (SEM) (JEOL, JSM-IT500HR) coupled with energy dispersive X-ray (EDS) with an accelerating voltage of 15.0 keV. The membrane surface was coated with gold under vacuum condition to avoid the electrostatic changing.

Results and Discussion:

Effect of plasma gases: The differences of WCA changed after modification under different plasma activation gases and different operating condition is demonstrated in Figure 1. The changing on WCA results of modified membrane with and without plasma activation were compared. In which, after grafted with 0.02M MTCS for 2 hours, all modified membranes activated by plasma gave higher water. After activated under the same plasma operating condition followed by grafted with 0.02M MTCS for 2h, the WCA of membrane activated by oxygen was much higher than which activated by argon plasma gas and air plasma gas. In particular, WCA of the modified membranes were increased from 70.5° (original) to 108.1° and 114.8° and by Ar and O_2 plasma activation, respectively. The reason of this result is that active plasma gas such as oxygen gas can directly introduce -OH groups to membrane surface; whereas, inert plasma gas such as argon only can generate active radicals on to membrane surface then form the -OH groups after exposure to the air.[8]

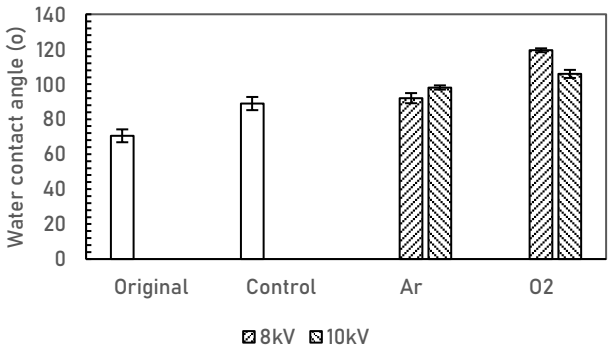

Figure 26. The WCA of grafted membranes activated by different plasma gases and different plasma applied voltage under operating pressure at 0.25 mbar, and grafting time of 1 shot and grafting condition of 0.02M MTCS for 2 hours

Effect of plasma operating conditions: After grafted by 0.02M MTCS for 2h, the WCA of membranes activated by argon plasma gas was increased from 92° to 98.1° when the applied voltage increased from 8kV to 10 kV, while that of membranes activated by oxygen plasma gas was declined from 119.4° to 105.9°. It could be explained that the amount of active radical increased with the increasing of applied voltage; thus, the WCA of membrane activated by argon plasma gas was increased when the applied voltage increased. Besides, the plasma temperature also increased when the applied voltage increased. However, plasma temperature poses a negative effect on the process of introducing -OH groups on to membrane surface of oxygen gas, leading to the decreasing of WCA.

Effect of chloroalkylsilanes and grafting time: Figure 2 shows the differences of WCA change of membrane grafted by two different chloroalkylsilanes and different grafting time, under the activation condition of oxygen plasma gas, applied voltage of 8 kV and plasma treatment time of 1 shot. The WCA after grafted by MTCS and TMCS increased with time. The WCA of membrane grafted by MTCS increased rapidly from 70.5° to 114.8° after 0.5h, then continuously increased to 123.1° after 4h, while the WCA of membrane grafted by TMCS did not change much, which increased from 70.5° to 76.2° after 4h. The reason of this difference is because MTCS has three functional sites available for bonding molecules with -OH groups on membrane surfaces, while TMCS has only one [4]. The modification process is shown in Figure 3.

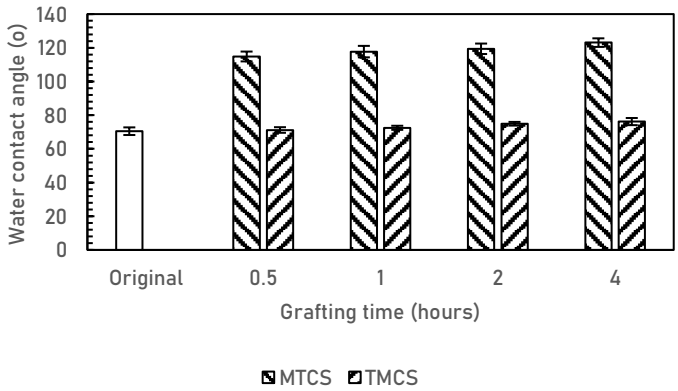

Figure 27. Effect of grafting time and chloroalkylsilanes under activation condition of oxygen plasma gas, 8kV, 1 shot.

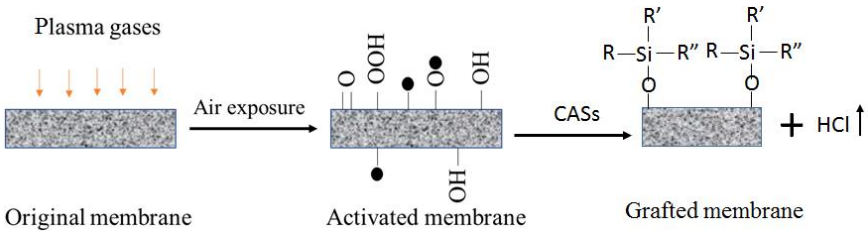

Figure 28. PVDF membrane modification by methods of plasma activation followed by CAS direct grafting

Figure 4 shows the SEM results of membrane surface after modifying with different grafting conditions. After grafted by chloroalkylsilanes solutions, membrane surface had considerable changes. It can be observed that while membranes grafted by TCMS was not change much, MTCS solution formed the particles on the membrane surface. The particles were found on the modified membranes by MTCS as shown in Figure 4 (c-d).

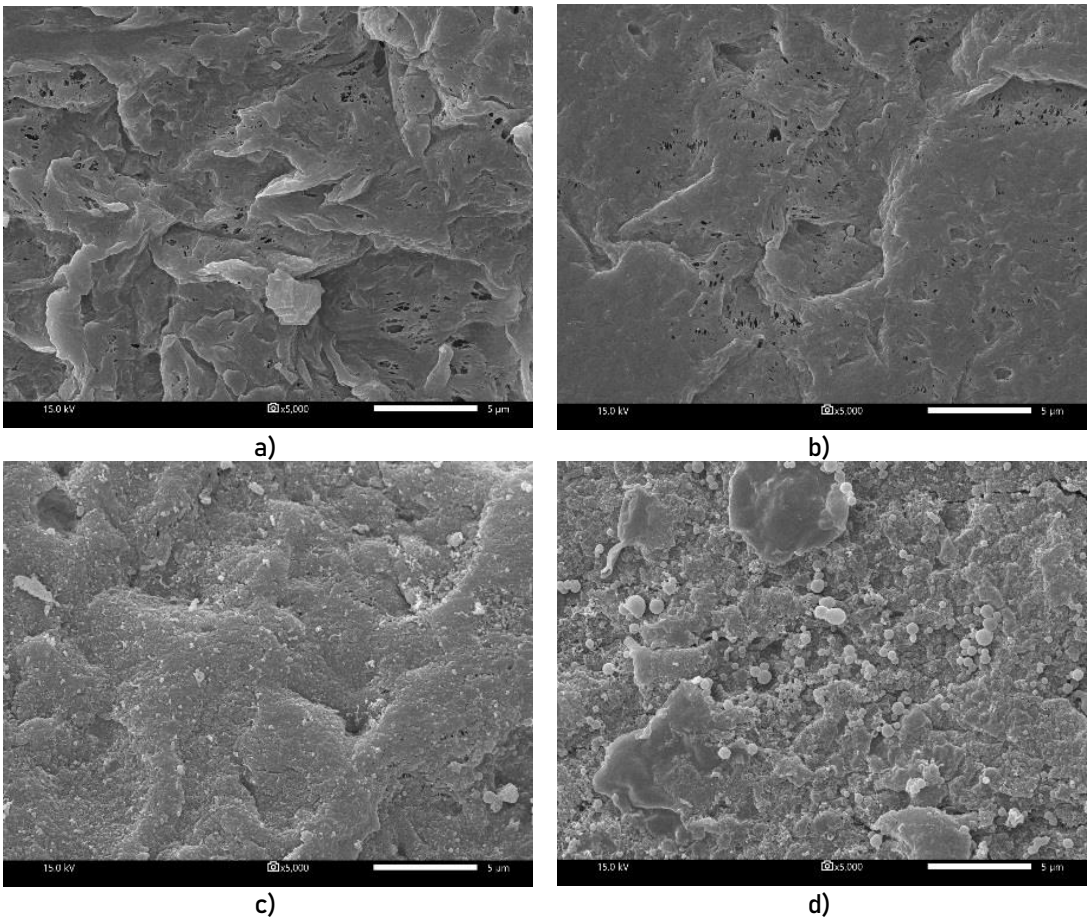

Figure 29: Outer surface morphology of modified PVDF membrane at different grafting solution and grafting time, activated by oxygen plasma gas at 8 kV, 1 shot: a) original PVDF membrane, (b-d) grafted membrane b) TMCS for 2h, c) MTCS for 0.5h, and d) MTCS for 2h

The hydrophobic particles formed are the results of horizontal reaction between MTCS chemical and the -OH groups present on membrane surface and vertical reaction between this chemical with the moisture of the air, then form the methylsilicon hydrophobic network on membrane surface,[9] as illustrated in Figure 5:

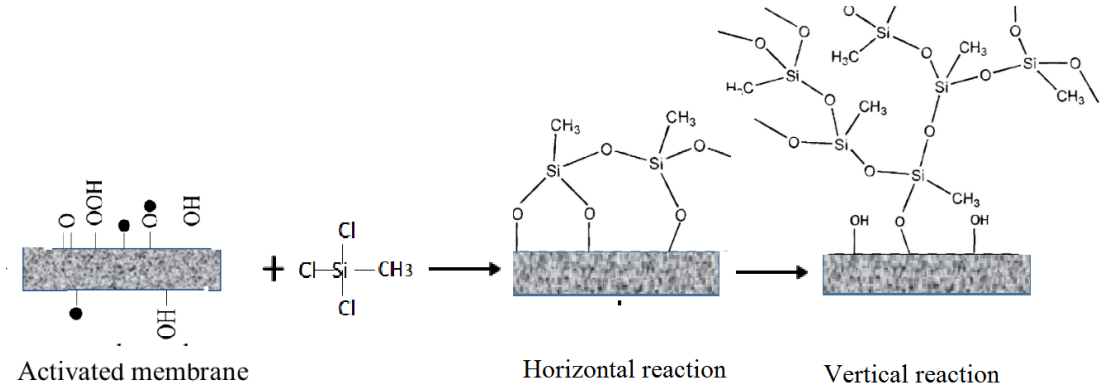

Figure 5. Reaction mechanisms between methyltrichlorosilane and the activated PVDF membrane surface [9]

It can be observed that the number and size of hydrophobic particles increased with the grafting time, due to the increase by vertical way of methylsilicon network on membrane surface by time. The formation of the hydrophobic network was further confirmed by EDS characterization and was summarized in Table 1.

Table 3. Changes of the chemical structure of membrane surface

Atomic concentration (%)	Original	Activated membrane	Grafted membranes	
			TMCS	MTCS
C	53.4	51.76	52.95	47.99
F	46.6	46.17	47.05	21.18
O	-	2.06	-	21.59
Si	-	-	-	8.24

(*) Note: Modification condition: 1 shot of oxygen plasma gas at applied voltage of 8 kV followed by 2h grafting time.

For the original membrane surface, there was only the presence of C and F showing in the table. After activated by oxygen plasma gas at the applied voltage of 8 kV, a small amount of O was added, due to the introducing of -OH groups on to membrane surface. The high percentage of Si and O on the surface of membrane grafted by MTCS proves that methylsilicon network successfully formed. In contrast, there was no Si presented on the surface of membrane grafted by TMCS. Therefore, the chemical compositions of modified PVDF membranes confirmed the successful of membrane modification by MTCS with the present of Si on the membrane surface.

Conclusion: PVDF membrane surface was successfully treated with plasma activation and chloroalkylsilanes direct grafting to enhance their hydrophobicity. Oxygen plasma gas gave the better results compared to other plasma gas. The results showed that the hydrophobic membranes were successfully produced by MTCS. SEM and EDS revealed that after grafted by MTCS, hydrophobic methylsilicone was formed on the membrane surface, making membrane surface be more hydrophobicity. In addition, the size and number of hydrophobic

particles were increased with time. After activated by oxygen plasma gas at condition of 8 kV, 1 shot and grafted with 0.02M MTCS for 4 hours, the WCA was increased from 70.5° (original) to 123.1°.

References:

1. Matsuyama H, Rajabzadeh S, Karkhanechi H, and Jeon S. Compr Memb Science & Engineering. 2017: p. 137.
2. Zheng Z, Gu Z, Huo R, and Ye Y. Appl Surf Sci. 2009; 255(16): p. 7263-7267.
3. Tang Z, Li H, Hess D W, and Breedveld V. Cellulose. 2016; 23(2): p. 1401-1413.
4. Hendren Z D, Brant J, and Wiesner M R. J Membr Sci. 2009; 331(1): p. 1-10.
5. Rabuni M, Sulaiman N N, Aroua M, Chee C Y, and Hashim N A. Chem Eng Sci. 2015; 122: p. 426-435.
6. Hashim N A, Liu Y, and Li K. Chem Eng Sci. 2011; 66(8): p. 1565-1575.
7. Kostov K G, dos Santos A L R, Honda R Y, Nascente P A P, Kayama M E, Algatti M A, and Mota R P. Surf Coat Technol. 2010; 204(18): p. 3064-3068.
8. Wang J, Chen X, Reis R, Chen Z, Milne N, Winther-Jensen B, Kong L, and Dumée L. Membranes. 2018; 8(3): p. 56.
9. Zhai T, Zheng Q, Cai Z, Turng L-S, Xia H, and Gong S. ACS Applied Materials & Interfaces. 2015; 7(13): p. 7436-7444.

Acknowledgements: This research was financially supported by the Commission on Higher Education, Thailand Research Fund (MRG6280181), HSM program, Chulalongkorn University. The authors would like to thank the Department of Environmental Science, Chulalongkorn University for experimental facilities provided and Department of Physics, Chulalongkorn University for plasma machine supported.

D_044_PF: PREPARATION AND CHARACTERIZATION OF KAFFIR LIME OIL MACROCAPSULES

Aungsana Prajaksangsiri[1,*], Pattara Thiraphibundet[2]
[1]Petrochemistry and Polymer Science, Faculty of Science, Chulalongkorn University, Bangkok 10330, Thailand
[2]Nanotec-CU Center of Excellence on Food and Agriculture, Department of Chemistry, Faculty of Science, Chulalongkorn University and, Bangkok 10330, Thailand
*e-mail: a.m._chain@hotmail.com

Abstract: Macrocapsules with the size of 3-4 mm were prepared by coaxial glass-tube apparatus. The shell-forming solution made from alginate, gellan gum and TEMPO-oxidized bacterial cellulose (TOBC). The core solution was kaffir lime oil (KLO). The various amount of TOBC with the degree of oxidation 0.1 was studied as the reinforcement agent for KLO capsule shell. Increase the amount of TOBC led to enhance the viscosity of shell-forming solution. The higher viscosity of solution caused the lower capsules formation efficiency percentage (%CFE) but gave larger size and higher weight of KLO capsules. Interestingly, the shell surface of KLO capsule with 0.2% of TOBC content was smoother and lesser shrinkage than other content. Moreover, addition of TOBC in the shell-forming solution showed the improvement of the compression strength of KLO capsules.

Introduction: Alginate is an anionic natural polymer isolated from marine brown algae. It is linear polysaccharides consisting of α-L-guluronic acid (G) and β-D-mannuronic acid (M) residues which can form a gel and widely used as thickener, stabilizer, gelling agent and emulsifier in food industry. Moreover, guluronic acid blocks of alginate can cross-linked with divalent cations such as Ca^{2+}, Ba^{2+} and Cu^{2+} by ionic bonds resulting in an a "egg-box" structure. Alginate has aqueous-solubility, biocompatibility, non-toxicity, non-immunogenicity and biodegradability. Thus, it is generally used for encapsulation many kinds of materials such as drug, gene, cell, enzymes, and lipids[1] in the form of alginate bead. Alginate beads can be produced by many techniques such as external, inverse, and internal gelation[2]. External gelation is a classical method in which alginate solution containing active compound is extruded and dropped into a $CaCl_2$ solution. Ca^{2+} ions diffuse into alginate droplets to initiate cross-linking on the bead surface. In contrast to the inverse gelation, liquid oil containing Ca^{2+} ions and active compound is extruded dropwise into an alginate solution bath. Upon contact, the Ca^{2+} ions diffuse to the outer periphery of the droplet and cross-link with the alginate polymer chains at the interface. Alginate bead prepared by the internal gelation method was formed by extruding the mixture of alginate solution, active compound and insoluble calcium salt ($CaCO_3$) into oil bath containing acetic acid. Acetic acid renders the release of Ca^{2+} from $CaCO_3$. Subsequently, Ca^{2+} ions further cross-linked with the alginate polymer chains inside the alginate droplet.

Alginate capsule is another type of encapsulation which the active compound is wrapped by alginate shell. Alginate capsule can prepare by various techniques such as electro-coextrusion and melt coaxial electrospray. The olive oil-loaded alginate macrocapsules was fabricated using electro-coextrusion through the coaxial nozzle controlled by a high voltage power machine[3]. The diameter of capsule and thickness of alginate shell were 0.89-1.61 and 17.4-66.4 mm, respectively in accordance to a variety of the alginate concentration, flow rate of solution and voltage power. The *n*-nonadecane-loaded alginate capsule was produced using melt coaxial electrospray[4]. The core solution was melted *n*-nonadecane before extruded through the coaxial nozzle together with alginate solution into $CaCl_2$ solution. In this study, the various concentrations of alginate solution and working distance affected the size of capsule (275-480 μM). Beyond our knowledges, there is no study reported the preparation of alginate macrocapsule with the size of 3-4 mm. Thus, the aim of

this work is to fabricate the alginate capsule using coaxial glass-tube and controlling the flow rate by syringe pumps. We prepared kaffir lime oil (KLO) macrocapsule in which the alginate shell was improved its mechanical strength by gellan gum and oxidized cellulose. In the dried form of alginate shell, it has low mechanical property, thus be easily broken. Gellan gum, which is widely used as a thickening agent, gelling agent and stabilizing agent in food, was used to expect the increasing of flexibility of alginate shell. Oxidized cellulose is obtained by oxidized hydroxyl group on bacterial cellulose (BC) chain to be carboxylic group using 2,2,6,6-tetramethyl-1-piperidine-N-oxy radical (TEMPO)[5,6]. The oxidized BC can easily disperse in water and be used as a reinforce agent in many materials[5-7].

The objective of this work was to prepare KLO macrocapsules which the physical property of capsule shell was improved by gellan gum and TOBC. Effect of the different TOBC contents on the mechanical property was studied by Texture analyzer. In addition, capsule formation efficiency was determined and surface appearance was observed by a digital camera at a magnification of x40 and Scanning electron microscopy (SEM),

Methodology:

Materials: Sodium alginate was purchased from Union Chemical 1986 Co., Ltd. (Thailand). Gellan gum was purchased from Siam Victory Chemicals. Calcium chloride ($CaCl_2$), (2,2,6,6-tetramethylpiperidin-1-yl) oxyl (TEMPO), sodium bromide (NaBr) and sodium hypochlorite (NaClO) were purchased from Sigma-Aldrich (USA). Bacterial cellulose (BC) pellicles or nata de coco was obtained from a local market in Chonburi, Thailand. Kaffir lime oil (KLO) was purchased from Thai-China Flavors and Fragrances Industry Co., Ltd.

Experimental:

Preparation of TEMPO-oxidized bacterial cellulose (TOBC). BC pellicles were treated in 0.5 M NaOH solution at 90 °C for 2 h and then neutralized by acetic acid. The filtrate treated BC was minced by a blender, filtered and freeze-dried. The freeze-dried BC was oxidized using a TEMPO-mediated system[5,6,8] (Fig 1). Firstly, 0.75 g of freeze-dried BC was suspended in 85 ml of distilled water containing 0.1 mmol of TEMPO and 1 mmol of NaBr. The oxidation reaction started by dropping 15 mL of NaClO to BC suspension at ambient temperature and the mixture was maintained at pH 10 by adding NaOH solution (0.1 M). After 5 h, the oxidation was quenched by adding ethanol to the suspension. The TOBC suspension was further centrifuged at 6000 rpm for 5 min to obtain the TOBC in the bottom layer. This TOBC were subsequently purified by dialysis for 1 day against distilled water. The dried TOBC sample was obtained by freeze-drying and kept in a desiccator before further experiment. The value of degree of oxidation (DO) (or carboxylate content) of TOBC was 0.10 which was determined by electric conductivity titration method[8].

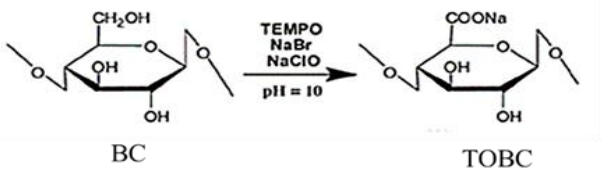

Figure 1. synthesis reaction of TOBC.

Preparation of alginate/GG/TOBC capsules from coaxial glass-tube. Shell-forming solution was made up of alginate (1 %w/v), gellan gum (1 %w/v), and various TOBC contents (0, 0.05, 0.1, 0.15 and 0.2 %w/v). TOBC was suspended in distilled water using ultrasonic treatment for 15 min before adding alginate and gellan gum powders. The mixture was then mechanical stirred for 6 h to obtain homogeneous shell-forming solution. After that, shell-

forming solution and KLO were loaded in syringes No.1 and 2, respectively, and set up the eject apparatus to fabricate macrocapsules as show in Fig 2. The inner and outer diameters of coaxial glass-tube tip were 4 and 6 mm, respectively. From the preliminary test, the appropriate flow rate of shell and core solutions was 10 and 2 mL/min, respectively. At these flow rates, it was founded that the shell and core substances fall from the tip together and gave the perfect capsule. Both solutions were dropped into 5% w/v of calcium chloride solution and soaked under mildly stirring for 10 minutes. The KLO macrocapsules were washed with distilled water and dried in an oven at 50°C for 16 h.

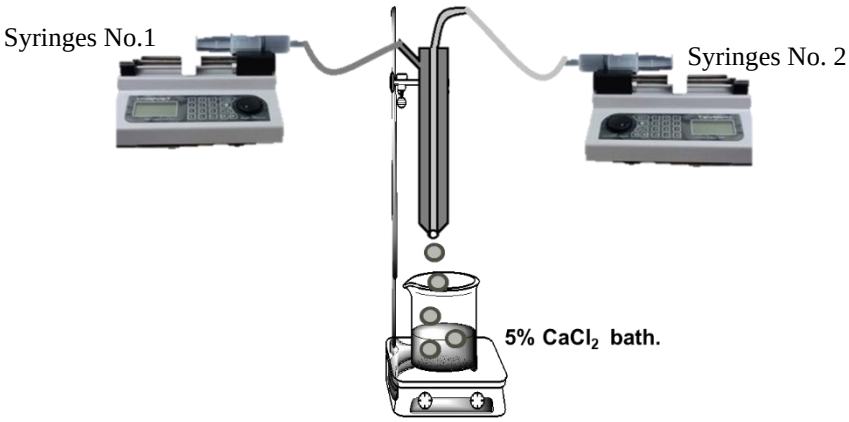

Figure 2. Device for the fabricated KLO macrocapsules.

Capsules characterization: The optical appearance was carried out on a digital camera at a magnification of x40. The surface morphology was observed using scanning electron microscopy (SEM, JSM-IT-500HR, JEOL, Japan) at an acceleration voltage of 5 kV. Capsule size was measured using a digital electronic Vernier caliper micrometer (Mitutoyo, Tokyo, Japan). Capsules formation efficiency (%CFE) was defined as follow;

$$\%CFE = \frac{\text{Number of oil loaded capsules (in 60s)}}{\text{Number of total drops (in 60s)}} \times 100$$

The mechanical property was analyzed by the compression test using a TA-XT2i (icon) Texture Analyzer (Stable Micro Systems, England). The instrument is equipped with a 0.05 N load cell fitted with a TA-P/6 separating rod fixture. The P/6 has short rods of 6 mm diameter each, protruding horizontally from the fixture. The alginate capsules were mounted onto the pair of rods. The probe moves downwards at a speed of 2 mm/sec until the capsules were chapped. The applied force is recorded as a function of 50% strain.

Results and Discussion: Kaffir lime oil (KLO) macrocapsules were successfully fabricated via a coacervation method using a coaxial glass-tube. The shell-forming solution composed of 1% w/v of alginate and gellan gum solutions together with a various amount of TOBC. The control KLO macrocapsule was the KLO capsule without TOBC and the %CFE of this capsule was 98.1%. The increasing amount of TOBC in shell-forming solution caused the increase of the viscosity of the shell-forming solution and also affected to the decrease of %CFE (Table 1.). The higher viscosity of shell solution led to the slower dripping and larger pendent droplet[3]. Therefore, the number of total drops in 60 seconds decrease. However, the slower fall of droplet resulted in the larger size and weight of capsule.

Table 1. The %CFE, size and weight of dried KLO macrocapsules fabricated from various TOBC contents

%TOBC in the shell-forming solution	%CFE	Capsule size (mm)	Capsule weight (mg)
0	98.1 ± 0.9	3.51 ± 0.27	33.74 ± 2.8
0.05	95.4 ± 1.3	3.70 ± 0.28	37.40 ± 0.63
0.1	92.6 ± 1.0	3.72 ± 0.23	38.37 ± 0.32
0.15	90.6 ± 1.1	3.75 ± 0.19	40.78 ± 0.43
0.2	86.2 ± 1.2	3.83 ± 0.13	41.82 ± 0.30

The appearance of KLO capsules was viewed under a digital camera at a magnification of 40X (Fig 3.). The surface of the control capsule was rough and transparent which the inside KLO can be observed. TOBC content was found to lessen the transparency of capsule shell. Interestingly, the surface of KLO capsule with 0.2%TOBC was smoother than others. The magnified images of capsule by SEM showed the shrinkage surface caused by the cross-linkage between the alginate chain and Ca^{2+} ion (Fig 4). In addition, the carboxylate groups of TOBC were reported that they can participate with the Ca^{2+} ion and the TOBC fiber can also form a semi-interpenetrating polymer network (SIPN) with other polymers[5,9]. The shrinkage of the shell surface was found in all formula of capsules but capsule with 0.2% TOBC content showed the lowest shrinkage. This might be the TOBC fiber at this amount can protect the collapse of polymer network from shrinkage.

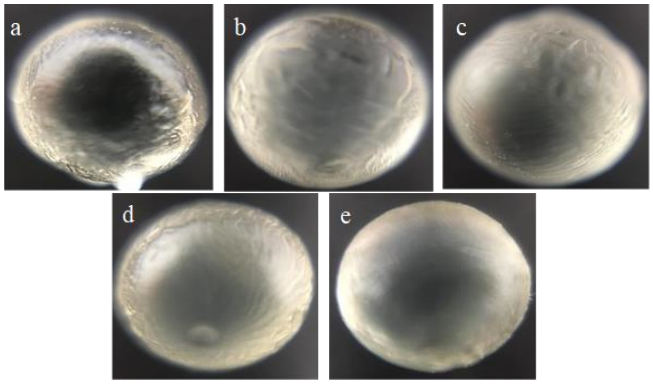

Figure 3. Digital camera images of KLO macrocapsules with the content of (a) 0% (b) 0.05% (c) 0.1% (d) 0.15% and (e) 0.2% of TOBC.

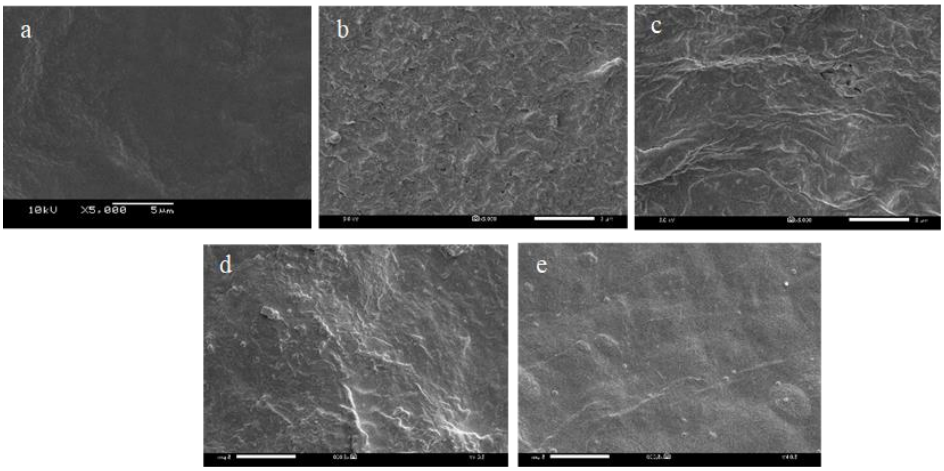

Figure 4. SEM images of KLO macrocapsules with the content of
(a) 0% (b) 0.05% (c) 0.1% (d) 0.15% and (e) 0.2% of TOBC.

The compression strength of each KLO macrocapsule was evaluated and the results were shown in Fig 5. The strength value of capsule with 0.05% of TOBC was closed to that of control capsule. Increasing the TOBC content can enhance the compression strength of capsule. However, the strength of capsule with 0.15 and 0.2% of TOBC showed the similar value. The higher amount of TOBC than 0.2% seems to not boost the compression strength.

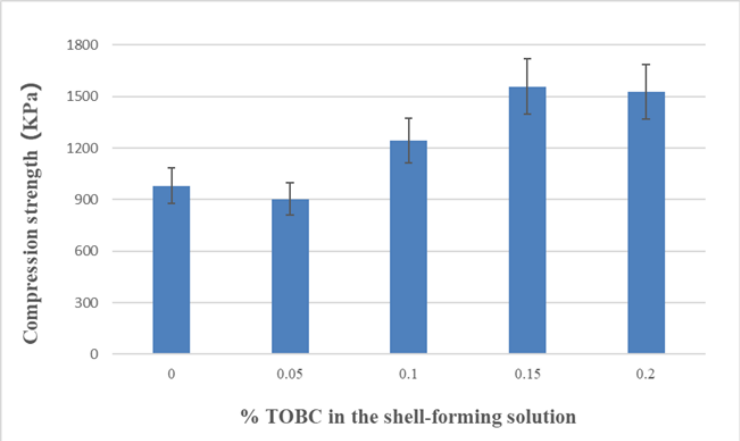

Figure 5. The compression strength of the KLO macrocapsules with various TOBC content.

Conclusion: Kaffir lime oil (KLO) macrocapsules were successfully fabricated by a coaxial glass-tube. The shell solution composed of alginate, gellan gum and TOBC whereas the core solution was KLO. TOBC was used as a reinforcing agent to improve the mechanical property of capsule shell. At the amount of 0.2 %w/v of TOBC, macrocapsules exhibited the lowest %CFE but the highest size and weight dried which were 86.2%, 3.83 mm and 41.82 mg/capsule, respectively. The SEM images showed that KLO macrocapsules containing 0.2%w/v of TOBC had smooth surface but turbidity. Moreover, these macrocapsules showed the higher compression strength due to formation of a semi-interpenetrating polymer network.

References:

1. Yue Y, Han J, Han G, French AD, Qi Y, Wu Q. Carbohydr. Polym. 2016;147:155-164.

2. Leong JY, Lam WH, Ho KW, Voo WP, Lee MFX, Lim HP, Lim SL, Tey BT, Poncelet D, Chan ES. Particuology. 2016;24:44-60.
3. Phawaphuthanon N, Behnam S, Koo SY, Pan CH, Chung D. Int. J. Biol. Macromol. 2014;65:267-274.
4. Moghaddam MK, Mortazavi SM, Khayamian T. J. Electrostat. 2015;73:55-64.
5. Lin N, Bruzzese C, Dufresne A. ACS Appl. Mater. Interfaces. 2012;4:4948–4959.
6. Parka M, Lee D, Hyuna J. Carbohydr. Polym. 2015;116:223–228.
7. Cheng F, Liu C, Wei X, Yan T, Li H, He J, Huang Y. ACS Sustainable Chem. Eng. 2017;5: 3819-3828.
8. Habibi Y, Chanzyl H, Vignonl MR. Cellulose. 2006;13:679-687.
9. Naseri N, Deepa B, Mathew AP, Oksman K, Girandon. Biomacromolecules. 2016;17:3714–3723.

Acknowledgements: This work was financially supported by the Thailand Research Fund (RDG595002) and the National Nanotechnology Center (NANOTEC), NSTDA, Ministry of Science and Technology, Thailand, through its program of Research Network NANOTEC (RNN).

D_054_OF: SYNTHESIS AND STRUCTURAL PROPERTIES OF METAL DOPED Li NIKEL-RICH NMC POWDER MATERIALS FOR HIGH SPECIFIC CAPACITY

Jaruwan Kanthachan[1,2], Uraiwan Intatha[3], Sukum Eitssayeam[2,*]
[1]Graduate School, Chiang Mai University, Chiang Mai 50200, Thailand
[2]Department of Physics and Materials, Faculty of Science, Chiang Mai University, Chiang Mai 50200, Thailand
[3]Materials for Energy and Environment Research Group, School of Science, MaeFahLuang University, Chiang Rai 57100, Thailand
*e-mail: sukum99@yahoo.com

Abstract: Lithium nickel manganese cobalt oxide(NMC) is positive electrodes in lithium-ion batteries. The $LiNi_{0.75}Mn_{0.15}Co_{0.10}O_2$ shows the highest specific capacity, with the potential range of 215 $mAhg^{-1}$. The fine NMC powder size was successfully synthesized by co-precipitation method. Addition of $Sn_3(PO_4)_2$ has distinct influence on the crystal structure of the materials. Study, different steps synthesis to mix with lithium hydroxide monohydrate. After doping with an appropriate amount tin phosphate, the electrochemical performance of $LiNi_{0.75-x}Mn_{0.15-x}Co_{0.10-x}(Sn_3(PO_4)_2)_xO_2$ or $Li_{1-y}(NiMnCo)_1(Sn_3(PO_4)_2)_yO_2$ cathode materials is significantly enhanced. The phase formation and structure were studied by X-ray Powder Diffraction (XRD). The morphological change is also investigated by field-emission scanning electron microscope (FE-SEM).

Introduction: Trend of the research data and market information reveal that the world's largest market research store are rapid growth, the energy technologies and big market size. In the future leads Compound Annual Growth Rate 38.34% during 2016-2024. Focus only the lithium battery market size of CAGR can get up to 17% in 2014-2025 with the estimation of USD 93.1 billion. Due to carbon dioxide destroys ozone because increases during transportation of the people. Now in Europe interest has been focused in using streetcar and electric car to decrease the carbon dioxide emission, and environmental friendliness[1,2]

Lithium rich oxide of $LiNi_{0.75}Mn_{0.15}Co_{0.1}O_2$ (equivalent to NMC) has been widely used as a cathode materials in commercial Li-ion batteries. Because its excellent electrical properties .The synthesis were carried out via co-precipitation method[3-8]. It is easy to preparation when compared with other methods such as hydrothermal[9] and sol-gel[10].

Doping of tin phosphate into a NMC powder by calcination was the key development. The doping effect with a microstructure caused by adding this element into powder. Adding of various concentrations of tin phosphate between 1wt% 3wt% 5wt% and 10wt% was carried out. The substitution of tin phosphate into NMC will be different. The calcination patterns bring to phase change.

The patterns are; calcination 1 time was calcination after doped tin phosphate into a NMC mixed with a lithium and bring into a furnace. Then tin phosphate will form with metal NMC. And calcination 2 times, this is bring a metal hydroxide to calcine before doping and followed by the process. Then for calcination 2 times, tin phosphate will be formed with lithium ions. The effects of tin phosphate doping on the structure and electrical properties of the $LiNi_{0.75}Mn_{0.15}Co_{0.1}O_2$ were investigated.

Methodology:

Preparation $[Ni_{0.75}Mn_{0.15}Co_{0.1}](OH)_2$: The precusor$[Ni_{0.75}Mn_{0.15}Co_{0.1}](OH)_2$was prepared using Nickel(II)Nitrate Hexahydrate($Ni(NO_3)_2*6H_2O$)98%,Manganese(II)Nitratetetrahydrate($Mn(NO_3)_2*4H_2O$)98%, Cobalt(II)Nitrate Hexahydrate($Co(NO_3)_2*6H_2O$)97.7% from Alfa Aesar, Ammonium hydroxide (NH_4OH)28-30%(LABALOCHEMIE) and NaOH as starting materials. The ($Ni(NO_3)_2*6H_2O$),($Mn(NO_3)_2*4H_2O$),($Co(NO_3)_2*6H_2O$) were mixed with molar ratio of 0.75:0.15:0.1 and dissolved by DI water, stirred by a magnetic bar for 30 minutes. The NH_4OH was

dropwisely added to adjust PH to about 9.0, stirred by magnetic bar for 30 mins. Concentration of NaOH was continually added to adjust PH to 11 and then stirred for 1-3 hrs followed by being filtered and wash suddenly with DI water until the PH of drop passing the filter having similar PH of water before filter. The powder left on the filter paper was dried at 120°C less than 12 hrs.

Preparation of $LiNi_{0.75-x}Mn_{0.15-x}Co_{0.10-x}(Sn_3(PO_4)_2)_xO_2$ powders by calcination 1 time: The 1,3,5,10wt% $Sn_3(PO_4)_2$ doped on $Ni_{0.75}Mn_{0.15}Co_{0.10}(OH)_2$ powders, Sn(II)acetate and $NH_4H_2PO_4$ were dissolved in DI water and stirred 1 hrs. Doped a $Sn_3(PO_4)_2$ solution in $Ni_{0.75}Mn_{0.15}Co_{0.10}(OH)_2$, after filtering and washing, the mixture was dried at 120°C less than 12 hrs.

Then the dry precursor and lithium hydroxide monohydrate were mixed uniformly in accordance with the mole ratio 1:1. The mixed powder was ground in a mortar by hand. The mixture was calcine at 550°C in the oxygen atmosphere for 5 hrs. The temperature was naturally cooled down to room temperature to obtain an active cathode materials, $LiNi_{0.75}Mn_{0.15}Co_{0.10}O_2$ dope $Sn_3(PO_4)_2$

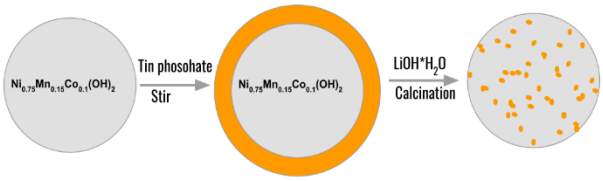

Figure 1. Synthesis process for tin phosphate doped $LiNi_{0.75}Mn_{0.15}Co_{0.1}O_2$ by calcination 1 times[11].

Preparation of $Li_{1-y}(Ni_{0.75}Mn_{0.15}Co_{0.10})(Sn_3(PO_4)_2)_yO_2$ powders by calcination 2 times: The obtained $Ni_{0.75}Mn_{0.15}Co_{0.10}(OH)_2$ powder was brought to calcine 550°C in the oxygen atmosphere for 5 hrs. Doping of $Sn_3(PO_4)_2$ into a $Ni_{0.75}Mn_{0.15}Co_{0.10}O_2$ was done. After that mixed the lithium hydroxide monohydrate by ratio 1:1 in a mortar. Then the mixture was calcine at 550°C.

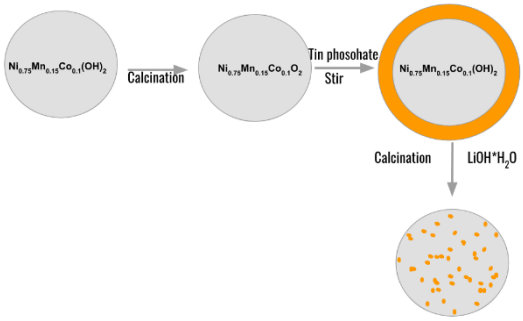

Figure 2. Synthesis process for tin phosphate doped $LiNi_{0.75}Mn_{0.15}Co_{0.1}O_2$ by calcination 2 times.

Results and Discussion:

Microstructure characterization by XRD: The XRD patterns of $LiNi_{0.75-x}Mn_{0.15-x}Co_{0.10-x}(Sn_3(PO_4)_2)_xO_2$ are shown in Fig 3. The XRD patterns of Li $Ni_{0.75}Mn_{0.15}Co_{0.10}O_2$ peaks can be matched with standard pattern(ICDD 01-076-6563). From the patterns phases of tin phosphate(ICDD 00-052-1536) and tin(ICDD 03-065-5224) were pronounced. The surface area affect with Li intercalation, then the crystal size affects with specific energy performance. Each peak listed were similarly with main peaks but, they are different on Full Width at Half

Maximum (FWHM). It was found that the concentrations, 1wt% to 5wt% increase the crystal size. But a concentration of 10wt% showed smaller size.
The synthesis of various concentrations of tin phosphate doped NMC powder was tabulated data in the table1.

Table1. The list of synthesis NMC; they are 2 main components about NMC(OH)2 is NMC hydroxide mix with each doped tin phosphate1wt% 3wt% 5wt% 10wt% and NMCO2 is NMC oxide mix with doped tin phosphate1wt% 3wt% 5wt% 10wt% .

NMC*		tin Phosphate			
$NMC(OH)_2$	$NMCO_2$	1wt%	3wt%	5wt%	10wt%
/		/	/	/	/
	/	/	/	/	/

* no mixed

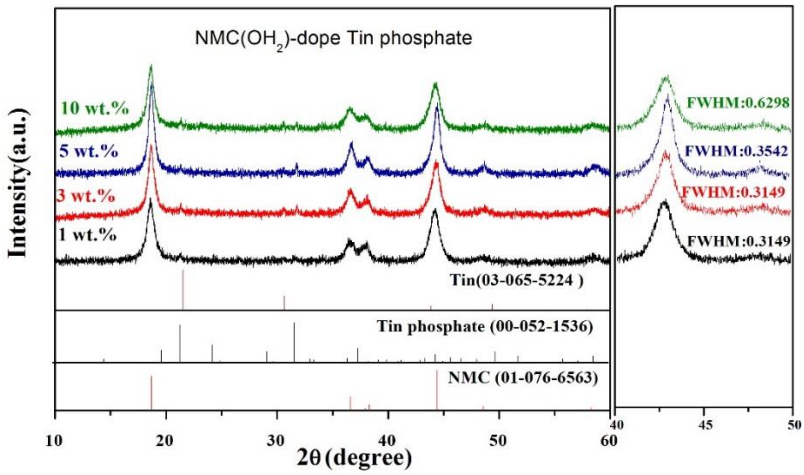

Figure 3. XRD patterns of $NMC(OH)_2$ dope tin phosphate by various concentration.

The $LiNi_{0.75-x}Mn_{0.15-x}Co_{0.10-x}(Sn_3(PO_4)_2)_xO_2$ affects with XRD pattern. The peaks at 2theta; 21.534, 30.638, and 31.739 increase when an increase concentration of tin phosphate. However, without a 10wt% of tin phosphate on peak height show decreasing.

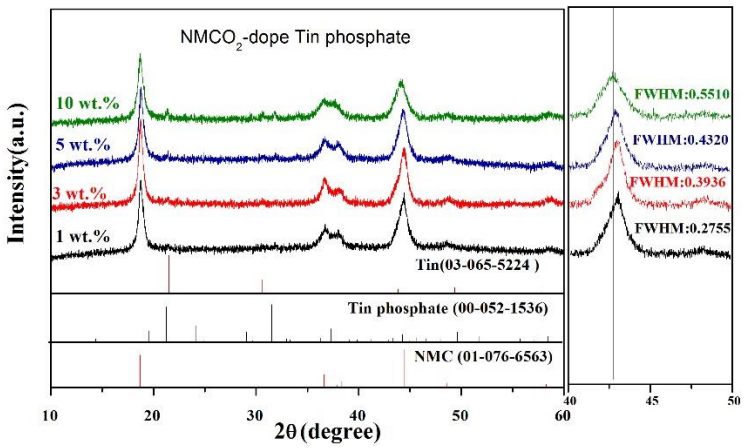

Figure 4. XRD patterns of $NMCO_2$ dope tin phosphate by various concentration.

On the $Li_{1-y}(NiMnCo)_1(Sn_3(PO_4)_2)_yO_2$ a concentration of tin phosphate affects on the XRD pattern. The peak list at 2theta; 21.534, 30.638, and 31.739 increased when an increase concentration of tin phosphate. The FWHM and peak high of 2theta on 44.2048 have the effect on crystal size. When compare with other conditions such as $NMC(OH)_2$ doped tin phosphate 10wt% the width of the peak is wider than other. The same effect was found in $NMCO_2$ doped tin phosphate 10wt%. And a crystal structure is a sheet stack and random size. Then it is hard to calculate. Therefore we employed the Scherrer's Formula for calculation.

The crystal sizes were calculated using a Scherrer's Formula:

$$\tau = K\lambda / (\beta\cos\theta)$$

τ = The mean size of crystalline
K = Scherrer constant. (K = 0.94)
λ = X-ray wavelength (CuKα = 1.5417 Å)
β = FWHM of XRD peak (Full Width at Half Maximum)
θ =XRD peak position

Table2. The crystal size of each conditions by scherrer's calculation.

NMC*		Crystal size(nm)				
**$NMC(OH)_2$	***$NMCO_2$	1wt%	3wt%	5wt%	10wt%	pure
/		183.45	241.29	302.79	208.63	
	/	231.61	263.82	377.06	216.90	
	/					271.55

**$NMC(OH)_2$ calcination 1 time
***$NMCO_2$ calcination 2 times

Microstructure characterization by SEM:

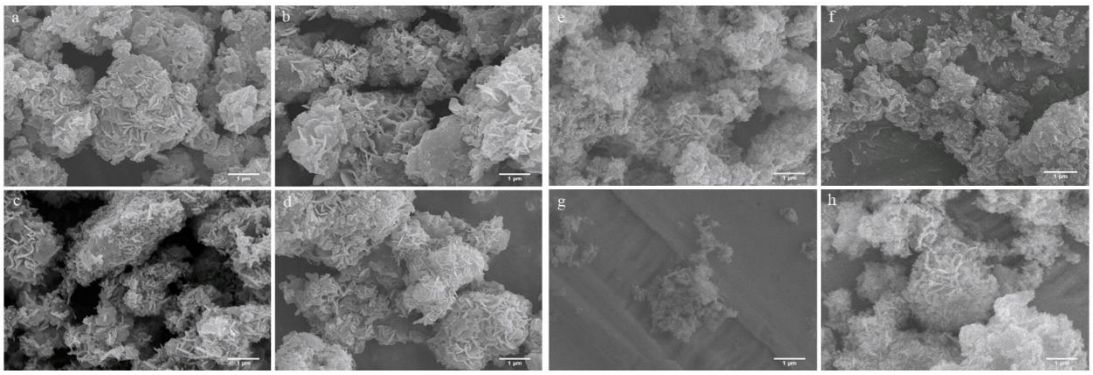

Figure 5. SEM image morphologies of tin phosphate dope in NMC powder, a; calcination 1time dope 1wt%, b; calcination 1times dope 3wt%, c; calcination 1times dope 5wt%, d; calcination 1times dope 10wt%, e; calcination 2times dope 1wt%, f; calcination 2times dope 3wt%, g; calcination 2times dope 5wt% and h; calcination 2times dope 10wt%

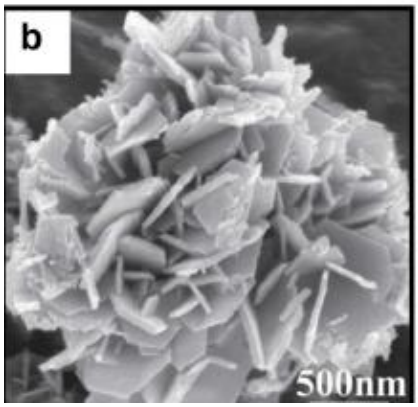

Figure 6. SEM image via $Li_{1.5}Ni_{0.25}Mn_{0.75}O_{2+d}$ by co-precipitation method [12].

The morphology of the sheet stacking on our results (Figure 5) were similarly to that of[12]. Some images in the figures show bar like. The results were supported by Seung-Taek Myung[12] who prepared the $Li_{1.5}Ni_{0.25}Mn_{0.75}O_{2+d}$ by co-precipitation. The high concentration showed a bigger sheet. But a calcination 2times showed less sheet stack more than calcination 1 time. Theoretically of synthesis amount of tin phosphate will increase size. This causes by a synthesis control, a time and rate of stir, then high concentration the powder will accumulate on the surface of NMC powder more. According to the experiment, a concentration of 1wt% 3wt% and 5wt% increase crystal size which is contradict to the theory. However, a concentration of 10wt% showed small size.

Conclusion: The tin phosphate doped NMC cathode materials via synthesized by co-precipitation method and different calcinations. Tin phosphate doped can change the crystal structure and size when compared with pure NMC. A concentration effect with crystal size directly causes an accumulated on NMC powder. Controlling of other factors such as a high concentration results produce large size and more other sheet stack. But the concentration in 10wt% of tin phosphate can produce a smaller size than other concentrations. Also a large surface area was found in other concentrations too. This may affect on intercalation mechanism of lithium. Then a doping tin phosphate 1wt% on $NMC(OH)_2$ was high specific energy because of the smallest size of particle or large surface area. The co-precipitation method can produce an average crystal size to 253.19 nm (183.45-377.06) all of samples as calculated via the Scherrer's Formula. The XRD pattern can show an increasing of each concentration of tin phosphate.

References:

1. Goodennough JB and Kim Y. Chem Mater. 2010; 22: 587–603.
2. Etacheri V, Marom R, Elazari R, Salitra G, and Aurbach D. Energy Environ Sci. 2011; 4: 3243-3262.
3. LIU and HA. Disseratation of City University of Hong Kong. 2010.1-50.
4. Yujing BI, Deuy Wang and Jun Li, U.S. Patent No.20150104708A1. 2015.
5. Myung-Hyoon Kim, Ho-Suk Shin , Dongwook Shin and Yang-Kook Sun. J. AM. CHEM. SOC. 2005; 127: 13411-13418.
6. Christian Julien , Alain Mauger , Karim Zaghib and Henri Groult . Materials. 2016; 9. 595: 1-26.
7. Seung-Taek Myung, Hyung-Joo Noh,Sung-June Yoon, Eung-Ju Lee and Yang-Kook Sun. J. Phys. Chem. Lett. 2014; 5: 671-679.
8. Enshan Han, Yanpu Li , Lingzhi Zhu and Ling Zhao. Solid State Ionics. 2014; 255: 113-119.

9. Sami Barkaoui, Marwa Haddaoui, Hassouna Dhaouadi, Noureddine Raouafi amd Fathi Touati. Solod State Chemistry(auther's accepted manuscript). 2015: 1-25.
10. Yanjing Hao, Qiongyu Lai, Zhihui Xu, Xueqi Liu and Xiaoyang Ji. Solid State Ionics. 2005; 176: 1201-1206.
11. D. Aurbach, Y. Einely, A. Zaban and J. Electrochem. Ceramics International. 2015; 41: 7133-7139.
12. Seung-Taek Myung,Khalil Amine , and Yang-Kook Sun. Power source. 2015; 283: 219-236.

Acknowledgements: This work was supported by Electroceramic laboratory at Chiangmai University, Thailand is gratefully acknowledged. We would like to express us thanks to financial support from the Graduated School, Chiangmai University. Investment form Product Machine Maintenance co., ltd., Lamphun Thailand.

SESSION E: ENERGY_ENVIRONMENTAL & EARTH SCIENCE

E_002_PF: ARCHITECTURE ELEMENTS AND STRATIGRAPHY OF ANCIENT MUN RIVER, NAKHON RATCHASIMA, NORTHEASTERN THAILAND

Thunchanok Kawinate*, Montri Choowong, Kantapon Suraprasit
Morphology of Earth Surface and Advanced Geohazards in Southeast Asia (MESA) Research Unit, Department of Geology, Faculty of Science, Chulalongkorn University, Bangkok 10330, Thailand
*e-mail: thunchanok-k@hotmail.com

Abstract: In order to understand the depositional mechanism of the meandering Mun river, the reconstruction of architecture elements coupled with detail stratigraphic correlation is essential. In this study, we recognized ten lithofacies that can be grouped into six architecture elements from meander belt of the Mun River, Nakhon Ratchasima province. Ten lithofacies include planar-cross-bedded gravel (Gp), matrix-supported gravel (Gmg), trough-cross-bedded sand (St), ripple cross-laminated sand (Sr), planar-cross-bedded sand (Sp), horizontally bedded sand (Sh), silt, mud (Fsm) mud, silt (Fr), massive mud, silt (Fm) and laminated sand, silt, mud (Fl). Six architecture elements were identified as sandy bedforms (SB), lateral accretion deposits (LA), levee deposits (LV), crevasse channel elements (CR), floodplain fines (FF) and abandoned channel (CH(FF)). All these facies and elements found within 13 m thick indicate the sedimentary process of the meandering river. Based on facies and architectures, the upper part shows fine-grained facies deposited mainly from suspension during a low flow regime and low energy. The lower part is mainly characterized by sand facies with medium to very coarse-grained and less commonly gravel facies at the base, It is interpreted to have deposited by high flow regime, rapid flow and high energy depositional mechanism.

Introduction: The Mun River is one major branch of the Mekong River originated from the western part of the Khorat Plateau, Nakhon Ratchasima province, northeastern Thailand. The Mun River floodplain is classified as part of the Quaternary sediments deposited in the Khorat Basin. Part of ancient meandered belt with traces of meandered scar, oxbow lake and paleo-channels has become geological important since some vertebrate and plant fossils have been reported.

Many researchers have studied and improved many aspects of the Quaternary sediments along the recent and ancient channel deposits of the Mun river and found that the depositions were formed by high-energy flood pulses[6]. As well as palaeomagnetic dating indicated that these flood pulses were contemporaneous with the tektite-forming event at c. 0.8 Ma[5]. In general, the Quaternary sediments comprise two distinct units[6-7]. The upper unit is dominated by a brown-yellow color indicating oxidizing environment[6,8-9]. The lower unit is markedly different by a grey color indicating chemically reducing environment[6]. Moreover, at the Khok Sung sandpit, some sedimentary facies were studied from the Pleistocene fossils site and interpreted that the sediments were deposited as two meandering channel sets[10]. Chronologically, the age of mammalian fauna collected from these Quaternary sediments inferred as the late Miocene[7]. They consist of hipparion, proboscideans, rhinocerotids, pigs, anthracotheres, bovid, and giraffid[7]. Moreover, the fauna fossils also indicated the paleo-climate that is differed from today. Heavier rainfall and more extensive grassland areas during the Pleistocene were suggested[10].

The study area is located along ancient Mun river meandered belt mainly at the Phimai District, 60 km northeast of Nakhon Ratchasima downtown (Figure 1). The purpose of this study is to characterize the lithofacies, architecture elements, and to reconstruct depositional mechanism.

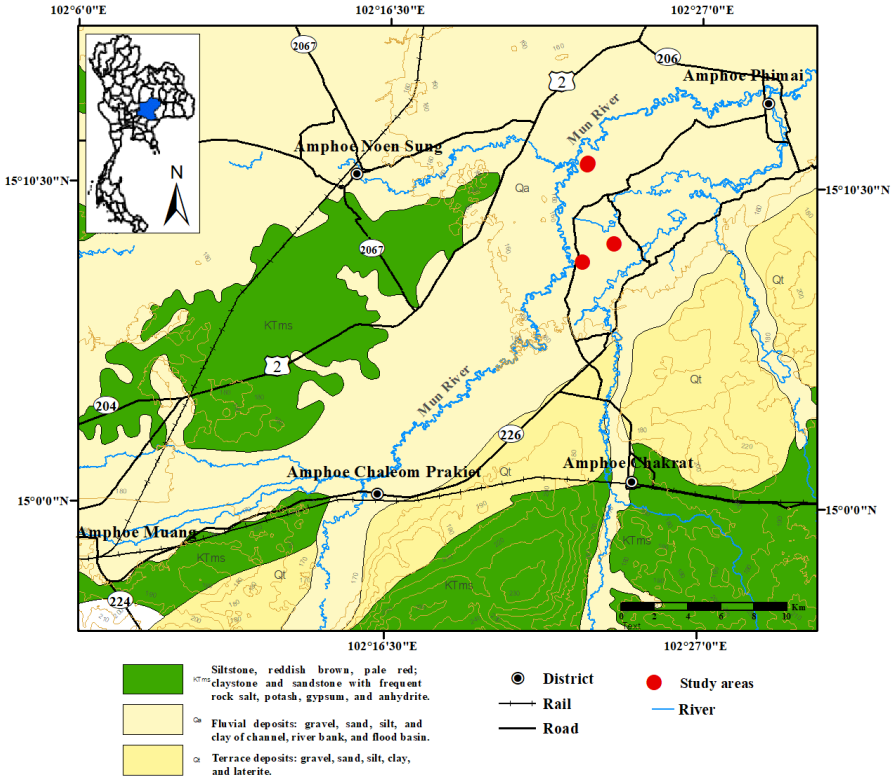

Figure 1. Geological map of the study area. Sandpits (circles) are located along the ancient Mun river, Nakhon Ratchasima Province.

Methodology: The exposure of sandpit in the study area provides an excellent opportunity for studying the facies, architecture elements and reconstructing Quaternary stratigraphy of the ancient Mun River. The field methods for facies and architectural interpretation in this study were based on those of Miall[1,3]. Detail of facies analysis including bedding characteristics, grain size, texture, sedimentary structures, biogenic structures, the degree of clast rounding and sorting and the other physical characteristics were considered to identify the different sedimentary facies and interpret the depositional environment. Also, analysis of the architecture elements was generally modified from Miall[1-2]. Generally, the facies and structural elements were drawn from photo-mosaics as well as the measurement of widths and thickness of the architecture elements. Ratios of all those dimensions were, then, calculated. The photo-mosaics were prepared as montages of partly overlapping photographs taken from a distance of several tens of meters to avoid distortion. Computer software programs are also used to explain and interpret the information obtained from the field studies. These programs include Adobe illustrator and Sedlog for profile drawing and final layout of the studies profiles and Agisoft photoscan for montages a photograph.

Results and Discussion: The lithofacies classification of the Quaternary sediments in the study area using Miall[1,3] can be divided into ten (10) facies (Table 1). Two gravel lithofacies consist of less commonly of clast-supported, planar-cross-bedded gravel (Gp) and matrix- supported gravel (Gmg). Four sand lithofacies are recognized including ripple cross-laminated sand (Sr), trough-cross-bedded sand (St), planar-cross-bedded sand (Sp), and horizontally bedded sand (Sh). Finally, four fine-grained clastic facies are subdivided into silt, mud (Fsm) mud, silt

(Fr), massive mud, silt (Fm) and laminated sand, silt, mud (Fl). Detail of lithofacies and the discussion on depositional mechanism are described below:

I - gravel lithofacies

Facies Gp; Planar-cross-bedded gravel: These facies are composed mainly of coarse to very coarse-grained, may be granules to pebbly, clast-supported grained, well sorted, rounded to well-rounded and display planar-cross-bedded, and iron concretion. These showing mottle zone deposits in a reducing and oxidizing environment. The facies is 0.4 m thick. Basal boundaries are mostly erosional.

Facies Gmg; Matrix- supported gravel: These facies are composed mainly of coarse to very coarse-grained, may be granules to pebbly, moderately to poorly sorted, angular to subangular, the facies is 0.1 m thick. Follow to Miall[1,3]; It is interpreted as pseudo-plastic debris flow (low strength, viscous).

II - sand lithofacies

Facies Sr; Ripple cross-laminated sand (Figures 2A and 2B)*:* These facies are composed of ripple cross-bedded sandstone, very fine to coarse-grained sand, granule, rounded to well rounded, moderately to well sorted. The facies is 2.0 m thick. It is interpreted as ripples (lower flow regime)[1,3].

Facies St; Trough-cross-bedded sand (Figure 2C, and 2D)*:* These facies are characterized by trough cross-bedded sand, fine to very coarse-grained sand. The thickness of this facies is 1 - 3 m. The geometry is a concave shape. The major internal structures consist of trough cross-bedding, wedge-shaped cross-bedding, and low-angle cross-bedded sand (Sl). The large-scale trough cross-beds may overlie the mud clasts. Basal boundaries are mostly erosional contact. Following Miall[1,3], it is interpreted as sinuous-crested and linguoid (3-D) dunes that stack up to general bar forms in a channel. Trough sets are larger than 1 meter in thickness, indicating correspondingly great water depths and dune heights.

Facies Sp; Planar-cross-bedded sand (Figures 2E and 2F)*:* These facies are characterized by planar-cross- bedded, fine to coarse-grained sand. The thickness of up to 0.7 to 1 m. It is interpreted[1,3] as a transverse bar underflow regime and linguoid and bedforms (2-D dunes).

Facies Sh; Horizontally bedded sand: These facies are characterized by horizontal lamination, very fine to fine-grained sand, well sorted, the thickness of this facies is 1 to 1.5 m. It is interpreted[1,3] as plane-bed flow to coarse, parting or streaming (critical flow).

III - fine-grained clastic facies

Facies Fsm; Silt, mud (Figures 2G and 2H)*:* These facies are characterized by silt, mud, mottles zone, desiccation cracks. The facies is 2.2 m thick. It is interpreted as deposits in the back swamp, abandoned channel deposits, and a reducing and oxidizing environment[1,3-4]

Facies Fr; Mud, silt: These facies are characterized by mud, silt, very fine to medium- grained sand, root bed, bioturbation, root traces, and mottles zone. They indicate oxidizing condition. Iron concretion was also observed in the lower part of this facies. The facies is 2.2 m thick. These facies are common in vegetated floodplains, representing soil development in a humid climate and deposits in a reducing and oxidizing environment[1,3-4].

Facies Fm; Massive mud, silt: These facies are characterized by massive mud, silt, desiccation cracks. The geometry is wedge-shaped. It is interpreted[1,3] as overbank deposits, abandoned channel, or drape deposits. Thus, it may represent the most distal floodplain.

Facies Fl; Laminated sand, silt, mud: These facies are consisted of very fine-grained sand, silt, mud. Fine lamination and very small-scale ripples are present. The thickness is 1 to 2 m. Miall[1,3] interpreted these facies that they were deposited in overbank, waning flood deposits.

Six architectural elements were recognized, including sandy bedforms (SB), lateral accretion deposits (LA), levee deposits (LV), crevasse channel elements (CR), floodplain fines

(FF), and abandoned channel (CH(FF)) shown in Table 2 and Figure 3. These elements were defined by their geometries and bounding surfaces. The interpretation of the depositional environment from architectural elements in this study was followed Miall[1-2].

Sandy bedforms (SB): Sandy bedforms comprise lithofacies St, Sr, Sh, Sp. They are characterized by massive, parallel, cross-bedded structures, and sharp bases. The geometry of the channel appears sheet-like, predominated by vertical aggradation. They are usually about 1 to 3 m thick. This element is interpreted as sandy bedforms and probably deposited in a channel.

Lateral accretion deposits (LA): Lateral accretion deposits (LA) are composed mainly of sandy facies St, Sp, Sh, and Gp. This element appears typically in the sandstone-dominated environment. They are characterized by wedge shape and internal- lateral-accretion 3rd-order surfaces. It is interpreted as channel-fill and point-bar deposits that formed by the lateral migration of channels.

Levee deposits (LV), and Crevasse channel elements (CR): These are composed of lithofacies St, Sr, Fl. Their geometries are of the wedge-shaped ridges, showing interfingering and small-scale ripples and parallel lamination. The thickness of the bed is 1 to 2 m. According to Miall[1-2], these elements are interpreted as overbank flooding when flood waters of a stream overtop its banks.

Floodplain fines (FF): Floodplain fines (FF) are represented mainly by fine-grained sand, and composed of lithofacies Fsm, Fr, Fm, and Fl. They show desiccation cracks, mottle zone, diffuse root traces, and iron concretion. These facies are interpreted as floodplain deposits.

Abandoned channel fills (CH(FF)): Abandoned channel fills (CH(FF)) is composed of lithofacies Fsm, Fr, Fm, and Fl. The geometry is of the lenticular in cross-section and interbedded with element SB. The clay plugs that commonly fill abandoned channels. Lithofacies and architectural elements throughout stratigraphy are shown in Figure 4.

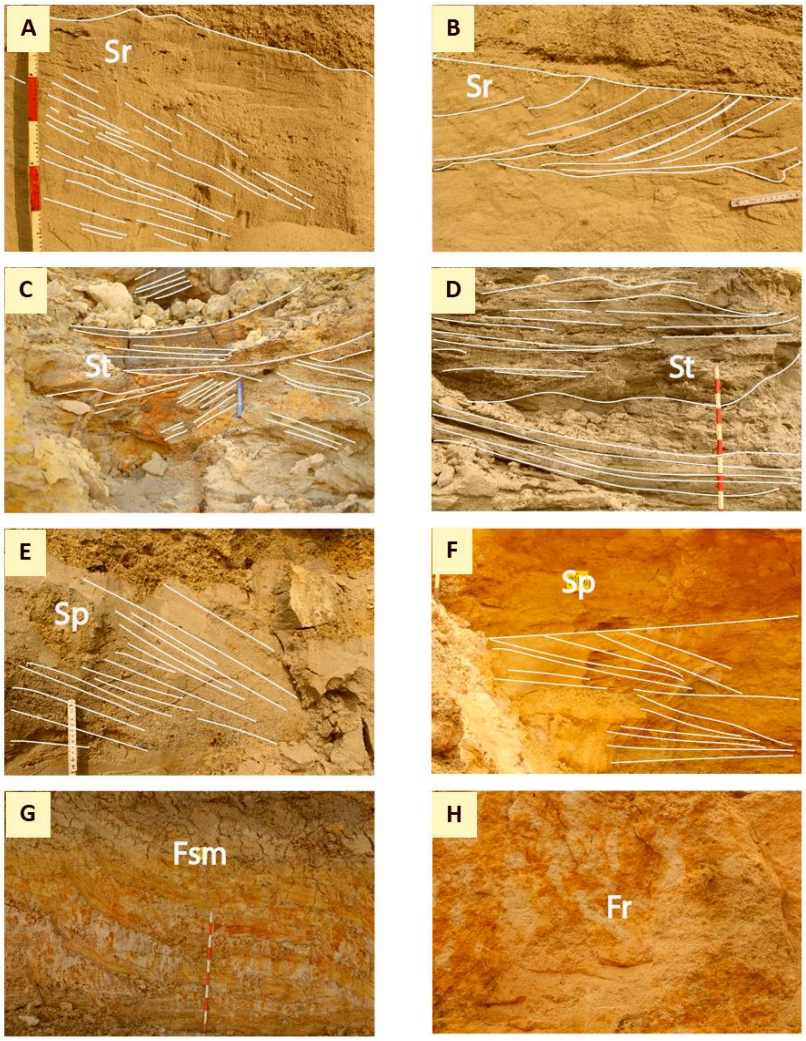

Figure 2. Lithofacies recognized in the study area.
(A-B) *ripple cross-laminated sand (Sr)*, (C-D) *trough-cross-bedded sand (St)*, (E-F) *planar-cross-bedded sand (Sp),* (G) *silt, mud (Fsm),* (H) *mud, silt, root bed (Fr).*

Table 1. Summary of lithofacies description and interpretation in the study area (modified from Miall[1,3]).

Facies code	lithofacies	Sedimentary structures	Interpretation
		I - Gravel lithofacies	
(Gmg)	Matrix-supported gravel	Normal grading	Pseudo-plastic debris flow
(Gp)	Gravel	Planar-cross-bedded	Transverse bedforms
		II - Sand lithofacies	
Sr	Sand, fine to coarse-grained sand	Ripple cross-laminated	Ripples (lower flow regime)
St	Sand, fine to very coarse-grained sand	Trough-cross-beds	Sinuous-crested and linguoid (3-D) dunes (High flow regime)
Sp	Sand, medium to coarse-grained sand	Planar-cross-bedded	Transverse and linguoid bedforms (2-D dunes
Sh	Sand, horizontally bedded sand	Horizontal lamination	Plane-bed flow to coarse, parting or streaming (critical flow)
		III - Fine-grained clastic facies	
Fsm	Silt, mud	Desiccation cracks, mottles zone, iron concretion	Back swamp or abandoned channel deposits
Fr	Mud, silt,	Root traces, mottles zone, bioturbation,	Root bed, incipient soil
Fm	Mud, silt	Massive, wedge-shaped, desiccation cracks	Overbank, abandoned channel, or drape deposits
Fl	Sand, silt, mud	Lamination, small ripples mark	Overbank, abandoned channel, or waning flood deposits

Table 2. Summary of architecture elements formed within channels in the study area (modified from Miall[1-2]).

Element	Code	Lithofacies	Geometry and relationships
Sandy bedforms	SB	St, Sp, Sh, Sl, Sr	Channel fills, minor bars
Lateral-accretion macroform	LA	St, Sp, Sh, Sl, Ss, Gp, Gmg	Wedge, characterized by internal-lateral-accretion 3rd-order surfaces
Abandoned channel fills	CH(FF)	Fsm, Fl, Fm, Fr	Product of chute or neck cutoff
Levee deposits	LV	Fl	Overbank flooding
Crevasse channel	CS	St, Sr, Fl	Break in main channel margin
Floodplain fines	FF	Fsm, Fl, Fm, Fr	Deposits of overbank sheet flow, floodplain ponds, and swamps

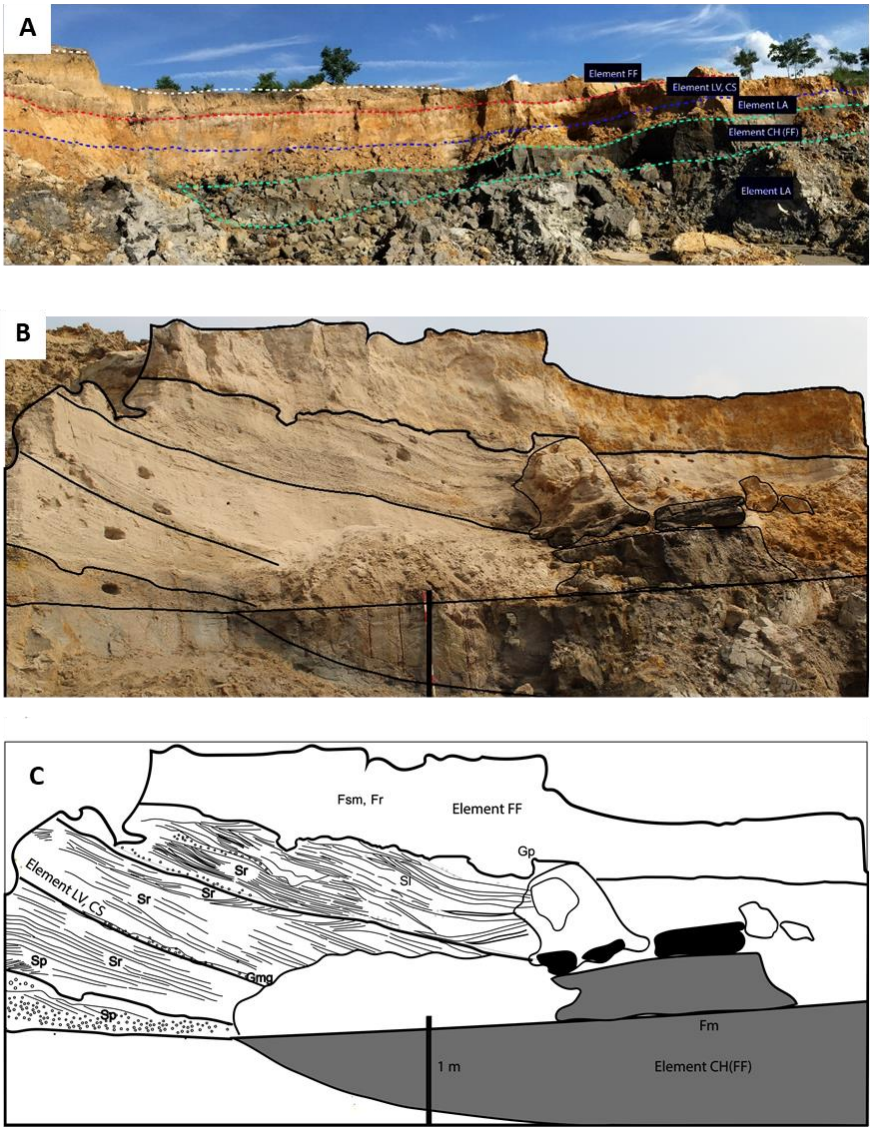

Figure 3. (A -B) Overview of sandpit in the study area, Nakhon Ratchasima Province. (C) Photo-mosaic of the study area and its interpretation of architecture elements. See table 2 for architectural code and elements. Black color represents wood fragments.

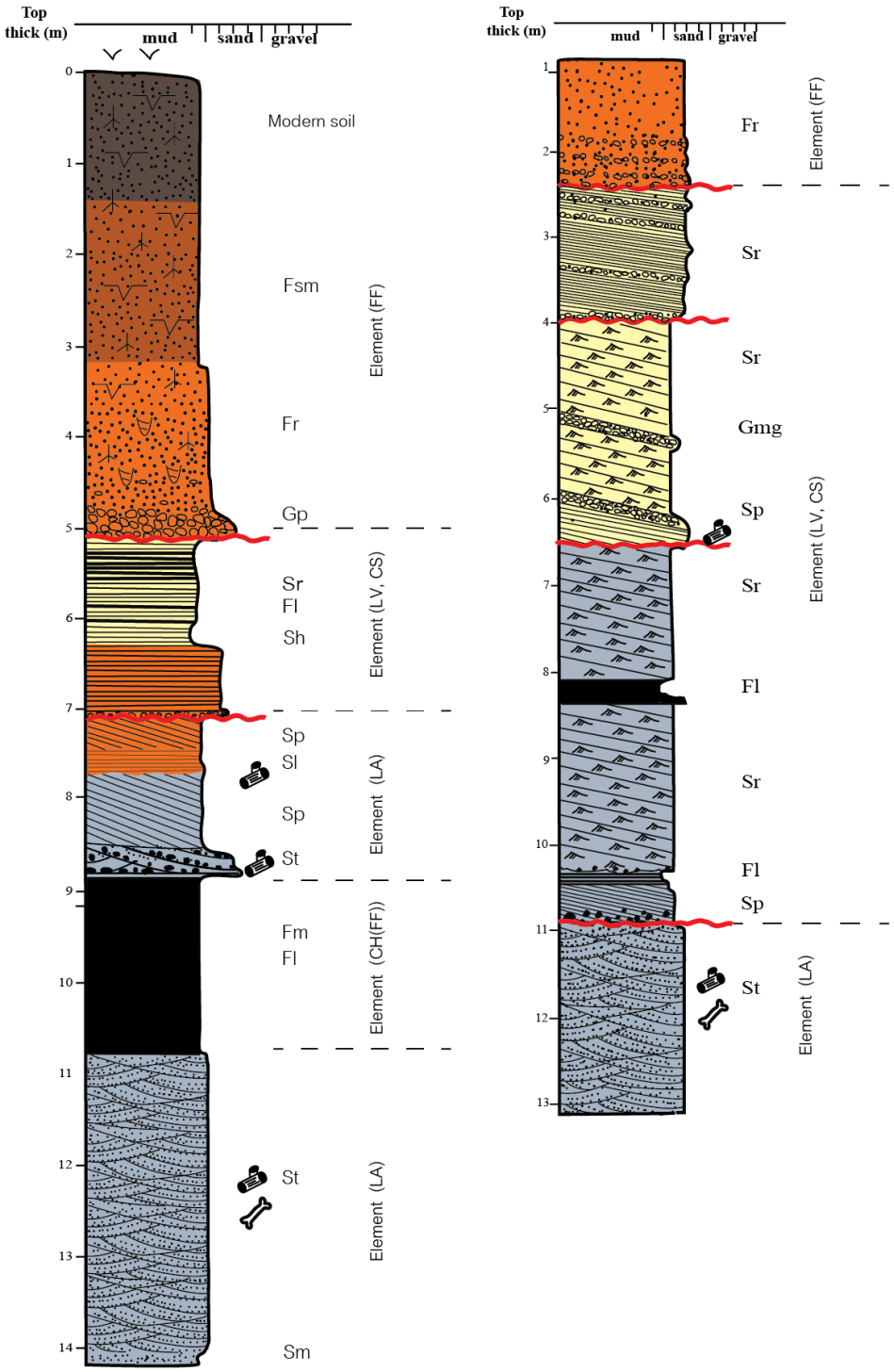

Figure 4. Detail stratigraphy of the studied section with architecture elements and lithofacies code. Depth of plant fossils and bone fragments and indicated. Sharp contacts are shown in red line.

Conclusion: The lithofacies and architecture elements of ancient Mun River found in stratigraphic unit from Nakhon Ratchasima sandpits consists of fine to coarse-grained sand with thick sand beds interbedded with thin mud to form numerous interfingering structures. Six architectural elements were classified correspondingly with depositional environments and mechanism including (1) sandy bedforms, (2) lateral accretion deposits, (3) levee deposits, (4) floodplain fines, (5) crevasse channel elements (CR) and (6) abandoned channel fills, respectively. A detail of architectural elements analysis from this study suggests that the sand-beds were mainly deposited by lateral migration of channels, reflecting growth, migration, abandonment and filling of channels in meandering river environment. All those lithofacies and architectural elements confirm the deposition environment of channel-fill and point-bar deposits in correspond with the lateral migration of channels. The upper part of the stratigraphic unit comprise fine-grained clastic facies suggesting the deposition from suspension as a low flow regime and low energy. However, the lower part is dominated by sand lithofacies, and less commonly gravel facies. It indicates high flow regime and rapid flow. Both of them were represented the meandering features of fluvial system with high sinuosity channels. The analysis in facies and architectural elements in this work improves our understanding in depositional mechanism and environment of the ancient Mun River as well as providing stratigraphic key facies in the correlation of future fossil layers that may probably discover in the similar depositional features.

References:

1. Miall A D. Springer. 1996; 75–190.
2. Miall A D. Elsevier Science Publishers B.V. 1985; 22:261–308.
3. Miall A D. Elsevier Scientific Publishing Company, Amsterdam. 1977;13:1–62.
4. 14Osman F I A, Ibrahim A, Abuobida Y, Eisawi A M A, Alhadi M, Mukhtar O, El Tijani A A. American Journal of Earth Sciences. 2015;2(6):236–241.
5. 16Howard T. The Geological Society London. 2011;573–591.
6. 17Haines W, Howard T, Ali R, Burrett F, Bunopas S. Earth and Pllanetary Science. 2004;225:19–28.
7. 18Chaimanee Y, Yamee C, Tian P, Khaowiset, Marandat B, Tafforeau P, Nemoz C, Jaeger J–J. American Journal of Physical Anthropology. 2006;131:311–323.
8. 19Dheeradilok P, Kaewyana W. Bulletin of the Geological Society of Malaysia. 1986;1: 515–532.
9. 20Choowong M. The Geological Society London. 2011;335–350.
10. 21Duangkrayom J, Ratanasthien B, Jintasakul P, Carling P A. Quaternary International. 2014;325:220–238.

Acknowledgements: This work is supported by the Research Grant for New Scholar Ratchadaphisek Somphot Endowment Fund, Chulalongkorn University. MESA Research Unit is also acknowledged for field and laboratory works.

E_004_PF: ACTIVITY OF $PtIrO_2$/C FOR REGENERATIVE PEM FUEL CELL

Ladawan Thupchai[1,2], Mali Hunsom[3], Kejvalee Pruksathorn[1,2,*]
[1]Department of Chemical Technology, Faculty of Science, Chulalongkorn University, Bangkok, Thailand
[2]Center of Excellence on Petrochemical and Materials Technology, Chulalongkorn University, Bangkok, Thailand
[3]Associate Fellow of Royal Society of Thailand, Bangkok, Thailand
*e-mail: kejvalee.p@chula.ac.th

Abstract:The $PtIrO_2$/C electrocatalysts for oxygen reduction reaction (ORR) and oxygen evolution reaction (OER) in regenerative PEM fuel cell were prepared by impregnation method at the ratio of Pt black and IrO_2 of 1:1. Activity of supported $PtIrO_2$ electrocatalyst was explored and compared to Pt/C catalyst. It was found that the $PtIrO_2$/C exhibited higher performance in ORR and OER activity, in term of kinetic current density with current density of 0.42 mA/cm^2 at 0.6 V and 1.11 mA/cm^2 at 1.35 V, respectively. Kinetic analysis shows that ORR of all catalysts follows four electron pathway mechanism.

Introduction: Fuel cell is a device that converts chemical energy into electricity. It has high efficiency rate to generate electricity and water as a byproduct without any toxic emissions. Unitized regenerative fuel cell (URFC), it is a reversible energy conversion device that combines fuel cell (FC) and water electrolyzer (WE). In fuel cell mode, hydrogen and oxygen are used to produce the electricity by hydrogen oxidation reaction at anode and oxidation reduction reaction (ORR) at cathode. On the other hand, in water electrolyzer mode, water can split to produce hydrogen and oxygen by hydrogen evolution reaction (HER) at cathode and oxygen evolution reaction (OER) at anode. Limitation of URFC is attributed to slow kinetic rate of ORR together with mass transport limitations of gaseous reactants to the reaction sites[1]. Thus, the electrocatalyst for both ORR and OER need to have high electrocatalytic activity, stability and electrical conductivity[2].

The most catalyst for ORR in fuel cell is the platinum-based supported on carbon because carbon material has high surface area to achieve high dispersion of metal particle. For OER in electrolyzer, the performance of metal follows the order Ru > Ir > Rh > Pd > Pt > Au[3]. However, OER in water electrolyzer occurs at high potential, metal oxide electrocatalysts are chosen for this reaction because the volcano plot in which metal oxides are in located on its top[4] and the IrO_2 exhibits a higher stability than RuO_2. Thus, bifunctional electrocatalyst obtained by the combination of Pt and IrO_2 should improve ORR and OER performance in URFC.

The objective of this work is to prepare $PtIrO_2$ on carbon by impregnation method. The ORR and OER activity of all prepared catalysts were tested in acid solution.

Methodology: The support used in this work was the carbon black (Vulcan XC-72). Prior use, carbon black were treated in 12M mixed HNO_3 and H_2SO_4 at volume ratio of 1:1 by dispersing of carbon black in mixed acid into flask with the volumetric ratio of 7:3 and stirred at 250 rpm for 6 h. The slurry was held afterwards in hood without stirring for 18 h and the treated carbon black was filtrated and washed by deionized water until pH constant and dried at 110°C for 24 h.

For the preparation of Pt, IrO_2 and $PtIrO_2$/C electrocatalysts, treated carbon black were used as the support. The catalysts with Pt:IrO_2 weight ratio 1:1 and metal loading of the support 20 wt% were prepared using impregnation synthesis method[5]. Both Pt black (99.99%, Alfa Aesar) and IrO_2 (99.99%, Alfa Aesar) were mixed mechanically with support, and the mixer was dispersed in isopropanol under sonication for 0.5 h. Then 2 M formic acid was added into solution and adjusted the pH to 2 by HCl under sonication at 80°C for 3 h.

Subsequently, the suspension was filtrated and washed by deionized water until the constant pH was reached and dried at 80°C for 24 h.

The morphology of the all prepared catalysts were analyzed using X-ray diffractometry (XRD) on D8 Discover-Bruker AXS machine, transmission electron microscopy (TEM) on JEOLJEM-3100F, Scanning electron microscopy (SEM) and energy dispersive X-ray spectrometry (EDX) on JEOLJSM-7610F.

The electrochemical characterization of all prepared electrocatalysts was performed in 0.5 M H_2SO_4 electrolyte at 25°C with three electrodes using saturated calomel electrode (SCE) as reference electrode and Pt rod as counter electrode. The prepared electrocatalyst loaded on glassy carbon was used as working electrode, which can prepared in-house by dispersing the catalyst in deionized water and sonicated for 1 h. Then isopropanol was added into solution and sonicated for 2 h. The 2 µL of catalyst ink was dripped onto glassy carbon. The electrochemical surface area (ESA) was estimated using cyclic voltammetry using Potentiostat/Galvanostat in N_2-saturated acid solution with the potential range of -0.2 to 0.8 V at scan rate of 20 mV/s. The ESA of each catalyst was calculated from H_2 desorption peak. The ORR activities were studied using the linear sweep voltammograms (LSV) in O_2-saturated acid solution at the potential between -0.2 to 1.0 V at scan rate of 10 mV/s as different rotation speeds varying from 500 to 2,000 rpm. The OER activity was studied in N_2-saturated acid solution between 1.0 to 1.6 V at scan rate 10 mV/s as rotating speed 1,500 rpm.

Results and Discussion:

Physicochemical characterization of prepared catalysts: The XRD pattern of all prepared catalysts together with that of carbon support, commercial Pt black and IrO_2 are shown in Figure 1. For Pt/C catalyst, the characteristic diffraction peaks of Pt were observed at 2θ of 39.89°, 46.28°, 67.53° and 81.54° corresponding to Pt(111), Pt(200), Pt(220) and Pt(311), respectively. For IrO_2/C catalyst, the characteristic diffraction peaks of IrO_2 were appeared at 2θ of 40.69°, 47.35°and 69.17° corresponding to IrO_2(200), IrO_2(211) and IrO_2(112) respectively and peak at 2θ of 24.86° corresponded to C(002) of graphitic carbon from carbon black support. The diffractograms of $PtIrO_2$/C catalysts exhibited the coexistence of peaks related to face centered cubic Pt and tetragonal rutile IrO_2[6], Indicating that both Pt and IrO_2 particles have been deposited on support. For Carbon black support, broad peaks were observed indicating the formation of less crystallite structure[7]. The average crystallite size of catalysts were calculated based on Pt(111) and IrO_2(200) by Scherrer equation. The results of crystallite size Pt/C, IrO_2/C and $PtIrO_2$/C were shown in Table 1. The crystallite size decreased importantly in the presence of mixed metal, probably due to the interaction between Pt and IrO_2 metal, providing a well dispersion of $PtIrO_2$ catalyst on support.

Figure 2 shows the TEM images of the metal for all catalysts. The Pt/C and IrO_2/C catalysts exhibited an agglomerated between particle whereas the $PtIrO_2$/C exhibited uniform distribution particle. The average particle size of Pt/C, IrO_2/C and $PtIrO_2$/C were determined to be 6.88, 7.35 and 1.81 nm, respectively. From EDX analysis, an average $PtIrO_2$ loading on carbon black were around 16.50-20.76 wt% as shown in Table 1. The distribution of Pt and Ir elements in the testing region is shown in Figure 3, displaying high degree of dispersion of Pt (blue dots) and Ir (green dots).

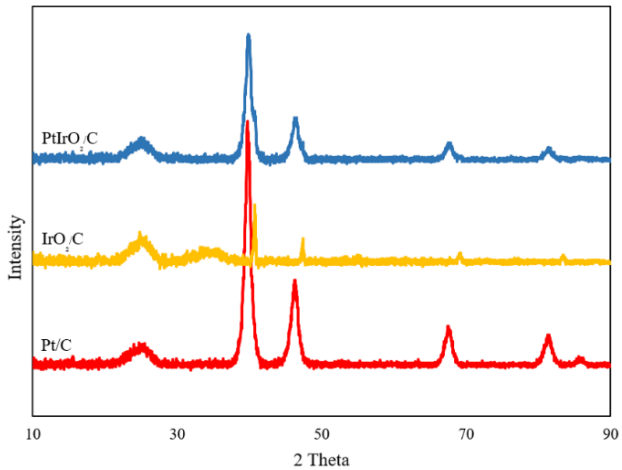

Figure 1. XRD patterns of Pt/C, IrO_2/C and $PtIrO_2$/C catalysts

Electrochemical characterization of catalyst.: The ESA of all catalysts was determined by cyclic voltammetry (CV) under N_2-saturated in acid solution as shown in Figure 4. As shown in Table 1, the ESA of Pt/C and $PtIrO_2$/C were 18.26 and 27.18 m^2/g of Pt, respectively, but no peaks behaviors could be observed on IrO_2/C. Indicating that $PtIrO_2$/C catalyst had the highest number of active sites on Pt surface. That is, its ESA increased by 1.5 times compared to that of Pt/C catalyst. The difference in ESA obtained for the difference catalyst could be attributed to Pt utilization efficiency of each catalyst as order $PtIrO_2$/C > Pt/C. A higher Pt utilization efficiency represented a number of three-phase boundaries in the structure where actual catalyst occurs and number of effective Pt active sites for ORR[9].

Table 1. Properties of Pt/C, IrO_2/C and $PtIrO_2$/C catalysts

Catalysts	Crystallite size (nm)		Average particle size (nm)	$PtIrO_2$ loading on support (wt%)	ESA (m^2/g of Pt)
	Pt	IrO_2			
Pt/C	9.898	-	6.88 ± 1.298	19.02	18.26
IrO_2/C	-	40.028	7.35 ± 1.337	16.50	-
$PtIrO_2$/C	9.143	29.483	1.81 ± 0.523	20.76	27.18

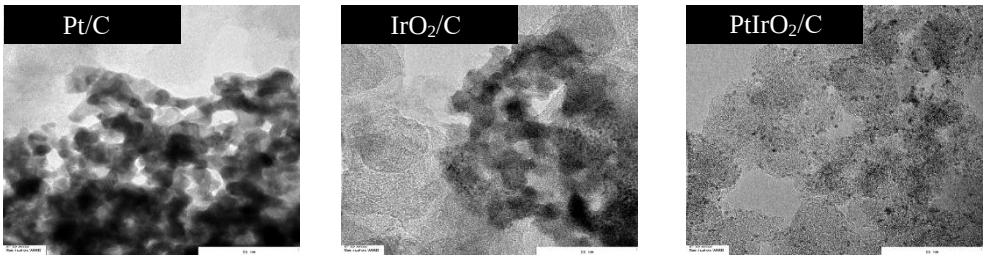

Figure 2. TEM and particle size distribution of catalysts

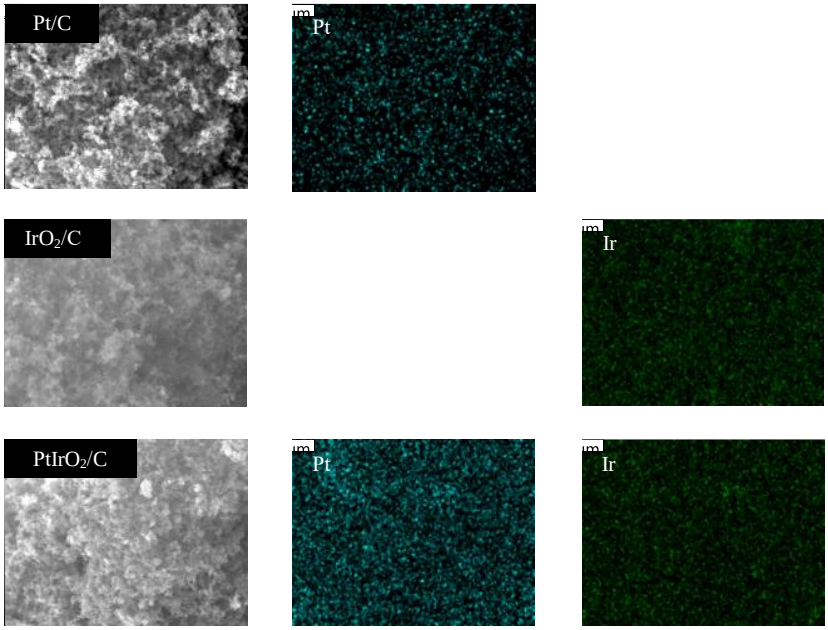

Figure 3. SEM micrographs of all catalysts and EDX mapping pattern of the element

The ORR activities of all catalysts were investigated in O_2-saturated acid solution using RDE linear sweep voltammograms at rotation rates between 500-2,000 rpm during a vary potential of 0.0 to 1.0 V and constant rate of 10 mV/S. The ORR polarization curves of all catalysts were shown in Figure 5(a). As expected, all prepared catalyst except IrO_2 showed three difference regions. The first region of 1.0 to 0.75 V was the kinetics control region, where the current density was not affected by rate of mass transfer and independent of the rotation rate (ω). The second region of 0.75 to 0.55 V was the intermediate region of mixed control by kinetics of electron transfer and mass transport, which the current increased with the rotation rate. The third region of 0.55 to 0.0 V was the mass transport control region, which showed a well-defined limiting current density that increases linear with $\omega^{1/2}$. The relation between the current density and the rotation rate could be expressed by the Koutecky-Levich equation as shown in Eq. (1).

$$\frac{1}{i} = \frac{1}{i_K} + \frac{1}{i_L} = \frac{1}{i_K} + \frac{1}{0.62nFAD^{2/3}\nu^{-1/6}\omega^{1/2}C_o^0} \qquad \text{(Eq. 1)}$$

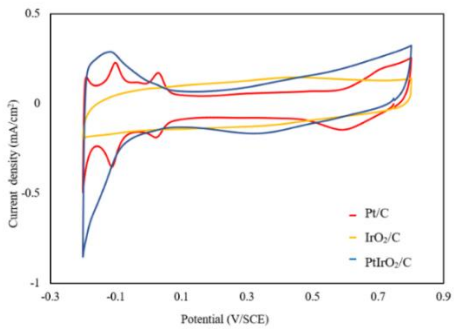

Figure 4. Cyclic voltammograms of Pt/C, IrO_2/C and $PtIrO_2$/C catalysts

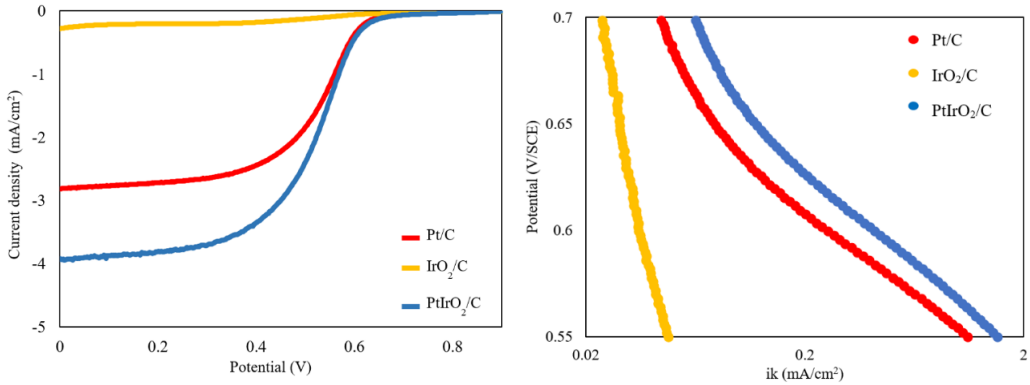

(a) (b)

Figure 5. (a) ORR polarization curve at 2000 rpm
(b) Kinetic current density of Pt/C, IrO_2/C and $PtIrO_2$/C catalysts

The kinetic currents (i_k) measured at 0.6 V on Pt/C, IrO_2/C and $PtIrO_2$/C were 0.36, 0.05 and 0.42 mA/cm^2 (Table 2), respectively. As shown in Figure 5(b), it could be seen that the kinetic current changed as the change of applied potential, suggesting that the catalyst activity toward the ORR increased in order of $PtIrO_2$/C > Pt/C > IrO_2/C. The $PtIrO_2$/C catalyst exhibited the highest catalytic ORR activity. The enhanced ORR activity may be also be associated with Pt dispersion, Pt particle size and interaction between Pt and IrO_2. It has been reported that Pt-M (M = Ir, Pd, Ru) catalysts with optimum composition of 2nd metal showed enhancement of ORR[2]. As shown in Table 2, the calculated number of transferred electrons for catalysts were ~ 4, similar to those reported for the Pt-based catalyst in acid solution[10]. It can be indicated that the ORR of the supported $PtIrO_2$ electrocatalyst followed the four- electron transfer pathway, which produces H_2O without the formation of H_2O_2[6].

Table 2. ORR and OER activities of Pt/C, IrO_2/C and $PtIrO_2$/C catalysts in 0.5 M H_2SO_4 solution

Catalysts	n	ORR at 0.6 V (mA/cm^2)	OER at 1.35 V (mA/cm^2)
Pt/C	3.8	0.36	0.08
IrO_2/C	-	0.05	1.62
$PtIrO_2$/C	3.9	0.42	1.11

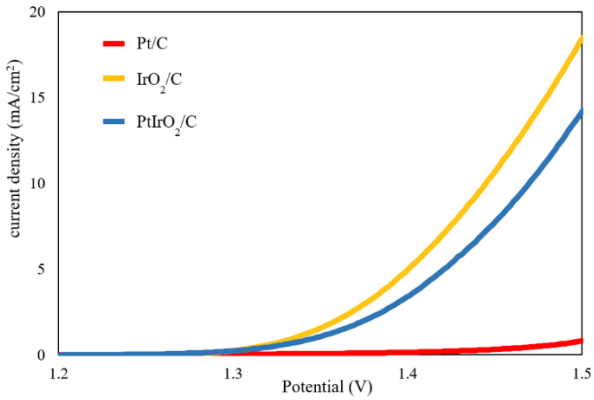

Figure 6. OER polarization curves of Pt/C, IrO_2/C and $PtIrO_2$/C catalysts at 1,500 rpm

The OER activities of all catalysts were investigated in N_2-saturated acid solution using RDE linear sweep voltammograms at the rotation rates of 1,500 rpm between potential 1.0 to 1.5 V and constant rate of 10 mV/S. As shown in Figure 6 and Table 2, the current density measured at 1.35 V of Pt/C, IrO_2/C and $PtIrO_2$/C were 0.08, 1.62 and 1.11 mA/cm^2, respectively. The IrO_2/C has lower onset potential and more active in high potential range. The $PtIrO_2$/C catalyst performance decreased also in the activation region indicating that IrO_2 covered Pt site reducing in catalytic activity of bimetallic catalyst for oxygen evolution reaction[11].

Conclusion: It was observed that mixing Pt and IrO_2 on carbon black prepared by impregnation method demonstrated a good uniformity and ordered distribution. From this study, it can be concluded that the $PtIrO_2$/C catalyst exhibited high ORR and OER activity. Kinetic analysis showed that the ORR of Pt and $PtIrO_2$ catalysts followed the four-electron pathway.

Reference:

1. Millet P. International Journal of Hydrogen energy. 2011;36:4156-4163.
2. Won JE, Kwak DH, Han SB, et al. Journal of catalysis. 2018;358:287-294.
3. Paoli EA, Masini F, Frydendal R, et al. Chemical Science. 2015;6:190-196.
4. Jeevagan AJ, Suzuki Y, Gunji T, et al. The Electrochemical Society. 2014;58:9-18.
5. Cruz JC, Rivas S, Beltran, et al. International Journal of Hydrogen energy. 2012;37: 13522-13528.
6. Silva GC, Fernandes MR, Ticianelli EA. Journal of American Chemical Society. 2018;8: 2081-2092.
7. Bharti A, Cheruvally G. Journal of Power Source. 2017;360:196-205.
8. Park S, Shao Y, Wam H, et al. Electrochemical. 2011;13:258-261.
9. Okamoto M, Fujigaya T, Nakashima N. Small. 2009;5:735-740.
10. Paulus U, Schmidt T, Gasteiger H, et al. Journal of Electroanalysis Chemical. 2001;495: 134-145.
11. Baglio V, Urso CD, Blasi AD, et al. International Journal of Electrochemistry. 2011;2011: 6205-6209.

Acknowledgement: This research was funded by Center of Excellence on Petrochemical and Material Technology, Chulalongkorn University and Department of Chemical Technology, Faculty of Science, Chulalongkorn University.

E_005_PF: $NiCo_2S_4$/N-rGO AS A BIFUCNTIONAL OXYGEN REACTION ELECTROCATALYST FOR RECHARGEABLE ZINC-AIR BATTERIES

Phonphiphat Suwannarak, Nisit Tantavichet
Department of Chemical Technology, Faculty of Science, Chulalongkorn University, Bangkok, Thailand
Center of Excellence on Petrochemical and Materials Technology, Bangkok, Thailand
*e-mail: phonphiphat.s@gmail.com

Abstract: Nowadays, zinc–air batteries the one of metal–air batteries have received interest because it has high energy density, the abundance of oxygen, the affluence of zinc, low cost and safety. Rechargeable zinc-air battery can store and release energy by using oxygen reduction reaction (ORR) and oxygen evolution reaction (OER). However, these reactions are slow, so it required catalyst. Recently, nickel cobalt sulfide ($NiCo_2S_4$) which has good performance, inexpensive and useful for both ORR and OER get more attention. Herein, $NiCo_2S_4$ with carbon-based support was investigated in term of electrocatalyst activity for oxygen reduction reaction (ORR) and oxygen evolution reaction (OER) comparing with commercial catalysts. Vulcan carbon (C), reduced graphene oxide (rGO) and nitrogen doped reduced graphene oxide (N-rGO) were used as supporters to improve electrocatalytic activity. The results show that $NiCo_2S_4$ on nitrogen doped rGO had higher electrocatalytic activity more than $NiCo_2S_4$ on non-doped rGO. When consider $NiCo_2S_4$/N-rGO compare with $NiCo_2S_4$/C and commercial catalysts, the result show that $NiCo_2S_4$/N-rGO had higher electrocatalytic activity than cobalt oxide (Co_3O_4) but still lower than $NiCo_2S_4$/C and the commercial platinum (Pt/C) for ORR.

Introduction: At present, global energy consumption is increasing over the years resulting in development of renewable energy technologies such as solar and wind energy technologies. However, they depend on the uncertain weather and environment. It is necessary to have energy storage systems that store generated energy and release later. This reason leads to the importance of energy storages such as batteries and capacitors. Among them, metal–air batteries have received increasing interest. The advantages of metal-air batteries are their high energy density and the use of oxygen as resource. Metal-air batteries is consisted of metal electrode, separator, air electrode and electrolyte. The type of metal-air batteries depends on the metal that use as metal electrode.

Zn–air batteries have a potential for future energy applications due to its high stability, high reactivity, high reversibility, low cost and safety.[1] Rechargeable zinc-air battery can store and release energy through the oxygen reduction reaction (ORR) and oxygen evolution reaction (OER). During discharge zinc will donate electrons and forms zincate ion.

$$\mathrm{Zn + 4OH^- \rightarrow Zn(OH)_4^{2-} + 2e^-} \qquad \mathrm{E^0 = -1.266\ V\ vs.\ NHE}$$

$$\mathrm{Zn(OH)_4^{2-} \rightarrow ZnO + H_2O + 2OH^-}$$

While, at air electrode oxygen from air will receive electrons and forms hydroxyl ions. This reaction is ORR.

$$\mathrm{\frac{1}{2}O_2 + H_2O + 2e^- \rightarrow 2OH^-} \qquad \mathrm{E^0 = 0.401\ V\ vs.\ NHE}$$

Overall reaction during discharge:

$$\mathrm{Zn + \frac{1}{2}O_2 \rightarrow ZnO} \qquad \mathrm{E^0cell = 1.667\ V\ vs.\ NHE}$$

And during charge the reverse reaction is occurred. Zincate in electrolyte is reduced to zinc and deposit to zinc electrode.

$$ZnO + H_2O + 2OH^- \rightarrow Zn(OH)_4^{2-}$$

$$Zn(OH)_4^{2-} + 2e^- \rightarrow Zn + 4OH^-$$

While, at air electrode hydroxyl ions form oxygen and release electrons. This reaction is OER.

$$2OH^- \rightarrow \frac{1}{2}O_2 + H_2O + 2e^-$$

Overall reaction during charge:

$$ZnO \rightarrow Zn + \frac{1}{2}O_2$$

The ORR and OER is important reactions for rechargeable Zn-air batteries.[2,3]

However, these reactions are slow, so it requires catalysts. Nowadays, the precious metal is known as highest performance electrocatalyst. Due to its cost and rarity, make them undesirable for commercial use. So, it is necessary to find alternative catalysts with low cost. Recently, oxides and sulfides of transition metal have received attention because of its good electrocatalytic activity and low cost. Among them, nickel cobalt sulfide ($NiCo_2S_4$) reveal good electrocatalytic activity for both the ORR and OER but it has low conductivity. So, it has been studied to improve electrocatalytic performance. Herein, the electrocatalytic activity of $NiCo_2S_4$ on nitrogen doped reduced graphene oxide is studied and compare with commercial catalyst.[4]

Methodology:

A. Chemicals: Sulfuric acid (98%) (H_2SO_4), hydrogen peroxide (H_2O_2) and potassium permanganate ($KMnO_4$) were purchased from Merck. Ammonia solution (25%) (NH_3OH) and ethylene glycol were supplied by Quality Reagent Chemical. Graphite powder, cobalt(II) acetate tetrahydrate ($Co(OAc)_2.4H_2O$), nickel(II) acetate tetrahydrate ($Ni(OAc)_2.4H_2O$) and thiourea were supplied by Aldrich. All chemicals were used as received without further purification.

B. Synthesis of Graphene oxides: The graphene oxide was synthesized by modified Hummers method. Graphite powder 5 g was added into 115 mL concentrated H_2SO_4 (98%) under stirring in an ice bath. After stirring for 1 h, $KMnO_4$ 30 g was slowly added under continuous stirring and the temperature of the mixture was kept below 5 °C for 3 h. After that the mixture was heated to 40 °C and kept at this temperature for 1 h. Cold deionized water 100 mL was dropwise added into the mixture under stirring for 1 h and kept temperature below 95 °C. After that deionized water 200 mL and H_2O_2 15 mL was added into the mixture. The mixture was centrifuged and washed several times with 5% HCl and deionized water. The slurry was dried at 60 °C. Finally, graphene oxide was obtained after sonicated for 3 h and freeze dried.

C. Synthesis of $NiCo_2S_4$/N-rGO: $NiCo_2S_4$/N-rGO was synthesized by solvothermal method. Firstly, GO 60 mg was dispersed in 60 mL ethylene glycol by sonicated for 1 h. Then, 0.3 mmol $Co(OAc)_2$ and 0.15 mmol $Ni(OAc)_2$ were dissolved in GO/EG suspension and stirred at 80 °C for 1 h. After that 10 mL 25% NH_3OH solution was introduced into the mixture. After stirring for 1 h, 0.9 mmol thiourea was added into the mixture. Then the mixture was transferred to a Teflon-lined autoclave (100 mL) and the reaction was continued at 180 °C for 12 h. The resulted product was collected by filtration, washed with deionized water, and freeze dried. $NiCo_2S_4$/rGO and $NiCo_2S_4$/C was prepared by the same method except NH_3OH solution addition.

D. Characterization: The morphology and element ratio of synthesized samples were characterized by scanning electron microscopy (SEM) equipped with an energy-dispersive spectrometer (EDS). The crystal structure was detected by X-ray diffraction (XRD, Bruker/D8 Advanced).

E. Electrochemical Measurements: The electrochemical tests were carried out on an AutoLab workstation (Autolab PGSTAT 30), using a three-electrode electrochemical cell. The synthesized sample coated glass carbon (GC) electrode, a silver chloride electrode, and a platinum pole were used as working, reference, and counter electrode, respectively. The catalyst ink was prepared as follows: 6 mg of the catalyst was dispersed in the mixture of 800 µL deionized water, 200 µL ethanol and 100 µL of 5 wt % Nafion solution by sonicating for 1 h to obtain a homogeneous ink. Then, 5 µL of the catalyst ink was loaded onto a GC electrode of 5 mm in diameter (the catalysts loading was ~0.139 mg cm^{-2} for all samples). The ORR performance was investigated by linear sweep voltammetry (LSV) in O_2-saturated 0.1 M KOH at room temperature, under constant O_2 gas flow, with a rotation speed of 1600 rpm and a sweeping rate of 10 mV s^{-1} in the potential range of 0.1 to −0.9 V vs Ag/AgCl. The OER performance was investigated by the LSV method, in 0.1 M KOH at room temperature, with a rotation speed of 1600 rpm and a sweeping rate of 10 mV s^{-1} in the potential range of −0.1 to 0.9 V vs Ag/AgCl.

Results and Discussion: $NiCo_2S_4$/N-rGO was synthesized by one-step solvothermal using $Co(OAc)_2$, $Ni(OAc)_2$, thiourea as precursor, NH_3OH as doping agent and GO as supporter. Firstly Co^{2+} and Ni^{2+} ions were anchored on negatively charged GO sheets and formed into $NiCo_2S_4$ after thiourea was added. During the solvothermal process, $NiCo_2S_4$ was formed and GO sheets was reduced to rGO. This synthesis process is similar to the formation of rGO sheets decorated with other nanoparticles.[5,6]

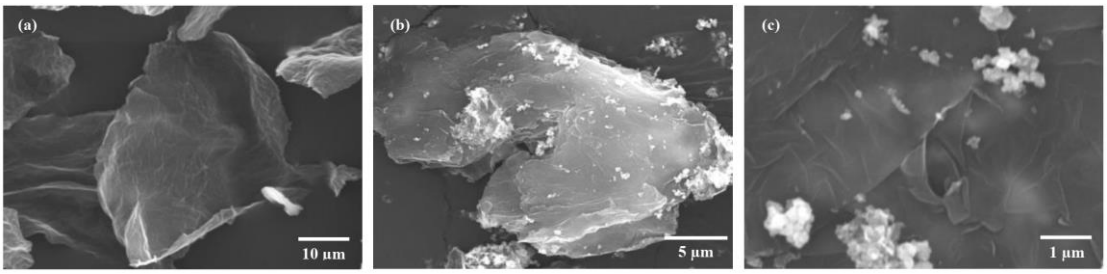

Figure 1. SEM images of (a) GO (b, c) $NiCo_2S_4$/rGO

The morphology and surface structure of synthesized GO and $NiCo_2S_4$/rGO were revealed by scanning electron microscopy. Figure 1 (a) show thin layer GO without obvious aggregation. Figure 1 (b, c) show $NiCo_2S_4$ particles grown on reduced graphene oxide sheets. The Element analysis from EDS (Table 1) reveals the atomic ratio of Ni to Co and S is 1 : 2 : 3.6 which is appropriate to 1 : 2 : 4 and confirms the formation of stoichiometric of $NiCo_2S_4$. The XRD pattern of $NiCo_2S_4$/N-rGO and $NiCo_2S_4$/rGO (Figure 2) show diffraction peak at 26.8°, 31.6°, 38.2°, 50.4° and 55.2° that indicating (220), (311), (400), (511) and (440) planes. These peaks were corresponding to cubic type $NiCo_2S_4$ (PDF 43-1477) for both $NiCo_2S_4$/rGO and $NiCo_2S_4$/N-rGO.

Table 1 elemental component of $NiCo_2S_4$/rGO

Element	Amount		Ratio / Ni
	%Atomic	%Weight	
Ni	5.68	13.46	1.0
Co	11.17	26.54	2.0
S	20.7	26.77	3.6
O	18.5	11.94	-
C	43.95	21.29	-

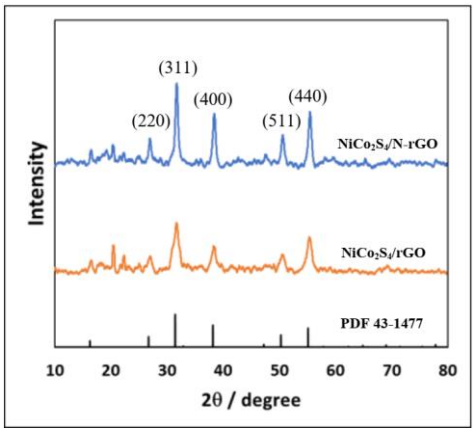

Figure 2. XRD pattern of $NiCo_2S_4$/N-rGO and $NiCo_2S_4$/rGO

The effect of doping nitrogen on reduced graphene oxide was studied by measuring electrocatalytic performance of $NiCo_2S_4$, $NiCo_2S_4$/rGO and $NiCo_2S_4$/N-rGO via three electrode system. The catalytic activity for ORR of $NiCo_2S_4$, $NiCo_2S_4$/rGO and $NiCo_2S_4$/N-rGO was examined by LSV in O_2-saturated 0.1 M KOH at room temperature, under constant O_2 gas flow, with a rotation speed of 1600 rpm as show in Figure 3 (a). The ORR onset is at -0.36, -0.27 and -0.18 V vs. Ag/AgCl respectively. The current density at -0.8 V is -1.53, -2.73 and -3.09 mA cm^{-2} respectively. The OER electrocatalytic performance was examined by the same method except O_2-saturated and O_2 gas flow as show in Figure 3 (b). The OER onset potential is 0.34, 0.25 and 0.22 V vs. Ag/AgCl respectively. From these results show that $NiCo_2S_4$/N-rGO has higher electrocatalytic activity than $NiCo_2S_4$ and $NiCo_2S_4$/rGO indicate by more positive onset potential and highest current density in ORR curves and more negative onset potential in OER curves. These results suggest that doping nitrogen on reduced graphene oxide can improve electrocatalytic activity of $NiCo_2S_4$ for both ORR and OER.

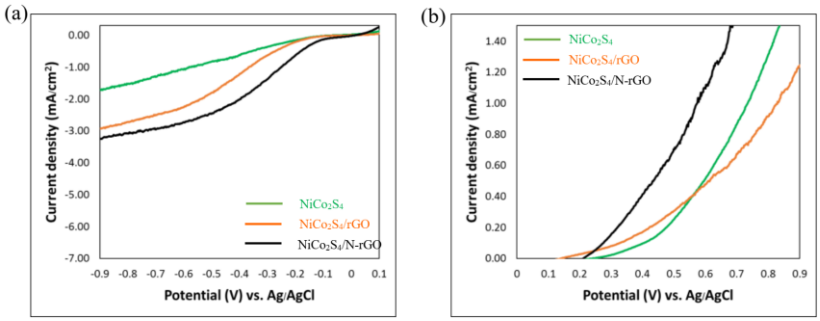

Figure 3. (a) ORR and (b) OER curves of $NiCo_2S_4$, $NiCo_2S_4$/rGO and $NiCo_2S_4$/N-rGO

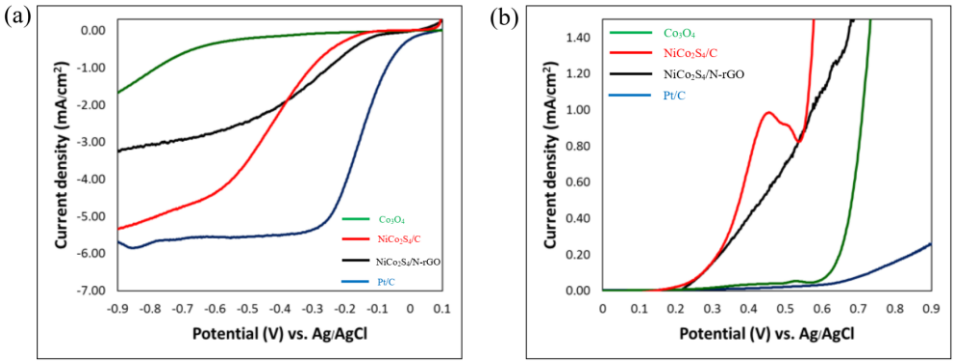

Figure. 5. (a) ORR and (b) OER curves of Co_3O_4, $NiCo_2S_4$/C, $NiCo_2S_4$/N-rGO and Pt/C 20%

In addition, $NiCo_2S_4$/N-rGO was compared with $NiCo_2S_4$/C and commercial electrocatalyst. The ORR curves (Figure 5 (a)) show that $NiCo_2S_4$/N-rGO has higher ORR electrocatalytic activity than Co_3O_4 but it is still lower than $NiCo_2S_4$/C and Pt/C. However, the OER curves (Figure 5(b)) show the good OER electrocatalytic performance of $NiCo_2S_4$/N-rGO which is higher than commercial electrocatalyst and similar to $NiCo_2S_4$/C.

Conclusion: The morphology of $NiCo_2S_4$/N-rGO which was successfully synthesized by the solvothermal method shows small particles of $NiCo_2S_4$ deposit on thin layers of graphene oxide. These $NiCo_2S_4$/N-rGO exhibit higher electrocatalytic activity for ORR and OER than $NiCo_2S_4$ and $NiCo_2S_4$/rGO. When compared to $NiCo_2S_4$/C and commercial electrocatalysts, $NiCo_2S_4$/N-rGO is much more effective than cobalt oxide (Co_3O_4) but still lower than $NiCo_2S_4$/C and the commercial platinum (Pt/C) for ORR. For OER, $NiCo_2S_4$/N-rGO is better than commercial electrocatalysts.

References:

1. Li Y, Dai H. Chem. Soc. Rev 2014;43:5257–5275.
2. Zhu A. L, Wilkinson D. P, Zhang X, Xing Y, Rozhin A. G, Kulinich S. A. Journal of Energy Storage 2016;8:35–50.
3. Haas O, Holzer F, Müller K, Müller S. Technology and Applications 2003;1:382–408.
4. Osgood H, Devaguptapu S. V, Xu H, Cho J, Wu G. Nano Today 2016;11:601–625.
5. Wu J, Dou S, Shen A, Wang X, Ma Zh, Ouyang C, Wang S. J. Mater. Chem. A 2014; 2:20990.
6. Wang M, Huang J, Wang M, Zhang D, Zhang W, Li W. J. Chen. Electrochem. Commun. 2013;34:299.

Acknowledgements: This research was conducted with financial support from Center of Excellence on Petrochemical and Materials Technology, Chulalongkorn University and made use of the facilities at department of Chemical Technology, Faculty of Science, Chulalongkorn University.

E_006_OF: THE STUDY OF BASEFLOW SEPARATION AT WATERSHEDS IN CHIANG RAI, THAILAND

Prach Sukkavee[1], Schradh Saenton[2], Rungrote Nilthong[1,*]
[1]School of Science, Mae Fah Luang University, Chiang Rai, Thailand
[2]Department of Geological Sciences, Chiang Mai University, Chiang Mai, Thailand
*e-mail: rungrote@mfu.ac.th

Abstract: This paper presents the parameter estimation process of baseflow separation method on 3 watersheds in Chiang Rai, ranging from 31.6 to 434.0 km^2. The main input for the process was daily stream flow data from each watershed. The stream flow analysis was conducted using 6 recursive digital filters (RDF: One-parameter, Boughton-two-parameter, IHACRES, Lyne & Hollick, EWMA, and Chapman algorithm) and hydrograph analysis (DGM: Fixed interval and Sliding interval). First, each method was calibrated by using daily stream flow data in dry periods (January to March and December) for each year (annually) for baseflow separation. Then, optimal parameters were obtained from annual median values. The calibration process was developed for each watershed. Furthermore, validation process was performed by applying the optimal parameters with stream flow data during dry periods in 2018 and 2019 and testing the result with BFI index, RMSE and correlation coefficient. The result showed both DGM and RDF methods give RMSE values less than 0 while BFI index and correlation values found in the RDF method are 0.800 and 0.999 respectively. Both values are better than those of DGM method which are 0.778 and 0.793 respectively. In analytical detail, the RDF method using the IHACRES algorithm provided the best performance. Also the DGM method with Fixed interval algorithm using $N=A^{0.2}$ can be used to separate the baseflow as well.

Keywords: baseflow; separation; digital filter; recursive digital filter; calibration.

Introduction: Stream runoff or runoff refers to water flow in the river. The stream runoff commonly changes according to different times of the year. Normally, the quantity of water in the river is abundant in the rainy season and becomes less in dry season. The analysis of the runoff primarily consists of two main parts, the first part is direct runoff caused by rain in the catchment area (ground cannot absorb, thus runoff will occur) and the second part is amount of water absorbed by soil and released later called "baseflow". Importantly, it sustains stream flow during dry periods, in spite of lower rainfalls in the watershed. Water content in each component is very important especially when considering the water resources management in terms of water storage or disaster event. For instance, flood or landslide will occur when the amount of water is excessive while drought during dry season will occur due to the baseflow is lower than the water requirement. Therefore, the understanding of the water in both components and the process of water flow conditions, such as the nature of the watershed and time period of the flow is a key part for forecasting. However, it's difficult to separate each component part of the water from measurement directly due to changes in watershed area, such as nature of land use, or condition changes in soil and climate, etc.

There are many different methods to separate baseflow from stream flow in the river. The most widely used methods for baseflow separation are Recursive Digital Filter algorithm (RDF) and Digital Graphical Method (DGM). The RDF relies on mathematical analysis in a runoff by filtering the signal from the high signal or average signal[1] depending on the threshold configuration. While the hydrographic analysis or DGM is processed by filtering out high signals from low signals. Both two methods are based on the analysis of hydrograph. The baseflow analysis was developed and reported by Boussinesq (1877) and Miller (1905)[2]. Some related works in baseflow separation were developed and reported. For example, Darlin and A Lott Mark T. Stewart (2016)[3] used these algorithms for baseflow separation on various

watersheds (both small and large area) and calibrated with the tracer or mass balance method. While Indarto Indator et al (2017)[1] studied calibration parameters and preliminary study for baseflow separation in East Java by RDF and the DGM method and calibrated data with stream flow in dry periods.

Recursive Digital Filter (RDF): In this study, the stream flow was separated to find baseflow using RDF method. The 6 RDF algorithms used in this study were: One-parameter, Boughton-two-parameter, IHACRES, Lyne & Hollick, EWMA, and Chapman algorithm. The six algorithms are presented in Table 1.

Table 1. Baseflow separation methods used for this study.

Alogorithm	Equation	Note
One parameter[4]	$q_{b(i)} = \frac{k}{2-k} q_{b(i-1)} + \frac{1-k}{2-k} q_{b(i)}$	$q_{b(i)} \leq q_{(i)}$
Boughton (two-parameter)[4,5]	$q_{b(i)} = \frac{k}{1+C} q_{b(i-1)} + \frac{C}{1+C} q_{b(i)}$	$q_{b(i)} \leq q_{(i)}$
IHACRES (three-parameter)[6]	$q_{b(i)} = \frac{k}{1+C} q_{b(i-1)} + \frac{C}{1+C} \left(q_{b(i)} + \alpha_q q_{b(i-1)}\right)$	
BFLOW (Lynie & Holick)[7,8]	$q_{f(i)} = \alpha q_{f(i-1)} + \left(q_{(i)} - q_{(i-1)}\right) \frac{1+\alpha}{2}$	$q_{f(i)} \geq 0, \alpha = 0.925$ for daily flow, $q_b = q - q_f$
Chapman[9,10]	$q_{f(i)} = \frac{3\alpha-1}{3-\alpha} q_{f(i-1)} + \frac{2}{3-\alpha} \left(q_{(i)} - q_{(i-1)}\right)$	$q_b = q - q_f$
EWMA filter[11]	$q_{b(i)} = \alpha q_{f(i)} + (1-\alpha) q_{b(i-1)}$	

Where:

$q_{(i)}$, $q_{(i-1)}$: total flow (observed flow) at day i and i-1.

$q_{b(i)}$, $q_{b(i-1)}$: calculated baseflow at day i and i-1.

$q_{f(i)}$, $q_{f(i-1)}$: calculated quick flow/direct run off at day i and i-1.

k, α, C : filter parameter

Each algorithm in Table 1 was used to compute the baseflow in each interval (day i) by using daily stream flow as input.

Digital Graphical Method (DGM): The conceptual of DGM method is connecting each intersection point of baseflow and direct flow upon the lowest of rising limb and a point of falling limb of hydrograph. The popular methods are local minimum, Fixed interval, and Sliding interval. In this study, we concerned on Fixed interval and Sliding interval which are simple and effective to apply for baseflow separation. Firstly, the time interval was determined by N values. In literature review N values were determined by empirical relation, $N = A^{0.2}$ where A is basin area in square miles (mi^2) or $N = 0.827A^{0.2}$ where A is basin area in square kilometers (km^2). Secondly, the minimum flow was searched in each interval. In Fixed interval method time interval is 2N*day while time interval method using time interval is 0.5 (2N*-1) day where 2N* is odd integer number (3, 5, ..., 7) is close to 2N[12].

Methodology: The study was conducted at Chiang Rai province in Kok- Mekong basin. The 3 main stream rivers that flow into reservoir were selected; Maesuai River from Maesuai sub-basin, Mae Ja Dee River from Lao sub-basin, and Huai Chang River form Lower-Ing sub-basin as shown in Figure 1.

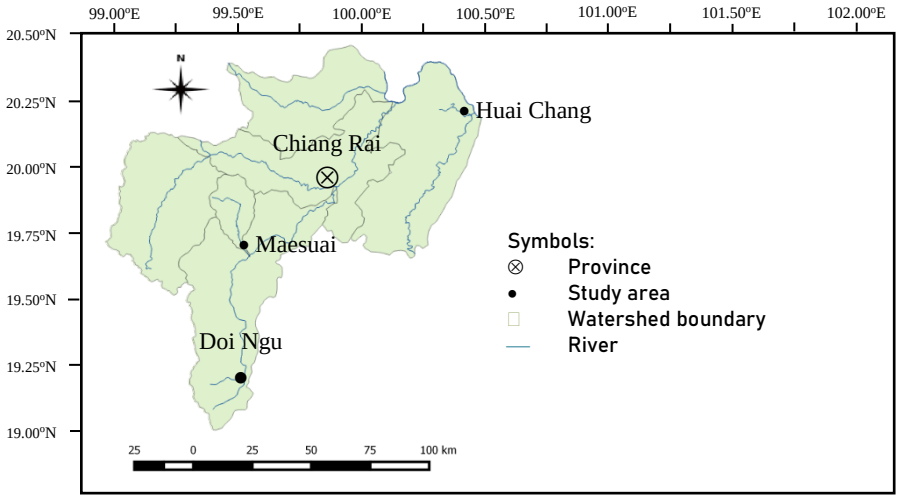

Figure 1. Three watershed sites: Maesuai, Huai Chang and Doi Ngu.

The main physical properties of watershed were summarized in Table 2.

Table 2. Main physical properties of watershed.

River	Reservoir/ watershed	Sub basin	Area (km^2)	Rainfall (mm./y)	discharge (10^6 m^3/y)	Period
Maesuai	Maesuai	Maesuai	434.0	1411.9	183.00	2009 – 2019
Mae Ja Dee	Doi Ngu	Lao	173.8	1089.0	44.55	2016 – 2019
Huai Chang	Huai Chang	Lower Ing	31.6	1726.6	14.12	2009 – 2019

The range of watershed area was 31.6 – 434.0 km^2 and annual discharge was recorded between 14.12 – 183.00 million m^3 while annual rainfall data ranged from 1089.0 – 1411.9 mm. At the same time, the discovery of land use showed that more than 50 percent of the area is forest, followed by agriculture (fruit trees, crops, and rice field), residential use and cultivation field.

Preparing data.: The data were collected by the Royal Irrigation Department from the year 2009 – 2019 in the form of text files (* .txt) with Excel. Then they were imported into the BFI+ program for baseflow separation with RDF and DGM approach. More result analysis, interpretation and visualization were prepared with Excel.

Calibration data.: Each watershed, baseflow parameters were extracted from daily stream flow data in dry period (unaffected by rain), in this study we used the daily runoff data from January to March and December for each year. Starting with EXCEL 2010 program, the parameters were estimated by using Solver tool to calculate the initial parameters. Then, the parameters were entered into BFI+ module by trial error on year basis. The calibration process would be stopped when the calculated baseflow curve (red-curve) was close to the observed discharge curve (blue area curve) as shown in Figure 2.

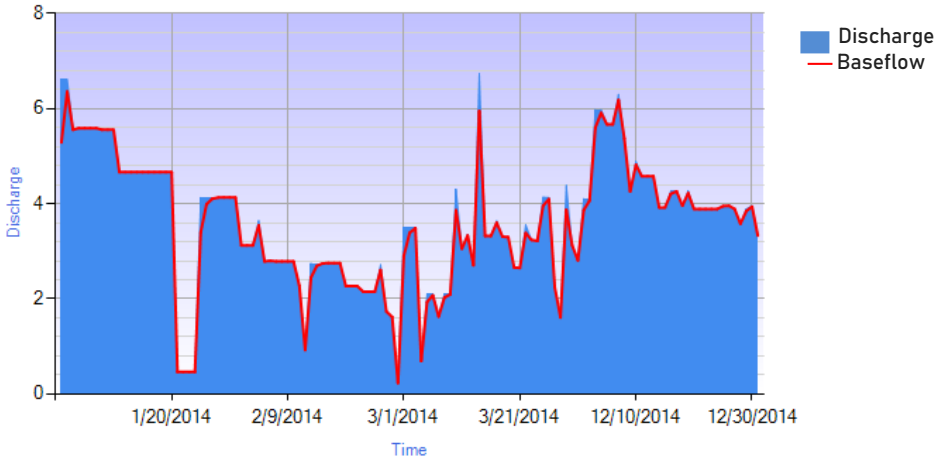

Figure 2. Calibration process for parameter value estimation.

Statistical Analysis: The statistical analysis was used for a comparison between the calculated baseflow and the actual runoff during dry periods (January to April and November to December) based on the assumption stream flow in river in this period was caused only by baseflow, Therefore, the direct flow (quick flow or direct runoff) was close or equal to 0. Furthermore, the effectiveness of parameters was measured by Root Mean Square Error (RMSE) as an equation.

$$\mathrm{RMSE} = \sqrt{\frac{1}{n}\sum(q_c - q_0)^2}$$

where:

q_c : calculated baseflow (m^3/s)
q_0 : measured total flow in the river (m^3/s)
n : number of samples

The lower RMSE values represent that the calculated baseflow are close to observed stream flow. Furthermore, the analysis of relationship between runoff and baseflow can be used as a correlation value. If the correlation coefficient is close to 1, it shows the relationship between baseflow and river discharge is linear while the + and – sign will indicate the direction of the relationship.

Validation.: In this step, the optimal parameter values for each watershed were estimated by the central values in each year. Then the values were tested with stream flow in 2018 and 2019 for each watershed area. The results were presented in Table 3 and 4.

Result and Discussion:

Range of parameter values: The range of parameter values explored for each watershed and each model were presented in Table 4. For this study, our main river was categorized as perennial river, therefore the BFI-max was set to 0.8 according to Eckhardt[13] filter (BFI-max).

Table 4. Range value of parameters explored for calibration.

Algorithm	Parameter				
	K	C	α	α_q	N
One parameter	0.001 – 0.956				
Boughton	0.019 – 3.870	0.290 – 6.274			
IHACRES	1.007 – 4.000	0.001		0.001	
BFLOW			0.001 – 2.010		
Chapman			0.001 – 0.973		
EWMA filter			0.029 – 0.800		
Fixed and Sliding					1.741 – 2.940

The representative parameters of each watershed were determined by using the median values of the parameter. For the parameters of baseflow separation by DGM method, the optimal values of the number of days (N) were determined form $N = 0.827A^{0.2}$ and rounded as integers according to BFI+ module. These parameters were displayed in Table 5.

Table 5. Optimal parameter values explored for baseflow separation.

Watershed	One para.	Boughton		IHACRES			BFLOW	Chapman	EWMA filter	Fixed, Sliding
	k	k	c	q	c	k	α	α	α	N
Maesuai	0.248	0.186	3.258	0.001	3.970	0.001	0.917	0.858	0.077	2.940 (3)
Doi Ngu	0.220	0.354	2.549	0.001	3.975	0.001	0.926	0.543	0.091	2.448 (2)
Huai Chang	0.001	0.460	2.465	0.001	3.976	0.001	0.940	0.001	0.053	1.741 (2)

Table 5 shows the parameter value obtained from the calibration process. These values are relatively similar for each method, except the parameters of Bouthon and Champman algorithm of the Huai Chang reservoir are different from other watersheds.

Statistical analysis: Table 6 shows the statistical analysis results of RMSE values and correlation coefficient (r) for all algorithms for each watershed. The RMSE and r values were calculated using baseflow separation result in dry periods (January to April and November to December) of the year 2018 – 2019.

Table 6. BFI, RMSE and r values of each model for each watershed.

Watershed	RDF											
	One parameter			Boughton			IHACRE			BFLOW		
	BFI	RMSE	r	BFI	RMSE	r	BFI	RMSE	r	BFI	RMSE	r
Maesuai	0.522	0.139	0.973	0.811	0.055	0.998	0.801	0.055	0.999	0.892	0.099	0.820
Doi Ngu	0.505	0.056	0.996	0.802	0.023	0.997	0.800	0.001	0.999	0.878	0.037	0.717
Huai Chang	0.500	0.018	1.000	0.834	0.008	0.995	0.800	0.007	0.999	0.861	0.022	0.717

Table 6 (continue). BFI, RMSE and r values of each model for each watershed.

Watershed	RDF						DGM					
	Chapman			EWMA filter			Fixed interval			Sliding interval		
	BFI	RMSE	r	BFI	RMSE	r	BFI	RMSE	r	BFI	RMSE	r
Maesuai	0.606	0.154	0.747	0.910	0.097	0.833	0.778	0.110	0.786	0.779	0.107	0.793
Doi Ngu	0.517	0.059	0.941	0.892	0.034	0.741	0.920	0.029	0.696	1.000	0.000	1.000
Huai Chang	0.529	0.020	0.942	0.886	0.022	0.742	0.858	0.020	0.697	1.000	0.000	1.000

This table shows the result of baseflow separation between RDF and DGM method. Most of RDF algorithms show the similar performance (except One parameter and Chapman algorithms) and are better than the DGM method according to BFI, RMSE and r values closer to 0.8, 0 and 1, respectively. In conclusion, IHACRE algorithm is the most effective method, followed by Boughton algorithm, the result is agreeable with the study of Indarto et al[15]. From the analysis, it was found that the DGM method with Fixed interval algorithm can separate the baseflow while the Sliding interval algorithm cannot distinguish baseflow effectively when watershed area is small. Notice from BFI values is 1, showing that baseflow is stream flow. However for a large basin, such as Maesuai watershed, both algorithms (Fixed and Sliding interval) provide similar performance. Moreover, the model performance was visualized by Flow Duration Curve (FDC) for each watershed as presented in Figure 3.

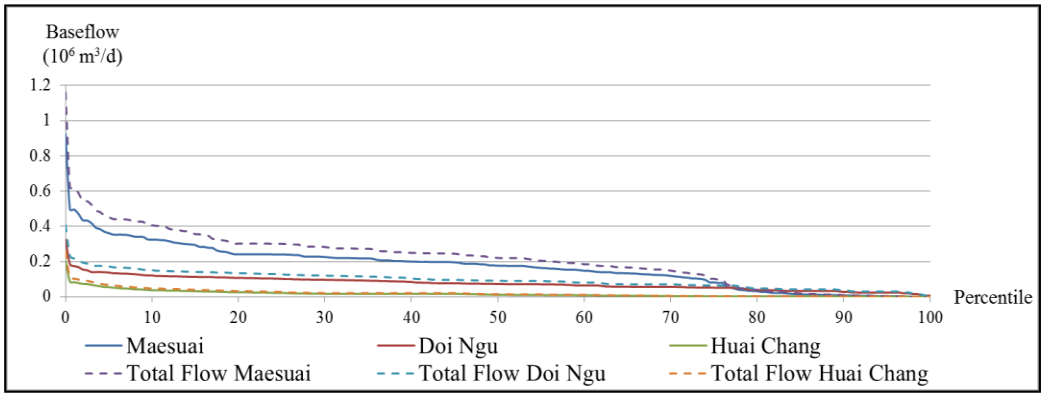

Figure 3. FDC Curve of each watershed for dry period only

Figure 3 visualizes the FDC in dry periods for all 3 sub-basins. The FDC shows the different between calculated baseflow (IHACRE) and observed stream flow, and percentile of water flow (baseflow and stream flow) in river. Clearly, the form of baseflow (continue-line) is relatively similar to the form of stream flow (dash-line).

Conclusion: Overall, for RDF method, most baseflow separation algorithms can be applied for Kok-Mekong basin in Chiang Rai. However, One parameter and Chapman algorithms are not as effective as other algorithms. The algorithm that shows very good performance is IHACRE and Boughton algorithm. On the other hand, the analysis with DGM method can separate the baseflow as well. Particularly, the Fixed interval algorithm provides good performance and can be applied in both small and large watershed areas, while the Sliding interval algorithm is suitable only for large watershed areas.

References:
1. Indarto Indarto, Ratnaningsih Anik, Wahyuningsih Sri. ARPN Journal of Engineering and Applied Sciences. 2017;12:3772-3778.
2. Tallaksen L. M.. Journal of Hydrology, 1995;165:349-370.
3. Lott A. Darline, Stewart T. Mark. Journal of Hydrology. 2016;535:525-533.
4. Champman, T. G., Maxwell A. I.. Institute Engineers Australia National Conference. 1996;96/05:539-545.
5. Boughton W. C.. Institute of Engineers Australia National Conference. 1993;93/14:317-324.
6. Jakeman A. J., Hornberger G. M.. Water Resources Research. 1993;29:2637-2649.
7. Lyne V., Hollick M. Institute of Engineers Australia National Conference. 1979;79/10:89-93.
8. Nathan R. J., McMahon T A. Water Resources Research, 1990;26(7):1465-1473.
9. Champman, T. G., Water Resources Research, 1991;27(7):1783-1784.
10. Mau D P, Winter T C. Ground Water,1997;35(2):291-304.
11. Lanen Henny A. J. van, Tallaksen Lena M.. Developments in Water Science, 2004;48:579.
12. Pettyjohn W.A., Henning Roger. University Water Resources Center Project Completion Report Number 552. 1979;-:31.
13. Eckhardt K. Hydrological Processes; 2005;19(2):507-515.

Acknowledgements: This research is supported financially by Mae Fah Luang University. Most of data used for this research were obtained from Water Watch and Monitoring System for Warning Branch, Regional Irrigation Office 2 (RIO 2), Royal Irrigation Department. In addition the BFI+ module for studying the composition of the stream flow was supported by Hydro Office.

E_008_PF: PREPARATION OF NiCoS CATALYSTS FOR RECHARGEABLE ZINC-AIR BATTERIES

N. Tangaemsakul[1,2,*], N. Tantavichet[1,2]
[1]Department of Chemical Technology, Faculty of Science, Chulalongkorn University, Bangkok 10330, Thailand
[2]Center of Excellence on Petrochemical and Material Technology, Chulalongkorn University, Bangkok 10330, Thailand
*E-mail: nuttasith@windowslive.com

Abstract: Nickle cobalt sulfide ($NiCo_2S_4$) was synthesized by a one-pot solvothermal strategy using $Co(OAc)_2$, $Ni(OAc)_2$ and thiourea as precursors and ethylene glycol as the dispersing agent with varied carbon-based support was investigated in term of bifunctional nonprecious electrocatalyst activity for oxygen reduction reaction (ORR) and oxygen evolution reaction (OER) comparing with commercial catalysts. Vulcan carbon (C), Vulcan carbon treated (CT), were used as supporters. The results show $NiCo_2S_4$/CT had higher electrocatalytic activity more than cobalt oxide (20% Co_3O_4/C) but still lower than the commercial platinum (20% Pt/C) for the ORR in 0.1 M KOH but in term of OER $NiCo_2S_4$/CT reveals much higher activity than other commercial catalysts. The result show that $NiCo_2S_4$/CT have the highest electrocatalytic activity for both ORR and OER.

Introduction: Nowadays renewable energy such as solar energy, water energy or wind energy are becoming competitive with technologies base on fossil fuels. However, Renewable energy have to work with batteries for storage energy in electrical form then electrical energy is used by electronic device such as electric cars, laptops, mobile phone, and other electronic appliances. There are many types of batteries but one of the most interesting is Metal-air batteries have much attention recently as a possible alternative, due to their extremely high energy density compared to the other rechargeable batteries[1]. Among the different types of metal–air batteries. The Zn-air battery system was intensively developed in the past, as it is relatively simple, easy to operate, inexpensive to manufacture, and has excellent reliability, recycle-ability, recharge-ability and also safety. At present, Rechargeable Zn-air batteries already have certain applications, for example, in hearing-aids and miniature medical devices. Rechargeable zinc-air battery can store and release energy through the oxygen reduction reaction (ORR) and oxygen evolution reaction (OER)[2]. However, both reactions are complicated for multielectron transfer, leading to the sluggish kinetics so it required good catalysts. Currently, Pt functions as the best ORR catalyst but its OER activity is unsatisfactory. Pt alloys, such as Pt/Ir and Pt/Au were investigated as promising bifunctional catalysts. However, the low abundance, prohibitive cost, and declining activity pose critical challenges for the practical use of the Pt-based catalysts. Nickel cobalt sulfide ($NiCo_2S_4$) has received attention because it potentially has good performance for both ORR and OER[3]. Herein, Nickel cobalt sulfide was synthesized from metal salts, thiourea, and carbon-based supports in the medium of ethylene glycol (EG) by a one-pot solvothermal strategy[4] and we report ORR and OER electrocatalytic performance of NiCo2S4 with carbon-based support compared with commercial catalyst (cobalt oxide and Pt/C)

Methodology:

Raw materials: Vulcan carbon, Cobalt (II) acetate, Nickel (II) acetate, thiourea, Ethylene glycol

Preparation of catalysts: Synthesis of $NiCo_2S_4$/CT. The Vulcan carbon treated (CT) was prepared by acid treatment.

In a typical synthesis of $NiCo_2S_4$/CT, Vulcan carbon treated (CT) 60 mg was dissolved in 60 mL of EG and sonicated for 1 h. Then added $Co(OAc)_2$ (0.6 mmol) and $Ni(OAc)_2$ (0.3 mmol) in the CT/EG suspension and stirred at 80 °C for 1 h. Then, thiourea (1.8 mmol) was introduced into the above suspension, and after transferring the mixture to an autoclave (100 mL), the

solvothermal reaction was followed at 180 °C for 12 h. The resulted product was collected by filtration, washed with plenty of deionized water, and lyophilized at last.

Characterization of catalysts: Structural Characterization. The samples were pressed to thin films for powder X-ray diffraction (XRD) detections on a Rigaku B/Max-RB X-ray diffractometer with a nickel filtrated Cu Kα radiation (Cu Kα, λ = 1.5406). and the energy dispersive spectroscopy (EDS) spectra were taken on a Tecnai-G2- F30(300 keV) field-emission TEM (FE-TEM).

Electrochemical Measurements: The electrochemical tests were carried out on a AutoLab workstation (μ Autolab III) assembled with a model of an ATA-1B rotational system, using a three-electrode electrochemical cell. The sample coated glass carbon (GC) electrode, a silver chloride electrode, and a platinum pole were used as working, reference, and counter electrode, respectively. The working electrode was prepared as follows: 100 μL of 5 wt % Nafion solution was added to 1 mL of 4:1 v/v water/ethanol, and then, 6 mg of the catalyst was dispersed in it by sonicating in an water bath to obtain a homogeneous ink. Then, 5 μL of the catalyst ink was loaded onto a GC electrode of 5 mm in diameter (the catalysts loading was ~0.139 mg cm^{-2} for all samples). A commercial 20%Pt/C electrode was also prepared for comparison. The ORR performance was first investigated by cyclic voltammetry (CV) in Ar and O_2-saturated 0.1 M KOH at room temperature, with a sweep rate of 10 mV s^{-1}. Linear sweep voltammetry (LSV) was conducted under constant O_2 gas flow, with a sweeping rate of 10 mV s^{-1} in the potential range of -0.2 to 0.9 V vs Ag/AgCl. The OER activities of all samples were investigated by the LSV method, with the sweep rate of 10 mV s^{-1} in 0.1 M KOH.

Results and Discussion: $NiCo_2S_4$/CT was prepared by a one-pot solvothermal approach using $Co(oAc)_2$, $Ni(oAc)_2$, thiourea, and CT as precursors in polyol (EG) medium. The polyol method is usually employed to synthesize nanosized materials. It is known that a catalyst with amorphous or nanocrystalline phase would be rendered a great performance on account of abundant accessible active sites. During the reaction, EG acts as a mild reductant to get CT and also the solvent with a chelating effect, which avoids agglomeration of particles. Thiourea is intended for the formation of metal sulfides. The solvothermal procedure is of significant importance, affording the crystallization of $NiCo_2S_4$.

Catalyst characterization:

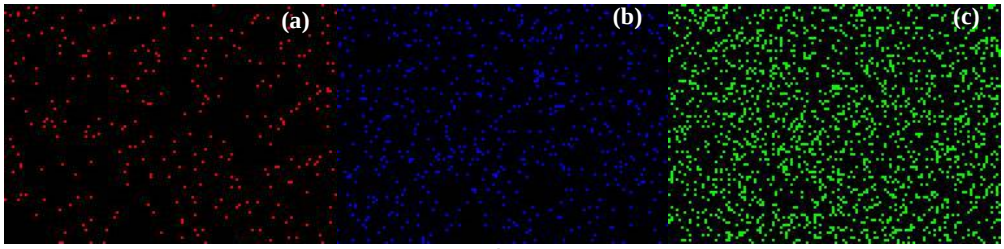

Figure 1. Elemental mapping of $NiCo_2S_4$/CT elemental nickel (a) cobalt (b) sulphur (c)

Table 1 elemental component of $NiCo_2S_4$/CT

Element	Weight%	Atomic%	Atomic ratio
C	56.57	71.02	-
O	23.50	22.14	-
S	8.10	3.81	4
Co	8.26	2.11	2
Ni	3.58	0.92	1

EDS and techniques were employed to investigate the elemental component and metal (Ni and Co) dispersion on the silica supports. EDS in Table 1 clearly indicated that the atomic ratio of Ni:Co:S as about 1:2:4

Electrochemical Measurements:

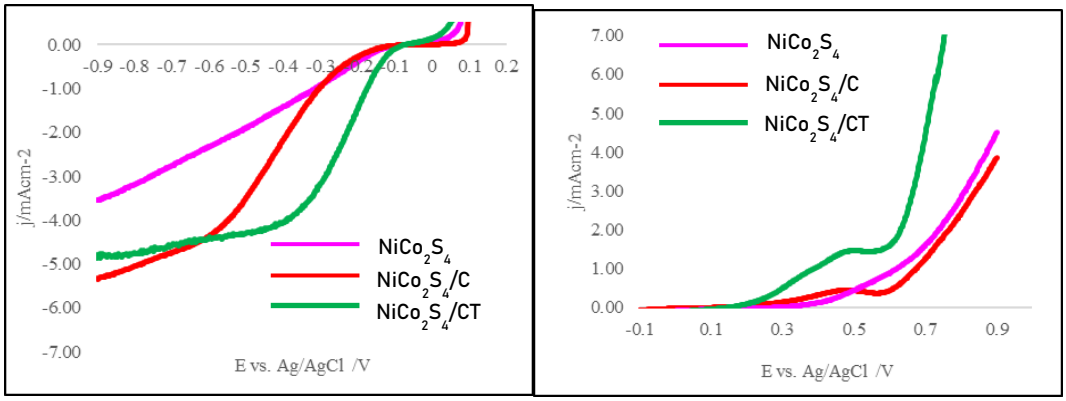

Figure 3. ORR and OER curves in O_2-saturated 0.1 M KOH at 1600 rpm with a sweep rate of 10 mV s^{-1}.

The rotating-disk electrode (RDE) measurement was applied to reveal the ORR kinetics of $NiCo_2S_4$ with varied carbon-based support in O2-saturated 0.1 M KOH. As shown in Figure 3, The ORR onset potential and limiting current density of $NiCo_2S_4$/CT are, respectively, at -0.14 V vs Ag/AgCl and -4.86 mA/cm^2. These values are more positive than those of $NiCo_2S_4$/C (onset of −0.24 V and limiting current density of −5.33 mA/cm^2) and $NiCo_2S_4$ (onset of −0.22 V and limiting current density of −3.55 mA/cm^2).In term of OER, onset of $NiCo_2S_4$/CT is 0.22 V that show higher activity than $NiCo_2S_4$/C (onset of 0.31 V) and $NiCo_2S_4$ (onset of 0.41 V), which may be due to $NiCo_2S_4$/CT has more than metal loading in the support. Small peak in OER curves[5,6] cause of changing the oxidation state of Co^{2+} to Co^{3+}.

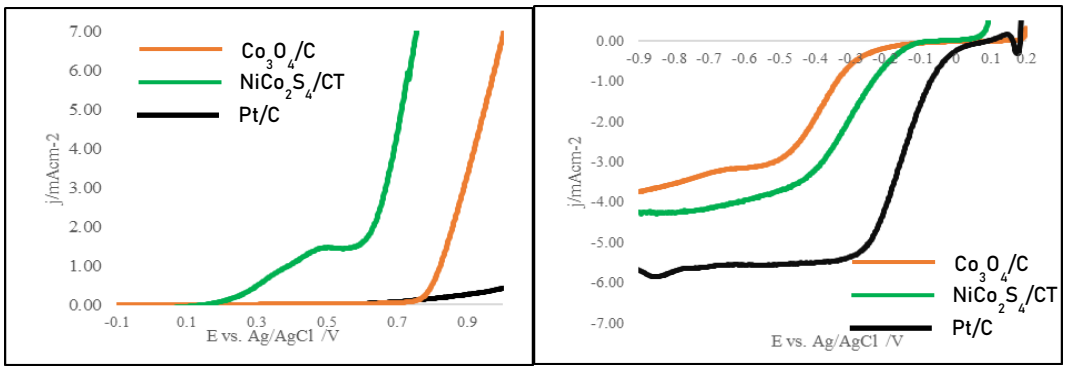

Figure 4. ORR and OER curves in O_2-saturated 0.1 M KOH at 1600 rpm with a sweep rate of 10 mV s^{-1}.

When compared with the commercial catalysts (20% Co_3O_4/C and 20% Pt/C) as shown in Figure 4. For ORR, Activity of $NiCo_2S_4$/CT is much higher than 20% Co_3O_4/C (onset of -0.29V and limiting current density of -3.74 mA/cm^2) but lower than that of commercial 20% Pt/C (onset of -0.034 V and limiting current density of -5.96 mA/cm^2). It indeed exhibits inferior ORR activity to Pt-based catalyst. Then, the OER performance of $NiCo_2S_4$/CT much better than both of 20% Co_3O_4/C (onset of 0.34V) and commercial 20% Pt/C (onset of 0.43 V).

Table 2. Summation of the catalytic performance of $NiCo_2S_4$ on different supports comparing to commercial catalysts.

Catalyst	ORR		OER
	onset (V)	limiting current density (mA/cm^2)	onset (V)
$NiCo_2S_4$	-0.22	-3.55	0.41
$NiCo_2S_4$/C	-0.24	-5.33	0.31
$NiCo_2S_4$/CT	-0.14	-4.86	0.22
Co3O4/C	-0.29	-3.74	0.34
Pt/C	-0.034	-5.96	0.43

Conclusion: We have prepared $NiCo_2S_4$ on vulcan carbon treated support ($NiCo_2S_4$/CT) as bifunctional electrocatalyst via a one-pot solvothermal using thiourea, metal acetates as precursors. $NiCo_2S_4$/CT has higher electrocatalytic activity for ORR and OER than other carbon-based supports. When compared to commercial electrocatalysts, For ORR $NiCo_2S_4$/CT is much more effective than 20% Co_3O_4/C but still lower than commercial 20%Pt/C. However, in term of OER $NiCo_2S_4$/CT is much higher than both of cobalt oxide (Co_3O_4) and commercial platinum (Pt/C).

References:

1. Zhu, Aaron L., David P. Wilkinson, Xinge Zhang, Yalan Xing, Alex G. Rozhin, and Sergei A. Kulinich. 2016. "Zinc regeneration in rechargeable zinc-air fuel cells — A Review." Journal of Energy Storage 8:35–50.
2. Li, Yanguang and Hongjie Dai. 2014. "Chem soc rev chemical society reviews recent advances in zinc-air batteries." Chemical Society Reviews 43:5257.
3. Wang, Shaolan, Wei Li, Lipeng Xin, Ming Wu, and Xiaojie Lou. 2016. "High-performance Nickel Cobalt Sulfide materials: via low-cost preparation for advanced asymmetric supercapacitors." RSC Advances 6(48):42633–42.
4. Wu, Jianghong, Shuo Dou, Anli Shen, Xin Wang, Zhaoling Ma, Canbin Ouyang, and Shuangyin Wang. 2014. "One-step hydrothermal synthesis of $NiCo_2O_4$-rGO as an efficient electrocatalyst for the oxygen reduction reaction." Journal of Materials Chemistry A 2(48):20990–95.
5. Sönmez, Turgut, Stephen J. Thompson, Stephen W. T. Price, Derek Pletcher, and Andrea E. Russell. 2016. "voltammetric studies of the mechanism of the oxygen reduction in alkaline media at the spinels Co_3O_4 and $NiCo_2O_4$." Journal of The Electrochemical Society 163(10):H884–90.
6. Pletcher, Derek, Xiaohong Li, Stephen W. T. Price, Andrea E. Russell, Turgut Sönmez, and Stephen J. Thompson. 2016. "comparison of the spinels Co_3O_4 and $NiCo_2O_4$ as bifunctional oxygen catalysts in alkaline media." Electrochimica Acta 188:286–93.

Acknowledgements: This research was conducted with financial support from Center of Excellence on Petrochemical and Materials Technology, Chulalongkorn University and made use of the facilities at department of Chemical Technology, Faculty of Science, Chulalongkorn University.

E_010_PF: HYDROGEN PRODUCTION AND COD REMOVAL FROM BIODIESEL WASTEWATER USING COUPLED SEMICONDUCTOR PHOTOCATALYST

Napat Chuenangkul[1,*], Mali Hunsom[2], Kejvalee Pruksathorn[3]
[1]Department of Chemical Technology, Faculty of Science, Chulalongkorn University, Pathumwan, Bangkok 10330, Thailand
[2]Associated Fellow of Royal Society of Thailand (AFRST), Bangkok 10300, Thailand
[3]Center of Excellence on Petrochemical and Materials Technology (PETROMAT), Chulalongkorn University, Pathumwan, Bangkok 10330, Thailand
*e-mail:napat_c-angkul@hotmail.com

Abstract: Nowadays, many products have been produced from industries together with the generation of wastewater. Thus, many processes have been developed for wastewater treatment such as chemical/physical treatment, electrochemical treatment, as well as biological treatment. In this study, organic pollutants in industrial wastewater was degraded by photocatalytic oxidation using semiconductors simultaneously with hydrogen (H_2) production via the photocatalytic oxidation process. Typically, titanium dioxide (TiO_2) is a common semiconductor used in heterogeneous photocatalysis because of its stability, low cost and non-toxic to the environment. However, TiO_2 has large band gap energy of 3.2 eV and has fast electron-hole recombination. One way to overcome the serious drawbacks of TiO_2 is the coupling of TiO_2 with other semiconductor. Recently, it was reported that the coupling of TiO_2 with semiconductor with different band gap energy such as Bi_2O_3, Nb_2O_5, and WO_3 can enhance the absorption capacity of TiO_2 and to hamper the electron-hole recombination. In this study, the simultaneous H_2 production and COD removal from biodiesel wastewater was tested by the photocatalytic oxidation via coupled semiconductor photocatalysts. It was obvious that the coupled semiconductor photocatalysts showed a higher hydrogen (H_2) production than the pure TiO_2 at 4.0 g/L with 5.93 mW/cm^2 UV-Visible irradiation, after 4 h irradiation. The presence of Bi_2O_3/TiO_2 showed the highest H_2 production rate of 941 µmol/h compared with others, while the WO_3/TiO_2 presented the highest COD removal of 32%.

Introduction: Due to a fast development of many industries, various types of industrial wastewater have been generated. Over the past decades, a great deal of effort has been devoted to investigate the photocatalytic degradation of organic water pollutants by photocatalysis because of several advantages, such as extremely fast degradation rate, high mineralization efficiency and low toxigenicity. Recently, it was reported that an organic pollutants in industrial wastewater can be degraded by the photocatalytic oxidation using semiconductors simultaneously with H_2 production by photocatalytic water splitting. As a brief, when the photocatalyst absorbs the light having the photon energy equal or greater than the band gap energy. Electrons (e_{cb}^-) are excited from the valence band (VB) by photon energy into the conduction band (CB), leaving holes (h_{vb}^+) behind. The excited electrons and holes can act as the reductant and oxidant to react with electron donors such as H_2O and electron acceptors such as O_2 or H_2O_2 to generate hydroxyl radicle ($OH^\bullet$) and superoxide radicle ($O_2^{-\bullet}$), which are the strong oxidizing agent and can oxidize organic molecules to the smaller one. Among all photocatalysts, the TiO_2 is the widely investigated photocatalyst because TiO_2 can generate strong oxidizing, non-toxic to the environment, good stability in photocatalytic reactions and low-cost. However, TiO_2 can only be excited by UV light due to its large band gap of 3.2 eV and the other drawbacks of TiO_2 is a fast charge recombination. To overcome these drawbacks, many strategies have been developed in the past and the most widely used one is coupling of TiO_2 with semiconductor having different band gap energy. In particular, the coupling of TiO_2 with semiconductors with different band gap energy has been proposed to extend the absorption wavelength range to the visible range and to hamper the e-/h+ recombination. When the CB level of semiconductor-B is lower than that of semiconductor-A

(Figure 1.), electrons in the CB of semiconductor-A can transfer to that of semiconductor-B under light irradiation. If the VB level of semiconductor-B is lower than that of semiconductor-A, holes in the VB of semiconductor-B can transfer to that of semiconductor-A. Therefore, the probability of electron–hole recombination can be reduced [1].

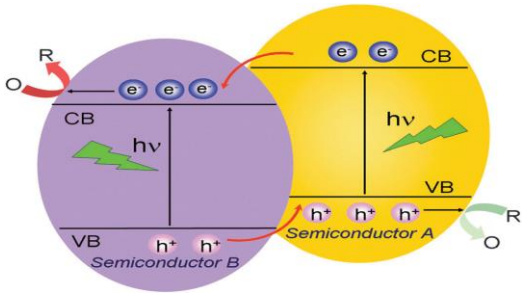

Figure 1. Schematic diagram showing the energy band structure and electron–hole pair separation in the semiconductor heterojunction [1].

In this work, the photocatalytic activity of TiO_2 was enhanced by coupling with various types of semiconductors including Bi_2O_3, Nb_2O_5, and WO_3. The photocatalytic activity of the coupled photocatalyst was tested via the H_2 production and COD removal from biodiesel wastewater.

Methodology:

Synthesis of coupled semiconductor photocatalysts: Firstly, the commercial of Bi_2O_3 (Sigma Aldrich) and TiO_2 (P25, Sigma Aldrich) were mixed in ethanol (Qrec, 99.9%) at the ratio of 5% mole. Then, the maleic acid (QRec) using as a binder to prepare coupled semiconductor photocatalysts [2] was dissolved in a mixed-oxide aqueous solution containing amount of Bi_2O_3 and TiO_2. After 5 h of sonication at room temperatures, the solution was stirred for 5 h at room temperatures and washed with ethanol to remove excess maleic acid. Finally, the obtained solution was dried at 80 °C overnight and calcined in furnace under air flow at 400 °C for 3 h. The similar method was used for the synthesis of Nb_2O_5/TiO_2 and WO_3/TiO_2 photocatalyst. For all coupled semiconductor photocatalysts, the loading of all semiconductors on TiO_2 was fixed at 5% mol.

Pretreatment of biodiesel wastewater: The pretreatment of biodiesel wastewater was carried out by the addition of concentrated H_2SO_4 (Qrec, 98%) to pH lower than 2.0-3.0 due to the high contaminants in the biodiesel wastewater (Table 1) [3]. The layers of oil and water were separated after addition of conc. H_2SO_4. The oil-layer was removed by slow decantation, leaving the water-layer (pretreated wastewater) for the photocatalytic reaction.

Photocatalytic activity test: The H_2 production and COD removal using coupled semiconductor photocatalysts were performed in a closed Pyrex glass cylinder at temperature of 30-32°C with the UV light intensity of 5.93 mW/cm^2 using the high pressure mercury lamp (RUV 533 BC, Holland, wavelength 100-600 nm) as a light source for 4 h, set at the middle of the UV-protected box. In each experiment, the 0.4 g of photocatalyst was dispersed in the 3.3-fold dilution biodiesel wastewater having a constant volume of 100 mL.

Results and Discussion:

Properties of the biodiesel wastewater: In comparison with the property of wastewater set by Thai Government for discharging into the environment, the fresh biodiesel wastewater cannot be discharged directly into the environment due to it contains a very high level of COD, BOD, oil&grease, TDS and TSS (Table 1). After the addition of conc. H_2SO_4, the quantities of soap,

COD, BOD and oil&grease in pretreated wastewater were reduced importantly causing by the H^+ dissociated from the utilized H_2SO_4 can combine with the pollutant in biodiesel [4]. Nonetheless, the pretreated biodiesel wastewater still had high levels of COD, BOD, oil&grease and TDS which were 86,430 ± 1,875 mg/L, 228 ± 76 mg/L, 744 ± 48 mg/L and 50,525 ± 4,182 (mg/L), respectively, which were higher than the property of wastewater set by Thai Government for discharging into the environment. Thus, the wastewater treatment is still required.

Table 1. Properties of the biodiesel wastewater

Property	Thai standard	Fresh wastewater	Pretreated wastewater	Treated wastewater[a]
pH	5.5-9.0	5.75 ± 0.06	2.06 ± 0.02	2.70 ± 0.04
Soap (wt.%)		77.35 ± 1.16	58.76 ± 1.48	4.65 ± 1.36
FFA (wt.%)		0.68 ± 0.02	6.47 ± 0.02	4.83 ± 0.03
COD (mg/L)	≤ 400	127,358 ± 2,110	86,430 ± 1,875	19,274 ± 2,502
BOD (mg/L)	≤ 60	557 ± 10	228 ± 76	20 ± 13
Oil & grease (mg/L)	≤ 15	1,429 ± 179	744 ± 48	250 ± 70
TDS (mg/L)	≤ 3000	18,880 ± 407	50,525 ± 4,182	14,500 ± 1,250
TSS (mg/L)	≤ 150	225 ± 5	75 ± 5	40 ± 15

[a]Photocatalytic reaction with WO_3/TiO_4 at 4.0 g/L, light intensity of 5.93 mW/cm^2, reaction time of 4 h with biodiesel wastewater at 3-fold dilution.

Morphology of the coupled semiconductor photocatalysts: Figure 2 shows the XRD patterns of commercial TiO_2 couple with different semiconductors at 5% mol. The XRD pattern of the commercial TiO_2 demonstrated the main characteristic peaks of the anatase phase at 2Θ of 25.26°, 37.76° and 48.04° and the rutile phase at 27.41°, 36.06° and 53.87°, corresponding to the (101), (004) and (200) planes for the anatase phase and (110), (101) and (211) planes for the rutile phase, respectively. This indicated that the commercial TiO_2 was in anatase-rutile mixed phase. The main diffraction peaks of the Bi_2O_3 at 2Θ of 27.35° is attributed to the (120) planes, which is presented at high intensity even in composites containing Bi_2O_3/TiO_2. The XRD peaks of Nb_2O_5 exists as biphasic containing orthorhombic (JCPDS file no. 71-0336) and monoclinic phases (JCPDS file no. 37-1468) [5]. Furthermore, it presents both of Nb_2O_5 and TiO_2 peaks. In the same way, there is the characteristic peaks of WO_3 in the XRD pattern of WO_3/TiO_2 photocatalyst. The commercial WO_3 is well crystallized in a single phase and all of the diffraction peaks can be indexed to monoclinic WO_3 (JCPDF 43-1035) [6]. According to Scherer equation, the crystallite size of anatase-TiO_2 was calculated from the XRD patterns of the examined samples and presented in Table 2. It was found that the average crystallite size of anatase-TiO_2 was almost the same for all samples, suggesting that loading types of semiconductor did not obviously change the crystallite size of TiO_2, probably because the calcination temperature of 400 °C was not high enough to stimulate the further growth of TiO_2 [7].

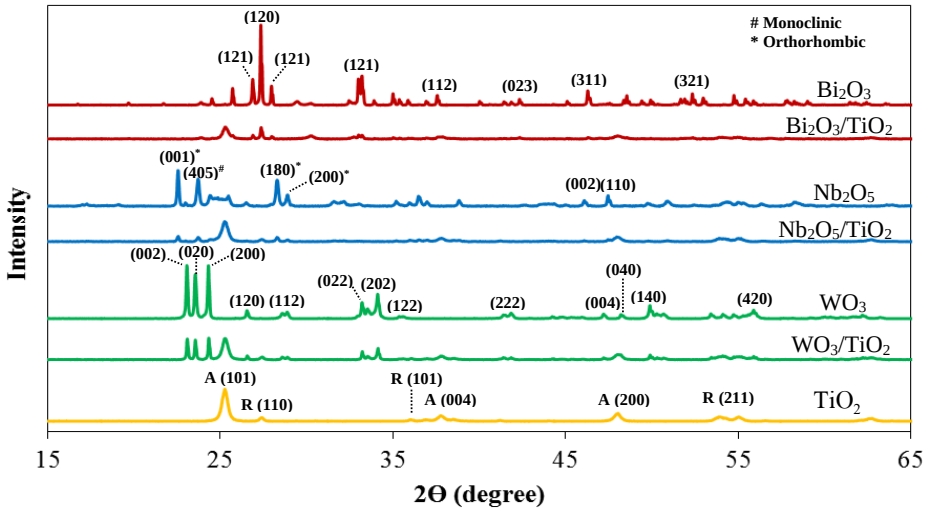

Figure 2. XRD patterns of commercial TiO_2, coupled semiconductor photocatalyst in different types of semiconductor and commercial of semiconductor.

Figure 3 shows the UV-visible light absorption spectra of commercial TiO_2, the coupled semiconductor photocatalyst and pure commercial of semiconductor photocatalysts. There was a red-shift of the absorption bands of the coupled semiconductor photocatalyst compared to the commercial TiO_2, indicating that the coupling of TiO_2 with semiconductor with different band gaps has been proposed to extend the absorption wavelength range to the visible range. The band gap energy estimated for commercial TiO_2 was 3.35 eV. The band gap energy of coupled semiconductor photocatalysts were shown in Table 2, modified the band gap values to 3.21, 3.24 and 3.24 eV for Bi_2O_3/TiO_2, WO_3/TiO_2 and Nb_2O_5/TiO_2 photocatalysts, respectively. The decrease in band gap energy caused the defective energy levels that formed within the forbidden band by coupling between commercial TiO_2 and semiconductor photocatalysts which resulted in the red-shift absorption of coupled semiconductor photocatalyst [8].

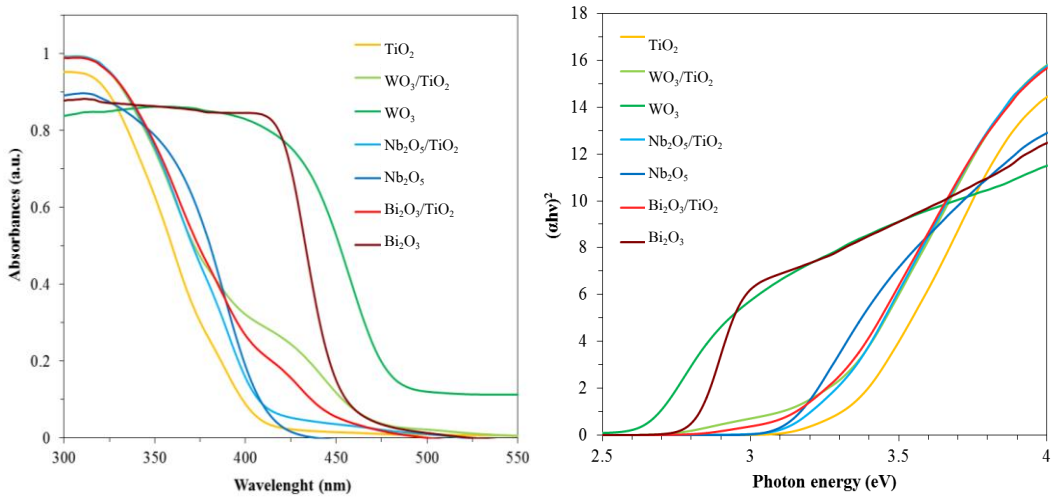

Figure 3. (a) UV-visible light absorption spectra of commercial TiO_2, coupled semiconductor photocatalyst in different types of semiconductor and commercial of semiconductor, (b) curves of $(\alpha h\nu)^2$ versus photon energy.

Table 2. Properties of photocatalysts

Type of photocatalyst	Actual loading (%mol) [a]	Anatase content (%) [b]	Crystallite size of TiO_2 (nm) [c]	Band gap energy (eV) [d]
TiO_2	-	90.75	21.90	3.35
Bi_2O_3	-	-	-	2.81
WO_3	-	-	-	2.64
Nb_2O_5	-	-	-	3.25
Bi_2O_3/TiO_4	5.03 ± 0.28	87.08	22.80	3.21
WO_3/TiO_4	5.23 ± 0.55	90.66	22.27	3.24
Nb_2O_5/TiO_4	4.79 ± 0.37	92.90	19.96	3.24

[a] from SEM-EDX
[b] calculated from Spurr's equation
[c] calculated from Scherrer equation
[d] calculated from plots of $(\alpha h\nu)^2$ against the photon energy

Photocatalytic activity test: The results of photocatalytic activity of H_2 production and photocatalytic degradation from 3.3-fold dilution pretreated biodiesel wastewater using the coupled semiconductor photocatalyst in different types of semiconductor under UV-visible irradiation is shown in Figure 4. It can be seen that the TiO_2 photocatalyst can enhance the H_2 production of 404 µmol/h, whereas that of Bi_2O_3/TiO_2, Nb_2O_5/TiO_2 and WO_3/TiO_2 showed higher H_2 production of 941 µmol/h, 838 µmol/h and 709 µmol/h, respectively. It was obvious that coupled semiconductor photocatalyst showed a higher H_2 production than the pure TiO_2. This is probably bacause the position of CB of coupled semiconductor photocatalysts was slightly above the H^+/H_2 position [9] and lower band gap energy than pure TiO_2 (Table 2). Therefore, the coupled semiconductor photocatalysts can produced hydrogen. On the other hand, the WO_3/TiO_2 photocatalyst can achieve the highest COD removal of 32% compared with the Bi_2O_3/TiO_2 and Nb_2O_5/TiO_2 photocatalysts. It was proposed that when WO_3/TiO_2 photocatalyst was excited by the UV-Visible irradiation light, the electrons of the VB of WO_3 and TiO_2 absorbed energy and jumped to the CB, leaving a holes in the VB to another. In this scenario, TiO_2 and WO_3 were positioned closely to each other, facilitating the photogenerated electrons and holes transfer from one semiconductor to another [8]. The effect of transferring the electrons and holes which resulted in presence of an efficient charge separation could prevent the fast electron-hole recombination. It is well known that Lewis surface acidity of WO_3 is much higher than that of TiO_2 and shows a higher affinity for chemical species having unpaired electrons. The WO_3/TiO_2 photocatalyst can adsorb more OH^- groups or H_2O molecules on the surface and generate a greater amount of hydroxyl radicals during the electron-hole pair formation [10].

The properties of treated wastewater by using the WO_3/TiO_2 photocatalyst were summaries in Table 1. It can be seen than after the photocatalytic process, a level of COD, BOD, oil&grease, TDS and TSS decreased importantly. Nonetheless, they were still higher than the acceptable value set by Thai Government. Thus, further study will be carried out with the addition of some clean oxidizing agent and the results will be reported soon.

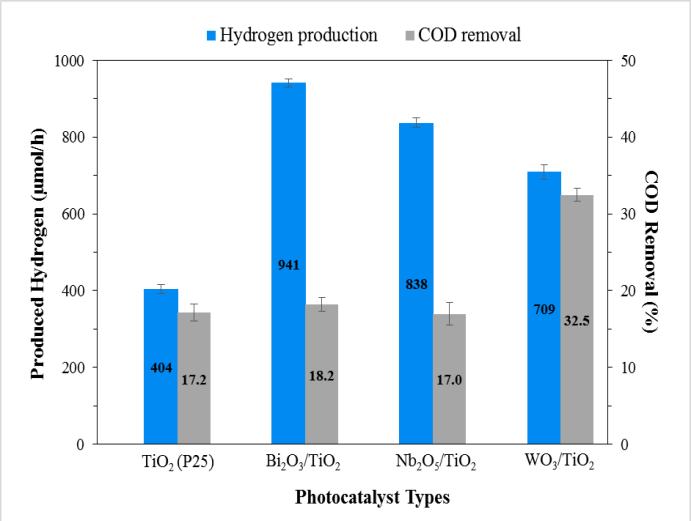

Figure 4. Effect of 3.3-fold dilution pretreated wastewater on the H_2 production and pollutant removal using coupled semiconductor photocatalyst at 4.0 g/L with 5.93 mW/cm^2 UV-Visible irradiation for 4 h.

Conclusion: The simultaneous H_2 production and pollutant removal from biodiesel wastewater was tested by the photocatalytic oxidation using Bi_2O_3, Nb_2O_5 and WO_3 photocatalysts in coupling with TiO_2. The coupled semiconductor photocatalyst showed the higher H_2 production than the pure TiO_2 at 4.0 g/L with 5.93 mW/cm^2 UV-Visible irradiation, after 4 h irradiation. That is the TiO_2 photocatalyst generated 404 µmol H_2 /h, whereas the Bi_2O_3/TiO_2, Nb_2O_5/TiO_2 and WO_3/TiO_2 showed higher H_2 production of 941 µmol/h, 838 µmol/h and 709 µmol/h, respectively. For COD removal, the WO_3/TiO_2 can enhance the highest COD removal up to 32.5% at the same condition. The coupling of different band gap semiconductor with TiO_2 can increase the efficiency of H_2 production and pollutant removal from biodiesel wastewater with photocatalytic oxidation.

References:

1. Wang H, Zhang L, Chen Z, Hu J, Li S, Wang Z, Liu J, Wang X. Chem Soc Rev. 2014;43: 5234-5244.
2. Ayekoe P.Y, Robert D, Goné D.L. Res Rev J Chem. 2017;6:77-83.
3. Jaruwat P, Kongjao S, Hunsom M. Energ Convers Manage. 2010;51:531-537.
4. Pansa-Ngat P, Jedsukontorn T, Hunsom M. J Taiwan Inst Chem E. 2017;78:386-394.
5. Ghugal S.G, Umare S.S, Sasikala R. RSC Advances. 2016;6:64047-64055.
6. Guo J, Li Y, Zhu S, Chen Z, Liu Q, Zhang D, Moon W.J, Song D.M. RSC Advances. 2012;2: 1356-1363.
7. Xu D, Hai Y, Zhang X, Zhang S, He R. Appl Surf Sci. 2017;400:530-536.
8. El-Yazeed W.S.A, Ahmed A.I. Inorg Chem Commun. 2019;105:102-111.
9. Lakshmana R.N, Emin S, Valant M, Shankar M.V. Int J Hydrogen Eerg. 2017;42:6627-6636.
10. Ismail A.A, Abdelfattah I, Helal A, Al-Sayari S.A, Robben L, Bahnemann D.W. J Hazard Mater. 2016;307:43-54.

Acknowledgements: The authors would like to thank the Center of Excellence on Petrochemical and Materials Technology and Department of Chemical Technology, Faculty of Science, Chulalongkorn University for financial support of this study and Bangchak Corporation Public Company Limited for samples.

E_012_OF: ORGANIC GEOCHEMICAL CHARACTERISTICS OF COAL DEPOSITS IN LAMPANG PROVINCE

Patthapong Chaiseanwang*, Piyaphong Chenrai
Department of Geology, Faculty of Science, Chulalongkorn University, Bangkok, Thailand
*e-mail: pchaiseanwang@gmail.com

Abstract: The five hand-picked samples from Mae Teep coal mine, located in Mae Teep basin, Lampang province, were studied on organic geochemical characteristics. The total organic carbon (TOC) content of the coals range from 44.0 to 73.7 wt.%, whereas oil shale and coaly mudstone values in the range of 19.5 wt.% and 4.96 wt.%, respectively. The extractable organic matter (EOM), which is yielded from bitumen extraction, values between 1,277-5,956 ppm representing good to excellent hydrocarbon potential generation for petroleum source rock associated with slightly high thermal maturity based on biomarkers maturity parameters. The coal samples are determined to be mature stage which can be related to high volatile bituminous coal in A.S.T.M. standards. On the condition of depositional environment, the analyzed Mae Teep coals are characterized by high Pr/Ph ratios indicating oxic condition. Whereas, oil shale is represented anoxic condition based on low Pr/Ph ratio and coaly mudstone in suboxic condition showing moderate Pr/Ph ratio. The samples were also investigated that the input of organic matter was derived from higher plant with minor influences of algae and/or bacteria in oil shale formation based on high CPI value, the occurrence of C_{27}, C_{28} and C_{29} regular steranes and the plot of Pr/*n*-C_{17} and Ph/*n*-C_{18}. The depositional environment have been believed to divide into three main system depends on the different rock types; 1) coal seams have been deposited in peat swamp environment, 2) oil shale is considered to be reducing-aquatic terrestrial deposits and 3) coaly mudstone is interpreted to be organic-lean sediment supply in terrestrial environment.

Keywords: Biomarker, Depositional environment, Mae Teep, Thermal maturity

Introduction: Coal is the one of important fossil-fuel resources in Thailand and is widely used to generate electricity in power plant and heating materials for other industries such as cement and iron and steel. Consumption of coal is expected to increase in the future due to industries' expansion. However, domestic coal production in Thailand is not sufficient for higher demand. Importing of coals from other countries can partly solve the high demand problem in Thailand. Thus, coal study and exploration in Thailand are needed for sustainable energy in the future.

Cenozoic sedimentary basins have been found to be widely distributed in several parts of Thailand, especially in the northwestern Thailand. These basins are mostly formed as half-grabens or grabens of normal fault bounded, N-S trending. It was formed in result of extensional regime influenced by the collision of the Indian Plate and Eurasian Plate which initiated in Oligocene age[6]. These basins are often covered by Quaternary sediments and associated with coal and oil shale deposits[2]. In Thailand, investigation of coal has been studied on physical characteristics such as depositional system from stratigraphy, petrography and proximate and ultimate analysis for coal rank and property[4,5,10]. There is a few organic geochemistry studies on Cenozoic coals in Thailand[4,9]. Thus, the organic geochemistry investigation of coal in Thailand is very limited and needed in order to get better understanding of coal deposits in Thailand. The aim of this study is to determine coal properties and depositional environment within Cenozoic sedimentary basins in Lampang, northern Thailand (Mae Teep coal mine) based on organic geochemical data such as TOC and GC-MS.

Geological setting: Mae Teep Basin is located in Ngao district, Lampang province covering 3 km wide and 10 km long. It is one of an intermontane basin containing coal deposits with

NE-SW trending structure and is operated as coal mine (Figure 1a.). The Cenozoic sequence in this area can be described and divided into 2 units including Tertiary coal-bearing sequence consisting of limestone, mudstone, coal and carbonaceous mudstone with minor oil shale overlying with Quaternary alluvium sequence containing gravel, pebbly sand, muddy sand and sandy clay as shown in Figure 1b. The lithostratigraphic log is studied from the mine wall and five hand-picked samples were collected to analyze for studying on organic geochemical characteristics (Figure 1c.) including oil shale (A), coal (1B-3B) and coaly mudstone (C).

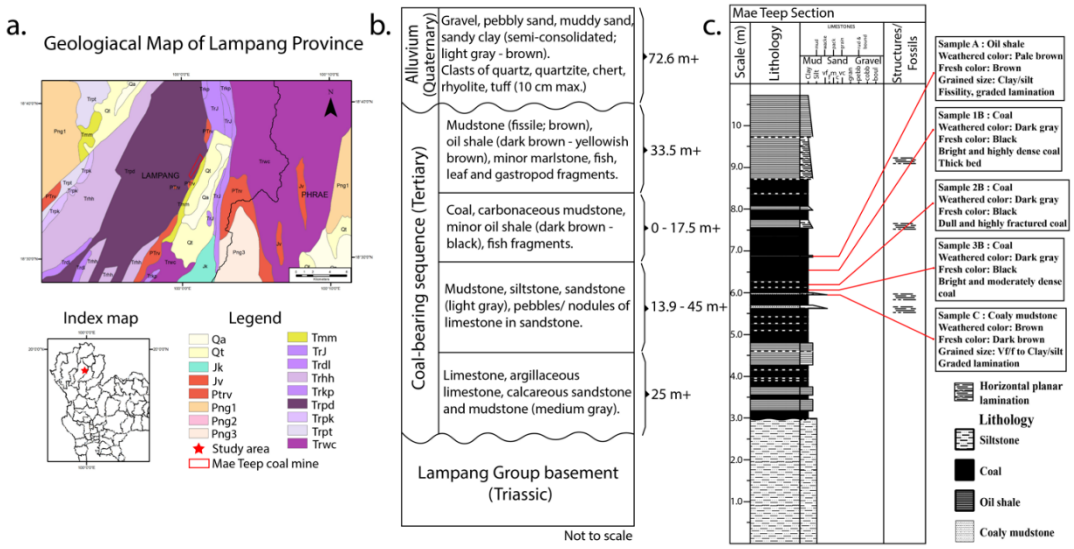

Figure 1. a. the geological map shows the study area, Mae Teep coal mine, Lampang province; b. stratigraphy of Mae Teep Basin (modified from Ukakimaphan et al., 1981); c. lithostratigraphic log from Mae Teep coal mine and hand-picked sample locations.

Methodology: Five rock samples are collected within the Mae Teep coal mine. The samples were collected using handpicked from non-weathered exposures after removing the weathering surface and stored in sealed bags. Bulk samples are crushed into powder by disc mill and stored in glass bottle for protecting humidity. All apparatuses are cleaned up using distilled, acetone and dichloromethane (DCM) in order to avoid contamination before use.

The bulk samples were analyzed total organic carbon content (TOC) using SHIMADZU TOC analyzer with solid sample module (SSM-5000A)[13]. Measured parameters are TOC, Bitumen (or extractable organic matter, EOM) content and biomarkers. Bitumen extractions were performed on the crushed samples using a Soxhlet apparatus for 48 hours extracted by the mixture of dichloromethane (DCM) and methanol (CH_3OH) (93:7). The extracts were separated into saturated hydrocarbon, aromatic hydrocarbon and NSO compound fractions by liquid column chromatography. A chromatographic column (50 x 2.5 cm) was cleaned by using acetone and dichloromethane, respectively and then packed silica gel of 40-370 mesh that was activated for 24 hours at 120 °C and capped with a few centimeters of alumina. Only saturated fraction was used to analyze in this study. The fractions of all samples were dissolved in hexanes and analyzed using gas chromatography-mass spectrometry (GC-MS). The gas chromatography used HP-5MS column with a temperature programmed at 50°C held for 6 min, then up to 130 °C with a rate of 20 °C/min, after that reduced rate to 3 °C/min held for 20 min at 250 °C. Later, using the rate of 5 °C/min until reached to 300 °C and held for 15 min. The GC-MS analysis was performed on an Agilent 7000C GC/MS Triple Quad with a gas chromatograph attached directly to the ion source (70 eV ionization voltage, 100 mA filament

emission current, 280 °C inlet temperature). Chromatograms were acquired in scanning: 35-700 molecular weight and selected-ion-monitored (SIM) for compound identification and integration. The distribution of organic compounds in the bitumen extracts was monitored by fragmentograms of *n*-alkane (m/z 85), terpanes and hopanes (m/z 191) and steranes (m/z 217).

Results and Discussion:

Quantity of organic matter: The quantitative analysis of the source rock is firstly considered consisting total organic carbon content (TOC) and bitumen (or EOM) content in order to evaluate hydrocarbon potential for petroleum source rock. In addition, the quality of the source rock is used to specify type of organic matter. The depositional environment is used to confirm source of organic matter by using biomarker identification.

The average TOC value of Mae Teep coal mine is 40.0 wt. %, in the range of 4.96 to 73.7 wt. %. The samples can be classified as excellent hydrocarbon potential at present day by TOC content based on literature review[7]. The coal samples contain the highest TOC value ranging from 44.0-73.7 wt.% from 1B-3B whereas the lowest TOC content was recorded in coaly mudstone from C.

The bitumen (or EOM) content of the samples from study area is extracted ranging from 1,277 to 5,956 ppm which can be evaluated as good to excellent generative potential for petroleum source rock[7]. The highest content appears on the coal samples from 1B-3B while coaly mudstone has the lowest value representing good potential source rock at present day.

These results indicate that TOC and bitumen (or EOM) contents can be reached to level of hydrocarbon generation (Table 1.). However, the presence of higher amount of TOC in coal samples causes organic matter of coal mostly consists of organic carbon which can generate only gas compared to oil shale showing both organic hydrogen and organic carbon which can generate oil and/or gas. Moreover, coaly mudstone showing lowest amount of organic matter can be explained that organic-lean sediments were deposited before coal formation.

Table 1. The geochemical results and biomarker ratios of saturated hydrocarbon of the samples from the Mae Teep coal mine.

Parameter \ Sample ID	A	1B	2B	3B	C	Average
Rock types	Oil shale	Coal	Coal	Coal	Coaly mudstone	
TOC[a] (wt. %)	19.5	73.7	57.7	44.0	4.96	40.0
EOM[b] (ppm)	5,956	4,886	3,170	4,819	1,277	4,022
CPI[c]	3.52	5.72	6.39	4.13	2.47	4.45
Pr/Ph[d]	1.07	8.71	6.09	6.29	2.98	5.03
Pr/*n*-C_{17}	3.16	3.78	3.79	4.31	0.44	3.10
Ph/*n*-C_{18}	4.28	0.50	0.80	0.77	0.16	1.30
C_{31} homohopane 22S/(22S+22R)	0.44	0.90	0.91	0.89	0.93	0.81
Ts/(Ts+Tm)[e]	0.37	0.96	0.93	0.98	0.83	0.81
%C_{27} regular sterane	26.8	16.4	20.4	15.1	7.67	17.3
%C_{28} regular sterane	5.4	7.9	8.48	12.4	31.5	13.1
%C_{29} regular sterane	67.8	75.7	71.2	72.5	60.9	69.6

[a]Total organic carbon content
[b]Extractable organic matter
[c]Carbon preference index
[d]Pristane/phytane
[e]Ts: C_{27}18α (H),22,29,30-trisnorneohopane and Tm: C_{27}17α (H),22,29,30-trisnorhopane

Molecular geochemistry: The study of type of organic matter and condition of depositional environment can be defined by using organic geochemistry such as biomarker distributions. The saturated hydrocarbon fraction (aliphatic hydrocarbon) extracted from studied samples was analyzed by using the gas chromatography-mass spectrometry (GC-MS) in order to determine biomarkers used for interpreting thermal maturity, depositional environment and type of organic matter.

n-Alkanes and isoprenoids: The presence of *n*-alkane in rocks can be used to evaluate type of organic matter by using GC-MS (m/z 85 mass chromatogram). Gas chromatograms were shown as results of the GC-MS analyze in Figure 2. and parameters were recorded in Table 1. comprising normal alkanes between n-C_7-n-C_{35} and isoprenoids, pristane (Pr) and phytane (Ph). The *n*-alkanes distribution can be used to indicate type of organic matter which can be divided into three types; short chain *n*-alkanes (lower than n-C_{20}) are represented as microbial input. In addition, middle chain *n*-alkanes (n-C_{11}-n-C_{20}) are indicated origin of algae and/or bacteria in organic matter. Long chain *n*-alkanes (more than n-C_{20}) are considered as input of terrestrial waxes, especially in the n-C_{25}-n-C_{33} range.

The distribution patterns of *n*-alkanes of the analyzed samples suggest that organic matters are mainly derived from terrestrial waxes input with minor microbial activity due to the presence of long chain *n*-alkanes and the prevalent of n-C_7-n-C_{10} range. However, oil shale sample (A) showing the higher peak of middle chain *n*-alkanes (n-C_{17}-n-C_{18}) is represented minor influence of algal and microorganism inputs[14].

The presence of isoprenoids in all analyzed samples are shown as gas chromatogram in Figure and parameters are listed in Table 1. Pristane ($C_{19}H_{40}$) and phytane ($C_{20}H_{42}$) are regular isoprenoid hydrocarbons derived from the phytol side chain of chlorophyll molecule. Phytol can be transformed to both pristane and phytane depending on the depositional environment. Pr/Ph is ratio using to determine oxic/anoxic conditions of paleoenvironment[3]. High Pr/Ph ratio (more than 3.0) indicates oxic conditions often associated with terrestrial organic matter input whereas low ratio (lower than 1.0) represents anoxic conditions, commonly hypersaline or carbonate environments[8] and ratio between 1.0 and 3.0 suggests intermediate conditions (suboxic conditions)[1]. In addition, Pr/Ph ratios can be divided into three groups including 1) ratio lower than 2.0 indicating reducing-aquatic deposition (including marine, fresh water, and brackish water), 2) intermediate ratios 2 to 4 indicating fluvio-marine and coastal swamp deposits and 3) ratio more than 4 indicating peat swamp in an oxidizing environment.

The average Pr/Ph ratio of analyzed samples is 5.03, in the range of 1.07 to 8.71. The coal samples (1B-3B) showing the highest value between 6.09 and 8.71 indicates oxic condition associated peat swamp deposits while oil shale sample (A) has the lowest value about 1.07 indicating anoxic associated aquatic deposition and coaly mudstone (C) showing suboxic condition.

Terpanes and steranes: The distributions of terpanes and steranes are analyzed by using GC-MS measuring the ions m/z 191 and m/z 217 mass chromatograms, respectively. Gas chromatograms of terpanes and steranes are shown in Figure 2. and parameters are listed in Table 1.

The regular steranes are used to distinguish the input of organic matter measured by using m/z 217 mass chromatogram in GC-MS. The distribution of regular steranes can be divided into three groups; C_{27} regular sterane infers to planktonic marine influenced system while C_{28} regular sterane is derived from yeast, fungi, plankton and algae in freshwater of lacustrine depositional environment and C_{29} regular sterane is derived from terrestrial higher plants and brown and green algae[15]. However, microalgae or cyanobacteria can also be important source of C_{29} steranes. On the other hand, the presence of higher C_{27} steranes content suggests a marine influenced system from micro-plankton and micro-marine algae. In addition, some C_{28} and C_{27} steranes may derive from fresh water plankton and/or algae[16].

The relative abundance of C_{27}, C_{28} and C_{29} regular steranes from this study was converted to a percentage and plotted in a ternary diagram as shown in Figure and listed in Table. In this study, all analyzed samples showing similar distributions of the regular steranes can be inferred that these samples may derived from the same organic matter source or same depositional environment. In addition, the significant presence of C_{29} regular sterane (more than 60%) can be indicated to terrestrial higher plant environment. However, oil shale sample (A) and coaly mudstone (C) may have minor influences of plankton and/or algae due to the significant presence of both C_{27} and C_{28} regular steranes.

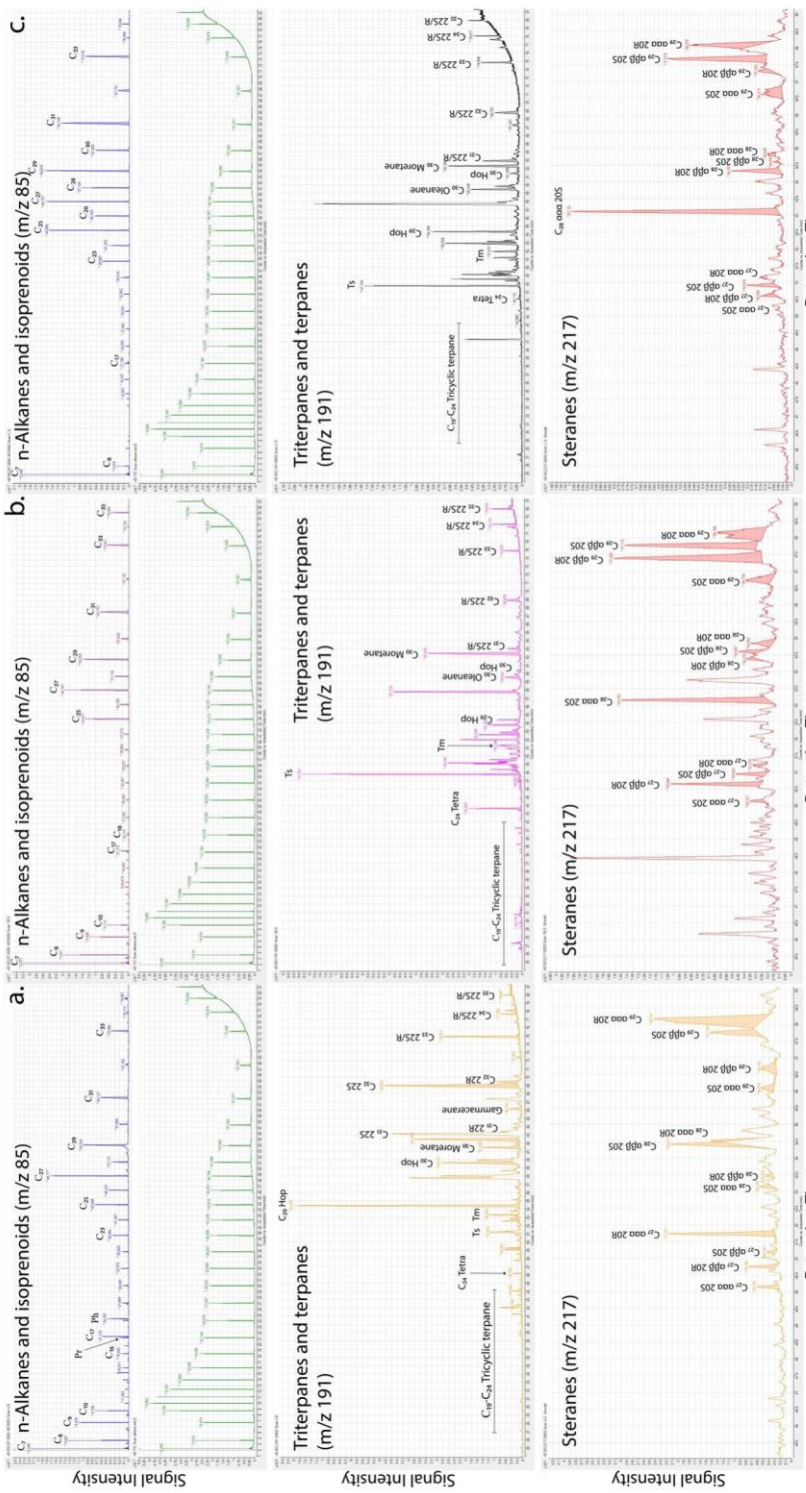

Figure 2. Gas chromatogram of the analyzed samples showing *n*-alkanes and isoprenoids (m/z 85) compared to reference alkanes chromatograms, terpanes (m/z 191) and steranes (m/z 217); an example of a. oil shale (sample A); b. coal (sample 1B) and c. coaly mudstone (sample C).

Thermal maturity: The study of thermal maturity is used to understand the change of organic matter in rocks during lithification or diagenetic process. In this study, the analyzed samples are mainly coal (1B-3B) and other sedimentary rock such as oil shale (A) and coaly mudstone (C). The change of organic matter of coal can be defined the difference in coal rank. The rank of coal reflects the degree of coalification which depends on time of burial depth, temperature and pressure from burial depth. Other factors (including igneous intrusions or heat flow in the basin) can play a part for transformation of peat into coal. Thus, thermal maturity can evaluate relatively to coal rank by using American Society for Testing and Materials (A.S.T.M.) standards. In this study, biomarker parameters are used to evaluate the level of thermal maturity including homohopane isomerization ratio and Ts/(Ts+Tm) ratio.

C_{31} homohopane 22S/(22S+22R) isomerization ratio: Homohopane isomerization ratio is used as a biomarker maturity parameter which is measured from the m/z 191 mass chromatogram. This ratio is determined the configuration of homohopane molecules between biological form (22R) and geological form (22S) (Figure 3a.). Ratio ranges 0-0.6 means equilibrium during maturation. Early state of oil generation values 0.50-0.54. Then, ratio can be reached from 0.57-0.62 indicating oil window maturity[11]. Homohopane isomerization ration can be calculated from any or all of C_{31}-C_{35} homohopanes.

In this study, C_{31} homohopane is used as biomarker maturity indicator showing 22S /(22S+22R) ratio in the range of 0.44 to 0.93. These ratios suggest that organic matter of analyzed samples have been reached at mature stage, except from oil shale (A) with 0.44 representing immature source rock.

Ts/(Ts+Tm): The ratio of Ts (C_{27}18α (H),22,29,30-trisnorneohopane) and Tm (C_{27}17α (H),22,29,30-trisnorhopane) is used to determine maturity (Figure 3a.). Tm is less stable than Ts during catagenesis. Therefore, the high value of this ratio refers to low amounts of Tm with higher thermal maturity of organic matter[11]. Both Ts and Tm can be calculated from peak area in the m/z 191 mass chromatogram. Mature state is evaluated ranging 0.35-0.95.

The analyzed samples showing Ts/(Ts+Tm) ratio in the range of 0.37 to 0.98 can be indicated as mature source rock. This ratio is consistent with homohopane isomerization ratio.

Coal rank: These biomarker parameters can be inferred that coal samples are at an early stage of oil generative potential. Based on evolution of the organic matter (modified from Tissot and Welte, 1984), all analyzed coal samples are considered as high volatile bituminous coal equivalent to the A.S.T.M. coal rank (Figure 3b.).

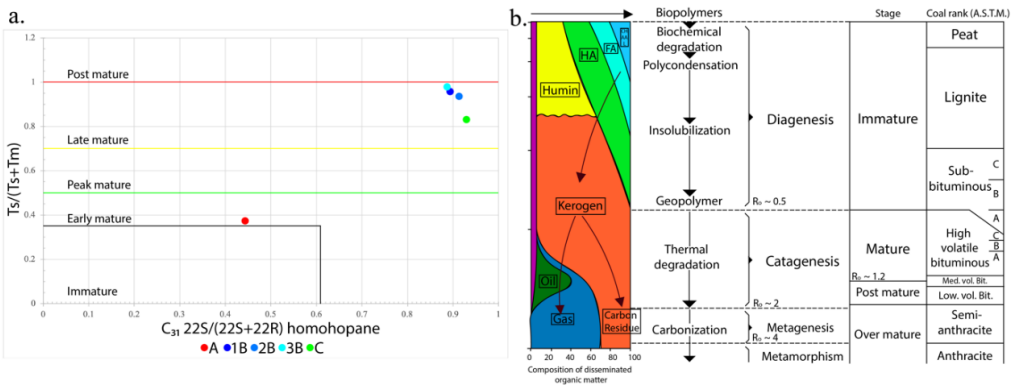

Figure 3. a. cross-plot between the ratios of the Ts/(Ts+Tm) and C_{31} 22S/(22S+22R) homohopane showing maturity of the studied samples; b. general scheme of evolution of the organic matter, from the freshly deposited sediment to the metamorphic zone. (*CH:* carbohydrates, *AA:* amino acids, *FA:* fluvic acids, *HA:* humic acids, *L:* lipids, *HC:* hydrocarbons, *N,S,O:* N, S, O compounds (non-hydrocarbon)) and comparison of the scale of equivalent A.S.T.M. coal rank (Modified from Tissot and Welte, 1984).

Depositional environment: The biomarker distributions can be also used to interpret the organic matter source and depositional environment. The ion m/z 85, m/z 191 and m/z 217 mass chromatograms are monitored in order to determine the peak area of *n*-alkanes, terpanes and steranes which can be calculated as parameters shown in Table 1. including carbon preference index (CPI), Pr/Ph, Pr/*n*-C_{17}, Ph/*n*-C_{18} and regular steranes.

The samples from Mae Teep coal mine have similar *n*-alkanes, isoprenoids and steranes distributions, except oil shale (A) showing different results. However, the long chain *n*-alkanes predominant suggests the mainly influence of terrestrial higher plant environment and are good agreement with the C_{29} regular sterane prevalent (Figure 4b.) while the formation of oil shale and coaly mudstone may have minor influence of different organic matter type such as algae and/or plankton due to the significant amount of C_{27} and C_{28} regular sterane.

Carbon preference index (CPI) is the ratio of *n*-alkane distribution containing the relative between odd carbon-numbered *n*-alkanes and even carbon-numbered *n*-alkanes. CPI can be used to describe maturity, biodegradation and also source of organic matter. CPI values above or below 1.0 indicating immature stage, while values close to 1.0 representing mature stage.

$$CPI = (2[n\text{-}C_{23}+n\text{-}C_{25}+n\text{-}C_{27}+n\text{-}C_{29}]/[n\text{-}C_{22}+2\{n\text{-}C_{24}+n\text{-}C_{26}+n\text{-}C_{28}\}+n\text{-}C_{30}])$$

In reducing environment, n-fatty acids, alcohols and phytol is dominant over decarboxylation resulted in predominance of even carbon-numbered n-alkanes over odd carbon-numbered n-alkanes (CPI<1.0) and phytane is dominant over pristane. While, oxidizing environment containing more decarboxylation increases odd carbon-numbered n-alkanes over even carbon-numbered n-alkanes (CPI>1.0) and pristane is dominant over phytane. In addition, depositional system can be characterized by the presence of *n*-alkanes patterns including 1) algal marine possessing lower molecular weight *n*-alkane (short chain) with no longer than *n*-C_{17} and without any odd or even chain length preference, 2) terrestrial source consists of higher molecular weight n-alkane (long chain) with odd numbered preference such as *n*-C_{27}, *n*-C_{29} and *n*-C_{31}. Moreover, freshwater algae comprise longer chain *n*-alkanes as same as terrestrial input.

On this study, the coal samples are believed to have been deposited in peat swamp environment under oxic condition caused of high CPI and high Pr/Ph ratio. Whereas, oil shale is considered terrestrial with minor aquatic deposition under anoxic condition due to high CPI with middle chain *n*-alkanes, low Pr/Ph ratio and coaly mudstone deposited with organic-lean sediment on terrestrial environment under suboxic condition (high CPI and moderate Pr/Ph ratio). Organic facies are confirmed by using Pr/*n*-C_{17} and Ph/*n*-C18 as shown in Figure 4a. as result of terrestrial environment.

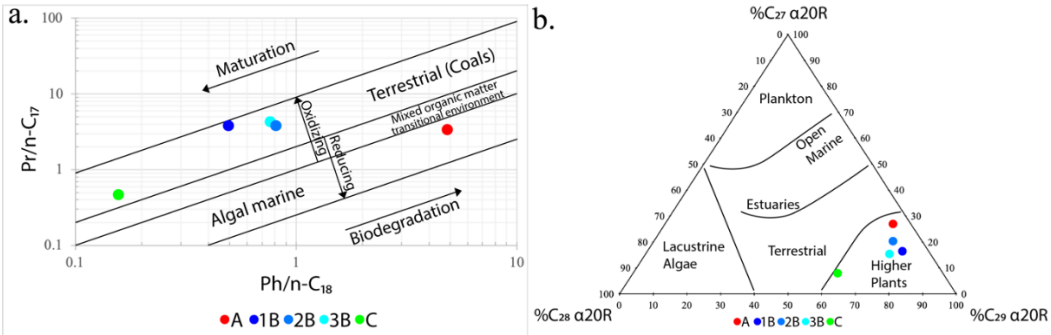

Figure 4.a. log plot between the ratios of phytane to *n*-C_{18} alkane (Ph/*n*-C_{18}) and pristane to *n*-C_{17} alkane (Pr/*n*-C_{17}) (modified after Shanmugam, 1985); b. ternary diagram of regular steranes (C_{27}:C_{28}:C_{29}) showing the relationship between sterane compositions, organic matter input, and depositional environment for the studied samples (modified after Huang and Meinschein, 1979).

Conclusions: The study of organic geochemical characteristics of the analyzed samples from Mae Teep coal mine leads to the conclusion that this study has high TOC values as well as bitumen (or EOM) content showing high value. These contents are considered as excellent hydrocarbon generative potential for petroleum source rock at present day. In addition, all analyzed samples are displayed slightly high in thermal maturity at present day as indicated by biomarkers maturity parameters, except from oil shale (A) showing immature stage. In term of coal rank, thermal maturity can be related to high volatile bituminous coal in all coal samples of this study.

The biomarker distribution of this study can be indicated source of organic matters in rock samples. There is higher plant of organic input with minor algae and/or bacteria based on the plot of Pr/*n*-C_{17} and Ph/*n*-C_{18} and CPI.

The depositional environment of organic matter of the Mae Teep coal mine in this study area can be divided into three systems depends the different rock types. Firstly, the coal samples (1B-3B) are interpreted to be peat swamp environment under oxic condition based on C_{27}, C_{28} and C_{29} regular steranes occurrence and high Pr/Ph ratio. While, oil shale sample (A) is considered to be reducing-aquatic terrestrial environment due to low ratio of Pr/Ph and the C_{29} regular sterane prevalence. Finally, coaly mudstone sample (C) showing low amount of organic matter is believed to be deposited on terrestrial environment with suboxic condition based on the C_{27}, C_{28} and C_{29} regular steranes occurrence and moderate Pr/Ph ratio.

References:

1. Amane W, Hideki N. Organic Geochemistry. 1997;28:27-41.
2. Coster P, Benammi M, Chaimanee Y, Yamee C, Chavasseau O, Emonet E, Jaeger J. GSA Bulletin. 2010;122:1180–1191.
3. Didyk B, Simoneit B, Brassell S, Eglinton G. Nature. 1978;272:216–222.
4. Gibling M, Tantisukrit C, Uttamo W, Thanasuthipitak T, Haraluck M. AAPG Bulletin. 1985;69:767–780.
5. Gibling M, Ukakimaphan Y, Srisuk S. AAPG Bulletin. 1985;69:760–766.
6. Morley C. Journal of the Geological Society. 2001;158:461–474.
7. Peters K, Cassa M. American Association of Petroleum Geologists, Memoir. 1994;60:93–120.
8. Peters K, Clark M, Das Gupta U, McCaffrey M, Lee C. AAPG Bulletin. 1995;79:1481-1494.
9. Petersen H, Foopatthanakamol A, Ratanasthien B. Journal of Petroleum Geology. 2006;29:337–360.

10. Ratanasthien B, Kandharosa W, Chompusri S, Chartprasert S. Journal of Asian Earth Sciences. 1999;17:301–306.
11. Seifert W, Moldowan J. Methods in Geochemistry and Geophysics. 1986;24:261-290.
12. Shanmugam G. American Association of Petroleum Geologists Bulletin. 1985;69:1241–1254.
13. Sleutel S, De Neve S, Singier B, Hofman G. Communications in Soil Science and Plant Analysis 2007;38(19-20):2647-2657.
14. Tissot B, Deroo G, Hood A. Geochimica et Cosmochimica Acta. 1978;42:1469–1485.
15. Volkman J. Organic Geochemistry. 1986;9:83–99.
16. Volkman J, Maxwell J. Amsterdam, the Netherlands: Elsevier. 1986;-:1-42.

Acknowledgements: The authors are grateful to Department of Geology, Faculty of Science, Chulalongkorn University for providing geochemical laboratory and any facilities to fulfill this research. Special thanks to Suntitranon Co. Ltd. for allowing coal mine accession. It is appreciated to Scientific and Technological Research Equipment Centre and Center of Excellence on Hazardous Substance Manage for providing analysis tools.

Appendix1. Peak distribution of gas chromatograms of aliphatic hydrocarbons measured m/z 85, m/z 191 and m/z 217.

Peak	Compound
Pr	Pristane ($C_{19}H_{40}$)
Ph	Phytane ($C_{20}H_{42}$)
C_{24} Tetra	C_{24} Tetrecyclic terpane
Ts	C_{27} 18α (H)-22, 29, 30-trisnorneohopane
Tm	C_{27} 17α (H)-22, 29, 30-trisnorhopane
C_{29} Hop	C_{29} 17α (H), 21β (H)-norhopane
Oleanane	C_{30} 18, 17α (H)-oleanane
C_{30} Hop	C_{30} 17α (H), 21β (H)-hopane
C_{30} Moretane	C_{30} 17β (H), 21α (H)-moretane
C_{31} 22S	C_{31} 17α, 21β (H)-homohopane (22S)
C_{31} 22R	C_{31} 17α, 21β (H)-homohopane (22R)
Gammacerane	C_{30} Gammacerane
C_{32-35} 22S	C_{32-35} 17α, 21β (H)-homohopane (22S)
C_{32-35} 22R	C_{32-35} 17α, 21β (H)-homohopane (22R)
C_{27} ααα 20S	C_{27} 5α,14α (H), 17α (H)-cholestane 20S
C_{27} αββ 20R	C_{27} 5α,14β (H), 17β (H)-cholestane 20R
C_{27} αββ 20S	C_{27} 5α,14β (H), 17β (H)-cholestane 20S
C_{27} ααα 20R	C_{27} 5α, 14α (H), 17α (H)-cholestane 20R
C_{28} ααα 20S	C_{28} 5α, 14α (H), 17α (H)-ergostane 20S
C_{28} αββ 20R	C_{28} 5α, 14β (H), 17β (H)-ergostane 20R
C_{28} αββ 20S	C_{28} 5α, 14β (H), 17β (H)-ergostane 20S
C_{28} ααα 20R	C_{28} 5α, 14α (H), 17α (H)-ergostane 20R
C_{29} ααα 20S	C_{29} 5α, 14α (H), 17α (H)-stigmastane 20S
C_{29} αββ 20R	C_{29} 5α, 14β (H), 17β (H)-stigmastane 20R
C_{29} αββ 20S	C_{29} 5α, 14β (H), 17β (H)-stigmastane 20S
C_{29} ααα 20R	C_{29} 5α, 14α (H), 17α (H)-stigmastane 20R

E_013_OF: RECONSTRUCTION OF SEA LEVEL FLUCTUATION AND PALEOENVIRONMENTAL CHANGES IN KHAO SAM ROI YOT NATIONAL PARK, CHANGWAT PRACHUAP KHIRI KHAN DURING THE LATE HOLOCENE

Worakamon Nudnara[1], Paramita Punwong[2], Akkaneewut Chabangborn[1,*]
[1]Morphology of Earth Surface and Advanced Geohazards in Southeast Asia Research Unit (MESA), Department of Geology, Faculty of Science, Chulalongkorn University, Bangkok, Thailand
[2]Faculty of Environment and Resource Studies, Mahidol University, Nakhon Pathom, Thailand
*e-mail: akkaneewut@gmail.com

Abstract: Sediment sequences from the Sam Roi Yot wetland provided the evidences of sea level fluctuation and paleoenvironmental changes in Khao Sam Roi Yot National Park area. Nine sediment sequences were correlated together. Core SRY CP-4 was further analyzed by loss on ignition (LOI) to access the organic and carbonate content and dated by radiocarbon technique. The sediment sequence were divided to 3 units i.e. unit A, B, and C from the bottom to the top respectively. Unit A, dominated by dark grey sandy to silty clay, suggested the tidal influenced deposition at approximately 3300 cal year BP. The gradual change to beige color sediment in unit B was possibly indicated the increase in marine influence at approximately 2075 cal year BP. The deposition of gyttja in unit C probably indicated the subsequently replaced of freshwater wetland at approximately 1150 cal year BP.

Introduction: Sea level changes in the Gulf of Thailand have been interested in many studies that showed their temporal fluctuations and spatial distributions (e.g. Choowong et al., 2004; Horton et al., 2005; Nimnate et al., 2014; Surakiatchai et al., 2018). It is caused by which the isostatic rebound after the Last Glacial Age can be possibly negligible (Horton et al., 2005). In addition, the evidences of seismic activities have not been found yet in this area (Charusiri et al., 2007). Therefore, the sea level fluctuation in this area is potentially reflecting of the eustatic changes (Horton et al., 2005; Hanebuth et al., 2011).

Khao Sam Roi Yot National Park is located on the west coast of the Gulf of Thailand in Prachuap Khiri Khan. The central part of the national park is the mountains of the Permain limestone. And the further west of the mountain is a large freshwater wetland called 'Thung Sam Roi Yot' (DNP, n.d.). The elevation around the wetland is approximately near the mean sea level (Koskelainen, 2014).

The coastal geomorphology, i.e. a coastal bay, beach ridge plains and tombolos, was developed by the transgression in this area at approximately 6500 – 6000 yr BP (Surakiatchai et al., 2018). Sam Roi Yot area gradually transferred from a coastal bay, beach ridge plains and tombolos to a tidal flat at about 3000 – 1000 yr BP after the tombolos connected to the mainland (Surakiatchai et al., 2018). These results consist well in time with the sea notches, which developed in the study area and indicate the stillstand of sea level at approximately 6000 and 3000 yr BP (Surakiatchai et al., 2018). These all together suggest a gradually sea level lowering after the mid-Holocene (Choowong et al., 2004; Dusitapirom et al., 2008; Nimnate et al., 2014; Surakiatchai et al., 2018).

Methodology:

Sample collection: Nine sediment sequences from the Sam Roi Yot (SRY) wetland were collected in the north-south and east-west transects by using the Russian corer with 1-meter length and 7.5 centimeters diameter (Figure 1). The samples were taken every 1-meter depth till penetration is not possible. To achieve a continuous sequence, sediment cores were taken at approximately 30-cm next to the first borehole with an overlap depth of 50-cm at each coring site. All samples were kept in a refrigerator until the further analysis. The sediment were detail described and correlated in the north-south transect (SRY-CP4, -CP7, -CP1 and

-CP2) and the east-west transect (SRY-CP4, -CP5 and –CP6) (Figure 1.). Sediment sequence of SRY-CP4 was here select for the further study by loss on ignition (LOI) because it is from the deepest part near the center of the wetland.

Loss on ignition (LOI) (Heiri et al., 2001): The consecutive 2-cm sediment samples from SRY-CP4 were dried at 105 °C for 12 hr. To assess the organic content in sediment, the dried samples were combusted at 550 °C for 6 hr and calculated as the percentage of weight loss of the dried sample (Heiri et al., 2001). The carbonate content were further analysis by the combustion of the samples at 950°C for 3 hr and calculated as the percentage of weight loss of 550°C (Heiri et al., 2001). The weight loss of 950°C was corrected by carbonate and carbon dioxide ratio of 2.27 in order to assess to the carbonate weight in the samples.

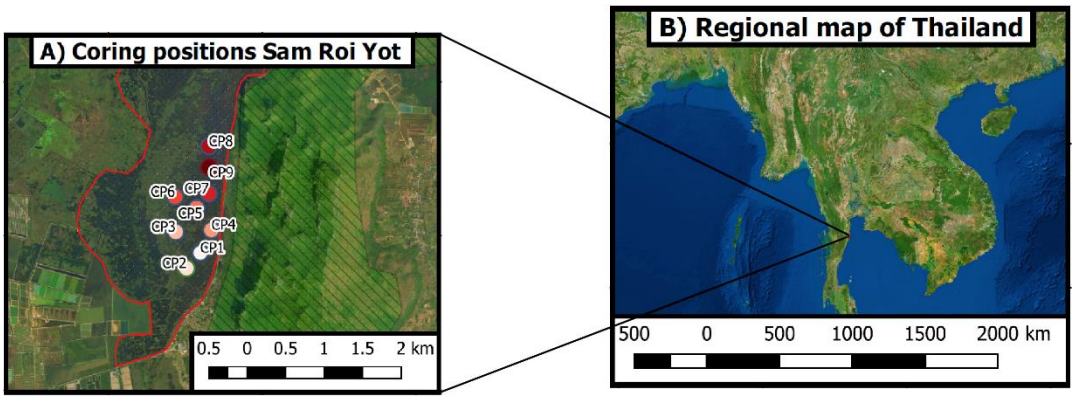

Figure 1. Location map of SRY coring point

Results: The sediment sequences derived from SRY can be divided into 3 units, i.e. unit A, B and C, based on their physical properties.

Unit A, which is the dark grey sandy to silty clay, is the lowermost sedimentary layer. The limestone gravels and shell fragments can be found in the bottom of SRY-CP-4 and the lower part of SRY-CP-5 (Figure 2.). However, unit A is indeterminable core SRY-CP8 caused by unable to penetrate below the overlain layer of unit B (Figure 3.). The topmost of unit A is approximately 2.7 m depth below water surface (DBWS) before it gradually transfer to beige color of sandy to silty clay of unit B (Figure 2., 3., 4.). The upper layer of unit B in core SRY-CP-6, -CP-8 and -CP-9 consists of the dark brown sandy clay (Figure 2., 3.). The brown gyttja clay was found in the upper part of unit B in CP-4. This sediment was grouped into the unit C. Unit B is about 0.6 m thick in SRY-CP1, -CP4 and –CP7, 0.8 m thick in SRY-CP5 and -CP9, and 1.2 m thick in SRY-CP2, -CP3 and –CP6 (Figure 2., 3., 4.). The sharp boundary can be found between unit B and C. Unit C, which is the uppermost part, is mainly composed of gyttja clay, clayey gyttja and gyttja (Figure 2., 3., 4.). Unit C thickness is approximately 0.05, 0.07 and 0.15 cm in core SRY-CP-6, -CP-5 and –CP-4, respectively, which is less than that in the other cores (Figure 2.). This unit is about 0.2 m thick in core SRY-CP-1, -CP-2 and –CP-7 (Figure 3., 4.). The unit C in core SRY-CP-9 is the thickest of about 0.25 cm (Figure 3.).

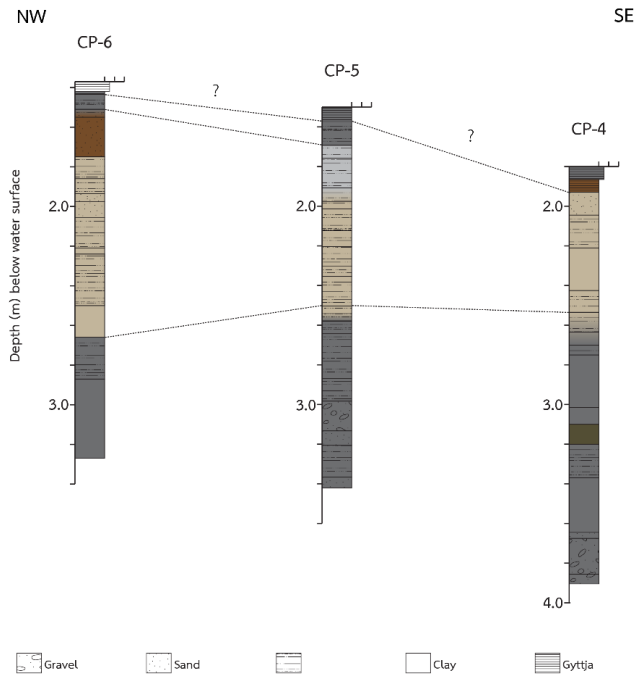

Figure 2.Lithostratigraphic correlation in 1st northwest – southeast transect

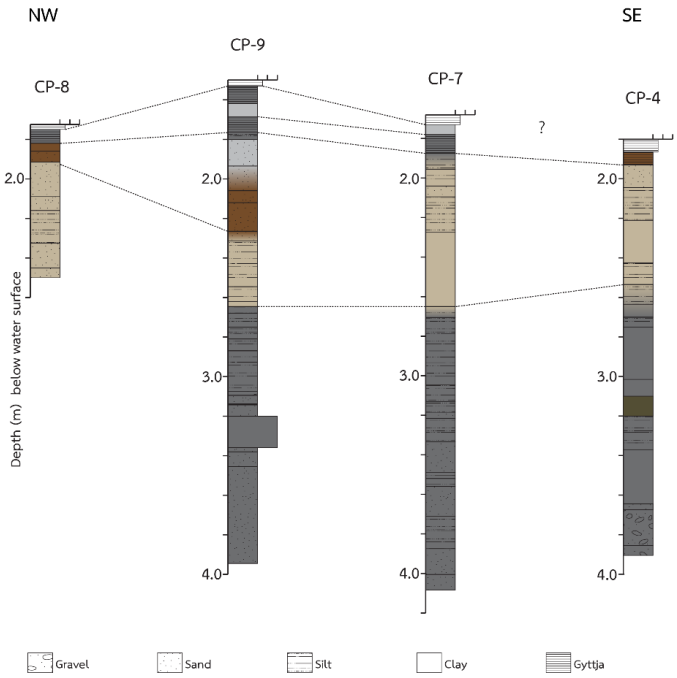

Figure 3.Lithostratigraphic correlation in 2nd northwest – southeast transect

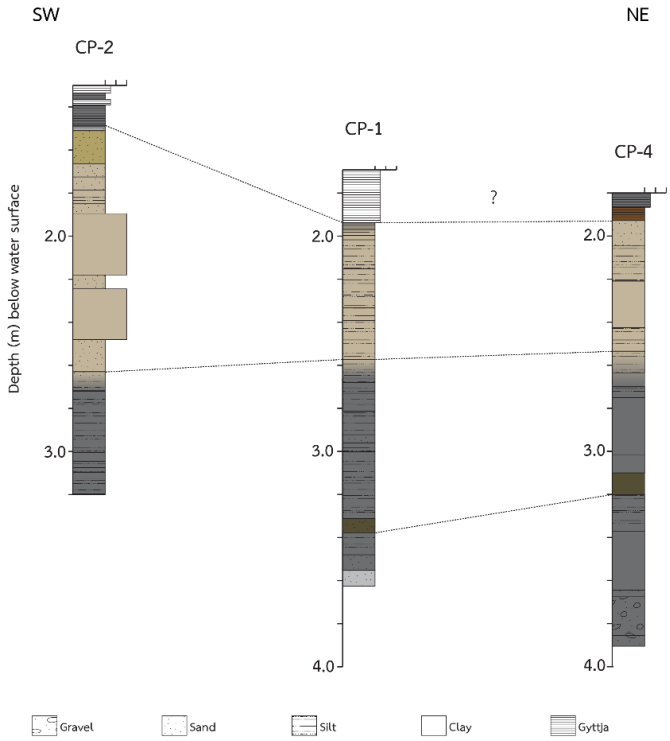

Figure 4.Lithostratigraphic correlation in northeast – southwest transect

We here selected core SRY-CP-4 for the further analysis because it was taken from the deepest part of the wetland. This sediment sequence composes of all 3 sediment units; A, B and C. It can be further divided to 13 subunits (Table 1.). LOI at 550°C in SRY-CP-4 gradually increase from 3 to 10% from layer 4 of unit A to layer 11 of the upper part of unit B. It becomes remarkably increase to 15% in layer 11 and reach its maximum of 30% in unit 13 (Figure 5.). However, the LOI at 950°C generally decrease from 7 to 4% between layer 4 to 11. It slightly increases from 4 to 6% between layer 12 and 13. Chronology of SRY-CP-4 was constructed in regarding to two ^{14}C dating of microscopic charcoals derived from 3.6 and 2.1 m DBWS. The radiocarbon dating results is approximately 3,296 and 1,466 cal year BP. These results suggest the deposition in the wetland during the late Holocene with rate of deposition of about 0.0833 cm/year (Figure 6.)

Table 1. Lithostratigraphic description of SRY CP-4

Depth (m) below water surface	Lithostratigraphic description	Unit	Layer
1.865 – 1.8	Clayey gyttja	C	13
1.93 – 1.865	Brown gyttja clay		12
2.045 – 1.93	Beige sandy clay	B	11
2.21 – 2.045	Beige silty clay		10
2.415 – 2.21	Beige clay		9
2.6 – 2.415	Beige silty clay		8
2.75 – 2.6	Dark grey silty clay	A	7
3.1 – 2.75	Dark grey clay		6
3.2 – 3.1	Dark grey clay (oxidized)		5
3.37 – 3.2	Dark grey silty clay		4
3.645 – 3.37	Dark grey clay with sand spot		3
3.675 – 3.645	Dark grey sandy clay		2
3.9 – 3.675	Dark grey sandy clay with gravel		1

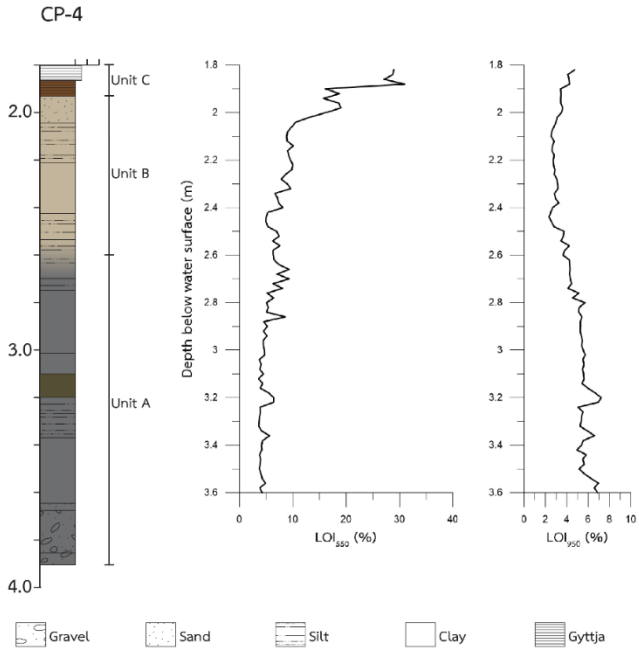

Figure 5. LOI results of SRY CP-4

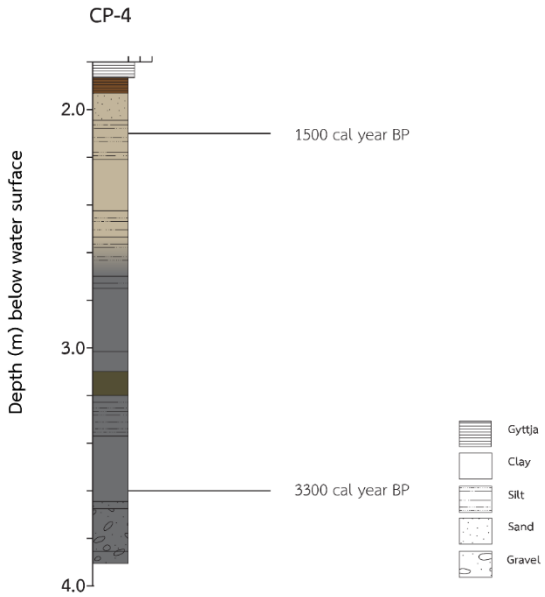

Figure 6. Chronology of SRY CP-4

Discussions and conclusions: The dark grey sandy to silty clay of unit A suggests the deposition under tidal-dominant environment at approximately 3300 cal year BP. This result agrees well in time with the regression period in regarding to Choowong et al. (2004) and Surakiatchai et al. (2018). The replacement of beige color of sandy to silty clay of unit B indicate an environmental change at approximately 2075 cal year BP. The change in sediment color possibly indicates the increase in the marine influence in the study area. This transgression however differs from the stillstand of sea level between 3000 and 900 cal year BP that was mentioned by Surakiatchai et al. (2018). Due to limit of information, the further investigation is necessary. In regarding to the deposition of gyttja of unit C, Sam Roi Yot was possibly replaced by the freshwater wetland at approximately 1150 cal year BP.

References:

1. Choowong M, Ugai H, Chareontitirat T, Charusiri P, Daorerk V, Songmuang R, Ladachart R. The Natural History Journal of Chulalongkorn University. 2004;4(2):1-18.
2. Dusitapirom U, Choowong M, Daorerk V. Bulletin of Earth Sciences of Thailand (BEST). 2008;1:35-39.
3. Hanebuth TJJ, Voris HK, Yokoyama Y, Saito Y, Okuno J. Earth-Science Reviews. 2011;104: 99-110.
4. Heiri O, Lotter AF, Lemcke G. Journal of Paleolimnology. 2001;25:101-110.
5. Horton BP, Gibbard PL, Milne GM, Morley RJ, Purintavarakul C, Stargardt JM. The Holocene. 2005;15,8:1199-1213.
6. Nimnate P, Chutakositkanon V, Choowong M, Pailoplee S, Phantuwongraj S. ScienceAsia. 2015;41:55-63.
7. Surakiatchai P, Choowong M, Charusiri P, Chareontitirat T, Chawchai S, Pailoplee S, Chabangborn A, Phantuwongraj S, Chutakositkanon V, Kongsen S, Nimnate P, Bissen R. Tropical Natural History. 2018;18(2):112-134.

E_014_OF: USING INFORMATION AND COMMUNICATION TECHNOLOGY TO SUPPORT THE MANAGEMENT OF HOUSEHOLD HAZARDOUS WASTE: A CASE OF CHIANG RAI PROVINCIAL ADMINISTRATIVE ORGANIZATION

Mudchima Unmuang[1], Panate Manomaivibool[2,*], Anant Eungwanichayapant[2], Kemachart Kemavuthanon[3], Nitisak Charoenroop[4]
[1]School of Science, Mae Fah Luang University, Chiang Rai, Thailand
[2]Circular Economy for Waste-free Thailand Research Group, School of Science, Mae Fah Luang University, Chiang Rai, Thailand
[3]School of Information Technology, Mae Fah Luang University, Chiang Rai, Thailand
[4]Faculty of Business Administration and Liberal Arts, Rajamangala University of Technology Lanna, Chiang Rai, Thailand
*e-mail: panate.man@mfu.ac.th

Abstract: The management of household hazardous waste (HHW) presents a major challenge for Thailand. Less than 0.2% of HHW was collected and sent for safe disposal. In 2017, Chiang Rai Provincial Administrative Organization (CR PAO) and Mae Fah Luang University developed an information center, named D-ToC (the Data-supporting system for the management of Toxic waste in Chiangrai), to coordinate the collection of HHW with the other 143 local governments in the province.

D-ToC employed information and communication technology (ICT) to support the management of HHW. All local governments in Chiang Rai had reported the quantity of HHW they collected through D-ToC mobile and web-based applications. The system allowed CR PAO to monitor the progress and coordinated with private contractors for an orderly shipment of HHW for safe disposal without the need of a central storage facility. CR PAO had managed 23 and 118 tons of waste in 2017 and 2018, respectively – the highest in the country for both years.

Introduction: The management of household hazardous waste (HHW) presents a major challenge for Thailand. The Pollution Control Department (PCD) reported that only 174 tons of hazardous waste could be recovered from households for safe disposal in 2016. This represented less than 0.2% of estimated generation of 600,000 tons in that year. The figure included the 3 types of HHW: fluorescent lamps, spent batteries, and chemical containers, and electronic waste. Although a fluorescent lamp is being replaced by a LED lamp, the latter is part of e-waste. Therefore, the waste stream in total was expected to grow at a faster rate than municipal solid waste[1].

Currently, there is no specific law for the management of HHW in Thailand. It is handled by local governments under the Public Health Act, B.E. 2535 and the Act on the Maintenance of Cleanliness and Public Order, B.E. 2535, which were were amended in 2017. However, in reality most if not all local governments at a sub-district level found it impossible to get sufficient volume on their own for proper transportation even when households and institutional users such as hotels separated HHW at source[2,3].

In 2017, the Ministry of Interior issued a new policy. The Clean Provinces Action Plan, B.E. 2560 had mandated the installment of a collection point for all villages in Thailand and encouraged the Provincial Administrative Organizations (PAO) to serve as a coordinator for the shipment of HHW. A blueprint for a centralized storage facility was attached to the Action Plan. However, for many provinces including Chiang Rai where the PAOs did not possess any waste treatment facility, it was extremely difficult to site such a facility due to the so-called not-in-my-backyard (NIMBY) syndrome.

To circumvent the obstacle, Chiang Rai PAO with the assistance from Mae Fah Luang University (MFU) developed an online clearing house, named "D-ToC" (the Data-supporting system for the management of Toxic waste in Chiangrai), to coordinate the management of

HHW from over 1,800 collection points with the other 143 local governments at a sub-district level in Chiang Rai. Figure 1 shows examples of collection points in the province.

Figure 1. Examples of collection points for household hazardous waste in Chiang Rai (Source: D-ToC System).

This paper reports the design of the D-ToC system and its achievements during the past years. It also discusses the benefits of using communication technology (ICT) for the management of solid waste as experienced in this case study and the updates to the system. Possibilities to improve the system are outlined for future study.

Methodology: PCD's Guideline for Local Governments (no.04-063) summarizes the management of HHW into 7 following steps:
Step 1: Develop a source separation mechanism(s) and raise the awareness of households and other waste generators;
Step 2: Provide containers or designate collection points for HHW separated from other waste to prevent contamination;
Step 3: Collect HHW from households and other sources by using a curbside collection, a bring system, or both;
Step 4: Put collected HHW in a safe storage until there is enough volume for transportation;
Step 5: Transport HHW by transporters with licenses and full compliance from the Department of Industrial Works (DIW);
Step 6: Sort materials that can be recovered from HHW and send them to authorized recycling facilities (with a 106-type license); and,
Step 7: Send the other waste containing hazardous materials for proper treatment and disposal at a 101-type facility.
According to the Ministry of Interior's Action Plan, a PAO will manage HHW from Step 4 onward with an erection of a centralized storage. It is worth noting that PCD has exempted the transportation of HHW from local governments to a central storage within the same province from the DIW's manifest system since 2017. This enabled CR PAO to replaced a physical storage with a virsual one, as depicted in Figure 2.

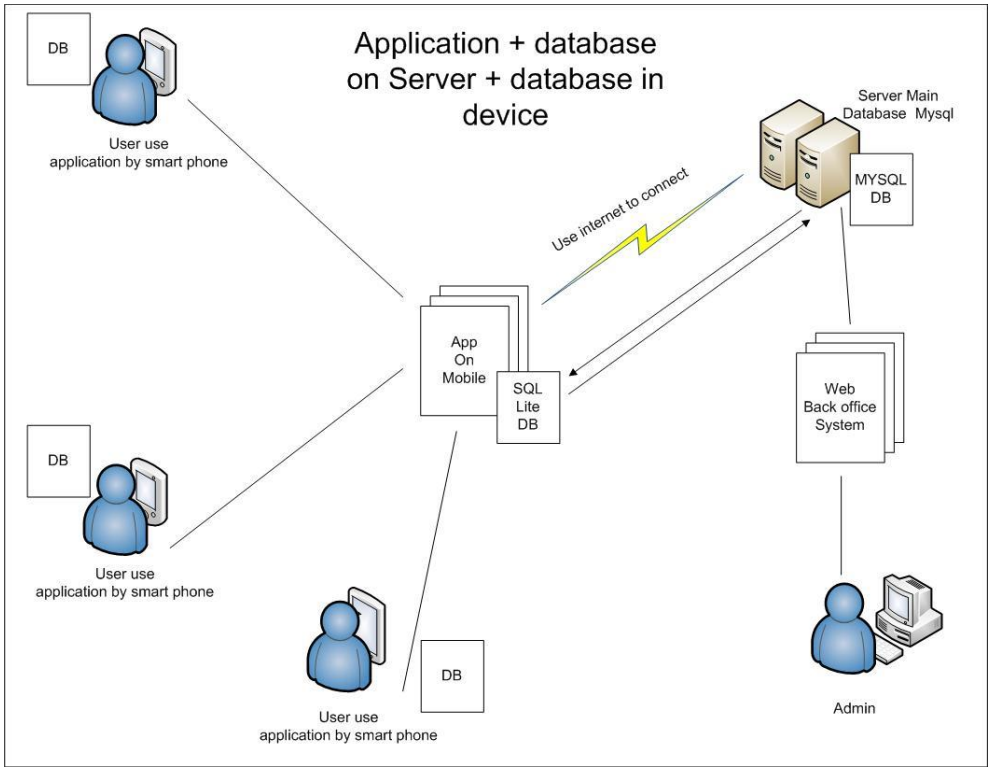

Figure 2. A schematic depiction of the D-ToC system for the management of household hazardous waste in Chiang Rai.

Accounts in the D-ToC system can be classified into 3 types. The administrators of the system, i.e. CR PAO and researchers, can monitor and make changes to all data in the system. The users, i.e. all other local governments at a sub-district level, can input, edit, and manage their own data via mobile and web-based applications. The observers such as other governmental offices at district and provincial levels that have a supervision role can see all data but cannot make any changes.

The system standardized the management of HHW. All users are required to work with the same 7 sub-categories of waste, as shown in Table 1. Waste glass is added into the system as a separate category despite not being hazardous waste because the field survey showed that it is often collected along side HHW. Spray cans are separated from other chemical containers because they are flammable and explodable. CR PAO organized a 2-day training session for the users from all local governments in May 2017 before the official launch of the system.

Table 2. The sub-categories of waste in the D-ToC system.

Sub-category	Hazards and risks
Fluorescent lamps	Toxicity, Sharp edge
Spent batteries	Toxicity, explodability
Spray cans	Toxicity, explodability, flammability
Chemical containers	Toxicity, flammability
Electronic waste	Toxicity
Waste glass	Sharp edge
Others	Toxicity

Results and Discussion: With the support of the D-ToC system, CR PAO managed to ship 141 tons of waste for safe disposal. The first shipment of 23 tons of HHW was on 29 August 2017. This was only 3 months after the launch of the system in May 2017. The second shipment was on 6 October 2018 and tallied 118 tons. 51 tons out of this figure were waste glass that had been accumulated in the province. But, the amount of HHW also increased by a factor of 3 from 23 to 68 tons owing to the fact that all local governments participated. For the next shipment, 130 had registered 53 tons of waste in the D-ToC system by 30 June 2019. According to the interview with CR PAO, they had prepared the budget for HHW but it was unlikely that they would be able to send 8 tons of waste glass this year. Table 2 shows the number of 1-m^3 bags, which were standard transport packaging, and trucks used in each shipment calculated from the quantity of different types of waste in the system. Figure 3 shows the actual shipment.

Table 2. The number of transport packaging and trucks for the shipments by types of waste from the D-ToC system, Chiang Rai.

Year		F. Lamp 90 kg/m^3	Spent battery 400 kg/m^3	Spray can 100 kg/m^3	Chem container 70 kg/m^3	E-waste 80 kg/m^3	Waste glass 400 kg/m^3	Others 400 kg/m^3	Total
2017	Bags	117	13	17	73	8	-	1	229
	Trucks	3.66	0.41	0.53	2.28	0.25	-	0.03	8
2018	Bags	292	22	49	288	60	127	9	847
	Trucks	9.13	0.69	1.53	9.00	1.88	3.97	0.28	27
2019[a]	Bags	207	14	34	219	21	-	3	498
	Trucks	6.47	0.44	1.06	6.84	0.66	-	0.09	16

[a]Based on the data on 30 June 2019. Actual shipment is expected in September 2019.

Figure 3. The shipments of household hazardous waste from Chiang Rai for safe disposal.

Figure 4 shows the composition of HHW that were collected and reported through the D-ToC system between 2017 and 2019 (as of June). It can be seen that fluorescent lamps had the largest shares for all the years. However, the share of chemical containers continued to rise between 2017 and 2019. This might reflect the fact that Chiang Rai was an agriculture-based area and used a lot of chemicals in the crop production. The amount of spent batteries in 2017 was higher than the other two years because batteries that had been sorted out and accumulated at the integrated composting and landfill site in Mae Sai District were released in the first year of operation.

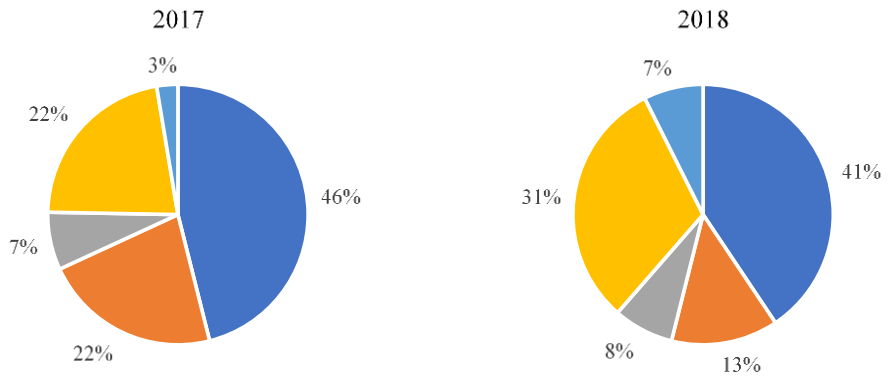

Figure 4. Composition of HHW in the D-ToC system between 2017 and 2019 (as of June).

Figure 5 shows the frequency of uses based on the survey with 105 users of D-ToC system that responded to an online questionnaire in January 2019. It also found that 68% of the users were 35 years or older. Only 29% had inputted the data through the mobile application and 16% had never used the system on mobile devices. The majority of the users tended to use the web-based application for filling the data and used the mobile devices for displaying the information. Although 80% had attended the training organized by CR PAO in 2017, 94% stated that they would attend a training again. Based on this survey, Mae Fah Luang University upgraded the system and organized a training on 19 July 2019. The new system allows a user to add information and attach the documents in line with the Ministry of Public Health's standard system for the management of toxic or hazardous waste from community, EHA 4003. After meeting all data requirements, the user can generate a compliance report automatically from the system.

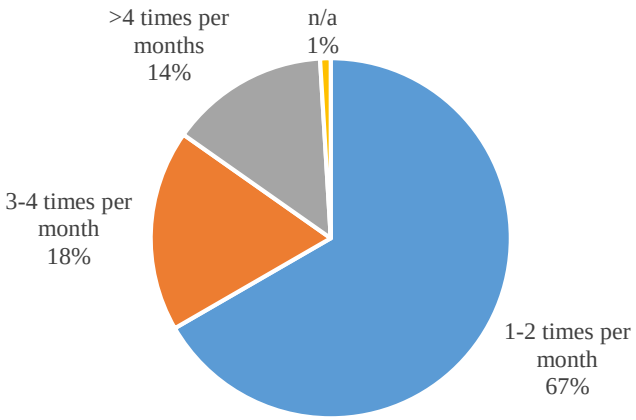

Figure 5. Frequency of uses of the D-ToC system based on a user survey, January 2019.

Conclusion: The D-ToC system proves the benefits of using ICT for environmental management. But for the potential to materialize, users' requirements must be studied and updated. In the future, the system can be further improved by increasing the automation at the front-end of HHW separation and collection. A smart bin can improve data reliability and ensure optimal waste collection[4]. In addition, the transportation of HHW from Chiang Rai can be rearranged to match with the amount of HHW stored in the province. The objectives should be to reduce the number of days waste has to be kept and the travelling distance within the province to improve safety and risk management[5].

References:

1. Manomaivibool, P, Vassanadumrongdee, S. 2011. Journal of Industrial Ecology. 2011; 15: 185-205.
2. Manomaivibool, P. Resources, Conservation and Recycling. 2015; 103: 69-76.
3. Manomaivibool, P, Mongkonkorn, S, Unroj, P, Dokmaingam, P. Resources, Conservation and Recycling. 2018, 136: 142-152.
4. Esmaeilian, B, Wang, B, Lewis, K, Duarte, F, Ratti, C, Behdad, S. Waste Management. 2018, 81: 177-185.
5. Inglezakis, VJ, Moustakas, K. Journal of Environmental Management. 2015, 150: 310-321.

Acknowledgements: The authors would like to acknowledge the funding from the Thai Government to the Integrated Research Program, "Comprehensive Decision Supporting System for Sustainable Solid Waste Management". Special thanks to the Chaing Rai Provincial Administrative Organization for its continuous supports to the D-ToC system.

E_015_OF: ESTIMATING LONG-TERM GROUND-LEVEL PM10 CONCENTRATIONS OVER NORTHERN THAILAND USING A SATELLITE-BASED

Saran Panjaruang, Pichnaree Lalitaporn*
Department of Environmental Engineering, Kasetsart University, Bangkok 10900, Thailand
*e-mail: fengprla@ku.ac.th

Abstract: Particulate Matters or PM_{10} (Particulate matters with a diameter of 10 microns or less) concentrations have adverse effects on human health and their required for long-term assessing population exposure to PM_{10} over heavily polluted areas. In this study, we developed geographically and temporally weighted regression (GTWR) model to derive estimated 10-years (January 2009 to December 2018) of ground-level PM_{10} concentrations over Northern Thailand, using 10 km resolution aerosol optical depth (AOD) data measurements from the Moderate Resolution Imaging Spectroradiometer (MODIS) aboard NASA's Terra and Aqua satellites with meteorological variables, including temperature, humidity, wind speed, pan evaporation and rainfall as predictors on a monthly basis. The GTWR model shows good performance in model prediction with the coefficient of determination (R^2) of 0.86 and root mean square errors (RMSE) and mean prediction error (MPE) of 11.67 and 8.20 μg/m^3, respectively. The GTWR model outperforms multiple linear regression, was fitted seasonally these obtained the highest R^2 value and the lowest RMSE and MPE values for this study. Satellite-derived population-weighted mean PM_{10} for Northern Thailand is 43.15 μg/m^3 over all the whole study period, which lower than Thailand's annual mean PM_{10} standards of 50 μg/m^3. These results are useful for evaluate short-term exposure and evaluate long-term trends of PM_{10} air pollution in the Northern Thailand, especially in dry season of seasonal open biomass burning when more heavily polluted events occur.

Introduction: Particulate Matters (PMs) is the public's concerns about air pollution that can be related to an increased risk of asthma, lung cancer, respiratory diseases chronic, obstructive pulmonary disease and cause serious health problems [1,2]. With its rapid agricultural and economic growth, Thailand is experiencing severe ambient air pollution. According to the Office of the Permanent Secretary Ministry of Public Health of Thailand is reported that over 26 million population has diseases of the respiratory system in 2017, or 44.78% of its 1,000 population were potentially exposed to ambient concentration of PM_{10} (PMs with a diameter of 10 microns or less) in excess annual mean PM_{10} of 50 μg/m^3 of the National Ambient Air Quality Standards (NAAQSs) of Thailand. In Northern Thailand, seasonal open biomass burning has generated PM_{10} air pollution, which occurred frequently over the past decades. The PM_{10} health effects study generally use PM_{10} measurements from ground monitoring stations, but there are many areas with no ground PM_{10} measurements available due to their sparse monitoring network. This limits the ability of PM_{10} to human exposures estimation.

Aerosol optical depth (AOD) was collected by the Moderate Resolution Imaging Spectroradiometer (MODIS) aboard NASA's Terra and Aqua satellites have been widely used to estimation of ground-level PM_{10} concentrations using simple linear regression models [3,4,5,6] and advanced statistical models [7,8,9] was developed to explain for spatial and temporal characteristics in the PM_{10}-AOD relationships. In this study, we aimed to present the first attempt to develop a geographically and temporally weighted regression (GTWR) model for estimation of ground-level PM_{10} concentrations over Northern Thailand based on MODIS AOD and meteorological data on a monthly basis. In addition, the quality model performance of GTWR model, we examine and compare model fitting with multiple linear regression (MLR) in dry season (about November through April) and wet season (about May through October) from January 2009 to December 2018. Statistics are represented with the coefficient of determination (R^2), root-mean-square error (RMSE) and mean prediction error (MPE).

Furthermore, we investigated seasonal patterns of PM_{10} over Northern Thailand based on monthly average concentrations during the study period.

Methodology:

Study Area.: The study area was Northern Thailand, covers located in nine provinces, including Chiang Rai, Chiang Mai, Nan, Phayao, Phrae, Mae Hong Son, Lampang, Lamphun and Tak, an area of 102,259 km^2 and have population greater than 6.1 million as of 2018 data.

Ground-Level Data.: 10-years (January 2019 to December 2018) of monthly average PM_{10} observed data at 15 monitoring stations over Northern Thailand were acquired from the Pollution Control Department (PCD) of Thailand (http://air4thai.pcd.go.th). All the PM_{10} data are measured based on beta ray attenuation and tapered element oscillating microbalance method. The location of all the stations are presented in Figure 1. To improve PM_{10}-AOD relationships, ancillary data are meteorological data (i.e., pressure (P), temperature (TEMP), relative humidity (RH), cloud amount (CA), wind speed (WS), pan evaporation (PE) and rainfall (RAIN) were considered in this study and there are obtained from the Northern Meteorological Center of Thailand website (http://www.cmmet.tmd.go.th/).

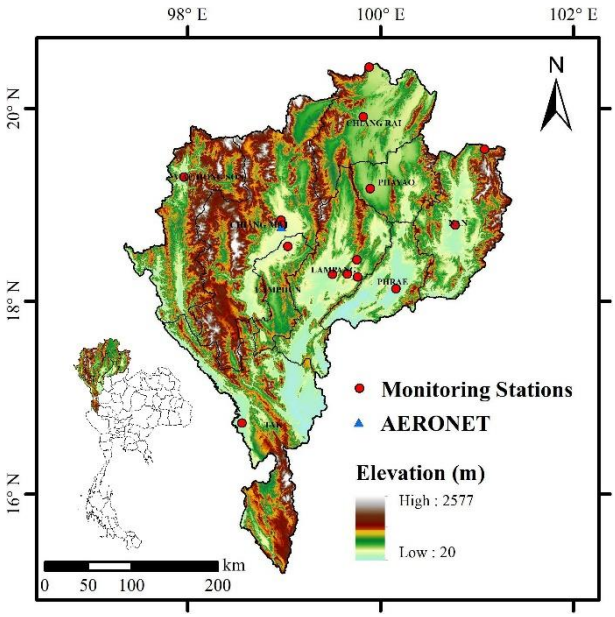

Figure 1. Spatial distribution of location of PM_{10} monitoring stations with the background of elevation.

MODIS AOD Data.: The MODIS aboard NASA's Terra and Aqua satellites is used to monitor AOD and size distribution of the ambient aerosol [10]. In this study, we used to MODIS AOD data from Terra (MOD04_L2) and Aqua (MYD04_L2) satellites, scientific dataset (SDS) Optical_Depth_Land_And_Ocean and retrieval algorithm at 550 nm wavelength. The satellite-derived MOD04_L2 and MYD04_L2 are the MODIS level-2 atmospheric aerosol product provided on a 10 km resolution (10×10 pixel scale at nadir) [11], there are obtained from the Level-1 and Atmosphere Archive & Distribution System Distributed Active Archive Center (LAADS DAAC) NASA website (https://ladsweb.nascom. nasa.gov/) for January 2009 to December 2018.

The ground-based Level-2 AOD data from the Aerosol Robotic Network (AERONET) in Chiang Mai site (Chiang_Mai_Met_Sta, 18.771N, 98.972E) was used to validation of MODIS AOD

data [12,13] and there used to compare with MODIS AOD spectrum at 550 nm. AERONET AOD at 550 nm was calculated by interpolating AERONET AOD at 440 and 675 nm using the reported angstrom exponents for respective wavelengths [14,15] were downloaded from AERONET website (http://aeronet.gsfc.nasa.gov/). The MODIS AOD within a 25 km radius retrieval boxes (at nadir) [10,16] around the AERONET site and data collected within monthly averages of the Terra and Aqua satellites overpass time were adopted. A validation of MODIS AOD results between MODIS AOD with AERONET AOD at 550 nm from the linear regression model during January 2009 to December 2018 shown to correlate well with the Pearson correlation coefficient (r) are both valued at 0.90 and 0.92 for Terra and Aqua MODIS, respectively (Figure 2a and 2b).

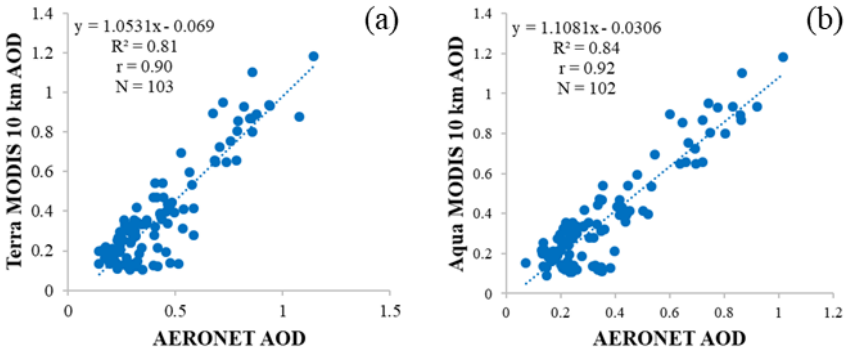

Figure 2. Validations of (a) Terra and (b) Aqua MODIS AOD with AERONET AOD at 550 nm over Chiang Mai AERONET site.

Model Development.: The spatial and temporal variations between ground-level PM_{10} concentrations and satellite-derived AOD relationships influenced by meteorological factors [15,16,17]. In this study, we developed GTWR model follow the approach proposed by Huang et al. [18] to represent the varying PM_{10}-AOD relationships, and improved PM_{10}-AOD relationships with meteorological variables. To independent variables selection, multiple linear regression has been carried out to determine the performance for each model was used to variance inflation factor (VIF), it was calculated as an approximate indicator of collinearity [8,19]. A VIF value of independent variables were more than 2 is regarded as a high collinearity in this study. Finally, Model 3 in Table 1 was developed to the final GTWR model with the structure presented in Eq. (1).

$$\begin{aligned} PM_{10(i)} = \beta_0(u_i,v_i,t_i) + \beta_1(u_i,v_i,t_i) \times AOD_i + \beta_1(u_i,v_i,t_i) \times TEMP_i \\ +\beta_3(u_i,v_i,t_i) \times RH_i + \beta_4(u_i,v_i,t_i) \times WS_i + \beta_5(u_i,v_i,t_i) \times PanE_i \\ +\beta_6(u_i,v_i,t_i) \times RAIN_i + \varepsilon_i \end{aligned} \quad (1)$$

where $PM_{10(i)}$ is the monthly average ground PM_{10} concentrations for sample i at location (u_i, v_i) on time (t_i); β_0 denotes the intercept value; β_1 - β_6 (or β_i) denotes the slope of monthly average AOD_i, $TEMP_i$, RH_i WS_i, $PanE_i$ and $RAIN_i$, respectively; and ε_i stands for the random error. To estimation of $\beta_i(u_i, v_i, t_i)$ at each location (u_i, v_i) on time (t_i) can be expressed as:

$$\hat{\beta}(u_i,v_i,t_i) = [X^T W(u_i,v_i,t_i) X]^{-1} X^T W(u_i,v_i,t_i) PM_{10(i)} \quad (2)$$

where $W(u_i, v_i, t_i)$ is a spatiotemporal weight matrix based on Gaussian distance-decay-based functions and Euclidean distance to estimate the intercept and slope. The spatiotemporal distance between two samples was calculated following Bai et al., Huang et al., and He and Huang [7,18,19].

Table 1. The results of collinearity analysis for independent variables selection.

Model	R^2	VIF							
		AOD	P	TEMP	RH	Cloud	WS	PanE	RAIN
1	0.50	2.00	4.09*	3.86*	4.01*	4.96*	1.33	1.47	1.85
2	0.47	1.89	3.67*	3.41*	1.88	-	1.23	1.47	1.83
3	0.45	1.81	-	1.77	1.68	-	1.21	1.42	1.66
4	0.42	1.72	-	1.48	1.11	-	1.16	1.41	-
5	0.42	1.72	-	1.13	1.11	-	1.14	-	-
6	0.08	1.08	-	-	-	-	1.05	1.08	1.02
7	0.19	1.23	-	1.53	-	-	1.12	1.41	1.53

*VIF > 2

Results and Discussion:

Descriptive Statistics.: Table 2 presents the descriptive statistics of ground-level PM_{10} concentrations measurements, fused Terra and Aqua MODIS AOD and meteorological data at 15 PCD monitoring stations during the study period when PM_{10}-AOD data are available (N = 1,432). Overall, the mean PM_{10} concentrations was 43.26 µg/m^3, which lower than Thailand's NAAQSs annual mean PM_{10} of 50 µg/m^3 and the standard deviation (SD) was 30.77 µg/m^3. The mean AOD was 0.36 with an SD 0.25. Although the time series and the scatter plot (Figure 4) showed high correlation between monthly average PM_{10} concentrations and AOD (r = 0.69), which results are also consistent with previous studies [3,5,20]. However, affected by meteorological conditions (Figure 3) were incorporated into GTWR model to estimate PM_{10} concentrations and improve PM_{10}-AOD relationships.

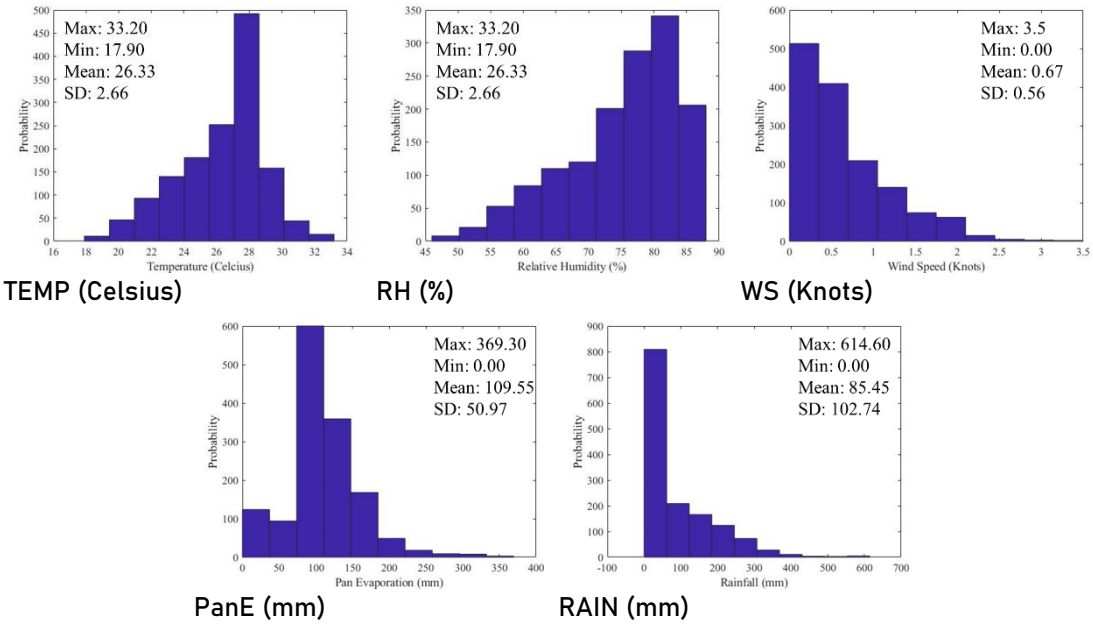

Figure 3. Histograms and descriptive statistics of all meteorological independent variables were used in this study.

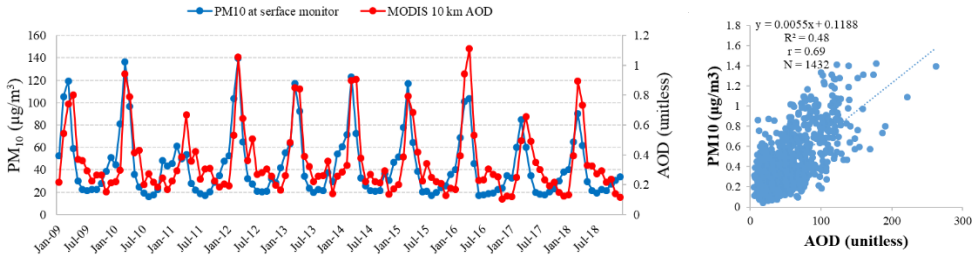

Figure 4. The time series and scatter plot between monthly average PM10 concentrations and MODIS AOD.

Table 2. Descriptive Statistics of measured PM_{10} concentrations at 15 PCD monitoring stations and AOD during the study period.

Station	Province	Lon	Lat	PM_{10} (µg/m³)			AOD (unitless)		
				N	Mean	SD	N	Mean	SD
1	Chiang Rai	99.82	19.91	119	44.78	33.34	119	0.42	0.30
2	Chiang Rai	99.88	20.43	86	50.40	39.75	86	0.41	0.32
3	Chiang Mai	98.97	18.84	119	43.36	26.09	119	0.38	0.22
4	Chiang Mai	98.99	18.79	115	43.47	27.02	115	0.38	0.22
5	Nan	100.77	18.79	108	41.26	26.26	108	0.37	0.30
6	Nan	101.08	19.58	33	32.21	25.91	33	0.33	0.32
7	Phayao	99.89	19.17	100	40.00	30.92	100	0.40	0.25
8	Phrae	100.16	18.13	102	46.43	27.94	102	0.37	0.23
9	Mae Hong Son	97.96	19.29	114	42.70	42.92	114	0.30	0.22
10	Lampang	99.50	18.28	115	46.53	33.11	115	0.35	0.21
11	Lampang	99.76	18.25	105	42.30	25.79	105	0.32	0.22
12	Lampang	99.76	18.43	88	38.56	29.18	88	0.30	0.21
13	Lampang	99.66	18.28	103	43.86	27.06	103	0.33	0.21
14	Lamphun	99.04	18.57	99	41.20	25.52	99	0.36	0.21
15	Tak	98.57	16.73	26	47.00	32.80	26	0.22	0.14

[a] Longitude
[b] Latitude

GTWR Model Performance and Comparisons.: After the model development process, a total of 1,432 datasets of PM_{10}-AOD and meteorological variables for GTWR model fitting were available. The GTWR model overall of R^2 between the predicted and measured PM_{10} is 0.86, that can be explained approximately 86% of the variability in ground-level PM_{10} concentrations and the overall of RMSE and MPE are valued at 11.67 and 8.20 µg/m³, respectively. In this study, GTWR model outperforms MLR, there obtained the highest R^2 value and the lowest RMSE and MPE values were fitted seasonally using the same testing datasets are listed in Table 3. However, it must be noted that the reported PM_{10} seasonal patterns may not be the representative of the entire study period, since Terra and Aqua AOD values were monthly average and less likely to be collected during the wet season due to clouds and high surface reflectance. In addition, Terra and Aqua AOD data are often missing due to retrieval errors. These data gaps inevitably affect the results and analysis of the AOD application [7,21,22].

Table 3. Model Fitting Performance for MLR and GTWR model for ground-level PM_{10} estimation.

Averaging period	MLR			GTWR		
	R^2	RMSE	MPE	R^2	RMSE	MPE
Overall	0.76	15.08	10.46	0.86	11.67	8.20
Dry season (about Nov-Apr)	0.70	18.53	13.11	0.84	13.08	9.28
Wet season (about May-Oct)	0.27	8.02	6.19	0.54	6.36	4.79

PM_{10} concentration estimations.: The GTWR model given high predicting power, it is used to derive ground-level PM_{10} concentrations over Northern Thailand areas at 10 km resolution MODIS AOD. Figure 5a presents the estimated map 10-years long-term mean ground-level PM_{10} concentrations as a whole is 43.15 µg/m^3 derived from the 10 km resolution MODIS AOD, and Figure 5b is shown boxplots of spatial pattern of monthly PM_{10} levels from January 2009 to December 2018. The interquartile ranges, that is the distances between the first and third quartiles of PM_{10} in dry season is around twofold higher than those in wet season. It demonstrates that high PM_{10} concentrations in dry season over Northern Thailand correspond well with seasonal open biomass burning and transboundary haze pollution in the upper part of Southeast Asia (Thailand, Myanmar and Laos), which are generated by open burning of agricultural crop residues, garbage burning and forest fires [23,24,25] over the past decades in dry season.

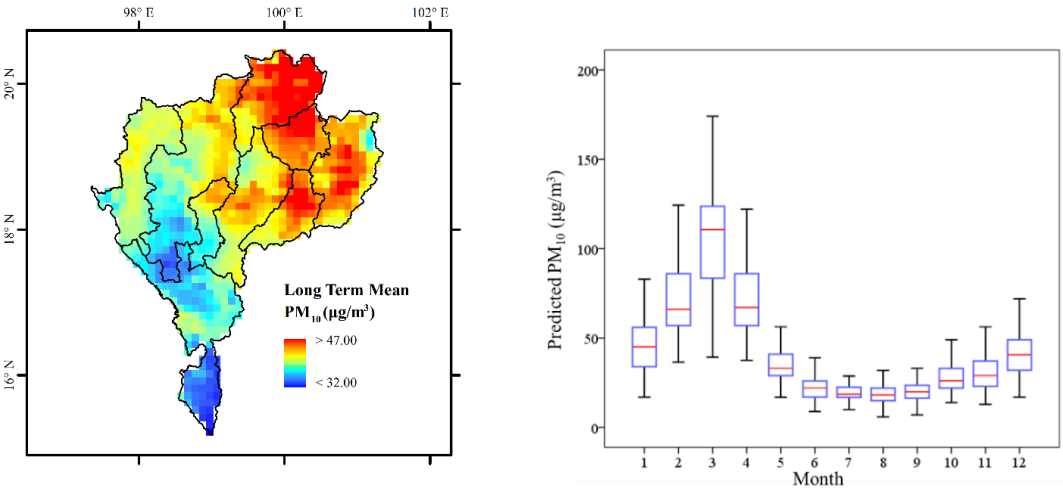

Figure 5. (a) Mean satellite-derived PM_{10} map for Northern Thailand average over all the whole study period and (b) Boxplots of GTWR model estimated the average monthly PM_{10} concentrations.

Conclusion: In this study, GTWR model presented here applies average MODIS AOD with meteorological variables, including TEMP, RH, WS, PanE and RAIN to estimate ground-level PM_{10} concentrations over Northern Thailand on a monthly basis. The GTWR model that can be explained approximately 86% of the variability in ground-level PM_{10} concentrations with RMSE and MPE are valued at 11.67 and 8.20 µg/m^3, respectively, which GTWR model outperforms when compared MLR were evaluated by using the same testing datasets. These results are useful for evaluate short-term exposure and evaluate long-term trends of PM_{10} air pollution in the Northern Thailand, especially in dry season of seasonal open biomass burning when more heavily polluted events occur.

References:
1. Kurt OK, Zhang J, Pinkerton KE. Curr Opin Pulm Med. 2016; 22(2): 138-143.
2. Li T, Hu R, Chen Z, Li Q, Huang S, Zhu Z, Zhou LF. Chronic Diseases and Translational Medicine. 2018; 4: 176-186.
3. Leelasakultum K, Kim Oanh NT. GeoHealth. 2017; 1: 165-179.
4. Sirimongkonlertkul N, Phonekeo V. APCBEE Procedia. 2012; 1: 304-308.
5. Kanabkaew T. EnvironmentAsia. 2013; 6(2): 65-70.
6. You W, Zang Z, Zhang L, Li Y, Pan X, Wang W. Remote Sens. 2016; 8(3): 184.
7. Bai Y, Wu L, Qin K, Zhang Y, Shen Y, Zhou Y. Remote Sens. 2016; 8(3): 262.
8. Guo Y, Tang Q, Gong DY, Zhang Z. Remote Sensing of Environment. 2017; 198: 140-149.
9. Chu HJ, Huang B, Lin CY. Atmospheric Environment. 2015; 102: 176-182.
10. Munchak LA, Levy RC, Mattoo S, Remer LA, Holben BN, Schafer JS, Hostetler CA, Ferrare RA. Atmospheric Measurement Techniques. 2013; 6: 1747-1759.
11. Remer LA, Mattoo S, Levy RC, Munchak LA. Atmospheric Measurement Techniques. 2013; 6(7): 1829-1844.
12. Holben B, Eck T, Slutsker I, Tanre D, Buis J, Setzer A, Vermote E, Reagan J, Kaufman Y, Nakajima T. Remote Sens. Environ. 1998; 66: 1-16.
13. Levy RC, Mattoo S, Munchak LA, Remer LA, Sayer AM, Patadia F, Hsu NC. Atmospheric Measurement Techniques. 2013; 6(11): 2989-3034.
14. Janjai S, Nunez M, Masiri I, Wattan R, Buntoung S, Jantarach T, Promsen W. Atmospheric and Climate Sciences. 2012; 2: 441-453.
15. Xie Y, Wang Y, Zhang K, Dong W, Lv B, Bai Y. Environ. Sci. Technol. 2015; 49: 12280-12288.
16. Gupta P, Remer LA, Levy RC, Mattoo S. Atmos. Meas. Tech. 2018; 11: 3145-3159.
17. Park S, Shin M, Im J, Song CK, Choi M, Kim J, Lee S, Park R, Kim J, Lee DW, Kim SK. Atmos. Chem. Phys. 2019; 19: 1097-1113.
18. Huang B, Wu B, Barry M. International Journal of Geographical Information Science. 2010; 24(3): 383-401.
19. He Q, Huang B. Environmental Pollution. 2018; 236: 1027-1037.
20. Phayungwiwatthanakoon C, Suwanwaree P, Dasananda S. EnvironmentAsia. 2014; 7(2): 133-141.
21. Lee HJ, Liu Y, Coull BA, Schwartz J, Koutrakis P. Atmos. Chem. Phys. 2011; 11: 7991-8002.
22. Yang J, Hu M. Science of The Total Environment. 2018; 633: 677-683.
23. Punsompong P, Chantara S. Atmospheric Pollution Research. 2018; 9(6): 1038-1051.
24. Moran J, NaSuwan C, Poocharoen OO. Environmental Science & Policy. 2019; 97: 1-15.
25. Pani SK, Chantara S, Khamkaew C, Lee CT, Lin NH. Atmospheric Research. 2019; 224: 180-195.

Acknowledgements: This research was funded by Kasetsart University Research and Development Institute (KURDI). We would like to thank the Pollution Control Department (PCD) of Thailand, the Northern Meteorological Center of Thailand, the Level-1 and Atmosphere Archive & Distribution System Distributed Active Archive Center (LAADS DAAC) NASA and The Aerosol Robotic Network (AERONET) for providing data publicly accessible.

E_020_PF: SOME PETROCHEMICAL FEATURES OF GRANITIC ROCKS ALONG HIGHWAY 1D, XIENGKHOUANG TO XAISOMBOUN PROVINCES, LAO PDR

Sisouphanh Souvongxay[1], Parichat Sriwan[2], Weerapan Srichan[3], Patcharin Kosuwan Jundee[3,*], Burapha Phajuy[3]
[1]Phu Bia Mining Company Limited, 7th Floor, Capital Tower, 23 Singha Road, Saysetha, Vientiane, Lao PDR
[2]Gemological Research (Thailand), 6th and 10th floors, U-Chu-Liang Building, 968, Rama IV Road, Silom, Bangrak, Bangkok 10500 Thailand
[3]Department of Geological Sciences, Faculty of Science, Chiang Mai University, Chiang Mai 50200, Thailand. Tel. 66(0)53943417-9; Fax. 66(0)53943444
*e-mail: patcharinkosuwan.j@cmu.ac.th

Abstract: The Late Carboniferous to Early Permian granitic rocks in the area of Xiengkhouang to Xaisomboun Provinces were constituted by monzogranite and granodiorite. The rocks have striking petrochemical features. They are I-type granitoid as they contain hornblende as a minor constituent but are S-type granitoid as they have normative corundum and Na_2O/K_2O ratios less than 1.03 at Na_2O in a range of 2.36-2.85 wt%. They are most likely to have high-K calc-alkalic affinity; however, their tectonic setting of formation appear to be non-orogenic.

Keywords: Truong Son fold belts, granitic rock, high-K calc-alkaline rocks, non-orogenic granite, transitional granite

Introduction: The presented granitic rocks are collecting along highway 1D, from Phonegneng Village, Khoun District, Xiengkhouang Province to Thasy Village, Thathom District, Xaisomboun Province, Lao People's Democratic Republic (Lao PDR), with distance approximately 15 kilometres (Figure 1). The intrusive bodies located nearby the intersection of Loei and Truong Son fold belts. The Loei fold belt situated in western Indochina Terrene and has NW–SE trending. It is 50-100 km wide and up to 1,500 km long that extends across western Cambodia through central Thailand to central Laos. The Truong son fold belt located in eastern Indochina Terrene with NW–SE trending. It is 50–100 km wide and 1,000 km long that extends northwest across Laos and northwest of Vietnam. The Loei and Truong Son fold belts are important magmatic and Cu–Au metallogenic belts in mainland Southeast Asia (Zaw *et al.*, 2014; Tran *et al.,* 2014; Manaka *et al.*, 2014).

The Truong Son fold belt separated and drifted northwards from Gondwana in the Early Devonian (Metcalfe, 2011, 2013). After drifting northwards, Indochina Terrene may have collided and amalgamated with the southern Eurasia margin during the Triassic, giving rise to the closure of Paleo-Tethys ocean and cessation of arc magmatism. Also, many workers suggested that Ailaoshan-Song Ma ocean plate was subducted under the Eastern Indochina Terrene during the Late Carboniferous to Permian (Liu, Tran *et al.,* 2012; Liu, Wang *et al.,* 2012; Burrett *et al.,* 2014). The presence of Late Carboniferous to Permian arc magmatism at the northernmost end of the Truong Son fold belt and the ophiolitic rock in Song Ma suture is the evidence of these subductions (Nakano *et al.*, 2004; Osanai *et al.*, 2004; Lai *et al.*, 2014). This southwest-dipping subduction probably induced adakitic and calc-alkaline magmatism and mineralization processes in central, eastern and southern Laos. These subductions led to a collision between Indochina and south China Terranes at about 270-260 Ma in central Vietnam and terminated Truong son arc magmatism along the eastern edge of the Indochina Terrene (Kamvong *et al.*, 2014). Therefore, the Truong Son fold belt has experienced a complex tectonic history, consists of Paleozoic to Early Mesozoic volcano-plutonic suites, and hosts

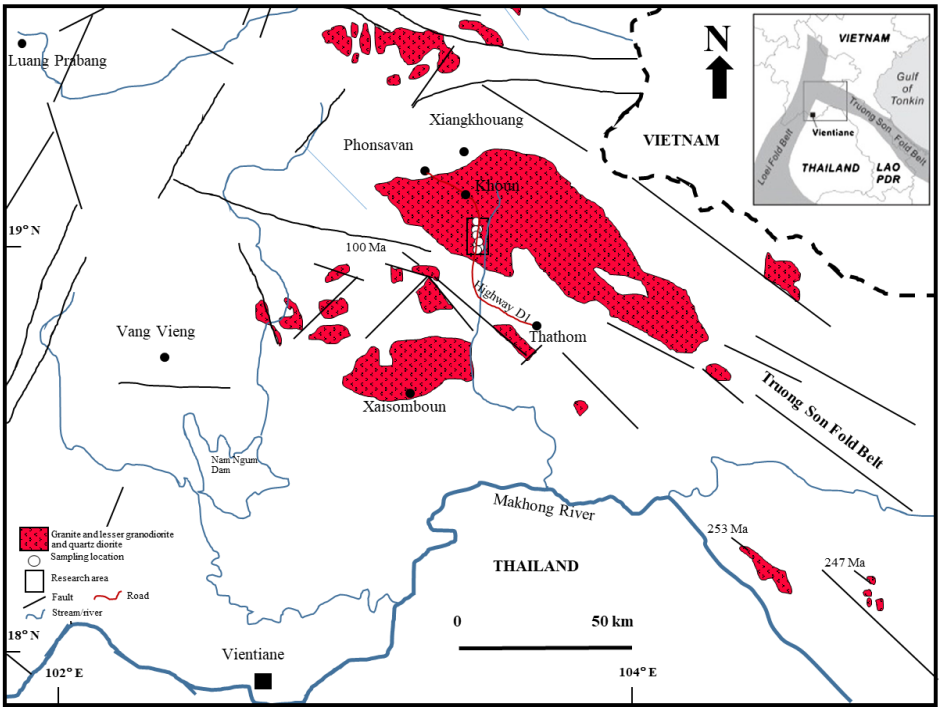

Figure 1. The enlarged map of the research area (see inset) illustrating the distribution of granitic rocks in Truong Son fold belt, northern Lao PDR, and the studied sample locations along the highway 1D from Xiangkhouang to Xaisomboun (modified from Manaka *et al.,* 2014, and Sanematsu *et al.,* 2011).

several Cu–Au deposits. The igneous suites are composed mainly of granite, with subordinate diorite. The plateau ages determined from biotite and muscovite in S-type granitoids that distributed in the Truong Son fold belt of central Laos. Ar^{40}/Ar^{39} incremental heating method indicted the ages range from 253 Ma to 247 Ma in the southwest and 244 Ma to 199 Ma in the northeast of the fold belt. In contrast, the plateau ages of the I-type granitoids, distributed in the Kontum massif of southeasternmost Laos, range widely from 414 Ma to 252 Ma. Carboniferous-Permian granitoids have adakitic characteristics (Sanematsu *et al.*, 2011). The purposed of this studied to investigate petrography and some geochemistry. The major and some trace elements used for discrimination of tectonic setting of emplacements.

Methodology:

Sample selection: Some granitic rock samples collected have been examined under the petrographic microscope and used alteration box plot (Large *et al.*, 2001) to obtain least-altered samples. The least-altered samples are generally excluded those with the extensive development of mesoscopic domains of secondary minerals such as quartz resulted from silicification, epidote minerals and chlorite, well-developed foliation or mineral layering, abundant vugs or druses, xenocrysts, and xenoliths and quartz, epidote, or calcite veining and/or patches totalling more than 5 modal%. The six least-altered granitic rock samples were selected to examine their petrography, modal composition and geochemistry in this study.

Sample Preparation: The least-altered samples prepared in the form of standard thin sections, stained rock slabs, and fusion discs and pellets for petrographic investigation, modal analysis and whole-rock chemical analysis, respectively. Standard thin sections made by cutting and polishing rocks samples until a thickness of approximately 0.03 mm reached. The stained rock slabs for modal analysis made by cutting off the weathering surfaces before

making slabs. The slabs soaked in hydrofluoric acid (HF) and then sodium cobaltinitrite solution ($CoN_6Na_3O_{12}$). The power samples for whole-rock chemical analysis done by cutting off the weathering surfaces of the least-altered samples, splitting them into conveniently-sized fragments, and crushing them to small chips, using a Rocklabs Hydraulic Splitter/Crusher. The cleaned rock chips were divided by quartering, and approximately 50-80 g of the cleaned chips were then pulverized for a few minutes by a Rocklabs Tungsten-Carbide Ring Mill. All the described procedures do at the Department of Geological Sciences, Faculty of Science, Chiang Mai University.

Analytical Technique for Geochemistry: The sample powders chemically analyzed for major oxides, trace elements, and loss on ignition (herein LOI). Chemical analyses of major oxides (SiO_2, TiO_2, Al_2O_3, total iron (FeO and Fe_2O_3) as Fe_2O_3, MnO, MgO, CaO, Na_2O, K_2O and P_2O_5) and some certain trace elements (Ba, Rb, Sr, Y, Zr, Nb, Ni, V, Sc, Cr and Th) were carried out using Philips Magix PRO X-ray fluorescence (XRF) spectrometer (wavelength dispersive system). The standards used were the USGS geochemical reference materials, AGV-2, BCR-2, BHVO-2G, BIR-1a, DTS-2b, DNC-1a, W-2a, GSP-2, QLO-1a, RGM-2 and STM-2. These chemical species were measured from fusion discs prepared with 1 g sample powder, 5 g di-lithium tetraborate ($Li_2B_4O_7$) and 0.06 g lithium bromide (LiBr) for major oxides, and from pressed powders prepared with 6 g sample powder and 0.3 g XRF MULTI-MIX PXR-200 for trace elements. Ignition loss by heating approximately 1 g of powdered samples at 1000 °C for 12 hours. All described procedures were done and measured at the Department of Geological Sciences, Chiang Mai University.

Results and Discussion:

Petrographic Investigation: Modal analysis, performed on the stained rock slabs, reveals that the studied least-altered samples have relative proportions of quartz, potassium feldspar and plagioclase, as shown in Table 1. They are compositionally monzogranite and granodiorite, based on the QAP diagram for plutonic rocks of Streckeisen *et al.* (1967) (Figure 2).

Table 1. Modal analyses of the least-altered granitic rocks show relative proportions of quartz, potassium feldspar and plagioclase.

Modal analysis (%)	Monzogranite					Granodiorite
Sample no.	1202	1208	1401	1405	1406	1410
Quartz	29	38	33	40	35	47
Potassium feldspar	42	29	34	30	35	7
Plagioclase	29	33	33	30	30	46

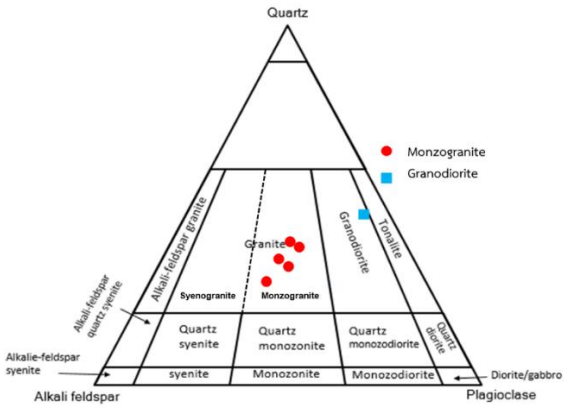

Figure 2. Modal quartz (Q) - alkali feldspar (A) - plagioclase (P) diagram (after Streckeisen *et al.,* 1976) for the least-altered granitic rocks.

Monzogranite (sample nos. 1202, 1208, 1401, 1405 and 1406) is the most abundant rock type in these batholiths. They have a coarse-grained and equigranular texture and consist largely of quartz, plagioclase and potassium feldspar, with minor biotite and muscovite. Quartz shows equant crystals, rounded edges, and embayed outlines. Potassium feldspar and plagioclase crystals have a sieve and graphic texture. Both of the feldspars are anhedral to subhedral and slightly altered to sericite. Chlorite occurred is an alteration product of biotite.

Granodiorite (sample no. 1410) occurs in the southern part of the research area. It has coarse-grained and equigranular textures and composed abundantly of plagioclase and quartz, with subordinate potassium feldspar and minor biotite. Plagioclase and potassium feldspar display subhedral to anhedral outlines and partly show a sieve texture and random orientation. Both of the feldspars slightly altered to sericite. Quartz show quant crystals rounded edge, and embayed outlines with various sizes range from 0.2 to 3 mm in diameter. Biotite is anhedral to subhedral and moderately altered to chlorite.

Whole-rock chemical analysis: Major oxides and some certain trace elements of the least-altered granitic samples report in Table 2. The data for major oxides, in terms of weight%, was used to calculate Ishikawa alteration index (AI) and chlorite-carbonate-pyrite index (CCPI), following the equations.

$$AI = \frac{100(MgO + K_2O)}{(FeO + K_2O + MgO + Na_2O)}$$

$$CCPI = \frac{100(FeO + MgO)}{(FeO + K_2O + MgO + Na_2O)}$$

The results (Table 2) show that the studied samples lie well within limits of the least-altered rocks of Large et al. (2001) as shown in Figure 3.

Table 2. Major oxides and some certain trace elements of the studied least-altered granitic rocks. Normative minerals were calculated, according to the principles of geochemistry.

	Monzogranite					Granodiorite
Sample no.	1202	1208	1401	1405	1406	1410
	major oxide (wt%)					
SiO_2	73.64	70.73	68.57	68.40	68.83	69.23
TiO_2	0.33	0.47	0.59	0.66	0.66	0.59
Al_2O_3	13.91	15.15	15.69	15.69	15.34	15.79
Fe_2O_3	2.62	3.32	4.25	4.56	4.59	4.23
MnO	0.05	0.07	0.09	0.08	0.07	0.07
MgO	0.35	0.90	1.15	1.29	1.31	1.27
CaO	1.45	2.31	2.60	2.68	2.48	3.13
Na_2O	2.85	2.61	2.47	2.42	2.36	2.78
K_2O	4.73	4.31	4.42	4.02	4.11	2.70
P_2O_5	0.06	0.14	0.17	0.21	0.21	0.21
LOI	1.06	0.98	0.98	0.96	0.05	1.04
Original sum	101.09	99.89	100.55	99.39	100.96	98.39
	Some trace elements (ppm)					
Ni	5.67	13.0	10.4	16.9	17.9	13.8
V	60.8	82.2	89.5	98.6	99.8	90.2
Rb	176	234	212	188	190	167
Y	98	92	86	84	81	56
Nb	16.3	13.7	12.8	13.3	14.0	14.6
Th	27.1	23.8	25.1	17.6	19.0	23.1
Cr	15.6	61.0	73.1	52.6	51.8	68
Sr	126	189	205	207	195	217
Ba	1,107	915	917	883	878	707
Sc	3.1	7.4	12.2	7.0	6.9	10.3
Zr	296	196	319	229	225	204
AI	54.2	51.4	52.4	51.0	52.9	40.2
CCPI	28.1	37.9	43.9	47.6	47.6	50.1
	CIPW (wt%)					
Quartz (Q)	34.79	32.57	29.87	31.26	32.10	34.18
Albite (Ab)	24.12	22.09	20.91	20.48	19.97	23.52
Anorthite (An)	6.83	10.57	11.85	11.98	10.98	14.23
Orthoclase (Or)	28.76	26.14	26.79	24.42	25.01	16.54
Corundum	1.43	2.17	2.35	2.82	2.83	2.95
Hypersthene	0.87	2.24	2.86	3.21	3.26	3.16
Rutile	0.27	0.4	0.49	0.58	0.59	0.52
Ilmenite	0.11	0.14	0.18	0.16	0.14	0.14
Hematite	2.62	3.31	4.24	4.55	4.58	4.22
Apatite	0.14	0.32	0.39	0.49	0.49	0.49
Zircon	0.06	0.04	0.06	0.04	0.04	0.04
Chromite	0	0.01	0.01	0.01	0.01	0.01

The least-altered granitic rocks quasi-chemically and chemically classified as monzogranite (sample nos. 1202, 1208, 1401, 1405 and 1406) and granodiorite (sample no. 1410), based on relative proportions of normative quartz, alkali feldspar and plagioclase (Figure 4), and normative anorthite, albite and orthoclase (Figure 5), and total alkalis against silica plot (Figure 6), respectively. These rock types are in agreement with those base on modal quartz,

alkali feldspar and plagioclase (Figure 2). The studied granitic rocks appears to be in the fields of subalkalic rock on total alkaline against silica diagram (Figure 6), calc-alkaline rock on FeO(total) - Na_2O+K_2O - MgO plot (Figure 7), almost totally calc-alkaline rock, except for granodiorite that is calcic (Figure 8), and high-K calc-alkaline rock (Figure 9). Consequently, the studied granitic rocks are most likely to have a high-K calc-alkaline affinity.

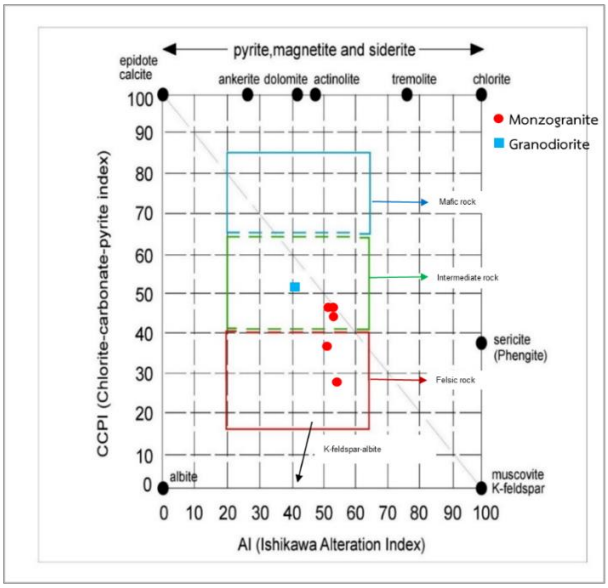

Figure 3. The alteration box plot of Large *et al.* (2001) show the studied least-altered granitic samples.

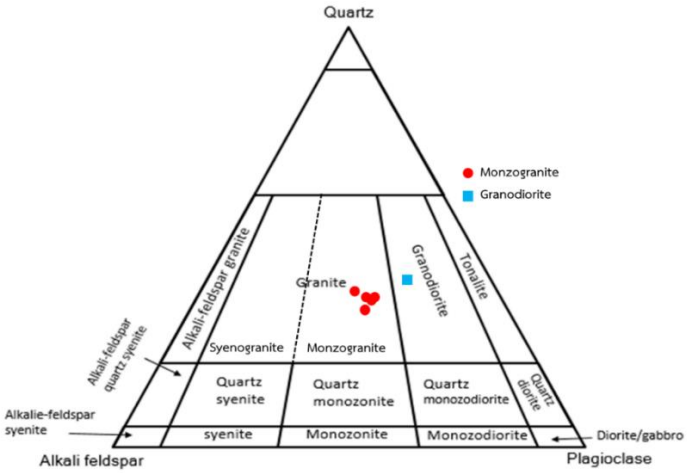

Figure 4. Positions of least-altered granitic rocks, using normative quartz, potassium feldspar and plagioclase, in modal quartz (Q) - alkali feldspar (A) - plagioclase (P) diagram of Streckeisen *et al.* (1967).

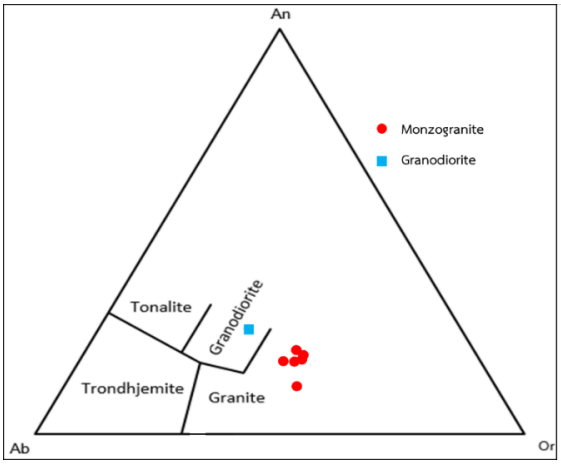

Figure 5. Normative anorthite (An) - albite (Ab) - orthoclase (Or) diagram (Barker, 1979) for the studied least-altered granitic rocks.

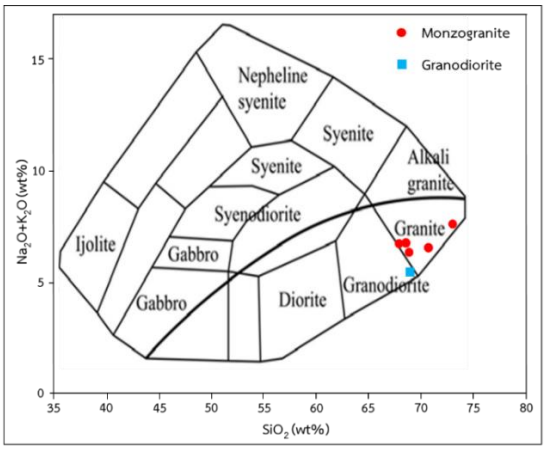

Figure 6. Total alkalis against silica (TAS) diagram for plutonic rocks (Wilson, 1989) showing the positions of least-altered granitic rocks present. The curved solid line separates alkaline (above) from subalkaline (below) rocks.

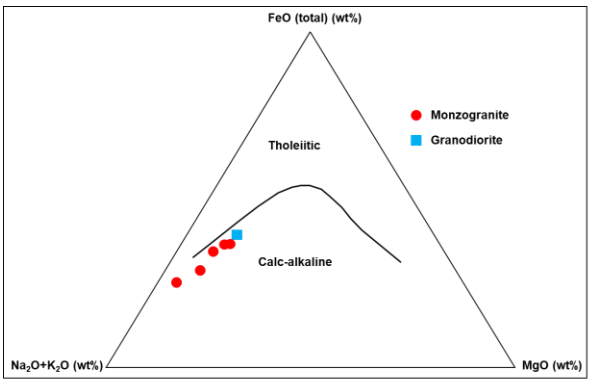

Figure 7. FeO (total) - Na_2O+K_2O - MgO (AFM) diagram for the studied granitic rocks. Tholeiitic and calc-alkaline fields are after Irvine and Baragar (1971).

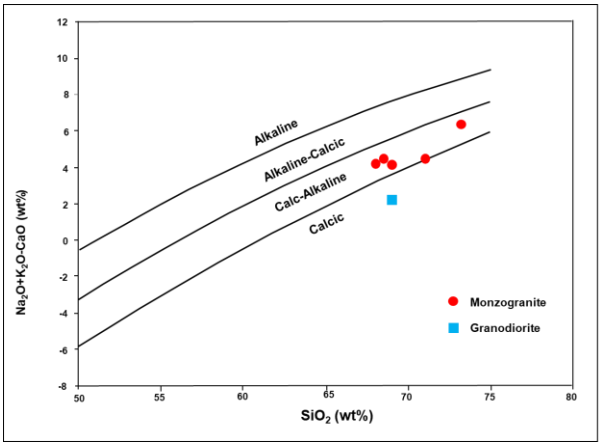

Figure 8. The studied granitic rocks plotted in Na_2O+K_2O-CaO versus SiO_2 diagram with fields of different magma series (after Frost *et al.,* 2001).

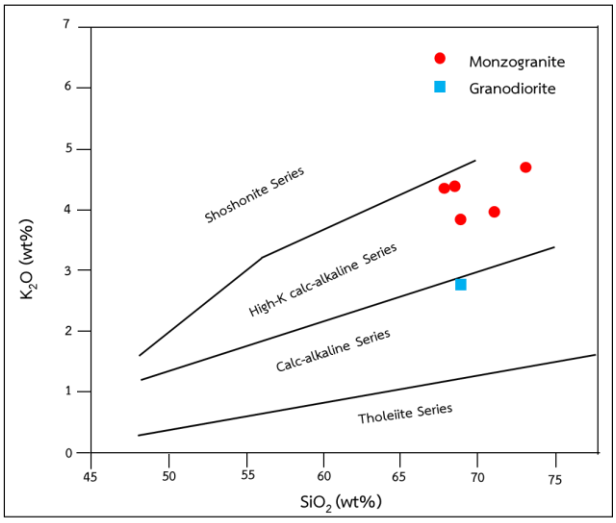

Figure 9. The studied granitic rocks plotted in K_2O versus SiO_2 diagram with fields of different magma series (after Peccerillo and Taylor (1976)).

These rocks are neither magnesian nor ferroan since they straddle on the demarcation line between ferroan and magnesian rocks of Frost and Frost (2008) as shown in Figure 10. The samples plotted in the field of S-type granite in Na_2O - K_2O diagram of Chappell and White (1984) as shown in Figure 11. Sanematsu *et al.* (2011) also mentioned that the Carboniferous Permian granite and granitoid in the northwestern part of Truong Son fold belt were S-type granite with calc-alkaline affinity. In terms of tectonic setting of formation, they are in the field of within-plate granite on Rb against Nb+Y diagram (Figure 12) and the boundary between ocean ridge granite, and within-plate granite and ocean ridge granite from the anomalous ridge (Figure 13).

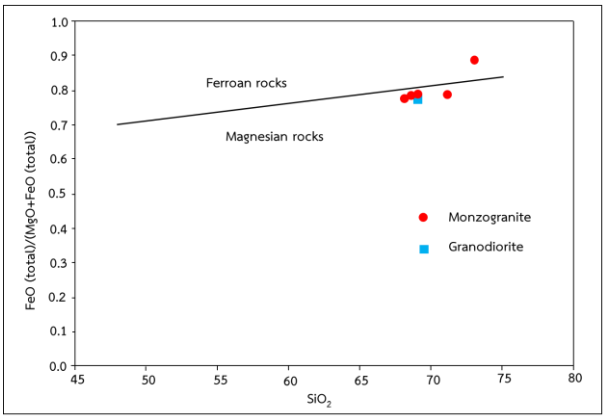

Figure 10. The studied granitic rocks plotted in FeO(total)/MgO+FeO(total) versus SiO_2 diagram with fields of ferroan and magnesian rocks (after Frost and Frost, 2008).

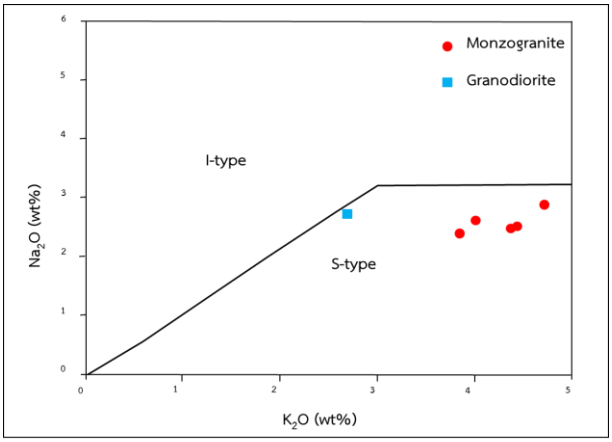

Figure 11. The studied granitic rocks plotted in Na_2O versus K_2O diagram with fields of I-type and S-type granite (after Chappell and White, 1992).

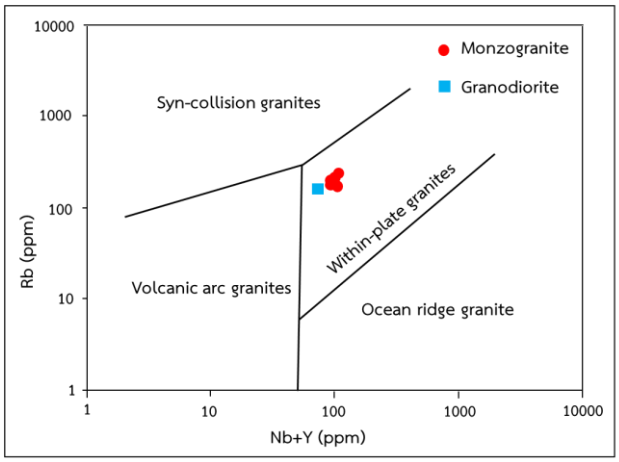

Figure 12. The studied granitic rocks plotted in Rb versus Nb+Y diagram with fields of different tectonic settings (after Pearce *et al.*, 1984).

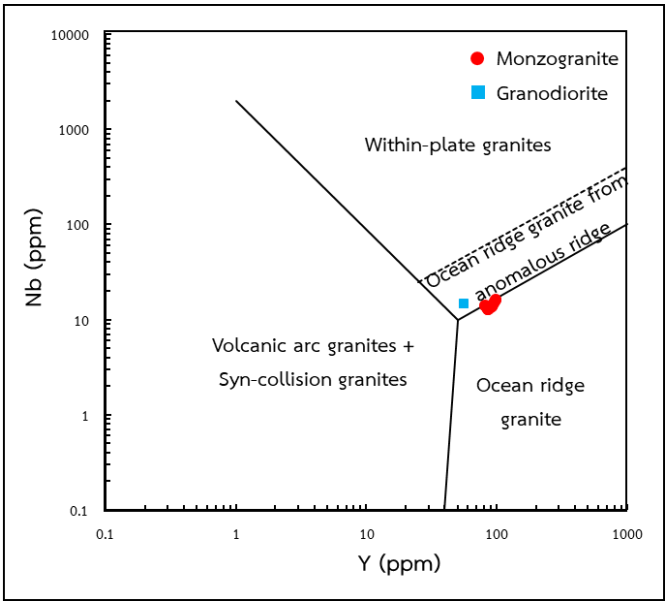

Figure 13. The studied granitic rocks plotted in Nb versus Y diagram with fields of different tectonic settings (after Pearce *et al.,* 1984).

Conclusion: The Late Carboniferous - Early Permian least-altered granitic rocks collected along highway 1D, from Xiengkhouang to Xaisomboun, Laos PDR. They are largely monzogranite, with minor granodiorite, based on modal analyses, quasi-chemical constituents and chemical compositions. The rocks have a coarse-grained, equigranular texture, and consist largely of quartz, plagioclase and potassium feldspar, with minor biotite and muscovite. Their whole-rock chemistry, i.e. the occurrence of normative corundum and the proportions of Na_2O/K_2O, is comparable with that of S-type granitic rocks. The studied granitic rocks are most likely to have a high-K calc-alkaline affinity, but according to tectonic discrimination diagrams, they might have formed in non-orogenic environments.

References:

1. Barker F. Developments in Petrology. 1979;6:1-12.
2. Burrett C, Zaw K, Meffre S, Lai CK, Khositanont S, Chaodumrong P, Udchachon M, Ekins S, Halpin JA. Gondwana Res. 2014;26(1):31–51.
3. Chappell BW, White AJR. Trans R Soc Edinburgh Earth Sci. 1992;83(1-2):1-26.
4. Frost BR, Barnes CG, Collins WJ, Arculus RJ, Ellis DJ, Frost CD. J Petrol. 2001;42(11):2033-2048.
5. Frost BR, Frost CD. J Petrol. 2008;49(11):1955-1969.
6. Irvine TN, Barager WRA. Can J Earth Sci. 1971;8(5):523-548.
7. Kamvong T, Zaw K, Meffre S, Maas R, Stein H, Lai C. Gondwana Res. 2014;26(1):165-184.
8. Lai CK, Meffre S, Crawford AJ, Zaw K, Halpin J, Xue CD, Salam A. Gondwana Res. 2014a;26:75–88.
9. Large R, Gemmell B, Paulick H. Econ Geol. 2001;96(5):957-971.
10. Liu J, Tran M, Tang Y, Nguyen QL, Tran TH, Wu W, Chen J, Zhang Z, Zhao Z. Gondwana Res. 2012;22(2):628-644.
11. Liu Y, Wang X, Wang D, He D, Song K, Gao C, Hu Z, Gong H. Chem Geol. 2012;328:89-108.
12. Manaka T, Zaw K, Meffre S, Vasconcelos P, Golding S, Cairns C. Gondwana Res. 2014;26(1):185–197.
13. Metcalfe I. Gondwana Res. 2011;19(1):3-21.

14. Metcalfe I. J Asian Earth Sci. 2013;66:1-33
15. Nakano N, Osanai Y, Owada M, Tran NN, Tsunogae T, Toyoshima T, Pham B. J Miner Petrol Sci. 2004;99(4):242-256.
16. Osanai Y, Nakano N, Owada M, Tran NN, Toyoshima T, Tsunogae T, Pham B. J Miner Petrol Sci. 2004;99(4):225-241.
17. Pearce JA, Harris NBW, Tindle AG. J Petrol. 1984;25:956-983.
18. Peccerillo R, Taylor SR. Contrib Mineral Petrol. 1976;58(1):63-81.
19. Sanematsu K, Marakami H, Duangsrigna S, Vilayhack S, Duncan R, Watanabe Y. J Miner Petrol Sci. 2011;106:13-25.
20. Streckeisen A. Neu Jb Mineral, Abh. 1967;107:144-240.
21. Tran HT, Zaw K, Halpin J, Manaka T, Meffre S, Lai CK, Lee YJ, Lee VH, Dinh S. Gondwana Res. 2014;26(1):144-164.
22. Wilson M. Igneous Petrogenesis - A global tectonic approach. 1st ed. 1989;466p.
23. Zaw K, Meffre S, Lai CK, Burrett C, Santosh M, Graham I, Manaka T, Salam A, Kamvong T, Cromie T. Gondwana Res. 2014;26(1):5-30.

Acknowledgements: This study supported by the Faculty of Science, Chiang Mai University and the 50th Anniversary Geology Fund, Chiang Mai University.

E_021_OF: DEVELOPMENT OF LITHIUM METAL OXIDE AS A CATHODE MATERIAL FOR LITHIUM ION BATTERIES

Piyaphat Sunthi[1,2], Sukum Eitssayeam[2,*], Uraiwan Intatha[3], Tawee Tunkasiri[2]
[1]Graduate Master's Degree Program in Faculty of Science, Chiang Mai University
[2]Electro-Ceramics Laboratory, Department of Physics and Materials Science, Faculty of Science, Chiang Mai University, Chiang Mai 50200, Thailand
[3]Materials for Energy and Environment Research Group, School of Science, Mae Fah Luang University, Chiang Rai 57100, Thailand
*e-mail: sukum99@yahoo.com

Abstract: The study on synthesis of lithium metal oxide for positive electrodes for lithium ion batteries was important to the development of the country in the automotive industry and energy storage equipment. This research was a study of the development of lithium metal oxide compound for cathode material. The metal of interest compound is Ni-Mn-Co (NMC) as high performance such as good cycle stability, higher energy and power density, better cycle life and safety for using. [1] The NMC compound was synthesized by co-precipitation method and then the NMC powder was doped and coated with $Ba_3(PO_4)_2$: BP by 1, 3, 5 and 10 wt.%. In doping method, the NMC powder was mixed with BP in solution using DI water as a solvent and then dried the mixture. The obtained powder was then mixed with LiOH and then the mixture was calcined at 550 °C for 5 hrs. While for the coating technique, the mixture of NMC and LiOH was calcined first and then coated with BP in solution of DI water. The obtained powders from 2 routes were characterized in terms of phase formation and microstructure via X-ray diffractometer (XRD) and scanning electron microscope (SEM), respectively. XRD patterns and microstructure of BP doped and coated (1, 3, 5, 10 wt.%) on LiNMC523 have not affected the structure. The average particle size was different due to doping and coating does affect the size of the particle.

Introduction: Lithium-ion batteries are the first-choice source of portable electrochemical energy storage due to it has advantages to using. Firstly, high energy density self-discharge low maintenance. Finally, variety of types available. One of the most successful Li-ion systems is a cathode combination of nickel-manganese (NMC). Nickel is known for its high specific energy but poor stability, manganese has the benefit of forming a spinel structure to achieve low internal resistance but offers a low specific energy. Combining the metals enhances other strengths, cobalt is the main active material that give good battery characters. Another successful combination is NMC_{523}. Other combinations using various amounts of cathode materials are also possible. [2-3]

The single crystal $Li[Ni_{0.50}Mn_{0.20}Co_{0.30}]O_2$: $LiNMC_{523}$ in cathode materials have excellent long term charge-discharge cycle lifetime and good electrochemical performance was successfully synthesized by co-precipitation method. The key synthesis steps including the impact of the Li to transition metal ratio, sintering temperature, precursor size and sintering time were discussed in [4]. In addition, the NMC_{523} compound is largely unknown for doping and coating some metal on NMC, phase and structure. Therefore, we studied the effects of BP doping and coating on phase formation and microstructure of $LiNMC_{523}$ for using as cathode in lithium ion batteries. However, the phosphorus compound has high of physical properties under high pressure therefore, it is interesting to dope and coat on LiNMC523 compound for development of lithium metal oxide. [5]

Methodology: The starting powder of $Ni_{0.50}Mn_{0.20}Co_{0.30}\cdot(OH)_2$: NMC_{523} were synthesized by co-precipitation method. Stoichiometric amounts of $N_2NiO_6\cdot6H_2O$ (Alfa Aeser, 98%), Manganese(II)nitrate tetrahydrate; $MnN_2O_6\cdot4H_2O$ (Alfa Aeser, 98%) and Cocall(II)nitrate

hexahydrate; $Co(NO_3)_2 \cdot 6H_2O$ (Alfa Aeser,98%) were dissolved in distilled water (molar ratio of Ni:Mn:Co = 5:2:3). NaOH and NH_4OH were added into the starting solution until a pH value between 11-12 and then the solution was filtered and dried at 120 °C for 12 hrs.

The solution of $Ba_3(PO_4)_2$: BP was prepared from stoichiometric amounts of $Ba(CH_3COO)_2$ (QReC, 99%) and $NH_4H_2PO_4$ (Fluka, 99%) with distilled water for 1 hrs.

The NMC_{523} powder was doped and coated with BP by 1, 3, 5 and 10 wt.% in different ways. In doping method, the NMC powder was mixed with BP in solution using distilled water as a solvent and then filtered and dried the mixture at 120 °C for 12 hrs. The obtained powder was then mixed with $LiOH \cdot H_2O$ (DAEJUNG, 95%). Then the mixture was calcined at 550 °C for 5 hrs (molar ratio of Li:(Ni:Mn:Co) = 1:1). While for the coating technique, the mixture of NMC_{523} and $LiOH \cdot H_2O$ was calcined first at 550 °C for 5 hrs (molar ratio of Li:(Ni:Mn:Co) = 1:1) and then coated with BP in solution of distilled water. Filtered and dried the coated powder at 120 °C for 12 hrs. The diagram process was shown in Figure 1.

The obtained powders from 2 routes were characterized in terms of phase formation and microstructure via X-ray Diffractometer, FE-Scanning Electron Microscope (JEOL JSM-6335 F) and Particle sizer analyzer (Zetasizer Nano Series, Malvern Instruments, DLS), respectively.

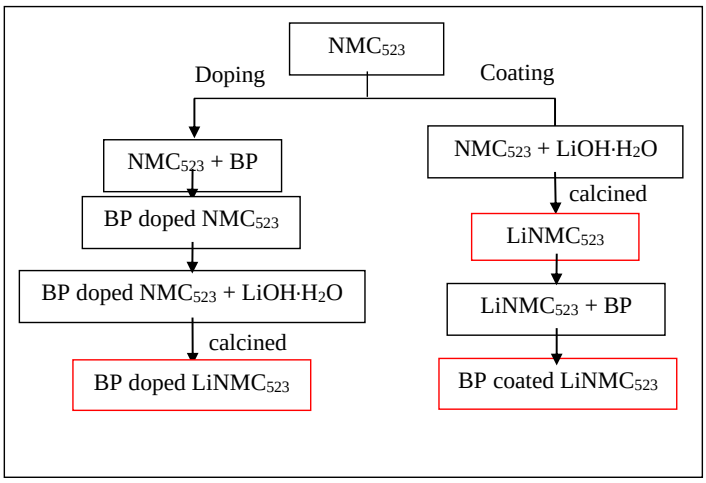

Figure 1. The diagram processes

Results and Discussion:

X-ray Diffractometer (XRD): Figure 2 shows the XRD patterns of these $LiNMC_{523}$ samples. The phase formation of BP doped $LiNMC_{523}$ are shown in Figure 2a, the patterns demonstrate that the materials have good crystallinity with strong diffraction peaks while the condition of BP dose does not affect the BP doped on structure due to the pattern phase are similar pattern in different way of 1,3,5 and 10 wt.%. The average particle size was calculated to be about 100 nm using the debye-Scherer formula. Figure 2b shows that the phase formation of BP coated $LiNMC_{523}$ and uncoat shows no different. The condition of BP also does not affect on coated structure of the powder. The average particle size was calculated to be about 200 nm.

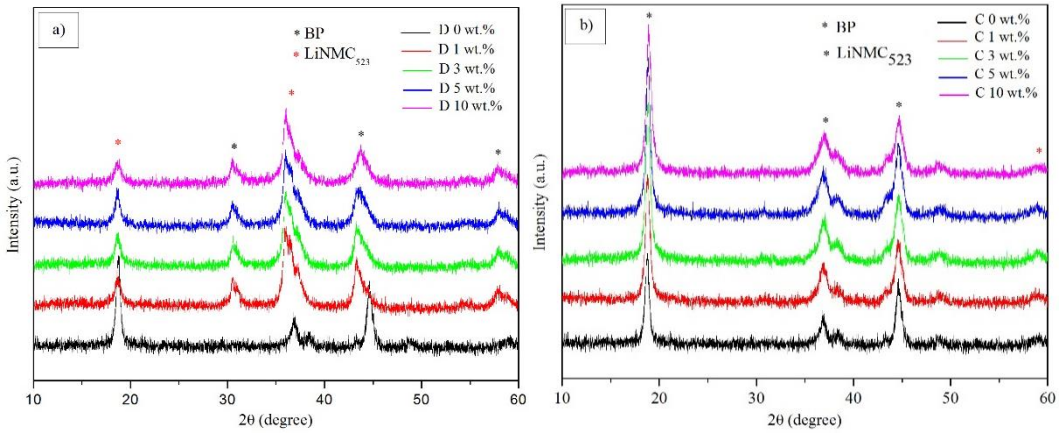

Figure 2. XRD patterns of BP doped (a) and coated (b) on $LiNMC_{523}$

FE-Scanning Electron Microscope (FE-SEM): Figure 3. shows the scanning electron microscopy (SEM) image of $LiNMC_{523}$ sample. The primary particles with a particle size of ~ 400 nm aggregated and formed rather spherical particles about 7 µm in an average diameter.

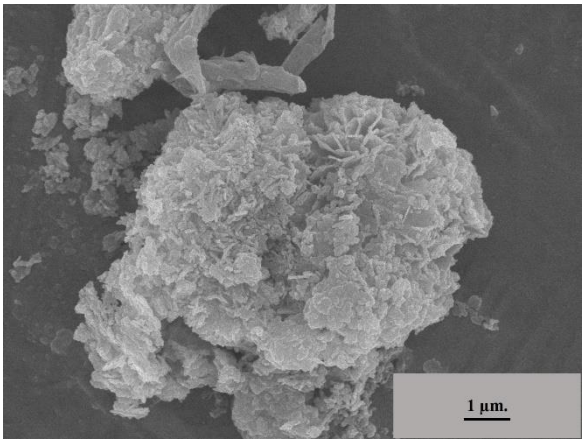

Figure 3. SEM image of $LiNMC_{523}$

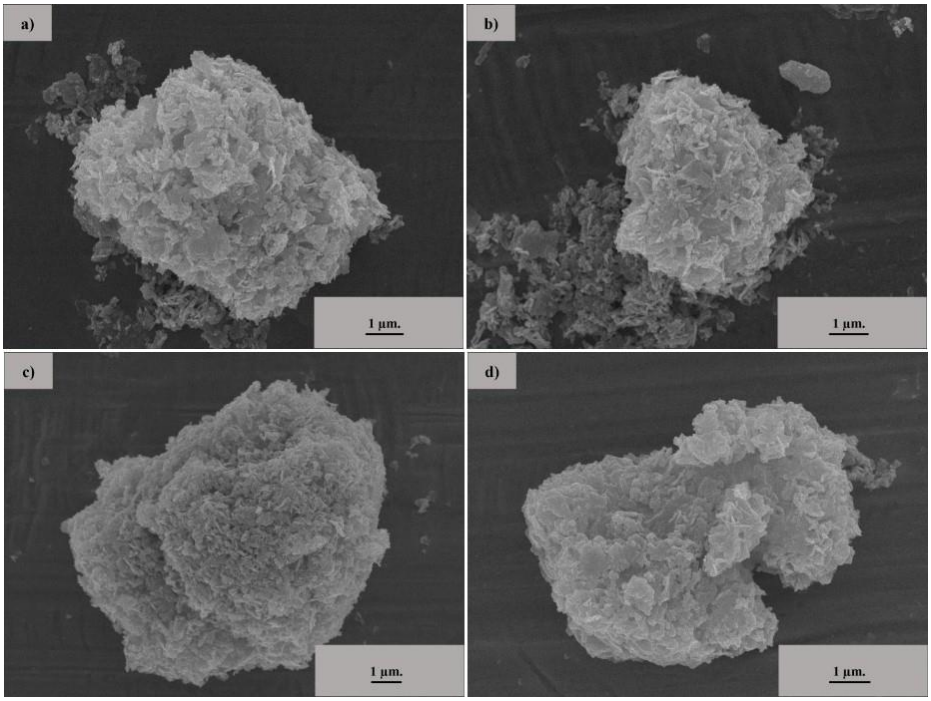

Figure 4. SEM images of BP doped (a) 1 wt.%, (b) 3 wt.%, (c) 5 wt.% and (d) 10 wt.% on $LiNMC_{523}$

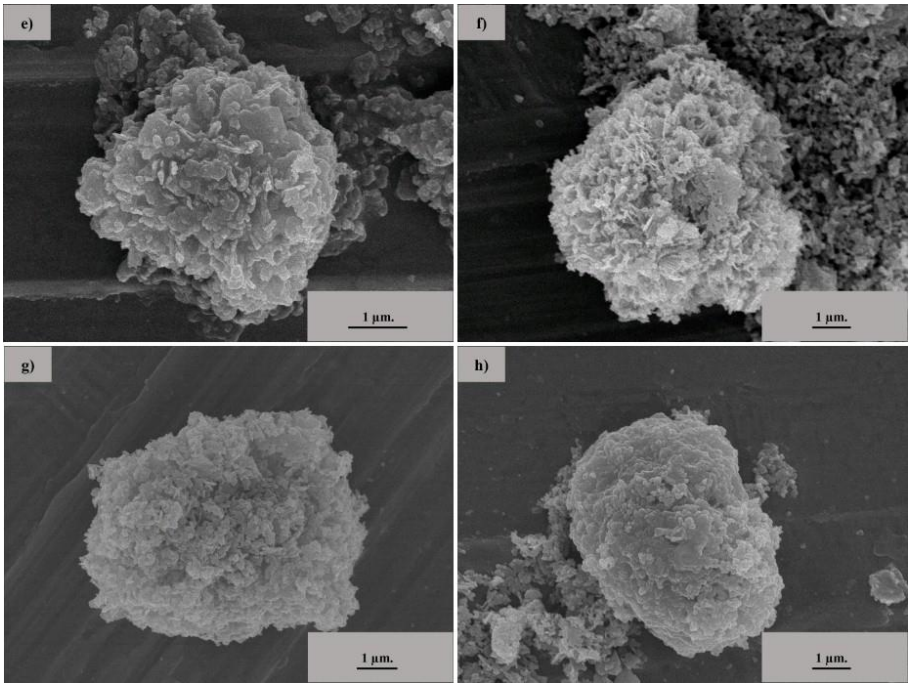

Figure 5. SEM images of BP coated (e) 1 wt.%, (f) 3 wt.%, (g) 5 wt.% and (h) 10 wt.% on $LiNMC_{523}$

Figure 4 (a-d). shows the SEM images of $LiNMC_{523}$ doped with BP (1,3,5 and 10 wt.%) samples. The particles shape are similar between these materials and other doping samples

with different concentration of BP. The primary particle with a particle size of ~ 100-200 nm was aggregated and formed irregular secondary particle about 5-6 µm in an average diameter.

Figure 5. shows the SEM images of $LiNMC_{523}$ coated with BP (1,3,5 and 10 wt.%) samples. The particles shape are similar between these materials and the samples coating with different concentration of BP same to the particles that BP-doped. The primary particle with a particle size of ~ 200 nm was aggregated and formed irregular secondary particle about 6-7 µm in an average diameter.

Particle size analyzer (DLS nano sizer):

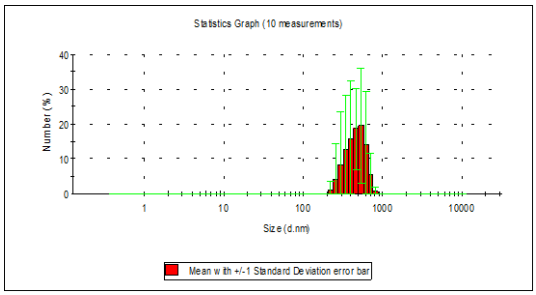

Figure 6. DLS nano sizer of $LiNMC_{523}$

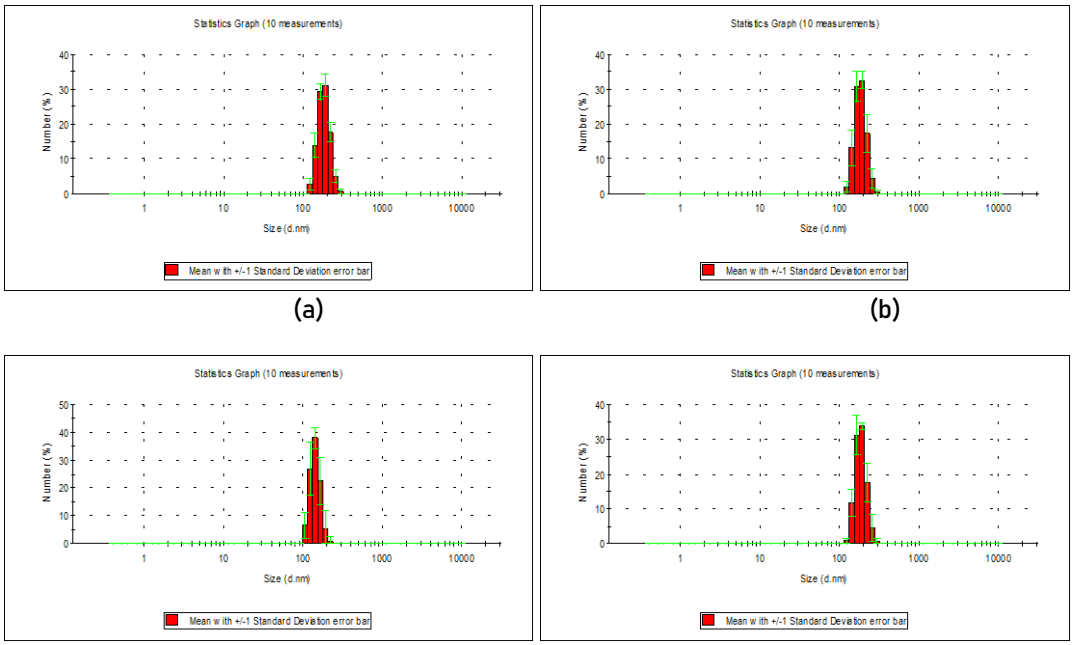

Figure 7. DLS nano sizer of BP doped (a) 1 wt.%, (b) 3 wt.%, (c) 5 wt.% and (d) 10 wt.% on $LiNMC_{523}$

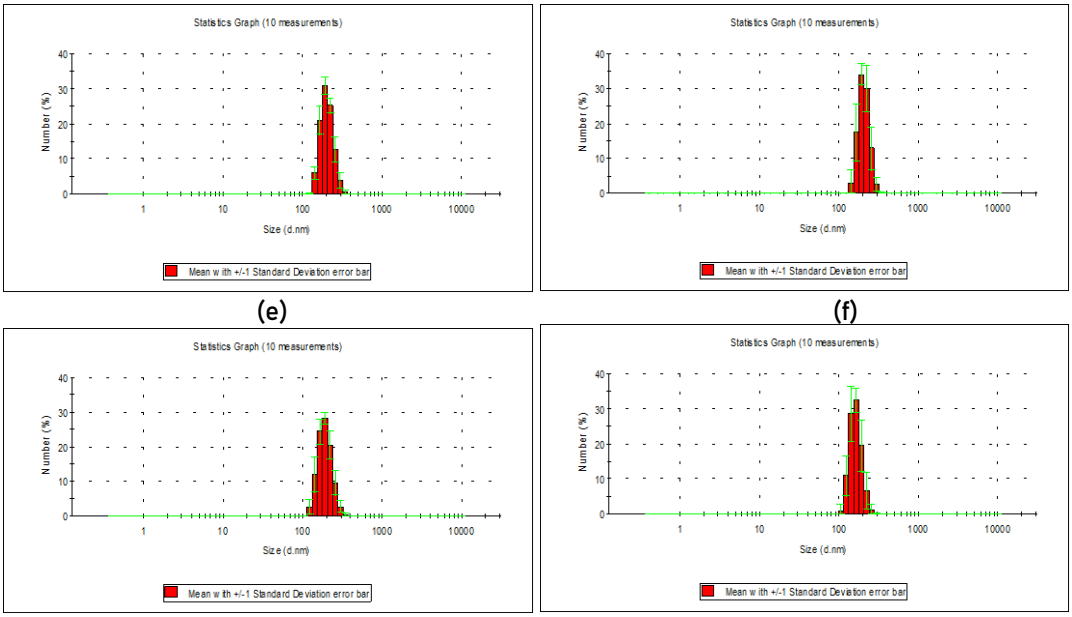

Figure 8. DLS nano sizer of BP coated (e) 1 wt.%, (f) 3 wt.%, (g) 5 wt.% and (h) 10 wt.% on $LiNMC_{523}$

Figure 6-8. shows the DLS nano sizes of $LiNMC_{523}$, BP doped and coated (1, 3, 5, 10 wt.%) on $LiNMC_{523}$, respectively. The average of particle size of $LiNMC_{523}$ is between 400-500 nm while the average of particle size of BP doped and coated (1, 3, 5, 10 wt.%) on $LiNMC_{523}$ are about 140 – 190 nm and about 150 – 210 nm, respectively shown in Table 1.

Table 1. The average of particle size of $LiNMC_{523}$, BP doped and coated (1, 3, 5, 10 wt.%) on $LiNMC_{523}$

Samples	The average of particle size (nm)
LiNMC523	426.5
BP doped on LiNMC523	
1 wt.%	183.3
3 wt.%	182.9
5 wt.%	142.7
10 wt.%	184.6
BP coated on LiNMC523	
1 wt.%	202.5
3 wt.%	204.4
5 wt.%	191.9
10 wt.%	162.5

Doping and Coating are improving the electrochemical performance and microstructure of LiNMC523 [6]. Doping section affects structure and particle size due to the stability structure on lithium extraction [7-9]. The coating has an impact on the surface structure layer and improves better stability particles [10-11]. Therefore, the particle size of LiNMC523 is the biggest while LiNMC523 coated by BP and doped-LiNMC523 smaller respectively.

Conclusion: In summary, the development of lithium metal oxide for cathode materials was studied with effect of doping and coating on $LiNMC_{523}$ samples were successfully synthesized by co-precipitation method. XRD patterns confirmed the doping and coating present the different structure while the condition of BP concentration. In addition, the microstructure of BP doped and coated on LiNMC523 were not different and showed the crystals of primary and secondary particles. The average of particle size of BP doped and coated (1, 3, 5, 10 wt.%) on $LiNMC_{523}$ are different.

References:

1. Naoki Nitta, Feixiang Wu, Jung Tae Lee, Gleb Yushin. Materials today. 2015; 18: 252-264.
2. Ruhul Amin, Yet-Ming Chiang. J.Electrochemical Soc. 2016; 163(8): A1512-A1517.
3. Eric Jianfeng, Chenga, Kicheol, Hong, Nathan John Taylor, Heeman Choe, Jeff Wolfenstinec, Jeff Sakamotoa. J. European Ceramic Society. 2017; 37(9): 3213-3217.
4. Jing Li, Hongyang Li, Will Stone, Rochelle Weber, Sunny Hy, J. R. Dahn. J. Electrochemical Society. 2017; 164(14): A3529-A3537.
5. Hyun-Soo Kim, Woo-Seong Kim, Hal-Bon Gu, Guoxiu Wang, J. New Materials for Electrochemical Systems. 2009; 12(4): 207-212.
6. Yin Ding, Rui Wang, Lei Wang, Kailin Cheng, Zhikun Zhao, DaoBin Mu, Boron Wu. Energy Procedia 105. 2017: 2941-2952.
7. M. Iftekhar, N. E. Drewett, A. R. Armstrong, D. Hesp, F. Braga, S. Ahmed, L. J. Hardwick. J.Electrochemical Soc. (2014); 161 (14): A2109-A2116.
8. Berke Pişkin, Cansu Savaş Uygur, Mehmet Kadri Aydınol. J. Energy Res. (2018); 42: 3888–3898.
9. Matthias Eilers-Rethwisch, Martin Winter, Falko Mark Schappachera. J. Power Sources. (2018); 387: 101–107.
10. Wenchang Zhu, Xue Huang, Tingting Liu, Zhiqiang Xie, Ying Wang, Kai Tian, Liangming Bu, Haibo Wang, Lijun Gao, Jianqing Zhao. Coatings. (2019); 9 (92): 1-12.
11. Dina Becker, Markus Börner, Roman Nölle, Marcel Diehl, Sven Klein, Uta Rodehorst, Richard Schmuch, Martin Winter, Tobias Placke. ACS Appl. Mater. Interfaces. (2019); 11: 18404–18414.

Acknowledgements: This work was financially supported by the Faculty of Science, Chiang Mai University, Chiang Mai, Thailand. This study was also supported by the electro-ceramic laboratory, department of Physics and Materials Science.

E_022_OF: CHARACTERISTICS OF BIOCHAR FROM TEA RESIDUAL FOR SOIL AMENDMENT

Patsara Danwittayakul[1,*], Thitipone Suwunwong[2,3], Khamphe Phoungthong[4,5], Kua-anan Techato[5]
[1]Faculty of Environmental Management, Prince of Songkla University, Songkla 90112, Thailand
[2]Center of Chemical Innovation for Sustainability (CIS), Mae Fah Luang University, Tasud, Muang, Chiang Rai 57100, Thailand
[3]School of Science, Mae Fah Luang University, Tasud, Muang, Chiang Rai 57100, Thailand
[4]Environmental Assesment and Technology for Hazardous Waste Management Research Center, Faculty of Environmental Management, Prince of Songkla University, Songkla 90112, Thailand
[5]Energy and environmental management Research Center, Faculty of Environmental Management, Prince of Songkla University, Songkla 90112, Thailand
*e-mail: patsara26@hotmail.com

Abstract: Biochar was produced from tea residual. For this work, the Elemental analysis, Fourier transform infrared analysis were employed to characterize the physicochemical character of the biochar. Biochar was prepared by pyrolysis process at 500 °C at 5 °C minute and hold for 1 hour at this temperature. From FT-IR spectra and elemental analysis information, the results showed that the composition of biochar derived from tea residual is mainly in organic carbon (OC). Hence, biochar preparation by this pyrolysis process in a close system, limit oxygen, is the way to control the organic carbon to use in soil amendment.

Introduction: Biochar is the process of producing charcoal or carbon black, which the biochar production must go through the process of decomposition with heat in conditions with low oxygen. The biochar or bio-charcoal is also useful in many areas, such as helping to store carbon in the soil, absorb toxins and contaminants in the environment, improve soil quality both physically and chemically, and alleviate global warming [4-6]. Moreover, the characteristics of the biochar will have mainly carbon and porous properties making it able to absorb well the plant nutrients to use in soil amendment and fertilizer, but the structure of biochar will vary according to each type of biomass material [1-3]. In this work, we used tea residual to produce biochar and studied the physicochemical property to assess the character of the obtained biochar as a soil amendment product.

Methodology: In this work, We used biochar from tea residual which received from northern Thailand. The first step is to wash the tea leaves with water twice. Then the biomass was ground and dried to feed to pyrolysis process at 500 °C at 5 °C/min in the furnace, limiting of oxygen. We held the pyrolysis process for 1 hour and studied the characteristics of biochar by CHNO Elemental analysis and FT-IR Spectroscopy.

Results and Discussion: Biochar derived from tea residual is shown in Figure 1. From this pyrolysis process, We obtained the soft powder of biochar in the black solid. The results of the CHNOS content showed that tea residual biochar has a carbon value of 64.137 which is an organic carbon. The FTIR spectrum shows that biochar from tea residual is composed mainly of organic carbon form in which the functional groups of C-O (1380-1470 cm^{-1}), aromatic groups, C=O, C=C (1500-1650 cm^{-1}), C-H (~3000 cm^{-1}) and hydroxyl group (~3440 cm^{-1}) were observed as shown in Figure 2.

Figure 1. Biochar from tea residual.

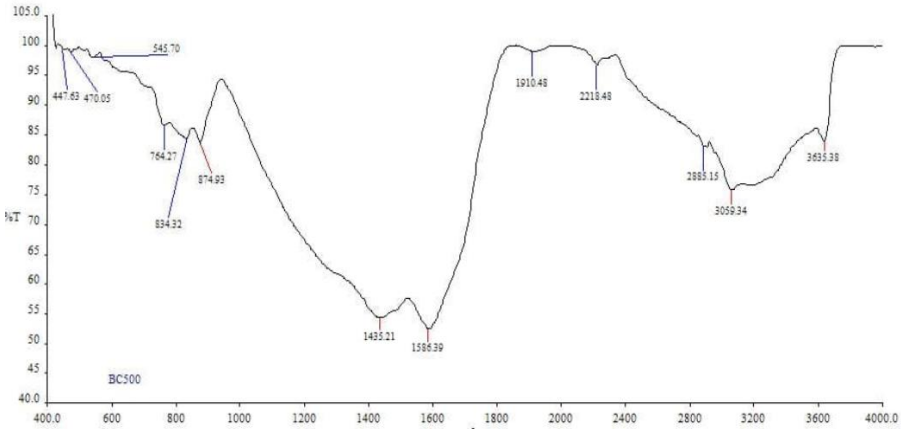

Figure 2. FT-IR Spectrum of biochar from tea residual.

Conclusion: In order to reduce the amount of biomass, the biochar from tea residual can be produced easily and environmentally friendly by the pyrolysis process in a closed system. The characteristics have content and the chemically functional groups which confirm the obtained biochar is composed mainly of organic carbon (OC). Hence, biochar derived from tea residue which grew in northern Thailand can use in soil amendment.

References:

1. Orasa Suksawang. 2010., 25-26.
2. Winsley, P. 2007., 64,1 : 5-10.
3. Lehmann, J., J. P. da Silva Jr., C. Steiner, T. Nehls, W. Zech, and B. Glaser. (2003). *249,* 343-357.
4. Steiner C., W. G. Teixeira, J. Lehmann, T. Nehls, J. L. V. d. Macedo. W. E. H. Bium, and W. Zech. (2007). *291*, 275-290.
5. Zeng, L., Li, X., Liu, J., (2004). *38*, 1318-1326.
6. Loyo, R.L.D.A., Nikitenko, S.I., Scheinost, A.C., Simonnoff, M., (2008). *42*, 2451-2456.

Acknowledgements: The authors acknowledge the facilities support of Mae Fah Luang University and facilities support of Prince of Songkla University.

E_024_OF: PALEOSEISMIC EVIDENCES OF THE DOI WIANG LA FAULT SEGMENT, MAE HONG SON FAULT, NORTHERN OF THAILAND

Chanista Chansom[1,*], Sukonmeth Jitmahantakul[1], Punya Charusiri[2]
[1]Basin Analysis and Structural Evolution Special Task Force for Activating Research (BASE STAR), Department of Geology, Faculty of Science, Chulalongkorn University, Bangkok 10330, Thailand
[2]Morphology of Earth Surface and Advanced Geohazards in Southeast Asia Research Unit (MESA RU), Department of Geology, Faculty of Science, Chulalongkorn University, Bangkok 10330, Thailand
*e-mail: Chanista.gg@gmail.com

Abstract: Paleoseismological investigation has been carried out to determine the fault evidence of the Mae Hong Son Fault (MHSF) in the Mae Hong Son province, northern Thailand. This is because the existence of an earthquake near the south of Mae Hong Son area on February 1975 with a magnitude of 5.6 at Ban Tha Song Young, Mae Hong Son Province with small earthquakes (Mw 1-3) around Mae Hong Son area till present. Thus, this research aims to explain characteristics of MHSF and to evaluate paleoearthquake magnitudes, recurrence intervals, and slip rate. Major techniques include remote-sensing, field investigation, and paleoseismic excavation together with optical stimulated luminescence (OSL) dating. Several morphotectonic features, particularly offset streams, linear valleys, shuttle ridges and scarplets have been recognized along the fault within the two basins, Mae Hong Son and Mae Sariang basin, in the Mae Hong Son province. The major strike-slip faults have been recognized with an approximate trend in N-S direction, displaying not only dextral but also normal movement faults. The dextral movement along the MHSF with a total length of 150 km, consisting of 45 fault segments ranging from 3.03 km up to 28.55 km. The results from OSL dating of one and earlier excavated paleoseismic trenches along the MHSF indicate at least 2 paleoearthquake events, ca. 34,000 years ago with the latest movement taking in ca. 34,000 to 31,000 years ago. Results also estimated that the maximum credible earthquake magnitudes of Mw 5.64 - 6.77. Therefore, the MHSF is still active till present with the dextral sense of movement and controls the development of the Mae Hong Son and Mae Sariang basin.

Introduction: Paleoseismic investigation is using geological and geomorphological data for identification of past earthquakes in terms of location, size and timing[1]. This study can reveal a seismic history even going back several thousand years, mostly from the Late Pleistocene to the present day[2]. The active faults in Thailand consists of 15 fault zones and the MHSF has been classified as one of the active faults[3]. The MHSF is a 150 km long right-lateral strike-slip fault that extends in north-south direction from Muang Mae Hong Son, Khun Yuam, Mae La Noi and Mae Sariang Districts of Mae Hong Son Province to the northern part of Tha Song Yang District, Tak Province. The MHSF consists of several fault segments with mostly trending in north-south direction. Evidences of surface deformation includes consistent right-lateral offsets of stream drainages crossing the fault, offset ridge crests, triangular facets, fault scarps and linear valleys. Narrow push up ridges or restraining bends occur where faults change the orientation to northwest, while linear valleys or pull-apart basins form associated with northeast-trending faults[4]. In addition, an analysis of the seismic hazard by probabilistic seismic hazard analysis (PSHA)[5] found that 22% of the Mae Hong Son region has the potential to generate earthquakes annual magnitude of 7.0 within 50 years. However, Wiwegwin et al. (2014)[6] have been investigated paleoearthquake in the MHSF (i.e. Mok Cham Pae, Phra That Chom Kitti and Mae La Noi no.1 fault segments), the earthquake was at least eight paleoearthquake events were occurred within the Mae Hong Son area in the last 78,000 years with the recurrence interval of 10,000 years. Thus, to better understand and clarify the nature

of seismicity in the Mae Hong Son region, there are essential to use new data and more detailed surveys for investigation paleoearthquake of the region. This research aims to describe the characteristics of the MHSF in term of paleoseismic trenching or road-cut along the fault segment.

Methodology: This research reviewed the earlier studied the morphotectonic landforms and investigated the Quaternary fault at the road cut wall which the wall perpendicular with the fault. The four soil samples were collected from the wall for Optical Stimulated Luminescence (OSL) dating by using the Riso TLD dosimeter. The single-aliquot regenerative (SAR) dose protocol technique was applied to measure the equivalent dose (De) for each sample[7](Figure 3). However, all the data and results from this research and previous work are used to determine the number of paleoearthquake events.

Results and discussion:
Morphotectonic landforms: From Chansom et al, 2017 based on satellite image interpretation founded that the MHSF consists of several fault segments with mostly trending in north-south direction. Evidences of surface deformation includes consistent dextral offsets of stream drainages crossing the fault, offset ridge crests, triangular facets, fault scarps and linear valleys. Narrow push up ridges or restraining bends occur where faults change the orientation to northwest, while linear valleys or pull-apart basins form associated with northeast-trending faults as show in Figure 2. The several lines of morphotectonic evidence shows the fault segments belonging to the MHSF, the wide range of from 3.03 km (Phra That Chom Kiti segment) up to 28.55 km (Mae La Noi segment). As a result, the determined fault segments of the MHSF zone can generate the credible earthquakes with the maximum around 5.64 to 6.77.
stratigraphic and structural evidence: The Doi Wiang La site is the road cut on the road to Khun Yuam District, located along the 18°53'32"N and 97°55'52"E have been observed the fault cutting Cenozoic deposit (Figure 1). The Quaternary stratigraphy and structural geology of the road-cut wall are shown 7 depositional units (A-G) as show in Figure 3, identification of units and structures was based on field data and sedimentological characteristics of the strata are described below;

Unit A, the oldest unit in the road cut, is an alluvial/colluvial unit consisting mainly of brown to yellowish sand with gravel. Grain sizes range from very coarse to fine sand. Most clasts are angular to subrounded, pebble sized, and comprised of sandstone and quartz. The minimum thickness of the unit ranges from 0.5 to 0.8 m.

Unit B is an alluvial unit comprised of light brown to yellowish sand. Grain sizes vary from coarse to fine sand; pebbles of quartz and sandstone are sparsely distributed in the unit. The thickness of the unit ranges from 0.2 cm to 0.4 m.

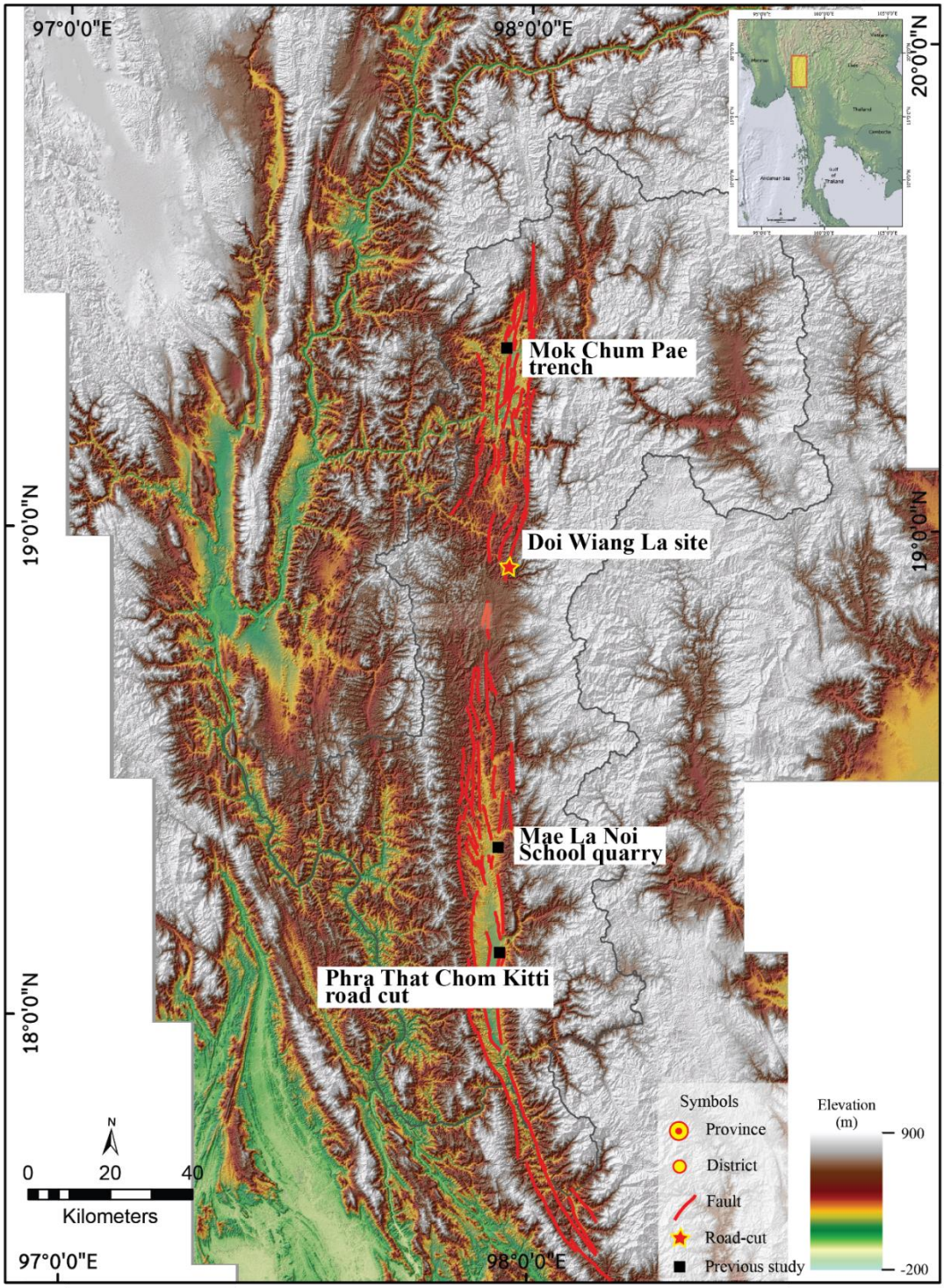

Figure 1. Map shows the location of road-cut exposure which were examined for a paleoearthquake study.

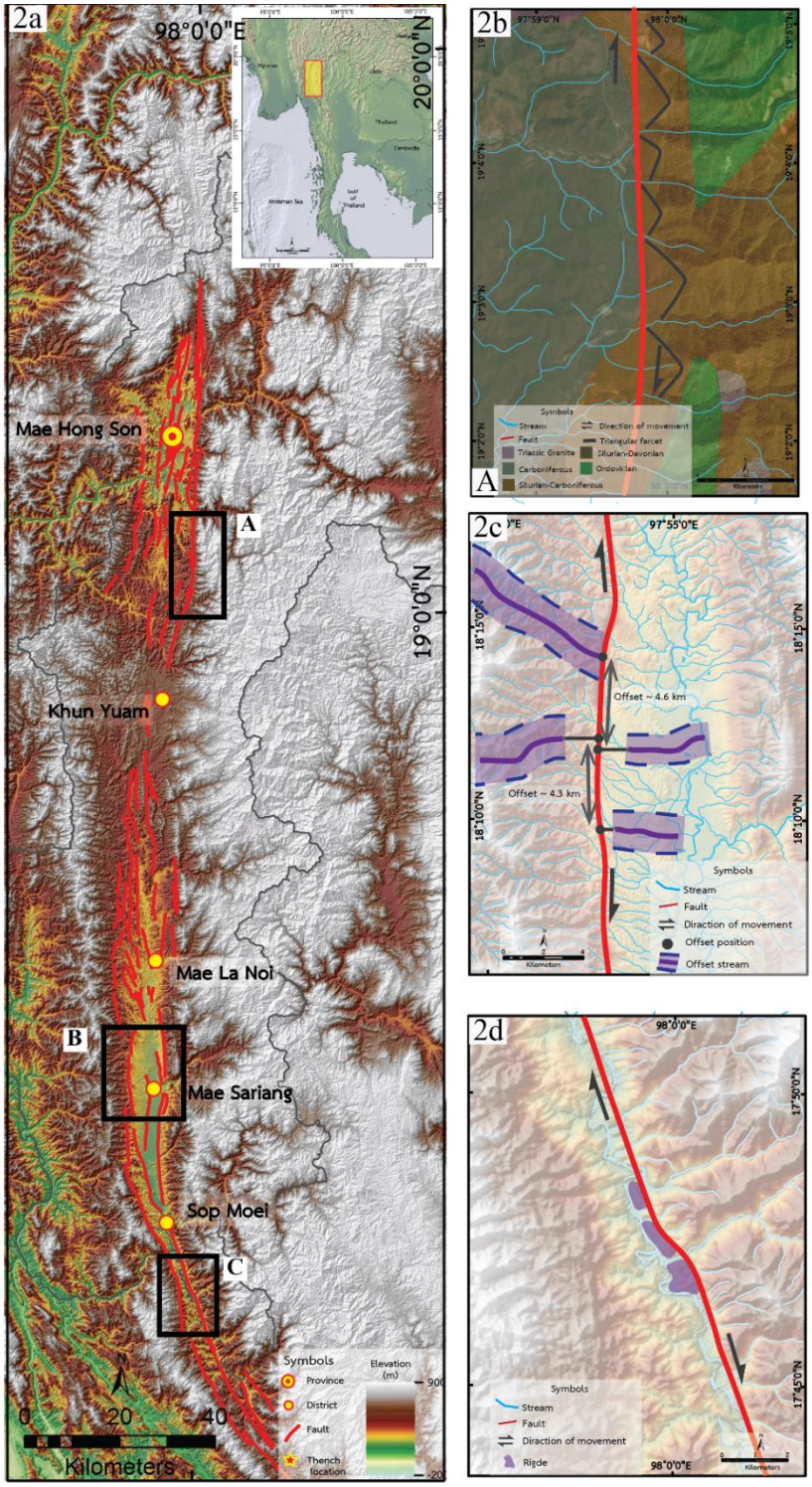

Figure 2. Enhanced SRTM DEM data illustrate the morphotectonic evidence in the MHSF (2a). The detail morphotectonic evidences shows triangular facets in Figures 2b, off set stream in Figure 2c and shuttle ridge in Figure 2d.

Unit C is an alluvial/colluvial unit containing brown to yellowish sand with gravel. Grain sizes range from very coarse to fine sand. Most clasts are subrounded and low sphericity, pebble sized, and comprised of sandstone and quartz. The thickness of the unit ranges from 0.2 to 1 m.

Unit D, with an average thickness of 1.3 m, is an alluvial unit comprised of light brown. Grain sizes vary from coarse to fine sand; pebbles of quartz and sandstone are sparsely distributed in the unit. This unit shows gradational deposit.

Unit E, with an average thickness of 0.3 m, is an alluvial unit comprised of gravel, sand, and clay. The gravel beds in unit F are clast-supported. The gravel clasts are mainly subrounded to rounded and consist mostly of quartz, sandstone, and shale.

Unit F, with an average thickness of 2.5 m, is an alluvial unit comprised of gravel, sand, and clay. The gravel beds in unit F are clast-supported. The gravel clasts are mainly subrounded to rounded and consist mostly of quartz, sandstone, and shale; their maximum diameter is 6 cm. Sand layers are prominent in the unit. The unit consists of intercalated graded beds with thicknesses of 30–50 cm.

Unit G, is the topmost layer with an average thickness of 0.3 m, is an alluvial unit containing light brown to yellowish sand with gravel. Most clasts are subrounded and moderate sphericity, pebble sized, and comprised of sandstone, quartz and shale.

The sediments of units B and E are mostly sand and gravel with minor clay and silt. They are considered to represent fluviolacustrine environments. The sediments of units A, B, F and G are poorly sorted and subangular, and are characterized by mixtures of sand, silt, clay, and gravel. The geometries of the sedimentary packages and structures indicate that these units were possibly deposited by matrix-rich debris flow. The clast-supported gravel of unit C, D and E. However, contains mostly subrounded clasts, the sediments are poorly to moderately sorted and graded beds have been encountered in unit D. The sediments of unit C, D and E were possibly deposited by clast-rich debris, as well as by occasional channel flood deposits similar to those reported by Larsen and Steel (1978)[8], Steel and Gloppen (1980)[9], and Rhodes et al. (2005)[10]. The mapped F1 fault strike N17°E and dip 87°S and F2 fault N63°W and dip 80°S.

Number and timing of depositional: The age estimates for the sediment deposits at the Doi Wiang La site are based on OSL analyses of quartz gains. A total of four samples from road cut wall were analyzed for OSL age determination in Figure 4 and the summary of OSL analyses shows in Table 1 using single-aliquot regenerative (SAR) technique. These analyze suggest that the composite stratigraphic record at the Doi Wiang La site extends from ca. 70,000 years to the present day. Based on stratigraphic position of four samples yielded age estimates that are representative of the alluvial and colluvial deposits containing them. The stratigraphic relationships exposed in the road cut wall at Doi Wiang La site provide evidence of multiple Pleistocene earthquakes at this site. The characteristics of units DWL1, DWL2, DWL3 and DWL4 in Doi Wiang La site strongly suggest alluvial deposition. Assuming that the OSL ages reflect the age of the alluvial deposits (as discussed above), the estimated ages of these deposits probably closely reflect the timing of individual ruptures. Thus, we interpret the occurrence of two large, surface-rupturing earthquakes within the past before ca. 34,000 years and the second or earlier earthquake ca. 34,000 to 31,000 years.

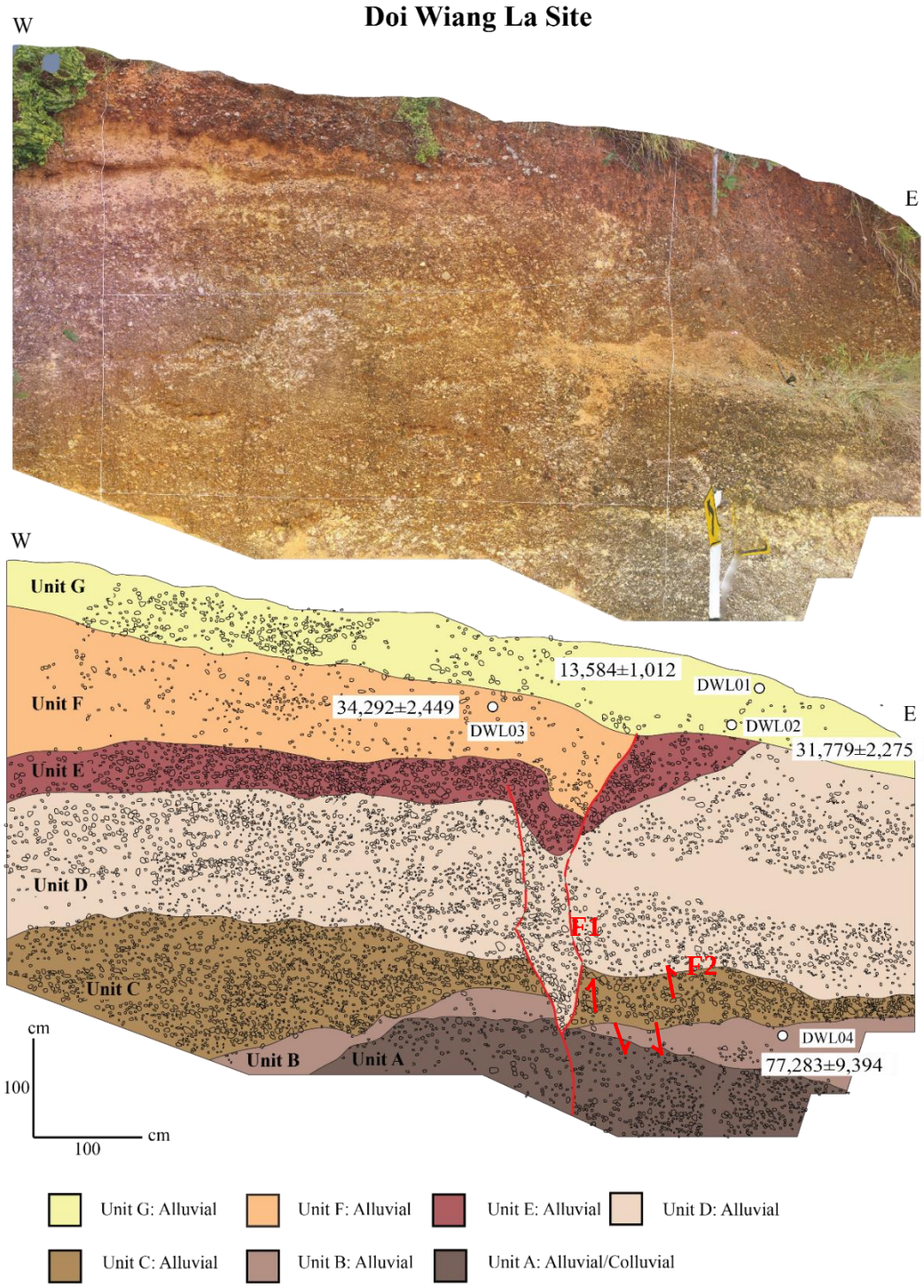

Figure 3. Sketch of road-cut wall of Doi Wiang La site and its interpretation. Red lines represent faults and black line show stratigraphic contracts. OSL dates are used to constrain the timing of paleoseismic event.

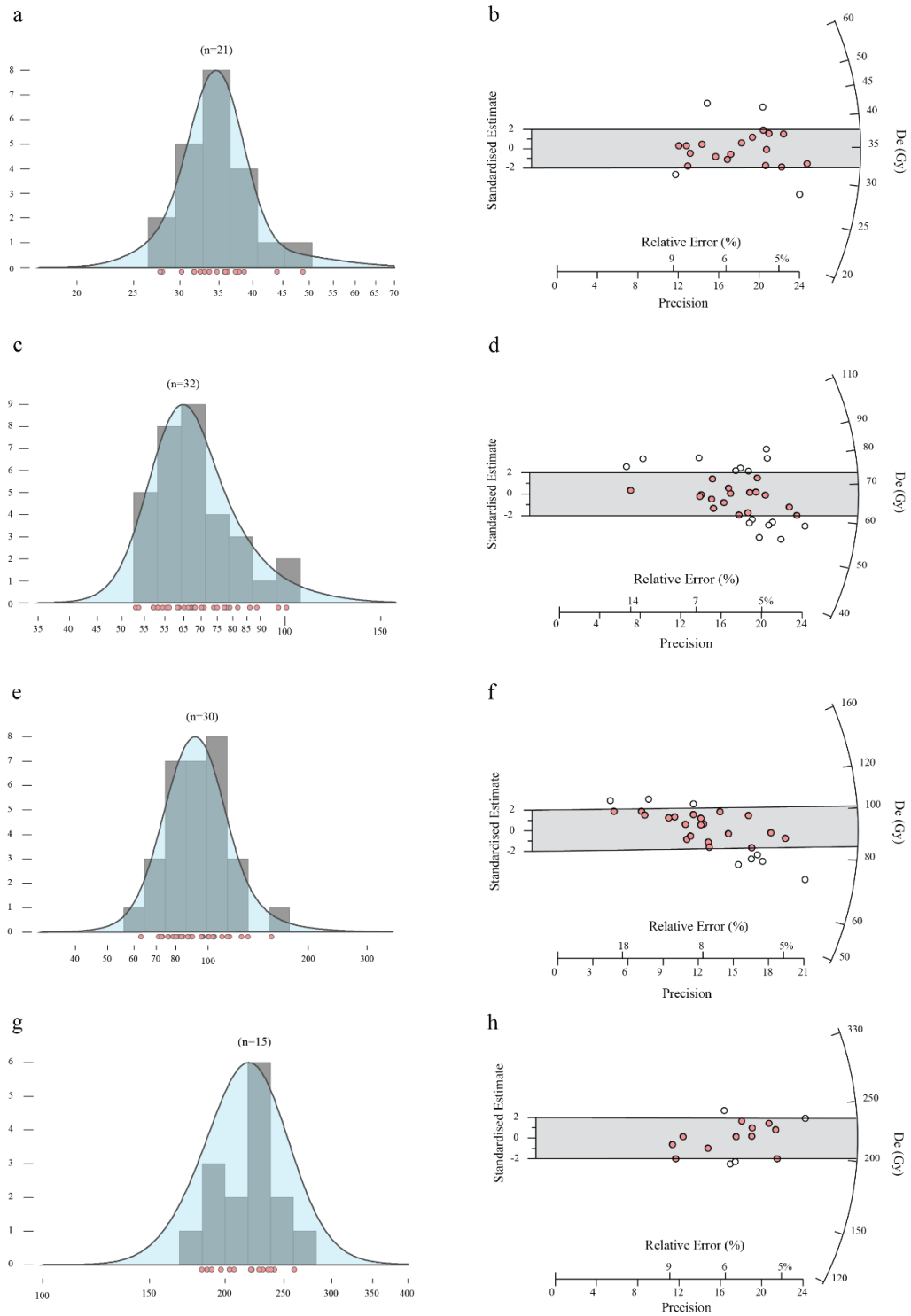

Figure 4. Radial plots and histograms of De distribution for the quartz samples of Doi Wiang La site (a and b: DWL1; c and d: DWL2; e and f: DWL3; g and h: DWL4).

Table 1. Summary of OSL analyses, Doi Wiang La site

Sample No.	U[a*] (ppm)	Th[a*] (ppm)	K[a*] (%)	W[b*] (%)	AD[c*] (Gy/ka)	De[d*] (Gy)	Age[e*] (yr)	Error[f*] (yr)
DWL1	0.99	23.61	1.67	45.49	2.57	34.85	13,584	1,012
DWL2	1.15	17.78	1.64	55.17	2.12	67.38	31,779	2,275
DWL3	1.07	18.79	1.30	52.43	1.97	67.38	34,292	2,449
DWL4	0.93	17.93	2.97	59.56	2.77	213.73	77,283	9,394

[a*]The concentrate of Uranium, Thorium and Potassium

[b*]The water content or moisture content

[c*]The annual dose to the sample is computed from water content and concentrations of K, U and Th described by Bell (1979)[11] using the DRAC[12] method

[d*] Mean equivalent dose determined from replicated single-aliquot regenerative-dose run

Conclusion: Paleoseismic investigation within Doi Wiang La provides data on the late Pleistocene rupture history of the Doi Wiang La segment of the MHSF. The road-cut outcrop across the east-west facing fault scarp at the Doi Wiang La site provide stratigraphic and structural evidence of the fault. These road-cut outcrop shows the presence of scarp-derived alluvial deposits that provide evidence of two possible surface ruptures. Correlation of deposits among the road-cut outcrop is based on lithologic characteristics, stratigraphic position, and a total of 4 OSL analyses of quartz gains. Based on stratigraphic ordering and a statistical comparison of OSL dates using the Radial Plotter program, the past surface ruptures at the Doi Wiang La site occurred within the ranges within the past before ca. 34,000 years and the second or earlier earthquake ca. 34,000 to 31,000 years. However, all the data and results from this research and previous work are used to determine the number of paleoearthquake events.

Reference

1. McCalpin J. P. and Nelson A. R. International Geophysics. 1996; 62: 1-32.
2. Akuz S. H., Zacbi C. and Karabacak V. Encyclopedia of Earthquake Engineering. 2014: 1-15.
3. Department of Mineral Resources. Technical Report: Active Faults Map in Thailand. 2018
4. Chansom, C., Jitmahantakul, S., and Charusiri, P. Journal of RESGAT. 2017; 19: 268-280.
5. Pailoplee, S and Charusiri, P. Earth, Planets and Space. 2016; 69:68
6. Wiwegwin, W., Hisada, K., Charusiri, P. Kosuwan, S., Pailoplee, S., Saithong, P., Khaowiset, K. and Won-in, K. Journal of Earthquake and Tsunami.2014; 8(2): 1450007-1–145007-35.
7. Rhodes E. J. Annu. Rev. Earth Planet. Sci. 2011. 39:461–88
8. Larsen, V. and Steel, R.J. Sedimentology. 1978; 25: 37–59.
9. Steel, R. and Gloppen, T.G. Spec. Publ. Int. Ass. Sediment. 1980; 4: 79–103.
10. Rhodes, B.P., Conejo, R., Benchawan, T., Titus, S. and Lawsan, R. Journal of the Geological Society of London. 2005; 162:51–63.
11. Bell, W. T. Archaeometry. 1979; 21: 243–245.
12. Durcan, J.A., King, G.E., and Duller, G.A.T. Quaternary Geochronology. 2015;28: 54-61.

Acknowledgements: This research was supported by the Science Achievement Scholarship of Thailand (SAST). Our appreciation also goes to Prof. Lewis A. Owen (Geochronology Laboratory at the University of Cincinnati) for completing OSL analyses. Anonymous reviewers are thanked for their useful and constructive comments.

E_027_OF: PHYSICOCHEMICAL CHARACTERIZATION OF SLOW PYROLYSIS BIOCHAR FROM *Robusta* SPENT COFFEE GROUNDS UTILIZED FOR SOIL AMENDMENT

Naeem Hussain[1,*], Khamphe Phoungthong[1,2], Suchada Chantrapromma[3], Thitipone Suwunwong[4,5], Kuaanan Techato[1]
[1]Environmental Assessment and Technology for Hazardous Waste Management Research Center, Faculty of Environmental Management, Prince of Songkla University, Songkhla 90112, Thailand
[2]Center of Excellence on Hazardous Substance Management (HSM), Bangkok 10330, Thailand.
[3]Department of Chemistry, Faculty of Science, Prince of Songkla University, Hat Yai, Songkhla 90110, Thailand
[4]School of Science, Mae Fah Luang University, Chiang Rai, 57100, Thailand
[5]Center of Chemical Innovation for Sustainability (CIS), Mae Fah Luang University, Chiang Rai, 57100, Thailand
*e-mail: naeemhussain912@gmail.com

Abstract: The waste from coffee is the main suppliers to biomass residue in Thailand. From biomass can produce chemical feedstocks, fuels and absorbents by the pyrolysis process because biomass has potential. In this study, the wastes of coffee i.e. spent coffee grounds were characterized and then pyrolyzed in a muffle furnace underneath the following parameters of pyrolysis: a temperature of 500 °C with heating rate 5 °C / min and residence time of 30 min. After pyrolysis, characterization of the products with an importance of biochar was achieved utilizing several methods such as Moisture content, Biochar yield, FTIR, XRF and CNH/O analyses. The results presented that the pyrolysis of spent coffee grounds biochar yield was 28.0 % the moisture content was 60 %. It was observed that all the coffee waste contained high levels of carbon and oxygen and lower levels of sulfur. It is also suitable for the environment. Additionally, the coffee waste contains 4.0 % minerals and 96.0% pure coffee.

Keywords: Coffee waste, Biochar, Pyrolysis

Introduction: Presently, the consumption of biomass energy is very significant in the future's expected renewable energy supply. The accessibility of biomass is an elementary constraint in the form of switch energy materials. In practice, the world's largest sustainable energy resources are biomass feedstocks. The biomass production annual is about 220 billion on dry bases [1]. For the production of an alternative energy, the biomass can be utilized by combustion or other energy materials, for example liquid biochar. In the last insufficient centuries, the growth of biomass feed stock has been investigated with the intensity of pyrolysis process.

Pyrolysis is a process to change biomass feedstock into biochar, biooil, and gases. Pyrolysis process was performed at a high temperature and without oxygen. In pyrolysis process both reactions have such as, endothermic and exothermic reactions. In the exothermic reaction the cracking of organic materials were occurred at the low temperature through pyrolysis process at the initial stage. The temperature is rise, some product is evaporated and cracked into secondary product. The process of vaporization and cracking is called endothermic reaction or process [2]. The biomass for instant wheat straw, oat hulls, rice hulls, peanut hulls, wood a bagasse are utilized in this process [3,4]. However, in the pyrolysis process the biochar yield is a byproduct and produced within a range of 25–35%.

Additionally, the produced biochar may be used in different industries, for example to produce activated carbon, chemicals, carbon fibers, carbon nanotubes, etc. [5]. In addition, biochar can be used as decrease the negative impact on the environment and also used to reduce the soil pollution. Biochar is an extremely absorbent, it is utilized to remove heavy metals from the wastewater and used in the soil as a fertilizer [6].

The production of Robusta coffee in Thailand is very high, 80,000-85,500 tons produced yearly in southern Thailand. 60% of Robusta coffee is exported and the remaining coffee commonly utilized in a local production of instant coffee. The production of waste per year is 22,000 tones [7].

In this study, coffee wastes (spent coffee ground) were pyrolyzed in the muffle furnace. After pyrolysis process, the pyrolyzed product were characterized. For the pyrolysis process the condition followed e.g., temperature, heating rate and set time. After the all sample were analyzed its physical and chemical properties by utilized different equipment.

Materials and methods:

Materials: In this study the Robusta spent coffee grounds were collected from the coffee shop in the southern Thailand.

Methodology:

Pyrolysis: Biochar produced from the spent coffee ground by using the pyrolysis process. The muffle furnace was used for pyrolysis process. The muffle furnace was set 500 °C, heating rate 5 °C/min and the residence time of pyrolysis process were 30 min. After pyrolysis the pyrolyzed product were characterized.

Characterization of biochar and spent coffee grounds: Physiochemical characteristic of coffee was determined with different instrument. Yield of biochar was determined by the following equation (1) [8]:

$$Biochar\ yield\ (\%) = \frac{Weight\ of\ biochar\ (g)}{Weight\ of\ spent\ coffee\ grounds(g)} \times 100 \qquad (1)$$

Spent coffee ground moisture content was calculated by the following equation (2): [9].

$$Moisture\ content = \left(\frac{Initial\ weight(g) - weight\ after\ drying(g)}{weight\ after\ drying(g)}\right) \times 100 \ (2)$$

The C, H, N, S and O content of spent coffee grounds were measured by using Elemental analysis (Elementary Analysis System GmbH, Germany). Spent coffee grounds chemical composition were calculated by using an X-ray fluorescence (XRF) spectrometer (Shimadzu XRF-1800 [10]. Adding biochar into distilled water reached the mass/water ratio will be 1:20 to calculate the pH of the biochar [11].

FTIR analysis: For the analysis of functional groups of spent coffee ground were used Perkin Elmer FTIR spectrometer. The sample scanned at the range 400-4,000 cm^{-1}. The resolution was set as 4 cm^{-1}.The sample 0.1 g and 1 g of KBr were mixed together [12].

Results and Discussion:

Physicochemical properties of spent coffee grounds and biochar: Biochar produced from coffee waste were characterized. Moisture content of the spent coffee ground was 60 %. The biochar production was high at low-temperature during the pyrolysis. Moreover, the biochar yields differed with different biomass types. The biochar yield was 27.87 %. The weight loss of biochar occurred by the decomposition of raw material at higher temperature and thus the decomposition of solid product was observed; because of this process the conversion of pyrolysis was increased [13,14]. Katyal [5] reported that increasing the temperature caused lower char production. At 400°C higher yield of biochar was observed as compared to 700°C. Various heating rates and the yields of biochar were compared i.e. 5 °C/min, 20 °C/min and 30 °C/min , at 5 °C/min the yield of char was increased as compare to 20 °C/min and 30 °C/min. The components of biomass play a significant role for the production of biochar. All cellulose

degraded in to smaller molecules by increasing the pyrolysis temperature at 400 °C [15]. The pH of biomass before and after were 5.6 and 10.4 respectively. Due to the un-pyrolyzed inorganic materials, the pH of the biochar increased with the increase in temperature of pyrolysis [17].

Additionally, Rawat et al. [18] reported that biochar is utilized for soil amendment. It improves the soil quality and soil fertility by increasing the soil pH. Biochar also decreases the soil hardening and increases the cation-exchange capacity and also changes its structure and physicochemical properties.

Elemental composition of biomass: The result showed that spent coffee ground showed higher percentage of carbon and oxygen content 52 and 34.1 %, respectively. The aromatic ration H/C is higher than O/C 2.0 and 0.5, respectively. Nguyen and Lehmann [17] reported that the H/C and O/C both are important indicator of biochar yield. Lehmann et al. [19] reported that the carbon content increased the soil remediation. The C content in the soil will increase the carbon sequential. Ahmad et al. [20] reported that soybean Stover have high amount of carbon. It is significant for soil remediation. From the Table 1 it can be observed that the H/C ratio of Robusta is higher than other biomass feedstocks. Rest of the biomass feedstocks e.g., cotton, wheat, oil-rape and rice were less in aromatic ratio. Chen et al [21] studied different biomass feedstocks for soil amendment. The biomass having higher H/C ratios showed significant amendments in soil texture and for the removal of heavy metals from waste water.

Table 1. Elemental composition of spent coffee grounds and other biomass (%w/w).

Biomass	N	C	H	O	O/C	H/C
Robusta	2.1	52.0	7.0	34.1	0.5	2.0
Cotton	0.66	44.8	6.1	44.3	0.74	1.6
Wheat	0.92	36.8	5.3	42.5	0.87	1.7
Oil -rape	1.11	42.3	5.9	41.4	0.75	1.7
Rice	0.71	39.1	5.7	40.9	0.8	1.8

Chemical composition of spent coffee grounds: The results of chemical composition of spent coffee grounds showed that K is in the highest concentration of 2.0 %, whereas, Ca, P and S were 0.88, 0.42 and 0.64 %, consecutively. Zajac et al. [22] reported that Ca, K, P and S were used for agricultural purposes. In addition, the amount of Zn, Cu and Mn noted in the spent coffee grounds were 0.01,0.03 and 0.04, successively. Zajac et al [22] reported that such minerals may enhance the capabilities of the biochar used as fertilizer.

Characteristic of Functional groups in biomass and biochar:

Table 2. Functional groups of biomass and biochar

Materials	Spectral region (cm^{-1})	Functional groups	Details
Biomass	2921	C-H	Stretching vibration for alkanes
	2855	C-H	Stretching vibration for alkanes
	1747	C=O	Easter stretch modes
	1542-1535	N-H, C-H	Amine and Easter stretch modes
	1435	C-H	Methylene bending vibration
	1249	C=O	Aldehydes
	832-674	C-H	Aromatic
Biochar	3100	C-H	Stretch aromatic
	1400	C=C	Stretch aromatic

From the Table 2. the result showed the wavenumber of 2921 and 2855 cm^{-1} (stretching vibration for alkanes C-H), 1747 cm^{-1} are ester C=O stretch modes, 1542 - 1535 $cm^{-1}$is amine N-H stretch modes and ester C-H stretch modes, 1435 cm^{-1} (Methylene bending vibration).

At 1249 cm^{-1} (aldehydes C=O) and the 832-674 cm^{-1} bands (aromatic C-H) [23]. The functional groups were reduced in the biochar respectively due to the high temperature. At 3100 cm^{-1} stretch aromatic and the 1400 cm^{-1} also (stretch aromatic bond C=C).

Conclusion: The results of analysis of the spent coffee grounds displayed that it contains high carbon and oxygen contents of 52.0 and 34.1 %. The moisture contents of spent coffee grounds were high 60 %. It investigates that spent coffee grounds has 96.0 % of pure coffee. This coffee biomass converts into biochar by pyrolysis process with the following conditions, 500°C, heating degree 5°C/min and for the set time is 30 min. The compounds of spent coffee grounds were determined by FTIR analyses which contains alkanes, aromatic compounds, carboxylic acids and aldehydes. Additionally, it was observed that slow pyrolysis increased the biochar yield.

References:

1. Moreira, J.R. Global biomass energy potential. Mitig. Adapt. Strateg. Glob. Chang. 2006;11: 313–342.
2. Cheung, K.Y., Lee, K.L., Lam, K.L., Chan, T.Y., Lee, C.W., Hui, C.W. Operation strategy for multi-stage pyrolysis. J. Anal. Appl. Pyrolysis. 2011; 91:165–182.
3. Ji-lu, Z. Bio-oil from fast pyrolysis of rice husk: Yields and related properties and improvement of the pyrolysis system. J. Anal. Appl. Pyrolysis. 2007; 80:30–35.
4. Mohan, D., Pittman, C.U., Steele, P.H. Pyrolysis of wood/biomass for bio-oil: A critical review. Energy and Fuels. 2006; 20:848–889.
5. Katyal, S., Thambimuthu, K., Valix, M. Carbonisation of bagasse in a fixed bed reactor: Influence of process variables on char yield and characteristics. Renew. Energy. 2003; 28: 713–725.
6. Mullen, C.A., Boateng, A.A., Goldberg, N.M., Lima, I.M., Laird, D.A., Hicks, K.B. Bio-oil and bio-char production from corn cobs and stover by fast pyrolysis. Biomass and Bioenergy. 2010; 34:67–74.
7. Angkasith, P. Coffee Production Status and Potential of Organic Arabica Coffee in Thailand .* 2001;26–28.
8. Kulaksiz, E., Gözmen, B., Kayan, B., Kalderis, D. Adsorption of Malachite Green on Fe-modified biochar: influencing factors and process optimization. Desalin. Water Treat. 2017; 74:383–394.
9. Reeb, J., Milota, M. moisture content by the oven-dry method for industrial testing Weight of water Weight of wood MC -Wdka. 1999; 66–74.
10. Zhou, Q., Liao, B., Lin, L., Qiu, W., Song, Z. Science of the Total Environment Adsorption of Cu (II) and Cd (II) from aqueous solutions by ferromanganese binary oxide – biochar composites. Sci. Total Environ. 2018; 615:115–122.
11. Sun, L., Chen, D., Wan, S., Yu, Z. Adsorption Studies of Dimetridazole and Metronidazole onto Biochar Derived from Sugarcane Bagasse : Kinetic , Equilibrium , and Mechanisms. J. Polym. Environ. 2018; 26:765–777.
12. Abnisa, F., Arami-Niya, A., Daud, W.M.A.W., Sahu, J.N. Characterization of Bio-oil and Bio-char from Pyrolysis of Palm Oil Wastes. Bioenergy Res. 2013; 6:830–840.
13. Şensöz, S., Kaynar, I. Bio-oil production from soybean (Glycine max L.); Fuel properties of Bio-oil. Ind. Crops Prod. 2006; 23:99–105.
14. Williams, P.T., Reed, A.R. Pre-formed activated carbon matting derived from the pyrolysis of biomass natural fibre textile waste. J. Anal. Appl. Pyrolysis. 2003; 70:563–577.
15. Yang, H., Yan, R., Chen, H., Lee, D.H., Zheng, C. Characteristics of hemicellulose, cellulose and lignin pyrolysis. Fuel. 2007; 86:1781–1788.
16. Lima, I., Steiner, C., Profile, S., Das, K.C., Novak, J.M., Lima, I., Xing, B., Gaskin, J.W., Ahmedna, M., Rehrah, D., Watts, D.W., Busscher, W.J., Schomberg, H. characterization of

designer biochar produced at different temperatures and their effects on a loamy sand. Ann. Environ. Sci. 2009;3:195–206.
17. Nguyen, B.T., Lehmann, J. Black carbon decomposition under varying water regimes. Org. Geochem. 2009; 40:846–853. Lehmann, J. "Black is the new green". Nature. 2006; 442: 624-626.
18. Ajema L. Effects of biochar application on beneficial soil organism review. Int. J. Rese. Studi, Sci., Eng. Technol. 2018;5(5):9-18.
19. Lehmann, J. "Black is the new green". Nature. 2006; 442: 624-626.
20. Ahmad, M., Lee S.S., Lee, S.E., Al-Wabel,M.I., Tsang, D.C.W., Ok, Y.S. Biochar-induced changes in soil properties affected immobilization mobilization of metals metalloids in contaminated soils. J Soils Sediments. 2017;17:717–30.
21. CHEN, X. J., LIN, Q. M., Rizwan, M., ZHAO, X. R., & LI, G. T. 2. Steam explosion of crop straws improves the characteristics of biochar as a soil amendment. J Intergr Agr. 2019; 18(7): 1486–1495.
22. Zając, G., Szyszlak-Bargłowicz, J., Gołębiowski, W., Szczepanik, M. Chemical Characteristics of Biomass Ashes. Energies. 2018; 11:2885.
23. Liu, Y., He, Z., Uchimiya, M. Comparison of Biochar Formation from Various Agricultural By-Products Using FTIR Spectroscopy. Mod. Appl. Sci. 2015; 9 : 246–253.

Acknowledgement: The authors would like thankfully acknowledge research Grants from Thailand's Interdisciplinary Graduate School of Energy System (Contract No. IGS-Energy 1/2018/13) funds for Master of Science research, in Sustainable Energy Management, Faculty of Environmental Management, Graduate School, Prince of Songkla University Thailand.

E_028_OF: SIMULATION OF SHALLOW LANDSLIDES SUSCEPTIBILITY MAP IN THE TOP OF PHU TUB BERK MOUNTAIN, PHETCHABUN, THAILAND

Apiwat Intiyakosat[1], Pawee Klongvessa[4], Srilert Chotpantarat[1,2,3,*]

[1]Department of Geology, Faculty of Science, Chulalongkorn University, Bangkok, Thailand

[2]Research Program on Controls of Hazardous Contaminants in Raw Water Resources for Water Scarcity Resilience, Center of Excellence on Hazardous Substance Management (HSM), Chulalongkorn University, Bangkok, Thailand

[3]Research Unit Control of Emerging Micropollutants in Environment, Chulalongkorn University, Bangkok, Thailand

[4]Department of Environmental Technology and Management, Faculty of Environment, Kasetsart University, Bangkok, Thailand

*e-mail: Srilert.C@Chula.ac.th

Abstract: Landslide frequently occurs in steep slope areas with high rainfall amount in Thailand and causes severe damages. Therefore, predicting landslides is useful. One of the methods to predict landslides is modeling. This study aimed to use the SHALSTAB model to determine shallow landslides susceptibility map in the top of Phu Tub Berk mountain area, which is the location of Doy Nam Peung Din village. Samples were collected in the field and tested in the laboratory. To obtain parameters used in the model. A result of the simulation classified the area by function of a hydrologic ratio (log Q/T) required to instability. into 5 classes as established by Dietrich and Montgomery. Of the total area, 64.82% (18.62 km2) is classified as stable area (log Q/T >-2.2), 6.51% (1.87 km2) has the value of log Q/T between -2.5 and -2.2, 13.09% (3.75 km2) has the value of log Q/T between -2.8 and -2.5, 10.51% (3.01 km2) has the value of log Q/T between -3.1 and -2.8, and 5.08% (1.45 km2) is classified as unstable area (log Q/T <-3.1). The Doy Nam Peung Din village is in the stable area, but some parts of the road number 2331, which is the way to this village, are on the less stable area.

Introduction: Landslide frequently occurs in steep slope areas with high rainfall amount in Thailand. The Phu Tub Berk Mountain, Phetchabun, often suffers from this disaster. Doy Nam Peung Din village is the most populated area in the Phu Tub Berk Mountain.

Landslides can be classified by the movement characteristics into falls, topples, slides, lateral spread, and flows (Highland and Bobrowsky, 2008). From the available data, there were a lot of landslides and debris flow in nearby areas. In 2001, the landslide caused 140 deaths, 109 injuries, and many damages to homes and agricultural areas in Tambon Nam Koh, Amphoe Lomsak (Yumuang 2006). A good landslide warning system is required. A late warning can lead to the uncontrollable damage. Therefore, landslide prediction is one of the possible ways help handling the damage.

The Shallow Landslide Stability Model (SHALSTAB) is quantitative model for assessing the topographic influence on shallow landslide. Models for the generation of soil saturation and slope instability are combined with digital terrain data to predict landslide susceptibility (Mongomery and Dietrich, 1994). The SHALSTAB model calculates landslide susceptibility map using digital elevation map, density of soil, soil thickness, effective cohesion, and internal friction angle.

This study aimed to collect data which includes Geographic Information System (GIS) and field data in Phu Tub Berk to predict the landslide susceptibility map using the SHALSTAB model.

Methodology: The study area was a formation of sandstone on the top of Phu Tub Berk Mountain. The total area of the study area was approximately 28.73 km^2.

The SHALSTAB model was a deterministic distributed model based on a combination of infinite slope and steady-state hydrological models. SHALSTAB was integrated into a GIS

by ArcView 3.2 through which the upslope drainage area, elevation, and slope values were calculated by using a digital elevation model (DEM), and these values were assigned to each pixel (Michel, 2014). The landslide susceptibility was generated by equation 1.

$$\frac{Q}{T}=\frac{b}{a}\times\sin\theta\times\{P\times(1-\frac{\tan\theta}{\tan\emptyset})+\frac{C}{\cos^2\theta\times\tan\emptyset\times P\times g\times Z}\} \quad (1)$$

Where Q was net rainfall, T was soil transmissivity, b/a was the contributing area per unit contour length, θ (degree) was the slope gradient, ∅ (degree) was the internal friction angle, C (N/m^2) was the effective cohesion, ρ (kg/m^3) was the density of soil, Z (m) was the soil thickness, and g (9.81 m/s^2) was the gravitational acceleration.

Results from SHALSTAB model was shown as a value of log Q/T, which could be classified into 5 classes include >-2.2, (-2.2) - (-2.5), (-2.5) - (-2.8), (-2.8) - (-3.1) and <-3.1. The higher value of log Q/T represented the more stability. The areas with values of log Q/T more than -2.2 were considered stable and those with the values of log Q/T less than -3.1 were considered unstable.

The parameters required in the SHALSTAB model were derived from GIS database and fieldwork with laboratory experiments. Table 1 showed the values of parameters used in the model.

DEM is data of elevation based on Geographic Information System. In study area, DEM was generated by contour lines with a resolution of 30 m (Figure 1) and was used to calculate the contributing area per unit contour length (b/a) and slope gradient (θ).

Soil thickness (Z) and density of soil (ρ) were obtained from a fieldwork. The soil thickness was measured from the soil layer to the base rock and the density of soil was determined from soil samples at 4 locations (Figure 2).

Effective cohesion (C) and internal friction angle (∅) were obtained from direct shear test (Figure 3) which was the test of maximum capacity of the soil mass to receive shear strength before break. The shear strength to trigger landslide was from external forces and the weight of the soil. The value of cohesion (C) and internal friction angle (∅) indicated the strength of soil mass (Strength parameters). Strength parameters could be determined by Mohr – Coulomb's equation as shown in equation 2.

$$\tau=c+\sigma\tan\emptyset \quad (2)$$

where τ was the shear strength, c was the cohesion, σ was the normal stress, and tan∅ was the coefficient of international friction.

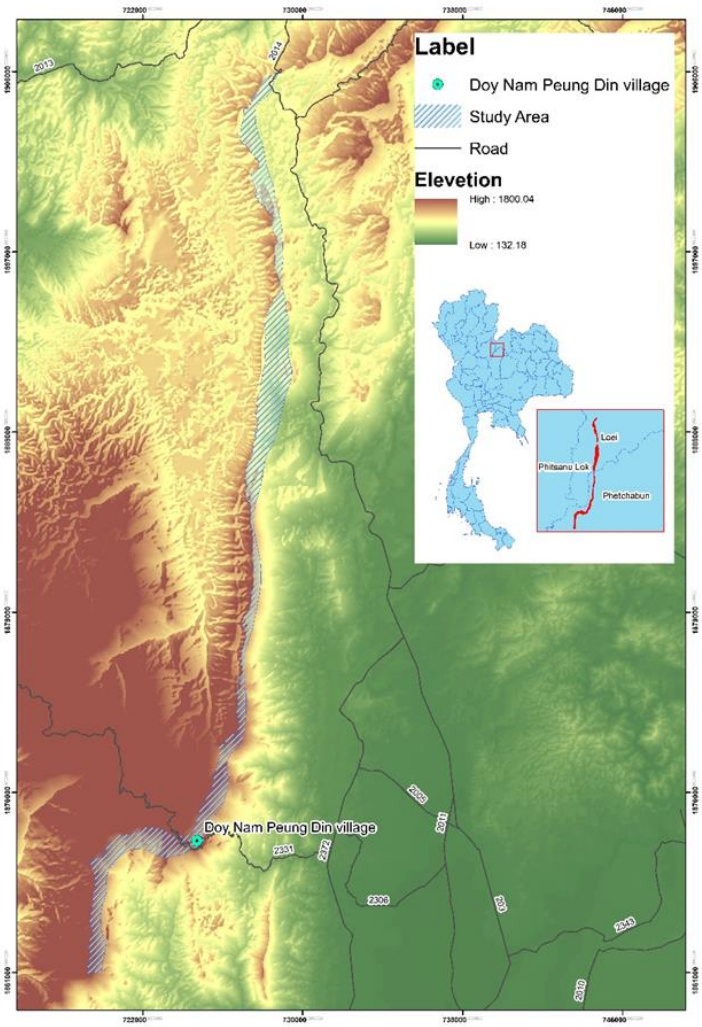

Figure 1. Study area

(a) (b) (c)

Figure 2. Sample collection in the field and laboratory experiment.
(a) Soil thickness measurement (b) Samples of soil density (c) Weighing for soil density

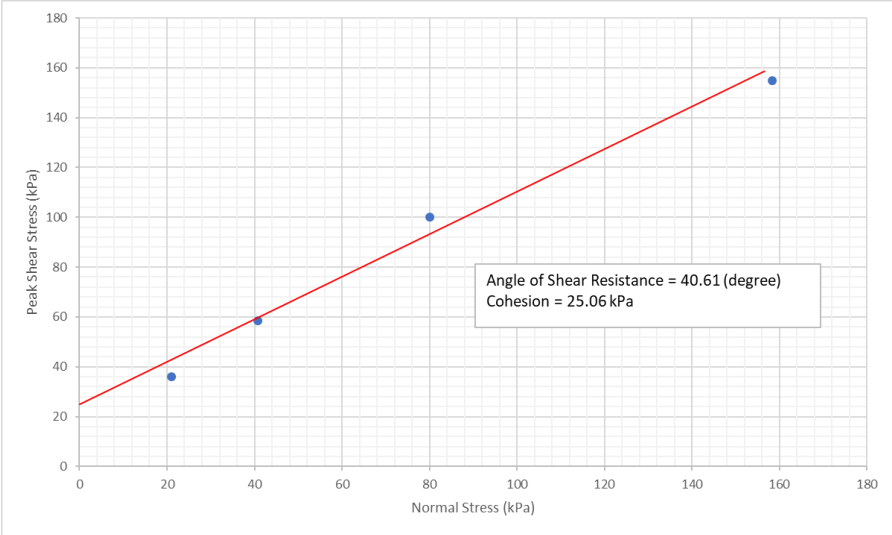

Figure 3. Results of direct shear test.

Table 1. The geotechnical parameters derived from fieldwork and laboratory experiments

Parameter	Value
soil thickness (Z)	1.2 (m)
density of soil (P)	1623 (kg/m^3)
effective cohesion (C)	2506 (N/m^2)
internal friction angle (∅)	40.61 (degree)

Results and Discussion: A Result of the simulation by SHALSTAB model is a landslide susceptibility map on the top of Phu Tub Berk Mountain as shown in Figure 4. The area can be classified by the value of log Q/T into 5 classes as established by Dietrich and Montgomery. Of the total area, 64.82% (18.62 km2) is classified as stable area (log Q/T >-2.2), 6.51% (1.87 km^2) has the value of log Q/T between -2.5 and -2.2, 13.09% (3.75 km^2) has the value of log Q/T between -2.8 and -2.5, 10.51% (3.01 km^2) has the value of log Q/T between -3.1 and -2.8, and 5.08% (1.45 km^2) is classified as unstable area (log Q/T <-3.1) as presented in Figure 5. From the landslide susceptibility map (Figure 4), it can be seen that the Doy Nam Peung Din village is located on a stable area, but some parts of the road number 2331, which is the way to this village, are on steep slope areas which is not very stable.

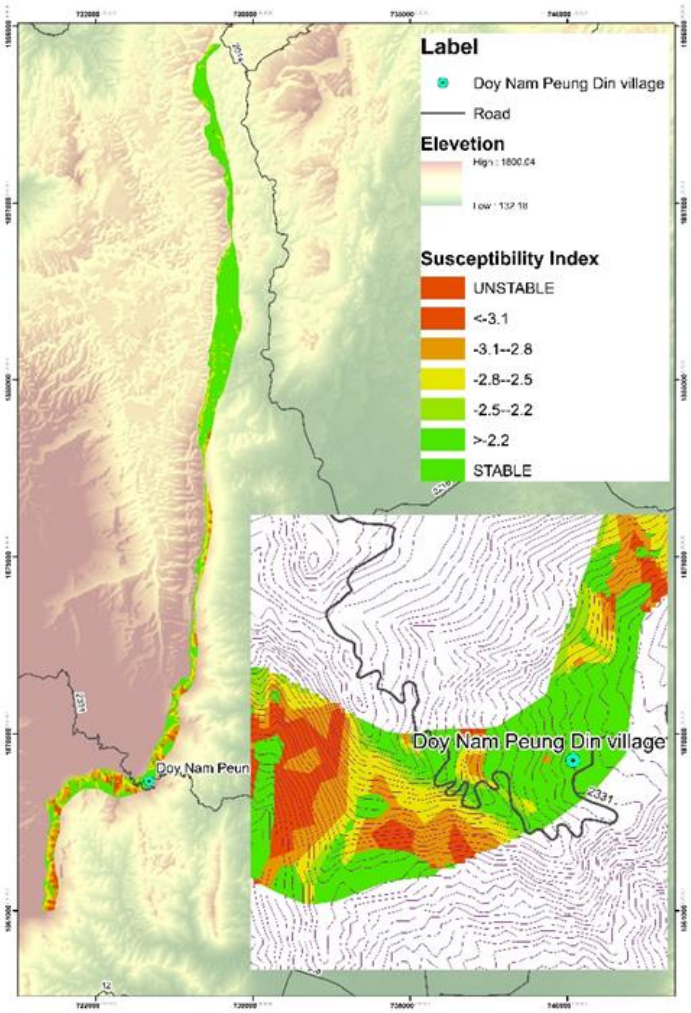

Figure 4. Landslide susceptibility map.

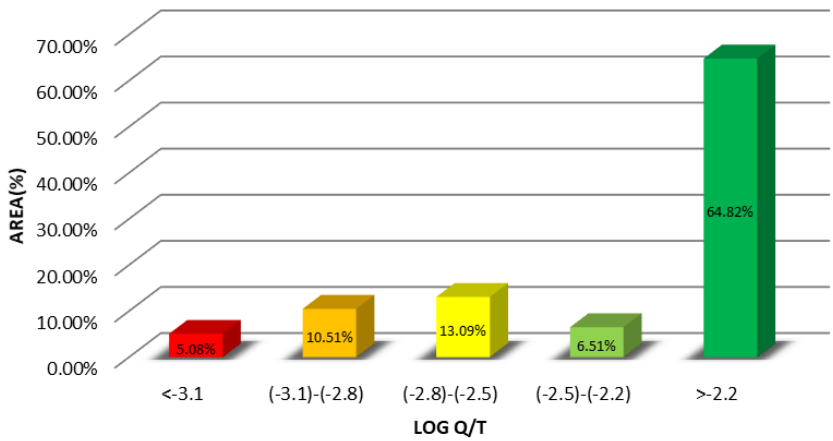

Figure 5. Classes from stable to unstable areas in the top of Phu Tub Berk Mountain.

Conclusion: The landslides susceptibility map simulated by the SHALSTAB model shows that the Doy Nam Peung Din village is located on a stable area which is not affected by landslides, but some parts of the road number 2331, which is the way to this village, are on steep slope areas which are not very stable. Even though this study successfully developed the landslide susceptibility map, this map needed to improve reliability because of the lack of landslide data in the area. Therefore, the calibration of the model with actual data in the area may help increasing the accuracy of the landslides susceptibility map in the current study.

References:

1. Beven KJ, Binley AM. Hydrological Processes. 1992; 6:279-298.
2. Highland L, Bobrowsky P. U.S. Geological Survey. 2008; 129.
3. Huang JC, Kao SJ, Hsu ML, Lin JC. Natural Hazards and Earth System Sciences. 2016; 6: 803-815.
4. Lee JH, Park HJ. Landslides. 2015; 13:885-903.
5. Michel GP, Kobiyama M, Goerl RS. J Soils Sediments. 2014; 14:1266-1277.
6. Montgomery DR, Dietrich WE. Water Resources Research. 1994; 30:1153-1170.
7. Pradhan AMS, Kim YT. Catena. 2016; 140:125-139.
8. Rosso R, Rulli MC, Vannucchi G. Water Resources Research. 2006; 42:W06410.
9. Yumuang S. Environmental Geology. 2006; 51:545-564.

Acknowledgements: This research was funded by the Ratchadaphisek Sompoch Endowment Fund (2019), Chulalongkorn University (762003-CC), the Center of Excellence on Hazardous Substance Management (HSM) and the International Postgraduate Programs in Environmental Management, the Grant for International Research Integration: Chula Research Scholar, Ratchadaphiseksomphot Endowment Fund (GCURS-59-06-79-01), and Graduate School, Chulalongkorn University. The authors are also thankful for assistance in the field studies from Mr. Rugkiet Chansorn

E_029_PF: LOW ASH BIOMASS PELLET FROM CORN STALK: EFFECT OF CALCIUM CARBONATE BASE ADDITIVE ON FUELS AND ASH QUANTITIES

Apisith Suebchompoo, Thanakit Kumwung, Nattakan Soykeabkeaw, Uraiwan Intatha, Nattaya Tawichai*
Center of Innovative Materials for Sustainability (iMatS), Mae Fah Luang University, Chiang Rai 57100, Thailand
School of Science, Mae Fah Luang University, Chiang Rai 57100, Thailand
*e-mail: nattaya.taw@mfu.ac.th

Abstract: This research was studied on effect of $CaCO_3$ on ash content of biomass pellets. The pellets were made from corn stalk and various amounts of $CaCO_3$ (0, 3 and 5%wt). The pellets were formed by using uniaxial compression machine at 80 MPa pressure. The physical properties of pellets such density, moisture content, heating value and ash content were measured. Heating value was measured by bomb calorimeter machine. Ash content and moisture content were measured following the EN standard test methods. According to the result density of pellets was 997 kg/m^3 and when $CaCO_3$, the density of pellets added were increase of 8.36%. Moisture content of pellets was 8.3% and when increased the content of $CaCO_3$, the moisture content was decreased of 17%. From the result, density and moisture content were affected to heating value. The heating value of the pellets was 16 MJ/kg and ash content of pellets was 22%. Heating value of pellets were decreased of 12% and ash content were reduced of 31.5% of add 5 wt% of $CaCO_3$.

Introduction: Biomass is renewable energy that collects from natural resources. There are many types of biomass sources such as agricultural wastes, solid wastes, landfill gas and wood. Among those sources, agricultural wastes from crops production wastes have gained interest because they are high production rate, low energy input to produce and low nutrient requirements. However, these sources contain high components of K, Na, P, Cl and others, they are the main cause of ash and slag transformation.

Corn is one of the most popular crops, it has many components such as corn cob, corn stalk and corn stover. From the previous works, corn stover contains ash content of 3.7%, corn cob contains ash content of 1.86% and corn stalk contains ash content of 8.25%[1-4]. Normally, ash is formed during biomass combustion process. The products from this process are alkali-metal and volatile elements. Alkali-metal were reacted with O_2 during combustion process and they are the primary ash forming. After that the primary ash forming would reaction together and transform to ash. Volatile elements were released into the atmosphere in forms of gas when temperature was decreased, then, volatile condense into ash and slag. Some of volatile components are condense to fly ash. Ash and slag can lead corrosion and erosion in boiler. Ash content can be reduced by two methods: physical treatments and chemical treatments[5,6].

Chemicals treatment is the method that used chemical solutions as an additive and the result of chemical treatments can be divided into 4 ways: Aluminum silicate (Al_2SiO_5) based additive[7], Calcium (Ca) based additive[8-9], Sulphur (S) based additive[10] and Phosphorus (P) rich based additive[8]. Aluminum silicate-based additive can reduce ash content of 51.83% and calcium-based additive can reduce of 67.24 %. The main objective of this research was study on effect of calcium carbonate ($CaCO_3$) on ash content of biomass pellets from corn stalk.

Methodology: This study, corn stalk was collected from Chiang Rai province, Northern Thailand and Calcium carbonate ($CaCO_3$) in calcite forms was received from Thai Poly Chemicals Company Limited. This research was divided into two. The first part, the raw materials were dried in hot air oven at 105 °C for 10 hours, then ground and sieved by using sieving tools to

get the particle size less than 1 mm. The second part, raw materials were mixed with $CaCO_3$ various content (0, 3 and 5 wt%). Then, the mixture was pressed into pellets by using uniaxial hydraulic compression machine with a 10 mm diameter die at pressure of 80 MPa and holding for 1 minute.

Apparent density: The density of individual pellets was calculated by dividing the mass of an individual pellet by its volume. A Vernier caliper was used to measure length and diameter to find volume of the pellets and a 4-digit balance was used to weigh the sample. The reported values are an average of 10 measurements and calculated by the following equation below:

$$Apparentdensity = \frac{m}{V}$$

where m is mass of sample (g) and V is volume of pellet (mm^3).

Moisture content: Moisture content characteristic method is following by EN 14774-2. First, alumina crucibles were weighed (m_1) then put sample in alumina crucible. Samples and crucibles were weighed together (m_2). Then, samples were dried at 105 ±2°C for 10 hours, after that dried samples were placed to desiccator for cooling down to room temperature. Finally, dried samples were weighed (m_3). Moisture content can estimate by using the equation below:

$$Moisturecontent(\%) = \left(\frac{m_2 - m_3}{m_2 - m_1}\right) \times 100$$

Heating value: The fuel properties of the obtained samples were measured by an IKA C6000 Calorimeter (Germany). Firstly, the samples were weighed in the crucible, with a weight around 0.5 g. The ignition wire was fastening between the electrodes in the bomb. Then, water was added to bomb before assembly and charged oxygen gas into bomb. The bomb was put into the instrument, and the weight of sample was input to the software and analyzes the sample. Then heating value was calculated by the equation below:

$$Highcalorificvalue = \frac{(W + w) \times (t_2 - t_1)}{m}$$

where m is mass of sample taken into calorimeter (g), W is mass of water taken into calorimeter (g), w is mass of calorimeter and thermometer (g), t_1 is initial temperature of water in calorimeter (°C) and t_2 is final temperature of water in calorimeter (°C).

Ash content: Determination of ash content is following by EN 14775. First, samples were weighing and dried in hot air oven at 110°C for 24 hours. Then, the samples after dried were put into muffle oven at 550°C for 12 – 18 hour. After temperature is cooling down to 250°C then the sample were moved into desiccator at room temperature. Last sample after burnt were weigh and calculate by the equation below:

$$Ashcontent(\%) = \left(\frac{m_1 - m_3}{m_2 - m_3}\right) \times 100$$

where m_1 is mass of ash (g) ,m_2 is initial mass of sample (g) and m_3 is mass of crucible (g).

Results and Discussion: Figure 1 shows the effect of $CaCO_3$ content on density of samples. From the standards of pellets, the density was in range of 600 – 650 kg/m^3 and the commercial pellets from corn stalk were in range of 1000±20 kg/m^3 and samples from experiment were 997±15 kg/m^3. When the content of $CaCO_3$ increased, the density was increasing of 8.36% by adding 5 wt% of $CaCO_3$. Because the density of $CaCO_3$ is (2711 kg/m^3) higher than raw materials, when raw materials were mixed with $CaCO_3$ the density may continuous increase.

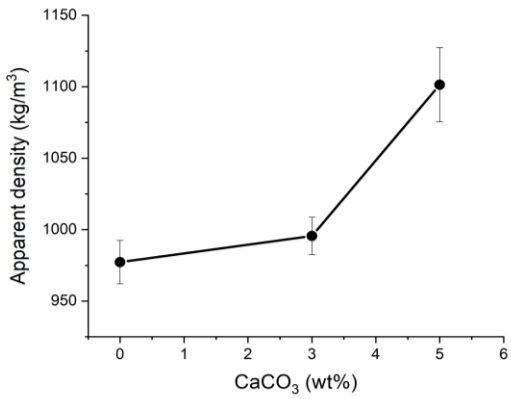

Figure 1. Effect of $CaCO_3$ content on density of samples.

Figure 2 shows the effect of $CaCO_3$ on moisture content of samples. From the standard could be allowed in range of 10 – 12% of moisture content. Moisture content of general pellets from corn stalk is in range of 5±1% but in this experiment the moisture content of cornstalk without $CaCO_3$ is 8.3±0.5%. When $CaCO_3$ were added the moisture content of samples were decrease of 17 % at 5 wt% of $CaCO_3$.

Figure 3 shows effect of $CaCO_3$ content on heating value on samples. The commercial heating value of pellets were in range of 18±0.75 and in this experiment heating value of pellets at 0 wt% $CaCO_3$ were in range of 16±0.08. When the samples from experiment were compared with the commercial samples, heating value of the experiment samples were lower than the commercial because the compositions compound and mineral in raw materials. Heating value was depended on the content of fuels elements such as C, H and N.

When increase the content of $CaCO_3$, heating value of samples were decreased of 12% by adding 5 wt% $CaCO_3$. The heating value of $CaCO_3$ is 1.78 MJ/kg. Density and moisture content are also affecting to heating value. Effect of density on heating value, when density of sample are increase but volume of samples were decrease because the weight of samples were fixed at 0.5 g per sample that cause of low quantity of carbon (C) that can be effect to heating value.

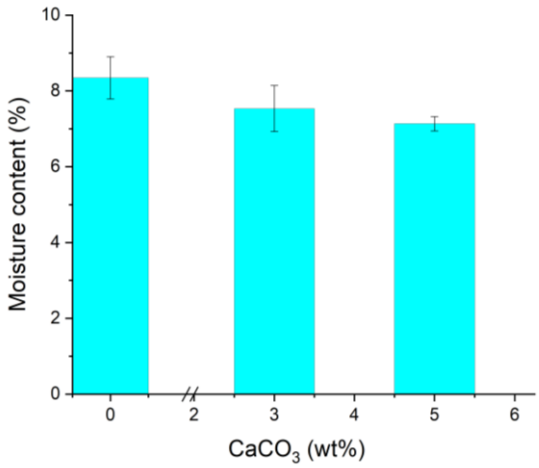

Figure 2. Effect of $CaCO_3$ content on moisture content of samples.

Effect of moisture content on heating value, when moisture content was increased heating value will be decrease because percentage of water or moisture content was high. During combustion process water became to vapor therefore, heating value refer to temperature of water in liquid state. But in this experiment the moisture content decrease and heating value also decrease cause of $CaCO_3$ had low heating value. When increase the content of $CaCO_3$ can lead the heating value content of samples were decreased[11].

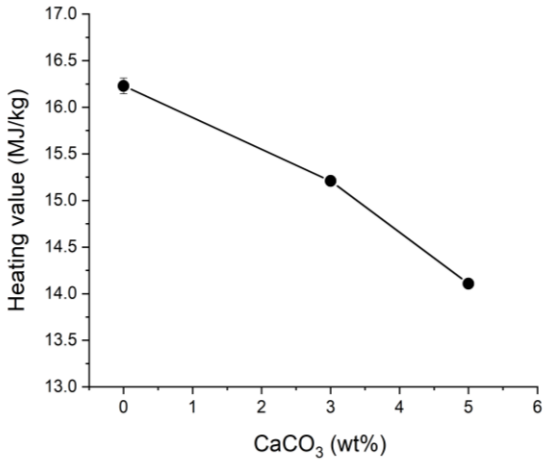

Figure 3. Effect of $CaCO_3$ content on heating value of samples.

Figure 4 shows the effect of $CaCO_3$ content on ash content of samples. In the commercial pellets from corn stalk, ash content was in range of 8±0.5% but in this experiment, ash content is 22±0.4%. Additives were added, at 5 wt% of $CaCO_3$ can lead ash reduction of 31.5%. Therefore, when increase the content of $CaCO_3$ ash content can be continuous decrease. $CaCO_3$ was increased melting temperature of ash by 100 – 200°C because Ca can dissolve in potassium silicate and fore potassium to gas phase. However, CaO is the component of ash but $CaCO_3$ in forms of calcite were completely eliminated at 1100°C[12].

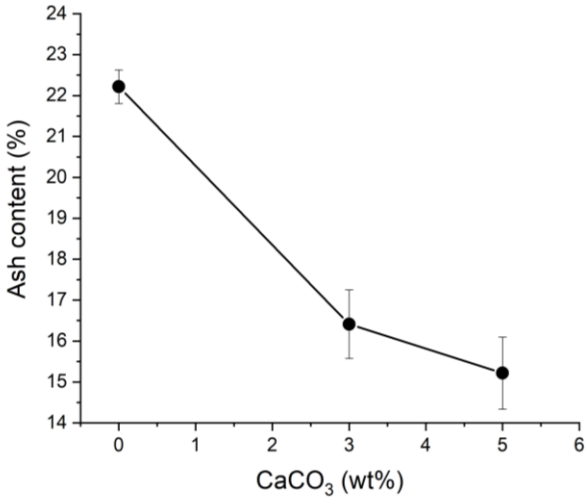

Figure 4. Effect of $CaCO_3$ content on ash content of samples.

Conclusion: This research is focusing on effect of $CaCO_3$ on ash content of biomass pellets that made from corn stalk. When increase the content of $CaCO_3$, they can lead the density of sample increase of 8.36% from 997 kg/m^3 but in the other hand, $CaCO_3$ were leaded moisture content and heating value decrease of 17% from 8.3% of moisture content and 12% from 16 MJ/kg of heating value. Ash content was decreased of 31.5% from 22% of ash content. Cause of ash reduction, during combustion process calcium carbonate is reaction with potassium silicate and force potassium into gas phase. Because potassium the main cause lead ash transformation and $CaCO_3$ was completely eliminated at 1100°C. Ca based additives such as lime, limestone and marble sludge are more efficient in abating ash sintering and slagging in bottom ash.

References:

1. Almeida L F P, Sola A V H, Behainne J J R. Acta Sci Techol. 2017;39:461-468.
2. Demirbas A. Energ Convers Manage. 2001;42:1357-1378.
3. Örberg H, Jansson S, Kalén G, Thyrel M, Xiong S. Energy Fuels. 2014;282:1103-1110.
4. Kaliyan N, Morey V R. Fuel Process Technol. 2010; 91:559-565.
5. Xiong S, Burvall J, Orberg H, Kalen G, Thyrel M, Ohman M, Bostrom D. Energy Fuels. 2008;225:3465-3470.
6. Wang L, Hustad J E, Skreiberg Ø, Skjevrak G, Gronli M. Energy Procedia. 2012;20:20-29.
7. Wang L, Skjevrak G, Hustad J E, Grønli M G. Energy Fuels. 2011:25(12):5775-5785.
8. Lindström E, Sandström M, Boström D, Öhman M. Energy Fuels. 2007;21 (2):710-717.
9. Wu H, Glarborg P, Frandsen F J, Dam-Johansen K, Jensen P A. Energy Fuels 2011;25(7):2862-2873.
10. Broström M, Kassman H, Helgesson A, Berg M, Andersson C, Backman R, Nordin A. Fuel Process Technol. 2007;88(11-12):1171-1177.
11. Lin S, Kiga T, Wang Y, Nakayama K. Energy Procedia. 2011:4:356-361.
12. Thy P, Jenkins B M, Grundvig S, Shiraki R, Lesher C E. Fuel 2006;85(5-6):783-795.

Acknowledgements: This work was financials supported by Center of Innovative Materials for Sustainability (iMats) and Mae Fah Luang University.

SESSION F:
PHYSICS &
APPLIED PHYSICS

F_001_PF: STRUCTURAL AND PHYSICAL PROPERTIES OF $SnS_{1-x}Se_x$ SOLID SOLUTION THIN FILMS PREPARED BYCLOSE SPACED SUBLIMATION METHOD

Parichat Cummon*, Ngamnit Wongcharoen, Thitinai Gaewdang
Department of Physics, Faculty of Science, King Mongkut's Institute of Technology Ladkrabang, Soi Chalongkrung 1, Ladkrabang District, Bangkok 10520, Thailand
*e-mail: bamparichat2@hotmail.com

Abstract: SnS thin films, as one of the important tin chalcogenide semiconductor materials, have attracted considerable attention in recent years as low-toxicity and cost-effective materials for use in solid state device fabrication like photoconductors, photovoltaic conversion, holographic recording media, solar control device and near-infrared detector. SnSe thin films have also been extensively studied in the photovoltaic application for its extraordinary advantages including excellent optoelectronic properties. In this work, $SnS_{1-x}Se_x$ solid solutions were prepared by close spaced sublimation method in vacuum using source temperature in the range 650-670°C. The different between source temperature and substrate temperature was controlled to be approximately 100°C. From XRD patterns, the all prepared films crystallized in orthorhombic structure with the preferred orientation of (400) plane. SEM and EDS were used to study the surface morphology and elemental composition of the samples. Optical properties were investigated by means of UV-Vis-NIR spectroscopy in range of 400-2000 nm. The direct band gap value of the films evaluated from the optical transmission spectra decreased from 1.18 to 0.95 eV as Se composition (x) increased from 0 to 1. In addition, it was found that SnSe films presented two extra indirect band gap values being 0.80 and 0.92 eV, respectively. The electrical properties were carried out by resistivity and Hall effect measurements with van der Pauw configuration. The temperature-dependent conductivity was performed in the temperature range of 20-300 K. It was shown that three types of conduction mechanisms can be expected such as Nearest-Neighbor hopping (NNH) at high temperature range (220-295 K), Mott variable-range hopping (Mott-VRH) at low temperature range (125-190 K) and Efros-Shklovskii variable-range hopping (ES-VRH) at very low temperature range (<105 K). The set of parameters describing the properties of localized electrons in each conduction behavior were determined.

Introduction: SnS and SnSe can be formed in a complete series of solid solutions with orthorhombic structure.[1] The band gap of these materials can be tuned from 1.18 eV in SnS to 0.95 eV in SnSe by controlling the alloy composition. Tunable large band gap materials are important for thin film photovoltaic[2] and optoelectronic applications.[3] In these applications, the importance of the variation of E_g with composition (x) lies in the possibility of growing layers of $SnS_{1-x}Se_x$ thin films with different composition values in the whole range ($0 \leq x \leq 1$). $SnS_{1-x}Se_x$ thin films have been prepared by different techniques depending on the growth system and on the growing parameters. Micro-crystalline thin films with different grain sizes can be deposited, leading to the variation of their optical and electrical properties. The close spaced sublimation (CSS) method is a simple, short time and inexpensive growth method in low pressure condition.[4] In this paper, $SnS_{1-x}Se_x$ thin films in the whole range ($0 \leq x \leq 1$) were prepared on glass substrate by CSS method. The XRD, SEM, EDS, FTIR and UV-Vis NIR spectroscopies were investigated. Moreover, electrical parameters such as resistivity, carrier concentration and Hall mobility were obtained from Hall measurements in van der Pauw configuration at room temperature. Electrical conduction mechanisms of all films were investigated at temperature down from 300 to 20 K. We have studied these solid solution thin films in order to improve the performance of $CdS/SnS_{1-x}Se_x$ solar cells.

Methodology: $SnS_{1-x}Se_x$ thin films in the whole composition ($0 \leq x \leq 1$) were deposited on the etched glass substrate with hydrofluoric acid by close spaced sublimation (CSS) method using mixed powders of SnS and SnSe materials with high purity 99.99% supplied by Sigma Aldrich. The starting powders were mixed and mashed during 60 min for obtaining the good homogeneity. For composition x=0.0, source and substrate temperatures were used at 670 and 550 °C, respectively. For other compositions ($0.2 \leq x \leq 1$), source and substrate temperatures were used at 650 and 550 °C, respectively. The deposited time for preparing the films was 20 min in vacuum chamber with low pressure of 3×10^{-3} mbar. The crystal structure of these films was checked by X-ray diffraction technique with a Brucker D 8 diffractometer using CuK_α radiation. Grain size and surface morphology were revealed in accordance to Zeiss EVO MA 10 Scanning Electron Microscopy (SEM). The EDS spectra were also recorded for confirmation of elemental composition. Optical transmission measurements were performed with UV-Vis-NIR double beam spectrophotometer in the wavelength range of 400-2,000 nm. FTIR spectra were performed by Thermo Scientific Nicollet 6700 in the range between 450 and 4000 cm^{-1}. Electrical properties of the films were evaluated by Hall effect and resistivity measurements in the van der Pauw configuration at room temperature. The temperature-dependent conductivity was measured using the two-point probe method in the temperature range 20-300 K.

Results and Discussion:

Crystal structure and surface morphology: The XRD patterns of the $SnS_{1-x}Se_x$ thin films are shown in Figure 1. They are well agreed with JCPDS data file 73-1859 and 32-1382 for SnS and SnSe phases, respectively. All samples belong to orthorhombic structure with preferred orientation (400) plane. There was no indication of phase separation or multiple sets of peaks, only a single phase diffraction pattern was observed, which confirms the formation of the solid solution. The position of peaks shifted towards a lower 2 theta value with increase in Se content. It was found that the value of lattice constant a, b and c linearly increased with increasing Se content as shown in Figure 2. Therefore, increasing lattice constant a, b and c of the films due to an expansion of the lattice parameters with substitution of the smaller S atom (1.84Å) by the larger selenium atom (1.98Å).[5] The linear variation of lattice parameters of $SnS_{1-x}Se_x$ thin films is in good agreement with the Vegard's law.[5]

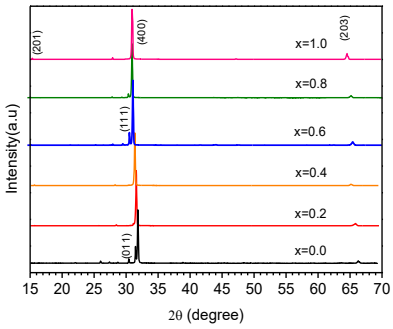

Figure 1. XRD patterns of CSS-$SnS_{1-x}Se_x$ thin films.

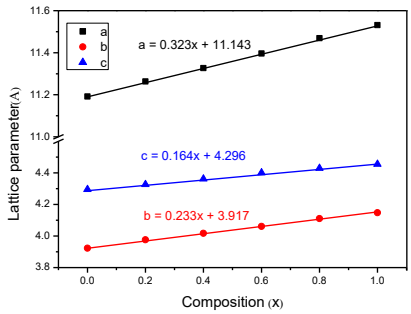

Figure 2. Variation of lattice parameters of CSS-$SnS_{1-x}Se_x$ thin films.

SEM micrographs of $SnS_{1-x}Se_x$ thin films are shown in Figure 3. The images are marked with different compositions of Se from x=0.0 to x=1.0. We noticed that the films at x=0.0 had a less preferred (400) plane orientation resemble a rectangular plate-like form with dimension around 7 µm in length, 5 µm in width and 0.5 µm in thickness. Increasing preferred

orientation was observed when the composition (x) increased. However, the thin square plate-like grain orientated perpendicularly to substrate plane was observed for x=1.0. The pronounced preferential orientation along the (400) direction observed in SnSe films was also reported elsewhere.[6] This result is consistent with the XRD data with the high texture coefficient of 2.163.

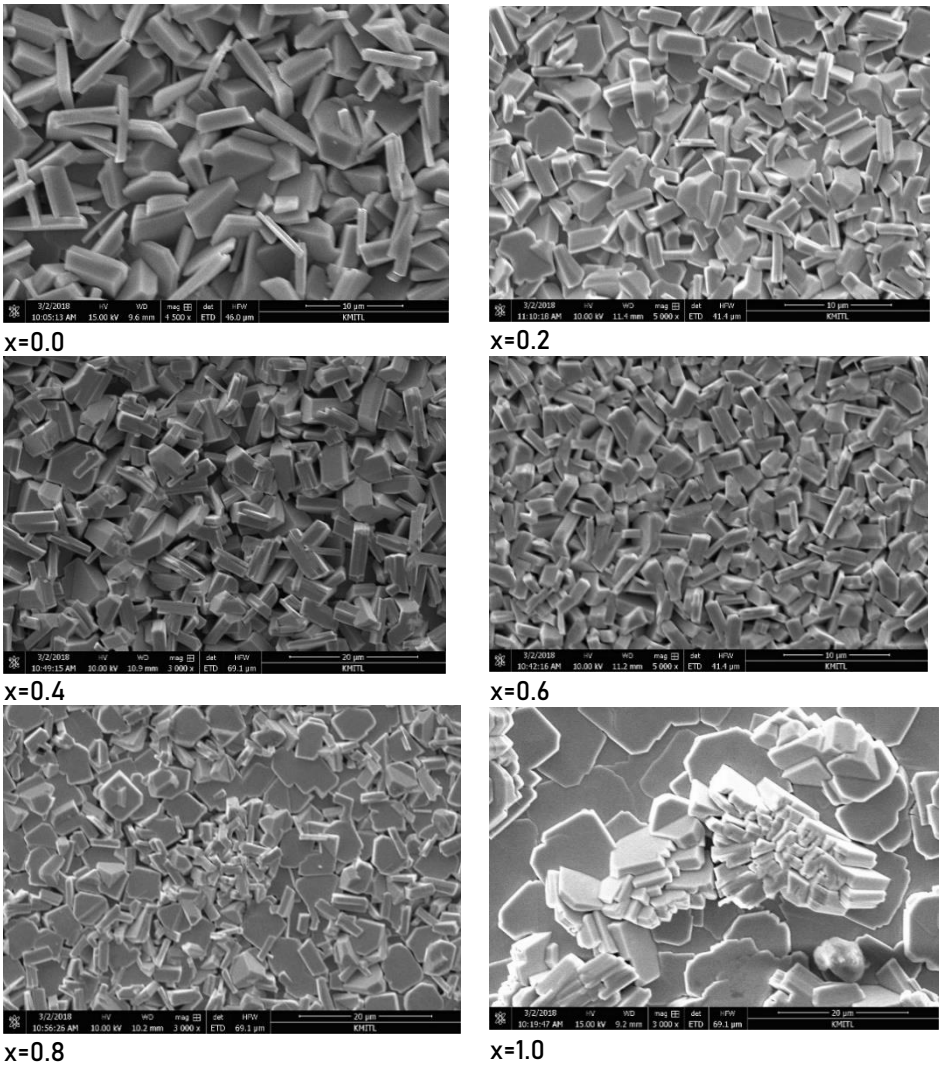

Figure 3. SEM images of CSS-$SnS_{1-x}Se_x$ thin films.

Elemental analysis: The percentage of all the elements presented in the synthesized $SnS_{1-x}Se_x$ thin films was determined by EDS spectroscopy (Figure 4). Qualitative analysis indicates the presence of only desired elements i.e. Sn, S and Se, whereas the quantitative analysis shows a successive increase in Se concentration with $SnS_{1-x}Se_x$ composition between x=0 to 1.0. The elemental compositions of the films corresponding to the different compositions of Se are provided the more detail in Table 1. The stoichiometry of the alloy films was found to be very close to the experimental value.

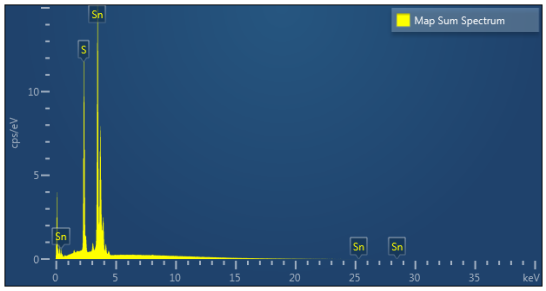

Full Scale 2765 Cursor.0.000

x =0.0

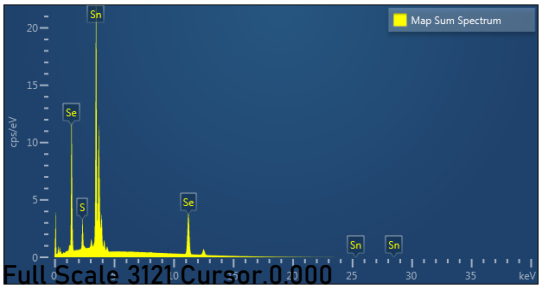

Full Scale 3121 Cursor.0.000

x =0.2

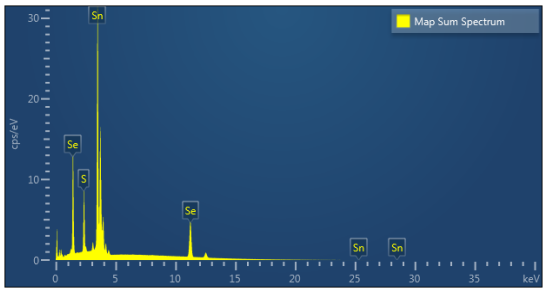

Full Scale 3105 Cursor.0.000

x =0.4

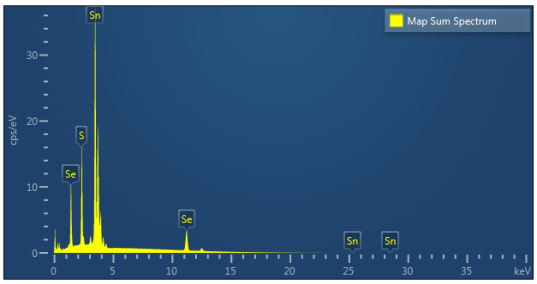

Full Scale 3176 Cursor.0.000

x =0.6

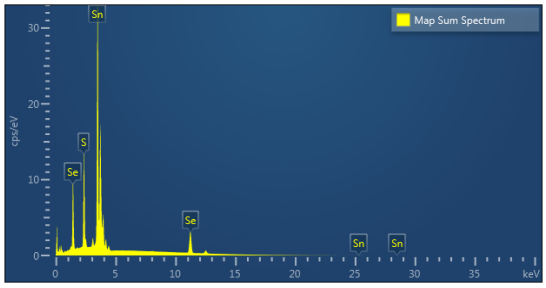

Full Scale 2765 Cursor.0.000

x =0.8

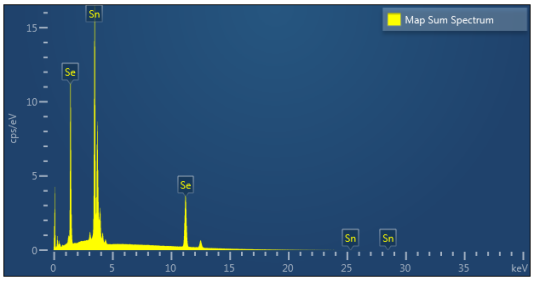

Full Scale 2765 Cursor.0.000

x =1.0

Figure 4. EDS images of CSS-$SnS_{1-x}Se_x$ thin films.

Table 1. Elemental analysis of CSS-$SnS_{1-x}Se_x$ thin films by EDS.

Composition (x)	Weight (%)			Atomic (%)		
	Sn	S	Se	Sn	S	Se
x=0.0	80.20	19.80	-	52.25	47.25	-
x=0.2	69.10	10.15	20.75	50.15	27.24	22.63
x=0.4	69.47	10.97	19.76	49.97	28.67	21.36
x=0.6	63.14	6.33	30.53	47.67	17.69	34.65
x=0.8	61.64	3.20	35.16	48.79	9.37	41.84
x=1.0	57.78	-	42.22	47.66	-	52.34

FTIR analysis: FTIR spectroscopy was used to investigate the information on the functional groups of organic and inorganic matters contained in $SnS_{1-x}Se_x$ thin films. The FTIR analysis was carried out on the films with different compositions by measurement in the range 400-4000 cm^{-1}. The FTIR spectra could be illustrated by all kinds of peaks obtained by SnS_{1-}

$_xSe_x$ samples as shown in Figure 5. The typical vibrational modes of films (for x=0) are given in Table 2. The characteristic peak of stretching vibration was observed at 665 cm^{-1} which was close to 686 cm^{-1} reported in the literature.[7] This peak showed a red-shift from 665 cm^{-1} to 640 cm^{-1} as the rising of Se composition from x = 0 to x = 1.0, indicating the substitution of Se atom in S site of the lattice.

Optical properties: The optical transmission spectra of films deposited with different Se contents in the wavelength rage of 400-2000 nm are shown in Figure 6. As the different Se contents, the gradual shift of absorption edge of $SnS_{1-x}Se_x$ thin films were clearly observed. These results guide that the optical band gap (E_g) value can be tuned as a function of Se content. The optical band gap value of the films was determined using Tauc's relation as the following equation:[8]

$$\alpha h\nu = A(h\nu - E_g)^n \qquad \text{(i)}$$

where α is the absorption coefficient can be calculated by lnT = -αd (d is thin film thickness and T is transmittance). A is a constant, E_g is the optical band gap and the exponent n value being 1/2, 2, 3/2 and 3 corresponds to the allowed direct, allowed indirect, forbidden direct and forbidden indirect transition, respectively. The plots in Figure 7a for direct transition show straight lines yielding band gap values which decrease from 1.18eV to 0.95eV with increasing composition (x). As for SnSe thin films in Figure 7b, it was found two extra indirect band gaps of 0.80 and 0.92, respectively. Figure 8 shows the variation of band gap value from 1.18eV (for SnS films) to 0.95eV (for SnSe films). The decreasing of direct band gap is resulted from the addition of Se atom in SnS lattice.

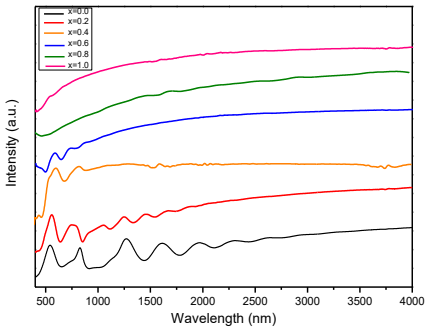

Figure 5. FTIR spectra of CSS-$SnS_{1-x}Se_x$ thin films.

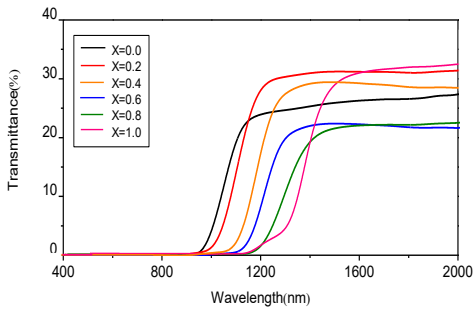

Figure 6. Transmittance spectra of CSS-$SnS_{1-x}Se_x$ thin films.

Table 2. Important IR stretching frequencies of $SnS_{1-x}Se_x$ (for x=0.0) thin films.

Wavenumber (cm^{-1})	Assignment Vibration Mode	References
665.0	stretching vibration of SnS	[7]
1030.0	SO_3 stretching vibration	[9]
1780.5	sulfide stretching vibration	[7]
2117.3	C=C vibration	[7]

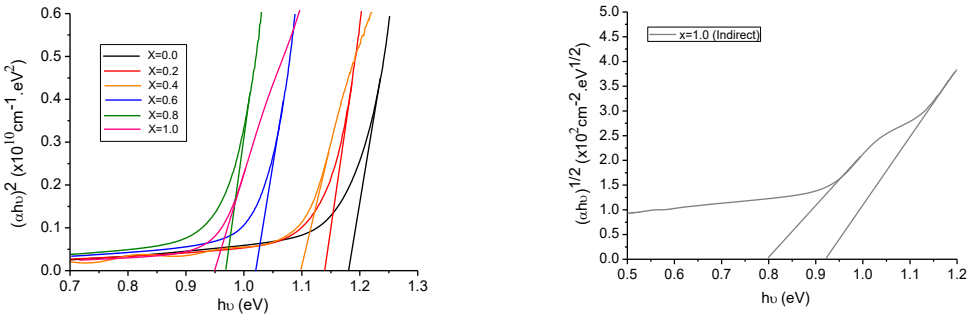

(a) (b)

Figure 7. (αhv)2 vs. hv plot for (a) direct band gap of $SnS_{1-x}Se_x$ thin films and $(\alpha h\nu)^{1/2}$ vs. hv plot for (b) indirect band gap of SnSe thin films.

Electrical properties: The electrical properties of $SnS_{1-x}Se_x$ thin films were investigated by resistivity and Hall effect measurements with van der Pauw method. Figure 9 shows the resistivity, hole concentration and Hall mobility of $SnS_{1-x}Se_x$ thin films with different compositions of Se. The positive sign of the Hall coefficient confirmed the p-type conductivity in all prepared films. The resistivity (ρ) of $SnS_{1-x}Se_x$ thin films is inversely proportional the product of hole concentration (p) and mobility (μ) as the following relation:[10]

$$\rho = 1/pe\mu \qquad \text{(ii)}$$

The resistivity value firstly increased from 0.38 Ω·cm at x = 0.0 to the maximum value of 1.40 Ω·cm at x = 0.2, then decreased to minimum value of 0.01 Ω·cm at x = 1.0. The hole concentration initially decreased with the increase of composition (x) down to x = 0.2 and then gradually increased to the minimum value at x = 1.0. The variation of Hall mobility value seemly exhibited the similar fashion to resistivity behavior.

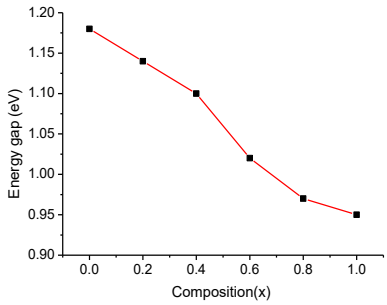

Figure 8. Variation of E_g of CSS-$SnS_{1-x}Se_x$ thin films.

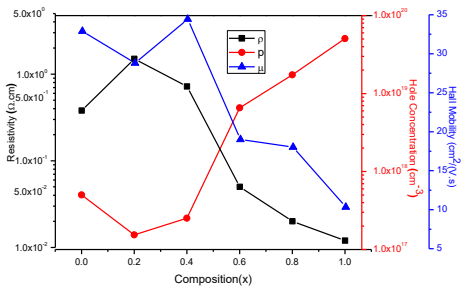

Figure 9. Variation of ρ, p and μ of CSS-$SnS_{1-x}Se_x$ thin films.

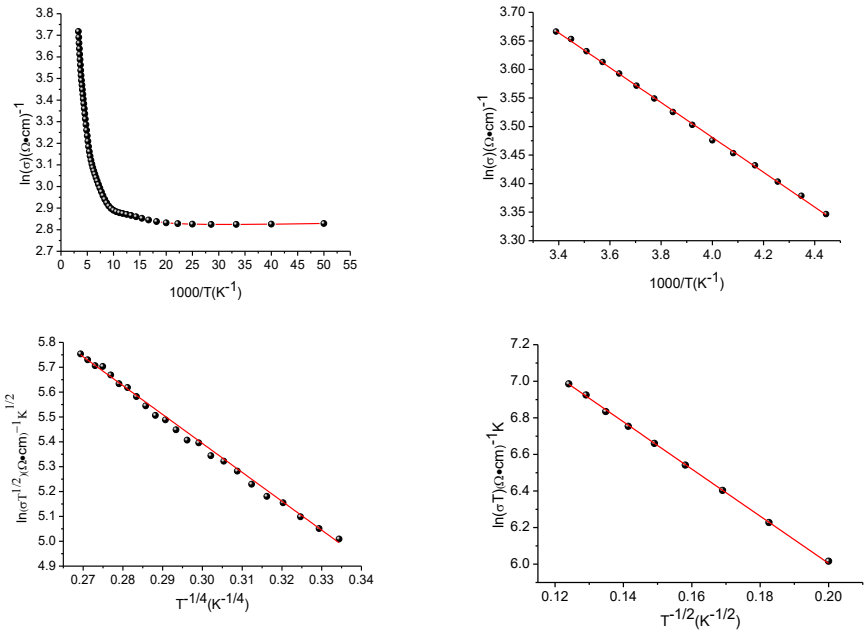

Figure 10. (a) ln(σ) vs 1000/T plot in the range of 300-20 K, (b) ln(σ) vs 1000/T plot in the range of 295-220 K, (c) ln(σ$T^{1/2}$) vs $T^{-1/4}$ plot in the range of 190-125 K and (d) ln(σT) vs $T^{-1/2}$ plot in the range of 105-50 K for CSS-$SnS_{1-x}Se_x$ thin films (at x=0.6).

The Arrhenius plot of ln(σ) and 1000/T for the films with x=0.6 is shown in Figure 10 (a), no single mechanism can be fitted in the entire curve of conductivity. At high temperature, the electrical conductivity of the sample is dominated by thermal activation across grain boundaries. The temperature dependence of the electrical conductivity of the films was firstly analyzed using Nearest Neighbor Hopping (NNH) as the following expression:[11]

$$\ln\sigma = \frac{E_{\mathrm{NNH}}}{k_B T} + \ln\sigma_{0,\mathrm{NNH}} \qquad \text{(iii)}$$

where $\sigma_{0,NNH}$ is a constant, E_{NNH} is the Nearest Neighbor activation energy, and *k* is the Boltzmann's constant.

The hole concentration (N_a) was calculated by using the following equation:[11]

$$N_a = \left[\frac{E_{NNH} 4\pi\varepsilon_s}{0.99e^2}\right]^3 \qquad \text{(iv)}$$

$$T_{C1} = \frac{e^2 N_d^{\frac{2}{3}} \xi_{Mott}}{k_B(4\pi\varepsilon_s)} \qquad \text{(v)}$$

As shown in Figure 10(b), a good linear relationship can be observed in the Arrhenius plot in the high temperature range (295-220 K). The important parameters obtained from fitting curve were listed in Table 3. Figure 10 (c) shows the plot of ln(σ$T^{1/2}$) vs $T^{-1/4}$. The plot was found to have been linear at temperature range of 190-125 K. This indicated that the conduction is governed by Mott variable-range hopping (Mott-VRH) instead of the NNH model at high temperature. The Mott's parameters can be calculated from the relation:[12]

$$\ln\left(\sigma T^{\frac{1}{2}}\right) = -\left(\frac{T_{0,\mathrm{Mott}}}{T}\right)^{\frac{1}{4}} + \ln\sigma_{0,\mathrm{Mott}} \quad \text{(vi)}$$

$\sigma_{0,\mathrm{Mott}}$ is a characteristic temperature coefficient which depends on the density of states $N_0(E_F)$ at the Fermi-level in the form:[12]

$$T_{0,\mathrm{Mott}} = \frac{18\alpha^3}{\frac{k}{q}N_0(E_F)} \quad \text{(vii)}$$

The localization length (ξ_{Mott}) is given as:

$$\xi_{Mott} = \frac{1}{\alpha} \quad \text{(viii)}$$

where α is the coefficient of the exponential decay of the localized states wave function and is assumed to be 1.24×10^{-7} cm^{-1}.The density of localized state ($N_0(E_F)$) at Fermi-level is

$$N_0(E_F) = \frac{18\alpha^3}{\frac{k}{q}T_{0,\mathrm{Mott}}} \quad \text{(ix)}$$

The hopping distance ($R_{hop,Mott}$) and average hopping energy ($W_{hop,Mott}$) are determined by using the following relation:[12]

$$R_{\mathrm{hop,Mott}} = \left(\frac{9}{8\pi\alpha\frac{k}{q}\mathrm{T}N_0(E_F)}\right)^{\frac{1}{4}} \quad \text{(x)}$$

and

$$W_{\mathrm{hop,Mott}} = \frac{3}{4\pi R^3_{\mathrm{hop,Mott}}N_0(E_F)} \quad \text{(xi)}$$

The Mott-VRH conduction parameters are listed in Table 4. The VRH conduction process exists in the grain boundary at temperatures at which the carriers do not have sufficient energy to cross the potential barrier and to transfer themselves into the crystallite by the process of thermionic emission. At very low temperature range (105-50 K), the measured data were satisfied the Efros-Shklovskii variable-range hopping (ES-VRH). In this electrical conduction mechanism region, the electron interaction caused the density of state at Fermi-level is separated and became to the coulomb gap. The conductivity in ES-VRH model is given by

$$\ln(\sigma T) = -\left(\frac{T_{0,\mathrm{ES}}}{T}\right)^{\frac{1}{2}} + \ln\sigma_{0,\mathrm{ES}} \quad \text{(xii)}$$

$T_{0,ES}$ is a characteristic temperature coefficient given by

$$T_{0,\mathrm{ES}} = \frac{2.8e^2}{k\xi_{\mathrm{ES}}\varepsilon_s} \quad \text{(xiii)}$$

The hopping distance ($R_{hop,ES}$) and average hopping energy ($W_{hop,ES}$) are determined by using the following relation:[13,14]

$$\frac{R_{hop,ES}}{\xi_{ES}} = \frac{1}{4}\left(\frac{T_{0,ES}}{T}\right)^{\frac{1}{2}} \quad \text{(xiv)}$$

$$W_{hop,ES} = \frac{1}{2} k_B T \left(\frac{T_{0,ES}}{T}\right)^{\frac{1}{2}} \quad \text{(xv)}$$

The Coulomb gap can be estimated from[13,14]

$$\Delta C = k_B \left(\frac{T_{0,ES}}{T_{0,Mott}}\right)^{\frac{1}{2}} \quad \text{(xvi)}$$

The ES-VRH conduction parameters are listed in Table 5.

Table 3. NNH parameters at high temperature of CSS-$SnS_{0.4}Se_{0.6}$ thin films.

Temperature (K)	Range	$\sigma_{0,NNH}$ (10^2S/cm)	E_{NNH} (meV)	T_{C1} (K)	N_a (10^{19} cm^{-3})
295-220		1.10	26.49	195	7.77

Table 4. Mott's parameters at low temperature of CSS-$SnS_{0.4}Se_{0.6}$ thin films.

Temperature Range (K)	$\sigma_{0,Mott}$ (S/cm)	$T_{0,Mott}$ (10^4 K)	$N_0(E_F)$ (cm^{-3}·eV^{-1})	$W_{hop,Mott}$ (meV)	$R_{hop,Mott}$ (nm)	$\frac{R_{hop,Mott}}{\xi_{Mott}}$
190-125	1.55x10^4	4.25	1.64x10^{24}	16.3	20.71	3.94

Table 5. ES's parameters at very low temperature of CSS-$SnS_{0.4}Se_{0.6}$ thin films.

Temperature Range (K)	$\sigma_{0,ES}$ (S/cm)	$T_{0,ES}$ (10^2 K)	ξ_{ES} (nm)	$W_{hop,ES}$ (meV)	ΔC (μeV)	$\frac{R_{hop,ES}}{\xi_{ES}}$
105-50	1.13	3.43	160.75	8.18	7.75	0.45

Conclusion: $SnS_{1-x}Se_x$ thin films in the entire range ($0 \leq x \leq 1$) were successfully prepared by close spaced sublimation method. The effect of addition of Se content on the structural, optical and electrical properties was studied. XRD results indicated that all of compositions (x) of $SnS_{1-x}Se_x$ belong to orthorhombic structure. The value of direct band gap decreased from 1.18 to 0.95 eV as Se composition (x) increased from 0 to 1.0. In addition, it was found that SnSe films presented two extra indirect band gap values being 0.80 and 0.92 eV, respectively. From FTIR transmission spectra, the characteristic peak of stretching vibration revealed a red-shift from 665 cm^{-1} to 640 cm^{-1} as increasing of Se composition from x = 0 to x = 1.0, indicating the substitution of Se atom in S site of the lattice. The positive sign of the Hall coefficient confirmed the p-type conductivity in all $SnS_{1-x}Se_x$ thin films. In the temperature range of 20-300 K, it was shown that three types of conduction mechanisms can be expected such as thermionic emission across grain boundary at high temperature range (220-295 K), the Mott variable-range hopping (Mott-VRH) at low temperature range (125-190 K) and the Efros-Shklovskii variable-range hopping (ES-VRH) at very low temperature range (50-105 K). The films with x=0.4 showed the highest mobility and low resistivity values which may suitable to solar cell application.

References:
1. Ektarawong A, Alling B. J. Phys.: Condens. Matter. 2018;30:29LT01-1-29LT01-5.
2. Kafashan H, Azizieh M, Balak Z. Appl. Surf. Sci. 2017;410:186-195.
3. Kul M. Vacuum. 2014; 107: 213-218.
4. Wongcharoen Ng, Gaewdang T. IOP Conf. Ser.: Mater. Sci. Eng. 2018;383:012007-1-012007-5.
5. Khan MD, Aamir M, Murtuza G, Malik MA, Revaprasadu N. Dalton Trans. 2013;330: 202-208.
6. Nicolas D, Claire J, Robert G, Ivan P. Thin Solid Films. 2008;516:4750-4757.
7. Mani P, Manikandon K, Joseph Prince J. J. Mater Sci: Mater Electron. 2016;27:9255-9264.
8. Huang CC, Lin YJ, Chuang CY, Yang YW. J.Alloys Compd. 2013;553:208-211.
9. Henry J, Mohanraj K, Kannan S, Barathan S, Sivakumar G. Nanoscience. 2015;10:78-85.
10. Asfandiyar A, Wei TR, Zhiliang L, Sun FH, Wu CF. Scientific Reports. 2017;7:43262-1-43262-7.
11. Kumar R, Khare N. Thin Solid Films. 2008;516:1302-1307.
12. Mott NF, J. Non Cryst. Solid. 1968;1:1-17.
13. Shklovskii BI, Efros AL. Electronic Properties of Doped Semiconductor (Springer- Verlag, Berlin, 1984).
14. Efros AL, Shklovskii BI. J.Phy. C. 1975;8:L49-L50.

Acknowledgements: This research is financially supported from Faculty of Science, King Mongkut's Institute of Technology Ladkrabang (KMITL) and thankful the Photonic Materials Research Laboratory (PMRL) facilities to carry out the research work.

F_002_PF: EFFECTS ON TRIBOLOGICAL BEHEVIORS OF SYNTHETIC HYDROCARBON BASED LUBRICANT FOR MICROELECTRONIC APPLICATIONS

Chanikan Polpattanakul[1], Duangamol Tungasmita[2], Panadda Dechadilok[3], Benjie L. Fernandez[4], Sukkaneste Tungasmita[3,*]
[1]Petrochemistry and Polymer Science Program, Faculty of Science, Chulalongkorn University, Bangkok 10330, Thailand
[2]Department of Chemistry, Faculty of Science, Chulalongkorn University, Bangkok 10330, Thailand
[3]Department of Physics, Faculty of Science, Chulalongkorn University, Bangkok 10330, Thailand
[4]Western Digital Co. Ltd., Bang Pa-in, Phra Nakhon Si Ayutthaya 13160, Thailand
*e-mail: Sukkaneste.T@chula.ac.th

Abstract: During the lapping process in the hard disk drive fabrication, petroleum-based lubricant is employed in order to reduce heat from the abrasive and prevent materials corrosion. In this work, the functional synthetic hydrocarbon-based lubricants, was characterized using the ball-on-disk tribometer for its tribological properties. The coefficient of friction (COF) of stainless steel ball on the lubricated alumina-titanium carbide surfaces was investigated and the friction regime was determined from the power law relationship. Unlike COF obtained in absence of the lubricant that was independent of the sliding speed, COF measured from an experiment employing synthetic hydrocarbon-based lubricant is found to decrease as a function of the sliding speed, indicating that the friction regime in the presence of synthetic hydrocarbon-based lubricant differs from that of the ball sliding on a dry surface.

Introduction: Hard disk drive (HDD) is known to be crucial in storing the digital data both inside and outside computer via cloud storage or external drive. Within the HDD, there is an important device called a magnetic read-write head or "slider" which is used for reading and writing the data on media disc by transform a magnetic field into an electrical current. During the slider fabrication, the lapping process improves the efficiency of the slider by removing the excess material of slider until the desired slider thickness is achieved. However, in the final lapping process, the surface of slider and lapping plate are grinded against one another, leading to the occurrence of friction and wear on the slider surface. The functional lubricant is employed in order to reduce dissipative heat, smear and wear in this process. [1-3]

Recently, the utilized lubricant is ethylene glycol (EG)-based lubricant. However, due to the lubricant being polar, the structure of slider that consists of multi-layers of thin film materials is found to be corroded. Petroleum-based lubricants, non-polar lubricants, are, then, introduced to prevent the corrosion in final lapping process. In addition to contributing to corrosion prevention, petroleum-based lubricants are found to exhibit a better wettability property than EG lubricants. In this application, a functional synthetic hydrocarbon-based lubricant, was chosen to be examined for its tribological properties.

In the research work, the effects on the tribological characteristics and lubrication behaviors of petroleum-based lubricant was studied by using the ball-on-disk tribometer. The coefficient of friction (COF) values corresponding to friction on the lubricated AlTiC surfaces were obtained by having stainless steel ball sliding against the alumina-titanium carbide (AlTiC) surface where different normal forces and surface sliding speeds were varied. The friction regime was also determined from the relationship between COF and sliding speed by using the power law relationship to identify the sliding behavior between both surfaces [4].

Methodology: The synthetic hydrocarbon-based lubricant employed in this work, is obtained from Western Digital (Thailand) Co., Ltd. This synthetic hydrocarbon-based lubricant has a hydrocarbon chain in the range of C_{12} to C_{20}, with the viscosity about 3.77 cP (at 25°C)

The tribological characterizations were measured by using the Bruker CETR-UMT-2 microtribometer with a ball-on-disk configuration as the schematic diagram shown in Figure 1 [5]. The alumina-titanium carbide (AlTiC) wafers were obtained from KYOCERA Asia Pacific Pte Ltd. This AlTiC wafer has three inches diameter with the surface hardness of 2000 HV and the surface roughness of 10 nm. COF values were obtained by having probe of AUS304 steel ball sliding against the AlTiC surface. To mimic the HDD slider lapping process, the sliding ball speeds and the load forces were set to match and comparable to the actual fabrication processes.

The friction regime and sliding behavior were determined from the relationship between COF and sliding speed by using the power law relationship. If COF is found to be independent from the sliding speed, the friction regime is the boundary regime where the surface roughness is much larger than the lubricant thickness, and the dissipative heat is generated from contacts between solid surfaces. If COF decreases as a function of sliding speed, it indicates that the lubricant thickness is comparable to the surface roughness, and the occurred friction belongs to a mixed regime where the friction is due to a combination of contacts between solid surfaces and those of solid-liquid interfaces. Based on the power law of ice friction [4], in this regime, COF α $v^{-1/2}$ where v is the sliding speed. If COF increases as a function of sliding speed, the lubricant thickness is much larger than the surface roughness, and the friction is due to the fluid shear stress within the lubricant layer; this regime is often referred to as a hydrodynamic regime. In this regime, COF α $v^{1/2}$ according to the power law of ice friction [4].

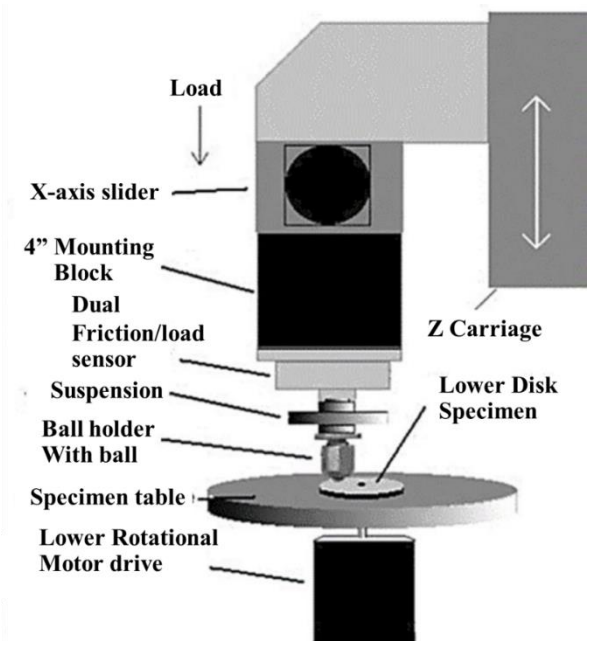

Figure 1. Schematic diagram of a ball-on-disk tribometer [5]

Results and Discussion: The typical COF characteristic COF graph of synthetic hydrocarbon-based lubricants on AlTiC surface is shown in Figure 2. The COF characteristic graph can be divided into 3 zones. The 1st zone is approaching process as the tip of steel ball approached

the AlTiC disk surface. the 2nd zone is from the process as the ball probe landed and bounced on the surface and the 3rd zone is the zone where the COF value became stable.

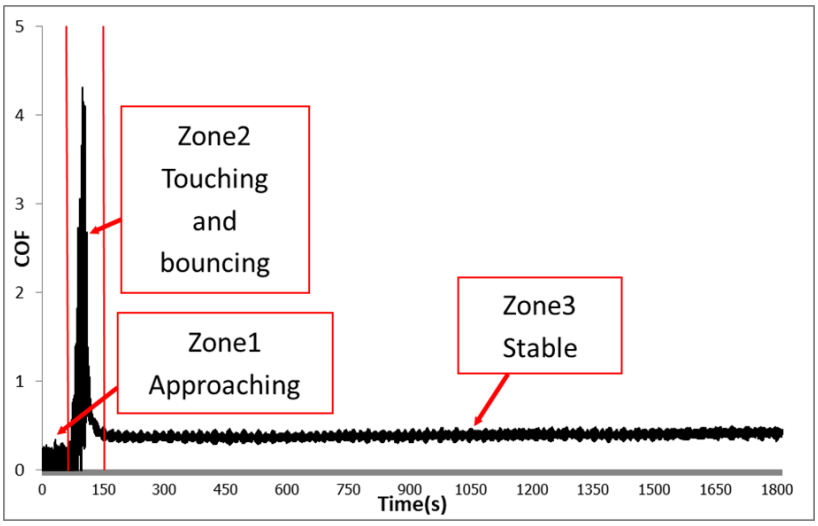

Figure 2. Zones observed for measured coefficients from the friction force exerted on a ball in relative motion with surfaces covered with functional synthetic hydrocarbon-based lubricants.

Moreover, it has been found in our previous study that, if the lubricant is not employed and the AlTiC surface was treated as a dry surface, the COF is independent of the sliding speed, indicating that the generated friction belongs to a boundary friction as expected [6]. In this present work, the effects of functional synthetic hydrocarbon-based lubricants on COF is examined: in Figure 3, obtained COF is presented as a function of the normal forces. Results indicated that COF decreased as the normal forces increased in accord with the ice friction model of Oksanen and Keinonen [4] where COF was predicted to decrease as a function of the applied normal force. This validated a further comparison between the obtained experimental data of the present work and their model.

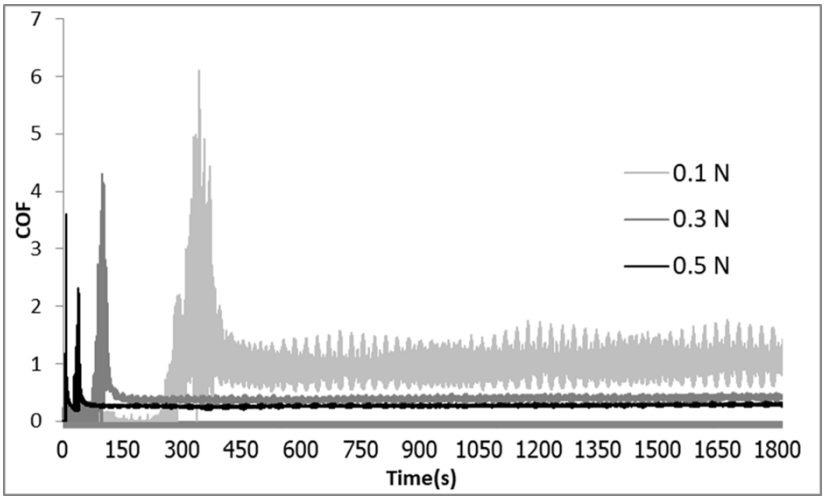

Figure 3. Temporal profiles of COF of functional synthetic hydrocarbon-based lubricants on AlTiC surface as a function of load force at the sliding speed of 4100 mm/min

To investigate the effects of sliding speed on COF, the value of the sliding speed was varied from 4100 mm/min to 6150, 8200, 10250 and 12300 mm/min. As shown in Figure 4, COF is presented as a function of the sliding speed in a log-log plot. These results show that the COF decreases as a function of $v^{-0.321}$ and $v^{-0.325}$ at the normal force of 0.3 N and 0.5 N, respectively. This power law relationship between COF and v is unprecedented. As the power of COF α $v^{0.3}$ lies in between that of the mixed regime (COF α $v^{1/2}$) and that of the boundary regime (COF α v^{0}), it can be speculated that the friction behavior is in transition between the boundary regime (where the friction is generated from contacts of solid surfaces) and the mixed regime (where the friction is generated from solid-solid and solid-liquid contacts). During the lapping process, the solid-solid contacts are preferred as it is likely to lead to a more efficient material removal rate and a faster method to achieve the designed slider thickness, as the COF characteristic is shown in Figure 5 [6]. To ensure that the friction would belong to a boundary regime and that COF is not varied as a function of sliding speed, an additive that has a properties of a surfactant should be added to this synthetic hydrocarbon-based lubricant. The surfactant is found to decrease the lubricant contact angle [7] and is likely to reduce the lubricant thickness relative to the surface roughness. This could lead to a friction regime transition back to the desired boundary friction regime. The effects of the surfactant additive within this functional synthetic hydrocarbon-based lubricant on friction on an AlTiC surface is one possible direction for future investigations.

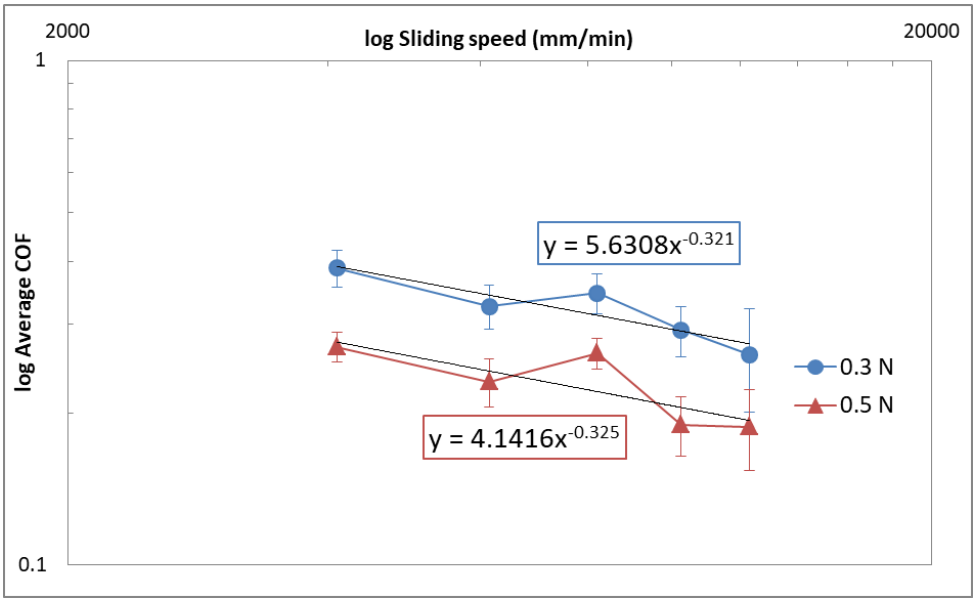

Figure 4. The relationship between COF as a function of sliding speed of functional synthetic hydrocarbon-based lubricant on AlTiC surface

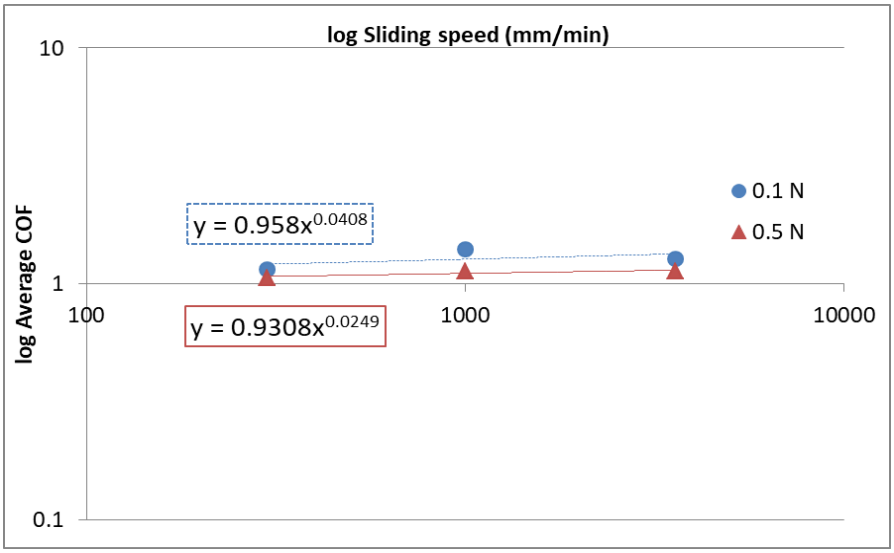

Figure 5. The relationship between COF as a function of sliding speed of dry surface contact (no lubricant on AlTiC surface) which COF values are independent from sliding speeds.[6]

Conclusions: The tribological characteristics and lubrication behaviors of the functional synthetic hydrocarbon-based lubricant, a petroleum-based lubricant, was studied by using the ball-on-disk tribometer. As the synthetic hydrocarbon-based lubricant was employed and the applied normal force was varied, the coefficient of friction decreased as the normal forces increased. Based on the relationship between COF and the sliding speed, the friction regime is found to be in a transition between the boundary regimes (friction generated from between solid-solid contacts) and the mixed regime (friction generated from a combination of solid-solid and solid-liquid contact). To ensure a transition back to a boundary regime where solid-solid contact would lead to a larger slider material removal rate, a surfactant additive should be added to this synthetic hydrocarbon-based lubricant in order to reduce the lubricant thickness; the effect of the surfactant on the tribological characteristics should be further investigated.

References:

1. Castillo J, Bhushan B. CRC Press: Florida. 2006;15-78.
2. Kim DE, Chung KH, Cha KH. Tribol Int. 2003;36:467-473.
3. Chiba H, Takeda M, Nakamura N, Watanabe K. Tribol Int. 2003;36: 367-369.
4. Oksanen P, Keinonen J. Wear. 1982;78:315- 324.
5. CETR-UMT Hardware Installation and Application Manual. Campbell USA: Center for Tribology. 2009.
6. Jitphayomkun S, Dechadilok P, Tungasmita D, Tungasmita S. JMMM. 2019;29(1):63-68.
7. Seesomdee C, Dechadilok P, Tungasmita S. (Senior's thesis) Department of Physics, Faculty of Science, Chulalongkorn University.2018.

Acknowledgements: The authors would like to acknowledge the supports on this work from the Western Digital Corporation, the petrochemistry and polymer science program, faculty of science and the graduate school (Chulalongkorn University Graduate School Thesis Grant), Chulalongkorn University.

F_003_PF: FABRICATION AND CHARACTERIZATION OF $(CdS)_{1-x}(ZnTe)_x$ AND $CuSbS_2$ THIN FILMS FOR PHOTODIODE APPLICATION

Dusit Thueman*, Ngamnit Wongcharoen, Thitinai Gaewdang
Department of Physics, Faculty of Science, King Mongkut's Institute of Technology Ladkrabang, 1, Soi Chalongkrung 1, Ladkrabang District, Bangkok 10520, Thailand
*e-mail: 59605090@kmitl.ac.th

Abstract: $(CdS)_{1-x}(ZnTe)_x$ ($0 \leq x \leq 1$) and $CuSbS_2$ thin films were deposited on glass substrate by a single source vacuum thermal evaporation method. The sets of CdS, ZnTe and Cu_2S, Sb_2S_3 powders with high purity grade were used as the precursors for the first kind and for the second kind of desired films, respectively. The XRD patterns showed that $(CdS)_{1-x}(ZnTe)_x$ thin films were crystallized in pure hexagonal phase with (002) preferred orientation at $x \leq 0.2$. While, $x \geq 0.8$, these films were crystallized in pure cubic phase with (111) preferred orientation. For the composition x=0.4 and 0.6, the hexagonal and the cubic phases were appeared to coexist in the system and the films became less preferentially oriented. However, $CuSbS_2$ phase belonging to orthorhombic crystal structure with small trace of Sb_2S_3 and $Cu_{1.8}S$ phases was formed after the films were annealed at 350°C in pure nitrogen atmosphere for 60 min. FESEM and AFM were used to study morphological features of the films. The optical transmission spectra is calculated to find the energy gap values of the films. Electrical properties were performed by Hall effect measurements with van der Pauw method. In addition, we fabricated $(CdS)_{0.9}(ZnTe)_{0.1}/CuSbS_2$ heterojunction thin films by thermal evaporation method deposited on ITO substrate. Electrical properties of the heterojunction were investigated by means of I-V and C-V characterizations. Under reverse bias condition, it showed a good photoresponse under illumination by ELH halogen lamp and a high pressure mercury vapor lamp. This behavior indicates that the device may be a suitable candidate for white light and UVA light photodiode applications.

Introduction: The II–VI compounds are very popular polycrystalline semiconducting materials studied for many years and a wide range of optoelectronic and photovoltaic applications.[1-3] Cadmium sulfide (CdS) and zinc telluride (ZnTe) belong to II–VI family and crystalline structure is hexagonal wurtzite for CdS and cubic zincblende for ZnTe, respectively.[4-7] The energy gap values of CdS and ZnTe are approximately 2.40 and 2.20 eV, respectively.[7-9] CdS and ZnTe can be mixed so as to provide $(CdS)_{1-x}(ZnTe)_x$ alloys which can lead to discover new semiconductor materials that may be suitable for achieving the tasks of enhanced resistance towards photo-corrosion and increased absorption of solar spectrum. Based on our literature investigation, a few reports are dealt with crystal structure of $(CdS)_{1-x}(ZnTe)_x$ alloys[9,10] but optical and electrical properties are are not yet well understood until now.[11,12] Therefore, it is important to understand in details the optical and electrical properties of these materials because the suitable optoelectronic properties is substantially essential the performance of $(CdS)_{1-x}(ZnTe)_x$ ($0 \leq x \leq 1$) thin films for photovoltaic and photosensor applications. Copper antimony sulfide ($CuSbS_2$) belongs to I-V-VI_2 compound family and crystalline structure is chalcostibite type with orthorhombic system.[13]Additionally, the low cost and application diversity of Sb against In and Ga ,as a result $CuSbS_2$ an popularity material for low cost and large amount of productions. $CuSbS_2$ are being presently studied as a choice to replacing $Cu(In,Ga)Se_2$ as the absorber layer in photovoltaic devices because of their optical properties and electrical properties can be substituted.[14] $CuSbS_2$ is p-type semiconductor with a hole concentration from 10^{16} to 10^{18} cm^{-3} and maximum charge carrier mobility of about 49 $cm^2/(V.s)$.[14] Moreover, $CuSbS_2$ has direct energy gap near the optimum value of 1.7 eV,[15-17] and also a high optical absorption coefficient of among 10^4 and 10^5 cm^{-1}. In this work, both $(CdS)_{1-x}(ZnTe)_x$ and $CuSbS_2$ thin films were prepared by vacuum thermal evaporation on glass substrate. Structural, optical and electrical properties of these films prepared on glass substrate were investigated.

Fabrication of a photodiode having the structure of ITO/$(CdS)_{0.9}(ZnTe)_{0.1}$/$CuSbS_2$ was achieved from the above optimized condition. Electrical properties of the heterojunction were investigated by means of I-V and C-V characterizations. Photoresponse measurements under illumination by an ELH halogen lamp and a high pressure mercury vapor lamp were performed. The reason for higher photosensitivity under UV excitation than under white light illumination will be discussed.

Methodology:

Preparation of $(CdS)_{1-x}(ZnTe)_x$ and $CuSbS_2$ thin films: The fabrication of $(CdS)_{1-x}(ZnTe)_x$ and $CuSbS_2$ thin films by a single source vacuum thermal evaporation method using tungsten boat. To make different compositions of $(CdS)_{1-x}(ZnTe)_x$, we used CdS and ZnTe compounds with high purity of 99.99%. CdS and ZnTe powders were weighed by taking the stoichiometric ratio in order to obtain different compositions of $(CdS)_{1-x}(ZnTe)_x$ films. The starting powders were mixed and mashed during 60 min for obtaining a good homogeneity and further baked at 150°C for 30 min in air. The substrate used to deposit thin films was glass substrate with dimension about 12x25 mm^2. To the cleanness of the glass surface, the glass substrate was subsequently cleaned with deionized water, acetone, ethanol and deionized water again in the ultrasonic bath, respectively. During the film growth processing, the substrate temperature was kept at around 100°C by using a PID temperature controller. The films thickness about 500 nm was used a crystal thickness monitor (Edwards type FTM6). $CuSbS_2$ thin films prepared by using Cu_2S and Sb_2S_3 powders with high purity of 99.99%. Then, the as-deposited films were subsequently annealed at 100-350 °C in nitrogen flow gas for 60 min. The crystalline structure of these films was investigated by XRD with a Brucker D 8 diffractometer using CuK_α radiation. The surface morphology was investigated using LEO 1455VP SEM. The grain size was examined by Park XE-100 AFM. Optical transmission measurements in the wavelength range of 400-1,000 nm were performed with thermos electron corporation, Heios model UV-Vis spectrophotometer. The optical transmittance (T) data can be find the absorption coefficient (α) of the films from using the equation $\alpha = (1/d)\ln(1/T)$ where d is the thickness of the film. Direct energy gap (E_g) of the films was derived by the equation $(\alpha h\nu)^2 = A(h\nu - E_g)$ where α is the absorption coefficient and $h\nu$ is the photon energy, A is a constant. The films electrical properties were interpreted by Hall effect and resistivity which Hall effect measures in the van der Pauw configuration.

Fabrication of $(CdS)_{0.9}(ZnTe)_{0.1}$/$CuSbS_2$ heterojunction: Commercially available ITO coated glass substrate having sheet resistance 60 Ω/square was used for thin film deposition. The preheated substrate was thoroughly rinsed in isopropyl alcohol and then dried under nitrogen flow gas. $(CdS)_{0.9}(ZnTe)_{0.1}$ thin films of 500 nm thickness were grown on ITO coated glass substrate by evaporation method at a base pressure of $5x10^{-5}$ torr and substrate temperature kept at 100°C. Subsequently, 800 nm thick $CuSbS_2$ films were coated on the $(CdS)_{0.9}(ZnTe)_{0.1}$ layer at substrate temperature of 100°C. Then, natural cooling to room temperature was performed by turning off electric power. The device was removed from the evaporation system and subsequently subjected to the pure nitrogen flow gas furnace. The device was annealed at 350°C for 60 min in order to obtain the $CuSbS_2$ phase. Finally, C/Ag contact was made by using carbon and silver paste and then annealed in air at 100°C for 20 min. The I-V characteristics were investigated by using a computer interfaced Keithley 236 current/voltage source. The C-V measurements were carried out with Agilent E4980A precision LCR meter with a frequency 300 kHz. Photoresponse of device was investigated under illumination by ELH halogen lamp and a high pressure mercury vapor lamp.

Results and Discussion:

$(CdS)_{1-x}(ZnTe)_x$ Thin Films: Figure 1 shows the XRD patterns of $(CdS)_{1-x}(ZnTe)_x$ thin films with different compositions (x). The diffraction angle (2θ) varied from 20 to 70°. For x≤0.2, XRD revealed that the films exhibited a hexagonal structure, and agreed well JCPDS file 77-2306, with the preferred orientation of (002) plane. However, when x≥ 0.8, they existed in cubic structure, and agreed well JCPDS file 15-746, with the preferred orientation of (111) plane. For the composition 0.4≤x≤0.6, the hexagonal and cubic phases coexisted in the system and the films became less preferentially oriented. For the composition x≤0.2, the strongest peak intensity of (002) plane shifted to a lower 2θ value with increasing composition (x). In contrast, the strongest peak intensity of (111) plane shifted to a higher 2θ value with increasing composition (x) for the composition x≥ 0.8. However, some small peaks corresponding to the excess Te element appeared in the films with x=1.0. Figure 2 shows the relation of the calculated lattice constants of $(CdS)_{1-x}(ZnTe)_x$ thin films with composition (x). It is clear from figure that the phase changes from hexagonal to cubic when the composition x beyond 0.6. The lattice constant "a" and "c" of hexagonal phase decreased linearly with increasing composition (x) from 0 to 0.6. This behavior in accordance with Vegard's law corresponds to earlier reports.[9,10] This is mainly attributed to the partial replacement of Cd^{2+} ions (ionic radius r=0.78 Å) by Zn^{2+} ions (r=0.60 Å), indicating a reduction in the lattice constant "a" and "c".[9] However, the lattice constant "a" of cubic phase increased linearly with increasing composition (x) from 0.4 to 1.0. This is mainly due to the partial replacement of S^{2-} ions (r=1.84 Å) by Te^{2-} ions (r=2.21 Å) indicating an enhancement in the lattice constant "a". The present lattice constant data clearly suggested that CdS and ZnTe can be combined in the intermediate range (0.4≤ x≤0.6) because the incongruity of ionic radius of S and Te normally excluded the formation of completely miscible lattice in II-VI chalcogenide alloy in bulk except very close when values of compositions x increased.[9]

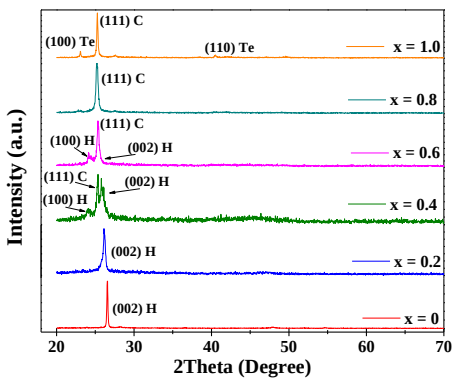

Figure 1. XRD patterns of $(CdS)_{1-x}(ZnTe)_x$ thin films.

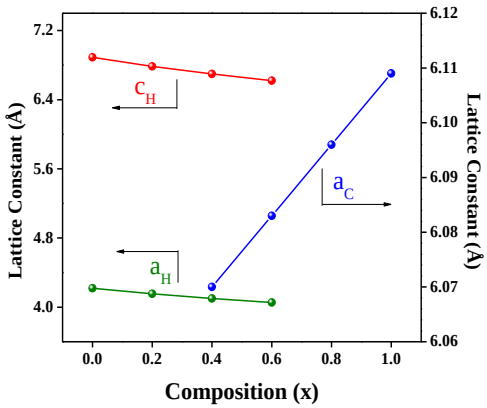

Figure 2. Variation of lattice constant "a"and "c" of $(CdS)_{1-x}(ZnTe)_x$ thin films.

Figure 3 shows AFM images of $(CdS)_{1-x}(ZnTe)_x$ thin films with different compositions. The main difference among films is the distribution of grain size. The grain size values of the thin films were 361, 156, 117, 88, 205 and 264 nm for x=0, 0.2, 0.4, 0.6, 0.8, 1.0, respectively. The corresponding roughness values were 33, 20, 7, 6, 16 and 18 nm, respectively. The morphological differences are possibly due to a change in the crystal structure from hexagonal to cubic system.

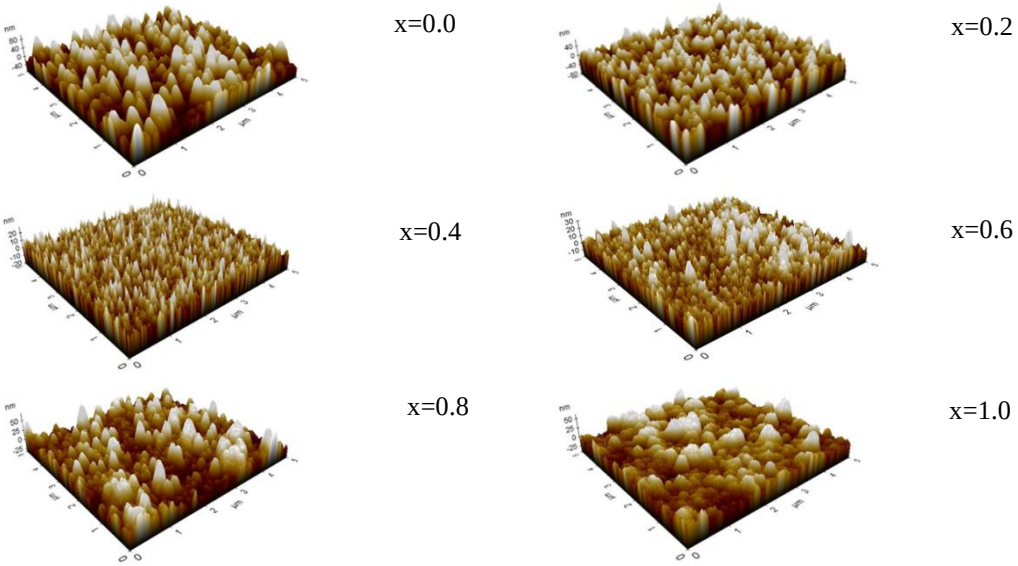

Figure 3. AFM images of $(CdS)_{1-x}(ZnTe)_x$ thin films.

Figure 4 presents the transmission spectra of the $(CdS)_{1-x}(ZnTe)_x$ thin films in the wavelength range 400-1,000 nm. It is seen from the absorption edge of the transmission spectra that shifted towards the larger wavelength with an increase in composition suggesting the decrease of energy gap. The indication that the film is of good quality can be seen from The interference fringes, which are found on some transmission spectrums. Figure 5 shows the energy gap (E_g) of the films estimated by plotting $(\alpha h\upsilon)^2$as a function of energy$(h\upsilon)$.[4,5] The energy gap value decreased from 2.43 eV (corresponding to the E_g value of a CdS bulk material) with a high increasing composition (x) by decreasing through a minimum value of 1.85 eV, and increased to 1.90 eV after that (corresponding to the E_g value of a ZnTe bulk material).

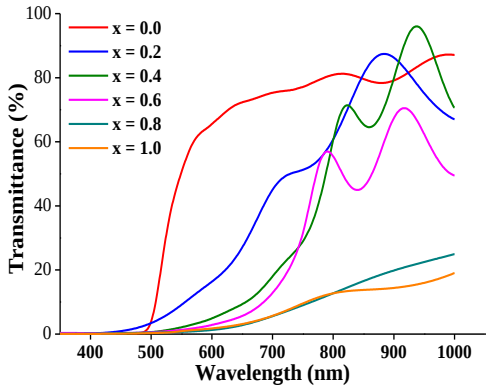

Figure 4. Transmission spectra of $(CdS)_{1-x}(ZnTe)_x$ thin films.

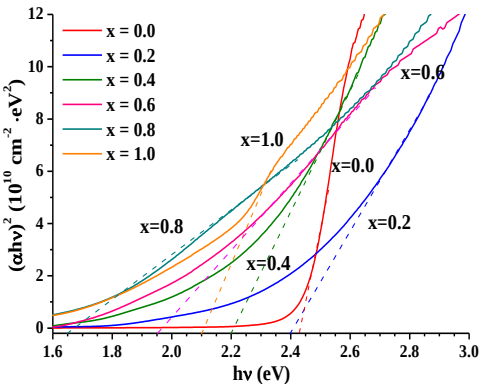

Figure 5. $(\alpha h\upsilon)^2$vs. $h\upsilon$of $(CdS)_{1-x}(ZnTe)_x$ thin films.

The films were investigated by Hall effect and resistivity measurements in van der Pauw configuration to study electrical properties. Variation of resistivity, carrier concentration and mobility against composition (x) is shown in Figure 6. The resistivity of the $(CdS)_{1-x}(ZnTe)_x$ thin films with the different compositions has a wide distribution, and has value in the range

from 10^{-1} to $10^{7}\Omega$ cm. The films conductivity type could be evaluated by considering the sign of Hall voltage. Normally, CdS exhibits n-type while ZnTe exhibits p-type. The conductivity type started to convert from n-type to p-type when composition (x) beyond 0.4 due to auto-compensation of the charge carrier between the electrons and hole.[10] The highest resistivity of 1.18×10^{7} Ω cm was observed for the films with x=0.4. It indicated that the amount of charge carrier between the electrons and hole is approximately the same order or refute. Moreover, CdS-rich phase (for x≤0.4) obviously manifested the higher mobility value than the one of ZnTe-rich phase (for x≥ 0.6).

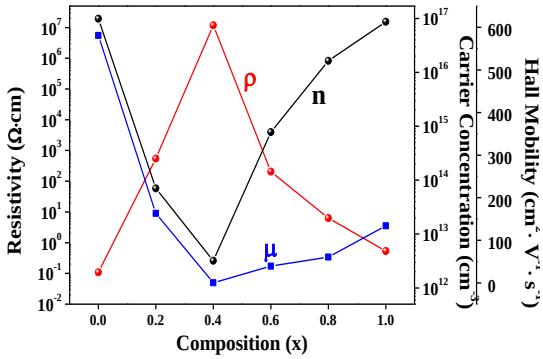

Figure 6. Variation of n, ρ and μ of $(CdS)_{1-x}(ZnTe)_x$ thin films.

$CuSbS_2$ Thin Films: Figure 7 shows XRD patterns of the as-deposited and annealed $CuSbS_2$ films at 100-350°C. It found that the as-deposited and films annealed at 100 and 200 °C had an amorphous structure due to the featureless XRD spectra. While the films annealed at temperature of 250 and 300 °C showed several peaks of the Sb_2S_3 and $Cu_{1.8}S$ phases but when the annealing at 350 °C appeared many peaks corresponding to $CuSbS_2$ orthorhombic phase with dominant (111) diffraction plane. However, Sb_2S_3 and $Cu_{1.8}S$ phases still exist with lower peak intensity compared to the other annealed films.[13] Deterioration of surface morphology was observed on the films annealed at temperature 400°C onwards.

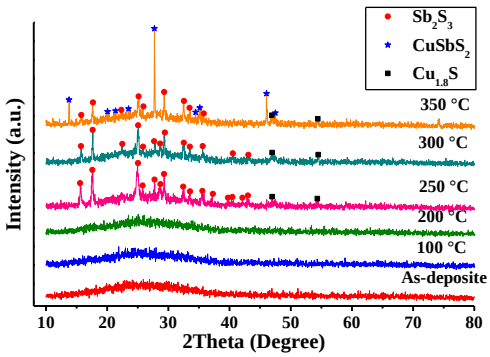

Figure 7. XRD patterns of $CuSbS_2$ thin films.

Figure 8 shows SEM image of $CuSbS_2$ thin films annealed at 350 °C. Surface morphology shows well defined grains with at least two types of grain shapes were observed: a hexagonal-like shape and an irregular shape. Figure 9 shows AFM image of $CuSbS_2$ thin films annealed at 350 °C. Clearly defined grains with the biggest grain size around 293 nm were obtained.

Figure 10 shows the optical transmission spectra of the as-deposited and annealed $CuSbS_2$ films prepared on glass substrate. As increasing annealing temperature from the as-prepared temperature to 350°C, a red-shift of absorption edge was clearly observed. Figure 11 shows $(\alpha h\upsilon)^2$vs. $h\upsilon$ plots in order to find the energy gap (E_g) value. The energy gap value decreased from 2.24 eV down to 1.65 eV when annealing temperature increased from the as-prepared temperature to 250°C and then increased to 1.72 eV when annealing temperature reached to 350 °C.

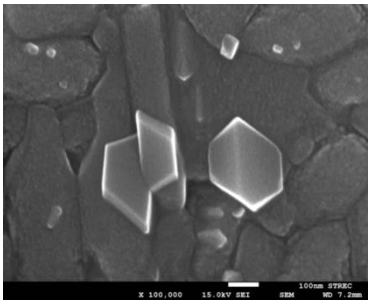

Figure 8. SEM image of $CuSbS_2$ thin films annealed at 350°C.

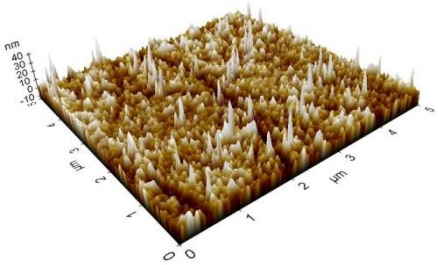

Figure 9. AFM image of $CuSbS_2$ thin films annealed at 350°C.

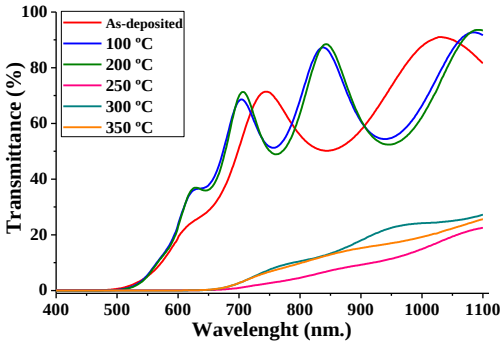

Figure 10. Transmission spectra of $CuSbS_2$ thin films.

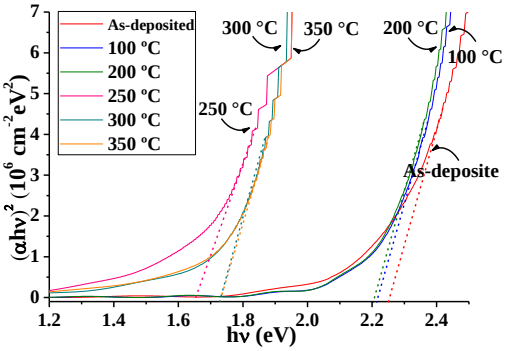

Figure 11. $(\alpha h\upsilon)^2$ vs. $h\upsilon$ of $CuSbS_2$ thin films.

Hall effect and resistivity measurements in the van der Pauw configuration of the films are used to evaluate Electrical properties. We found that all studied films behaved p-type conductivity. Variations between the carrier concentration, resistivity and mobility against the temperature of annealing are shown in Figure 12. The resistivity value increased from 5.62×10^4 to 9.49×10^4 Ω.cm as increasing annealing temperature. In contrast, carrier concentration decreased from 6.85×10^{15} to 3.69×10^{14} cm^{-3} with an increase in annealing temperature. The carrier mobility (μ) of the films increased from 0.02 attain maximum at 0.17 $cm^2/(V.s)$ with annealing temperature increased from the as-prepared temperature to 300°C and then decreased to 0.12 $cm^2/(V.s)$ when annealing temperature further increased to 350°C.

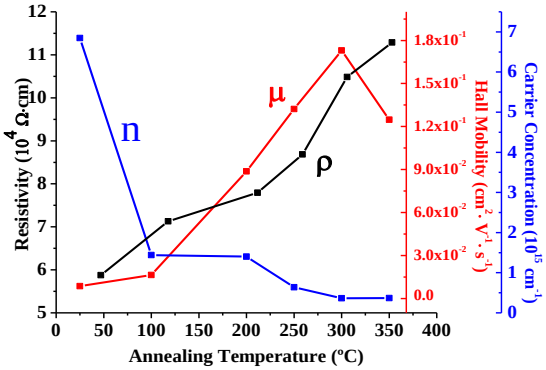

Figure 12. Variation of n, ρ and μ of $CuSbS_2$ thin films.

$(CdS)_{0.9}(ZnTe)_{0.1}/CuSbS_2$ heterojunction: Figure 13a shows I-V characteristics of the $(CdS)_{0.9}(ZnTe)_{0.1}/CuSbS_2$ heterojunction performed at three conditions: in dark (no light), under ELH light illumination and under UVA excitation, respectively. These I-V characteristics show the rectifying behavior confirming the formation of n-$(CdS)_{0.9}(ZnTe)_{0.1}$/p-$CuSbS_2$ heterojunction. Comparing between the illuminated and the dark condition increased current values in both forward and reverse bias voltage. The fabricated p-n heterojunction it confirmed that can behave as a photodiode. As for photosensitivity measurements in this paper, the voltage bias of measurements was set a fixed value of -3V. When the light illumination, the measured absolute current increased significantly: the dark current was about 9.5×10^{-4} A, and the current increased to 2.19×10^{-3} A under ELH light illumination and further increased to 3.97×10^{-3} A under UVA excitation. The sensitivity (S) of the device defined as the ratio of the generated photocurrent to the dark current given by $S = (I_{light} - I_{dark})/I_{dark}$. Thus, sensitivity (S) of the photodiode equals to 22.05 and 40.79, respectively. According to the thermionic emission (TE) theory, the forward current varies with the voltage according to the equation[18]

$$I = I_S[exp(qV/kT) - 1] \quad (1)$$

and

$$I_S = AA^*T^2 exp(q\varphi_B/kT) \quad (2)$$

where q is the charge, A is the device area, A* is the Richardson's constant, n is the ideality factor, k is the Boltzmann's constant, T is the absolute temperature, I_s is the reverse saturation current and ϕ_B is the zero bias barrier height of the diode. From Equation (1), the ideality factor n which is given by[18]

$$n = (q/kT)[dV/d(ln\, I)] \quad (3)$$

Then, we have operated least square fits of Equation (1) to the linear part of the measured lnI-V plots (as shown in Figure 13b) within bias voltage about 0.25-0.6 V. From these fits, the experimental values of I_S were determined at different illumination conditions. Using Equations (2) and (3), the experimental values of the barrier height and ideality factor were determined. The $(CdS)_{0.9}(ZnTe)_{0.1}/CuSbS_2$ heterojunction with a large value of n about 5.78, in dark condition, is far from ideal due to particular distribution of interfacial layer and interface states between $(CdS)_{0.9}(ZnTe)_{0.1}$ thin films and $CuSbS_2$ layer.[18] Ideality factor (n) slightly increased to 6.22 and 6.54 under ELH light illumination and under UVA excitation, respectively. The value of the barrier height was found to be 0.54 eV in dark condition. Its value decreased

to 0.52 and 0.51 eV under ELH light illumination and under UVA excitation, respectively. Figure 13c shows the forward bias logarithmic I-V characteristics for $(CdS)_{0.9}(ZnTe)_{0.1}/CuSbS_2$ heterojunction in dark, under ELH light illumination and under UVA excitation, respectively. The graph is divided into three regions. Region I appears at low voltage (<0.25V) having slope ≈1 corresponding to the Ohmic conduction case. Region II (0.25V<V<0.6V) shows a non-linear graph representing the thermionic emission (TE) mechanism. Region III (V>0.6V) is suggested to a space charge limited conduction (SCLC) mechanism described with exponential trap distribution in bulk material which locates outside of the depletion layer. From the forward bias I-V data can be calculated to find the value of R_s using the Cheung's method. Figure 13d and 13e are shown experimental dV/d(lnI) vs. I and H(I) vs. I plots in dark, under ELH light illumination and under UVA excitation, respectively. Then, the slope of dV/d(lnI) vs. I plot will give R_s and nkT/q as the y-axis intercept. The plotting of H (I) and I given n value out, will also give a $n\phi_{B0}$ from straight line intercept with y-axis. In addition, the checking consistency of this approach can be used other two methods to calculate the values of R_s. The values of R_s obtained from dV/d(lnI)-I and H(I)-I plots are approximately equal to each other's. The calculated n, ϕ_{B0} and R_S are listed in Table 1. Norde's method is another way to calculate the ϕ_{B0} and R_s values.[18] Figure 13f shows the plot of F(V) vs. V in dark, under ELH light illumination and under UVA excitation, respectively. The values of ϕ_{B0} and R_s evaluated from the F(V) vs. V plot are also reported in Table 1.

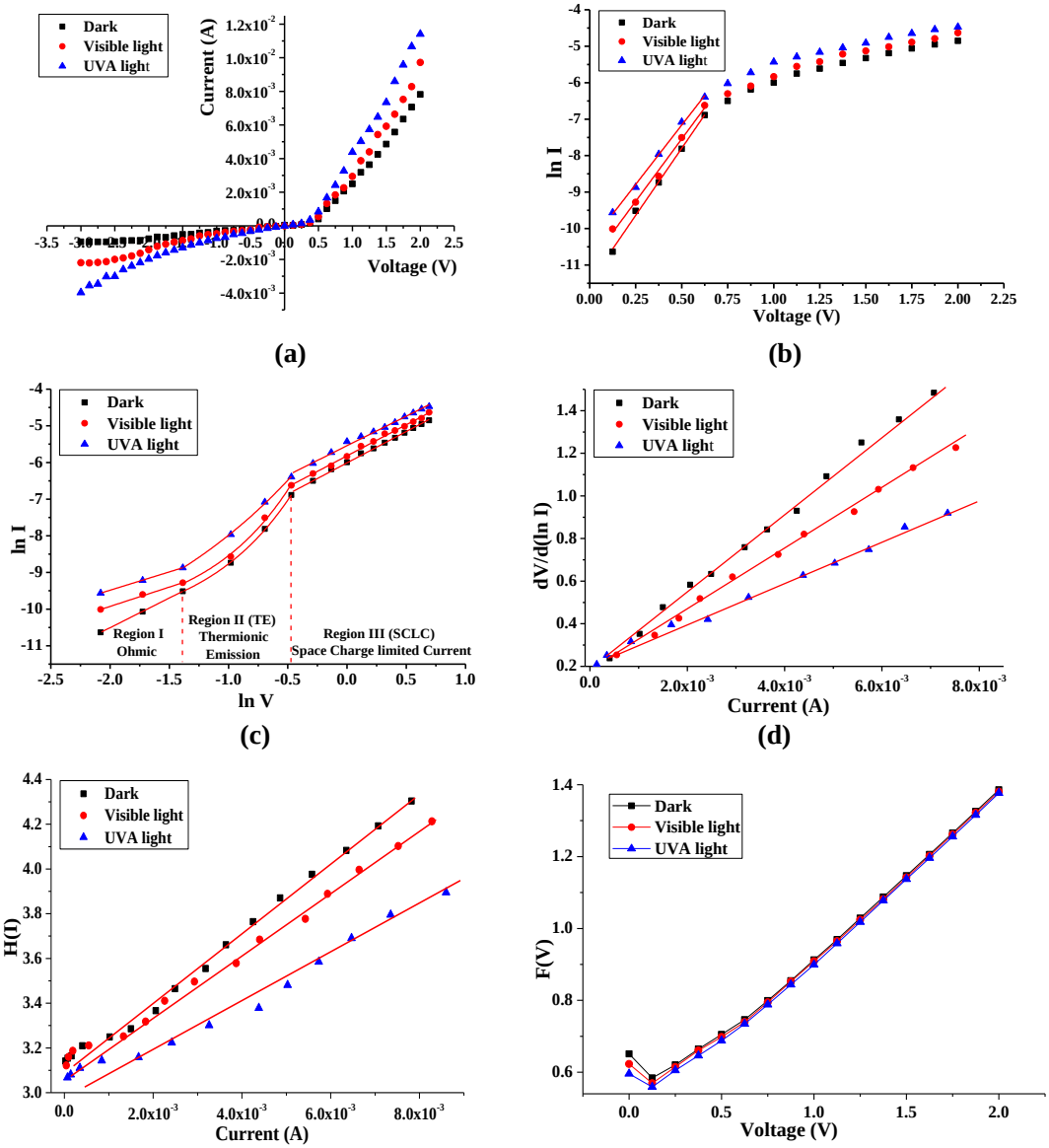

Figure 13 (a) I-V plot, (b) lnI-V plot, (c) lnI-lnV plot, (d) dV/dlnI-I plot, (e) H(I)-I plot and (f) F(V)-V plot of $(CdS)_{0.9}(ZnTe)_{0.1}/CuSbS_2$ diode.

Table. 1 Values of n, φ_B, R_S measured at different light sources.

Light Source	Saturation Current (A)	Ideality Factor (n)		Barrier Height, ϕ_B (eV)			Series Resistance, R_s (Ω)		
		TE	Cheung	TE	Cheung	Norde	Cheung	Cheung	Norde
		I–V	dV/dln(I)–I	I–V	H(I)–I	F(V)–V	H(I)–I	dV/dln(I)–I	F(V)–V
Dark	1.04×10^{-5}	5.78	5.97	0.54	0.52	0.58	151.83	155.12	164.59
ELH light	1.74×10^{-5}	6.22	6.47	0.52	0.51	0.56	126.80	145.82	154.37
UVA light	3.00×10^{-5}	6.54	6.83	0.51	0.49	0.55	101.41	145.08	148.25

Hole concentration of $CuSbS_2$ layer around 3.62×10^{14} cm^{-3} was evaluated from the slope of $1/C^2$- V plot as shown in Figure 14. This value is very close to 3.69×10^{14} cm^{-3} obtained from Hall effect measurements. Based on some important parameters obtained from optical and electrical properties of $CdS_{0.9}(ZnTe)_{0.1}$ and $CuSbS_2$ thin films deposited on glass substrate, energy band diagram of $CdS_{0.9}(ZnTe)_{0.1}/CuSbS_2$ heterojunction can be approximately made by using Anderson model as shown in Figure 15. When device is illuminated with ELH light, excess electron and hole are generated in $CuSbS_2$ layer. These carriers can be easily moved towards the electrode due to the influence of built-in electric field appearing at depletion region. In fact, the energy of the photons obtained from the high pressure mercury vapor lamp is higher than the energy of the photons obtained from the ELH halogen lamp. Therefore, under UVA excitation some more extra electron and hole can be generated in $CdS_{0.9}(ZnTe)_{0.1}$ layer besides generated in $CuSbS_2$ layer. Thus, the photocurrent is more enhanced under UVA light radiation.

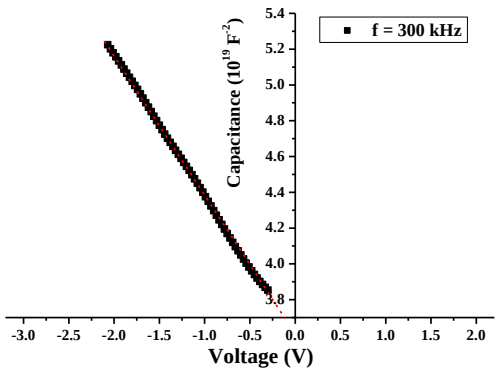

Figure 14. $1/C^2$-V of $(CdS)_{0.9}(ZnTe)_{0.1}/CuSbS_2$ diode.

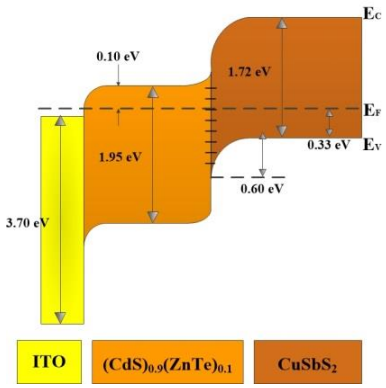

Figure 15. The proposed energy band diagram of $(CdS)_{0.9}(ZnTe)_{0.1}/CuSbS_2$ diode.

Conclusion: $(CdS)_{0.9}(ZnTe)_{0.1}/CuSbS_2$ heterojunction was successfully fabricated on ITO substrate using a single source thermal evaporation method. Structural investigations of both $(CdS)_{0.9}(ZnTe)_{0.1}$ and $CuSbS_2$ thin films deposited on glass substrate are in good crystalline quality. Optical and electrical properties of the both films also studied. The fabricated $(CdS)_{0.9}(ZnTe)_{0.1}/CuSbS_2$ heterojunction responds to light in UVA region (from high pressure mercury vapor lamp) better than the visible region (from ELH halogen lamp). It indicated that the device can be more suitably used as UVA photodiode or UVA photosensor for various optoelectronic device applications.

References:

1. Huang L, Wei Z L, Zhang F M, Wu X S. J. Alloy.Compd. 2015;648:591–594.

2. Hussain T, Al–Kuhaili M F, Durrani S M A, Qayyum H A. Ceram. Int. 2018;44:10130–10140.
3. Gassoumi A, Saad H.–E M M, Alfaify S, Nasr T B, Bouarissa N. Alloy.Compd. 2017;725:181–189.
4. Vinayakumar V, Shaji S, Avellaneda D A, Aguilar Martinez J A, Krishnan B. Mat. Sci. Semicon. Proc. 2019;91:81–89.
5. Kumar M, Persson C. Energy. Proced. 2014;44:176–183.
6. Feng X, Singh K, Bhavanam S, Palekis V, Morel D L, Ferekides C. Thin Solid Films. 2013;535:202–205.
7. Akaltun Y, Yildirim M A, Ates A, Yildirim M. Mater. Res. Bull. 2012;47:3390–3396.
8. Felimban A, Naby M A. Phys. Stat. Sol. 1989;115:K27–K29.
9. Lakshmi N, Rao N M, Venugopal R, Reddy D R, Reddy B K. Mater. Chem. Phys. 2003;82:764–770.
10. Raju K N,Vijayalakshmi R P, Reddy D R, Reddy B K. J. Phys. Chem. Solids. 1992;53:341-344.
11. Karpova E O, Nagibina I Y, Makarova A S. Russ. J. Phys. Chem. A. 2015;89:144-147.
12. Pfisterer F, Schock H W. J. Cryst. Growth. 1982;59:432-439.
13. Souza-Lucus F W, Zakutayev A. APL Materials. 2018;6:084501-1-084501-13.
14. Ramirez-Esquivel O Y, Mazon-Montijo D A, Montiel-Gonzalez Z, Aguirre-Tostado F S. Sol. Energy Sol. Cells. 2018;185:392-398.
15. Edley M, Opasanont B, Conley J, Tran H, Smolin S, Li S, Dillon A, Fafarman A, Baxter J. Thin. Solid. Films. 2018;646:180–189.
16. Wada T, Maeda T. Phys. Status. Solidi. C. 2017;1600196
17. Ornelas–Acosta R E, Shaji S, Avellaneda D, Castillo G A, Das Roy T K, Krishnan B. Mater. Res. Bull. 2014;61:215–225.
18. Aksoy S, Caglar Y. J. Alloys Compd. 2014;613:330-337.

Acknowledgements: This work is financially supported by Faculty of Science, King Mongkut's Institute of Technology (KMITL) and it provided the necessary facilities for complete this work.

F_004_OF: FLOW CROSSOVER DURING COLLISIONLESS MAGNETIC RECONNECTION

Pakkapawn Prapan[1,*], Kittipat Malakit[2], David Ruffolo[1]
[1]Department of Physics, Faculty of Science, Mahidol University, Bangkok, Thailand
[2]Department of Physics, Faculty of Science and Technology, Thammasat University, Pathum Thani, Thailand
*e-mail: p_dv99@hotmail.com

Abstract: Magnetic reconnection is a magnetic field line rearrangement in a plasma (ionized gas) that transfers magnetic energy into kinetic energy and thermal energy of plasma in the outflow regions. In this work we use a particle labeling technique to study symmetric reconnection, especially in the outflow regions. We performed Particle-In-Cell (PIC) simulations, which treat both ions and electrons using representative particles, with labeling to indicate the source region as one of the two inflow regions or the interface region. Finally, we discovered a flow crossover between the two inflow plasmas as they stream out from the reconnection region into an outflow region.

Introduction: Magnetic reconnection is a magnetic-field-rearrangement process that changes field line topology allowing the system to achieve a lower energy state through converting the energy stored in the magnetic field into the kinetic energy of the plasma outflow. Magnetic reconnection is associated with important astrophysical phenomena such as the solar flares and coronal mass ejections. It also plays a key role in the interaction between the solar wind plasma and the magnetospheric plasma. Furthermore, it can occur inside tokamaks, a type of man-made fusion devices. Magnetic reconnection is indeed a universal process in magnetized plasma systems.

To allow the magnetic field lines to rearrange and change its topology, a region called diffusion region is required. In this region, the frozen-in condition is broken, which means the magnetic field is free from the motion of plasma and the reconfiguration of the magnetic field is therefore possible. Understanding how plasma behaves going through the diffusion region is important in understanding magnetic reconnection.

Influenced by a classic model of plasma going through the diffusion region by Sweet (1958) and Parker (1957), it is conventional to think of plasma outside the diffusion region as frozen-in fluid and the plasma inside the diffusion region as non-frozen-in fluid. With this way of thinking, we have fluid flowing into the diffusion region from two upstream sides. The two inflows meet at a stagnation point, turn the corner, and exit the diffusion region on the downstream sides becoming the outflows (Figure 1). This is probably applicable for collisional reconnection, which is very much successfully explained by the Sweet-Parker model. With the success of the Sweet-Parker model, this idea of how plasma flow through the diffusion region is thought to be general and applicable for the case of collisionless reconnection as well[1].

An advance in understand how the outflow plasma is made by the introduction of the idea of mixing[1]. The inflow from the two sides mix in the diffusion region before becoming the outflow. This mixing idea is reasonable especially for collisionless reconnection. Treating plasmas as fluids fails to capture this effects[2], but the mixing is proved to be the case by Particle-In-Cell (PIC) simulations of collisionless reconnection[3], which treat plasma as particles and therefore include all the kinetic effects not included by fluid models of plasma. The idea of mixing is important in advancing the understanding reconnection with asymmetric inflow conditions[1].

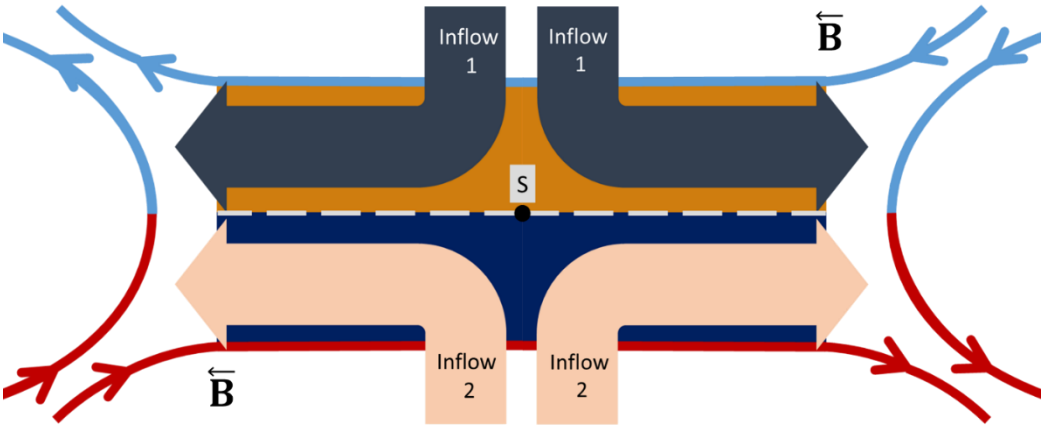

Figure 1. Stagnation point (S) and plasma flows (dark blue and light orange arrows) as usually assumed for magnetic reconnection at the border of the two plasma inflows.

In this work we make a step further in understanding how the plasmas from the two inflows flow through the diffusion region before becoming the outflows by labelling plasma particles in a PIC simulation from the two input regions. in symmetric reconnection outflow regions. The results from the simulation shows that the inflow plasmas do not just turn the corner within the diffusion region and randomly mix with its counterpart when flowing out the diffusion region becoming the outflows. Instead, the inflow from the two sides demonstrate a flow crossover which is a new feature not yet reported by previous studies.

Methodology:

Particle-in-cell model using the P3D code: The Particle-In-Cell (PIC) model is a model in which individual representative particles are tracked for every time step. For running this model on millions of particles, we use the P3D code which is a massively parallel full particle code that can simulate up to one billion particles on a supercomputer. The simulations were "2.5 dimensional", meaning that all vector quantities are three-dimensional but particle locations are only stored in two dimensions, *x* and *y*.

Initial simulation parameters: The simulation box was divided into three regions as shown in Figure 2. Simulation regions 1 and 2, with oppositely directed B, provide the inflows for reconnection to take place near locations marked by an "X" with dashed lines. Region 3 comprise the initial transition regions between regions 1 and 2, with strong current sheets according to the transitions in B. We consider symmetric reconnection, in which regions 1 and 2 have the same parameters except oppositely directed magnetic fields. Both regions initially have plasma β=0.25. Before running the simulation, we normalized all parameters to initial values in regions 1 and 2 to minimized numerical problems.

To study mixing, we labeled the particles "1", "2", or "3" according to the region of their initial location (see Figure 2). The simulation box has length l_x = 102.4 and width l_y=51.2 in units of the initial ion initial length in region 1 or 2. The two current sheets between oppositely directed magnetic field lines are initially located at y_1 = l_y/4 and y_2 = (3/4) l_y. From these locations of the two current sheets, the particles initially located in the area inside $y_1 \pm 2.5$ or $y_2 \pm 2.5$ are marked as "3".

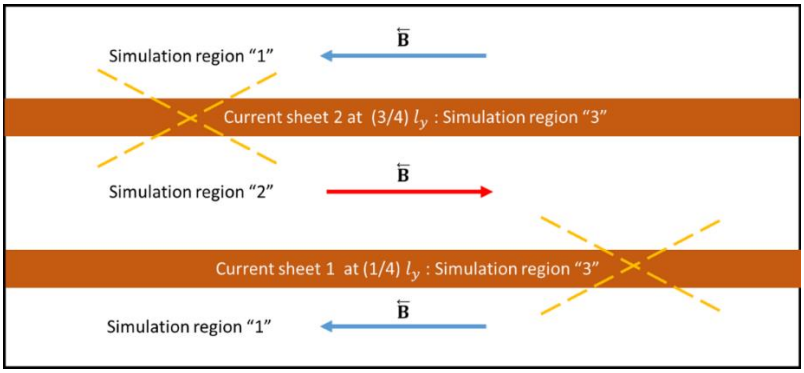

Figure 2. Simulation diagram for labeling particles based on their initial locations in this box with periodic boundary conditions. The simulation initially perturbs the particle distribution so that magnetic reconnection occurs at two points, indicated by crossing dashed lines. The two inflow regions are separated by current sheets at y_1 = l_y/4 and y_1 = (3/4) l_y. The magnetic field is oppositely directed in regions 1 and 2. Particles with label number "3" are initially located in the area that contains the current sheets.

Performing the PIC simulation: After we built in the label identification code into the main P3D code and performed initial assignments, we started to run a simulation of symmetric reconnection for 210 time units (i.e., 210 ion cyclotron times), when the reconnection rate was stable. Afterward, we continued to run and we report data averaged over 100 snapshots separated by 1 time unit.

Results and Discussion: The results combining all plasma labels show the x-point where magnetic field lines change topology and the stagnation point where is no plasma flow. This type of data is well known from previous research.

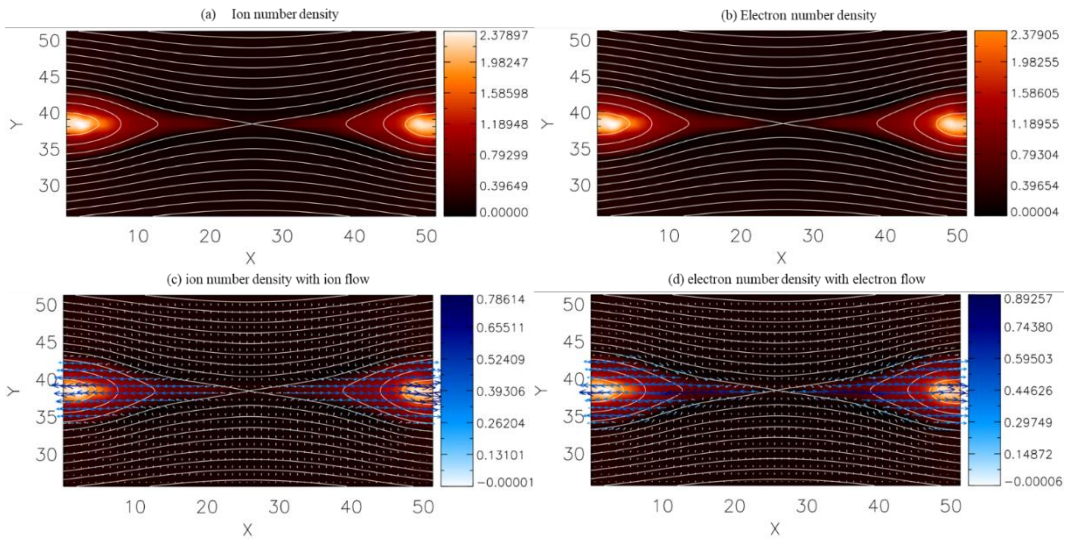

Figure 3. Graphs combining all plasma labels with superposed magnetic field lines (white). (a) and (b): 2 dimensional contour graphs of ion and electron number density, representatively, according to the color scale. (c) and (d): As above, now with superposed ion and electron flow vectors, respectively (blue vectors). The color scale indicates the magnitude of the flow.

The results for labeled populations reveal additional behavior that is not visible from the combined results. The ions and electrons from simulation region 1 flowed across the current sheet, where magnetic field changes sign, as shown in Figures 4 and 5. Ion inflow from both regions exhibits a flow crossover directly to the outflow region as show in Figures 4(b) and 6(b). The electrons also have a flow crossover, mostly flowing inward along a magnetic field line and then flowing out from the middle along the outflow as shown in Figures 5(b) and 7(b).

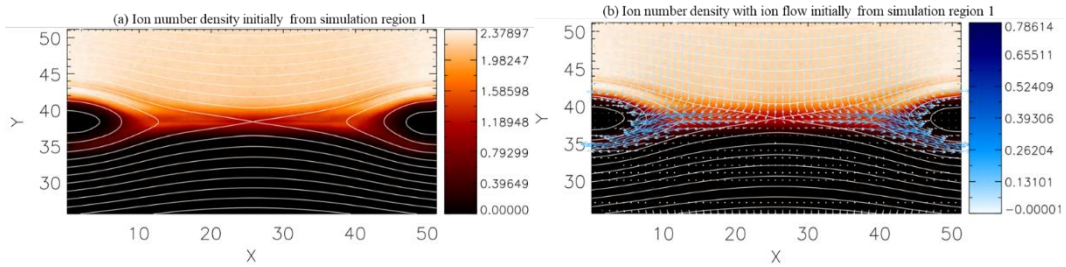

Figure 4. Graphs with labeled ions initially from simulation region 1 with superposed magnetic field lines (white). (a): 2 dimensional contour graph of ion "1" number density according to the color scale. (b): As (a), now with superposed ion flow vectors (blue vectors). The color scale indicates the magnitude of the flow.

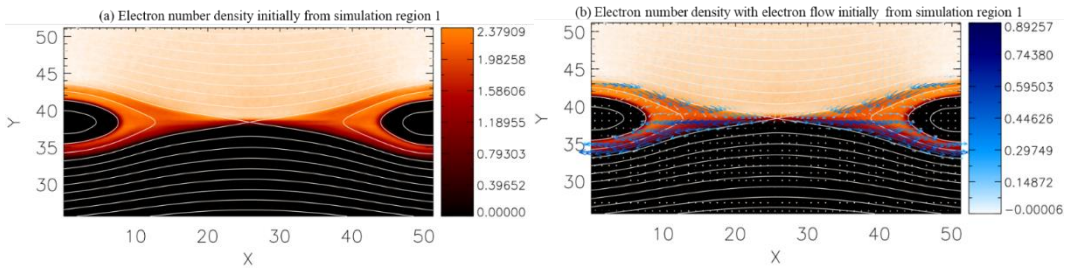

Figure 5. Graphs with labeled electrons initially from simulation region 1 with superposed magnetic field lines (white). (a): 2 dimensional contour graph of electron "1" number density according to the color scale. (b): As (a), now with superposed electron flow vectors (blue vectors). The color scale indicates the magnitude of the flow.

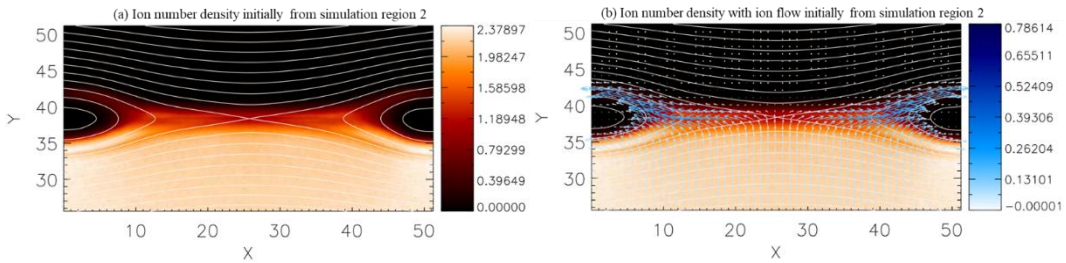

Figure 6. Graphs with labeled ions initially from simulation region 2 with superposed magnetic field lines (white). (a): 2 dimensional contour graph of ion "2" number density according to the color scale. (b): As (a), now with superposed ion flow vectors (blue vectors). The color scale indicates the magnitude of the flow.

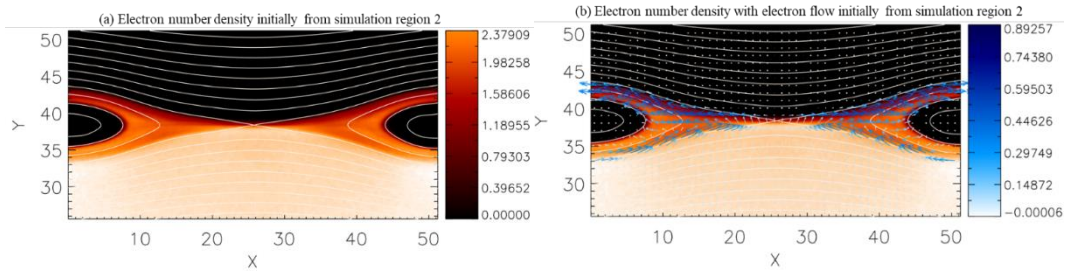

Figure 7. Graphs with labeled electrons initially from simulation region 2 with superposed magnetic field lines (white). (a): 2 dimensional contour graph of electron "2" number density according to the color scale. (b): As (a), now with superposed electrons flow vectors (blue vectors). The color scale indicates the magnitude of the flow.

Conclusions: We explored the behavior of two labelled inflows in collisionless, symmetric magnetic reconnection with no guide field using fully kinetic PIC simulation with the P3D code. The two inflows contained the same initial parameters such as magnetic field, number density of both ions and electrons, etc. Instead of seeing a stagnation point and the border between two inflow plasmas in the outflow region, we discovered a flow crossover between the two plasma populations for both ions and electrons.

References:

1. Cassak PA, Shay MA. Phys Plasmas. 2007;14;102114.
2. Cassak PA, Shay MA. Phys Plasmas. 2009;16;055704.
3. Malakit K, Shay MA, Bard C. J. Geophys. Res. 2010;115; A10223.
4. Parker EN. J. Geophys. Res. 1957;62;509
5. Sweet PA. Electromagnetic Phenomena in Cosmical Physics edited by Lehnert B. 1958;6;123

Acknowledgements: We thank http://terpconnect.umd.edu/~swisdak/p3d/ for sharing useful knowledge of the P3D code. This work was supported by grant RTA5980003 and grant MRG6180176 from the Thailand Research Fund.

F_005_OF: VERIFICATION OF CURLING PROBE MEASUREMENT IN DC PLASMA

Chatchai Sirithipvanich, Natthapong Jimpaiboon, Boonchoat Paosawatyanyong
Chulalongkorn University, Bangkok, Thailand
e-mail: chatchai.sirithipvanith@gmail.com, mnnatthapong@gmail.com, paosawat@gmail.com

Abstract: The curling probe is one of the active resonance absorption spectroscopic plasma analysis methods, the methods utilized the reflection coefficient of a probe over frequency to determine the plasma density. The proposed model of the curling probe uses the deviation of frequency in which the minimum reflection coefficient occurs when the probe is submerged in different mediums. The probe structure is simple and is claimed to be robust and efficient. The experiment of the curling probe and the simulation of the probe reflection coefficient are repeated. The probe was constructed, the simulations of the previously reported article were followed, and the simulations of the constructed probe were done. Our simulation results of the previously reported probe contradicted with the reported article; however, agreed with experiments in which the frequency where the minimum reflection coefficient occurs did not change when the plasma density changed.

Introduction: The low-temperature plasma technologies have been being constantly developed and recently has a great number of applications. Without them, the development of microelectronics or surface modifications of advanced materials would not be possible [1]. In the last few decades, its applications have been broadened to the medication such as plasma treatments and biocompatible material fabrications [2]. To optimize and control conditions for the specific application, plasma parameters such as electron temperature and electron density must be determined [1].

Conventionally, the plasma parameters of the low-temperature plasma usually obtained by well-established techniques such as Langmuir probe technique, optical emission spectroscopy or microwave interferometry. The Langmuir probes are simple conducting wires, the technique is simple and robust, more importantly, they can be used for locally measuring plasma parameters. However, the probe must be exposed directly to plasma, the perturbation and contamination are unavoidable [3]. The optical emission spectroscopy uses the spectrum of electromagnetic waves, emitted by the plasma, for determining the plasma parameter [3]. The technique does not perturb plasma but the measured parameters are not local and the accuracy is low for molecular plasma [4]. Microwave interferometry is a legacy technique. It is robust, simple and does not perturb or contaminate plasma moreover, it is more accurate than the optical emission spectroscopy, but the method can only measure electron density and the measurement is not local. It is usually used for calibrating the Langmuir probe [3].

Active plasma resonance spectroscopy is one of plasma diagnostic techniques. It is the terminology for the probes which are composed of dielectric materials and conductors, such as microwave resonator probe, multipole resonance or curling probe. When the probes are inserted into plasma, we consider probe and plasma as a system of electrical networks. The system's reflection coefficients over a range of frequencies are measured and analyzed into the plasma density [5].

The curling probe is the most recently developed active plasma resonance spectroscopic methods. It could be the most promising technique because of their durable and simple design. Basically, It is a metal cylinder filled with dielectric material with one end etched into a spiral slot antenna [6]. If the curling probe is covered with an inert dielectric, it can measure plasma parameters locally and does not contaminate plasma. However, the probe can only measure electron density. The curling probe was first proposed in 2011 by Iji Liang [6], and it has been used in experiments [7-10] since 2013, but it is not widely applicable and only verified by a single group of researchers [6-11]. our study aims to test the validity of

the curling probe by constructing a curling probe and simulating the probe to compare the results with the previously reported article's. If the probe worked as it was claimed, the techniques would be a good candidate for another well-established and robust method of plasma diagnostics.

Methodology: Our curling probe study introduced both experimental and simulated verifications. In the experiments, we constructed the probe using a hollow female-SMA, wire-cut the end into a spiral slot. The end of the SMA is 0.5mm thick, the drilled center diameter is 0.6mm, the slot width is 0.3mm and the spiral length is 35mm. the dimension of the probe was chosen by the limitation of our vacuum chamber and the spiral length is chosen to be the same as previously reported article's [6] which claimed that the measurement greatly depended on the spiral length so we can expect the results to be closed to what is reported and be able to be used for comparison to the report. the schematics and constructed probe are shown in Figure 30.

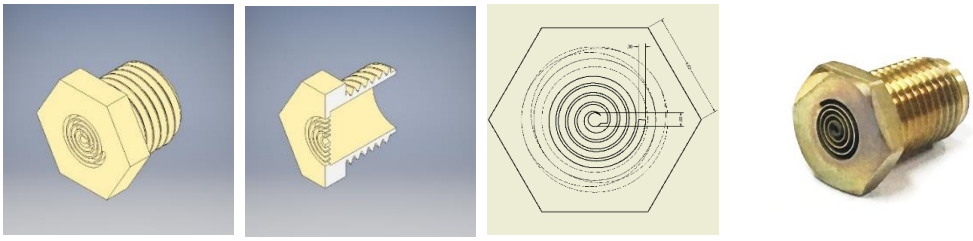

Figure 30. The first 3 left pictures are the diagrams of the probe.
The right picture is the picture of the actual probe.

The plasma was generated in a vacuum chamber filled with argon gas as shown in Figure 31. Inside the chamber, there are two electrodes where the direct current voltage is applied to generate plasma. The curling probe is connected to the coaxial transmission line RG-142 and covered with the Pyrex tube. The probe is then inserted into the chamber to diagnose the plasma.

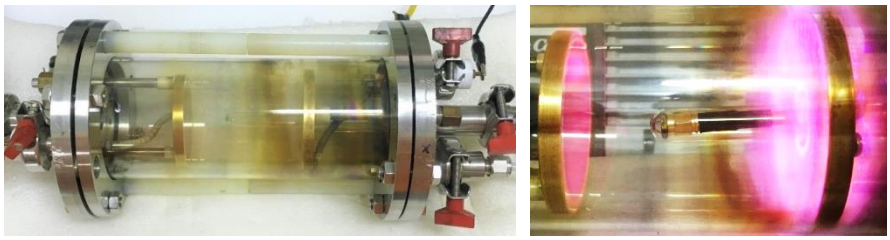

Figure 31. The vacuum chamber (left)
and the probe inside the chamber when the plasma was generated (right).

The experiments were performed in 8 different conditions, which the plasma densities measured by the home-made Langmuir probe are the difference, shown in

Table 4. the chamber was evacuated until the pressure reached 0.10 mbar and then the mass flow controller was turned on to feed the argon gas into the chamber. The mass flow controller was adjusted to achieve the designated pressure.

Table 4. The 8 different conditions of performed experiments.

Experiment No.	Pressure (mbar)	Power (Watt)
1	0.55	0.000
2	0.55	7.539
3	0.55	26.230
4	0.55	48.654
5	0.65	3.792
6	0.65	17.280
7	0.65	34.182
8	0.65	47.17

When the pressure had been stable, the power supply GW GPR-60H15D was turn on to generate plasma. The reflection coefficient over the range of frequency was then measured by Agilent E5071C Network Analyzer.

In the simulations, the CST microwave studio environment was used to simulate the reflection coefficient. We simulated two configurations of the probe, the first configuration is the probe proposed by the previously reported article and another configuration is close to our constructed probe. The first configuration is chosen to directly compare the results to the previously reported article's [6] while the second configuration is chosen to compare with the constructed probe in the experiments. The configurations used in the simulation are shown in Figure 32. The previously reported probe was configured to be filled with 3.75 relative permittivity medium while our constructed probe is configured to be filled with vacuum. The ends of both probes are configured to be connected to the RG142 50Ω coaxial transmission line. The probes were immersed in a dispersive medium which is configured as plasma with variable electron density. The electron density was varied with the logarithmic step because we expected to observe changes in the reflection coefficient profile. Once, the medium has been configured and waveguide port has been specified, the simulation can be started. The simulations are performed in the time domain by generating the input pulse which is the sum of the interested spectrum of electromagnetic waves, using this method, the simulation of different frequencies can be done at once. The simulation environment automatically generated the input signal to match the coaxial transmission line mode. The criteria required for simulation to stop are that the electromagnetic wave has dissipated, or that the simulation time has exceeded 200 times of the input pulse duration. If the electromagnetic wave does not fully dissipate, the truncation error will occur which causing ripples in reflection coefficient results [12]. An example of the input and response signals of a low truncation error simulation is shown in Figure 33.

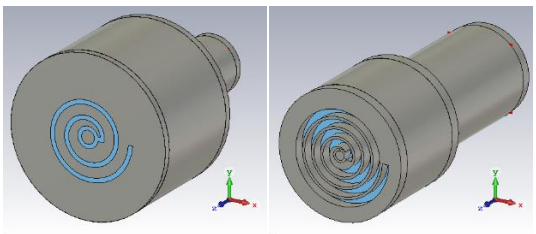

Figure 32. The previously reported probe configuration [6] (left) and the constructed probe configuration (right) used to simulate the reflection coefficient in the CST microwave studio.

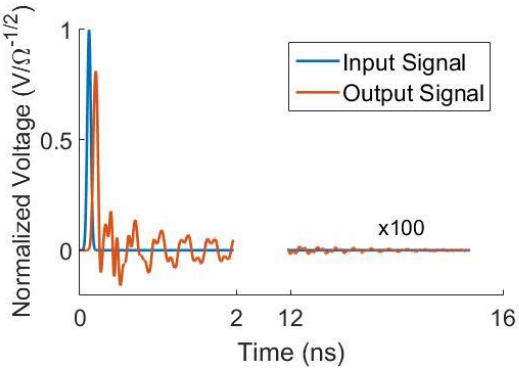

Figure 33. An example of simulated signals of a low truncation error simulation.

Results and Discussion: In the experiments, the minimum reflection coefficient occurs approximately at the frequency around 4.1956 GHz as shown in Figure 34., This frequency did not change when the plasma density is assumed to be changed. In the simulations, when probes were subjected to different plasmas with different densities, the simulated reflection coefficient also did not changes for both previously reported and our constructed configurations as shown in

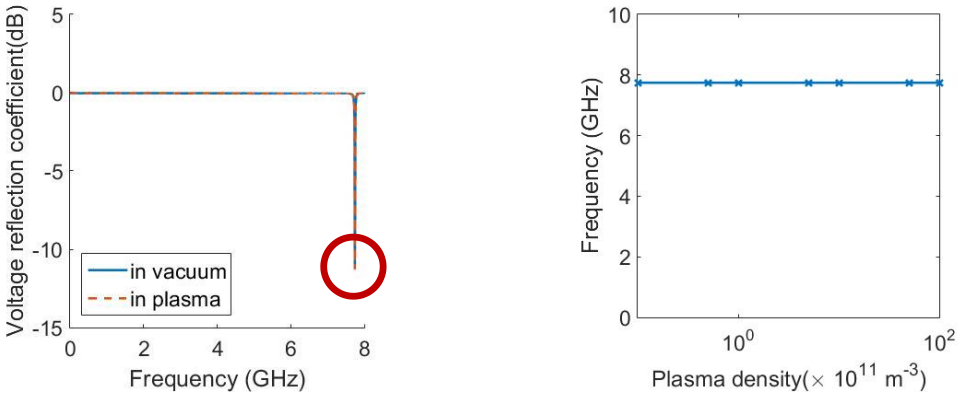

Figure 35. and

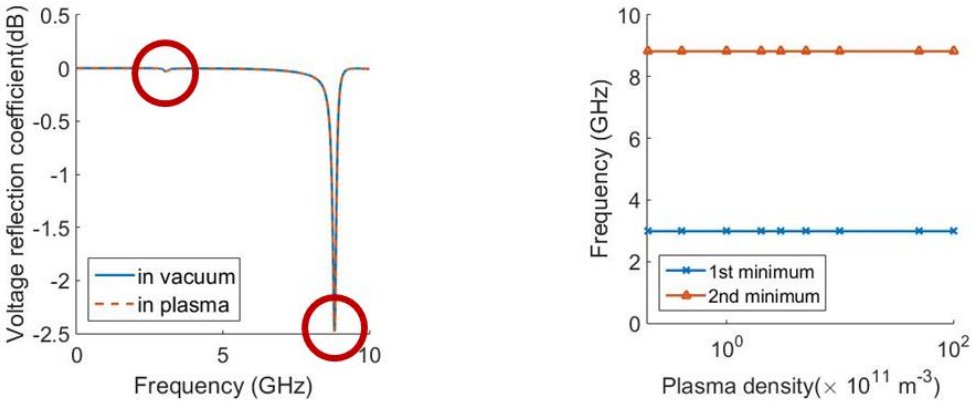

Figure 36. The previously reported configuration's simulated reflection coefficient [6] has one minimum reflection coefficient, occurs at 7.744 GHz, while our constructed configuration shows two local minimum reflection coefficients, which occurs at 3.095 GHz and 8.955 GHz.

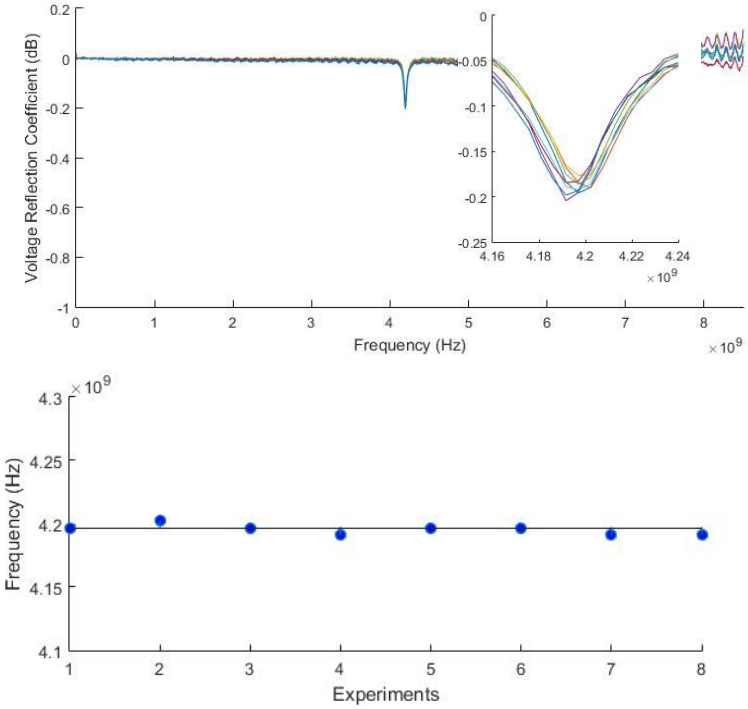

Figure 34. The reflection coefficients from 8 experiments plotted in the same coordinate and the magnification of the reflection coefficient around the minimum (top) and frequencies where the minimum reflect coefficient occurred in each experiment (bottom).

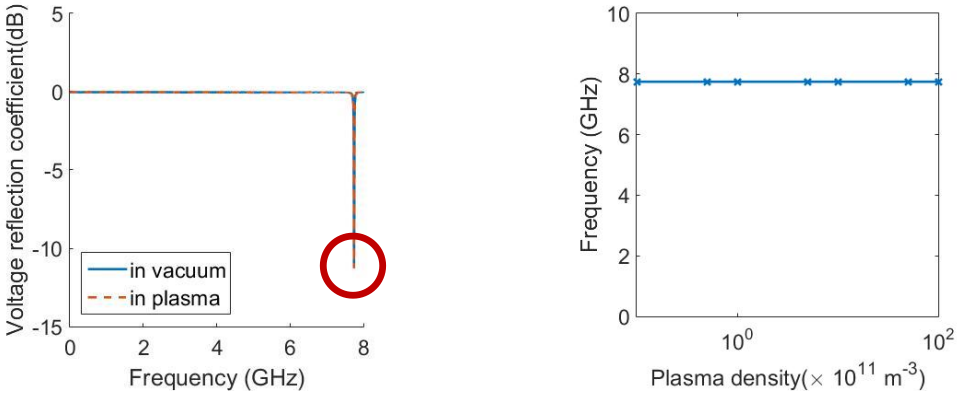

Figure 35.The simulated reflection coefficient of the previously reported probe which immersed in plasmas with different densities (left) and the frequencies where the local minimums of reflected coefficient occur (right).

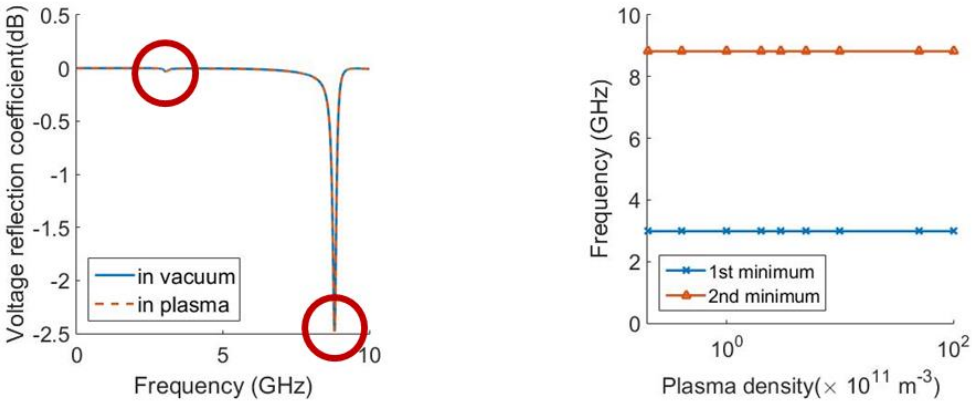

Figure 36. The simulated reflection coefficient of our constructed probe which immersed in plasmas with different densities (left) and the frequencies where the minimum reflected coefficient occurs (right).

The probe reported by Iji Liang [6] simulated results contradicted with the previously reported article where the frequency in which the minimum reflect coefficient occurs changes proportional to plasma density. Our constructed probe experiment and simulation results show that the frequency in which the minimum reflect coefficient occurs did not change when the plasma density changed. The frequency where minimum reflect coefficient occurs of constructed probe differs from the frequency, where the first local minimum occurs, of simulation by approximately 1 GHz and in the experiment, the frequency range of the instrument is limited to 8.5 GHz thus the second local minimum of our constructed probe cannot be observed.

The frequency in which the minimum reflect coefficient occurs is clearly does not depends on only the spiral slot length but also the inner radius shell, the height, the thickness of the end, and the inner core radius of the probe. We do not yet understand why the minimum reflection coefficients were present, the More investigation is needed to determine where the minimum reflection coefficient would occur. According to our simulations which is not shown here, there would be the minimum reflection coefficient only when the spiral slot was present otherwise total reflection occurs overall frequency. This is to be expected from a closed transmission line resonator [13]. Our hypothesis is that the reflected wave is excited into higher modes of the coaxial transmission line by the spiral slot which are attenuating modes and they dissipated along the transmission line before they reach the waveguide port [13]. The 1 GHz different between the simulations and the experiments of constructed have not yet determined, but we hypothesize that because the simulation configuration is slightly different from the constructed probe.

Conclusion: The curling probe principle uses the difference of frequencies in which the minimum reflection coefficient occurs when the probe is submerged in different mediums to determine the plasma density. The probe structure is simple and is claimed to be robust and efficient. The probe was manufactured, and the experiment found that the frequency where the minimum reflection coefficient occurs does not change when the plasma density changes. The simulations of the previously reported article were performed and the results are contradicted with the article proposed in 2011 [6]. The frequency in which the minimum reflection coefficient occurs does not change, the frequency stays the same at 7.744 GHz when the plasma density is changed. The simulations of the constructed probe indicated the same conclusion but with two noticeable local minimum occurs at 3.095 GHz and 8.955 GHz.

However, the simulation results do not agree with the published article, the simulated results agree with the experiments on the constructed probe. The reasons why the minimum reflection coefficients were present are not yet determined but our hypothesis is that the reflected wave is excited by the spiral slot into attenuating modes which they will dissipate before reaching the waveguide port.

References:

1. Auciello O, Flamm DL. Plasma Diagnostics: Academics Press; 1989.
2. Chu PK, Lu X. Low Temperature Plasma Technology: Taylor & Francis; 2014.
3. Chen FF, Chang JP. Lecture Notes on Principle of Plasma Processing: Springer; 2002.
4. Fantz U. Basics of plasma spectroscopy. Plasma Sources Science and Technology. 2006;15(4):S137-S47.
5. Lapke M, Oberrath J, Mussenbrock T, Brinkmann RP. Active plasma resonance spectroscopy: A functional analytic description. Plasma Sources Science and Technology. 2013;22(2).
6. Liang I, Nakamura K, Sugai H. Modeling microwave resonance of curling probe for density measurements in reactive plasmas. Applied Physics Express. 2011;4(6).
7. Pandey A, Nakamura K, Sugai H. Opto-curling probe for simultaneous monitoring of optical emission and electron density in reactive plasmas. Applied Physics Express. 2013;6(5).
8. Pandey A, Sakakibara W, Matsuoka H, Nakamura K, Sugai H. Curling probe measurement of electron density in pulse-modulated plasma. Applied Physics Letters. 2014;104(2).
9. Pandey A, Sakakibara W, Matsuoka H, Nakamura K, Sugai H. Time-resolved curling-probe measurements of electron density in high frequency pulsed DC discharges. Japanese Journal of Applied Physics. 2016;55(1).
10. Pandey A, Tashiro H, Sakakibara W, Nakamura K, Sugai H. Curling probe measurement of a large-volume pulsed plasma with surface magnetic confinement. Plasma Sources Science and Technology. 2016;25(6).
11. Arshadi A, Brinkmann RP, Hotta M, Nakamura K. A simple and straightforward expression for curling probe electron density diagnosis in reactive plasmas. Plasma Sources Science and Technology. 2017;26(4).
12. CST Microwave Studio: Work Flow and Solver Overview: CST GmbH–Computer Simulation Technology; 2008.
13. Pozar DM. Microwave Engineering. 4th ed: John Wiley & Sons; 2012.

Acknowledgements: We would like to thank Sahaporntool limited partnership for advising the details on how to construct a curling probe and constructing the probes used in our experiments.

F_006_PF: HEAT TREATMENT OF MOGOK ZIRCON, MYANMAR

Chanisara Srimuang, Kanyarat Kwansirikul*
Department of Geological Sciences, Faculty of Science, Chiang Mai University, Chiang Mai 50200, Thailand
*e-mail: kanyarat.k@cmu.ac.th

Abstract: The studied yellowish green to greenish brown zircons were mined from alluvial deposits in Mogok city, Myanmar, related to metasomatism process within the Mogok metamorphic belt (MMB). Thirty rough zircon samples were characterized using gemological standard methods, FTIR and UV-Vis-NIR spectroscopy. Chemical compositions were analysed using SEM-EDS. The specific gravity of the samples ranged from 4.61 - 4.76 indicating high type of zircon. All samples fluoresced moderate to strong yellow under both long-wave and short-wave ultraviolet radiation. Internal features consisted of fluid inclusions, healed fracture, apatite crystals, iridescence cracks, needle inclusions and oxide-strain. Ten samples were chosen for chemical compositions analysis. They revealed major elements of ZrO_2 and SiO_2. Minor and trace elements were composed of HfO_2 and Al_2O_3. In the darker-tone samples contained greater amounts of Hf than the lighter-tone samples. Heat treatments were carried out under reducing conditions at 900°C, 1000°C and 1100°C soaked for 1 hour at each temperature. After heating, the samples showed reducing of brown color and became near colorless to slightly yellowish green. The internal fractures in the heated stones were more developed and the yellowish brown oxide-strain turned into dark brown and near colorless. Tension cracks were generated around mineral inclusions upon heating. UV-Vis-NIR absorption spectra showed decreasing of the color-center absorption band intensity between 300 - 400 nm which caused the brown color in zircon. The spectra also showed the U^{4+} peaks between 400 - 700 nm and U^{5+} peaks between 1,000 - 1,700 nm which had no significant change after heating. Infrared spectra showed absorption spectra of $[SiO_4]^{4-}$, O-H stretching, U^{4+} and U^{5+} which had no significant change after heating.

Introduction: Zircon has been popular in gem market for a long time due to its high refractive index and dispersion which resulting in high brilliant and adamantine luster. Zircon is a nesosilicate mineral and its chemical formula is $ZrSiO_4$. Zircon crystallizes in tetragonal structure with a unit cell composed of four $[SiO_4]^{4-}$ and four $[ZrO_8]^{12-}$ groups. Trivalent rare-earth elements (REE^{3+}) as well as Hf^{4+}, Ti^{4+}, Th^{4+}, U^{4+}, U^{5+}, P^{5+}, Nb^{5+} and Ta^{5+} can incorporate in the zircon structure[1]. U and Th, the radioactive elements which substitute for Zr^{4+} in zircon structure as trace elements, generate radioactive radiation and cause structural defects in zircon. Generally, the colors of zircon are caused by the trace element composition (transition metals, lanthanides, actinides and REEs) and radiation damage (radiation induced color centers)[2].

Brown, reddish brown to yellowish brown zircons are commonly found in nature. Those colors are caused by color center upon the radiation. However, they are not the desirable colors in gem market, unlike blue and colorless zircon. Natural reddish brown zircon can turn into blue or colorless by suitable heat treatment. Heating zircon under oxidizing conditions up to 600 °C can turn the natural brown color into colorless while heating zircon under reducing conditions at 900 - 1400 °C will turn the natural brown color into blue. However, not zircon from every location can turn into blue by this process. Ratanakiri, one of the north-eastern provinces of Cambodia, is the promising source for the well-known vivid blue heat-treated zircon. However, zircon from Kanchanaburi province in Thailand, which seems to have initial color before heating similar to Ratanakiri zircon, does not turn into vivid blue after heating under reducing atmosphere at the same conditions[3].

Zircon is a common accessory mineral occurred in igneous and metamorphic rocks. Relatively large, gem-quality crystals grow predominantly in felsic pegmatites and more

rarely in metasomatic rocks. Gem-quality zircon has produced in Sri Lanka, Cambodia, Vietnam, Thailand, Myanmar, India, Pakistan, China, Russia, France, Tanzania, Madagascar, the USA, Canada, Australia and other countries[1]. For zircon deposits in Myanmar, Mogok is one of the most productive gemstone deposits including zircon. Mogok is a city in the Pyin Oo Lwin District, Mandalay Region of Myanmar. Mogok zircons occur in alluvial deposits related to metasomatism process between their host-rock and local metamorphic rocks in the southern part of the Mogok metamorphic belt (MMB). They occur in biotite syenogranitic rock in the area of zircon rim during a poscollisional high-grade metamorphic event in the late Eocene-Oligocene[4]. Mogok zircons are mined from alluvial deposits as a byproduct from corundum mining[6].

From previous studies, zircon from central highlands of Vietnam and Ratanakiri province of Cambodia turn easily into blue after heating under reducing atmosphere at suitable conditions[5]. Zircon from both locations occur associated with alkali basaltic rocks. Heat treatment of zircons which occur associated with the metasomatism process has rarely been reported. Therefore, this study aims to characterise gemological properties and heat zircon from Mogok, Myanmar, under reducing conditions to observe the change of color after heating.

Methodology: 30 rough transparent zircon samples, ranging from 0.363 to 0.976 ct. from Mogok city in Myanmar were studied. The samples were doubly polished parallel to c-axis for analyzing including their gemological characteristics, chemical compositions and spectroscopic features. Gemological properties, specific gravity, fluorescence and internal features were investigated using standard gemological instruments. 10 samples were selected for chemical compositions analysis by a JSM-IT300 Scanning Electron Microscope with Energy Dispersive X-ray Spectrometer (SEM-EDS). Ultraviolet-visible-near infrared (UV-Vis-NIR) absorption spectra were recorded over an interval of 250 - 1800 nm using a Hitachi U4001 spectrophotometer, with a slit width of 2 mm and a scan speed of 300 nm/min. Infrared spectra were collected in the 500 - 7000 cm^{-1} range using a Bruker Tensor 27 Fourier Transform Infrared Spectrophotometer. Heat treating experiments were carried out with a SANTE electric furnace, under reducing conditions at 900, 1000 and 1100 °C soaked for 1 hour at each temperature. The furnace was slowly cooled down to room temperature before samples removing. All experiments and analyses methods were done at Faculty of Science, Chiang Mai University, Chiang Mai, Thailand. (Leave a blank line between section

Results and Discussion: The studied 30 rough Mogok zircon samples were transparent and varied from subhedral to euhedral crystal. Their colors ranged from pale yellow to greenish brown (Figure 1). The samples were divided into 4 groups depending on their appearance colors. They included pale yellow, intense yellowish brown, pale yellowish brown and greenish brown groups. Color of the studied Mogok zircons is different from alkaline basaltic zircon which is commonly found in reddish brown[5]. The specific gravity of all samples ranged from 4.61 - 4.76 (average 4.67) which indicated the high type of zircon[6]. All samples fluoresced moderate to strong yellow under long-wave and short-wave ultraviolet radiation. For internal features, fluid inclusion was found in every samples. Apatite crystals, healed fractures, iridescence cracks, needles and yellowish-brown iron oxide stains were also found in some samples (Figure 2).

Four samples for chemical analysis were selected from pale yellow and pale yellowish groups and six samples were selected from pale yellowish brown and greenish brown groups. The chemical data of the studied samples were summarized in Table 1. The samples revealed major elements of ZrO_2 (54.12 - 61.80 wt.%) and SiO_2 (28.85 - 36.63 wt.%). Minor and trace elements detected were composed of HfO_2 (5.36 - 12.5 wt.%) and Al_2O_3 (0.33 - 1.00 wt.%). In the darker-tone samples contained greater amounts of Hf than the

lighter-tone samples similar to alkaline basaltic zircons from central highland of Vietnam. The darker reddish brown Vietnamese zircon samples contain greater Hf concentration than the lighter samples[5]. The concentrations of U, Th and some trace elements were below detection limit of SEM-EDS analysis technique.

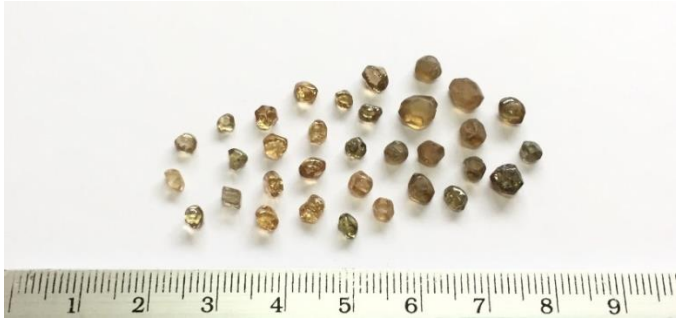

Figure 1. Natural Mogok zircon samples varying from pale yellow to greenish brown and from subhedral to euhedral crystals.

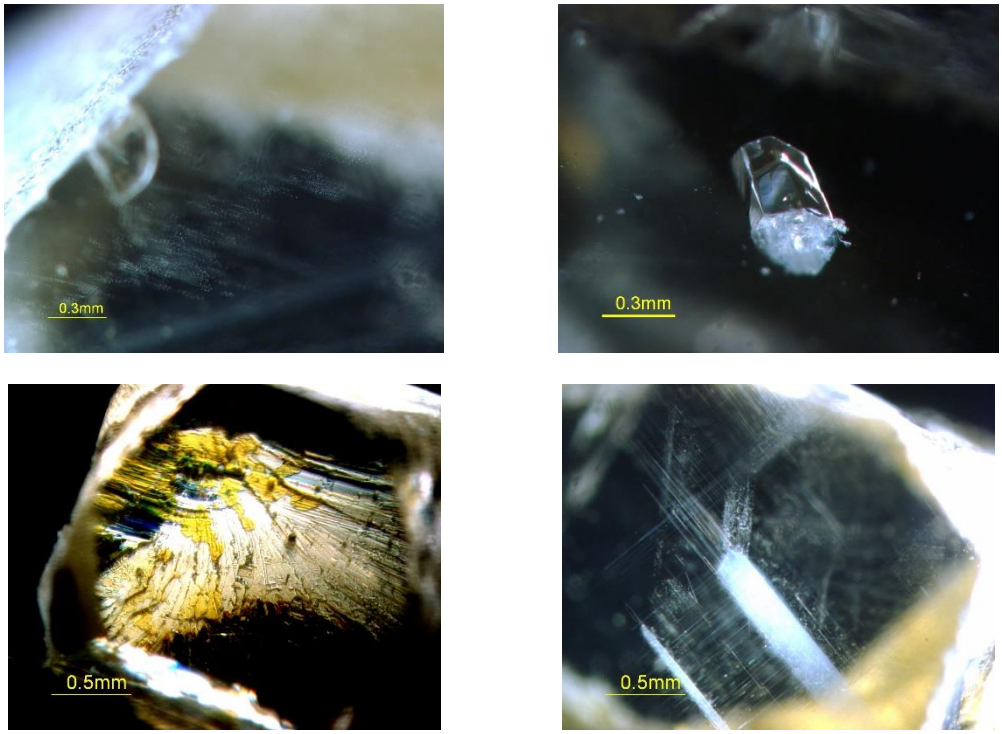

Figure 2. Example of internal features found in unheated Mogok zircon showing fluid inclusion (top left), an apatite crystal (top right), yellowish-brown iron oxide stain (bottom left) and needle inclusions (bottom right).

Table 1. Average chemical compositions of the studied Mogok zircons determined by SEM-EDS.

Chemical composition (wt.%)	Pale yellow	Intense yellowish brown	Pale yellowish brown	Greenish brown
ZrO_2	61.80	58.03	54.12	57.65
SiO_2	32.51	34.04	36.63	28.85
HfO_2	5.36	7.26	8.29	12.50
Al_2O_3	0.33	0.67	0.96	1.00

The zircon samples were heated under reducing conditions at 900, 1000 and 1100 °C. After heat treatment, the pale yellow to greenish brown samples showed brown discoloration and turned into near colorless to pale yellowish green (Table 2). All samples were inert under long-wave and short-wave ultraviolet radiation. There was no change on the specific gravity significantly. Fractures in the heated stones were more developed, yellowish-brown oxide stain turned into dark brown and partially turned into colorless, and some tension cracks were generated by heat (Figure 3).

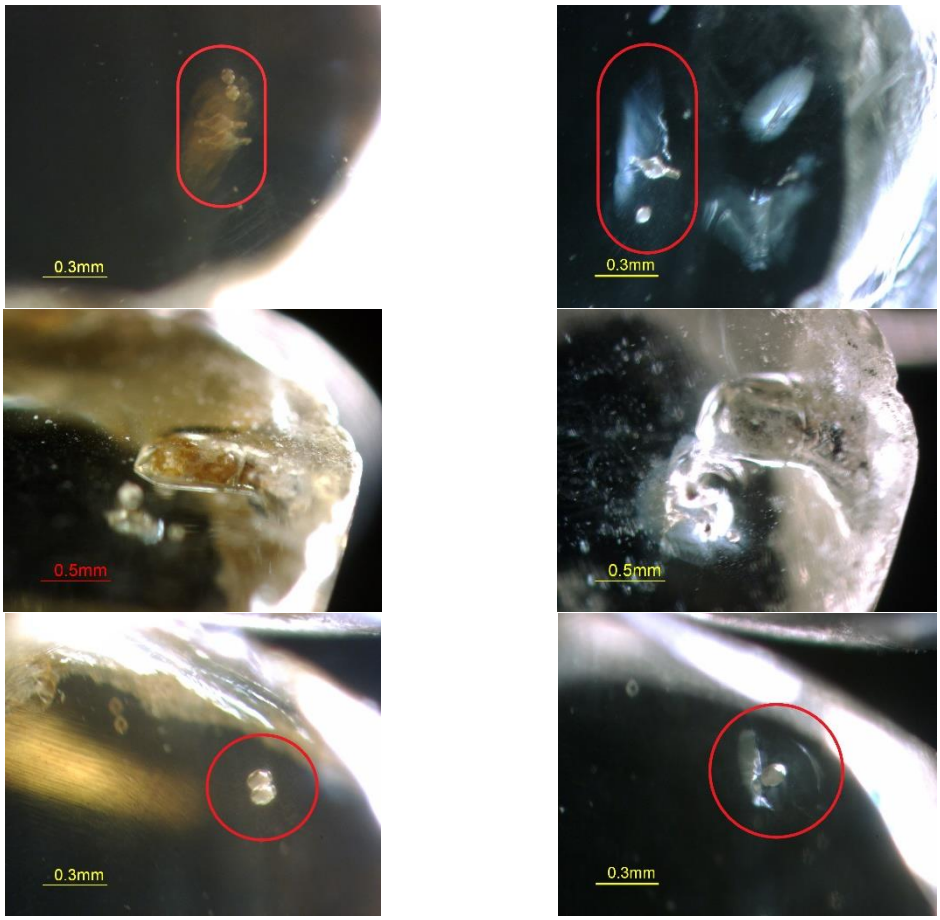

Figure 3. Internal features before (left column) and after heating (right column); fractures (top row), iron oxide stain (middle row) and tension crack (bottom row).

Table 2. Change of color of Mogok zircon samples before and after heat treatment at different temperatures.

Initial color	Unheat	900 °C	1000 °C	1100 °C
Pale yellow	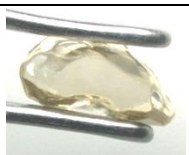			
Intense yellowish brown	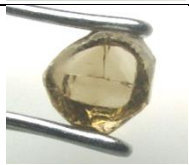	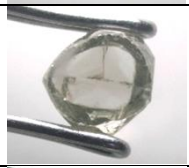	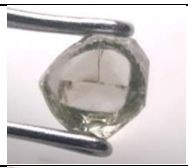	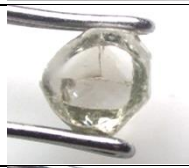
Pale yellowish brown			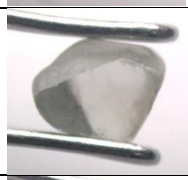	
Greenish brown	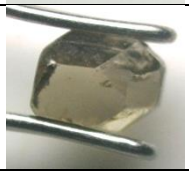	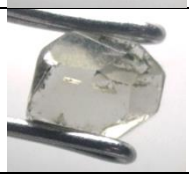	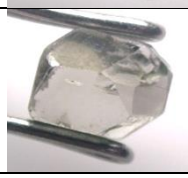	

The UV-Vis-NIR absorption spectra of 30 unheated Mogok zircon samples showed a broad absorption between 300 - 400 nm which its center was in ultraviolet range with an absorption tail extending into the visible region. This band is due to the absorption of color center which caused brown color in zircon[2]. The samples also showed the absorption peaks of U^{4+} between 400 - 700 nm and the peaks of U^{5+} at 1050 1108 1430 1500 and 1660 nm[1]. The absorption intensity of dark-color tone samples is higher than the light- color tone ones.

After heating under reducing conditions, the samples showed decreasing of the color-center absorption band between 300 - 400 nm which resulted in brown discoloration in the heated samples. The absorption peaks of U^{4+} and U^{5+} has no significant change. The UV-Vis-NIR absorption spectra of natural Mogok zircon are different from alkaline basaltic zircon which normally shows the O-hole center absorption bands between 400 - 600 nm (center at 505 nm) and between 600 - 1000 nm (center at 800 nm). These bands are the causes of reddish brown color in natural alkaline basaltic zircon. After heating up to 600 ℃ in both oxidizing and reducing conditions, the O-hole center bands disappeared[1].

FTIR spectra of 30 unheated Mogok zircon samples were dominated by the following features: an absorption peak at 2740 cm^{-1} is due to $[SiO_4]^{4-}$ [7], the peak at 3580 cm^{-1} (can be varied to 3480 cm^{-1} in some samples) is due to O-H stretching and the absorption peaks of Uranium ion between 4567-6779 cm^{-1} [8]. After heating under reducing conditions, the samples showed decreasing of the absorption peak of U^{5+} at 6669 cm^{-1} which could be the result of U^{5+} changed to U^{4+} upon reducing heating.

Conclusion: The Mogok zircons are classified as high type zircon, and range from pale yellow to greenish brown. Their shapes are subhedral to euhedral. Chemical compositions data show ZrO_2 and SiO_2 as major elements, HfO_2 and Al_2O_3 as minor and trace elements. The studied Mogok zircons turn near colorless to pale yellowish green upon heat treatment under

reducing conditions at 900 - 1100°C soaked for 1 hour at each temperature. The brown coloration in Mogok zircons caused by the color center absorption between 300 - 400 nm which decreased after heating. From this experiment, heating zircons under reducing condition at 1100 °C causes more change of color with the highest saturation than the temperatures at 900 °C and 1000 °C . However, it cannot turn the studied samples into blue color.

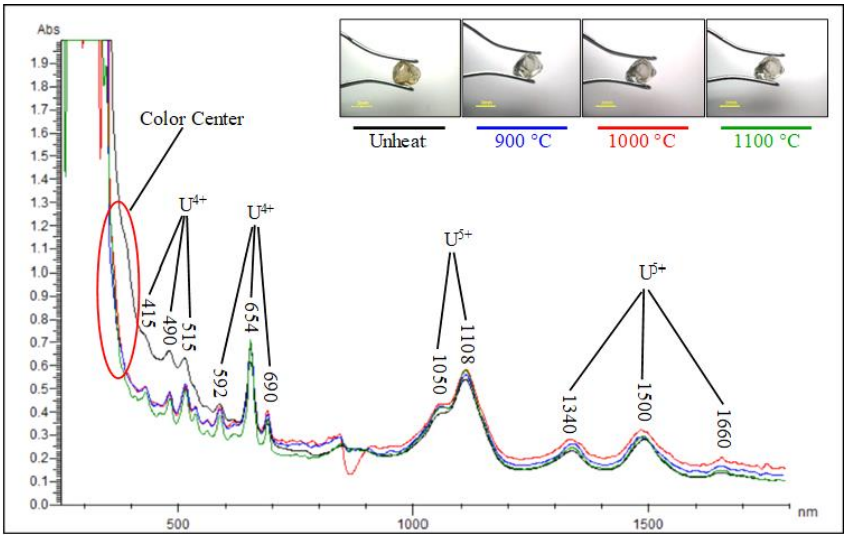

Figure 4. The UV-Vis-NIR absorption spectra of Mogok zircon samples before and after heat treatment under reducing conditions.

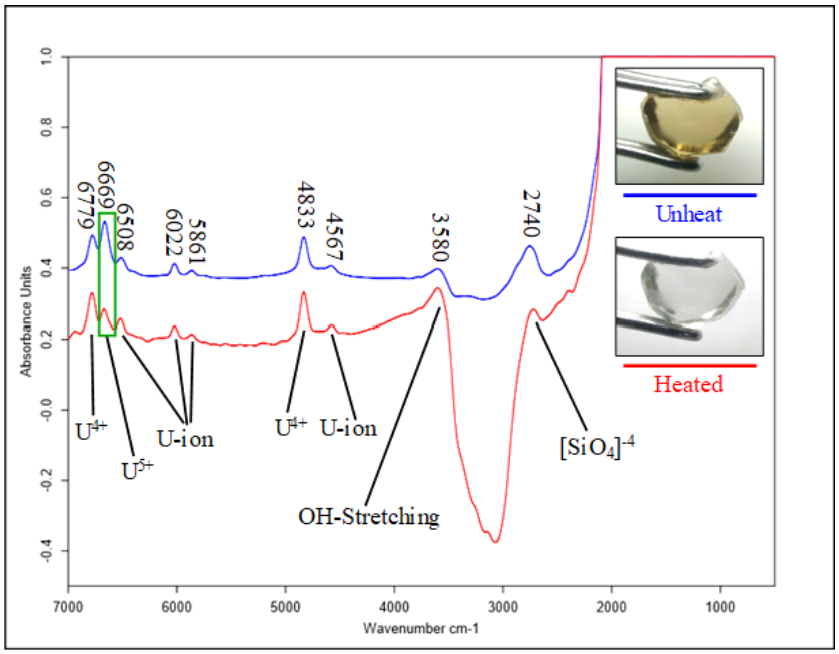

Figure 5. The Infrared spectra of Mogok zircon samples before and after heat treatment under reducing conditions.

References:
1. Zeug M, Nasdala L, Wanthanachaisaeng B, Balmer WA, Corfu F, Wildner M. J. Gemm. 2018;36(2):112-132.
2. Vuong BTS, Huong LTT. VNU Journal of Science: Earth and Environmental Sciences. 2015;31(3):60-66.
3. Satitkune S, Wanthanachaisaeng B, Won-in K, Wongkokau W, Chantaratat P, Leelawattanasuk T, Wathanakul P. IGC. 2013:158-160.
4. Searle MP, Noble SR, Cottle JM, Waters DJ, Mitchell AHG, Hlaing T, Horstwood MSA. Tectonics. 2007;26:1-24.
5. Huong LT-T, Vuong BS, Thuyet NTM, Khoi NN, Satitkune S, Wanthanachaisaeng B, Hofmeister W, Häger T, Hauzenberger C. J. Gemm. 2016;35(4):308-318.
6. Chen T, Ai H, Yang M, Zheng S, Liu Y. GEMS GEMOL. 2011;47(1):36-41.
7. Woodhead JA, Rossman GR, and Thomas AP. Am. Mineral. 1991b;76:1533-1546.
8. Zhang M, Salje EKH, Ewing RC. J. Phys: Condensed Matter. 2002;14(12): 3333-3352.

Acknowledgements: The authors would like to thank Mr. Sutas Singbamroong for samples providing and 50th Geological Anniversary Chiang Mai University for providing the financial support of this research project. Thanks are also extended to Assoc. Prof. Dr. Phisit Limtrakun for his suggestions, Mr. Siwakon Chimnakphant and Department of Geological Sciences, Faculty of Science, Chiang Mai University for providing the facilities.

F_008_PF: EFFECT OF SINTERING TEMPERATURES ON DENSITY AND VICKERS MICRO-HARDNESS OF BZT CERAMICS PREPARED BY MOLTEN SALT METHOD

Chompoonuch Warangkanagool*
Department of Physics, Faculty of Science, Naresuan University, Phitsanulok 65000, Thailand.
Research Center for Academic Excellent in Applied Physics, Faculty of Science, Naresuan University, Phitsanulok 65000, Thailand.
*e-mail: chompoonuchp@nu.ac.th

Abstract: In this research, the $Ba(Zr_{0.05}Ti_{0.95})O_3$ powders were prepared by molten salt method. The powders were calcined at 1000°C for 3 h with heating rate of 5°C/min. The sintering procedure was carried out at 1200, 1250 and 1300°C for 2 h with a heating/cooling rate of 5°C/min. Phase formation and microstructure were examined by XRD and SEM, respectively. The density of the sintered samples was measured by Archimedes method with distilled water as the fluid medium. The Vickers micro-hardness was determined using the Vickers indentation techniques. It was found that, the perovskite BZT cubic phase was found for all samples. The analysis was carried out based on the basis of Joint Committee on Powder Diffraction Standard (JCPDS) data. The morphology showed that, the ceramics more densification increased with increasing sintering temperature. The optimum sintering temperature for BZT ceramic was found at 1300°C. The highest relative density was about 90.3%, and the Vickers micro-hardness was 6.2 GPa.

Introduction: BZT or $Ba(Zr_xTi_{1-x})O_3$ solid solution has attracted considerable attention for its special characteristics. it has been shown that piezoelectricity, dielectric relaxation and tunability can be developed with specific zirconium content, resulting in a wide use for various device applications, such as piezoelectric transducers, tunable microwave devices, dynamic random access memories, and so on [1-4]. BZT in formula $Ba(Zr_{0.05}Ti_{0.95})O_3$ has excellent piezoelectric performance [5] and relatively high Curie temperature, it was therefore chosen as the matrix material. The molten salt method was used to prepare the BZT powder in this research because of its high reaction rate and lower reaction temperature, and it can improve the degree of homogeneous [6]. However, while these ceramics are used in the real applications, they are often applied in the devices that heats and vibrations are generated. This research, therefore, also study the hardness properties. So, the effects of sintering temperatures on density and Vickers micro-hardness of the $Ba(Zr_{0.05}Ti_{0.95})O_3$ ceramics prepared by molten salt method were investigated.

Methodology: The present material was prepared according to the formula $Ba(Zr_{0.05}Ti_{0.95})O_3$ powders by the molten salt method. All starting powder had a purity of 99.0% except for NaCl, which was 99.5%. The starting materials of $BaCO_3$, ZrO_2 and TiO_2 in molar ratio of 1:0.05:0.95 were mixed in a ball-mill for 24 h with ethyl alcohol and a zirconia ball. The slurry was dried and ground into powders (mixture BZT powders). The raw materials of NaCl and KCl in a molar ratio of 1:1 were mixed by hand-grinding for 20 min (mixture salt). The BZT mixture powders and mixture salts were mixed by hand-grinding at a 1:1 weight ratio and calcined at 1000°C for 3 h with heating rate of 5°C/min. The product was washed with distilled water many times. The remaining salt was washed with hot de-ionized water until no free chloride ions were detected by silver nitrate solution. The calcined powders of the BZT were ball milled with 1% PVA in ethanol for 12 h using the same method as mentioned earlier. The slurry was dried, sieved and pressed into a disc shape and sintered at 1200-1300°C for 2 h with heating rate of 5°C/min. Phase formation of the sintered pellets was determined by X-ray diffraction (XRD). The microstructure was examined by scanning electron microscopy. Bulk densities of the sintered ceramics were measured by the Archimedes method with distilled water as the fluid medium.

The Vickers micro-hardness of these ceramics was investigated by Vickers micro-hardness tester. Indentations were applied on the polished surfaces of the BZT ceramics. The applied loads were in the range of 500 g with an indentation period of 15 s.

Results and Discussion:

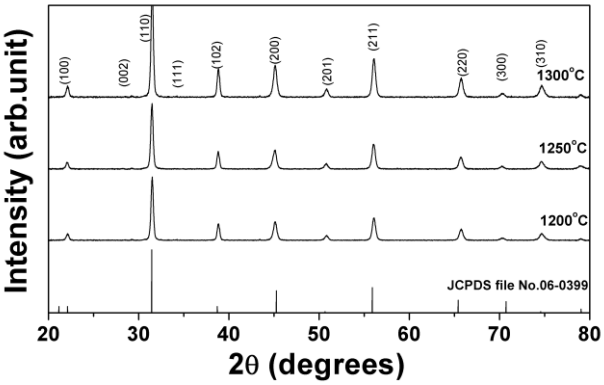

Figure 1. XRD patterns of BZT ceramics sintered at 1200-1300°C

Figure 1 shows the XRD patterns of the BZT ceramics sintered at 1200-1300°C for 2 h. All XRD patterns display a cubic phase structure. These patterns could be matched with a JCPDS file number 06-0399 [7]. The XRD data in this study were compared with $BaTiO_3$ phase (JCPDS data file number 06-0399) because the $Ba(Zr_{0.05}Ti_{0.95})O_3$ in this research has only a small amount of Zr. It can be seen that the cubic phase structure of $Ba(Zr_{0.05}Ti_{0.95})O_3$ was found for all samples.

Figure 2 shows microstructure of BZT ceramics sintered at 1200, 1250 and 1300°C, the grain morphology have rather rectangular shape. The porosity decreases with increasing sintering temperature.

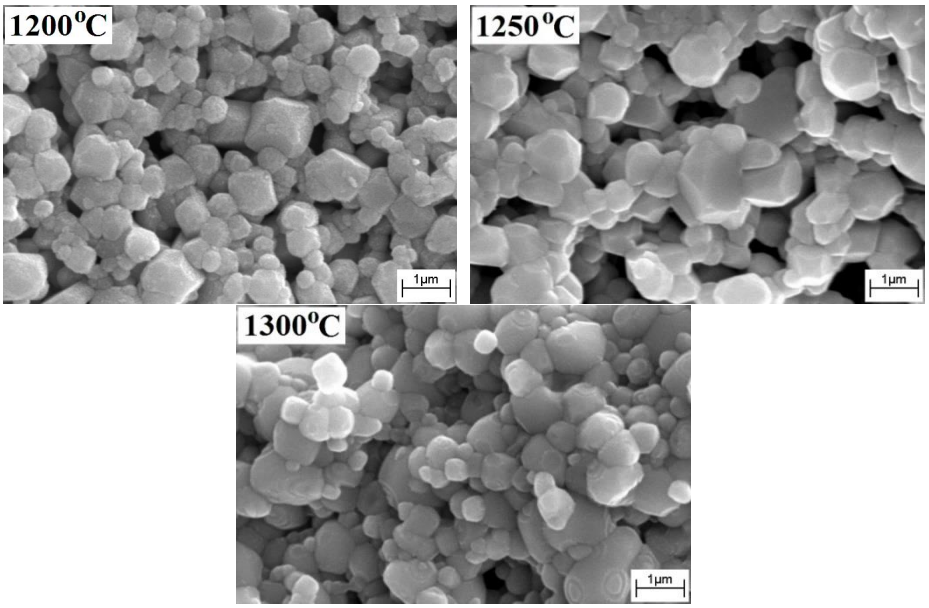

Figure 2. SEM photographs of BZT ceramics sintered at 1200-1300°C

The relative density and Vickers micro-hardness of BZT ceramics were plotted as a function of sintering temperature as shown in Figure 3, the values of density of BZT ceramics are shown in Table 1. The value of relative density is in the range of 77.5-90.3%. The highest density as shown in BZT ceramic sintered at 1300°C corresponded well to SEM results in which a highly dense grain-packing was observed.

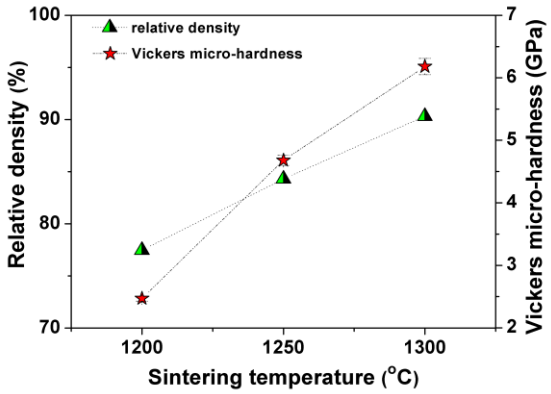

Figure 3. Relative density and Vickers micro-hardness of BZT ceramics sintered at 1200-1300°C

Table 1. Relative density and Vickers micro-hardness of BZT ceramics.

Sintering temperature (°C)	Relative density (%)	Vickers hardness (GPa)
1200	77.5	2.5 ± 0.04
1250	84.3	4.7 ± 0.08
1300	90.3	6.2 ± 0.13

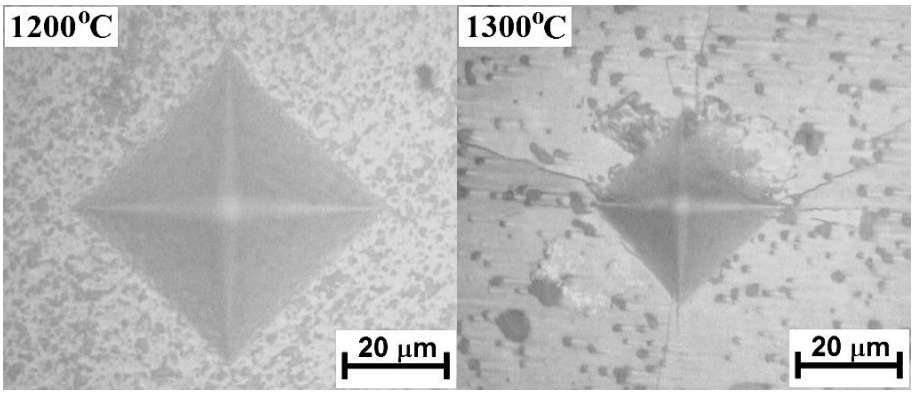

Figure 4. Optical micrographs of Vickers micro-hardness prints of BZT ceramics sintered at 1200 and 1300°C

The micro-hardness of the BZT ceramics was performed by using the Vickers micro-hardness tester. The OM photographs of Vickers prints are shown in Figure 4. The values of Vickers micro-hardness of BZT ceramics are shown in Table 1. The highest values of Vickers micro-hardness values of BZT ceramics was found at sample sintered at 1300°C. The OM photographs of Vickers micro-hardness prints of the lowest values of BZT ceramic sintered at 1200°C compared with SEM photographs of BZT ceramics sintered at 1200°C. The OM photographs of Vickers micro-hardness prints of the highest values of BZT ceramic sintered at 1300°C compared with SEM photographs of BZT ceramics sintered at the same temperature.

The result from our study is consistent with Yuan *et al.* [8], which reported the increase in hardness with increasing density.

Conclusion: $Ba(Zr_{0.05}Ti_{0.95})O_3$ ceramics prepared powders by molten salt method. The effect of sintering temperatures on density and Vickers micro-hardness of BZT ceramics were investigated. All of BZT samples were showed the perovskite cubic phase. The morphology showed that, the ceramics more densification and more value of Vickers micro-hardness increased with increasing sintering temperature. The optimum sintering temperature for BZT ceramic was found at 1300°C. The highest relative density was about 90.3%, and the Vickers micro-hardness was 6.2 GPa.

References:

1. Cao WQ, Xiong JW, Sun JP. Mater Chem Phys. 2007;106:338-342.
2. Tang XG, Wang J, Wang XX, Chan HLW. Solid State Commun. 2004; 131:163-168.
3. Wang YL, Li LT, Qi JQ, Gui ZL. Ceram Int.2002;28:657-661.
4. Zheng P, Zhang JL, Qin HB, Song KX, Wu J, Ying ZH, Zheng L, Deng JX. J Electron Mater. 2013;42:1154-1157.
5. Liang D, Zhun X, Zhu J, Zhu J, Xiao D. Ceram Int. 2014; 40:2585-2592.
6. Rahaman MN. Ceramic Processing and Sintering (2nd edition), Marcel Dekker, 0-82470-988-8 York, USA. 2003.
7. Powder Diffraction File, Card No. 06-0399, Joint Committee for Powder Diffraction Standards (JCPDS) PDF-4, International Centre for Diffraction Data (ICDD) 2000.
8. Yuan X, Liu X, Wang L, Lu X. IOP Conf Ser.: Earth Environ Sci. 2017; 61:012140.

Acknowledgements: This research was supported by National Research Council of Thailand (NRCT), Department of Physics, Faculty of Science, Naresuan University. The author would like to thank Prof. Dr. Tawee Tunkasiri and Prof. Dr. Gobwute Rujijanagul for his help in many facilities [Materials Science Research Laboratory (MSRL), Department of Physics and Materials Science, Chiang Mai University].

SESSION G:
MATHEMATICS / STATISTICS / COMPUTER SCIENCE

G_001_PF: EDGE-ODD GRACEFUL LABELING IN THE CONTEXT OF DUPLICATION OF GRAPH ELEMENTS

Pijittra Sangthong[1], Siwaporn Saewan[2,*]
[1]Students, Department of Mathematics and Statistics, Faculty of Science, Thaksin University, Phatthalung 93210, Thailand
[2]Assist. Prof. Dr., Department of Mathematics and Statistics, Faculty of Science, Thaksin University, Phatthalung 93210, Thailand
*e-mail: si_wa_pon@hotmail.com

Abstract: Let G be a simple connected and undirected graph with vertex set $V(G)$ and edge set $E(G)$. An edge-odd graceful labeling of a graph G with p vertices and q edges is a bijection function f from the set of edges $E(G)$ to the set $\{1, 2, 3, \ldots 2q-1\}$ with the property that, for each vertex $v \in V(G)$ is assigned the sum of all edges incident to it $mod\, 2\, q$. The edge labels and the vertex labels are distinct. A graph is called edge-odd graceful if it admits an edge-odd graceful labeling. In this paper we show that the graph obtained by duplication of an element of a cycle with even vertices are edge-odd graceful.

Introduction: Let G be a simple connected and undirected graph with vertex set $V(G)$ and edge set $E(G)$. Let $p = |V(G)|$ be the number of the vertices and $q = |E(G)|$ be the number of the edges of G. A labeling of a graph G is a rule that assign an integers either to the vertices or edges or both subject to certain conditions. Rosa [1] introduced a labeling called *β-valuation*, later Golomb [2] called as graceful labeling.

Definition 1 Let G be a graph with q edge. A function f is called a *graceful labeling* of a graph G if f is an injection from the set of vertices $V(G)$ to the set $\{0, 1, \ldots, q\}$ and each edge $e = uv$ is assigned the label

$$|f(u) - f(v)|,$$

the resulting edge labels are $\{1, 2, 3, \ldots, q\}$. A graph which admits a graceful labeling is called a graceful graph.

Vaidya and Bijukumar [3] shown that the graphs obtained by duplication of an arbitrary vertex in cycle C_n as well as duplication of an arbitrary edge in even cycle C_n are graceful graphs

Later, Solairaju and Chithra [4] introduced a new type of labeling of a graph G called an edge-odd graceful labeling.

Definition 2 A function f is called an *edge-odd graceful labeling*. If f is a bijection function from the set of edges $E(G)$ to the set $\{1, 3, \ldots, 2q - 1\}$ such that the induced function $f+$ from the set of vertices $V(G)$ to $\{0, 1, 2, \ldots, 2q - 1\}$ given by

$$f + (u) = \sum_{uv \in E(G)} f(uv) (mod\, 2\, q).$$

The edge labels and vertex labels are distinct. A graph which admits an edge-odd graceful labeling is called an *edge-odd graceful graph*.

Solairaju and Chithra [4] showed edge-odd graceful labelings of graphs related to paths: the Hoffman tree, the Bistar, the graph $< K_{1,n} : 2 >$ and the Double star. Daoud [5] proved necessary and sufficient conditions for some path and cycle related graphs to be an edge-odd graceful. Solairaju et.al. [6] showed the edge-odd graceful labelings of graphs as the sum of a path with n vertices and each path with 2, 3, 4, 5, and 6 vertices.

Definition 3 The duplication of an edge $e=uv$ of a graph G produces a new graph by adding a new edge $e^*=u^*v^*$ such that

$$N(u^*)=N(u)\cup\{v^*\}-\{v\}$$

and

$$N(v^*)=N(v)\cup\{u^*\}-\{u\},$$

where $N(u^*)$ denotes the set of vertices adjacent to u^* and is called the Neighbours of u^*.

Definition 4 The duplication of a vertex edge $e=uv$ of a graph G produces a new graph by adding a new edge $e^*=u^*v^*$ such that $N(u^*)=N(u)\cup\{v^*\}-\{v\}$ where $N(u^*)$ denotes the set of vertices adjacent to u^* and is called the Neighbours of u^*.

A cycle graph or cycle is a connected graph that consists of a single cycle and number of vertices at least 3. The number of vertices in a cycle equals the number of edges and every vertex has degree 2. The cycle graph with n vertices is denoted by Cn.

In this paper, we show that the new graphs obtained by duplication of an arbitrary edge of a cycle C_n, where $n\equiv 0(mod6)$, duplication of an arbitrary vertex of a cycle C_n, where n is even are edge-odd graceful.

Results and Discussion: In this section, we prove the following results.

Theorem 1: The graph obtained by duplicating an arbitrary edge in a cycle C_n, where $n\equiv 0(mod6)$ is edge odd graceful.

Proof.: Let C_n be a cycle with n vertex, where $n\equiv 0(mod6)$ and let v_i where $1 \le i \le n$ be the successive vertices of the cycle C_n such that v_i is adjacent to v_{i+1}. Let G be the graph obtained by duplicating an arbitrary edge $v_k v_{k+1}$ of C_n by a new edge $v_k{}'v_{k+1}{}'$. Without loss of generality, duplicating an edge v_1v_2 by a new edge $v_1{}'v_2{}'$. Let the vertex set and the edge set of G be

$$V(G) = \{v_i : i = 1,2,3,\dots,n\} \cup \{v_i{}', v_{i+1}{}'\}$$
$$E(G) = \{v_i v_{i+1} : i = 1,2,3,\dots,n-1\} \cup \{v_1{}'v_n, v_1{}'v_2{}', v_2{}'v_3\}.$$

Hence we have $|V(G)| = n+2$ and $q = |E(G)| = n+3$.

First, we define the edge labeling $f: E(G) \to \{1,3,5,\dots,2q-1 = 2n+5\}$ as follows.

$$f(v_1{}'v_n) = 1$$
$$f(v_1{}'v_2{}') = 3$$
$$f(v_2{}'v_3) = 5$$
$$f(v_1v_n) = 7$$
$$f(v_i v_{i+1}) = 2i+7, i = 1,2,3,\dots,n-1.$$

Hence $\{f(v_iv_{i+1})\} = \{9, 11, 13, \dots, 2n+5 \mid i = 1,2,3,\dots,n-1\}$.

Let A be the set of all edges of C_n in G and let B be the set of new edges of G. Let A^* and B^* be the sets of edge labels of the edges in the sets A and B respectively. We observe that

$A^* = \{7, 9, 11, \dots, 2n+5\}$

$B^* = \{1,3,5\}$.

It is obvious that f is bijective and the edge labels are odd. Also, we observe the induced vertex labels that

$$f+(v_1{}') = 4$$
$$f+(v_2{}') = 8$$
$$f+(v_1) = 16$$
$$f+(v_2) = \begin{cases} 2, & \text{if } n = 6 \\ 20, & \text{if } n > 6 \end{cases}$$
$$f+(v_3) = f+(v_2) + 9$$
$$f+(v_n) = 7$$
$$f+(v_i) = (4i+12)(mod\ 2q) \text{ for } i = 4,5,6,\dots,n-1.$$

Therefor the set of the vertex labels are distinct. So f is an edge-odd graceful labeling. □

As an example, the graph G obtained by duplicating an arbitrary edge in a cycle C_6 is given in Figure 1. The edge-odd graceful labeling of the graph G shown in the proof for Theorem 1 is given in Figure 2.

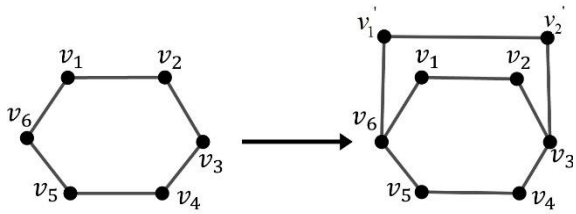

Figure 1.

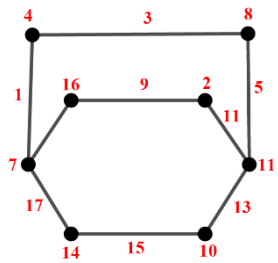

Figure 2.

Theorem 2: The graph obtained by duplicating an arbitrary vertex in a cycle C_n, where n is even, is edge odd graceful.

Proof.: Let C_n be a cycle with n vertex, where n is even and let v_i where $1 \le i \le n$ be the successive vertices of the cycle C_n such that v_i is adjacent to v_{i+1}. Let G be the graph obtained by duplicating an arbitrary vertex v_k of C_n by a new edge uw. Without loss of generality, duplicating an vertex v_1 by a new edge uv. Let the vertex set and the edge set of the graph G be

$$V(G) = \{v_i : i = 1,2,3,\dots,n\} \cup \{u, w\}$$

and $$E(G) = \{v_i v_{i+1} : i = 1,2,3,\dots,n-1\} \cup \{v_1 u, v_1 w, uw\}.$$

Hence we have $|V(G)| = n + 2$ and $q = |E(G)| = n + 3$.

First, we define the edge labeling $f: E(G) \to \{1,3,5,\dots,2q - 1 = 2n + 5\}$ as follows.

$$f(v_1 w) = 2n + 5$$
$$f(uw) = 2n + 3$$
$$f(v_1 u) = 2n + 1$$
$$f(v_1 v_2) = 2n - 1$$
$$f(v_i v_{i+1}) = 2i - 1 \text{ for } i = 1, 2, 3,\dots, n - 1.$$

Hence $\{f(v_i v_{i+1} \mid i = 1, 2, 3,\dots, n - 1)\} = \{1, 3, 5, \dots, 2n - 3\}$.

Let A be the set of all edges of C_n in G and let B be the set of new edges of G. Let A^* and B^* be the sets of edge labels of the edges in the sets A and B respectively. We observe that

$A^* = \{1, 3, 5, \dots, 2n - 3, 2n - 1\}$

$B^* = \{2n + 1, 2n + 3, 2n + 5\}$.

It is obvious that f is bijective and the edge labels are odd. Also, we observe that

$$f^+(v_1) = 2n - 6$$
$$f^+(v_n) = (4n - 4) \bmod (2n + 6)$$
$$f^+(u) = 2n - 2$$
$$f^+(w) = 2n + 2$$
$$f^+(v_{i+1}) = 4i \bmod (2n + 6) \text{ for } i = 1, 2, 3, \dots, n - 2.$$

Therefor the set of the vertex labels are distinct. So f is an edge-odd graceful labeling. □

As an example, the graph G obtained by duplicating an arbitrary vertex in a cycle C_4 is given in Figure 3. The edge-odd graceful labeling of the graph G shown in the proof for Theorem 2 is given in Fig 4.

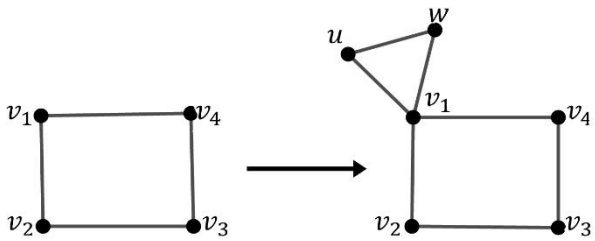

Figure 3.

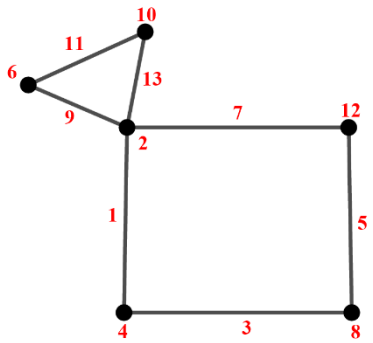

Figure 4.

Conclusion: Motivated by the recent work of edge-odd graceful labeling, we introduced an edge-odd graceful labeling of new graphs obtained by duplication of an arbitrary edge and obtained by duplication of an arbitrary vertex of a cycle C_n.

References:

1. Rosa A. On certain valuations of the vertices of a graph. in: Theory of Graphs (Internat. Symposium, Rome, (July 1966), Gordon and Breach), N. Y. and Dunod Paris 1967; 349-355.
2. Golomb S. W. How to number a graph. in: Graph Theory and Computing, R C Read, ed., Academic Press. New York. 1972; 23-37.
3. Vaidya, S.K., & Bijukumar, Lekha. Some new graceful graphs. International Journal of Mathematics and Soft Computing. 2011; 37 - 45
4. Solairaju A. and Chithra K. Edge-Odd Graceful Graphs, Electronic Notes in Discrete Math. 2009; 15-20.
5. Daoud S. N. Edge odd graceful labeling of some path and cycle related graphs. AKCE International Journal of Graphs and Combinatorics. 2017; 178–203.
6. Solairaju1 A. Balasubramanian G. Ambika B. Edge-Odd Graceful Labeling for Sum of a Path and a Finite Path. Global Journal of Mathematical Sciences: Theory and Practical. 2017; 323-335.

Acknowledgements: This work was supported by Thaksin University.

G_002_OF: EXPLORING DATA CLASSIFICATION MODELS FOR IDENTIFICATION OF CKD PROGRESSION INTERVAL: A CASE STUDY

Theeranai Sangjan*, Natthakan Iam-On, Pattariya Singpant, Sujitra Arwachananukul
IQD-IT Research Group, School of Information Technology, Mae Fah Luang University, Chiang Rai 57100, Thailand
*e-mail: thesangjan@gmail.com

Abstract: Chronic kidney disease (CKD) has become one of the major health problems, witnessed globally over decades. Given a high rate of death, patients with CKD are to receive an appropriate treatment as soon as they are diagnosed as stage 3rd. Sooner or later, depending on medical treatment and personal conditions, CKD will progress to stage 5th. The cost of kidney dialysis in this later stage can be very high, with a number of patients normally overwhelm the treatment capacity. Ability to predict the translational interval between these stages may well be useful for both patients and medical service providers. This paper responses to the quest by investigating a classification model for a real case study. Given the original data obtained from Phan hospital, Chiang Rai, different approaches have been explored to improve predictive performance of conventional classifiers. These include feature selection, dimensionality reduction and imbalanced data classification. Based on 10-fold cross validation, the model yielding the best accuracy is K-Nearest Neighbors (K = 1), with the rate of 84.60%.

Introduction: Chronic Kidney Disease (CKD) is a condition which is abnormal in the kidney; It is means kidney cannot work efficiently for a long time. Most of CKD will often cause to deteriorate permanently, unable to return a normal again. Moreover, CKD is a significant factor cause of heart disease and coronary artery disease (CAD) those problems lead to humans die prematurely. CKD is one world-wide public health problem because its end of the stage and high possibility of death are using high-cost treatment. Incidence and prevalence of CKD in Thailand approximately from the prevalence in Thailand 4.3% to 13.8% of the population[1]. As the cost of dialysis for the CKD 5th stage of patients in Thailand is about 1500 baht/session and 4500 baht/week reported by Thailand Security Service Officer. According to 2017 Clinical Practice Guideline for the Evaluation and Management of Chronic Kidney Disease from Kidney Disease Improving Global Outcome (KDIGO) Clinical Practice Guideline Update for the Diagnosis, Evaluation, Prevention, and Treatment of CKD-MBD has divided chronic kidney disease into six stages based on glomerular filtration rate (GFR) as CKD1, CKD2, CKD3a, CKD3b, CKD4, CKD5.[2] As such, various data mining techniques exploited in related works will be explored as to support the value of this paper. In fact, algorithms have been widely used for prediction in the medical context. They provide different accuracy levels depending on the nature of data under examination.

B. V. Ravindra, N. Sriraam and M. Geetha propose a clinical decision support tool for chronic kidney using Artificial Neural Network (ANN). It is to predict whether a case is categorized as CKD or Non-CKD. They have collected the dataset from local hospital with 230 records. Backpropagation Neuron Network used as the classification model. The stimulation shows the result with the overall accuracy of 95.3%.[3]

M. Ahmad, V. Tundjungsari, D. Widianti, P. Amalia and U. A. Rachmawati have presented a decision support system that makes use of Support Vector Machine (SVM), one of the most well-known algorithms in classification. The research area focuses on the diagnostic tool of Kidney Disease, which helps a doctor to determine whether the patient's condition signifies chronic kidney disease or not. The underlying data is expressed by five attributes and 400 records. The experimental result suggests the accuracy of 98.34%.[4]

Charleonnan A., T. Fufaung, T. Niyomwong, W. Chokchueypattanakit, S. Suwannawach and N. Ninchawee6 produce a predictive analytics system for Chronic Kidney Disease. They

propose four machine-learning algorithms for the empirical study, which are K-nearest Neighbors, logistic regression (LR), Decision Tree, and Support Vector Machine, respectively. The best model from comparative assessment will be chosen to build the target classifier. In particular, the best classification is Support Vector Machine that reaches the high accuracy of 98.3%.[5]

To explore data classification models for the identification of CKD progression interval, the common five steps of data mining process are followed; namely data collection and preparation, data preprocessing, data transformation, design and generation of classification models, and model evaluation, respectively. For the details of each step will be explained in the next section.

Methodology: Data Mining method was proposed as a technique to find the meaning of the medical data. We proposed the data mining method following by Data Mining Concepts and Techniques as a conceptual framework. This research focused on methodology to optimization classification model in imbalanced data to improve the accuracy score of classification model. A detail in every process proposed following

Data collection and preparation.: Phan hospital, Chiang Rai, Thailand, who provi ded the medical data set to support this study. The processes to collecting the data start from the first process of hospitality by Phan hospital until the doctor diagnosed that the patient has condition of CKD. Not only collecting the data in the process of disease diagnosed but also collecting in follow-up processes. The doctors and nurses interviewed the patient and view patient's medical history. They are concerned latent symptoms in CKD such as hypertension, diabetes and ischemic heart disease. There are some missing parameters in the data. some values are missing because of two main problem in this context. First, they are no laboratory result that including CKD stage because the patient they are wanting to meet a doctor for another disease diagnosis. The last one is having no laboratory test when they got a dialysis.

Data Preprocessing: Due to the two main problems in the data collection process, we applied to fill in the missing values and delete insignificant attributes such as HN and citizen ID. This process will be explained below. CKD stage of the patient calculation: In case of incorrected stage at the data set we have to calculate the CKD stages of patient based on CKD EPI formulas and replaced it. For the CKD-EPI formulas has divided into four formulas based on gender and amount of Creatinine.

$$GFR_{Female(Creatinine\leq 0.7)} = 114 \times (\frac{Creatinine}{0.7})^{(-0.329)} \times (0.993)^{Age} \quad (1)$$

$$GFR_{Female(Creatinine>0.7)} = 114 \times (\frac{Creatinine}{0.7})^{(-1.209)} \times (0.993)^{Age} \quad (2)$$

$$GFR_{Male(Creatinine\leq 0.9)} = 114 \times (\frac{Creatinine}{0.9})^{(-0.411)} \times (0.993)^{Age} \quad (4)$$

$$GFR_{Male(Creatinine>0.9)} = 114 \times (\frac{Creatinine}{0.7})^{(-1.209)} \times (0.993)^{Age} \quad (3)$$

Then the size of data set is 168 records. Which contain 80 records of male and 88 records of female, and 62-year-old is the average patient's age where the range from 49 to 91-year-old. Moreover, there are patients with diabetes approximately 63% and 70% of records with hypertension.

Transformation: The range of some selected attributes are too wide. That is not suitable to provide classification model development. Rescaling the range was provided to rescale the range of the data in this process. There are many methods to rescaling depends on the pattern of the values in the data set. For high and normal of sugar value, high and normal of fat value, high, normal and low of waste value in blood. All of them are rescaling into the range [0,1], the equation which are

$$FBS_{high} = \frac{fbs_{high}}{fbs_{total}} \quad (5)$$

$$FBS_{normal} = \frac{FBS_{normal}}{FBS_{total}} \quad (6)$$

$$HDL_{high} = \frac{hdl_{high}}{hdl_{total}} \quad (7)$$

$$HDL_{normal} = \frac{hdl_{normal}}{hdl_{total}} \quad (8)$$

$$BUN_{high} = \frac{bun_{high}}{bun_{total}} \quad (9)$$

$$BUN_{low} = \frac{bun_{low}}{bun_{total}} \quad (10)$$

$$BUN_{normal} = \frac{bun_{normal}}{bun_{total}} \quad (11)$$

There are 41 to 61 year of the patient's age range by using the equation 12 for rescaling the range of age into [0,1], The equation 12 was applied from max-min scalar. the equation explained below.

$$age_{norm} = \frac{age - age_{min}}{age_{max} - age_{min}} \quad (12)$$

After that, the range of value will be rescaled in the same range. furthermore, for the value that is not a number such as Yes and No; Yes as 0 and No as 1. For example, diabetes, BMI high, and NSAIDs. 19 parameters were chosen and there can be divided into two types which are numeric and nominal. For a list of chosen parameters, we explanation on table 1.

Table 1. A list of selected parameters for generating the classification model.

Attributes / Parameter	Data Type	Value Domain
Gender	Nominal	{0, 1}
Age	Numeric	[0,1]
High-sugar value in blood (FBS-high)	Numeric	[0,1]
Normal-sugar value in blood (FBS-normal)	Numeric	[0,1]
High-fat value in blood (HDL-high)	Numeric	[0,1]
Normal-fat value in blood (HDL-normal)	Numeric	[0,1]
High-waste value in blood (BUN-high)	Numeric	[0,1]
Low-waste value in blood (BUN-low)	Numeric	[0,1]
Normal-waste value in blood (BUN-	Numeric	[0,1]
normal)	Nominal	{0, 1}
BMI high	Nominal	{0, 1}
NSAIDs	Nominal	{0, 1}
Diabetes (DM)	Nominal	{0, 1}
Hypertension (HT)	Nominal	{0, 1}
Stone (N20)	Nominal	{0, 1}
Ischemic heart disease (I200)	Nominal	{0, 1}
Disease related to hearth failure (I500)	Nominal	{0, 1}
Gout or Rheumatoid (M109)	Nominal	{0, 1}
Albumin		

These are the list of selected parameters after a process of transformation and normalization. The next step is utilizing the period of the time between the first day of stage 3rd and 5th as answer of a model called class label. Due to treatment year of a patient have collected from the first day of hospitality to ninth years of hospitality in CKD stage 5 patient. That become the reasons we divided a group of patients into two groups which are patients

that have treatment history less than or equal to 3.5 years and patient that have treatment history more than 3.5 years. These data consist of 108 records for less than or equal to 3.5 years and 60 records for more than 3.5 years. That is two categories for classification model generation.

Design and Generating Classification models: We proposed Python Scikit-Learn as a model builder and model evaluation. There are many classification algorithms in Scikit-learn, we use Decision Tree, K-nearest neighbor, Bayesian Naïve Bayes, and Support Vector Machine as a model classifier. In additional, there are might be a problem called imbalanced data that we mentioned. This problem must be resolved because a classification algorithm may focus on majority class. The result of model that created by imbalanced data will have low accuracy score; this means that the result of prediction would be wrong. Therefore, we use Synthetic Minority Over-sampling (SMOTE) to manipulate this problem.

Model Evaluation: The next step after Design and generating classification model is model evaluation. In this step we proposed k-fold cross validation, k = 10, as algorithm for the classifier evaluation. Equation 13 is formula of confusion matrix classifier. For the result of equation of accuracy score will range in [0,100].

$$Accuracy = \left(\frac{TP+TN}{TP+FP+TN+FN}\right) \times 100 \quad (13)$$

Table 2 Shown confuse Matrix of binary classes of class label that was applied to evaluation classifier model.

Table 2. Confuse matrix of binary classes.

		Actual Values	
		Positive	Negative
Predictive Values	Positive	TP	FN
	Negative	FP	TN

Results and Discussion: As mentioned before, this data set has a problem called imbalanced data. An experimentation including Synthetic Minority Over-sampling (SMOTE), SMOTE with Distance selection, and SMOTE with Kernel Principal Components Analysis (KPCA) to find a method that is the best practice. Due to the original data consist of 168 records, 19 attributes, and 1 class label. Table 3 will present accuracy of difference classification model used for this study in original dataset. 10-fold cross validation was preferring as model evaluation. The accuracy in the table 3 is average across ten repetitions of evaluation with standard deviation (S.D.). From the table 3, the highest accuracy was K-nearest Neighbor.

Table 3. A result of original data set when generating a classification model.

No.	Classifier	Technique	Accuracy	S.D.
1	K-nearest Neighbor	k = 1	65.70	0.26
2	Decision Tree	Entropy	58.20	1.02
3	Bayes Sian	Naïve Bayes	61.90	0.54
5	Support Vector Machine	Support Vector Classification	59.90	0.77

From the table 3, Accuracy of classifier is not satisfactory because effect of an imbalanced data. Therefore, we are using SMOTE as technique of resampling a new data to manipulate imbalanced data. The accuracy result of SMOTE shown on table 4. K-nearest neighbors also the highest accuracy but the second highest is Support Vector Machine.

Table 4. A result of resampling by using SMOTE and accuracy result from generating a classification model.

No.	Classifier	Technique	Accuracy	S.D.
1	K-nearest Neighbor	k = 1	84.60	0.55
2	Decision Tree	Entropy	61.50	0.53
3	Bayesian	Naïve Bayes	59.60	0.58
5	Support Vector Machine	Support Vector Classification	77.00	0.65

Although SMOTE can improve an accuracy score but that is not enough to accept as expected result. So, the next experimentation we tried to applied statistics method to improve an accuracy score. KPCA was proposed as a technique to reduce parameters that make confused rate in classifier. Table 5 show an accuracy score after applied KPCA combined with SMOTE to reduce attributes from 19 parameters into 5 parameters.

Table 5. A result reduce attribute from 19 parameters to 5 parameters using KPCA.

No.	Classifier	Technique	Accuracy	S.D.
1	K-nearest Neighbor	k = 1	75.60	0.74
2	Decision Tree	Entropy	62.10	0.65
3	Bayesian	Naïve Bayes	63.30	0.77
5	Support Vector Machine	Support Vector Classification	69.70	0.43

The last experimentation we reduce the attributes by applied Ensemble random forest to find a meaningful feature. We chose the first thirteen of parameters for generating classification model again. The result of using random forest show on table 6.

Table 6. A result reduce attribute from 19 parameters to 13 parameters using Random Forest.

No.	Classifier	Technique	Accuracy	S.D.
1	K-nearest Neighbor	k = 1	80.80	0.78
2	Decision Tree	Entropy	61.80	0.52
3	Bayesian	Naïve Bayes	61.30	0.68
5	Support Vector Machine	Support Vector Classification	76.90	0.61

From accuracy score on the table 6, K-nearest Neighbor is also the best classifier for this data. Support Vector Machine is the second-best classifier. We compare all of accuracy score that improved data in difference method, illustrated in figure 1.

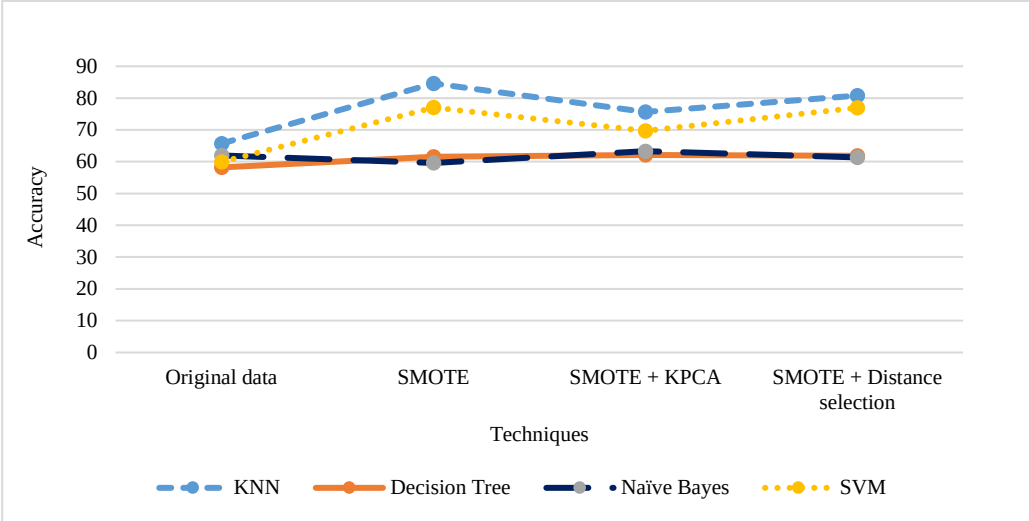

Figure1. The comparison of experimentation result.

Conclusion: Provided the empirical results given above, the biggest problem with this set of data is imbalance between classes. This can be solved to a certain extent, such that the best accuracy rate of 84.60 is achieved by one of the classifiers under examination. On the other hand, both dimensionality reduction and feature selection seem to be less effective, based on the results shown for the last two experiments. Perhaps, all the current attributes are equally informative to the final classification model, where less accurate classifiers may be obtained by cutting out some of those attributes. Hence, collecting more informative attributes is likely to be a better solution for enhancing the predictive capacity. Also, a use of classifier ensemble might also be another good research in the future.

References:

1. Ingsathit A., et al., NEPHROL DIAL TRANSPL. 2010; 5: 1567–1575.
2. Kidney Disease Improving Global Outcome, KI supplements. 2017; 7: 8.
3. Ravindra B, Sriraam N, Geetha M, International Conference on Communication, Computing and Internet of Things (IC3IoT). 2018, Feb 15-17;Chennai, India
4. Ahmad M., et al, Second International Conference on Informatics and Computing (ICIC). 2017, Nov 1-3;Papua, Indonesia.
5. Charleonnan A., et al. Management and Innovation Technology International Conference. 2016, Oct 12-14;Chonburi, Thailand.

Acknowledgements: Thanks to Phan Hospital for the provision of data exploited in this research, and to IQD-IT research group for technical and financial support.

SESSION H:
FOOD SCIENCE & TECHNOLOGY

H_009_PF: COMPARISON OF EXTRACTION TECHNIQUES USING DHS-TENAX TA, SBSE AND SPME FOR ANALYSIS OF DRIED CHILI VOLATILES

Ersa Aurora Ria Diani, Suwimon Keeratipibul, Panita Ngamchuachit*
Department of Food Technology, Faculty of Science, Chulalongkorn University, Phayathai Road, Pathumwan, Bangkok 10330, Thailand
*e-mail: Panita.N@chula.ac.th, panita.nuun@gmail.com

Abstract: The volatile compounds in dried chili samples were extracted using three different solvent-free techniques: dynamic headspace-Tenax TA (DHS-Tenax TA), headspace – stir bar sorptive extraction (HS-SBSE), headspace – solid phase micro extraction (HS-SPME). Seven groups of compound were found in dried chili. The result showed that DHS had highest number of compounds followed by headspace SBSE and SPME which 34, 13 and 17 compounds, respectively. DHS was efficient to adsorb hexanal, hydrocarbons and alcohols. Eventough HS-SPME had lowest identified compound, it was efficient to adsorb esters, hydrocarbons, and sesquiterpene hydrocarbons compared to HS-SBSE. Hexanal appeared as a compound with highest % peak area found in DHS-Tenax TA and HS-SBSE.

Introduction: Dried chili is one of the famous spice mostly used as flavoring and coloring ingredients in Asian dishes.[1] The quality of dried chili can be determined by moisture content, ascorbic acid content, microbial contamination, flavor and color.[2,3] Besides the quality related to physicochemical properties, the aroma characteristics of dried chili play important role in consumer acceptance and the subtances related to aroma are volatile compounds.

Numerous extraction techniques have been previously conducted to obtain volatile compounds such as steam distillation, solvent extraction and soxhlet extraction. However, these extraction methods are time-consuming which might not suitable for a large number of samples. Moreover, high temperature with long extraction time could induce loss of volatile compounds, degradation of volatile compounds to unrelated artifacts, and contamination of non-volatile compounds.[4,5] Other headspace extraction methods such as headspace solid-phase micro extraction (SPME), headspace – stir bar sorptive extraction (SBSE), and dynamic headspace (DHS) have been widely used for volatile analysis due to their rapid, sensitive, solvent-free, less contamination of non-volatile compounds, and less artifact formation.[7,12-15]

For headspace – solid phase micro extraction (HS-SPME), the fused-silica fiber is placed in the headspace of vial contains liquid or solid sample during extraction. The vial is heated then volatile compounds are released from food matrix and adsorbed into fiber. The fiber is coated with thin layer of polymeric stationary phases for concentrating the analytes during adsorption. After the extraction, the fiber is removed and desorbed by heating the fiber in GC injection port.[7] A headspace stir bar sorptive extraction (HS-SBSE) has been developed using stir bar coated with polydimethylsiloxane (PDMS) to adsorb volatile compounds.[9] The use of PDMS as extraction medium has been used due to the desorption of analytes can be done in lower temperature thus minimizing the losses of thermolabile analytes and the capacity of PDMS for a certain analytes is not influenced by the presence of water since the analytes are partitioned into the PDMS phase. The amount of PDMS varies based on the length of 10 mm (55 µL of PDMS) to 40 mm (219 µL of PDMS) and is higher compared to the PDMS coated onto SPME fiber with maximum amount of 0.5 µL. Therefore, the extraction efficiency is improved compared to SPME.[8] After extraction, the stir bar is rinsed with distilled water, dried on a lint-free tissue and then subjected to thermal desorption analysis.[9] For a dynamic headspace extraction, the carrier gas is purged through the sample leading to the release of volatile compounds from the sample to the headspace. The released volatile compounds are then trapped into an adsorptive trap for further gas chromatography (GC) analysis.[6]

Many fiber coating materials of SPME are available including PDMS, CAR/PDMS, DVB/CAR/PDMS and PDMS/DVB. Based on fiber properties. PDMS, CAR/PDMS, and

DVB/CAR/PDMS are effective to extract low polarity compound. PDMS/DVB can be used to extract medium polarity compound.[7] A lot of studies had been conducted using HS-SPME technique to identify volatile compound. The presence of hexanal, 2-isobutyl-3-methoxypyrazine, 2,3-butanedione, 3-carene, trans-2-hexenal and linalool appeared as major compounds in fresh chili.[16] Esters, alcohols, terpenes and aldehydes found in fresh chili pepper.[10,17]

PDMS is used as sorbent in SBSE technique. A study was performed for identification of volatile and semi-volatile compounds in traditional Korean fermented rice wines using DHS Tenax TA and SBSE. It was found that the identified compounds varied depend on the extraction technique. DHS technique was effective to extract low molecular-weight polar compounds (acetic acid, 3-ethoxy-1-propanol and ethyl lactate). In other hand, SBSE was better than DHS to analyze semi-volatile compound and relatively high molecular weight compound (fatty acid ethyl esters).[18]

In previous studies, several sorbents have been used in DHS including Tenax, silica gel, chromosorb, carbotrap and carbon molecular sieves. Tenax sorbent is the most popular since it has wide volatility range, high temperature stability, low water affinity and long shelf life.[22] Manzini et al. (2011) compared two different sorbents (Tenax TA and Tenax GR) to trap the furfurals and suggested that Tenax TA had higher reproducibility compared to Tenax GR.[23] A study was conducted for compound identification in butter samples using DHS- Tenax TA and SPME (DVB/CAR/PDMS) techniques and found that DHS had higher extracted compounds compared to SPME.[11]

Even though few studies reported the major volatiles compound, the comparative volatile profile of dried chili extracted by DHS, SPME, SBSE headspace extraction is still lacked. The objective of this study is to compare extraction technique using DHS, headspace SPME and SBSE for identification of volatile compounds in dried chili.

Methodology:

Sample collection: Whole commercially dried chili samples *(Capsicum frutescens* L. cv 'Jinda') was received from dried chili manufacture in Nakhon-Pathom province in 2019.

Sample preparation: For each replicate (3 replicates in total), fifteen grams of dried chili without peduncle were immersed in liquid nitrogen and ground homogenously to powder using a grinder (LAB MILL Osaka Chemical Co., Ltd.; Japan). Five grams of ground powder was differentiated for each extraction techniques.

Headspace-Solid phase micro ectraction (HS-SPME): A 1.5 grams of ground sample placed in a 20 mL vial with a polytetrafluoroethylene (PTFE)/silver screw cap and were spiked with 10 µL of 2-methyl-3-heptanone (0,1632 g/L in methanol) as internal standard. The sample in the vial was heated in a water bath (40 °C) for 20 min and then subjected to a HS-SPME fiber coating with divinylbenzene/carboxan/polydimethylsiloxane (DVB/CAR/PDMS, 50/30 µm, Supelco, Bellefonte, PA, USA). The volatiles were extracted at 40 °C for 20 min. The volatiles were then thermally desorbed at 220 °C for 5 min in a GC injection port.

Headspace-Stir bar sorptive extraction (HS-SBSE): A 1.5 grams of ground sample placed in a 20 mL vial with a polytetrafluoroethylene (PTFE)/silver screw cap and were spiked with 10 µL of 2-methyl-3-heptanone (0,1632 g/L in methanol) as internal standard. Headspace insert vial was placed before heating the sample in a water bath. The sample in the vial was heated in a water bath (40 °C) for 20 min. A stir bar (Twister bar; polydimethyl siloxane, 0.5 mm film thickness × 10 mm length, Gerstel) was then put in headspace insert vial and exposed to the sample at 40 °C for 20 min. After sampling had finished, the water droplets on the stir bar were removed with a lint-free tissue and then the stir bar was placed in a Gerstel thermal desorption unit (TDU) tube. The volatiles were then thermally desorbed at 220 °C for 5 min in a GC injection port.

Dynamic headspace-Tenax TA extraction (DHS-Tenax TA): A 1.5 grams of ground sample placed in a 20 mL vial with a polytetrafluoroethylene (PTFE)/silver screw cap and were spiked with 10 µL of 2-methyl-3-heptanone (0,1632 g/L in methanol) as internal standard. The volatile compounds in the headspace were trapped in a Tenax TA adsorbent tube (60/80 mesh, Gerstel, Mülheim an der Ruhr, Germany). The trapping volume was 800 mL with a nitrogen purge stream at a flow rate of 20 ml/min and the trapping temperature held at 40°C. The volatiles were then thermally desorbed at 220 °C for 5 min in a GC injection port.
Gas chromatography–olfactometry–mass spectrometry analyis: The volatile compounds were analyzed using a GC-MS (7890B GC and 5977B MSD; Agilent Technologies Inc., Santa Clara, CA, USA) equipped with an olfactory detector port (ODP3; Gerstel). The volatile separation was conducted using an HP-5MS column (30 m × 0.25 mm internal diameter, 0.25-µm film thickness; Agilent). The initial temperature of the CIS was 20 °C and raised to 300 °C at a rate of 10 °C/s and held at this temperature for 5 min. The initial GC oven temperature was 40 °C that held for 3 min then increased to 280 °C at a ramp rate 3 °C/min and held for 10 min. The flow rate of the helium carrier gas was 1.5 mL/min. The electron impact ionization energy was 70 eV. The mass scan range was between 35 and 350 amu. The ODP was maintained at 200 °C (ODP transfer line) and at 200 °C (ODP mixing chamber). Humidified air was supplied (50 mL/min) to the ODP to prevent drying of the nasal mucosa. The odor-active compounds were perceived by three panelists in separate time. The panelists were also required to note the perceived odor characteristic and the retention time of odor-active compound individually.
Volatile compound identification: The identification of volatile compounds was performed by linear retention index (LRI), mass spectra and odor. The mass spectra and the linear retention index (LRI) were matched with references obtained from NIST MS 14.0 library (National Institute of Standards and Technology, Gaithersburg, MD, USA). The odor of compound was perceived from GC-O and matched with reference odor of compound. The criteria for compound identification required a mass spectrum matching score of ≥60 and an LRI difference of ≤20 units between the calculated LRI and the LRI from the database for the same stationary phase. The LRIs of the compounds were calculated by the Kovats method using co-injection series of n-alkanes (C8-C20) under the same chromatographic conditions, which were calculated using equation (1):

$$\mathrm{RI} = 100 \times \left[\frac{t - t_n}{t_{n+1} - t_n}\right] + n \qquad (1)$$

Where t is the retention time of the compound, n is the carbon number of the alkane eluting immediately before the compound, t_n is the retention time of the n-alkane eluting immediately before the compound and t_{n+1} is the retention time of the n-alkane eluting immediately after the compound.

Statistical analysis: Stastical analysis of compounds identified by each extraction technique was performed using MetaboAnalyst 4.0 software (http://www.metaboanalyst.ca). Prefentially, the data transformation was performed by cube root transformation and data scaling was set to pareto centering. A principal component analysis (PCA) plot was constructed based on data normalization. In addition, a heatmap was constructed as intensity for identified compounds from each extraction techniques.

Results and Discussion: A principal component analysis (PCA) was performed as data visualization to evaluate whether the data of volatile compounds identified in dried chili samples can be used to differentiate based on extraction techniques using DHS-Tenax TA, HS-SBSE and HS-SPME. PCA was performed according to the peak area (%) of 34 volatile compounds (variables) from 9 dried chili samples as an input dataset for calculation and the data were standardized before processing. Figure 1 showed the result of PCA score plot which

PC1 and PC2 represent data object with the highest variation (77.3% and 17.9%, respectively). The figure clearly showed the grouping tendencies of each extraction techniques of dried chili.

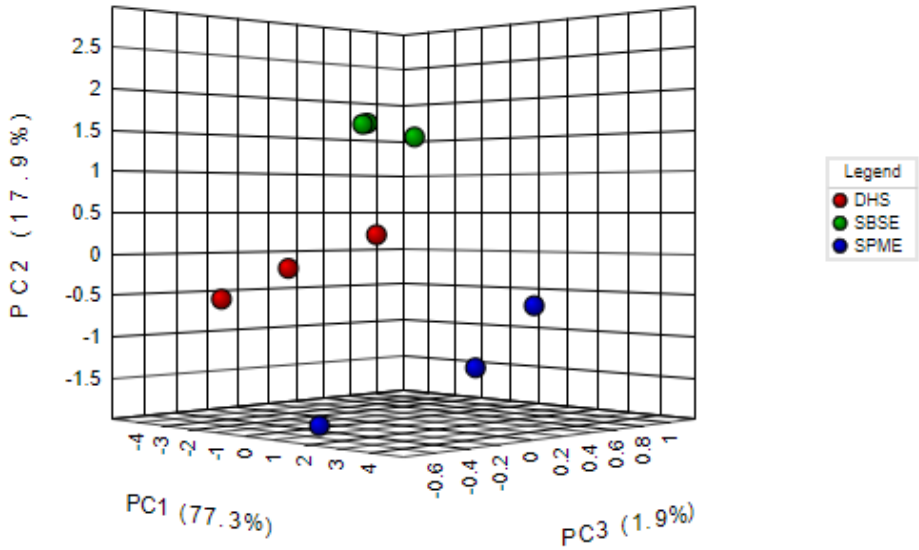

Figure 1. PCA score plot of 9 dried chili samples with 34 variables

Eight groups of volatile compounds were found in dried chili including alcohols, aldehydes, furan, esters, ketones, hydrocarbons, monoterpenes hydrocarbons and sesquiterpene hydrocarbons. The identified compound for each technique was shown in Table 1. DHS-Tenax TA had the highest identified compounds (34 compounds), whereas HS-SBSE and HS-SPME had 13 and 7 compounds, respectively.

The heatmap was performed to compare each compound using % peak area as input dataset (Figure 2). HS-SBSE and HS-SPME showed similarity that could not extract several compounds including undecane, pseudolimonene, 1,3,5,8-undecatetraene, 2-methyl-hexadecane, heptadecane, 1-pentanol, α-gurjunene, methyl hexanoate, 2,2,6-trimethyl-cyclohexanone, pentadecane, α-longicyclene, 2-methyl-pentadecane, β-cyclocitral, humulene, dihydroactinolide, tridecane, 3-methyl-pentadecane, 3,4-dimethylcyclohexanol, trans-β-ionone, heptanal, 2,2,4,6,6-pentamethyl-heptane (shown as light blue color). However, those compounds were extracted by DHS-Tenax TA.

Based on % peak area of functional groups, HS-SPME absorbed esters (1.40%), hydrocarbons (2.81%) and sesquiterpene hydrocarbons (0.45%). HS-SBSE absorbed alcohols (0.32%), aldehydes (13.19%), furan (0.25%), esters (0.35%), hydrocarbons (0.97%) and sesquiterpene hydrocarbons (0.09%). DHS-Tenax TA absorbed alcohols (2.62%), aldehydes (26.76%), furan (1.34%), esters (2.12%), ketones (0.28%), hydrocarbons (5.46%), monoterpene hydrocarbons (0.05%) and sesquiterpene hydrocarbons (0.75%).

Table 1. Volatile compounds of dried chili sample extracted using different techniques

No	Volatile compounds	RT (min)	RI_{ref}[a]	RI_{hp5}[b]			Peak Area (%)			Attributes[c]
				DHS	SBSE	SPME	DHS	SBSE	SPME	
	Alcohols									
1	1-pentanol	7.62	765	774	-[d]	-	0.65	-	-	sweet balsamic
2	4-methyl-1-pentanol	10.98	846	853	847	-	1.76	0.32	-	nutty
3	3,4-dimethylcyclohexanol	23.46	1126	1123	-	-	0.21	-	-	-
	Aldehydes									
4	hexanal	9.51	800	816	800	-	26.54	13.19	-	grass green*
5	heptanal	13.83	901	920	-	-	0.20	-	-	fat rancid*
6	β-cyclocitral	28.67	1220	1238	-	-	0.02	-	-	tropical herbal
	Furan									
7	2-pentyl-furan	17.91	993	1006	995	-	1.19	0.25	-	fruity*
8	dihydroactinidiolide	41.76	1538	1555	-	-	0.15	-	-	fruity
	Esters									
9	methyl hexanoate	14.93	925	943	-	-	0.40	-	-	fruity*
10	4-methylpentyl 2-methylbutanoate	27.66	1201	1215	1202	1203	1.11	0.24	1.23	pungent acidic
11	4-methylpentyl 3-methylbutanoate	27.95	1206	1221	1208	-	0.18	0.05	-	fruity peach
12	4-methylpentyl 4-methylpentanoate	32.68	1315	1330	1320	1320	0.43	0.06	0.17	fruity herbal
	Ketones									
13	2,2,6-trimethyl-cyclohexanone	19.97	1036	1049	-	-	0,14	-	-	pungent*
14	trans-β-ionone	39.72	1486	1505	-	-	0.14	-	-	floral fruity
	Hydrocarbons									
15	2,2,4,6,6-pentamethyl-heptane	17.78	991	1004	-	-	0.04	-	-	-
16	undecane	23.15	1100	1115	-	-	0.06	-	-	herbal*
17	1,3,5,8-undecatetraene	25.51	1177	1168	-	-	0.02	-	-	-
18	tridecane	32.06	1300	1315	-	-	0.08	-	-	mild waxy
19	2-methyl-tridecane	34.67	1364	1378	1363	1364	1.27	0.33	1.19	mild waxy*

Table 2. (Continued)

No	Volatile compounds	RT (min)	RI_{ref}[a]	RI_{hp5}[b]			Peak Area (%)			Attributes[c]
				DHS	SBSE	SPME	DHS	SBSE	SPME	
20	tetradecane	36.19	1400	1415	1401	-	0.19	0.05	-	mild waxy
21	2-methyl-tetradecane	38.01	1463	1478	1462	1463	1.49	0.33	1.17	-
22	2-methyl-1-tetradecene	38.69	1467	1462	1447	1446	1.15	0.19	0.45	-
23	pentadecane	40.13	1500	1516	-	-	0.10	-	-	waxy*
24	2-methyl-pentadecane	42.49	1563	1579	-	-	0.22	-	-	-
25	3-methyl-pentadecane	42.79	1570	1587	-	-	0.04	-	-	-
26	hexadecane	43.85	1600	1616	1601	-	0.28	0.07	-	-
27	2-methyl-hexadecane	46.12	1664	1679	-	-	0.25	-	-	-
28	heptadecane	47.41	1700	1716	-	-	0.27	-	-	-
	Monoterpene Hydrocarbons									
29	pseudolimonene	17.17	1004	991	-	-	0.05	-	-	citrus
	Sesquiterpene Hydrocarbons									
30	α-longipinene	34.22	1353	1367	1352	1353	0.19	0.05	0.11	-
31	α-longicyclene	35.07	1374	1388	-	-	0.08	-	-	-
32	α-gurjunene	36.66	1409	1427	-	-	0.09	-	-	woody*
33	α-himachalene	38.21	1449	1468	1450	1452	0.16	0.04	0.34	floral*
34	humulene	39.38	1505	1497	-	-	0.23	-	-	woody

[a] Retention index from NIST14.0 mass spectral database.
[b] Retention index on HP-5 MS column
[c] Attributes obtained from olfactometer and online database (the good scent company (http://www.thegoodscentscompany.com) and flavournet (http://www.flavournet.org))
[d] not detected
* detected in GC-O

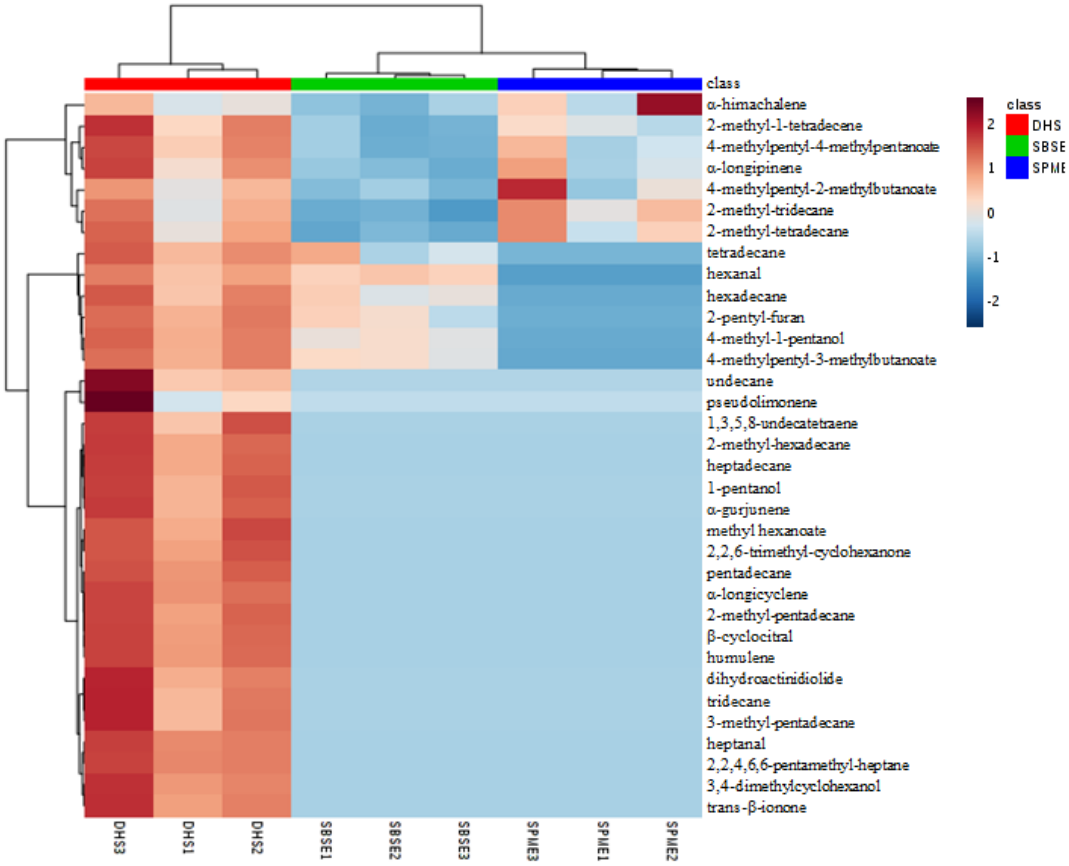

Figure 2. Heatmap of identified compounds in dried chili

DHS-Tenax TA absorbed highest number of compound and % peak area compared to other techniques in dried chili sample. It might due to Tenax TA provided larger surface area and higher reproducibility than other techniques, therefore it yielded highest extraction.[11,23] In our samples, DHS-Tenax TA was effective to absorp hexanal, hydrocarbons and alcohols. Another study found that DHS-Tenax was efficient to absorb alcohols compared to SPME in cheese.[19] In agreement with previous study, the extraction technique in dried chili sample using DHS-Tenax TA showed not only the highest identified compound, but also had the most odor characteristics perceived during GC-O analysis (Figure 3) due to the larger surface area of DHS-Tenax TA than fiber of SPME.[11]

Six classes of functional groups were identified in HS-SBSE. The result showed that HS-SBSE had higher number of extracted compounds than HS-SPME. It might due to different absorbent used in each techniques. PDMS and DVB/CAR/PDMS were used as extraction medium in HS-SBSE and HS-SPME, respectively. The amount of PDMS in HS-SBSE was higher compared to HS-SPME thus improved the extraction efficiency.[8] Therefore, HS-SBSE had higher number of identified compounds.

Eventough HS-SPME absorbed lowest number of compounds, the peak area of esters, hydrocarbons and sesquiterpene hydrocarbons in HS-SPME were higher than HS-SBSE. Therefore, HS-SPME was effective to absorb esters, hydrocarbons and sesquiterpene hydrocarbons in dried chili compared to HS-SBSE. Based on fiber properties, a DVB/CAR/PDMS of HS-SPME was efficient to absorb low polarity compounds.[7] A study was

conducted to identify volatile compounds in three varieties of Brazillian chili peppers using SPME extraction. They found that esters and alcohols appeared as major compounds in the malagueta chili pepper. Monoterpenes and aldehydes were identified in dedo-de-moca chili pepper and mostly esters and sesquiterpenes found in the murupi chili pepper.[10]

Aldehydes especially hexanal was found to be the major compound extracted using DHS-Tenax TA and HS-SBSE. The previous study was conducted in fresh chili found hexanal as one of the six major compounds for fresh chili aroma[16] and known as lipid oxidation product.[21] Hexanal also found in fresh green chili pepper and after drying between 60 to 100 °C for up to 15 hours the amount of hexanal was decreased.[3] In other hand, the spice paprika powder was heated at 90 °C for 60 min resulted increasing the content of hexanal caused by autooxidative linoleic acid degradation.[20] α-himachalene appeared as one of compounds found in dried chili samples using all extraction techniques. The appearance of α-himachalene also found in Cachucha peppers and Habanero peppers eventough it was not major compounds.[24,25] However, Apichartsrangkoon (2013) stated that α-himachalene was one of compounds that relatively stable in Thai green chili paste during processing.[26]

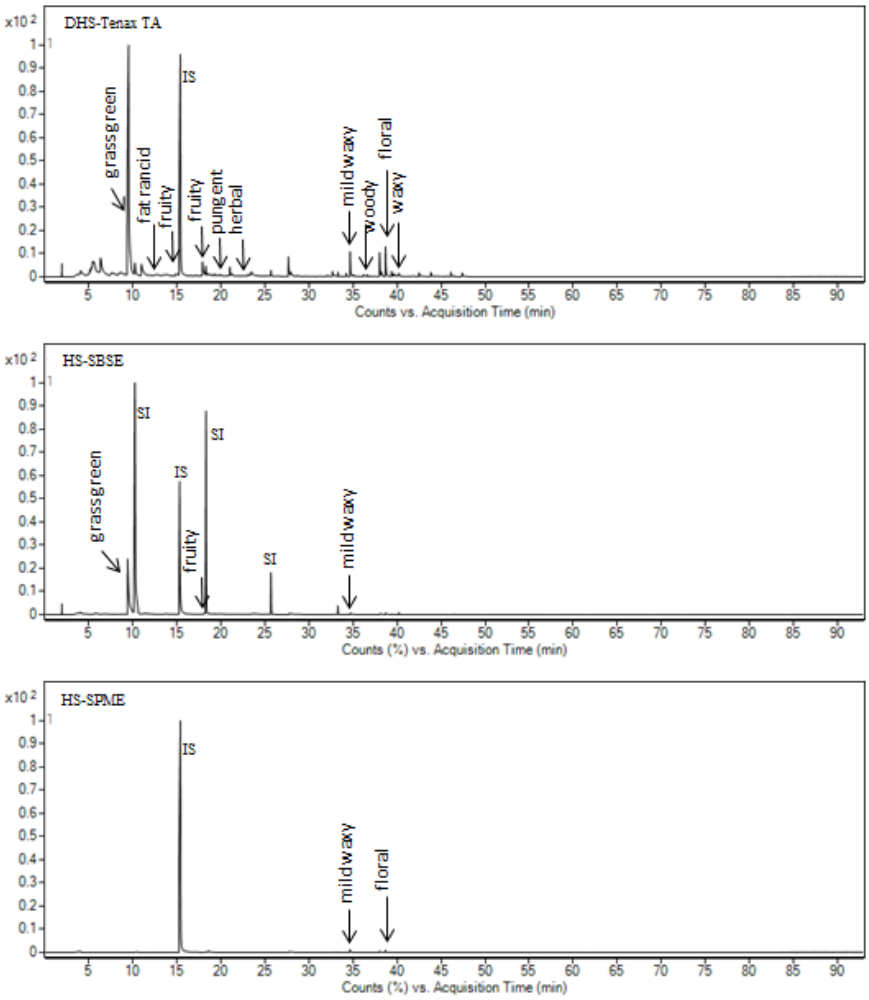

Figure 3. DHS-SBSE-SPME chromatogram in dried chili
(IS=internal standard; SI=siloxane from column)

Conclusion: DHS-Tenax TA had highest number of identified compound followed by HS-SBSE and HS-SPME. HS-SPME was effective to absorb esters, hydrocarbons and sesquiterpene hydrocarbons eventough HS-SPME had lower identified compound compared to HS-SBSE. Based on all extraction techniques, DHS was the best of extraction technique used in dried chili and hexanal appeared as volatile compound with highest % peak area in dried chili.

References:

1. Toontom N, Meenune M, Posri W, Lertsiri S. International Food Research Journal. 2012; 19:1023-1031.
2. Al-Sebaeai MA, Chauhan AK, Arvind, Hemalatha S. International Journal of Innovative Research in Science, Engineering and Technology. 2017;6:18595-18602.
3. Chairote EO, Intachum S. International Journal of Applied Chemistry. 2016;12:129-138.
4. Berka-Zougali B, Ferhat M, Hassani A, Chemat F, Allaf, KS. International Journal of Molecular Sciences. 2012;12:4673-4695.
5. Zhang QW, Lin LG, Ye WC. Chinese Medicine. 2018;13:1-26.
6. Werkhoff P, Bretschneider W. Journal of Chromatography. 1987;405:87-98.
7. Kataoka H, Lord HL, Pawliszyn. Journal of Chromatography A. 2000;880:35-62.
8. Baltussen E, Sandra P, David F, Cramers C. J. Microcolumn Separations. 1999;11:737-747.
9. Telgheder U, Bader N, Alshelmani N. Asian Journal of Nanoscience and Materials. 2018;1:56-62.
10. Junior SB, Tavares AM, Filho JT, Zini CA, Godoy HT. Food Research International. 2012;48:98-107.
11. Povolo M, Contarini G. Journal of Chromatography A. 2003;985:117-125.
12. Mamede MEO, Pastore GM. Food Chemistry. 2006;96:586-590.
13. Zellner B, Dugo P, Dugo G, Mondello L. Journal of Chromatography A. 2008;1186:123-143.
14. Soria AC, Garcia-Sarrio MJ, Sanz ML. Trends in Analytical Chemistry. 2015; doi:10.1016/j.trac.2015.04.015.
15. Jerkovic I, Marijanovic Z. Croat. J. Food Sci. Technol. 2009;1(2):28-34.
16. Mazida MM, Salleh MM, Osman H. Journal of Food Composition and Analysis. 2005;18: 427-437.
17. Garruti D, Pinto N, Alves V, Penha M, Tobaruela E, Araujo I. Ciencia e Tecnologia de Alimentos. 2013;33:102-108.
18. Ha J, Wang Y, Jang H, Seog H, Chen X. Food Chemistry. 2014;142:79-86.
19. Mallia S, Fernandez-Garcia E, Olivier Bosset J. International Dairy Journal. 2005;15:
20. 741-758.
21. Cremer DK, Eichner K. J. Agric. Food Chem. 2000;48:2454-2460.
22. Martin A, Hernandez A, Aranda E, Casquete R, Velazquez R, Bartolome T, Cordoba MG. Food Research International. 2017;doi:10.1016/j.foodres.2017.07.068.
23. Soria AC, Garcia-Sarrio MJ, Sanz ML. Trends in Analytical Chemistry. 2015;doi: 10.1016/j.trac.2015.04.015.
24. Manzini S, Durante C, Baschieri C, Cocchi M, Sighinolfi S, Totaro S, Marchetti A. Talanta. 2011;85:863-869.
25. Pino J, Fuentes V, Barrios O. Food Chemistry. 2011;125:860-864.
26. Pino J, Gonzalez M, Ceballos L, Centurion-Yah AR, Trujillo-Aguirre, Latournerie-Moreno L, Sauri-Duch E. Food Chemistry. 2007;104:1682-1686.
27. Apichartsrangkoon A, Chaikham P, Srisajjalertwaja S, Chunthanom P, Dajanta K. International Food Research Journal. 2013;20(4):1739-1746.

H_010_PF: EFFECTS OF JIAOGULAN ON HEXANAL CONTENT IN *SAI-UA* (NORTHERN STYLE HERBAL-PORK SAUSAGE)

Sirichanut Thongsew[1], Atikorn Panya[2], Nipa Khuankuab[3], Siriporn Riebroy Kim[1,*]
[1]Major of Food and Nutrition, Department of Home Economics, Faculty of Agriculture, Kasetsart University, Bangkok, Thailand
[2]National Center for Genetic Engineering and Biotechnology, NSTDA, Pathum Thani, Thailand
[3]Doi Pui Research Station, Faculty of Agriculture, Kasetsart University, Bangkok, Thailand
*e-mail: siriporn.r@ku.th

Abstract: The effect of ground jiaogulan addition on hexanal content in *Sai-ua* was studied. Three formulas of *Sai-ua* (S1, S2, and S3) were produced and analyzed. Different amounts and types of ingredients contributed to the contents of protein and lipid as well as color. Hexanal content in cooked S1 and S3 were not different ($p>0.05$) but S3 had the lowest hexanal content even pork backfat added ($p<0.05$). For sensorial properties, S2 had the highest likeness scores for appearance, color, flavor and overall liking ($p<0.05$). S2 added with ground jiaogulan at 0% (SJ-0), 0.5% (SJ-0.5), 1.0% (SJ-1.0), 1.5% (SJ-1.5), and 2.0% (SJ-2.0) were produced and analyzed. Before grill, the free fatty acid content of all samples were slightly different ($p<0.05$). Decrease in free fatty acid content was observed in each sample after grill ($p<0.05$). This might be resulted from free fatty acid oxidation. Before grill, hexanal content in SJ-0, SJ-1.0 and SJ-2.0 was lower than SJ-0.5 and SJ-1.5 ($p<0.05$). After grill, hexanal content of each sample sharply increased, particularly SJ-0 ($p<0.05$). As compared to sample without addition of ground jiaogulan (SJ-0), sample added with ground jiaogulan had lowered hexanal content ($p<0.05$). No differences in L*, a*, and b* in all samples before grill ($p>0.05$), but a* and b* of all samples after grill were slightly different ($p<0.05$). No difference in appearance of all samples but SJ-2.0 had the lowest this liking score ($p<0.05$). Sample added with ground jiaogulan had lower liking score for color. Lower flavor liking score was found in samples added with ground jiaogulan ($p<0.05$). The bitter flavor in samples was detected in those added with 1% and 2% ground jiaogulan. However, the taste liking score of SJ-0.5 was similar to SJ-0 ($p>0.05$). Among samples added with ground jiaogulan, SJ-0.5 showed a greater acceptability ($p<0.05$). Although the bitter flavor of ground jiaogulan effect to *Sai-ua*, the addition of ground jiaogulan at 0.5% was possible to improve the hexanal development and its sensorial property can be equivalent to *Sai-ua* without ground jiaogulan addition.

Introduction: Jiaogulan (*Gynostemma pentaphyllum*) has been widely used as an herbal tea, dietary supplement, and vegetable in Asian countries.[1] Gypenosides have been isolated from jiaogulan with various bioactivities, such as antioxidant, anti-inflammatory, antilipidemic, cardiovascular, and hepatoprotective effects.[1,2] Many health products and beverages based on jiaogulan have been developed and sold in Chinese market, for example, total jiaogulan saponin tablets and jiaogulan tea.[2] Generally, the cultivation of jiaogulan in the north of Thailand has been developed and in local area as a secondary crop. Doi Pui Research Station studied on both cultivation and tea preparation process of jiaogulan. Dried jiaogulan can be sold as an herbal tea mixed with chrysanthemum, stevia, safflower, etc. Total phenolic content (TPC) and antioxidant activity of jiaogulan tea extract from Doi Pui Research Station have been tested.[3] The jiaogulan extract with phosphate buffer (pH 3.0 and 7.0) showed higher TPC and antioxidant activity than those extract with methanol.[3] Additionally, ground jiaogulan could be applied to salad dressing at 0.25% though bitter taste detected by sensory evaluation.

Sai-ua, a northern Thai style herbal-pork sausage, is generally produced by mixing of minced pork, spices and herbs, and curry paste. *Sai-ua* is generally cooked by grill and it can be served as an appetizer with cooked glutinous rice. Owing to the flavorful aroma from spices and herbs, *Sai-ua* has a desirable odor after grill. Although spices and herbs added to

Sai-ua can act as antioxidants, but the lipid oxidation occurs during preparation and cooking. In general, lipid oxidation plays a major role in a quality of lipid-containing food, such as meat, by producing volatile compounds that contribute both to the typical flavor of meat and to the development of off flavor.[4] Lipid oxidation is a problem on meat products quality, particularly oxidative flavor. Cooking destroys the integrity of cell membrane releasing phospholipids, and inactivates several protective antioxidants e.g. catalase.[5] Hexanal has become a well-known indicator, being a major product of lipid oxidation. For meat and meat product, hemoproteins such as myoglobin are denatured allowing the release of the prooxidant iron, which can result in the warmed-over flavor (WOF). The WOF becomes predominant with precooking and is characterized by undesirable organoleptic qualities.[6] Destruction of membranes, decreased catalase activity, and the increase in non-heme iron can elevate the rate of lipid oxidation in cooked pork, therefore, it is important to apply strategies to prolong the shelf-life of cooked pork products.[5,7] The fat portion of meat, and especially the phospholipid fraction, undergoes auto-oxidation phenomena, producing an overwhelming number of volatiles, such as acids, aliphatic aldehydes, ketones, and alcohols, and promoting the formation of some other such as nitrogen- and sulfur-containing compounds.[8] The adverse qualities are due to the secondary products of lipid oxidation such as hexanal, octanal, and nonanal. According to the antioxidant activity and various therapeutic efficacies of jiaogulan, it can be applied to food, especially meat or lipid-containing food products. The bitter flavor and taste should be considered for organoleptic property. To our knowledge, no studies have investigated the addition of jiaogulan as an antioxidant in *Sai-ua*. Due to its delicacy, the ready-to-eat *Sai-ua* had been produced continuously and it is delivered to homes, restaurants, and supermarkets. While the convenience appeals to consumers, precooking before packing and storing can accelerate oxidation, deteriorating product quality. Therefore, the objectives of this study were to study the proximate composition and hexanal as well as acceptability of *Sai-ua* produced from different three formulas and to investigate the hexanal development in *Sai-ua* added with and without ground jiaogulan.

Methodology:

Preparation of jiaogulan: Dried jiaogulan (*Gynostemma pentaphyllum*) were obtained from Doi Pui Research Station, Agricultural Research and Technology Transfer Center (ARTTC), Faculty of Agriculture, Kasetsart University, Thailand. The dried jiaogulan sample was prepared from harvested fresh jiaogulan in December 2018. Dried jiaogulan sample was vacuum packed in aluminum bag (200 g/bag) and transferred to Food and Nutrition Laboratory within 24 h. Before addition into *Sai-ua*, dry jiaogulan was ground by a grinder and passed through a 1.0 mm sieve (18-mesh size).

Preparation of Sai-ua added with ground jiaogulan: Sai-ua samples were produced by different three formulas (S1, S2, and S3) (Table 1). These formulas have been studied and developed in Food and Nutrition Demonstration Cooking Laboratory. Lean pork (sirloin) was purchased from a local market (Bangkhen, Bangkok, Thailand) and kept in ice (0-2°C) before transportation to Food and Nutrition Laboratory, Kasetsart University. Pork was ground with an electric meat mincer (TC-22, Sunling, China) at speed level 2, for 5 min (4°C). For S3, pork back fat was frozen (-20°C) for 12 h before used and it was ground with mince pork for 3 min. All ingredients were added to processed pork and mixed thoroughly for 5 min. Spices and herbs for this experiment were kaffir lime leave and fruit (peel), green onion, coriander leave and root, dried chili, galangal rhizome, lemongrass, shallot, garlic, turmeric rhizome. Each *Sai-ua* mix was stuffed into natural casing by manual excise. Sai-ua samples were grill by an electric barbecue stove (EL-280, Wellborn, China) until internal temperature was reached 70°C for 15 min. Cooked *Sai-ua* samples were cooled for 1 h before analyses. *Sai-ua* sample that had the highest overall liking score was chosen for the study of effect of ground jiaogulan

on hexanal development. The levels of ground jiaogulan were 0% (SJ-0), 0.5% (SJ-0.5), 1% (SJ-1.0), 1.5% (SJ-1.5), and 2% (SJ-.2.0). The analyses were performed before and after grill. Sensorial properties of samples were evaluated cooked samples.

Table 1. Formulas* for *Sai-ua* production (g/100 g).

Ingredients	S1	S2	S3
Pork (kg)	85.98	85.91	66.09
Back fat (g)	-	-	21.81
Vegetable oil (g)	2.41	2.41	-
Salt (g)	0.43	0.43	0.33
Fish sauce/soy sauce (g)	2.41	2.41	0.99
Fermented shrimp paste (g)	0.6	1.72	1.32
Sugar (g)	-	-	0.99
Spices and herbs (g)	8.17	7.13	8.46
Total	100	100	100

Proximate chemical analysis: Sample was ground by a grinder (Moulinex, France). The pH of samples was determined by a pH meter (Seven Compact, Mettler Teledo, USA). The water activity (A_w) was carried out by a water activity meter (4TE, AquaLab, USA). Samples were analyzed for moisture content.[9] Protein content was determined by the Kjeldahl method.[9] The crude fat content was determined by a Soxhlet extraction apparatus using the solvent petroleum ether.[9]

Determination of hexanal: Hexanal content was determined by using solid phase microextraction gas chromatography and mass spectrometry (SPME-GC/MS).[10] Sample (3 g) was weighted into 20-ml vial and distilled water (6.95 ml) was added. The internal standard was 2-methyl-3-heptanone (0.01 nmol/□l). The mixture was incubated at 40°C for 10 min then SPME-GC/MS analysis.

Determination of color: The color (L*, a*, and b*) of cooked samples was measured by colorimeter (HunterLab, USA). The measurement was done in five replications.

Sensorial evaluation

The acceptability of cooked Sai-au produced fro, different formulas was evaluated by 9-point hedonic scale.[11] The un-trained panelists were students in Food and Nutrition of age ranging from 19-25 years. Sample was sliced perpendicular to the long axis to obtain the length of 1.0 cm. Samples were placed on dish and cover with aluminum foil. Samples were randomly selected and coded with three-digit random number. The panelists evaluated for appearance, color, odor, taste, flavor, texture and overall liking.

Statistical analysis

One-way ANOVA was used and mean comparison was performed by Duncan's multiple range test.[12] Statistical analysis was carried out using SPSS statistic program (Version 10.0) for Window (SPSS Inc. Chicago, IL).

Results and Discussion:

Characteristics and acceptability of Sai-ua produced from different formulas: The pH of all samples ranged from 6.22 to 6.25. No difference in A_w was observed (0.98) ($p>0.05$) (Data are not shown). *Sai-ua* produced from different three formula (S1, S2, and S3) had differences in protein, fat and moisture contents ($p<0.05$) (Table 2). According to the formula (100 g), the pork mince was a major ingredient for *Sai-ua* production. S2 had the highest protein content, compared with other samples ($p<0.05$). The amount of pork mice in S1 and S2 was not different but fermented shrimp paste in S2 was a protein source (Table 1). In general, fermented fish shrimp had 20-25% protein content.[13] In addition, the lowest protein content in S3 was

observed ($p<0.05$). S3 had the highest content of fat because of pork backfat addition ($p<0.05$). S2 had higher fat content than that in S1 ($p<0.05$). Additionally, the lowered moisture content might be caused by addition of pork backfat. Although, higher fat content was observed in S2 ($p<0.05$) but no fat or oil was added to formula as S1 and S3 samples.

Table 3 shows color of *Sai-ua* produced from different formula. Generally, color of cooked *Sai-ua* is golden brown or turmeric yellowish.[14] Due to the different amount of ingredients affected on color of cooked Sai-ua. S2 had the lowest L* when compared with others ($p<0.05$). The highest a* was observed in S1 and S2 ($p<0.05$). This might be resulted from higher amount of dried chili addition. S1 had the highest b* ($p<0.05$).

Table 2. Chemical composition (% by wet weight) of cooked *Sai-ua* produced from different formulas.

Chemical composition	S1	S2	S3
Protein	19.31±0.33[b]	21.65±0.90[a]	18.17±0.36[b]
Fat	5.07±0.10[c]	8.32±0.18[b]	21.33±0.72[a]
Moisture	64.94±0.55*[a**]	61.17±0.32[b]	49.82±0.44[c]

*Mean ± standard deviation from triplicate determination.
**Different letters in the same row indicate significant differences ($p<0.05$).

Table 3. Color of cooked *Sai-ua* produced from different formula

Color	S1	S2	S3
L*	46.96±1.55*[a**]	39.98±1.32[b]	48.08±1.65[a]
a*	16.52±0.33[a]	15.06±0.96[b]	13.93±0.83[c]
b*	31.37±0.94[a]	24.47±1.15[b]	25.08±1.40[b]

*Mean ± standard deviation from five determinations.
**Different letters in the same row indicate significant differences ($p<0.05$).

The lipid oxidation of *Sai-ua* samples was also investigated. Hexanal content of cooked *Sai-ua* samples are depicted in Figure 1. S3 had the lowest hexanal content ($p<0.05$) though it was added with backfat. Generally, most of fatty acids in pork backfat were saturated and mono-unsaturated fatty acids.[15] They were not susceptible to oxidation, compared to polyunsaturated fatty acids. No difference hexanal content in S1 and S2 ($p>0.05$). They had 2 times higher haxanal content than that in S3. Considering major lipid ingredient, S1 was added with vegetable oil while S2 added with palm oil. Both oils composed of polyunsaturated fatty acids which were prone to oxidation.[15] Hexanal is aldehydes, lipid-derived volatiles, which is generally found in cooked meat.[10] Hexanal was dominant aldehyde in cooked meat. Most of the straight chain aldehydes are derived from the oxidation of unsaturated fatty acids. In contrast, the generation of volatiles occurs quickly and provides a different volatiles profile related to the desirable flavor of cooked pork. Cooked meat from lean pig showed a higher number of volatile compounds which were related to lipid oxidation.[16] From the result, different ingredients, particularly type of lipid, contributed on lipid oxidation. Also, some antioxidants (spices and herbs) might contribute to lipid oxidation because of minerals as a prooxidants (Fe and Cu) such as lemongrass and turmeric.[17] In addition, the mild cooking of meats, to temperatures of 70-80 °C leads to the disruption of muscle membrane structure and facilitates the interaction of lipid oxidation catalysis with unsaturated fatty acids, resulting in the generation of free radicals and the propagation of WOF.[10]

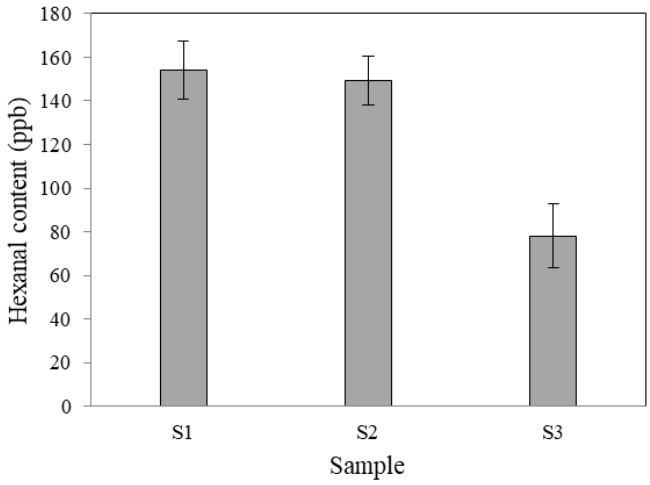

Figure 1. Hexanal content (part per billion, ppb) in cooked *Sai-ua* produced from different formulas. Bars indicated standard deviation from triplication determinations.

The acceptability score of *Sai-ua* produced from different formulas is shown in Table 4. S2 had the highest score for appearance liking, color liking, odor liking, flavor liking and overall liking ($p<0.05$). No differences in taste liking and texture liking scores in all samples ($p>0.05$). Although S2 was no added lipid and S1 and S3 were added with vegetable oil and pork backfat, respectively. However, all samples had different liking score for flavor. The flavor of *Sai-ua* is normally variety of herbs and spices flavors. These might be due to the differences of lipid types and some spices and herbs added. Chili and turmeric can act as antioxidant because of some active compounds (capsaicin and curcumin).[18] The lowest scores for appearance liking, color liking, flavor liking and overall liking were observed with S1 ($p<0.05$). These might be due to S1 had vegetable oil which affected on shiny surface and rancid flavor. Generally, flavor mainly affects the sensory quality of foods, and is strongly related to lipid oxidation (Figure 1). Therefore, S2 which had the highest scores for all attributes was chosen for study on the effect of jiaogulan addition on hexanal development.

Table 4. Likeness scores of *Sai-ua* produced from different formulas.

Color	S1	S2	S3
Appearance	6.00±0.93*^{c**}	7.70±1.02^{a}	7.20±1.13^{b}
Color	5.52±1.27^{c}	7.72±1.20^{a}	7.02±1.35^{b}
Odor	6.06±1.25^{b}	7.18±1.40^{a}	6.68±1.81^{a}
Taste^{ns}	5.96±1.18	6.32±1.80	6.44±1.73
Texture^{ns}	6.28±1.03	6.20±1.59	6.36±1.58
Flavor	5.94±1.08^{c}	7.16±1.04^{a}	6.64±1.35^{b}
Overall	6.20±0.81^{c}	8.02±0.74^{a}	6.88±1.00^{b}

*Mean ± standard deviation from fitty evaluations.
**Different letters in the same row indicate significant differences ($p<0.05$).

Effect of ground jiaogulan on lipolysis and lipid oxidation of Sai-ua: Free fatty acid content in *Sai-ua* added with different levels of ground jiaogulan is shown in Table 5. Before grill, in *Sai-ua* added with ground jiaogulan at 0.5% had lower free fatty acids than other samples ($p<0.05$). After grill, decrease in free fatty acids in all sample was observed ($p<0.05$). As the free fatty acid content developed before grill, it indicates lipolysis of Sai-ua during

manufacture. The lipolysis in meat occurs by enzyme action or by heat and moisture, resulting in the liberation of free fatty acids.[19] Additionally, lipolysis occurs during heating due to the water introduced from food and relative high temperature used. Oxidative and thermal degradation taking place in unsaturated fatty acid is responsible for the production of free fatty acids. Generally, heating by grill is cooking method for *Sai-ua*. However, the decrease of free fatty acid content revealed with lipid oxidation reaction. The release of free fatty acid is responsible for the development of an undesirable rancid flavor (hydrolytic rancidity).[15] Hexanal is one of compound markers of warmed-over-flavor (WOF) occurred in meat products.[15] Figure 2 shows hexanal content of *Sai-ua* before and after grill. Samples added with ground jiaogulan had higher hexanal content when compared with those without ground jiaogulan addition ($p<0.05$). Higher hexanal content was observed after heating. After grill, *Sai-ua* had higher hexanal content, indicating lipid oxidation (Figure 2). Considering ground jiaogulan addition, grilled samples had lower hexanal content ($p<0.05$). The antioxidant activities of acid polysaccharices in jiaogulan have been reported.[20] From the result, the addition ground jiaogulan might reduce hexanal development.

Table 5. Free fatty acid (mg/g) in *Sai-ua* added with different levels of ground jiaogulan before and after grill.

	Samples*				
	SJ-0	SJ-0.5	SJ-1.0	SJ-1.5	SJ-2.0
Before grill	7.12±0.74**aA***	5.37±0.75bA	6.18±0.08abA	6.92±0.43aA	7.11±1.05aA
After grill	3.99±0.17bB	4.18±0.15bB	4.70±0.58abB	5.87±1.66aB	4.44±0.35abB

**Sai-ua* added with ground jiaogulan at 0% (SJ-0), 0.5% (SJ-0.5), 1.0% (SJ-1.0), 1.5% (SJ-1.5), and 2.0% (SJ-2.0). **Mean ± standard deviation from five determinations. ***Different letters and capital letters indicate significant differences ($p<0.05$) in the same row and column, respectively.

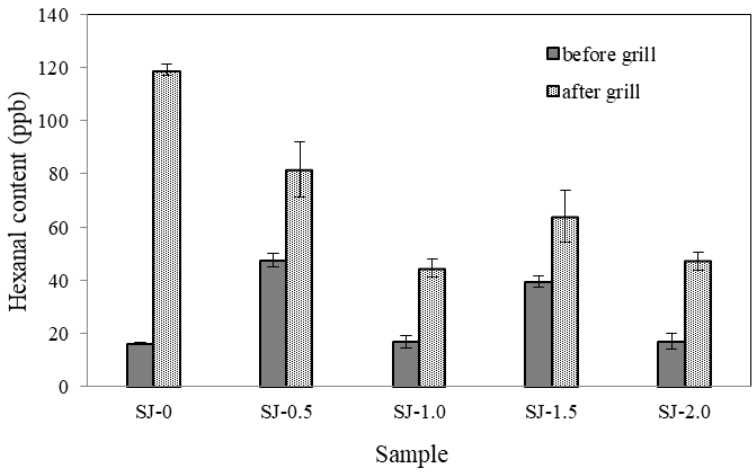

Figure 2. Hexanal content (part per billion, ppb) in Sai-ua added with different levels of ground jiaogulan. *Sai-ua* added with ground jiaogulan at 0% (SJ-0), 0.5% (SJ-0.5), 1.0% (SJ-1.0), 1.5% (SJ-1.5), and 2.0% (SJ-2.0). Bars indicated standard deviation from triplication determinations.

Before grill, ground jiaogulan did not effect on color of *Sai-ua* samples (Table 5). In general, ground jiaogulan is grey-greenish color. Considering color after grill, the b* value

of *Sai-ua* samples increased. The b* value indicates yellowness/blueness of product. Increase in b* might be due to the non-enzymatic browning reaction (Maillard reaction). From the results, the addition of jiaogulan into *Sai-ua* might affect to color after heating.

Table 6.Color of *Sai-ua** added with ground jiaogulan before and after grill

Color	SJ-0	SJ-0.5	SJ-1.0	SJ-1.5	SJ-2.0
Before grill					
L^{ns****}	42.21±2.16*	43.29±2.17	43.54±2.13	43.17±1.59	42.62±2.23
a^{*ns}	17.66±4.02	17.19±5.34	15.67±4.82	15.79±4.62	15.04±4.39
b^{*ns}	18.29±5.95	18.80±7.27	16.57±8.01	17.74±7.01	16.39±6.25
After grill					
L^{*ns}	44.93±4.01	45.84±3.81	46.17±3.95	42.60±4.88	45.07±3.74
a^{*}	18.42±1.06^{ab***}	18.52±0.91^{ab}	18.93±1.03^{a}	17.72±0.97^{bc}	17.39±0.77^{c}
b^{*}	27.81±1.49^{c}	28.73±1.43^{ab}	29.72±1.60^{a}	27.84±1.88^{c}	28.79±1.04^{ab}

**Sai-ua* added with ground jiaogulan at 0% (SJ-0), 0.5% (SJ-0.5), 1.0% (SJ-1.0), 1.5% (SJ-1.5), and 2.0% (SJ-2.0). **Mean ± standard deviation from five determinations. ***Different letters in the same row indicate significant differences ($p<0.05$).

The acceptability evaluation is shown in Table 4. The appearance liking score of SJ-0, SJ-0.5, SJ-1.0, and SJ-1.5 were not different ($p>0.05$). As color tested (Table 6), sample added with ground jiaogulan had lower color likeness score, compared with those without jiaogulan addition ($p<0.05$). At higher than 1.0% of jiaogulan addition, a lower flavor likeness of sample was observed ($p<0.05$). However, SJ-0.5 had higher bitterness and taste likeness scores that those added with ground jiaogulan ($p<0.05$). Due to the gypenoside compound in jiaogulan effects on bitter and sweet tastes and the low content of this compound is caused for bitterness.[21] Additionally, the bitter flavor and taste in salad dressing has been reported.[3] No difference in texture likeness score in all samples ($p>0.05$). At 0.5% jiaogulan addition, the taste and overall likeness scores of SJ-0.5 was similar to SJ-0 (without jiaogulan addition). From the results, ground jiaogulan can be incorporated into *Sai-ua* production without bitterness effect.

Table 7. Likeness scores of *Sai-ua** added with different levels of ground jiaogulan.

Attributes	SJ-0	SJ-0.5	SJ-1.0	SJ-1.5	SJ-2.0
Appearance	7.48±1.18**^{a}	7.06±1.15^{ab}	7.00±1.23^{ab}	7.08±1.19^{ab}	6.58±1.18^{b}
Color	7.90±0.74^{a}	7.24±1.14^{bc}	7.42±0.86^{b}	7.16±0.77^{bc}	7.04±0.88^{c}
Odor	7.84±0.68^{a}	7.70±0.68^{ab}	7.60±0.54^{ab}	7.54±0.54^{b}	7.58±0.50^{b}
Flavor	7.88±1.10^{a}	7.44±0.88^{b}	7.14±0.93^{b}	6.72±0.99^{c}	6.46±0.93^{c}
Bitterness	6.88±0.82^{a}	7.00±0.90^{a}	6.84±1.04^{a}	5.98±1.10^{b}	5.54±0.81^{c}
Texture^{ns}	6.76±1.24	6.66±1.17	6.36±1.21	6.40±1.20	6.30±1.11
Taste	7.12±1.17^{a}	7.12±1.30^{a}	6.56±1.25^{bc}	6.72±1.21^{ab}	6.22±0.74^{c}
Overall	7.50±1.07^{a}	7.20±0.90^{a}	6.82±0.92^{b}	6.48±1.07^{b}	5.96±0.76^{c}

**Sai-ua* added with ground jiaogulan at 0% (SJ-0), 0.5% (SJ-0.5), 1.0% (SJ-1.0), 1.5% (SJ-1.5), and 2.0% (SJ-2.0). **Mean ± standard deviation from fifty evaluations.
***Different letters in the same row indicate significant differences ($p<0.05$).
^{ns} Means within the same row are not significantly different ($p>0.05$)

Conclusion: *Sai-ua* produced with different formulas showed different protein and fat contents. The lipid source was very important for hexanal development and organoleptic property. Higher ground jiaogulan addition showed a lower hexanal content in *Sai-ua*.

However, the bitter flavor of ground jiaogulan affected on sensorial properties. The addition ground jiaogulan at 0.5% can be applied for *Sai-ua* production with a lower hexanal content.

References:

1. Wang J, Yang JL, Zhou PP, Meng XH, Shi YP. J Agric Food Chem. 2017;65:5926-5934.
2. Xie Z, Liu W, Huang H, Salvin M, Zhao Y, Whent M, Blackford J, Lutterodt H, Zhou H, Chen P, Wang TTY, Wang S, Yu L. J Agric Food Chem. 2010;58:11243-11249.
3. Kim SR, Khuankuab N, Yaoop B, Kim J, Chaijan M. Proceedings of the 15th ASEAN Conference on Food Science and Technology. 2017; 267-273.
4. Meynier A, Genot C, Gandemer G. J Am Oil Chem'Soc. 1998; 75(1): 1-7.
5. Rhee KS, Anderson LM, Sams AR. J Food Sci.1996;61(1):8-12.
6. Rojas MC, Brewer MS. J Food Sci.2007;72(4):S282-S288.
7. Fernan-Lopez J, Sevilla L, Sayas-Barbera E, Navarro C, Marin F, Perez-Alvarez JA. J Food Sci.2003;68(2):660-664.
8. Mottram DS. Food Chem. 1998;62:415-424.
9. AOAC. Official Methods of Analysis.2000.
10. Estévez M, Morcuende D, Ventanas S, Cava R. J Agric Food Chem. 2003;51:3429-3435.
11. Chamber IV, Wolf MB. Sensory testing methods.1996.
12. Steel RGD, Torrie JH. Principle and procedure of statistics. 1980.
13. Kongpun S. The Complete Thai Cook Book. 2015;178.
14. Faithong N, Benjakul S, Patcharat S. Binsan W. Food Chem. 2010;119: 133-140.
15. Nawar WW. Food Chemistry. 1996; 225-320.
16. Jully KMM, Toto CS, Were L. LWT-Food Sci Technol.2016;66:244-251.
17. Raghavan S. Handbook of spices, seasonings, and flavorings.2007.
18. Suresh D, Manjunatha H, Srinivasan K. J. Food Comp. Anal. 2007;20:346-351.
19. Thai Community Product Standard 294/2004. (in Thai)
20. Li B, Zhang X, Wang M, Jiao L.Carbohydr. Polym. 2015;127:209-214.
21. Wu PK, Tai WCS, Choi RCY, Tsim KWK, Zhou H, Liu X, Jiang ZH, Hsiao WLW. Food Chem. 2011;128:70-80.

Acknowledgement: Authors would like to thank staffs of Doi Pui Research Station (Chaing Mai), Kasetsart University for providing jiaogulan sample.

H_013_PF: INFLUENCE OF STEVIA CONCENTRATION AND GUAR GUM ON RHEOLOGY AND PHYSICO CHEMICAL PROPERTIES OF GUAVA JUICE

Napassorn Peasura*, Pornrat Sinchaipanit
Institute of Nutrition, Mahidol University, Thailand
*e-mail: napassorn.pea@mahidol.ac.th

Abstract: In the beverage section is mainly focused on the achievement of an adequate sweetness while improving health and appearance. Sugar is often reduced or replaced with natural non-nutritive sweeteners which often changes food texture. Rheological behaviors of guava juice are the most important features. Guava juice is one of a most preferred non-alcoholic beverage in Thailand. They had unique flavour, taste, and health-promoting qualities. Therefore, the effect of stevia and guar gum in guava juice on the physicochemical, antioxidant and rheological at different concentration were studied. Guava juice was added stevia at 0.1, 0.125 and 0.15% and guar gum at 0.1 and 0.3%. The result showed that guava juice with 1.5% stevia and 0.3% guar gum had the highest antioxidant capacity. The appearance was uniformly which pulp did not precipitate. In addition, the viscosity of guava juice was increased with increasing guar gum. This study indicated that 0.3% guar gum could improve physico chemical properties of guava juice in term of stability and turbidity. It was not observed phase separation and sedimentation. Moreover, stevia could promote antioxidant capacity in guava juice when compared to non-added stevia.

Introduction: Guava (*Psidium guajava*) is a tropical fruit with a pleasant aroma and flavor. They have high nutritional value which is carotenoid (Campoli S.S et al., 2018). The major carotenoids present in guava are β-carotene and lycopene (Rodriguez-Amaya D.B et al., 2008). The guava fruit can be processed in form of pulp, jellies, pasta, fruit in syrup, puree, baby food, soft drinks, juices and syrups. Guava juice is one of a most preferred non-alcoholic beverage in Thailand with its unique flavour, taste, and health-promoting qualities. The consumption of guava juice is steadily increasing as consumers seek its health benefits. Although sucrose is the most common sweetener in juice, beverage section is mainly focused on the achievement of an adequate sweetness. Hence, sucrose is trying to substitute with other sweetener which increased use of the artificial sweeteners such as aspartame, acesulfame-k, saccharin and sodium cyclamate, or polyalcohols. They have negative connotations due to their possible risk to health and they must be subject to a rigorous assessment before their use in food products and beverages (de Queiroz Pane et al. 2015). In addition, food industry has shown increased interest in plant extracts from *Stevia rebaudiana* (Stevia) Bertoni, because it can be a nutritional strategy in order to replace or substitute sugar energy content due to its high content in non-nutritive sweeteners (Nehir El & Simsek, 2012). Stevia except of sweetness contains a high content of phytochemicals strong antioxidant activity (Šic Žlabur J et al., 2018). Moreover, it has been reported that Stevia is nutrient-rich, containing substantial amounts of minerals, vitamins, polyphenols and other antioxidant compounds. In some countries, Stevia has been consumed as a food and medicine (ethnobotanical) for many years, including most notably Japan and Paraguay (Lemus-Mondaca R et al., 2012). Moreover, the important quality of guava juice is visual appearance and cloud stability. Therefore, guar gum was added in fruit juice to achieve a visual appearance similar to fresh juice. In order to avoid undesirable sedimentation in the bottle during storage. Guar gum is extracted from the endosperm of *Cyamopsis tetragonolobus*. It is a rapid hydration in cold water and formation of viscous solutions and wide range of viscosity stability with pseudoplastic behavior (Nieto and Akins, 2011). However, guava drink is one of a most preferred non-alcoholic beverage. They have an interesting potential for the development of healthful and functional products due to its

antioxidant properties (Ferrari G et al., 2010). In addition, there is not any reported about the effect of the addition of stevia combine with guar gum on physico chemical and rheology of guava juice. The objective of present study was to investigate the stevia and guar gum concentration effect on physico chemical and rheological of guava juice.

Methodology:

Guava juice based formulation: Guava fruits were purchased from local market which were washed with tap water. Guava pulp were mixed with water at a ratio of 60% and 40% w/w, respectively. The juice was filtered and adjust to 5 °Brix. The formulations were obtained proportion of different three components. Juice formulation were formulated using optimal formulations. The proportion levels were 0.3-0.7% of citric acid, 0.21-0.25 of salt and 0.1-0.14% of color, following to the mixture design for optimal formulation. Citric acid in dry powdered form and freshly color solution in distilled water was added to guava juice. The formulated juice was pasteurized at 80°C for 30 seconds, then filled in the pasteurized bottle and cooling in water bath. Guava juice was stored at 4°C for later measurements.

Preparation of guava juice-stevia mixture: In order to produce guava juice, One formulation of guava juice based was added sweetener at various concentrations (0.1, 0.125 and 0.15%) which combined with guar gum solution at 0.1 and 0.3%. The juice was pasteurized at 80°C for 30 second, aseptic bottling and held in cool water. The physico chemical antioxidant and rheology were measured.

Table 1. Optimal mixture design matrix for ingredient formulations.

	Components		
Formulation	citric acid (X_1)	salt (X_2)	color (X_3)
F1	0.61	0.25	0.14
F2	0.65	0.21	0.14
F3	0.65	0.23	0.12
F4	0.65	0.22	0.13
F5	0.67	0.22	0.11
F6	0.65	0.24	0.11
F7	0.65	0.25	0.10
F8	0.69	0.21	0.10
F9	0.63	0.24	0.13

Physicochemical properties: The pH of guava juice formulated (10 mL) was measured using a pH meter (Denver instrument model 225, Calorado, USA.) at 25°C.

The titratable acidity (based on citric acid) of guava juice was determined using 0.1 N NaOH to a pH value of 8.1 (Poyrazog˘lu E et al. 2002).

$$\%\ Citric\ acid = \frac{V_{NaOH} \times 0.1\ \times\ MW_{NaOH}\ \times 100}{\text{Sample weight}\ \times 1000}$$

Color of guava juice with different stevia and guar gum concentration were evaluated color using a Hunter lab colorimeter. Color measurement was placed guava juice in the test cup in colorimeter which distilled water used as a standard. The color measurements were taken in triplicate (Bolin & Huxsoll, 1991).

Where Lightness (0=black, 100=white), a* (−a*=greenness, +a*=redness) and b* (−b*=blueness, +b*=yellowness)

Turbidity: The turbidity of guava juice was centrifuged at 618 ×g, 20 min, 20 °C. The absorbance was measure absorbance at 660 nm by an UV-1800 UV–VIS spectrophotometer (Shimadzu, Kyoto, Japan). All measurements were conducted at 25 °C. The turbidity was calculated as the following formation: (Schoniger, W., 1955)

$$T = -In\left(\frac{I}{I_0}\right)$$

where I is the optical density that passes through a volume of solution with 1 cm length.
I_0 is the incident light intensity.

Antioxidant by DPPH (2,2-Diphenyl-1-picrylhydrazyl (DPPH) assay: Guava juice was evaluated antioxidant activity according to with modified method. Juice sample (100 µL) was added 2 mL of 0.1 DPPH in 95% ethanol. Incubation was performed in dark condition for 30 min, the absorbance of reaction mixture was measure at 517 nm. The DPPH radical scavenging activities of guava juice were calculated as a percentage according to the following equation. (Shimada, K.K. et a., 1992)

$$\%Scavenging\ activity = [(1 - Asample)/Acontrol] \times 100$$

Rheological measurements: Rheological measurements of guava juice were carried out using a rheometer (model Haake Rheometer 400, Germany). The viscosity was performed to determine the dependence of apparent viscosity and shear rate. The condition was performed using shear rate which ranged from 0 to 200 s^{-1} at constant temperature (Borchani, M., et al., 2019).
Statistical analysis: Juice based was optimized using response surface methodology (RSM), mixture design with three variables in three levels. The independent variables were citric acid (X1) (0.3, 0.5 and 0.7%), salt (X2) (0.21, 0.23 and 0.25%) and color (X3) (0.1, 0.12 and 0.14%). In addition, dependent variables included pH. Guava juice with various stevia concentration were conducted in triplicate in a Randomized Complete Block Design. The statistical analysis was per-formed using the Statistical Analysis System (SAS, version 6.0) (SAS Institute, Cary, NC, USA). Duncan's Multiple Range Test was used to determine significant differences between means ($p < 0.05$).

Results and Discussion:
Guava juice based formulation: Mixture design was to optimize guava juice formulation which was performed by applying the desirability function (titratable acidity, pH and color). Table 2 shows the individual desirability of each response. The proportion of three ingredients were citric acid (0.3-0.7%), salt (0.21-0.25%) and color (0.1-0.14%) which are shown in Table 1.

Table 2 Optimal mixture design matrix for ingredient formulations.

Formulation	Titratable acidity (%citric acid)	pH	Color		
			L*	a*	b*
F1	0.61±0.02 ^{c}	3.50±0.02^{c}	22.00±0.39 ^{b}	-0.69±0.05 ^{a}	-1.97±0.08 ^{a}
F2	0.65±0.03^{a}	3.52±0.02^{c}	22.87±0.34 ^{b}	-0.88±0.06 ^{c}	-2.15±0.11 ^{c}
F3	0.63±0.01^{b}	3.55±0.03^{b}	25.25±0.25 ^{a}	-1.28±0.11 ^{d}	-2.00±0.19 ^{b}
F4	0.63±0.05^{b}	3.56±0.01^{b}	21.59±0.30 ^{c}	-0.72±0.04 ^{a}	-1.92±0.06 ^{a}
F5	0.64±0.01^{a}	3.57±0.01^{a}	21.93±0.24 ^{c}	-0.74±0.05 ^{b}	-2.05±0.06 ^{b}
F6	0.65±0.02^{a}	3.57±0.02^{a}	22.36±0.12 ^{b}	-0.80±0.04 ^{c}	-2.14±0.05 ^{c}
F7	0.63±0.02^{b}	3.57±0.02^{a}	21.78±0.20 ^{c}	-0.71±0.03 ^{a}	-2.01±0.06 ^{b}
F8	0.66 ±0.03^{a}	3.58±0.01^{a}	24.36±0.18 ^{a}	-1.17±0.04 ^{d}	-1.95±0.11 ^{a}
F9	0.65±0.02^{a}	3.56±0.02^{b}	25.30±0.22 ^{a}	-1.26±0.08 ^{d}	-2.10±0.17 ^{c}

Values are displayed as mean ± standard deviation. Different superscript letters in the same column represent significantly different values.

Titratable acidity is determines acid:sugar ratio in juice. Organoleptic qualities of fruit juice were indicated by acidity (Sadler & Murphy, 2010) which the major acid in guava is citric acid. The TA is shown in Table 2. The high level of TA (0.66%) was found in F8. The result showed that the values obtained for TA were in the range 0.61–0.66 g citric acid L^{-1}. After citric acid added from 0.61 to 0.69%, their content increased by 0.61 to 0.66, respectively.

Formulation different citric weight ranged from 0.63-0.69% were not significantly different TA value. In addition, compounds contributing to guava juice pH value are mainly organic acids, including citric, succinic, and malic acids. The pH can be defined as the amount of free hydronium ions in a solution, and represents active acidity (Sadler and Murphy, 2010). A pH of 4.6 is a recognized critical value to control against bacterial growth, specifically spore-forming pathogenic growth (Tucker and Featherstone, 2011). However, less variation was found in the pH values, ranging from 3.50 to 3.58. As shown in Table 2, the pH values of F5-F9 were not significantly different. In addition, the pH decreased with increasing TA which might be due to hydrolysis non reducing sugar in polysaccharide chain converted to reducing sugar (Bhardwaj & Pandey, 2011). According to (Abid et al., 2015) reported that decrease in pH and increase in acidity was found in apple juice. Moreover, color is an important parameter that plays a large role in consumer acceptance of a juice (Wrolstad and Smith, 2010). The color system is frequently utilized L^* a^* b^* system, where L^* indicates lightness (0 to 100), a^* (−80 to +80) indicates the green-red color, and b^* (−80 to +80) indicates the blue-yellow color (Wrolstad & Smith, 2010). As seen in Table 2, color of guava juice was significantly different. The result showed that F8 and F9 had the brightest, whereas it had the lowest reddish values. The decrease of a* value was probably due to carotenoid compounds affecting red color in guava juice (Drożdż W et al., 2014). In addition, low a^* was lost during pasteurization process for a prolonged shelf time (Davis AR et al., 2003). However, guava juices were slightly cloudy and translucent, due to no hydrocolloid in the juices. According to mixture design optimization samples were associated to the highest TA and pH and brightest.

Table 3 Regression analysis data used in prediction model for guava juice based

Coefficient	Acidity	pH	Color		
			L*	a*	b*
Constant	0.235	4.2	20.35	7.20	1.84
Linear					
b_1	5.43	2.93	5.501	-6.34	-8.72
b_2	-1.16	-6.28	-1.17	1.35	1.86
b_3	-4.0	-2.16	-4.05	4.67	6.42
Quadratic					
b_{11}	0.502	-1.5	12.80	-1.35	4.269
b_{22}	1.533	6.78	1.27	-1.46	-2.015
b_{33}	-2.982	6.55	-3.69	5.26	-6.33
Interaction					
b_{12}	1.25	-4.63	-5.06	8.43	-2.83
b_{13}	2.955	-5.06	-9.49	1.09	1.50
b_{23}	-9.3	-3.52	-1.04	1.92	7.04
R^2	0.994	0.998	0.94	0.927	0.953
F	1.41	3.85	2.54	2.98	2.902
Sig F	0	0	0.07	0.008	0.05

Note: The model selected properties (acidity, pH and color) as a function of X1 (citric acid), X2 (salt) and X3 (color) were calculated as $Y=b_0+b_1(X_1)-b_2(X_2)-b_3(X_3)+b_{12}(X_1X_2)+b_{13}(X_1X_3)-b_{23}(X_2X_3)+b_{11}(X_1)^2+b_{22}(X_2)^2-b_{33}(X_3)^2$

The linear and quadratic models were used in the desirability physicochemical properties (Table 3). The optimal formulation and predicted physico-chemical properties from different model are showed in equation (1) (2) (3) (4) and (5).

Acidity: $Y= 0.235+5.43(X_1)-1.16(X_2)-4.0(X_3)+1.25(X_1X_2)+2.95(X_1X_3)-9.3(X_2X_3)+0.502(X_1)^2+1.53(X_2)^2-2.982(X_3)^2$ (equation 1)

pH: $Y= 4.2+2.93(X_1)-6.28(X_2)-2.16(X_3)-4.63(X_1X_2)-5.06(X_1X_3)-3.52(X_2X_3)-1.5(X_1)^2+6.78(X_2)^2+6.55(X_3)^2$ (equation 2)

color (L*): $Y= 20.35+5.50(X_1)-1.17(X_2)-4.05(X_3)-5.06(X_1X_2)-9.49(X_1X_3)-1.04(X_2X_3)+12.80(X_1)^2+1.27(X_2)^2-3.69(X_3)^2$ (equation 3)

color (a*): $Y=7.20-6.34(X_1)+1.35(X_2)+4.67(X_3)+8.43(X_1X_2)+1.09(X_1X_3)+1.92(X_2X_3)-1.35(X_1)^2-1.46(X_2)^2+5.26(X_3)^2$ (equation 4)

Equation color (b*): $Y=1.84-8.72(X_1)+1.86(X_2)+6.42(X_3)-2.83(X_1X_2)+1.50(X_1X_3)+7.04(X_2X_3)+4.26(X_1)^2-2.01(X_2)^2-6.33(X_3)^2$ (equation 5)

Optimization are created using a mixture design when the factors are ingredients of a mixture for a four component system (citric, salt and color). The result showed that acidity and salt were most important in predicting acidity pH and color. Optimal conditions were generated by high acidity and low pH. Therefore, the guava juice formation (F8) with 0.69% of citric, 0.21% of salt and 0.1% of color was selected to produce guava juice which were added stevia and guar gum in the future. The guava juice prepared with stevia (0.1, 0.125 and 0.15%) and guar gum (0.1 and 0.3%) at various concentration which physical properties are given in Table 4.

Table 4 Physical properties and antioxidant activity of guava juice with various stevia and guar gum concentration.

Formulation	Physical properties		Antioxidant activity (DPPH•)
	Appearance	Turbidity (%T)	
Stevia 0%+ GC 0% (Control)	Pulp separate from the juice and settle at bottom of the bottle	20.50±0.15[d]	3.15±0.01[d]
Stevia 0.1%+ GC 0.1% (GJ1)	Pulp separate from the juice and settle at bottom of the bottle	20.70±0.17[d]	3.53±0.11[c]
Stevia 0.1% + GC 0.3% (GJ2)	Pulp is uniformly distributed. It does not precipitate	23.43±0.2[b]	3.50±0.18[c]
Stevia 0.125% + GC 0.1% (GJ3)	Pulp separate from the juice and settle at bottom of the bottle	22.57±0.21[c]	3.61±0.12[b]
Stevia 0.125% + GC 0.3% (GJ4)	Pulp separate from the juice and settle at bottom of the bottle	24.40±0.17[b]	3.60±0.25[b]
Stevia 0.15% + GC 0.1% (GJ5)	Pulp separate from the juice and settle at bottom of the bottle	20.40±0.53[c]	3.83±0.19[a]
Stevia 0.15% + GC 0.3% (GJ6)	Pulp is uniformly distributed. It does not precipitate	26.43±0.15[a]	3.81±0.15[a]

The appearance of guava was observed after 1 day. As seen in Table 4, phase separation was

observed from GJ1, GJ3 and GJ5, while GJ2, GJ4 and GJ6 did not show phase separation. Increasing guar gum content to 0.3% in GJ2, GJ4 and GJ6 could hold water in the structure and delay the particle sedimentation. Similar results were reported by Kubo M.T.K. et al. (2013) for tomato juice and by Betoret E et al. (2009) for citrus juices. Moreover, turbidity was used as an indicator for formation of cloud juice. Therefore, addition of guar gum produced an important increase in turbidity values, while increased the total number of suspended particles and soluble solids. The total antioxidant capacity of the guava juice was evaluated using the DPPH· free radical method. The antioxidant capacity values of guava juice decreased throughout the stevia concentration ($p \leq 0.05$) (Table 3). The highest antioxidant capacity was obtained from GJ5 and GJ6 which also contained the highest stevia concentration. As expected, guava juice with 0.15% stevia presented the highest antioxidant values which compared to the juice with 0.1 and 0.125% stevia. The high antioxidant capacity of the guava juice is exerted by stevia via several mechanisms, including scavenge free radicals and reactive oxygen species.

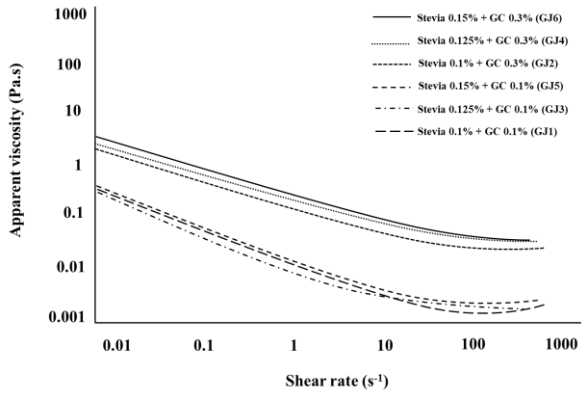

Figure 1. Apparent viscosity of guava juice as a function of shear rate (0.01–300 s^{-1})

As shown in Figure 1, the apparent of guava juice was increased with increasing guar gum from 0.1 to 0.3%. It might be swelling of the guar gum which resulted in a reduction of fluidity, thereby increasing viscosity. However, food contained hydrocolloid with random coil structure. It exhibited viscous response at sufficiently high concentrations when sheared over a wide shear rate range (Naji-Tabasi and Razavi, 2016). Roberts GP et al. (2001) reported that by increasing gum concentration, the zero shear viscosity ($\eta 0$) is increased. In addition, viscosity of GJ6 had a lower than GJ2 with same guar gum concentration. This differentiation was attributed by its different levels of stevia concentration in the juice (Juszczak L et al., 2010). Moreover, the viscosity of guava juice strongly dependent on inter-molecular forces between the molecules and solute-solvent interactions. It is due to inter-molecular spacings and strength of bonding between the molecules. They are affected by the concentration (Krokida MK et al. 2001).

Conclusion: In this study, the addition of stevia and guar gum affected physiochemical properties antioxidant and rheology. Stevia and guar gum concentration seemed to influence the apparent viscosity which confirmed the rheological results by observation. At 0.3% guar gum, Guava juice contributed to increasing viscosity. Consequently, this study showed that stevia could be successful improve antioxidant activity in guava juice. However, further

studies require to be validated influence of stevia and guar gum concentration on shelf life and antioxidant in guava juice.

References:

1. Campoli SS, Rojas M L, do Amaral J E P G, Canniatti-Brazaca S G, Augusto P E D. Food Chem. 2018; 594-601.
2. Rodriguez-Amaya, D B, Kimura M, Godoy HT, Amaya-Farfan J. J Food Compos Anal. 2008; 445-463.
3. de Queiroz Pane D, Dias C B, Meinhart A D, Ballus C A, Godoy H T. J Food Sci Tech. 2015; 6900-6913.
4. Nehir El S, Simsek S. Compr Rev Food Sci f. 2012; 2-12.
5. Šic Žlabur J, Dobričević N, Galić A, Pliestić S, Voća S. J Food Process Pres. 2018;
6. Lemus-Mondaca R, Vega-Gálvez A, Zura-Bravo L, Ah-Hen K. Food Chem. 2012; 1121-1132.
7. Nieto M B, Akins M. Food Hydrocoll. 2010; 67.
8. Ferrari G, Maresca P, Ciccarone R. J Food Eng. 2010; 245-253.
9. Poyrazoğlu E, Gökmen V, Artk N. J Food Compos Ana. 2002; 567-575.
10. Bolin H R, Huxsoll C C. J Food Sci. 1991; 60-62.
11. Schoniger, W., Mikrochim. Acta 1955, 123-9
12. Shimada, K. K., Fujikawa, K. Y., Nakamura, T. J. Agric. Food Chem. 199; 945–948
13. Borchani, M., Masmoudi, M., Amira, A. B., Abbès, F., Yaich, H., Besbes, S. LWT. 2019; 108314
14. Sadler G D, Murphy P A. Food Ana. 2010; 219-238.
15. Tucker G, Featherstone S, Wiley-Blackwell. 2011.
16. Wrolstad R E, Smith D E. Food Ana. 2010; 573-586.
17. Drożdż W, Tomaszewska-Ciosk E, Zdybel E, Boruczkowska H, Boruczkowski T,
18. Regiec P. Pol J Chem Technol. 2014; 7.
19. Davis A R, Fish W W, Perkins-Veazie P. Postharvest Biol Tec. 2003; 425-430.
20. Kubo M T K, Augusto P E, Cristianini M. Food Res Int. 2013; 170-179.
21. Betoret E, Sentandreu E, Betoret N, Fito P. J Food Eng. 2012; 28.
22. Naji-Tabasi S, Razavi S M A, Mohebbi M, Malaekeh-Nikouei B. Food Hydrocoll. 2016; 350-358.
23. Roberts G P, Barnes H A, Carew P. Chem Eng Sci. 2001; 5617-5623.
24. Juszczak L, Witczak M, Fortuna T, Solarz B. Int J Food Prop. 2010; 1364-1372.
25. Krokida M K, Oreopoulou V, Maroulis Z B, Marinos-Kouris D. J Food Eng. 2001. 347-354.

Acknowledgements: This work was supported by a New Researcher Grant from Mahidol University, Thailand

SESSION SP1: CRYSTALLOGRAPHY

SP1_004_PF: THERMAL ANALYSIS OF PHASE TRANSITION AND CRYSTALLIZATION OF $EuBa_2Cu_3O_{7-\delta}$ POWDER PREPARED BY SOLID-STATE REACTION

Paitoon Boonsong[1, 2], Anucha Watcharapasorn[1, 3, 4,*]
[1]Department of Physics and Materials Science, Faculty of Science, Chiang Mai University, Chiang Mai 50200, Thailand.
[2]Graduate Ph.D.'s Degree Program in Applied Physics, Faculty of Science, Chiang Mai University, Chiang Mai 50200, Thailand.
[3]Center of Advanced Materials for Printed Electronics and Sensors, Materials Science Research Center, Faculty of Science, Chiang Mai University, Chiang Mai 50200, Thailand.
[4]Center of Excellence in Materials Science and Technology, Materials Science Research Center, Faculty of Science, Chiang Mai University, Chiang Mai 50200, Thailand.
*e-mail: anucha@stanfordalumni.org

Abstract: $EuBa_2Cu_3O_{7-\delta}$ (Eu-123) powders were synthesized using the solid-state reaction technique. The mixed powders were prepared using a stoichiometric ratio (i.e. Eu:Ba:Cu = 1:2:3) of high-purity Eu_2O_3, $BaCO_3$ and CuO precursors. The powders were analyzed using thermo analytical (DSC/TGA) techniques. The exotherm was related to the formation of Eu-123 which occurred at around 900-930°C. This temperature was selected for calcination process with various time of 12-24 h. Phase identification was determined using an X-ray diffractometer (XRD) and the quantitative phase analysis was performed by fitting the XRD pattern using the GSAS-II program. The morphology was observed by scanning electron microscopy (SEM) with chemical composition identification from EDS mode. For the calcination temperature of 930°C, X-ray diffraction performed at room temperature along with Rietveld analysis showed single phase of an orthorhombic structure Eu-123 for all samples. Rietveld refinement confirmed a good agreement between observed and calculated intensity and a low value of goodness of fit (*GOF*). Orthorhombicity decreased but the oxygen content tended to increase with increasing time which might be a factor that caused the enhancement of the transport properties. Scanning electron microscope (SEM) revealed that the particles had irregular shapes which are randomly distributed. Average particle sizes were < 30 µm in the Eu-123 powders. The approximated stoichiometry of the powder was near the expected nominal composition of Eu-123.

Keywords: Eu-123, solid state reaction, powder synthesis

Introduction: $YBa_2Cu_3O_{7-\delta}$ (Y-123), has been known as a representative of the $REBa_2Cu_3O_{7-\delta}$ superconductors (RE = Rare Earths), is considered a potential oxide thermoelectric material (TE) due to its high electrical conductivity, moderately high Seebeck coefficient and low thermal conductivity [1-5]. $EuBa_2Cu_3O_{7-\delta}$ (Eu-123) provides an opportunity to reveal the effect of the ionic radius of a rare-earth element (0.93 Å for Y^{3+} and 1.03 Å for Eu^{3+}) on structure and electrical conductivity. Compared to the Y-123, the Eu-based systems have better applicability such as a better surface morphology and high T_c temperature [6,7]. Besides, Eu^{3+} has an ionic size almost the same as that of Ba^{2+} and this leads to the introduction of point defects into the RE-123 system. This is advantageous since the high density of point defects can act as strong pinning centers in the RE-123 systems [8]. Even though the Eu-123 possesses a superior potential for various applications, relatively few studies have been done on synthesis, electrical and thermal transport properties of this compound.

Generally, there are two non-equivalent Cu sites, the linear chain Cu(1) in the O(1) Cu(1) O(1) units and the planar Cu(2) in the CuO_2 planes containing O(2) and O(3) in RE-123 system. The electrical properties of the RE-123 system is believed to occur in the CuO_2 planes through hole charge carriers and the oxygen content of Cu-O chains governs the hole carries

concentration in the CuO_2 planes. The non-stoichiometry of Eu-123 is closely related to average copper valence, carrier concentration and high temperature conductivity [9] so that synthesizing pure Eu-123 powders are important. Therefore, the Rietveld method in the quantitative phase analysis was applied to prepared Eu-123 powders. This technique offers advantages over traditional analytical methods which was originally developed for crystal structure refinement using quantitative X-ray powder phase analysis [10].

In this work, we studied the influence of variable calcination time on the synthesis of Eu-123 powder by the solid-state reaction technique. Thermal analysis of the synthesized Eu-Ba-Cu-O precursor powders during heat treatment without flowing O_2 was studied. These samples are studied using the Rietveld refinement of the X-ray diffraction (XRD) data for calculation of structural parameters to confirm the Eu-123 phase using the General Structure Analysis System II (GSAS-II) program which is a comprehensive software package for all aspects of crystallographic data analysis [11]. Surface morphology and elemental composition were investigated by SEM with EDS analysis.

Methodology: The $EuBa_2Cu_3O_{7-\delta}$ powders were prepared by a standard solid-state reaction method from the commercial 99.99% purity oxide powders of Eu_2O_3, CuO and $BaCO_3$. The constituents were weighed in the stoichiometric ratio of Eu: Ba: Cu = 1: 2: 3. In advance, the powder mixtures were ball milled in ethanol for 24 h and dried to attain homogeneous mixture. DSC/TGA analysis (Netzsch STA 449 F3 Jupiter) was used to obtain the temperature of calcination. The dried powder was placed in a Pt crucible and heated up to a temperature of 1100°C with a heating rate of 10°C/min under a normal atmosphere. According to DSC/TGA result, the powders were calcined at 920 and 930°C for 12-24h in air atmosphere. The structural characterization of the powders prepared was investigated by X-ray diffraction (XRD) in the range of $2\theta = 20-80^{o}$. Phillips Xpert pro Diffractometer having CuK_a radiation was used. The lattice parameters of the samples were calculated by Rietveld-Refinement method using GSAS-II software [11]. The microstructural and compositional characterization of the samples was performed using JSM -IT300 scanning electron microscope (SEM) and Energy Dispersive X-ray Spectroscope (EDX).

Results and Discussion: DSC/TGA as a function of temperature for precursor compositions have been performed, taken upon heating and cooling the samples at a rate of 10°C/min, as shown in Figure 1. The mixed precursors have transformed during a pre-reaction at elevated temperatures. The first weight loss which started from 200 °C and ended at 300 °C was due to the evaporation of the water hydration and finally with intermolecular dehydration reactions. According to DSC/ TGA data reported for this process, mass loss began gradually at about 700°C. The mass loss was mostly due to evolution of CO_2 from $BaCO_3$ in the range of 790-810°C. The calcination temperature was expected to be in the range of 900-930°C as the enxotherm was related to the formation of Eu-123. The endothermic peak observed at above 1040°C indicated that Eu-123 decomposed peritectically to Eu-211 phase and a liquid consisting of $BaCuO_2$ and CuO_x. In this work, the calcination process at 920°C and 930°C for 12-24h in air were selected to investigate the effect of variable calcination temperature on the synthesized Eu-123.

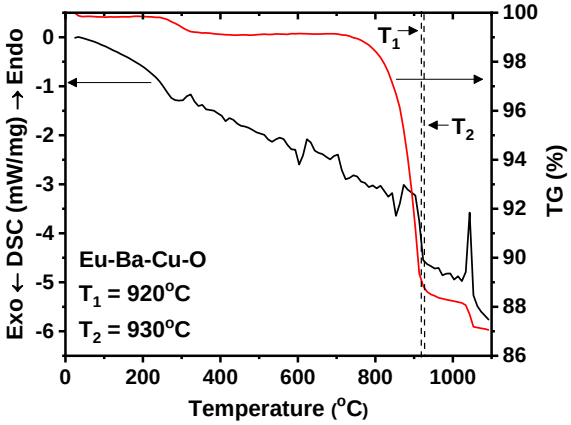

Figure 1. DSC/TGA heating curve of the pre-calcined Eu-Ba-Cu-O powder heated under air atmosphere with a heating rate 10°C/min.

Figure 2 shows the X-ray diffraction patterns of the Eu-123 powders. The diffraction pattern is indexed using High score Plus 3.0 software. The identification of this phase was firstly obtained from the comparison with the standard COD files in which the standard phase Eu-Ba-Cu-O was referenced. The result clearly shows that in all cases, the desired Eu-123 phase was identified as the main crystalline phase. The XRD pattern of the powders corresponded well with the $EuBa_2Cu_3O_7$ phase (COD file no. 96-154-0792), indicating an orthorhombic perovskite structure with the space group Pmmm.

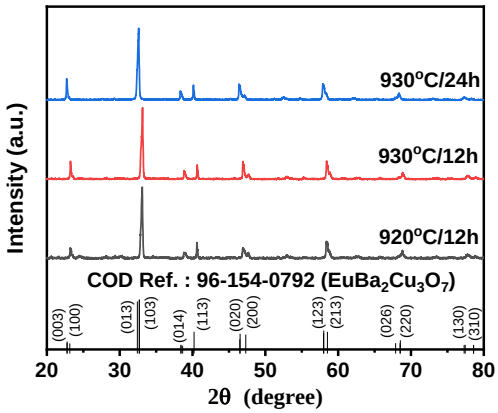

Figure 2. XRD patterns of the calcined Eu-123 powders.

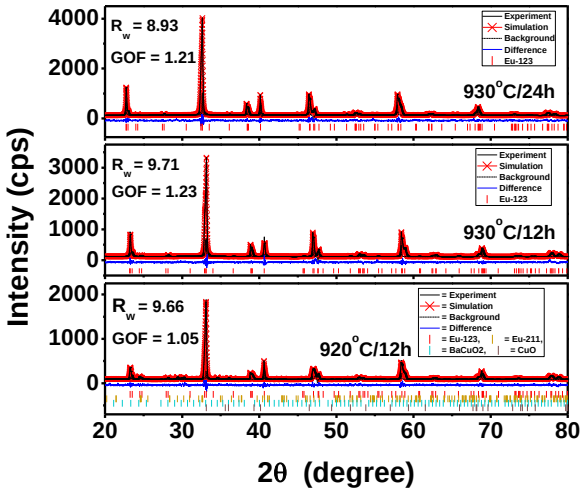

Figure 3. Experimental and simulated XRD patterns of the calcined Eu-123 powders.

The Rietveld refinement of samples has also been performed using GSAS II program. Figure 3 shows the experimental and fitted XRD patterns for all the presently studied compositions. Rietveld refinement requires a structural model that has an approximation for the actual crystal structure. Normally, it is well known that at high temperature of calcination, the chemical reactions can be expressed by

$$2EuBa_2Cu_3O_{7-\delta} \rightleftharpoons Eu_2BaCuO_5 + 3BaCuO_2 + 2CuO \quad (1)$$

Therefore, Rietveld refinement of the XRD patterns of all samples was performed using the structural model (COD database) of all possible occurring secondary phases such as $EuBa_2Cu_3O_{7-\delta}$ (Eu-123), Eu_2BaCuO_5 (Eu-211), $BaCuO_2$ and CuO phases. To evaluate quantitatively the best fit of the data, the most accepted factor is the weighted residual (R_w) minimized in Rietveld refinement which is commonly defined as

$$R_w^2 = \frac{\Sigma_i \omega_i \left(y_i^{(exp)} - y_i^{(a)}\right)^2}{\Sigma_i \omega_i \left(y_i^{(exp)}\right)^2} \quad (2)$$

where $y_i^{(exp)}$ and $y_i^{(a)}$ are the observed and calculated intensities at a point i, respectively, while ω_i is the weight, which is inversely proportional to $y_i^{(exp)}$. The calculated intensities $y_i^{(a)}$ depend on the vector of the refined parameters. In the case of purely statistical errors, the expected *R* value limit is

$$R_{exp}^{2\frac{N-P}{\Sigma_i \omega_i \left(y_i^{(exp)}\right)^2}} \quad (3)$$

where *N* is the number of observations and *P* is the number of parameters. The ratio between the two *R* values defines the goodness-of-fit (GOF)

$$\mathrm{GOF} = S^2 = R_w^2 / R_{exp}^2 \quad (4)$$

A *GOF* value or S^2 of 1.0 is the best obtainable statistical value for the refinement and it also indicates that the refinement is complete. Nevertheless, The *S*-value of 1.3 or less is

empirically considered to be satisfactory for the best fitting with an appropriate model [12]. Low deviation values for the statistical parameters R_w and *GOF* were found as shown in Figure 3 which indicated a good quality of structural refinement. The lattice parameters and orthorhombicity values of RE-123 structure as a function of temperature and time are given in Table 1. The result showed that the orthorhombic lattice parameters a and b became closer with the increase of temperature and time. The asymmetric distribution of oxygen leads to an orthorhombicity (b – a/b + a), which is a measure of ordering. The large difference between b and a corresponded to the higher ordering degree [13]. It is noticed that orthorhombicity started to decrease, which was a signal of the beginning of phase transition from orthorhombic to tetragonal structure [14]. At 930°C, the result of refined XRD data showed that the samples exhibited the pure Eu-123 phase. However, the Eu-211 (0.8 wt.%), BaCuO2 (0.1 wt.%) and CuO (0.3 wt.%) were observed at calcination at 920°C.

Table 1. Lattice parameters, volume and orthorhombicity of Eu-123 structure.

Sample	Parameters					Oxygen deficiency (δ)	Hole concentration (n (CuO_2))
	a (Å)	b(Å)	c(Å)	Vol(Å^3)	(a-b/a+b) 10^{-3}		
920°C/12h	3.8493	3.9001	11.6663	175.139	6.550	-	-
930°C/12h	3.8512	3.8976	11.6960	175.563	5.981	0.18	0.07
930°C/24h	3.8533	3.8958	11.6714	175.208	5.481	0.01	0.24

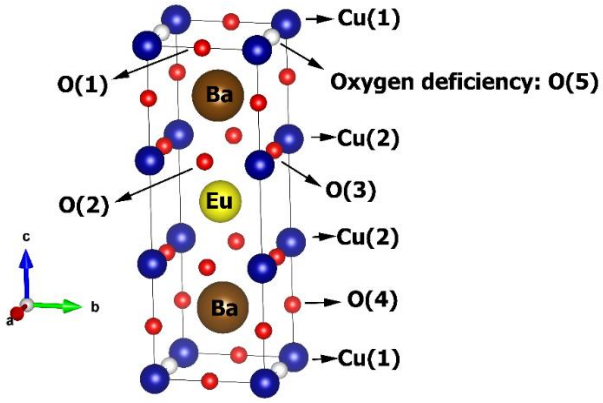

Figure 4. Crystal Structure of orthorhombic Eu-123.

The RE-123 is orthorhombic structure and also related to the perovskite. Its main features are CuO_5 pyramids whose square bases, which include the Cu(2) atoms, form the CuO_2 plane and CuO chains with the Cu(1) atoms running along the b-axis as shown in Figure 4. It is well known that oxygen content is responsible for charged reservoir CuO_2 planes in a RE-123 system. A reduction in oxygen content lowers the number of oxygen atoms in Cu–O chains in the unit cell. The oxygen content in the Eu-123 was calculated from X-ray diffraction data by the formula [15, 16] as:

$$\int_{c/3=3.890}^{c_{exp}/3} dc = 0.047x \int_0^{\delta} d\delta \quad (5)$$

It is observed that the oxygen content depends on c-axis in the Eu-123 samples. The results of calculated oxygen content suggested that the oxygen content tended to increase

with increasing calcination time at 930°C (low oxygen deficiency) as shown in Table 1. Moreover, the hole concentration in the CuO_2 plane is calculated using the formula [16,17] as:

$$n\,(\mathrm{CuO_2}) = (0.5 - 2\delta)/2 \qquad (6)$$

The value of n (CuO_2) for optimum value is 0.24, which is in good agreement with the reported literature [18,19]. The value of n (CuO_2) showed an increasing trend with increasing time.

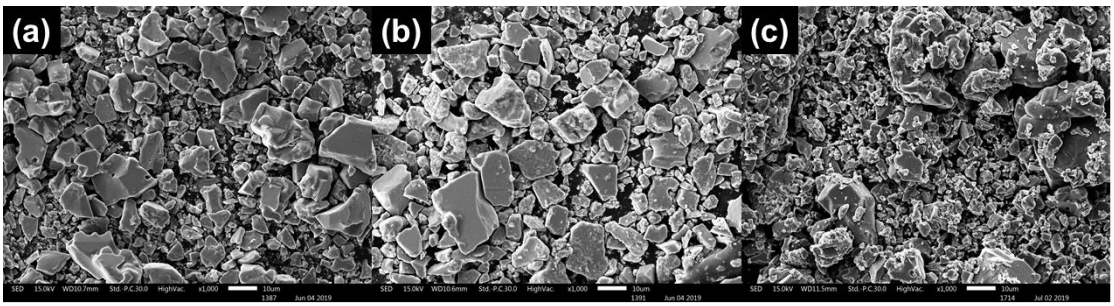

Figure 6. SEM micrographs of Eu-123 powders calcined at
(a) 920 and (b) 930°C for 12h and calcined at 930°C for (c) 24h

Table 2. Evaluated elemental composition and particle sizes for samples calcined at various conditions.

Sample	Evaluated elemental composition (at. %)			
	Eu	Ba	Cu	O
920°C/12h	9.52	17.59	25.20	47.69
930°C/12h	8.59	19.08	28.56	43.77
930°C/24h	8.05	15.95	25.92	50.08

The morphology and particle size of the powders produced by the solid-state reaction technique were determined by a scanning electron microscope (SEM) as shown in Figure 5. It was observed that most samples exhibited irregular-shape with size range of <30 µm which were linked together in agglomerates of different sizes. EDS was performed on the samples for the quantitative elemental analysis and the results are listed in Table 2. It revealed that the approximate stoichiometric composition was near the Eu-123 phase. However, these results appeared slightly different chemical composition compared to stoichiometric Eu-123 due partly to error measurements from agglomerates having particle size distribution or secondary phase.

Conclusion: The Eu-123 powders were successfully synthesized via solid state reaction technique. Thermal analyses via DSC/DSC show identical thermal behavior for Eu-Ba-Cu-O precursors, which undergo different chemical processes during their formation. The calcination temperature suggests a good calcination to be at 930°C as the exotherm related to obtain fine powders with high purity Eu-123. With increasing time, the quantitative analysis of XRD results using GSAS-II program indicated that all samples showed the pure Eu-123 phase with orthorhombic perovskite structure with space group Pmmm. An increase in calcination time decreased the oxygen deficiency. The microstructures of the powders were consisted of irregular-shaped particles, which were linked together in agglomerates. The

average sizes of most particles were < 30 µm. These results suggested that the calcination process at 930°C for 24h are suitable for the fabrication process of Eu-123 powders.

References:

1. Rodríguez JE. Phys. Stat. Sol. (a). 2008; 205:1173–1176.
2. Rodriguez JE. Phys. Stat. Sol. (c). 2005; 2:3605–3608.
3. Rodríguez JE, López J. Physica B. 2007; 387(1–2):43–146.
4. Prayoonphokkharat P, Watcharapasorn A. Sci. Adv. Mater., 2017; 9:1872–1875.
5. Wannasut P, Prayoonphokkharat P, Jaiban P, Keawprak N, Watcharapasorn A. Mater. Lett., 2019; 236:378–382.
6. Jia QX, Maiorov B, Wang H, Lin Y, Foltyn SR, Civale L, MacManus-Driscoll JL. IEEE Trans. Appl. Supercond. 2005; 15:2723.
7. Zhou H, Maiorov B, Wang H, MacManus-Driscoll JL, Holesinger TG, Civale L, Jia QX, Foltyn SR. Supercond. Sci. Technol. 2008; 21:025001
8. Civale L, Maiorov B, Serquis A, Willis JO, Coulter JY, Wang H, Jia QX, Arendt PN, MacManus-Driscoll JL, Maley MP, Foltyn SR. Appl. Phys. Lett. 2004; 84:2121–2123.
9. Ghigna P, Spinolo G, Malavasi L, Chiodelli G, Flor G. Phys. Chem. Chem. Phys. 2001; 3: 606–612
10. Post JE, Bish DL. Rev. Mineral. 1989; 20:277–308.
11. Toby BH, Von Dreele RB. J. Appl. Cryst. 2013; 46:544–549.
12. Tsubota M, Kitagawa J. Scientific Reports. 2017; 7:15381.
13. Kulpa A, Chaklader ACD, Osborne NR, Roemer G, Sullivan B, Williams DL. Solid State Commun. 1989; 71:265–268.
14. Akduran N. J. Low Temp. Phys. 2015; 181:183–196.
15. Jung J, Mohamed MAK, Cheng SC, Franck JP. Phys. Rev. B. 1990; 42:6181.
16. Huse VR, Mote VD, Dole BN. Ceram. Intern. 2013; 39(7):7317–7321.
17. Khosroabadi H, Daadmehr V, Akhavan M. Mod. Phys. Lett. B. 2002; 16:943.
18. Tokura Y, Torrance JB, Huang TC, Nazzal AI. Phys. Rev. B. 1988;38:7156.
19. Booth CH, Bridges F, Boyee JB, Claeson T, Zhao ZX, Cervantes P, Phys. Rev. B. 1994; 49:3432.

Acknowledgements: This research was supported by a Science Achievement Scholarship of Thailand (SAST) and instrument analysis support was given by CMU. Center of Excellence in Materials Science and Materials Technology, Department of Physics and Materials Science, Faculty of Science and the Graduate School, Chiang Mai University are also acknowledged.

SP1_005_PF: A NEW ZINC(II) COORDINATION POLYMER BASED ON 5-NITROISOPHTHALATE; SYNTHESIS, CRYSTAL STRUCTURE AND HIGHLY SENSITIVE FLUORESCENCE SENSING PROPERTIES OF SMALL MOLECULES AND METAL IONS

Pornsan Lueangseephet[1], Supakorn Boonyeun[1,*], Sukanya Mingphimai[1], Kittipong Chainok[2], Premjit Arpornmaeklong[3], Yuki Shirosaki[4]
[1]Department of Chemistry, Faculty of Science and Technology, Thammasat University, Pathum Thani 12120, Thailand
[2]Materials and Textile Technology, Faculty of Science and Technology, Thammasat University, Pathum Thani 12120 Thailand
[3]Faculty of Dentistry, Thammasat University, Pathumthani 12120, Thailand
[4]Department of Materials Science, Faculty of Engineering, Kyushu Institute of Technology, Kitakyushu, Japan
*e-mail: chemistrytu@gmail.com

Abstract: A new Zn(II) coordination polymers $[Zn(Nip)(apm)(DMF)]_n$ (1) was synthesized by direct method thru the reactions of $Zn(NO_3)_2$ with 5-nitroisophthalate and 2-aminopyrimidine in the mixture of solvent. The compound was characterized by IR spectroscopy, single and powder X-ray diffraction. The compound crystallizes in the triclinic crystal system and *P*$\bar{1}$ space group. The Zn(II) ion adopts four-coordinated in a distorted tetrahedral geometry that is constructed to give 1D polymeric chain through carboxylate group of 5-nitroisophthalate ligands. The double layers of 1D chain is created by π - π interaction. The 2 and 3 dimension was encouraged by hydrogen bond interactions and CH - π interactions. The Zinc(II) compound represented as fluorescence sensing highly sensitive for acetone and Fe^{3+} ion.

Introduction: Coordination polymers architectures are increasing interested constructed by coordination bond and supramolecular interactions (hydrogen bonding and π-π stacking) using first row transition metal ions and bridging organic linkers.[1] Coordination polymers were prepared using a lot of synthetic methods such as direct, hydrothermal (solvothermal, diffusion, mechanochemical, electrochemical, microwave assisted and sonochemical. Dicarboxylate derivatives ligands are an organic compound, which containing two carboxyl functional groups (-COOH).[2] The general molecular formula is HO_2C-R-CO_2H, where R can be represented an aliphatic or aromatic, which adducts mainly aromatic dicarboxylic acids. The metal dicarboxylate derivatives have been used as model compound in physical chemistry studies.[3] They have been used as bridging organic linkers for lanthanides and transition metals.[4-5] The coordination polymers can be designed and synthesized as a novel of the coordination polymers by working on potential applications such as molecular separation, gas storage, catalyst, magnetic materials and optical properties.[6-8] The new Zinc(II) compound was designed and synthesized to form new coordination polymer. Ligand dicarboxylate has been selected following factor N,O-ligand such as 5-nitroisophthalic acid (Nip) and 2-aminopyrimidine (apm). Structure confirmation considered the interaction from X-ray spectroscopy. The Zinc(II) compound was used focusing on the fluorescence sensing properties of small organic solvent molecules and metal ions.

Methodology: All chemicals were of commercial grade from Aldrich. All solvents and reagents were purchased from RCI Lab scan, Thailand and it was distilled prior use. The CHN Elemental analysis was determined by using a Perkin-Elmer analyzer (2400). The FT-IR spectra were recorded in the range 4000-400cm^{-1} on Perkin-Elmer infrared spectrophotometer (spectrum GX), using KBr pellets. UV-vis spectra were recorded on Shimadzu UV-vis spectrophotometer (UV-1700) and Shimadzu UV-spectrophotometer (UV-2600 Serier) (for solid state UV-Vis).

The photoluminescence (PL) studies were carried out using a Horiba Fluoro Max4 spectrofluorometer with a 180 W Xenon lamp.

Synthesis of [Zn(Nip)(apm)(DMF)]$_n$: A mixture of $Zn(NO_3)_2.6H_2O$ (1 mmol) and 5-nitroisophthalic acid (1 mmol) in mixed solvent MeOH : DMF (10:5 mL) was add to a solution of 2-aminopyrimidine (1 mmol) into the first solution. The mixture solution would be heated and stirred for 20 min. After cooling to room temperature for two days, colorless crystals of complex were collected by filtration, washed and dried. Yield: $[Zn(Nip)(apm)(DMF)]_n$, 67%.

X-ray crystallographic analysis : Diffraction data were collected on a Bruker D8 QUEST CMOS diffractometer equipped with graphite-monochromatic Mo-Kα radiation (λ = 0.71073 Å) at Faculty of Science and Technology, Thammasat University, operating at 296 ± 2 K. Empirical absorption corrections were applied to all data using SADABS.[9] The structures were solved by SHELXT-2015 and refined by full-matrix least-squares based on F^2 using the SHELXL-97 with Olex2 as a graphics interface.[10-12] Anisotropic displacement parameters were refined for all non-hydrogen atoms except for the disordered atoms. Hydrogen atoms were added theoretically and were riding on their parent atoms.

Fluorescence sensing properties: The $[Zn(Nip)(apm)(DMF)]_n$ (1 mg) was soaked in different solvents [Methanol, Ethanol, N-propanol, isopropanol, butanol , benzene (BZ), acetone, DMF, DMSO, ethyl acetate (EtOAc), tetrahydrofuran (THF), chloroform ($CHCl_3$), acetone, toluene, acetonitrile (ACN)] with an equal volume of 3 mL and treated by ultrasound for 30 min, and then the suspensions were promptly used for luminescence measurement. Sensing of metal ions test, $[Zn(Nip)(apm)(DMF)]_n$ (1 mg) were soaked in ethanol solutions (3mL) containing 1×10^{-3} mol.L^{-1} $M(NO_3)_x$ (M = Al^{3+}, Mg^{2+}, Mn^{2+}, Fe^{2+}, Co^{2+}, Ni^{2+}, Cu^{2+}, Cd^{2+}, Cr^{3+},Pb^{2+} ,Ag^{+} and Fe^{3+}),and then treated by ultrasound for 30 min for luminescence detection. Then, excitation at 300 nm were detected from 310 to 350 nm.

Results and Discussion:

Synthesis and IR spectroscopic studies of [Zn(Nip)(apm)(DMF)]$_n$: The $[Zn(Nip)(apm)(DMF)]_n$ complex was obtained as colorless crystals by reaction of ligand 5-nitroisophthalic acid (Nip), 2-aminopyrimidine (apm) and Zinc (II) nitrate in a 1:1:1 ratio in mixed solvent MeOH : DMF. The infrared spectra and element analyses of $[Zn(Nip)(apm)(DMF)]_n$ confirm the main functional group on the structure. The IR spectra represented the significant vibrational mode that were observed include NH stretching at 3337.89, 3196.12 cm^{-1} of 2-aminopyrimidine (apm). The strong spectral bands of C=C stretching are revealed at 1455.79. The bands of C=O stretching observed in the experimental spectra at1630.20 cm^{-1}. In all cases, the IR spectra are significantly different from the starting materials, confirming the presence of the bridging ligand in the metal coordination sphere.

Structural description of [Zn(Nip)(apm)(DMF)]$_n$: X-ray crystallography reveals that $[Zn(Nip)(apm)(DMF)]_n$ crystallizes in the triclinic crystal system and *P*1 space group as shown in Table 1. The asymmetric unit consists one crystallographically unique Zn(II) ion, one Nip, one apm and one DMF ligand. The Zn1 ion formed a four coordinated complex, with three oxygen atoms from two different Nip and DMF ligands and one nitrogen atoms from apm ligand. The Zn(II) complex exhibits a distorted tetrahedral geometry from bond lengths of Zn – O1 1.9563(17), Zn – O4^{i} 1.9790(18), Zn1 – O7 1.9940(2), Zn – N1 2.0430(2) and bond angles 98.75(8) – 117.67(8)$^{\circ}$ in Table 2. The Zn(II) ion is linked to near Zn(II) ion by bridge of Oxygen atom of carboxylic group in Nip resulting one-dimensional chain structure as shown in Figure 1. The one-dimensional is constructed by π - π interactions to give double layers (Figure 2.). The double layers are connected by hydrogen bonding and CH - π interactions to form 2D and 3D structure, respectively. (Figure 3. and Table 3.).

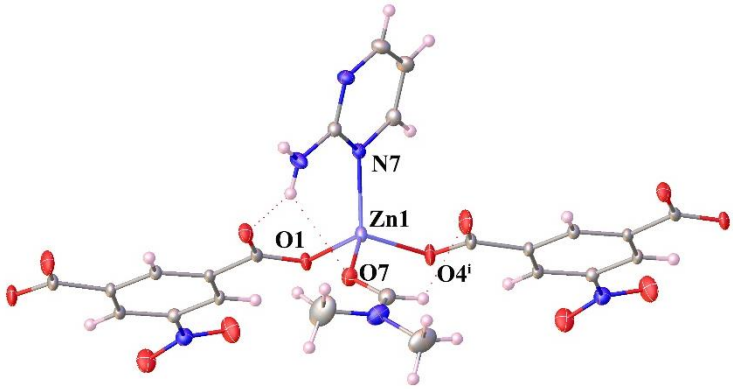

Figure 1. Coordination environment of Zn(II) atoms of $[Zn(Nip)(apm)(DMF)]_n$

Table 1. Crystal data and structure refinements for $[Zn(Nip)(apm)(DMF)]_n$

Compound	$[Zn(Nip)(apm)(DMF)]_n$
Empirical formula	$C_{15}H_{15}N_5O_7Zn$
M (g mol^{-1})	442.69
Crystal system	Triclinic
Space group	*P*1
Temperature (K)	296
a (Å)	8.529 (4)
b (Å)	9.750 (1)
c (Å)	12.596 (4)
α (°)	70.748 (1)
β (°)	87.520 (1)
γ (°)	66.887 (1)
V (Å^3)	905.10 (5)
Z	2
D_{calc} (gcm^{-3})	1.624
μ (Mo K*α*) (mm^{-1})	1.41
Reflections collected	3699
Independent reflections (R_{int})	0.036
$R[F^2>2\sigma(F^2)]$	0.034
$wR_2(F^2)$	0.090

Table 2. Selected bond distances (Å) and angles(°) for complex $[Zn(Nip)(apm)(DMF)]_n$

Parameter	Value (Å)	Parameter	Value (Å)
Zn1 - O1	1.9563 (17)	O1 – Zn1 – O7	107.01 (8)
Zn1 – O4^i	1.9790 (18)	O1 – Zn1 – N1	117.67 (8)
Zn1 – O7	1.9940 (2)	O4^1 – Zn1 – O7	114.15 (9)
Zn1 – N7	2.0430 (2)	O4^1 – Zn1 – N1	112.57 (9)
O1 – Zn1 – O4^i	98.75 (8)	O7 – Zn1 – N1	112.74 (8)

Symmetry codes: (i) -1+X,1+Y,+Z

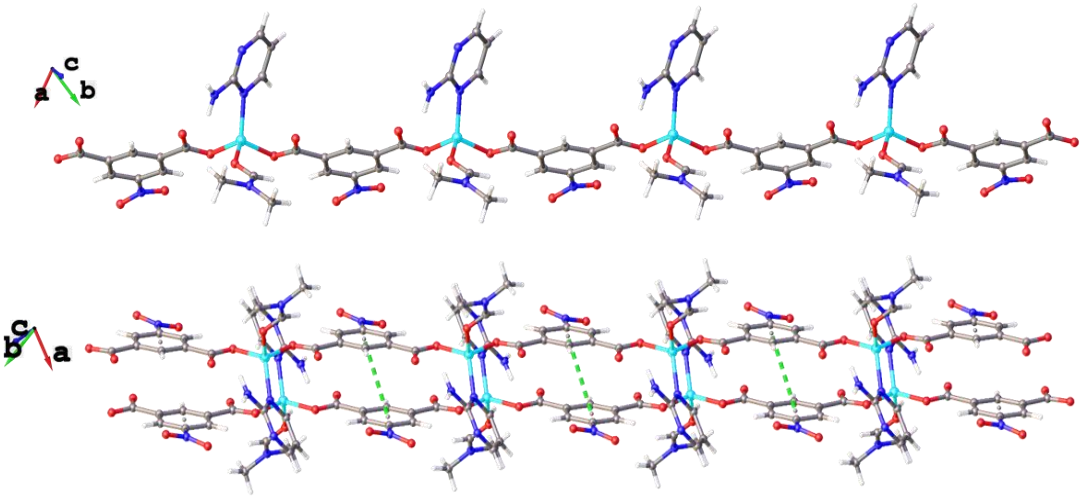

Figure 2. The one-dimensional (above) and double layers (bottom) of $[Zn(Nip)(apm)(DMF)]_n$

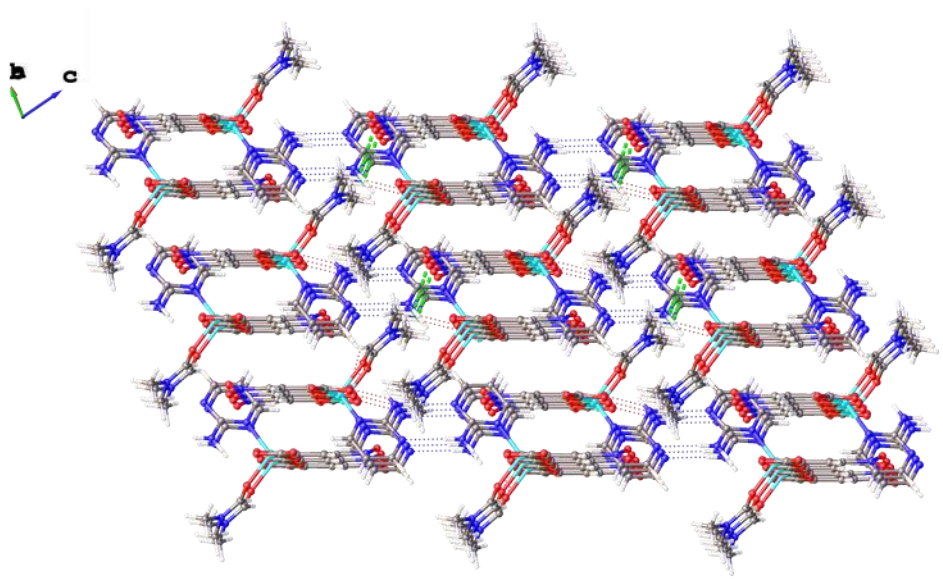

Figure .3 The 3D structure of $[Zn(Nip)(apm)(DMF)]_n$ compound

Table 3. The hydrogen bond geometries for $[Zn(Nip)(apm)(DMF)]_n$

D – H --- A	D – H (Å)	H --- A(Å)	D – A(Å)	D – H --- A (°)
N3 – H3A … N2^{i}	0.86	2.26	3.121(3)	174.5
N3 – H3B … O2	0.86	2.26	2.958(3)	137.8
N3 – H3B … O7	0.86	2.46	3.088(3)	130.6
C4 – H4 … O4^{ii}	0.93	2.68	3.283(3)	123.2
C13 – H13 … O^{iii}	0.93	2.41	3.010(4)	122.2
C14 – H14B … O3^{iv}	0.96	2.31	3.249(5)	165.8

Symmetry codes: (i) -1+X,1+Y,+Z (ii) 1-X,1-Y,1-Z (iii) -1+X,1+Y,+Z (iv) 1-X,1-Y,2-Z

Powder X-ray diffraction: Powder X-ray diffraction, an analytical technique used for checked phase purity of a crystalline material and can provide information on unit cell dimensions, shows PXRD patterns of $[Zn(Nip)(apm)(DMF)]_n$. The simulated PXRD pattern for the single crystals of material obtained from single crystal X-ray diffraction displayed a non-solvated adduct all compounds and also coincided with patterns obtained for polycrystalline. The simulated and experimental patterns are in good acceptance with X-ray data. That the bulk materials and single crystals are homogeneous as shown in Figure 4.

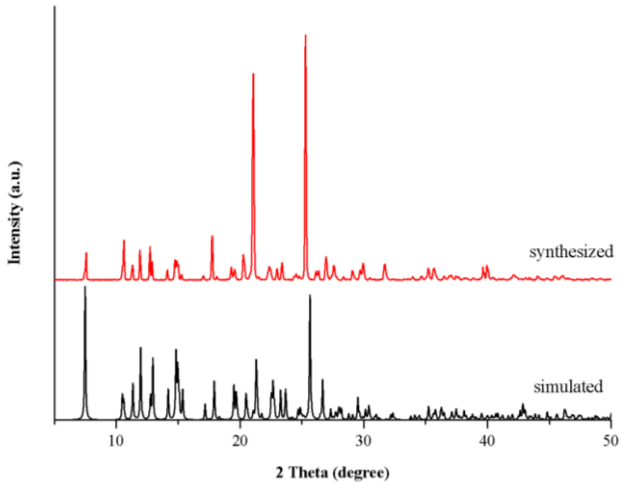

Figure 4. The PXRD patterns of $[Zn(Nip)(apm)(DMF)]_n$ compound

Solid-state emission: The solid-state emission spectra $[Zn(Nip)(apm)(DMF)]_n$ compound with emission spectra of Nip ligands was obtained at room temperature upon excitation at 300 nm. The emission of Nip ligand displays an emission maximum at 438 nm. The maxima emission peaks were observed at about 420 nm for $[Zn(Nip)(apm)(DMF)]_n$ compounds , as shown in Figure 5.

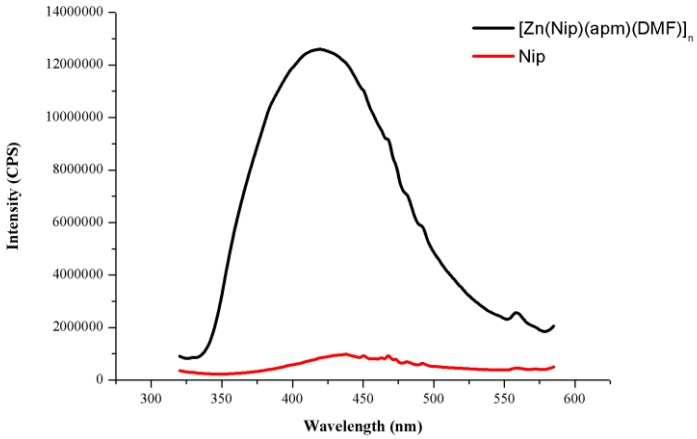

Figure 5. Solid-state emission spectra of Nip and $[Zn(Nip)(apm)(DMF)]_n$ compound at room temperature when excited at 300 nm

Fluorescence sensing properties: $[Zn(Nip)(apm)(DMF)]_n$ compound was selected to study the luminescence responses to various organic solvent and metal ions. The luminescent intensities of $[Zn(Nip)(apm)(DMF)]_n$ compound is depend on the solvent molecules, especially acetone and THF, respectively (Figure 6). Explicitly, acetone represented turn on quenching efficiency of $[Zn(Nip)(apm)(DMF)]_n$ compound about 84.86 %. [quenching efficiency = $(I_0 - I) / I_0$ x 100 %, where I_0 is fluorescent intensities of ethanol solution and I is fluorescent intensities of aim solution]

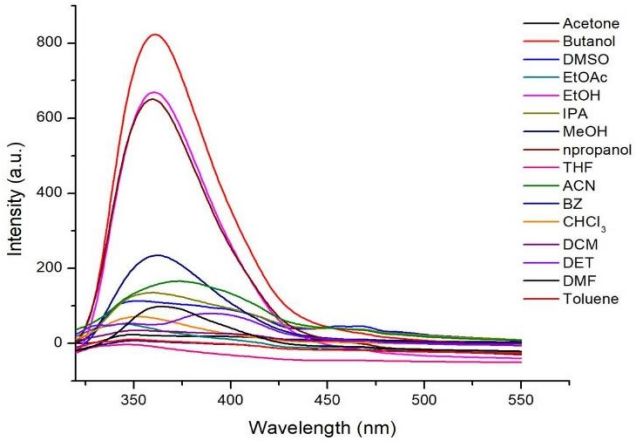

Figure 6. The luminescence intensity of $[Zn(Nip)(apm)(DMF)]_n$ compound with various organic solvents

In addition, $[Zn(Nip)(apm)(DMF)]_n$ compound was grinded into powder and dispersed in ethanol solution (10 mL) containing 10^{-3} M of $M(NO_3)_x$ (M = Ag^+, Cd^{2+}, Co^{2+}, Cu^{2+}, Mg^{2+}, Mn^{2+}, Ni^{2+}, Pb^{2+}, Zn^{2+}, Al^{3+}, Cr^{3+}, Fe^{3+}), as shown in Figure 7 Fe^{3+} ion exhibits quenching effect towards $[Zn(Nip)(apm)(DMF)]_n$ compound. The quenching percentage was about 98.54 % [quenching efficiency = $(I_0 - I) / I_0$ x 100 %, where I_0 is fluorescent intensities of ethanol solution and I is fluorescent intensities after addition of aimed species]

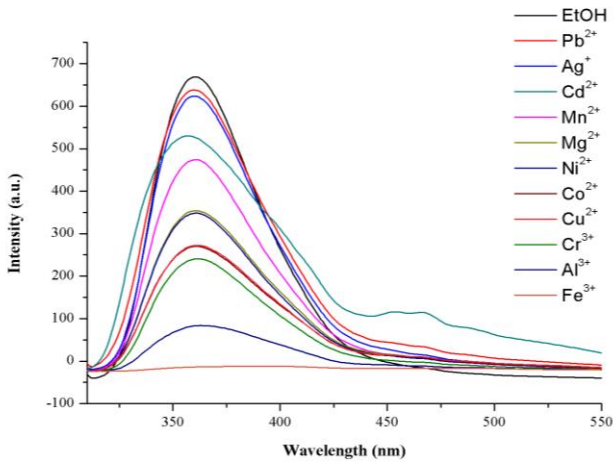

Figure 7. The luminescence intensity of $[Zn(Nip)(apm)(DMF)]_n$ compound with various metal ions

Conclusions: Zinc(II) coordination polymer was synthesized by direct method and characterized. The crystal structure of $[Zn(Nip)(apm)(DMF)]_n$ showed a distorted tetrahedral geometry, which determined by X-ray diffraction. $[Zn(Nip)(apm)(DMF)]_n$ compound exhibits a 1D chain from Nip ligand and connected by π - π interactions to form 2D supramolecular. The significantly hydrogen bond interactions reveals 2D and 3D structure, respectively. The quenching effect display sensitivity and selectivity for detection acetone and Fe^{3+}.

References:

1. Xiangxiang Z, Shilin W, Liyan Z, Suya L, Guozan Y. Inorg. Chem. 2019;58:2444–2453.
2. Whitfield T, Zheng L, Wang X, Jacobson AJ. Solid state Science.2001;3:829-835.
3. Tomar K, Gupta AK, Grupta M. J.Name. 2013;00:1-3.
4. Jie Z, Tong Y, Yong-Feng Q, Yi-Dan Z, Xiao W, Lin D, Min-Jin X, Jian X, Qi-Hua Z. Inorg. Chem. Commun. 2016;73:161-165.
5. Chengfang Q, Yi Z, Youliang R, Xia G, Meili Z, Chunsheng Z, Guochum Z, Sanping C, Shengli G. J Solid State Chem 2019;270:443-449.
6. Bo X, Jie L, Nana K, Cuncheng L. Inorg. Chem. Commun. 2014;47:119-122.
7. Xiao-Jie W, Dong L, Yue-Hue L, Guang-Hua C. Polyhedron 2019;158:357-364.
8. Bei L, Xiaofang W, Huai-Ming H, Yi-Fan Z, Meng-Lin Y, Ganglin X.Inorg. Chim Acta 2016;453:771-778.
9. Xiong Y., Liu G., Wang X., Zhang J., Lin H. and Sha X. Cryst Eng Comm. 2016,19;31:1-12.
10. Klongdee F., Boonmak J., Moubaraki B., Murray K. S. and Youngme S. Polyhedron. 2017;126:8-16.
11. Kuriakose, Daly.: Ambili Aravindakshan, A.: Prathapachandra Kurup, M.R. Polyhedron. 2017;127:84-96.
12. Sheldrick, G.M. Acta Cryst. 2015b;C71:3-8
13. Jian-Long D, Xuan L, Tian-Li S, Chao-Ping L, Ya-Juan M, Li-Jun L. Mater Lett 2015;158:225-228.
14. Piromchom J, Wannarit N, Boonmak J, Chainok K, Pakawatchai C, Youngmea S, Inorg. Chem. Commun. 2014;44:111-113.
15. Huang Q.Y, Lin X.Y, Meng X.R. Acta. Cryst. 2016;72(6):480-484.
16. Hou Y.N, Song J.,Bai F. Y., Xing Y.H. Inorg. Chim. Acta. 2016;440:69-76.
17. Parmar B, Rachuri Y, Bisht K.K, Laiya R, Suresh E. Inorg. Chem. 2017;56:2627-2638.
18. Wang X, Zhao J, Lin H, Le Mao, Liu G, J. Coord. Chem. 2018;71:8.
19. Yan Y.T, Liu J, Yang G. P, Zhang F, Fan Y. K, Zhang W. Y, Wang Y. Y. Cryst. Eng. Comm. 2018;20:477-486.
20. Jinting G, Jinjin Y, Zhanhui T, Yaqing L, Xiaodong L, Jiankang D, Shuo W. ACS Omega. 2018;3:3045-3050.
21. Joseph W. N., Hyunjung L, Hee-Seung L, Jeseph H. R., Robert D. H. Inorg. Chem. 2014;53:9014-9026.
22. Abir El M, Cyril C, Isabelle D, Bernard T, Francoise C. Inorg. Chem. 2011;50:4029-4038.
23. Klongdee F, Boonmak J, Youngme S. Dalton. T. 2018;47:45.

Acknowledgements: The financial and all experiments equipment were supported by Department of Chemistry, Physics and Biotechnology, Faculty of Science and Technology, Thammasat University. Central Scientific Instrument Center (CSIC) of Faculty of Science and Technology, Thammasat University.

Author Index

A-aesoh Luebaesa 437
Akio Ojida 254
Akkaneewut Chabangborn 545
Amnat Phetrungnapha 95
Amornpun Sereemaspun 449
Ampapan Naknaen 120
Anant Eungwanichayapant 40, 551
Anirut Suppasombut 325
Anupan Kongbangkerd 8, 437
Apicha Maharat 342
Apichart Suksamrarn 348, 407
Apinun Limmongkon 8
Apinya Huskul 240
Apisith Suebchompoo 603
Apiwat Intiyakosat 597
Archrob Khuhapinant 178
Aroonsiri Shitangkoon 282
Asada Leelahavanichkul 184
Asmita Khaniya 126
Athit Chaiwichien 33, 50, 56
Atikorn Panya 679
Aungsana Prajaksangsiri 485
Banthot Chomsawan 332
Benjie L. Fernandez 619
Benya Nontaleerak 109
Boonchoat Paosawatyanyong 640
Boon-ek Yingyongnarongkul 336
Burapha Phajuy 564
Chainarong Tocharus 407
Chaiwat Boonpeng 82
Chaiya Prasittichai 461
Chalermchai Mitrpant 178
Chanapimon Keerathiwattanarat 150
Chanikan Polpattanakul 619
Chanisara Srimuang 647
Chanista Chansom 584
Charinee Thonthong 421
Chatchai Putson 271
Chatchai Sirithipvanich 640
Chatchawan Chaisuekul 212
Chawanakorn Kongsak 308
Chayaphon Sripannam 95
Chidkamon Thunkhamrak 295
Chiraphat Phromthong 388
Chitsanuphong Phanthian 212
Chompoonuch Warangkanagool 654
Chongdee Thammakhet-Buranachai 259
Chopaka Thongbumrer 336
Chotika Neamchey 259
Chutimon Tangaiad 157
Damratsamon Surangkul 95
David Ruffolo 635
Decha Dechtrirat 472
Depicha Jindatip 449
Dhassida Sooksawat 259, 325
Duangamol Tungasmita 619
Dusit Jit-ueakul 178
Dusit Thueman 624
Eliot Cline 40
Ersa Aurora Ria Diani 670
Gun Anantasomboon 73
Hanh Le Thi My 479
Htoo Pyei Hlaing 178
Indiah Ratna Dewi 271
Intira Tampayak 73
Itaru Hamachi 254
Iyarit Thaipisuttikul 126
Janista Thumrongtharadol 109
Janpen Tangjitjaroenkun 67
Jarichad Toosaranont 178
Jaroon Jakmunee 295
Jaruwan Kanthachan 491
Jes Kettratad 240
Jinda Sirita 332
Jintana Duangnkern 150, 157
Jintana Duang-nkern 163, 169
Jirapant Dutchaneephet 431
Jirarut Wongkongkatep 254
Jumroensri Thawonsuwan 120
Kalyarat Kaewnirat 115
Kamonwan Meesuwan 303
Kanchana Kiriyadee 25
Kanet Wongravee 412
Kanlaya Jumpatong 332
Kansri Boonpargob 82
Kantapon Suraprasit 498
Kanyamas Choocheep 194
Kanyanat Dee-ying 461
Kanyarat Kwansirikul 647
Kawinnat Buaruang 62, 229, 235
Kawinthida Moolsarn 295
Kazumichi Fujii 87
Kejvalee Pruksathorn 507, 529
Kemachart Kemavuthanon 551

Khamphe Phoungthong 582, 592
Khanobporn Tangtrakulwanich..... 20, 25
Khwannarin Khemsom 109, 150
Kiattikhun Manokruang 442
Kitiphong Khongphinitbunjong 20
Kittipat Malakit 635
Kittipong Chainok 703
Krai Meemon 33, 50, 56
Krit Tantanarat 95
Krit Won-in 431
Kritsakorn Saninjuk 163
Kuaanan Techato 592
Kua-anan Techato 582
Ladawan Thupchai 507
Luckika Panthiya 407
Mali Hunsom 507, 529
Manatchanok Pattanasing 336
Mangheny Godfrey 295
Mongkol Phaengphech 62, 82
Montakan Tamtin 33, 50, 56
Montri Choowong 498
Morakot Kaewpet 325
Mudchima Unmuang 551
Muthita Molsil 62
N. Tangaemsakul 525
N. Tantavichet 525
Naeem Hussain 592
Nakorn Niamnont 33, 50, 56
Napassorn Peasura 687
Napat Chuenangkul 529
Napida Hinchiranan 467
Narin Changklungmoa 33, 50, 56
Natavudh Townamchai 184
Nattakan Soykeabkeaw 603
Nattaya Wongyai 95
Nattha Yongwattana 254
Natthakan Iam-On 663
Natthapol Chittamart 87
Natthapong Jimpaiboon 640
Natthaya Chuaypen 348
Nattida Pankaew 135
Nattiya Hirankarn 184
Natwara Dangnordang 120
Netiya Karaket 102
Ngamnit Wongcharoen 609, 624
Nipa Khuankuab 679
Nisit Tantavichet 513
Nitisak Charoenroop 551
Nontawat Sricharoen 412
Nontivich Tandavanitj 200, 247
Nootcharee Kunkit 442
Nutthanun Khantasup 200
Onuma Piasai 62
Orawan Wanachewin 194
Paitoon Boonsong 696
Paitoon Rashatasakhon 342
Pakkapawn Prapan 635
Pakorn Varanusupakul 303
Pakwuan Wongshaya 8
Panadda Dechadilok 619
Panate Manomaivibool 551
Panchika Prangkio 381
Panita Ngamchuachit 670
Panote Thavarungkul 259
Panupun Limpachayaporn 348
Panuwat Padungros 401
Paramita Punwong 545
Parichart Onsri 472
Parichat Cummon 609
Parichat Sriwan 564
Patchara Mongkolsuk 62, 235
Patcharapon Jumsri 247
Patchararujee Ngamdee 467
Patcharin Kosuwan Jundee 564
Patsara Danwittayakul 582
Pattara Thiraphibundet 485
Pattarin Tangtanatakul 184
Pattariya Singpant 663
Patthapong Chaiseanwang 535
Pawee Klongvessa 597
Pawnprapa Pitakjakpipop 314
Peeravat Natrsanga 364
Peerawat Saejong 381
Phanupol Mongkolsiri 102
Phimchanok Jaturapiree 77
Phimpisa Phraphuchamnong 235
Phonphiphat Suwannarak 513
Phurich Boonsanit 205
Pichamon Srisawad 135
Pichayanan Srisuwan 325
Pichnaree Lalitaporn 557
Pijittra Sangthong 659
Pimonsri Mittraparp-arthorn 135
Pipat Sudying 77
Pisit Tangkijvanich 348
Pisutti Dararutana 431
Piyada Yodsoontorn 332
Piyaphat Sunthi 575
Piyaporn Phukhatmuen 393
Pongchai Dumrongrojwatthana 221

Poorichaya Somparn 184
Pornanan Kueakhai 50, 56
Pornanan Kuekai 33
Pornrat Sinchaipanit 687
Pornsan Lueangseephet 703
Pornthip Boonsri 421
Prach Sukkavee 518
Prachya Kongtawelert 194
Pranpariya Ponpakdee 401
Praput Thavornyutikarn 308
Prasert Sobhon 33, 50, 56
Premjit Arpornmaeklong 319
Proespichaya Kanatharana 259
Prompong Pienpinijtham 412
Puncharat Promsuvong 20
Punya Charusiri 584
Puttachard Hensanghong 67
Puttinan Meepowpan 456
Ratchanaporn Chokchaisiri 407
Rattachat Mongkolnavin 479
Rattanaruji Pomwised 115
Rattaphan Lamoon 178
Rawiwan Charoensup 393
Roongkan Nuisin 479
Rujirek Chaiwongsa 194
Rungnapa Noina 407
Rungnapa Tangchitcharoenkhul 67
Rungrote Nilthong 518
Saifon Nopnipa 109, 157
Sanong Ekgasit 412
Santi Tip-pyang 364
Saowanuch Tawornpruek 87
Saowapa Chotisuwan 437
Saran Panjaruang 557
Sarawut Sattayakawee 95
Sarinya Palakhachane 348
Sarunyou Chusri 115
Sasikarn Looprasertkul 449
Schradh Saenton 518
Scorn Mongkolsuk 157
Sermpong Sairiam 479
Sirichanut Thongsew 679
Sirikanya Anantasena 189
Siriphong Somprasong 359
Siriporn Riebroy Kim 679
Siritron Samosorn 421
Sisouphanh Souvongxay 564
Siwaporn Saewan 659
Songsuda Promthong 265
Srilert Chotpantarat 597
Suchada Chantrapromma 592
Suchada Muangsri 282
Sujitra Arwachananukul 663
Sukanya Mingphimai 703
Sukkaneste Tungasmita 619
Sukonmeth Jitmahantakul 584
Sunaree Saejong 184
Supakorn Boonyeun 703
Supakorn Boonyuen 319
Supanut Pairohakul 205
Supasara Ounsuk 254
Supawadee Osotprasit 33, 50, 56
Surachet Aramrak 87
Sutanan Pinmaneenopparat 221
Sutima Preeprem 135
Suvimol Soithongsuk 14
Suwimon Keeratipibul 670
Tassapon Krajangdara 240
Teerapong Jantarat 259
Tepparit Samrit 50
Tepprit Samrit 33, 56
Thanakit Kumwung 603
Thanaphat Auwattanamongkol 169
Thanapon Deekaikam 442
Thapong Teerawatananond 319
Theeranai Sangjan 663
Thitinai Gaewdang 609, 624
Thitipone Suwunwong 582, 592
Thongchai Ngamprasertwong 200, 247
Thunchanok Kawinate 498
Tittita Aksonkird 135
Torsak Luanphaisannont 381
Torsak Luanphaisarnnont 359
Torsak Luanphisarnnont 374
Tossapon Phromsatit 319
Tu Thi Phuong Nguyen 314
Tulyapruek Tawonsawatruk 254
Udomrak Meethong 229
Vasun Poengsungnoen 62
Wachira Jaengkhao 143
Walaiphan Chuwongpanich 87
Waleed Alahmad 303
Wandee Udomuksorn 189
Wanich Limwanich 456
Wannee Thepsing 254
Warabhorn Boonyarat 388
Waraluck Chaichompoo 407
Warapond Wanna 143
Watanalai Panbangred 109
Watchara Kaewsuwan 265

Watcharapon Prasitwatcharakorn 374
Weerapan Srichan..... 564
Wetchasart Polyiam 82
Wimonsiri Kaewsamer 25
Winita Punyodom..... 456
Wipark Anutrasakda..... 314
Wipawan pukumpuang.....194
Wisanu Maneerat.....25, 393
Worakamon Nudnara 545
Yuki Shirosaki 319
Yupakanit Puangwerakul 14
Yuwaporn Ketkaew 348

สมาคมวิทยาศาสตร์แห่งประเทศไทยในพระบรมราชูปถัมภ์

http://www.scisoc.or.th/stt/